CODEN: JASMAN 4966

THE JOURNAL of the Acoustical Society of America

Vol. 107, No. 2 February 2000

SOUNDINGS SECTION

GENERAL LINEAR ACOUSTICS [20]

NONLINEAR ACOUSTICS [25]

UNDERWATER SOUND [30]

(Continued)

CONTENTS—*Continued from preceding page*

ULTRASONICS, QUANTUM ACOUSTICS, AND PHYSICAL EFFECTS OF SOUND [35]

TRANSDUCTION [38]

NOISE: ITS EFFECTS AND CONTROL [50]

ARCHITECTURAL ACOUSTICS [55]

ACOUSTIC SIGNAL PROCESSING [60]

PHYSIOLOGICAL ACOUSTICS [64]

PSYCHOLOGICAL ACOUSTICS [66]

(Continued)

CONTENTS—*Continued from preceding page*

(Continued)

CONTENTS—*Continued from preceding page*

ACOUSTICS RESEARCH LETTERS ONLINE

CUMULATIVE AUTHOR INDEX

NOTES CONCERNING ARTICLE ABSTRACTS

1. The number following the abstract copyright notice is a Publisher Item Identifier (PII) code that provides a unique and concise identification of each individual published document. This PII number should be included in all document delivery requests for copies of the article.
2. PACS numbers are for subject classification and indexing. See June and December issues for detailed listing of acoustical classes and subclasses.
3. The initials in brackets following the PACS numbers are the initials of the JASA Associate Editor who accepted the paper for publication.

(Continued)

Acoustical imaging through a multiple scattering medium using a time-reversal mirror

Philippe Roux, Arnaud Derode, Aymeric Peyre, Arnaud Tourin, and Mathias Fink

Laboratoire Ondes et Acoustique, Université Paris 7, ESPCI, 10 rue Vauquelin, Paris 5
philippe.roux@espci.fr, arnaud.derode@espci.fr, arnaud.tourin@espci.fr, mathias.fink@espci.fr

Abstract: Acoustical imaging is based on the ability to focus an acoustic beam inside the zone of interest. This remains an issue through a high-order multiple scattering medium because the electronic delay lines that enable one to focus through a multiple scattering medium are *a priori* unknown. Using time-reversal principles, we show that images can be obtained through a very disordered medium. Surprisingly, the images are better than those obtained in a homogeneous medium with a classical imaging device.

PACS numbers: 43-35.Bf, 43-60.Gk, 43-60.Pt

Introduction

The use of ultrasound for medical imaging dates back more than 50 years and has matured in the last two decades to the level of routine use in hospitals.[1-2] The last developed techniques use ultrasonic arrays. An image is classically constructed using a repetitive procedure. First, a beam is focused at a given point through the zone of interest using adapted delay lines, and the array records the back-scattered field; second, the brightness of the image at the focus is the correlation coefficient between the back-scattered field and the emitted delay lines; last, the delay lines are changed to focus at another point, thus closing the loop. To reduce the run time and obtain images in real time, only a few delay lines are used, and it is assumed that the time of arrival of the back-scattered echoes corresponds to depth via the sound velocity. In a homogeneous medium, the quality of the image classically depends on the size of the focal spot, which is itself defined by the array aperture according to diffraction laws. Roughly speaking, the larger the array, the smaller the focal spot and the better the image. However, this procedure no longer works when a multiple scattering medium is placed between the array and the treatment volume. First, delay lines do not permit a focus through multiple scattering; second, the time of arrival of the back-scattered echoes no longer corresponds to depth. Thus, acoustical imaging through a multiple scattering medium remains an issue.

The aim of this study is to show that images can be obtained through a multiple scattering medium using time-reversal principles. More precisely, we compare the quality of images obtained with the same ultrasonic array in two configurations: in the first case, the phantom to be imaged is placed in water in front of the array; in the second case, a multiple scattering medium is placed between the array and the phantom. It appears that the detection of scatterers is better through multiple scattering than in water.

This study is divided into three parts. The first section deals with time-reversal principles and their application to ultrasonic focusing through a multiple scattering medium. In the second section, we describe the procedure used to construct the image of a phantom through a high-order multiple scattering medium. Finally, we compare in the final section the quality of images obtained with the same array in a homogeneous medium and through a multiple scattering medium.

Time-reversal focusing

A classic time-reversal experiment consists of :

1. transmitting a short pulse from a source;
2. recording the acoustic field on an array of transducers (the time-reversal mirror or TRM) after refraction and/or scattering through the propagation medium;
3. time-reversing and retransmitting the time-reversed field through the same propagation medium;

Because of the reversibility of acoustic propagation in a motion-less and loss-less medium, the time-reversed field temporally and spatially focuses back onto the source whatever the heterogeneity of the medium. Since the early 1990s, experimental demonstrations of time-reversal focusing have been achieved through various media, such as ultrasonic or underwater acoustic wave guides, human skull, metallic plates and high-order multiple scattering media.[3-6] It has been shown that the larger the heterogeneities of the propagation medium, the smaller the focal spot after time-reversal. Actually, after time-reversal, the heterogeneities of the medium act as a set of secondary sources, which serve to increase the wave number diversity, thereby decreasing the size of the focal spot. For example, TRMs achieve good focusing in wave guides.[3-4] However, the TRM must then span the whole wave guide section to correctly sample the wave number diversity, and the optimal size of the guide[3] may prevent practical applications to ultrasonic imaging. Therefore, in this work, we prefer to use a multiscattering medium with which a part of the acoustic field is naturally redirected with wide-angle wave numbers toward a small TRM.

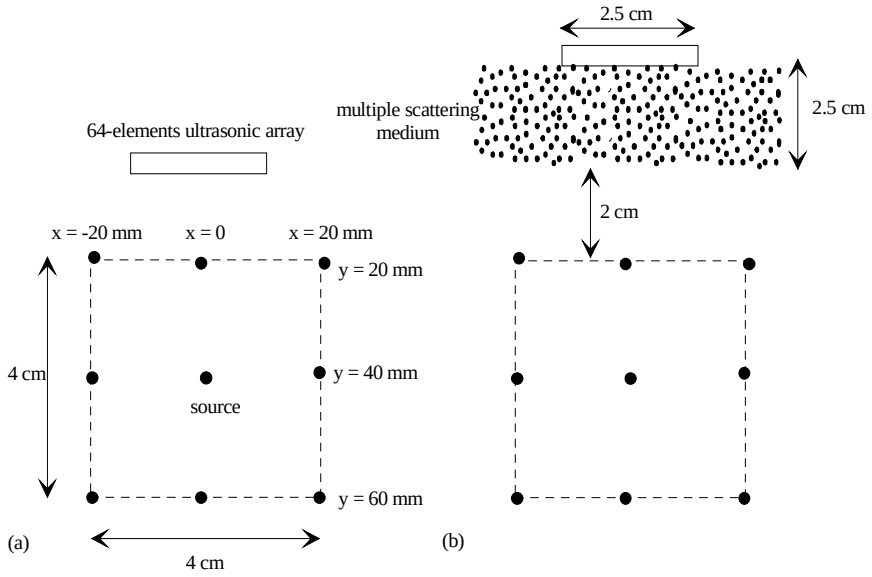

Fig. 1. Schematic of the experimental set-up: (a) the homogeneous case; (b) the multiple scattering case. The nine positions of the source correspond to the results of Figs. 2 and 3.

In the following, we compare the focal spot after time-reversal in two configurations. In the first case, a point source is placed in the water in front of a 64-elements linear array (Fig. 1a). Each element width is 0.4 mm with central frequency 3.3 MHz (wavelength ~ 0.45 mm). The total aperture of the array is 25 mm. Both the source and the array are reversible devices: they work as transmitters as well as receivers.

In the second case, a high-order multiple scattering medium is placed between the source and the array (Fig. 1b). The multiple scattering medium is a random set of parallel steel rods.[7] The rods are 0.8 mm in diameter, approximately 10 cm in length, and the average distance between two rods is 2.3 mm. Since the source and the array elements are 12 mm in length, which is significantly larger than the wavelength and the width of each element, the set-up can be considered two-dimensional in the xy plane. The rod concentration is ~18

rods/cm^2, the multiple scattering region is 2.5cm x 5cm, and its front face is stuck on the array.

A time-reversal experiment is achieved following stages 1-3 described above. After stage 3, the maximum of the time-reversed field is recorded at and around the initial point source now using the source as a receiver. Figures 2 and 3 show the focal spots obtained at nine different positions (see Fig. 1) of the point source relative to the array in the two studied configurations. Two points are important. First, the focal spot is more concentrated when the multiple scattering medium is present between the source and the array; the focal spot is smaller and the average maximum is 5 times larger. Second, the maximum of the time-reversed field is more stable over the nine focal spots. The average maximum has a 18% standard deviation in the multiple scattering case whereas it reaches 48% in the case of a homogeneous medium. These results are important to ultrasonic imaging. Indeed, the quality of an image depends on the size of the focal spot as well as the variation of amplitude of the focused field in the region of interest.

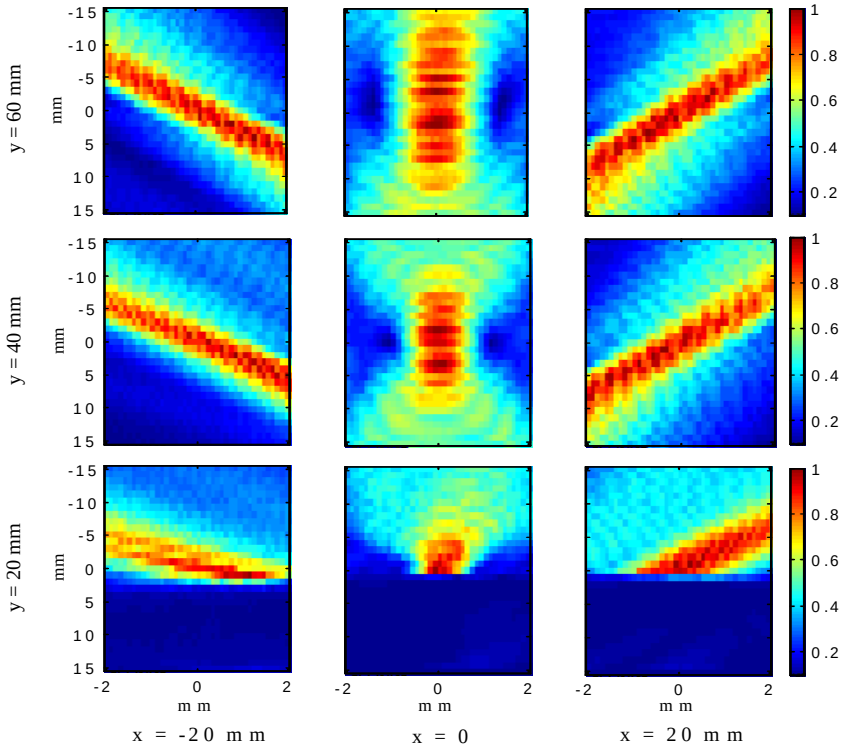

Fig. 2. Focal spots after time-reversal in a homogeneous medium for 9 positions of the source. It was not possible to scan the pressure field at less than 20 mm from the array. Each picture is normalized by its own maximum. The standard deviation between the maxima is equal to 48% of the average maximum.

Ultrasonic imaging through multiple scattering

Usually, acoustical imaging is performed with arrays. Here, we define the ensemble “array plus multiple scattering medium” as a new imaging device. The quality of an imaging system lies in its ability to focus an acoustic wave at any point inside the region of interest. We have shown that the focusing quality of an array is improved after time-reversal when the propagation medium is a multiple scattering medium. This requires knowledge of the complicated electronic signals that focus back onto the source after time-reversal from the array. This first point differs significantly from a classic imaging system for which focusing is performed with simple electric delay lines. However, this set of signals can be recorded only

once when the ensemble “array plus multiple scattering medium” is built. Indeed, these signals depend only on the geometry of the system and are completely independent of the medium to be imaged. A second point is also important: with a classic imaging system, the back-scattered energy comes only from the medium to be imaged. In our case, the multiple scattering medium will back-scatter more energy than the treatment volume. This acoustic field has then to be subtracted from the total back-scattered field before the construction of the image.

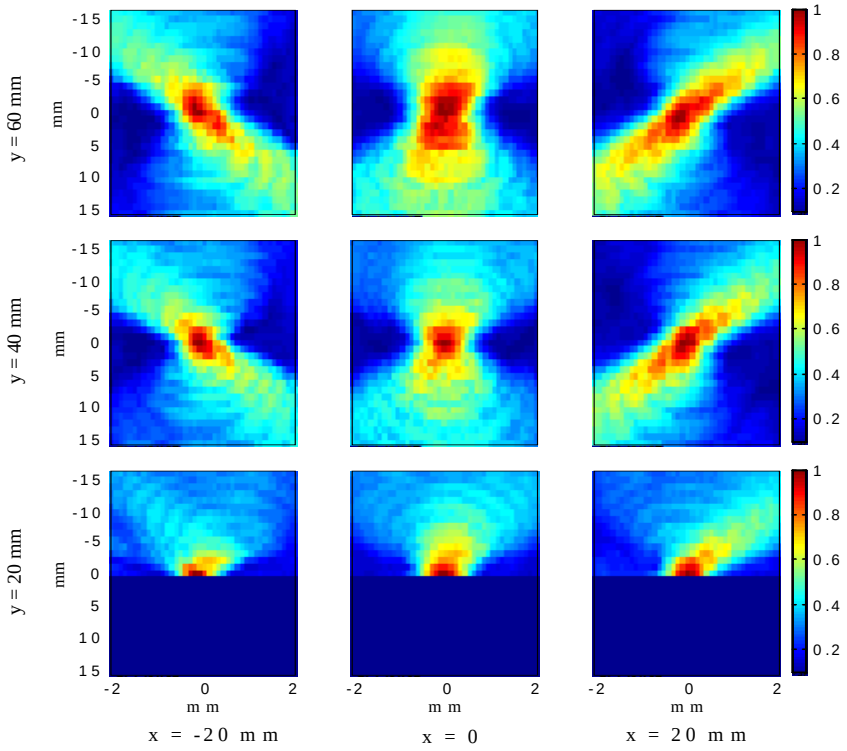

Fig. 3. Focal spots after time-reversal through a multiscattering medium for 9 positions of the source. For consistency with Fig. 2, the pressure field has not been scanned at less than 20 mm from the multiple scattering medium. Each picture is normalized by its own maximum. The standard deviation between the maxima is equal to 18% of the average maximum.

As a consequence, the procedure to create an image through a multiple scattering medium is the following :

1. We define the size and the resolution of the future image. We place a point source at the center of each pixel and, for each transducer of the array, we record the electronic signals which will allow us to focus back onto the source after time-reversal;
2. For each pixel, we transmit the previously-recorded time-reversed field and record the pressure field back-scattered by the multiple scattering medium alone. This is called the reference field;

Stages 1 and 2 are performed without the medium to be imaged and done only once when the system “array plus multiple scattering medium” is built. We now place the “array plus multiple scattering medium” in front of the region of interest.

3. For each pixel, we transmit the electronic time-reversed codes from the array and record the back-scattered field;
4. For each pixel, we subtract the reference field from the back-scattered field and correlate the difference with the electronic signal recorded during stage 1. The correlation coefficient corresponds to the brightness of the image for this pixel.

Experimental results

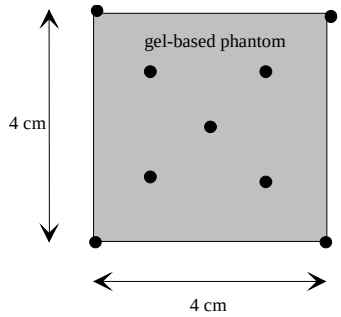

Fig. 4. Schematic of the phantom, made of 9 rods included in a gel-based phantom.

We have tested this algorithm on a medium made of 9 rods placed in a gel-based phantom. The rods are identical to the ones that compose the multiscattering medium, and the medium is also considered two-dimensional. Four rods were placed at the corners of a 4 cm square, and the other 5 were arranged regularly on the diagonal of the square (Fig. 4). The two-dimensional imaging device is placed in the same plane as the two-dimensional medium at two centimeters from one side of the square (see Fig. 1). Everything is immersed in a water bath. The imaging device is either the 2.5-cm 64-elements array described above alone or the system "array plus multiple scattering medium". In the latter case, the phantom is placed at two centimeters from the multi scattering medium (see Fig. 1b).

Considering the size of the phantom, we choose to image a 50mm x 60mm area sampled by 51 x 21 pixels (stage 1 is performed with a 1-mm resolution along the x axis and a 3-mm resolution along the y-axis). Figures 5 and 6 show the images of the phantom obtained with the two different imaging devices. In the case of the multiscattering imaging system, the phantom has not been well centered on the predefined image area, which explains why the extreme left side of the phantom misses the image. As expected, we get a better detection of the phantom scatterers with the multiscattering imaging system: the axial and lateral resolutions are better, and each rod appears with the same strength. On the other hand, the noise level is 10-dB higher. This is due to the subtraction between the total and the reference back-scattered field done imperfectly during our experiment. Actually, some rods of the multiscattering medium have moved slightly between the recording of the reference field (stage 2) and the acquisition of the total back-scattered field (stage 3). More generally, the noise level is due to small heterogeneities of the phantom and should be comparable to the noise observed with a classic imaging device.

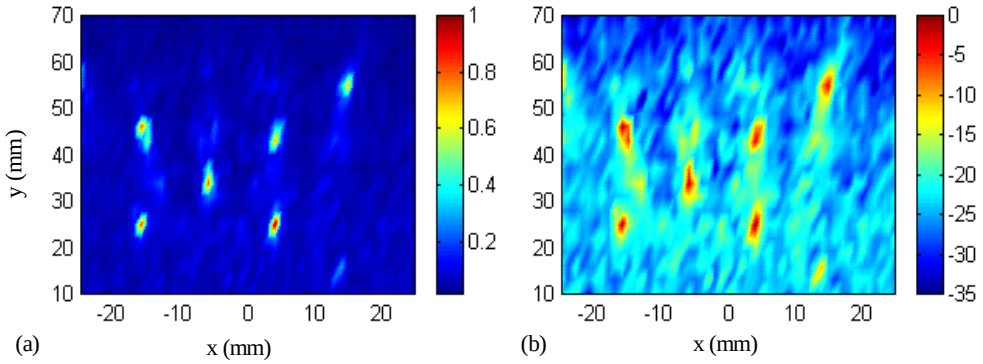

Fig. 5. Image of the phantom obtained with the multiscattering imaging device:
(a) in a linear scale; (b) in decibel.

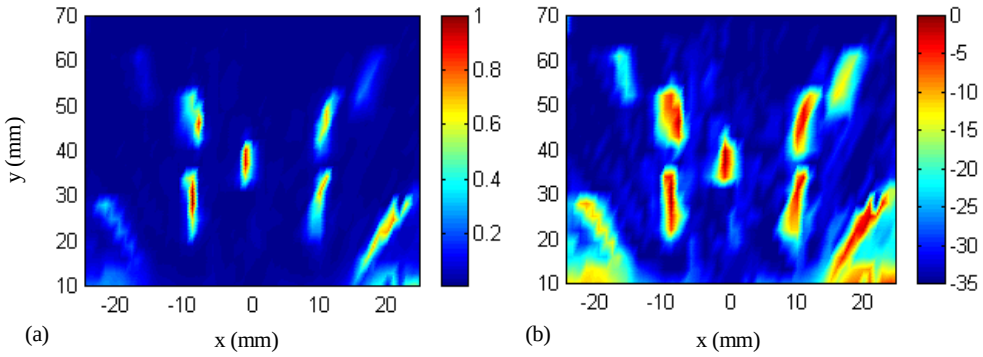

Fig. 6. Image of the phantom obtained with a classic imaging device:
(a) in a linear scale; (b) in decibel.

Finally, an image of a phantom is feasible as long as the low-amplitude signal (A) received from a phantom scatterer is measurable compared to the high-amplitude signal (B) backscattered by the multiple scattering medium itself. By measurable, we mean that the phantom signal, which is the subtraction between the total field (stage 3) and the reference field (stage 2) is higher than the electronic noise of the experiment. In our case, we have $20\log_{10}(B/A) \approx 20\,\mathrm{dB}$ which is far above the noise threshold of our transducers. Another limitation of the system is that an image cannot be obtained in real time with the multi-scattering imaging device. The time cost to transmit the electronic signals, record the back-scattered field and correlate it with the electronic codes is relatively heavy (2 hours for 51 x 21=1071 pixels on a Pentium 2 computer). On the other hand, this imaging device has many advantages besides the quality of the images. We study, for example, the possibility of reducing the number of elements in the array without degrading the quality of the image.

In conclusion, we have shown that time reversal is a solution for performing ultrasonic imaging through a multiple scattering medium. The resolution of the image of a phantom is better than the one obtained in a homogeneous medium. In future work, we will carefully investigate the influence of the number of array elements and the size of the multiscattering medium on the quality of the images (noise level, axial and lateral resolution) obtained with this new ultrasonic imaging device.

References and links

[1] J.J. Wild, “The use of ultrasonic pulses for the measurement of biologic tissues and the detection of tissue density changes,” Surgery **27**, 183-188 (1950).

[2] J.A. Jensen, “Estimation of blood Velocities using Ultrasound,” Cambridge Univ. Press (1996).

[3] P. Roux, B. Roman, and M. Fink, “Time-reversal in an ultrasonic waveguide,” Appl. Phys. Lett. **70** (14), 1811-1813 (1997).

[4] W.A. Kuperman, W.S. Hodgkiss, H.C. Song, T. Akal, C. Ferla, and D. Jackson, “Phase conjugation in the ocean: experimental demonstration of an acoustic time-reversal mirror,” J. Acoust. Soc. Am. **103**, 25-40 (1998).

[5] J.L. Thomas and M. Fink, “Ultrasonic beam focusing through tissue inhomogeneities with a time reversal mirror: Application to transkull therapy,” IEEE Trans. Ultrason. Ferr. Freq. Cont. **43** (6), 1122-1129 (1996).

[6] R.K. Ing and M. Fink, “Self-focusing and time recompression of Lamb waves using a time reversal mirror,” Ultrasonics **36**, 179-186 (1998).

[7] A. Derode, P. Roux, and M. Fink, “Robust Acoustic time reversal with high order multiple scattering,” Physical Review Letters **75** (23), 4206-4209 (1995).

[8] To see a picture of the experimental set up and get more information about the work done in Paris about ultrasonic time-reversal, consult the laboratory web site : http://www.loa.espci.fr

SOUNDINGS

Section Editor: Richard Stern

This front section of the *Journal* includes acoustical news, views, reviews, and general tutorial or selected research articles chosen for wide acoustical interest and written for broad acoustical readership.

ACOUSTICAL NEWS—USA

Elaine Moran
Acoustical Society of America, Suite 1NO1, 2 Huntington Quadrangle, Melville, NY 11747-4502

Editor's Note: *Readers of this Journal are asked to submit news items on awards, appointments, and other activities about themselves or their colleagues. Deadline dates for news items and notices are 2 months prior to publication.*

Call for Business Meeting of the Society

Notice. A business meeting of the Society will be held starting at 3:30 p.m. on Thursday, 1 June 2000 at the Westin Peachtree Plaza Hotel in Atlanta, Georgia. All Fellows and Members are urged to attend for the purpose of voting on proposed amendments to Articles VI and VIII, and part of Article IX of the Bylaws of the Society.

Rationale for proposed Bylaw amendments. Articles VI and VIII of the Bylaws specify the composition of the Executive and Technical Councils respectively, and the voting status of the members of each Council; Article IX concerns the election of Officers and Executive Council, and in Section 1 specifies the terms of office.

In recent years the Society has strengthened and broadened its technical activities by forming Technical Specialty Groups and an Interdisciplinary Technical Group. To coordinate technical activity it is necessary for the chairs of these technical groups to attend meetings of the Technical Council, and they have until now attended as nonvoting visitors. Also, on a trial basis, the immediate past Vice President (being the previous chair of the Technical Council) has attended meetings of the Technical Council for one additional year to strengthen the continuity of the Society's technical activities. The purpose of the proposed amendments to Article VIII is to formally recognize the position of the immediate past Vice President and the chairs of technical groups as nonvoting members of the Technical Council.

The purpose of the proposed amendments to Articles VI and IX of the Bylaws is to add the immediate past Vice President as a voting member of the Executive Council for one year. The result of the proposed amendments to these two Articles is that the person elected as Vice President Elect will serve and vote on Executive Council for three years (one year as Vice President Elect, one year as Vice President, and one year as immediate past Vice President). This corrects the anomaly that the Vice President Elect currently serves for a total of only two years on the Executive Council, whereas the President-Elect and all other elected members of the Executive Council serve and vote for three years.

Motions to be presented for vote at the business meeting. Three motions to ammend Articles VI, VIII and part of IX of the Bylaws, respectively, will be presented for vote during the business meeting. A proposed ammendment may be adopted by a two-thirds vote of the Members and Fellows present and voting in person. Changes to the wording of Articles VI, VIII and part of IX are shown below in bold type and were approved by the Executive Council on 5 November 1999.

Motion 1. To approve the following revised version of Article VI:

> Article VI. Executive Council
> The affairs of the Society shall be managed by an Executive Council which shall consist of the President, the President-Elect, the Vice President, the Vice President-Elect, the Treasurer, the Editor-in-Chief, the Executive Director, the Standards Director, the **immediate past** President **and immediate past Vice President**, and six members elected from the Members and Fellows of the Society. The Treasurer, the Editor-in-Chief, the Executive Director, and the Standards Director shall be members of the Executive Council without vote.

Motion 2. To approve the following revised version of Article VIII:

> Article VIII. Technical Council
> The Technical Council shall consist of the **Chairs** of the Technical Committees, the Vice President, the Vice President-Elect, and as *ex-officio* members without vote, **the immediate past Vice President, the Chairs of technical groups appointed by the President, and** the other officers of the Society. The Technical Council shall be responsible for coordinating the policies and activities of the Technical Committees **and technical groups**, and advising the Executive Council by formal resolutions on matters of policy concerning technical considerations. The Technical Council shall be presided over by the Vice President, or in his or her absence, by the Vice President-Elect.

Motion 3. To approve the following revised version of the first two paragraphs of Article IX, Section 1:

> Article IX. Election of Officers and Executive Council
>
> Section 1. Terms of office
> The term of office of the President shall be one year and, as **immediate** past President, he or she shall continue as a member of the Executive Council for an additional year. The President-Elect shall be elected for a term of one year and, at the expiration of his or her term, shall succeed automatically to the office of President.
> The term of office of the Vice President shall be one year **and, as immediate past Vice President, he or she shall continue as a member of the Executive Council for an additional year**. The Vice President-Elect shall be elected for a term of one year and, at the expiration of his or her term, shall succeed automatically to the office of Vice President.

Charles Schmid
Executive Director

Regional Chapter News

Madras, India: At its meeting on 19 and 20 August, the Madras-India Regional Chapter awarded two student paper awards and six science and engineering fair awards. Binu Jose received a best student paper award in Bioacoustics (see Fig. 1) and B. Prakash received a best student paper award

FIG. 1. Chapter President C. P. Vendhan (r) and Chapter Representative H. S. Paul (c) present the Best Student Paper Award in Bioacoustics to Binu Jose (l).

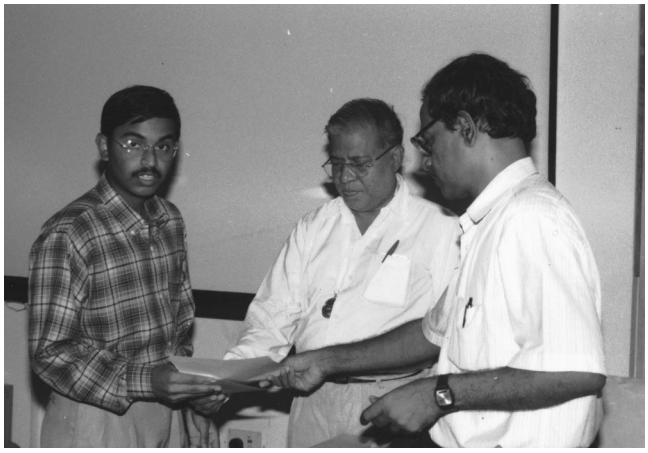

FIG. 2. Chapter President C. P. Vendhan (r) and Chapter Representative H. S. Paul (c) present the Best Student Paper Award in Speech Communication to B. Prakash (l).

in Speech Communication (see Fig. 2).

The following people received science and engineering fair awards: S. Gayatri (see Fig. 3), First; N. Prajwal, Second; Arun Kumaran, S. V. Krishnan, C. Susmita, Chandrasekar.

FIG. 3. Chapter President C. P. Vendhan (r) and Chapter Representative H. S. Paul (c) present the first place science and engineering fair award to S. Gayatri (l).

The General body elected the following officers for 2000–2001: Vice President: S. K. Tomar, Member-at-Large: B. K. Kuthiala.

USA Meetings Calendar

Listed below is a summary of meetings related to acoustics to be held in the U.S. in the near future. The month/year notation refers to the issue in which a complete meeting announcement appeared.

2000

17–19 Feb.	National Hearing Conservation Association (NHCA) 25th Annual Conference, Denver, CO [NHCA, 9101 E. Kenyon Ave., Suite 3000, Denver, CO 80327, Tel.: 303-224-9022; Fax: 303-770-1812; E-mail: nhca@gwami.com; WWW: www.hearingconservation.org].
6–9 March	Society of Automotive Engineers Congress, Detroit, MI [SAE Headquarters, 400 Commonwealth Dr., Warrendale, PA 15096-0001; Fax: 724-776-1830; E-mail: congress2000@sae.org].
17–19 May	ASNE Day 2000, Arlington, VA [Andrea Zari, Meetings Department, American Society of Naval Engineers, 1452 Duke St., Alexandria, VA 22314-3458; Tel.: 703-836-6727; Fax: 703-836-7491; E-mail: azari@navalengineers.org].
30 May–3 June	139th Meeting of the Acoustical Society of America, Atlanta, GA [Acoustical Society of America, Suite 1NO1, 2 Huntington Quadrangle, Melville, NY 11747-4502. Tel.: 516-576-2360; Fax: 516-576-2377; E-mail: asa@aip.org; WWW: asa.aip.org].
13–16 July	ClarinetFest 2000, Norman, OK [Dr. Keith Koons, Music Dept., Univ. of Central Florida, P.O. Box 161354, Orlando, FL 32816-1354, Tel.: 407-823-5116; E-mail: kkoons@pegasus.cc.ucf.edu].
4–8 December	Joint Meeting: 140th Meeting of the Acoustical Society of America/Noise Con 2000, Newport Beach, CA [Acoustical Society of America, Suite 1NO1, 2 Huntington Quadrangle, Melville, NY 11747-4502. Tel.: 516-576-2360; Fax: 516-576-2377; E-mail: asa@aip.org; WWW: asa.aip.org].

2001

30 April–3 May	2001 SAE Noise & Vibration Conference & Exposition, Traverse City, MI [Patti Kreh, SAE Int'l, 755 W. Big Beaver Rd., Suite 1600, Troy, MI 48084, Tel.: 248-273-2474; Fax: 248-273-2494; E-mail: pkreh@sae.org]. Deadline for submitting abstracts: 14 July 2000.

ACOUSTICAL NEWS—INTERNATIONAL

Walter G. Mayer
Physics Department, Georgetown University, Washington, DC 20057

Canadian Audiology Centre to be created

It was recently announced that a National Centre for Audiology (NCA) will be created at the University of Western Ontario. The center will provide an environment in which to expand knowledge of hearing functions and problems, the needs of people with hearing impairment, and methods to assist persons with hearing loss. The new establishment is expected to assume a national leadership role in the education of audiologists and audio engineers and other qualified personnel. Over the next few years the University of Western Ontario will be adding faculty in key areas of the discipline, educational programs will be expanded and revised, and research programs will be strengthened. Funding will come from various private and public sources who will contribute more than $3 million for the purchase of equipment and space. More information on the NCA is available by contacting kieffer@audio.hhcru.uwo.ca
(Based on a report in Canadian Acoustics/Acoustique Canadienne, vol. 27, 1999)

Papers published in JASJ(E)

A listing of Invited Papers and Regular Papers appearing in the latest issue of the English language version of the *Journal of the Acoustical Society of Japan*, JASJ(E), was published for the first time in the January 1995 issue of the Journal. This listing is continued below.

The September issue of JASJ(E), Vol. 20, No. 5 (1999) contains the following contributions:

A. Hussain, S. Asghar, and T. Hayat, ''The impulse response of an acoustic wave from coupling of absorbing elastic plates''
Z. Yaohua and L. Yuwei, ''The study of prosodic adjustment in Chinese speech synthesis''
Y. Iwaya, Y. Suzuki, M. Sakata, and T. Sone, ''Active control of vibration intensity flow in a beam in the far-field''
I. Al-harthy and A. Tamura, ''Sound environment evaluation and categorization of audible sounds—The first survey of the human response to the sound environment in Muscat City (Oman)''
G. Remijn, G. vander Meulen, G. ten Hoopen, Y. Nakajima, Y. Komori, and T. Sasaki, ''On the robustness of time-shrinking''

International Meetings Calendar

Below are announcements of meetings to be held abroad. Entries preceded by an * are new or updated listings with full contact addresses given in parentheses. Month/year listings following other entries refer to meeting announcements, with full contact addresses, which were published in previous issues of the *Journal*.

March 2000

01–02 (New venue) **Measuring Noise Outdoors**, Bedford, UK. (Fax: +44 1727 850 553; e-mail: ioa@ioa.org.uk) *8/99*

15–17 **Acoustical Society of Japan Spring Meeting**, Tokyo. (Fax: +81 3 3379 1456; e-mail: kym05145@nifty.ne.jp) *8/99*

19–22 **25th International Acoustical Imaging Symposium**, Bristol. (Web: www.bris.ac.uk/epts/medphys) *10/99*

20–24 **Meeting of the German Acoustical Society (DAGA)**, Oldenburg. (Fax: +49 441 798 3698; e-mail: dega@aku.physik.uni-oldenburg.de) *10/98*

April 2000

3–4 **Structural Acoustics 2000**, Zakopane, Poland. (Fax: +48 12 423 3163; Web: www.cyf-kr.edu.pl/ghpanusz) *8/99*

May 2000

17–19 **9th International Meeting on Low-Frequency Noise and Vibration**, Aalborg. (Fax: +44 1277 223 453) *6/99*

23–26 **Russian Acoustical Society Meeting**, Moscow. (Fax: +7 095 126 8411; e-mail: ras@akin.ru) *10/99*

23–26 ***6th International Conference on Tactil Aids, Hearing Aids and Cochlear Implants**, Exeter, UK. (I. Summers, School of Physics, University of Exeter, EX4 4QL, UK; Fax: +44 1392 264111; Web: newton.ex.ac.uk/medphys/pages/isasc.html)

24–26 **Joint International Symposium on Noise Control & Acoustics for Educational Buildings** (24–25 May) and **5th Turkish National Congress on Acoustics** (25–26 May), Istanbul. (Fax: +90 212 261 0549; Web: www.takder.org) *10/99*

June 2000

5–9 **International Conference on Acoustics, Speech, and Signal Processing (ICASSP-2000)**, Istanbul. (Fax: +1 410 455 3969; Web: icassp2000.sdsu.edu) *6/99*

6–9 **5th International Symposium on Transport Noise and Vibration**, St. Petersburg. (Fax: +7 812 127 9323; e-mail: noise@mail.rcom.ru) *6/99*

14–17 **IUTAM Symposium on Mechanical Waves for Composite Structures Characterization**, Chania. (Fax: +30 821 37438; Web: www.tuc.gr/iutam) *10/99*

July 2000

4–7 **7th International Congress on Sound and Vibration**, Garmisch-Partenkirchen. (Fax: +49 531 295 2320; Web: www.iiav.org/icsv7.html) *12/98*

9–13 **19th International Congress on Education of the Deaf & 7th Asia-Pacific Congress on Deafness**, Sydney, Australia. (ICED 2000 Secretariat, GPO Box 128, Sydney, NSW 2001 Australia; Fax: +61 2 9262 3135; Web: www.iced2000.com)

10–13 **5th European Conference on Underwater Acoustics**, Lyon. (Fax: +33 4 72 44 80 74; Web: www.ecua2000.cpe.fr) *12/99*

August 2000

28–30 ***INTER-NOISE 2000**, Nice. (Fax: +33 1 47 88 90 60; *New Web: internoise2000.loa.espci.fr) *6/99*

31–2 **International Conference on Noise & Vibration Pre-Design and Characterization Using Energy Methods (NOVEM)**, Lyon. (Fax: +33 4 72 43 87 12; Web: www.insa-lyon.fr/laboratoires/lva.html) *6/99*

September 2000

3–6 **5th French Congress on Acoustics—Joint Meeting of the Swiss and French Acoustical Societies**, Lausanne. (Fax: +41 216 93 26 73) *4/99*

13–15 **International Conference on Noise and Vibration Engineering (ISMA 25)**, Leuven. (Fax: +32 16 32 24 82; e-mail: lieve.notre@mech.kuleuven.ac.be) *12/99*

17–21 **Acoustical Society of Lithuania 1st International Conference**, Vilnius. (Fax: +370 2 223 451; e-mail: daumantas.ciblys@ff.vu.lt) *8/99*

October 2000

3–5 **WESTPRAC VII**, Kumamoto. (Fax: +81 96 342 3630; Web: cogni.eecs.kumamoto-u.ac.jp/others/westprac7) *6/98*

 0001-4966/2000/107(2)/677/2/$17.00

3–6 **EUROMECH Colloquium on Elastic Waves in NDT**, Prague. (Fax: +420 2 858 4695; e-mail: ok@bivoj.it.cas.cz) *10/99*

12–14 ***International Conference on Newborn Hearing Screening**, Milan, Italy. (F. Grandori, Medical Engineering, CNR, Piazza Leonardo da Vinci 32, 20133 Milan, Italy; Fax: +39 2 23993367/.60; Web: www.biomed.polimi.it/nh2000)

16–18 **2nd Iberoamerican Congress on Acoustics, 31st National Meeting of the Spanish Acoustical Society, and EAA Symposium**, Madrid. (Fax: +34 91 411 7651; e-mail: ssantiago@fresno.csic.es) *12/98*

16–20 **6th International Conference on Spoken Language Processing**, Beijing. (Fax: +86 10 6256 9079; Web: www.icslp2000.org) *10/98*

August 2001

28–30 **INTER-NOISE 2001**, The Hague. (Web: internoise2001.tudelft.nl) *6/99*

September 2001

2–7 **17th International Congress on Acoustics (ICA)**, Rome. (Fax: +39 6 4424 0183; Web: www.uniromal.it/energ/ica.html) *10/98*

10–13 **International Symposium on Musical Acoustics (ISMA 2001)**, Perugia. (Fax: +39 75 577 2255; e-mail: perusia@classico.it) *10/99*

October 2001

17–19 **32nd Meeting of the Spanish Acoustical Society**, La Rioja. (Fax: +34 91 411 76 51; Web: www.ia.csic.es/sea/index.html) *10/99*

September 2002

16–21 ***Forum Acusticum 2002 (Joint EAA-SEA-ASJ Meeting)**, Sevilla, Spain. (Spanish Acoustical Society, 144 Serrano, 28006 Madrid, Spain; Fax: +34 91 411 7651; Web: www.cica.es/aliens/forum2002)

OBITUARIES

Daniel William Martin • 1918–1999

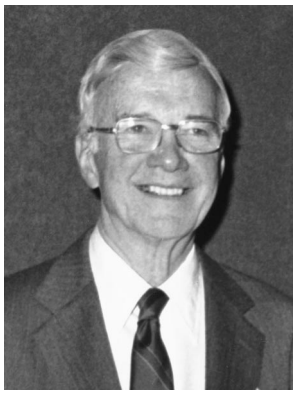

Daniel William Martin, Fellow of the Acoustical Society of America (ASA) and of the Audio Engineering Society, died in Cincinnati on January 7, 1999. At the time he was the editor in chief of *The Journal of the Acoustical Society of America* (JASA), a position that he had held with distinction since 1985.

Dan Martin was born in Georgetown, Kentucky in 1918 and later moved to Harbor Springs, Michigan where he was class salutatorian with his high school class of 1934. Following undergraduate study in physics and mathematics at Georgetown College he received his A. B., summa cum laude in 1937. He pursued graduate studies in the Physics Department at the University of Illinois receiving his MS in 1939. Subsequently he did his doctoral work at Illinois under the direction of the noted acoustician Floyd Watson. Watson was actually the first editor of JASA as well as one of the Society's founding members and its sixth President. Dan was fond of telling his ASA colleagues that it was Professor Watson who first sparked his lifelong love affair with acoustics and in the affairs of the Society. For his thesis work Dan studied brass musical instruments. He did a stroboscopic analysis of the vibrations of the player's lips and made anechoic measurements of the radiation patterns for the brass family.

In 1940 he joined the Acoustical Society, and a year later married Martha E. Parker, a high school teacher at the time. That same year he began to work for the Radio Corporation of America (RCA) on acoustical aspects of military communications, particularly on the development of throat microphones, for which he received the first of his 26 U.S. Patents. Dan continued working in various RCA groups in Indianapolis and later in Camden, NJ through the WWII period and immediately afterward. In 1949 he joined the Baldwin Piano Company (later the Baldwin Piano and Organ Company) which allowed him to continue to pursue his favorite topic, musical acoustics. In 1957 he became the director of research at Baldwin, a position that he held until his nominal retirement in 1983. While at Baldwin Dan did extensive research on the decay of piano tones, tone color in electronic organs, musical scales, and the effects of room environments on piano and organ sounds. As part of his work at Baldwin, Dan reviewed acoustical patents. In 1951 he joined the team of patent reviewers for JASA, and his reviews regularly appeared in the pages of that journal for the next 48 years. He served as JASA's Associate Editor for Patent Reviews and in a similar capacity for the *Journal of the Audio Engineering Society*. This period of time comprehended the explosive development of electronic and electroacoustic musical instruments, and in the end Dan reviewed nearly 4000 patents.

Dan's career was notable for service to scientific and technical organizations. He was Chairman of the Institute of Radio Engineers (later the Institute of Electrical and Electronics Engineers) Professional Group on Audio (1955–57), President of the Audio Engineering Society (1964–65), and President of the Acoustical Society of America (1984–85). Few people have served the Acoustical Society as long and as well as Dan. He served on innumerable committees and was a member of the Executive Council (1957–60). He chaired two Cincinnati meetings, 1961 and 1983. He played a continuing role in the development of acoustical standards, and received the Society's Distinguished Service Citation in 1989. Dan was one of the Society members who regularly sang in barbershop quartets at Society meetings—''barbershop harmonies'' were sung at his funeral.

In 1983, following retirement from the Baldwin Piano and Organ Company, Dan began in earnest a second career as an independent acoustical consultant. Already a licensed Professional Engineer in the State of Ohio, he opened an office in Cincinnati offering professional services in acoustics to the public and, at the urging of his ASA consulting colleagues joined, as a member firm, the National Council of Acoustical Consultants.

Dan had actually been introduced to acoustical consulting and, more particularly, to consulting in architectural acoustics during his graduate studies at the University of Illinois (1937–41). He assisted his mentor, Floyd Watson, in teaching classes in architectural acoustics at a time when few such courses were available at Schools of Architecture despite the efforts of such pioneers as Wallace and Paul Sabine at Harvard, as well as at the new Riverbank Acoustical Laboratory, and Vern Knudsen at the University of California at Los Angeles. Dan assisted Dr. Watson in acoustical testing at the Purdue Music Hall, the Indianapolis Coliseum, and the Indiana University Auditorium among other assignments on which Dr. Watson served as consultant.

From 1966 through 1970, Associate Professor Martin taught courses in architectural acoustics at the University of Cincinnati's College of Design, Art and Architecture supplementing his long service in teaching courses in music acoustics and in the psychology of music in the University's College-Conservatory of Music. Good teachers generally make good consultants and, indeed, Dan Martin was a prolific and busy consultant as attested to by the number of repeat clients in his project files. In all, his consulting files list over 500 projects including schools, worship spaces, auditoriums, theaters, broadcast studios, and practically every other building type. That total excludes the hundreds of *pro bono* consultations given to churches and other organizations of modest means.

During his many years at Baldwin he served as ''in-house'' consultant to the research and product applications staff on all matters acoustical. Likewise, earlier during his years on various military related research assignments at RCA (1941–49), Dan did part-time consulting on hundreds of applications of sound amplification and recording equipment in motion picture theaters and auditoriums, as well as in broadcast and recording studios.

One of Dan's most cherished publications was one he authored in 1986 as a consultant to his former employer Baldwin entitled ''Providing for Sounds of Worship.'' This concise, comprehensive and highly readable advice to organizations considering building new or renovating old worship spaces is still appropriate today. Dan's introductory promise in the brochure ''...this is intended to help non-technical people understand more clearly the effects of both room acoustics and electroacoustics (audio) upon the worship experience...'' is still more than fulfilled in the brochure, as it apparently was for hundreds of Dan's consulting clients over the years. The Society's Technical Committee on Architectural Acoustics, whose regular meetings along with those of the Musical Acoustics Committee Dan rarely missed, has recommended that ''Providing for Sounds of Music'' be reprinted and made available through the Society's books program ...a fitting legacy to future architectural and music acousticians as well as future builders of spaces for worship.

Another legacy Dan Martin leaves our Society is its continuing and growing interest in encouraging younger and promising new members of the Acoustical Society. Dan, always conscious of the encouragement he received from his early mentor Professor Watson and others during the formative years of the Society, was a strong supporter and promoter of the new member receptions and other such activities that abound now at our semiannual meetings. Dan Martin was one of the first to offer a kind and welcoming word to an apprehensive young fledgling acoustical consultant, Bill Cavanaugh, at his very first Acoustical Society meeting in 1957. The profound effect on that new Society member's introduction to and future in the Society was undoubtedly repeated manyfold by Dan and so many others like him whose allegience to the goals and objectives of the Acoustical Society of America knew no bounds. It is this societal ''kinship,'' if you will, that distinguishes ours from many other organizations. Dan played no small part in developing this valuable asset of our Society.

Dan was active in the Presbyterian church and served as Chair of the Presbyterian Work Group on Faith, Science and Technology. From 1977 to 1978 he was National President of the Presbyterian Men's Organization.

Dan is survived by Martha, his wife of 58 years and valuable assistant in the task of editing JASA. He is survived also by his three children, Mary Kilpatrick, David Martin, and Nancy Glasgow, and by seven grandchildren.

With the loss of our beloved colleague Dan Martin, the field of acoustics and the acoustical consulting profession are at once saddened and forever grateful that we had an opportunity to share at least a part of his almost six decades spent doing acoustics.

WILLIAM CAVANAUGH
WILLIAM HARTMANN

Transient acoustic wave propagation in rigid porous media: A time-domain approach

Z. E. A. Fellah and C. Depollier[a)]
Laboratoire d'Acoustique de l'Université du Maine, IAM UMR-CNRS 6613, Ave O. Messiaen, 72085 Le Mans Cedex 9, France

(Received 20 May 1999; revised 9 August 1999; accepted 1 October 1999)

Wave propagation of acoustic waves in porous media is considered. The medium is assumed to have a rigid frame, so that the propagation takes place in the air which fills the material. The Euler equation and the constitutive relation are generalized to take into account the dispersive nature of these media. It is shown that the connection between the fractional calculus and the behavior of materials with memory allows time-domain wave equations, the coefficients of which are no longer frequency dependent, to be worked out. These equations are suited for direct and inverse scattering problems, and lead to the complete determination of the porous medium parameters. © *2000 Acoustical Society of America.* [S0001-4966(00)02701-6]

PACS numbers: 43.20.Bi, 43.20.Hq [ANN]

INTRODUCTION

During the last two decades, there has been a reborn interest in sound propagation in porous materials. The main reason is not only the necessity of noise control in architectural acoustics or in transport vehicles, but also a better theoretical understanding of wave propagation in complex media. Special attention has been paid to wave propagation in porous media having a rigid frame, and nowadays the monochromatic wave propagation in these media is well understood. Some of the recent progress in this area is reviewed in Refs. 1 and 2. If many applications like medical imaging or inverse scattering problems[3] require the study of the behavior of pulses traveling in porous media, it is only recently that the response of these media to such excitations has been addressed.[4] To efficiently cope with the specific problems appearing in the transient acoustic field propagation, suited methods not related to fixed frequency formulation must be applied. Among them, one can cite the hereditary mechanics[5] or the time-domain approaches. The time-domain response of a material is described by an instantaneous response and a ''susceptibility'' kernel responsible for the memory effects. Evidently, the Fourier transformation translates the fixed frequency results into the time domain. However, in the analysis of the transient behavior of the fields, especially the short time behavior near the wave front, the investigations of the problem as a time-domain problem are more appropriate. A time-domain approach differs from the frequency analysis in that the susceptibility functions of the problem are convolution operators acting on the velocity and the pressure fields and therefore a different algebraic formalism has to be applied to resolve the wave equation. In the past, many authors have used the fractional calculus as an empirical method of describing the properties of viscoelastic materials.[6,7] The observation that the asymptotic expressions of stiffness and damping in porous materials are proportional to fractional powers of frequency suggests the fact that time derivatives of fractional order might describe the behavior of sound waves in this kind of material. In addition to that, fractional-order time derivatives simultaneously model relaxation and frequency dependence.

The outline of the paper is as follows. In Sec. I the model of equivalent fluid is presented and the basic equations in the frequency domain are given. Section II is devoted to the connection between fractional derivative and wave propagation in rigid porous media. Section III contains the asymptotic analyses for the low and high frequencies; the generalized Euler equation and constitutive relation and the time-domain wave equations are worked out.

I. MODEL OF THE EQUIVALENT FLUID

Let a homogeneous isotropic porous material with porosity ϕ be saturated with a compressible and viscous fluid of density ρ_f and viscosity η. It is assumed that the frame of this porous solid is not deformable when it is subjected to an acoustic wave. It is the case, for example, for a porous medium which has a large skeleton density or very large elastic modulus or weak fluid-structure couplings. To apply the results of linear elasticity it is required that the wavelength of sound waves should be much larger than the sizes of pores or grains in the medium.

In these porous materials, acoustic waves propagate only in the fluid. They can be seen as an equivalent fluid, the density and the bulk modulus of which are ''renormalized'' by the fluid-structure interactions. Viscous and thermal effects are well described by the Kirchhoff theory of the sound propagation in cylindrical tubes. Unfortunately, the fundamental equations of acoustics that are used in this theory can be very difficult to solve in the case of tubes with a noncircular cross section. Zwikker and Kosten[8] have worked out a simplified model of the sound propagation in the case of a circular cross section where viscous and thermal effects are treated separately. They derived the important result that the correction factor of bulk modulus of the fluid only contains the thermal effect and that of density only the viscous one. The validity of this model has been justified later for a large

a)Electronic mail: Claude.Depollier@univ-lemans.fr

range of radii at acoustical frequencies. Taking this result into consideration, it is assumed that the basic equations of the model of the equivalent fluid are the Euler equation (E) and the law of the mass conservation (M) associated with the behavior (or adiabatic) equations, and we will henceforth refer to them as EM equations,

$$\rho_f \alpha(\omega) \frac{\partial v_i}{\partial t} = -\nabla_i p, \quad \frac{\beta(\omega)}{K_a} \frac{\partial p}{\partial t} = -\nabla \cdot \mathbf{v}. \tag{1}$$

In these relations, $\mathbf{v}$ and p are the particle velocity and the acoustic pressure, $K_a = \gamma P_0$ is the compressibility modulus of the fluid, $\alpha(\omega)$ and $\beta(\omega)$ are the dynamic tortuosity of the medium and the dynamic compressibility of the air included in the porous material. These two response factors are complex functions which heavily depend on the frequency $f = \omega/2\pi$. Their theoretical expressions are given by Allard[1] and Lafarge,[2]

$$\alpha(\omega) = \alpha_\infty \left(1 + \frac{\eta\phi}{j\omega\alpha_\infty\rho_f k_0} \sqrt{1 + j \frac{4\alpha_\infty^2 k_0^2 \rho_f \omega}{\eta \Lambda^2 \phi^2}} \right), \tag{2}$$

$$\beta(\omega) = \gamma - (\gamma - 1) \times \left(1 + \frac{\eta\phi}{j\omega\rho_f k_0' \,\mathrm{Pr}} \sqrt{1 + j \frac{4 k_0'^2 \rho_f \omega \,\mathrm{Pr}}{\eta \phi^2 \Lambda'^2}} \right)^{-1}, \tag{3}$$

where $j^2 = -1$, γ represents the adiabatic constant, Pr the Prandtl number, α_∞ the tortuosity, k_0 the static permeability, k_0' the thermal permeability and Λ and Λ' the viscous and thermal characteristic lengths.[9] This model was initially developed by Johnson, Koplik and Dashen,[10] and completed by Allard and Champoux by adding the description of thermal effects.[11] Later on, Lafarge introduced the parameter k_0' which describes the additional damping of sound waves due to the thermal exchanges between fluid and structure at the surface of the pores.[2]

The functions $\alpha(\omega)$ and $\beta(\omega)$ express the viscous and thermal exchanges between the air and the structure which are responsible for the sound damping in acoustic materials. These exchanges are due on the one hand to the fluid-structure relative motion and on the other hand to the air compressions-dilatations produced by the wave motion. The parts of the fluid affected by these exchanges can be estimated by the ratio of a microscopic characteristic length of the media, as, for example, the sizes of the pores, to the viscous and thermal skin depth thickness $\delta = (2\eta/\omega\rho_0)^{1/2}$ and $\delta' = (2\eta/\omega\rho_0 P_r)^{1/2}$. For the viscous effects this domain corresponds to the region of the fluid in which the velocity distribution is perturbed by the frictional forces at the interface between the viscous fluid and the motionless structure. For the thermal effects, it is the fluid volume affected by the heat exchanges between the two phases of the porous medium. In this model, the sound propagation is completely determined by the five following parameters: ϕ, α_∞, $\sigma = \eta/k_0$, Λ and Λ'. In the next section, we will show that the values of these parameters are given by the low- and high-frequency wave equations.

The sound velocity in the porous material is derived from Eqs. (2) and (3) and yields the usual equation,

$$c(\omega) = \sqrt{\frac{K_a}{\rho_f \alpha(\omega) \beta(\omega)}}. \tag{4}$$

In this expression, the velocity is a complex function of the frequency, which is not very convenient to investigate the propagation of ultrasonic short pulses or to deduce the values of the parameters of the medium. This is due to the fact that the EM equations are neither expressed in time domain nor in frequency domain: they are correct only for monochromatic waves. To restore their validity for transient signals, we need to write them in the time domain.

II. FRACTIONAL DERIVATIVE AND BEHAVIOR OF MATERIALS

The constitutive relation between the strain $\epsilon(t)$ at time t and the driving stress $\sigma(t)$ is at the heart of the conventional description of the theory of elasticity. In the ''classical'' theory, the stresses and strains are related by constants. Accordingly, the time histories of these values are similar and the deformation process is completely reversible. It was found out, however, that most elastic materials exhibit an explicit departure from this type of behavior due to the fact that they partially absorb energy. These deviations from pure elasticity may be taken into account by replacing the elastic constants by integral or differential time operators.

A. Fractional derivative and viscoelasticity

The fractional calculus model of viscoelastic behavior employs derivatives of fractional orders to relate stress fields to strain fields in viscoelastic materials and it has been shown that constitutive equations employing such derivatives are linked to the microscopic theories describing the macroscopic behavior of the media. Bagley and Torvik[7] have explored the models of the form

$$\sigma(t) + bD^\lambda[\sigma(t)] = G_0 \epsilon(t) + G_1 D^\nu[\epsilon(t)],$$

where b, G_0, G_1, λ and ν are five parameters to be determined by least-squares fit to experimental data. $D^\nu[x(t)]$ is the fractional derivative of order ν defined by

$$D^\nu[x(t)] = = \frac{1}{\Gamma(-\nu)} \int_0^t (t-u)^{-\nu-1} x(u) du, \tag{5}$$

where ν is a real number and $\Gamma(x)$ is the gamma function. A fractional derivative no longer represents the local variations of the function but on the contrary, it acts as a convolution integral operator. More details about the properties of fractional derivatives and about fractional calculus are given in Ref. 12.

In view of the success obtained with these models, one is inclined to ask if they can be generalized to the case of wave motion in rigid porous materials.

B. Fractional derivative relationship for a porous medium

To write the basic equations in the time domain we use a quite different method than the one described in Ref. 7.

As seen above, the complex susceptibilities $\alpha(\omega)$ and $\beta(\omega)$ have been worked out in the framework of the equivalent fluid model. They must be mapped into the time domain. For that, the trick is to expand these functions into series of ω,

$$\alpha(\omega)=\sum_{\nu} a_{\nu}(j\omega)^{\nu}, \quad \beta(\omega)=\sum_{\lambda} b_{\lambda}(j\omega)^{\lambda}, \tag{6}$$

where ν and λ may be fractional numbers. Then we use the rules of the fractional calculus and the Fourier transform

$$F[g(t)]=\int_{-\infty}^{\infty} g(t)e^{j\omega t}dt, \tag{7}$$

to write the useful relationship

$$F[D^{\nu}g(t)]=(j\omega)^{\nu}F[g(t)]. \tag{8}$$

At last, we substitute the fractional derivatives for the powers of ω,

$$(j\omega)^{\nu} \overset{t}{\rightarrow} D^{\nu}[\cdot].$$

Unfortunately, this method leads to very complicated equations if valid expressions are required for all values of ω and exact solutions for general conditions are not easily obtained. For example, in this framework the EM equations have the following general form:

$$\rho_f \sum_{\nu} a_{\nu} D^{\nu}\left[\frac{\partial v_i}{\partial t}\right]=-\nabla_i p, \quad \frac{1}{K_a}\sum_{\lambda} b_{\lambda} D^{\lambda}\left[\frac{\partial p}{\partial t}\right]=-\nabla\cdot\mathbf{v}. \tag{9}$$

Another way to tackle this problem is to consider the asymptotic expressions of $\alpha(\omega)$ and $\beta(\omega)$, when ω tends to zero or to infinity, which are generally very simple functions of ω.

III. WAVE EQUATIONS IN THE TIME DOMAIN

The fact that more than one time-domain equation must be considered, one equation for each particular range of frequencies, appears to be the drawback of this approach. Of course, it would be better to have only one model to describe the sound propagation in the whole time domain. However, we know that the relative importance of the effects responsible for the behavior of a fluid in a porous media is significantly modified when the frequency goes from zero to high values. In this case it seems reasonable that the physics laws which govern the wave propagation may be quite different from one domain to the other. We now consider the cases of low- and high-frequency responses.

A. Low-frequency approximations

The range of frequencies such that viscous skin thickness $\delta=(2\eta/\omega\rho_0)^{1/2}$ is much larger than the radius of the pores r,

$$\frac{\delta}{r}\gg 1, \tag{10}$$

is called the low-frequency range. For these frequencies, the viscous forces are important everywhere in the fluid. At the same time, the compression-dilatation cycle in the porous material is slow enough to favor the thermal exchanges between fluid and structure. At the same time, the temperature of the frame is practically unchanged by the passage of the sound wave because of the high value of its specific heat: the frame acts as a thermostat. In this case the isothermal compressibility is directly applicable.

We consider the low-frequency approximations of the response factors $\alpha(\omega)$ and $\beta(\omega)$. When $\omega\rightarrow 0$, Eqs. (2) and (3), respectively, become

$$\alpha(\omega)\approx\alpha_0\left(1+\frac{\eta\phi}{j\omega\alpha_0\rho_f k_0}\right), \tag{11}$$

$$\beta(\omega)\approx\gamma. \tag{12}$$

α_0 is the the low-frequency approximation of the tortuosity given by Lafarge in Ref. 2 and also obtained by Norris[13] from homogenization theory,

$$\alpha_0=\frac{\langle\mathbf{v}(\mathbf{r})^2\rangle}{\langle\mathbf{v}(\mathbf{r})\rangle^2}, \tag{13}$$

where $\langle\mathbf{v}(\mathbf{r}\rangle$ is the average velocity of the viscous fluid for direct current flow within a volume element small compared to the relevant wavelength, but large compared to the individual grains/pores of the solid.

The time-domain expression for α becomes

$$\alpha(\omega)\overset{t}{\rightarrow}\alpha_0\left(I+\frac{\eta\phi}{\alpha_0\rho_f k_0}\partial_t^{-1}\right), \tag{14}$$

where I is the unit operator and $\partial_t^{-1}g(t)=\int_0^t g(t')dt'$. For a wave traveling along the direction $0x$, the generalized forms of EM equations in the time domain are now

$$\rho_f\alpha_0\frac{\partial v}{\partial t}+\frac{\eta\phi}{k_0}v=-\frac{\partial p}{\partial x} \quad \text{and} \quad \frac{\gamma}{K_a}\frac{\partial p}{\partial t}=-\frac{\partial v}{\partial x}. \tag{15}$$

In this approximation, the Euler equation expresses the balance between the driving forces of the wave, the drag forces $\eta\phi v/k_0$ due to the flow resistance of the material and the inertial forces.

The wave equation is derived from these two relations by elementary manipulations,

$$\frac{\partial^2 v}{\partial x^2}-a\frac{\partial^2 v}{\partial t^2}-d\frac{\partial v}{\partial t}=0. \tag{16}$$

The first coefficient of this equation,

$$a=\frac{\rho_f\alpha_0\gamma}{K_a}, \tag{17}$$

leads to the sound velocity $c=a^{-1/2}$ in the air filling the structure of the material. This result shows that the viscous forces and the shape of the pores increase the fluid density by the factor $\alpha_0\geqslant 1$. The second coefficient,

$$d=\frac{\eta\phi\gamma}{k_0K_a}, \tag{18}$$

is the damping-distortion term due to viscous and thermal effects which take place in the porous material. From these equations it is possible to estimate α_0 and the flow resistivity $\sigma=\eta/k_0$. At very low frequency, the asymptotic expressions for $\alpha(\omega)$ and $\beta(\omega)$ are

$$\alpha(\omega)\approx\frac{\eta\phi}{j\omega\rho_f k_0}, \quad \beta(\omega)\approx\gamma. \tag{19}$$

In this range of frequencies, EM equations become

$$\frac{\eta\phi}{k_0}v=-\frac{\partial p}{\partial x} \quad \text{and} \quad \frac{\gamma}{K_a}\frac{\partial p}{\partial t}=-\frac{\partial v}{\partial x}, \tag{20}$$

where the Euler equation is reduced to the Darcy's law which defines the static flow resistivity $\sigma=\eta/k_0$. The fields which are varying in time, the pressure, the acoustic velocity, etc., follow a diffusion equation with the diffusion constant

$$D=\frac{K_a k_0}{\eta\phi\gamma}.$$

A quite similar result is given by Johnson in Ref. 14. However, the adiabatic constant γ does not appear in Johnson's model in which the thermal expansion is neglected.

B. High-frequency approximation

When the frequency increases, the skin thickness becomes narrower and the viscous effects are concentrated in a small volume near the frame $\delta/r\ll 1$. In this case, the viscous effects in the fluid can be neglected: the fluid behaves almost like a perfect fluid (without viscosity).

At high frequencies the compression/dilatation cycle is much faster than the heat transfer between the air and the structure, and in this case, it is a good approximation to consider that the compression is adiabatic.

The high-frequency approximations of the response factors $\alpha(\omega)$ and $\beta(\omega)$ when $\omega\to\infty$ are given by the relations

$$\alpha(\omega)\approx\alpha_\infty\left(1+\frac{2}{\Lambda}\left(\frac{\eta}{j\omega\rho_f}\right)^{1/2}\right), \tag{21}$$

$$\beta(\omega)\approx 1+\frac{2(\gamma-1)}{\Lambda'}\left(\frac{\eta}{j\omega\,\mathrm{Pr}\,\rho_f}\right)^{1/2}. \tag{22}$$

In the time domain, the expressions of the responses α and β become

$$\alpha(\omega)\overset{t}{\to}\alpha_\infty\left(\delta(t)+\frac{2}{\Lambda}\left(\frac{\eta}{\rho_f}\right)^{1/2}t^{-1/2}\right)*, \tag{23}$$

$$\beta(\omega)\overset{t}{\to}\left(\delta(t)+\frac{2(\gamma-1)}{\Lambda'}\left(\frac{\eta}{\mathrm{Pr}\,\rho_f}\right)^{1/2}t^{-1/2}\right)*, \tag{24}$$

where * denotes the time convolution and $\delta(t)$ is the Dirac function. The tortuosity α_∞ is real-valued and defined as in Eq. (13) but from the field of the microscopic velocity $\mathbf{v}(\mathbf{r})$ in a perfect fluid. Brown[15] has shown that this quantity is related to the electrical formation factor F by $\alpha_\infty=F\phi$. When the wave propagates along the coordinate axis $0x$, the EM equations are generalized as follows in the time domain:

$$\rho_f\alpha_\infty\frac{\partial v}{\partial t}+2\frac{\rho_f\alpha_\infty}{\Lambda}\left(\frac{\eta}{\pi\rho_f}\right)^{1/2}\int_{-\infty}^{t}\frac{\partial v/\partial t'}{\sqrt{t-t'}}dt'=-\frac{\partial p}{\partial x}, \tag{25}$$

$$\frac{1}{K_a}\frac{\partial p}{\partial t}+2\frac{\gamma-1}{K_a\Lambda'}\left(\frac{\eta}{\pi\,\mathrm{Pr}\,\rho_f}\right)^{1/2}\int_{-\infty}^{t}\frac{\partial p/\partial t'}{\sqrt{t-t'}}dt'=-\frac{\partial v}{\partial x}. \tag{26}$$

A consequence of this is a surprising result: the retarding force is no longer proportional to the time derivative, it is found to be proportional to a fractional derivative of order 1/2 of the acoustic velocity. This occurs because the volume of fluid participating in the motion is not the same for all motion, as it is for a fully developed steady flow. The phenomena may be understood by considering such a volume of fluid in a pore to be in harmonic motion. At a higher frequency, only a thin boundary layer is excited: the average shear stress is high. At a lower frequency, the same amplitude of the fluid motion allows a thicker layer of fluid to participate in the motion, and consequently the shear stress is less. The penetration distances of the viscous forces and therefore the excitation of the fluid depend on the frequency. In the time domain, such a dependence is associated with a fractional derivative. The generalized mass conservation equation is interpreted in the same way. In these equations, the convolutions express the dispersive nature of the porous material. They take into account the memory effects due to the fact that the response of the medium to the wave excitation is not instantaneous but needs some time to take place.

The wave equation is derived from these two relations by elementary calculation and can be written as

$$\frac{\partial^2 v}{\partial x^2}-A\frac{\partial^2 v}{\partial t^2}-B\int_{-\infty}^{t}\frac{\partial^2 v/\partial t'^2}{\sqrt{t-t'}}dt'-C\frac{\partial v}{\partial t}=0, \tag{27}$$

where the coefficients are given by

$$A=\frac{\rho_f\alpha_\infty}{K_a}, \quad B=\frac{2\alpha_\infty}{K_a}\sqrt{\frac{\rho_f\eta}{\pi}}\left(\frac{1}{\Lambda}+\frac{\gamma-1}{\sqrt{\mathrm{Pr}}\,\Lambda'}\right),$$

$$C=\frac{4\alpha_\infty(\gamma-1)\eta}{K_a\Lambda\Lambda'\sqrt{\mathrm{Pr}}}.$$

The first one gives the velocity $c=A^{-1/2}$ of the wave in the air included in the porous material. In this case the fluid density is modified by the factor α_∞. The other coefficients are essentially dependent on the characteristic lengths Λ and Λ', and express the viscous and thermal interactions between the fluid and the structure. The knowledge of these three coefficients allows the determination of the three parameters α_∞, Λ and Λ'. This can be achieved from the measurements of the damping and broadening of ultrasonic pulses during the propagation in the porous medium.

With this model, one can hope to get an easier estimation of the characteristic lengths than for example Ref. 16. In this paper, the characteristic lengths are deduced from the high-frequency asymptotic behavior of either the velocity or

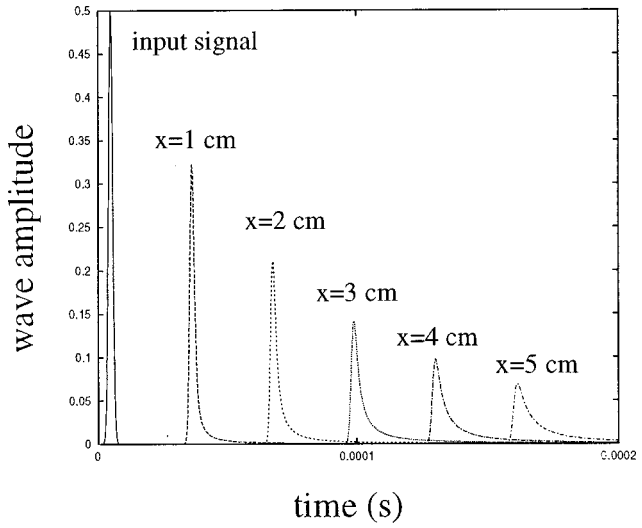

FIG. 1. Space evolution of a Gaussian pulse in a porous medium. The medium parameters are those of the polyrethan foam Bulpren R60, manufactured by Recticel. $\alpha_\infty = 1.04$, $\phi = 0.98$, $\Lambda = 2\times10^{-4}$ m, $\Lambda' = 5\times10^{-4}$ m, $\sigma = 2850$ Nm^{-4} s.

the attenuation curves which allow only the determination of the length $L = [\Lambda^{-1} + (\gamma - 1)(\sqrt{\mathrm{Pr}}\,\Lambda'^{-1}]^{-1}$. In this case, the estimation of the characteristic lengths needs the data obtained from the dispersion curves in air- and helium-filled materials. On the contrary, by using inverse scattering methods, the time-domain approach provides the viscous Λ and the thermal Λ' characteristic lengths from the coefficients B and C of Eq. (27). On the other hand, Eq. (27) is well suited for analytical solutions and numerical applications. Figure 1 shows the evolution of a Gaussian pulse in an air-filled porous medium as a time function. These results are obtained by convolution of the Green's function of Eq. (27) with the pulse. During the propagation, the pulse gets wider while its amplitude decreases; the result is a warped Gaussian pulse due to the combined effects of dispersion and attenuation where high frequencies are faster but more attenuated than the low frequencies. Figure 2 presents numerical simulations for two values of the B coefficient of Eq. (27). Warping of the input signal is mainly due to this effect. [The contribution of the other term of Eq. (27) is not significant.] Other numerical applications and comparisons with experimental results will be given in Ref. 17. Accordingly, it seems possible to get the specific contribution of viscous and thermal effects to the spreading and attenuation of ultrasonic pulses by standard inverse scattering methods.

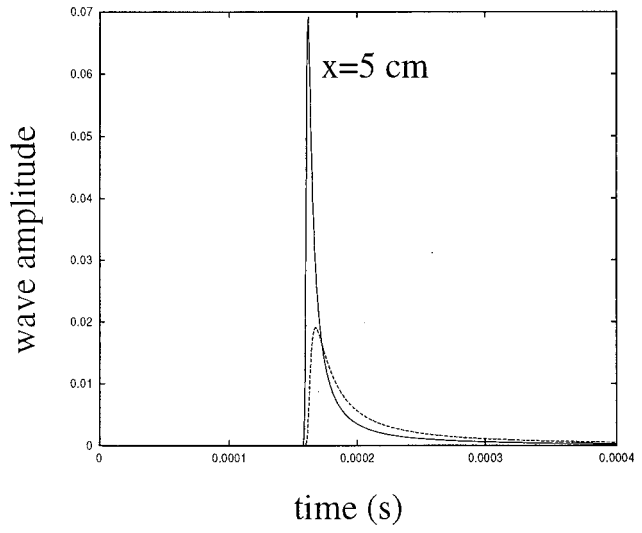

FIG. 2. Numerical simulations of warped Gaussian pulse for $x = 5$ cm for two values of B coefficient [Eq. (27)]; solid line: $B = 2.41\times10^{-4}$ and broken line: $B = 4.41\times10^{-4}$.

IV. CONCLUSION

In this paper the time-domain equations for the transient wave propagation in a porous medium have been derived in the low- and high-frequency ranges. In each range, the coefficients of the wave equation are no more frequency dependent, and viscous and thermal effects can be distinguished. At very low frequency, the viscous forces and the thermal exchanges are strong enough to prevent the waves from propagating in these materials: the field's evolution follows a diffusion equation. At low frequency the damping is weaker and the fields can propagate. In the high-frequency range, the wave propagation is described by hereditary mechanics. As a consequence of the relaxation phenomenon, the fluid density and the bulk modulus are no longer constant numbers but they are signal dependent.

The results of preliminary numerical simulations tend to indicate that studies of the propagation of transient waves may yield useful data. Ultrasonic impulses seem to be an efficient tool to probe the properties of sound absorbing materials. Last, the time-domain wave equations have a well adapted form for the analysis of the direct and inverse scattering problems.

ACKNOWLEDGMENTS

The authors express their thanks to Professor B. Castagnède, and Professor M. Fellah and Dr. D. Lafarge for useful comments. They are indebted to the referees for careful reading of the manuscript and for many suggestions on improving its presentation.

[1] J. F. Allard, *Propagation of Sound in Porous Media: Modeling Sound Absorbing Materials* (Chapman and Hall, London, 1993).
[2] D. Lafarge, ''Propagation du son dans les matériaux poreux à structure rigides saturéx par un gaz,'' Ph.D. dissertation, Université du Maine, 1993.
[3] *Inverse Problems in Mathematical Physics*, edited by L. Päivärinta and E. Somersalo (Springer, Berlin, 1993).
[4] Z. E. A. Fellah, B. Castagnède, and C. Depollier, ''Forum Acusticum 1999,'' J. Acoust. Soc. Am. **105**, 1384(A) (1999).
[5] Yu. N. Rabotnov, *Elements of Hereditary Solid Mechanics* (Mir, Moscow, 1980).
[6] M. Caputo, ''Vibrations of an infinite plate with a frequency independent Q,'' J. Acoust. Soc. Am. **60**, 634–639 (1976).
[7] R. L. Bagley and P. J. Torvik, ''On the Fractional Calculus Model of Viscoelastic Behavior,'' J. Rheol. **30**, 133–155 (1983).
[8] C. Zwikker and C. W. Kosten, *Sound Absorbing Materials* (Elsevier, New York, 1949).
[9] D. Lafarge, J. F. Allard, and B. Brouard, ''Characteristic dimensions at high frequencies of the surface impedance of porous layers,'' J. Acoust. Soc. Am. **93**, 2474–2478 (1993).
[10] D. L. Johnson, J. Koplik, and R. Dashen, ''Theory of dynamic permeability and tortuosity in fluid-saturated porous media,'' J. Fluid Mech. **176**, 379–402 (1987).

[11] J. F. Allard and Y. Champoux, ''New empirical equations for sound propagation in rigid frame fibrous materials,'' J. Acoust. Soc. Am. **91**, 3346–3353 (1992).
[12] S. G. Samko, A. A. Kilbas, and O. I. Marichev, *Fractional Integrals and Derivatives: Theory and Applications* (Gordon and Breach Science, Amsterdam, 1993).
[13] A. N. Norris, ''On the viscodynamic operator in Biot's equations of poroelasticity,'' J. Wave Mat. Interact. **1**, 365–380 (1986).
[14] D. J. Johnson, ''Recent developments in the acoustic properties of porous medium,'' in *Proceedings of the International School of Physics Enrico Fermi, Course XCIII*, edited by D. Sette (North-Holland, Amsterdam, 1986), pp. 255–290.
[15] R. J. S. Brown, ''Connection between formation factor of electrical resistivity and fluid-solid coupling factor in Biot's equations for acoustic waves in fluid-filled porous media,'' Geophysics **45**, 1269–1275 (1980).
[16] P. Leclaire, L. Kelders, W. Lauriks, N. R. Brown, M. Melon, and B. Castagnède, ''Determination of the viscous and thermal characteristics lengths of plastic foams by ultrasonic measurements in helium and air,'' J. Appl. Phys. **80**, 2009–2012 (1996).
[17] Z. E. A. Fellah, B. Castagnède, and C. Depollier (unpublished).

Backscattering enhancements for tilted solid plastic cylinders in water due to the caustic merging transition: Observations and theory

Florian J. Blonigen and Philip L. Marston
Department of Physics, Washington State University, Pullman, Washington 99164-2814

(Received 4 October 1999; accepted for publication 16 November 1999)

Bulk shear and longitudinal waves give rise to important contributions to the scattering of ultrasound by tilted finite plastic and rubber cylinders in water. This occurs in situations where either the shear or longitudinal speed is less than the speed of sound in the surrounding water. At a certain critical tilt angle, large backscattering enhancements are observed for finite cylinders, where the wave vector can reverse direction upon reflection from the cylinder truncation. The scattering process is analogous to the enhancement produced by the merging of rainbow caustics of primary rainbow rays in the scattering of light by long dielectric cylinders, also known as the caustic merging transition [C. M. Mount, D. B. Thiessen, and P. L. Marston, Appl. Opt. **37**, 1534–1539 (1998)]. A ray theory was developed to model the backscattering mechanism at the critical tilt angle. It employs the idea of the Bravais effective refractive index, convenient for constructing ray diagrams for the projections of rays in the base plane of the cylinder. There is general agreement between the theory and the experiment down to relatively low ultrasonic frequencies (*ka* as small as 10). The enhancement is the most significant backscattering contribution for a wide range of tilt angles. © *2000 Acoustical Society of America.* [S0001-4966(00)05402-3]

PACS numbers: 43.20.Fn, 43.30.Ft, 43.35.Mr [ANN]

INTRODUCTION

In the studies of the scattering of ultrasound by truncated solid metallic cylinders in water, it has been found that surface guided waves make important contributions to the backscattering at large tilt angles.[1,2] Incident sound couples to surface modes on the cylinder, which may backscatter upon reflection at the cylinder's end. Specifically, supersonic Rayleigh surface waves that run along the meridian of the cylinder have been observed to give rise to strong backscattering enhancements due to short ray paths along the cylinder's surface (which reduces the effect of radiation damping) and a flat outgoing scattered wave front.[1,2] A similar meridional ray enhancement has also been observed for generalizations of Lamb waves in finite thick cylindrical shells.[3,4] Typical plastic materials will not support Rayleigh waves which are supersonic relative to water and will no longer yield a meridional Rayleigh ray enhancement as was just described. (Recent evidence shows the existence of subsonic Rayleigh waves on polymer plastic-water interfaces where the sound speed in the water is located between the values of the longitudinal and shear speed in the solid.[5]) In the present work, we show that bulk transmitted waves must be considered when identifying candidate backscattering mechanisms for penetrable cylinders at large tilt angles when the phase velocity of the transmitted wave is less than the speed of sound in water. For typical polymer plastics, the shear velocity is less than the speed of sound in water.[6,7] Transmitted longitudinal waves are also considered for rubber cylinders in situations where the intrinsic material damping is small.

In this paper, we present a novel backscattering mechanism of sound by tilted penetrable cylinders in water where the shear and, for rubber, the longitudinal wave speeds are subsonic. The mechanism is an analog of the optical ray phenomenon of rainbow caustics observed in the scattering of laser light by dielectric cylinders and of sunlight by nearly cylindrically shaped icicles.[8–11] When light is incident on cylinders (shown schematically in Fig. 1), far-field caustics (analogous to rainbow caustics of sunlit raindrops) are observed at some scattering angle, which depends on the tilt angle of the incident light relative to the cylinder's axis. At a certain critical tilt angle, the two rainbow caustics of the cylinder merge in the merdional plane to produce a double caustic in the far-field specular direction. For a finite cylinder, however, light rays may backscatter if reflected off the cylinder's end. Thus, in the acoustic analog of this ray effect, the scattering of sound by finite, penetrable cylinders in water at ultrasonic frequencies should produce the possibility of a strong backscattering enhancement. This scattering enhancement mechanism will be referred to as the caustic merging transition (CMT).

To understand this effect using ray concepts, it is convenient to introduce the notion of the Bravais effective refractive index, n_{eff}, most commonly used to calculate the propagation of skew rays through prismatic ice crystals.[12,13] It is the effective index of refraction of the cylinder as seen by the projections of rays onto the cylinder's base plane (the plane perpendicular to the cylinder's axis) and is given by the following formula derived in Appendix A:

$$n_{\mathrm{eff}}(\gamma,n)=(n^2-\sin^2\gamma)^{1/2}/\cos\gamma, \tag{1}$$

where $n\geqslant 1$ is the actual refractive index of the cylinder material and γ is the tilt angle of an incident ray with respect to the cylinder (see Fig. 1) axis. Using this effective index, ray tracing can be done in the base plane and rainbow caustic

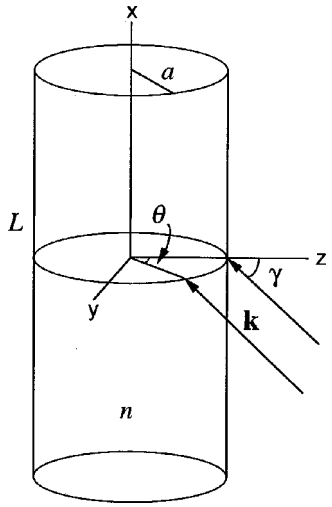

FIG. 1. Schematic diagram of the scattering problem. A plane wave of wave vector **k** is incident on a penetrable cylinder of refractive index n and length L. The wave vector is tilted at an angle γ with respect to broadside incidence ($\mathbf{k}=-k\mathbf{z}$ corresponds to broadside incidence). In this diagram, the x-z plane is the meridional plane and the y-z plane is the base plane.

rays identified (see Fig. 2), just as has been done for light rays in spherical raindrops.[12–15]

Consider the scattering of an incident plane wave by a dielectric cylinder. The scattering angle of rainbow rays as projected onto the base plane, denoted by ϕ, will depend on the effective index of refraction, n_{eff}, which by Eq. (1) depends on the tilt angle, γ, of the cylinder with respect to all incident rays. In particular, consider the two-chord rainbow caustic rays shown in Fig. 2, also known as Descartes rays.[12–15] It can be demonstrated[8–11] that at a certain critical tilt angle, γ_c, corresponding to an index of $n_{\text{eff}}=2$, the rainbow caustics on both sides of the cylinder merge in the meridional plane (the plane defined by the incident wave vector and the cylinder's axis). The critical tilt angle is given by the formula

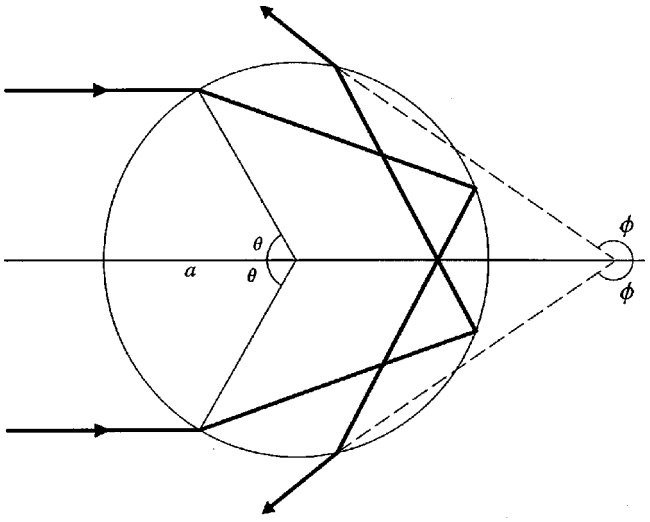

FIG. 2. This figure shows the ray paths of two Descartes rays as projected onto the base plane which leave the cylinder with zero lateral curvature and result in far-field rainbow caustics. The rays have a projected angle of incidence, θ, and scattering angle ϕ, which depend on the effective index of refraction. In the caustic merging transition, the rainbow rays merge at $\phi=180°$.

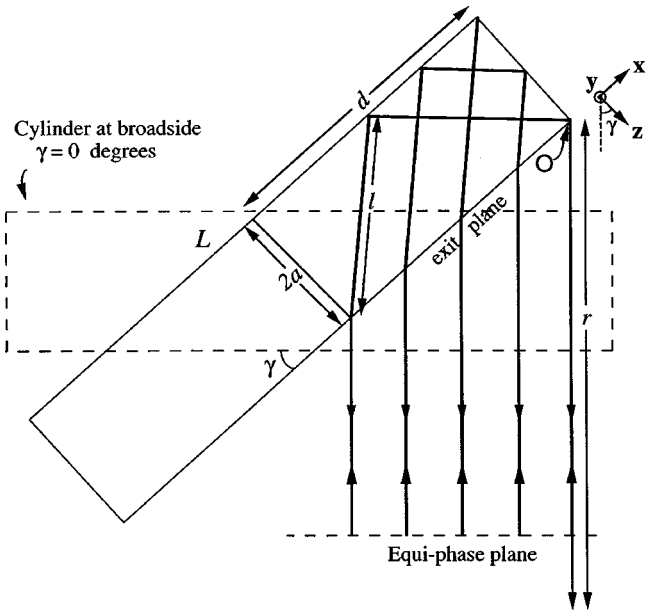

FIG. 3. Rays confined to the meridional plane which are backscattered by a finite titled cylinder of tilt angle γ. The rays shown are only twice internally reflected. Such rays must enter the cylinder at a distance $\leqslant d$ from the far end of the cylinder, and all rays have a path length of $2l$ inside the cylinder. It is evident from this diagram that the outgoing pressure is constant in amplitude with only a linear phase ramp along the x-axis. Note that all rays shown in this diagram are reversible.

$$\gamma_c=\arccos\{[(n^2-1)/3]^{1/2}\}, \tag{2}$$

which can be derived by setting $n_{\text{eff}}=2$ in Eq. (1) and solving for γ. This result has also been derived without introducing the Bravias index, n_{eff}, by direct analysis of the curvature of waves transmitted by a tilted cylinder.[8] It is apparent from Fig. 2 that the Descartes rays merge in the meridional plane at $\phi=180°$. This does not necessarily mean that the rays are backscattered; they only appear to be in the base plane. In the meridional plane, rays will only backscatter if they reflect off the end of a finite or semi-infinite cylinder, as shown in Fig. 3. The flatness of the outgoing wave front for the backscattered caustic rays then leads to the scattering enhancement.

The CMT enhancement has already been observed in the study of the scattering of laser light by transparent fibers.[9,10] The purpose of this work was to study the CMT enhancement in the backscattering of ultrasound by bluntly truncated plastic and rubber cylinders in water. Experiments were carried out on cylinders composed of materials where either the bulk shear or longitudinal sound speed, c_b, was less than the speed of sound in water, c. This ensures that the index of refraction of the cylinder is greater than one: $n=c/c_b\geqslant 1$. The experimental setup and general observations are discussed in Sec. I. The ray theory used to calculate approximate backscattered pressure amplitudes is described in Sec. II. A comparison of ray theory and experimental data is done in Sec. III. Section IV gives a discussion of the results. The problem of thin shells filled with low velocity materials is not considered here, but when the shell wall is sufficiently thin, the CMT should produce a backscattering enhancement in that case also.

TABLE I. Material parameters for polystyrene, silicone rubber, and water. The data for polystyrene were taken from the references below. The density and longitudinal speed values for the silicone rubber were provided by G. Kaduchak in private communication.

	Density (in g/cm^3)	Longitudinal speed (in mm/μs)	Shear speed (in mm/μs)	Attenuation constant, α (Np/m-MHz)	Relevant refractive index, $n=c/c_b$
Polystyrene[a]	1.056	2.350	1.120	15[b]	1.322
Silicone rubber (RTV 615)	1.02	1.08		12[c]	1.37
Water	0.998	1.481			

[a]See Reference 6.
[b]See Reference 26.
[c]See Reference 18.

I. EXPERIMENT AND OBSERVATIONS

Backscattering experiments were performed on solid plastic and rubber cylinders in a large water-filled redwood tank. A 1.5-in diameter piston transducer (Panametrics model V3386) was used as both a sound source and receiver, though to obtain the frequency-scan data discussed in Sec. III, a composite transducer was used instead. The transducer was placed 230 cm from the cylinder targets. The experimental setup was similar to the one used by Gipson in her backscattering experiments with solid metallic cylinders, including the single transducer send-receive system (see Fig. 2 of Ref. 1 for a schematic of the experimental setup along with the electronics setup).

Plastic and rubber cylinder targets were used: a polystyrene cylinder of length 9.6 cm and diameter 3.2 cm, and a silicone rubber cylinder (RTV 615) of length 11.1 cm and diameter 2.7 cm. The material parameters for these cylinders are given in Table I, along with the relevant refractive index of each cylinder corresponding to the shear or longitudinal wave in the material which yields $n \geqslant 1$. In the polystyrene cylinder, it is the shear waves which are subsonic and can make a strong backscattering contribution through CMT. In the rubber cylinder, it is the longitudinal waves which are the relevant subsonic waves. The shear wave in the rubber is also subsonic but the sound speed for this wave is too slow to make any important contribution to the scattering. The temperature of the experiment (typically 20 °C) is significantly below the glass transition temperature for polystyrene (approximately 100 °C) and the range of frequencies is limited to 140–370 kHz. As a consequence, the effects of dispersion on the changes in the polystyrene shear wave velocity are small and the material attenuation factor is approximated as linear in the frequency. These approximations are supported by studies of the viscoelastic behavior of polystyrene[16] and we use similar approximations to model the longitudinal wave behavior in RTV 615.

Time records of the backscattering of tone bursts by the cylindrical targets were recorded on a digital oscilloscope as a function of tilt angle. These time plots were cascaded to show the backscattering as a function of time and angle in Figs. 4 and 5. The results for polystyrene are shown in Fig. 4. Here, a 15-cycle tone burst of frequency 250 kHz was used, and time plots were recorded at angular intervals of 0.5°. In Fig. 4, we see a significant signal at a tilt angle of 0° corresponding to the broadside specular reflection. There is also a rather large backscattered signal in the angular region of 50–70° at a somewhat later time. This is close to the predicted critical tilt angle of $\gamma_c = 59.9°$ for polystyrene. Thus, we claim that this backscattering enhancement is due to the caustic merging transition. This was confirmed by calculating the time delay of the backscattered rays in the meridional plane with respect to those of the broadside reflection and comparing that with the same delay observed in the experimental time records.

Figure 5 shows a similar cascade plot for the silicone rubber cylinder. In this case, a 10-cycle tone burst of frequency 250 kHz was used, and the time plots were recorded at angular intervals of 1.6°. There is also a large backscatter-

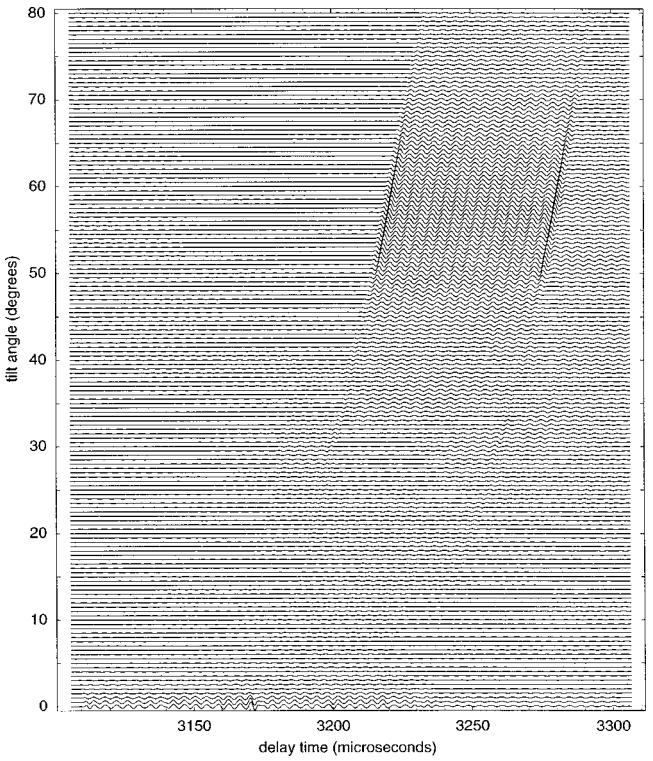

FIG. 4. Time records of the backscattering of 250-kHz 15-cycle tone bursts by a tilted polystyrene cylinder in water, cascaded as a function of angle. There is significant backscattering at broadside incidence (at 0°). There is also a backscattering enhancement at 50–60° due to the caustic merging transition (CMT). The critical tilt angle for the polystyrene is 59.9°. The time delay of the CMT signal at the critical tilt relative to the broadside reflection was 109 μs. This is in good agreement with the theoretical value of 110 μs which was calculated geometrically for refracted shear waves.

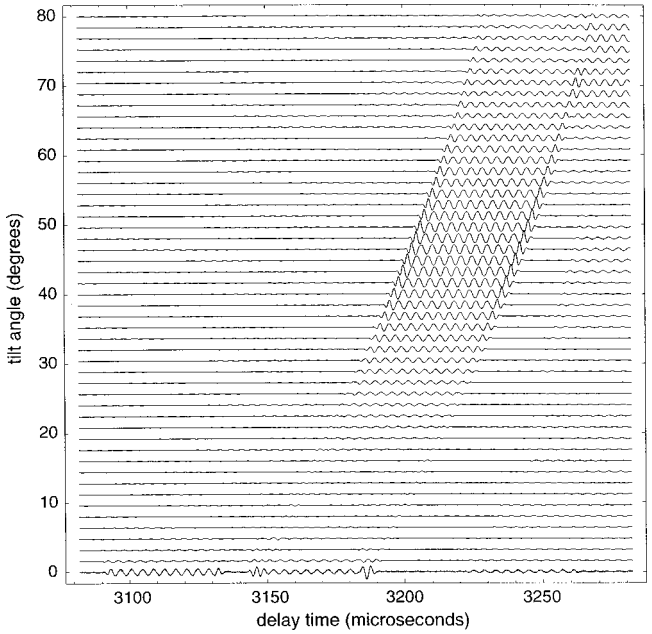

FIG. 5. Similar to Fig. 4, but this time using the RTV 615 rubber cylinder with 250 kHz 10-cycle tone bursts and a coarser angle scan. Again, a CMT enhancement is observed. The critical tilt angle for the silicone rubber is 57°. Unlike for the polystyrene cylinder in Fig. 4, the rotation axis of the target was offset from the center of mass. Consequently, the time delay of the CMT signal at the critical tilt relative to the broadside reflection differed from the theoretical value for longitudinal waves calculated geometrically by as much as 14 μs.

ing enhancement around the predicted critical tilt angle of $\gamma_c = 57°$ for the silicone rubber due to CMT, associated with longitudinal waves.

II. RAY THEORETIC PREDICTION OF BACKSCATTERED AMPLITUDES

A ray approximation used to predict the amplitude of the backscattering enhancement of the cylinder specimens at the critical tilt angle γ_c will now be described. Consider the scattering problem of a plane wave of wave vector **k** incident on a finite penetrable cylinder of radius a, length L, refractive index n, and tilt angle γ measured from broadside incidence (Fig. 1). Possible backscattered rays can be identified by finding their projections scattered at an angle of $\phi = 180°$ in the base plane. Three such rays are shown in Fig. 6. These comprise all the two-chord backscattered rays for the scattering situation in question. One such ray is confined to the meridional plane and appears to lie on the diameter of the circular base when projected onto the base plane. It is labeled as ray B in Fig. 6 and will be referred to as the axial ray. The two other rays, A and C, have nonzero impact parameter and are scattered with $\phi = 180°$ upon reflection from the far side of the cylinder in the meridional plane. Both rays travel along the same ray path, only in opposite directions. They will simply be referred to as the proper two-chord rays.

When the two-chord rainbow rays merge in the meridional plane at the critical tilt angle, when $n_{\text{eff}} = 2$, the proper two-chord rays merge with the axial ray. As they merge, the outgoing wave front flattens; the vanishing curvature of the wave front leads to the backscattering enhancement.[17] To model this evolution of the shape of the outgoing wave front

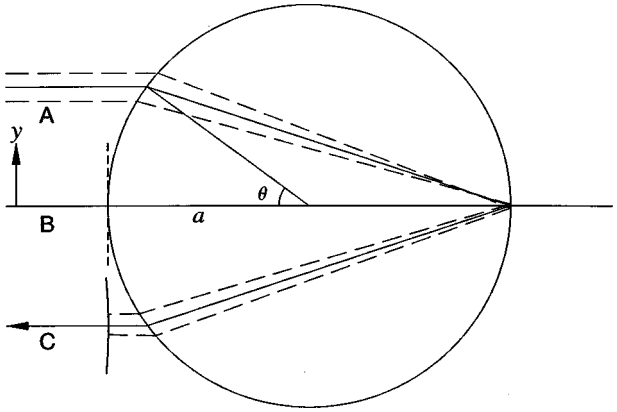

FIG. 6. The three two-chord backscattered rays as projected onto the base plane. Ray A, a proper two-chord ray, enters the cylinder with a projected angle of incidence, θ, and leaves with a negative wave front curvature along the y-axis, with wave front displacements measured relative to the short dashed line. Ray B, which enters the scatterer at an angle $\theta = 0°$, is called the axial ray. Ray C, the third two-chord ray, follows the path of ray A, only in the opposite direction.

as the effective index passes through $n_{\text{eff}} = 2$, we define a wave front shape function, W, which is the displacement of some specified wave front from a reference plane in space, called an exit plane. The displacement of the wave front defined by $W(x=0, y=0) = 0$ is measured relative to the short dashed line in Fig. 6. The shape of this wave front is given by the following function of y, where the y-axis is perpendicular to the incident rays shown in Fig. 6:

$$W(x=0, y) = a_4 y^4 - a_2 y^2, \tag{3}$$

where, a_4 and a_2 are given by (see Sec. 4.8 of Ref. 15)

$$a_4 \approx 2/a^3 n_{\text{eff}}^3 (2 + n_{\text{eff}}), \tag{4}$$

$$a_2 \approx (2 - n_{\text{eff}})/a n_{\text{eff}}. \tag{5}$$

These approximations become exact in the limit $n_{\text{eff}} \to 2$.

Figure 7 gives representative plots of this function near

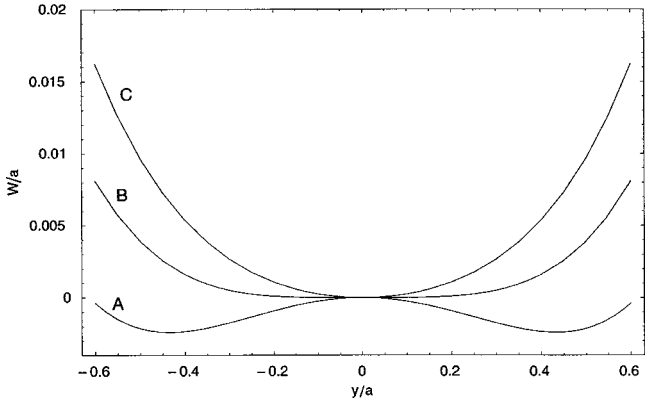

FIG. 7. Plots of a normalized wave front shape function W/a near the CMT condition $n_{\text{eff}} \approx 2$, shown as a function of y/a. Curve A gives the shape function for $n_{\text{eff}} = 1.95$. It has two minima, corresponding to the proper two-chord rays, and a local maximum at $y = 0$, corresponding to the axial ray. For curve B, $n_{\text{eff}} = 2$ exactly and $W \propto y^4$, so that the two minima in Curve A merge with the local maximum at $y = 0$. The wave front flattens, resulting in the CMT enhancement in the far-field backscattering direction. Curve C gives the shape function for $n_{\text{eff}} = 2.05$. In this case, the axial ray is the only remaining two-chord ray.

the critical tilt, $n_{\text{eff}} \approx 2$. For $n_{\text{eff}} \leqslant 2$, the wave front shape function has three extrema (curve A). The three two-chord backscattered rays run perpendicular to the wave front through these extremum points. As $n_{\text{eff}} \rightarrow 2$, the three extrema merge in the meridional plane and the curvature of the wave front at this point vanishes (curve B). This flattening of the wave front gives rise to the CMT backscattering enhancement in the far-field.

Once the three rays merge, they are confined to the meridional plane. Figure 3 shows a diagram of the backscattered rays in this plane. It is clear from this diagram that the pressure has a simple phase ramp along the *x*-coordinate parallel to the cylinder's axis, so that the shape function $W(x,y=0)$ is linear in x. We restrict our attention to rays which enter and leave the cylinder within a distance d from the cylinder's end, where d has the significance shown in Fig. 3 and is given by

$$d = 4a \tan \gamma / n_{\text{eff}}, \tag{6}$$

where $d \rightarrow 2a \tan \gamma$ as n_{eff} approaches 2. These rays suffer the least number of internal reflections in the cylinder. It should also be mentioned that all the ray paths shown in Fig. 3 are reversible and each path has the same phase delay with respect to the broadside reflection, including the same path length inside the cylinder, $2l$, where $l = 2an \sec \gamma / n_{\text{eff}}$. Figure 3 also contains information about the reflection and transmission coefficients which need to be calculated for the rays, to be discussed in more detail in Appendix D.

Knowing the coefficients and the shape of the backscattered wave front, as given by the function $W(x,y)$, we can propagate the outgoing wave to the far-field by evaluating a Rayleigh-Sommerfeld propagation integral as outlined in Appendix B. The result is the far-field backscattered pressure, p_{bs}. For finite scatterers, it is convenient to express this pressure in terms of a dimensionless form function, $f(ka,\gamma)$, defined by the following expression (and also in Ref. 1):

$$p_{bs} = p_{\text{inc}}(a/2r) f(ka,\gamma) e^{ikr}, \tag{7}$$

where p_{inc} is the amplitude of the incident plane wave and r is the distance from the scatterer to the far-field observation point. Under this definition for the form function, $f(ka,\gamma)$ is unimodular for the scattering of sound rays by a fixed-rigid sphere having the same radius, a, as that of the cylinder.

The derivation in Appendix B gives the following expression for the form function modulus at the critical tilt angle γ_c:

$$|f(ka,\gamma_c)| = (2/\pi)\Gamma(1/4)|B| \tan \gamma_c (ka \cos \gamma_c)^{3/4} e^{-2\alpha l k c/2\pi}. \tag{8}$$

This includes only the two-chord ray contributions, since other contributions are predicted to be much weaker when $ka \gg 1$. In this expression, $|B|$ is the magnitude of a product of reflection and transmission coefficients which were calculated as summarized in Appendix D. The exponential factor at the end takes into account the attenuation of the sound rays inside the cylinder, where α is the attenuation constant of the cylinder material. The far-field caustic results in the $(ka)^{3/4}$ scaling.

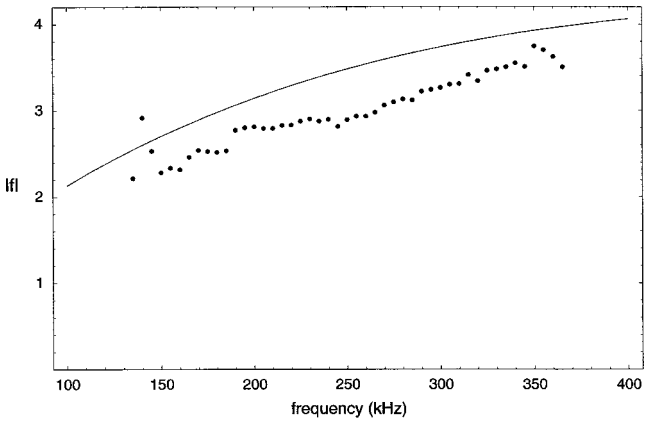

FIG. 8. The backscattering form function for the rubber cylinder at the critical tilt angle as a function of frequency, beginning with *ka* of 8. The solid points are experimentally determined form function amplitudes. The solid curve is the theoretical prediction given by Eq. (8).

III. COMPARISON OF RAY THEORY PREDICTIONS WITH EXPERIMENTAL MEASUREMENTS

According to Eq. (8), the backscattering form function at γ_c is a function of frequency through the parameter *ka*. In order to compare this theoretical result with experiment, backscattering measurements were done at varying frequencies using the rubber and polystyrene cylinders fixed at their respective critical tilt angles. The same experimental setup was used as described in Sec. I, except that a four panel 1–3 composite transducer (Material Systems, Inc.) was used because of its flat frequency response. One panel was used for sending sound signals and another one was used for receiving. The transducer was placed 290 cm from the cylinder so that far-field approximations are applicable. The transducer was driven using 10-cycle tone bursts. Time records of the backscattered tone bursts were recorded on a digital oscilloscope for frequencies in the range of 135–365 kHz at intervals of 5 kHz. The signal amplitudes were computed using a root-mean-square (rms) averaging scheme: the data were averaged over five cycles of the backscattered signal near the central part of the tone burst where it was determined that the signal had reached a steady state condition. Backscattered specular reflections from a stainless steel calibration sphere were used to convert the computed voltage amplitudes to a form function amplitude at each frequency, with the form function defined according to Eq. (7). A detailed discussion of the calibration technique can be found in Appendix B of Ref. 1.

The experimental values for the form function amplitudes were then plotted as a function of frequency as shown in Figs. 8 and 9. Figure 8 shows the plot for the rubber cylinder (RTV 615). The form function is plotted as a function of frequency in the range of 135–365 kHz, which for the rubber cylinder corresponds to a *ka* range of about 8–21. The individually plotted points are the experimental values. The solid curve plotted in the range of 100–400 kHz is the theoretical prediction given by Eq. (8). The theoretical curve is in general agreement with the experimental data. The experimental data points do form the same basic shape as the theoretical curve, though there does seem to be an offset be-

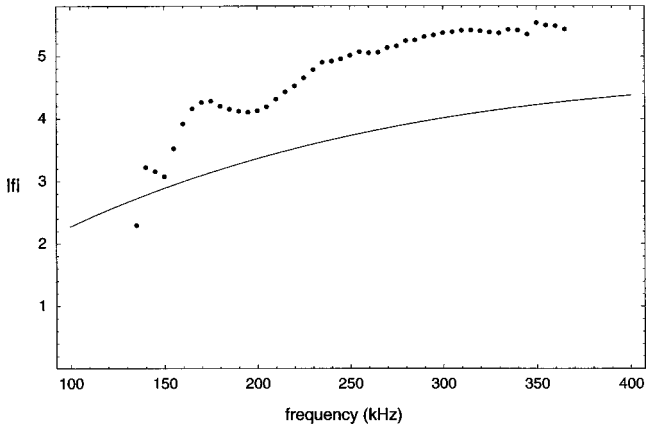

FIG. 9. Similar to Fig. 8, but for the polystyrene cylinder, beginning with *ka* of 9.

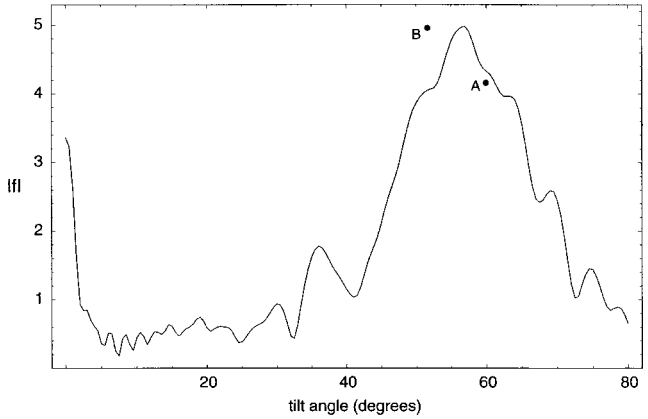

FIG. 10. The solid curve gives the experimentally determined backscattering form function for the polystyrene cylinder for a wide range of angles at a fixed frequency of 250 kHz. Point A is the theoretical form function amplitude at the critical angle, given by Eq. (8). Point B is a theoretical approximation for the amplitude and angular location of the peak value of the form function as a function of angle, as discussed at the end of Appendix B.

tween them, indicating a systematic error. This may be the result of an error in the value of the product of coefficients, $|B|$, due to the uncertainty in the material parameters of the rubber. There may also be a significant error in the exponential factor in Eq. (8), which takes into account the sound attenuation. This is because the value for the attenuation coefficient in the rubber was not directly available from literature, and was inferred from insertion loss data.[18]

Figure 9 shows a similar plot for the polystyrene cylinder. The form function is plotted as a function of frequency in the range of 135–365 kHz, which for the polystyrene cylinder corresponds to a *ka* range of about 9–25. Again, the plotted points are the experimental values and the solid curve is the theoretical prediction. There is also some general agreement between the theoretical and experimental curves for the polystyrene, though an offset between them is evident here as well. This may be due to the uncertainty in the material parameters which have a significant effect on $|B|$ for polystyrene.

It should be restated that Figs. 8 and 9 show plots of the backscattered form function only at the predicted critical tilt angle γ_c. We were also interested in how the theoretical form function amplitude compares with the experimental values for a wide range of tilt angles. The raw data from the backscattered time records for polystyrene, which are displayed in Fig. 4, were used to compute experimental form function amplitudes utilizing the rms averaging and calibration techniques already mentioned. A plot of the experimental form function values as a function of tilt angle is given by the solid curve in Fig. 10. Figure 10 also has two individually plotted points. Point A gives the theoretical value of the backscattering form function plotted at the critical tilt γ_c, as given by Eq. (8). Point B gives a theoretical value for the form function plotted at a tilt angle, γ_m, which is an approximate predicted location of the maximum of the form function angle scan. Due to diffraction, the largest enhancement does not occur at the critical tilt angle but at a slightly smaller angle, as explained in Appendix B.

IV. DISCUSSION

The cascade plots of Figs. 4 and 5 clearly show that there can be large backscattering enhancements from finite plastic and rubber cylinders at large tilt angles. This can be useful in sonar applications where it is desirable to detect low impedance cylindrical targets tilted at oblique angles with respect to the source. To substantiate the claim that these enhancements are due to CMT, a ray theoretic backscattering form function was calculated and compared with the values computed from experimental data. In Figs. 8 and 9, they are compared as a function of frequency. The agreement between theory and experiment in these plots is good considering the uncertainty in our knowledge of the material parameters of the cylinder and the uncertainties involved in the experiment, as well as the low *ka* values at which we are applying our ray theory. What should be emphasized is that our ray model does at least predict the right order of magnitude for the form function amplitude. One should also note from our experiments that the CMT effect exists even at low *ka* (*ka* as small as 8), so that the effect is not severely restricted to high frequencies where attenuation effects might start to dominate. From the measurements, $\log(|f|/(ka)^{3/4})$ is approximately linear in *ka* with the slope indicative of the material absorption. In Fig. 10, the form function was plotted as a function of tilt angle. There appears to be better agreement between theory and experiment as compared to the frequency scan in Fig. 9 obtained in a different series of experiments. This may be a consequence of a variation in water temperature between experimental runs. The frequency range and target dimensions would make it difficult to obtain independent measurements of the material parameters for these targets. The theoretical values for form function amplitudes vary significantly within the range of literature values for the material parameters of polymer plastics and rubbers. Thus, the quality of the agreement we find between theory and experiment in Fig. 10 may be fortuitous, though the results shown in Figs. 4, 5, 8, and 9 leave no doubt as to the existence of the CMT enhancement. Other contributions to backscattering associated with external reflection from the cylinder are only present for tilts close to 0° as can be seen by inspection of Figs. 4 and 5. This is in general agreement with predictions.[19,20]

As an additional test of the correctness of our models, related ray theory predictions were compared with computed wave theory predictions. Such a test is insensitive to uncertainties in material parameters and need not include attenuation effects. A ray theory far-field scattering amplitude in the specular direction was calculated for the case of plane wave scattering by an *infinite* elastic cylinder at the critical tilt angle, as summarized in Appendix C. This was compared with a numerical partial wave series solution, which was modified so as to subtract off a background due to specular reflection. The two theoretical results are plotted together in Fig. C1 for the case of the rubber (RTV 615) cylinder in water. The agreement between the two predictions is excellent for the broad trend. There was less agreement under this computational test for the polystyrene cylinder, though there is evidence that the ray model and partial wave series results slowly converge to each other at large *ka*.

ACKNOWLEDGMENT

This work was supported by the Office of Naval Research.

APPENDIX A: DERIVATION OF THE BRAVAIS LAW OF REFRACTION

Using a simple ray analysis, we can derive the expression for the Bravais effective refractive index in Eq. (1). We begin by considering a ray incident on a cylinder of refractive index n, and tilt angle γ as shown in Fig. 1. The incident wave vector, $\mathbf{k}$, has magnitude $|\mathbf{k}|=k$; and if the tilt angle γ is measured from broadside incidence, the projection of the wave vector along the direction of the cylinder's axis (the x-coordinate in Fig. 1) has magnitude

$$k_x = k \sin\gamma. \tag{A1}$$

The projection of the wave vector in the base plane gives back the original wave vector, $\mathbf{k}$, when added to the x-component. Therefore, it must have magnitude

$$k_b = k \cos\gamma. \tag{A2}$$

Note in passing that the results of Eqs. (A1) and (A2) will be used to compute phase changes along projected ray paths in Appendix B.

The transmitted wave vector in the cylinder, $\mathbf{k}'$, has magnitude $|\mathbf{k}'|=k'=kn$. Its direction can be determined by matching the components of the transmitted wave vector with those of the incident wave vector on the cylinder's surface. One set of components is given by the x-components. Setting the x-component of the transmitted wave vector, k_x', equal to that of the incident wave vector, k_x, in Eq. (A1) gives us $k_x'=k\sin\gamma$. The other set of components lies in the base plane and tangent to the cylinder. Since the projections of the rays in the base plane obey the effective Snell's law, with effective refractive index n_{eff}, we can immediately write down the magnitude of the component of the transmitted wave vector in the base plane, k_b', as the product of the magnitude of the incident wave vector component in the base plane [Eq. (A2)] and the effective index in the base plane n_{eff}: $k_b'=k_b n_{\text{eff}}=kn_{\text{eff}}\cos\gamma$.

Adding these two components of the transmitted wave vector in quadrature yields, by the Pythagorean theorem, the squared magnitude of $\mathbf{k}'$: $(k_x')^2+(k_b')^2=|\mathbf{k}'|^2=k^2n^2$. Substituting in our expressions for k_x' and k_b' gives

$$k^2\sin^2\gamma + k^2 n_{\text{eff}}^2 \cos^2\gamma = k^2 n^2. \tag{A3}$$

Solving Eq. (A3) for n_{eff}, gives Eq. (1).

APPENDIX B: BACKSCATTERING FORM FUNCTION MAGNITUDE AT THE CRITICAL TILT ANGLE

In this Appendix, we derive the expression for the form function of a finite penetrable cylinder for the two-chord backscattering contribution given by Eq. (8) and evaluated at the critical tilt angle γ_c. Figure 3 shows the ray diagram for the backscattered rays in the meridional plane. A coordinate system is defined as indicated by the axes set shown in the upper-right-hand corner. The origin is located in the meridional plane on the far end of the cylinder at the corner nearest to the source. The plane tangent to the cylinder and perpendicular to the meridional plane on the near side of the cylinder will be referred to as the exit plane (the x-y plane). The far-field backscattered pressure is calculated by evaluating a Rayleigh-Sommerfeld propagation integral[21] in the exit plane,

$$p_{bs} = (-ik\cos\gamma/2\pi r)\int\int_{-\infty}^{\infty} dx'dy' p(x',y') e^{ikr'}. \tag{B1}$$

This is a simplified version of the formula for far-field scattering by finite objects. In this expression, $r=(x^2+y^2+z^2)^{1/2}$ is the distance from the origin to the backscattering observation point, and $r'=[(x-x')^2+(y-y')^2+z^2]^{1/2}$ is the distance from the observation point to a source point in the exit plane. From Fig. 3, we can infer that $x=-r\sin\gamma$, $y=0$, $z=r\cos\gamma$. Inserting this into our expression for r' gives $r'\approx r+x'\sin\gamma$ for large r.

To calculate a backscattering amplitude due to the two-chord ray contribution at the critical tilt, we need to know the corresponding outgoing pressure in the exit plane. Much of the information about the outgoing pressure wave was already provided in Sec. II. Equation (3) gives the shape of the wave front as seen in the base plane (see Fig. 7). To convert the shape function W to a phase function, φ, we must multiply it by the wave number projected onto the base plane, $k_b=k\cos\gamma$, as given by Eq. (A2). At the critical tilt where $n_{\text{eff}}=2$, the coefficients of the shape function W reduce to: $a_2\to 0$ and $a_4\to a/(2a)^4$, according to Eqs. (4) and (5); and the phase, φ, as a function of y becomes

$$\varphi(x=0,y) = (ka\cos\gamma_c) y^4/(2a)^4. \tag{B2}$$

It was determined in Sec. II that the phase of the outgoing wave depends linearly on x, the coordinate running parallel to the cylinder's axis. The proportionality constant in the phase is given by the magnitude of the projection of the incident wave vector onto the x-axis, $k_x=k\sin\gamma$, as given by Eq. (A1). Thus, the phase of the outgoing wave as a function of x is

$$\varphi(x,y=0) = -kx\sin\gamma; \quad -d\leqslant x\leqslant 0. \tag{B3}$$

The negative sign takes into account the fact that the x-component of the wave vector reverses direction upon reflection from the cylinder's end. Furthermore, Eq. (B3) only holds within a distance d from the cylinder's end as discussed earlier in Sec. II. Equations (B2) and (B3) addictively combine to give the approximate phase as both a function of x and y,

$$\varphi(x,y) \approx -kx \sin\gamma_c + (ka\cos\gamma_c)y^4/(2a)^4. \tag{B4}$$

Here, the phase has been evaluated at the critical tilt γ_c.

Besides the phase, knowledge of the amplitude of the outgoing wave is needed. The amplitude of the incident wave is given by p_{inc}. This initial amplitude is reduced by a product of reflection and transmission coefficients. The magnitude of this product is given by $|B|$. There may also be attenuation along ray paths inside the cylinder. The attenuation coefficient is $\alpha(kc/2\pi)$, where α is the attenuation constant of the material given in Table I, and where $(kc/2\pi)$ is an expression for the frequency. The length of the ray paths inside the cylinder is $2l$, where $l = an\sec\gamma_c$ for $n_{\text{eff}}=2$. Thus, the initial amplitude is also reduced by the factor $e^{-2\alpha l(kc/2\pi)}$. In general, the outgoing amplitude may also be reduced relative to the incoming amplitude by wave front spreading, but this does not occur for the caustic rays focused at infinity. Therefore, the incoming wave amplitude is only modified by the product of coefficients and the attenuation factor. Combining the amplitude and phase expressions, the outgoing pressure in the exit plane due to the two-chord backscattering contribution is given by

$$\begin{aligned} p(x',y') &= p_{\text{inc}}|B|e^{i[\varphi(x',y')+\varphi_0]}e^{-2\alpha l(kc/2\pi)} \\ &= p' e^{i\varphi(x',y')}, \quad -d \leqslant x \leqslant 0, \end{aligned} \tag{B5}$$

where $p' = p_{\text{inc}}|B|e^{i\varphi_0}e^{-2\alpha l(kc/2\pi)}$ and φ_0 is a phase shift resulting from propagation through the cylinder. Outside the region $-d \leqslant x \leqslant 0$, it should be understood that $p'=0$.

Inserting Eq. (B5) into Eq. (B1), we obtain

$$p_{bs} = (-ik\cos\gamma/2\pi r)\int\int_{-\infty}^{\infty} dx'\,dy'\,p' e^{i\varphi(x',y')}e^{ikr'}. \tag{B6}$$

Using the far-field approximation $r' \approx r + x'\sin\gamma$, the x' dependence drops out of the phase of the integrand so that Eq. (B6) becomes

$$\begin{aligned} p_{bs} = (-ik\cos\gamma_c e^{ikr}/2\pi r)&\int_{-d}^{0} dx' \int_{-\infty}^{\infty} dy'\,p' \\ &\times \exp[i(ka\cos\gamma_c)y'^4/(2a)^4], \end{aligned} \tag{B7}$$

where we have evaluated p_{bs} at the critical tilt. The integral over x' is trivial, giving

$$\begin{aligned} p_{bs} = (-ip'kd\cos\gamma_c e^{ikr}/2\pi r)&\int_{-\infty}^{\infty} dy' \\ &\times \exp[i(ka\cos\gamma_c)y'^4/(2a)^4], \end{aligned} \tag{B8}$$

where p' has been approximated by its value at $y'=0$ and taken outside the y' integral. Using the Pearcey function, $P_{\pm}(w_1,w_2)$, defined as[22,23]

$$P_{\pm}(w_1,w_2) = \int_{-\infty}^{\infty} ds \exp[\pm i(s^4 + w_2 s^2 + w_1 s)], \tag{B9}$$

the y' integral can be expressed as a Pearcey function of zero argument, where $w_1=0$, $w_2=0$. From contour integral methods and the definition of the gamma function, it is known[22] that $|P_{\pm}(0,0)| = (1/2)\Gamma(1/4)$. Using this result, Eq. (B8) becomes

$$p_{bs} = -ip'\Gamma(1/4)d(ka\cos\gamma_c)^{3/4}e^{ikr}/2\pi r. \tag{B10}$$

Finally, we insert the expression for d from Eq. (6) evaluated at $n_{\text{eff}}=2$ as well as the expression for p'. Taking the absolute value of Eq. (B10) and using Eq. (7), yields Eq. (8): the magnitude of the backscattering form function contribution due to the two-chord class of rays evaluated at the critical tilt.

To conclude this Appendix, the method for calculating the maximum in the angle scan of Fig. 10 will now be discussed. As mentioned in Sec. III, the peak in the backscattering amplitude of finite cylinders is not expected to occur precisely at the critical tilt angle, γ_c, but at a slightly smaller tilt angle γ_m. This is a result of the fact that the maximum in the Pearcey function as a function of w_2 does not occur at $w_2=0$ but at a somewhat smaller value: $w_2=-2.2$.[22] To find the magnitude of the backscattering peak, the y' integral in Eq. (B8) will have to be reevaluated. Writing the phase as a function of y' in the more generic form $\varphi(x'=0,y') = ka\cos\gamma W(x'=0,y')$, Eq. (B8) can be rewritten as

$$\begin{aligned} p_{bs} = (-ip'kd\cos\gamma e^{ikr}/2\pi r)&\int_{-\infty}^{\infty} dy' \\ &\times \exp[i(ka\cos\gamma)W(x'=0,y')], \end{aligned} \tag{B11}$$

where the wave front shape function, W, at $\gamma_m \neq \gamma_c$ has three extrema, as shown by curve A in Fig. 7. This indicates that the axial ray and the proper two-chord rays are now separate. The y' integral in Eq. (B11) can also be expressed in terms of a Pearcey function. Evaluated at its maximum, corresponding to $\gamma=\gamma_m$, the Pearcey function is larger by a factor of about 1.456 as compared to its value at zero argument.[22] Multiplying the expression for p_{bs} at the critical angle, γ_c, [Eq. (B10)] by the factor of 1.456 and reevaluating the factor p' at the angle γ_m, then gives us an approximate value for the magnitude of the backscattered pressure at the maximum in the angle scan.

Finally, we discuss how the value for the angle corresponding to the maximum amplitude itself, γ_m, was calculated. Combining Eq. (3) with Eqs. (4) and (5), we can reconstruct the general form of the wave front shape function as a function of y,

$$\begin{aligned} W(x=0,y) = &[2/a^3 n_{\text{eff}}^3(2+n_{\text{eff}})]y^4 \\ &-[(2-n_{\text{eff}})/an_{\text{eff}}]y^2. \end{aligned} \tag{B12}$$

To write the y-integral of Eq. (B11) in Pearcey function form, define an integration variable $s = [2/a^3 n_{\text{eff}}^3(2+n_{\text{eff}})]^{1/4}y$. Then, Eq. (B12) becomes

$$W(s) = s^4 - [[(2-n_{\text{eff}})/an_{\text{eff}}]/[2/a^3 n_{\text{eff}}^3(2+n_{\text{eff}})]^{1/2}]s^2. \tag{B13}$$

Comparing this expression with the exponent of the integrand in Eq. (B9), the defining equation for the Pearcey function, we find that we can make the identification,

$$w_2 = -(ka\cos\gamma)^{1/2}[[(2-n_{\text{eff}})/n_{\text{eff}}]/[2/n_{\text{eff}}^3(2+n_{\text{eff}})]^{1/2}]. \tag{B14}$$

Expand this expression in a Taylor series around the critical tilt angle $\gamma=\gamma_c: w_2(\gamma)\approx[(dw_2/d\gamma)(\gamma_c)](\gamma-\gamma_c)$, where $[(dw_2/d\gamma)(\gamma_c)]=(ka\cos\gamma_c)^{1/2}[[(dn_{\text{eff}}/d\gamma)(\gamma_c)]/n_{\text{eff}}]/[2/n_{\text{eff}}^3(2+n_{\text{eff}})]^{1/2}]$, and where one can easily show $[(dn_{\text{eff}}/d\gamma)(\gamma)]=\tan\gamma(n_{\text{eff}}-1/n_{\text{eff}})$ using Eq. (1). Evaluating functions at the critical tilt where indicated, we find

$$w_2(\gamma)\approx 3(ka\cos\gamma_c)^{1/2}\tan\gamma_c(\gamma-\gamma_c). \tag{B15}$$

Finally, setting $w_2(\gamma_m)=-2.2$ gives us an equation for the angle shift of the peak in the backscattering angle scan away from the critical angle,

$$(\gamma_m-\gamma_c)\approx -2.2/[3(ka\cos\gamma_c)^{1/2}\tan\gamma_c]. \tag{B16}$$

Using Eq. (B16), the angle corresponding to the maximum backscattering amplitude in Fig. 10, as indicated by Point B, is approximated to be $\gamma_m\approx 54°$ for $ka=17$. Here, the Taylor expansion of $w_2(\gamma)$ out to first order in $(\gamma_m-\gamma_c)$ is only a rough approximation since the quantity $(\gamma_m-\gamma_c)$ is appreciable at low frequencies. This may account for the overestimation in the angle shift apparent in Fig. 10.

APPENDIX C: NUMERICAL COMPARISON OF RAY THEORY WITH PARTIAL WAVE SERIES SOLUTION FOR AN INFINITE CYLINDER

The ray theory prediction for scattering at the critical tilt angle was tested against a numerical partial wave series solution. Since an exact solution for the scattering by a finite cylinder is unavailable, the ray theory and the partial wave series solution were compared for the case of a plane wave obliquely incident on an infinitely long elastic cylinder. Since the cylinder is infinite and has no truncation, there will be no CMT effect in the backscattering direction. Instead, the two-chord CMT contribution in the specular direction was considered.[8,9] The outline for the ray solution to the problem is analogous to the discussion given in Sec. II and Appendix B.

For the problem of the infinite cylinder, the form function is defined as[2]

$$p_{\text{spe}}=p_{\text{inc}}(a/2r)^{1/2}f(ka,\gamma)e^{ik\cos\gamma r}, \tag{C1}$$

where r is now the distance from the observation point to the cylinder's axis, rather than the distance to any particular origin. The pressure symbol is subscripted with ''spe'' to indicate our interest in the pressure in the specular direction as opposed to the backscattering direction. The ray theoretic form function in the specular direction at the critical tilt angle due to the two-chord CMT is given by

$$|f(ka,\gamma_c)|=[\Gamma(1/4)/\pi]|B|(ka\cos\gamma_c)^{1/4}, \tag{C2}$$

where for simplicity no absorption factor is included and attenuation effects were neglected in the infinite cylinder partial wave series.[2] Only the ray contribution from the first internal reflection is included in Eq. (C2). The subsequent reflections produce curved wave fronts which give much weaker contributions that fail to increase in proportion to $(ka)^{1/4}$. The product of coefficients, $|B|$, is discussed in Appendix D. The numerical value of the complex f from the partial wave series solution was computed. A background was subtracted off from f to remove interfering contributions from the direct specular reflection. Figure C1 shows a comparison of the ray theory with the background-subtracted solution using the material parameters of silicone rubber (RTV 615), neglecting absorption. The solid curve gives the partial wave series solution while the dashed curve is Eq. (C2). For the case of rubber, the ray theory seems to rapidly converge to the partial wave series solution at moderately low ka. In general, good agreement between the ray theories and wave theories is found for fluidlike material parameters.

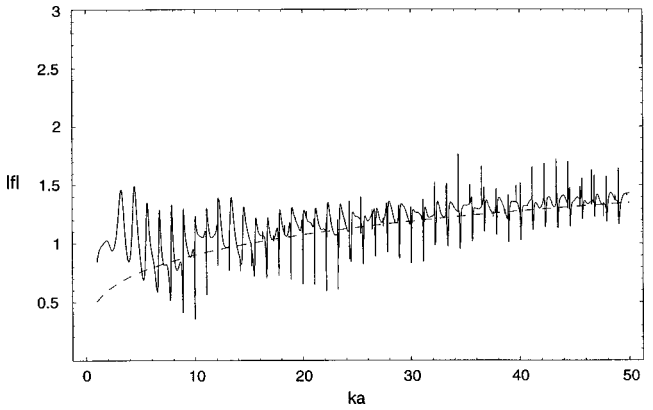

FIG. C1. Plot of the form function at the critical tilt angle of 57.25° in the far-field specular direction for an infinite RTV 615 rubber cylinder, neglecting attenuation and using a shear speed value of 0.005 mm/μs. The solid curve is a numerical partial wave series result, as discussed in Appendix C. The dashed curve is the ray theoretic result given by Eq. (C2), which describes the most significant scattering contribution while omitting the fine structure. The significance of the CMT scattering enhancement is evident by comparing the magnitude of the dashed curve with the magnitude of the specular contribution, $|f_{\text{specular}}|=0.32$, at large ka.

APPENDIX D: THE PRODUCT OF REFLECTION AND TRANSMISSION COEFFICIENTS $|B|$

Consider first, the finite cylinder. Figure 3 indicates the reflection and transmission coefficients needed for the CMT backscattering problem. Rays are transmitted into the cylinder, undergo two internal reflections, one on the opposite side of the cylinder and one on the cylinder truncation, and then are finally transmitted back into the surrounding water. For the polystyrene cylinder, the relevant rays inside the cylinder are the shear rays. Thus, the product of plane surface amplitude coefficients, $|B|$, takes on the following form:

$$|B|=|T_{WS}|\,|R_{SS1}|\,|R_{SS2}|\,|T_{SW}|. \tag{D1}$$

Here, T_{WS} is the transmission coefficient for a sound ray in water converted to a shear ray in the polystyrene cylinder. The coefficient is evaluated at an angle of incidence equal to the critical angle γ_c. The angle of refraction is given by Snell's law, with the index now being the actual index of refraction of the cylinder $n=c/c_s$, where c_s is the shear speed of polystyrene. R_{SS1} is the reflection coefficient of the first internal reflection of the shear ray, evaluated at an angle

of reflection equal to the aforementioned angle of refraction. R_{SS2} is the reflection coefficient of the second internal reflection evaluated at an angle of reflection which complements the angle of reflection corresponding to the coefficient R_{SS1}. Finally, T_{SW} is the transmission coefficient for the shear ray conversion back into a longitudinal wave in water. The reflection and transmission coefficients are given by the square roots of Knott's energy coefficients.[24] These coefficients can also be found in the Appendix of Ref. 25. Evaluating Eq. (D1) for rays in the meridional plane yields the result $|B| = 0.2567$.

For the silicone rubber cylinder (RTV 615), the relevant rays inside the cylinder are the longitudinal rays. Thus, the product of coefficients, $|B|$, takes on the form

$$|B| = |T_{WL}|\,|R_{LL1}|\,|R_{LL2}|\,|T_{LW}|, \tag{D2}$$

where subscripts L denote longitudinal waves and the refraction angle is given by Snell's law with $n = c/c_l$, where c_l is the longitudinal wave speed of the rubber. Evaluation of Eq. (D2) gives $|B| = 0.2897$ at $\gamma = \gamma_c$.

The product of coefficients $|B|$ is slightly different for the infinite cylinder problem. There is no longer a second internal reflection off a cylinder truncation, and the angle of incidence for the one internal reflection is the angle of refraction at the first interface. Thus, for the case of an infinite polystyrene cylinder, the product of coefficients becomes $|B| = |T_{WS}|\,|R_{SS1}|\,|T_{SW}| = 0.2854$, and in the rubber case, it becomes $|B| = |T_{WL}|\,|R_{LL1}|\,|T_{LW}| = 0.2897$.

[1] K. Gipson and P. L. Marston, ''Backscattering enhancements due to reflection of meridional leaky Rayleigh waves at the blunt truncation of a tilted solid cylinder in water: Observations and theory,'' J. Acoust. Soc. Am. **106**, 1673–1680 (1999).

[2] P. L. Marston, ''Approximate meridional leaky ray amplitudes for tilted cylinders: End-backscattering enhancements and comparisons with exact theory for infinite solid cylinders,'' J. Acoust. Soc. Am. **102**, 358–369 (1997); **103**, 2236 (1998).

[3] G. Kaduchak, C. M. Wassmuth, and C. M. Loeffler, ''Elastic wave contributions in high-resolution acoustic images of fluid-filled, finite cylindrical shells in water,'' J. Acoust. Soc. Am. **100**, 64–71 (1996).

[4] S. F. Morse, P. L. Marston, and G. Kaduchak, ''High-frequency backscattering enhancements by thick finite cylindrical shells in water at oblique incidence: Experiments, interpretation, and calculations,'' J. Acoust. Soc. Am. **103**, 785–794 (1998).

[5] F. Padilla, M. de Billy, and G. Quentin, ''Theoretical and experimental studies of surface waves on solid-fluid interfaces when the value of the fluid sound velocity is located between the shear and longitudinal ones in the solid,'' J. Acoust. Soc. Am. **106**, 666–673 (1999); B. T. Hefner and P. L. Marston, ''Backscattering enhancements associated with subsonic Rayleigh waves on polymer spheres in water: Observation and modeling for acrylic spheres,'' *ibid* (submitted).

[6] W. P. Mason, ''Acoustic properties of solids'' in *American Institute of Physics Handbook*, 3rd ed., edited by D. E. Gray (McGraw-Hill, New York, 1972), Sec. 3, p. 104.

[7] B. Hartmann, ''Acoustic properties,'' in *Physical Properties of Polymers Handbook*, edited by J. E. Mark (AIP, Woodbury, NY, 1996), Part IX, Chap. 49, pp. 677–686.

[8] P. L. Marston, ''Descartes glare points in scattering by icicles: Color photographs and a tilted dielectric cylinder model of caustic and glare-point evolution,'' Appl. Opt. **37**, 1551–1556 (1998).

[9] C. M. Mount, D. B. Thiessen, and P. L. Marston, ''Scattering observations for tilted transparent fibers: Evolution of Airy caustics with cylinder tilt and the caustic merging transition,'' Appl. Opt. **37**, 1534–1539 (1998).

[10] J. A. Lock and C. L. Adler, ''Debye-series analysis of the first-order rainbow produced in scattering of a diagonally incident plane wave by a circular cylinder,'' J. Opt. Soc. Am. **14**, 1316–1328 (1997).

[11] C. L. Adler, J. A. Lock, B. R. Stone, and C. J. Garcia, ''High-order interior caustics produced in scattering of a diagonally incident plane wave by a circular cylinder,'' J. Opt. Soc. Am. **14**, 1305–1315 (1997).

[12] W. J. Humphreys, *Physics of the Air* (Dover, New York, 1964), pp. 476–506.

[13] R. A. R. Tricker, *Introduction to Meteorological Optics* (American Elsevier, New York, 1970).

[14] H. M. Nussenzveig, *Diffraction Effects in Semiclassical Scattering* (Cambridge University Press, Cambridge, 1992).

[15] P. L. Marston, ''Geometrical and catastrophe optics methods in scattering,'' in *Physical Acoustics*, edited by A. D. Pierce and R. N. Thurston (Academic, Boston, 1992), Vol. 21, pp. 1–234.

[16] N. Lagakos, J. Jarzynski, J. H. Cole, and J. A. Bucaro, ''Frequency and temperature dependence of elastic moduli of polymers,'' J. Appl. Phys. **59**, 4017–4031 (1986).

[17] See Sec. 4.8 of Ref. 15.

[18] D. L. Folds, ''Speed of sound and transmission loss in silicone rubbers at ultrasonic frequencies,'' J. Acoust. Soc. Am. **56**, 1295–1296 (1974).

[19] T. K. Stanton, ''Sound scattering by cylinders of finite length. I. Fluid cylinders,'' J. Acoust. Soc. Am. **83**, 55–63 (1988).

[20] See Sec 2.12 of Ref. 15, pp. 34–37.

[21] See Sec. 2.1 of Ref. 15, Eq. (6).

[22] See Sec. 3.2 of Ref. 15, pp. 71–73.

[23] C. K. Frederickson and P. L. Marston, ''Transverse cusp diffraction catastrophes produced by the reflection of ultrasonic tone bursts from a curved surface in water: Observations,'' J. Acoust. Soc. Am. **92**, 2869–2877 (1992).

[24] G. B. Young and L. W. Braile, ''A computer program for the application of Zoeppritz's amplitude equations and Knott's energy equations,'' Bull. Seismol. Soc. Am. **66**, 1881–1885 (1976).

[25] K. L. Williams and P. L. Marston, ''Mixed-mode acoustical glory scattering from a large elastic sphere: Model and experimental verification,'' J. Acoust. Soc. Am. **76**, 1555–1563 (1984). In Eq. (A9), t_{LS} should be t_{LW}. In Eq. (A10), D^{-1} should have been printed as D. In Eq. (A12), $-c_s^2$ should be $+c_s^2$; and in Eq. (A14), $+Z_W$ should be $-Z_W$.

[26] I. A. Viktorov, ''Damping of surface and spatial ultrasonic waves,'' Sov. Phys. Acoust. **10**, 91–92 (1964).

Acoustic scattering by a modified Werner method

Patrice Ravel[a)]
ISTIV, Modélisation Numérique et Couplage, Avenue Georges Pompidou, 83162 La Valette du Var, France

Ahmed Trad[b)]
Laboratoire de Modélisation en Mécanique des structures, URA 1776, Université Paris 6, Tour 66, 4 place Jussieu, 75252 Paris cédex 05, France

(Received 21 July 1998; revised 26 July 1999; accepted 1 October 1999)

A modified integral Werner method is used to calculate pressure scattered by an axisymmetric body immersed in a perfect and compressible fluid subject to a harmonic acoustic field. This integral representation is built as the sum of a potential of a simple layer and a potential of volume. It is equivalent to the exterior Helmholtz problem with Neumann boundary condition for all real wave numbers of the incident acoustic field. For elastic structure scattering problems, the modified Werner method is coupled with an elastodynamic integral formulation in order to account for the elastic contribution of the displacement field at the fluid/structure interface. The resulting system of integral equations is solved by the collocation method with a quadratic interpolation. The introduction of a weighting factor in the modified Werner method decreases the number of volume elements necessary for a good convergence of results. This approach becomes very competitive when it is compared with other integral methods that are valid for all wave numbers. A numerical comparison with an experiment on a tungsten carbide end-capped cylinder allows a glimpse of the interesting possibilities for using the coupling of the modified Werner method and the integral elastodynamic equation used in this research.
[S0001-4966(00)04501-X]

PACS numbers: 43.20.Fn, 43.20.Bi, 43.20.Gp, 43.20.Rz [ANN]

INTRODUCTION

The purpose of this article is the numerical study of acoustic scattering by rigid or elastic structures by a modified integral Werner method. Acoustic scattering can be modeled by the Helmholtz partial derivative equation with Neumann boundary condition.

At low and medium frequencies, integral methods are often used to transform the exterior Neumann problem. The advantage of these methods is to restore the problem from one of an unbounded area to a problem in which the bounded support is, in general, the surface of the soundproof object.

Nevertheless, this reduction is not without drawbacks. Mathematical difficulties appear. Most of the integral operators intervening in the different formulations are singular. Moreover, representations using either an indirect representation constructed with the aid of a potential simple layer or a potential double layer or using a direct Helmholtz type integral formulation are not valid for all wave numbers of incident acoustic fields.[1,2] These wave numbers, called irregular wave numbers, are the eigenvalues of a Dirichlet interior problem for which there is no uniqueness.

Numerous studies were carried out on the problems of irregular wave numbers and a synopsis of studies prior to 1983 appears in the book by Kolton and Kress.[3]

In our point of view, we may distinguish two large families of integral methods to resolve the problem of the irregular wave numbers.

The first family uses, in most cases, techniques of overdetermination of Helmholtz's surface integral equation.

Schenck's method[2] consists in increasing the number of equations through Helmholtz's interior representation. Nevertheless, when a computational node appearing in the Helmholtz interior representation coincides with a nodal surface of a structure, the rectangular system obtained is very poorly conditioned. Numerous improvements[4,5] complicating the use of Schenck's method consisted, for example, in increasing the number of supplementary equations to take the derivatives of order n of the Helmholtz interior representation.

Piaszczyk and Klosner[6] use Helmholtz's integral exterior representation to overdetermine Helmholtz's integral surface equation. The problem of nodal surfaces no longer exists, but the convergence of iterative processes permitting the calculation of pressure is numerically slower and more costly in the number of operations than Schenck's method.

Null field equations[7] form a countable set of equations obtained from the Helmholtz equation decomposed on an orthogonal basis of L^2 spherical waves. Jones[8] and Stupfel *et al.*,[9] for axisymmetric structures, define a criterion for overdetermining Helmholtz's integral surface equation with the help of a finite number of null field equations. This method remains relatively complex to be carried out numerically.

The T matrix method[10] uses a truncation of the set of equations obtained starting this time from the exterior representation of Helmholtz. This method is relatively sensitive to the eccentricity of the bodies studied according to the basis of chosen decomposition.

The number of supplementary equations for all these

a)Electronic mail: ravel@balard.pharma.univ-montp1.fr
b)Electronic mail: trad@ccr.jussieu.fr

methods increases as the wavelength of the incident field decreases.

The second family contains integral methods constructed with the help of indirect integral formulations. Their principle is to define an extension ending in a solvable interior problem. Most of these methods start from the work of Brakhage and Werner[11] who constructed a solvable integral representation for the exterior Dirichlet problem.

Burton and Miller[12] and then Filippi[13] represent the solution of the problem as a linear combination of a single-layer and double-layer potential with a particular condition on the coefficients of the combination in order to obtain uniqueness.

The major inconvenience of the Burton–Miller method is the hyper-singular kernel of the integral equation. Treating the kernel has been undertaken by numerous authors. The most precise works[14,15] consist in using a regularization of the integral equation through Laplace's equation.

The Hwang and Chang[16] modification of the Burton–Miller method makes possible the use of an arbitrary surface in the interior of the structure. The unknown of the problem is no longer defined on the singular surface of the structure, which eliminates numeric singularities.

Another variation is the coupled Helmholtz integrals (CHI) method of Fahnline and Koopman.[17] It uses a linear combination of Helmholtz's integral surface equation with a gradient of Helmholtz's integral interior representation instead of Helmholtz's integral surface representation. This technique has the advantage of removing the hyper-singular integrals since the computational nodes are taken from the interior of the structure.

Hamdi[18] introduced into the interior of the field of integration a surface on which an adequate boundary condition is defined. Pressure is equally decomposed as a sum of a potential of single and double layers, but with different densities. Hamdi's method is resolved with the help of a variational formulation that decreases the singularity of the hyper-singular kernel.[19]

These methods remain, nevertheless, sensitive to the choice of the different parameters that compose them and have been validated for relatively weak wave numbers ($ka < 15$).

The Werner decomposition[20] is a valid method whatever the number of real wave numbers of the incident waves. It consists in writing the solution of the scattering problem as the sum of a surface potential and a volume potential.

A modification of the Werner method[21] consists in choosing an arbitrary and simple volume B inside the structure instead of the total volume as in the Werner method. With this modification, the following results are obtained:

(i) The removal of part of the singular integrals and
(ii) The simplification of the numeric treatment of certain elementary matrices

Nevertheless, the introduction of a volume inside the structure necessitates an important number of finite elements in order to ensure a convergence of satisfactory results. A weighting factor, introduced by Ravel,[22] overcame this handicap and optimized the method.

The modified Werner integral method was applied to the study of diffraction and acoustic radiation of axisymmetric structures for all real wave numbers of the incident harmonic field. Problems of scattering in elastic structures were also studied by coupling the modified Werner method with a direct integral representation[23,24] of the displacement field on the surface. This purely integral approach is preferred to a variational formulation[25,26] for the structure coupled with integral equations for the fluid.

As a matter of fact, a variational formulation of the dynamic structure problem leads to looking for the displacement field in the entire structure[26] while only the normal component of the displacement field on the surface of the elastic structure is useful to resolve the scattering problem. Furthermore, as we are going to see in what follows, the coupling of the direct integral equation of the displacement field on the surface structure with the modified Werner method is performed quite simply.

Methods using the T matrix[27,28] to represent the contribution of the displacement field are built on the same principle as that of fluid acoustics. They share the same inconveniences: difficulty in accounting for geometric shapes other than the sphere and spheroid and difficulty in evaluating the near field.

The modified Werner method applied to the acoustic scattering problem was resolved with the help of a boundary elements method: the collocation method. A calculus code, the PWM code, was developed and used to treat problems of scattering in axisymmetric structures.

The modified Werner method as well as different numeric integration techniques were validated in numerous test cases. It was also contrasted with other methods (Burton and Miller[12]) with the help of results drawn from articles.

Finally, comparisons between the modified Werner method and experimental results were made for a full end-capped cylinder (straight cylinder ended by two hemispheres) in tungsten carbide.

I. BACKGROUND OF THE PROBLEM

Let us consider the acoustic pressure field P which is scattered by a rigid or elastic structure. This body, with a regular boundary surface S, occupies the finite volume Ω_S in space. Let us also assume that the body is immersed in a perfect fluid of density ρ_f which occupies the unbounded domain Ω_f in which a harmonic acoustic wave is propagating (Fig. 1). This wave is defined at any point M of Ω_f by a displacement field $\mathbf{U}^*$, corresponding to an incident pressure P^*. Then one type of wave is produced in the exterior fluid: A wave field of diffraction is caused by the diffraction of the incident field on the structure. The harmonic problem is supposed with a time dependence in $\exp(-i\omega t)$, where ω is the angular frequency of the incident wave. The wave number $k=\omega/c$ is supposed to be real where c is the speed of sound in the fluid.

Then, in this case, the stationary part of the scattered pressure P is governed by the following system (1):

$$\Delta P + k^2 P = 0, \quad \forall M \in \Omega_f, \tag{1a}$$

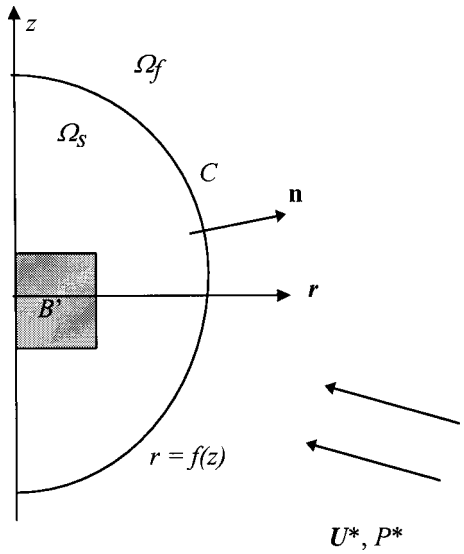

FIG. 1. Scattering problem.

$$\left|\frac{\partial P}{\partial r}-ikP\right|=O(r^{-2}),\quad P=O(r^{-1}),\quad r=\|OM\|\to+\infty, \tag{1b}$$

$$\frac{\partial P}{\partial n}=-\rho_f\omega^2\mathbf{U}^*\cdot\mathbf{n},\quad \forall M\in S. \tag{1c}$$

Equation (1a) represents the wave equation in a perfect fluid. The first part of Eq. (1b) is the Sommerfeld radiation condition. This condition ensures the uniqueness of the problem (1). The boundary condition Eq. (1c) expresses the conservation of the normal component of the displacement on S.

Conversely, if we suppose that Ω_S is a homogeneous elastic isotrope body with constant Lamé coefficients λ and μ and density ρ_S, the scattered pressure is defined as the sum of a diffraction wave and a wave provoked by the elastic vibrations of the structure. In this case the stationary parts of the scattered pressure P and of the displacement field $\mathbf{U}$ of the structure are governed by the following system (2):

$$\Delta P+k^2P=0,\quad \forall M\in\Omega_f, \tag{2a}$$

$$\left|\frac{\partial P}{\partial r}-ikP\right|=O(r^{-2}),\quad P=O(r^{-1}),\quad r\to+\infty, \tag{2b}$$

$$\rho_S\omega^2\mathbf{U}+(\lambda+\mu)\mathbf{Grad}(\operatorname{div}\mathbf{U})+\mu\Delta\mathbf{U}=0,\quad \forall M\in\Omega_S, \tag{2c}$$

$$\frac{\partial P}{\partial n}=\rho_f\omega^2\mathbf{U}\cdot\mathbf{n}-\rho_f\omega^2\mathbf{U}^*\cdot\mathbf{n},\quad \forall M\in S, \tag{2d}$$

$$\sigma(\mathbf{U})\mathbf{n}=-P\mathbf{n}-P^*\mathbf{n},\quad \forall M\in S. \tag{2e}$$

Equation (2c) is the Navier equation. The boundary condition Eq. (2e) expresses the conservation of the stress vector at the fluid–structure interface. Systems (1) admit a unique solution.[29] The system (2) has at least one solution in the general case.[29,30] However, in rare cases, certain angle frequencies ($\omega^2>0$) may be eigenvalues, associated with a motion of the solid without interaction with the fluid. The so-called ''Jones modes'' are free vibrations of the elastic structure. Consequently, they do not modify the scattering of the structure. These modes appear notably for axisymmetric structures; however, for the end-capped cylinder and for the wave numbers studied, they were not identified.

II. INTEGRAL REPRESENTATION

For every structure the second-order systems (1) and (2) do not accept simple theoretical solutions because of the Sommerfeld radiation condition. The integral representations are well adapted to solve this type of problem numerically. They consist in writing a coupled system of integral equations governing the pressure and the normal component of the displacement vector, on the boundary S of the structure. So, with the numerical solution, the pressure at any point of the fluid is calculated very quickly.

The irregular wave numbers are well known for bodies with simple geometric shapes, such as a sphere, a cylinder, or a cone. In these cases the Helmholtz integral representation is well suited to the problem when the frequency is regular. This simple representation with a surface's potential is neither very difficult to compute nor expensive in terms of calculation time.

Nevertheless, the number of irregular wave numbers has an accumulation point at infinity. Their density increases as the frequency increases. The Helmholtz method quickly becomes numerically unusable for medium frequencies.

The originality of the modified Werner method[20] results from the fact that it splits up the pressure P into a surface potential and a volume potential, not in the whole interior domain but in a nonzero arbitrary part B strictly inside Ω_S (Fig. 1).

The pressure P is written as follows:

$$P(M_0)=\Phi_1(M_0)+\Phi_2(M_0)\quad \forall M_0\in S, \tag{3}$$

with

$$\Phi_1(M_0)=\int_S \nu(M)g(M_0,M)\,ds, \tag{4a}$$

$$\Phi_2(M_0)=\int_B \rho(M)g(M_0,M)\,d\nu, \tag{4b}$$

where g is the Green function, in dimension 3, associated with the Helmholtz equation (1a): $g(M_0,M)=\exp(ikD\times(M_0,M))/4\pi D(M_0,M)$, $D(M_0,M)$ being the Euclidian distance between points M and M_0.

These two potentials have some properties of regularity[31] with ν and ρ supposed to be continuous. Two equations are necessary for determining the new unknowns ν and ρ.

Let's take the normal derivative—exterior normal—of the expression (3), when M tends to M_0:

$$\frac{\partial P(M_0)}{\partial n}=\frac{\partial \Phi_1(M_0)}{\partial n}+\frac{\partial \Phi_2(M_0)}{\partial n}. \tag{5}$$

For $\nu(M)$, we calculate the normal derivative of Eq. (4a). This limit is well defined if the surface S is a Liapunov surface.[32]

For $\rho(M)$, as the volume B is strictly included in the domain Ω_S, there is no singularity and the limit is also well defined. It is a direct application of a Lebesgue theorem. Thus we obtain, $\forall M_0 \in S$,

$$\frac{\partial \Phi_1(M_0)}{\partial n} = \frac{-\nu(M_0)}{2} + \int_S \nu(M) \frac{\partial g(M_0,M)}{\partial n(M_0)}\, ds, \quad (6a)$$

$$\frac{\partial \Phi_2(M_0)}{\partial n} = \int_B \rho(M) \frac{\partial g(M_0,M)}{\partial n(M_0)}\, d\nu. \quad (6b)$$

With the boundary condition Eq. (1c) and the relations (6a) and (6b), we find the first equation:

$$\frac{\nu(M_0)}{2} = \rho_f \omega^2 \mathbf{U}^*(M_0).\mathbf{n} + \int_S \nu(M) \frac{\partial g(M_0,M)}{\partial n(M_0)}\, ds + \int_B \rho(M) \frac{\partial g(M_0,M)}{\partial n(M_0)}\, d\nu \quad \forall M_0 \in S. \quad (7)$$

A second equation between ν and ρ is necessary. Inside the domain B, we impose the following condition:

$$-(\Delta + k^2) P(M) = iC^* P(M) \quad \forall M \in B, C^* \in \Re. \quad (8)$$

The potentials Φ_1 and Φ_2 are governed by the wave equation (9a) and the inhomogeneous wave equation (9b) (in the distribution sense), respectively:

$$(\Delta + k^2)\Phi_1(M) = 0, \quad \forall M \in B. \quad (9a)$$

$$-(\Delta + k^2)\Phi_2(M) = \rho(M), \quad (9b)$$

Then,

$$iC^* P(M) = \rho(M) \quad \forall M \in B. \quad (10)$$

Thus

$$\rho(M_0) = iC^* \int_S \nu(M) g(M_0,M)\, ds + iC^* \int_B \rho(M) g(M_0,M)\, d\nu \quad \forall M_0 \in B. \quad (11)$$

The imaginary constant iC^* is fundamental. In the demonstration of Werner,[20] $C^* = 1$ and allows us to solve the problem of irregular frequencies. This way, we obtain the existence and the uniqueness of the two coupled equations (7) and (11) for ν and ρ. Then the existence and the uniqueness of ν and ρ justify the decomposition in Eq. (3) and prove the uniqueness of the solution of the problem (1).

The real constant C^*, called a weighting factor, does not exist in Werner demonstration.[20] Trad[21] includes it to obtain an equation having good physical dimensions. His choice is to take $C^* = 1/a^2$, where a is a characteristic length of the soundproof object. Ravel[22] finds that this choice is not optimum. It is necessary to take a significant number of elements of volume to mesh the interior volume B in order to obtain a good convergence of results in the vicinity of the irregular wave numbers. Additionally, the introduction of interior volume B quickly becomes prohibitive in calculation time as the wave numbers increase.

A study of conditioning permitted improvement of the modified Werner method. Ravel[22] shows that a good compromise for the weighting factor is to take

$$C^* = k^2 \frac{\text{Volume}\,(\Omega_S)}{\text{Volume}\,(B)}. \quad (12)$$

The advantage of such a choice rests on the very clear improvement in conditioning for the numeric system matrix. Additionally, a single finite volume element to net volume B is sufficient to ensure the convergence of results. A comparative study, with or without a weighting factor, was conducted in Ravel's thesis.[22] The gain in precision is variable according to the situation. On average, for the wave numbers studied, the results with a weighting factor are approximately 100 times more precise when the same number of volume elements is used. The comparisons were made on cylinders, end-capped cylinders, and spheres. The introduction of the weighting factor thus reduces the calculation time necessary for the solution of the system of integral equations (7) and (11), which makes it comparable to the calculation time obtained by the Helmholtz method for problems of diffraction and acoustic scattering.

When the structure is elastic (2), only the contribution of the displacement field of the interface S of the structure must be taken into account in the acoustic scattering. This way, we apply the Maxwell–Betti formula,[23] using the boundary conditions Eqs. (2d) and (2e), and we obtain a general integral representation of the displacement vector. Then, for a full homogeneous elastic structure, the unknown scalar functions P, ν, ρ and the displacement field's three components U_j, $j = 1,2,3$, at the interface S are governed by the system (13) of six Fredholm integral equations of second order:

$$P(M_0) = \int_S \nu(M) g(M_0,M)\, ds + \int_B \rho(M) \underline{g(M_0,M)}\, d\nu, \quad \forall M_0 \in S, \quad (13a)$$

$$\frac{\nu(M_0)}{2} = \rho_f \omega^2 (\mathbf{U}^*(M_0) - \mathbf{U}(M_0))\mathbf{n} + \int_S \nu(M) \frac{\partial g(M_0,M)}{\partial n(M_0)}\, ds + \int_B \rho(M) \underline{\frac{\partial g(M_0,M)}{\partial n(M_0)}}\, d\nu, \quad \forall M_0 \in S, \quad (13b)$$

$$\rho(M_0) = iC^* \int_S \nu(M_0) \underline{g(M_0,M)}\, ds + iC^* \int_B \rho(M_0) g(M_0,M)\, d\nu, \quad \forall M_0 \in B, \quad (13c)$$

$$\frac{1}{2}U_j(M_0)=F_j(M_0)-\int_S[\mathbf{G}^j(M_0,M)\cdot\mathbf{n}P(M)+\mathbf{T}(\mathbf{G}^j(M_0,M))\cdot\mathbf{U}(M)]\,ds,\quad \forall M_0\in S, \tag{13d}$$

where free terms F_j, $j=1,2,3$, are defined by

$$F_j(M_0)=\int_S P^*(M)\mathbf{G}^j(M_0,M)\cdot\mathbf{n}\,ds,\quad \forall M_0\in S. \tag{14}$$

The kernels $\mathbf{G}^j$, $j=1,2,3$, are the solutions in terms of Navier operator distribution Eq. (2c). They are defined by[23]

$$\mathbf{G}^j(M_0,M)=\frac{1}{\rho_S\omega^2}[\mathbf{Curl}\,\mathbf{Curl}\,\mathbf{W}^j(M_0,M)-\mathbf{GRAD}\,\mathrm{Div}\,\mathrm{V}^j(M_0,M)],\quad j=1,2,3, \tag{15}$$

where

$$\mathbf{W}^j(M_0,M)=\delta^j\frac{\exp(ik_tD(M_0,M))}{4\pi D(M_0,M)},\quad k_t=\left(\frac{\rho_s\omega^2}{\mu}\right)^{1/2}, \tag{16a}$$

$$\mathbf{V}^j(M_0,M)=\delta^j\frac{\exp(ik_lD(M_0,M))}{4\pi D(M_0,M)},\quad k_l=\left(\frac{\rho_S\omega^2}{\lambda+2\mu}\right)^{1/2}. \tag{16b}$$

The components of the vector δ^j are $(\delta^j)_i=\delta_{ij}$; δ_{ij} is the Kronecker symbol; σ, k_t, and k_l are respectively the stress vector, the transversal wave number, and the longitudinal wave number; and $\mathbf{T}(\mathbf{u})=\sigma(\mathbf{u})\mathbf{n}$ is the stress vector. Thanks to the introduction of volume B, the three underlined integrals coming from Werner modified method are regular. Their evaluation can be carried out in a simple manner.

III. NUMERICAL TREATMENT

A numerical program (PWM) based on a finite element method[33] has been developed. It simulates the acoustic scattering resulting from axisymmetric structures. The interpolation of the unknown elements of the problem is quadratic. The volume B is generated by the rotation around the axis z of the generating surface B' (Fig. 1). This surface is meshed by quadrangles with nine-pointed quadrangles (Q2 element).

The surface S is also generated by the rotation of the contour C around the axis z. It is meshed with three-pointed arcs (P2 element).

The calculus of the elementary matrices corresponds to the kernels and the free terms of the integral equations, calculated on the elements. When the integrals are of regular type, the Gauss–Legendre quadrature is used, with only four integration points (unless otherwise indicated). However, when the calculus node belongs to the element which is integrated, the integrals become improper. They require a special treatment.

It consists in using adapted Gauss quadratures for the different types of encountered singularities.

For the surface operators of the modified Werner method, Eqs. (13a) and (13b), and for the structure under study, two types of singularities exist: $\mathrm{Ln}(x)$ outside the extremities, $1/x^{1/2}$ in the vicinity of the extremities of the axisymmetric structure.[22] Then Gauss's quadratures with a weight $\mathrm{Ln}(1/x)$[22,34] and Tchebychev quadratures are used respectively.

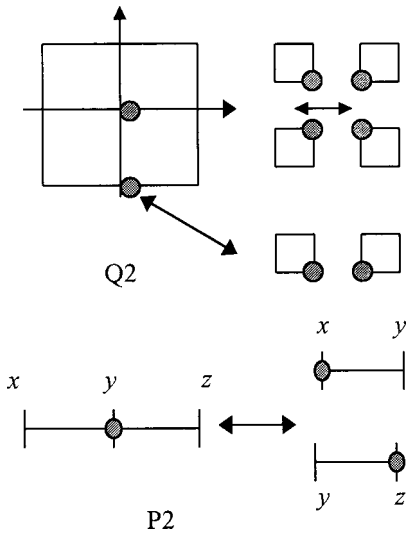

FIG. 2. Treatment of singularities.

For the volume operators of the modified Werner method, Eq. (13c), only one type of singularity exists: $x\,\mathrm{Ln}(x)$. The quadratures adapted to the weight $\mathrm{Ln}(1/x)$ or Gauss–Legendre quadratures can be used to evaluate singular volume integrals.

Using the special quadratures requires certain changes in the variables. Because of the positions of the quadrature points, it is necessary to put the singularity at the end of the integration element for the calculation of the integral to be efficient.

Thus, for the P2 element type, there are two possibilities. In the first case the computational node is on (y), in the middle of the segment (Fig. 2), then the element (xz) is divided into two segments. This technique puts the singularity at the extremities of the element. In the second case the node is on x or z, and we do not perform any transformation.

For the Q2 element, the method is similar. The element is split into four or two elements if the computational node does not belong to an extremity of the element (Fig. 2).

This numerical procedure is helpful. It allows us to obtain, for the same number of quadrature points, a calculus precision equivalent to that of regular integrals evaluated by the Gauss–Legendre method.

However, the integral formulation Eq. (13d) of the problem of the dynamic nature of the structure brings about problems of the singularities of the integral operators.[35] The singularities of the kernels of the integral equations for elastodynamics are of an order greater than those for the modified Werner method. These nonintegrable kernels exist in the sense of the Cauchy principal value.

A numerical method to evaluate these integrals consists first in regularizing them using integral equations obtained with the help of the associated static structure problem.[35,36] Nevertheless, the numeric treatment remains complex and is limited to low wave numbers.

The use of adapted quadratures was not kept for elasto-

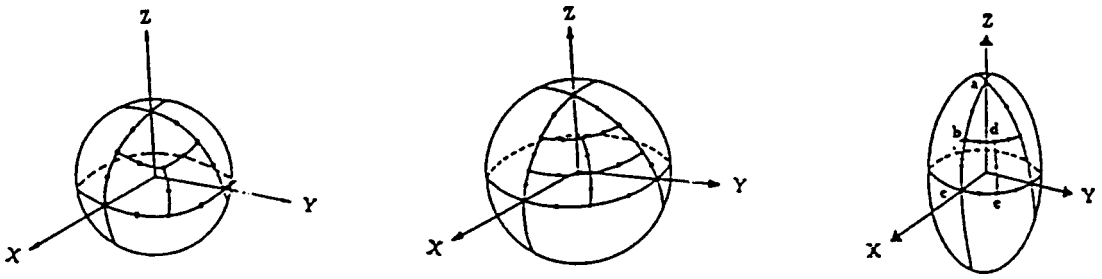

FIG. 3. Meshes of the sphere and the spheroid by quadrilaterals of eight nodes. Large mesh: 24 elements. Finer mesh: 40 elements.

dynamic operators because of the complexity of their expressions and the numerous algebraic manipulations required to apply them. By using the Gauss–Legendre quadrature with an even number of points, we obtain satisfactory results with certain types of boundary elements for not very large wave numbers. As a first approximation, the symmetric position of the Gauss–Legendre points makes it possible to approximately calculate the limit in the sense of the Cauchy principal value.

Henceforward, we can use the collocation method to describe the discretization for a fluid/structure problem: for example, the problem (2) of acoustic scattering of an elastic structure fully immersed in a perfect fluid. The surface S is discretized by the elements P2 with a total number NS nodes. The volume B is discretized by the elements Q2 with a total number of NV nodes.[37] The coupled system with simplified notation will be represented as follows:

$$\begin{array}{c} \\ \\ \\ \\ \end{array}\!\!\begin{array}{c} \begin{array}{cccc} & & \mathbf{1} & \mathbf{2} \end{array} \\ \left[\begin{array}{cccc} [-\delta] & [\mathbf{g}_{SS}] & [\mathbf{g}_{SB}] & [0] \\ [0] & \left[\dfrac{-1}{2}\,\delta+\dfrac{\partial \mathbf{g}_{SS}}{\partial \mathbf{n}}\right] & \left[\dfrac{\mathbf{g}_{SB}}{\partial \mathbf{n}}\right] & [-\delta\mathbf{n}] \\ [0] & [\mathbf{g}_{BS}] & \left[\dfrac{1}{iC^*}\,\delta+\mathbf{g}_{BB}\right] & [0] \\ [\mathbf{G}_{SS}(\mathbf{n})] & [0] & [0] & [(\mathbf{T}(\mathbf{G})_{SS}] \end{array}\right] \end{array}$$

$$\times\left\{\begin{array}{c}\{\mathbf{P}\}_{NS}\\ \{\nu\}_{NS}\\ \{\rho\}_{NV}\\ \{\mathbf{U}\}_{NS}\end{array}\right\}=\left\{\begin{array}{c}\{0\}_{NS}\\ \{-\rho_f\omega^2\mathbf{U}^*\cdot\mathbf{n}\}_{NS}\\ \{0\}_{NV}\\ [(\mathbf{G})_{SS}(\mathbf{n})]_{NS.NS}\{\mathbf{P}^*\}_{NS}\end{array}\right\}. \tag{17}$$

The notation $[\mathbf{A}_{xy}]$ represents an assembled elementary matrix relative to different operators. The letters **x** and **y** can take the values S or B to designate respectively the surface S or the volume B. The first letter corresponds to the position of the computational node in the collocation method. The second letter corresponds to the integration element.
For instance, let us show the writing of the matrix in detail $[\mathbf{g}_{SS}]$:

$$\begin{aligned}[\mathbf{g}_{SS}]_{ij}&=\sum_{k\in A_j}\int_{\Gamma_k}N_j^k g(M_i,M)\,ds_M,\\ &A_j=\{q/M_j\in\Gamma_q\},\quad M_i\in S\ \text{ and }\ S=\cup\Gamma_i,\\ &i=1,\ (NS-1)/2,\end{aligned} \tag{18}$$

where M_i is one of computational node and N_j^k is the interpolation function associated with the node M_j for the surface element Γ_k.

The notation $\{\mathbf{A}\}_{\mathbf{N}^*}$ represents the function **A** on the N^* nodes of the surface mesh if $N^*=NS$, or the volume mesh if $N^*=NV$.

Block (1) corresponds to operators of the modified Werner method. It resolves problems of diffraction and acoustic scattering.

Matrix $[\mathbf{G}_{SS}]$ contains the elastic fluid/structure coupling, matrix $[\mathbf{T}(\mathbf{G})_{SS}]$ governs the dynamic behavior of the elastic structure, and finally the diagonal matrix $[-\delta\mathbf{n}]$ describes the geometry of the surface S. The latter contains the three components of the normals in each surface node. The second member of Eq. (17) contains the component from the modified Werner method to which was added a vector representing a stress vector imposed on the surface of the structure.

IV. NUMERICAL RESULTS

In this part, the modified Werner method is compared with the Burton–Miller method in the case of a sphere and a spheroid for radiation problems. Subsequently, an experimental comparison of a scattering problem with an end-capped cylinder with results obtained by the PWM code will complete this study.

A. Burton and Miller method[12]

The results of the modified Werner method were also compared with the work of Meyer *et al.*[14] and Chien *et al.*[15] These authors successively improved the Burton and Miller method by proposing a procedure for regularizing the hypersingular kernel as follows:

$$I(M_0)=\int_s\frac{\partial^2 g(M,M_0)}{\partial n_M\partial n_{M_0}}\,ds_M. \tag{19}$$

Only the type of interpolation differentiates the work of these two authors: Chien *et al.* proceed with the help of quadratic elements while Meyer *et al.* use an interpolation constant per element.

Two structures are considered: the sphere and the spheroid. The tridimensional meshes of the sphere and the spheroid are constructed with isoparametric quadrilaterals of eight nodes in Chien *et al.* and Meyer *et al.* Two meshes are used: a large mesh with 24 elements and a finer mesh with 40 elements (Fig. 3). The numerical evaluation of regular inte-

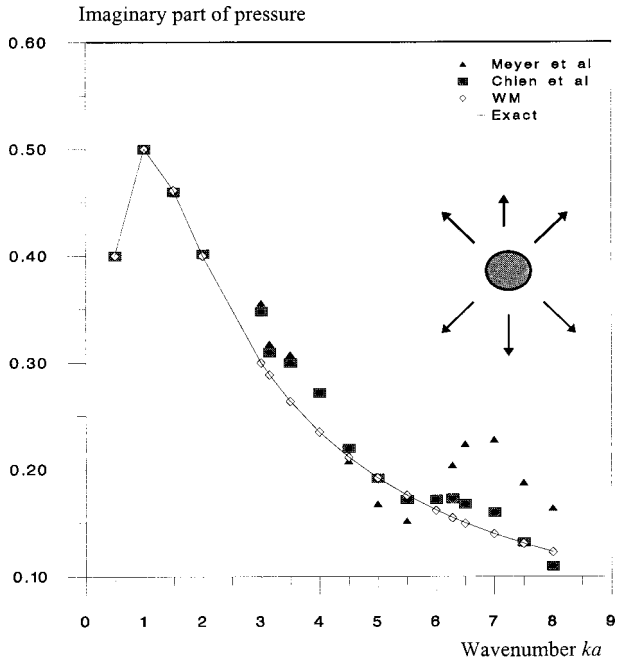

FIG. 4. Imaginary part of pressure at the surface of a sphere subjected to a uniform traction for the large mesh of the sphere. Comparisons between the Burton–Miller and modified Werner methods.

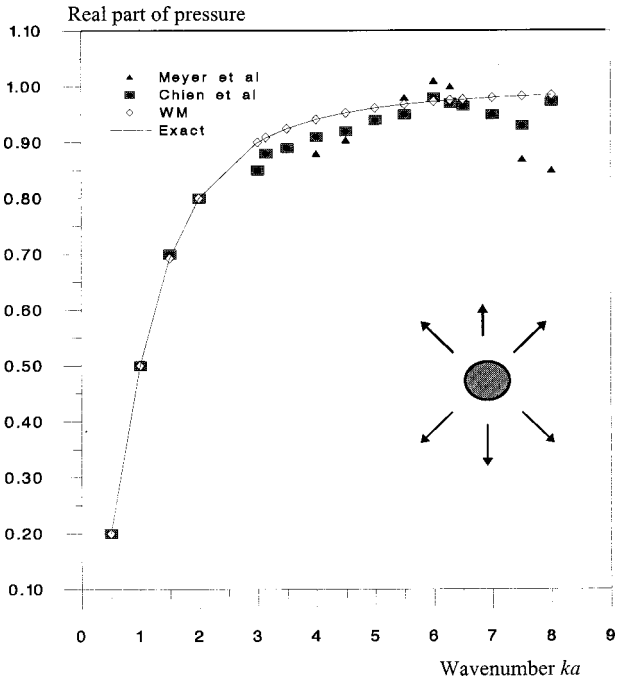

FIG. 5. Real part of pressure at the surface of a sphere subjected to a uniform traction for the large mesh of the sphere. Comparisons between the Burton–Miller and modified Werner methods.

grals and singular integrals (after regularization) of the Burton and Miller method is carried out with three Gauss points per element.

In order to make a comparison, we developed an equivalent axisymmetric mesh. For the larger and finer meshes, four and six quadratic elements served for the discretization of the contour of the generating surface C (Fig. 1). The interval of the polar angle $\theta\,[0, 2\pi]$ was divided into six subintervals for the two meshes. The large axisymmetric mesh is relatively close to its tridimensional counterpart. The finer axisymmetric mesh comprises four elements less than its tridimensional counterpart. The treatment of the singularities was carried out with the help of eight special quadrature points per element. A single volume element of nine nodes was placed at the center of the structure. This element represents 1% of the volume of the studied structure.

The first test case considered is a radiating sphere (of an a radius) for which the normal speed V_a at the surface is given. This speed is uniform and radial. This situation corresponds to the problem of Eqs. (2a), (2b), and (2d), defined in the first section with the following givens:

$$\mathbf{U}^*\cdot\mathbf{n}=0, \quad \frac{\partial P}{\partial n}=i\rho_f\omega V_a\,. \tag{20}$$

In spherical coordinates the solution to this problem is the following:

$$\frac{P(r)}{\rho_f c V_a}=\left(\frac{a}{r}\right)\frac{ika}{(ika-1)}\exp\left(ik(r-a)\right). \tag{21}$$

The real and imaginary parts of the pressure that are represented are on a point of the surface situated on the equator. The results obtained by the modified Werner method are very precise and on the whole better than those produced by Meyer *et al.* and Chien *et al.* (Figs. 4 and 5). The convergence of the modified Werner method is very rapid since the large mesh is sufficient to ensure a relative precision inferior to 1%.

In the vicinity of the two irregular wave numbers π and 2π, the curves obtained by the Burton and Miller method are less good than for the other wave numbers. This perturbation is more clearly distinguished for $ka=2\pi$. We note also the importance of the precision of the calculation concerning the conditioning of the matrices obtained by Meyer *et al.* and Chien *et al.* The numerical treatment proposed by Chien *et al.* is more precise than that of Meyer *et al.* As a consequence, the perturbations produced by the irregular frequencies are more attenuated on the curve of Chien *et al.*

The second test case is similar to the first, except for the surface speed which is not constant this time. The speed module is defined as $V_a\cos(\theta)$, where θ is the angle made by the z axis with the radial direction (Fig. 6). In this case,

$$\mathbf{U}^*\cdot\mathbf{n}=0, \quad \frac{\partial P}{\partial n}=i\rho_f\omega V_a\cos(\theta). \tag{22}$$

In spherical coordinates the solution of this problem is the following:

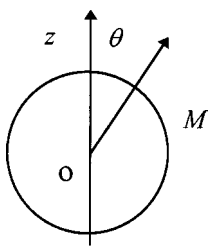

FIG. 6. Angle θ.

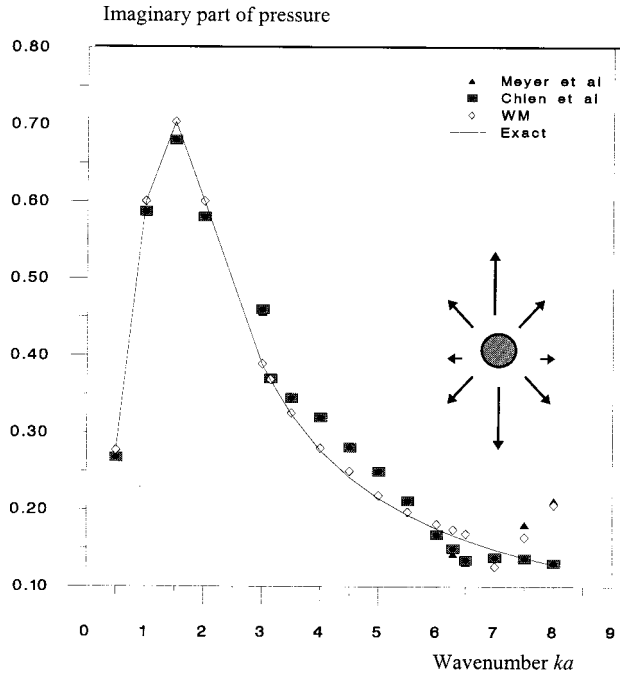

FIG. 7. Imaginary part of pressure on the surface of an oscillating sphere for the finer mesh of the sphere. Comparison between the methods of Burton–Miller and modified Werner.

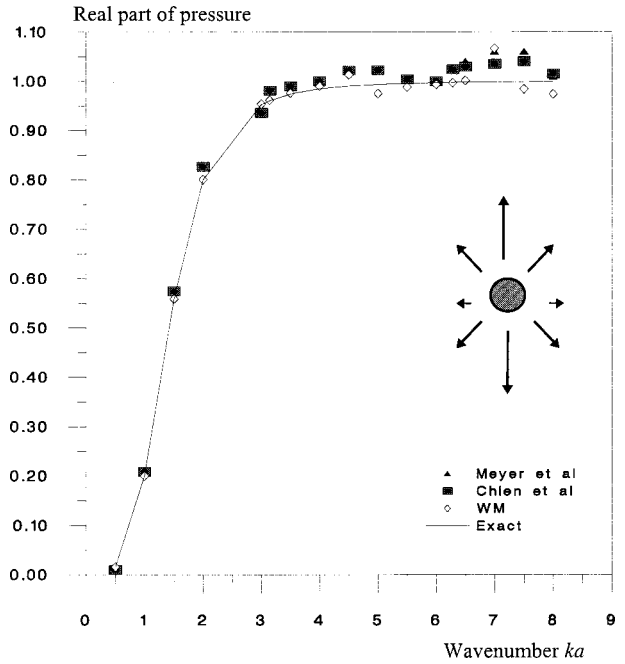

FIG. 8. Real part of pressure on the surface of an oscillating sphere for the finer mesh of the sphere. Comparison between the methods of Burton–Miller and modified Werner.

$$\frac{P(r,\theta)}{\rho_f c V_a} = \left(\frac{a}{r}\right)^2 \cos(\theta)\, \frac{ika(1-ikr)}{k^2a^2+2(-1+ika)} \exp\left(ik(r-a)\right). \tag{23}$$

In this case, the computational node is the north pole of the sphere. The results obtained are those calculated for the fine mesh. The precision obtained for the modified Werner method is good until $ka=7$, afterwards it is comparable with the Meyer *et al.* results (Figs. 7 and 8). This lack of precision for the real part of the pressure is probably explained by the position of the computational node of the north pole and by the important variations of the second member of system (17). A finer mesh with 52 elements is sufficient to obtain a precision inferior to 1%, for the collection of the mesh nodes.

Finally, the last test case treated is a spheroid submitted to a point source, situated at the center of the structure for a wave number $ka=\pi$ close to an irregular wave number. The ratio between the length b of the long axis of the ellipse and the length of the small axis a is $b/a=1.6$. The comparison is made for certain nodes of the mesh (Fig. 3). The results recorded in Table I represent the real part of the pressure for the three methods.

For the test cases studied the modified Werner method is more precise than the other methods. It is necessary to note that the pressure calculated at the North pole has low precision with the Burton–Miller method. This difficulty comes probably from the eccentricity of the spheroid and the stronger singularity at that point.

B. A tungsten carbide end-capped cylinder

In this paragraph we are interested in the study of scattering by an elastic end-capped cylinder ($L/2a=2$) with the help of a combination of the modified Werner method and integral equations of elastodynamics (13).

Comparisons between numerical and experimental results obtained respectively by the PWM code and by the L.A.U.E.[38] (Laboratoire d'Acoustique Ultra sonore et d'Electronique du Havre) were established.

The full end-capped cylinder (Fig. 9) which was used for these comparisons is composed of tungsten carbide. The structure has the following characteristics: volume mass: 13 800 kg/m^3, longitudinal speed and transversal speed: 6490 and 4120 m/s, and characteristic length: $a=10^{-2}$ m.

This object is immersed in water in where a plane harmonic wave is propagated in the direction of z positives (Fig. 9).

At first the proper longitudinal modes of the target were identified with the help of the PWM code. This identification

TABLE I. Real part of the pressure on the surface of a spheroid for particular nodes for $ka=\pi$ for the two different meshes: 24 elements (24 el.), and 40 elements (40 el.).

		Meyer *et al.*		Chien *et al.*		Werner	
Nodes	Theory	24 el.	40 el.	24 el.	40 el.	24 el.	40 el.
a	−0.0036	0.0008	−0.0010	−0.0002	−0.0019	−0.0036	−0.0036
b	0.7543	0.7502	0.7505	0.7504	0.7511	0.7501	0.7541
c	0.9080	0.8944	0.8989	0.8995	0.9016	0.910	0.9082

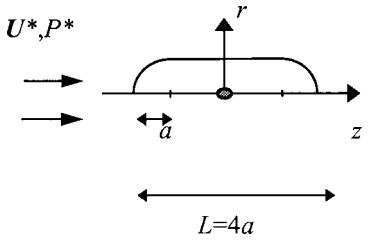

FIG. 9. Target generatrice.

was carried out by graphical research of the peaks of resonance. These values are to be compared with those obtained by the L.A.U.E.[39] (Table II). The relative maximum gap is of the order of 2.1% for the fourth mode.

Next, in the vicinity of the fourth longitudinal end-capped cylinder mode, the bistatic experimental diagram in forced regime is compared to its numerical equivalent (Fig. 10). The transmitter **E** is fixed, the receiver **R** is situated at 1 m from the target. It turns around the target and the radiated pressure is thus measured for all degrees. Two critical zones in the vicinity of 180 and 0 degrees do not allow correct measurement. In these two particular zones, the receiver passes in front of the transmitter. The bistatic diagram is symmetric to the *z* axis, which is why the comparison between the lower and the upper parts is possible. It is noteworthy that this symmetry gives the experimenters partial control over the coherence of their measures.

The editing of the two curves was carried out by the L.A.U.E. Using the L.A.U.E. bistatic diagrams data bank, the most significant results were obtained for a wave number $ka=8.665$ for the PWM code and $ka=8.89$ for the L.A.U.E. This difference between the wave numbers is effectively the same as that obtained for the fourth mode (Table II).

The results obtained (Fig. 10) are satisfactory from a qualitative point of view. There is good agreement between the angular dispositions of eight different lobes appearing on the diagram for the two methods. From the quantitative point of view, it is not currently possible to make a comparison using this experiment because it is very difficult for the experimenter to dimension his measurements.

V. CONCLUSION

The Werner method is an integral representation of the diffraction and acoustic radiation problem. This representation is built with the help of a linear combination of a potential of a simple layer and potential of volume. The introduction of the volume potential plays a major role in the decomposition since it permits obtaining an integral representation that is strictly equivalent to the Neumann exterior problem.

The modified Werner method applied in this manuscript is developed by Trad[21] and improved by Ravel.[22] It is well adapted to the solution of acoustic scattering problems of elastic structures because the normal component of the displacement field at the fluid structure interface is directly exploitable. A direct integral representation of the displacement field at the interface can be coupled in a simple fashion with the modified Werner method.

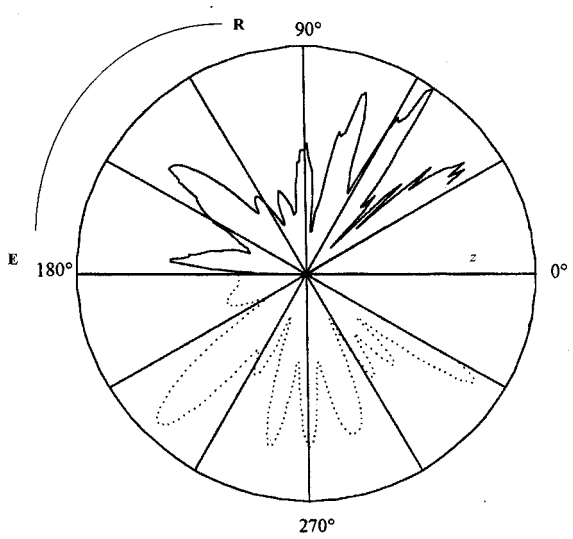

FIG. 10. Bistatic diagram of a tungsten carbide end-capped cylinder. Comparison: code PWM ($ka=8.665$), dotted curve, and L.A.U.E. experiment ($ka=8.89$), continuous feature curve.

The amount of numerical work was the reason for the creation of a calculus code—the PWM code—for modeling of axisymmetric structure scattering.

Different integral representations were solved numerically by the collocation method with a quadratic interpolation.

The contribution of the singular integrals in the case of the operators in the modified Werner method was given particular attention. A numerical regularization procedure built on using quadratures adapted to different singularities provided a lot of precision in the calculations.

The introduction of the weighting factor in the decomposition of Werner significantly reduced the numerical cost of the potential of volume. A single finite element of volume was sufficient to obtain satisfactory results.

These two combined advantages gave the modified Werner method high performance marks in comparison with the work of Chien *et al.*[15] in the classic test cases for acoustic scattering of axisymmetric structures.

A comparison of numerical results with an experiment on the end-capped cylinder also gave satisfactory results with the different numerical treatments carried out on the hyper singular kernels of elastodynamics. A study, currently being undertaken, should permit improvement to these results with the help of special quadratures for integrals defined in the sense of the principal Cauchy value.

TABLE II. Research of eigen longitudinal modes of the end-capped cylinder.

Mode No.	PWM (ka)	L.A.U.E. (ka)
4	8.5	8.68
5	10	10
6	11.75	11.8
7	13.75	13.4

ACKNOWLEDGMENTS

We extend our appreciation to Professor Maze Décultot and Professor Dominique Décultot of the L.A.U.E, le Havre University, for the excellent help they provided us in analyzing the experimental results.

[1] L. G. Copley, ''Fundamental results concerning integral representations in acoustic radiation problems,'' J. Acoust. Soc. Am. **44**, 28–33 (1968).
[2] H. A. Schenck, ''Improved integral formulation for acoustic radiation problems,'' J. Acoust. Soc. Am. **44**, 41–58 (1968).
[3] D. Colton and R. Kress, *Integral Equation Methods in Scattering Theory* (Wiley, New York, 1983).
[4] T. W. Wu and A. F. Seybert, ''A weighted residual formulation for the CHIEF method in acoustics,'' J. Acoust. Soc. Am. **90**, 1608–1614 (1991).
[5] D. J. Segalman and D. W. Lobitz, ''A method to overcome computational difficulties in the exterior acoustics problem,'' J. Acoust. Soc. Am. **91**, 1855–1861 (1991).
[6] C. M. Piaszczyk and J. M. Klosner, ''Acoustic radiation from vibrating surfaces at characteristic frequencies,'' J. Acoust. Soc. Am. **75**, 363–372 (1984).
[7] F. Ursell, ''On the Exterior Problems of Acoustics,'' Proc. Cambridge Philos. Soc. **74**, 117–125 (1973).
[8] D. S. Jones, ''Integral equations for the exterior acoustic problem,'' Q. J. Mech. Appl. Math. **27**, 129–142 (1973).
[9] B. Stupfel, A. Lavie, and J. N. Decarpigny, ''Combined integral equation formulation and null-field method for the exterior acoustic problem,'' J. Acoust. Soc. Am. **83**, 927–941 (1988).
[10] P. C. Waterman, ''New formulation of acoustic scattering,'' J. Acoust. Soc. Am. **45**, 1417–1429 (1969).
[11] H. Brakhage and P. Werner, ''Über das dirichletsche aussenraumproblem für die Helmholtzsche Schwingungsgleichung,'' Arch. Math. **16**, 325–329 (1965).
[12] A. J. Burton and G. F. Miller, ''The application of integral equation methods to the numerical of some exterior boundary-value problems,'' Proc. R. Soc. London, Ser. A **323**, 201–210 (1971).
[13] P. J. T. Filippi, ''Layer potentials and acoustic diffraction,'' J. Sound Vib. **54**(4), 473–500 (1977).
[14] W. L. Meyer, W. A. Bell, and B. T. Zinn, ''Boundary integral solutions of three dimensional acoustic radiation problems,'' J. Sound Vib. **59**(2), 245–262 (1978).
[15] C. C. Chien, H. Rajiyah, and S. N. Atluri, ''An effective method for solving the hypersingular integral equations in 3-D acoustics,'' J. Acoust. Soc. Am. **88**, 918–937 (1990).
[16] J. Y. Hwang and S. C. Chang, ''A retracted boundary integral equation for exterior acoustic problem with unique solution for all wavenumbers,'' J. Acoust. Soc. Am. **90**, 1167–1180 (1991).
[17] J. B. Fahnline and G. H. Koopmann, ''A numerical solution for the general radiation problem based on the combined methods of superposition and singular-value decomposition,'' J. Acoust. Soc. Am. **90**, 2808–2819 (1991).
[18] M. A. Hamdi, ''Une formulation variationnelle par équations intégrales pour la résolution de l'équation de Helmholtz avec des conditions aux limites mixtes,'' C. R. Acad. Sci **292**(II), 17–20 (1981).
[19] J. C. Nedelec, ''Approximation par potentiel de double couche du problème de Neumann extérieur,'' C. R. Acad. Sci. URSS Ser. A **286**(A), 103–106 (1978).
[20] P. Werner, ''Randwertprobleme der mathematischen akustic,'' Arch. Ration. Mech. Anal. **10**, 29–66 (1962).
[21] A. Trad, ''Acoustic scattering by rigid line, in an oblique acoustic field, at arbitrary real frequencies,'' J. Acoust. **4**, 201–214 (1991).
[22] P. Ravel, ''Rayonnement acoustique de structures rigides ou élastiques, validation numérique de la méthode de Werner modifiée,'' Thèse de doctorat, Université Pierre et Marie-Curie, 1996.
[23] V. D. Kupradze, *Potential Methods in the Theory of Elasticity* (I.P.F.S.T., Jerusalem, 1965).
[24] F. J. Rizzo, D. J. Shippy, and M. Rezayat, ''A boundary integral equation method for radiation and scattering of elastic waves in three dimensions,'' Int. J. Numer. Methods Eng. **21**, 115–129 (1985).
[25] J. P. Coyette and O. Bjorndahl, ''A mixed variational FEM/BEM model for submerged elastic structures with thin appendages,'' 2nd European conference on Underwater Acoustics (Copenhagen, Denmark, 1994).
[26] B. Dubus, ''Coupling finite element method and boundary element methods on a mixed solid-fluid/fluid-fluid boundary for radiation or scattering problems,'' J. Acoust. Soc. Am. **96**, 3792–3799 (1994).
[27] A. Boström, ''Scattering of stationary acoustic waves by an elastic obstacle immersed in a fluid,'' J. Acoust. Soc. Am. **67**, 390–398 (1980).
[28] V. K. Varadan, V. V. Varadan, J. H. Su, and T. A. K. Pillai, ''Comparison of sound scattering by rigid and elastic obstacles in water,'' J. Acoust. Soc. Am. **71**, 1377–1383 (1982).
[29] J. Sanchez-Hubert and E. Sanchez-Palencia, *Vibration and Coupling of Continuous Systems: Asymptotic Methods* (Springer-Verlag, Berlin, 1989).
[30] C. J. Luke and P. A. Martin, ''Fluid-solid interaction: Acoustic scattering by a smooth elastic obstacle,'' SIAM (Soc. Ind. Appl. Math.) J. Appl. Math. **55**, 904–921 (1995).
[31] E. Sanchez-Palencia, ''Non-homogeneous media and vibration theory,'' in *Lectures Notes in Physics* (Springer-Verlag, Berlin, 1975), pp. 293–324.
[32] S. G. Mikhlin, ''Mathematical physics, an advanced course,'' in *Applied Mathematics and Mechanics* (North Holland, London, 1975).
[33] G. Dhatt and G. Touzot, Une représentation de la méthode des éléments finis (Col. Uni. de Compiégne, 1984).
[34] J. P. Boujot and P. Maroni, ''Algorithme général de construction de tables de Gauss pour les problèmes de quadratures,'' Institut Blaise Pascal, Compiégne, France, Publication No. NMX/8.1.8/AI (1968).
[35] F. J. Rizzo, D. J. Shippy, and M. Rezayat, ''On time-Harmonic elastic-wave analysis by the boundary element method for moderate to high frequencies,'' Comput. Methods Appl. Mech. Eng. **55**, 349–367 (1986).
[36] M. Bonnet, *Equations intégrales et éléments frontières* (C.N.R.S, Eyrolles, 1995).
[37] F. J. Rizzo and D. J. Shippy, ''An advanced boundary integral equation method for three-dimensional thermoelasticity,'' Int. J. Numer. Methods Eng. **11**, 1753–1768 (1977).
[38] G. Maze, D. Décultot, F. Lecroq, J. Ripoche, X. L. Bao, and H. Überall, ''Resonance identifications of a solid axisymmetric finite length target,'' J. Acoust. Soc. Am. **96**, 944–950 (1994).
[39] D. Décultot, ''Diffusion acoustique par des objets axisymétriques immergés. Cas d'un cylindre limité par deux hémisphères,'' Thèse de doctorat de l'université du Havre (1993).

New explicit solutions in acoustics of closed spaces on the basis of divergent series

M. A. Sumbatyan
Research Institute of Mechanics and Applied Mathematics, Stachki Prospect 200/1, Rostov-On-Don, 344090, Russia

A. Pompei and M. A. Rigano
Department of Mathematics, University of Catania, Viale A. Doria 6, Catania-95125, Italy

(Received 4 November 1998; revised 20 July 1999; accepted 10 August 1999)

A new approach to the acoustics of closed spaces is developed that involves solutions for polygonal shapes in explicit form. It is shown that exact solutions can be constructed for polygonal geometries where all the interior angles are equal to π/n (n is an integer). It is stated that the set of such polygons consists of the rectangle (known result) and three types of triangles. Some new explicit formulas are obtained for the eigenfrequencies of the triangles. It is demonstrated that the proposed technique also permits an exact representation of the impulse response function for the geometries described. © *2000 Acoustical Society of America.* [S0001-4966(99)01012-7]

PACS numbers: 43.20.Ks [ANN]

INTRODUCTION

The structure of the wave field in closed spaces is very complex, even if one only considers polygon and polyhedron scale models. Some explicit analytical results have been obtained for rectangular spaces (both two- and three-dimensional), on the basis of the classical modal representation in the form of trigonometric series.[1] At the same time, an alternative ''image'' representation is well known in acoustics, and it is proved in Ref. 2 that an exact solution, given by the image method for rectangular spaces, can be derived directly from the modal solution.

Let us assume that the wave process is harmonic with respect to time. Then the wave function $p(x,y)$ satisfies the Helmholtz equation:

$$P(x,y,t)=p(x,y)\exp(-i\omega t), \quad \Delta p+k^2p=0, \quad k=\omega/c, \tag{1}$$

where c is the wave speed. The main idea of the image method for the rectangular rigid-wall room is clear from Fig. 1. If there is a point source (x_0,y_0): $p_0=H_0^{(1)}[k\sqrt{(x_0-x)^2+(y_0-y)^2}]$ placed inside the space, then to satisfy the trivial boundary condition for the normal derivative, $\partial p/\partial n=0$, one may organize a two-dimensional array of virtual images that provides intrinsic symmetry with respect to an arbitrary boundary point on the wall. The response at the receiving point is then given by a two-dimensional series. This technique has been applied by several authors to the case of impulse sources,[1,2] when this series is convergent, since only a finite number of virtual sources can contribute to the response at a certain moment.

One can apply this approach to the harmonic process which leads, in the two-dimensional case, to the following result:

$$\begin{aligned} p(x_1,y_1)=&S(x_0-x_1,y_0-y_1,a,b)+S(x_0+x_1,y_0-y_1,a,b)\\ &+S(x_0-x_1,y_0+y_1,a,b)\\ &+S(x_0+x_1,y_0+y_1,a,b), \end{aligned} \tag{2}$$

where the function S is given by the double series

$$S(x,y,a,b)=\sum_{m,n=-\infty}^{\infty} H_0^{(1)}[k\sqrt{(x+2am)^2+(y+2bn)^2}]. \tag{3}$$

Although the solution is expressed in explicit form (3), the series does not converge in a classical sense. Thus, one cannot use result (3) for direct computations.

I. AN ALTERNATIVE REPRESENTATION FOR RECTANGULAR SPACE

One may treat the series in the framework of a ''small attenuation'' principle. If a small imaginary component is added to the wave number: $k_\varepsilon=k+i\varepsilon$, $0<\varepsilon\ll 1$, then series (3) becomes exponentially convergent, and it has a finite limit when $\varepsilon\to 0$, as in the Poisson–Abel method of generalized summation.[3] However, it is not clear how this approach can be treated directly. That is why we have developed another idea. Since the function $S(x,y,a,b)$ is periodic with respect to both its arguments, let us assume that $0\leqslant x<2a$, $0\leqslant y<2b$. Then we use the integral representation of the Hankel function

$$H_0^{(1)}(k_\varepsilon\sqrt{x^2+y^2})=\frac{1}{\pi i}\int_{-\infty}^{\infty} e^{-\gamma(\alpha)x}\frac{e^{-i\alpha y}}{\gamma(\alpha)}d\alpha,$$

$$\gamma(\alpha)=\sqrt{\alpha^2-k_\varepsilon^2}. \tag{4}$$

Thus, series (3) may be rewritten as

$$\begin{aligned} S(x,y,a,b)=\frac{1}{\pi i}\sum_{n=-\infty}^{\infty}\int_{-\infty}^{\infty}\Bigg[&\sum_{m=0}^{\infty} e^{-\gamma(\alpha)(2am+x)}\\ &+\sum_{m=1}^{\infty} e^{-\gamma(\alpha)(2am-x)}\Bigg]\frac{e^{-i\alpha|2bn+y|}}{\gamma(\alpha)}d\alpha. \end{aligned} \tag{5}$$

The branching function $\gamma(\alpha)$ has a positive real part: $\mathrm{Re}[\gamma(\alpha)]>0$ when $\varepsilon>0$ (see Ref. 4). Hence, the last series is a geometric progression, which yields

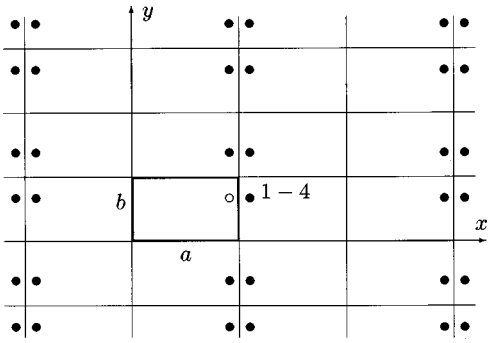

FIG. 1. Arrangement of virtual sources for the rectangular domain.

$$
\begin{aligned}
&S(x,y,a,b)\\
&\quad=\frac{1}{\pi i}\sum_{n=-\infty}^{\infty}\int_{-\infty}^{\infty}\frac{\exp[-\gamma(\alpha)x]+\exp[\gamma(\alpha)(x-2a)]}{1-\exp[-2a\gamma(\alpha)]}\\
&\qquad\times\frac{e^{-i\alpha|2bn+y|}}{\gamma(\alpha)}d\alpha\\
&\quad=\frac{1}{\pi i}\sum_{n=-\infty}^{\infty}\int_{-\infty}^{\infty}\frac{\cosh[(a-x)\gamma(\alpha)]}{\sinh[a\gamma(\alpha)]}\\
&\qquad\times\frac{e^{-i\alpha|2bn+y|}}{\gamma(\alpha)}d\alpha. \qquad (6)
\end{aligned}
$$

Obviously, there is no obstacle here to applying a standard expansion in residues at simple poles, because the integrand is an exponentially decaying meromorphic function with the integration contour removing down to infinity. By so doing, one obtains the following result:

$$
\begin{aligned}
S(x,y,a,b)&=-i\sum_{m=0}^{\infty}\delta_m\frac{\cos(\pi mx/a)}{q_m}\\
&\quad\times\sum_{n=-\infty}^{\infty}\exp(-|2bn+y|q_m/a),\\
&\quad q_m=\sqrt{(\pi m)^2-(ak_\varepsilon)^2},\quad \delta_0=1,\quad \delta_m=2\\
&\quad (m=1,2,\ldots). \qquad (7)
\end{aligned}
$$

Since the real part of the quantities q_m is positive with $\varepsilon>0$, the last series is again a geometric progression, its sum being equal to

$$
\begin{aligned}
&\sum_{n=0}^{\infty}\exp\left[-\frac{(2bn+y)}{a}q_m\right]+\sum_{n=1}^{\infty}\exp\left[-\frac{(2bn-y)}{a}q_m\right]\\
&\quad=\frac{\exp[-yq_m/a]+\exp[(y-2b)q_m/a]}{1-\exp[-2bq_m/a]}\\
&\quad=\frac{\cosh[(b-y)q_m/a]}{\sinh[bq_m/a]}. \qquad (8)
\end{aligned}
$$

Therefore, the final representation ($\varepsilon\to 0$) may be obtained from (7) and (8), as follows:

$$
\begin{aligned}
S(x,y,a,b)&=-i\sum_{m=0}^{\infty}\delta_m\frac{\cos(\pi mx/a)}{\sqrt{(\pi m)^2-(ak)^2}}\\
&\quad\times\frac{\cosh[\sqrt{(\pi m)^2-(ak)^2}(b-y)/a]}{\sinh[\sqrt{(\pi m)^2-(ak)^2}b/a]}. \qquad (9)
\end{aligned}
$$

II. TESTING THE MAIN RESULT

Formula (9) is worthy of special discussion. First of all, it admits the following exchange in notations: $x\to y$, $y\to x$, $a\to b$, $b\to a$, since the same development procedure can be performed (as in the previous section), starting to sum first over parameter n, and then over parameter m.

Further, for an arbitrary fixed dimensionless frequency parameter ak only a finite number of the series terms in (9) have an oscillating character (for $\pi m<ak$), and the others decay exponentially when the parameter m increases. Thus, Eq. (9) is indeed an efficient alternative explicit representation for the double divergent series (3).

The result obtained has also been tested by a boundary element technique. In order to create a wave field without singularities inside the closed space, we may remove the point-source, which leads to the nontrivial boundary condition:

$$
\begin{aligned}
&\frac{\partial p}{\partial n}=-\frac{\partial H_0^{(1)}(kr)}{\partial n}=kH_1^{(1)}(kr)\frac{\partial r}{\partial n},\\
&r=[(x-x_0)^2+(y-y_0)^2]^{1/2},\quad (x,y)\in l. \qquad (10)
\end{aligned}
$$

Then the Kirchhoff integral formula determines the wave field at an arbitrary point (x_1,y_1) inside the boundary contour l, as follows:

$$
\begin{aligned}
p(x_1,y_1)&=H_0^{(1)}(kr_0)+\frac{ki}{4}\int_l\Big[H_0^{(1)}(kr_1)H_1^{(1)}(kr)\frac{\partial r}{\partial n}\\
&\qquad+u(x,y)H_1^{(1)}(kr_1)\frac{\partial r_1}{\partial n}\Big]dl_{xy},\\
r_0&=[(x_1-x_0)^2+(y_1-y_0)^2]^{1/2}, \qquad (11)\\
r_1&=[(x-x_1)^2+(y-y_1)^2]^{1/2},
\end{aligned}
$$

which contains the unknown boundary value of the regular wave function $u(x,y)=p(x,y)-H_0^{(1)}(kr)$, $(x,y)\in l$. This function can be defined from the boundary integral equation given by the same Kirchhoff formula:

$$
\begin{aligned}
&\frac{1}{2}u(x_1,y_1)-\frac{ki}{4}\int_l u(x,y)H_1^{(1)}(kr_1)\frac{\partial r_1}{\partial n}dl_{xy}\\
&\quad=\frac{ki}{4}\int_l H_0(kr_1)H_1^{(1)}(kr)\frac{\partial r_1}{\partial n}dl_{xy},\quad (x_1,y_1)\in l, \qquad (12)
\end{aligned}
$$

which holds for the arbitrary smooth boundary contour l. If the contour l contains some corners, then the product $\frac{1}{2}$ in the first term should be replaced by a coefficient coupled with the value of the angle measured in radians (see Ref. 5).

In the numerical treatment we used the simplest version of the boundary element method (BEM) in the following way: If one takes a mesh with a small elementary arc Δl_j

TABLE I. Comparison of explicit solution (2) and (7) with BEM computations for rectangular space: $k=3.0$, $a=1.0$, $b=0.8$, $x_0=0.5$, $y_0=0.4$, $y=0.2$.

x	(2), (7)	BEM ($N=200$)	BEM ($N=300$)	BEM ($N=400$)
0.05	0.824 i	−0.0018+0.810 i	−0.0014+0.815 i	−0.0012+0.817 i
0.10	0.800 i	−0.0018+0.781 i	−0.0014+0.786 i	−0.0012+0.789 i
0.15	0.758 i	−0.0018+0.735 i	−0.0015+0.740 i	−0.0012+0.743 i
0.20	0.697 i	−0.0019+0.672 i	−0.0016+0.678 i	−0.0013+0.681 i
0.25	0.619 i	−0.0021+0.597 i	−0.0017+0.603 i	−0.0014+0.606 i
0.30	0.530 i	−0.0022+0.512 i	−0.0018+0.518 i	−0.0015+0.522 i
0.35	0.441 i	−0.0024+0.424 i	−0.0019+0.430 i	−0.0016+0.434 i
0.40	0.363 i	−0.0025+0.343 i	−0.0020+0.350 i	−0.0016+0.353 i
0.45	0.310 i	−0.0025+0.284 i	−0.0020+0.291 i	−0.0017+0.294 i
0.50	0.292 i	−0.0026+0.262 i	−0.0020+0.269 i	−0.0017+0.272 i

$=(l_j, l_{j+1})$, then the method applied is based upon a ''stepped'' approximation of the integrand: $f_j \equiv \text{const}$, $\forall j$, so that $\int f_j dl = f_j \cdot \Delta l_j$ (the integral is taken over the arc Δl_j).

Comparison between the exact explicit solution given by (2) and (9) and direct numerical computations is shown in Table I. Note that the explicit formula (9) assumes the wave function to be imaginary. The results of the numerical simulation by the BEM show a nontrivial but in fact very small real part when compared with the imaginary one.

III. EXTENSION TO MORE COMPLEX POLYGONS

It is not easy to extend the image method to more complex polygonal shapes. Irregular shapes involve a more complicated procedure to find the positions of the virtual sources. Some studies try to develop a general algorithm to detect their arrangement;[6] however, they seem to sketch a general methodological basis rather than a concrete algorithm with formulas.

It is important to clarify the property of the exact solution for rectangular spaces. If we look at Fig. 1 again, it becomes clear that four virtual sources crowd around each corner of the main rectangle, symmetrically with respect to its faces, at equal distances from the corner. They correspond to virtual sources in an exact solution for a point source placed in a quarter-plane. It is known[7] that for an arbitrary wedge with the angle $0<\vartheta<2\pi$, the total wave field consists of the geometric–optic component and the wave diffracted by the wedge corner. The latter disappears when $\vartheta=\pi/n$, where n is an arbitrary positive integer. Essentially, this property is connected with the evident statement that only for these values of ϑ is the number of virtual sources outside the wedge finite, being equal to $2n$ (including the real source). Obviously, the case $n=2$ is related to the quarter-space.

The main statement of the present section is that one can construct an exact explicit solution for polygonal spaces where only a geometric–optic wave component is present. In other words, each angle of the polygon has to be taken in the form π/n.

Let us study this set of polygons in more detail. Let l denote the number of the sides; the sum of the interior angles is thus $\pi(l-2)$. On the other hand, if each angle $\vartheta=\pi/n \leqslant \pi/2$, then this sum is not greater than $\pi l/2$, which means $\pi(l-2)\leqslant \pi l/2$, or $l\leqslant 4$. A trivial treatment shows that there are only four possible cases: (1) rectangle ($n=2$ for each angle); (2) equilateral triangle ($n=3$ for each angle); (3) isosceles right-angled triangle ($n=2$ for one angle and $n=4$ for others); (4) right-angled triangle ($\vartheta_1=\pi/2, n=2$) with $\vartheta_2=\pi/3$ ($n=3$) and $\vartheta_3=\pi/6$ ($n=6$). The permissible geometries of the triangles are shown in Fig. 2(a)–(c).

The exact explicit solutions for them are the following:

$$\text{(a) } a=\frac{3}{2}c, \quad b=\frac{\sqrt{3}}{2}c,$$
$$p(x_1,y_1)=\sum_{i=1}^{12} S(\xi_i-x_1, \eta_i-y_1, a, b), \tag{13}$$

$$\text{(b) } p(x_1,y_1)=\sum_{i=1}^{8} S(\xi_i-x_1, \eta_i-y_1, a, a), \tag{14}$$

$$\text{(c) } a=\frac{\sqrt{3}}{2}c, \quad b=\frac{3}{2}c \ (c \text{ is the hypotenuse})$$
$$p(x_1,y_1)=\sum_{i=1}^{24} S(\xi_i-x_1, \eta_i-y_1, a, b), \tag{15}$$

where (ξ_i, η_i) are the Cartesian coordinates of the virtual sources, $(\xi_1, \eta_1)=(x_0, y_0)$ being the real source. The function S is given by (9). The arrangement of the virtual sources, marked in Fig. 2, is evidently given by certain analytical expressions, which are omitted for reasons of space. Table II demonstrates a spectral response for the equilateral triangle when the source is placed in its central point.

IV. ESTIMATE OF THE EIGENFREQUENCIES

Obviously, the eigenvalues of the wave number k are determined by Eq. (9) when the hyperbolic sine becomes equal to zero:

$$\begin{aligned}\sinh[\sqrt{(\pi m)^2-(ak)^2}\, b/a]=0 &\sim \sqrt{(\pi m)^2-(ak)^2}\, b/a \\ &= -\pi n i \sim k_{mn} \\ &= \pi\sqrt{\frac{m^2}{a^2}+\frac{n^2}{b^2}}\end{aligned} \tag{16}$$

for arbitrary integer values of m and n. For the rectangular domain with the sides a and b this result is well known in literature. For triangular spaces it involves some new exact estimates:

(a) equilateral triangle with side-length c:

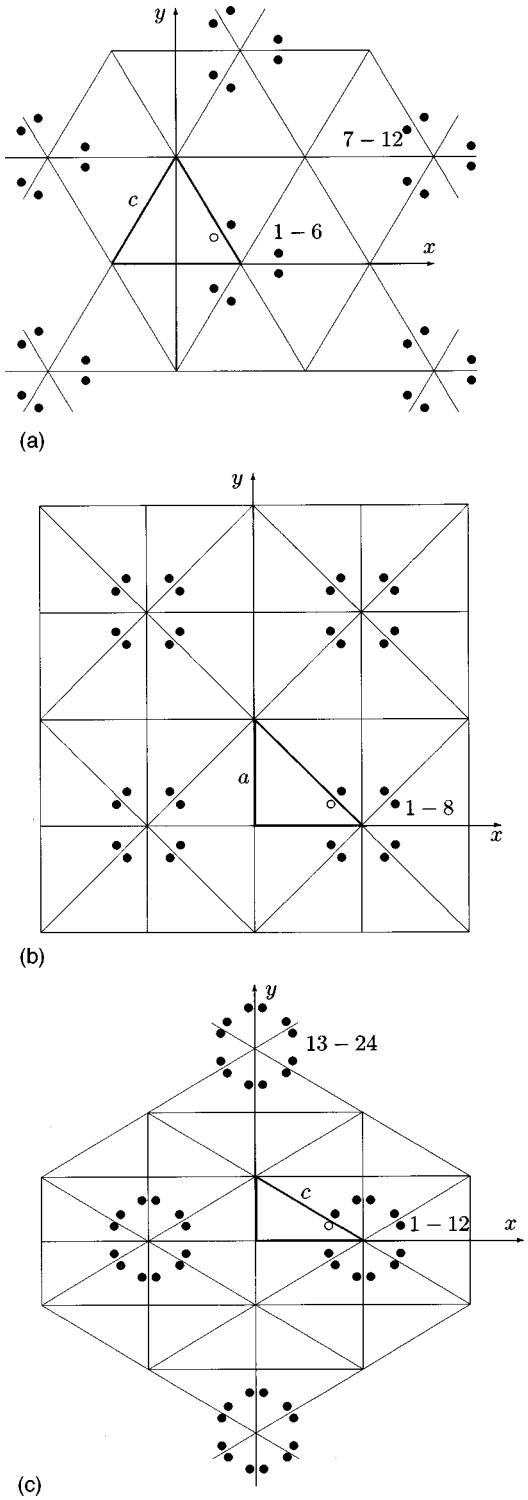

FIG. 2. Arrangement of virtual sources for triangular spaces: (a) equilateral triangle with side-length c; (b) isosceles right-angled triangle with leg a; (c) right-angled triangle with the acute angles equal to 30 and 60 degrees and the hypotenuse c.

$$k_{mn}=\frac{2\pi}{3c}\sqrt{m^2+3n^2}, \tag{17}$$

(b) isosceles right-angled triangle (Table III) with the length of the leg equal to a:

$$k_{mn}=\frac{\pi}{a}\sqrt{m^2+n^2}, \tag{18}$$

TABLE II. Comparison of explicit solution (13) and (7) with BEM computations for equilateral triangle: $k=2.0$, $c=1.0$, $x_0=0.25$, $y_0=0.25/\sqrt{3}$, $y=0.4$.

x	(13), (7)	BEM ($N=300$)	BEM ($N=600$)
−0.25	3.19 i	−0.0374+3.15 i	−0.0222+3.17 i
−0.20	3.16 i	−0.0378+3.12 i	−0.0225+3.14 i
−0.15	3.10 i	−0.0380+3.06 i	−0.0226+3.08 i
−0.10	3.02 i	−0.0381+2.97 i	−0.0227+2.99 i
−0.05	2.92 i	−0.0381+2.85 i	−0.0227+2.88 i
0.00	2.78 i	−0.0379+2.71 i	−0.0227+2.73 i
0.05	2.63 i	−0.0376+2.55 i	−0.0225+2.57 i
0.10	2.44 i	−0.0371+2.37 i	−0.0222+2.39 i
0.15	2.24 i	−0.0365+2.18 i	−0.0219+2.20 i
0.20	2.03 i	−0.0357+1.99 i	−0.0214+2.01 i
0.25	1.82 i	−0.0347+1.80 i	−0.0209+1.82 i

(c) right-angled triangle (Table IV) with the acute angles equal to 30 and 60 degrees and the hypotenuse c:

$$k_{mn}=\frac{2\pi}{3c}\sqrt{3m^2+n^2}. \tag{19}$$

It is interesting to note that (b) proves the identity of the eigenfrequencies for the isosceles right-angled triangle and a square of the same size c. Note that the wave fields in these two types of closed spaces are absolutely different, even if the point–source is placed in the same position.

In fact, cases (a) and (c) involve identical eigenvalues, although the wave fields in these two triangles are also different.

V. CONCLUDING REMARKS

(1) A comparison between the exact solutions and the direct numerical method is only possible for low and moderate frequencies, because when the frequency increases the number of nodes should be taken proportionally to the frequency parameter. However, the main result is that (9) guar-

TABLE III. Comparison of explicit solution (14) and (7) with BEM computations for isosceles right-angled triangle: $k=1.0$, $a=3.0$, $x_0=1.0$, $y_0=1.0$, $x=0.5$.

y	(14), (7)	BEM ($N=300$)	BEM ($N=450$)	BEM ($N=600$)
0.15	0.705 i	−0.0468+0.659 i	−0.0300+0.675 i	−0.0142+0.692 i
0.30	0.672 i	−0.0470+0.626 i	−0.0301+0.643 i	−0.0145+0.660 i
0.45	0.618 i	−0.0469+0.576 i	−0.0300+0.594 i	−0.0147+0.610 i
0.60	0.547 i	−0.0463+0.517 i	−0.0295+0.535 i	−0.0148+0.551 i
0.75	0.494 i	−0.0452+0.464 i	−0.0287+0.481 i	−0.0146+0.497 i
0.90	0.468 i	−0.0434+0.438 i	−0.0275+0.455 i	−0.0143+0.470 i
1.05	0.488 i	−0.0410+0.466 i	−0.0259+0.483 i	−0.0137+0.494 i
1.20	0.569 i	−0.0379+0.553 i	−0.0240+0.570 i	−0.0129+0.582 i
1.35	0.694 i	−0.0343+0.682 i	−0.0216+0.698 i	−0.0119+0.708 i
1.50	0.849 i	−0.0300+0.828 i	−0.0020+0.843 i	−0.0017+0.852 i
1.65	0.992 i	−0.0252+0.978 i	−0.0158+0.992 i	−0.0093+0.998 i
1.80	1.112 i	−0.0198+1.122 i	−0.0124+1.134 i	−0.0078+1.139 i
1.95	1.190 i	−0.0140+1.257 i	−0.0124+1.268 i	−0.0078+1.269 i
2.10	1.331 i	−0.0078+1.380 i	−0.0048+1.389 i	−0.0042+1.388 i
2.25	1.475 i	−0.0013+1.490 i	−0.0006+1.498 i	−0.0023+1.493 i
2.40	1.580 i	0.0055+1.586 i	0.0037+1.591 i	−0.0004+1.582 i

TABLE IV. Comparison of explicit solution (15) and (7) with BEM computations for right-angled triangle with the acute angles 30 and 60 degrees: $k=2.0$, $c=1.0$, $x_0=0.25\sqrt{3}$, $y_0=0.125$, $x=0.4$.

y	(15), (7)	BEM ($N=300$)	BEM ($N=600$)	BEM ($N=900$)
0.025	3.51 i	0.097+3.66 i	0.075+3.61 i	0.061+3.58 i
0.050	3.45 i	0.099+3.58 i	0.076+3.53 i	0.062+3.51 i
0.075	3.35 i	0.101+3.44 i	0.078+3.40 i	0.063+3.37 i
0.100	3.20 i	0.102+3.26 i	0.079+3.22 i	0.064+3.19 i
0.125	2.99 i	0.103+3.16 i	0.080+3.11 i	0.065+3.08 i
0.150	3.26 i	0.105+3.33 i	0.080+3.28 i	0.065+3.25 i
0.175	3.47 i	0.106+3.59 i	0.081+3.54 i	0.066+3.51 i
0.200	3.64 i	0.107+3.80 i	0.082+3.75 i	0.067+3.72 i
0.225	3.78 i	0.108+3.97 i	0.083+3.92 i	0.067+3.89 i
0.250	3.89 i	0.109+4.12 i	0.084+4.06 i	0.068+4.03 i

antees that a finite number of series terms is sufficient for precise calculations at arbitrary frequencies.

The results given in the tables show that error of the calculations by the BEM decreases when the number of the nodes N increases, which is quite natural.

(2) The proposed technique may be applied to the classical problem of room acoustics[1] as regards the impulse response function (time domain Green's function), by analogy to the single-frequency point source. The exact solution is of the same form (2) (rectangular room) and (13)–(15) (triangular spaces), the function S being given as

$$S(t,x,y,a,b) = \frac{1}{2\pi}\sum_{m,n=-\infty}^{\infty}\frac{\mathrm{H}[t-\sqrt{(x+2am)^2+(y+2bn)^2}/c]}{\{c^2t^2-[(x+2am)^2+(y+2bn)^2]\}^{1/2}}, \tag{20}$$

where H( ) is the Heaviside step function.

Unlike the divergent double series representation (3), which is valid for the harmonic wave process, only a finite number of terms can contribute to the sum of the last series at a certain moment, as noted in the Introduction.

(3) The approach developed is also applicable to three-dimensional problems, in that the image method gives an exact solution for three-dimensional rectangular spaces. The divergent series arising may be treated by analogy to the two-dimensional case, which will be the subject of future work by the authors.

[1] P. M. Morse and K. U. Ingard, *Theoretical Acoustics* (McGraw–Hill, New York, 1968).
[2] J. B. Allen and D. A. Berkley, ''Image method for efficiently simulating small-room acoustics,'' J. Acoust. Soc. Am. **65**, 943–950 (1979).
[3] C. S. Rees, S. M. Shah, and C. V. Stanojevic, *Theory and Applications of Fourier Analysis* (Marcel Dekker, New York, 1981).
[4] R. Mittra and S. W. Lee, *Analytical Techniques in the Theory of Guided Waves* (MacMillan, New York, 1971).
[5] P. K. Banerjee and R. Butterfield, *Boundary Element Methods in Engineering Science* (McGraw–Hill, Oxford, 1981).
[6] J. Borish, ''Extension of the image model to arbitrary polyhedra,'' J. Acoust. Soc. Am. **75**, 1827–1836 (1984).
[7] E. Skudrzyk, *The Foundation of Acoustics* (Springer–Verlag, Vienna, 1971).

Acoustics of a flanged cylindrical pipe using singular basis functions

N. Amir[a] and H. Matzner
Center for Technological Education Holon, Golomb 52, Holon 58102, Israel

S. Shtrikman
Department of Electronics, Weizmann Institute of Science, Rehovoth 76100, Israel and Department of Physics, UCSD, La Jolla, California 92093

(Received 29 March 1999; accepted for publication 26 October 1999)

The problem of acoustic radiation from a cylindrical pipe with an infinite flange has been discussed in a number of papers. The most common approach is to decompose the field inside the pipe over a basis of Bessel functions. A very large number of basis functions is usually required, with a large degree of ripple appearing as an artifact in the solution. In this paper it is shown that a close analysis of the velocity field near the corner yields a new family of functions, which are called ''edge functions.'' Using this set of functions as test functions and applying the moment method on the boundary between the waveguide and free space, a solution is obtained with greatly improved convergence properties and no ripple. © *2000 Acoustical Society of America.*
[S0001-4966(00)02902-7]

PACS numbers: 43.20.Mv, 43.20.Bi [DEC]

LIST OF SYMBOLS

p	acoustic pressure
k_0	free space wave number
k_i	confined wave number, cylindrical coordinate system
$\vec{v}$	acoustic particle velocity
$\vec{n}$	normal
ρ	density of air
c	speed of sound in air
ω	angular frequency
β_i	eigenvalues for higher-order modes in a cylindrical system
β_i'	zeros of the first-order Bessel function
$J_0(\cdot)$	Bessel function of order 0
z	axial coordinate
r	radial coordinate
R	radius of the aperture

INTRODUCTION

The interaction of acoustic waves propagating in a cylindrical waveguide with the waves they excite outside the end of the waveguide has been treated widely in the literature. The main aspects discussed are the internal reflections created by the open termination, the pressure and velocity fields on the opening itself, the waves excited in free space beyond the opening, and the end correction. The basic problem has two basic variations: a flanged opening and an unflanged one, though some works treat the intermediate case of a finite flange.[1]

Initial studies of this subject date to Rayleigh.[2] Rayleigh calculated upper and lower bounds on the static end correction. This work was carried further by Daniell[3] and King[4]—all of these being for an infinite flange. Many later works[5–7] mention this parameter also and calculate it to varying degrees of precision. Some of these, such as Levine and Schwinger, extend the idea of the static end correction to a frequency-dependent end correction, calculated up to the cutoff frequency of the second mode.

A convenient formulation for the acoustic field in a cylindrical waveguide is the decomposition of the longitudinal field into forward and backward traveling waves, and decomposition of the lateral field into normal modes based on Bessel functions. Solution of the field inside and outside the waveguide is obtained by assuming an impinging forward traveling pressure wave (most often the plane wave mode only) and then matching the internal and external fields on the aperture; the values that are matched are pressure and axial velocity. The boundary conditions for a perfectly rigid guide and flange are zero normal particle velocity.

In order to match the internal and external fields, one must find an appropriate formulation for the external fields. Morse[8] used a Green's function integral, adopted also by Nomura *et al.*[9] and Zorumski,[10] Norris and Sheng,[5] Wendolowski *et al.*,[7] and others. Bom and Park,[11] on the other hand, use a Fourier–Bessel integral, which proves to be slightly simpler. This approach is adopted in the current paper.

Matching the external and internal fields gives the solution inside the waveguide as an infinite set of equations for the coefficients of the reflected waves. This set of equations must be truncated at some finite value and solved. The resultant coefficients can be used for two purposes: as the cross-reflection coefficients, and for calculating the internal pressure and velocity fields. Zorumski gives a very complete analysis of the reflection coefficients,[10] treating cases where

[a]Electronic mail: noamoto@wine.cteh.ac.il

the impinging wave is not necessarily the plane wave mode, treating annular ducts, and also discussing modes which are not axisymmetric. In such a case there is no special importance to the number of coefficients found in the solution; this depends solely on the cross-reflection coefficient desired. The various coefficients and their frequency dependance is also discussed by Nomura *et al.*[9] and Norris and Sheng.[5] Few papers, on the other hand, attempt to calculate the actual pressure and velocity fields on the aperture. Notably, Wendoloski *et al.*[7] demonstrate that the convergence of this calculation is very slow, requiring a large number of coefficients to reduce the ripple in the numerical solution. This is due to the presence of the sharp edge at the corner of the waveguide and flange. In fact, the velocity there is singular. The Bessel function decomposition attempts to follow this singularity, though such a decomposition is very inefficient in this case. Wendoloski *et al.* point this out, and suggest an improved expansion based on the general form of the singularity.

The present paper presents a moment method solution for the acoustic field on the aperture. The same set of functions is used as expansion functions and test functions; in this case they are commonly termed ''basis functions.'' Those used here are somewhat similar to those presented by Wendoloski *et al.*[7] In order to obtain the best possible set of basis functions they are derived analytically from the behavior of the velocity field at the corner. A similar study of a magnetic field demonstrated that this approach results in greatly improved convergence.[12] In the present study we show that using less than five such basis functions can give a solution better than that obtained with hundreds of normal modes.

The next section presents the general derivation of the problem. In Sec. III we then present the moment method solution using the proposed basis functions (termed here ''edge functions''). The derivation of the edge functions themselves is left to Appendix A. For completeness, in Sec. III we repeat the normal mode solution, as found in a number of other papers.[5,7,11] In Sec. IV the results obtained from applying the two methods are presented and compared, from the point of view of pressure and velocity fields, end correction, and convergence of the solutions. Finally, we conclude in Sec. V with a discussion of the results and of a number of open points. Appendix B includes a discussion of a number of numerical issues encountered when solving the equations.

I. FORMULATION

In this work we consider the acoustic field in a system composed of a cylindrical pipe terminated by an infinite flange, as shown in Fig. 1. Propagation throughout the system is assumed to be lossless. We denote the region in the pipe as region I, and the region outside the pipe as region II. In the cylindrical coordinate system (r,φ,z), the positive z direction is towards the flanged end of the pipe. Denoting the acoustic pressure as p, and considering sinusoidal steady state, the pressure wave must obey the Helmholtz equation

$$\nabla^2 p + k_0^2 p = 0, \tag{1}$$

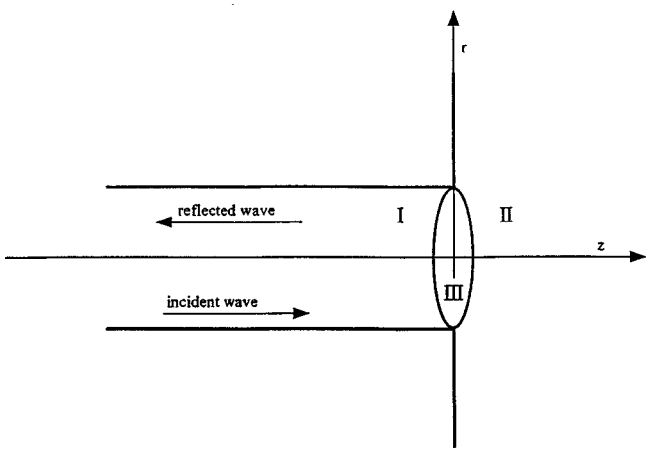

FIG. 1. The geometry of the problem being studied.

where k_0 is the wave number in free space. The particle velocity is given by

$$\vec{v} = -\frac{1}{j\rho\omega}\nabla p, \tag{2}$$

where ω is angular frequency and ρ is the density of air. The boundary condition for a perfectly reflecting surface is zero velocity into the surface. In other words

$$\vec{n}\cdot\vec{v} = 0, \tag{3}$$

where $\vec{n}$ is the normal to the surface of the flange and the pipe.

The acoustic wave inside the pipe (region I) is assumed to be circularly symmetric. Separating into forward and backward propagating waves, these can be decomposed in cylindrical coordinates as infinite sums. In the most general case, the forward propagating wave will be

$$p_I^+(z,r) = \sum_{i=0}^{\infty} a_i J_0(\beta_i r) e^{-jk_i z}, \tag{4}$$

where J_0 is the zeroth-order Bessel function;

$$\beta_i = \begin{cases} 0, & i=0, \\ \beta_i'/R, & i=1,2,\ldots; \end{cases} \tag{5}$$

R is the radius of the pipe; β_i', $i=1,2,\ldots$ are the zeros of the first-order Bessel function J_1; k_i are the confined wave numbers,

$$k_i = \begin{cases} \sqrt{(k_0^2-\beta_i^2)}, & k_0 > \beta_i, \\ -j\sqrt{(\beta_i^2-k_0^2)}, & k_0 < \beta_i; \end{cases} \tag{6}$$

and k_0 is the propagation constant ω/c.

In this work we will consider the more degenerate case, where the forward propagating wave is composed solely of the lowest-order mode; thus in our case,

$$p_I^+(z,r) = e^{-jk_0 z}. \tag{7}$$

The radiation impedance at the flanged opening will excite higher-order modes in the backward propagating wave, thus it will be

$$p_I^-(z,r)=\sum_{i=0}^{\infty} b_i J_0(\beta_i r)e^{jk_i z}, \tag{8}$$

where the b_i are unknown constants. The total pressure in region I is the sum of the forward and backward propagating pressure waves (this basic formulations appears in many previous papers[5,7,10,11]):

$$p_I(z,r)=e^{-jk_0 z}+\sum_{i=0}^{\infty} b_i J_0(\beta_i r)e^{jk_i z}. \tag{9}$$

The acoustic wave in region II is assumed to have only a forward traveling component, caused by radiation from the pipe. In order to receive a mathematically tractable expression for the pressure in this region, we will go through a number of steps. Defining $p_{\mathrm{II}}(x,y,z)$ as the pressure in this region and $\tilde{p}(k_x,k_y)$ as its Fourier transform, we can express the relationship between them in Cartesian coordinates as follows:

$$p_{\mathrm{II}}(x,y,z)=\frac{1}{4\pi^2}\int_{-\infty}^{\infty}\int_{-\infty}^{\infty}\tilde{p}(k_x,k_y) \times e^{-jk_x x}e^{-jk_y y}e^{-j\gamma(k_t)z}\,dk_x\,dk_y. \tag{10}$$

Here $k_t=\sqrt{k_x^2+k_y^2}$; conversely $k_x=k_t\cos\varphi$, $k_y=k_t\sin\varphi$. $\gamma(k_t)$ is defined as

$$\gamma(k_t)=\begin{cases}\sqrt{(k_0^2-k_t^2)}, & k_0>k_t,\\ -j\sqrt{(k_t^2-k_0^2)}, & k_0<k_t.\end{cases} \tag{11}$$

We wish to transform this expression to a cylindrical coordinate system, as used above for the pressure wave inside the waveguide. Assuming circular symmetry, in cylindrical coordinates the same pressure function will be simply a function of r and z, so that in fact there exists a function $p_{1,\mathrm{II}}(r,z)$ such that $p_{\mathrm{II}}(rz\cos\varphi,r\sin\varphi,z)=p_{1,\mathrm{II}}(r,z)$. The above Fourier transform in cylindrical coordinates will then be

$$p_{1,\mathrm{II}}(r,z)=\frac{1}{4\pi^2}\int_{-\infty}^{\infty}\int_{-\infty}^{\infty}\tilde{A}(k_t) \times e^{-jk_x x}e^{-jk_y y}e^{-j\gamma(k_t)z}\,dk_x\,dk_y \tag{12}$$

$$=\frac{1}{4\pi^2}\int_0^{2\pi}d\varphi_k\int_0^{\infty}\tilde{A}(k_t) \times e^{-jk_x x}e^{-jk_y y}e^{-j\gamma(k_t)z}k_t\,dk_t, \tag{13}$$

where $\tilde{A}(k_t)$ is an unknown function to be found. Using the identity[13]

$$\int_0^{2\pi}d\varphi_k e^{j(k_x x+k_y y)}\begin{Bmatrix}\cos m\varphi_k\\ \sin m\varphi_k\end{Bmatrix}=2\pi j^m\begin{Bmatrix}\cos\varphi\\ \sin\varphi\end{Bmatrix}J_m(k_t r), \tag{14}$$

where J_m is the mth-order Bessel function, and setting $m=0$ in our case due to circular symmetry, we obtain the relationship

$$p_{1,\mathrm{II}}(r,z)=\frac{1}{2\pi}\int_0^{\infty}\tilde{A}(k_t)J_0(k_t r)e^{-j\gamma(k_t)z}k_t\,dk_t. \tag{15}$$

Finally, on the interface between the cylinder and free space, marked as region III, we choose to decompose the axial velocity as follows:

$$v_{z,\mathrm{III}}=\sum_{i=1}^{\infty} c_i(R-r)^{\alpha_i}, \quad i=1,2,4,5,7,8,\ldots \quad (i\neq 3,6,9,\ldots), \tag{16}$$

where $\alpha_i=2i/3-1$. The set of functions $(R-r)^{\alpha_i}$, $i=1,2,4,5,7,8,\ldots$, is the proposed set of basis functions, which we call also ''edge functions.'' This scheme was originally suggested in Ref. 12 and will prove to be very computationally effective. The considerations for choosing this decomposition are presented in Appendix A.

Given the above equations, our aim is to find the unknown coefficients c_i, b_i, and an expression for the unknown function $\tilde{A}$.

II. MOMENT METHOD SOLUTION

To find the unknowns stated above, we equate pressure and particle velocity over region III. This is done in three stages: First we equate axial particle velocity in region I for $z=0$ to axial particle velocity on region III. Then we also equate axial particle velocity in region II for $z=0$ to axial particle velocity on region III. Finally we equate pressure in regions I and II for $z=0$. The first two equalities eliminate b_i and $\tilde{A}$, and the third gives us a moment method equation for c_i.

First, equating particle velocity in the axial (z) direction in region II at $z=0$, $r<R$, to particle velocity on region III, and to zero over the flange, gives

$$v_{z,\mathrm{II}}(r,0)=\begin{cases}v_{z,\mathrm{III}}(r), & r<R,\\ 0, & r>R,\end{cases} \tag{17}$$

where v_z signifies axial velocity. Further, particle velocity in region I at $z=0$ is also equal to particle velocity on region III, giving

$$v_{z,\mathrm{I}}(r,0)=v_{z,\mathrm{III}}(r). \tag{18}$$

The acoustic pressures should also be equal for $z=0$, giving

$$p_{1,\mathrm{II}}(r,0)=p_I(0,r), \quad r<R. \tag{19}$$

Our purpose is now to obtain a moment method equation for the expansion over region III. From (2) we obtain

$$v_{z,\mathrm{II}}(r,z)=-\frac{1}{j\rho\omega}\frac{\partial}{\partial z}p_{1,\mathrm{II}}(r,z). \tag{20}$$

Obtaining $v_{z,\mathrm{II}}(r,z)$ from (15) using (20) and inserting it in (17) along with (16) gives

$$\frac{1}{2\pi\rho\omega}\int_0^{\infty}\tilde{A}(k_t)J_0(k_t r)\gamma(k_t)k_t\,dk_t =\begin{cases}\sum_{i=1}^{\infty} c_i(R-r)^{\alpha_i}, & r<R\\ 0, & r>R.\end{cases} \tag{21}$$

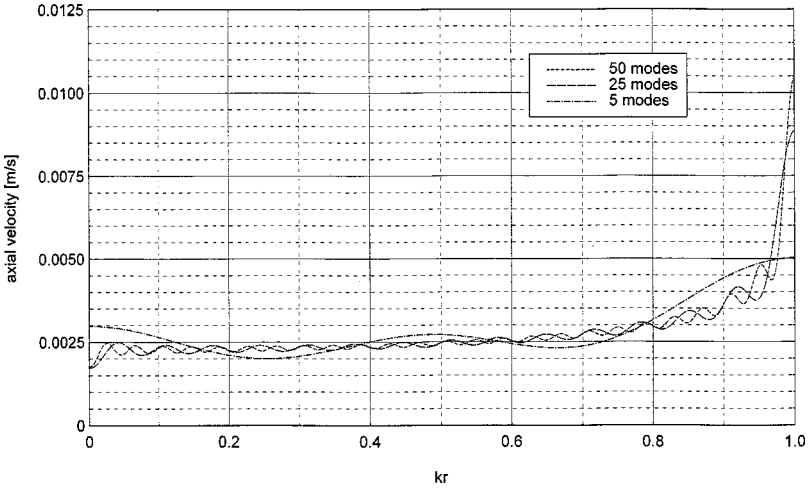

FIG. 2. The axial velocity over the aperture, calculated with 5, 25, and 50 normal modes ($kR=1$).

Similarly, applying (2) to (9) and inserting it with (16) into (18) gives

$$\frac{k_0}{\rho\omega}+\sum_{i=0}^{\infty}\frac{-k_i}{\rho\omega}b_iJ_0(\beta_i r)=\sum_{i=1}^{\infty}c_i(R-r)^{\alpha_i}. \tag{22}$$

Multiplying (21) by $rJ_0(kr)$ and integrating with respect to r from 0 to infinity gives[14]

$$\frac{\gamma(k)}{2\pi\rho\omega}\tilde{A}(k)=\sum_{i=1}^{\infty}c_i\tilde{f}_i(R,k), \tag{23}$$

where $\tilde{f}_i(R,k)$ is a hypergeometric function (see Appendix B),

$$\tilde{f}_i(R,k)=\int_0^R(R-r)^{\alpha_i}J_0(kr)r\,dr$$

$$=R^{2+\alpha_i}\frac{{}_1F_2(\frac{3}{2};\frac{3}{2}+\alpha_i/2,2+\alpha_i/2;-\frac{1}{4}R^2k^2)}{(1+\alpha_i)(2+\alpha_i)}. \tag{24}$$

Multiplying (22) by $rJ_0(\beta_j r)$ and integrating with respect to r from 0 to R gives

$$\frac{k_0R^2}{2\rho\omega}\delta_{0j}-\frac{k_jR^2J_0^2(\beta_jR)}{2\rho\omega}b_j=\sum_{i=1}^{\infty}c_i\tilde{f}_i(R,\beta_j). \tag{25}$$

The last three equations give us expressions for $\tilde{A}$ and b_j, which can be plugged into (15) and (9). Equating them in as in (19) at $z=0$ gives

$$2-\sum_{j=0}^{\infty}\sum_{i=1}^{\infty}c_i\tilde{f}_i(R,\beta_j)\frac{2\rho\omega}{k_jR^2J_0^2(\beta_jR)}J_0(\beta_j r)$$

$$=\int_0^{\infty}\frac{\rho\omega}{\gamma(k_t)}\sum_{i=1}^{\infty}c_i\tilde{f}_i(R,k_t)J_0(k_t r)k_t\,dk_t. \tag{26}$$

This equation still has the free parameter r. Here we apply the basis functions once more: Multiplying (26) by $r(R-r)^{\alpha_l}$ and integrating r from 0 to R gives a matrical equation:

$$\sum_{i=1}^{\infty}c_iA_{il}=d_l, \tag{27}$$

where

$$A_{il}=\sum_{j=0}^{\infty}\frac{2\rho\omega}{k_jR^2J_0^2(\beta_jR)}\tilde{f}_i(R,\beta_j)\tilde{f}_l(R,\beta_j)$$

$$+\int_0^{\infty}\frac{\rho\omega}{\gamma(k_t)}\tilde{f}_i(R,k_t)\tilde{f}_l(R,k_t)k_t\,dk_t, \tag{28}$$

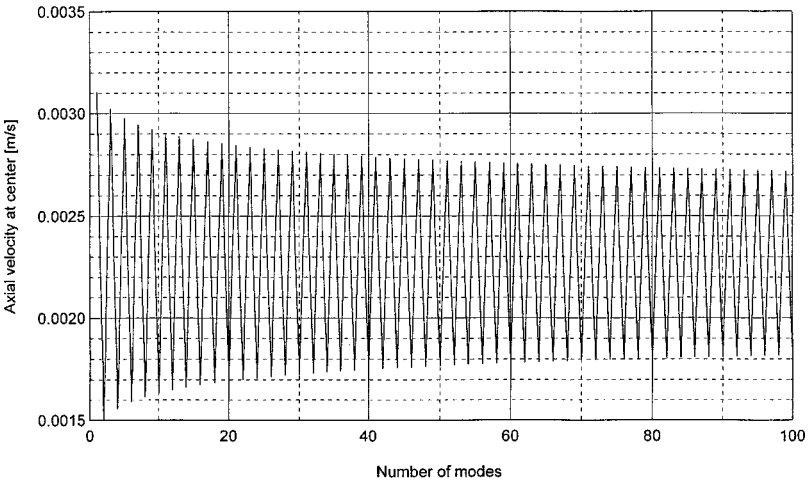

FIG. 3. The axial velocity at the center of the aperture, calculated with 1 to 100 normal modes ($kR=1$).

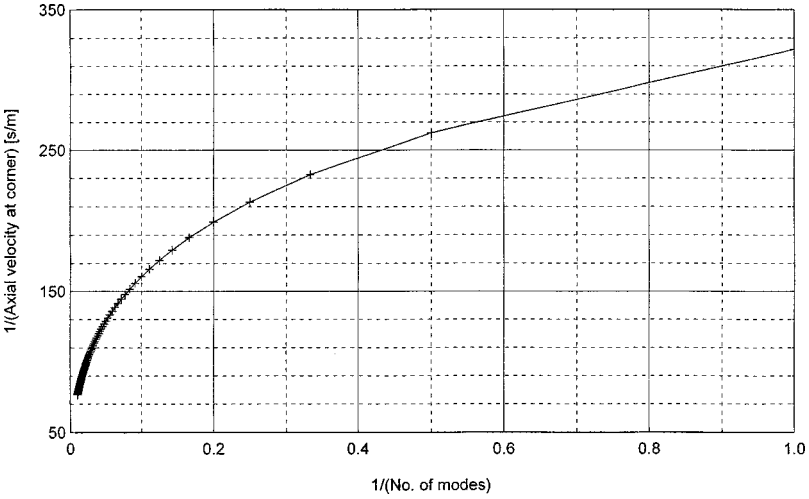

FIG. 4. The reciprocal of the axial velocity at the guide/flange corner versus the reciprocal of the number of normal modes used, calculated with 1 to 100 normal modes ($kR=1$).

$$d_l=\frac{2R^{(2+\alpha_l)}}{(1+\alpha_l)(2+\alpha_l)}, \quad l=1,2,4,5,7,8,\ldots \quad .$$

This is simply an infinite set of linear equations for c_i. The infinite sums and integrals are the coefficients of these equations. A discussion of the numerical issues involved in computing these sums and integrals can be found in Appendix B; the main problem with this set of equations is that it is infinite. An approximate solution can be obtained by truncating and solving a finite subset of equations. It remains to be seen how many equations should be used to achieve a degree of accuracy comparable to that obtained with other methods.

III. NORMAL MODE FORMULATION

As a basis for comparing the above method to more standard formulations, the solution was also obtained using the Bessel functions as basis functions. This solution appears in similar form in papers by Norris and Sheng, Wendoloski *et al.*, and others,[5,7] though it appears that only Bom[11] used the Fourier–Bessel sum to express the external field. This approach is adopted here.

In this analysis we do not define region III as a separate region; instead, pressure and axial velocity are equated at $z=0$ in regions I and II.

Equating axial velocity at $z=0$ gives

$$\frac{1}{2\pi}\int_0^\infty \tilde{A}(k_t)J_0(k_t r)\gamma(k_t)k_t\,dk_t = \begin{cases} k_0-\sum_{i=0}^{\infty} k_i b_i J_0(\beta_i r), & r<R, \\ 0, & r>R. \end{cases} \tag{29}$$

Equating pressure at $z=0$ gives

$$1+\sum_{i=0}^{\infty} b_i J_0(\beta_i r)=\frac{1}{2\pi}\int_0^\infty \tilde{A}(k_t)J_0(k_t r)k_t\,dk_t, \quad r<R. \tag{30}$$

Multiplying (29) by $rJ_0(kr)$ and integrating r from 0 to infinity gives

$$k_0 s_0(R,k)-\sum_{i=0}^{\infty} k_i b_i s_i(R,k)=\frac{\gamma(k_t)}{2\pi}\tilde{A}(k), \tag{31}$$

where we define

$$s_i(R,k)=\int_0^R J_0(\beta_i r)J_0(kr)r\,dr = -\frac{Rk}{\beta_i^2-k^2}J_1(kR)J_0(\beta_i R). \tag{32}$$

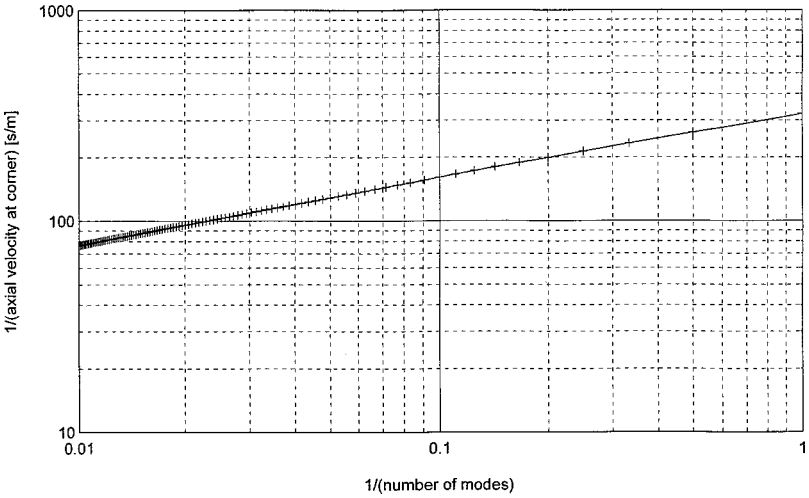

FIG. 5. Log-log of the reciprocal of the axial velocity at the guide/flange corner versus the reciprocal of the number of normal modes used, calculated with 1 to 100 normal modes ($kR=1$). Slope is -0.33.

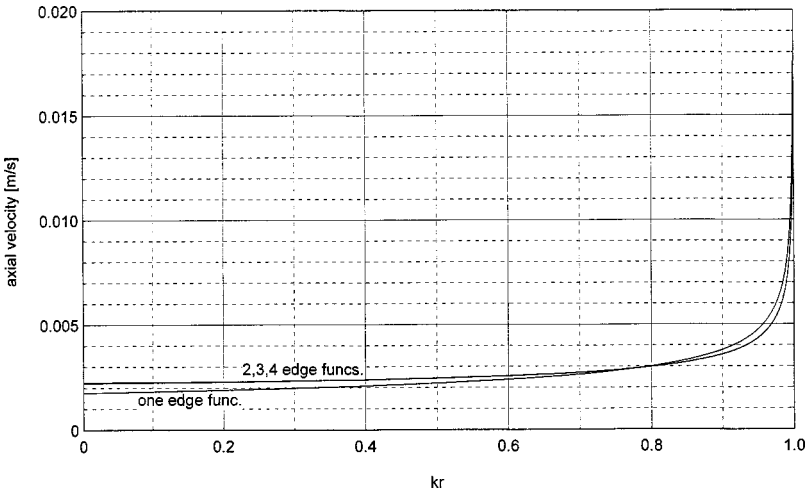

FIG. 6. The axial velocity over the aperture, calculated with one to four edge functions. Calculations with two to four edge functions are nearly indistinguishable ($kR=1$).

Taking the expression for $\tilde{A}(k)$ from (31) and putting into (30) gives

$$1+\sum_{i=0}^{\infty} b_i J_0(\beta_i r)=\int_0^{\infty}\frac{1}{\gamma(k_t)} \times\left(k_0 s_0(R,k_t)-\sum_{i=0}^{\infty} k_i b_i s_i(R,k_t)\right) \times J_0(k_t r)k_t\,dk_t, \quad r<R. \tag{33}$$

Here we use $rJ_0(\beta_j r)$ as basis functions. Multiplying (33) by $rJ_0(\beta_j r)$ functions and integrating over r from 0 to R gives

$$\frac{R^2}{2}\delta_{0j}+b_j J_0(\beta_j)\frac{R^2}{2} =\int_0^R\int_0^{\infty}\frac{1}{\gamma(k_t)}k_0 s_0(R,k_t)J_0(\beta_j r)J_0(k_t r)k_t\,dk_t r\,dr -\int_0^R\int_0^{\infty}\frac{1}{\gamma(k_t)}\sum_{i=0}^{\infty} k_i b_i s_i(R,k_t)J_0(\beta_j r) \times J_0(k_t r)k_t\,dk_t r\,dr. \tag{34}$$

Rearranging then gives

$$\sum_{i=0}^{\infty} b_i\left[k_i\int_0^{\infty}\frac{1}{\gamma(k_t)}s_i(R,k_t)s_j(R,k_t)k_t\,dk_t+\delta_{ij}J_0(\beta_j R)\frac{R^2}{2}\right] =\int_0^{\infty}\frac{1}{\gamma(k_t)}k_0 s_0(R,k_t)s_j(R,k_t)k_t\,dk_t-\frac{R^2}{2}\delta_{0j}, \quad j=0,1,2,3,\ldots\ . \tag{35}$$

Finally, using (32) gives

$$\sum_{i=0}^{\infty} b_i B_{ij}=e_j, \tag{36}$$

where

$$B_{ij}=k_i J_0(\beta_i R)J_0(\beta_j R) \times\int_0^{\infty}\frac{k_t^3}{\gamma(k_t)(\beta_i^2-k_t^2)(\beta_j^2-k_t^2)}J_1^2(k_t R)\,dk_t +\delta_{ij}J_0(\beta_j R)\frac{R^2}{2}, \tag{37}$$

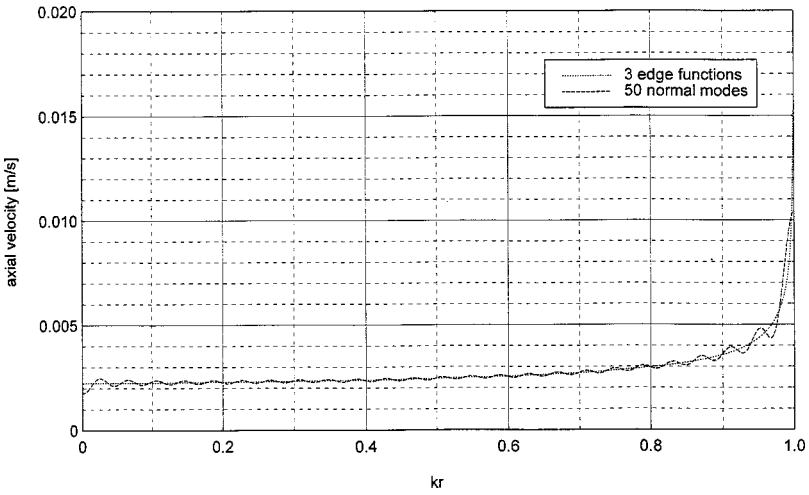

FIG. 7. Comparison of axial velocity over aperture, calculated with 50 normal modes and three edge functions ($kR=1$).

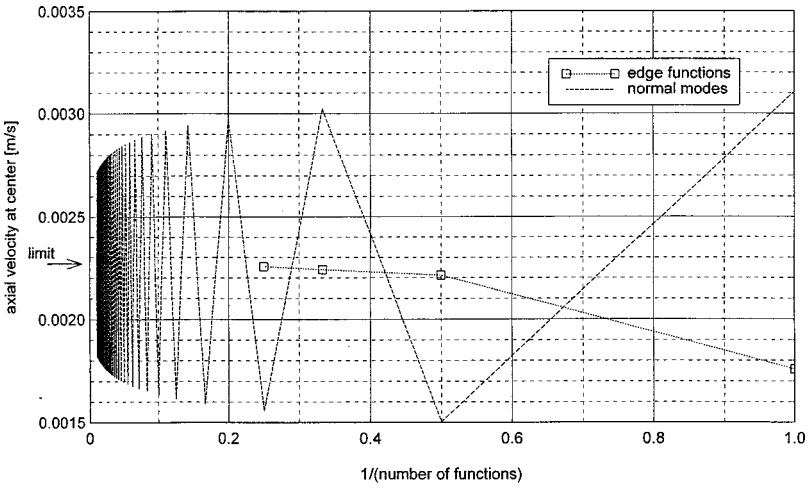

FIG. 8. Convergence of axial velocity at center of aperture. Dashed line—1 to 100 normal modes; dotted line—one to five edge functions. Graph is plotted versus reciprocal of number of modes ($kR=1$).

$$e_j = \int_0^\infty \frac{k_t}{\gamma(k_t)(\beta_j^2 - k_t^2)} k_0 J_1^2(k_t R)\, dk_t - \frac{R^2}{2}\delta_{0j},$$

$$j = 0,1,2,3,\ldots .$$

To solve for the coefficients b_i we must evaluate the infinite integrals in this equation. Once more, this gives an infinite set of linear equations for b_i to be truncated and solved through matrix inversion. The integrals in this case prove to be simpler to evaluate than those encountered in the moment method. A discussion of the numerical issues involved in computing these sums and integrals can be found in Appendix B.

IV. RESULTS

The numerical details of solving Eqs. (27) and (36) are discussed in Appendix B. Therefore, in this section we will discuss only the full solutions to these equations. First we wish to demonstrate the improved convergence obtained with the use of the proposed basis functions—the edge functions.

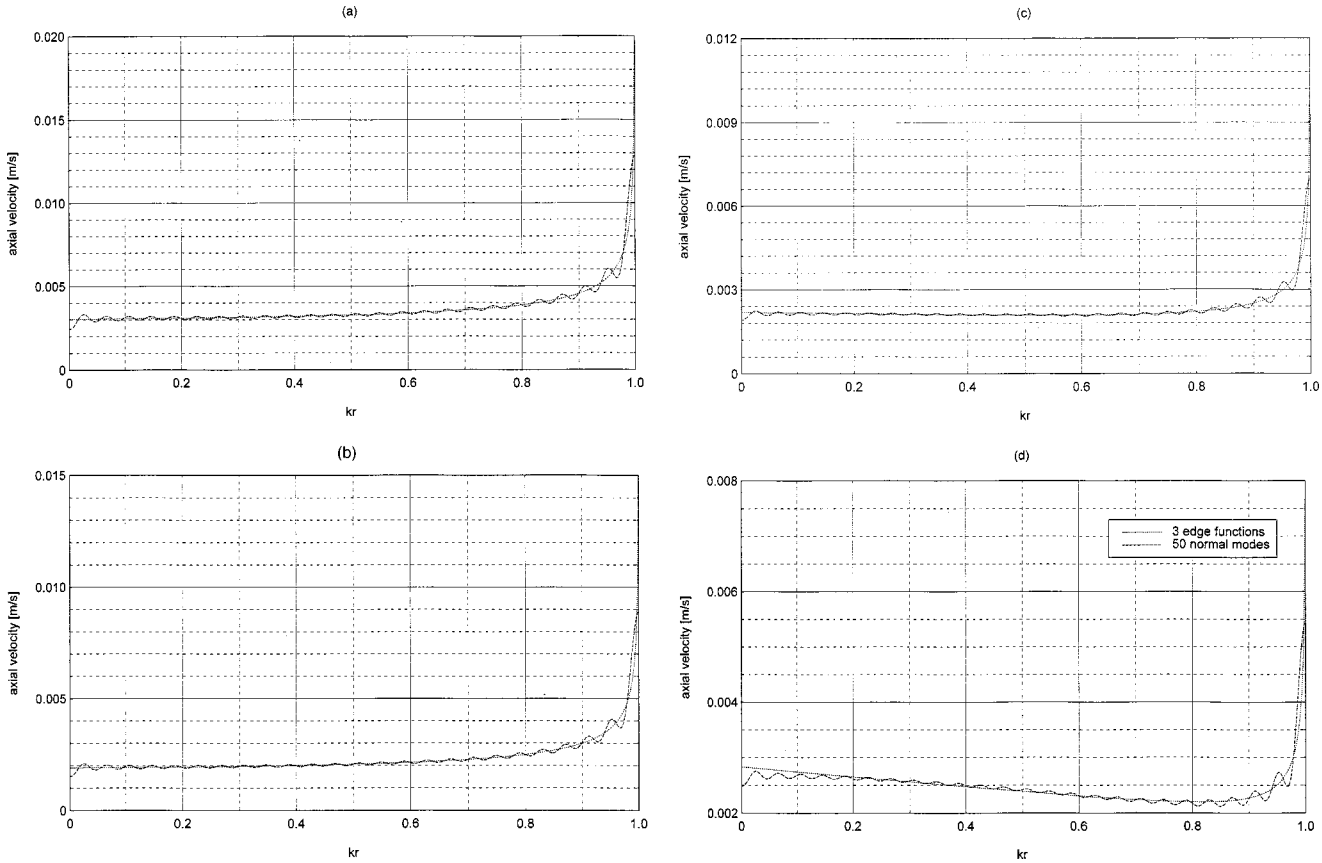

FIG. 9. Comparison of axial velocity over aperture, calculated with 50 normal modes and three edge functions, for (a) $kR=0.5$, (b) $kR=1.5$, (c) $kR=2.5$, and (d) $kR=3.5$.

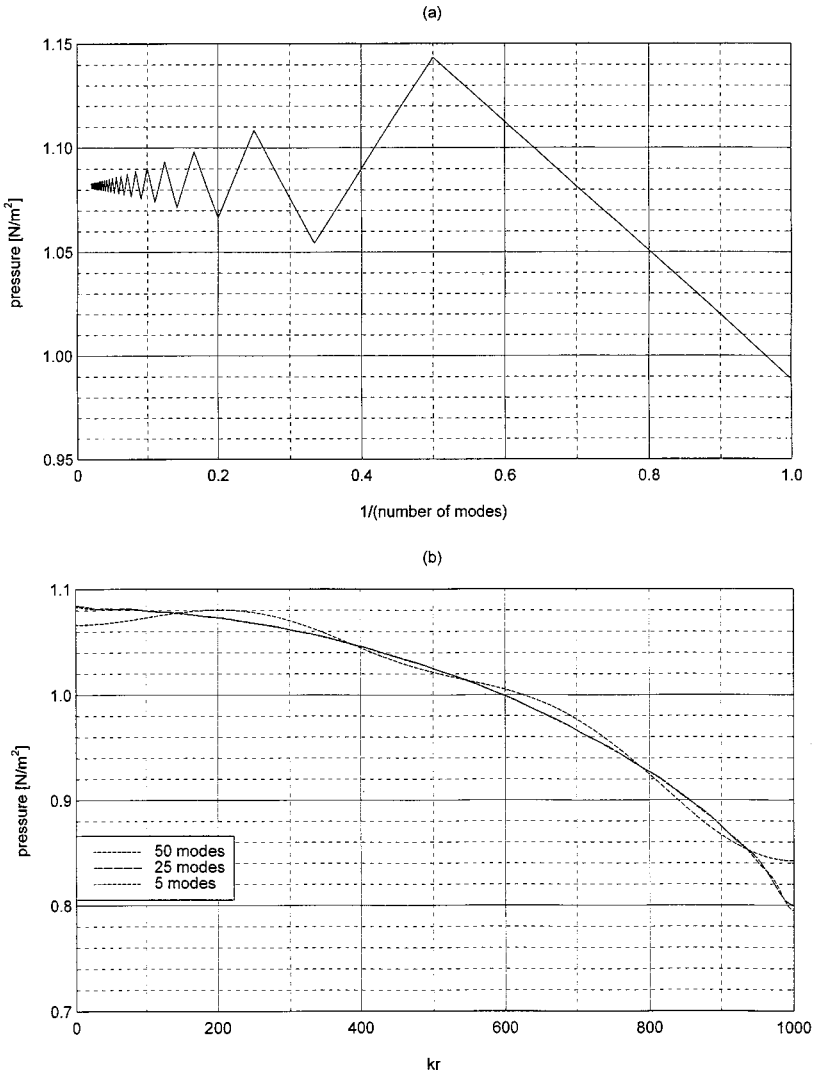

FIG. 10. (a) Pressure at center of aperture, calculated with 1–50 normal modes. (b) Pressure profile over aperture, calculated with 5, 25, and 50 normal modes ($kR=1$).

A. Comparison of the two methods

We first consider the case where $kR=1$. Using the normal mode (NM) solution with progressively more modes, shows that convergence is slow. A noticeable ripple is present even when using 50 modes, as shown in Fig. 2. Plotting the axial velocity at the center of the waveguide versus the number of modes used also demonstrates this, as in Fig. 3. The limit value of the velocity at the center was estimated as the average of the last 50 points in this figure. Even with 100 modes, the velocity at the center still oscillates 10% around this estimated limit. The velocity at the edge is theoretically infinite—though the numerical values using the NM solution cannot reflect this. Using progressively more modes, the edge velocity rises monotonically. Plotting the reciprocal of the velocity versus the reciprocal of the number of modes in Fig. 4 shows indeed that the end of this curve points to the origin. This is consistent with the results obtained by Wendoloski *et al.*[7] Plotting this graph on a log-log scale as in Fig. 5, this curve becomes linear, indicating the edge velocity behaves according to the following power law:

$$v_{z,\mathrm{I}}(R)=\frac{1}{2.54}N^{0.33}, \tag{38}$$

where N is the number of modes used, and $v_{z,\mathrm{I}}(R)$ is the axial velocity at the corner.

Considering now the moment method (MM) solution, we observe that using one to four edge functions, the solutions are nearly indistinguishable when using more than one, with no ripple, as in Fig. 6. The velocity at the edge of the waveguide is truly infinite in this case, due to the first edge function which is singular there. Comparing the velocity profile over the aperture to the NM solution, we see that the MM solution is very near what we would expect from the NM solution if the ripple was absent, as shown in Fig. 7. Comparing convergence of the velocity in the center of the waveguide, we observe that with four edge functions we are 0.7% from the limit, whereas the NM solution is still 10% from the limit with 100 modes, as shown in Fig. 8.

It is interesting to note that the MM method solution is valid over a wide range of frequencies. The edge functions were developed mainly with the behavior at the corner in mind, which is independent of frequency; indeed Wendoloski *et al.*, who propose a similar set of edge functions, state that they are valid for the static case but may not be for the frequency range of $0<kR<3.831\,71$. In fact, there is extremely good agreement between the MM and NM solutions

up to $kR=3.831\,71$. Figure 9 demonstrates this for a number of frequencies. It can be seen, though, that in Fig. 9(d) the two solutions diverge somewhat at small radii. It seems that for higher frequencies the edge functions may have difficulties in following the correct velocity profile near the center of the aperture.

The pressure profile over the aperture does not have any singular points, and therefore behaves well even when using NM. The profile with progressively more modes is shown in Fig. 10. The ripple is much weaker here, and convergence of pressure at the center of the aperture is much better than for the velocity.

V. DISCUSSION AND CONCLUSIONS

We have presented two methods for calculating the velocity and pressure field at the end of a flanged cylindrical waveguide. One is based on decomposition using Bessel functions, which comprise a complete basis. Despite this mathematical advantage, we have demonstrated that such a basis has a difficulty in describing the velocity field, due to its singularity at the waveguide/flange corner. This results in a large degree of ripple in the solution and poor convergence. Closely observing the behavior of the velocity field at this corner, we have shown that a new family of basis functions (termed here ''edge functions''), containing the expected singularity, behaves much better from a numerical point of view: no ripple is present in the solution, and convergence is better by at least two orders of magnitude. This behavior is present at least up to the cutoff frequency of the first higher-order mode.

Fundamentally, this is an interesting result. It shows that the behavior at the edge dominates the solution over the entire aperture; though no proof was presented that the suggested edge functions are a complete basis, they provided a very good solution simply due to the fact that they are closely related to the solution at the corner. It has been suggested by one of the reviewers that the edge functions in fact do comprise a complete basis. This is definitely a point worth looking into. However, some preliminary simulations at higher frequencies such as $kR=9$ show that the solution using edge functions has difficulties following the correct velocity profile at these frequencies. The authors expect to examine these issues in a future paper.

From a computational standpoint, the equations involving the edge functions are more complex. Solving the moment method equation involves evaluation of a large number of hypergeometric functions; lacking good numerical routines for these means that a very large number of integrals must be evaluated numerically. Though the results are impressive, it is not automatically clear that the additional computational effort is worthwhile in practical cases. A further study of various parameters such as end correction, radiation impedance, etc., will be presented in a future paper.

APPENDIX A: DERIVATION OF THE ''EDGE FUNCTIONS''

In this section we explain the choice of the edge functions as used in the decomposition of axial velocity in region III. Observing the 90° corner at the junction of the waveguide and the flange, the solution p for the Laplacian in the vicinity of the corner is

$$p\sim\left\{\begin{array}{c}\rho^{a_n}\\ \rho^{-a_n}\end{array}\right\}\left\{\begin{array}{c}\sin(a_n\varphi)\\ \cos(a_n\varphi)\end{array}\right\}, \tag{A1}$$

where ρ is the radius in a polar coordinate system with the origin at the corner. Since p must converge at $\rho=0$, we discard the solution containing ρ^{-a_n}. The gradient of p is

$$v\sim\frac{\partial p}{\partial\rho}\hat{\rho}+\frac{1}{\rho}\frac{\partial p}{\partial\varphi}\hat{\varphi}. \tag{A2}$$

Applying the boundary condition that the gradient of p is zero at the walls, i.e., for $\varphi=0$ and $\varphi=3\pi/2$, requires therefore that the second term in (A2) is equal to zero for $\varphi=0$ and $\varphi=3\pi/2$. This means we must require

$$a_n\rho^{a_n-1}\left\{\begin{array}{c}\cos(a_n\varphi)\\ -\sin(a_n\varphi)\end{array}\right\}=0,\quad \varphi=0\ \text{ and }\ \varphi=\frac{3\pi}{2}. \tag{A3}$$

This is possible only for solutions involving the sin function, and requiring $a_n 3\pi/2=n\pi$, which holds for

$$a_n=\tfrac{2}{3}n,\quad n=1,\ldots,\infty. \tag{A4}$$

Therefore we obtain the general solution

$$p=\sum_{n=1}^{\infty}d_n\rho^{(2/3)n}\cos\left(\frac{2}{3}n\varphi\right). \tag{A5}$$

Returning to our original problem, the expansion on region III is an expansion for v, for which we are interested in $\varphi=\pi$ only. The axial velocity for the original problem coincides with the $\hat{\varphi}$ direction in the current discussion, so that

$$v_{z,\mathrm{III}}\sim\frac{1}{\rho}\frac{\partial p}{\partial\varphi}\hat{\rho}=\sum_{n=1}^{\infty}d_n\rho^{(2/3)(n-1)}\sin\left(\frac{2}{3}n\pi\right). \tag{A6}$$

This expression becomes zero for all n's that are integer multiples of 3. Further, in the original cylindrical coordinate system, $\rho=R-r$. Therefore, in that coordinate system we obtain the expansion

$$v_{z,\mathrm{III}}=\sum_{n=1}^{\infty}c_n(R-r)^{\alpha_n},\quad n\neq 3,6,9,\ldots, \tag{A7}$$

and $\alpha_n=2n/3-1$, as above.

APPENDIX B: NUMERICAL ISSUES

Solving Eqs. (27) and (36) require large amounts of numerical programming, involving infinite integrals, integrals with singular and oscillatory integrands, and calculation of special functions. This is very demanding in terms of programming time and computer time, therefore we find it suitable to discuss certain aspects of this issue.

1. Special functions

There are two sets of special functions used in this analysis: Bessel functions and the 1F2 hypergeometric function. There are many well-documented libraries for calculating the Bessel function, so these do not normally prove prob-

lematic. Press *et al.*[15] provide simple routines for calculating them. The hypergeometric functions are less widespread in use and often more problematic numerically. Certain series or iterative methods are presented by Luke.[16] The problem we encountered was that these expressions diverged for arguments beyond a certain value. Since these functions appear in our analysis as integrands in infinite integrals such as (27), the usefulness of these methods was limited. Therefore, we resorted to computing the hypergeometric functions numerically, using the integral (24). This increases computation time considerably, but the results are more reliable.

2. Numerical integrations

The integrals in Eqs. (27) and (36) can be difficult to evaluate numerically. The least problem is that the integrand is oscillatory; thus care must be taken to provide for a sufficient number of points in each oscillation. The rate of oscillation is nearly fixed, since the asymptotic expression for the Bessel functions is a decaying cosine; therefore, it is relatively straightforward to perform the integration properly in this sense.

The second problem is that some of the integrands have singular points, though the integrals converge, such as

$$I=\int_0^\infty \frac{1}{\gamma(k_t)} s_0(R,k_t)s_j(R,k_t)k_t\,dk_t. \tag{B1}$$

Performing a straightforward integration requires is problematic due to the singular point at k_0. Rewriting the integral as follows,

$$\begin{aligned} I&=I_1+I_2\\ &=\int_0^{k_0}\frac{s_0(R,k_t)s_j(R,k_t)k_t\,dk_t}{\sqrt{(k_0^2-k_t^2)}}\\ &\quad+j\int_{k_0}^{\infty}\frac{s_0(R,k_t)s_j(R,k_t)k_t\,dk_t}{\sqrt{(k_0^2-k_t^2)}}, \end{aligned} \tag{B2}$$

the integrand of I_1 approaches infinity as k_t approaches k_0. The behavior of the integrand can be improved by rewriting it as

$$\begin{aligned} I_1&=\int_0^{k_0}\frac{(s_0(R,k_t)s_j(R,k_t)-s_0(R,k_0)s_j(R,k_0))k_t\,dk_t}{\sqrt{(k_0^2-k_t^2)}}\\ &\quad+\int_0^{k_0}\frac{s_0(R,k_0)s_j(R,k_0)k_t\,dk_t}{\sqrt{(k_0^2-k_t^2)}}. \end{aligned} \tag{B3}$$

The top integral can be evaluated analytically; the integrand on the bottom integral is now convergent and can be easily calculated numerically. The same procedure must be carried out for I_2 in the vicinity of k_0.

Finally, infinite integrals such as I_2, though convergent, may require a large number of integrations points in order to be calculated to a reasonable degree of accuracy. In certain cases an improvement in the calculation time can be achieved using asymptotical expressions. Consider, for example, the integral

$$I_3=\int_{2k_0}^{\infty}\frac{k_t}{\gamma(k_t)(\beta_j^2-k_t^2)}J_1^2(k_tR)\,dk_t. \tag{B4}$$

The asymptote of the integrand is

$$\frac{2\cos^2(k_tR-0.75\pi)}{\pi k_t^3}. \tag{B5}$$

The integral of this asymptote has an analytical solution; on the other hand, subtracting it from the original integrand gives the integral

$$\int_{2k_0}^{\infty}\left(\frac{k_t}{\gamma(k_t)(\beta_j^2-k_t^2)}J_1^2(k_tR)-\frac{2\cos^2(k_tR-0.75\pi)}{\pi k_t^3}\right)dk_t, \tag{B6}$$

which converges much more rapidly than the original integral I_3.

APPENDIX C: ASYMPTOTIC BEHAVIOR OF THE NM METHOD

Viewing the rather poor convergence of the velocity profile using the NM method, it is of interest to note whether the asymptotic behavior of the coefficients b_i can be determined analytically. The following is an analysis of this behavior, which in turn can also predict the convergence of the velocity at the center of the aperture.

The velocity for $z=0$ is given by

$$v_z=k_0-\sum_{i=0}^{\infty}k_ib_iJ_0(\beta_ir),\quad \rho<1 \tag{C1}$$

(for simplicity taking $R=1$).

$$k_i=\begin{cases}\sqrt{k_0^2-\beta_i^2}, & k_0>\beta_i,\\ -j\sqrt{\beta_i^2-k_0^2}, & \beta_i>k_0,\end{cases} \tag{C2}$$

and $J_1(\beta_i)=0$.

The linear behavior observed in Fig. 5 suggests that a power law correctly describes the asymptotic behavior of b_i. Since they are also observed to have alternating signs, we assume that asymptotically they can be written as

$$b_i=(-1)^i i^{\alpha}. \tag{C3}$$

Taking $t=1-r$, a small number, we have

$$\begin{aligned} I&=-\sum_{i=0}^{\infty}k_ib_iJ_0(\beta_ir)\\ &\sim\sum_{n=0}^{\infty}\beta_n\cos(\pi n)n^{\alpha}J_0[\beta_n(1-t)]. \end{aligned} \tag{C4}$$

Applying the asymptotic formulas

$$\beta_n\approx(n+\tfrac{1}{4})\pi \tag{C5}$$

(Ref. 17, p. 981) and

$$J_0(x)\approx\sqrt{\frac{2}{\pi x}}\cos\left(x-\frac{\pi}{4}\right) \tag{C6}$$

(Ref. 17, p. 961), we have

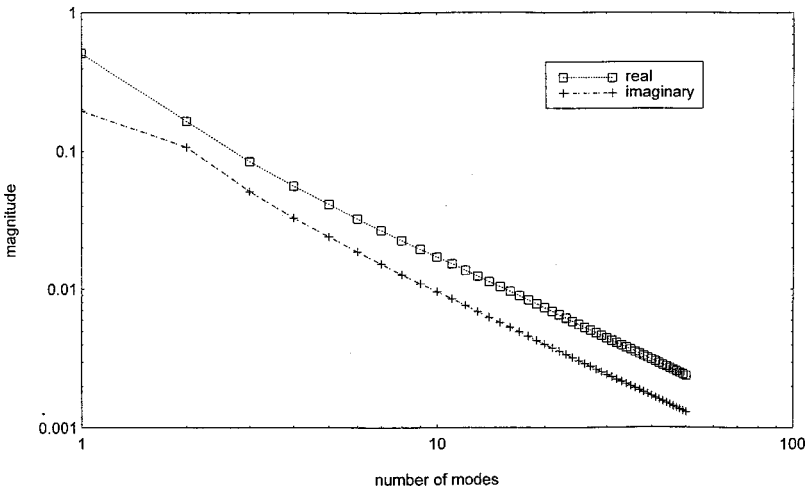

FIG. C1. The log-log plot of real and imaginary part of b_i coefficients ($kR=1$). Theoretical slope is $-7/6$; actual slopes are -1.21 for real part, -1.2 for imaginary.

$$I\sim\sum_{n=0}^{\infty}\left(n+\frac{1}{4}\right)\cos(\pi n)n^{\alpha}\times\sqrt{\frac{2}{\pi\beta_n}}\cos\left[\beta_n(1-t)-\frac{\pi}{4}\right], \tag{C7}$$

$$I\sim\sum_{n=0}^{\infty}\cos(\pi n)n^{\alpha+1/2}\cos\left[\left(n+\frac{1}{4}\right)\pi(1-t)-\frac{\pi}{4}\right], \tag{C8}$$

$$I\sim\sum_{n=0}^{\infty}\cos(\pi n)n^{\alpha+1/2}\cos\left[n\pi-n\pi t-\frac{1}{4}\pi t\right], \tag{C9}$$

$$I\sim\sum_{n=0}^{\infty}n^{\alpha+1/2}\cos\left[n\pi t-\frac{1}{4}\pi t\right]. \tag{C10}$$

Applying

$$\int_0^{\infty}x^a\cos(bx-c)dx=b^{-1-a}\Gamma(1+a)\sin\left(c-\frac{a\pi}{2}\right), \tag{C11}$$

in order that v_z will behave like $t^{-1/3}$, we need

$$t^{-1-\alpha-1/2}=t^{-1/3} \tag{C12}$$

and

$$\alpha=-\tfrac{7}{6}. \tag{C13}$$

In Fig. C1 we present the real and imaginary parts of the coefficients as a function of their order, on a log-log scale. Taking the last five points we perform a linear regression in order estimate the asymptotical behavior of the coefficients. The slopes of the real and imaginary parts are -1.21 and -1.20, respectively, which is quite close to the calculated value.

[1] Y. Ando, ''On the sound radiation from semi-infinite circular pipe of certain wall thickness,'' Acustica **22**, 219–225 (1969/1970).
[2] Lord Rayleigh, *The Theory of Sound*, 1896 (reissued in Dover, New York, 1945).
[3] P. J. Daniell, ''The coefficient of the end correction—part I,'' Philos. Mag. **XXX**, 137–146 (1915).
[4] L. V. King, ''On the electrical and acoustical conductivity of cylindrical tubes bounded by infinite flanges,'' Philos. Mag. **21**, 128–144 (1936).
[5] A. N. Norris and I. C. Sheng, ''Acoustic radiation from a circular pipe with infinite flange,'' J. Sound Vib. **135**, 85–93 (1989).
[6] H. Levine and J. Schwinger, ''On the radiation of sound from an unflanged circular pipe,'' Phys. Rev. **73**(4), 383–406 (1948).
[7] J. C. Wendoloski, F. R. Fricke, and R. C. McPhedran, ''Boundary conditions of a flanged cylindrical pipe,'' J. Sound Vib. **162**(1), 89–96 (1993).
[8] P. M. Morse, *Vibration and Sound* (McGraw–Hill, New York, 1948).
[9] Y. Nomura, I. Yamamura, and S. Inawashiro, ''On the acoustic radiation from a flanged circular pipe,'' J. Phys. Soc. Jpn. **15**(3), 510–517 (1960).
[10] W. E. Zorumski, ''Generalized radiation impedances and reflection coefficients of circular and annular ducts,'' J. Acoust. Soc. Am. **54**, 1667–1673 (1973).
[11] H. J. Bom and T. J. Park, ''A series solution for acoustic radiation from a flanged circular pipe,'' Acustica **80**, 315–316 (1994).
[12] H. Matzner and S. Shtrikman, ''Some improved formulas for the Westmijze head,'' IEEE Trans. Magn. **33**(1), 820–825 (1997).
[13] P. M. Morse and H. Feshbach, *Methods of Theoretical Physics* (McGraw–Hill, New York, 1953).
[14] J. D. Jackson, *Classical Electrodynamics*, 2nd ed. (Wiley, New York, 1975).
[15] W. H. Press, S. A. Teukolsky, W. T. Vetterling, and B. P. Flannery, *Numerical Recipes* (Cambridge U.P., Cambridge, 1988).
[16] Y. L. Luke, *Algorithms for the Computation of Mathematical Functions* (Academic, New York, 1977).
[17] I. S. Gradshtein and I. M. Ryzhik, *Table of Integrals, Series and Products* (Addison-Wesley, Reading, MA, 1988).

Intensity streamlines and vorticity streamlines in three-dimensional sound fields

Jiang Zhe
Vibration and Noise Research Division, Jiangsu University of Science and Technology, Zhen Jiang, Jiangsu, 212013, The People's Republic of China

(Received 9 December 1997; accepted for publication 11 October 1999)

The properties of intensity streamlines and vorticity streamlines are discussed in this paper. It is found that the properties in three-dimensional sound fields are different from the properties in two-dimensional sound fields. The integral behavior of intensity streamlines is that the beginning and the end are attached to a sound source surface or that the beginning is on the sound source surface and the end extends into the infinite. For the vorticity streamlines, the integral behavior is that it is a closed curve or that the beginning and the end are attached to the sound source surface. Three examples are given for intensity and vorticity streamlines. © *2000 Acoustical Society of America.* [S0001-4966(00)05801-X]

PACS numbers: 43.20.Rz, 43.20.Bi [DEC]

INTRODUCTION

Sound energy is transferred by the sound intensities. The curves of integrating the sound intensities are called intensity streamlines which are tangential to the sound intensities at all points and which describe the way of sound energy transfer. In two-dimensional sound fields, some examples are given for the intensity streamlines and the local properties have been studied.[1–4] The local properties are concerned principally with the singular points of intensity streamlines, which are divided into two kinds, the saddle points and the vortex points. But a little is known about the properties of intensity streamlines in three-dimensional sound fields. The results obtained in two-dimensional sound fields cannot be applied completely to every case in three-dimensional sound fields. The aim of this paper is to discuss the properties of the intensity streamlines in three-dimensional sound fields.

In general the sound intensity is rotational and the curl of sound intensity is called sound vorticity. Similarly, the curves of integrating sound vorticities are called vorticity streamlines. In this paper the properties of the vorticity streamlines are discussed also.

I. FUNDAMENTAL VARIABLES IN A SOUND INTENSITY FIELD (Ref. 5)

At any point $X(x,y,z,)$ in a steady three-dimensional sound field, let the instantaneous sound pressure be $p(x,y,z,t)$. Transforming time domain into frequency domain, the sound pressure becomes $P(x,y,z,\omega)$, which is the finite Fourier transform of $p(x,y,z,t)$, where ω is the circle frequency. In the frequency domain, the sound pressure P can be expressed by a complex exponential function and takes the form

$$P(x,y,z,\omega)=|P|e^{-j\varphi(x,y,z,\omega)}, \tag{1}$$

where $\varphi(x,y,z,\omega)$ is the phase function of sound pressure. Set

$$G_p(x,y,z,\omega)=\frac{1}{T}PP^*, \tag{2}$$

where T is an averaging time, G_p is the auto-spectrum of sound pressure and the asterisk * denotes the complex conjugate. In a sound field, the independent fundamental variables are G_p and φ.

Using the phase function φ and the auto-spectrum G_p of sound pressure, the sound intensity **I** and the reactive sound intensity **Q** can be written as

$$\mathbf{I}(x,y,z,\omega)=\frac{G_p}{\rho ck}\nabla\varphi \tag{3}$$

and

$$\mathbf{Q}(x,y,z,\omega)=-\frac{1}{2\rho ck}\nabla G_p, \tag{4}$$

where ρ is the density of the medium, c is the speed of sound and k is the wave number, $k=\omega/c$.

Let G_0 be constant with the same dimension as G_p, then

$$\frac{\nabla G_P}{G_p}=\nabla\ln\left(\frac{G_p}{G_0}\right). \tag{5}$$

We put

$$\psi(x,y,z,\omega)=\ln\left(\frac{G_p}{G_0}\right) \tag{6}$$

and have[5]

$$\nabla^2\varphi+\nabla\psi\cdot\nabla\varphi=0, \tag{7}$$

$$\nabla^2\psi+\tfrac{1}{2}\nabla\psi\cdot\nabla\psi=2k^2(\varepsilon^2-1), \tag{8}$$

where

$$\varepsilon^2=\frac{\nabla\varphi\cdot\nabla\varphi}{k^2}=\frac{\mathbf{I}\cdot\mathbf{I}}{(Gp/\rho c)^2} \tag{9}$$

and the function ϵ denotes the uniformity in a sound field. Obviously the independent fundamental variables $G_p(\Psi)$ and φ are the functions with second order continuous derivative, and the sound intensity **I** and the reactive sound intensity **Q** have first order continuous derivative.

Taking the curl of the sound intensity $\mathbf{I}$, the sound vorticity $\mathbf{\Omega}$ is obtained and takes the following form:

$$\Omega(x,y,z,\omega)=\nabla\times\mathbf{I}=\frac{1}{\rho ck}\nabla G_p\times\nabla\varphi. \tag{10}$$

The sound intensity $\mathbf{I}$ and the sound vorticity $\mathbf{\Omega}$ are continuous.

II. INTENSITY STREAMLINES

An intensity streamline is defined as a continuous line of which the tangent at all point is in the direction of the sound intensity. The differential equations of intensity streamlines are given by

$$\frac{dx}{I_x}=\frac{dy}{I_y}=\frac{dz}{I_z}, \tag{11}$$

where I_x, I_y and I_z are the components of $\mathbf{I}$ in Cartesian coordinate. Giving a point $X_0(x_0,y_0,z_0)$ and integrating Eqs. (11), the solution is the intensity streamline passing through point X_0.

Because $\nabla\cdot\mathbf{I}=0$ and $\mathbf{I}$ is continuous, no source exists in the sound intensity fields and the intensity streamlines cannot break off suddenly and cannot intersect. The integral behavior of the intensity streamlines could have three kinds of possibilities: (a) the intensity streamline is closed itself in the sound field; (b) the beginning and the end are attached to the sound source surface; and (c) the beginning is on the sound source surface and the end extends into the infinite. We demonstrate that possibility (a) is not true for the intensity streamlines.

Taking a small closed curve in the sound field, the intensity streamlines passing through all the points on the closed curve form a intensity streamtube. Because the intensity streamlines cannot intersect, the same intensity streamlines pass through the intensity streamtube at all cross sections and the intensity streamtube exchanges no energy with the outside. Taking any two cross sections A_1 and A_2 along the intensity streamtube, it is followed from $\nabla\cdot\mathbf{I}=0$ that

$$\int\int_{A_1}\mathbf{I}\cdot\mathbf{n}_1\,dA_1=\int\int_{A_2}\mathbf{I}\cdot\mathbf{n}_2\,dA_2, \tag{12}$$

where $\mathbf{n}_1$ and $\mathbf{n}_2$ are the normal unit vector on A_1 and A_2, respectively.

Suppose that a close intensity streamline exists in the sound field. An intensity streamtube which is annular can be obtained around the closed intensity streamline. This means that there is an energy flow in the annular streamtube which does not exchange energy with the outside. If the damping of the medium is ignored, the energy flow does not vanish perpetually. Apparently, this result cannot be accepted. Furthermore, since no energy comes into the annular streamtube, any energy flow cannot be formed. Therefore the annular streamtube dose not exit and the intensity streamline cannot be closed itself in the sound field.

Physically, the intensity streamline presents the way on which the energy is transferred, and the transferred energy comes only from the sound source. The energy radiated by the sound source is transferred along the intensity streamlines into the infinite or back to the sound source. Thus the integral behavior of the intensity streamlines in three-dimensional sound field is that the beginning and the end are attached to the sound source surface or that the beginning is on the sound source surface and the end extends into the infinite.

Using parameter γ, an intensity streamline can be described by the trajectory of radial vector $\mathbf{r}_I(\gamma)$, $\mathbf{r}_I(\gamma)=\{x(\gamma),y(\gamma),z(\gamma)\}$.

If the parameter γ denotes distance along the intensity streamline, the derivative $\mathbf{r}_I'(\gamma)$ with respect to γ is the tangent unit vector on the intensity streamline. According to the definition of intensity streamline, we have

$$\mathbf{I}=\lambda_I\mathbf{r}_I'(\gamma), \tag{13}$$

where λ_I is a proportion function. From Eqs. (3) and (9), λ_I can be determined as

$$\lambda_I^2=\varepsilon^2(G_p/\rho c)^2$$

and Eq. (13) becomes

$$\frac{1}{k}\nabla\varphi=\varepsilon\mathbf{r}_i'(\gamma). \tag{14}$$

Taking derivative of Eq. (14) with respect to γ yields

$$\frac{1}{k}(\nabla\varphi)'=\varepsilon\mathbf{r}_I''(\gamma)+\varepsilon'\mathbf{r}_I'(\gamma), \tag{15}$$

where

$$\frac{1}{k}(\nabla\varphi)'=\frac{1}{k}(\mathbf{r}_I'\cdot\nabla)\nabla\varphi=\frac{1}{k^2\varepsilon}(\nabla\varphi\cdot\nabla)\nabla\varphi=\nabla\varepsilon.$$

Then, Eq. (15) is written as

$$\varepsilon\mathbf{r}_I''(\gamma)+\varepsilon'\mathbf{r}_I'(\gamma)=\nabla\varepsilon. \tag{16}$$

Taking the dot product of Eq. (14) with $\mathbf{r}_I'(\gamma)$ yields

$$\frac{d\varphi}{d\gamma}=k\varepsilon. \tag{17}$$

Integrating this equation along an intensity streamline, we have

$$\varphi=\varphi_0+\int_0^{\gamma}k\varepsilon\,d\gamma, \tag{18}$$

where φ_0 is an initial phase.

Let $\mathbf{n}$ be the principal normal unit vector of intensity streamline, and we have

$$K\mathbf{n}=\mathbf{r}_I''(\gamma), \tag{19}$$

where K is curvature. Equation (16) becomes

$$\varepsilon K\mathbf{n}+\varepsilon'\mathbf{r}_I'(\gamma)=\nabla\varepsilon$$

and taking the dot product of this equation with $\mathbf{n}$ yields

$$K=\frac{1}{\varepsilon}\nabla\varepsilon\cdot n. \tag{20}$$

If ϵ is constant, the curvature $K\equiv 0$ and the intensity streamline is a straight line. If the gradient direction of ϵ is always

parallel to $\mathbf{r}_I'$, the curvature $K\equiv 0$ and the intensity streamline is a straight line.

III. LOCAL PROPERTIES OF INTENSITY STREAMLINES

When $\mathbf{I}=0$, the direction of intensity streamline cannot be determined. The point at which $\mathbf{I}=0$ is called the singular point of the differential equations of intensity streamlines. Because the independent fundamental variables about $\mathbf{I}$ are G_p and φ, we discuss the following three cases.

(a) At a singular point $X_a(x_a,y_a,z_a)$, $G_p=0$ but $\nabla\varphi\neq 0$. The differential equations (11) hold formally and become

$$\frac{dx}{\partial\varphi/\partial x}=\frac{dy}{\partial\varphi/\partial y}=\frac{dz}{\partial\varphi/\partial z}. \tag{21}$$

Mathematically, the singular point X_a can be canceled and the curve of integrating Eqs. (21) passing through the point X_a exists. But the curve cannot present the way of energy flow and is not an actual intensity streamline.

Let L_a be the integral curve passing through the point X_a. Since $\nabla\cdot\mathbf{I}=0$, the energy flow along L_a cannot break off suddenly. At the point X_a, $G_p=0$ and $\mathbf{I}=0$. It can be found that no energy flow exists or that $\mathbf{I}\equiv 0$ along L_a. Because $\nabla\varphi\neq 0$, then $G_p\equiv 0$ along L_a. Thus the point X_a is not isolated. All the point like the point X_a can form a subspace M_a in which there is no energy flow.

Since $G_p\geqslant 0$ in the sound fields, at the points of $G_p=0$, $\nabla G_p=0$. From Eqs. (3), (4), and (10), we arrive at the fact that on the subspace M_a the sound intensity $\mathbf{I}$, the reactive sound intensity $\mathbf{Q}$ and the sound vorticity $\mathbf{\Omega}$ vanish and the subspace M_a is a silent space.

(b) At a singular point $X_b(x_b,y_b,z_b)$, $G_p\neq 0$ but $\nabla\varphi=0$. In the vicinity of the point X_b, we have

$$\frac{\partial\varphi}{\partial x}=\left(\frac{\partial^2\varphi}{\partial x\,\partial x}\right)_{X_b}\cdot(x-x_b)+\left(\frac{\partial^2\varphi}{\partial y\,\partial x}\right)_{X_b}\cdot(y-y_b)+\left(\frac{\partial^2\varphi}{\partial z\partial x}\right)_{X_b}\cdot(z-z_b),$$

$$\frac{\partial\varphi}{\partial y}=\left(\frac{\partial^2\varphi}{\partial x\,\partial y}\right)_{X_b}\cdot(x-x_b)+\left(\frac{\partial^2\varphi}{\partial y\,\partial y}\right)_{X_b}\cdot(y-y_b)+\left(\frac{\partial^2\varphi}{\partial z\partial y}\right)_{X_b}\cdot(z-z_b),$$

and

$$\frac{\partial\varphi}{\partial z}=\left(\frac{\partial^2\varphi}{\partial x\,\partial z}\right)_{X_b}\cdot(x-x_b)+\left(\frac{\partial^2\varphi}{\partial y\,\partial z}\right)_{X_b}\cdot(y-y_b)+\left(\frac{\partial^2\varphi}{\partial z\partial z}\right)_{X_b}\cdot(z-z_b).$$

Using parameter τ, the differential equations of intensity streamline become

$$\begin{Bmatrix}\dfrac{dx}{d\tau}\\[2mm]\dfrac{dy}{d\tau}\\[2mm]\dfrac{dz}{d\tau}\end{Bmatrix}=[J_b]\begin{Bmatrix}x-x_b\\y-y_b\\z-z_b\end{Bmatrix}, \tag{22}$$

where

$$[J_b]=\begin{bmatrix}\dfrac{\partial^2\varphi}{\partial x\,\partial x} & \dfrac{\partial^2\varphi}{\partial y\,\partial x} & \dfrac{\partial^2\varphi}{\partial z\partial x}\\[2mm]\dfrac{\partial^2\varphi}{\partial x\,\partial y} & \dfrac{\partial^2\varphi}{\partial y\,\partial y} & \dfrac{\partial^2\varphi}{\partial z\partial y}\\[2mm]\dfrac{\partial^2\varphi}{\partial x\,\partial z} & \dfrac{\partial^2\varphi}{\partial y\,\partial z} & \dfrac{\partial^2\varphi}{\partial z\partial z}\end{bmatrix}_{X_b} \tag{23}$$

evaluated at the point X_b. Apparently, the coefficient matrix $[J_b]$ is real and symmetrical, so that the eigenvalues λ_i $(i=1,2,3)$ of $[J_b]$ are real and satisfy.

$$\lambda_1+\lambda_2+\lambda_3=\left(\frac{\partial^2\varphi}{\partial x\,\partial x}\right)_{X_b}+\left(\frac{\partial^2\varphi}{\partial y\,\partial y}\right)_{X_b}+\left(\frac{\partial^2\varphi}{\partial z\partial z}\right)_{X_b}=(\nabla^2\varphi)_{X_b}. \tag{24}$$

At the point X_b, $G_p\neq 0$ and $\nabla\varphi=0$, and from Eq. (7) we have $(\nabla^2\varphi)_{X_b}=0$ and

$$\lambda_1+\lambda_2+\lambda_3=0. \tag{25}$$

Of the eigenvalues there is at least one to be positive. The point X_b is an unstable point which is called saddle point. Considering that the energy flow cannot break off suddenly, we can obtain that no intensity streamline passes through the point X_b and that the point X_b is a separating point of intensity streamlines.

At the point X_b, $\mathbf{I}=0$ and $\Omega=0$, but $G_p\neq 0$, so that the reactive sound intensity $\mathbf{Q}\neq 0$. Although no energy flow passes through the point X_b, yet at the point X_b exists energy that has a relation with $\mathbf{Q}$ and cannot be transferred.

(c) At a singular point $X_c(x_c,y_c,z_c)$, $G_p=0$ and $\nabla\varphi=0$. According to the discussion above, the point X_c is also a saddle point and no intensity streamline passes through the point X_c. From Eqs. (3), (4) and (10), it is followed that at the point X_c, $\mathbf{I}=0$, $\mathbf{Q}=0$ and $\mathbf{\Omega}=0$. Thus the point X_c is a silent point.

At all the singular points of the differential equations of intensity streamlines, the sound vorticity $\Omega=\nabla\times\mathbf{I}=0$. It also implies that the intensity streamline cannot be closed in three-dimensional sound fields.

IV. VORTICITY STREAMLINES

When the sound intensity $\mathbf{I}$ is rotational, the curves of integrating sound vorticities are called vorticity streamlines, on which the tangent is in the direction of sound vorticity $\mathbf{\Omega}$. A vorticity streamline satisfies the following equations

$$\frac{dx}{\Omega_x}=\frac{dy}{\Omega_y}=\frac{dz}{\Omega_z}, \tag{26}$$

where Ω_x, Ω_y, and Ω_z are the components of sound vorticity $\mathbf{\Omega}$ in Cartesian coordinates.

From Eq. (10), we have that $\nabla \cdot \Omega = 0$ and the vorticity streamlines cannot break off suddenly. A vorticity streamtube can be formed by vorticity streamlines in the same way as the intensity streamtube. At any two cross sections A_1 and A_2 along the vorticity streamtube, we find

$$\int \int_{A_1} \Omega \cdot \mathbf{n}_1 \, dA_1 = \int \int_{A_2} \Omega \cdot \mathbf{n}_2 \, dA_2 . \tag{27}$$

The integral behavior of vorticity streamlines could have also three kinds of possibilities. But one of them, that the beginning is on the sound source surface and the end extends into the infinite, is not true.

Suppose that it is true. Then a vorticity streamtube can be formed around the vorticity streamline of which the beginning is on the sound source surface and the end extends into the infinite. Let r be the distance between the beginning and any point along the vorticity streamline. In the far field, as $r \to \infty$, $|\mathbf{I}|$ tends to zero by the order $1/r^2$ and $|\Omega|$ tends to zero by the order $1/r^3$. The area of the cross section A_2 along the vorticity streamtube can tends to infinity by the order r^2. Therefore, in the far field, $\int\int_{A_2} \Omega \cdot \mathbf{n}_2 \, dA_2$ becomes zero. It is in contradiction with Eq. (27) and the supposition is not true.

The integral behavior of vorticity streamlines in three-dimensional sound field is that the beginning and the end are attached to the sound source surface or that the vorticity streamline is closed itself.

Let $\mathbf{r}_\Omega(\gamma)$ be the radial vector of vorticity streamline,

$$\mathbf{r}_\Omega(\gamma) = \{x(\gamma), y(\gamma), z(\gamma)\},$$

where γ is distance along a vorticity streamline, from Eq. (10), we have

$$\nabla G_p \times \nabla \varphi = \lambda_\Omega \mathbf{r}'_\Omega(\gamma), \tag{28}$$

where λ_Ω is a proportion function and $\mathbf{r}'_\Omega(\gamma)$ is the tangent unit vector on the vorticity streamline. Taking the dot product of Eq. (28) with ∇G_p yields

$$\mathbf{r}'_\Omega(\gamma) \cdot \nabla G_p = 0$$

or

$$\frac{dG_p}{d\gamma} = 0. \tag{29}$$

Equation (29) shows that along a vorticity streamline G_p is constant. Thus a vorticity streamline lies on a constant potential surface (G_p=constant). Taking the dot product of Eq. (28) with $\nabla \varphi$ yields

$$\mathbf{r}'_\Omega(\gamma) \cdot \nabla \varphi = 0$$

or

$$\frac{d\varphi}{d\gamma} = 0. \tag{30}$$

Equation (30) shows that along a vorticity streamline, φ is constant. Thus a vorticity streamline lies on a constant phase surface (φ=constant).

From the point of geometry, a vorticity streamline is a curve intersected by a constant potential surface and a constant phase surface. If the curve is intersected again by the sound source surface, the beginning and the end of the vorticity streamline are attached to the sound source surface. If the curve is not intersected by the sound source surface, the vorticity streamline is a closed curve. If the constant potential surfaces coincide with the constant phase surfaces correspondingly, $\nabla G_p // \nabla \varphi$ at any point and it is followed from Eq. (10) that the sound intensity field is irrotational.

V. EXAMPLES

We discuss simple source, dipole source and quadrupole source which are harmonic and lie at the original point of the coordinates. Let r be the distance between a point $X(x,y,z)$ in the sound field and the origin, $r^2 = x^2 + y^2 + z^2$.

A. Simple source

The sound pressure P at any point X is

$$P = \frac{jk\rho c S_0}{4\pi r} e^{-jkr}, \tag{31}$$

where S_0 is the source strength. Equation (31) is rewritten in the complex exponential form as

$$P = \frac{k\rho c S_0}{4\pi r} e^{-j(kr - \pi/2)}.$$

From Eqs. (1) and (2), the phase function φ and the autospectrum G_p of sound pressure are, respectively,

$$\varphi = kr - \frac{\pi}{2} \tag{32}$$

and

$$G_p = \frac{G_0}{k^2 r^2}, \tag{33}$$

where

$$G_0 = \frac{1}{2}\left(\frac{k^2 \rho c S_0}{4\pi}\right)^2.$$

Then we find

$$\nabla \varphi = k \nabla r, \tag{34}$$

$$\mathbf{I} = \frac{G_0}{\rho c k^2 r^2} \nabla r, \tag{35}$$

and

$$\Omega = \nabla \times \mathbf{I} = 0. \tag{36}$$

Using Eq. (34), we obtain that $\varepsilon^2 = (1/k^2)\, \nabla\varphi \cdot \nabla\varphi = 1$, so that $\nabla \varepsilon = 0$ and the intensity streamlines are straight lines. In the sound field, G_p and $\nabla \varphi$ do not vanish and there is no singular point. Equations (32) and (33) show that the constant potential surface and the constant phase surfaces are spherical, and they coincide correspondingly. It just reflects the fact that the sound intensity field of simple source is irrotational.

B. Dipole source

Let the source strength be D_x. The sound pressure P at any point X is

$$P=\frac{jk\rho cD_x}{4\pi}\frac{\partial}{\partial x}\left(\frac{e^{-jkr}}{r}\right)$$

$$=\frac{k\rho cD_x}{4\pi}\frac{x}{r^3}\sqrt{1+k^2r^2}\cdot e^{-j[kr+tg^{-1}(1/kr)]}. \tag{37}$$

Then, the phase function φ and the auto-spectrum G_p of sound pressure are, respectively,

$$\varphi=kr+tg^{-1}\frac{1}{kr} \tag{38}$$

and

$$G_p=G_0\frac{x^2}{k^4r^6}(1+k^2r^2), \tag{39}$$

where

$$G_0=\frac{1}{2}\left(\frac{k^3\rho cD_x}{4\pi}\right)^2.$$

It is not difficult to obtain that

$$\nabla\varphi=\frac{k^2r^2}{1+k^2r^2}k\ \nabla r, \tag{40}$$

$$\mathbf{I}=\frac{G_0}{\rho c}\cdot\frac{x^2}{k^2r^4}\nabla r, \tag{41}$$

and

$$\Omega=\nabla\times\mathbf{I}=\frac{2G_0}{\rho c}\cdot\frac{x}{k^2r^4}\left(-\frac{z}{r}\mathbf{n}_y+\frac{y}{r}\mathbf{n}_z\right), \tag{42}$$

where $\mathbf{n}_x$, $\mathbf{n}_y$ and $\mathbf{n}_z$ are the unit vectors in the directions of the coordinates.

Using Eq. (40), we have

$$\varepsilon^2=\left(\frac{k^2r^2}{1+k^2r^2}\right)^2. \tag{43}$$

Equation (14) reduces to

$$\nabla r=\mathbf{r}_I'(\gamma). \tag{44}$$

Thus $\nabla\varepsilon//\nabla r//\mathbf{r}_I'(\gamma)$, and the intensity streamlines are straight lines.

In the sound field, $\nabla\varphi\neq 0$, but on the plane of $x=0$, $G_p=0$. Therefore on the plane of $x=0$, the straight lines are not actual intensity streamlines, there is no energy flow and $\Omega=0$. The plane is a silent subspace.

In order to obtain the vorticity streamlines, substituting Eq. (42) into Eq. (26) yields

$$dx=0, \tag{45}$$

$$\frac{dy}{-z}=\frac{dz}{y}. \tag{46}$$

Equation (46) is rewritten as

$$d(y^2+z^2)=0. \tag{47}$$

Giving a point $X_0(x_0,y_0,z_0)$ in the sound field and integrating Eqs. (45) and (47), the vorticity streamline passing through the point X_0 is obtained as

$$x=x_0, \tag{48}$$

$$y^2+z^2=y_0^2+z_0^2. \tag{49}$$

Apparently the vorticity streamlines are the circles of which the centers are on the x axis.

C. Quadrupole source

Let the source strength be Q_{xy}. The sound pressure P at any point X is

$$P=\frac{jk\rho cQ_{xy}}{4\pi}\cdot\frac{\partial^2}{\partial x\,\partial y}\left(\frac{e^{-jkr}}{r}\right)$$

$$=\frac{k\rho cQ_{xy}}{4\pi}\cdot\frac{xy}{r^5}\sqrt{9k^2r^2+(3-k^2r^2)^2}$$

$$\cdot e^{-j[kr+tg^{-1}(3-k^2r^2/3kr)]}. \tag{50}$$

From this equation, the phase function φ and the auto-spectrum G_p of sound pressure are, respectively,

$$\varphi=kr+tg^{-1}\left(\frac{3-k^2r^2}{3kr}\right) \tag{51}$$

and

$$G_p=G_0\frac{x^2y^2}{k^6r^{10}}(9+3k^2r^2+k^4r^4), \tag{52}$$

where

$$G_0=\frac{1}{2}\left(\frac{k^4\rho cQ_{xy}}{4\pi}\right)^2.$$

Further we have

$$\nabla\varphi=\frac{k^4r^4}{(9+3k^2r^2+k^4r^4)}k\ \nabla r, \tag{53}$$

$$\mathbf{I}=\frac{G_0}{\rho c}\cdot\frac{x^2y^2}{k^2r^6}\nabla r, \tag{54}$$

and

$$\Omega=\nabla\times\mathbf{I}=\frac{2G_0xy}{k^2r^7}\cdot[xz\mathbf{n}_x-yz\mathbf{n}_y+(y^2-x^2)\mathbf{n}_z]. \tag{55}$$

It is easy to demonstrate that $\nabla\varepsilon//\nabla r//\nabla\varphi//\mathbf{r}_I'(\gamma)$ and the intensity streamlines are straight lines.

In the sound field $\nabla\varphi\neq 0$, but on the plane of $x=0$ or the plane of $y=0$, $G_p=0$. The straight lines on the plane of $x=0$ or on the plane of $y=0$ are not actual intensity streamlines, where there is no energy flow. From Eqs. (54) and (55), $\mathbf{I}=0$ and $\Omega=0$ on the plane of $x=0$ or on the plane of $y=0$.

Substituting Eq. (55) into Eq. (26), the differential equations of vorticity streamlines become

$$\frac{dx}{xz}=\frac{dy}{-yz}=\frac{dz}{y^2-x^2}. \tag{56}$$

From the first equation, we have

$$y\,dx + x\,dy = 0 \tag{57}$$

and from the second equation, we have

$$-\frac{x^2}{y}dy + y\,dy + z\,dz = 0. \tag{58}$$

Equations (57) and (58) reduce to

$$d(xy) = 0 \tag{59}$$

and

$$d(x^2 + y^2 + z^2) = 0. \tag{60}$$

Giving a point $X_0(x_0, y_0, z_0)$ in the sound field and integrating above equations, the vorticity streamline passing through the point X_0 is obtained as

$$xy = x_0 y_0, \tag{61}$$

$$x^2 + y^2 + z^2 = x_0^2 + y_0^2 + z_0^2. \tag{62}$$

The vorticity streamline is a closed curve intersected by a spherical surface described by Eq. (62), which is a constant phase surface, and a quadratic surface described by Eq. (61), which is a constant potential surface.

VI. CONCLUSIONS

In three-dimensional sound fields, the integral behavior of intensity streamlines is that the beginning and the end are attached to the sound source surface or that the beginning is on the sound source surface and the end extends into the infinite. The intensity streamlines depend on ϵ. If ϵ is constant or if the direction of gradient of ϵ is parallel always to the direction of the corresponding sound intensity, the intensity streamlines are straight lines.

All the points at which $G_p = 0$ and $\nabla\varphi \neq 0$ form a subspace on which the curves of integrating sound intensities exist, but are not actual intensity streamlines. In the subspace there is no energy flow. The point at which $\nabla\varphi = 0$ is a separating point of intensity streamlines, called as the saddle point. No intensity streamline passes through the saddle point.

The integral behavior of vorticity streamlines is that the beginning and the end are attached to the sound source surface or that the vorticity streamline is closed itself. The vorticity streamline is the curve intersected by a constant potential surface and a constant phase surface. When the sound intensity field is irrotational, the constant potential surfaces coincide with the constant phase surfaces each other.

[1] R. V. Waterhouse, T. W. Yates, D. Feit, and Y. N. Liu, ''Energy streamlines of a sound source,'' J. Acoust. Soc. Am. **78**, 758–762 (1985).

[2] R. V. Waterhouse and D. Feit, ''Equal-energy streamlines,'' J. Acoust. Soc. Am. **80**, 681–684 (1986).

[3] R. V. Waterhouse, D. G. Crighton, and J. E. Ffowcs-Williams, ''A criterion for an energy vortex in a sound field,'' J. Acoust. Soc. Am. **81**, 1323–1326 (1987).

[4] C. F. Chien and R. V. Waterhouse, ''Singular points of intensity streamlines in two-dimensional sound fields,'' J. Acoust. Soc. Am. **101**, 705–712 (1997).

[5] Jiang Zhe, ''Variational principle and energy integrals in a complex sound intensity field,'' J. Acoust. Soc. Am. **98**, 1163–1168 (1995).

Modified impulse method for the measurement of the frequency response of acoustic filters to weakly nonlinear transient excitations

F. Payri, J. M. Desantes, and A. Broatch
CMT, Departamento de Máquinas y Motores Térmicos, Universidad Politécnica de Valencia, Aptdo. 22012, E-46071 Valencia, Spain

(Received 3 February 1999; accepted for publication 14 October 1999)

In this paper, a modified impulse method is proposed which allows the determination of the influence of the excitation characteristics on acoustic filter performance. Issues related to nonlinear propagation, namely wave steepening and wave interactions, have been addressed in an approximate way, validated against one-dimensional unsteady nonlinear flow calculations. The results obtained for expansion chambers and extended duct resonators indicate that the amplitude threshold for the onset of nonlinear phenomena is related to the geometry considered. © *2000 Acoustical Society of America.* [S0001-4966(00)00402-1]

PACS numbers: 43.25.Cb, 43.25.Ed, 43.25.Zx [MFH]

INTRODUCTION

Acoustic filters are generally conceived so that an optimum sound attenuation is attained in the linear regime. Indeed, most of the literature, either related to theoretical prediction or to experimental characterization, confirms this statement. The only exceptions are related to mufflers with perforated ducts, where the importance of the intrinsic nonlinear behavior of the flow at the holes is apparent even in the case of low-amplitude excitations.[1] However, in practice it is possible that acoustic filters optimized for attenuation of low-amplitude perturbations may be subject to higher-amplitude, nonlinear excitations. This is the case, for instance, of intake and, mainly, exhaust systems of internal combustion engines. In these cases there may exist a reasonable uncertainty with respect to the actual acoustic performance of the filter, and therefore, an estimation of the eventual differences expected is required.

Such an estimation should be obtained from experiment, since only relatively simple elements admit a suitable representation in the frame of nonlinear flow calculations, and this only for the low-frequency range.[2,3] This is one of the main reasons for the wide use of linear theory in acoustic filter design, even when it is known in advance that nonlinear excitations will be present, as in the case of internal combustion engines. Hence, an experimental procedure must be devised which permits the characterization of nonlinear and dissipative effects on the acoustic performance of a filter, while keeping the results essentially dependent on the filter characteristics, not on the particular excitation chosen.

In order to achieve this goal, several measurement procedures have been analyzed, in order to evaluate their possibilities to be modified in this sense. The classical evaluation method is the impedance tube,[4] where pure tones are used as excitation and an anechoic termination is needed. This method is not well suited for this work, as the determination of the filter characteristics from the standing waves established in the impedance tube assumes linear behavior of the flow field all throughout the system. Hence, the excitation must be kept necessarily small if uncertainties due to the use of some nonlinear propagation model are to be avoided. Other possibilities come from the use of two-sensor methods, such as the two-microphone method[5] and the transfer function method.[6–8] These methods do not require a separate measurement for each frequency, but instead use a pseudorandom excitation that allows for the simultaneous determination of the acoustic properties at all the frequencies of interest. With these methods, which can all be proved to be equivalent,[9] any exchange of spectral content between the different harmonics present in the pseudorandom excitation cannot be accounted for. However, since in this case the hypothesis of linear propagation is assumed only between the two sensors, and the space between them cannot be too large due to spatial aliasing,[10] the results obtained may give an estimate of the actual influence of flow nonlinearity on filter performance. Two-sensor methods may be extended to include the presence of a mean flow and acoustic damping,[11] thereby approaching realistic conditions. The main drawback of these methods for the present work is the need for an anechoic termination, due to the expectable changes in the reflection properties of any termination associated with the amplitude of the perturbations used. A further development that avoids the use of an anechoic termination is the two-source location method,[12] where two pairs of sensors are used. Although this method is theoretically well founded,[13] in the literature there is no evidence of its application, even for the purely linear regime.

By comparison, the impulse method[14] seems to be particularly well suited for the present investigation. In this method, the muffler is excited by means of a pressure pulse which, in the original method, is generated by means of a digital/analog (D/A) converter in order to obtain a spectrum as flat as possible and within the linear range. The incident, reflected and transmitted pulses are isolated in the time domain by means of a suitable windowing of the pressure records obtained, and the transmission loss is obtained directly from the frequency analysis of these signals.

In this paper, some modifications of the impulse method

are proposed and validated to allow a more flexible approach to the determination of the influence of the excitation characteristics on acoustic filter performance. Problems associated with nonlinear propagation, due both to wave steepening and to wave interactions, have been solved in an approximate way that provides sufficient accuracy, as has been verified by means of one-dimensional unsteady nonlinear flow calculations. The method is applied to expansion chambers and extended duct resonators, indicating that the amplitude threshold for the onset of nonlinear phenomena depends on the geometry considered.

I. MEASUREMENT METHOD

In order to justify the development of the measurement method proposed, first the application of the original impulse method, with some minor modifications, will be discussed. From the analysis of the results obtained, the main issues in the application of the method to the case of weakly nonlinear excitations will be discussed, and then the modified impulse method will be described.

A. Original impulse method: Discussion

Since the study focuses on the influence of the excitation, it is convenient to dispose of isolated pressure pulses, of which characteristics such as amplitude, duration, and shape may be controlled. In the original impulse method, the only requirement is that the incident spectrum is flat, so that the pulse can be generated by means of a D/A converter.[15] Furthermore, the actual exciting signal was not a single pulse, but a train of pulses modulated by the windowing function used. Therefore, for the purposes of the present work, the original impulse method was first modified in two senses,[16]

(i) The incident pulse is generated by means of an electrovalve that controls the discharge from a high-pressure reservoir. By modifying the upstream pressure it is possible to obtain excitations of different amplitudes, and therefore, it is possible to obtain pressure pulses close to those impinging on the filter when it operates in realistic conditions. In addition, by changing the opening time of the valve it is possible to ensure that the spectrum associated with the incident pulse remains essentially flat.

(ii) The length of the ducts placed between the valve and the first transducer, the first transducer and the muffler, and the muffler and the open end, have been chosen so that no windowing is necessary in order to isolate the incident, the reflected, and the transmitted pulses.

The experimental setup resulting from these modifications is shown in Fig. 1. The first transducer was located 15 m away from both the valve and the filter, and the second one was placed 0.1 m downstream of the filter, and 15 m away from the open end. Typical pressure records from transducers 1 and 2 in the case of an expansion chamber are shown in Fig. 2, where it is observed that the above requirements are fulfilled. It should be noted that the duct lengths were large enough to avoid overlap between incident and reflected pulses.

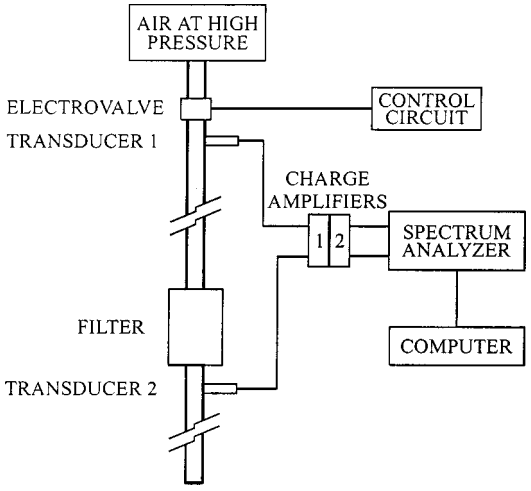

FIG. 1. Scheme of the measurement setup.

These signals allow a simple processing, isolating the incident, the reflected, and the transmitted pulses in the time domain. By performing the fast Fourier transform of the processed signals, one may estimate the modulus of the reflection and transmission coefficients, R and T, of the filter, as a function of frequency f,

$$|R(f)| = |B(f)/A(f)|, \tag{1}$$

$$|T(f)| = |C(f)/A(f)|, \tag{2}$$

where A, B, and C are, respectively, the complex amplitudes of the incident, the reflected, and the transmitted pulses. Of course, the phase might also be obtained, but it will be mainly determined by the intermediate ducts. The results of applying Eqs. (1) and (2) are shown in Figs. 3 and 4, compared with a theoretical linear prediction accounting for mean flow and viscothermal dissipation.[17] It can be observed that, while the transmission coefficient shown in Fig. 3 follows the linear behavior quite closely, especially at low frequencies, this is not the case for the reflection coefficient, where a certain similitude is observed only at very low frequencies. As demonstrated below, this is due to the fact that the pulses recorded by transducer 1 are not exactly those incident on and reflected by the filter, but are affected by nonlinear development along the connecting duct, whereas

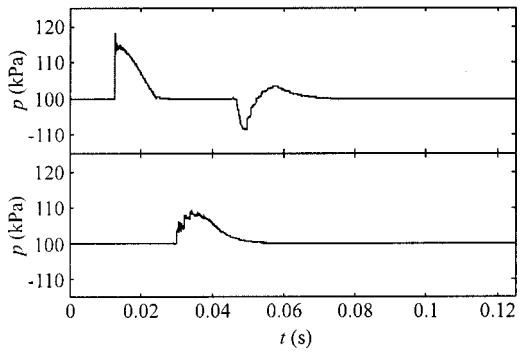

FIG. 2. Pressure recorded by transducers 1 (top) and 2 (bottom).

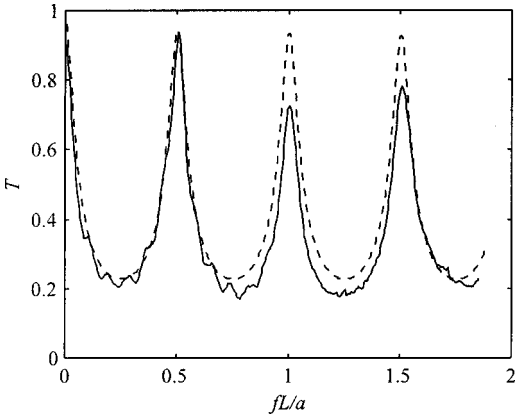

FIG. 3. Transmission coefficient (modulus) of expansion chamber as a function of nondimensional frequency fL/a (L: chamber length, a: speed of sound): Measured (solid), calculated (dash).

the transmitted pulse, being recorded just downstream of the filter, does not incorporate this feature to the same extent.

Although duct lengths are kept to the minimum, ensuring the absence of wave overlapping, the distance to be covered by the pressure pulse from the upstream transducer to the filter and back is considerably long. Thus a certain deformation of the pulse may be expected due to the nonlinear development associated with the amplitude considered, as indicated by Earnshaw's equation for simple homentropic waves,

$$u/a_0 = \pm[(p/p_0)^{\xi} - 1]/(\gamma\xi), \tag{3}$$

where u is the local velocity, p is the pressure, a_0 and p_0 are, respectively, the speed of sound and the pressure of the unperturbed medium, $\xi = (\gamma - 1)/2\gamma$ (γ is the adiabatic coefficient), and the plus sign $+$ corresponds to a forward simple wave and the minus sign $-$ corresponds to a backward simple wave. Equation (3) expresses the dependence of propagation speed on pressure amplitude, which implies the steepening of pressure pulses and the smoothing of rarefaction pulses. Thus pulses recorded by transducer 1 contain information related not only to the reflection properties of the filter, but also to the particular propagation path.

In order to assess the influence of this fact quantitatively, a numerical simulation has been performed by using a

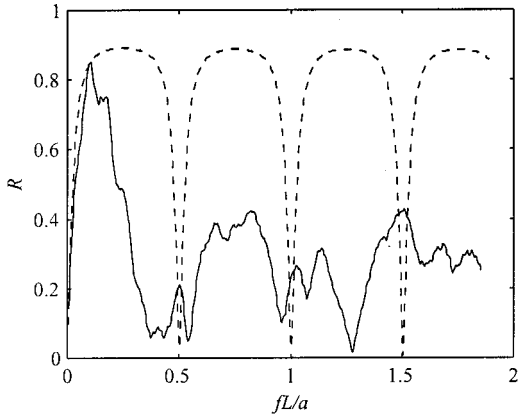

FIG. 4. Reflection coefficient (modulus) of expansion chamber (x-axis as in Fig. 3): Measured (solid), calculated (dash).

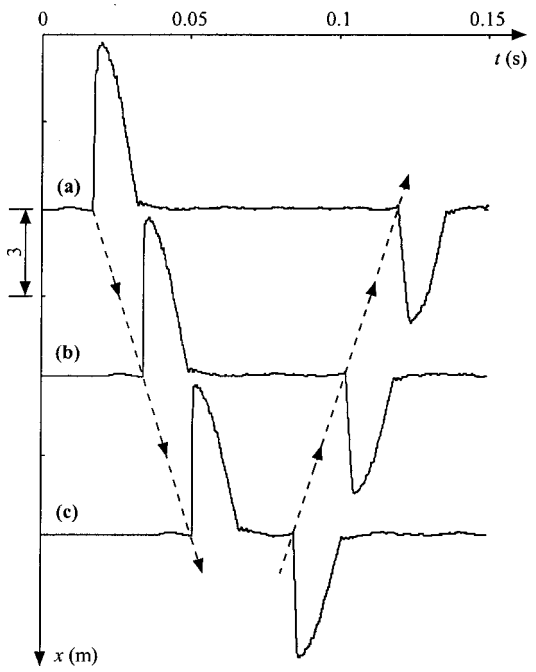

FIG. 5. Development of pressure and rarefaction pulses (numerical results): time domain.

version of the MacCormack finite differences scheme[18] to solve the unsteady one-dimensional flow equations. The pressure pulse recorded at transducer 1 has been imposed as a boundary condition at the inlet of a simple duct. At the outlet of the duct, an open end has been considered, so that the development of both a pressure wave (the incident pulse) and a rarefaction wave (the pulse reflected from the open end) may be studied. The results of this calculation are shown, in the time domain, in Fig. 5, where pulse deformation associated with the distances involved can be appreciated. It should be noticed that, while the incident pressure pulse exhibits small variations in shape once it reaches a certain degree of development, the reflected rarefaction pulse experiences a considerable deformation. The corresponding frequency-domain representations are shown in Fig. 6: in the upper part, the evolution of the incident spectrum is depicted, while in the lower part the same evolution for the reflected

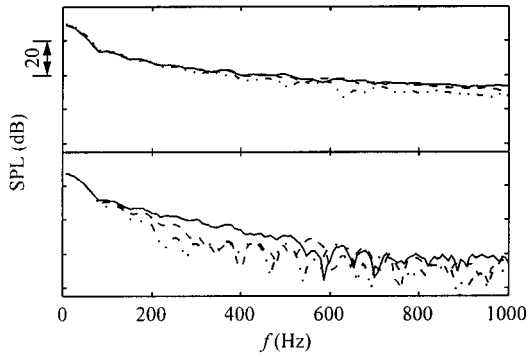

FIG. 6. Development of pressure and rarefaction pulses (numerical results): frequency domain. Top: pressure pulses; bottom: rarefaction pulses. Section (a) (dash-dot), section (b) (dash), and section (c) (solid) (sections labeled as in Fig. 5).

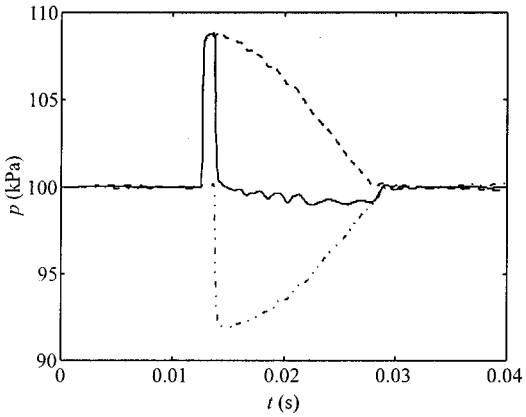

FIG. 7. Nonlinear local pressure decomposition: Pressure (solid), incident component (dash), and reflected component (dash-dot).

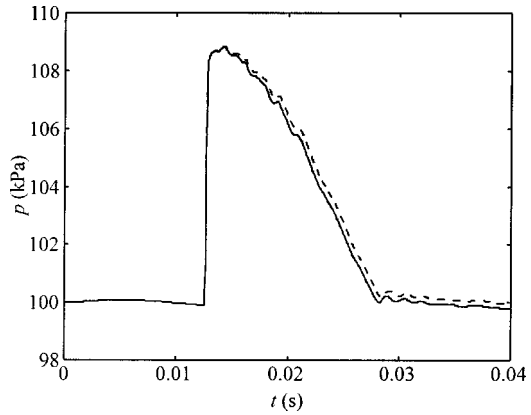

FIG. 8. Incident component as given by Eq. (5) (solid) and pressure pulse with anechoic termination (dash).

spectrum is shown. It is apparent that, although differences are observed in the evolution of pressure pulses, they are much lower than for the development of rarefaction pulses. Of course, this cannot be explained attending only to the eventual losses associated with pulse propagation, since such losses should be independent of the direction of propagation. The explanation lies in the intrinsic differences in behavior between pressure and rarefaction pulses in nonlinear conditions. Actually, the nonlinear development of a pressure pulse leads to the formation of an asymptotic singularity (in the limit, a shock wave). Therefore, once the pulse has reached the asymptotic region any further nonlinear development should be scarcely noticeable, both in the time and the frequency domains. On the contrary, the development of a rarefaction pulse does not lead to any asymptotic singularity, but to a continuous deformation of the pulse shape. This determines the changes in the frequency spectrum observed in Fig. 6, which arise not only in the level but also in the very shape of the spectrum. This difference in behavior, on the one hand, justifies the differences observed between the transmission and reflection coefficients, but on the other hand, indicates the need to take measurements closer to the filter in order to obtain the actual response of the filter itself. It should be noted that, if wave development is not to be noticeable, then the possibility to isolate the incident and the reflected pulses in the time domain is lost. This limitation may only be overcome with a substantial modification of the method.

B. Modified impulse method

Consider the same experimental setup as shown in Fig. 1, but adding a third pressure transducer located 0.1 m upstream of the filter. The pressure recorded by this new transducer will be the result of the nonlinear addition of the incident and the reflected pulses, according to[19]

$$[p/p_0]^{\xi}=[p_i/p_0]^{\xi}+[p_r/p_0]^{\xi}-1, \tag{4}$$

where p_i and p_r are, respectively, the incident and the reflected pulses whose Fourier coefficients should be used in Eqs. (1) and (2). Of course, is it not possible to identify these pressure components from a single pressure measurement. One possible solution would be to move transducer 1 to the vicinity of the filter, and then apply wave decomposition[9] in order to extract this information from a conventional two-sensor measurement. However, apart from the fact, already commented upon, that linear propagation must be assumed between the two transducers, a pulsed excitation such as the one considered here is not well suited for conventional decomposition algorithms. Therefore, an alternative solution has been devised, where the isolated incident pulse recorded by transducer 1 is propagated up to the position of the transducer just upstream of the filter, as detailed below.

First, it should be recalled that the propagation of the incident pulse is intrinsically nonlinear. Therefore, a simple translation of the pulse recorded by transducer 1 to the new measurement station is not possible. Second, the existence of nonlinear wave interactions upstream of the filter implies that, even if one is able to propagate the incident pulse up to the filter inlet, the result will not be the same as in the real situation, where the incident pulse is modified by the presence of the reflected one,[19] which is not known in advance. Therefore, the influence of this second issue will be addressed first in order to determine the importance of the interaction effect, and then the possibilities to propagate the incident pulse will be discussed.

1. Upstream pressure decomposition

To determine the influence of interaction on the incident pulse, the same numerical calculation as before has been used, taking advantage of the fact that, with a full knowledge of the flow variables, it is possible to compute the two components of the pressure at a given point as[3]

$$p_i=p_0[(1+a/a_0+\gamma\xi u/a_0)/2]^{1/\xi}, \tag{5}$$

$$p_r=p_0[(1+a/a_0-\gamma\xi u/a_0)/2]^{1/\xi}, \tag{6}$$

where a is the local speed of sound at the point considered. Comparison of p_i, as given by Eq. (5), with the pressure $\tilde{p}_i$, computed at the same point but removing any reflecting singularity (that is, with an anechoic termination), will indicate the influence of wave interaction and hence the feasibility of propagating, by any means, the pulse recorded at transducer 1 to the location of the transducer just upstream of the filter.

To consider flow conditions as much adverse as possible, an open end has been taken as the reflecting singular-

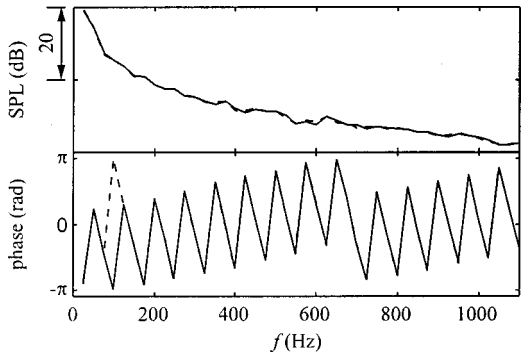

FIG. 9. Incident component spectrum (solid) and pressure spectrum with anechoic termination (dash). Top: modulus; bottom: phase.

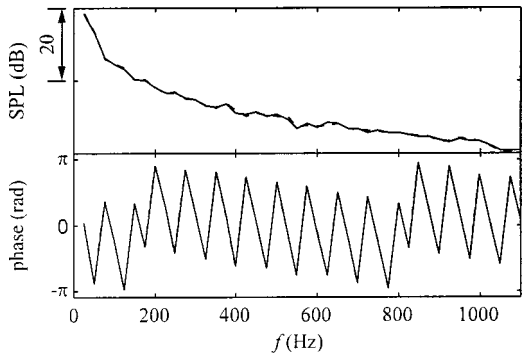

FIG. 11. Reflected component spectrum from Eq. (6) (solid) and reflected pulse spectrum from Eq. (7) dash. Top: modulus; bottom: phase.

ity. The results of the computation are shown in Fig. 7, where the pressure near the open end, together with the incident and reflected components computed from Eqs. (5) and (6), are represented. A comparison between this incident pulse and the one computed with an anechoic termination is shown in the time domain in Fig. 8, where it can be observed that, even though the shape of both pulses is substantially the same, there appear some differences in the level. Nevertheless, as can be observed in the corresponding spectrum shown in Fig. 9, differences in modulus are at most of the order of 1 dB, while the phase is not affected in any noticeable manner. Since the amplitude of the pulse reflected by a given filter will be, in general, lower than that of the pulse reflected by an open end, one may thus conclude that the propagation of the incident pulse to the inlet section of the filter, neglecting the influence of the interaction with the reflected pulse, gives a sufficient approximation to the actual pulse exciting the filter. The value of the corresponding reflected signal is then obtained as

$$\tilde{p}_r = p_0[1+[p/p_0]^{\xi}-[\tilde{p}_i/p_0]^{\xi}]^{1/\xi}. \tag{7}$$

Comparison of p_r, as computed from Eq. (6), and $\tilde{p}_r$, as given by Eq. (7), is shown in Figs. 10 and 11, where it is observed that the accuracy obtained is comparable to that found for the incident pulse. Notice that, according to Eqs. (1) and (2), the reflection coefficient will be affected by the approximation proposed both in the numerator and the denominator, whereas the transmission coefficient is affected only in the denominator, since no additional processing is required for the transmitted pulse.

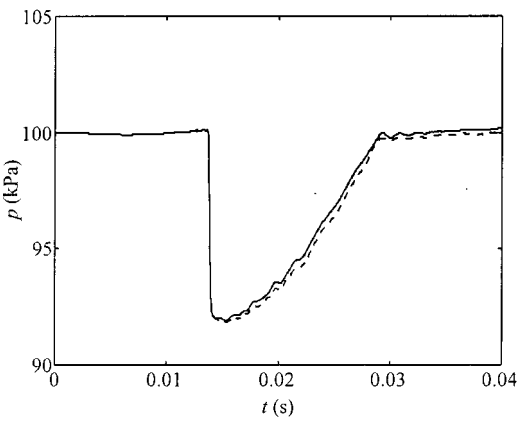

FIG. 10. Reflected component as given by Eq. (6) (solid) and reflected pressure pulse computed with Eq. (7) (dash).

2. Incident pulse determination

The possibilities to propagate the incident pulse from transducer 1 to the muffler inlet section will be now considered. One possibility would be the use of a nonlinear propagation model similar to the one used earlier in order to determine the importance of wave development. However, this numerical solution of the unsteady nonlinear flow equations may be affected by the presence of numerical dispersion, even when using the MacCormack scheme,[18] especially considering the duct lengths involved in the experiment. Consequently, the use of such a propagation method would introduce additional uncertainties in the measurement results. Therefore, an experimental solution has been preferred, where an additional test is performed. Here, the filter is removed from the measurement system, so that the pressure pulse recorded at the position corresponding to the filter inlet is precisely $\tilde{p}_i$, the anechoic termination being simulated by the absence of overlapping. For this solution to be suitable, it is imperative to ensure that the pulses used in both tests, with and without filter, are comparable. This is checked by evaluating the difference between the autocorrelation of the pulse recorded by transducer 1 in the test without filter, and the cross correlation between the pulses recorded with and without filter. The repeatability of the pulse generator used permits values of this difference below 5%, which are sufficient in practice.

3. Summary of the method

Summarizing the previous discussion, the measurement method consists of the following steps:

(1) Determination of the incident pulse at the inlet of the filter $\tilde{p}_i$, by means of a test without the filter.
(2) Measurement of the instantaneous pressure at the inlet of the filter (composition of incident and reflected signals) and the outlet (transmitted signal), checking the comparability of the incident pulse to that used in step 1.
(3) Determination of the reflected pulse at the filter inlet $\tilde{p}_r$ by means of Eq. (7).

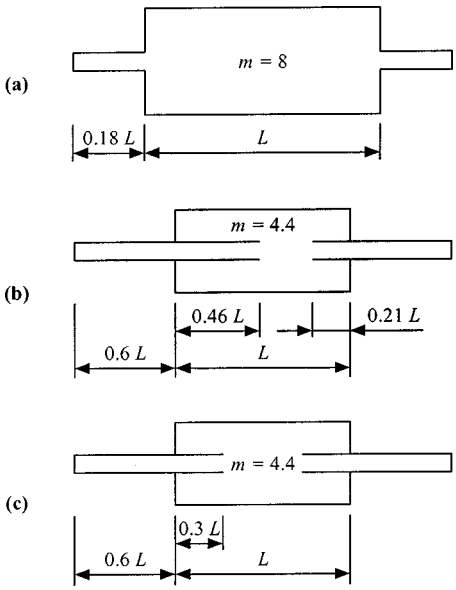

FIG. 12. Systems considered: (a) simple expansion chamber, (b) nonsymmetric extended duct resonator, (c) symmetric extended duct resonator.

(4) Frequency analysis of the incident, reflected, and transmitted signals, and computation of the complex transmission and reflection coefficients.

It should be noticed that the reflected pulse recorded by transducer 1 is no longer used for the filter characterization.

II. RESULTS

In order to check the proposed measurement method, two simple filter geometries with well-known acoustic responses have been chosen: the expansion chamber and the extended duct resonator. The schemes of the cases considered are shown in Fig. 12. Apart from the simple expansion chamber [Fig. 12(a)], two different designs of extended duct resonator have been considered: with extended inlet and outlet ducts of different lengths [nonsymmetric configuration, Fig. 12(b)], so that the resonator characteristic frequencies are located at the chamber passbands, and with equal lengths [symmetric configuration, Fig. 12(c)]. In all the cases, comparisons are presented between the results of the measurement and linear one-dimensional models,[17] in order to assess both the reliability of the method and its ability to account for eventual nonlinear and dissipative features.

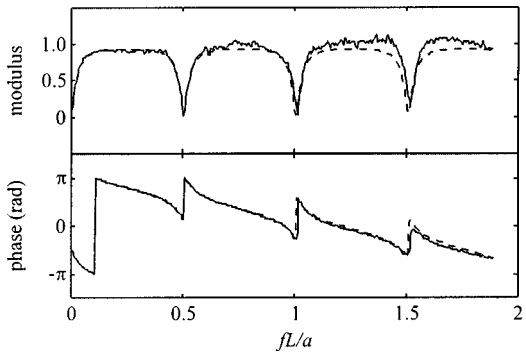

FIG. 14. Reflection coefficient of expansion chamber: measured (solid) and calculated (dash).

Results for the simple expansion chamber are shown in Figs. 13 and 14. In the theoretical calculation, the end correction proposed by Davies[20] has been used. The complex transmission coefficient represented in Fig. 13 exhibits an excellent agreement between measurement and calculation, in both the modulus and the phase, considering that no smoothing has been performed on the experimental results. By comparing these results with those shown in Fig. 3, a considerable improvement in the determination of the transmission coefficient can be appreciated. Looking at the reflection coefficient shown in Fig. 14, the agreement may be regarded as good, with the same trends in the measurement and the calculation. The differences found in the precise values are relatively small, especially if these results are compared with those obtained using the original method, and shown in Fig. 4. The deviations from the theoretical results, however, are higher than in the case of the transmission coefficient. This is partly due to the fact, as previously commented upon, that the uncertainty in the determination of the reflection coefficient is higher than for the transmission coefficient, since the assumptions associated with pressure decomposition upstream of the filter appear in the two signals used. However, this can only explain a part of the difference observed, the rest being due to nonlinear dissipation (since linear dissipation is accounted for by the calculation). The results found would suggest that this dissipative behavior arises mainly in its reflection properties.

In the case of the extended-duct resonators, the end cor-

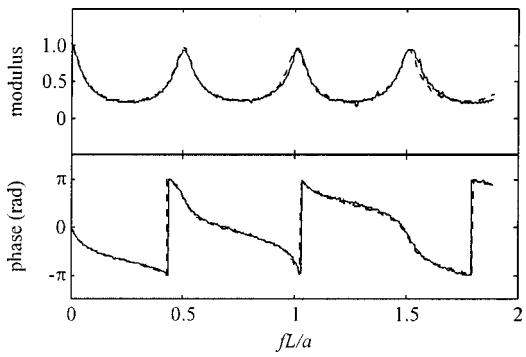

FIG. 13. Transmission coefficient of expansion chamber: measured (solid) and calculated (dash).

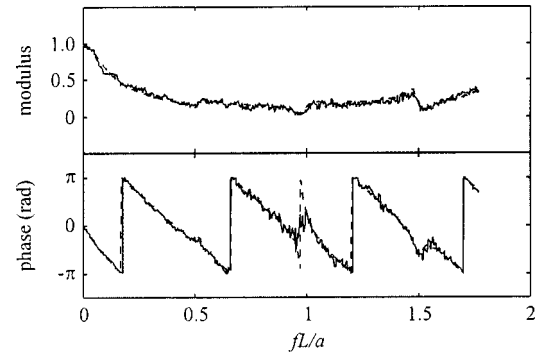

FIG. 15. Transmission coefficient of nonsymmetric extended duct resonator: measured (solid) and calculated (dash).

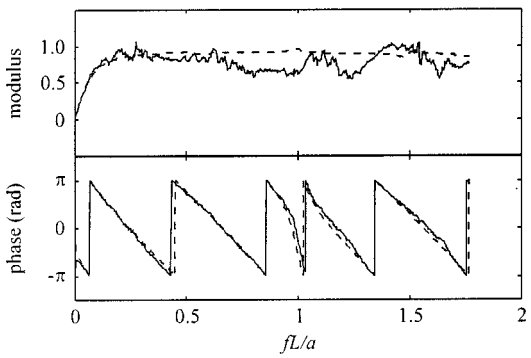

FIG. 16. Reflection coefficient of nonsymmetric extended duct resonator: measured (solid) and calculated (dash).

rection used was that proposed in Ref. 21. Considering first the nonsymmetric configuration, the results shown in Figs. 15 and 16 exhibit the same trends as for the expansion chamber, with an excellent agreement in the transmission coefficient and differences in value, but not in the shape, in the case of the reflection coefficient. However, a closer look at the results indicates that a new feature has appeared, mainly at low frequencies, where the differences between the measured and the calculated moduli present a certain periodicity, which could be related to nonlinear exchange of energy between different harmonics. The effect is of similar importance both in the transmission and the reflection coefficients.

A clearer assessment of this effect is obtained from the study of the symmetrical configuration, whose results are shown in Figs. 17 and 18. Here, the coupling between the effects of both resonators may give rise to local flow conditions inside the filter producing, on the one hand, an increase in dissipation and, on the other hand, a magnification of nonlinear energy transfer mechanisms, which are essentially dependent on the geometry, since the pulses used have been comparable in both cases. Both issues are confirmed by the results obtained: near the resonance frequency of the extended ducts, the measured behavior is much more dissipative than the predicted one, and for the low frequencies it can be clearly observed that the measured behavior oscillates around the predicted curve, the effect being more observable for higher frequencies than in the nonsymmetric case.

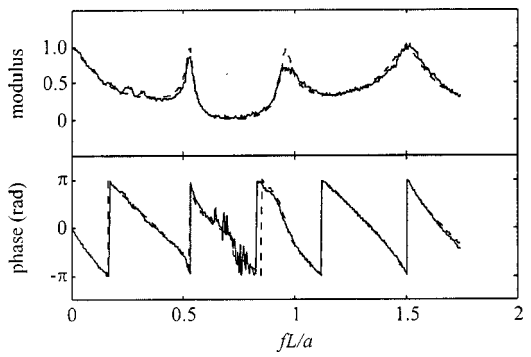

FIG. 17. Transmission coefficient of symmetric extended duct resonator: measured (solid) and calculated (dash).

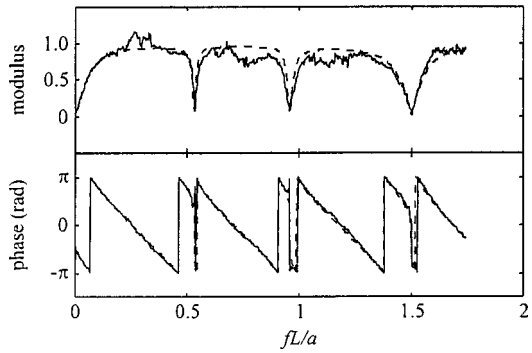

FIG. 18. Reflection coefficient of symmetric extended duct resonator: measured (solid) and calculated (dash).

III. CONCLUSIONS

A modified impulse method has been proposed that allows for the study of the frequency response of acoustic filters when subject to a weakly nonlinear pulse. Nonlinear issues in pulse propagation and interaction have been addressed in an approximate but sufficiently accurate fashion, as verified by means of numerical unsteady flow calculations. The application of the method to simple filter geometries indicates that, depending on the geometry considered, different results may be obtained with the same excitation characteristics. In some cases, only quantitative deviations from the expected linear behavior are observed, due to the extra amount of dissipation associated with nonlinear flow. In other cases, however, qualitative differences appear, with changes in the detail of the curves which, in principle, can be explained by attending to the possibility of nonlinear energy exchange between harmonics.

Further work is being performed in order to establish the origin of this phenomenon and highlight the relationship between the geometry and the amplitude threshold for the onset of this feature.

ACKNOWLEDGMENT

This work has been supported by CICYT through Project No. TAP97-1270-C02-01.

[1] A. J. Torregrosa, A. Broatch, and F. González, ''A theoretical and experimental study of the behavior of concentric perforated duct automotive mufflers,'' SAE Paper 960300 (1996).
[2] A. Onorati, ''Nonlinear fluid dynamic modeling of reactive silencers involving inlet/outlet and perforated ducts,'' Noise Control Eng. J. **45**, 35–51 (1997).
[3] F. Payri, J. M. Desantes, and A. J. Torregrosa, ''Acoustic boundary condition for unsteady one-dimensional flow calculations,'' J. Sound Vib. **188**, 85–110 (1995).
[4] V. B. Panicker and M. L. Munjal, ''Impedance tube technology for flow acoustics,'' J. Sound Vib. **77**, 573–577 (1981).
[5] A. F. Seybert and D. F. Ross, ''Experimental determination of acoustic properties, using a two-microphone random-excitation technique,'' J. Acoust. Soc. Am. **61**, 1362–1370 (1977).
[6] J. Y. Chung and D. A. Blaser, ''Transfer function method of measuring in-duct acoustic properties. I. Theory,'' J. Acoust. Soc. Am. **68**, 907–913 (1980).
[7] J. Y. Chung and D. A. Blaser, ''Transfer function method of measuring in-duct acoustic properties. II. Experiment,'' J. Acoust. Soc. Am. **68**, 914–921 (1980).
[8] W. T. Chu, ''Extension of the two-microphone transfer function method

for impedance tube measurements,'' J. Acoust. Soc. Am. **80**, 347–348 (1986).
[9] A. F. Seybert, ''Two-sensor methods for the measurement of sound intensity and acoustic properties in ducts,'' J. Acoust. Soc. Am. **83**, 2233–2239 (1988).
[10] M. Åbom and H. Bodén, ''Error analysis of two-miocrphone measurements in ducts with flow,'' J. Acoust. Soc. Am. **83**, 2429–2438 (1988).
[11] M. L. Munjal and A. G. Doige, ''The two-microphone method incorporating the effects of mean flow and acoustic damping,'' J. Sound Vib. **137**, 135–138 (1990).
[12] M. L. Munjal and A. G. Doige, ''Theory of a two source-location method for direct experimental evaluation of the four-pole parameters of an aeroacoustic element,'' J. Sound Vib. **141**, 323–333 (1990).
[13] M. Åbom, ''A note on the experimental determination of acoustical two-port matrices,'' J. Sound Vib. **155**, 185–188 (1992).
[14] R. Singh and T. Katra, ''Development of an impulse technique for measurement of muffler characteristics,'' J. Sound Vib. **56**, 270–298 (1978).
[15] R. Singh and T. Katra, ''On the digital generation of an acoustic excitation impulse,'' J. Sound Vib. **56**, 459–462 (1978).
[16] A. Broatch, ''Metodología experimental para el estudio de la respuesta acústica de elementos silenciadores de motores de combustión interna,'' Ph.D. thesis, Universidad Politécnica de Valencia, 1995.
[17] M. L. Munjal, *Acoustics of Ducts and Mufflers* (Wiley, New York, 1987).
[18] F. Payri, A. J. Torregrosa, and M. D. Chust, ''Application of MacCormack schemes to I. C. engine exhaust noise prediction,'' J. Sound Vib. **195**, 757–773 (1996).
[19] G. F. Mucklow and A. J. Wilson, ''The attenuation and reflection of compression waves propagated in pipes,'' Proc. Inst. Mech. Eng. **169**, 69–80 (1955).
[20] P. O. A. L. Davies, ''Practical flow duct acoustics,'' J. Sound Vib. **124**, 91–115 (1988).
[21] A. J. Torregrosa, A. Broatch, R. Payri, and F. González, ''Numerical estimation of end corrections in extended-duct and perforated-duct mufflers,'' Trans. ASME, J. Vib. Acoust. **121**, 302–308 (1999).

Matched-field processing using measured replica fields

Laurie T. Fialkowski, Michael D. Collins, W. A. Kuperman,[a] and John S. Perkins
Naval Research Laboratory, Washington, D.C. 20375

Lesley J. Kelly and Ashley Larsson
Defence Science and Technology Organisation, Salisbury, South Australia

John A. Fawcett
Defence Research Establishment Atlantic, Dartmouth, Nova Scotia

Lindsay H. Hall
Defence Operational Technology Support Establishment, Auckland, New Zealand

(Received 19 July 1999; revised 28 October 1999; accepted 12 November 1999)

An approach for avoiding the problem of environmental uncertainty is tested using data from the TESPEX experiments. Acoustic data basing is an alternative to the difficult task of characterizing the environment by performing direct measurements and solving inverse problems. A source is towed throughout the region of interest to obtain a database of the acoustic field on an array of receivers. With this approach, there is no need to determine environmental parameters or solve the wave equation. Replica fields from an acoustic database are used to perform environmental source tracking [J. Acoust. Soc. Am. **94**, 3335–3341 (1993)], which exploits environmental complexity and source motion. © *2000 Acoustical Society of America.* [S0001-4966(00)04602-6]

PACS numbers: 43.30.Wi, 43.30.Es [DLB]

INTRODUCTION

There has recently been a great deal of interest in inverse problems in ocean acoustics.[1–11] One of the main motivations for this line of research is the demand for techniques for locating sources. Matched-field processing techniques for solving this problem are based on generating replica fields by solving the wave equation for a source at an arbitrary location, comparing with acoustic data, and searching for the source location that gives the best fit.[12] Although there have been many advances in the development of these approaches,[13–25] the problem of environmental uncertainty severely restricts their practicality. The sound speed, density, attenuation, bathymetry, and other parameters of the ocean and sediment layers must be input to the propagation model that is used to generate replica fields. Relatively small errors in this information can cause matched-field processing techniques to break down.[26–28]

Environmental uncertainty can be eliminated by solving the inverse problem before solving the localization problem, but this approach is extremely difficult in the large regions that are typically of interest (source ranges of a few to many kilometers). Focalization is an alternative approach for dealing with environmental uncertainty that involves searching for the source location and environmental parameters simultaneously.[19,25] This approach exploits a parameter hierarchy in which source location outranks environmental parameters and avoids over-resolving the medium for the given frequency, system configuration, and source location. Focalization reduces the emphasis on the environmental inverse problem, which is of great interest for some applications but may be of no direct interest when the goal is to localize a source. In this paper, we investigate an approach for overcoming environmental uncertainty that completely avoids the inverse problem.

Acoustic data basing involves measuring replica fields rather than computing them, which can be performed by towing a source throughout the region of interest. In some scenarios, this approach requires a small fraction of the effort that is required to determine the environmental parameters throughout the region. It does not require solving the wave equation or making difficult decisions regarding accuracy and resolution in the measurement of environmental parameters. We test this approach using data from the TESPEX experiments, which were conducted in 1993 and 1994 by Australia, Canada, New Zealand, and the United States. We discuss the TESPEX experiments in Sec. I. We discuss and illustrate acoustic data basing in Sec. II. We present matched-field processing results based on acoustic databases in Sec. III.

I. THE TESPEX EXPERIMENTS

The feasibility of acoustic data basing was tested in the TESPEX experiments, which involved shallow-water environments. TESPEX-93 was conducted in May 1993 in the region off the eastern coast of New Zealand that is depicted in Fig. 1. TESPEX-94 was conducted in June 1994 in the region off the northern coast of Australia that is depicted in Fig. 2. These experiments also tested the possibility of exploiting complexities associated with variations in the properties of the medium and source motion.

Environmental uncertainty can be an overwhelming problem when a large number of parameters is required to characterize a region of the ocean. Environmental uncertainty and environmental complexity are closely related; there is usually uncertainty where there is complexity. Environmental complexity may therefore be regarded as a serious

[a]Present address: Marine Physical Laboratory, Scripps Institution of Oceanography, La Jolla, CA 92093.

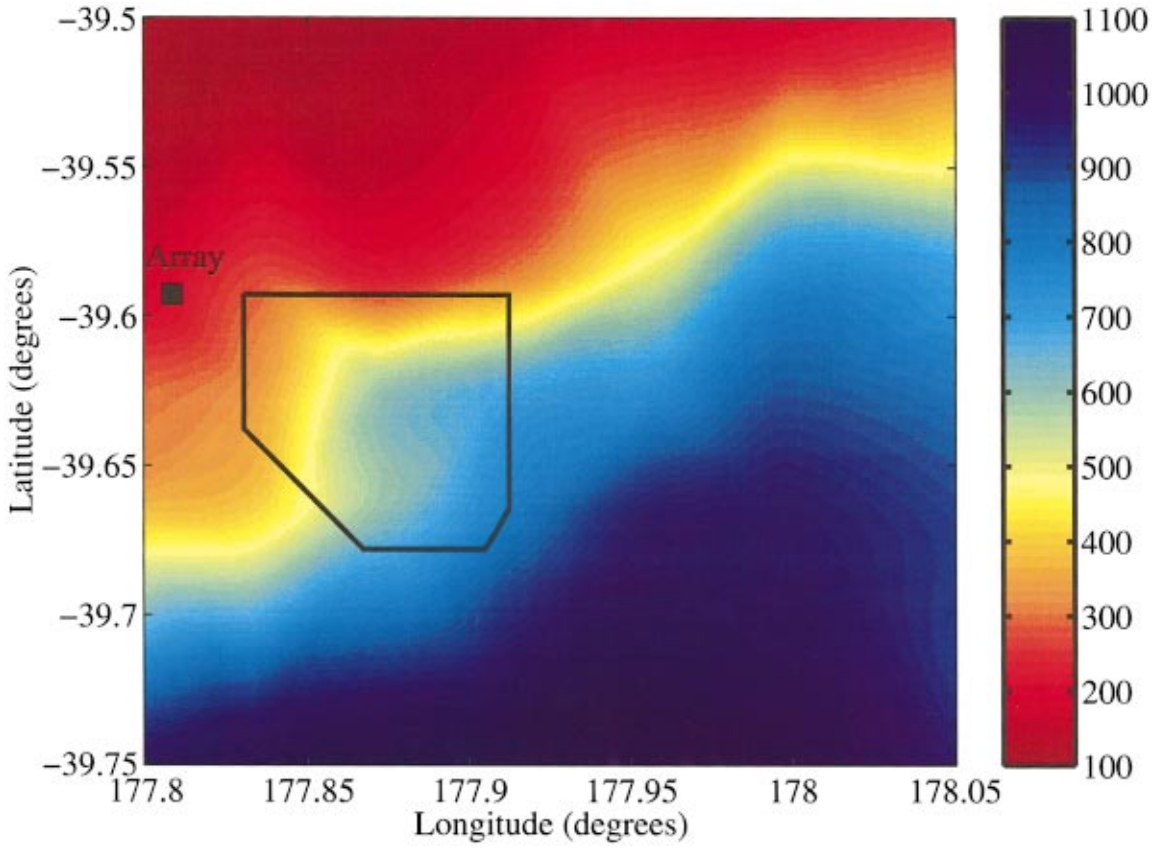

FIG. 1. Location and bathymetry in meters of TESPEX-93. The receiver was placed 176 m below the surface in 198 m of water. An acoustic database was obtained by towing a 75-Hz source 47 m below the surface throughout the region marked by the polygon. The length of the northern boundary of the polygon is approximately 11 km. The bathymetry variations at this site were exploited to perform environmental source tracking with a single receiver at a single frequency.

difficulty in matched-field processing. One of the goals of the TESPEX experiments was to test the idea that environmental complexity can also be regarded as an advantage that can be exploited.[15] The ambiguity of the source location tends to decrease as the complexity of the environment increases. In a homogeneous medium, it is only possible to determine the elevation angle of a distant source with a vertical array of receivers. Sufficient depth dependence in the properties of the medium makes it possible to determine range and depth. Sufficient three-dimensional dependence makes it possible to determine all three source coordinates.

Another goal of the TESPEX experiments was to test the idea that source motion also introduces complexity that can be exploited, especially in a complex environment.[23] It is impossible to determine anything about the location of a fixed source with a single receiver at a single frequency. Sufficient depth dependence makes it is possible to partially determine the track of a moving source with a single receiver at a single frequency. Sufficient three-dimensional dependence makes it possible to completely determine the track of a moving source with a single receiver at a single frequency.

II. ACOUSTIC DATA BASING

An acoustic database can be obtained by towing a source throughout the region of interest and measuring the acoustic field on an array of receivers. In some scenarios, acoustic data basing is much easier than environmental data basing. At low frequencies in shallow water, for example, an acoustic database can be obtained by performing tows at a relatively small number of source depths while avoiding the difficult inverse problem for sediment parameters.

The quality of an acoustic database depends on several factors. Navigation is important because the source positions must be known accurately. The source level must be sufficiently high to reduce contamination by noise to an acceptable level. The source level must be kept constant (or its variations must be taken into account) for some applications.[23] The depth of the source must be controlled carefully as it is towed. The source must be towed slowly enough so that high-quality covariance matrices can be obtained by averaging over time windows of sufficient duration. The acoustic field must be adequately sampled in space. Noise can be suppressed by using the eigenvector that corresponds to the largest eigenvalue of the covariance matrix as the quantity stored in the acoustic database.[24] Even if all of these requirements are met, the quality of an acoustic database may degrade over time as the environmental parameters vary. This problem can be reduced by working at relatively low frequencies and taking acoustic databases under different environmental conditions. Experimental results in Ref. 29 indicate that it takes more than a week for some acoustic databases to degrade.

We obtained a 75-Hz acoustic database in the region depicted in Fig. 1 during TESPEX-93. The length of the

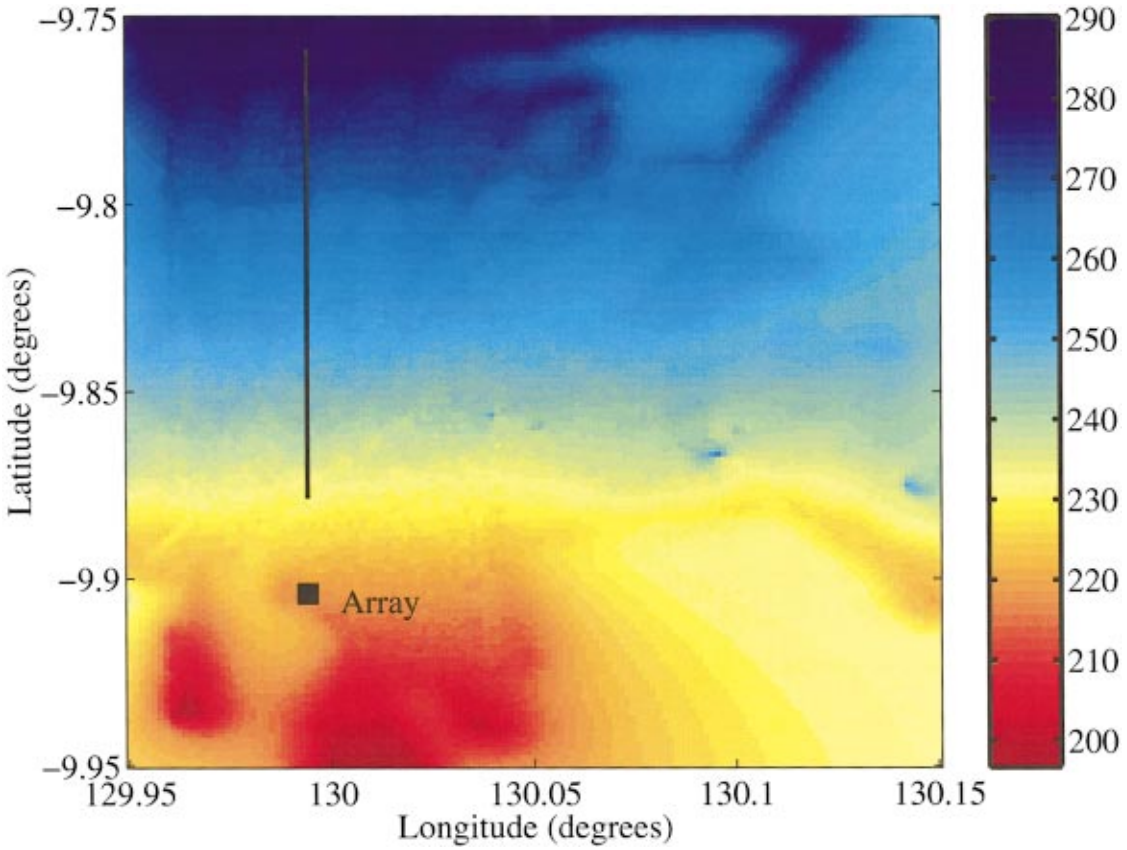

FIG. 2. Location and bathymetry in meters of TESPEX-94. An array of 32 receivers was placed in 220 m of water. An acoustic database was obtained by towing a 160-Hz source 50 m below the surface along the track to the north of the array. The tows along this track ranged between approximately 3 and 15 km from the array.

northern boundary of this region is approximately 11 km. A receiver was placed 176 m below the surface in 198 m of water at 39° 35.57′ S and 177° 48.50′ E. The source was towed 47 m below the surface along radial tracks, which pass through the receiver location, and cross tracks, which were not used in the acoustic database. Table I contains a summary of the tows and an explanation of the notation that is used to designate the tows. The ten radial tracks were separated in azimuth by 5° and spanned from 90° (east) to 135° (southeast). The end points of the radial tracks were approximately 5.6 and 16.7 km from the receiver. The tow speeds ranged from approximately 2 to 2.5 m/s. The radial tows took approximately 80 min apiece. Turning and positioning the ship prior to each tow took approximately 20 min. The acoustic field was mapped out in approximately 26 h, which is a small fraction of the time it would take to obtain the same information by mapping out the environmental parameters and then solving the wave equation. Since cross tracks were also obtained during this period, the actual time required to obtain the acoustic database was approximately 17 h.

TABLE I. The source tows of TESPEX-93. The notation includes the letters A, B, and C, which designate ranges of 5.6, 11.1, and 16.7 km, and bearings measured clockwise from north. For example, the first tow A090C090 was due east from the receiver beginning 5.6 km from the receiver and ending 16.7 km from the receiver. The tows marked with asterisks were used to form an acoustic database.

Tow	Date	Start time	End time
*A090C090	May 23	13:00	14:30
C090A090	May 23	14:50	16:10
*A095C095	May 23	16:20	17:40
*C100A100	May 23	18:00	19:20
*A105C105	May 23	19:40	21:00
*C110A110	May 23	21:30	22:56
*A115C115	May 23	23:20	00:32
*C120A120	May 24	01:06	02:36
A120C090	May 24	02:50	04:20
C090A120	May 24	04:50	06:34
A120B090	May 24	06:50	07:35
B090C125	May 24	08:05	09:20
*C125A125	May 24	09:40	11:00
*A130C130	May 24	12:09	13:23
*C135A135	May 24	13:26	15:20

The acoustic database appears in Fig. 3. Each point in this database was obtained by processing 16-sec slices of data. This initial attempt at obtaining an acoustic database was not performed under ideal conditions. After being delayed by hardware problems, time limitations forced us to use a relatively coarse azimuthal sampling. Large swells made it difficult to control the depth of the source, which varied by perhaps a few meters during the tows. Working with a single receiver, we were not able to suppress noise by forming a covariance matrix and extracting the leading eigenvector.[24] The database may contain degradations due to variations in source level, which is a crucial issue for single-receiver acoustic database.[23] Despite these limitations, the main features in the acoustic field appear to vary smoothly in

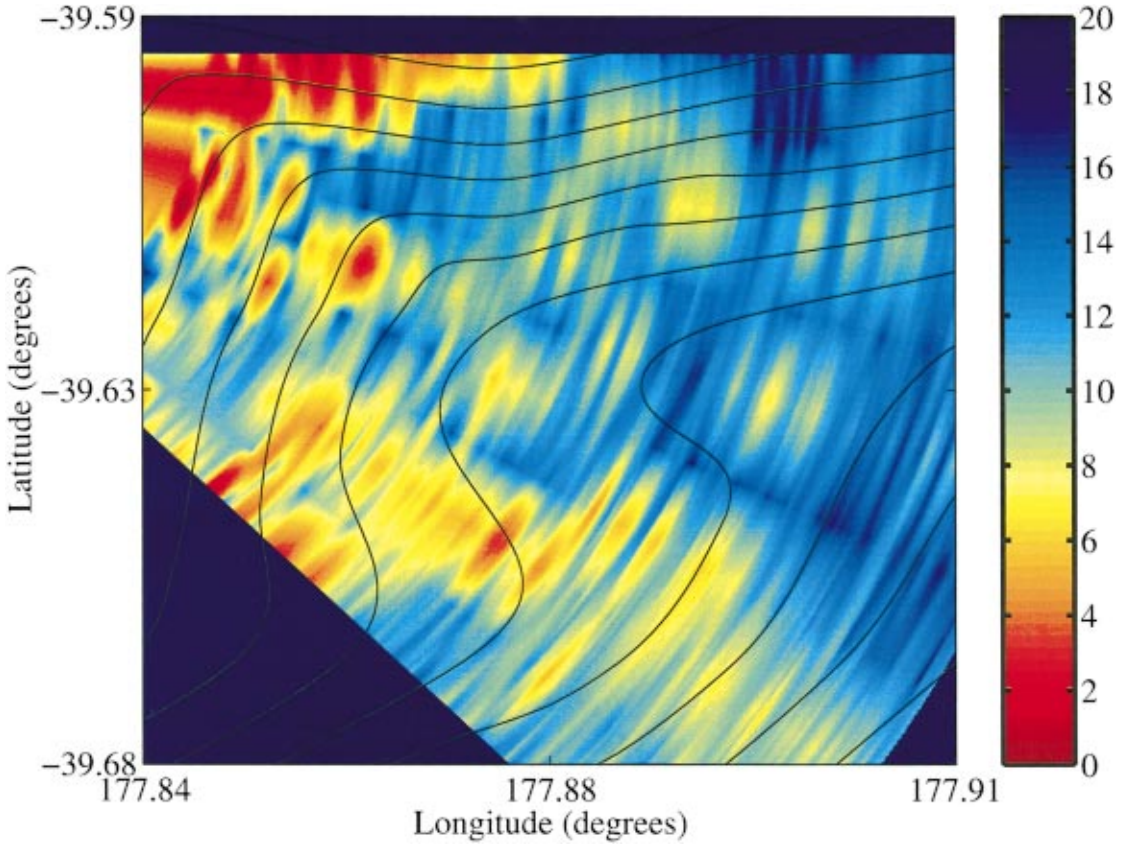

FIG. 3. The 75-Hz acoustic database obtained during TESPEX-93. The amplitude of the acoustic field is shown in decibels on a relative scale. The contours indicate the main features in the bathymetry, which is provided quantitatively in Fig. 1.

both range and azimuth. The azimuthal dependence of the acoustic field is evidently due mostly to variations in bathymetry.

III. MATCHED-FIELD PROCESSING RESULTS

During TESPEX-93, we performed environmental source tracking,[23] which is a matched-field processing technique for determining the path of a moving source. This approach is based on the fact that the field at a fixed receiver varies as a source moves through a waveguide. In sufficiently complex environments, the variations are sufficiently unique to the path that tracking can be performed using only a single receiver and a single frequency.[23] Tracking problems are very difficult in general. For example, it takes five parameters to describe a path in the relatively simple scenario in which the source level, velocity, and depth are assumed to be constant. We reduce the problem to two dimensions by assuming that the initial or final position of the source is known.

We perform environmental source tracking using a least-squares fit of amplitudes along tracks.[23] We consider segments of a radial track and two cross tracks. The radial track C090A090, which is not part of the acoustic database, was obtained immediately after the first radial track in the acoustic database was obtained. We use a segment of this track between ranges of 6 and 12 km. One of the cross tracks is a 9.58-km segment along A120C090 that begins at a range of 5.9 km and ends at a range of 14.6 km. The other cross track is a 9.27-km segment of C090A120 that begins at a range of 14.3 km and ends at a range of 5.9 km.

Source tracking ambiguity surfaces appear in Fig. 4 for the radial track. One of these surfaces corresponds to assuming that the initial location was known. The other surface corresponds to assuming that the final location was known. The end point locations are recovered fairly accurately for both cases. Source tracking ambiguity surfaces appear in Fig. 5 for the cross tracks. The main peak is fairly close to the location of the unknown end point for one of the cross tracks. The breakdown in the tracking for the other case is probably due to a combination of noise contamination, variations in source depth, and coarse azimuthal sampling in the acoustic database. Much better tracking results should be achievable in this region by reducing these data quality limitations.

During TESPEX-94, we investigated the effects of environmental variability on acoustic data basing. A vertical array of 32 receivers was placed in 220 m of water at 9° 54.23′ S and 129° 59.62′ E. The receivers were spaced by 5 m, with the top receiver 56.8 m below the surface. Over a period of four days, a 160-Hz source was towed several times along the track north of the array that is illustrated in Fig. 2. The tow speed averaged approximately 1.7 m/s but was varied during some of the tows in an attempt to keep the source 50 m below the surface. The tows ranged from approximately 3 km from the array out to approximately 15 km

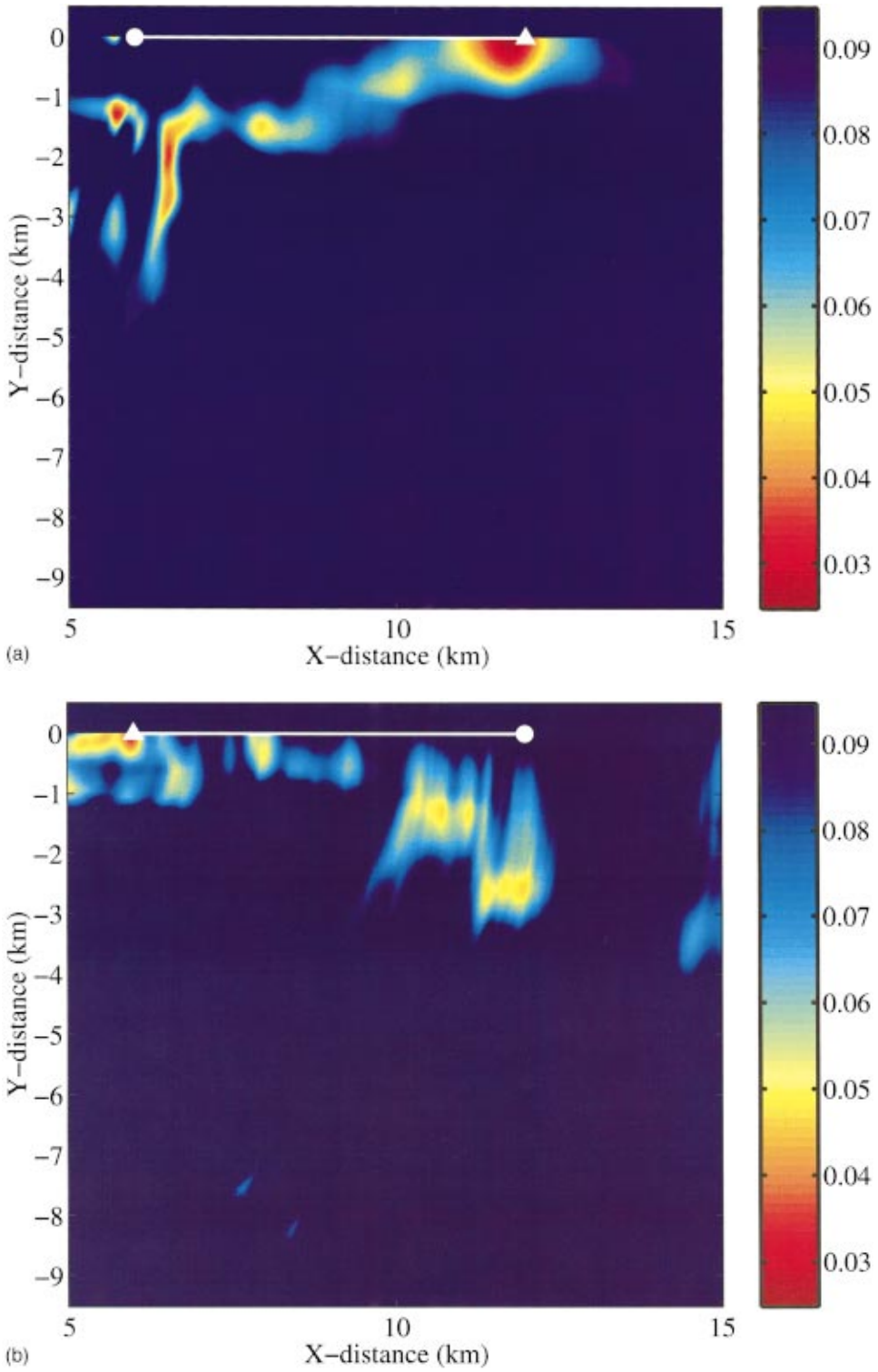

FIG. 4. Environmental source tracking results for a segment of a radial track from TESPEX-93. The ambiguity surface was constructed using the cost function defined in Ref. 23. Red corresponds to close agreement between the data and the replicas, which were obtained from the acoustic database. Blue corresponds to poor agreement. The circles mark the known positions. The triangles mark the unknown positions. (a) The initial range is assumed to be known and the final range is assumed to be unknown. (b) The final range is assumed to be known and the initial range is assumed to be unknown.

and took approximately 2 h. An acoustic database was constructed from the first tow by forming covariance matrices from 20-sec segments of data and extracting the leading eigenvector.

We performed matched-field processing using data from a tow that was performed immediately after the acoustic database was taken and a tow that was performed four days later. Appearing in Fig. 6 are ambiguity surfaces that were obtained by taking the inner products of eigenvectors from the acoustic database and from the subsequent tows. For the tow that was performed on the same day, the largest peaks correctly occur along the main diagonal, which stands out

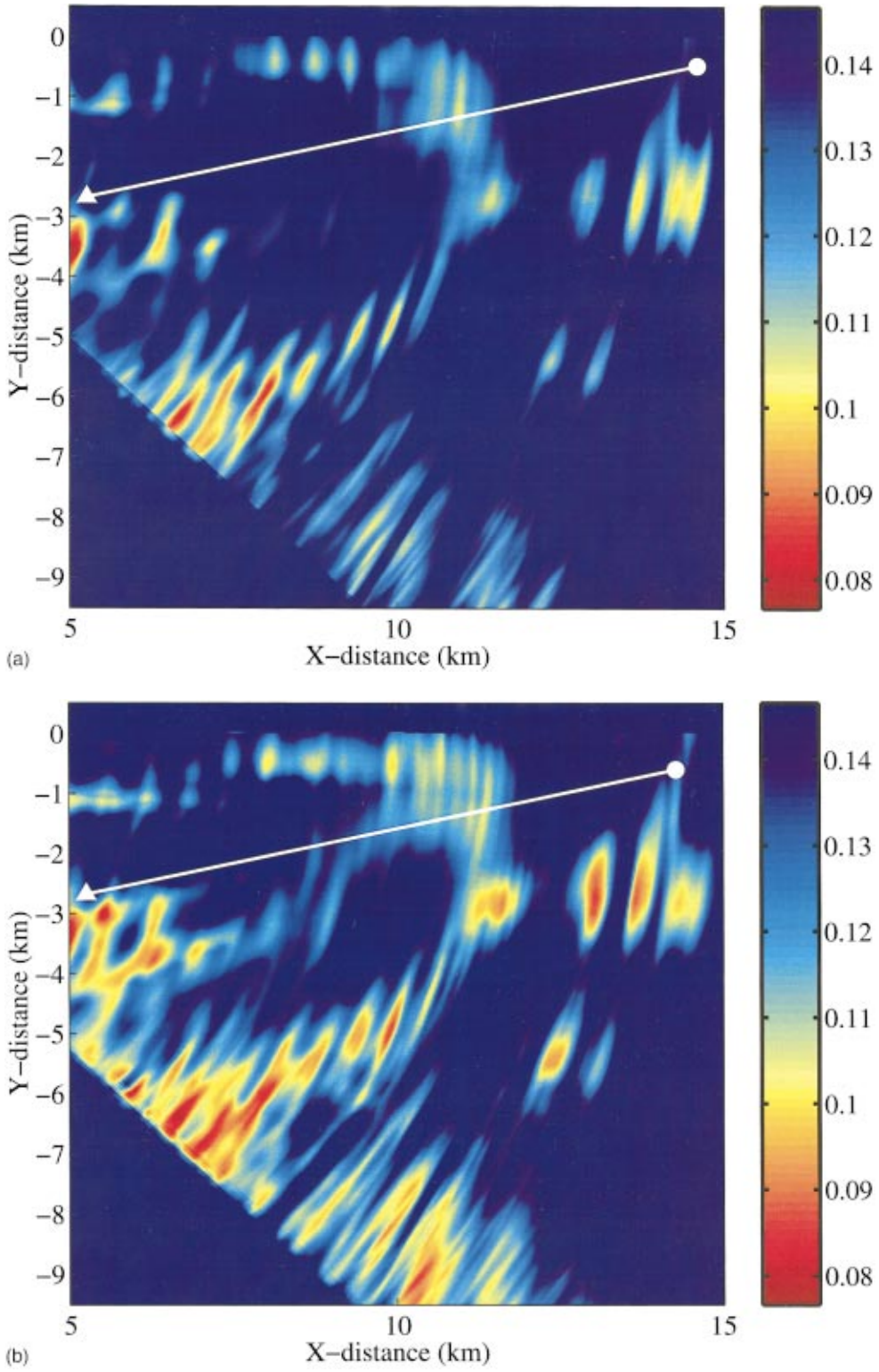

FIG. 5. Environmental source tracking results for segments of cross tracks from TESPEX-93. The ambiguity surface was constructed using the cost function defined in Ref. 23. Red corresponds to close agreement between the data and the replicas, which were obtained from the acoustic database. Blue corresponds to poor agreement. The circles mark the known positions. The triangles mark the unknown positions. The far end point is assumed to be known for each case. (a) The main peak is fairly close to the correct location for track A120C090. (b) The ambiguity surface contains similar features for track C090A120 but is severely corrupted by false peaks.

prominently in the ambiguity surface. The relatively minor breakdowns that occur along this track (e.g., near a range of 10 km) are probably due to variations in source depth. For the tow that was performed four days later, the largest peaks occur along the main diagonal out to a range of about 8 km. The complete breakdown at longer ranges is apparently due to changes in the sound-speed profile in the water column that occurred during the four-day interval between tows.

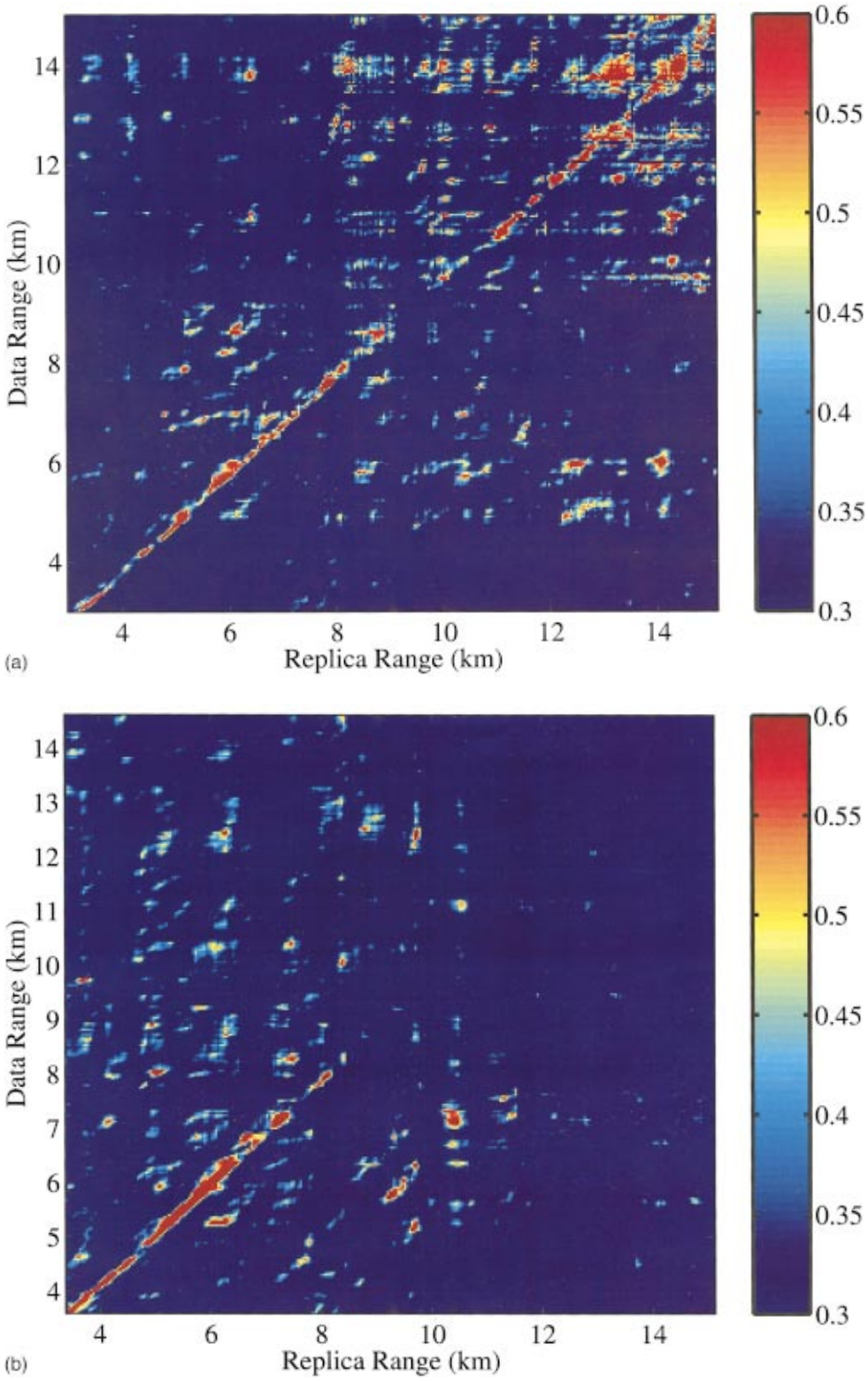

FIG. 6. Degradations of the 160-Hz acoustic database of TESPEX-4 that were apparently caused by environmental variations. Matched-field processing ambiguity surfaces for the source range. Red corresponds to close agreement between the data and the replicas, which were obtained from the acoustic database. Blue corresponds to poor agreement. Strong peaks along the main diagonal correspond to successful localizations. (a) Immediately after the database was obtained, the source was localized out to 15 km. (b) Four days later, the source was localized out to about 8 km.

IV. CONCLUSION

Acoustic data basing is a direct approach for avoiding the problem of environmental uncertainty. Acoustic fields can be measured directly and stored in a small fraction of the time that it takes to obtain the same information by determining the environmental parameters and solving the wave equation. The feasibility of this approach was investigated during the TESPEX experiments. The acoustic database obtained during TESPEX-93 was applied to perform environmental source tracking. The acoustic database obtained dur-

ing TESPEX-94 was used to illustrate the effects of environmental variations.

ACKNOWLEDGMENTS

This work was supported by the Office of Naval Research. We gratefully acknowledge the contributions of Ross Barrett, Ian Cox, Ossy Grotto, Mark Hentschke, Steve Hoefs, Kathy Leak, Rod MacLeod, Ashley Martin, Matthew Steed, Simon Taylor, Terry Trainor, Andrew Tynan, Ian Woon (Australia), Anthony Hoffmann (Canada), George Crook, Siew Wah Mak, Ralph Marrett, Rodney Patterson, John Pope, Chris Price, Dave Rafferty, Zhiyong Zhang (New Zealand), John Bashista, Joe Goldstein, Dick Harriss, Jon Jannucci, Tim Krout, Mike Rupar (United States), and the crews of the FRV Southern Surveyor, HMNZS Manawanui, HMNZS Tui, HMAS Geelong, and P-3C Maritime Patrol Aircraft of 92 WG, Royal Australian Air Force, Edinburgh.

[1] J. F. Lynch, S. D. Rajan, and G. V. Frisk, ''A comparison of broadband and narrow-band modal inversions for bottom properties at a site near Corpus Christi, Texas,'' J. Acoust. Soc. Am. **89**, 648–665 (1991).
[2] M. D. Collins, W. A. Kuperman, and H. Schmidt, ''Nonlinear inversion for ocean-bottom properties,'' J. Acoust. Soc. Am. **92**, 2770–2783 (1992).
[3] S. E. Dosso, ''Estimation of ocean-bottom properties by matched-field inversion of acoustic field data,'' IEEE J. Ocean Eng. **18**, 232–239 (1993).
[4] P. Gerstoft, ''Inversion of acoustic data using a combination of genetic algorithms and the Gauss-Newton approach,'' J. Acoust. Soc. Am. **97**, 2181–2190 (1995).
[5] M. D. Collins and L. Fishman, ''Efficient navigation of parameter landscapes,'' J. Acoust. Soc. Am. **98**, 1637–1644 (1995).
[6] N. R. Chapman, ''Matched-field inversion for geoacoustic model parameters in shallow water,'' IEEE J. Ocean Eng. **21**, 347–354 (1996).
[7] A. Caiti, S. M. Jesus, and Å. Kristensen, ''Geoacoustic seafloor exploration with a towed array in shallow water in the Strait of Sicily,'' IEEE J. Ocean Eng. **21**, 355–366 (1996).
[8] L. Xiao, R. H. Zhang, and F. H. Li, ''A novel nonlinear optimization method of inversion for sea-bottom properties,'' Chin. Phys. Lett. **14**, 853–856 (1997).
[9] R. J. Cederberg and M. D. Collins, ''Application of an improved self-starter to geoacoustic inversion,'' IEEE J. Ocean Eng. **22**, 102–109 (1997).
[10] P. Gerstoft and C. F. Mecklenbräuker, ''Ocean acoustic inversion with estimation of *a posteriori* probability distributions,'' J. Acoust. Soc. Am. **104**, 808–819 (1998).
[11] D. K. Dacol, M. D. Collins, and J. F. Lingevitch, ''An efficient parabolic equation solution based on the method of undetermined coefficients,'' J. Acoust. Soc. Am. **106**, 1727–1731 (1999).
[12] H. P. Bucker, ''Use of calculated sound fields and matched-field detection to locate sound sources in shallow water,'' J. Acoust. Soc. Am. **59**, 368–373 (1976).
[13] A. B. Baggeroer, W. A. Kuperman, and H. Schmidt, ''Matched-field processing: Source localization in correlated noise as an optimum parameter estimation problem,'' J. Acoust. Soc. Am. **83**, 571–587 (1988).
[14] J. M. Ozard, ''Matched-field processing in shallow-water for range, depth, and bearing estimation: Results of experiment and simulation,'' J. Acoust. Soc. Am. **86**, 744–753 (1989).
[15] J. S. Perkins and W. A. Kuperman, ''Environmental signal processing: Three-dimensional matched-field processing with a vertical array,'' J. Acoust. Soc. Am. **87**, 1553–1556 (1990).
[16] L. N. Frazer and P. I. Pecholcs, ''Single-hydrophone localization,'' J. Acoust. Soc. Am. **88**, 995–1002 (1990).
[17] C. A. Zala and J. M. Ozard, ''Matched-field processing in a range-dependent environment,'' J. Acoust. Soc. Am. **88**, 1011–1019 (1990).
[18] H. Schmidt, A. B. Baggeroer, W. A. Kuperman, and E. K. Scheer, ''Environmentally tolerant beamforming for high-resolution matched field processing: Deterministic mismatch,'' J. Acoust. Soc. Am. **88**, 1851–1862 (1990).
[19] M. D. Collins and W. A. Kuperman, ''Focalization: Environmental focusing and source localization,'' J. Acoust. Soc. Am. **90**, 1410–1422 (1991).
[20] E. K. Westwood, ''Broadband matched-field source localization,'' J. Acoust. Soc. Am. **91**, 2777–2789 (1992).
[21] J. A. Fawcett and B. H. Maranda, ''A hybrid target motion analysis/matched-field processing localization method,'' J. Acoust. Soc. Am. **94**, 1363–1371 (1993).
[22] B. H. Maranda and J. A. Fawcett, ''Localization of a maneuvering target using simulated annealing,'' J. Acoust. Soc. Am. **94**, 1376–1384 (1993).
[23] M. D. Collins, L. T. Fialkowski, W. A. Kuperman, and J. S. Perkins, ''Environmental source tracking,'' J. Acoust. Soc. Am. **94**, 3335–3341 (1993).
[24] M. D. Collins, L. T. Fialkowski, W. A. Kuperman, and J. S. Perkins, ''The multivalued Bartlett processor and source tracking,'' J. Acoust. Soc. Am. **97**, 235–241 (1995).
[25] L. T. Fialkowski, M. D. Collins, J. S. Perkins, and W. A. Kuperman, ''Source localization in noisy and uncertain shallow water environments,'' J. Acoust. Soc. Am. **101**, 3539–3545 (1997).
[26] D. R. Del Balzo, C. Feuillade, and M. M. Rowe, ''Effects of water-depth mismatch on matched-field localization in shallow water,'' J. Acoust. Soc. Am. **83**, 2180–2185 (1988).
[27] R. M. Hamson and R. M. Heitmeyer, ''Environmental and system effects on source localization in shallow water by the matched-field processing of a vertical array,'' J. Acoust. Soc. Am. **86**, 1950–1959 (1989).
[28] D. F. Gingras, ''Methods for predicting the sensitivity of matched-field processors to mismatch,'' J. Acoust. Soc. Am. **86**, 1940–1949 (1989).
[29] W. S. Hodgkiss, H. C. Song, W. A. Kuperman, T. Akal, C. Ferla, and D. R. Jackson, ''A long-range and variable focus phase-conjugation experiment in shallow water,'' J. Acoust. Soc. Am. **105**, 1597–1604 (1999).

Predicting acoustic effects of internal waves from the basic climatology of the world ocean

Kimberly J. Noble and Stanley M. Flatté
Physics Department and Institute of Tectonics, University of California at Santa Cruz, Santa Cruz, California 95064

(Received 28 September 1998; revised 23 April 1999; accepted 22 September 1999)

Internal waves of a given strength will produce acoustic effects that vary from water mass to water mass. Presented here is a means of predicting the strength of acoustic fluctuations due to internal waves, given the basic climatology, that is, measurements of depth, temperature, and salinity of an oceanic region. An acoustic fluctuation strength parameter F is defined as the ratio of the fractional potential sound-speed change to the fractional potential-density change. Here F is calculated at three depth levels (275, 550, and 850 m), on a one-degree grid of latitude and longitude, using NODC/OCL's World Ocean Atlas 1994. Representative values of F are presented for 15 upper water masses that range from $F=5$ in the North Pacific to $F=34$ in the North Atlantic, with a typical value for most of the upper waters being $F=15$. Results for two depth levels within 12 intermediate water masses range from $F=7$ in the North Pacific to $F=62$ in the North Atlantic, with a typical value of $F=20$, although there is considerable variation. In general, F exhibits higher values in the Atlantic Basin than in the Indian or Pacific, and has a maximum at 550 m. The main use of F will be the prediction of travel-time fluctuations in acoustic propagation experiments, which will be proportional to the value of F, given a universal strength of internal waves. © *2000 Acoustical Society of America.* [S0001-4966(00)02302-X]

PACS numbers: 43.30.Pc, 43.30.Re [DLB]

INTRODUCTION

Over the past 20 years, internal waves have been established as a dominant contributor to the fluctuations in the travel time of acoustic pulses sent over long distances through the ocean.[1–5] A first-order view of the world-ocean internal-wave field has been provided to us by Garrett and Munk[6,7] (GM) and has been verified by many acoustic experiments such as those referenced above. GM's original view had the internal-wave strength having a universal value represented by a specific energy density E_0. Later, the internal-wave strength was expressed in terms of a displacement variance of about 50 m^2 at a depth at which the buoyancy frequency has a value of 3 cph. More recent analysis of megameter-scale measurements has yielded consistent values more like 25 m^2.[8] In this article, we will return to the original statement of GM in terms of energy density because we want to relate ocean regions that have different buoyancy frequencies.

It is the purpose of this article to survey the world's ocean for variations in the travel-time fluctuations in long-range acoustic propagation, under the assumption of universal internal-wave strength. We will find that there is a significant variation in the expected travel-time fluctuations in different parts of the ocean. We will also find that dividing the world ocean into water masses, following long-standing oceanographic analysis,[9,10] will help to systematize our understanding of internal-wave acoustic effects.

We define an acoustic fluctuation strength parameter F as the ratio of the fractional sound-speed variation to the fractional density variation, both due to internal waves. Since both sound speed and density are dependent on temperature T and salinity S, it is the $T-S$ behavior of ocean waters that determine F. We perform the calculation of F for all geographic locations, and are therefore able to map regions that are acoustically ''sensitive'' to internal waves. We also determine representative values of F for each of the water masses defined by oceanographers.

The parameter F is related to a parameter G defined in the book by Flatté *et al.*[1] in Equation (1.1.9). However, G is a local variable that is not dimensionless, while F takes into account more of the water column, is dimensionless, and is defined independently of vertical gradients.

The significance of F is mainly for acoustic measurements of internal-wave strength. In order to calculate the travel-time fluctuations due to internal waves (as well as other acoustic effects of internal waves) it is necessary to know the specific profiles of sound speed, density (buoyancy frequency), and the strength of internal waves. Even if a universal strength of internal waves is assumed, the internal-wave-induced density fluctuations depend on the profile of buoyancy frequency, and thus the size of travel-time fluctuations will depend on the profiles of both the buoyancy frequency and the parameter F. We present results at three depths in order to provide a partial view of depth dependences. More detailed calculations of internal-wave effects on acoustic propagation can be done with a code named CAFI (calculations of acoustic fluctuations due to internal waves) written by Flatté and Rovner,[11] and available through the internet at URL: http://www.es.ucsc.edu/~smf/research.html.

The profile of sound speed in most of the world's ocean has a negative gradient in the top 1000 m, due to temperature decreasing with depth. As a result, acoustic energy propagates along rays that have upper turning points in the top 1000 m, and the effect of internal waves on these rays is

maximum in those depth regions. For this reason we have concentrated on the behavior of water masses in these upper depth regions (but not the very shallow mixed layers).

I. ACOUSTIC FLUCTUATIONS FROM INTERNAL WAVES

A combination of geometrical-acoustics ray theory and numerical integration of statistical quantities along these rays has provided successful predictions of acoustic fluctuation quantities for ocean-acoustic experiments.[11] One of the most important examples of acoustic fluctuation quantities is the travel-time variance for a pulse. The expression for such a variance in terms of ocean-medium properties is the following:

$$\tau^2 = \frac{1}{C^2}\int_0^R dx\,\langle\mu^2\rangle L_p, \tag{1}$$

where the integral is along a deterministic ray from a source at the origin to a receiver at range R; $\overline{C}$ is a reference sound speed in the deep ocean, typically 1500 $\mathrm{m\,s^{-1}}$; μ is the fractional deviation of the sound speed from its mean value at the point of evaluation; and L_p is the correlation length of internal waves along the deterministic ray at the point of evaluation.

We wish to express $\langle\tau^2\rangle$ more explicitly in terms of the ocean medium. We need to express both $\langle\mu^2\rangle$ and L_p in terms of the buoyancy frequency and the $T-S$ relation for the water being traversed. Because L_p involves integrals over both the frequency and the vertical mode number spectrum of internal waves, it contains information about the dispersion relation of internal waves. In particular, vertical and horizontal wave number components, k_V and k_H, are related to frequency and vertical mode number through the following equations:

$$k_V = \alpha j n(z), \tag{2}$$

$$k_H = \alpha j \sqrt{\omega^2 - \omega_i^2}, \tag{3}$$

where j is the vertical mode number, $n(z)$ is the local buoyancy frequency, ω is the internal-wave frequency, ω_i is the inertial frequency, and α is a constant that depends on the buoyancy-frequency profile,

$$\alpha^{-1} = \frac{1}{\pi}\int_0^D n(z)\,dz, \tag{4}$$

and D is the depth of the ocean.

In terms of these quantities, the internal-wave horizontal correlation length can be expressed as

$$L_p(0) = \frac{N}{\alpha\omega_i}, \tag{5}$$

where N is a dimensionless normalization constant whose value is 0.3.[12]

The expression for $\langle\mu^2\rangle$ in terms of appropriate quantities is more complicated. We will present the relationship between internal-wave energy density and internal-wave displacement variance, and then relate displacement variance to $\langle\mu^2\rangle$. In this way, we will develop an expression for $\langle\tau^2\rangle$ in terms of the buoyancy frequency and water-mass properties.

The energy density of internal waves can be expressed as

$$E_0 = -\overline{\rho}[n(z)]^2\langle\zeta^2\rangle, \tag{6}$$

where ζ is the displacement of the internal-wave field. Thus a constant internal-wave energy requires the rms displacement to vary inversely as the buoyancy frequency. This can be confusing, because the Wentzel–Kramers–Brillouin–Jeffreys (WKBJ) solution of a particular displacement eigenfunction scales inversely as the square root of the buoyancy frequency. One cannot use an individual eigenfunction to draw conclusions about scaling of the internal-wave field.

Once the scaling of displacement with buoyancy frequency is established, we can relate $\langle\mu^2\rangle$ to $\langle\zeta^2\rangle$.

First, we consider the fractional changes in sound speed caused by internal waves:

$$\left(\frac{\delta C}{C}\right) = \left(\frac{1}{\overline{C}}\frac{\Delta C_\theta}{\Delta z}\right)\zeta. \tag{7}$$

In order to evaluate this quantity under the constraint of constant internal-wave strength, we need to express it in terms of water-mass quantities and the buoyancy frequency. In other words, we want to avoid any gradients with depth other than the buoyancy frequency. We do this by transferring the gradient in potential sound speed to a gradient in potential density:

$$\left(\frac{\delta C}{C}\right) = \left(-\frac{\overline{\rho}}{\overline{C}}\frac{\Delta C_\theta}{\Delta\rho_\theta}\right)\left(\frac{1}{\overline{\rho}}\frac{\Delta\rho_\theta}{\Delta z}\right)\zeta. \tag{8}$$

However, the gradient in potential density can be expressed in terms of the buoyancy frequency:

$$\left(\frac{\delta C}{C}\right) = \left(-\frac{\overline{\rho}}{\overline{C}}\frac{\Delta C_\theta}{\Delta\rho_\theta}\right)\left(\frac{n^2(z)}{g}\right)\zeta. \tag{9}$$

We note the important fact that the first factor in this expression is a water-mass property and not dependent on any gradient that has substantial variability over the world's oceans. We designate this factor as a new parameter F, whose value will enter into the evaluation of acoustic fluctuation quantities:

$$F \equiv -\frac{\overline{\rho}}{\overline{C}}\frac{\Delta C_\theta}{\Delta\rho_\theta}. \tag{10}$$

The final definition of F does not involve gradients, but it does involve the evaluation of density and sound speed at two different points within a water mass. Those two different points might be at different depths (the case we will use) or they might be at different geographical locations; as long as they are within the water mass they can be used.

Squaring Eq. (9) and taking its expectation value, we find the relation we seek between $\langle\mu^2\rangle$ and $\langle\zeta^2\rangle$,

$$\langle\mu^2\rangle = F^2\frac{n^4(z)}{g^2}\langle\zeta^2\rangle, \tag{11}$$

and, returning to the internal-wave energy density, we find

$$\langle \mu^2 \rangle = F^2 \frac{n^2(z)}{\overline{\rho} \overline{g}^2} E_0 . \tag{12}$$

We now have the results with which to express the local contribution to $\langle \tau^2 \rangle$ at position x along the deterministic ray. Although both $\langle \mu^2 \rangle$ and L_p are functions of the details of the ray, it is known that for long-range propagation in the deep ocean, the main contributions to $\langle \tau^2 \rangle$ come from the upper turning points of the ray, and thus depend on $\langle \mu^2 \rangle$ and L_p at one particular depth, and near where the ray is horizontal. Therefore we can write this differential contribution to $\langle \tau^2 \rangle$ as

$$\frac{d}{dx} \langle \tau^2 \rangle = \left(\frac{N}{\pi \overline{\rho} \overline{C}^2 \overline{g}^2} \right) \left(\frac{E_0 F^2}{\omega_i} \right) \left([n(z)]^2 \int_0^D n(z)\, dz \right). \tag{13}$$

The first factor on the right is a constant independent of geographic position. The second factor is a function of geographic position because the inertial frequency depends on latitude, because the internal-wave energy E_0 might not be universal, and more interestingly because F is a function of geographic position. The third factor depends only on the buoyancy frequency. Munk[13] suggested a universal function for the buoyancy frequency as a function of depth, at least in the deep ocean. If this ''canonical profile'' was valid, the last factor would not vary with geographical position, and the only term whose geographical variability is not easily understood would be F^2. Taking a canonical buoyancy profile and example values of $E_0 = 4\ \mathrm{Jm}^{-3}$ and $F = 25$, we find a τ^2 contribution from a 10-km path length to be about 1 ms^2.

Again note that $\langle \tau^2 \rangle$ does not depend in an explicit way on the details of the sound-speed profile. The sound-speed profile enters mainly in controlling the path of the deterministic geometrical-optics ray through the ocean. However, the exact shape of this path does not strongly affect the value of $\langle \tau^2 \rangle$.[11] In order to make detailed calculations, rather than try to make a systematic overview such as we are doing in this paper, it is helpful to have a complete compendium of sound-speed profiles. This is available in an atlas compiled by Worcester and Ma.[14]

II. DATABASE DETAILS

For our calculations of F, we have used the *World Ocean Atlas 1994* (WOA94),[15] which was initiated by Levitus and Gelfeld,[16] and from which we have used the temperature and salinity means by month and within bins of one degree in latitude and longitude. Two technical papers[17,18] describe the objective analysis techniques used to check the quality of the data. There is a modification of this database called ''Replacement CTD data'' that has corrected some data in the original. We have checked that these modifications do not affect our analysis, mainly because we did not use raw data and we have restricted ourselves to depths in the upper ocean.

For each of our three chosen depths, we need two nearby depths from which to obtain differences in sound speed and density. Thus, we extracted the temperature and salinity data for six standard depths as shown in Table I.

TABLE I. WOA94 standard depths (from WOA94 documentation).

Standard level	Depth (m)
11	250
12	300
14	500
15	600
17	800
18	900

Although we carried out the calculations for every month, we present details just for the month of June, as the results show the same general patterns for every month. This is not surprising because the $T-S$ relation below the top few hundred meters is insensitive to season. We used the formulas of Chen and Millero[19] for calculating density and sound speed from temperature, salinity, and pressure. We inverted Fofonoff's formulas[20] for calculating depth from pressure and latitude.

III. RESULTS

This section describes our results for F and some associated quantities. The F results for 275, 550, and 850 m are given in Fig. 1.

We first discuss the results at 275-m depth. For temperate and equatorial latitudes, F lies in the range of 10–30. Regions of high latitude, $\geqslant$50 degrees, on the other hand, exhibit F values $\leqslant$10. There are some regions in which F goes below zero; later we will show that negative values for F do not imply a problem with unstable stratification. They come rather from the fact that the sound speed is quite a different function of temperature and salinity than is the density, so that a reverse gradient of sound speed is possible in the presence of a stable density gradient.

Continuing at 275-m depth, we can contrast the Pacific and Indian Oceans between plus and minus 40 degrees latitude, where F is 10–20, with most of the Atlantic, where F is 20–30. Thus experiments in the shallow Atlantic will tend to encounter larger internal-wave effects, other parameters being equal. Furthermore, the very northern Pacific, near Alaska, has quite small values of F.

The Circumpolar Ocean shows low values of F interspersed with a few regions with high values of F. We have investigated these regions of high horizontal gradient, and they are not associated with very sparse data or some other artifact of the database.

Descending to the 550-m depth, some significant changes are noted. F in the temperate and equatorial latitudes has generally increased from 10–20 to 20–50. The Southern Atlantic Ocean has particularly large F values of about 30–40, or greater. A distinct band between ≈ -15 degrees and ≈ -45 degrees latitude shows values of F that vary between 30 and 60; it is particularly well developed in the narrower Indian and Atlantic Ocean Basins, although it is present in the Pacific. The Circumpolar Ocean again shows large areas of low F containing smaller regions of high F, though the

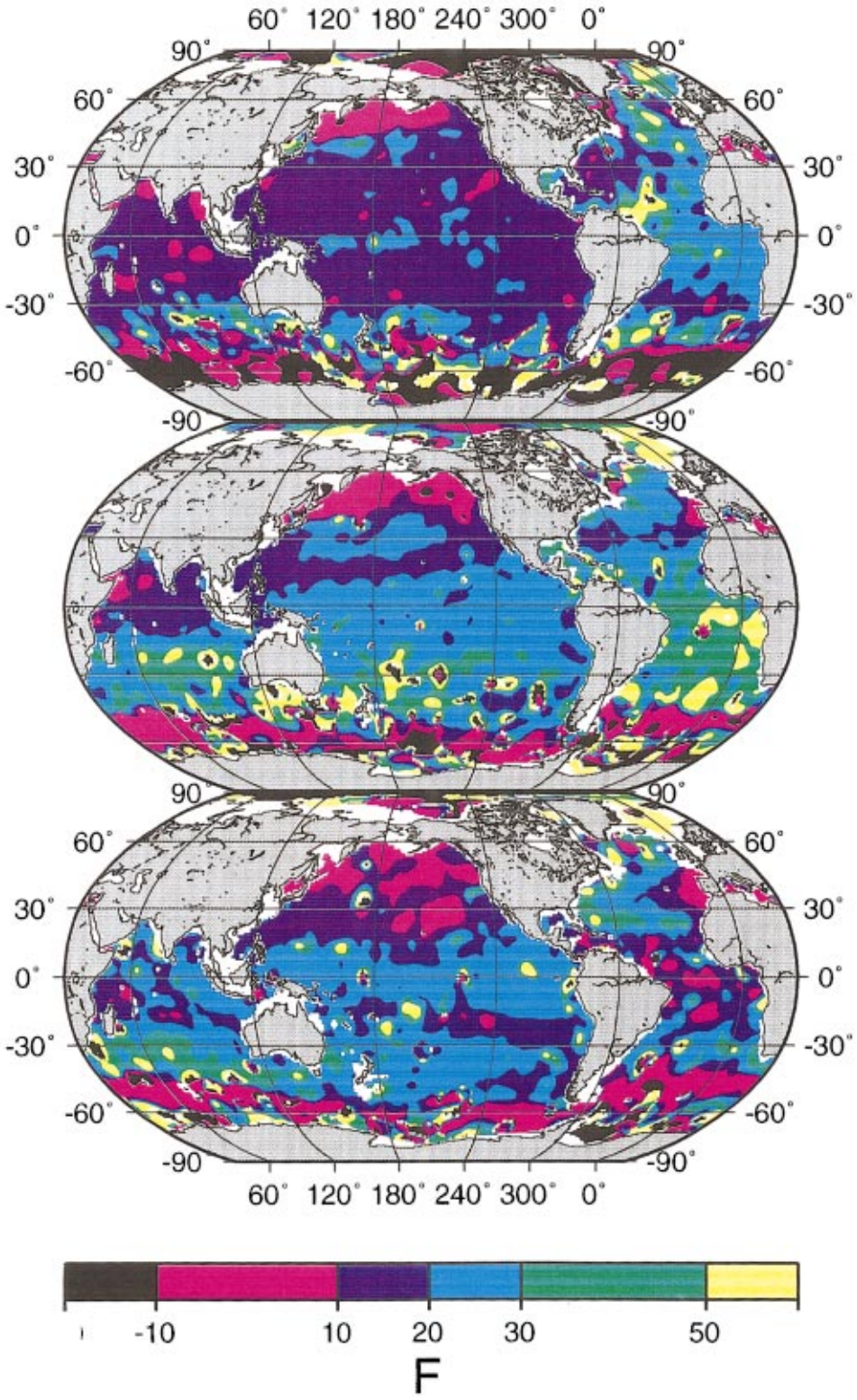

FIG. 1. Contour plots of F: The top, middle, and bottom plots are for ocean depths of 275, 550, and 850 m, respectively.

values of F are generally higher than at 275-m depth, and F is varying in a smoother fashion. The Arctic Ocean shows more variability than it did at 275 m.

The F values at 850-m depth have substantially decreased in the Southern Atlantic, where F lies mostly in the range 0–20. The Western North Atlantic, on the other hand, shows a definite increase in F, to about 30–40. The regions of high F that were apparent in the Southern Pacific have disappeared in favor of smooth areas with F between 20 and 30. Changes in the Indian and Circumpolar Oceans are relatively mild. The Arctic Ocean has an overall decrease in F value ($\leqslant -10$), although there are widespread, discontinuously changing regions of high F. Throughout each of the depths studied, F has consistently been quite high ($\geqslant 50$) in the area of the Greenland and Norwegian Seas.

We remind the reader here that an increase in F from one ocean region to another of a factor of 2 means an increase in the travel-time fluctuation due to internal waves of

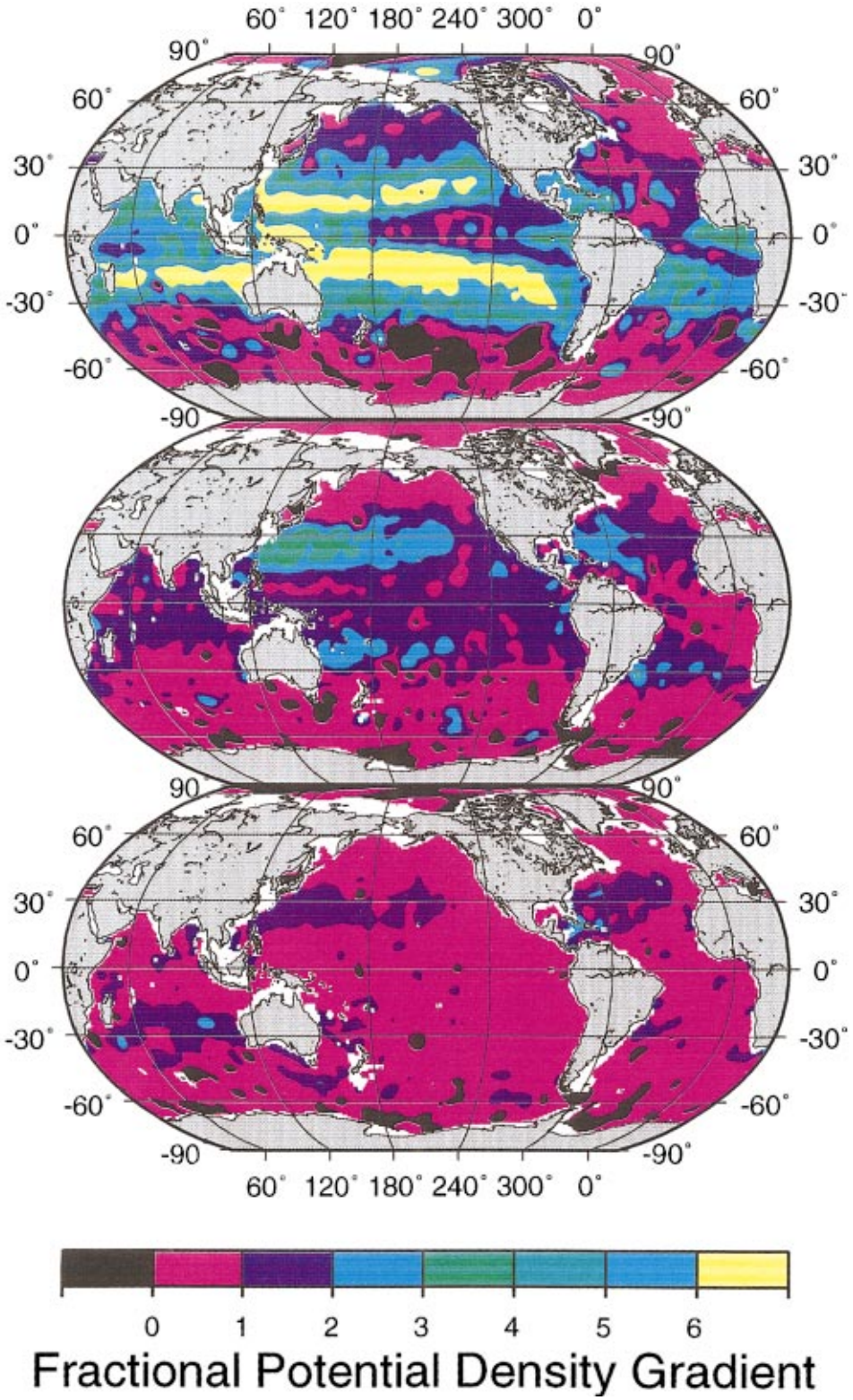

FIG. 2. Contour plots of fractional potential gradient of density: The top, middle, and bottom plots are for ocean depths of 275, 550, and 850 m, respectively. The units are $10^{-6}\,\mathrm{m}^{-1}$.

a factor of 2, even when the internal-wave energy level has the same universal value in the two ocean regions.

Since $\langle \tau^2 \rangle$ depends on the buoyancy frequency as well as F, even if E_0 is constant, it should be relevant to plot the buoyancy frequency as a function of geographic location and depth. Figure 2 shows the fractional potential gradient of density for our three depths. This plot shows very distinct maxima near the tropics, particularly in the Pacific Ocean. The fractional potential gradient plots of density for the 550- and 850-m depths are less dramatic. There are relatively few areas of negative (unstable) gradient, showing that most of the structure in F in the polar regions comes from the sound-speed behavior, not from unstable density gradients.

We have attempted to avoid a dependence on the entire sound-speed profile as a function of geographical location by showing three representative depths. We remind the reader that acoustic rays receive most of their internal-wave effects from the shallow depths where the rays have their upper

TABLE II. Characteristics of the upper water masses (0–500 m) (from Ref. 10).

Atlantic	Indian	Pacific
At. Subarc. Up. (ASUW)	Bengal Bay (BBW)	Pa. Subarc. Up. (PSUW)
0.0–4.0 °C; 34.0–35.0	25.0–29.0 °C; 28.0–35.0	3.0–15.0 °C; 32.6–33.6
W. N. At. Cen. (WNACW)	Arab. Sea (ASW)	W. N. Pa. Cen. (WNPCW)
7.0–20.0 °C; 35.0–36.7	24.0–30.0 °C; 35.5–36.8	10.0–22.0 °C; 34.2–35.2
E. N. At. Cen. (ENACW)	ln. Eq. (IEW)	E. N. Pac. Cen, (ENPCW)
8.0–18.0 °C; 35.2–36.7	8.0–23.0 °C; 34.6–35.0	12.0–20.0 °C; 34.2–35.0
S. At. Cen. (SACW)	Indo. Up. (IUW)	E. N. Pa. Tr. (ENPTW)
5.0–18.0 °C; 34.3–35.8	8.0–23.0 °C; 34.4–35.0	11.0–20.0 °C; 33.8–34.3
	S. In. Cen. (SICW)	Pa. Eq. (PEW)
	8.0–25.0 °C; 34.6–35.8	7.0–23.0 °C; 34.5–36.0
		W. S. Pa. Cen. (WSPCW)
Circumpolar		6.0–22.0 °C; 34.5–35.8
Subant. Surf. (SASW)		E. S. Pa. Cen. (ESPCW)
3.2–15.0 °C; 34.0–35.5		8.0–24.0 °C; 34.4–36.4
Antarctic Surf. (AASW)		E. S. Pa. Tr. (ESPTW)
−1.0–1.0 °C; 34.0–34.6		14.0–20.0 °C; 34.6–35.2

turning points. Thus the information needed is mainly provided by the upper two depths of Figs. 1 and 2.

IV. *F* VALUES FOR SPECIFIC WATER MASSES

In 1986, W. J. Emery and J. Meincke[10] updated existing maps and tables of water masses which had first been compiled and published in 1942 by Sverdrup *et al.*,[9] and had remained largely unchanged since then. Emery and Meincke list the names and (temperature and salinity) characteristics of water masses for three depth regions: upper water masses (0–500 m), intermediate water masses (500–1500 m), and deep water masses (>1500 m). In addition, they give distribution maps which include the location of source waters, and $T-S$ diagrams for the major water masses in each ocean basin. Since we considered depths in the upper 1000 m only, we will focus on the upper and intermediate water masses.

Table II summarizes Emery and Meincke's results for the upper water masses. Figure 3 shows the geographic locations of the water masses and locations of their sources.[10]

Table III lists the names and temperature and salinity characteristics that Emery and Meincke associated with the intermediate waters, while Fig. 4 shows their geographic locations as well as the locations of their sources.[10]

Figure 5 gives the $T-S$ curves for the water masses of the Atlantic, Pacific, and Indian Oceans. Note that these $T-S$ curves include the deep water masses which we have neglected in our discussion. Table IV provides a key to the acronyms for the deep waters.[10]

We identified the latitudes and longitudes of the water masses defined by Emery and Meincke[10] by comparing the temperature and salinity characteristics identified for each water mass (see Tables II and III) with our own potential temperature and salinity plots.

Our selections of the latitude and longitude ranges for the upper waters at 275 m are given in Table V, and the selections for the intermediate waters at 550 and 850 m are

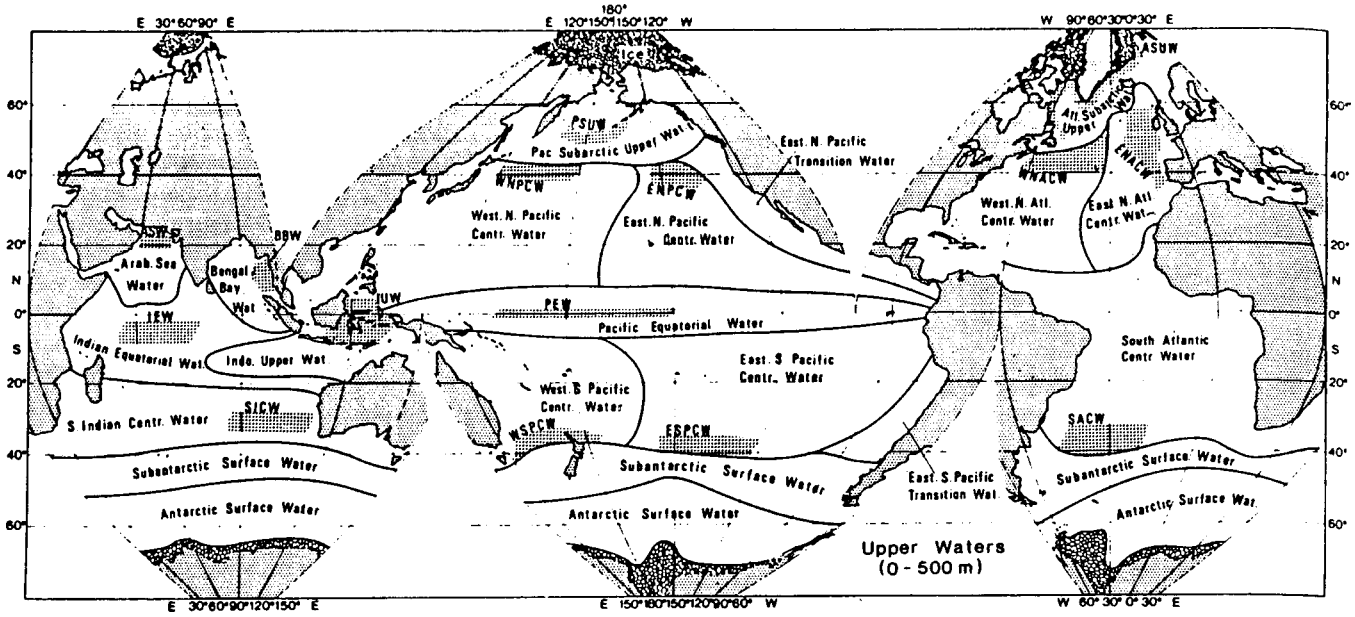

FIG. 3. Global distribution of upper waters (0–500 m). Water masses are labeled in abbreviated form with their boundaries indicated by solid lines. Formation regions for these water masses are marked by cross hatching and labeled with the corresponding acronym title (from Ref. 10).

TABLE III. Characteristics of the intermediate water masses (500–1500 m) (from Ref. 10).

Atlantic	Indian	Pacific
W. At. Subarc. Int. (WASIW)	Antarctic Int. (AAIW)	Pa. Subarc. Int. (PSIW)
3.0–9.0 °C; 34.0–35.1	2.0–10.0 °C; 33.8–34.8	5.0–12.0 °C; 33.8–34.3
E. At. Subarc. Int. (EASIW)	Indonesian Int. (IIW)	California Int. (CIW)
3.0–9.0 °C; 34.4–35.3	3.5–5.5 °C; 34.6–34.7	10.0–12.0 °C; 33.9–34.4
Antarctic Int. (AAIW)	Red Sea/Persian	E. S. Pa. Int. (ESPIW)
2.0–6.0 °C; 33.8–34.8	Gulf Int. (RSPGIW)	10.0–12.0 °C; 34.0–34.4
Mediterranean (MW)	5.0–14.0 °C; 34.8–35.4	Antarctic Int. (AAIW)
2.6–11.0 °C; 35.0–36.2		2.0–10.0 °C; 33.8–34.5
Arctic Int. (AIW)		
−1.5–3.0 °C; 34.7–34.9		

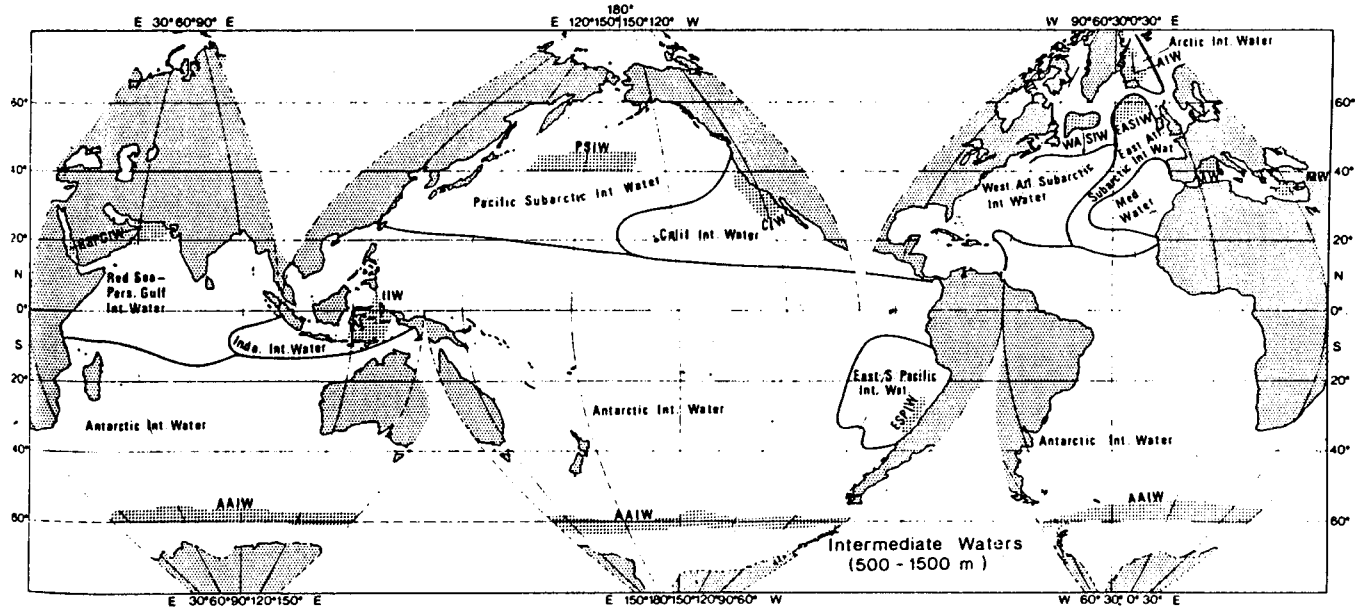

FIG. 4. Global distribution of intermediate water (500–1500 m). Lines, labels, and hatching follow the same format as described for the upper waters (from Ref. 10).

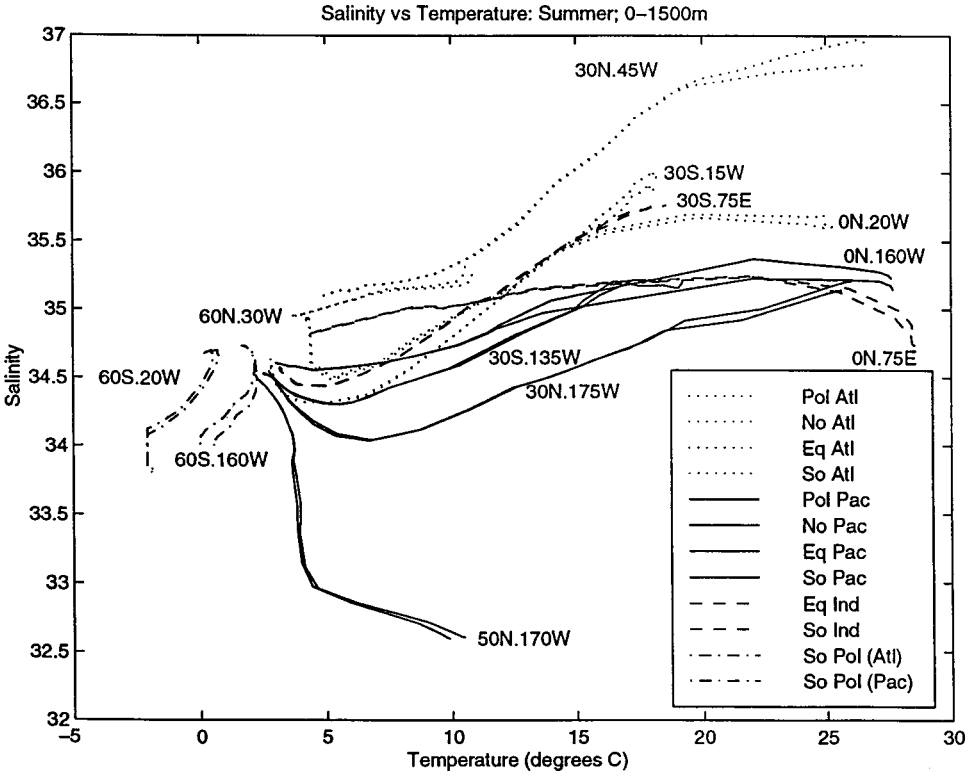

FIG. 5. The $T-S$ curves for the world's water masses. Note that the Pacific, Atlantic, Indian, and Circumpolar Oceans are represented by solid, dotted, dashed, and dash-dot lines, respectively.

TABLE IV. A Key to Emery and Meincke's acronyms for deep water masses.

Atlantic	Indian	Pacific
N. At. Deep (NADW) Antarctic Bottom (AABW) Arctic Bottom (ABW)	Circ. Deep (CDW)	Circ. Deep (CDW)

TABLE V. Latitude/longitude limits of the upper water masses (275 m).

Atlantic	Indian	Pacific
(ASUW) 45–80 N/0–20 and 305–360 E (WNACW) 15–40 N/275–320 E (ENACW) 25–60 N/330–355 E (SACW) 35–15 S/320–345 E	(IEW) 20 S–0/45–80 E (IUW) 20–5 S/80–125 E (SICW) 30–20 S/30–115 E	(PSUW) 45–60 N/145–215 E (WNPCW) 10–35 N/125–190 E (ENPCW) 10–35 N/190–220 E (ENPTW) 10–35 N/220–250 E (PEW) 5.S–10 N/150–240 E (WSPCW) 35–10 S/150–215 E (ESPCW) 35–5 S/215–250 E (ESPTW) 40–5 S/250–290 E

TABLE VI. Latitude/longitude limits of the intermediate water masses (550 and 850 m).

Atlantic	Indian	Pacific
(WASIW) 25–40 N/275–320 E (EASIW) 35–60 N/320–345 E (AAIW) 45 S–20 N/305–360 E (MW) 25–45 N/320–355 E (AIW) 65–85 N/0–20 and 350–360 E	(AAIW) 45–15 S/40–115 E (IIW) 15–5 S/80–125 E (RSPGIW) 15 S–20 N/45–90 E	(PSIW) 20–35 N/125–215 E (CIW) 10–35 N/200–245 E (ESPIW) 40 S–0/260–290 E (AAIW) 45–15 S/155–230 E

TABLE VII. Latitude/longitude of the characteristic point for the upper water masses (275 m).

Atlantic	Indian	Pacific
(ASUW) 45 N/0 E (WNACW) 25 N/295 E (ENACW) 25 N/335 E (SACW) 25 S/330 E	(IEW) 1 S/45 E (IUW) 7 S/85 E (SICW) 23 S/45 E	(PSUW) 50 N/180 E (WNPCW) 20 N/130 E (ENPCW) 26 N/200 E (ENPTW) 31 N/225 E (PEW) 5 N/200 E (WSPCW) 17 S/160 E (ESPCW) 20 S/225 E (ESPTW) 20 S/250 E

TABLE VIII. Latitude/longitude of the characteristic point for the intermediate water masses (550 and 850 m).

Atlantic	Indian	Pacific
(WASIW) 550 m: 25 N/275 E 850 m: 30 N/295 E (EASIW) 550 m: 45 N/330 E 850 m: 40 N/320 E (AAIW) 550 m: 20 S/345 E 850 m: 20 S/345 E (MW) 550 m: 30 N/325 E 850 m: 30 N/320 E (AIW) 550 m: 70 N/10 E 850 m: 65 N/0 E	(AAIW) 550 m: 29 S/55 E 850 m: 20 S/75 E (IIW) 550 m: 13 S/80 E 850 m: 15 S/100 E (RSPGIW) 550 m: 0 N/55 E 850 m: 10 S/45 E	(PSIW) 550 m: 30 N/160 E 850 m: 30 N/160 E (CIW) 550 m: 20 N/230 E 850 m: 20 N/240 E (ESPIW) 550 m: 25 S/260 E 850 m: 25 S/260 E (AAIW) 550 m: 20 S/155 E 850 m: 30 S/220 E

TABLE IX. Average values of F_0 and θ_0 for the upper water masses (275 m).

Atlantic	Indian	Pacific
(ASUW) $F_0=34/\theta_0=4$ °C (WNACW) $F_0=12/\theta_0=18$ °C (ENACW) $F_0=28/\theta_0=13$ °C (SACW) $F_0=15/\theta_0=15$ °C	(IEW) $F_0=16/\theta_0=12$ °C (IUW) $F_0=8/\theta_0=12$ °C (SICW) $F_0=9/\theta_0=17$ °C	(PSUW) $F_0=5/\theta_0=4$ °C (WNPCW) $F_0=11/\theta_0=18$ °C (ENPCW) $F_0=19/\theta_0=14$ °C (ENPTW) $F_0=14/\theta_0=10$ °C (PEW) $F_0=18/\theta_0=10$ °C (WSPCW) $F_0=12/\theta_0=17$ °C (ESPCW) $F_0=17/\theta_0=12$ °C (ESPTW) $F_0=16/\theta_0=11$ °C

TABLE X. Average values of F_0/θ_0 for the intermediate water masses (550 and 850 m).

Atlantic	Indian	Pacific
(WASIW) 550 m: 20/15 °C 850 m: 36/10 °C (EASIW) 550 m: 28/9 °C 850 m: 20/8 °C (AAIW) 550 m: 34/6 °C 850 m: 12/4 °C (MW) 550 m: 14/11 °C 850 m: 11/10 °C (AIW) 550 m: 62/1 °C 850 m: 35/0 °C	(AAIW) 550 m: 33/11 °C 850 m: 17/6 °C (IIW) 550 m: 21/8 °C 850 m: 22/6 °C (RSPGIW) 550 m: 14/10 °C 850 m: 13/7 °C	(PSIW) 550 m: 21/7 °C 850 m: 7/4 °C (CIW) 550 m: 14/6 °C 850 m: 9/5 °C (ESPIW) 550 m: 24/6 °C 850 m: 12/5 °C (AAIW) 550 m: 33/8 °C 850 m: 24/6 °C

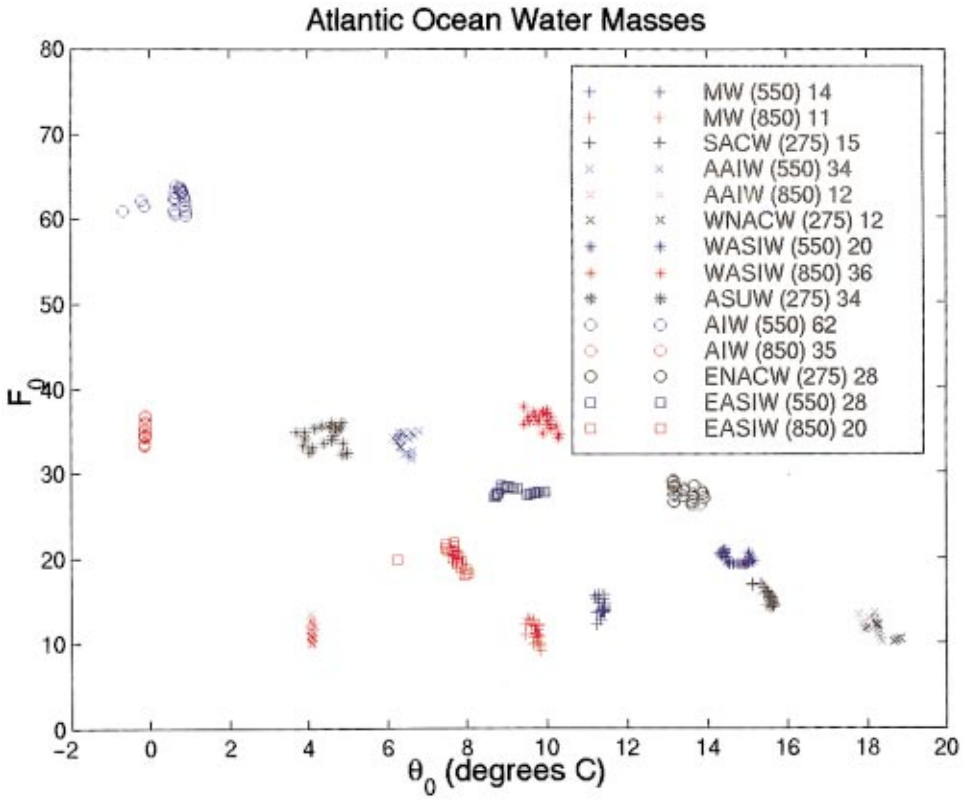

FIG. 6. Scatter plot of characteristic values of F and potential temperature for water masses of the Atlantic Ocean. Symbols for depths of 275, 550, and 850 m are black, blue, and red, respectively.

given in Table VI. (The Bengal Bay and Arabian Sea water masses are at depths shallower than our smallest depth of 275 m.)

We then extracted the subset of data enclosed by the chosen rectangles from the full data set. Scatter plots of F versus potential temperature for each subset were generated, and, on the basis of these plots, *representative* values of F and θ were identified. We call these representative values F_0 and θ_0, respectively.

The Circumpolar upper water masses revealed such a large variation in the value of F that we omitted them from our analysis of water masses.

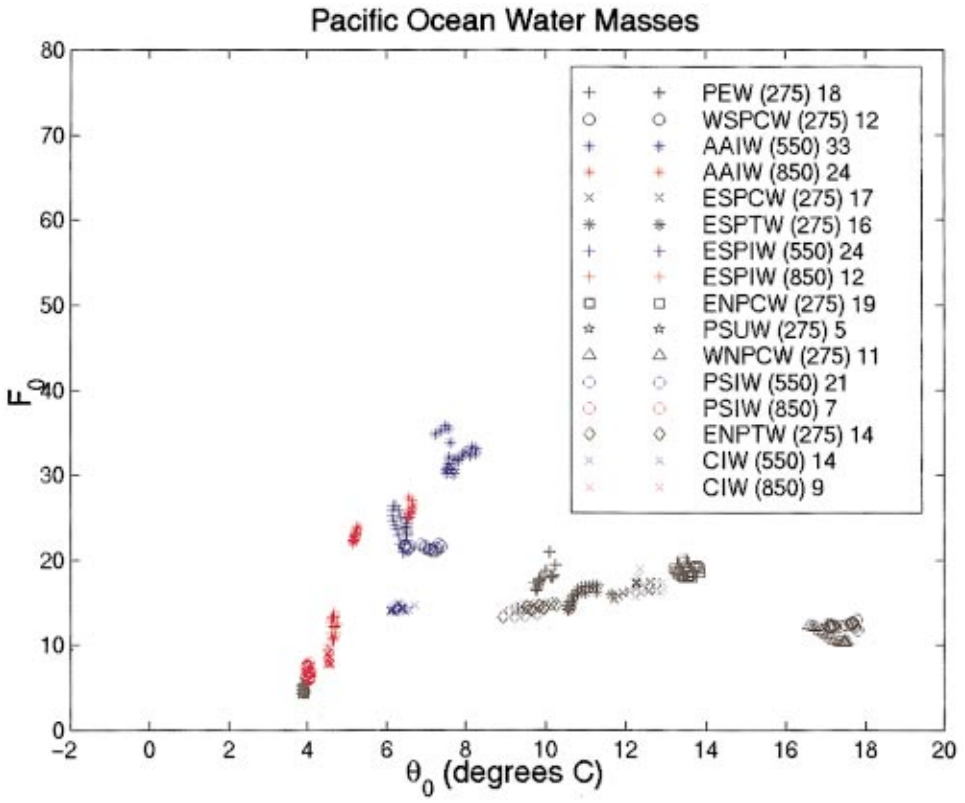

FIG. 7. Scatter plot of characteristic values of F and potential temperature for water masses of the Pacific Ocean. Symbols for depths of 275, 550, and 850 m are black, blue, and red, respectively.

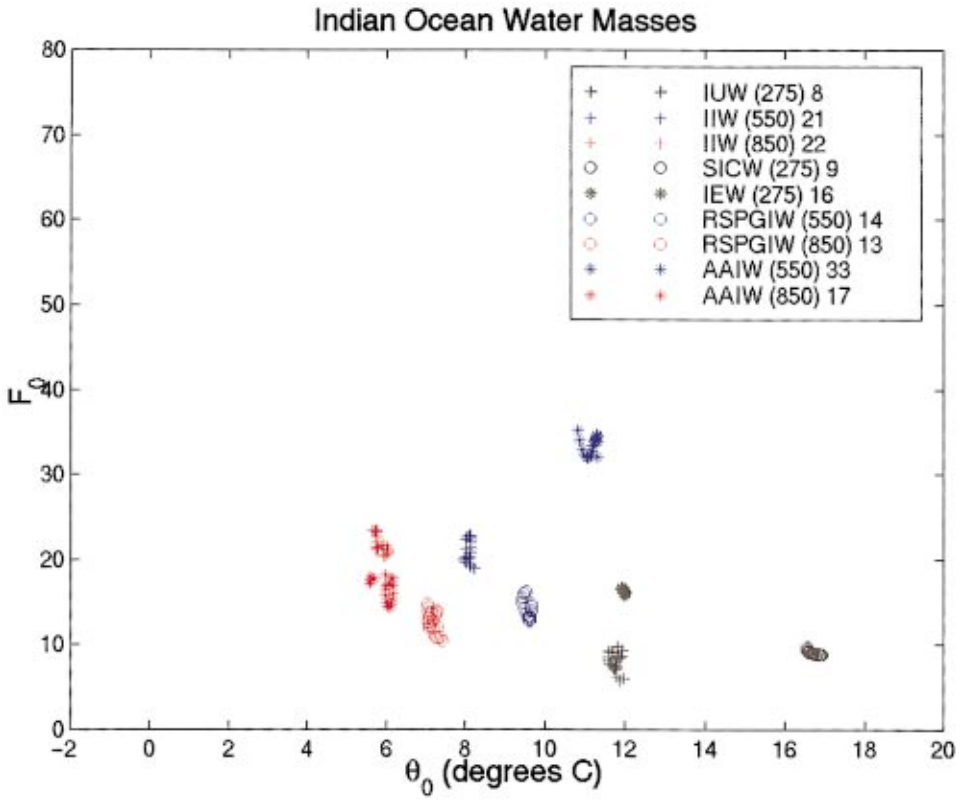

FIG. 8. Scatter plot of characteristic values of F and potential temperature for water masses of the Indian Ocean. Symbols for depths of 275, 550, and 850 m are black, blue, and red, respectively.

With F_0 and θ_0 identified from the scatter plots, we again examined the contour plots of F, plus the contour plots of θ. A point enclosed within each latitude/longitude rectangle exhibiting the identified representative values of F_0 and θ_0 for that water mass was selected, and we further required that this point be surrounded by a neighborhood of other points with similar F and θ characteristics. The latitude and longitude of each of these selected points for the 275-m depth are given in Table VII.

Then for each water mass, we began at the selected characteristic location identified in Table VII for upper waters and Table VIII for intermediate waters, and chose data for water-mass membership by requiring F and θ to be within a small interval of the reference location values.

Table IX summarizes the average values of F_0 and θ_0 for the clusters representing the upper water masses, and Table X summarizes the same quantities for the intermediate water masses.

Comparing the source locations identified by Emery and Meincke[10] with the same geographic locations on our color contours, we find that F often attains a large negative value at the location of a water mass source, particularly at high latitudes ($\geqslant$40 degrees), which is where most of the upper waters are formed. We did not include these regions in our plots of water-mass results for F_0.

Color scatter plots of F_0 vs θ_0 for all of the representative clusters are found in Figs. 6–8. These figures will be valuable for experimental work: either for deciding where to carry out an experiment or for predicting the acoustic fluctuations that will be seen in an experiment. By connection to a particular water mass that extends over a substantial geographical region, a prediction will be that much more robust than would be the case of judging from a map of F at a particular depth.

V. CONCLUSIONS

A dimensionless factor F has been defined that provides a measure of acoustic travel-time fluctuations in the presence of a universal internal-wave field. The systematics of F have been presented for the world ocean, showing that F varies by a considerable factor among ocean basins. The values of F for different water masses have also been presented. In high-latitude water-mass source regions, F tends to become negative. Within temperate-latitude locations, the travel-time fluctuation observed in an experiment could vary by as much as a factor of 3 depending on the particular ocean basin chosen.

ACKNOWLEDGMENTS

This work was presented in partial satisfaction of the requirements of a Master's Degree in Physics at the University of California at Santa Cruz by one of us (KJN).[21] More details on a number of aspects of this study may be found in that thesis. This research was supported in part by the U.S. Office of Naval Research Ocean Acoustics Program. We are grateful for a grant from the W. M. Keck Foundation. This is Contribution No. 396 of the Institute of Tectonics.

[1] S. M. Flatté, R. Dashen, W. H. Munk, K. W. Watson, and F. Zachariasen, *Sound Transmission Through a Fluctuating Occan* (Cambridge U.P., Cambridge, 1979).
[2] S. Flatté, ''Wave propagation through random media: Contributions from ocean acoustics,'' Proc. IEEE **71**, 1267–1294 (1983).
[3] T. Duda, S. M. Flatté, J. Colosi, B. Cornuelle, J. Hildebrand, W.

Hodgkiss, Jr., P. Worcester, B. Howe, J. Mercer, and R. Spindel, ''Measured wavefront fluctuations in 1000-km pulse propagation in the Pacific Occan,'' J. Acoust. Soc. Am. **92**, 939–955 (1992).
[4] J. Colosi, S. M. Flatté, and C. Bracher, ''Internal-wave effects on 1000-km oceanic acoustic pulse propagation: Simulation and comparison with experiment,'' J. Acoust. Soc. Am. **96**, 452–468 (1994).
[5] J. Colosi *et al.*, ''Comparisons of measured and predicted acoustic fluctuations for a 3250-km propagation experiment in the eastern North Pacific Ocean,'' J. Acoust. Soc. Am. **105**, 3202–3218 (1999).
[6] C. Garrett and W. H. Munk, ''Spacetime scales of internal waves: A progress report,'' J. Geophys. Res. **80**, 291–297 (1975).
[7] W. Munk and C. Garrett, ''Internal waves in the ocean,'' Annu. Rev. Fluid Mech. **11**, 339–369 (1979).
[8] S. M. Flatté, ''Megameter-scale oceanography of internal waves: Past, present, and future,'' J. Acoust. Soc. Am. **102**, 3080 (1997).
[9] H. Sverdrup, M. Johnson, and R. Fleming, *The Oceans: Their Physics, Chemistry and General Biology* (Prentice-Hall, Englewood Cliffs, NJ, 1942).
[10] W. Emery and J. Meincke, ''Global Water Masses: Summary and Review,'' Oceanologica Acta: European Journal of Oceanology **9**, 383–391 (1986).
[11] S. M. Flatté and G. Rovner, ''Calculations of internal-wave-induced fluctuations in ocean-acoustic propagation,'' submitted to J. Acoust. Soc. Am.
[12] S. Flatté and R. Esswein, ''Calculation of the phase-structure function density from oceanic internal waves,'' J. Acoust. Soc. Am. **70**, 1387–1396 (1981).
[13] W. H. Munk, ''Sound channel in an exponentially stratified ocean, with application to SOFAR,'' J. Acoust. Soc. Am. **55**, 220–226 (1974).
[14] P. Worcester and B. Ma, ''Ocean Accoustic Propagation Atlas,'' Technical report, Scripps Institution of Oceanography Reference Series 95-36, University of California at San Diego, La Jolla, CA (1995).
[15] *World Ocean Atlas 1994 Exabyte Tape Data Set Documentation, Informal Report No. 14* (Ocean Climate Laboratory at the National Oceanographic Data Center, Washington, DC, 1994).
[16] S. Levitus and R. Gelfeld, *NODC Inventory of Physical Oceanographic Profiles: Global Distributions by Year for All Countries* (U.S. Department of Commerce, National Oceanic and Atmospheric Administration, National Environmental Satellite, Data, and Information Service, Washington, DC, 1992).
[17] T. Boyer and S. Levitus, *Quality Control and Processing of Historical Temperature, Salinity and Oxygen Data* (National Oceanographic Data Center, Ocean Climate Laboratory, Washington, DC, 1994).
[18] M. Conkright, T. Boyer, and S. Levitus, *Quality Control and Processing of Historical Nutrient Data* (National Oceanographic Data Center, Ocean Climate Laboratory, Washington, DC, 1994).
[19] C. Chen and F. Millero, ''Precise equation of state of seawater for oceanic ranges of salinity, temperature, and pressure,'' Deep-Sea Res. **24**, 365–369 (1977).
[20] N. Fofonoff and J. R. C. Millard, ''Algorithms for computation of fundamental properties of seawater,'' UNESCO technical papers in Marine Science (1983).
[21] K. J. Noble, Master's thesis, University of California at Santa Cruz, 1998.

Long time-base observations of surf noise

Grant B. Deane
Marine Physical Laboratory, Scripps Institution of Oceanography, UCSD, La Jolla, California 92093-0238

(Received 25 June 1999; revised 7 October 1999; accepted 27 October 1999)

A year of surf noise observations in the very near shore region of La Jolla Shores beach are presented. Ambient sound levels and surface wave height were recorded for 9 min every hour from July 1997 through June 1998 at a monitoring station located 360 m seaward of the beach in 8-m deep water. Sound segments that were dominated by the noise from breaking surf formed the basis of a correlation analysis between surf noise level and wave height, wave period, wind speed, and mean water depth. The analysis shows that surf noise is primarily determined by wave height, and scales approximately with the wave height squared. The surface wave energy flux onto the beach also scales with wave height squared, leading to the conclusion that the conversion of the mechanical energy of the surface wave field into noise energy is approximately constant. In fact, the ratio of noise energy to surface wave energy flux varies by up to a factor of 3 over the range of energy fluxes considered (100–3000 W per m).
[S0001-4966(00)01602-7]

PACS numbers: 43.30.Nb, 43.30.Pc [DLB]

INTRODUCTION

Although quite a lot is known about ambient noise in the open ocean,[1] considerably less is known about surf noise. Bardyshev *et al.*,[2] Zakharov and Kirshov,[3] and Wilson *et al.*[4] published some of the first surf noise measurements in the early 70's and 80's. More recent studies are those of Wilson *et al.*[5] and Fabre and Wilson[6] who presented source level densities for surf noise at Monterey Bay, CA, and Duck, NC. The source level densities were calculated from surf noise measurements made a few km offshore over a period of a few days during heavy surf. Didenkulov and Korotkov[7] have also published measurements of the spectral-correlational characteristics of surf noise. Studies of individual breaking waves in the surf zone have been published by Deane[8,9] and Bass and Hay.[10] However, none of these earlier works have considered the relationship between surf noise level and the driving environmental parameters, such as surface wave height and wind speed, which is the topic of this paper.

A description of the surf noise experiment can be found in Sec. I, which gives an overview of the ambient noise monitoring station and its surrounding environment. Because there are many sources of sound in the very near shore region in addition to the noise of breaking surf, it was necessary to review the entire data set and remove any 9-min segments dominated by sources other than breaking surf. A survey of the identifiable noise sources is given in Sec. II, and Sec. III presents a correlation analysis of segments of surf-dominated noise with wave height and wind speed. Section IV contains the concluding remarks.

I. DESCRIPTION OF THE EXPERIMENT

The surf noise measurements began in July 1997 with the deployment of a sound and wave height monitoring station at 32° 51.997′ North, 117° 15.521′ West, approximately 150 m Southwest of Scripps Pier. A scale drawing of the deployment site detailing the position of the array relative to the pier and the average of the lower low water height is shown in Fig. 1. The gray rectangle is a contour plot of the sea floor bathymetry, and the image to the right shows an underwater photograph of the monitoring station. The hydrophones were cleaned regularly to remove marine growth, and the photograph was taken during one of the monthly maintenance operations.

The array consisted of four International Transducer Corporation 6050C hydrophones positioned on the vertices of a cube, nominally 1 m apart and 0.8 m above the sea floor. The average water depth at the array location was 8 m. The spatial arrangement of the hydrophones allowed sound power spectral density and coherence to be measured in the vertical and along two horizontal axes. A pressure sensor was deployed with the hydrophones to measure average water depth and the pressure fluctuations associated with waves passing overhead. Signals from the hydrophones and pressure sensor were brought to the pier and a computer-controlled recording station through a steel armored cable. The hydrophones and digital-audio recording system provided broadband data in the frequency range 10 Hz–22.5 kHz. Nine-minute segments of ambient noise and pressure time series were recorded hourly until mid June, 1998 providing over 8000, 9-min data records over the 12-month operating period. The monitoring array was augmented with a meteorological station in mid-December of 1997. The station was mounted at the end of Scripps Pier and recorded samples of the wind speed and direction every minute at a height of 20 m above sea level.

The beach around Scripps Pier is representative of the west coast of the continental United States. The sea floor is composed of a medium grained, lithogenous sand with a mean grain diameter of 570 m overlying a denser, rocky substrate. The sand layer thickness varies throughout the year, from 2 m or more during the summer months to zero after winter storms. The average beach angle in the wave breaking zone is 1.4 degrees, which corresponds to a slope of 1 in 40. Thus a typical 2-m change in water depth due to the

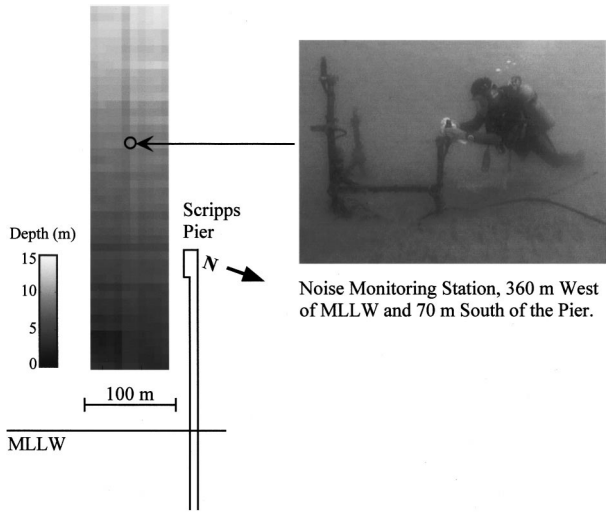

FIG. 1. A scale drawing of Scripps Pier and the location of the ambient noise monitoring state. The gray rectangle is a contour map of the bathymetry around the monitoring station. The image to the right was taken during one of the monthly maintenance operations and shows a diver cleaning the marine growth off one of the hydrophones.

tide varies the range between the breaking surf and the monitoring station by approximately 80 m over a 6-h period.

II. SOURCES OF AMBIENT SOUND IN THE SURF ZONE

Figure 2 shows a time series plot of the root mean square (rms) wave height and a sound pressure density spectrogram of the ambient sound recorded at the monitoring station during the month of January 1998 (see Sec. III) for a description of the data processing method). The significant wave height is often quoted as a measure of wave activity, and is four times the rms height. The sound levels are plotted in dB relative to 1 μPa^2/Hz. Although breaking surf generates noise up to at least 20 kHz,[8] the sound at the monitoring array at frequencies above 1 kHz is dominated by colonies of snapping shrimp that live beneath Scripps Pier, and for this reason the spectrogram has been cutoff at 1 kHz. From the ambient noise analysis (described in Sec. III) it was determined that the dominant noise source at the monitoring array during January was breaking surf. As will be shown, the surf noise scales approximately with the energy of the incident swell, which explains the strong visual correlation between wave height and ambient noise level evident in the figure.

There are, in addition to surf noise, a large number of sound sources operating in the very near shore region. A close inspection of the spectrogram in Fig. 2 shows sudden, large variations in sound level (see, for example, the two broadband lines around Julian Day 5) that are not accompanied by increased wave activity. Such events are more clearly seen in Fig. 3, which shows a summary of rms wave height and ambient noise for the month of September 1997. Although there is still a visual correlation between sound level and wave height during this month, it is clear that there are noise sources that are not correlated with breaking activity. The daily peaks in level centered on 200 Hz around Julian Day 255, for example, are due to a species of drum fish that chorus in the evening hours during the months of February through October.

As Fig. 3 suggests, there are many sources of sound active in the near shore region in addition to surf noise. Hydrodynamical, biological, and mechanical sources were all recorded during the 12-month observation period, and an extensive and detailed analysis was required to isolate segments of surf noise. The entire data set consists of roughly 1200 h of recordings, the entirety of which were processed into 1200 spectrograms (the processing details are provided in Sec. III). Visual examination of the spectrograms was the primary method of analysis used to determine if a given 9-min sound segment contained noise from sources other than surf. Although tedious, and subjective, the method is quite effective if the individual evaluating the spectrograms

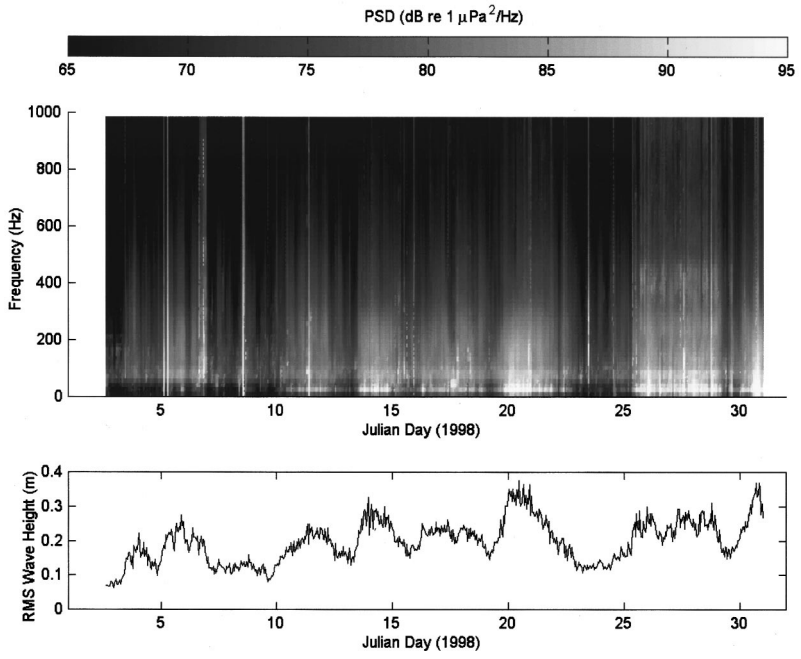

FIG. 2. A summary plot of ambient noise power spectral density and rms wave height for the month of January 1998. The time series have been formed by concatenating 9-min segments of noise and wave height into a continuous plot. Ambient noise levels can be seen to rise and fall with the rms wave height of the incident wave field.

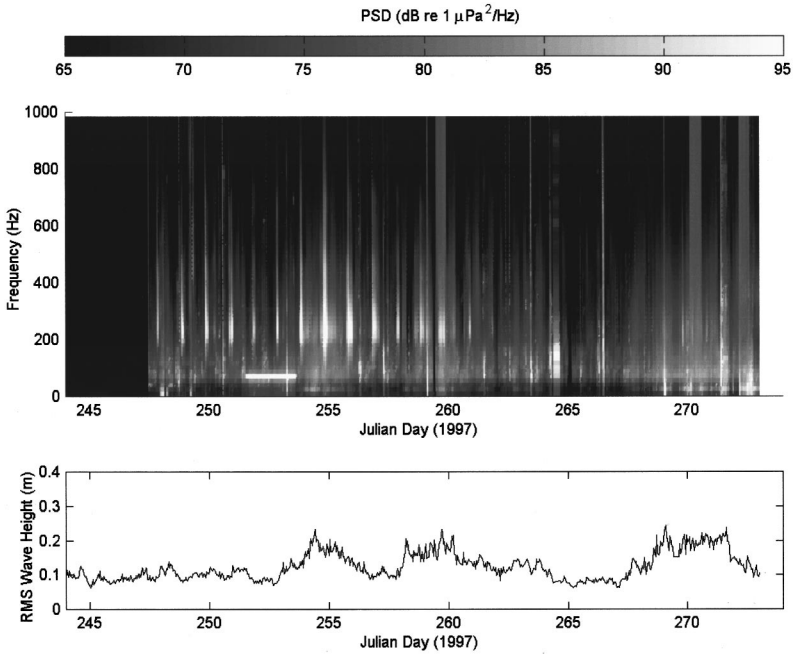

FIG. 3. A summary plot of ambient noise power spectral density and rms wave height for the month of September 1997. Ambient noise levels were not recorded for the first four days of the month. The large variations in ambient level are due to biological and manmade sources which were active during the summer months.

is familiar with the time-frequency patterns of interfering sources. This issue is discussed further in the concluding remarks.

Since the variety and characteristics of acoustic sources operating in the surf zone are of interest in their own right, examples of the hydrodynamical, biological, and mechanical sources identified in the data set are given below. The identification of a given sound with a category of source was made by identifying similar patterns of time-frequency variation in the spectrograms and then listening to the recording. It is relatively easy, for example, to distinguish between biological and mechanical noise this way. Spectrograms illustrating the noise from the various source categories are shown in Figs. 4, 5, and 6. In order to emphasize the relevant features of each source, the spectrograms are plotted on different time and frequency scales, so inter-comparisons should be made with care.

A. Biological sources

The biological sources identified at La Jolla Shores were snapping shrimp, members of the Sciaenidae family of fish (i.e., croakers, also known as Drum fish), seals, and dolphins. There are three marine mammals commonly observed in the vicinity of the SIO pier. These are the harbor seal, *Phoca vitulina*, the California sea lion, *Zalophus californianus*, and the bottle-nose dolphin, *Tursiops truncatus*. The gray whale, *Eschrichtius robustus*, are also observed in the pier vicinity during their yearly migration.

Snapping shrimp create distinctive broadband, impulsive snaps with source levels as high as 190 dB *re*: 1 μPa^2 s at 1 m and containing frequencies up to 200 kHz and beyond.[11] In concert, the shrimp sound similar to frying bacon. Colonies of shrimp are known to live among the mussels and barnacles that encrust the pilings of Scripps Pier, and the sound of their activity was ubiquitous and dominated the surf noise spectrum above about 1 kHz. Species of snapping shrimp known to live along the San Diego coastline are *Synalpheus lockingtoni*, *Alpheus californiensis*, *Alpheus bellimanus*, and *Alpheus clamator*.[12] The randomly placed, thin, white vertical lines seen throughout the spectrogram in Fig. 4(a) are due to snapping shrimp. The constant and high levels of shrimp noise effectively limited the analysis of surf noise to frequencies below 1 kHz.

Members of the Sciaenidae family of fish, also known as croakers or drum fish, have drumming muscles attached to their air bladder which they use to produce sound. Individuals produce a short burst of taps every 3 to 7 s.[13] Croakers are known to congregate in schools and chorus between the hours of dusk and early morning.[14] The vocalizations we are attributing to croakers were observed in the frequency band 200 Hz–800 Hz during the months of February through October for about 3–5 h after sunset. A spectrogram of a 10-s segment of the noise is shown in Fig. 4(c). There are ten species of croakers known to inhabit the coastal regions of California.[15] Recordings of croaker choruses made by Johnson[14] around Scripps Pier between 1942 and 1947 indicated the presence of one or more of the species: black croaker, *Sciaena saturna*, spotfin croaker, *Roncadro stearnsi*, and yellowfin croaker, *Umbrina roncador*.

Unlike snapping shrimp (colonies of which create sound continuously) and croakers (which exhibit regular seasonal and diurnal patterns of vocalization), seals and dolphins were heard at seemingly random intervals throughout the data set. A spectrogram containing dolphin vocalizations is shown in Fig. 4(a). Both broadband clicks and whistling tones can be seen. The whistles and clicks were not a significant source of sound below 1 kHz, which is the upper limit of the band for the surf noise analysis.

Seal vocalizations, which sound like a series of barks, are illustrated in Fig. 4(b). As the spectrogram shows, the calls are a significant source of sound within the surf noise analysis band (10 Hz–1 kHz), and 9-min segments containing seal barks were excluded from the data set. Seal calls were sometimes accompanied by loud taps on one of the

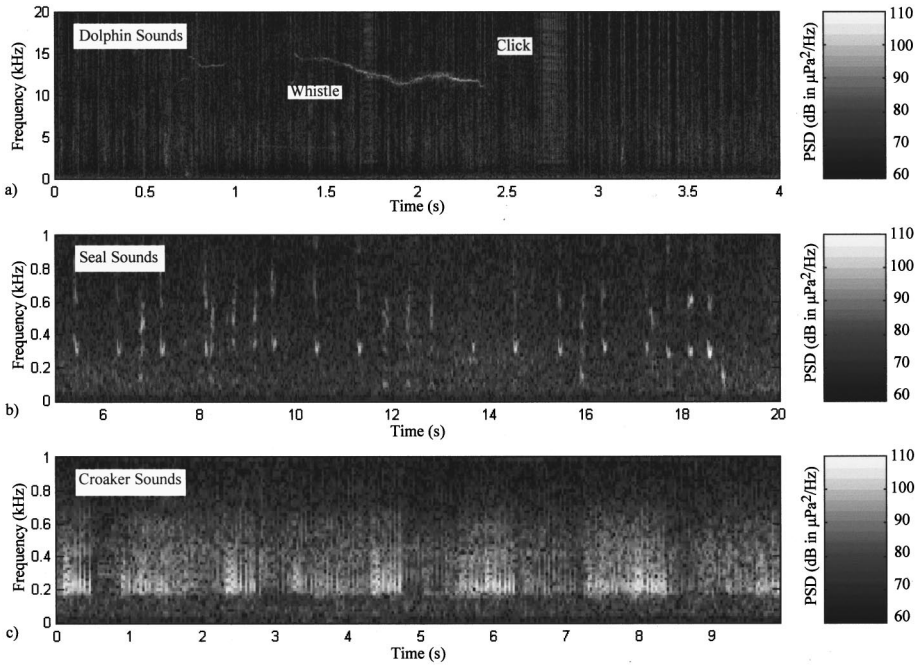

FIG. 4. Spectrograms showing examples of biological noise. (a) Both whistles and clicks from dolphins and broadband snaps from shrimps living on Scripps Pier can be seen. (b) Seal sounds. (c) Chorusing vocalizations of drum fish.

hydrophones. The strong impression gained by listening to the recording is that the hydrophone, possibly the object of a seal's curiosity, was being knocked or chewed on.

B. Hydrodynamical sources

The category of ''hydrodynamical sources'' includes breaking surf, wind-induced wave breaking (white caps), rain, flow noise caused by wave-induced water flow past the hydrophones and pressure variations caused by wave motion over the hydrophones. Hail and snow also create underwater sound, but these meteorological conditions were not encountered during the recording period.

1. Surf noise

Figure 5 shows a short segment of ambient noise recorded at 3 am on February 4, 1998 when the surf was heavy and dominated the sound field below 1 kHz. The spectrogram at the top of the figure shows 4 min of noise processed into sound pressure density and plotted in dB *re*: 1 μPa^2/Hz over the frequency band 10 Hz–1 kHz. The lower plot shows the surface wave field over the same time period. At the range of the monitoring station, approximately 360-m seaward of the mean lower low water line, the sound of individual waves breaking were distinguishable above the ensemble of more distant events. The white, vertical bands that persist of 5 s or so and extend over the entire frequency

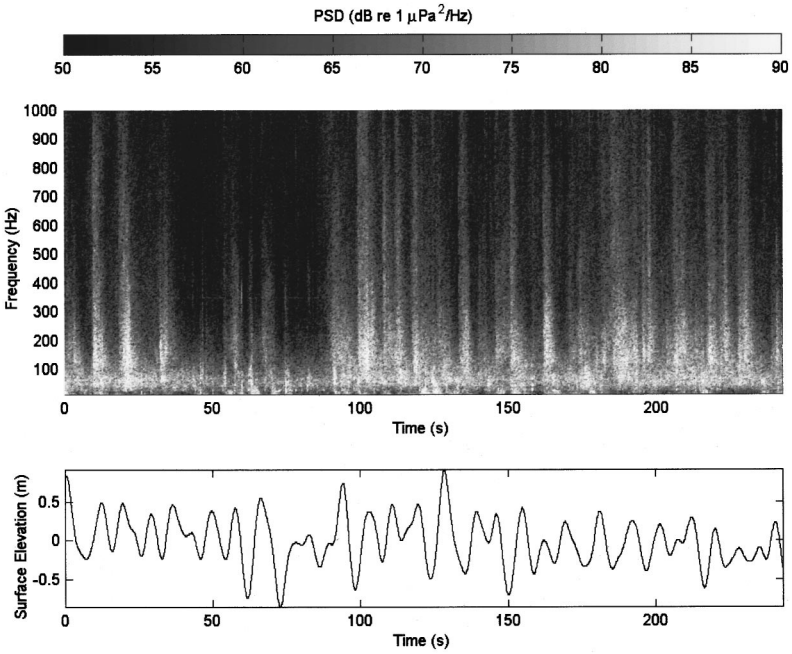

FIG. 5. A spectrogram of surf noise and a time series plot of ocean surface elevation taken during a period of moderate surf activity. The sound of individual breaking waves appears a broadband bursts of noise that persist for 5 s or so.

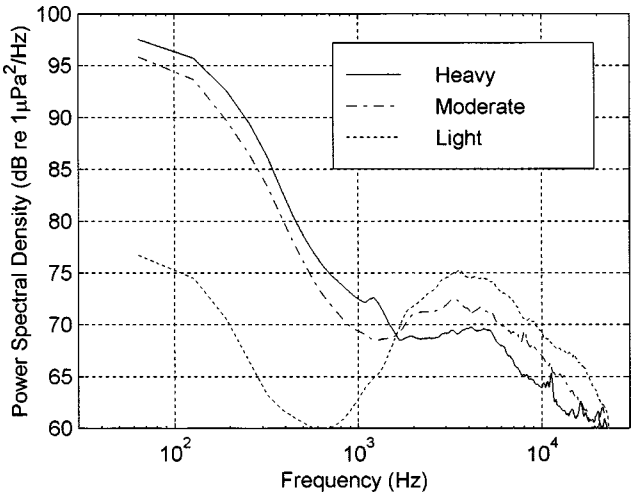

FIG. 6. Plots of the ambient noise power spectral density calculated from 4-min segments of noise recorded during heavy, moderate, and light surf conditions. The noise segments were selected from recordings free of biological and mechanical sounds. The spectrum between 100 Hz and 1.6 kHz is dominated by surf noise; the spectrum above 1.6 kHz comes from the sound shrimps living on Scripps Pier.

spectrum in the spectrogram are the sound of individual waves breaking on the beach. This fact was easy enough to verify during the course of the experiment by visually correlating wave breaking activity on the beach with the sound at the monitoring state. There is not a one-to-one correspondence between the sound signature of a breaking wave and the wave height peaks because of the time delay between waves passing over the monitoring station and breaking on the shore.

The surf noise is loudest below 300 Hz, but extends up to 1 kHz and beyond. Breaking surf is known to generate noise up to at least 20 kHz,[8] but ambient noise above about 1.6 kHz in the present data set was dominated by the sound of snapping shrimp living on Scripps Pier. Figure 6 shows the average broadband, power spectral density, estimated from 4 min of noise data taken during light, moderate, and heavy surf. The broad peak in the power spectrum between 2 and 8 kHz is due to snapping shrimp, and shows an anticorrelation with surf activity. Although this might be caused by an increasing reluctance of the shrimp to snap with rising surf activity, a more likely explanation is that the drop in sound level is caused by the acoustic absorption due to the large numbers of bubbles created by the surf between the monitoring station and the shrimp colonies on the pier. In the absence of other biological and mechanical noise sources, the power spectral density below 1 kHz is dominated by surf noise and increases with increasing surf activity.

Of the possible noise-generating mechanisms associated with surf breaking over sand, including free bubble oscillations and collective oscillations of bubbles in bubble plumes, splashes, sediment disturbance, hydrodynamic pounding of the sea floor (''surfseisms''), and bubble amplified turbulence, the dominant source of noise between about 500 Hz and 50 kHz is the oscillation of newly crated bubbles.[8]

2. Whitecap noise

When the wind speed exceeds about 5 m/s, wind-induced wave breaking occurs across an extended region of ocean surface forming whitecaps which contribute sound to the ambient noise field. The noise from whitecaps extends well below 1 kHz, and it was not possible to distinguish between noise from whitecaps and surf noise by examining the ambient noise spectrograms. This is not entirely surprising given the similarity between the physical processes occurring beneath breaking surf and wind-induced whitecaps. The contribution of whitecaps to the ambient noise field have not been removed from the noise analysis, and wind-induced effects on the ambient noise field are discussed in greater depth in Sec. III.

3. Rain noise

The underwater noise of rain has been well-studied.[16–21] As discussed by Nystuen *et al.*,[17] the underwater sound produced by rain depends on the total rainfall rate. Light rain with total rainfall rate of less than 2.5 mm per h produces a broad, wind-sensitive, spectral peak at 15 kHz. Heavy rainfall with a total rainfall rate greater than 7.5 mm per h produces broadband noise at least in the range 4–21 kHz. Rain noise was fairly easy to identify in the data set as continuous, broadband noise well below 1 kHz and lasting for several hours or days. In addition, a log book was maintained on a daily basis throughout the experiment into which weather conditions, including rain, were noted. Nine-minute noise records containing rain noise were excluded from the surf noise analysis.

4. Flow noise

Pressure fluctuations associated with the flow of water past a hydrophone produce low frequency pseudo-sound.[22] In the absence of turbulence caused by the physical presence of the hydrophone, the main source of noise is the advection of any existing turbulent pressure field past the hydrophone. Wave-induced water flow around the noise monitoring station had the dual effect of creating a turbulent flow around the supporting structure during one-half of the wave cycle, and then advecting the induced turbulence over the hydrophones as the flow direction reversed. It is not possible to estimate the amplitude of the resulting infrasonic noise without measurements of the turbulent velocity field at the noise monitoring station, but a reasonable assumption is that the noise measurements contain some component of flow noise below about 50 Hz. This view is supported by measurements of the ambient noise coherence between pairs of hydrophones. Figure 7 shows a plot of the real and imaginary parts of the coherence between the two hydrophones lying parallel to the shore line. The broadband coherence between two hydrophones with a fixed separation is defined as

$$\Gamma(\omega,r_1,r_2)=\frac{\langle S_1(\omega,r_1)S_2^*(\omega,r_2)\rangle}{\sqrt{\langle S_1(\omega,r_1)S_1^*(\omega,r_1)\rangle\langle S_2(\omega,r_1)S_2^*(\omega,r_1)\rangle}}, \tag{1}$$

where S_j is the pressure spectral density at hydrophone j located at r_j, ω is the angular frequency, * denotes complex conjugation, and $\langle\ \rangle$ denotes the expected value. The coherence function for acoustic noise fields has the property that it tends to unity as frequency tends to zero and the hydrophone

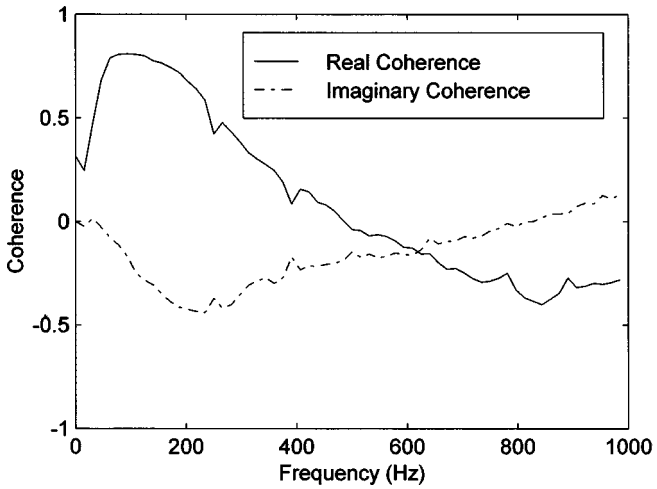

FIG. 7. The real and imaginary components of ambient noise coherence plotted as a function of frequency during a period of moderate surf activity. The noise field is not well correlated at frequencies less than about 50 Hz, indicating that the ambient noise recordings are contaminated by low frequency flow noise.

separation becomes a small fraction of a wavelength. The plot in Fig. 7, however, shows the coherence rapidly dropping to zero for frequencies less than about 50 Hz. This is a clear indication that the pressure fluctuations measured at frequencies less than 50 Hz are local to the hydrophone and are not associated with a propagating acoustic field. Because of the flow noise, the surf noise analysis is restricted to frequencies greater than 50 Hz.

C. Mechanical noise

The main source of mechanical noise was associated with human activity during the summer months and mainly came from small fishing and pleasure craft within a few kilometers of the monitoring station, although occasionally noise was heard from much larger vessels further off the coast or light aircraft passing over the monitoring station [see Fig. 8(a), (b)]. These sources of noise were present largely during the daylight hours, and created both broadband and narrow-band noise across the entire spectrum of interest. Nine-minute records containing identifiable ship or aircraft noise were removed from the data set.

Additional mechanical noise can from Scripps Pier which supports two large submersed pumps to supply seawater to the Stephen Birch Aquarium and various research laboratories on the Scripps campus. The pumps operate at irregular intervals depending on the varying demand for seawater, and create underwater sound between 40 Hz and 1 kHz [see Fig. 8(c)]. This is in frequency band of interest and 9-min records with low surf noise levels which also contained pump noise were largely eliminated from the data set. However, too many records contained pump noise for all of them to be removed and the pumps remained a noticeable source of noise contamination at low surf levels.

III. AMBIENT NOISE ANALYSIS

Each day of data collection resulted 24, 9-min segments of noise. Roughly 8000 noise segments were collected during the course of the experiment, but because many of these contained interfering sources of noise only a relatively small subset of the total were selected for the surf noise analysis. Figure 9 shows how the data set was processed. Spectrograms of the noise power spectral density were generated by playing the noise recordings through a 10-Hz to 1.6-kHz band-pass filter and sampling the filtered noise at 4 kHz with a 12 bit analogue to digital converter. The resulting data stream was transformed with a real-time Fast Fourier Transform processor and averaged into 2-s power spectral density estimates. All the noise recordings were processed into spectrograms and 9-min surf noise segments that were not obviously contaminated by other sources were selected manually.

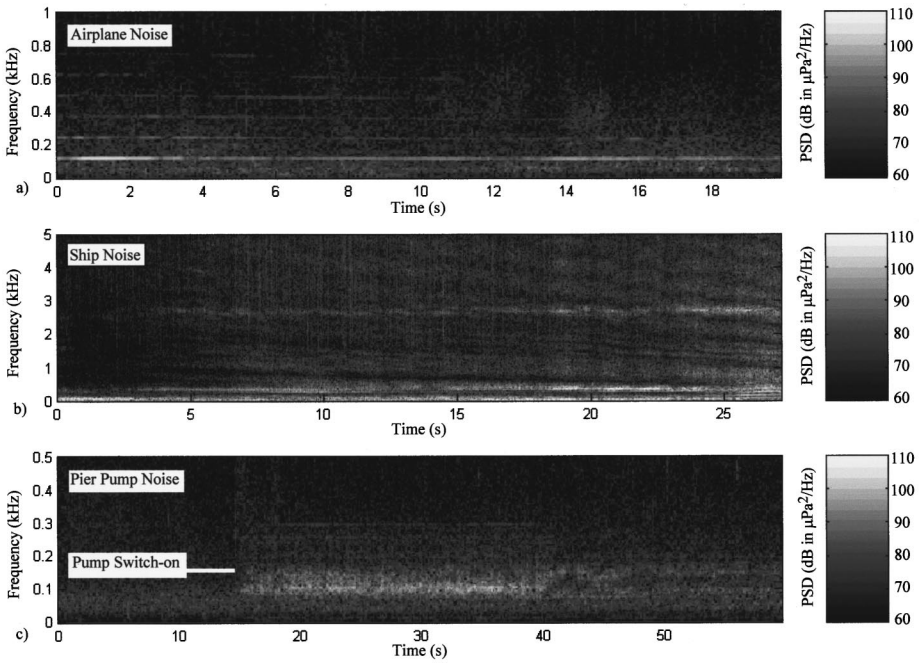

FIG. 8. Spectrograms showing examples of mechanical noise. (a) Airplane noise. (b) Ship noise. (c) Noise from one of the seawater pumps operating on Scripps Pier.

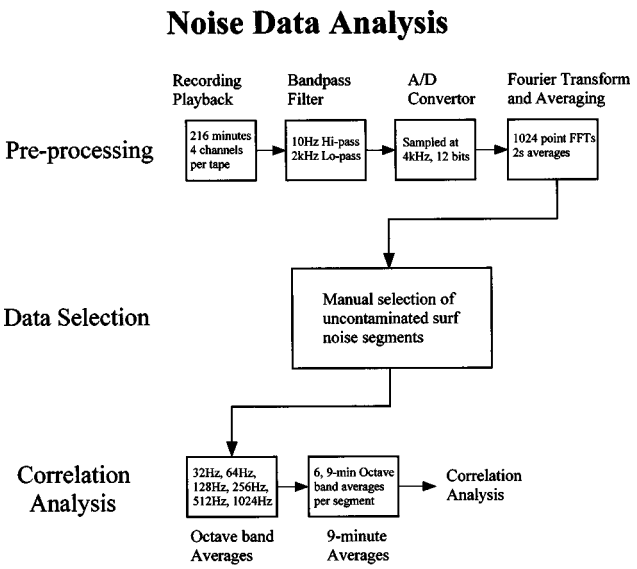

FIG. 9. A flowchart of the noise data analysis and 9-min segment selection process for the surf noise analysis. The 32-Hz and 64-Hz octave band averages are contaminated with flow noise and did not form part of the correlation analysis.

Eliminating noise segments contaminated by noise sources other than surf noise left a data set of approximately 1300 data points.

The noise segments selected as being surf noise dominated were processed further by forming six octave-band averages between 32 Hz and 1024 kHz and then time averaged over an entire segment. The octave bands centered on 32 and 64 Hz were contaminated by flow noise, and were not included in the correlation analysis. Thus every 9-min noise segment was reduced to four numbers, each of which represents the time-averaged energy level in an octave frequency band between 128 and 1024 Hz. In addition to the noise measurements, the average rms wave height, mean water depth, peak wave period, mean wind speed, and mean wind direction were calculated for each 9-min data segment. The calculation of the instantaneous surface elevation from the pressure time series is described in the Appendix.

A. The correlation between surf noise and wave height

Table I shows the results of a correlation analysis of the octave-band average noise levels and the rms wave height, wave peak frequency, mean water depth (representing tidal variations), and wind speed. Of the four environmental variables, rms wave height stands out as having the strongest correlation with the average noise levels, followed by wind speed. Scatter plots of mean noise level plotted in dB *re*: 1 μPa^2/Hz versus rms wave height for the four octave bands are shown in Fig. 10. As expected from the correlation coefficients, there is a strong, positive correlation between noise level and wave height. The scatter plots can be processed into mean noise levels by sectioning the wave height axis into bins and averaging all the points that lie within a given bin. The resulting curves are plotted in Fig. 11. The dots indicate the linear mean noise level and the length of the vertical bars passing through the dots indicate the standard deviation of the noise level within a bin.

The curves show a systematic trend to lower noise level with increasing frequency, and increasing noise level with rms wave height. Across the four octave bands the noise power density scales roughly as the rms wave height squared. This is a suggestive dependence. The mechanical energy in the incident surface wave field is also proportional to the rms wave height squared, implying that the noise power density at the monitoring station is proportional to the flux of wave energy incident on the beach. This idea is supported by the plots in Fig. 12, which show the ratio of ambient noise intensity, averaged over an octave band, to the surface wave field energy flux (calculation of the surface wave energy flux is described in Appendix A). Note that the surface wave energy flux is integrated over the depth of the water column but the noise intensity is not, so the ratio of these two quantities has dimensions of per m per Hz. The ratio is a measure of the efficiency of breaking waves in turning mechanical energy into sound energy measured at the recording station location. As the measurement site is remote from the breaking surf, the ratio is a result of both sound source mechanisms acting within the breaking surf and the absorption and scattering of sound between the surf and the monitoring station.

The numerical value of the energy flux ratio is very small because the conversion of mechanical energy in the surface wave field to sound energy is a very inefficient process. Although the points in the scatter plots show considerable variability, there are frequency and wave-energy-flux dependent trends in the ratio. These trends can be seen more clearly in Fig. 13, which shows average ratio values, found by sectioning the wave energy flux axis into bins and aver-

TABLE I. The cross-correlation coefficients between the 1340 9-min surf noise level averages, rms wave height, wave peak frequency, mean water depth, and rms wind speed. Frequencies refer to the center frequency of surf noise octave band averages. The cross-correlation coefficients are for the log of the octave band average levels.

	128 Hz	256 Hz	512 Hz	1024 Hz	Wave height	Wave freq.	Mean depth	Wind speed
128 Hz	1.00	0.95	0.91	0.89	0.94	−0.15	−0.19	0.30
256 Hz		1.00	0.98	0.91	0.87	−0.19	−0.27	0.23
512 Hz			1.00	0.95	0.83	−0.15	−0.31	0.28
1-24 Hz				1.00	0.84	−0.14	−0.29	0.39
Wave height					1.00	−0.18	−0.09	0.35
Wave freq.						1.00	−0.16	0.18
Mean depth							1.00	−0.13
Wind speed								1.00

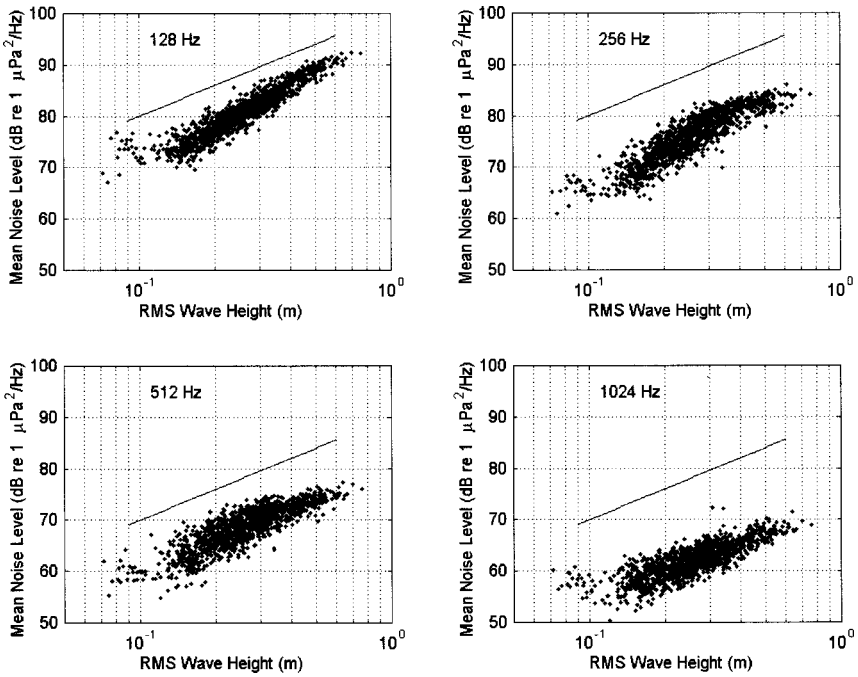

FIG. 10. Scatter plots of the octave-band-averaged noise level versus rms wave height. Each plot corresponds to noise level averages across the indicated octave band. Reference lines showing rms wave height squared scaling are also plotted.

aging all the points that lie within a given bin. For wave energy fluxes greater than 100 W per m, the maximum and minimum values of the average ratio generally differ by no more than a factor of 3. The scatter in the ratio for wave energy fluxes less than 100 W per m is probably due to interfering sound sources that become important at low surf levels and were not successfully eliminated from the data set.

At octave-band frequencies of 128, 256, and 512 Hz, there is an obvious peak in the ratio. Since the acoustic energy level at the monitoring station is a function of both the breaking wave source strength and wave guide propagation through the near shore region, it would be an oversimplification to infer that the peak is due to an optimal conversion of mechanical energy to sound (although this could, in fact, be the case). An alternative explanation is that acoustic absorption by the increasingly large numbers of bubbles generated by high surf levels causes an apparent decrease in the efficiency of mechanical to sound energy conversion. Such a mechanism would be a low frequency analogue of the high frequency absorption of surface generated noise at high wind speeds described by Farmer and Lemon.[23] A similar effect is also seen in rain-generated noise during heavy rain, as described by Nystuen, McGlothin, and Cook.[17] Although appealing, this explanation requires acoustical absorption by quite large bubbles. From Minnaert's equation,[24] the peak in the 128-Hz octave band implies absorption from bubbles about 5 cm in diameter. Although bubbles of this size may well be generated by breaking surf,[25] buoyancy forces will

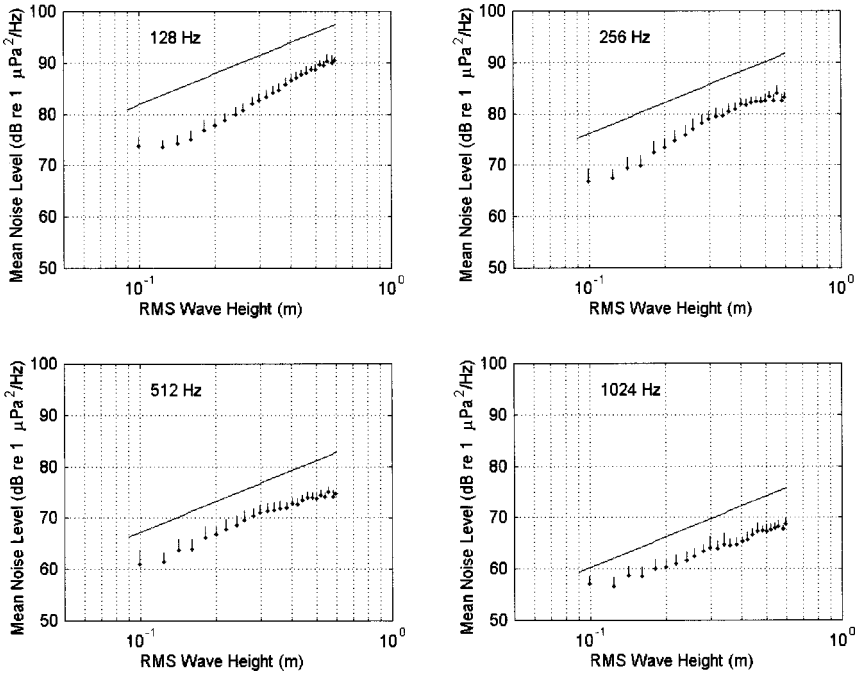

FIG. 11. Average values of noise level. The scatter plots in Fig. 10 have been processed into mean noise levels by sectioning the rms wave height axis into bins and averaging the points that lie within a given bin. The resulting mean noise level for each bin is plotted as a dot; the length of the vertical line above the dot shows the standard deviation of the levels lying within the bin. The reference lines show rms wave height squared scaling.

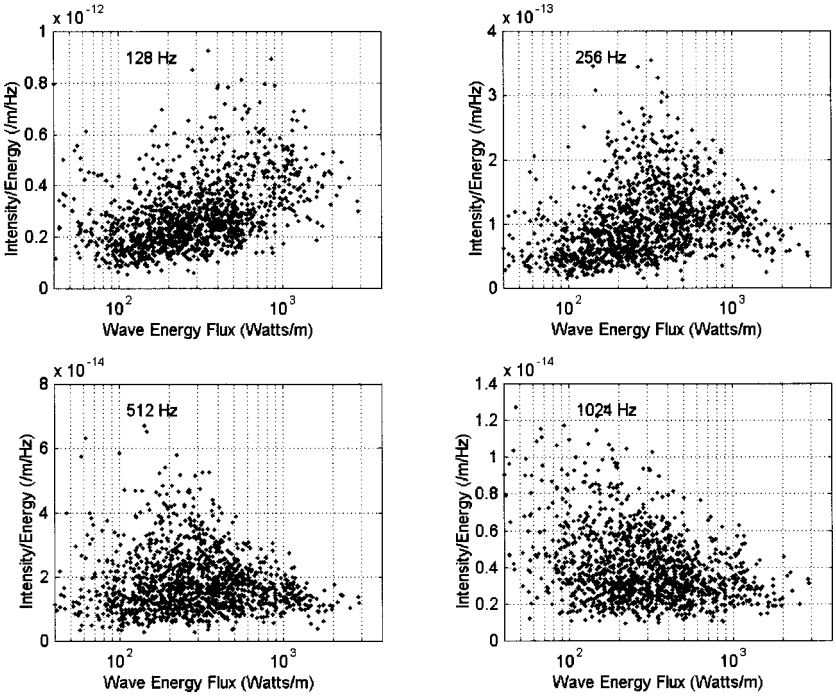

FIG. 12. Scatter plots of the ratio of ambient noise intensity to the surface wave field energy flux, plotted as a function of the wave field energy flux. The ratio is a measure of the efficiency of the conversion of mechanical energy in the surface wave field into sound energy at the monitoring station. The conversion process includes both noise generation processes within the breaking surf and sound propagation from the surf to the monitoring station.

rapidly remove them from the water column. The absorption of sound by assemblages of bubbles at low frequencies is another possibility. The collective oscillation of bubble clouds was independently suggested as a source of low frequency sound in the ocean by Carey[26] and Prosperetti.[27] These structures certainly exist in the surf zone, and their passive acoustic behavior represents an alternative mechanism for the scattering and absorption of low frequency sound.

B. The correlation between ambient noise and wind speed

Figure 14 shows a scatter plot of the (linear) avenge noise level versus rms wind speed for each of the octave bands. Positive values of wind speed indicate the wind is blowing from offshore toward the beach. There is considerable variance in the distribution of points within the plots because the noise level is primarily determined by wave height, not wave speed. The scatter plots have been processed into mean levels by sectioning the wind speed axis into bins and averaging all the points that lie within a given bin. The resulting curves are plotted in Fig. 15. The average curves show that the noise level averaged over wave height is independent of wind speed, for speeds less than about 5 m/s. Above 5 m/s the noise level increases with increasing wind speed, an effect almost certainly due to the additive noise generated by wind-induced white caps. Although the white caps are not as energetic as the breaking surf, they

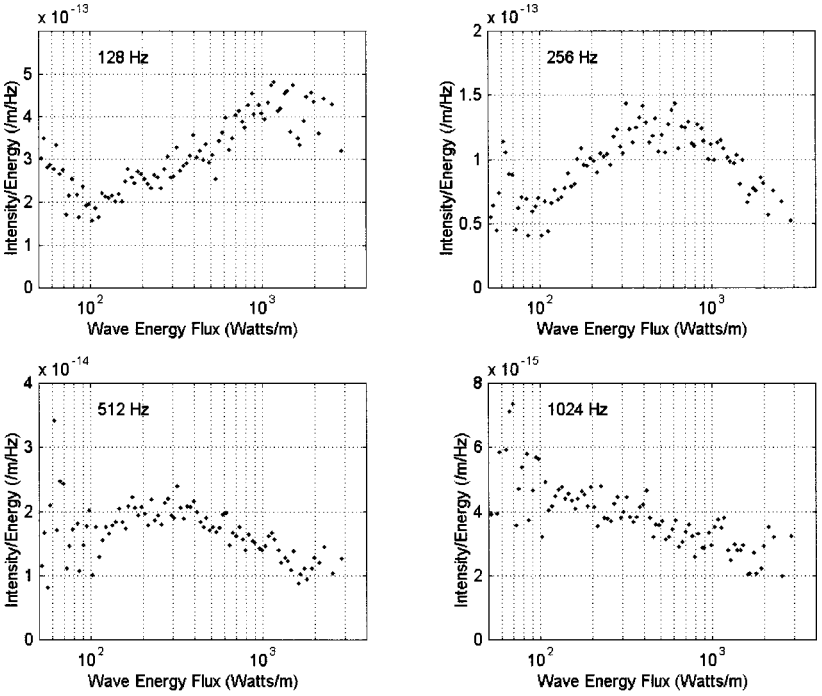

FIG. 13. Average values of the noise intensity and surface wave energy flux ratio, formed by sectioning the wave energy flux axis into bins and averaging the points that lie within a given bin.

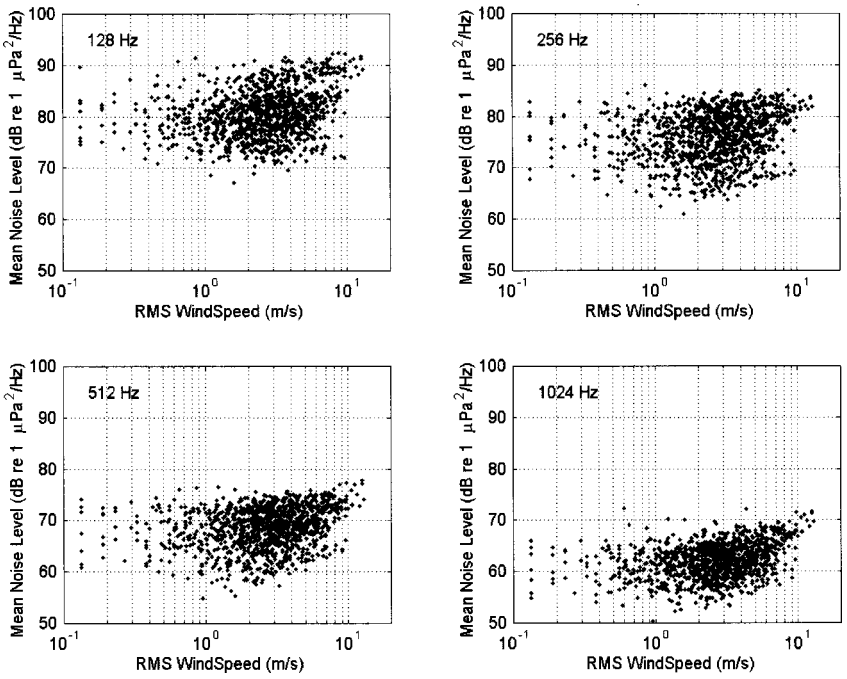

FIG. 14. Scatter plots of the octave-band-averaged noise level versus rms wind speed. Each plot corresponds to noise level averages across the indicated octave band.

occur over a larger area of ocean surface and their integrated radiation adds noticeably to the ambient noise level. Representative values for the noise due to white caps alone can be calculated by taking the power spectral density at a wind speed of 10 m/s and subtracting the surf noise component, estimated from the noise level at wind speeds less than 2 m/s. The resulting 10-m/s wind speed levels are: 89 dB at 128 Hz, 81 dB at 256 Hz, 75 dB at 512 Hz, and 71 dB at 1024 Hz.

Douglas[28] has studied the influence of wind on breaking surf in a laboratory flume. He found that onshore winds cause waves to break in deeper water and form spilling breakers while offshore winds tend to form plunging breakers in shallower water. Given the dependence of breaker location and type on the direction of the wind, it might be expected that the noise generated by breaking surf would also depend on wind direction. Figure 16 shows a plot of power spectral density versus the East/West component of wind speed for the four octave bands. The wind speed component is positive for winds out of the West. Any differences in noise level induced by an offshore versus an onshore breeze would be apparent in the plots as an asymmetry in the placement of data points about the vertical axis of the scatter plot. The plots are, however, quite symmetrical and it appears from this data set that the noise level does not show a dependence on wind direction over the 100-Hz to 1000-Hz frequency band.

IV. CONCLUDING REMARKS

The ambient noise recorded in the near shore region off La Jolla Shores beach arose from a multitude of hydrodynamical, biological, and manmade mechanical sources. Noise from snapping shrimp, drum fish, seals, dolphins, ships, airplanes, pumps on Scripps Pier, rain, and open-ocean white caps were recorded in addition to the sound of breaking surf. Noise levels were highly variable depending on which sources happened to be radiating within a given recording segment. It seems likely that noise levels measured at a different site, with a different resident marine population and different levels of cultural activity, would be different. The noise due to breaking surf, however, should be typical of any beach with a similar bathymetry and seafloor. Recording many noise segments over the course of a year has made it possible to select periods of surf dominated noise for a variety of wind and surface wave conditions.

The main result of this study is the discovery that between 100 and 1000 Hz, surf noise scales with the squared rms wave height of the incident surface waves. Figure 10 shows the relationship between mean noise power density in an octave band and the rms wave height of the surface wave field, measured 1.8 m above the sea floor in 8-m deep water, 360-m seaward of the mean lower low water line. The proportionality between surf noise and rms wave height squared implies that the conversion of wave mechanical energy into breaking wave noise is approximately constant. In fact, the ratio of noise power spectral density to surface wave energy flux varies by a factor of 2–3 over the range of surface wave energy fluxes measured (roughly 100–3000 W per m of wave crest).

For the 128-, 256-, and 512-Hz octave bands, the ratio of noise power spectral density and surface wave energy flux has a local maximum that moves systematically to lower values of surface wave energy flux with increasing frequency. If a peak exists in the ratio for the 1024-Hz band, it is masked by the presence of interfering noise sources that become important at surface wave energy fluxes less than 100 W per m. It is not obvious from the data set whether the peak in the ratio is due to an optimal conversion of mechanical energy to sound occurring in the breaking surf for a par-

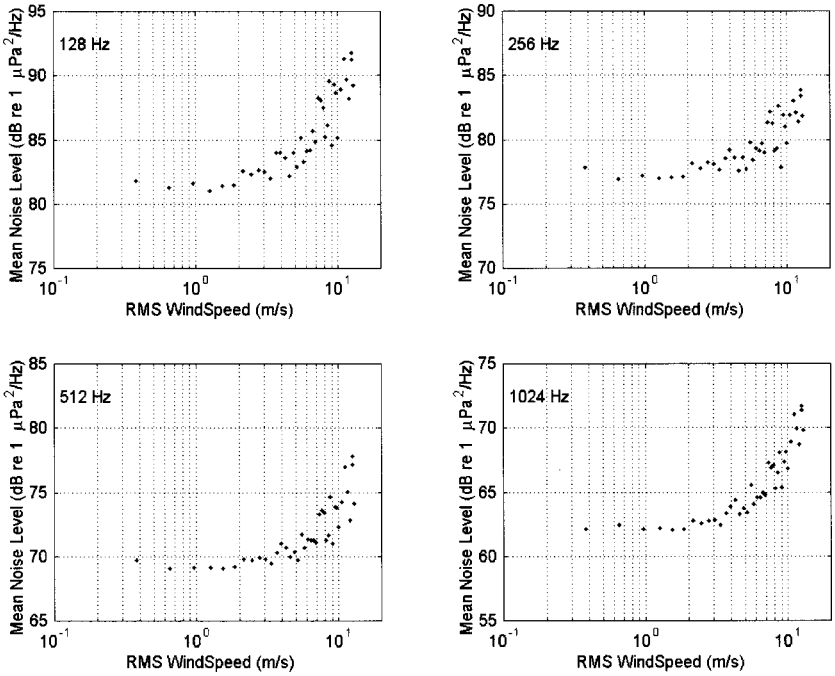

FIG. 15. Average values of the noise level computed from the points in Fig. 14 by sectioning the rms wind speed axis into bins and averaging the points that lie with a given bin. The ambient noise levels increase across the four octave bands when the wind speed exceeds about 5 m/s.

ticular value of surface wave energy flux, or whether acoustic absorption by the increasingly large numbers of bubbles generated by high surf levels causes an apparent decrease in the efficiency of mechanical to sound energy conversion at large values of surface wave energy flux.

The analysis of the correlation between ambient noise and wind speed showed that noise from wind-induced white caps begins to contribute noticeably to the ambient noise level across the four octave bands at the monitoring station when the wind speed exceeded 5 m/s. A study of the effect of on-shore versus off-shore wind direction did not show any influence of wind direction on surf noise generation over the 100-Hz to 1000-Hz frequency band.

One of the limiting factors of this study is the mixture of surf noise with other shallow water sound sources, which were numerous at the La Jolla Shores site (cf. Fig. 3). A resolution of this problem, and the one adopted here, is to find periods of time when surf noise dominates the sound field and include only these in the noise analysis. The difficulty with this method lies in its implementation; it is difficult to be certain whether a particular noise segment is dominated by surf noise when the emissions from competing sources have a similar time-frequency pattern to surf noise. This is the case with wind-induced, wave breaking noise, for example. In addition, manual selection of sound segments dominated by surf noise introduces a subjective element into the analysis. Automated selection, however, brings its own pitfalls and in this study the flexibility offered by a thinking

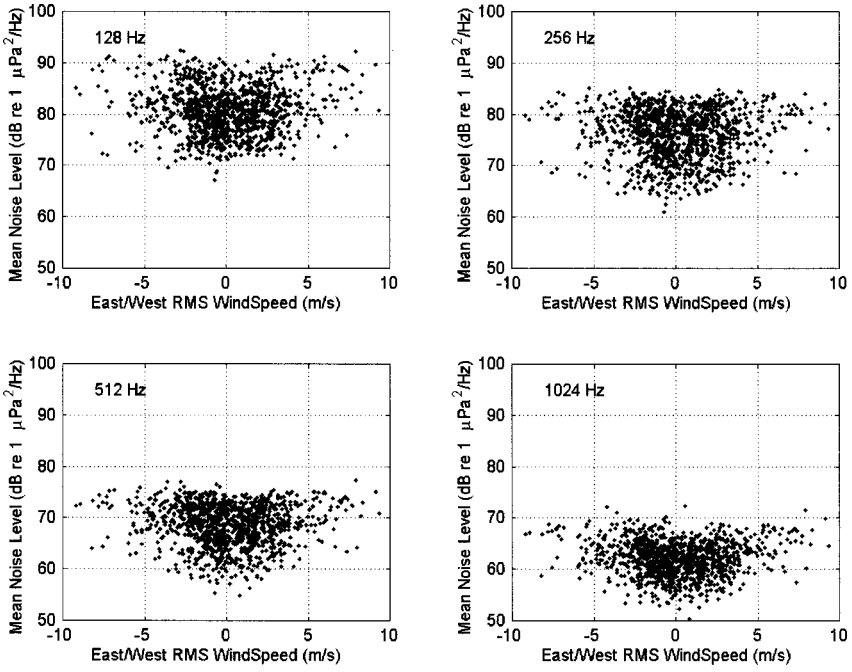

FIG. 16. Scatter plots of the octave-band-averaged noise level versus the East/West component of the rms wind speed. Offshore and onshore breezes are, respectively, plotted as positive and negative values. The plots do not show any obvious differences between onshore and offshore winds.

analyst was preferred over the repeatability of an automated analysis. Probably the most significant improvement to this study would be to make measurements at a site less subject to competing sound sources, particularly at high or low latitudes where snapping shrimp noise is absent.

ACKNOWLEDGMENTS

I am pleased to acknowledge the assistance of James Uyloan and Fernando Simonet who maintained the noise monitoring station. I also wish to acknowledge Professor Kendall Melville who first pointed out the importance of recording meteorological conditions simultaneously with surf noise. This work was generously supported by the Office of Naval Research through Grant No. N00014-96-1-0120.

APPENDIX. CALCULATION OF SURFACE ELEVATION AND ENERGY FLUX

The calculation of the instantaneous free surface elevation and surface wave energy flux discussed below is based on linear, shallow water wave theory. The tacit assumption is that nonlinear effects are small, so that the principle of superposition can be applied. The requirement for linear wave theory is that $kH/2$ be small, where k is the wave number and H is the peak-to-trough wave height. For the shortest period waves of interest (about 5 s), and the largest peak-to-trough wave heights observed (about 2 m), $kH/2$ has a value of 0.17 in the 8 m of water at the noise monitoring station. Thus we can expect linear theory to provide a good approximation for the surface wave properties.

A. Calculation of the surface elevation

The calculation of surface elevation from the measured pressure time series at the monitoring station requires some explanation. Linear, shallow water wave theory provides a relationship between the pressure field associated with a harmonic, progressive wave and the surface displacement (see, for example, Dean and Dalrymple,[29] p. 83):

$$p = -\rho g z + \rho g \, \eta K_p(z), \tag{A1}$$

where

$$K_p(z) = \frac{\cosh(k(h+z))}{\cosh(kh)}, \tag{A2}$$

ρ is the water density, g is the acceleration due to gravity, z is depth measured from the still water surface, η is the instantaneous surface displacement, k is the wave number, and h is the water depth. The first term on the right-hand side of Eq. (A1) is the hydrostatic term determined by the mean water depth. The second term is known as the dynamic pressure and is a function of the instantaneous wave height, wave frequency (through the wave number), and depth. The instantaneous wave height can be determined from a pressure time series segment as follows. The mean value of the pressure is subtracted from the time series, leaving the dynamic pressure. The dynamic pressure is Fourier transformed into spectral components, each of which is then scaled by the factor $1/(K_p \rho g)$ before inverse Fourier transforming. Note that the calculation of K_p requires determining the wave number for a given frequency component. The relationship between wave number and frequency is given by the gravity wave dispersion relationship:

$$k = \frac{\omega^2}{g} \frac{1}{\tanh(kh)}, \tag{A3}$$

where ω is the angular frequency of the wave. An approximate solution for k as a function of ω that is accurate to within about 5% is given by Eckart[30]

$$k = \frac{\omega^2}{g} \frac{1}{\sqrt{\tanh(\omega^2 h/g)}}. \tag{A4}$$

A practical problem encountered when compensating for the filtering effect of the water column is that K_p decreases rapidly from increasing frequency and water depth. Thus the dynamic pressure variation caused by short period waves decays rapidly with depth and there is some frequency at which the signal becomes lost in the noise of the transducer used to record the pressure variations and attempts to recover the signal result in the amplification of electronic noise. This practical difficulty can be overcome by limiting the range of frequencies for the inversion process.

B. Calculation of the surface wave energy flux

The surface wave energy flux for a harmonic, progressive wave is given by (see, for example, Dean and Dalrymple,[29] p. 98)

$$F = H^2 K_e, \tag{A5}$$

where

$$K_e = \frac{1}{16} \rho g \frac{\omega}{k} 1 + \frac{2kh}{\sinh(2kh)}, \tag{A6}$$

and H is the wave amplitude measured from the peak to trough. Equation (5) can be used to calculate the surface wave energy flux in an analogous manner to the free surface elevation. Using Parseval's theorem, the total energy flux in the surface wave train is estimated by summing the surface elevation power spectral density components weighted by K_e.

[1] R. J. Urick, *Ambient Noise in the Sea* (Peninsula, Los Altos, CA, 1986).
[2] V. I. Bardyshev, A. M. Velikanov, and S. G. Gershman, ''Experimental studies of underwater noise in the ocean,'' Sov. Phys. Acoust. **16**, 512–513 (1971).
[3] L. N. Zakharov and V. A. Kirshov, ''Undersea noise in a coastal region,'' in *Eight All-Union Acoustics Conference* (Moscow, 1973).
[4] O. B. Wilson, S. N. Wolf, and F. Ingenito, ''Measurements of acoustic ambient noise in shallow water due to breaking surf,'' J. Acoust. Soc. Am. **78**, 190–195 (1985).
[5] O. B. Wilson, M. S. Stewart, J. H. Wilson, and R. H. Bourke, ''Noise source level density due to surf—Part I: Monterey Bay, CA'' IEEE J. Ocean Eng. **22**, 425–433 (1997).
[6] J. P. Fabre and J. H. Wilson, ''Noise source level density due to surf—Part II: Duck, NC,'' IEEE J. Ocean Eng. **22**, 434–444 (1997).
[7] I. N. Didenkulov and A. S. Korotkov, ''The measurement of underwater noise characteristics in shallow water,'' in *Natural Physical Sources of Underwater Sound* (Kluwer, Dordrecht, 1993), pp. 45–49.
[8] G. B. Deane, ''Sound generation and air entrainment by breaking waves in the surf zone,'' J. Acoust. Soc. Am. **102**, 2671–2689 (1997).

[9] G. B. Deane, ''Acoustic hot-spots and breaking wave noise in the surf zone,'' J. Acoust. Soc. Am. **105**, 3151–3167 (1999).
[10] S. J. Bass and A. E. Hay, ''Ambient noise in the natural surf zone: Wave-breaking frequencies,'' IEEE J. Ocean Eng. **22**, 411–424 (1997).
[11] D. H. Cato and M. J. Bell, ''Ultrasonic ambient noise in Australian shallow waters at frequencies up to 200 kHz,'' DSTO Materials Research Laboratory, Technical Report MRL-TR-91-23, February, 1992.
[12] C. L. Epifanio, ''Acoustic daylight: Passive acoustic imaging using ambient noise,'' Ph.D. thesis, University of California, San Diego, 1997, pp. 311.
[13] V. O. Knudsen, R. S. Alford, and J. W. Emling, ''Underwater ambient noise,'' J. Mar. Res. **7**, 4109–429 (1948).
[14] M. W. Johnson, ''Sound as a tool in marine ecology, from data on biological noises and the deep scattering layer,'' J. Mar. Res. **7**, 443–458 (1948).
[15] D. J. Miller and R. N. Lea, ''Guide to the coastal marine fishes of California'' (Publications Division of Agriculture and Natural Resources, University of California, 6701 San Pablo Avenue, Oakland, CA 94608-1239, Oakland, 1972), pp. 249.
[16] A. Prosperetti, L. A. Crum, and H. C. Pumphrey, ''The underwater noise of rain,'' J. Geophys. Res. **94**, 3255–3259 (1989).
[17] J. A. Nystuen, C. C. McGlothin, and M. S. Cook, ''The underwater sound generated by heavy rainfall,'' J. Acoust. Soc. Am. **93**, 3169–3177 (1993).
[18] J. A. Nystuen, ''Rainfall measurements using underwater ambient noise,'' J. Acoust. Soc. Am. **79**, 972–982 (1986).
[19] M. S. Longuet-Higgins, ''An analytical model of sound produced by raindrops,'' J. Fluid Mech. **214**, 395–410 (1990).
[20] N. Bom, ''Effect of rain on underwater noise level,'' J. Acoust. Soc. Am. **45**, 150–156 (1969).
[21] T. E. Heindmsmann, R. H. Smith, and A. D. Arneson, ''Effect of rain upon underwater noise levels,'' J. Acoust. Soc. Am. **27**, 378–379 (1955).
[22] M. Strasberg, ''Nonacoustic noise interference in measurements of infrasonic ambient noise,'' J. Acoust. Soc. Am. **66**, 1487–1493 (1979).
[23] D. M. Farmer and D. D. Lemon, ''The influence of bubbles on ambient noise in the ocean at high wind speeds,'' J. Phys. Oceanogr. **14**, 1762–1778 (1984).
[24] M. Minnaert, ''On musical air-bubbles and the sounds of running water,'' Philos. Mag. **16**, 235–248 (1933).
[25] G. B. Deane and M. D. Stokes, ''Air entrainment processes and bubble size distributions in the surf zone,'' J. Phys. Oceanogr. **29**, 1393–1403 (1999).
[26] W. M. Carey and D. Browning, ''Low frequency ocean ambient noise: Measurement and theory,'' in *Natural Mechanism of Surface Generated Noise in the Ocean* (Kluwer, Dordrecht, 1988), pp. 361–376.
[27] A. Prosperetti, ''Bubble dynamics in oceanic ambient noise,'' in *Natural Mechanisms of Surface Generated Noise in the Ocean* (Kluwer, Dordrecht, 1988), pp. 151–171.
[28] S. L. Douglas, ''Influence of wind on breaking waves,'' Journal of Waterway, Port, Coastal and Ocean Engineering **116**, 651–663 (1990).
[29] R. G. Dean and R. A. Dalrymple, *Water Wave Mechanics for Engineers and Scientists* (World Scientific, New Jersey, 1991), p. 353.
[30] C. Eckart, ''The propagation of waves from deep to shallow water,'' in *Gravity Waves*, Circular No. 521: 165-73, National Bureau of Standards, 1952.

Collective oscillations of fresh and salt water bubble plumes

Gregory J. Orris and Michael Nicholas
Naval Research Laboratory, Washington, DC 20375

(Received 4 June 1996; revised 7 December 1998; accepted 30 July 1999)

Bubble plumes of various void fractions and sizes were produced by varying the flow velocity of a water jet impinging normally on a water surface. The bubbles entrained at the surface were carried downwards by the fluid flow to depths ranging from 33 to 65 cm, and formed roughly cylindrical plumes with diameters ranging from 12 to 27 cm. The acoustic emissions from the plumes were recorded onto digital audio tape using a hydrophone placed outside the cloud at distances ranging from 50 cm to 16.0 m. Closeup video images of the individual bubbles within the plume were also taken in order to gain knowledge of the bubble size distributions. The experiments were performed in both fresh-water and salt-water environments. The fresh-water clouds emitted sounds with a modal structure that was significantly different from that produced by the salt-water clouds. Furthermore, the smaller bubbles present in the salt-water clouds have a fundamental effect on the amplification of turbulence noise, generating sound at significant levels for frequencies up to several hundred Hertz. [S0001-4966(99)03012-X]

PACS numbers: 43.30.Nb, 43.30.Es [SAC-B]

INTRODUCTION

A. Bubbles in the ocean

In recent decades there has been much work related to understanding and modeling the wide array of mechanisms responsible for generating underwater ambient noise in the ocean.[1–4] Over the past several years the impact that subsurface bubbles and bubble clouds have on this ambient noise field has been realized.[5] In particular, the work described here is concerned with bubble-related noise generation following breaking wave events: These will typically be characterized by the entrainment of many thousands of bubbles in highly excited states, occupying a localized region of space ($\leqslant m^3$) and occurring over a fairly short period of time ($\sim$ seconds). Such bubble clouds will typically have quite complex distributions of bubbles (in both size and density), and will be influenced by such things as surface interactions, dissolution, coalescence, bubble shearing, and bubble transport by various fluid flows beneath the ocean surface. Following a breaking wave event one would typically expect to find a bubble cloud with a relatively dense core (high void fraction) surrounded by an outer sheath with substantially lower bubble density; the transition between the two is likely to be exponential in character. Simplified structures are often used to model the general shape and structure of these bubble clouds; to date the types of structures actively being considered include fractals, hemispheres, cylinders, and more extended shapes such as horns.[6–10]

The importance of bubbly structures to ocean acoustic propagation and noise modeling can be seen from the fact that compact bubble clouds distributed throughout a region of the ocean can dramatically affect the bulk acoustical properties: They are essentially pockets of media with acoustic phase speeds around an order of magnitude slower (at frequencies well below individual bubble resonance) than the sound speed of the surrounding sea water. For these low frequencies the acoustic phase speed can be expressed approximately as a function of the void fraction β via Wood's equation,[11]

$$c_{\text{Wood}} \approx \sqrt{\frac{P_0}{\rho_w \beta(1-\beta)}}. \tag{1}$$

This equation is valid for void fractions in the range $0.002 < \beta < 0.94$,[9] this upper limit being a gross overestimate for bubble clouds formed under even the most violent of breaking waves. P_0 is the ambient pressure ($\sim 1.01 \times 10^5$ Pa for near-surface clouds), and ρ_w is the density of the bubbly water which, for the bubble clouds in the ocean which will be considered in this work, is still quite close to 1000 kg/m^3. From (1) it is evident that even for void fractions of only 1% the acoustic phase speed is reduced to about 300 m/s. To a good approximation such a compact bubble cloud is equivalent to introducing a resonant cavity: If such a cavity were roughly cylindrical in shape with a length of 1 m, the fundamental longitudinal mode of oscillation would occur at around 150 Hz.

Low-frequency collective oscillations of clouds of bubbles can be sharply contrasted with the relatively high-frequency spectrum of individual bubble resonance for bubble sizes typically found in the ocean. From very general physical considerations (i.e., conservation of energy) Minnaert[12] and later Strasberg[13,14] have shown that for a spherical bubble pulsating radially, the natural frequency, f_0, will be given by the formula

$$f_0 = \frac{1}{2\pi}\sqrt{\frac{3\gamma P_0}{\rho_w R_b^2}}, \tag{2}$$

where γ (=1.4) is the ratio of specific heats, and R_b is the radius of the bubble.[12] In the experiment described in this paper even the largest fresh-water bubbles had radii well below 3.5 mm, for which the Minnaert frequencies as calculated by (2), are well above 1 kHz. Thus it is expected that a typical cloud's resonance frequencies are sufficiently far below the main resonance peaks of the individual bubbles

within the cloud, and as such the extremely high attenuation associated with driving a bubble at resonance is absent.[15] This has prompted many researchers to suggest that a group of bubbles can behave as a collective mass, provided that the bulk acoustical properties of the bubbly medium occur in a sufficiently compact region of space.[6–10,15–23]

Much still remains to be determined about bubble cloud resonances and excitation mechanisms, particularly in the ocean, where it is not an easy task to catch a freely resonating cloud while simultaneously making comprehensive measurements of the bubble field and other pertinent parameters. Several attempts have been made to produce bubbly structures in a more hospitable (controlled) environment;[6–9,24] in each case they are found to mimic certain aspects of bubble clouds found in the ocean. In particular, experiments usually have inaccurate bubble-field realizations with respect to real ocean parameters. In this study, a jet of water impinging on a horizontal water surface at normal incidence is used to continuously entrain a cloud of bubbles. (See Sec. I for details.) This experiment was carried out with the specific intent of looking for signs of clouds resonating while maintaining the gross dimensions of the cloud over a long time period, and allowing only those processes involved in entrainment to excite the cloud. In particular, we were looking for differences in the acoustic emissions of these bubble clouds when going from a fresh-water environment to a salt-water environment.

The analysis of the data collected in this experiment strongly suggests that any data concerning ambient noise in the ocean should be conducted in saline conditions. Certain conclusions one might infer from fresh-water experiments may be misleading or possibly erroneous in salt-water environments. While much of the physics of the entrainment and resonance processes are the same for the two environments, there are crucial differences (particularly those concerned with the surface properties) that lead to drastic differences in the bubble populations which, in turn, have marked effects on the acoustic properties.

B. Effects of salt and other surfactants

A detailed examination of the bubble entrainment process is beyond the scope of the work presented here. In terms of the effect on the acoustics, of most concern to us is that the bubble populations in the fresh-water and salt-water parts of our experiments are markedly different, and, furthermore, that the smaller-sized bubble populations we observed in the salt-water environment are to be expected in the ocean. However, we will briefly mention the effect salt has on the physics of bubbles and offer directions to some of the earlier work done by others that concern the entrainment process and give indications as to why the bubble sizes are so much smaller in salt water.

Salt, comprising NaCl and the impurities that come with it, alter the surface properties of the air–water interface. A water jet impinging on a still water surface will drag down the surface of the water, opening up a small wedge-shaped cavity from which bubbles are entrained (see Fig. 1). In reducing the surface tension by introducing salt into the water, the cavity opened up is smaller and results in the production

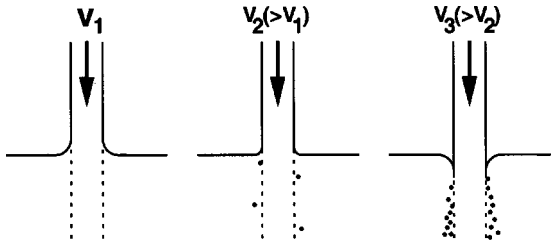

FIG. 1. This figure shows the different degrees of entrainment as a function of jet velocity. Below the threshold velocity v_2, the surface tension causes the water surfaces to adhere to one another. There are no sharp edges or pockets to collapse and form bubbles. As the velocity increases to v_2, the radius of curvature of the meniscus becomes progressively smaller. This is a particularly critical regime for bubble entrainment in that even small deformations of the surface of the water jet can cause bubble entrainment when they hit the horizontal water surface. As the jet velocity is increased even further, the water surface can no longer support the jet and sharp corners and pockets are created, entraining hundreds to thousands of bubbles at a time.

of smaller bubbles. In addition, there are other agents present in ocean waters which impede bubble coalescence, dissolution, and bursting at the surface: The net effect is that in the ocean we expect to see much smaller bubble size distributions within the bubble clouds, and that these bubbles will remain in the water column for longer times. As a direct result of this, salt-water (and in particular, ocean) bubbles and bubble clouds have ''long-term'' properties, occurring over time scales beyond those of typical acoustic emissions from, say, breaking waves. All of these properties, but particularly the extended life of the bubbles in the water column, combine with hydrodynamic effects (such as swell, Langmuir circulation, and turbulence) to cause dramatic changes in the acoustic behavior of such clouds.

Koga[25] performed some controlled experiments involving bubble entrainment when a laminar fluid jet impinges normally on the surface of an identical fluid. He noticed that a cavity opens up alongside the jet which varies in size and shape depending upon the conditions (such as angle of incidence, flow rate, etc.), and that the larger the cavity the more unstable it was. These larger cavities were found to entrain both more and bigger bubbles than those produced by the smaller, more stable cavities. He went on to describe the interaction of the jet with the surface as a balance of forces between the downward, dynamic force produced by the jet flow opposing an upward restoring force from the surface tension. As the flow increases the horizontal surface experiences more downward pull by the jet (which manifests itself as a progressively smaller radius of curvature for the fluid at the jet–surface interface, as illustrated in Fig. 1) until the surface tension is overcome, at which point the surface is then bent downwards and regular entrainment of air bubbles ensues.

Lin and Donnelly[26] also noticed the air cavity between the incoming jet and the deformed surface: For viscous fluids they observed that a thin cavity could extend down to several millimeters below the surface. They also showed that the addition of even a small amount of surfactant has the effect of entraining smaller bubbles. In the light of Koga's work, we see that the addition of a surfactant lowers the surface tension of the fluid and hence reduces the size of the cavity formed by the deformation of the surface. The result is the

TABLE I. Flow rates and mean jet velocities measured over the useful range of the pump controller settings. Below a setting of 35 the pump was not able to force enough water through the system to produce a steady cloud at the pontoon. At a setting of 75 and above the pump was operating at maximum rpm and no further increase in flow rate was possible.

Pump setting (%)	Flow rate (l/s)	Jet velocity (m/s)
35	0.91	1.42
40	1.01	1.57
45	1.12	1.74
50	1.28	1.98
55	1.44	2.23
60	1.54	2.39
65	1.61	2.50
70	1.64	2.54
75	1.67	2.59

entrainment of smaller bubbles. At higher flow rates (with Reynolds numbers of 2000 or more) the fluid jet is no longer laminar and surface irregularities were observed: Upon impact with the horizontal water surface these irregularities also open up cavities and lead to what Lin and Donnelly described as ''vigorous'' entrainment. For the jets investigated in these experiments the Reynolds numbers were in excess of 10 000, putting us well into the regime where we would expect a great deal of entrainment to be continually occurring at the plunging point of the jet.

It is important to point out that tabulated values of the surface tension of water with dissolved NaCl show that the values increase slightly with increasing NaCl concentration. However, Scott[27] points out that ''salt'' contains much more than just NaCl; even the table salt we use in the home contains soaps and other impurities that have surfactant properties. The salt water encountered in the ocean is actually ''dirty'' water in the sense that it will contain a variety of chemical agents that will lower the surface tension. (This will, of course, vary from location to location, but will always be much smaller than for fresh water.) Thorpe and Stubbs[28] did quote measurements of surface tension for both clean and dirty bubbles where the dirty bubbles had a surface tension half of that of the clean bubbles. They also note that the surface action on the dirty bubbles stops them from dissolving as quickly as clean bubbles. Furthermore, in Scott's careful experiments reported in Ref. 27 it was shown that, in the absence of all other impurities, NaCl alone has surface properties which make it more difficult for bubbles to coalesce in NaCl solutions at concentrations relevant to the ocean. Once the small bubbles are produced, there are mechanisms present which inhibit their disappearance by dissolution or coalescence and even retard their bursting at the surface.

I. THE EXPERIMENT

The experiments described in this work were carried out in two parts: One was conducted in the fresh water of Lake Washington, east of Seattle, while the other was carried out in the brackish water of Puget Sound, west of Seattle. With the exception of needing to use portable electrical generators on the Puget Sound part of the experiment, the equipment (see Fig. 2) used was identical to both.

A pontoon platform was constructed from a rigid frame mounted over four large styrofoam floats: these floats were of such a large footprint that they only extended below the water surface by a few centimeters even when the platform was fully loaded. This platform was used to hold a water jet nozzle, an underwater camera and lighting (on adjustable mounts), and a hydrophone and preamplifier. To isolate this system from the noise of the pump and water intake, this float was allowed to drift roughly 20 m away from a boat holding the remainder of the equipment. The intensity of the underwater lighting could be controlled from the boat (2×500 W maximum), as could the pan, tilt, and zoom features of the underwater camera. The bubble plume was generated by directing a fast stream of water from the nozzle at normal incidence onto the water surface.

Figure 3 shows a schematic for the data acquisition system. Video images from the underwater camera for which Figs. 4 and 5 are representative were stored on a high-quality SVHS recorder while simultaneous audio from the hydrophone (after filtering) was recorded onto the audio track: this audio track was used as a reference to match events on the recordings of the DAT recorder which were of much higher fidelity. A digital oscilloscope was used to perform some on-site analysis using its built-in fast Fourier transform (FFT) capabilities.

Water was fed to the nozzle down a 30-m hose held at the surface by floats: the intake end was at the boat, where the water was sucked in using a centrifugal pump driven by a variable-speed motor. (The flow rates were calibrated for each setting of the motor controller as listed in Table I.) A (fairly crude) measure of the void fraction was made by sampling the water for a specific period of time and measuring the volume of air present.

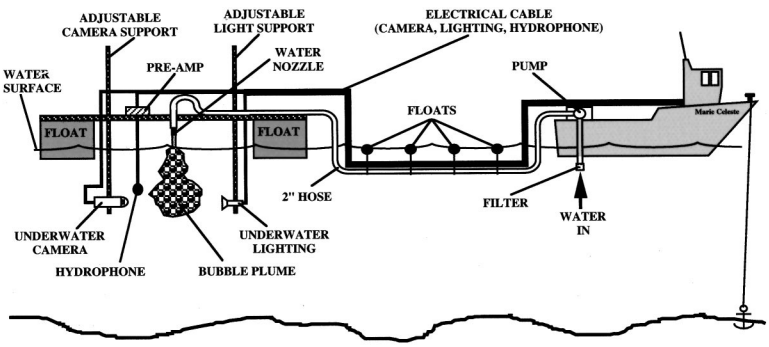

FIG. 2. A schematic of the experimental setup. A pump with its intake hose submerged nearby the boat forced water out through a nozzle approximately 20 m away forming a jet that impinged normally onto the surface. A typical cloud was roughly cylindrical in shape with a length of 50 cm and a diameter of 20 cm. The acoustic emissions were detected using a hydrophone placed outside the cloud and, after filtering, were recorded on a DAT recorder. Simultaneous video images were also recorded on a SVHS VCR.

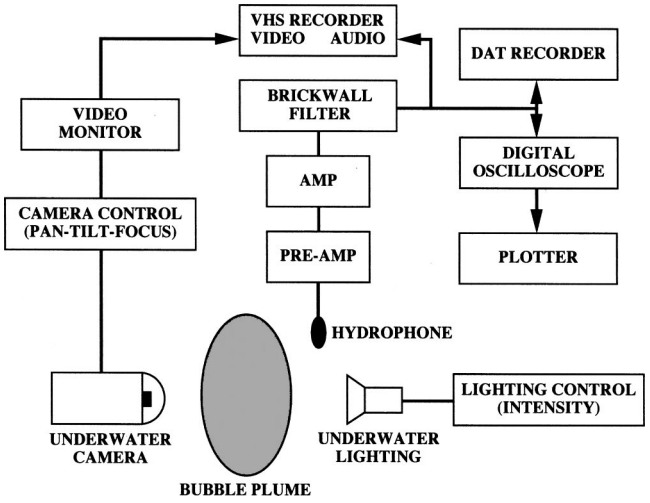

FIG. 3. A schematic for the data acquisition system. Video images from the underwater camera were stored on a high-quality SVHS recorder while simultaneous audio from the hydrophone (after filtering) was recorded onto the audio track: this audio track was used as a reference to match events on the recordings of the DAT recorder which were of much higher fidelity. A digital oscilloscope was used to perform some on-site analysis using its built-in FFT capabilities.

All bubble cloud sizes and individual bubble size measurements were made from images obtained using the underwater video camera. Digital images were later grabbed onto a computer and enhanced using commercially available software. Suitable scales were used *in situ* in order to calibrate these images. When sizing clouds we assumed that, on average, they were azimuthally symmetrical. For sizing the bubbles, the semi-major and semi-minor axes of their elliptical images were measured and their volumes were calculated assuming they are prolate ellipsoids. From this volume a radius is calculated for the equivalent spherical bubble, since it is this quantity that dominates in the calculation of individual bubble resonance frequencies. (Strasberg[13] showed that even drastically deformed bubbles still resonate close to the Minnaert frequency based on spherical bubbles.)

For cloud sizing the camera was mounted several meters away from the cloud, with a meter ruler periodically placed in the field of view for calibration purposes. For individual bubble size measurements, the camera was placed inside the bubble cloud: The camera that was used had a sufficiently small focal length to enable it to clearly see bubbles right outside its pressure dome. In order to reduce bubble-image overlap, a frosted screen was mounted a few centimeters beyond the pressure dome so that only those bubbles passing between the screen and the camera would be viewed. This screen was illuminated from behind using one of the underwater lamps, and a small scale with 1-mm markings was mounted to the bottom edge so that it was continuously in the view of the camera. There was sufficient light present to enable the video camera to be shuttered down to $\frac{1}{500}$ s which prevented blurring of the bubble images as they passed in front of the camera.

Figure 6 shows the bubble size distribution measured in the fresh water of Lake Washington. With the exception of the 60% flow rate, the distributions are similar in shape: The maxima occur at bubble radii between 0.5 and 1 mm with tails on the upper end and very few bubbles with radii below

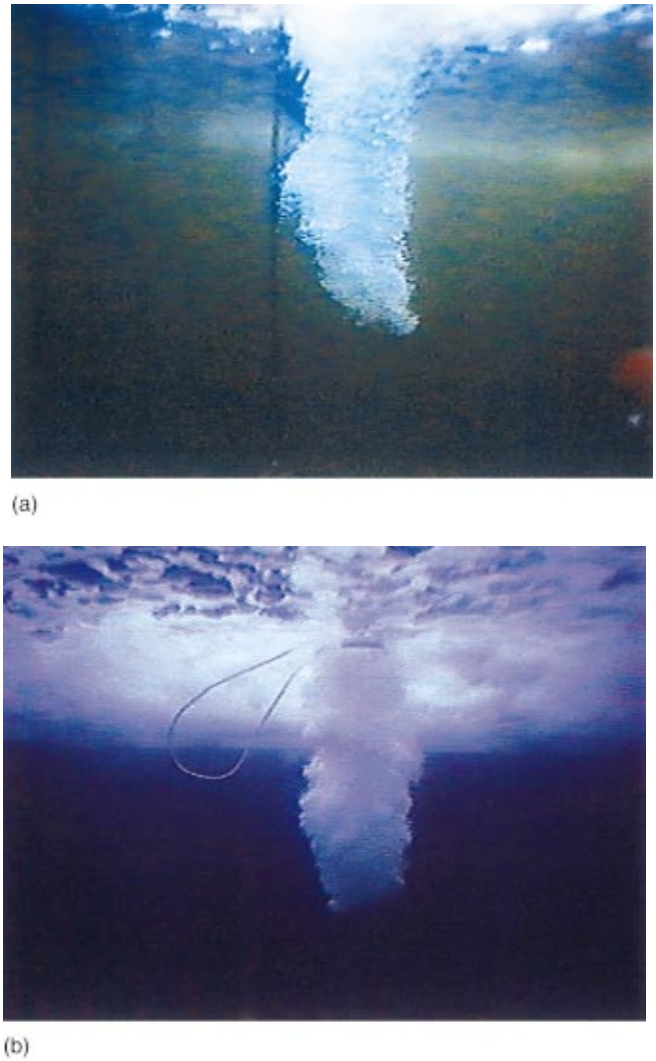

FIG. 4. Typical bubble clouds entrained by a water jet at the surface as observed from below using the underwater video camera. The image in (a) is from the fresh-water phase of the experiment, while the one in (b) is from the salt-water phase. The salt-water cloud had more diffuse edges than the fresh-water cloud and was composed of much smaller bubbles.

0.5 mm. At flow rates of 60% and above there was some difficulty in accurately measuring the bubble size distribution due to excessive image overlapping. However, given the similarity of all the distributions at the lower flow rates we do not expect any significant changes to be occurring at these slightly higher flow rates. In any case, most of the acoustic data used in this current work was for the flow rates where we do have clear measurements of the bubble size distributions.

Figure 7 shows the bubble size distribution for the combined data of all measurements below the 60% flow rate. This figure is based on 632 measurements of bubble volumes, which now enables us to divide the results into smaller bins. One can infer from this figure that the bubble size distribution is log-normal in nature: Fig. 8(a) shows a log-normal least squares fit to the data binned in 0.5-mm bins. We should not be too surprised at this since it has been known for some time[29] that gas bubbles in a turbulent liquid flow are distributed according to a log-normal distribution. We would further expect to see this bubble size distribution in results of ongoing studies looking at bubble fields close to

(a)

(b)

FIG. 5. Portions of the bubble clouds in fresh-(a) and salt-water (b) environments. In the salt-water image one can see the scale used for calibration purposes. The field of view in both cases is roughly the same, which illustrates that the bubbles entrained in the fresh-water environment are much larger than those of the salt-water case.

the surf zone, where there will be more fully developed turbulence present from the action of breaking waves.

Extracting the bubble size distribution for the salt-water experiments proved to be far more difficult than for the fresh-water experiments. On each captured video image there were many hundreds of bubble images, all of which had to be carefully measured in order to avoid any biasing that might be occurring from one part of the image to another. (By contrast, each fresh-water image contained only a few tens of bubbles to be sized.) Furthermore, the bubbles were much smaller in the salt water, and it was clear from the images that there were clouds of microscopic bubbles present that were far too small to be resolved on the video images. However, we were able to make measurements for the upper sizes in the distribution, the results of which are shown in Fig. 9 for two flow rates. (Making comprehensive and accurate measurements from the salt-water bubble images was too time consuming to allow more than two flow rates to be analyzed. Additional measurements would in any case have very little further to add to the experiment.) The sharp dropoff on the low end of the distribution at radii of 0.2 mm is a direct result of the minimum bubble sizes that could be measured: Bubbles with volumes below roughly 0.034 mm^3 could not be resolved. Figure 8 shows the log-normal fit to the salt-water bubble size distribution in which a minimum size (radius) cutoff of 20 μm has been assumed: This is likely to be a slight underestimate of the minimum size given that many experimenters in the past have measured distributions in sea water that cut off anywhere from roughly 10 μm up to roughly 40 or 50 μm, depending on the conditions present.[30–32] Sea water has higher salinity and, when breaking events are present, higher dissolved gas concentrations than the brackish waters encountered in Puget Sound: higher salinity and higher dissolved gas concentrations both tend to raise the lower cutoff for the bubble size distribution. (The lower salinity causes larger bubbles to be entrained at the surface, and the lower dissolved gas means that any small bubbles present will tend to dissolve into solution more rapidly.)

Measurement of the gross bubble cloud dimensions was a relatively straightforward task since the object being sized, namely the bubble plume, was quite large and filled a substantial portion of the video images. As mentioned earlier, calibration of the images was achieved by periodically placing a suitable measure in the field of view of the underwater video camera. The results for fresh and salt water are shown in Figs. 10 and 11, respectively. The cloud widths were found by measuring the vertical cross-sectional area of the cloud and then dividing by the length. Each point on the four plots in these two figures are based on ten measurements, the error bars being the standard deviation of these ten measurements.

Only a fairly crude measurement of the cloud void fraction was available at the time of these experiments. The air entrained close to the surface was carried down to depth by the fluid flow and then moved outwards and upwards, returning to the surface primarily due to its own buoyancy. It was these returning bubbles that were collected by allowing them to displace water from a cylindrical container of known volume and cross-sectional area. From the cloud video images we calculated an approximate rise velocity for these bubble clouds, and hence were able to estimate the void fraction from this. The results are shown in Fig. 12: It should of course be emphasized that this method only samples the returning air, and we would certainly expect some variation towards the core of the cloud (where entrainment is occurring and the bubbles are carried downwards) and out towards the edge of the cloud (where the bubble density becomes more diffuse).

There are several sources of uncertainty in the measurement of the void fraction. By far the largest is the determination of the average bubble rise velocity, but there are also uncertainties in the volume of air collected, the time taken to perform this collection, the effect that the measurement process itself has on the quantity being measured, and the possibility that a portion of (especially) the smaller bubbles are evading detection. All combined, we estimate our measurement of the void fraction to have uncertainty between 15% and 20%.

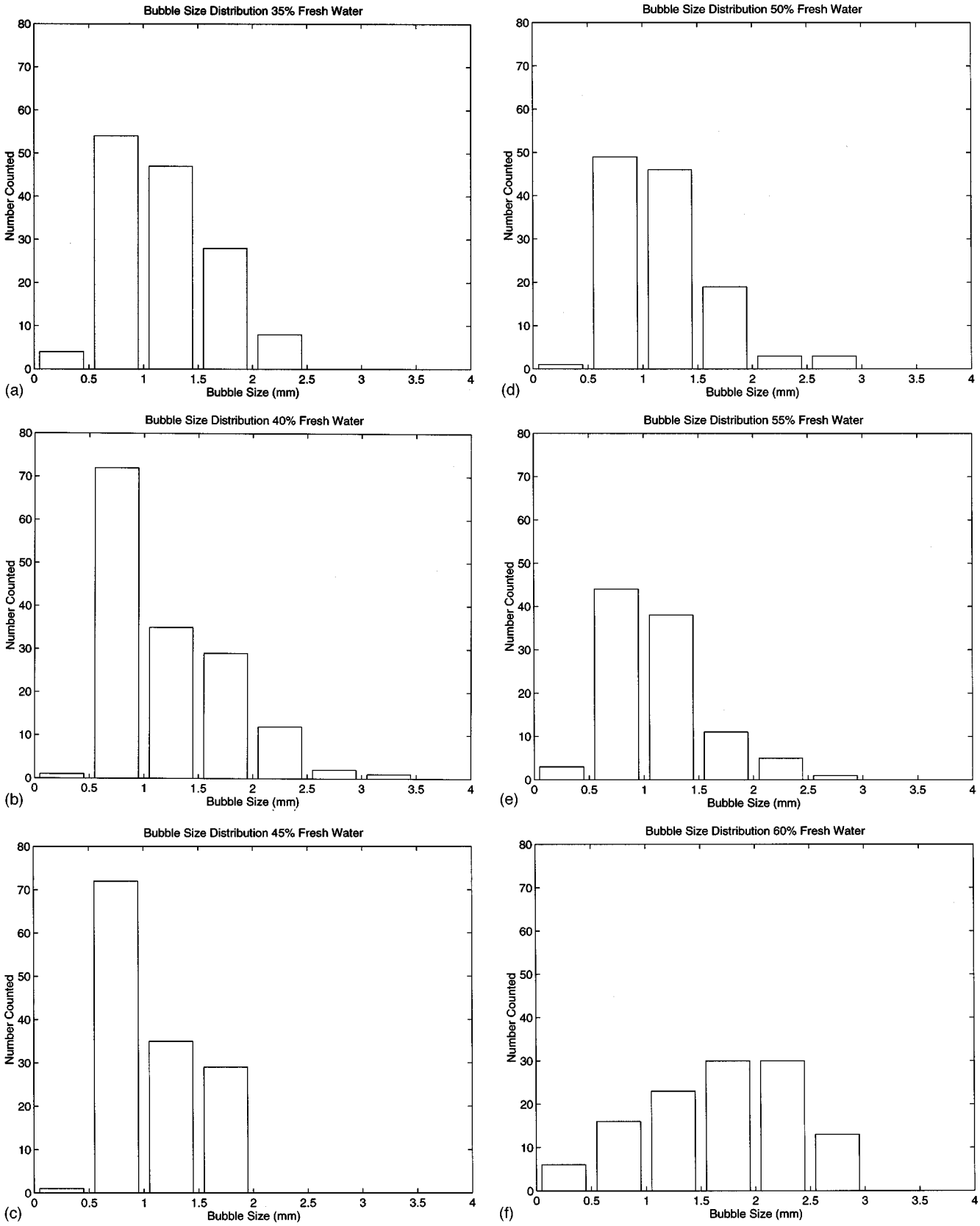

FIG. 6. Bubble size distributions measured in the fresh-water of Lake Washington. The sequence of (a)–(f) is for flow rates of 35%, 40%, 45%, 50%, 55%, and 60% respectively, and are compiled using 142, 151, 116, 121, 102, and 119 bubble images, respectively. At flow rates of 60% and above there were difficulties in measuring the bubble sizes due to image overlap, which resulted in the bubble size distribution losing its log-normal shape: These higher flow-rate distributions in fresh water were therefore taken to be unreliable. The bubble sizes were measured from images obtained with an underwater video camera: the recorded images were grabbed onto a computer and reduced using commercially available software.

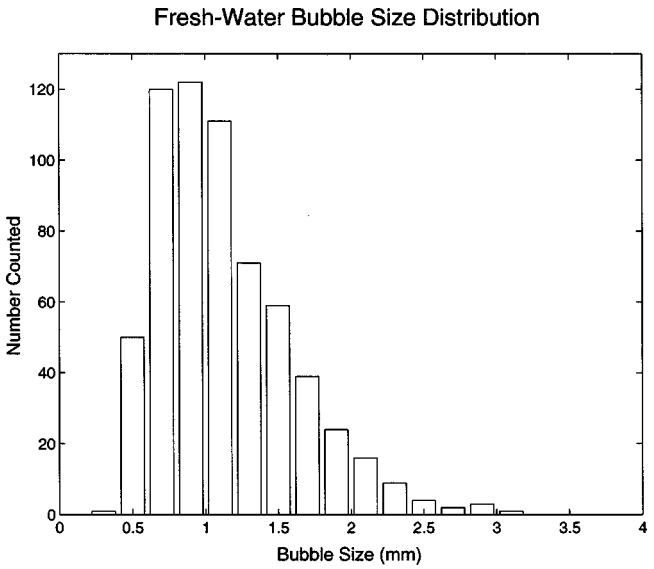

FIG. 7. The bubble size distribution in fresh water for the combined data from flow rates of 35%–55%. These data encompass all the flow rates where there are reliable bubble size measurements and where most of the acoustic measurements were made. There is a theoretical basis (see Ref. 29) for expecting this log-normal distribution of bubble sizes in such a turbulent flow field.

II. THEORETICAL CONSIDERATIONS OF LOW-FREQUENCY AMBIENT NOISE DUE TO BUBBLE ENTRAINMENT

A. Collective oscillations as resonant cavities

While there have been several previous works addressing many of the issues surrounding low-frequency collective bubble oscillations, the bubble cloud geometries have been limited in nature. The two most often used geometries are cylindrical clouds which span the entire water column within fresh-water tanks and semi-spherical clouds in the open ocean.[6,22,23] Neither of these geometries are close to that currently under investigation, the former because the cloud in this experiment occupied only about 5% of the water column, and the later because we are in the near field for the frequencies being considered here whereas open ocean studies have concentrated on the far field. A further complication is that the wave-guide nature of the experimental locations creates boundary conditions that differ from those used in the literature and which must be addressed in order to solve the problem correctly.

The collective oscillation of bubbles within a cloud is essentially acoustic energy within a leaky resonant cavity. This can be seen by considering more closely the phase speed in the interior of the cloud. Acoustic energy is trapped within the cloud by virtue of the fact that the cloud has a large impedance mismatch with the liquid outside the cloud; this is due to a large positive gradient in the phase speed as one moves from the interior of the cloud through the less densely populated outer sheath and on out to the pure liquid. A correct treatment of the physics of the cloud results in a formula for the wave number spectrum in the bubbly mixture, the real part of which reduces to (1) at frequencies well below bubble resonance.[6,10] The imaginary part of the wave number spectrum corresponds to the dampening effect cre-

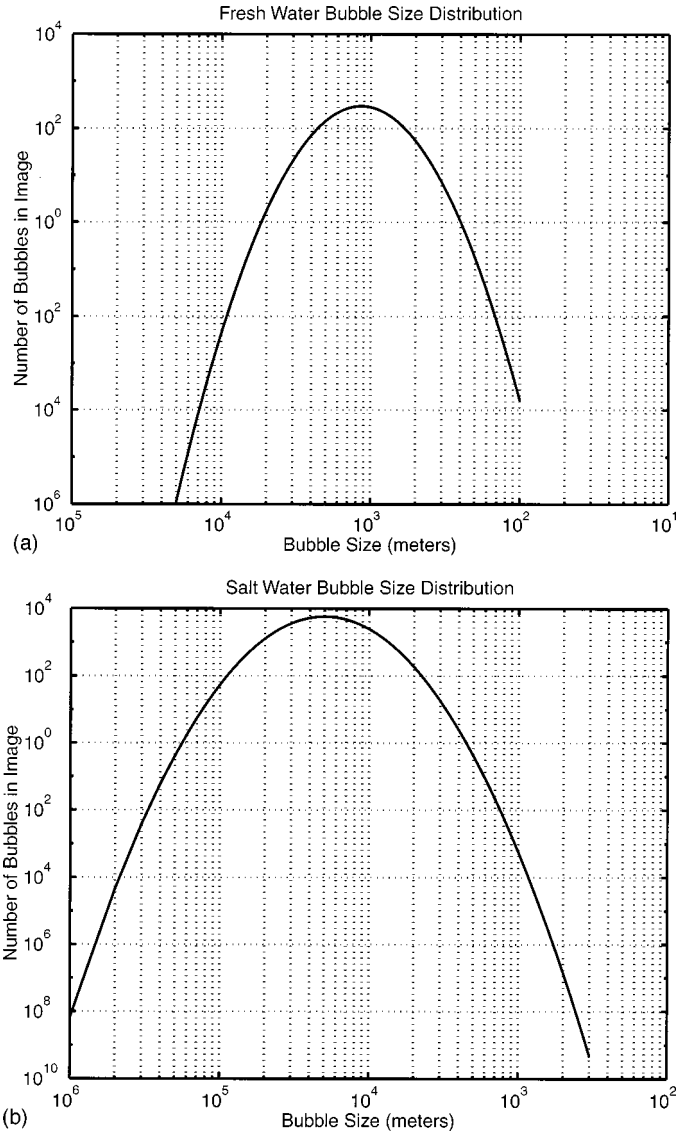

FIG. 8. In (a) we show the least-squares fit to the fresh-water bubble size distribution as presented in Fig. 7, while (b) shows the least-squares fit to the salt-water bubble size distribution as presented in Fig. 8. As can be seen from the log-log plots, the curves are parabolas, indicating that the best fits to the bubble size distributions are log-normal.

ated by the acoustic absorption (i.e., conversion of acoustic energy into the heat). As different sized bubbles resonate and absorb at different rates the wave number must be a quantity which is a function of the bubble size distribution[10,20]

$$k_{\text{int}}^2=\frac{\omega^2}{c_{\text{ext}}^2}+4\pi\omega^2\overline{n}\int_0^\infty\frac{a\phi(a)\,da}{\omega_0^2-\omega^2+2ib\omega}, \tag{3}$$

where the subscripts ''int'' and ''ext'' refer to values internal and external, respectively. In (3) $\overline{n}$ is the average number of bubbles per unit volume, and $\phi(a)$ is the bubble-size distribution, normalized such that

$$\int_0^\infty\phi(a)\,da=1. \tag{4}$$

The resonance angular frequency, ω_0 $(=2\pi f_0)$, and dampening constant b appearing in (3) are functions of the the ratio of specific heats γ $(=1.4)$, the surface tension

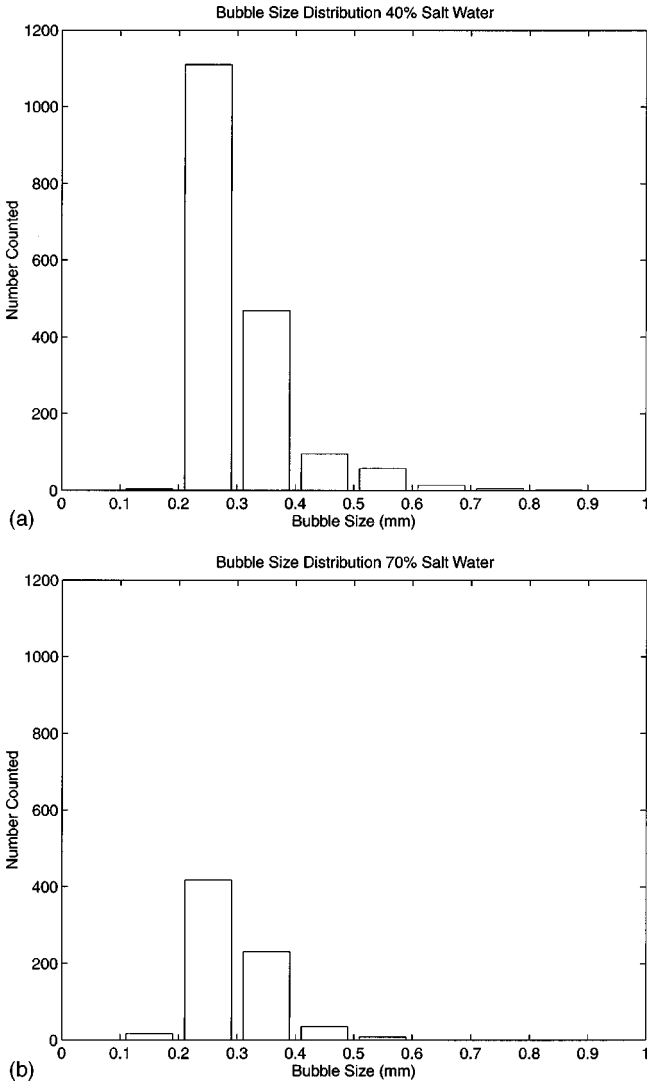

FIG. 9. Bubble size distributions measured in the brackish water of Puget Sound. (a) is the distribution for a flow setting of 40%, based on 1755 bubble images. In (b) is the distribution for a flow setting of 70%, based on 708 bubble images. One can immediately see how much smaller the bubbles are in the salt-water: the image overlap problems present for the higher flow rates in the fresh water of Lake Washington were not present here, making it possible to size the bubbles at the maximum flow rates. Unlike the situation for the fresh-water bubble size measurements, the sharp drop in (equivalent) bubble radii below roughly 0.2 mm is a direct result of the resolution of the digitized images; bubbles with volumes less than roughly 0.034 mm^3 could not be resolved.

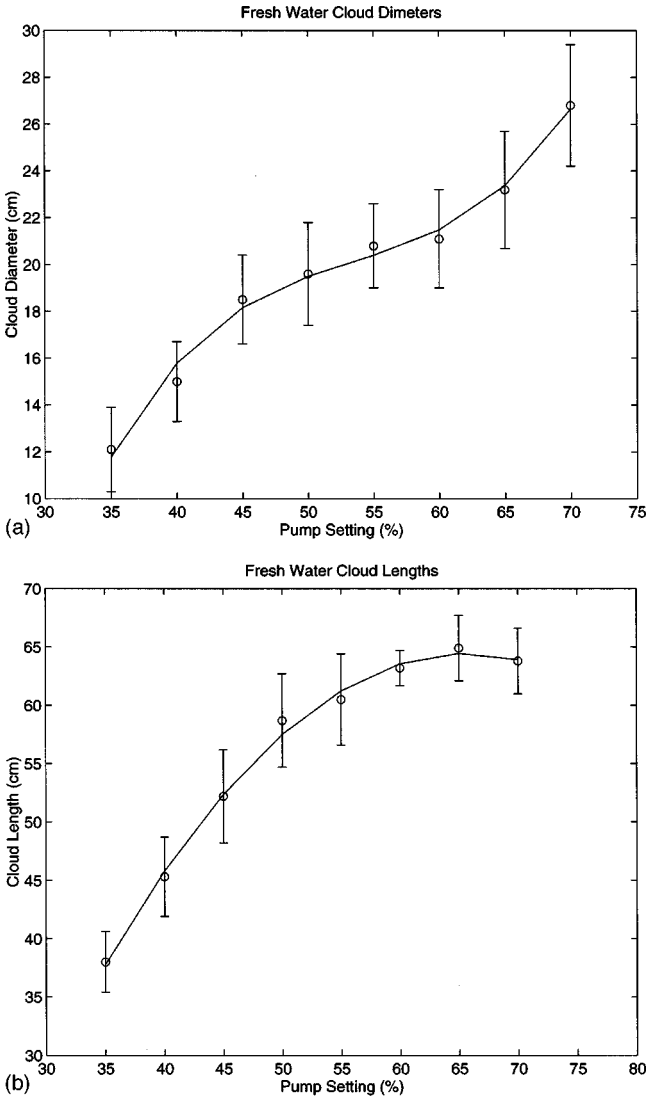

FIG. 10. Cloud sizes [cloud width in (a), cloud length in (b)] for the fresh-water environment of Lake Washington, as a function of the jet flow rate (in arbitrary units). Each point is the average of ten measured values, the error bars being the standard deviations of those ten values. The solid lines represent the least-squares fit to the data using a cubic polynomial.

σ (=0.079 N/m for fresh water and =0.06 N/m for salt water), the kinematic viscosity μ (=0.001307 Ns/m^2), the bubble radius a, the ambient pressure P_∞ ($=1.11135\times10^5$ Pa), the *Laplace* pressure P_{Laplace}, the thermal diffusivity D, the thermal conductivity in water $\kappa=0.024\,42$ W/(mK), and the angular frequency ω ($=2\pi f$) through the set of equations[10,20]

$$P_{\text{Laplace}}=2\sigma/a, \tag{5}$$

$$D=\frac{(\gamma-1)\kappa T}{\gamma P_\infty}, \tag{6}$$

$$P_0=P_\infty+P_{\text{Laplace}}=P_\infty+\frac{2\sigma}{a}, \tag{7}$$

$$\chi=\frac{D}{\omega a^2}, \tag{8}$$

$$\Phi=\frac{3\gamma}{1-3(\gamma-1)i\chi[\sqrt{i/\chi}\coth(\sqrt{i/\chi})-1]}, \tag{9}$$

$$\omega_0^2=\frac{P_0}{\rho a^2}\left(\mathrm{Re}(\Phi)-\frac{2\sigma}{aP_0}\right), \tag{10}$$

$$b=\frac{2\mu}{\rho a^2}+\frac{P_0}{2\rho a^2\omega}\mathrm{Im}(\Phi)+\frac{\omega^2 a}{2c_{\text{ext}}}. \tag{11}$$

At the frequencies of interest here, well below the resonance frequency of the biggest of bubbles, both the phase speed and attenuation are relatively insensitive functions of the void fraction. As can be seen from Fig. 12, jet velocities in the salt-water portion of the experiment have corresponding void fractions to those found in fresh water at about a 10% reduction in jet velocity. Yet, to investigate whether the

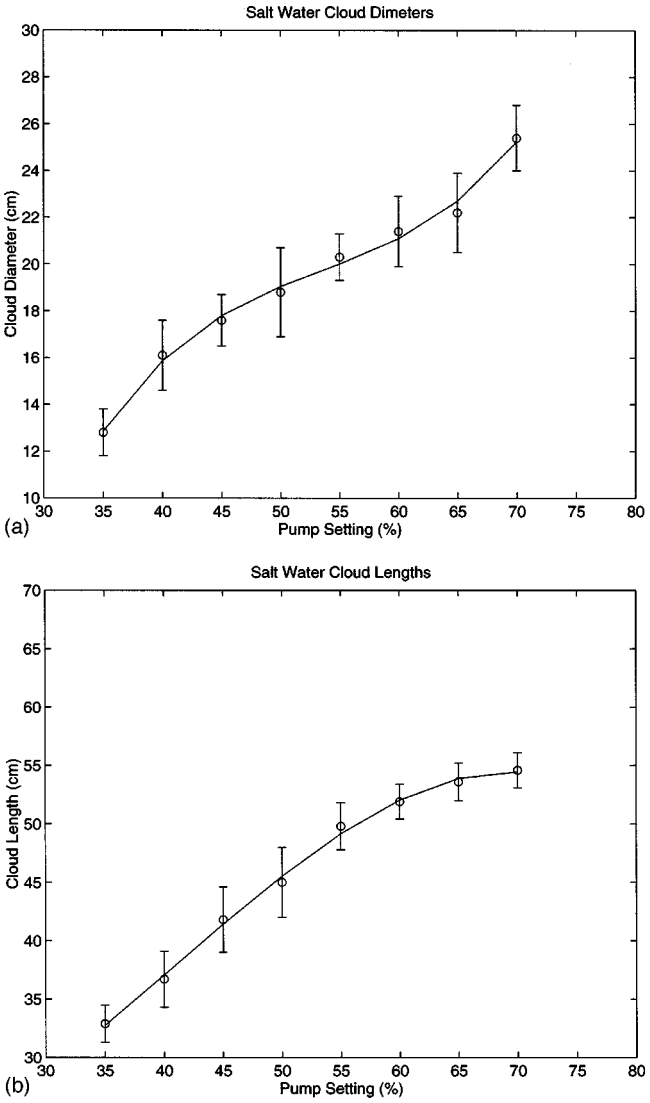

FIG. 11. Cloud sizes [cloud width in (a), cloud length in (b)] for the salt-water environment of Puget Sound, as a function of the jet flow rate (in arbitrary units). Each point is the average of ten measured values, the error bars being the standard deviations of those ten values. The solid lines represent the least-squares fit to the data using a cubic polynomial.

acoustic emissions from the clouds were due to collective effects, a fair basis of comparison was determined to be the corresponding cloud size. Picking the closest void fraction to 1% and clouds with approximately the same length, we will use data from the 40% flow rate from the fresh-water portion of the experiment and 50% flow rate from the salt-water portion. These flow rates correspond to a void fraction of 1.25% (i.e., $\beta = 0.0125$) and a cloud height of $h = 0.45$ m. Using the log-normal bubble size distributions fit to the experimental data we have calculated the phase-speed and attenuation curves using (3) and the relations

$$c_0 = \frac{\omega}{\mathrm{Re}\,(k_{\mathrm{int}})}\ \mathrm{m/s}, \tag{12}$$

$$A = 20 \log_{10}(e)\,\mathrm{Im}\,(k_{\mathrm{int}})\ \mathrm{dB/m} \tag{13}$$

(see Figs. 13 and 14). The phase speed in both the fresh and salt water are more than an order of magnitude less than that of the surrounding liquid (c_{ext} is taken to be iso-velocity and

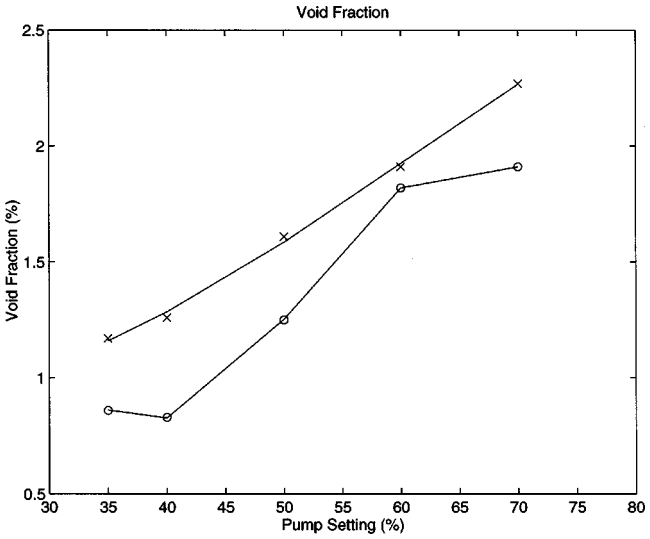

FIG. 12. Cloud void fraction as a function of jet flow rate (in arbitrary units) for the fresh-water (×'s) and salt-water (○'s) environments. Because of the importance of void fraction a proper comparison of the two phases of the experiment is valid only for flow rates which produce similar void fractions. Thus the data for a 50% flow in salt water was compared with the data for a 40% fresh-water flow (both generating clouds with a void fraction of approximately 1.25%).

1500 m/s): Yet, the maximum difference between the phase speeds (that is between fresh and salt water) represents only 0.67% of the phase speed in water. Also it can be seen from Figs. 10 and 11 that the cloud geometries are very similar for these flow rates. Consequently, one would expect, *a priori*, that the resonant behavior will be similar between the 40% fresh-water and 50% salt-water data.

Having defined the geometry and the wave number spectra in the interior of the cloud, we must relate the physics of sound-generating mechanisms of individual bubbles to the acoustical properties of the cloud in order to determine

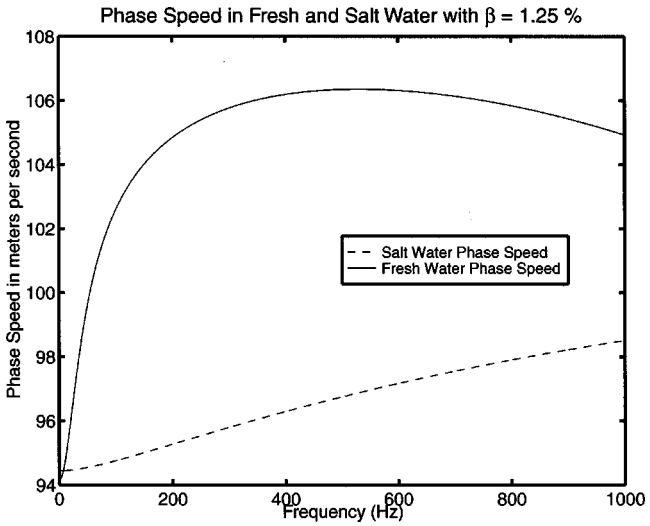

FIG. 13. Phase speed in the bubbly mixture as a function of frequency. The difference between these curves is only about 0.67% of the phase speed in the water outside the clouds. We can conclude that changes in the resonant behavior are minimally affected by differences in the bubble size distributions for frequencies this far below the resonant frequencies of the bubbles. In this frequency regime only the gross void fraction of the bubble cloud drives the phase speed.

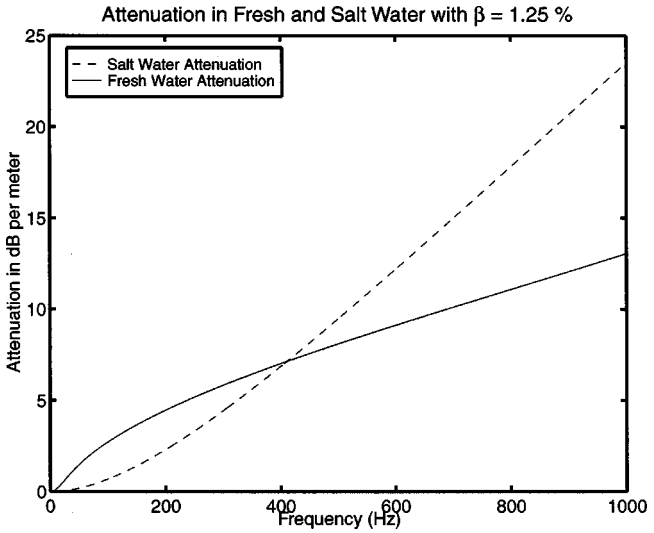

FIG. 14. Attenuation as a function of frequency in a bubbly mixture with a void fraction of 1.25%. For the clouds considered in this experiment sound generated at the center of these clouds will be attenuated by no more than 5–6 dB in traversing to the exterior.

the resonant behavior. This is because the resonant cavities created by the jet are acoustically driven by the combined contributions of the bubbles set into excited states by the entrainment process. The measured quantity is the sound level (SL), defined in dB by[33]

$$\mathrm{SL}=10\log_{10}|\tilde{S}(\mathbf{r},\omega)|^2, \tag{14}$$

where $\tilde{S}(\mathbf{r},\omega)$ is the spectral function

$$|\tilde{S}(\mathbf{r},\omega)|^2=\frac{4\pi|\tilde{P}(\mathbf{r},\omega)|^2}{TP_{\mathrm{ref}}^2/\mathrm{Hz}}. \tag{15}$$

Here T is the total time of the sampling interval, P_{ref} is the reference pressure level taken as 1 μPa, and $\tilde{P}(\mathbf{r},\omega)$ is the time-averaged Fourier transform of the pressure.[6,22,33]

To start we make the usual *ansatz* of superposition, i.e., that $\tilde{P}(\mathbf{r},\omega)$ can be represented as a sum of complex pressures; each contribution to the total field comes from the pressure field created by an individual bubble. Furthermore, we suppose that the field contribution from each bubble can be separated into that portion due to the strength of the source and that which is the solution to the boundary-value problem with a unit source at each bubble position $\mathbf{r}_n$, so that

$$\tilde{P}(\mathbf{r},\omega)=\sum_n \tilde{P}_{BV}(\mathbf{r},\mathbf{r}_n',\omega)\times\tilde{P}_B(\mathbf{r}_n',\omega), \tag{16}$$

where $\tilde{P}_B(\mathbf{r}_n',\omega)$ is the spectral contribution from a bubble at position $\mathbf{r}_n'$, and $\tilde{P}_{BV}(\mathbf{r},\mathbf{r}_n',\omega)$ is the solution to the boundary-value problem [i.e., $\tilde{P}_{BV}(\mathbf{r},\mathbf{r}_n',\omega)=\mathrm{G}_\omega(\mathbf{r}|\mathbf{r}')$ where $\mathrm{G}_\omega(\mathbf{r}|\mathbf{r}')$ is the Green's function for the acoustic wave equation].

Clearly the physical system under consideration (i.e., jet, bubbles, and cloud) is dynamic, and as such (16) will be implicitly, if not explicitly, time dependent. A solution to this type of deterministic problem is beyond the scope of this work, since this would require a full solution to the *Navier–Stokes* equation. Fortunately the acoustic data are composed of long records that the effects associated with time dependence can be averaged out and a relatively good spectrum can be obtained. Henceforth we will consider all quantities to be their time-averaged ones and thus T in (15) can be normalized to one. As long as we are interested in the field outside the cloud we may redefine the averaged pressure field as

$$\langle\tilde{P}(\mathbf{r},\omega)\rangle=\tilde{P}_{bv}(\mathbf{r},\omega)\times\tilde{P}_S(\omega), \tag{17}$$

where now $\tilde{P}_{bv}(\mathbf{r},\omega)$ is the solution to the boundary-value problem with a constant boundary condition defined over the cross-sectional area at the top of the cloud. $\tilde{P}_S(\omega)$ is now the effective source function over the disk at the top of the cloud [see Fig. 15(a)], which accounts for all of the bubbles en-

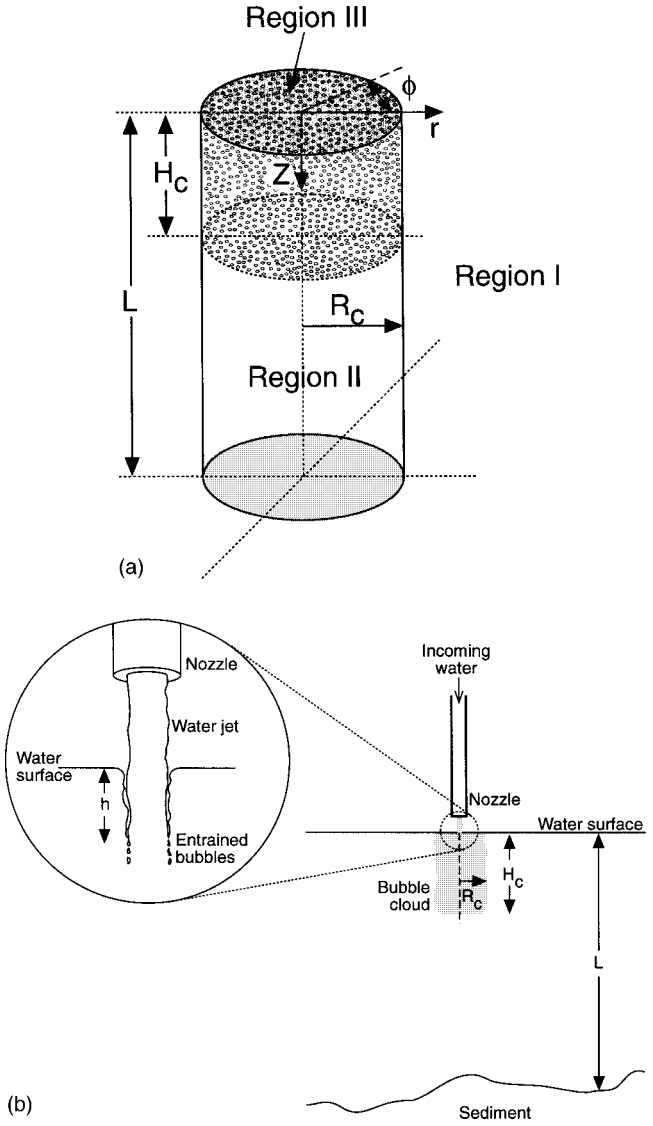

FIG. 15. The geometry encountered in this experiment, shown here, is that of a cylindrical bubble cloud entrained at the surface, occupying only a fraction of the water column, extending from the water surface down to a depth of H_c. The fluid flow created by the jet flow forces the bubbles to some depth, H_c, before they leave the area of the downward forces and begin to rise under their own buoyant forces. The boundary conditions on the bottom at $z=L$ are now either of Neumann or mixed type, depending on the composition of the bottom.

trained. By equating the acoustic energy flux of $\tilde{P}_S(\omega)$ through the disk at the top of the cloud with that due to the total sum of the bubbles themselves through the surface area of the cloud we can apply Gauss' theorem to find the relation[6,22]

$$\pi R_c^2 |\tilde{P}_S(\omega)|^2 = \int_{\Sigma_C} d \sum_C \left(N_T \int_{a_{\min}}^{a_{\max}} da\ \phi(a) |\tilde{P}_b(\mathbf{r},\omega)|^2 \right), \tag{18}$$

where N_T is the average number of bubbles entrained in a given time T, R_c is the radius of the cloud, Σ_C is a cylindrical surface surrounding the bubble cloud, and $\tilde{P}_b(\mathbf{r},\omega)$ the pressure field induced by a single bubble of radius a.

B. Dipole source functions

The method of describing the strength of the bubbles as acoustic sources is accomplished by considering an oscillating bubble close to a pressure-release surface: Together with its image source formed by reflection through that surface this pair forms a dipole. This approximation is strictly speaking only valid in the regime $kd \ll 1$, where d is the magnitude of the dipole separation vector (for our experimental setup this is essentially twice the depth of average bubble formation). Counter-intuitively this condition is certainly met for the lower frequencies under consideration here (i.e., $f < 500$), but not necessarily for higher frequencies; this is entirely due to the functional dependence of the phase speed upon the frequency. (See Fig. 13.) Nevertheless, we assume for the purposes of this calculation that this condition is satisfied.

Consider a time-dependent acoustic field in the far-field from a single oscillating bubble. The dipole strength is determined from the leading-order contribution of a series expansion of the pressure field: The term we seek is that proportional to $1/r$ and is given through the relation

$$\lim_{r\to\infty} P_b(t - r/c_0) = \frac{D_0 \cos\theta}{r} \exp[-b(t - r/c_0)] \times \cos[\omega_0 t - k_0 r + \theta_0], \tag{19}$$

where ω_0 is the natural resonance frequency of the bubble, c_0 is the phase speed of the bubbly mixture at that resonance frequency, k_0 is the associated wave number, θ_0 is the phase of oscillation of the bubble at $t=0$, and D_0 is the ''dipole strength.'' To determine the frequency response of the term $P_b(t - r/c_0)$ we Fourier transform (19) and hence $|\tilde{P}_b(\mathbf{r},\omega)|^2$ is defined as

$$|\tilde{P}_b(\mathbf{r},\omega)|^2 \approx |\tilde{D}(\omega)|^2 \frac{\cos^2\theta}{r^2}, \qquad |\tilde{D}(\omega)|^2 = \frac{D_0^2}{2\pi} \frac{\omega_0^2}{(b^2 - \omega^2 + \omega_0^2)^2 + 4\omega^2 b^2}. \tag{20}$$

We are left only with determining the appropriate value to use for the dipole strength.

Pumphrey and Ffowcs-Williams discussed three different causes of bubble oscillations that might give large enough sound levels and derived their respective dipole strengths.[34] They are *hydrostatic* and *Laplace* pressures, surface oscillations that couple into the volume oscillation modes, and forces associated with the liquid and the initial bubble wall velocity. Of these three only the last mechanism is thought to be significantly large enough to explain the rather high observed source levels. The dipole strength due to this mechanism is given by

$$D_0 = 2\rho c_0 k_0^2 a^2 h U_0, \tag{21}$$

where h is the depth of the bubble at pinch-off, and U_0 is the initial velocity of the bubble wall. Some recent studies have corroborated this by suggesting that it is this converging fluid flow around the neck of a pocket of air near pinch-off which is the most important for setting the bubble into an oscillating excited state. Basically the fluid (at the moment of pinch-off) has nowhere to go except up and down. This results in upward and downward directed jets, the downward one being responsible for exciting the bubble.[22]

C. The boundary-value problem

From the video images captured during these experiments it is evident that the source mechanisms could not possibly have been well localized. The dynamical effects of the incoming jet caused bubble pinch-off, turbulence, and the pinch-off of smaller clouds that separated from the main bubble plume, all of which occur at different places within the overall structure of the cloud. The dipole strength of an individual bubble is linearly (21) dependent upon its distance from the surface, and so bubbles formed at greater depths will have a much larger contribution to the acoustic excitation of the whole bubble cloud. We will err on the side of weaker stimulation and assume that the vast majority of the bubbles are created within a few centimeters of the surface. Thus the impulse response (i.e., P_{BV}) of the cloud is calculated by solving the relevant boundary-value problem where the field is identity at the top of the cloud (i.e., $z=0$ and $r < R_c$) and zero at the other boundaries.[6,22]

The composition of the sediment in the vicinity of the experiment consisted of several meters of silt. The relatively low sound speed of this type of medium allows us to simplify the problem considerably by making the bottom boundary conditions approximately Dirichlet, i.e., $P=0$. Following the definitions in Fig. 15(b), we define $P^{(1)}$ as the pressure in the cloud itself, $P^{(2)}$ to be the pressure beneath the cloud, and $P^{(3)}$ as the pressure outside the cylindrical surface defined by $r=R_c$. The boundary conditions for such a physical system are

$$P^{(1)}(z=0) = 1, \tag{22}$$

$$P^{(3)}(z=0) = 0, \tag{23}$$

$$P^{(2)}(z=L) = 0, \tag{24}$$

$$P^{(3)}(z=L) = 0, \tag{25}$$

$$P^{(1)}(z=H_c; 0 \le r \le R_c) = P^{(2)}(z=H_c; 0 \le r \le R_c), \tag{26}$$

$$P^{(1)}(0 \le z \le H_c; r=R_c) = P^{(3)}(0 \le z \le H_c; r=R_c), \tag{27}$$

$$P^{(2)}(H_c \le z \le L; r=R_c) = P^{(3)}(H_c \le z \le L; r=R_c), \tag{28}$$

$$\left.\frac{\partial P^{(1)}}{\partial z}\right|_{\substack{z=H_c \\ 0\leqslant r\leqslant R_c}} = \left.\frac{\partial P^{(2)}}{\partial z}\right|_{\substack{z=H_c \\ 0\leqslant r\leqslant R_c}}, \tag{29}$$

$$\left.\frac{\partial P^{(1)}}{\partial r}\right|_{\substack{0\leqslant z\leqslant H_c \\ r=R_c}} = \left.\frac{\partial P^{(3)}}{\partial r}\right|_{\substack{0\leqslant z\leqslant H_c \\ r=R_c}}, \tag{30}$$

$$\left.\frac{\partial P^{(2)}}{\partial r}\right|_{\substack{H_c\leqslant z\leqslant L \\ r=R_c}} = \left.\frac{\partial P^{(3)}}{\partial r}\right|_{\substack{H_c\leqslant z\leqslant L \\ r=R_c}}. \tag{31}$$

Technically all axial modes will be present, yet we will use the simplifying approximation that the time average shape of the cloud is that of a cylinder and thus only axially symmetric solutions time average to nontrivial values. The general solutions, $P^{(1)}$, $P^{(2)}$, and $P^{(3)}$, can easily be written as a combination of a *Fourier* and *Dini* series.[35] Because of the physical prescription for the wave number in the bubbly mixture the boundary conditions at the radial boundary of the cloud and the water column ($r=R_c$), as well as the base of the cloud ($z=H_c$), must be matched through the constant coefficients of the series representations. In view of this, the most general form of the solution field for each region is

$$P^{(1)}=\sum_{N=1}^{\infty}\left[A_N^{(1)}\sin[\lambda_n^{(1)}z]\frac{J_0(\mu_n^{(1)}r)}{J_0(\mu_n^{(1)}R_c)} + B_n^{(1)}\frac{\cos[\gamma_n^{(1)}(z-H_c/2)]}{\cos[\gamma_n^{(1)}H_c/2]}J_0(\nu_n r)\right], \tag{32}$$

$$P^{(2)}=\sum_{n=1}^{\infty}\left[A_n^{(2)}\sin[\gamma_n^{(2)}(z-L)]\frac{J_0(\mu_n^{(2)}r)}{J_0(\mu_n^{(2)}R_c)} + B_n^{(2)}\frac{\sin[\gamma_n^{(2)}(z-L)]}{\sin[\gamma_n^{(2)}(H_c-L)]}J_0(\nu_n r)\right], \tag{33}$$

and

$$P^{(3)}=\sum_{n=1}^{\infty}\left[A_n^{(3)}\sin[\lambda_n^{(3)}z]\frac{H_0^{(1)}(\mu_n^{(3)}r)}{H_0^{(1)}(\mu_n^{(3)}R_c)}\right]. \tag{34}$$

For the *Fourier* series part of the solutions in (32)–(34) the vertical wave numbers $\lambda_n^{(1)}$, $\lambda_n^{(2)}$, and $\lambda_n^{(3)}$ are given by

$$\lambda_n^{(1)}=\frac{n\pi}{H_c}, \tag{35}$$

$$\lambda_n^{(2)}=\frac{n\pi}{H_c-L}, \tag{36}$$

$$\lambda_n^{(3)}=\frac{n\pi}{L}, \tag{37}$$

and the radial wave numbers $\mu_n^{(1)}$, $\mu_n^{(2)}$, and $\mu_n^{(3)}$ are given by

$$\mu_n^{(1)}=\sqrt{k_{\text{int}}^2-\lambda_n^{(1)^2}}, \tag{38}$$

$$\mu_n^{(2)}=\sqrt{k_{\text{ext}}^2-\lambda_n^{(2)^2}}, \tag{39}$$

$$\mu_n^{(3)}=\sqrt{k_{\text{ext}}^2-\lambda_n^{(3)^2}}. \tag{40}$$

The second terms in (32) and (33) are formally called a *Dini* series.[35] As opposed to a *Bessel* series the ν_n's are the zeros of the derivative of the Bessel function J_0, i.e., $J_1(\nu_n R_c)=0$. By using this fact in conjunction with the boundary conditions of (22) and (26), we can immediately set all of the constants $B_n^{(1)}$ and $B_n^{(2)}$ to zero, except for $B_1^{(1)}$ and $B_1^{(2)}$, which are both one identically [because $\nu_1=0$ and $J_0(0)=1$]. Thus (32) and (33) become

$$P^{(1)}=\frac{\cos[k_{\text{int}}(z-H_c/2)]}{\cos[k_{\text{int}}H_c/2]} + \sum_{n=1}^{\infty}A_n^{(1)}\sin[\lambda_n^{(1)}z]\frac{J_0(\mu_n^{(1)}r)}{J_0(\mu_n^{(1)}R_c)} \tag{41}$$

and

$$P^{(2)}=\frac{\sin[k_{\text{ext}}(z-L)]}{\sin[k_{\text{ext}}(H_c-L)]} + \sum_{n=1}^{\infty}A_n^{(2)}\sin[\lambda_n^{(2)}(z-L)]\frac{J_0(\mu_n^{(2)}r)}{J_0(\mu_n^{(2)}R_c)}. \tag{42}$$

It is seen that (41) and (42) represent solutions which satisfy the boundary conditions on the surface and bottom and the conservation of pressure between regions one and two. The conservation of particle velocity between regions one and two, (29), and the other interface conditions (26) and (27) and (30) and (31) all have to be satisfied by matching the series coefficients $A_n^{(1)}$, $A_n^{(2)}$, and $A_n^{(3)}$. This is accomplished by taking various inner products of the solution series and equating terms. In this way a set of simultaneous equations is developed for each frequency that is solved using standard linear algebra techniques.

III. RESULTS AND DISCUSSION

Long acoustic time series (several minutes) were recorded in both the fresh- and salt-water environments for a range of jet flow rates. From listening to a loudspeaker set to broadcast the incoming signal, it was noted that there were marked differences between the two environments. In the case of the fresh-water environment there were three distinct types of sounds that could be discerned. The most prominent of the three was loud slapping sounds that appeared as a rapid succession of discrete events with a period on the order of 0.1–0.5 s: from the video recordings it could be seen that these loud events occur when parts of the bubble plume thrust outwards from the main body of the bubble plume, or when small clouds of bubbles broke away from the main plume. A sample time series is shown in Fig. 16 where one can see a continuous succession of loud and discrete events. Closer inspection of these discrete events within the time series show that the sound emitted has frequencies ranging from a few hundred hertz up to about a kilohertz. The second type of sound is similar to what is heard when pouring a glass of water, the source of which is the oscillation of several individual bubbles. These sounds were very intermittent in nature and are likely to be dominated by the acoustic emissions from the other two sources. Figure 17 shows a portion of the time series from the fresh-water environment

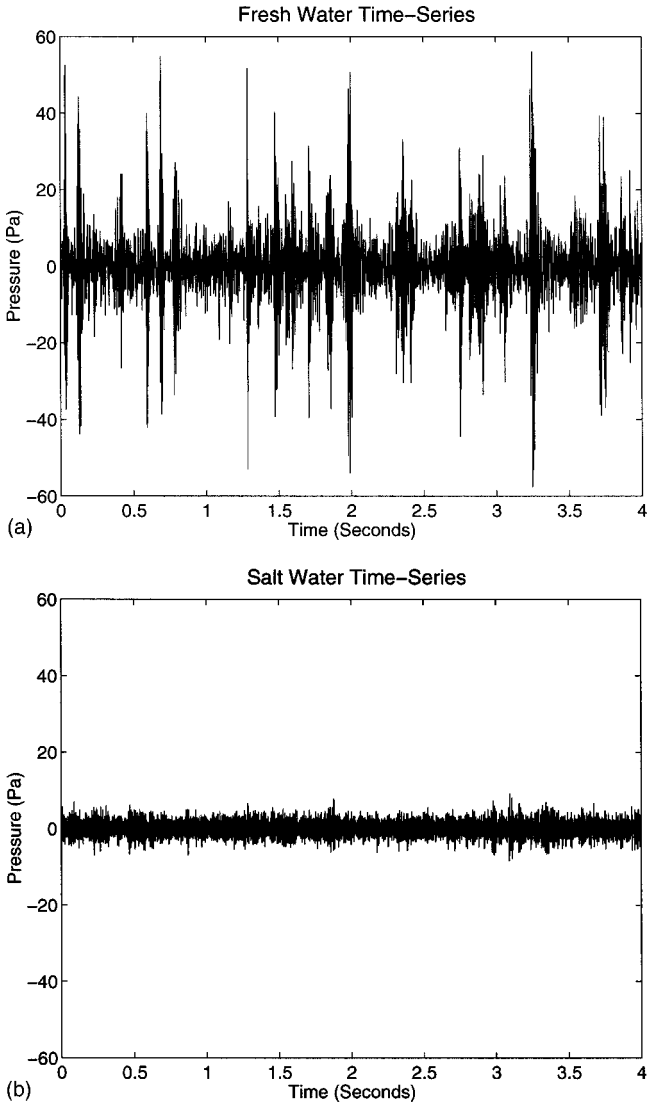

FIG. 16. Typical time series for the acoustic emissions of continuous bubble plumes in fresh-water and salt-water environments. In fresh-water (a) we can see several discrete, loud events that occur in intervals of 0.1 to 0.5 s. These are the result of the growth and detachment of small bubble clouds around the edge of the main bubble plume, and are the dominant noise generation mechanism for frequencies ranging from roughly 300–1100 Hz. By comparison, in salt-water (b) this mechanism does not exist since the bubble cloud, while grossly the same dimensions as the fresh-water clouds, remains intact around its edges. The pressure amplitudes seen in the salt-water time series are similar to the sections of the fresh-water time series occurring between the large-amplitude discrete events.

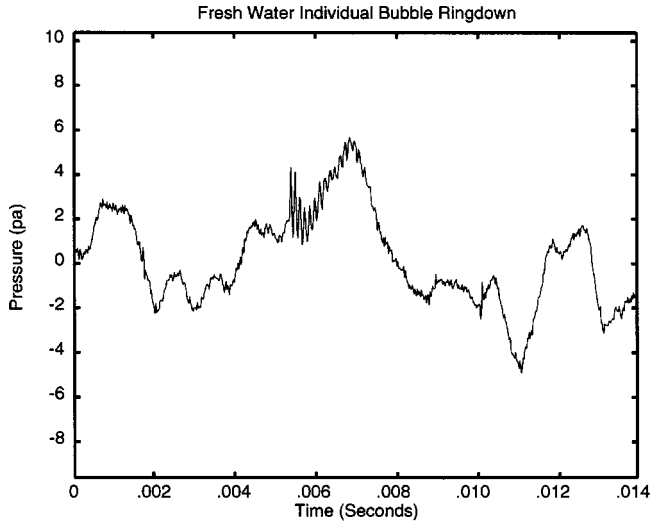

FIG. 17. Time series of the acoustic emissions of a bubble plume in a fresh-water environment. In fresh water, the acoustic emissions contain a continuous series of loud, discrete events: This particular data is taken from the background region between these events. Such data bears a strong resemblance to the emissions from bubble clouds in a salt-water environment, both of which are the result of amplification of noise from turbulence. Also notice the creation and ringdown of an individual bubble beginning at roughly 0.005 s: This oscillation is at a frequency of roughly 8.5 kHz, which means a bubble with a radius of roughly 0.4 mm was formed. In the fresh-water environment the oscillation of individual bubbles (or a few bubbles) could sometimes be heard, but these sounds were so intermittent that they will have very little influence on the long-term (tens of seconds) characteristics of the acoustic emission spectra.

in which one can see the ring-down of an individual bubble oscillation superimposed upon a lower-frequency background: this particular portion of the time series was taken from between two of the large discrete events described above. From this figure we estimate the bubble oscillation to be roughly 8500 Hz, which from (2) means this particular bubble had a radius of about 0.4 mm. Finally the third type of sound was a continuous whooshing that was always present in the background: in the time series of Fig. 16 this sound forms the bulk of what can be seen between the louder discrete events. In contrast to the three types of sound present in the fresh-water environment, the salt-water environment exhibited only the third type of (whooshing) sound: Fig. 16 shows a typical portion of the time series for the salt-water environment. This salt-water time series resembles the portions of the fresh-water time series *between* the discrete large events.

The loud slapping sounds in the fresh-water environment, while discrete in nature, did not exhibit any stochastic behavior over the long term (minutes), as is evident from the spectrogram of the data [see Fig. 18(a)]. Here we see a strong and persistent structure to the sounds emitted, indicating that the source must be quite constant over time. The spectrogram for the salt-water environment exhibits sound levels that are much lower and display less structure, although it is evident that this structure is nonetheless persistent; we shall address it presently.

A time average of the fresh-water spectrogram yields the plot shown in Fig. 19(a), which has several obvious features. First, there are several large peaks clustered below roughly 200 Hz, followed by another cluster of peaks between roughly 300 and 1100 Hz. All of these structures sit on a sloping background that can clearly be seen for the lower flow rates at frequencies above 1200 Hz: As the jet flow velocity rises the sound emissions increase in intensity. The second group of peaks (~300–1100 Hz) was identified earlier as being from bubbly structures that grow out from the main bubble plume or detach from it. The structure of this group of peaks is similar for all the flow rates, which leads us to conclude that the formation and detachment of smaller bubbly structures around the edge of the plume is a process that is already fully developed even at the lowest flow rate of the experiment, and higher flow rates serve only to produce more of the structures and generate higher levels of sound.

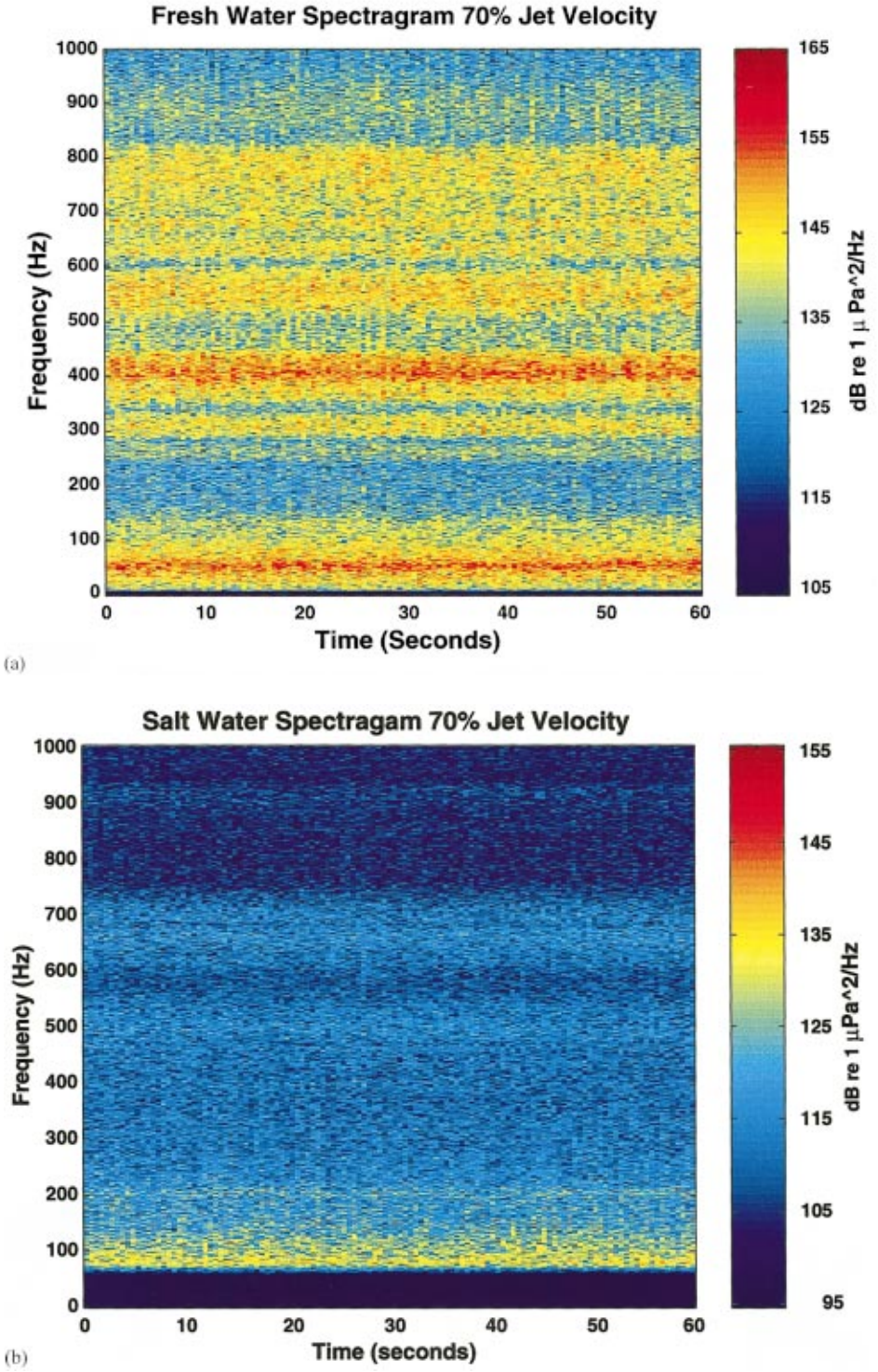

FIG. 18. Spectrogram of 60 s of data for both the fresh water (a) and salt water (b). This figure represents only the first 1000 Hz of the total bandwidth of 22 kHz, and shows several strong resonant peaks that are stable over long periods of time. In comparison the emissions from the salt-water cloud were much quieter with the strong resonant peaks being completely absent. However, there are three weaker emissions at frequencies of 200, 500, and 675 Hz which apparently result from collective cloud oscillations.

For reference, we have also shown a noise background curve in Fig. 19(a) in red at the bottom of the plot: It corresponds to the sound levels when no plume is present but the instrumentation and machinery is running, i.e., pump, generator, etc.

To compare with the fresh-water environment, Fig. 19(b) shows an equivalent time-averaged spectrogram for the salt-water portion of the experiment. The most obvious difference is the lack of the large peaks between 300 and 1100 Hz: the bubble plumes in the salt-water environment, while grossly the same size and shape as those in the fresh-water environment, remain more uniform and intact around the edges, providing no mechanism for the continuous series of loud slapping events responsible for the elevated sound levels in the fresh-water environment. The absence of the loud events in the salt-water environment exposes the two peaks in Fig. 19(b) at frequencies of roughly 500 and 675 Hz that result from collective modes of the bubble plume. One would expect similar such peaks in the fresh-water environment also, but they are hidden beneath sound from the other sources described earlier. (Below 80 Hz in the salt-water spectra there is a rapid drop off in the measured sound levels.

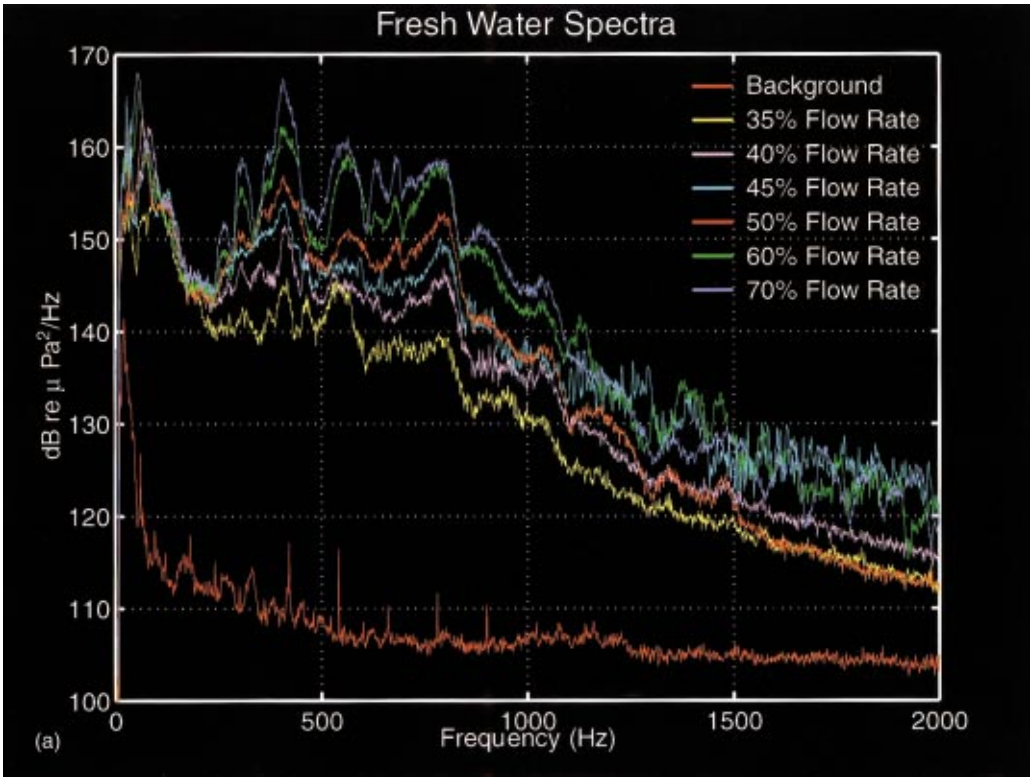

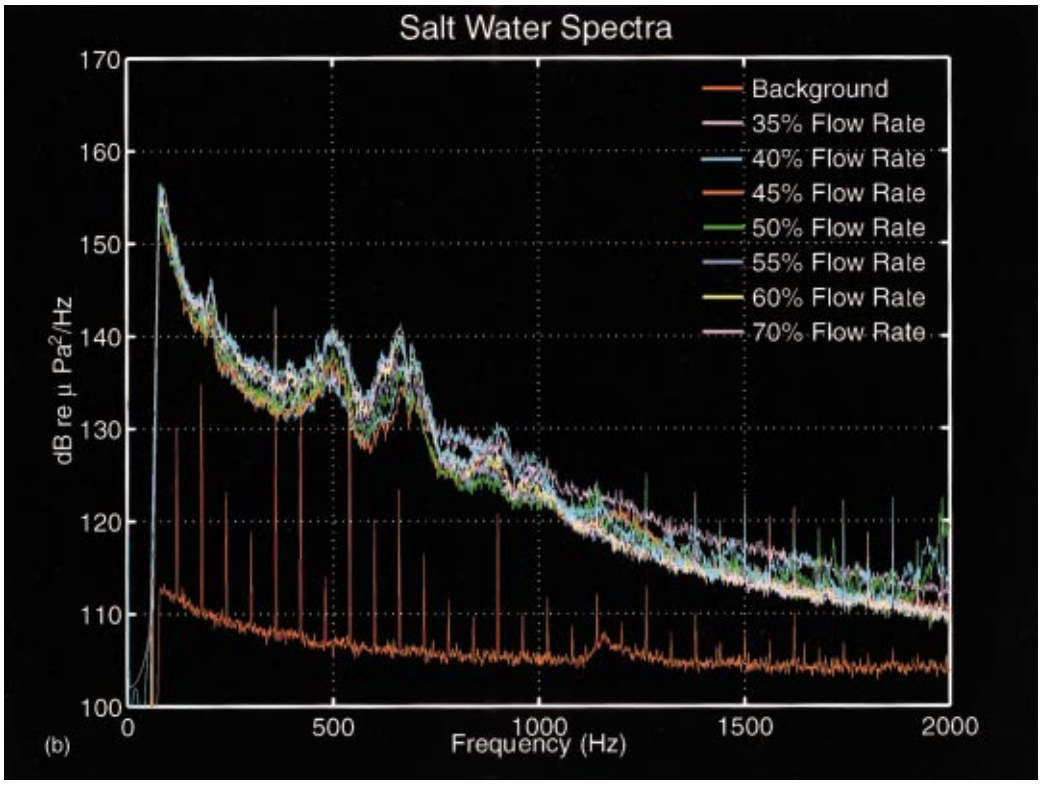

FIG. 19. Acoustic emissions measured in the fresh- and salt-water environments for a variety of jet flow velocities. As one might expect, the sound level increases monotonically with the flow rate. For comparison the orange (bottom) curves are the sound levels recorded when no bubble cloud is present but all of the mechanical and electronic instruments were operating (i.e., background reference level). There are large emissions that we associated with hydrodynamic noise generated by the incoming water jet. In fresh water (a) we see that from 300 to 1100 Hz there are several large resonant peaks. These result when small bubbly structures break away from the main bubble plume. Both of these sets of emissions lie on a background of turbulent noise generated within the body of the bubble cloud. In (b), the two sets of loud emissions present in the fresh-water environment are now absent in the salt-water environment. However, we still see the turbulent noise background spectrum and three weaker emissions at frequencies of roughly 200, 500, and 675 Hz. These weaker emissions correspond to theoretical results from an analysis of the collective modes of oscillation of the bubble plume.

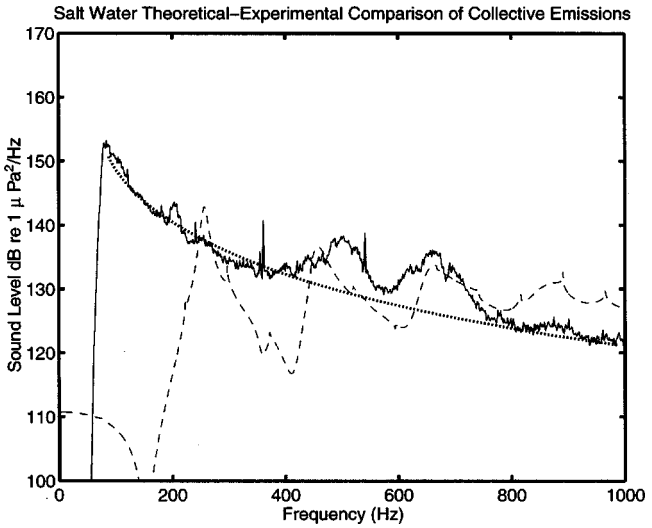

FIG. 20. Comparison of the measured acoustic emissions from a continuous bubble plume in salt water (solid line) with theoretically calculated values (dashed line). The theoretical calculations are for a vertical cavity acoustically driven by the noise generated by the continuous bubble pinch-off occurring at the surface, where the incoming water jet is entraining bubbles. Gross features present in the measured data that are not related to hydrodynamic noise are reproduced in the calculations, other than some uncertainties in frequency. To resolve these differences it would be necessary to further refine the calculations by using a model that accounts for the fact that the bubble plume is not a uniform cylinder, and that it contains a dense core of bubbles where the incoming jet is entraining air. We have also included a curve that would correspond to turbulence-induced noise (dotted curve). Despite the fact that it is not possible to ascertain the correct absolute levels, its shape alone is suggestive.

This is a direct result of filtering due to a large 60-Hz noise component in the salt-water phase of the experiment.) Increasing the flow rate from minimum to maximum has the effect of increasing the sound level by about 5–6 dB: the higher flow rate entrains more bubbles at the surface and hence there are more sound sources present to drive the resonant modes of the plume. We have already described in some detail how to model this cloud as a cylindrical resonant cavity standing vertically at the top of a wave guide and driven from above by the bubbles being entrained at the surface. Modeled in this way, the system will generate the spectrum shown in Fig. 20, which shows qualitative agreement with the measured values. Indeed, all of the features present in the measurements are also present in the results from the model, other than the curved background, of course, which must be generated by an entirely different mechanism.

The absence of the large peaks present in the fresh-water environment between 300 and 1100 Hz make the background curve present in the salt-water environment very clear. The acoustic power spectrum resulting from turbulence induced noise will behave as[36]

$$|P_{\text{turb}}| \sim \rho c^2 \left[\frac{v}{c}\right]^{22/2} \left(\frac{c}{\omega L}\right)^{7/2}, \tag{43}$$

and thus have a characteristic slope of $\omega^{-7/2}$. In Fig. 20 we have included such a theoretical spectrum with the measured power spectrum in the salt-water environment for a flow of 50%: clearly the background portion of the measured spectrum results from the amplification of turbulence noise. At frequencies below 500 Hz the sound levels become quite high and contribute to the noise spectrum just as much as the collective bubble plume oscillations. In the measured data one can also see a small peak near 875 Hz for which there is a corresponding theoretical peak: In this instance the measured levels are now lower than the theoretical values by approximately 8 dB due to a combination of absorption in the sediment and uncertainties in the dipole strength of the entrained bubbles as a function of frequency.

In the fresh-water environment, where we were not suffering from interference by noise at low frequencies, there appears to be some structure to the sound below 200 Hz. We digitally low-pass filtered the data to 200 Hz and listened to only this low-frequency portion, which sounded very much the same as the wooshing sound from the plumes in the salt-water environment with the obvious difference that it contains a much stronger low-frequency component that had to be filtered out in the experiment performed in the salt-water environment. These sounds could not have been produced by large individual bubble oscillations or acoustically excited bubbly structures ringing down. Rather, they were the result of hydrodynamic noise, and almost certainly related to the water jet at the core of the bubble cloud, where the flow velocities and length scales are of suitable magnitude to produce such low-frequency sound. However, in the case of the salt-water environment this part of the experiment was so contaminated by low-frequency noise that the signal had to be filtered below 70 Hz and the quality of the information is not good enough to be able to say a great deal more about the similarities between the fresh-water and salt-water environments down at these very low frequencies.

IV. CONCLUSIONS

Like all laboratory experiments, this study mimics only certain aspects of what happens at the air–water boundary in the open sea. It has been known for some time that bubbles entrained in a salt-water environment are a great deal smaller than in fresh water, and more recently there have been studies showing how the presence of bubbles has such a dramatic influence on the phase speed and attenuation of underwater sound. Here we were looking for differences in the noise generated by continuous bubble plumes in fresh-water and salt-water environments.

Several differences were found between the two environments. In particular, the greatest impact was brought about by the growth and detachment of small bubbly structures around the edge of the main plume—a mechanism that was present only in the fresh-water environment. These were found to generate a great deal of sound between 300 and 1100 Hz, often elevating the power spectrum levels by 15 dB or more (depending on the jet flow rates producing the bubble plumes, and the frequency) over the levels measured in the salt-water environment. In contrast to the fresh-water clouds, the salt-water environment produced bubble plumes that, while grossly the same sizes, remained smoother and intact around the edges: This has important ramifications on the final analysis of some experiments performed in fresh-water tanks.

Modeling the plumes as resonant cavities in a wave guide yielded results that, while not in exact agreement with the measured values, produced not only approximate sound levels but also reproduced all the major features in the spectra. Modeling the bubble cloud as a vertical cylinder that does not fill the entire water column makes the problem far more difficult than the geometries previously attempted by others.

One result of this work that warrants future investigation is the finding of such high levels of turbulence-induced noise and amplification produced by the presence of bubbles. While rather obscured by other mechanisms in the freshwater environment, this turbulence noise is profuse in the salt-water environment and appears to be the dominant mechanism over large parts of the low-frequency spectrum.

ACKNOWLEDGMENTS

We are indebted to Dr. Ronald Roy (Boston University) and Karl Steffin for their help in performing the experimental portion of this work, and to Tony Cesario of Photosea (now Simrad Osprey) for his help with the underwater video cameras. We would also like to thank the National Oceanic and Atmospheric Administration (NOAA) for furnishing us with a vessel with which to do these experiments. Our particular thanks go to David Gardner of NOAA (now with Los Alamos National Laboratory) who captained this vessel and provided extensive additional help without which this work would not have been possible.

[1] G. M. Wenz, ''Acoustic ambient noise in the ocean: Spectra and sources,'' J. Acoust. Soc. Am. **34**, 1936 (1962).
[2] B. Kerman (editor), *Sea Surface Sound: Natural Mechanisms of Surface Generated Noise in the Ocean*, Vol. 238 of *NATO Advanced Workshops*, Dordrecht, NATO (Kluwer, Lerici, Italy, 1987).
[3] B. Kerman (editor), *Natural Physical Sources of Underwater Sound: Sea Surface Sound (2)*, Dordrecht (Kluwer, Cambridge, UK, 1990).
[4] N. Chapman and J. Cornish, ''Wind dependence of deep ocean ambient noise at low frequencies,'' J. Acoust. Soc. Am. **93**, 782–789 (1993).
[5] P. M. Ogden and F. T. Erskine, ''Surface and volume scattering measurements using broadband explosive charges in the Critical Sea Test 7 experiment,'' J. Acoust. Soc. Am. **96**, 2908–2920 (1994).
[6] M. Nicholas, R. Roy, L. Crum, H. Oğuz, and A. Prosperetti, ''Sound emissions by a laboratory bubble cloud,'' J. Acoust. Soc. Am. **95**, 3171–3182 (1994).
[7] A. Kolani, R. A. Roy, and D. Gardner, ''Low-frequency acoustic emissions in fresh and salt water,'' J. Acoust. Soc. Am. **96**, 1766–1772 (1994).
[8] A. Kolani and L. A. Crum, ''Observations of underwater sound from laboratory breaking waves and the implications concerning ambient noise in the ocean,'' J. Acoust. Soc. Am. **96**, 1755–1765 (1994).
[9] W. M. Carey, J. W. Fitzgerald, E. C. Monahan, and Q. Wang, ''Measurements of the sound produced by a tipping trough with fresh and salt water,'' J. Acoust. Soc. Am. **93**, 3178–3192 (1993).
[10] K. W. Commander and A. Prosperetti, ''Linear pressure waves in bubbly liquids: Comparison between theory and experiments,'' J. Acoust. Soc. Am. **85**, 732–746 (1989).
[11] A. B. Wood, *A Textbook of Sound* (Bell, London, 1932).
[12] M. Minneart, ''On musical air-bubbles and the sounds of running water,'' Philos. Mag. **16**, 235–248 (1933).
[13] M. Strasberg, ''The pulsation frequency of nonspherical gas bubbles in liquids,'' J. Acoust. Soc. Am. **25**, 536–537 (1953).
[14] M. Strasberg, ''Gas bubbles as sources of sound in liquids,'' J. Acoust. Soc. Am. **28**, 20–26 (1956).
[15] A. Prosperetti, ''The equation of bubble dynamics in a compressible liquid,'' Phys. Fluids **30**, 3626–3628 (1987).
[16] A. Prosperetti and A. Lezzi, ''Bubble dynamics in a compressible liquid. part 1. first-order theory,'' J. Fluid Mech. **168**, 457–478 (1986).
[17] A. Lezzi and A. Prosperetti, ''Bubble dynamics in a compressible liquid. part 2. second-order theory,'' J. Fluid Mech. **185**, 289–321 (1987).
[18] A. Prosperetti, ''Application of the subharmonic threshold to the measurement of damping of oscillating gas bubbles,'' J. Acoust. Soc. Am. **61**, 11–16 (1977).
[19] A. Prosperetti, ''Thermal effects and damping mechanisms in the forced radial oscillations of gas bubbles in liquids,'' J. Acoust. Soc. Am. **61**, 17–27 (1977).
[20] A. Prosperetti, L. A. Crum, and K. W. Commander, ''Nonlinear bubble dynamics,'' J. Acoust. Soc. Am. **83**(2), 502–514 (1988).
[21] A. Prosperetti, ''Bubble-related ambient noise in the ocean,'' J. Acoust. Soc. Am. **84**, 1042–1054 (1988).
[22] H. N. Oğuz, ''A theoretical study of low-frequency oceanic ambient noise,'' J. Acoust. Soc. Am. **95**, 1895–1912 (1994).
[23] N. Q. Lu, A. Prosperetti, and S. W. Yoon, ''Underwater noise emissions from bubble clouds,'' IEEE J. Ocean Eng. **15**(4), 275–281 (1990).
[24] K. Gilbert and X. Di, ''Spectral decomposition and propagation of scattered fields in an ocean waveguide,'' in *Computational Acoustics*, edited by D. Lee, A. Cakmak, and R. Vichnevetsky (North-Holland, Amsterdam, 1990), Vol. 2, pp. 46–63.
[25] M. Koga, ''Bubble entrainment in breaking wind waves,'' Tellus **34**, 481–489 (1982).
[26] T. J. Lin and H. G. Donnelly, ''Gas bubble entrainment by plunging laminar liquid jets,'' AIChE. J. **12**(3), 563–571 (1966).
[27] J. Scott, ''The role of salt in whitecap persistence,'' Deep-Sea Res. **22**, 653–657 (1975).
[28] S. A. Thorpe and A. R. Stubbs, ''Bubbles in a freshwater lake,'' Nature (London) **279**(5712), 403–405 (1979).
[29] V. I. Ilichev and F. F. Neuimin, ''Size distribution law of gas bubbles in a turbulent liquid flow,'' Sov. Phys. Acoust. **11**(4), 390–393 (1966).
[30] S. A. Thorpe and D. K. Woolf, ''Some factors affecting the size distribution of oceanic bubbles,'' J. Phys. Oceanogr. **22**, 382 (1992).
[31] B. D. Johnson and R. C. Cooke, ''Bubble populations and spectra in coastal waters: A photographic approach,'' J. Geophys. Res. **84**(C7), 3761–3766 (1979).
[32] M. A. Haines and B. D. Johnson, ''Injected bubble populations in seawater and freshwater measured by a photographic method,'' J. Geophys. Res. **100**(C4), 7057–7068 (1995).
[33] C. S. Clay and H. Medwin, *Acoustical Oceanography: Principles and Applications* (Wiley, New York, 1977).
[34] H. C. Pumphrey and J. E. Ffowcs-Williams, ''Bubbles as Sources of Ambient Noise,'' IEEE J. Ocean Eng. **15**(4), 268–274 (1990).
[35] N. N. Lebedev, *Special Functions and their Applications* (Dover, New York, 1972).
[36] P. M. Morse and K. U. Ingard, *Theoretical Acoustics* (Princeton U. P., Princeton, NJ, 1968).

Ultrasonic absorption in critical binary mixture of perfluoromethylcyclohexane and carbon tetrachloride

Issam R. Abdelraziq
Physics Department, An-Najah National University, Nablus, West Bank, Israel

(Received 27 July 1998; accepted for publication 1 June 1999)

The results of ultrasonic absorption and velocity measurements for the system perfluoromethylcyclohexane-carbon tetrachloride are presented. In addition, viscosity measurements were made. Ultrasonic absorption at 5, 7, 10, 15, 21, and 25 MHz, above critical temperature T_c, is analyzed using the dynamic scaling theory of Ferrell and Bhattacharjee. The values of α/f^2 vs $f^{-1.06}$ show a good agreement with the theory. The experimental values of α/α_c for the binary mixture are compared to the scaling function $F(\omega^*)$. © *2000 Acoustical Society of America.* [S0001-4966(99)02409-1]

PACS numbers: 43.35.Bf [HEB]

INTRODUCTION

There are several theories available to analyze ultrasonic absorption measurements.[1–3] However, in this article, the dynamic scaling theory of Ferrell and Bhattacharjee[4] is applied to analyze the absorption and velocity data for the critical binary mixture of perfluoromethylcyclohexane and carbon tetrachloride. This binary mixture has an upper critical temperature T_c of 301.622 K and a critical composition of 0.5527 volume fraction carbon tetrachloride.[5]

In the literature, the available ultrasonic absorption data are not enough to evaluate measurements using the dynamic scaling theory. The ultrasonic absorption was measured by Kruus[6] for the frequencies 3.5, 10.0, and 16.6 MHz at the critical temperature and two other temperatures. Accordingly, in the present work further absorption data are measured for an extended temperature range 301.62–333.16 K and frequency range of 5–25 MHz to support FB theory which enables us to measure and calculate some thermodynamic quantities. The experimental results of absorption are compared to the prediction of the dynamic scaling theory.[4] The theory indicates that α/α_c in Eq. (10) should be a function of the reduced frequency ω^*, and should scale with the scaling function $F(\omega^*)$.

The shear viscosity of the perfluoromethylcyclohexane and carbon tetrachloride as a function of temperature at critical concentration has also been studied in order to determine the value of ω_0 in Eq. (2). The critical amplitudes of the shear viscosity, mutual diffusion coefficient, thermal expansion, and specific heat of the mixture have been obtained. The adiabatic coupling constant g and the change in critical temperature with respect to pressure (dT_c/dp) are calculated. In addition, values of adiabatic and isothermal compressibilities are calculated

I. THEORETICAL CONSIDERATIONS

In the dynamic scaling theory the total absorption coefficient at the critical temperature and concentration can be simply expressed as[7]

$$\alpha(\mathrm{crit},T_c)/f^2 = Sf^{-1.06} + b, \tag{1}$$

where b represents the contribution of the frequency-independent background absorption. The S value is given by[4]

$$S = [\{\pi C_{pc} g^2 v_c \text{œ}\}/\{2z\gamma T_c C_p^2(t_f)\}][a\omega_0/2\pi]^{\text{œ}/z\gamma}. \tag{2}$$

Here œ=0.11 and $z\gamma$=1.9 are the critical exponents,[8] C_{pc} is the critical amplitude in the following expression for the specific heat at constant pressure of a mixture of critical composition:[9]

$$C_p = C_{pc} t^{-\text{œ}} + C_{pb}. \tag{3}$$

C_{pb} is the background specific heat, $a=(\omega/\omega_0)^{t_f - z\gamma}$ is a dimensionless scaling factor of order unity,[10] ω_0 is a characteristic temperature-dependent relaxation rate, g is the adiabatic coupling constant, v_c is the adiabatic sound velocity at T_c, and $C_p(t_f)$ is the specific heat at a characteristic reduced temperature t_f, which can be approximated by $t=(T-T_c)/T_c$ value at which $\alpha(\mathrm{crit},T_c)/f^2$ for a given frequency is one-half its value at T_c.[7]

The adiabatic coupling constant g was introduced by Ferrell and Bhattacharjee and is given by[4]

$$g = \rho_c C_p[(dT_c/dP) - (T\alpha_p/\rho C_p)] \cong (C_{pc}\alpha_{pc}T_c/C_{pc}) - \alpha_{pb}T, \tag{4}$$

where ρ_c is the density at critical temperature and concentration, α_p is the isobaric thermal expansion coefficient which can be represented by a power law of the form[11]

$$\alpha_p = \alpha_{pc} t^{-\text{œ}} + \alpha_{pb}. \tag{5}$$

Note that α_{pc} and α_{pb} being the critical and background parts of the thermal expansion coefficients.

The absorption coefficient $\alpha(\mathrm{crit},\omega,T)$ can also be expressed as a function of the dimensionless reduced frequency ω^*,

$$\omega^* = \omega/\omega_D = 2\pi f/\omega_0 t^{z\gamma}, \tag{6}$$

where ω_D is given by[7]

$$\omega_D = k_B T/3\pi\,\eta\xi^3 = (k_B T_c/3\pi\,\eta_0\xi_0^3)t^{z\gamma} = \omega_0 t^{z\gamma}. \tag{7}$$

Here k_B designates Boltzmann's constant, and the correlation length ξ and the shear viscosity η are given by

$$\xi = \xi_0 t^{-\gamma} \tag{8}$$

and

$$\eta = \eta_0 t^{-x_\eta \gamma}, \tag{9}$$

where $x_\eta = 0.06$ is the critical exponent.

The expression for the critical term of the absorption as a function of reduced frequency ω^* is[4]

$$\alpha(\text{crit}, \omega, T)/\alpha(\text{crit}, \omega, T_c) = \alpha/\alpha_c = F(\omega^*) = (1+\omega^{*-0.5})^{-2}, \tag{10}$$

where $\alpha(\text{crit}, \omega, T)$ is the critical term at critical concentration and temperature T, and $\alpha(\text{crit}, \omega, T_c)$ is the critical term at critical concentration and critical temperature T_c.

The isothermal β_T and adiabatic β_s compressibilities and specific heat at constant volume C_v can be represented under the assumptions that all the quantities are expressed as power laws of the form[11]

$$\beta_T = \beta_{Tc} t^{-\alpha} + \beta_{Tb}, \tag{11}$$

$$\beta_s = \beta_{sc} t^{-\alpha} + \beta_{sb}, \tag{12}$$

$$C_v = C_{vc} t^{-\alpha} + C_{vb}, \tag{13}$$

where β_{Tc}, β_{sc}, C_{vc} and β_{Tb}, β_{sb}, C_{vb} are critical and background parts of the mentioned quantities, respectively.

II. EXPERIMENT

The purified carbon tetrachloride CCl_4 and perfluoromethylcyclohexane C_7F_{14} were obtained from Fisher Scientific. The chemicals were used without any further purification. The absorption and velocity measurements were made with a Matec pulse-echo system. The shear viscosity was measured using a Brookfield digital viscometer. Setup and operational procedures are discussed in our previous papers.[12–17]

III. RESULTS AND ANALYSIS

The binary mixture C_7F_{14}–CCl_4 has an upper critical temperature of 301.622 K and a critical composition of 0.5527 volume fraction carbon tetrachloride.[5] The thermostatic control error was ± 0.01 °C. The absorption measurements were made for the frequencies 5, 7, 10, 15, 21, and 25 MHz in one region starting at 60 °C toward critical temperature $T_c = 28.47$ °C.

In Fig. 1 the temperature dependence of the absorption α/f^2 for the critical binary mixture of C_7F_{14}–CCl_4 at six different frequencies are shown. The error in the absorption measurements was less than 3%.

Figure 2 shows a plot of absorption α_c/f^2 at critical mixture and temperature T_c vs $f^{-1.06}$. A least-square fit yields an experimental slope S of $0.99\times10^{-7}\pm0.08\times10^{-7}\,\text{cm}^{-1}\,\text{s}^{0.94}$ and an intercept of $529.25\times10^{-17}\,\text{cm}^{-1}\,\text{s}^2$ which represents the frequency-independent background term of α_c/f^2. The data form a straight line as predicted by FB theory. The calculated value of S using Eq. (2) and the calculated value of $g = 0.158\pm0.009$ is $S = 0.74\times10^{-7}\pm0.08\times10^{-7}\,\text{cm}^{-1}\,\text{s}^{0.94}$. Using our calculated values of (dT_c/dP) and $(\partial T/\partial P)_s$, the adiabatic coupling constant g is 0.222 ± 0.008, so the corresponding value of S is $1.28\times10^{-7}\pm0.09\times10^{-7}\,\text{cm}^{-1}\,\text{s}^{0.94}$. Kruus[6] has measured the absorption coefficient for C_7F_{14}–CCl_4 binary mixture for the frequencies 3.5, 10.0, and 16.6 MHz at critical temperature and two other temperatures. His data were evaluated using the Fixman's theory and α_c/f^2 is plotted versus $f^{-1.06}$ along

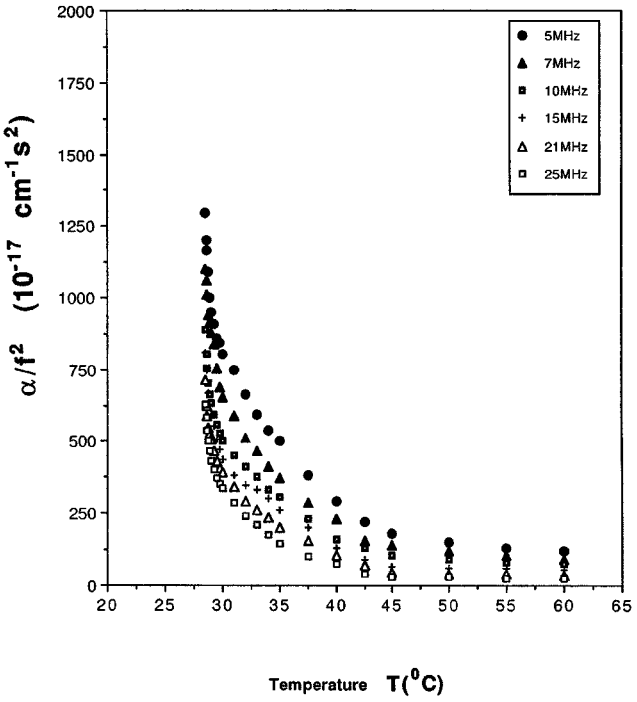

FIG. 1. Temperature dependence of α/f^2 for the critical binary mixture of perfluoromethylecyclohexane and carbon tetrachloride.

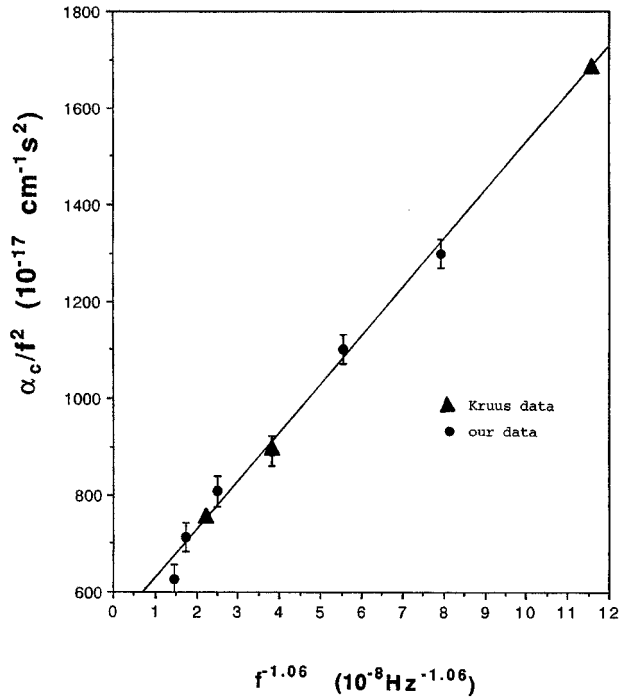

FIG. 2. α_c/f^2 values versus $f^{-1.06}$ at T_c of Kruus (Ref. 6) data along with our data for the critical mixture of perfluoromethylecyclohexane and carbon tetrachloride.

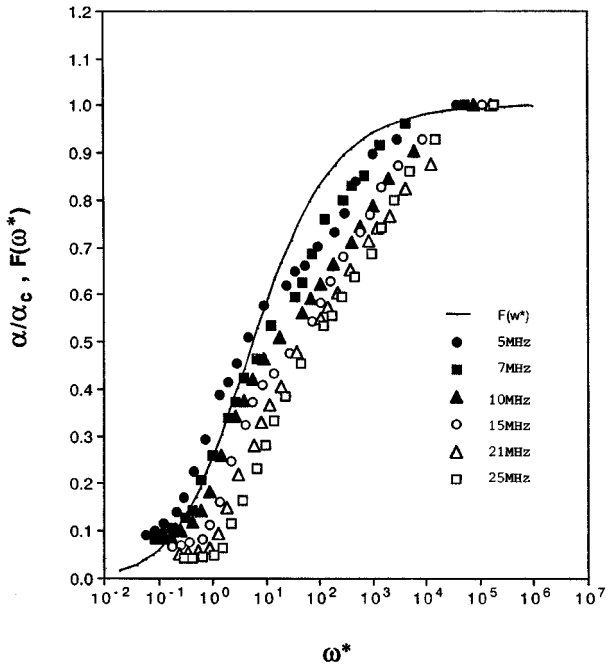

FIG. 3. Plot of α/α_c versus the reduced frequency ω^*. The smooth curve is the scaling function $F(\omega^*)$ given by Eq. (10).

with our data as shown in Fig. 2. From a least-square fit of his data, the slope is $S=1.01\times10^{-7}\,\mathrm{cm}^{-1}\,\mathrm{s}^{0.94}$ and the intercept is $516\times10^{-17}\,\mathrm{cm}^{-1}\,\mathrm{s}^{2}$. Our values (absorption, slope, and intercept) show good agreement with Kruus's data. For example, at frequency 10 MHz and $T=28.37\,^{\circ}\mathrm{C}$ his measurement of absorption is $\approx900\times10^{-17}\,\mathrm{cm}^{-1}\,\mathrm{s}^{2}$, and our measurement at the same frequency and temperature $T=28.50\,^{\circ}\mathrm{C}$ is $891\times10^{-17}\,\mathrm{cm}^{-1}\,\mathrm{s}^{2}$.

The experimental values of α/α_c at different frequencies are plotted versus the reduced frequency ω^* along with the theoretical curve $F(\omega^*)$ as shown in Fig. 3. The value of ω_0 was calculated using the measured shear viscosity $\eta_0=0.737\pm0.012$ centipoise shown in Fig. 4.

The velocity versus temperature and frequency at critical concentration are shown in Figs. 5 and 6. A least-square fit

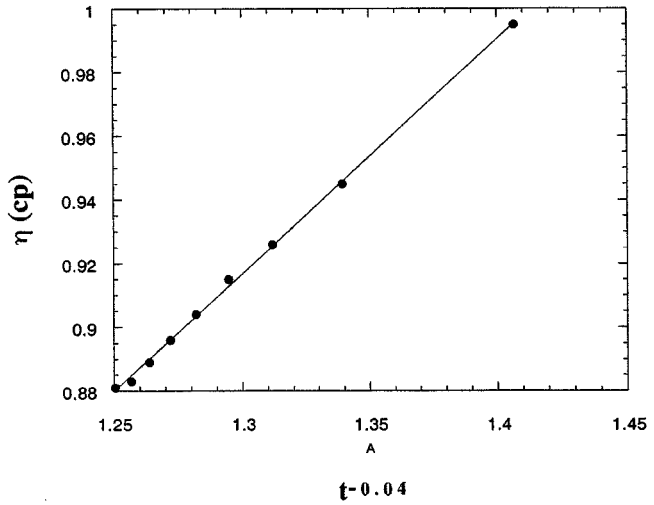

FIG. 4. The measured values of the shear viscosity $\eta(cp)$ vs $t^{-0.04}$ for the critical mixture of perfluoromethylecyclohexane and carbon tetrachloride.

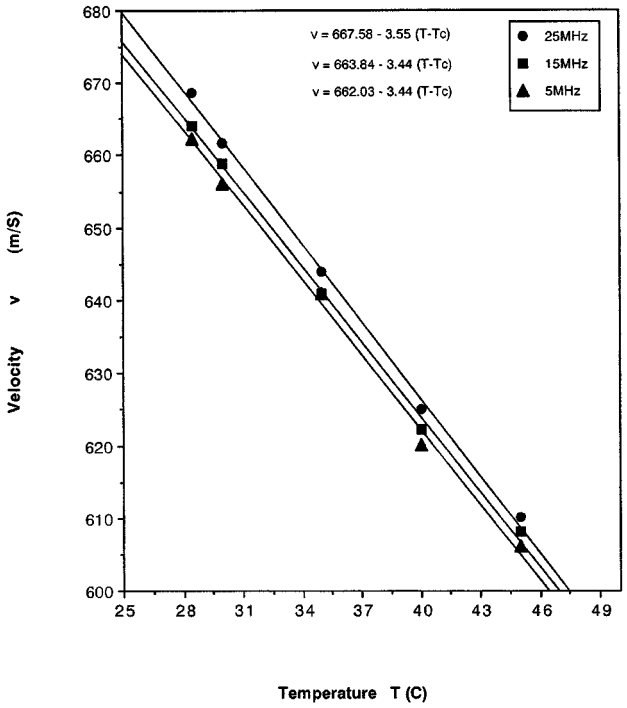

FIG. 5. The velocity versus temperature at critical concentration at three different frequencies.

of 5, 15, and 25 MHz yields the values of critical velocities and slopes at different temperatures. The sound velocity as a function of temperature at a critical concentration can be expressed by

$$v=662.03-3.44(T-T_c)\ \text{in m/s}\quad \text{for 5 MHz},$$

$$v=663.84-3.44(T-T_c)\ \text{in m/s}\quad \text{for 15 MHz},$$

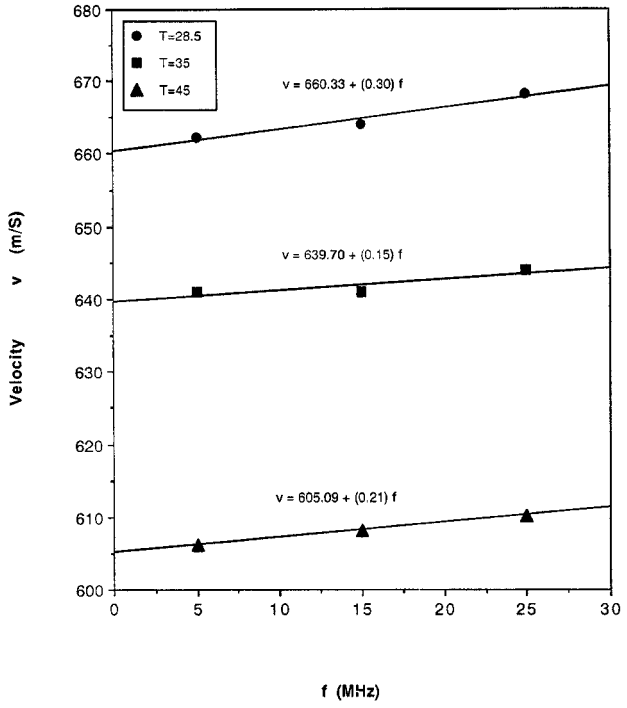

FIG. 6. The velocity versus frequency at critical concentration at three different temperatures.

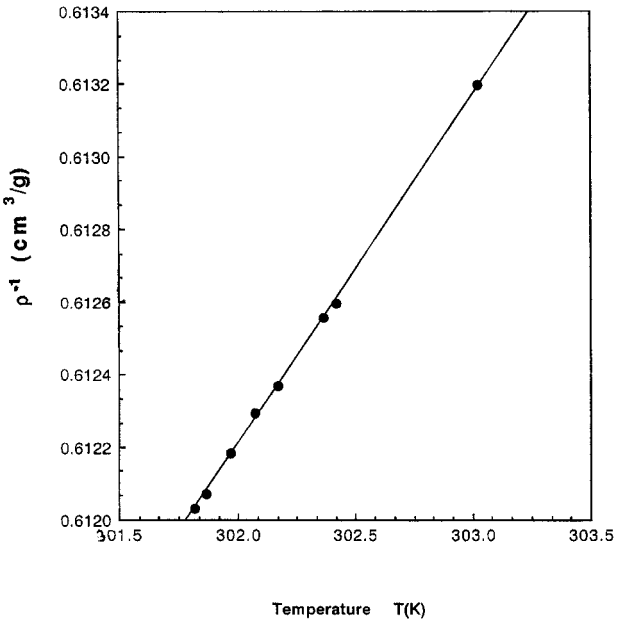

FIG. 7. The reciprocal density ρ^{-1} versus the temperature for the critical mixture of perfluoromethylecyclohexane and carbon tetrachloride. Points represents the data obtained by Darrell *et al.* (Ref. 18).

$$v = 667.58 - 3.55(T - T_c) \text{ in m/s for 25 MHz.}$$

The error in the velocity measurements was less than 0.2%. No anomaly was observed near the critical temperature.

The regular part (background) of the specific heat at constant pressure has been given by[5]

$$C_{pb} = 0.818 \times 10^7 \text{ erg/g K.}$$

Using this value and the two-scale factor universality,[4] α_{pc} and C_{pc} can be calculated, where

$$\xi_0[\text{œ}\rho_c C_{pc}/k_B]^{1/3} = \xi_0[\text{œ}T_c\alpha_{pc}/k_B T_c']^{1/3} = 0.270.$$

The density data for the critical mixture of C_7F_{14}–CCl_4 as a function of temperature has been reported by Darrell *et al.*[18] From their density data, Fig. 7, the slope $(\partial\rho^{-1}/\partial T)_p$ has been estimated from the linear fit of ρ^{-1} at various temperatures, where $(\partial\rho^{-1}/\partial T)_p = 9.58 \times 10^{-4}$ cm^3/g K. Using the thermal expansion coefficient $\alpha_p \equiv \rho(\partial\rho^{-1}/\partial T)_p$ and the power law of α_p, Eq. (5), yields a value of α_{pb}. The values of the thermal expansion and specific heat are then calculated to be

$$\alpha_p = 2.683 \times 10^{-4} t^{-0.11} + 9.795 \times 10^{-4} \text{ K}^{-1},$$

$$C_p = 0.128 \times 10^7 t^{-0.11} + 0.818 \times 10^7 \text{ erg/g K.}$$

The thermodynamic quantities, C_{pc}, C_{pb}, α_{pc}, α_{pb}, T_c, and $(dT_c/dP) = T_c'$ enable us to determine the adiabatic coupling constant g and the thermodynamic quantities mentioned in Eqs. (11), (12), and (13). Some measured and calculated quantities are given in Table I.[19]

IV. CONCLUSION

It can be seen from Fig. 1 that the absorption coefficient for the critical concentration increases as the critical temperature is approached from the high-temperature region for all frequencies. The velocity for the critical mixture increases with increasing frequency. This indicates the dispersion in the sound velocity as expected for binary liquid mixtures. The experimental values of ω^* for the critical binary mixture at different frequencies show good agreement with the theo-

TABLE I. Some measured and calculated values.

Quantity	Measured	Calculated	From references
T_c (K)			301.622[a]
ξ_0 (Å)			2.28[b]
η_0 (cp)	0.737		
ω_0 (Hz)		4.73×10^{10}	
D_0 (cm^2/s)		1.31×10^{-5}	
ρ_c (g/cm^3)			1.633[c]
v_c (cm/s)	66 220		
α_{pc} (K^{-1})		2.683×10^{-4}	
α_{pb} (K^{-1})		9.795×10^{-4}	
C_{pc} (erg/g K)		0.128×10^7	
C_{pb} (erg/g K)			0.818×10^{7}[a]
(dT_c/dP) (cm^2 K/dyne)		3.879×10^{-8}	
$(\partial T/\partial P)_s$ (cm^2 K/dyne)		2.636×10^{-8}	
S (cm^{-1} s$^{0.94}$)	0.99×10^{-7}	1.28×10^{-7}	1.01×10^{-7}[d]
		0.74×10^{-7}	
g		0.158	
β_{Tc} (cm^2/dyne)		1.04×10^{-11}	
β_{Tb} (cm^2/dyne)		50.63×10^{-11}	
β_{sc} (cm^2/dyne)		0.12×10^{-11}	
β_{sb} (cm^2/dyne)		48.46×10^{-11}	
C_{vc} (erg/g K)		0.108×10^7	
C_{vb} (erg/g K)		0.783×10^7	

[a]Reference 5.
[b]Reference 19.
[c]Reference 18.
[d]Reference 6.

retical function $F(\omega^*)$ at the low ($\omega^*<10$) and high ($\omega^*>10^3$) reduced frequencies ω^*. The measured absorption of the α_c/f^2 vs $f^{-1.06}$ yields a straight line as predicted by the FB theory. The coupling constant g is positive which indicates that the phase separation near the critical point is induced by a sudden increase of the pressure.

[1] K. Kawasaki, Phys. Rev. A **1**, 1750 (1970).
[2] L. Mistura, J. Chem. Phys. **57**, 2311 (1973).
[3] D. M. Kroll and J. M. Ruhland, Phys. Rev. A **23**, 371 (1981).
[4] J. K. Bhattacharjee and R. A. Ferrell, Phys. Rev. A **24**, 1643 (1981); E. A. Clerke, J. V. Sengers, R. A. Ferrell, and J. K. Bhattacharjee, *ibid.* **27**, 2140 (1983); R. A. Ferrell and J. K. Bhattacharjee, *ibid.* **31**, 1788 (1985).
[5] M. Pelger, H. Klein, and D. Woermann, J. Chem. Phys. **67**, 5362 (1977).
[6] P. Kruus, Can. J. Chem. **42**, 1712 (1964).
[7] C. W. Garland and G. Sanchez, J. Chem. Phys. **79**, 3090 (1983).
[8] P. Calmettes, Phys. Rev. Lett. **39**, 1151 (1977).
[9] M. Pelger, H. Klein, and D. Woermann, Ber. Bunsenges. Phys. Chem. **85**, 356 (1981).
[10] J. K. Bhattacharjee and R. A. Ferrell, Phys. Lett. A **88**, 77 (1982).
[11] H. Tanaka, Y. Wada, and H. Nakajima, Chem. Phys. **68**, 223 (1982).
[12] S. Fast and S. S. Yun, J. Acoust. Soc. Am. **83**, 1384 (1988).
[13] P. Spickler, I. Abdelraziq, S. S. Yun, and F. B. Stumpf, J. Acoust. Soc. Am. **85**, 1363 (1989).
[14] I. Abdelraziq, S. S. Yun, and F. B. Stumpf, J. Acoust. Soc. Am. **88**, 1831 (1990).
[15] I. R. Abdelraziq, S. S. Yun, and F. B. Stumpf, J. Acoust. Soc. Am. **91**, 844 (1992).
[16] R. Esqivel-Sirvent, B. Tan, I. Abdelraziq, S. S. Yun, and F. B. Stumpf, J. Acoust. Soc. Am. **93**, 819 (1993).
[17] I. R. Abdelraziq, J. Islamic Univ. **4**, 90 (1996).
[18] Darrell R. Thompson and O. K. Rice, J. Chem. Phys. **86**, 3547 (1964).
[19] D. Thiel, B. Chu, A. Stein, and G. Allen, J. Chem. Phys. **62**, 3689 (1975).

Comparison between the dispersion curves calculated in complex frequency and the minima of the reflection coefficients for an embedded layer

A. Bernard[a] and M. Deschamps
Laboratoire de Mécanique Physique, Université Bordeaux I, UPRES A 5469 C.N.R.S., Cours de la Libération, 33405 Talence Cedex, France

M. J. S. Lowe
Department of Mechanical Engineering, Imperial College of Science and Technology, Exhibition Road, London SW7 2BX, United Kingdom

(Received 1 April 1999; revised 27 September 1999; accepted 27 September 1999)

Analytical solutions of Lamb functions for symmetric and antisymmetric elastodynamic modes propagating within a solid layer embedded in an infinite medium are presented. Alternative theoretical analyses of such modes are performed, first in terms of the usual approach of harmonic heterogeneous plane waves (real frequency and complex slowness) and then in terms of transient homogeneous plane waves (complex frequency and real slowness). An example structure of a 0.1-mm-thick ''alpha case'' (an oxygen-rich phase of titanium that is relatively stiff) plate embedded in titanium is used for the study. A large difference between the usual dispersion curves calculated in real frequency and complex slowness and those calculated in complex frequency and real slowness is shown. Thus the choice between a spatial and a temporal parameter to describe the imaginary part of the guided waves is shown to be significant. The minima and the zeros of the longitudinal and shear plane-wave reflection coefficients are calculated and are compared with the dispersion curves. It is found that they do not match with the dispersion curves for complex slowness, but they do agree quite well with the dispersion curves for complex frequency. This implies that the complex frequency approach is better suited for the comparison of the modal properties with near-field reflection measurements.
[S0001-4966(00)03101-5]

PACS numbers: 43.35.Cg [HEB]

INTRODUCTION

Nondestructive testing and measurement of material properties by ultrasonic methods are key research areas. The techniques are based on the use of acoustic waves that propagate in the material being tested. They normally rely on the analysis of short-duration signals and their interactions with interfaces within the material. When the waves are incident at oblique angles, then the techniques can include the generation and detection of guided modes within layered structure. Within this context, researchers have, for a number of years, studied the properties of guided waves in plates and particularly Lamb waves. The well-known free (lossless) wave propagation modes of an elastic plate in vacuum were first described by Rayleigh and Lamb.[1] Wave interactions and guided waves in the liquid/solid/liquid configuration have already been studied by many authors, for example Chimenti and Nayfeh,[2] Chimenti and Rokhlin,[3] Nafeh and Chimenti,[4,5] Plona *et al.*,[6] Fiorito *et al.*,[7] Fiorito and Uberall,[8] Worlton,[9] Lenoir *et al.*,[10] Izbicki *et al.*,[11] and Junru and Zhemin.[12]

The usual approach, relating the excitation of guided modes to obliquely incident waves, assumes that the zeros of the plane-wave reflection coefficient indicate directly the modal properties of the plate. Thus the reflection coefficients for an immersed plate in water are measured using the coincidence angle hypothesis, and it is concluded that each zero of the longitudinal plane-wave reflection coefficient corresponds to the generation of a plate mode. The dispersion curves for the plate can thus be plotted from measured reflection coefficient minima over ranges of angle and frequency. For many configurations this approach is accurate, for example for most of the modes in an aluminum plate immersed in water (Fig. 1).

However, it has been shown that the modal properties and the zeros of the longitudinal plane-wave reflection coefficient for a fluid-coupled elastic layer are both modified under fluid loading[2–5] or solid loading[13–17] and are not in general coincident. In fact the hypothesis that the minima of the plane-wave reflection coefficients correspond to the modal properties of the plate appears to be accurate only when the impedance of the loading material is very much lower than that of the layer.

The conventional approach when modeling guided waves in an immersed or embedded plate is to assume a steady-state condition with real frequency and complex slowness.[14] This is easy to understand physically. As the (continuous) waves propagate along the layer, they can leak energy into the embedding material (liquid or solid) in the

[a]Alternate address: Department of Mechanical Engineering, Imperial College of Science and Technology, Exhibition Road, London SW7 2BX, United Kingdom.

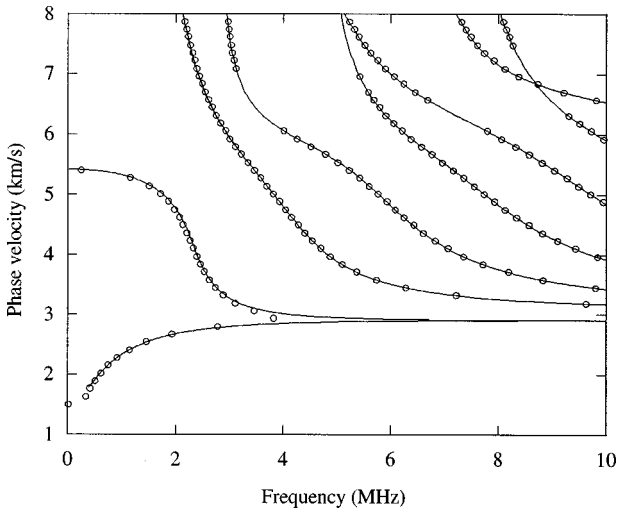

FIG. 1. Comparison between the reflection coefficient zeros (○) and dispersion curves (—) calculated in real frequency and complex slowness for 1-mm-thick aluminum plate immersed in water.

form of outgoing waves. The amplitudes of the plate waves must then decay as they travel and a complex parameter is needed to describe their spatial attenuation.

Thus the analysis has almost always been done in terms of real frequency and complex wave number, which is also equivalent to a real frequency and a complex slowness. The calculation of the dispersion curves for this problem then involves calculating the roots of a function F of the form: $F(\omega,{}^*S)=0$, where the prefix * denotes a complex quantity.

However, in general, we should also consider the possibility of a complex frequency, allowing, for the direct representation, waves that are transient in time. Thus the completely general form of the wave function should have complex parameters for both frequency and slowness, so that the characteristic equation is of the form $F({}^*\omega,{}^*S)=0$. In this paper we study this but we will restrict the complex frequency calculation to the special case in which the slowness is real, so that the characteristic equation is of the form $F({}^*\omega,S)=0$. The attenuation of the wave is then described in time. This kind of transient approach has already been considered in seismology and identified as an attractive model for calculating the modal properties of the waves excited by an earthquake or explosion point source.[18,19] In that context the interest was focused on temporal solutions rather than on the space. The complex frequency approach is different from the complex slowness approach and there is no reason to expect the dispersion curves should be the same.

Very recently, results have been obtained and examined by Poncelet and Deschamps for the propagation of transient heterogeneous waves in a fluid-loaded plate using the concept of complex frequency. They showed that, since in practice the excitation signals are bounded both spatially (by the size of the transducers) and temporally (by the switching on and off of the electric source), the use of transient (time attenuation) heterogeneous waves (spatial attenuation) seems to allow a more realistic modeling; the complex slowness models the space effects and the complex frequency models the time effects. They argue that it is preferable to represent the spatial properties by the slowness rather than the wave

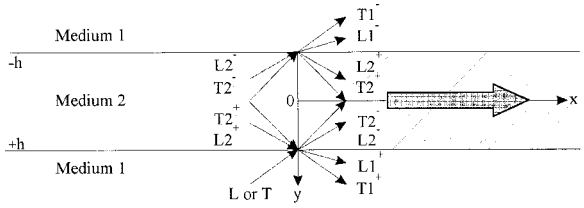

FIG. 2. Plate configuration: layer embedded in a solid medium showing partial waves.

number because the slowness is truly independent of the frequency, whereas the wave number contains a dependence on frequency: $*\mathbf{K}=*\omega*\mathbf{S}$. Their work in this topic has thus shown that waves which are characterized by amplitudes which decay in time are of key importance when Lamb waves are excited by transient signals in an immersed isotropic or anisotropic plate.[20–23] One of the findings of their studies of fluid-loaded plates is that there is a very good correlation between the dispersion curves calculated in complex frequency and the zeros of the reflection coefficient. Their results tend then to suggest that the coincidence angle principle is still valid for fluid-loaded plates if the attenuation is described by complex frequency. The modal properties of the plate can then still be linked directly with the zeros of the reflection coefficient.

Multilayered plates such as adhesive joints and diffusion-bonded joints are of great interest in nondestructive testing, and Lamb wave properties could potentially be used to detect defects including poor cohesion and poor adhesion, as considered by a number of authors and reviewed by Lowe and Cawley.[17] However, Lowe and Cawley studied such joints and showed that the zeros of the reflection coefficient when an incident wave in the adherent material reflects from the bond layer do not match the dispersion curves (for the bond layer) calculated in real frequency and complex slowness.[13,15–17] The purpose of this paper is therefore to investigate a bonded joint example using complex frequency and real slowness to see whether better agreement is obtained with this choice of solution. The geometry of the structure is similar to that considered by Poncelet and Deschamps except that the plate, which is now the bond layer, is ''immersed'' in a solid (the adherent material) instead of a fluid.

I. THEORY

The theory for elastic waves in multilayered plates is well established and was, for example, reviewed by Lowe.[14] Here we state the problem in summary and present specific forms of solution that have been derived for a single loaded layer and which are amenable to analytical study. We adopt the Cartesian coordinate system $\mathbf{X}(x,y,z)$ and arbitrarily assign **x** to the direction of propagation of the guided waves along the plate, **y** to the normal to the plate surface, and **z** to form an orthogonal set (Fig. 2). We denote the particle displacements by the vector **u**, the Lamé constants by λ and μ, and the density by ρ. The dynamic equilibrium in an infinite elastic isotropic solid is then satisfied by the equation

$$\rho \frac{\partial^2 \mathbf{u}}{\partial t^2} = (\lambda + 2\mu)\nabla(\nabla \mathbf{u}) + \mu \Delta \mathbf{u}, \tag{1}$$

where $\nabla = (\partial/\partial x, \partial/\partial y, \partial/\partial z)$ and $\Delta = (\partial^2/\partial x^2 + \partial^2/\partial y^2 + \partial^2/\partial z^2)$.

In an infinite solid, two possible equations for displacement satisfy this equation of motion, one describing longitudinal plane waves (L) and the other describing shear plane waves (T). Both have the form

$$\mathbf{u}^{\pm}_{L,T} = \mathrm{Re}\{{}^*\xi^{\pm}_{L,T} {}^*\mathbf{P} e^{i({}^*\omega t - {}^*\mathbf{K}.\mathbf{M})}\}, \tag{2}$$

where ${}^*\xi$ is the complex amplitude ($+$ for the waves traveling toward the positive **y**-direction, $-$ otherwise) and ${}^*\mathbf{P} = \mathbf{P}' - i\mathbf{P}''$ represents the unit length polarization vector (${}^*\mathbf{P} \cdot {}^*\mathbf{P} = 1$). Because the polarization is complex, the displacements are described by ellipses whose major and minor axes are defined, respectively, by $\mathbf{P}'$ and $\mathbf{P}''$, the imaginary part of the amplitude representing therefore the position of the displacement vector in the reference ($\mathbf{P}', \mathbf{P}''$). Furthermore, ${}^*\mathbf{K} = \mathbf{K}' - i\mathbf{K}''$ stands for the complex wave number, ${}^*\omega = \omega' + i\omega''$ is the complex angular frequency, **M** is the position vector in space, and the notation Re{} denotes the real part.

The real part of the wave number $\mathbf{K}'$ is the propagation vector and the imaginary part $\mathbf{K}''$ is the attenuation vector. However, as the frequency is considered as a complex quantity, and in order to separate the information due to the space from the information due to the time, as discussed earlier, a more convenient notation to express the wave number is to split it into ${}^*\mathbf{K} = {}^*\omega {}^*\mathbf{S}$, where ${}^*\mathbf{S}$ is the well-known slowness (inverse of the velocity). Therefore, the displacements become

$$\mathbf{u}^{\pm}_{L,T} = \mathrm{Re}\{{}^*\xi^{\pm}_{L,T} {}^*P e^{i[\omega'(t - \mathbf{S}' \cdot \mathbf{M}) - \omega'' \mathbf{S}'' \cdot \mathbf{M}]}\} \times e^{-\omega''(t - \mathbf{S}' \cdot \mathbf{M}) - \omega' \mathbf{S}'' \cdot \mathbf{M})}. \tag{3}$$

The real positive scalar ω' stands for the angular frequency. The parameter ω'' is the extinction coefficient ($\omega'' > 0$) or the switching-on coefficient ($\omega'' < 0$) of the source. This coefficient describes the time dependence in terms of an exponential transient. From an experimental point of view, the hypothesis of real slowness is satisfied if very large transducers are used such that an incident wave can be considered to be a plane wave rather than a bounded beam. Also, the hypothesis of complex frequency is satisfied if the signal presents a discontinuity in time. As a result, it is interesting to note that if the slowness vector is real ($\mathbf{S}'' = \mathbf{0}$), and if a plane of constant phase is considered, then the attenuation factor in the amplitude term of Eq. (3) disappears, which means that the waves do not leak. Further information concerning the notion of complex frequency and the differences it implies compared to the usual harmonic heterogeneous plane waves is presented in Refs. 20–23.

All the quantities being complex, the superscript indices * on the left-hand side of the quantities will now be omitted.

Let us now consider an infinite plane parallel elastic plate of thickness 2h, density ρ_2, longitudinal bulk velocity c_{L2}, and shear bulk velocity c_{T2}, embedded in a solid of density ρ_1, longitudinal bulk velocity c_{L1}, and shear bulk velocity c_{T1}, shown in Fig. 2. Because the connections between medium 1 and medium 2 are assumed to be ideal, the continuity of the displacements and of the stresses on the two boundaries must be satisfied. The resolution of these limit conditions leads to a system of eight equations with eight unknowns (represented by four partial waves in medium 2 and four outgoing waves in the embedding medium: two in the top half-space and two in the bottom half-space).

At this stage, two different problems can be examined: either the response problem, which consists of determining the reflection and the transmission coefficients of waves when a wave is incident, or the modal problem, which relates to the guided wave propagation properties of the system in the absence of an incident wave.

A. Response problem

In this section, the longitudinal plane-wave reflection coefficient for an incident longitudinal plane wave and the shear plane wave reflection coefficient for an incident shear plane wave are calculated, the incident wave characteristics being known. The following problem has to be solved:

$$[\mathcal{A}]\{\chi\} = \begin{Bmatrix} \mathbf{B}_{L,\mathbf{T}} \\ \mathbf{0} \end{Bmatrix}, \tag{4}$$

where

$$[\mathcal{A}] = \begin{bmatrix} \mathbf{L}_1^+ & \mathbf{T}_1^+ & -\mathbf{L}_2^- & -\mathbf{T}_2^- & \mathbf{0} & \mathbf{0} & -\mathbf{L}_2^+ & -T_2^+ \\ \mathbf{0} & \mathbf{0} & -\mathbf{L}_2^- & -\mathbf{T}_2^- & \mathbf{L}_1^- & \mathbf{T}_1^- & -\mathbf{L}_2^+ & -\mathbf{T}_2^+ \end{bmatrix}, \tag{5}$$

$$\{\chi\} = \{\xi_{L1}^+ \ \xi_{T1}^+ \ \xi_{L2}^- \ \xi_{T2}^- \ \xi_{L1}^- \ \xi_{T1}^- \ \xi_{L2}^+ \ \xi_{T2}^+\}^T. \tag{6}$$

The first and the second lines of Eq. (5) represent the boundary conditions on the top and on the bottom interfaces of the embedded layer, the vector $\mathbf{B}_{\mathbf{L},\mathbf{T}}$ stands for the longitudinal or shear incident wave, and **L** and **T** describe the longitudinal and shear partial waves traveling within the embedded layer. The indices on the bottom right-hand side of **L** or **T** indicate the medium in which the waves propagate and the sign ''+'' or ''−'' on the top right-hand side shows whether the waves travel in the positive or in the negative **y**-direction.

In this kind of problem, the orientation of the shear wave polarization vectors is arbitrary. However, in order to simplify, we set the polarization vectors of the partial shear waves within the plate such that their projection on the **x**-axis is positive and at the contrary we fix the polarization vectors of the shear waves outside the plate such that their projection on the **x**-axis is negative. Hence Eq. (5) can be expressed in terms of two matrices of dimension 4×4,

$$[\mathcal{A}] = [\mathcal{M}] + [\mathcal{C}] = \begin{bmatrix} M & 0 \\ 0 & M \end{bmatrix} + \begin{bmatrix} 0 & C \\ C & 0 \end{bmatrix}, \tag{7}$$

where

$$M=\begin{pmatrix} S_x\phi_1 & -S_{yT1}\phi_3 & -S_x\phi_6 & -S_{yT2}\phi_8 \\ -S_{yL1}\phi_1 & -S_x\phi_3 & -S_{yL2}\phi_6 & S_x\phi_8 \\ \alpha_1\phi_1 & \gamma_1 S_{yT1}\phi_3 & -\alpha_2\phi_6 & \gamma_2 S_{yT2}\phi_8 \\ -\gamma_1 S_{yL1}\phi_1 & \alpha_1\phi_3 & -\gamma_2 S_{yL2}\phi_6 & -\alpha_2\phi_8 \end{pmatrix} \tag{8}$$

and

$$C=\begin{pmatrix} 0 & 0 & -S_x\phi_5 & -S_{yT2}\phi_7 \\ 0 & 0 & S_{yL2}\phi_5 & -S_x\phi_7 \\ 0 & 0 & -\alpha_2\phi_5 & \gamma_2 S_{yT2}\phi_7 \\ 0 & 0 & \gamma_2 S_{yL2}\phi_5 & \alpha_2\phi_7 \end{pmatrix}. \tag{9}$$

The incident wave components (longitudinal or shear) are defined by

$$\mathbf{B_L}=\begin{vmatrix} -S_x\phi_2 \\ S_{yL1}\phi_2 \\ -\alpha_1\phi_2 \\ \gamma_1 S_{yL1}\phi_2 \end{vmatrix}, \tag{10}$$

$$\mathbf{B_T}=\begin{vmatrix} -S_{yT1}\phi_4 \\ -S_x\phi_4 \\ \gamma_1 S_{yT1}\phi_4 \\ \alpha_1\phi_4 \end{vmatrix}, \tag{11}$$

and all the variables used in these equations by

$$\begin{aligned} &\phi_1=e^{-imh}, \quad \phi_5=e^{-iph}, \quad p^2=\omega^2 S_{yL2}, \\ &\phi_2=e^{imh}, \quad \phi_6=e^{iph}, \quad q^2=\omega^2 S_{yT2}, \\ &\alpha_{1,2}=-i\rho_{1,2}(1-c_{T1,2}^2 S_x^2), \\ &\phi_3=e^{-inh}, \quad \phi_7=e^{-iqh}, \quad m^2=\omega^2 S_{yL1}, \\ &\gamma_{1,2}=-2i\rho_{1,2}c_{T1,2}^2 S_x \\ &\phi_4=e^{inh}, \quad \phi_8=e^{iqh}, \quad n^2=\omega^2 S_{yT1}, \end{aligned} \tag{12}$$

where S_x represents the projection of the slowness bivector on the **x**-axis, S_{yL} and S_{yT} the projection of the longitudinal and shear slowness bivectors on the **y**-axis, respectively, and 1 and 2 indicate medium 1 and 2. The matrix M refers to each interface and the matrix C represents the coupling between the two interfaces.

Because of the properties of the matrices $\mathcal{M}$ and $\mathcal{C}$, a matrix $\mathcal{R}$ is then introduced to simplify the reflection coefficients formulation as follows:

$$[\mathcal{A}]=[\mathcal{M}]([\mathcal{I}]-[\mathcal{R}]), \tag{13}$$

where

$$[\mathcal{R}]=-[\mathcal{M}]^{-1}[\mathcal{C}]=\begin{bmatrix} 0 & R \\ R & 0 \end{bmatrix} \text{ with } R=-M^{-1}C. \tag{14}$$

Then, the problem reduces to

$$\{\mathbf{X}\}=([\mathcal{I}]-[\mathcal{R}])^{-1}\{\mathbf{S}\}, \tag{15}$$

with

$$\{\mathbf{S}\}=\begin{Bmatrix} \mathbf{S_1} \\ \mathbf{0} \end{Bmatrix}, \tag{16}$$

$$\mathbf{S_1}=M^{-1}\mathbf{B_{L,T}} \tag{17}$$

and

$$([\mathcal{I}]-[\mathcal{R}])^{-1}=\begin{bmatrix} (I-R^2)^{-1} & 0 \\ 0 & (I-R^2)^{-1} \end{bmatrix}\begin{bmatrix} I & R \\ R & I \end{bmatrix}. \tag{18}$$

Finally, using the following relation, the solution of the equation can be immediately obtained by

$$\begin{pmatrix} \xi_{L1}^+ \\ \xi_{T1}^+ \\ \xi_{L2}^- \\ \xi_{T2}^- \end{pmatrix}=(I-R^2)^{-1}\mathbf{S_1}, \tag{19}$$

$$\begin{pmatrix} \xi_{L1}^- \\ \xi_{T1}^- \\ \xi_{L2}^+ \\ \xi_{T2}^+ \end{pmatrix}=(I-R^2)^{-1}R\mathbf{S_1}, \tag{20}$$

where I stands for the identity matrix, ξ_{L1}^+ is the longitudinal plane-wave reflection coefficient, and ξ_{T1}^+ the shear plane-wave reflection coefficient, the incident wave having a unit amplitude.

This method ultimately requires only a division of two determinants of dimension 4×4 and is therefore substantially faster than using a full expansion using Cramers method, which requires solution of two determinants of dimension 8×8.

B. Modal problem

The modal problem is defined by Fig. 2 without any incident wave. In fact, the system is supposed to be unforced and the guided wave is able to propagate without input of energy. Because the geometry is completely symmetric about the **x**-axis in terms of waves and layers, the problem can then be reduced by half. The determinant of dimension 8×8 linked to the matrix $\mathcal{A}$ [Eq. (5)] can then be transformed into a multiplication of two determinants of dimension 4×4 by decomposition into symmetric and antisymmetric modes.

1. Equation for symmetric case

For the symmetric modes, the displacements in the plate are given by[24]

$$\begin{aligned} u_1&=[-ik_xA_2\cos(py)+qB_1\cos(qy)]e^{i\omega(t-S_xx)} \\ u_2&=[-pA_2\sin(py)+ik_xB_1\sin(qy)]e^{i\omega(t-S_xx)}, \end{aligned} \tag{21}$$

where: A_2 stands for the amplitude of the longitudinal partial wave and B_1 defines the amplitude of the shear partial wave. The displacements in the bottom half-space are given by

$$\begin{aligned} u_1&=[-ik_xCe^{-imy}-inDe^{-iny}]e^{i\omega(t-S_xx)} \\ u_2&=[-imCe^{-imy}+ik_xDe^{-iny}]e^{i\omega(t-S_xx)}, \end{aligned} \tag{22}$$

where C and D denote the amplitudes of the longitudinal and the shear plane waves, respectively. The displacements in the top half-space are the mirror image. Applying the limit condition on the interface located at $y=h$, that is the continuity

of the displacements and of the stresses, a system of four equations with four unknowns (amplitudes of the waves) is obtained. The trivial solution to this system is to set the amplitudes of the waves to zero: no waves propagate. The other solution is to find the couple $(*\omega, *S)$ such that the determinant of the matrix is zero. Thus after expansion of the determinant, the analytical solution for the symmetric Lamb function (Cs) propagating in a plate embedded in a solid is presented,

$$Cs = A\cot(ph) + B\cot(qh) + C\cot(ph)\cot(qh) + D = 0; \tag{23}$$

with

$$\begin{aligned} A &= 4k_x^6U^2 + mnU^2[\rho_2 V + 2k_x^2]^2 \\ &\quad + k_x^2\omega^2(\rho_1 - \rho_2)U[(\rho_1 - \rho_2)V - 4k_x^2], \\ B &= pqU^2\{4k_x^2mn + [\rho_1 - 2k_x^2]^2\}, \\ C &= -i\rho_1\rho_2 qm\omega^4, \quad U = \rho_1 c_{T1}^2 - \rho_2 c_{T2}^2, \quad k_x = \omega S_x, \\ D &= i\rho_1\rho_2 pn\omega^4, \quad V = \frac{\omega^2}{U}. \end{aligned} \tag{24}$$

2. Equation for antisymmetric case

The antisymmetric Lamb function (Ca) propagating in a plate embedded in solid is easily found by changing the cotangents into tangents and by taking the conjugates of C and D. Therefore,

$$Ca = A\tan(ph) + B\tan(qh) - C\tan(ph)\tan(qh) - D = 0. \tag{25}$$

3. Solution

The dispersion curves are the loci of solutions of the transcendental equation $Cs = 0$ or $Ca = 0$. They are calculated in complex frequency and real slowness with a Newton–Raphson algorithm providing fast computation. The dispersion curves calculated using the conventional assumption of real frequency and complex slowness are calculated using a general purpose model developed by Lowe[14] and Pavlakovic *et al.*[25]

II. RESULTS AND DISCUSSION

The example that has been chosen for study relates to diffusion-bonded titanium. Previous work by Lowe and Cawley[13,17] examined the reflection coefficient minima and the real frequency dispersion curves for an idealized defective bonded joint, and those results form a useful basis for comparison with the dispersion curves for complex frequency. The idealized defective joint consists of a uniform layer of alpha case (or hard alpha) at the bond line between the two titanium adherents. The alpha case is brittle and may be established if oxygen or nitrogen is present during bonding. It has been shown that the bulk velocities of the alpha case are about 5% to 10% faster than those of the titanium but that its density is roughly the same.[26,27] The properties of those materials have therefore been chosen to be, for titanium, $c_{L1} = 6.06$ km/s, $c_{T1} = 3.23$ km/s, $\rho_1 = 4.46$ T/m^3, and for alpha case, $c_{L2} = 6.66$ km/s, $c_{T2} = 3.553$ km/s, $\rho_2 = 4.46$ T/m^3. In this section, the dispersion curves calculated either in real frequency and complex slowness or in complex frequency and real slowness will be compared to the minima and the zeros of the shear and longitudinal plane-wave reflection coefficients.

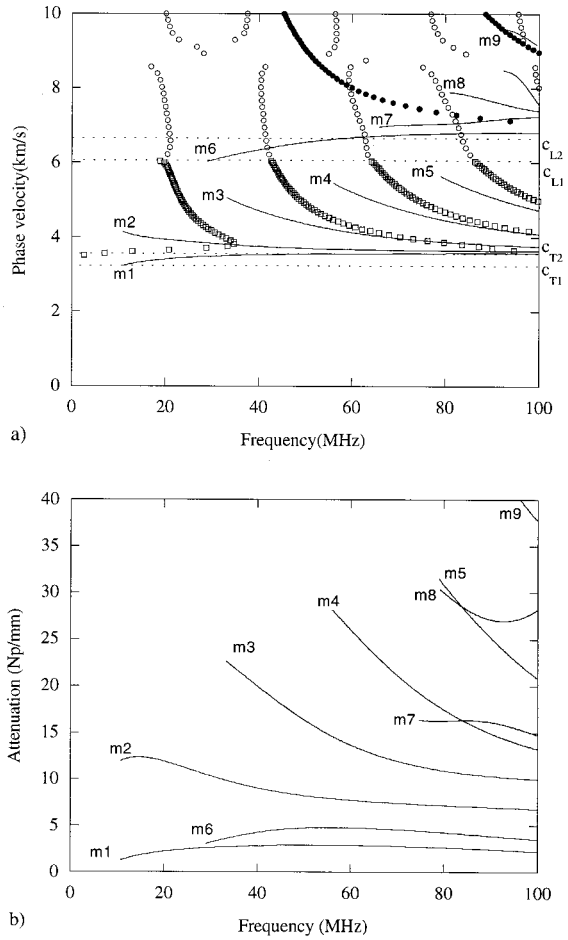

FIG. 3. (a) Comparison between the dispersion curves (—) calculated in real frequency and complex slowness (Refs. 13 and 17), the minima (○) and the zeros (□) of the shear plane-wave reflection coefficient and the minima of the longitudinal plane wave reflection coefficient (●) for a 0.1-mm-thick layer of alpha case embedded in titanium. (b) Attenuation (imaginary wave number) of these curves versus frequency.

A. Comparison between plane-wave reflection coefficients and dispersion curves for real frequency and complex slowness ($\omega = \omega'$)

Predictions of the reflection coefficient results and the conventional complex slowness dispersion curves for the layer of alpha case embedded in titanium are shown in Fig. 3. Part (a) of the figure shows the phase velocity ($1/S_x'$) and part (b) presents the attenuation factor $K_x'' = -\omega S_x''$ expressed in nepers per millimeters, both versus the frequency.[13,15–17] Two categories of reflection coefficient results are shown in part (a): ''zeros'' (□) correspond to the identification of zero values of the reflection coefficient; ''minima'' (○) correspond to the identification of locations where there is a clear dip of the function but not to zero value. Empty symbols (□, ○) correspond to the shear plane-wave reflection coefficient (shear incident, shear reflected), filled symbols (●) corre-

spond to the longitudinal plane-wave reflection coefficient. The horizontal dashed lines show the bulk velocities of the two materials. It should be noted that due to their very high attenuation leading to nonphysical solutions, some modes have not been traced or pursued.

It can be seen that there is no region, in this frequency range, where the minima or the zeros of the reflection coefficients coincide with the dispersion curves, although they show some similar trends and the leaky shear modes and the zeros seem to correlate reasonably well near the shear bulk velocity of the titanium as the frequency increases. The convergence of the zeros toward the modes at high frequency is also accompanied by a reduction in attenuation [Fig. 3(b)] and led Lowe and Cawley to suggest that the separation of zeros and modes is related to the rate of leakage. It is clear, therefore, that the measurement of zeros of the reflection coefficient do not reveal the (conventional) harmonic heterogeneous modal properties.

B. Comparison between plane-wave reflection coefficients and dispersion curves for complex frequency and real slowness

For the same configuration, let us now analyze the zeros and the minima of both the shear and the longitudinal plane-wave reflection coefficients and the dispersion curves calculated using the alternative approach of complex frequency and real slowness, shown in Fig. 4. Again, part (a) shows the phase velocity $(1/S_x')$ and part (b) presents the dimensionless attenuation factor $\Omega = \omega''/\omega'$. Both are plotted versus the real part of the frequency $(\omega'/2\pi)$. The imaginary parts of the different modes have been plotted just to point out that Ω is always positive. Therefore, the transient parts of the signals will be characterized by exponential decreases in time. The labels $m1$ to $m6$ are arbitrary. It is interesting to observe that modes $m2$ and $m4$ exhibit a cutoff in frequency when Ω tends to infinity. This characteristic was already observed in the case studied by Poncelet and Deschamps.[20]

Two different zones of the solution can be differentiated. Exactly below the longitudinal bulk velocity of the titanium (c_{L1}), there only exist zeros of the shear plane-wave reflection coefficient (squares) and, contrary to Fig. 3, they agree very well with the dispersion curves. The existence of zeros instead of minima could be because one wave, and one only, is reflected from the layer, the longitudinal plane wave being a surface wave beyond the critical angle associated with c_{L1}. This observation concerning the simultaneous existence of the zeros and of a single reflected wave would be in accordance with the liquid/solid/liquid geometry discussed earlier. In that case, only longitudinal plane waves can be reflected, of course, and the zeros exist for any incidence angle. The correlation between the zeros and the dispersion curves for a resolution in complex frequency is then always observed, even when the immersed solid is anisotropic.[20,22,23]

Returning to the present embedded solid case, above c_{L1} (second zone) the spectra of the plane-wave reflection coefficients do not present any zeros but only minima (circles). As an example of the minima, Fig. 5 illustrates the shear plane-wave reflection coefficient versus the frequency at a phase velocity of 8.4 km/s, where clearly the values of the minima are nonzero.

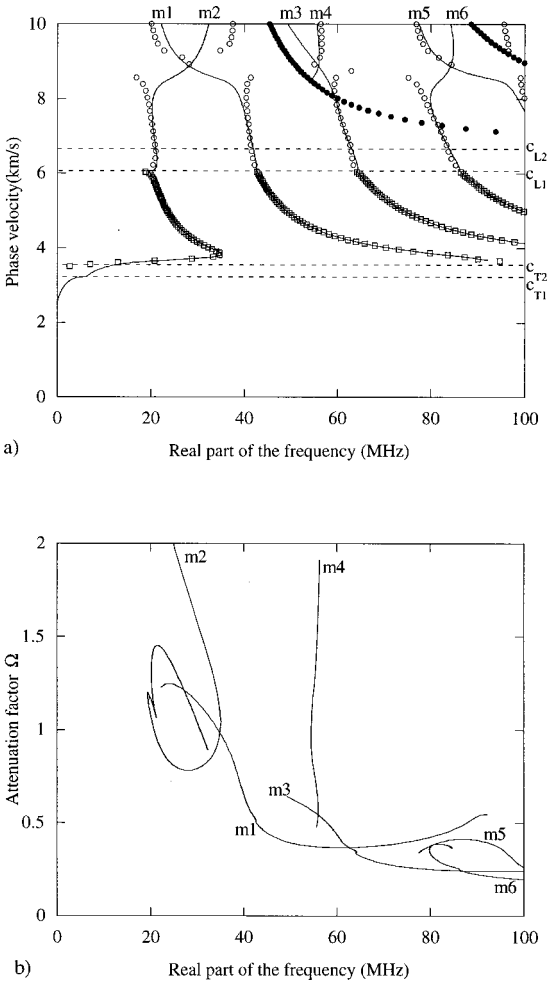

FIG. 4. (a) Comparison of the dispersion curves (—) calculated in complex frequency and real slowness, with the reflection coefficient results as shown in Fig. 3. (b) Attenuation factor Ω versus the real part of the frequency for a 0.1-mm-thick alpha case plate embedded in titanium.

The agreement between the minima of both the shear and the longitudinal plane-wave reflection coefficients and

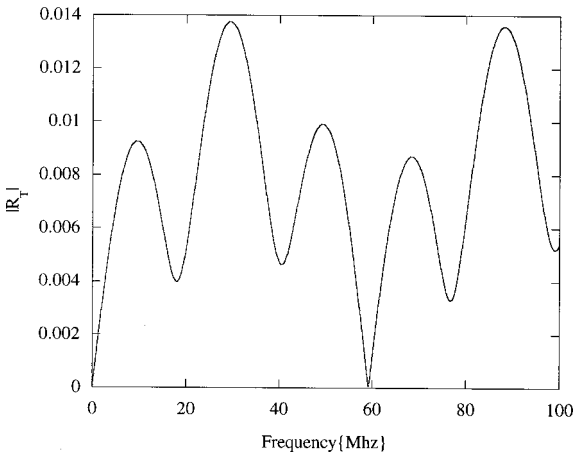

FIG. 5. Example of poor minima in the titanium/0.1-mm alpha case/titanium structure for the shear plane-wave reflection coefficient at a phase velocity of 8.4 km/s.

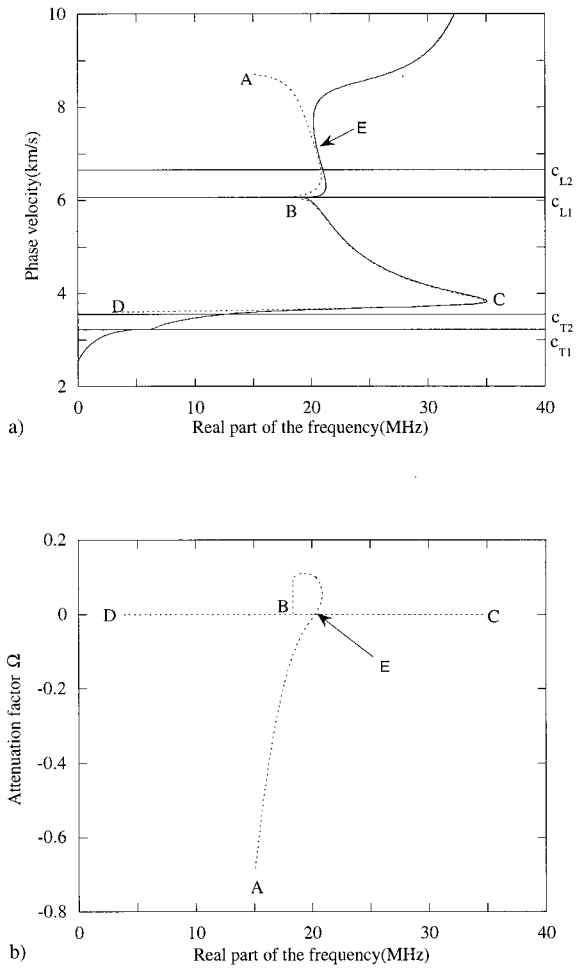

FIG. 6. (a) Comparison between the shear plane-wave reflection coefficient (···) and the mode labeled $m2$ in Fig. 4 (—), both calculated in complex frequency and real slowness, (b) attenuation factor ($\Omega = \omega''/\omega'$) of the zeros of the reflection coefficient.

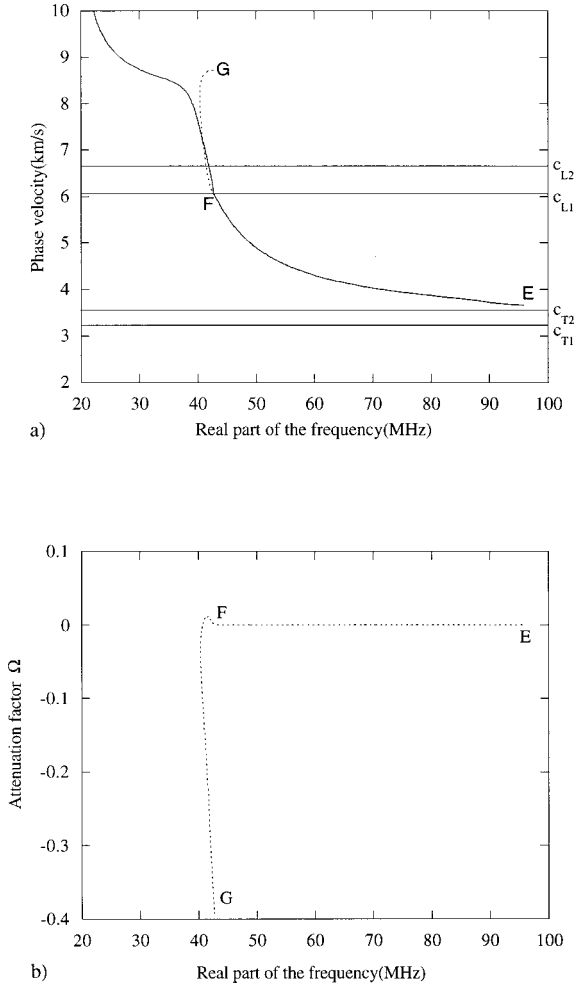

FIG. 7. As Fig. 6 but for the mode m1.

the dispersion curves degenerates progressively as the phase velocity increases, with the exception of just a few localized points. Above velocities of about 8 km/s, the minima and the dispersion curves are almost totally separated. The minima of the longitudinal plane-wave reflection coefficient (●), for example, do not correspond to any dispersion curves. The presence of minima instead of zeros above c_{L1} may be explained by the fact that in general both shear and longitudinal plane waves are reflected when either shear or longitudinal is incident.

C. Consideration of minima of the complex reflection coefficient, assuming complex frequency

The minima and zeros of the reflection coefficients were obtained assuming, conventionally, continuous plane waves (real frequency and real slowness). Let us now consider the possibility of reflection coefficients calculated with complex frequency and real slowness (transient incident waves). This will enable us to reduce the minima to zeros by searching in the (now) complex solution space. We study, for example, the modes labeled $m1$ and $m2$ in Fig. 4.

We consider first the mode $m2$. Figures 6(a) and 6(b) present the comparison between the real and the imaginary part (characterized by the dimensionless quantity $\Omega = \omega''/\omega'$) of the zeros of the shear plane-wave reflection coefficient (dashed line), and the dispersion curves (solid line) calculated in complex frequency and real slowness versus the real part of the frequency.

The two zones of solution identified earlier are clearly seen here since obviously the zeros plotted earlier in Fig. 4 must appear here with zero imaginary part, whereas the minima must now appear with nonzero imaginary part. For example, in Fig. 6, the path between *A* and *B*, above the longitudinal bulk velocity of the titanium c_{L1}, has a non-null Ω. The roots of the reflection coefficients are therefore complex and do not correlate with the dispersion curves. However, the path between *B* and *D*, below the longitudinal bulk velocity of the titanium c_{L1}, has null imaginary parts. We can also observe that despite now being able to identify loci of reflection coefficient zeros (rather than minima) throughout this solution space, we are still left with a divergence between the dispersion curves and the zeros when the velocity is greater than c_{L1}. The difference is therefore clearly a fundamental characteristic, and cannot simply be a result of poor identification of minima. In addition, the larger the imaginary part of the roots, the greater the divergence between the minima and the dispersion curves. Moreover, it can be observed that above c_{L1}, the point (*E*) which has a

null Ω, that is when the sign of Ω is changing from positive to negative values, is exactly on the dispersion curve even though both longitudinal and shear plane waves are being reflected.

The same analysis can be drawn for the other mode, $m1$, shown in Fig. 7. Again, as soon as the imaginary part of the root of the shear plane-wave reflection coefficient becomes non-null (path between F and G), the zeros (dashed line) move away from the dispersion curves (solid line). The two sets of curves have then only one point of agreement after this separation, exactly when the imaginary part crosses the **x**-axis to go from positive to negative values. The same phenomenon has been observed to occur for all the other modes.

III. CONCLUSIONS

Computational solutions of symmetric and antisymmetric Lamb functions and reflection coefficient have been presented for a plate embedded in a solid. A comparison between the dispersion curves obtained either in complex slowness and real frequency or in real slowness and complex frequency with the minima of the shear and longitudinal reflection coefficient has been achieved. A better correlation with the resolution in complex frequency has been shown, although some regions still exhibit some disagreements. Those differences occur where the minima are poorly defined. At such locations, clearly defined zeros of the shear and longitudinal plane-wave reflection coefficients may still be found by using a calculation with real slowness and complex frequency. However, these solutions still exhibit poor correlation with the dispersion curves in these regions. Regarding the implication on experimental work, it seems that the coincidence principle may be used reliably to measure the modal properties if the modes are calculated using complex frequency and real slowness and if measurements are restricted to velocities lower than c_L in the embedding medium.

ACKNOWLEDGMENT

The authors gratefully acknowledge support from the British Council for their collaboration in this research, via a British Council fellowship for A. Bernard.

[1] H. Lamb, ''On waves in an elastic plate,'' in Conference of the Royal Society, London, 1917.
[2] D. E. Chimenti and A. H. Nayfeh, ''Anomalous ultrasonic dispersion in fluid-coupled fibrous composite plates,'' Appl. Phys. Lett. **49**(9), 492–493 (1986).
[3] D. E. Chimenti and S. I. Rokhlin, ''Relationship between leaky Lamb modes and reflection coefficient zeros for a fluid-coupled elastic layer,'' J. Acoust. Soc. Am. **88**(3), 1603–1611 (1990).
[4] A. H. Nayfeh and D. E. Chimenti, ''Ultrasonic wave reflection from liquid-coupled orthotropic plates with application to fibrous composites,'' J. Appl. Mech. **55**, 863–870 (1988).
[5] A. H. Nayfeh and D. E. Chimenti, ''Propagation of guided waves in fluid-coupled plates of fiber-reinforced composite,'' J. Acoust. Soc. Am. **83**(5), 1736–1743 (1988).
[6] T. Plona, M. Behravesh, and W. Mayer, ''Rayleigh and Lamb waves at liquid-solid boundaries,'' Ultrasonics **1**, 171–174 (1975).
[7] R. Fiorito, W. Madigosky, and H. Uberall, ''Resonance theory of acoustic waves interacting with an elastic plate,'' J. Acoust. Soc. Am. **66**(6), 1857–1866 (1979).
[8] R. Fiorito and H. Überall, ''Resonance theory of acoustic reflection and transmission through a fluid layer,'' J. Acoust. Soc. Am. **65**(1), 9–14 (1979).
[9] D. Worlton, ''Experimental confirmation of Lamb waves at megacycle frequencies,'' J. Appl. Phys. **32**(6), 967–971 (1961).
[10] O. Lenoir, J. Duclos, J. M. Conoir, and J. L. Izbicki, ''Study of Lamb waves based upon the frequency and angular derivatives of the phase of the reflection coefficient,'' J. Acoust. Soc. Am. **94**(1), 330–343 (1993).
[11] J. Izbicki, G. Maze, and J. Ripoche, ''Etude de la réémission libre d'une plaque résonnante,'' Int. J. Acoust. **55**, 27–29 (1984).
[12] W. Junru and Z. Zhemin, ''The propagation of Lamb waves in a plate bordered with layers of a liquid,'' J. Acoust. Soc. Am. **91**(2), 861–867 (1992).
[13] M. Lowe and P. Cawley, ''Comparison of reflection coefficient minima with dispersion curves for ultrasonic waves in embedded layers,'' in *Review of Progress in Quantitative NDE* (Plenum, New York, 1994).
[14] M. Lowe, ''Matrix techniques for modeling ultrasonic waves in multilayered media,'' IEEE Trans. Ultrason. Ferroelectr. Freq. Control **42**(4), 525–542 (1994).
[15] M. J. S. Lowe and P. Cawley, ''The influence of the modal properties of a stiff layer embedded in a solid medium on the field generated in the layer by a finite-sized transducer,'' J. Acoust. Soc. Am. **97**(3), 1638–1649 (1995).
[16] M. J. S. Lowe and P. Cawley, ''Comparison of the modal properties of a stiff layer embedded in a solid medium with the minima of the plane-wave reflection coefficient,'' J. Acoust. Soc. Am. **97**(3), 1625–1637 (1995).
[17] M. J. S. Lowe and P. Cawley, ''The applicability of plate wave techniques for the inspection of adhesive and diffusion bonded joints,'' J. Nondestruct. Eval. **13**(4), 185–199 (1994).
[18] J. H. Rosenbaum, ''The long-time response of a layered elastic medium to explosive sound,'' J. Geophys. Res. **65**(5), 1577–1613 (1960).
[19] R. A. Phinney, ''Leaking modes in the crystal waveguide,'' J. Geophys. Res. **66**(5), 1445–1469 (1961).
[20] O. Poncelet and M. Deschamps, ''Lamb waves generated by complex harmonic inhomogeneous plane waves,'' J. Acoust. Soc. Am. **102**(1), 292–300 (1997).
[21] O. Poncelet, ''Ondes planes hétérogènes à fréquence complexe: Modes propres de plaques immergées,'' University Bordeaux I, France, 1996.
[22] M. Deschamps and O. Poncelet, ''Plate waves with complex frequency and total transmission,'' in Proceedings of Ultrasonics World Congress, 1997, Yokohama.
[23] M. Deschamps and O. Poncelet, ''Transient Lamb waves: Comparison between theory and experiments,'' J. Acoust. Soc. Am. (in press).
[24] J. D. Achenbach, *Wave Propagation in Elastic Solids* (North-Holland, Amsterdam, 1973), p. 223.
[25] B. Pavlakovic, M. J. S. Lowe, D. Alleyne, and P. Cawley, ''Disperse: A general purpose program for creating dispersion curves,'' in *Review of Progress in Quantitative NDE* (Plenum, New York, 1996).
[26] R. B. Thompson, F. Margetan, J. Rose, and N. Batia, ''Effects of interstitial oxygen on the ultrasonic properties of titanium alloys,'' in *Review of Progress in Quantitative NDE* (Plenum, New York, 1992).
[27] M. Lowe and P. Cawley, ''The detection of a brittle layer at the bondline in diffusion bonded titanium,'' in *Review of Progress in Quantitative NDE* (Plenum, New York, 1993).

Measurement of acoustic dispersion using both transmitted and reflected pulses

Ping He
Department of Biomedical, Industrial and Human Factors Engineering, Wright State University, Dayton, Ohio 45435

(Received 10 August 1999; accepted for publication 10 November 1999)

Traditional broadband transmission method for measuring acoustic dispersion requires the measurements of the sound speed in water, the thickness of the specimen, and the phase spectra of two transmitted ultrasound pulses. When the sound speed in the specimen is significantly different from that in water, the overall uncertainty of the dispersion measurement is generally dominated by the uncertainty of the thickness measurement. In this paper, a new water immersion method for measuring dispersion is proposed which eliminates the need for thickness measurement and the associated uncertainty. In addition to recording the two transmitted pulses, the new method requires recording two reflected pulses, one from the front surface and one from the back surface of the specimen. The phase velocity as well as the thickness of the specimen can be determined from the phase spectra of the four pulses. Theoretical analysis and experimental results from three specimens demonstrate the advantages of this new method. © *2000 Acoustical Society of America.* [S0001-4966(00)04002-9]

PACS numbers: 43.35.Cg, 43.35.Yb [HEB]

INTRODUCTION

Determination of acoustic dispersion (phase velocity as a function of frequency) in the frequency domain using a broadband transmission method has recently found many applications. Since introduced by Sachse and Pao in 1978, this method has been used to study the dispersion properties of metal (Sachse and Pao, 1978), epoxy resin (Rokhlin *et al.*, 1986), paper materials (Brodeur *et al.*, 1993), polymeric materials (Zellouf *et al.*, 1996), and ultrasound contrast agent (Mobley *et al.*, 1998), as well as to verify Kramers–Kronig relationship for acoustic waves (Lee *et al.*, 1990; Brodeur *et al.*, 1993).

Determination of dispersion using the above transmission method requires the measurements of a reference velocity—usually the sound speed in water, the thickness of the specimen, and the phase spectra of two transmitted ultrasound pulses. Since the magnitude of dispersion for most materials is very small (less than 1% within the frequency range of 1–10 MHz), minimizing measurement uncertainties is particularly important in such applications. In many cases, the overall accuracy of the dispersion measurement is limited by the uncertainty of the thickness measurement. In some cases, the specimen may have irregular surfaces; in other cases, the specimen may not be rigid enough that the action of measuring its thickness causes a certain degree of deformation. Even under ideal surface conditions, it has been shown that the overall uncertainty of the dispersion measurement is dominated by the uncertainty of the thickness measurement when the sound speed in the specimen is significantly different from that in water (Mobley *et al.*, 1998).

In this paper, a new water immersion, broadband method for determining dispersion in the frequency domain is described which does not require measuring the specimen's thickness. This new method is essentially an extension of a time-domain method, first proposed by Kuo *et al.* (1990) and later expanded by Hsu and Hughes (1992), which determines the sound speed in the specimen using times-of-flight data. The instruments and setup used in the new method are the same as that used in the traditional immersion, broadband transmission method for measuring dispersion. In addition to recording two transmitted pulses, the new method requires recording two reflected pulses, one from the front surface and one from the back surface of the specimen. The phase velocity of the specimen is determined from the phase spectra of the four recorded pulses. In addition, using an approach parallel to the one used by Hsu and Hughes (1992), it is shown that the thickness of the specimen can also be determined from the phase spectra of the four pulses. Results from three specimens are reported and an error analysis is presented.

I. THEORY

Figure 1 shows the signal paths in the immersion experiment for the dispersion measurement. $P_0(t)$ is the initial pulse launched by the transducer labeled as T_1. $P_s(t)$ and $P_w(t)$ represent the transmitted pulses with and without the specimen inserted, respectively, and $P_1(t)$ and $P_2(t)$ represent the pulses reflected back from the front and back surfaces of the specimen, respectively. If we use $A(f)e^{-j\theta(f)}$ to represent the Fourier transform of a pulse $P(t)$, and assume that the dispersion of water is negligible (Rokhlin *et al.*, 1986), the phase velocity of the specimen can be obtained from the phase spectra of the two transmitted pulses, $P_s(t)$ and $P_w(t)$ (Wu, 1996; He, 1999)

$$\frac{1}{V_p(f)} = \frac{\theta_s(f) - \theta_w(f)}{2\pi f L} + \frac{1}{c_w}, \tag{1}$$

where $V_p(f)$ is the phase velocity in the specimen, c_w is the sound speed in water, $\theta_s(f)$ and $\theta_w(f)$ are the phase spectra

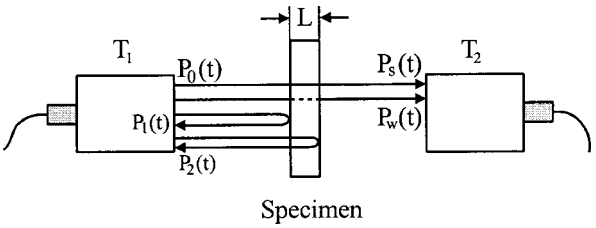

FIG. 1. Signal paths in the immersion experiment for the dispersion and thickness measurements.

of $P_s(t)$ and $P_w(t)$, respectively, and L is the thickness of the specimen.

Using the same analysis (He, 1999), $V_p(f)$ can also be obtained from the phase spectra of the two reflected pulses

$$\frac{1}{V_p(f)}=\frac{\theta_2(f)-\theta_1(f)}{4\pi fL}, \tag{2}$$

where $\theta_1(f)$ and $\theta_2(f)$ are the phase spectra of $P_1(t)$ and $-P_2(t)$, respectively (to take account of the inherent extra 180°-phase shift between P_2 and P_1, the recorded P_2 is always inverted first in all the data processing described in this paper). From the above two equations, we cancel L and obtain the phase velocity

$$V_p(f)=c_w\left[1+2\times\frac{\theta_w(f)-\theta_s(f)}{\theta_2(f)-\theta_1(f)}\right]. \tag{3}$$

This is the basic equation for determining $V_p(f)$ without measuring the specimen's thickness. It should be noted that each $\theta(f)$ in Eq. (3) is the absolute phase calculated using an origin of time ($t=0$) that is the instant when $P_0(t)$ is launched. Due to the large time delays between $P_0(t)$ and the transmitted or reflected pulses, the absolute phases of these pulses change rapidly with frequency, and phase unwrapping is required. In order to accurately determine the true absolute phase, a large number of zeros are usually appended to the original pulse to increase the sample density of the phase function, and the $2m\pi$ phase ambiguity needs to be carefully account for (Wu, 1996; Mobley, 1998). In order to simplify the process of phase calculation and reduce the ambiguity, we employ the following technique to determine the absolute phase.

We first assume that each of $P_s(t)$, $P_w(t)$, $P_1(t)$, and $P_2(t)$ is acquired using a long sampling window that starts from $t=0$. Instead of directly performing Fourier transform to the recorded pulse, we first shift the center of the pulse to the beginning of the sampling window (by circularly rotating to the left all the samples within the sampling window) and then calculate the phase spectrum of the shifted pulse. The relation between the phase spectra of the original and shifted pulses is

$$\theta(f)=\phi(f)+2\pi ft, \tag{4}$$

where $\phi(f)$ is the phase spectrum of the shifted pulse, and $t=n/f_s$ is the time shift, where f_s is the sampling frequency and n is the number of samples being shifted. Substituting Eq. (4) into Eq. (3), the equation for determining dispersion becomes

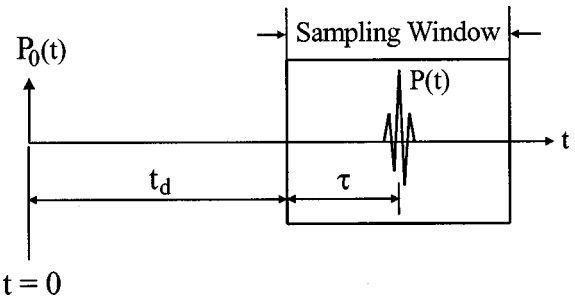

FIG. 2. Temporal relations of the initial pulse $P_0(t)$, sampling window, and recorded pulse $P(t)$.

$$V_p(f)=c_w\left[1+2\times\frac{\phi_w(f)-\phi_s(f)+2\pi f(t_w-t_s)}{\phi_2(f)-\phi_1(f)+2\pi f(t_2-t_1)}\right], \tag{5}$$

where $\phi_w(f)$, $\phi_s(f)$, $\phi_2(f)$, $\phi_1(f)$ are the phase spectrum of shifted $P_w(t)$, $P_s(t)$, $-P_2(t)$, $P_1(t)$, respectively, and t_w, t_s, t_2, t_1 are the respective time shifts.

We next consider that in a typical experiment, the pulse is recorded using a relatively small sampling window that starts not at $t=0$ but after a trigger delay t_d, as shown in Fig. 2. In this case, the recorded pulse is still shifted to the beginning of the sampling window and the phase spectrum of the shifted pulse is then calculated as $\phi(f)$. The total time shift, t, used in Eqs. (4) and (5) in this case should include both the time shift, τ, within the sampling window and the trigger delay, t_d, of the sampling window

$$t=t_d+\tau. \tag{6}$$

In both cases, the change (with frequency) of the phase spectrum, $\phi(f)$, can be minimized by adjusting the amount of time shift, and phase unwrapping is normally not needed (or rather easy to perform) in determining $\phi_w(f)$, $\phi_s(f)$, $\phi_2(f)$, and $\phi_1(f)$ (as we will show later in Fig. 4). As a result, $V_p(f)$ can be determined accurately by Eq. (5).

Equations (3) and (5) indicate that the absolute phase velocity $V_p(f)$ determined by the above method is directly proportional to c_w which changes with temperature (Del Grosso and Mader, 1972). If we express dispersion as the relative change in phase velocity, then the need for measuring c_w can also be eliminated:

$$\frac{V_p(f)-V_p(f_0)}{V_p(f_0)}=\frac{F(f)-F(f_0)}{1/2+F(f_0)}, \tag{7}$$

where f_0 is a reference frequency, and the function $F(f)$ is defined as

$$F(f)=\frac{\phi_w(f)-\phi_s(f)+2\pi f(t_w-t_s)}{\phi_2(f)-\phi_1(f)+2\pi f(t_2-t_1)}. \tag{8}$$

In this case, the uncertainty of the dispersion measurement is solely determined by the uncertainty of the time measurement.

If we cancel V_p in Eq. (1) and Eq. (2), and make use of Eq. (5), we obtain an estimate for the thickness L:

$$\hat{L} = \frac{c_w}{4\pi f}[\theta_2 - \theta_1 + 2(\theta_w - \theta_s)]$$

$$= \frac{c_w}{4\pi f}[\phi_2 - \phi_1 + 2(\phi_w - \phi_s) + 2\pi f(t_2 - t_1 + 2t_w - 2t_s)]. \quad (9)$$

In theory, the frequency dependence of all the components on the right side of Eq. (9) should be completely canceled out, making $\hat{L}$ a perfect constant. In practice, however, $\hat{L}$ calculated from the experimental data will not be a perfect constant, but will change with frequency. The mean of $\hat{L}$ within the frequency range of the measurement system is used as the estimated thickness L and the standard deviation of $\hat{L}$ can be used to judge the reliability of the new method in estimating thickness and measuring dispersion.

A comparison between the method presented here and the methods proposed earlier by Kuo *et al.* (1990) and Hsu *et al.* (1992) can be made at this point. The method presented here is based on the frequency-domain analysis and it measures the phase velocity of the specimen as a function of frequency. The methods proposed by Kuo *et al.* and Hsu *et al.* are performed in the time domain, and both measure the speed of sound of the specimen at unspecified frequency. If the time shift, t, in Eq. (4) is adjusted in such a way that $|\phi(f)|$ is minimized within the frequency range of interest, the time shifts, t_w, t_s, t_2, and t_1 in Eq. (5) and Eq. (9) then represent the gross propagation delay of P_w, P_s, P_2, and P_1, respectively. Then, if one ignores dispersion by assuming $\phi_w(f) = \phi_s(f)$, and $\phi_2(f) = \phi_1(f)$, Eq. (5) is reduced to Eq. (6) in the paper by Kuo *et al.* (1990) and Eq. (9) is reduced to Eq. (10) in the paper by Hsu *et al.* (1992). In other words, the time-domain methods proposed by Kuo *et al.* and Hsu *et al.* can be considered as approximations to the frequency-domain method presented here.

II. EXPERIMENT AND RESULTS

A typical setup for immersion experiment is used to test the new method (He, 1999). A focused transducer (Panametrics V382, 3.5 MHz, 13-mm aperture, 8.9-cm focal distance) is used as the transmitter/receiver (T_1 in Fig. 1) and a nonfocused transducer (Panametrics V384, 3.5 MHz, 6.35-mm aperture) is used as the receiver (T_2 in Fig. 1). This pair of transducers gives a useful frequency range of 1–5 MHz in all the experiments reported in this paper. The distance between T_1 and the front surface of the specimen is approximately 10 cm. The pulser/receiver used in the experiment is Panametrics 5052 PR. The amplified pulse is A/D converted by a SONY/TEK 390 AD programmable digitizer which has an adjustable digital delay for triggering the sampling window. Each sampling window contains 512 samples and the sampling frequency is 60 MHz. The samples are transferred to a PC and processed using a software package MATLAB (Math Works, MA). The water temperature is 21.2 °C, which gives $c_w = 1485.968$ m/s (Del Grosso and Mader, 1972).

A Plexiglas, a high-density polyethylene, and a low-density polyethylene sample are used in the experiment. The origin of the Plexiglas sample is unknown. The two polyethylene samples are both obtained from Poly Hi Solidur (Scranton, PA). The densities of the three samples are 1.176, 0.966, and 0.918 g/cm^3, respectively. The thickness of each sample is measured at five locations using a digital caliper (model 599-571-4, Brown & Sharpe, North Kingstown, RI), and the mean and standard deviation are listed in Table I. The mean thickness is used for calculating dispersion using the traditional method as well as for comparing with the thickness estimated using the new method.

TABLE I. Measured thickness using a digital caliper (average at five locations) and estimated thickness using Eq. (9) within the frequency range of 1 to 5 MHz for three specimens.

	Measured thickness (mm) (five locations)	Estimated thickness (mm) (1–5 MHz)
Plexiglas	39.942 ± 0.008	39.888 ± 0.004
High-density polyethylene	18.76 ± 0.03	18.706 ± 0.004
Low-density polyethylene	3.156 ± 0.009	3.149 ± 0.006

Figure 3 shows the four pulses obtained using the Plexiglas sample and Fig. 4 shows their phase spectra (P_2 is first reversed) after being shifted to the beginning of the respective sampling window. As shown in the figure, all the phase spectra change slowly with frequency. As a result, phase unwrapping is not needed in determining these spectra.

Figure 5(a) compares the phase velocity of the Plexiglas sample determined using the new method (solid line) and the traditional method (dashed line). The solid line is obtained using Eq. (5) based on the phase spectra (ϕ_1, ϕ_2, ϕ_w, and ϕ_s) shown in Fig. 3. In this particular experiment, the time shifts t_1, t_2, t_w, and t_s are 96.517, 125.450, 108.150, and 75.783 μs, respectively. Only four representative error bars at frequencies 1.5, 2.5, 3.5, and 4.5 MHz are presented in the figure. These error bars are calculated using Eq. (12), which will be derived later in Sec. III, based on an uncertainty of 0.1 °C in the temperature measurement and an uncertainty of 8.33×10^{-9} s in the time measurement. The dashed line in the figure is calculated using Eq. (1) with a measured $L = 39.942$ mm, as listed in Table I.

Figure 5(b) plots the estimated thickness using Eq. (9). As expected, $\hat{L}$ calculated from the experimental data is not a perfect constant, but the change (with frequency) is very small. Since the apparent flatness of this curve can be arbitrarily changed by changing the vertical scale of the plot, we chose the vertical plot range to be approximately ±1% around the mean value (in this case, it is from 39.9–0.4 mm to 39.9+0.4 mm). The mean and standard deviation of the estimated thickness are calculated within the frequency range of 1–5 MHz, and the results are listed in Table I.

Figure 6 shows the experimental results from the high-density polyethylene sample, and Fig. 7 shows the experimental results from the low-density polyethylene sample. Again, the mean and standard deviation of the thickness estimation for each specimen are listed in Table I.

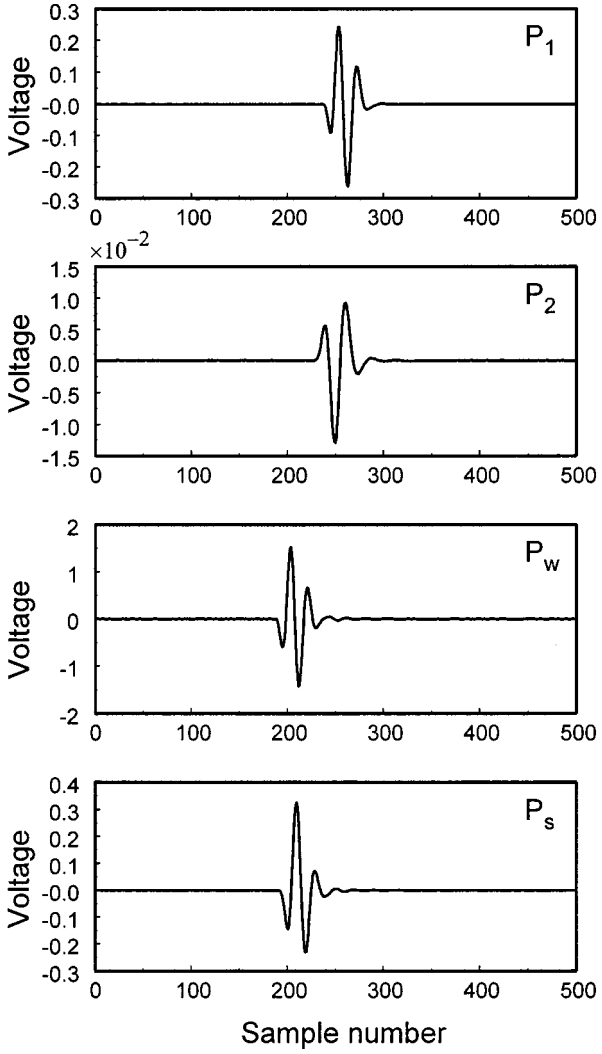

FIG. 3. Actual waveforms of the four recorded pulses: P_1 and P_2 are the pulses reflected back from the front and back surfaces of the specimen, respectively, and P_s and P_w are the transmitted pulses with and without the specimen inserted between the two transducers, respectively. Notice the extra 180°-phase shift of P_2 with respect to P_1. The time interval per sample is 1/60 μs.

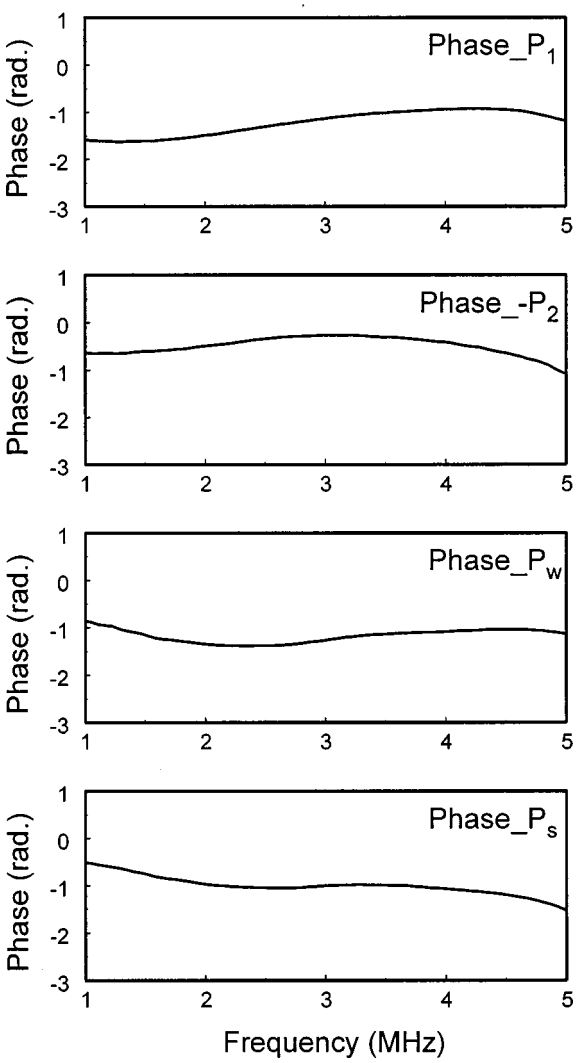

FIG. 4. The phase spectra of the four pulses shown in Fig. 3 after their centers being shifted to the beginning of the respective sampling window. Notice the second curve from the top is the phase of the inverted P_2.

III. DISCUSSION

The most directly noticeable fact exhibited by the experimental results is the excellent agreement between the measured and estimated thickness of the samples, as seen in Table I. The discrepancy between the measured and estimated thickness for each sample is 0.14% (Plexiglas), 0.29% (high-density polyethylene), and 0.22% (low-density polyethylene), respectively. This accuracy of thickness estimation is slightly better than the accuracy (from 0.16% to 0.80%) obtained by Hsu and Hughes using the time-domain, pulse-overlap method (1992). The results in Table I also show that within the frequency range of 1–5 MHz, deviation of $\hat{L}$ from a perfect constant is very small: 0.01% (Plexiglas), 0.02% (high-density polyethylene), and 0.19% (low-density polyethylene), respectively. On the one hand, this high degree of flatness of $\hat{L}$ obtained in the present experiment provides a strong support to the proposed method of using mixed spectra (of transmitted and reflected pulses) to determine dispersion. On the other hand, the degree of flatness of $\hat{L}$ obtained in a particular experiment may be used to judge the validity of the dispersion measurement for that experiment. The relatively large fluctuation of $\hat{L}$ from the low-density polyethylene sample is associated with the low amplitude of P_2, which is in turn caused by the large attenuation of the material (measured as 21 dB/cm at 3 MHz, as compared with 3.5 dB/cm for the Plexiglas sample and 5.2 dB/cm for the high-density polyethylene sample). It is expected that if the signal-to-noise ratio of the reflected signal were too weak, the fluctuation of $\hat{L}$ would be very large, indicating that the calculated dispersion using the mixed spectra would be no longer reliable.

Direct validation of the new method for measuring dispersion is more difficult because there are no standard dispersion data for the three samples used in this experiment. Kuo *et al.* (1990) measured the sound speed in three Plexiglas samples and obtained values ranging from 2750 to 2766 m/s. The solid curve shown in Fig. 5 is in the same range. In addition, the attenuation and dispersion properties of the same Plexiglas sample have been carefully studied before and the results presented in this paper are in excellent agree-

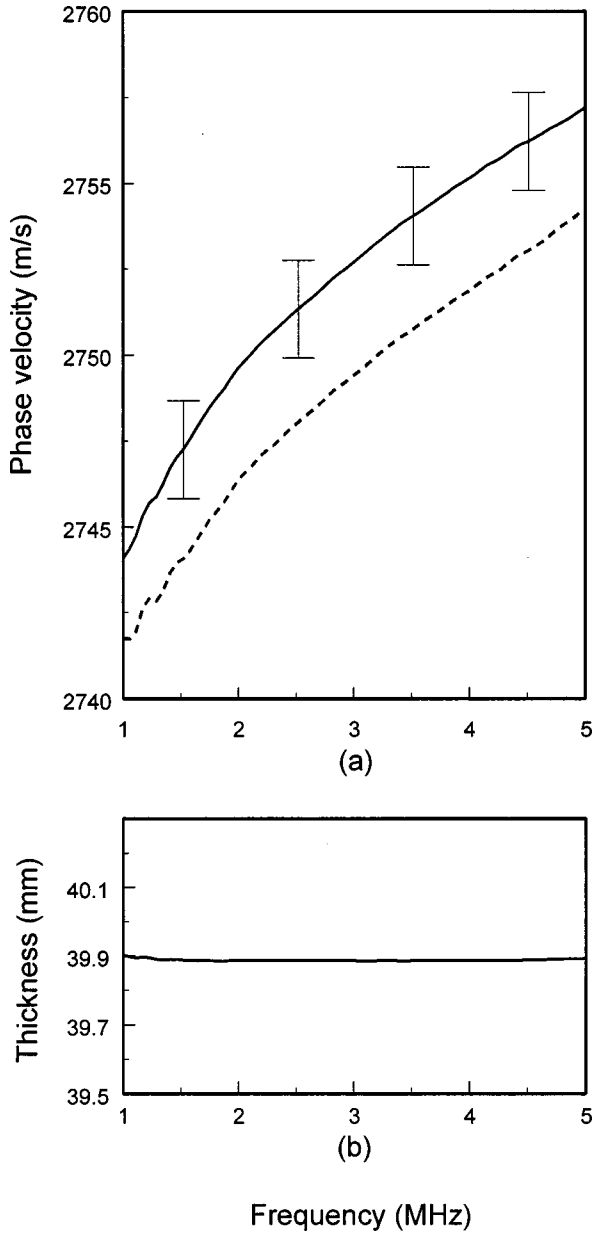

FIG. 5. (a) Solid line—phase velocity of the Plexiglas sample determined using the new method. Representative error bars are shown at 1.5, 2.5, 3.5, and 4.5 MHz. Dashed line—phase velocity determined using the traditional method with a thickness of 39.942 mm. (b) Thickness of the same sample determined using the proposed method. The plot range in the vertical direction is approximated ±1% around the mean value.

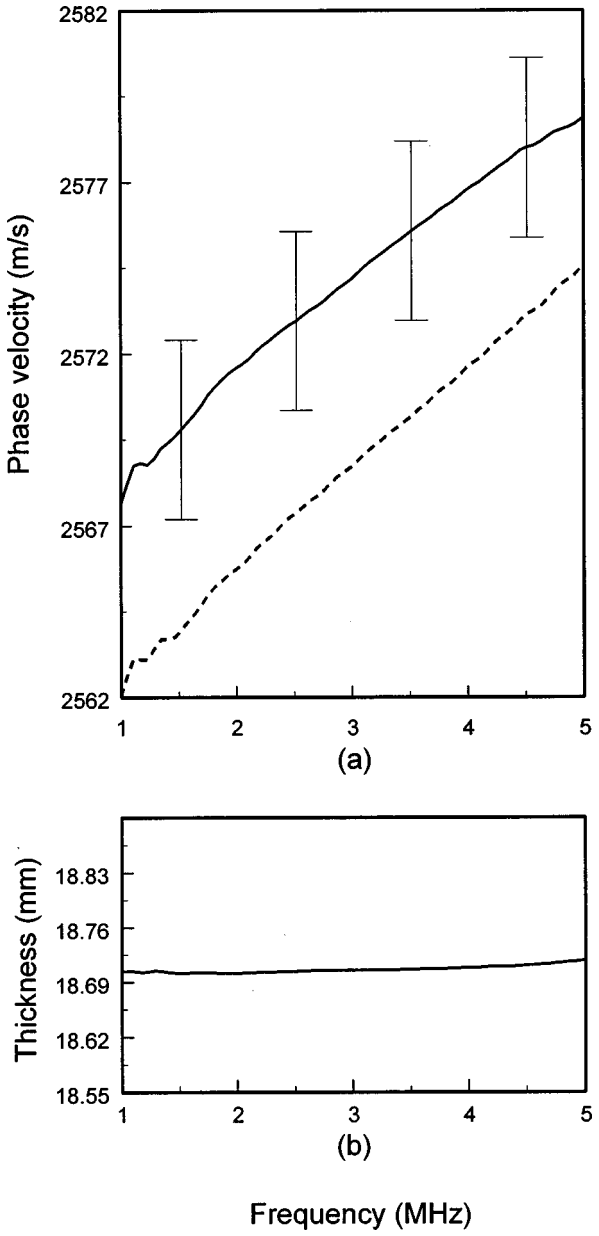

FIG. 6. (a) Solid line—phase velocity of the high-density polyethylene sample determined using the new method. Representative error bars are shown at 1.5, 2.5, 3.5, and 4.5 MHz. Dashed line—phase velocity determined using the traditional method with a thickness of 18.76 mm. (b) Thickness of the same sample determined using the proposed method. The plot range in the vertical direction is approximated ±1% around the mean value.

ment with the results obtained in the previous experiments (He, 1990). O'Donnell *et al.* (1981) measured the attenuation and dispersion of polyethylene in the frequency range of 1 to 10 MHz but did not specify the density of the specimen. From the large attenuation value (16 dB/cm at 3 MHz) reported by these investigators, it is judged that the acoustic properties of their specimen are close to that of the low-density polyethylene sample used in this study. Their dispersion curve shows a 45-m/s change in the phase velocity when the frequency is changed from 1 to 5 MHz. The dispersion curve plotted in Fig. 7(a) shows a similar change in the phase velocity. Wu (1996) measured dispersion of both high-density and low-density polyethylene. The dispersion curve of the high-density polyethylene sample plotted in Fig. 6 is in good agreement with the dispersion curve reported by Wu [Fig. 5(a), 1996]. However, that curve in Wu's paper is labeled as from the low-density polyethylene. It is noticed that the phase velocity of the low-density polyethylene reported by Wu is higher than that of the high-density polyethylene, which is in contradiction with the results obtained by this author. To further examine this discrepancy, we used the time-domain, pulse-overlap method (Hsu and Hughes, 1992) to measure the sound speed in these two samples, and obtained a speed of 2560 m/s for the high-density polyethylene and a speed of 2066 m/s for the low-density polyethylene. This independent measurement verified that the high-density polyethylene used in this study indeed has a higher sound speed than the low-density polyethylene. The exact source of

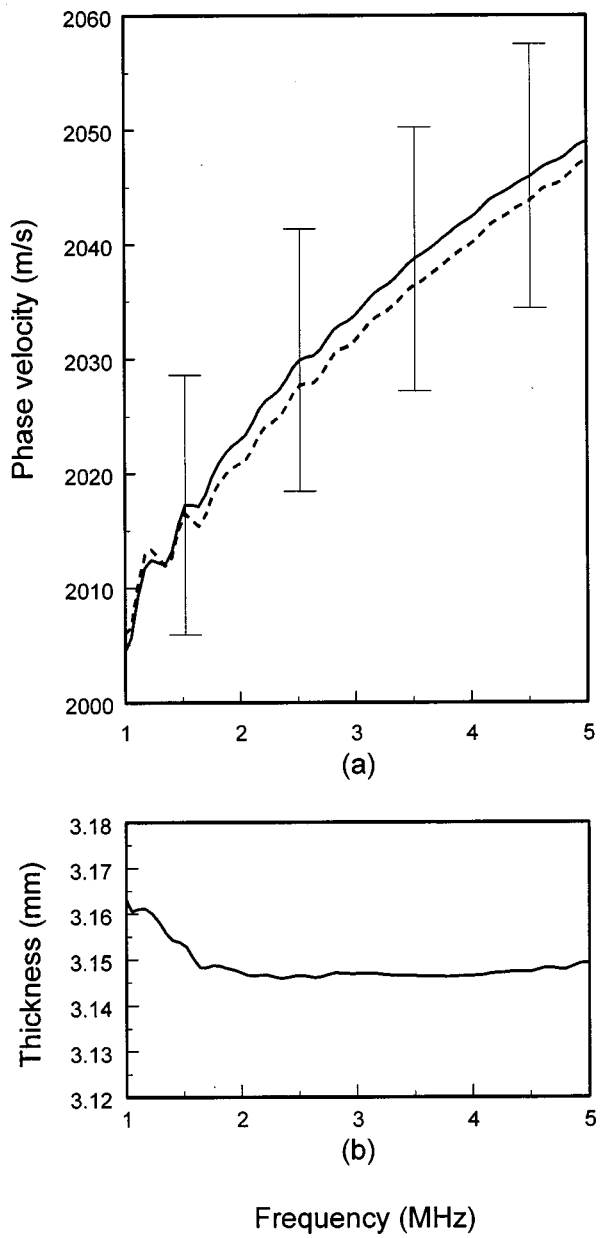

FIG. 7. (a) Solid line—phase velocity of the low-density polyethylene sample determined using the new method. Representative error bars are shown at 1.5, 2.5, 3.5, and 4.5 MHz. Dashed line—phase velocity determined using the traditional method with a thickness of 3.156 mm. (b) Thickness of the same sample determined using the proposed method. The plot range in the vertical direction is approximated ±1% around the mean value.

the discrepancy between Wu's results and our results is not known at this time.

Several observations can be made from the plots in Figs. 5(a), 6(a), and 7(a). In each figure, the solid line is obtained using both the transmitted and reflected pulses but without using the specimen's thickness, while the dashed line is obtained by the traditional method that uses the transmitted pulses only and a particular value for the sample's thickness. Although it appears that the two methods produce different dispersion curves, the discrepancy between the two curves in each figure is very small: 0.1% in Fig. 5(a), 0.2% in Fig. 6(a), and 0.1% in Fig. 7(a). In fact, if the thickness of the sample used to calculate the dashed curve in Fig. 5(a) is decreased by 0.054 mm (a mere 0.14% change), the new dashed curve would move up and overlap almost exactly with the solid curve. The same results can also be produced with the curves in Fig. 6(a) and Fig. 7(a). Since the immersion broadband transmission method for dispersion measurement is a well-established method, the above observations validate the accuracy of the new method in measuring dispersion that does not need to know the specimen's thickness. On the other hand, the above observations also suggest that the traditional method is very sensitive to the choice of the specimen's thickness. By eliminating the need for measuring the specimen's thickness, it is expected that the overall uncertainty of the dispersion measurement will be reduced in the new method. We now perform an error analysis to quantitatively investigate the improvement of the new method in reducing the uncertainty of the dispersion measurement.

For the traditional method that determines the phase velocity based on Eq. (1), the variance of the phase velocity can be determined based on the theory of error propagation to first order in the measurement uncertainties (Bevington, 1969; Mobley *et al.*, 1998)

$$\sigma_{v_p}^2 = \left(\frac{\partial V_p}{\partial L}\right)^2 \sigma_L^2 + \left(\frac{\partial V_p}{\partial \theta_s}\right)^2 \sigma_{\theta_s}^2 + \left(\frac{\partial V_p}{\partial \theta_w}\right)^2 \sigma_{\theta_w}^2 + \left(\frac{\partial V_p}{\partial c_w}\right)^2 \sigma_{c_w}^2 = V_p^4 \left[\frac{(\theta_s-\theta_w)^2}{\omega^2 L^4}\sigma_L^2 + \frac{1}{\omega^2 L^2}\sigma_{\theta_s}^2 + \frac{1}{\omega^2 L^2}\sigma_{\theta_w}^2 + \frac{1}{c_w^4}\sigma_{c_w}^2\right], \tag{10}$$

where $\omega = 2\pi f$, σ_L^2, $\sigma_{\theta_s}^2$, $\sigma_{\theta_w}^2$, and $\sigma_{c_w}^2$ are the measurement uncertainties (variances) of L, θ_s, θ_w, and c_w, respectively. Using Eq. (4), we can separate θ into two parts: a linear-with-frequency part, ωt, where t is the gross propagation delay, and a nonlinear part, ϕ, which contains the dispersion effect. Since the first part (ωt) is much larger then the second part (ϕ), we can use the following approximations in estimating the measurement uncertainty: $(\theta_s - \theta_w) \cong \omega(t_s - t_w) = \omega L(1/V_p - 1/c_w)$, $\sigma_{\theta_s}^2 \cong \sigma_{\theta_w}^2 \cong \omega^2 \sigma_t^2$, where σ_t^2 is the variance of the time measurement. With these approximations, Eq. (10) can be reduced to

$$\sigma_{V_p}^2 = \frac{2V_p^4}{L^2}\sigma_t^2 + \left(\frac{V_p}{c_w}\right)^4 \sigma_{c_w}^2 + \left(1 - \frac{V_p}{c_w}\right)^2 \frac{V_p^2}{L^2}\sigma_L^2. \tag{11}$$

Equation (11) indicates that if $V_p \cong c_w$, the contribution of the uncertainty of the thickness measurement may not be significant. On the other hand, if V_p is significantly different from c_w, the contribution of the last term in Eq. (11) can be very large. To demonstrate this, we substitute in Eq. (11) the following values found in the Plexiglas experiment: $V_p = 2753$ m/s (at about 3 MHz), $L = 4$ cm, and $c_w = 1486$ m/s. For the sampling frequency $f_s = 60$ MHz, σ_t is estimated as $0.5 \times 1/f_s = 8.33 \times 10^{-9}$ s. For the temperature within the range of 19.2 °C ± 0.1 °C, c_w changes from 1479.546 m/s to 1480.174 m/s (Del Grosso and Meder, 1972). Consequently, σ_{c_w} is estimated as 0.3 m/s. With these data, the first two terms on the right side of Eq. (11) can be first determined as 4.97 $(\text{m/s})^2$ and 1.06 $(\text{m/s})^2$, respectively. In this case, if the fractional uncertainty of thickness, σ_L/L, is larger than 0.095%, or $\sigma_L > 0.0038$ cm, the last term in Eq. (11) will be dominant. Mobley *et al.* (1998) used a fractional uncertainty

$\sigma_L/L=7\%$ in their error analysis in measuring the phase velocity in Albunex® suspensions. Such an uncertainty may be too large for solid specimens. If we use a more conservative $\sigma_L/L=0.5\%$, or $\sigma_L=0.02$ cm, the last term in Eq. (11) becomes 136.9 $(\text{m/s})^2$, that is, 22 times larger than the sum of the first two terms on the right side of Eq. (11).

For the new method that determines phase velocity based on Eq. (3), the variance of phase velocity can be evaluated using the same analysis

$$\begin{aligned}\sigma_{V_p}^2 &= \left(\frac{\partial V_p}{\partial \theta_s}\right)^2 \sigma_{\theta_s}^2 + \left(\frac{\partial V_p}{\partial \theta_w}\right)^2 \sigma_{\theta_w}^2 + \left(\frac{\partial V_p}{\partial \theta_2}\right)^2 \sigma_{\theta_2}^2 \\ &\quad + \left(\frac{\partial V_p}{\partial \theta_1}\right)^2 \sigma_{\theta_1}^2 + \left(\frac{\partial V_p}{\partial c_w}\right)^2 \sigma_{c_w}^2 \\ &= \frac{2V_p^2}{L^2}\left[c_w^2 + \left(\frac{c_w - V_p}{2}\right)^2\right]\sigma_t^2 + \left(\frac{V_p}{c_w}\right)^2 \sigma_{c_w}^2. \end{aligned} \tag{12}$$

Comparing Eq. (12) with Eq. (11), one notices that the potential major source of uncertainty associated with the thickness measurement is eliminated in the new method. The magnitudes of the remaining two terms associated with σ_t and σ_{c_w} are not significantly changed from that in Eq. (11) (in this particular example, they are slightly decreased to 1.71 and 0.31 $(\text{m/s})^2$, respectively).

The proposed method can also be used to improve the accuracy of attenuation measurement. It is typical that in a broadband transmission experiment, both attenuation and dispersion are measured at the same time (Lee *et al.*, 1990; Wu, 1996; He, 1999). Just like dispersion, the measured attenuation is dependent on the thickness of the specimen. If the specimen's thickness cannot be determined accurately, a large error may occur in the attenuation measurement. Using the proposed method, the specimen's thickness can be first determined from the transmitted and reflected pulses. The estimated thickness is then used to determine the attenuation.

The method proposed in this paper may be particularly useful for real-time measurement of dispersion/attenuation when the thickness of the specimen changes with time. Rokhlin *et al.* (1986) reported a measurement of frequency dependence of ultrasound velocity and attenuation during the curing reaction of epoxy resin. According to the authors, the shrinkage of the sample during the curing reaction was 1%–2%. Based on Eq. (11) and the related arguments, one would expect that (relatively) significant errors would occur when a fixed initial thickness is used to calculate the phase velocity and attenuation. By eliminating the need for thickness measurement, the new method is immune from the error produced by the change in the sample's thickness.

There are several limitations of this new method; all are related to the requirement of obtaining two reflected pulses. First, in order to obtain two nonoverlapping echoes, the thickness of the specimen cannot be smaller than the axial resolution of the ultrasound system. Second, two surfaces of the specimen should be parallel to each other and should be kept normal to the beam. Otherwise, significant distortion in echo waveform and phase spectrum may occur. Finally, if the acoustic impedance of the specimen is very close to that of the surrounding medium, or if the attenuation of the specimen is too large, the magnitude of the echo from the back surface may be reduced to the noise level. This last limitation may be the major obstacle in applying this method to certain biological tissues.

IV. CONCLUSIONS

In the measurement of acoustic dispersion using the traditional water-immersion broadband transmission method, if one can also reliably obtain reflected pulses from the front and back surface of the specimen, the phase velocity as well as the thickness of the specimen can be determined from the two transmitted and two reflected pulses. The degree of flatness of the estimated thickness within the useful frequency range of the system can be used to judge the reliability of the dispersion measurement. Experimental results from three specimens demonstrate the accuracy of the new method in determining the thickness and measuring the phase velocity. Theoretical analysis indicates that when the sound speed in the specimen is much different from that in water, the overall accuracy of the dispersion measurement can be significantly improved by eliminating the uncertainty associated with the measurement of the specimen's thickness.

Bevington, P. R. (**1969**). *Data Reduction and Error Analysis for the Physical Sciences* (McGraw-Hill, New York), Chap. 4, pp. 56–65.

Brodeur, P. H., Hall, M. S., and Esworthy, C. (**1993**). ''Sound dispersion and attenuation in the thickness direction of paper materials,'' J. Acoust. Soc. Am. **94**, 2215–2225.

Del Grosso, V. A., and Mader, C. W. (**1972**). ''Speed of sound in pure water,'' J. Acoust. Soc. Am. **52**, 1442–1446.

He, P. (**1999**). ''Experimental verification of models for determining dispersion from attenuation,'' IEEE Trans. Ultrason. Ferroelectr. Freq. Control **46**, 706–714.

Hsu, D. K., and Hughes, M. S. (**1992**). ''Simultaneous ultrasonic velocity and sample thickness measurement and application in composites,'' J. Acoust. Soc. Am. **92**, 669–675.

Kuo, I. Y., Hete, B., and Shung, K. K. (**1990**). ''A novel method for the measurement of acoustic speed,'' J. Acoust. Soc. Am. **88**, 1679–1682.

Lee, C. C., Lahham, M., and Martin, B. G. (**1990**). ''Experimental verification of the Kramers–Kronig relationship for acoustic waves,'' IEEE Trans. Ultrason. Ferroelectr. Freq. Control **37**, 286–294.

Mobley, J., Marsh, J. N., Hall, C. S., Hughes, M. S., Brandenburger, G. H., and Miller, J. G. (**1998**). ''Broadband measurements of phase velocity in Albunex® suspensions,'' J. Acoust. Soc. Am. **103**, 2145–2153.

O'Donnell, M., Jaynes, E. T., and Miller, J. G. (**1981**). ''Kramers–Kronig relationship between ultrasonic attenuation and phase velocity,'' J. Acoust. Soc. Am. **69**, 696–701.

Rokhlin, S. I., Lewis, D. K., Graff, K. F., and Adler, L. (**1986**). ''Real-time study of frequency dependence of attenuation and velocity of ultrasonic waves during the curing reaction of epoxy resin,'' J. Acoust. Soc. Am. **79**, 1786–1793.

Sachse, W., and Pao, Y. H. (**1978**). ''On the determination of phase and group velocities of dispersive waves in solids,'' J. Appl. Phys. **49**, 4320–4327.

Wu, J. (**1996**). ''Determination of velocity and attenuation of shear waves using ultrasonic spectroscopy,'' J. Acoust. Soc. Am. **99**, 2871–2875.

Zellouf, D., Jayet, Y., Saint-Pierre, N., Tatibouët, J., and Baboux, J. C. (**1986**). ''Ultrasonic spectroscopy in polymeric materials. Application of the Kramers–Kronig relations,'' J. Appl. Phys. **80**, 2728–2732.

The effect of gas loading on the RUS spectra of spheres

R. S. Sorbello, J. Feller, and Moisés Levy
Physics Department, University of Wisconsin-Milwaukee, Milwaukee, Wisconsin 53201

D. G. Isaak, J. D. Carnes, and O. L. Anderson
Institute of Geophysics and Planetary Physics, University of California at Los Angeles, California 90095-1567

(Received 25 January 1999; revised 27 July 1999; accepted 17 September 1999)

Resonant Ultrasound Spectroscopy (RUS) of a spherical sample in a pressurizing gas atmosphere was investigated experimentally and theoretically. Measurements were made on a fused silica sphere in He, Ar, and N_2 gases up to pressures of 120 bar. The pressure-dependent shift in the resonant frequency, Δf, and the Q-factor were measured for the S00, S11, and T02 modes. A theoretical model based on acoustic radiation impedance was used to calculate Δf and the radiation-resistance component, Q_r, of the Q-factor. Agreement between theory and experiment was good for Q_r, but there were discrepancies for Δf. It was found that the theoretical Δf due to gas-loading effects associated with acoustic radiation was very small and consistent with the observed dependence on pressure and gas species for the T02 mode but not for the S00 and S11 modes. We conclude that the T02 mode is the most reliable of these modes to use in measuring third-order elastic constants by RUS. © *2000 Acoustical Society of America.*
[S0001-4966(00)03601-8]

PACS numbers: 43.35.Cg [HEB]

INTRODUCTION

Over the past 30 years, resonant ultrasound spectroscopy (RUS) has emerged as a powerful tool to study the elastic properties of small specimens[1] and single crystals.[2] In recent years the RUS technique has been extended to high temperatures, albeit at ambient pressures.[3,4] High temperature RUS measurements have been used to extract the elastic constants of minerals in the Earth's mantle at high temperature, and to show that the specific heat at constant volume, C_v, of MgO obeys the Dulong and Petit limit exactly up to 1800 K,[5] and that its bulk modulus, K_s is linearly dependent upon the enthalpy.[6] Armed with this latter fact, Anderson[6] obtained extrapolated values of K_s up to about 3000 K, which is the upper limit of reliable measurements of the enthalpy of MgO.

RUS single crystal measurements are generally done with specimens prepared as right-rectangular parallelepipeds[2,7] or spheres.[8,9] There are excellent reviews of the RUS technique given in two articles by Maynard[10] and by Leisure and Willis[11] and a comprehensive book by Migliori and Sarrao.[12] There is also a review covering the beginning of RUS on spheres by Anderson.[13]

The RUS technique may also be used to determine third-order elastic properties of minerals and single crystals by performing RUS measurements under pressure attained with various gases. This procedure is attractive since it is relatively simple to perform. Thus a full set of elastic moduli may be obtained from one frequency scan under pressure, rather than requiring several measurements using different wave polarizations and crystal directions. However, gas pressure loading of the vibrating surfaces of the resonating specimens does provide a complication. In previous RUS measurements, it was correctly assumed that gas loading of the surfaces provided by ambient pressure does not significantly affect the resonance spectrum of the specimens being measured.[2,7,12] But under pressure, when the density of the surrounding gas can approach a significant fraction of the density of the specimen, it is possible that the increased acoustic coupling to the surrounding gas could displace the resonance curves by a measurable amount. Ohno *et al.*[14] attempted to circumvent this problem by using He as the pressurizing gas. They measured the pressure dependence of the shear modulus G of isotropic steel spheres, and found a value for $(\partial G/\partial p)_T$ equal to 1.8 which was within the range of values 1.5–2.0 found by other acoustic techniques. Thus they certainly demonstrated experimentally that the acoustic impedance mismatch between He and steel bracketed whatever effect gas loading would have on the value of the third-order elastic constants to less than 15% of the accepted value. However, no precise estimate was provided for the effect of gas loading.

Recently, RUS pressure measurements on a rectangular parallelepiped of fused quartz were reported by Zhang *et al.*[15] They included an analysis of the effect of gas pressure on both the quality factor Q and the resonance frequency of the peaks obtained in the RUS frequency spectrum. Both quantities were investigated in order to ascertain the validity of the theoretical model and of the approximations that were made. The shift in the resonance peaks could be produced by two factors: one, the effect of pressure on the elastic constants of fused quartz; and, two, the shift in frequency due to acoustic gas loading of the surfaces of the specimen, which is a dynamic effect arising from the creation of acoustic waves in the surrounding gas by the vibrating surfaces of the specimen. The frequency shift due to acoustic gas loading was described by Zhang *et al.*[15] as a ''mass-loading'' effect and was related to the reactive component of radiation impedance.

Because both sources of frequency shift are simultaneously present, it is not possible to determine from the experiments how much of the observed frequency shift is due to the third-order elastic constants and how much is due to acoustic gas loading. On the other hand, the change in the quality factor of the peaks produced by the pressurizing gas may be totally ascribed to acoustic gas loading, once it is experimentally deduced that the background losses are pressure independent. Therefore, Zhang *et al.*[15] proceeded under the assumption that if the theoretical model could account for the shift in quality factor as a function of pressure and also as a function of the molecular mass of the pressurizing gas, then the values predicted by the model for the shift in frequency due to acoustic gas loading would be justified. The authors found both quantitative and qualitative agreement between the experimental values for the changes in quality factor as a function of pressure and molecular mass for the compressional modes of the specimen. It was deduced that the shift in frequency produced by acoustic gas loading for this mode was a small fraction of the experimentally observed shifts. However, for the torsional modes the theoretical Q's were as much as three and a half times lower than seen experimentally and the theoretical changes in frequency were somewhere between a quarter and a twelfth of the experimental ones.

In their theoretical model, Zhang *et al.*[15] made two simplifying assumptions: one, they treated the six radiating rectangular surfaces of the parallelepiped independently, and then obtained the total radiation loading effect by adding the contributions from each surface; and, two, each surface was treated as a baffled planar source. It was not known if these assumptions caused the discrepancy for the torsional modes. Therefore, one of those authors, D. E. Beck, is working on a method to solve the radiation from a rectangular parallelepiped exactly. In the meantime, it was felt that the validity of the assumption that the change in acoustic losses was entirely due to acoustic radiation into the surrounding gas should be checked with a specimen shape that was more amenable to an exact theoretical solution. Therefore, the present authors initiated a RUS investigation of fused silica spheres. Isaak *et al.*[16] have published a preliminary account of this investigation where they report the value $(\partial G/\partial p)_T = -3.43$ obtained by extrapolating their experimental results with helium, nitrogen, and argon to a pressurizing gas of zero mass. Their extrapolated value falls within the range obtained by Meister *et al.*[17] of -3.39 and Gerlich and Kennedy,[18] -3.48, found by ultrasonic interferometry. In this paper, we will compare our theoretical results with the experimental values found for the changes in quality factor for both spheroidal modes and toroidal modes, and the frequency shift found for toroidal modes.

I. SPECIMENS AND EXPERIMENTAL CONDITIONS

We obtained a spherical specimen of fused silica whose radius is 2.414 mm. Table I lists the lowest seven modal frequencies calculated by Oda *et al.*[9] when 2.210 g/cm^3 is the density, ρ, and 37 and 31.3 GPa are the respective adiabatic bulk modulus, K_S, and shear modulus, G. The T's represent toroidal modes, the S's spheroidal modes. The mode number n is given first, followed by the harmonic, l corresponding to Y_{lm} in spherical harmonic notation, where l refers to the total angular momentum and m refers to the projection of angular momentum in the z direction.

TABLE I. Lowest calculated modal frequencies for fused silica sphere.

Mode	f_0 (MHz)
T02	0.620 58
S02	0.652 04
S11	0.804 53
S00	0.944 70
T03	0.958 90
S03	0.961 98
S02	1.147 91
S04	1.226 34

Pressure measurements for three different pressurizing gases, helium, nitrogen, and argon, were done on the sphere. The maximum pressure attained was in the range of 0.011–0.015 MPa (110–150 bar), depending on the gas used. Pressure was measured with a Bourdon tube pressure gauge that was accurate to about 1%.

The sample was placed between lead zirconium titanate (PZT) transducers that had 500-kHz natural frequencies. We used two mechanisms to ensure contact between transducers and specimen. One method was to fix a transducer and gently press the other, movable transducer to the specimen with a small spring on the back side of this second transducer. An alternative method was to gravity load with a small weight attached to the second transducer. There were no meaningful differences in the data acquisition using these two methods of contacting the transducers to the specimen. Further, the Q-factor for the PZT transducers is orders of magnitude less than for the specimen, resulting in no discernable shift in the specimen frequencies from the transducer resonances.

Temperature inside the pressure cell was monitored with two Type T Cu–CuNi thermocouples. Temperature was measured to 0.1°. The two thermocouples, placed on opposite sides of the specimen, never showed a difference of more than 0.1° from each other. After increasing or decreasing pressure, we waited for the temperature inside the vessel to stabilize to within 0.1°, or so, of room temperature. In our pressure runs, room temperature was usually within a degree of 25° throughout the run. We generally found excellent agreement in the up- and down-pressure data once they were all referenced to isothermal conditions.[16]

We recorded pressure data in intervals of 0.0005 MPa (5 bar) while increasing pressure up to 0.005 MPa (50 bar), after which intervals of 0.001 MPa (10 bar) were used. When decreasing pressure, we used 10-bar intervals throughout the pressure range. We made three separate pressure runs for each of the three pressurizing gases (He, N, Ar) and recorded data only when going up in pressure. The one exception was that we also recorded data while decreasing pressure for the last argon pressure run. No hysteresis was observed during this run.

II. EXPERIMENTAL RESULTS

This work will concentrate on resonance peaks associated with three modes of the fused silica spherical specimen.

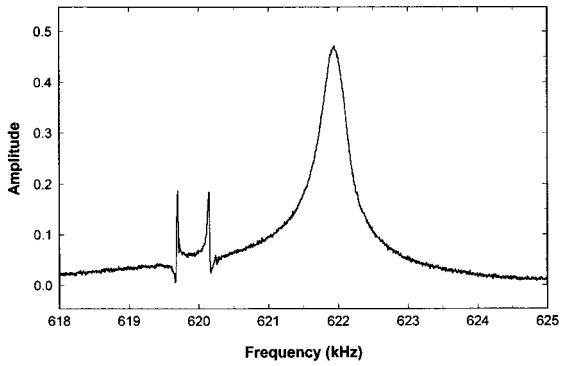

Degenerate modes: $n = 0,\ l = 2,\ m = 0, \pm 1, \pm 2$

$m = 0$:

$u_\theta = 0$

$u_\phi = A \sin 2\theta \cos \omega t$

$m = \pm 1$:

$u_\theta = A \cos\theta \cos(\omega t \pm \phi)$

$u_\phi = A \cos 2\theta \cos(\omega t \pm \phi)$

$m = \pm 2$:

$u_\theta = A \sin\theta \cos(\omega t \pm 2\phi)$

$u_\phi = \frac{1}{2} A \sin 2\theta \cos(\omega t \pm 2\phi)$

FIG. 1. Measured resonance peak for T02 mode. The lower half of the figure contains expressions for the displacement patterns on the sphere, with the $m = 0$ pattern displayed.

The curve in Fig. 1 shows the resonance peak for the toroidal T02 mode. The diagram in the bottom half of the figure indicates the displacement at the surface of the sphere for $m = 0$. Formulas for the displacements in the θ and ϕ directions for the three degenerate modes $m = 0 \pm 1, \pm 2$ are given next to this diagram. The angles θ and ϕ are defined in the figure. This is a pure shear mode with no motion in the radial direction. It is the lowest frequency mode for this sphere. As may be seen, there are three closely spaced peaks associated with this mode. We believe that this is caused by a break in the degeneracy due to a small asphericity in the specimen.[19] It is obvious that the peak around 622 kHz is better coupled to the transducer. We believe that this is the $m = \pm 1$ mode, since it contains motion in the θ direction at the poles, and therefore the shear transducers could more easily couple to this mode and both deliver more energy to it and more sensitively detect its oscillations. Since this mode is more tightly coupled to the transducers, the half-width of the peak is also more dependent on the Q of the transducers and therefore it was not used in the analysis of the data (presented in Fig. 4).

The resonance peak for the pure breathing mode S00 is shown in Fig. 2. At the bottom is the relation for the radial displacement u_r at the surface of the sphere. This figure also contains the S00 peak at a pressure of 25 bar of He. Peaks for the spheroidal mode S11 are shown in Fig. 3. These were obtained at zero pressure and at a pressure of 20 bar of He. The displacements for the degenerate modes are shown at the bottom.

As may be seen in Fig. 1, at least two of the peaks are visibly non-Lorentzian. In order to extract the quality factor

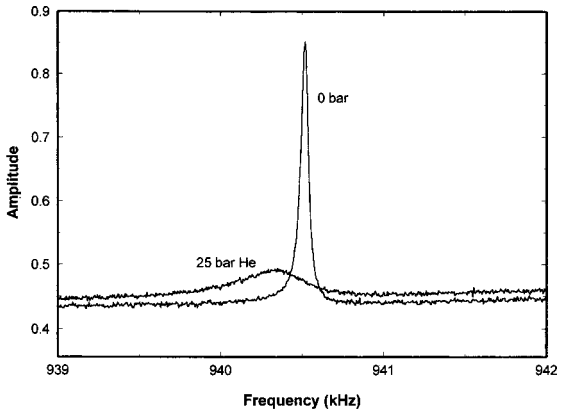

$n = 0,\ l = 0,\ m = 0$

$u_r = A \cos \omega t$

$u_\theta = u_\phi = 0$

(Pure radial breathing mode)

FIG. 2. Measured resonance peak for S00 mode. The lower half of the figure contains expressions for the displacement pattern.

and the resonant center frequency from the resonance peak, an appropriate background has to be subtracted from the data. This was done for all the data reported in this paper following the procedure described in Zhang *et al.*[15] The data points for the three modes as a function of pressure for three different gases are plotted in Figs. 4(a), (b), 5, and 6, except

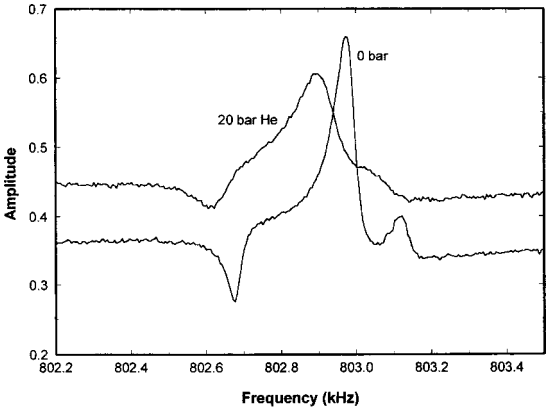

Degenerate modes: $n = 1,\ l = 1,\ m = 0, \pm 1$

$m = 0$:

$u_r = A \cos\theta \cos \omega t$

$u_\theta = B \sin\theta \cos \omega t$

$u_\phi = 0$

$m = \pm 1$:

$u_r = A \sin\theta \cos(\omega t \pm \phi)$

$u_\theta = B \cos\theta \cos(\omega t \pm \phi)$

$u_\phi = B \cos(\omega t \pm (\phi + \frac{\pi}{2}))$

FIG. 3. Measured resonance peaks for S11 modes. The lower half of the figure contains expressions for the displacement patterns.

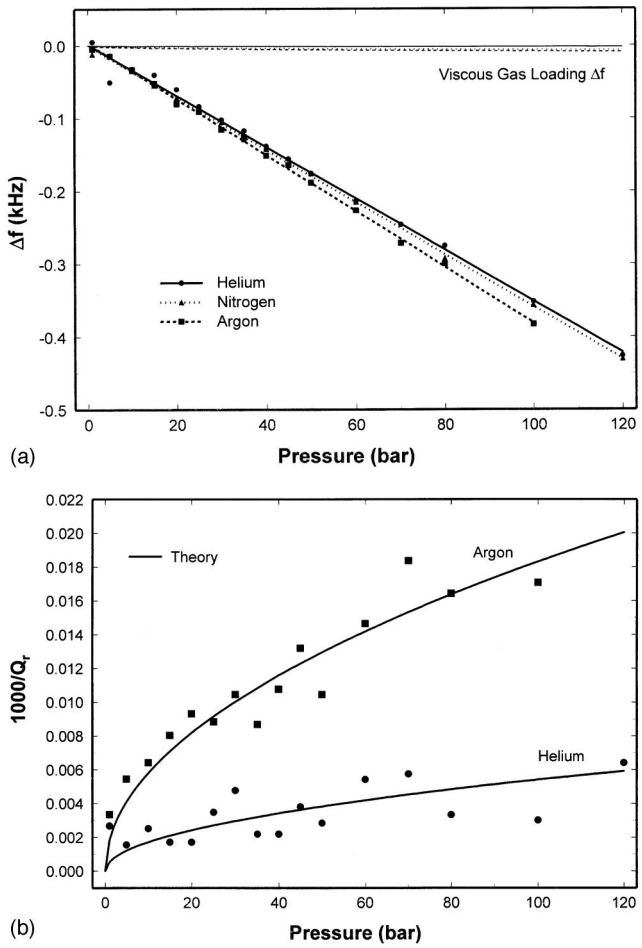

FIG. 4. (a) Measured frequency shift versus pressure for the T02 mode. The theoretical Δf due to acoustic gas loading by the viscous gas is labeled as ''viscous gas loading.'' (b) Measured and calculated $1/Q_r$ vs pressure for the T02 mode. ($1/Q_r$ is the part of the total $1/Q$ that is due to the presence of the gas.)

for Fig. 4(b), which contains data for Ar and He only. Figure 4(a) shows the experimental shift in central frequency as a function of pressure. Figures 4(b), 5, and 6 plot the experimental energy loss due to acoustic radiation $1/Q_r$ vs pressure. As described in Zhang *et al.*,[15] this latter quantity is

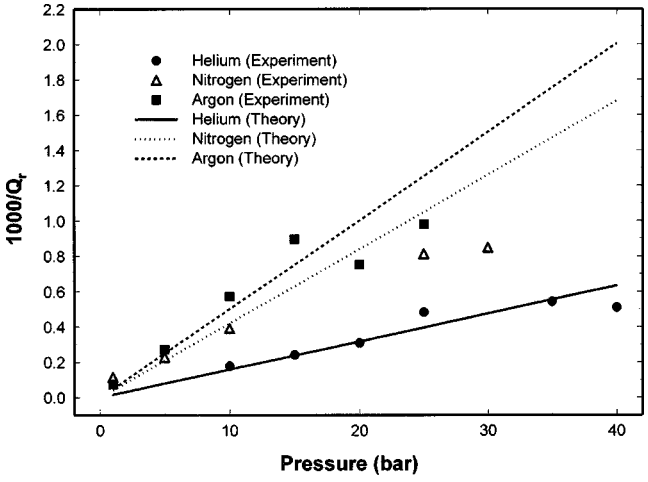

FIG. 5. Measured and calculated $1/Q_r$ vs pressure for the S00 mode.

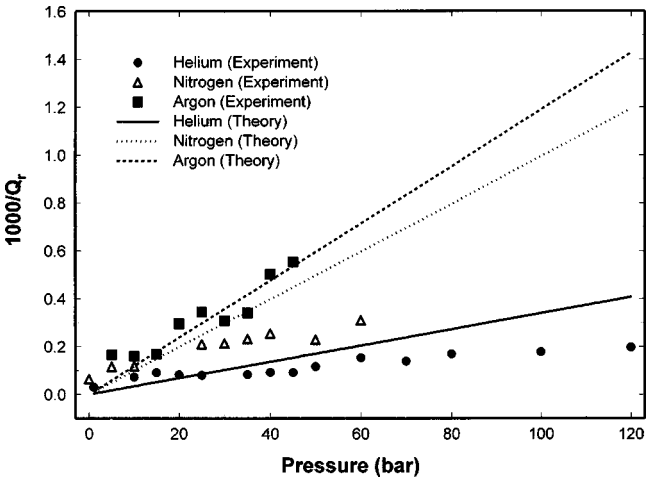

FIG. 6. Measured and calculated $1/Q_r$ vs pressure for the S11 mode.

obtained by subtracting a constant loss due to sample support and electronic losses.

It is evident that except for Fig. 4(b) the data may be fit with straight lines. As was mentioned earlier, the effect of third-order elastic constants would be to shift the central frequency linearly with pressure. The changes in losses $1/Q$ due to gas loading should not depend significantly on the third-order elastic constants. The toroidal mode shown in Fig. 1 has no radial motion, so that the coupling to the surrounding gas is through viscous motion. We shall see that this yields the square root dependence shown in Fig. 4(b).

III. THEORY OF ACOUSTIC GAS LOADING

The equations for the resonant frequencies of a vibrating isotropic sphere were derived by Lamb[20] and developed in greater detail by Lapwood and Usami,[21] whose approach we follow for the oscillations of an isotropic sphere in the absence of a surrounding gas. Later, we introduce the effects of a surrounding gas through an acoustical impedance at the surface of the sphere.

The oscillations of an isotropic material are governed by the wave equation

$$\rho \frac{\partial^2 u_i}{\partial t^2} = \sum_j \frac{\partial T_{ij}}{\partial x_j}, \tag{1}$$

where ρ is the mass density, u_i is the ith component of the displacement $\mathbf{u}$, and T_{ij} is the stress tensor, which for an isotropic material is given by

$$T_{ij} = \lambda \nabla \cdot \mathbf{u} \delta_{ij} + \mu \left(\frac{\partial u_i}{\partial x_j} + \frac{\partial u_j}{\partial x_i} \right), \tag{2}$$

where λ and μ are the Lamé coefficients, and δ_{ij} is the Kronecker delta function. As elucidated by Lamb in 1882, the basic solutions of the wave equation for an isotropic sphere can be categorized into the following three classes: I. Irrotational; II. Equivoluminal with zero radial displacement; and III. Equivoluminal with nonzero radial displacement. Following Lapwood and Usami[21] we assume time dependence of the form $\exp(i\omega t)$, where ω is the angular frequency

of oscillation, and modifying their notation slightly, we write the first class of solutions (irrotational) as

$$\mathbf{u}_{\mathrm{I}}=\nabla\Phi e^{i\omega t}, \tag{3}$$

where Φ is a scalar function that satisfies the Helmholtz equation

$$\nabla^2\Phi+h^2\Phi=0, \tag{4}$$

and $h=\omega/c_L=\omega/\sqrt{(\lambda+2\mu)/\rho}$, with c_L being the longitudinal velocity of sound. The physical solutions of Eq. (4) in spherical coordinates (r,θ,ϕ) are finite at the origin and have the form

$$\Phi=j_l(hr)Y_{lm}(\theta,\Phi), \tag{5}$$

where j_l is the spherical Bessel function and Y_{lm} are spherical harmonics.[22]

The second class solutions (equivoluminal with $u_r=0$) can be written as

$$\mathbf{u}_{\mathrm{II}}=\nabla\times\hat{\mathbf{r}}\psi e^{i\omega t}, \tag{6}$$

where ψ is a scalar function that satisfies the Helmholtz equation

$$\nabla^2\psi+k^2\psi=0, \tag{7}$$

and $k=\omega/c_T=\omega/\sqrt{\mu/\rho}$ with c_T being the transverse velocity of sound. In Eq. (6) $\hat{\mathbf{r}}$ is the unit vector along $\mathbf{r}$. The physical solutions of Eq. (7) have the form

$$\psi=j_l(kr)Y_{lm}(\theta,\phi). \tag{8}$$

The third class of solutions (equivoluminal with $u_r\neq0$) can be written as

$$\mathbf{u}_{\mathrm{III}}=(1/k)\nabla\times\nabla\times\mathbf{r}\chi e^{i\omega t}, \tag{9}$$

where χ is the scalar function that satisfies the Helmholtz equation

$$\nabla^2\chi+k^2\chi=0, \tag{10}$$

which has the physical solutions

$$\chi=j_l(kr)Y_{lm}(\theta,\phi). \tag{11}$$

It is customary to group these three sets of solutions into spheroidal modes, which have some radial displacement, and toroidal modes, which have only rotational displacement. Thus for the spheroidal modes we have

$$\mathbf{u}=A\mathbf{u}_{\mathrm{I}}+B\mathbf{u}_{\mathrm{III}}, \tag{12}$$

where A and B are constants. While for toroidal modes, we have

$$\mathbf{u}=C\mathbf{u}_{\mathrm{II}}, \tag{13}$$

where C is a constant.

For an unloaded sphere of radius a, the eigenfrequencies, or resonance angular frequencies, ω_0, are found by applying the free-surface boundary conditions that all stresses vanish at the surface of the sphere $(r=a)$. In terms of the stress tensor elements in spherical coordinates, this condition is

$$T_{rr}=T_{r\theta}=T_{r\phi}=0 \quad \text{at } r=a. \tag{14}$$

For a sphere that is gas loaded, the boundary conditions are

$$T_{rr}=-P \quad \text{at } r=a \tag{15}$$

and

$$T_{r\theta}=T_{r\phi}=0 \quad \text{at } r=a, \tag{16}$$

where in Eq. (15), P is the dynamic pressure of the gas. (Only the dynamic, or time varying part, of the pressure is relevant here.) The boundary condition Eq. (16) applies only if the viscosity of the gas is neglected. Later, when we consider the toroidal modes in detail, we will need to take into account the viscosity of the gas, and this will cause Eq. (16) to be modified.

To determine the eigenfrequencies of the loaded sphere, we need to use the pressure field of the gas in Eq. (15), and relate it to the displacement of the surface of the sphere. This leads to a transcendental equation for the angular frequency ω. The solutions of this equation give the eigenfrequencies of the sphere, which are now complex numbers. The real part of the complex frequency is associated with the frequency shift due to gas loading and the imaginary part is associated with radiation losses due to gas loading. The analysis is simplified by introducing the radiation impedance, Z, for the sphere. By definition,

$$Z\equiv P/v_g \quad \text{at } r=a, \tag{17}$$

where v_g is the (radial) velocity of the gas particles. By continuity of displacement at the surface of the sphere, v_g at $r=a$ is equal to the radial velocity of the surface. Therefore, $v_g=i\omega u_r$ and

$$Z=P/i\omega u_r \quad \text{at } r=a. \tag{18}$$

A useful expression for Z can be found in terms of the properties of the gas, independent of the properties of the sphere. To do this, we use the equation of motion for the gas

$$-\frac{\partial P}{\partial r}=\rho_g\frac{\partial v_g}{\partial t}, \tag{19}$$

where ρ_g is the mass density of the gas. In the region outside the sphere, there is only outgoing radiation emanating from the sphere. Consequently, the pressure in the gas must be of the form

$$P=Dh_l^{(2)}(k_gr)Y_{lm}(\theta,\phi)e^{i\omega t}, \tag{20}$$

where D is a constant, $h_l^{(2)}$ is the Hankel function of the second kind [necessitated by our adoption of the Lapwood and Usami convention of $\exp(i\omega t)$ time dependence], $k_g=\omega/c_g$ is the wave vector in the gas, and c_g is the speed of sound in the gas. Noting that $v_g\propto\exp(i\omega t)$, we can use Eqs. (19) and (20) in the expression Eq. (17) to find

$$Z=-i\rho_gc_gh_l^{(2)}(k_ga)/h_l^{(2)\prime}(k_ga). \tag{21}$$

The above expression for Z has all the information we need concerning the acoustic gas loading, assuming that the viscosity of the gas is negligible. To obtain the complex eigenfrequencies we define the function $F(\omega)$ as follows:

$$F(\omega)\equiv T_{rr}/u_r \quad \text{at } r=a, \tag{22}$$

and combine this with Eqs. (15) and (18) to get

$$F(\omega) = -i\omega Z. \tag{23}$$

As shown below, the function $F(\omega)$ can be found from Eq. (22) by explicitly evaluating T_{rr} in terms of u_r for the mode of interest. This function depends only on ω, a and the material parameters ρ, λ and μ.

By itself, Eq. (23) guarantees that boundary condition Eq. (15) is satisfied, but it is also necessary to satisfy boundary condition Eq. (16). The latter is automatically satisfied for the case of the purely radial breathing mode, or S00 mode, because the tangential stresses $T_{r\theta}$ and $T_{r\phi}$ identically vanish in that mode. For other spheroidal modes, it is necessary to explicitly require that the boundary condition Eq. (16) is satisfied. This is done by evaluating $T_{r\theta}$ and $T_{r\phi}$ in terms of the displacement **u** and using these expressions in Eq. (16). As illustrated below for the S11 mode, the result is a linear homogeneous equation relating the coefficients A and B that appear in expression Eq. (12) for **u**. This determines the ratio A/B. Evaluation of $F(\omega) \equiv T_{rr}/u_r$ yields an expression that depends on A and B only through the ratio A/B. Upon substituting the previously determined value of A/B into this $F(\omega)$ expression, we finally obtain an expression for $F(\omega)$ that contains neither A nor B, but rather is a function of only ω, a, ρ, λ, and μ. Subsequent solution of Eq. (23) now guarantees that both boundary conditions, Eqs. (15) and (16), have been satisfied.

Solution of the transcendental equation (23) for the complex frequency ω is simplified in the small-loading limit, where one can write $\omega = \omega_0 + \Delta\omega$, where ω_0 is the real eigenfrequency corresponding to the unloaded sphere and $\Delta\omega$ is a small correction. For the unloaded sphere, Z vanishes, as can be seen by taking the limit of vanishing gas density in Eq. (21), in which case Eq. (23) reduces to

$$F(\omega_0) = 0. \tag{24}$$

We emphasize that Eq. (23) is the equation satisfied by the complex eigenfrequency ω for arbitrary gas loading, while Eq. (24) is the equation satisfied by the real eigenfrequency ω_0 in the absence of gas loading. In the limit of vanishing gas density, $Z \to 0$ and the two equations become equivalent.

To obtain an approximate solution for the complex frequency shift $\Delta\omega$, we expand the left-hand side of Eq. (23) to the first order in $\Delta\omega$ and formally regard Z on the right-hand side of Eq. (23) to be small since Z vanishes for the unloaded sphere. After making use of Eq. (24) in this expansion, we obtain

$$\Delta\omega = -i\omega_0 Z(\omega_0)/F'(\omega_0), \tag{25}$$

where $Z(\omega_0)$ is the value of Z obtained by setting $k_g = \omega_0/c_g$ in the expression Eq. (21) for Z. Expression Eq. (25) is an excellent approximation for the complex frequency shift provided that $|\Delta\omega| \ll \omega_0$, which is the case for our experiments.

Now $F(\omega_0)$ is a real function (to ensure that ω_0 is real). Thus $F'(\omega_0)$ is also real and we deduce from Eq. (25) that

$$\mathrm{Re}\frac{\Delta\omega}{\omega_0} = \frac{\mathrm{Im}\, Z(\omega_0)}{F'(\omega_0)} \tag{26}$$

and

$$\mathrm{Im}\frac{\Delta\omega_0}{\omega_0} = -\frac{\mathrm{Re}\, Z(\omega_0)}{F'(\omega_0)}. \tag{27}$$

The real part of $\Delta\omega$ is the shift in the resonance angular frequency due to gas loading. Denoting the corresponding frequency shift (in Hz) as Δf, Eq. (26) implies that

$$\frac{\Delta f}{f_0} = \frac{\mathrm{Im}\, Z(\omega_0)}{F'(\omega_0)}, \tag{28}$$

where f_0 is the original resonance frequency for the unloaded sphere. The imaginary part of $\Delta\omega$ is related to the quality factor by the expression $1/Q = 2\,\mathrm{Im}\,\Delta\omega/\omega_0$. Applying this to the contribution $1/Q_r$ due to acoustic gas loading, and using Eq. (27), we find that

$$\frac{1}{Q_r} = -2\frac{\mathrm{Re}\, Z(\omega_0)}{F'(\omega_0)}. \tag{29}$$

We now apply these results to the spheroidal modes S00 and S11, and extend our analysis to the toroidal modes as well. In our calculations we use the following known values for the physical parameters for the sphere: $a = 0.2414$ cm, $\rho = 2.210$ g/cm^3, $c_T = 3.7634 \times 10^5$ cm/s, and $c_L = 5.9687 \times 10^5$ cm/s. The loading gases He, N_2, and Ar are treated as ideal gases.

A. S00 mode

The first spheroidal mode, S00, corresponds to the first solution of the form given by Eq. (12) with $l = 0$ and $m = 0$. This is the pure radial breathing mode whose pattern is given by

$$u_r = A j_0'(hr) e^{i\omega t}, \tag{30}$$

with $u_\theta = u_\phi = 0$. [For this mode, only the irrotational solutions $\mathbf{u}_{\mathrm{I}}$ contribute in Eq. (12), since $\mathbf{u}_{\mathrm{III}} = 0$ for $l = m = 0$.] The stress tensor elements T_{rr} for a mode having only radial displacement is given by[21]

$$T_{rr} = (\lambda + 2\mu) du_r/dr + 2\lambda u_r/r, \tag{31}$$

and the resulting $F(\omega)$, defined by Eq. (22), is

$$F(\omega) = (\lambda + 2\mu) h j_0''(ha)/j_0'(ha) + 2\lambda/a. \tag{32}$$

For the unloaded sphere, ω_0 is found by numerical solution of Eq. (24), and leads to a natural frequency of oscillation, $f_0 = \omega_0/2\pi$, equal to 0.944 68 MHz, in excellent agreement with the value in Table I. To find the complex frequency shift by Eqs. (26) and (27), we need the impedance expression Eq. (21) for the $l = 0$ case, and this is given by

$$Z(\omega_0) = \rho_g c_g \left[\frac{1 + i(k_g a)^{-1}}{1 + (k_g a)^{-2}}\right], \tag{33}$$

where $k_g = \omega_0/c_g$ is the wave vector for sound in the gas. Z can also be expressed in terms of the static pressure p and the molecular mass M of the gas by using the ideal gas expressions $\rho_g = pM/k_B T$, and $c_g = (\gamma p/\rho_g)^{1/2}$, where k_B is Boltzmann's constant and γ is the ratio of specific heats.

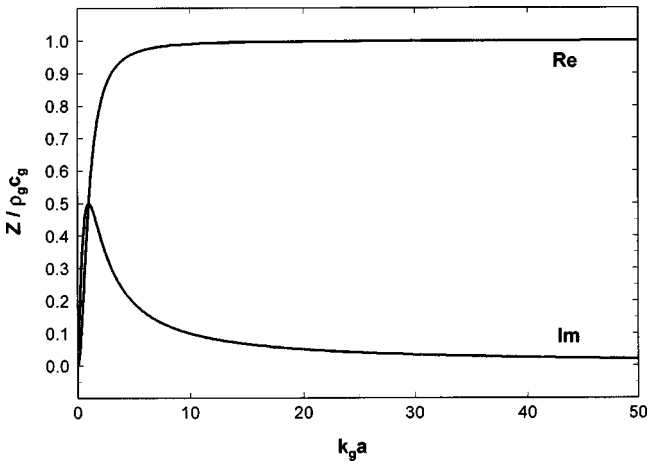

FIG. 7. Real and imaginary parts of the impedance Z vs $k_g a$.

The real and imaginary parts of Z are shown in Fig. 7. We note that for the experiments reported here, $k_g a \gg 1$ so that we are in the asymptotic regions of the curves. (The values of $k_g a$ are 15.5 for He, 41.0 for N_2, and 49.1 for Ar.) We remark that the impedance curves for modes with higher l values, e.g., the S11 mode, are similar to the curves in Fig. 7.

From Eqs. (28), (32), and (33), we obtain theoretical values for the real frequency shift Δf, plotted in Fig. 8. From Eqs. (29), (32), and (33), we obtain values for $1/Q_r$. These results are plotted along with the experimental data in Fig. 5. The theoretical dependence of Δf and $1/Q_r$ on the static pressure p and molecular mass M of the gas can be easily understood from the relations $\Delta f \propto \mathrm{Im}\, Z$ and $1/Q_r \propto \mathrm{Re}\, Z$ and from the behavior of $Z(\omega_0)$ in the $k_g a \gg 1$ regime. Thus $\Delta f \propto \mathrm{Im}\, Z \approx \rho_g c_g / k_g a = \rho_g c_g^2/\omega_0 a \propto p$, and independent of the molecular mass M, where we have used the fact that for an ideal gas at constant temperature $\rho_g \propto pM$ and $c_g \propto M^{-1/2}$. Similarly, $1/Q_r \propto \mathrm{Re}\, Z \approx \rho_g c_g \propto pMM^{-1/2} = pM^{1/2}$.

B. S11 mode

The S11 mode is the first spheroidal mode with $l=1$. It is triply degenerate, with $m=-1$, 0, or $+1$. According to Eq. (12), both $\mathbf{u}_{\mathrm{I}}$ and $\mathbf{u}_{\mathrm{III}}$ displacement classes contribute. The displacement pattern for the $m=0$ mode has the form

$$u_r = \left(Ahj_1'(hr) + \frac{2B}{kr} j_1(kr) \right) \cos\theta e^{i\omega t}, \tag{34}$$

$$u_\theta = -\left(\frac{Ahj_1(hr)}{r} + \frac{B}{kr}\frac{d}{dr}[rj_1(kr)] \right) \sin\theta e^{i\omega t}, \tag{35}$$

$$u_\phi = 0, \tag{36}$$

where A and B are constants. The displacement pattern for $m=\pm 1$ is

$$u_r = \left(Ahj_1'(hr) + \frac{2B}{kr} j_1(kr) \right) \sin\theta e^{i(\omega t \pm \phi)}, \tag{37}$$

$$u_\theta = \left(\frac{Ahj_1(hr)}{r} + \frac{B}{kr}\frac{d}{dr}[rj_1(kr)] \right) \cos\theta e^{i(\omega t \pm \phi)}, \tag{38}$$

$$u_\phi = \left(\frac{Ahj_1(hr)}{r} + \frac{B}{kr}\frac{d}{dr}[rj_1(kr)] \right) e^{i(\omega t \pm \phi \pm \pi/2)}, \tag{39}$$

where the upper sign is for $m=+1$ and the lower sign is for $m=-1$.

To find ω_0, the real eigenfrequency in the absence of gas loading, the free stress boundary condition Eq. (14) must be used. Evaluating the elements of the stress tensor for the displacement patterns given by either Eqs. (34)–(36) or (37)–(39) leads to the condition that

$$\alpha(\omega_0)\delta(\omega_0) - \beta(\omega_0)\gamma(\omega_0) = 0, \tag{40}$$

where

$$\alpha(\omega) = -(\lambda + 2\mu)h^2 j_1(ha) + (4\mu h/a) j_1'(ha) + (4\mu/a^2) j_1(ha), \tag{41}$$

$$\beta(\omega) = (4\mu/k)[kj_1'(ka)/a - j_1(ka)/a^2], \tag{42}$$

$$\gamma(\omega) = \mu[hj_1'(ha)/a - j_1(ha)/a^2], \tag{43}$$

$$\delta(\omega) = \mu k j_1''(ka). \tag{44}$$

The ω-dependence of α, β, γ, and δ arises through the quantities h and k, which as introduced in Eqs. (4) and (7), are defined by $h=\omega/c_L$ and $k=\omega/c_T$, respectively. The solution of the transcendental equation (40) gives the real frequency ω_0, which, as in the case of the S00 mode, is in excellent agreement with the corresponding f_0 value given in Table I.

To find the complex eigenfrequency ω for the S11 mode in the presence of gas loading, it is necessary to satisfy the boundary condition equations (15) and (16). Using the standard expressions[21]

$$T_{r\theta} = \mu\left(\frac{1}{r}\frac{\partial u_r}{\partial \theta} + \frac{\partial u_\theta}{\partial r} - \frac{u_\theta}{r} \right), \tag{45}$$

$$T_{r\phi} = \mu\left(\frac{1}{r\sin\theta}\frac{\partial u_r}{\partial \phi} + \frac{\partial u_\phi}{\partial r} - \frac{u_\phi}{r} \right), \tag{46}$$

we find that for the S11 mode, Eq. (16) yields the single relation

$$\gamma(\omega)A + \delta(\omega)B = 0, \tag{47}$$

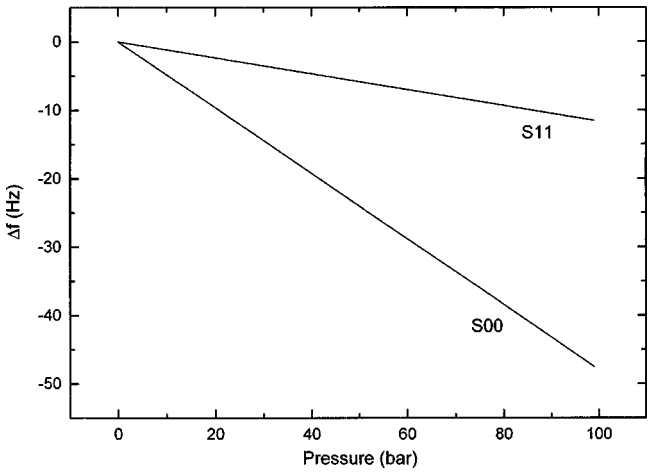

FIG. 8. Theoretical frequency shift due to acoustic gas loading for the S00 mode and S11 mode.

where A and B are the coefficients appearing in expression Eq. (12) for $\mathbf{u}$.

Using the standard expression[21]

$$T_{rr}=\lambda\nabla\cdot\mathbf{u}+2\mu\frac{\partial u_r}{\partial r}, \tag{48}$$

and the definition $F(\omega)\equiv T_{rr}/u_r$, we find that for the S11 mode

$$F(\omega)=\frac{\alpha(\omega)A+\beta(\omega)B}{Ahj_1'(ha)/a+(2B/ka)j_1(ka)/a^2}. \tag{49}$$

Substitution of the value of A/B from Eq. (47) into Eq. (49) yields

$$F(\omega)=\frac{\alpha(\omega)\delta(\omega)-\beta(\omega)\gamma(\omega)}{h\delta(\omega)j_1'(ha)/a-(2\gamma(\omega)/ka)j_1(ka)/a^2}. \tag{50}$$

Note that our final expression for $F(\omega)$ depends only on ω, a and the material parameters ρ, λ, and μ, just as we assumed in the theoretical development following Eq. (23). The ω-dependence arises through the quantities h and k that appear in Eq. (50) and that appear in the definitions Eqs. (41)–(44) of the quantities $\alpha(\omega)$, $\beta(\omega)$, $\gamma(\omega)$, and $\delta(\omega)$. Also note the consistency check: If we were to set $F(\omega)=0$, which would be appropriate only in the absence of gas loading, we obtain $\omega=\omega_0$, where ω_0 is the solution to Eq. (40).

Using our final $F(\omega)$ expression in Eqs. (28) and (29), along with $Z(\omega)$ from Eq. (21) for $l=1$, we obtain $1/Q_r$ and Δf. The results shown in Figs. 6 and 8. Following the same argument as for the S00 mode, but with the appropriate $Z(\omega_0)$ expression in place of Eq. (33), we find that $\Delta f\propto p$ and $1/Q_r\propto pM^{1/2}$, which is the case for all spheroidal modes.

C. T02 mode

Toroidal modes have zero radial displacement, and hence, there is no direct coupling to the pressure field of the surrounding gas. This means that for a nonviscous gas we would have $\Delta f=0$ and $1/Q_r=0$. If we include viscous coupling, the new boundary condition replacing Eq. (16) is that the tangential stress of the material matches the viscous stress in the gas at the surface of the sphere.

Since the toroidal modes are $(2l+1)$-fold degenerate for a given l value, it is simplest to restrict attention to the case of toroidal modes having $m=0$, in which case the displacement pattern is

$$u_r=u_\theta=0, \tag{51}$$

$$u_\phi=Cj_l(kr)\frac{\partial P_l(\cos\theta)}{\partial\theta}e^{i\omega t}, \tag{52}$$

where P_l is the Lengendre polynomial. The only nonvanishing elements of the stress tensor within the sphere are $T_{r\phi}$ and $T_{\phi r}$, which are identical. When the displacement components given by Eqs. (51) and (52) are used in Eq. (46), we find that

$$T_{r\phi}=C\mu\left(kj_l''(kr)-\frac{j_l(kr)}{r}\right)\frac{\partial P_l(\cos\theta)}{\partial\theta}e^{i\omega t}. \tag{53}$$

The resonant frequency ω_0 is found from the transcendental equation obtained from the unloaded sphere boundary condition $T_{r\phi}=0$ at $r=a$. For the T02 mode, $l=2$ and the resonant frequency is given by the first solution of this transcendental equation for $l=2$. As in the previous cases, the resulting value of $\omega_0/2\pi$ is in excellent agreement with the corresponding f_0 value in Table I.

For the loaded sphere, the new boundary condition to be satisfied at $r=a$ is that the tangential stress within the sphere matches the tangential stress due to viscosity in the gas. That is,

$$T_{r\phi}=T_{r\phi}^g \quad \text{at} \quad r=a, \tag{54}$$

where $T_{r\phi}^g$ is the viscous stress in the gas, and is given by[23]

$$T_{r\phi}^g=\eta_g\frac{\partial v_{g\phi}}{\partial r}, \tag{55}$$

where η_g is the viscosity coefficient of the gas, and $v_{g\phi}$ is the ϕ-component of the velocity field of the gas.

A relevant measure of the viscosity of a gas is the viscous length δ_v, which is defined by $\delta_v=\sqrt{2\eta_g/\rho_g\omega}$.[23] In the present experiments, $\delta_v\ll a$, which implies that to an excellent approximation the velocity field for the viscous wave created in the boundary layer outside the sphere has the form similar to that in a planar boundary layer; thus, $v_{g\phi}\propto\exp(-k'r)$, where $k'=(1+i)/\delta_v$.[23] In this case, Eq. (55) reduces to

$$T_{r\phi}^g=-\eta_g\frac{(1+i)}{\delta_v}v_{g\phi} \quad \text{at} \quad r=a. \tag{56}$$

The boundary condition equation (54) can now be cast into the same form as Eq. (23) if we define the impedance Z for toroidal modes as follows:

$$Z\equiv -T_{r\phi}^g/v_{g\phi} \quad \text{at} \quad r=a. \tag{57}$$

The expression Eq. (56) is analogous to the impedance definition Eq. (17), which was appropriate to spheroidal modes. Combining Eqs. (56) and (57), we obtain

$$Z=\frac{\eta_g(1+i)}{\delta_v}. \tag{58}$$

Finally, we can cast Eq. (54) into the desired form Eq. (23) if we define

$$F(\omega)\equiv\frac{T_{r\phi}}{u_\phi} \quad \text{at} \quad r=a, \tag{59}$$

in which case we find

$$F(\omega)=\mu\left(k\frac{j_l''(ka)}{j_l(ka)}-\frac{1}{a}\right), \tag{60}$$

where we have used Eqs. (57) and (59) and the relation $u_\phi=v_{g\phi}/i\omega$ at $r=a$, which follows from continuity of displacement at the surface of the sphere.

Theoretical values for Δf and $1/Q_r$ are obtained from Eqs. (28), (29), (58), and (60). The results are shown in Fig. 4 along with experimental data. The values used for η_g were the Handbook of Chemistry values at 20 °C, namely, 1.94, 1.75, and 2.22 in units of 10^{-5} Ns/m^2 for He, N_2, and Ar,

respectively. We note that the theoretical values for Δf and $1/Q_r$ are proportional to $p^{1/2}$, though the values of Δf are so small that the $p^{1/2}$ behavior of Δf is not visible in the figure. The $p^{1/2}$ behavior follows from the fact that $Z \propto \eta_g / \delta_v$ and that η_g is independent of p while δ_v is proportional to $\rho_g^{-1/2}$. Thus $Z \propto \rho_g^{1/2} \propto (Mp)^{1/2}$, which implies, via Eqs. (28) and (29), that Δf and $1/Q_r$ are also proportional to $(Mp)^{1/2}$.

D. Other modes

The theoretical method presented above can be used for all the modes of a gas-loaded spherical sample. All relevant details concerning the gas are contained in the impedance Z, which is given by Eq. (21) for spheroidal modes and Eq. (58) for toroidal modes. All relevant details concerning the elastic medium are contained in the function $F(\omega)$, which is defined by Eq. (22) for spheroidal modes and Eq. (59) for toroidal modes. To obtain the complex eigenfrequency ω for any mode, the key equation that needs to be solved is Eq. (23). For the weak-coupling case considered here, this leads to expressions Eqs. (28) and (29) for Δf and $1/Q_r$, respectively. These expressions can be combined to give the very general result

$$\frac{\Delta f / f_0}{1/Q_r} = \frac{-\operatorname{Im} Z(\omega_0)}{2 \operatorname{Re} Z(\omega_0)}, \tag{61}$$

which shows that the ratio of $\Delta f / f_0$ to $1/Q_r$ depends only on the properties of the surrounding gas and the resonance frequency of the unloaded sample. Because of this dependence and the general structure of our derivation, we conjecture that Eq. (61) may be applied to more general shapes than the sphere, provided that the appropriate impedance is evaluated at the surface of the sample.

IV. DISCUSSION

The theoretical results for the losses $1/Q_r$ for the spheroidal S00 mode, which is the fundamental pure radial displacement mode, are plotted as straight lines in Fig. 5. It is apparent that the fit is excellent for the helium data, very good for the argon data, and good for the nitrogen data. The slope of these straight lines is proportional to the square root of the molecular mass of the gases. This relation appears to yield a reasonable fit to the data. It should be emphasized that these are absolute value fits for the changes in losses as a function of applied pressure. Therefore, our model for the source of the change in Q, namely the increase in acoustic radiation into the surrounding gas due to the increase in density of the gas and the resultant decrease in acoustic impedance mismatch between the fused silica sphere and the surrounding gas, appears to be justified. Thus by extension, we can safely say that our model accounts for the full effect of acoustic gas loading on the frequency shift of the central frequency of the S00 resonance peak. This acoustic gas-loading frequency shift has been plotted in Fig. 8. It is linear with pressure and independent of the molecular mass of the gas. The effect of acoustic gas loading is one or two orders of magnitude smaller than the experimentally observed frequency shifts, which are not shown.

The theoretical results for $1/Q_r$ and Δf for the S11 mode are plotted in Figs. 6 and 8, respectively. We note that the theoretical results for the S11 mode are approximately a factor of 4 smaller than for the S00 mode. This is expected from the fact that for a given total energy in each of these modes, the average amplitude of the radial displacement over the surface of the sphere is considerably smaller for the S11 mode than for the S00 mode. Thus the coupling to the gas is smaller for the S11 mode than for the S00 mode. [Indeed, if one calculates the average square of the displacement pattern for the S11 mode as given in Eqs. (34) and (35), one finds that by virtue of the θ dependence of u_r and u_θ that only one-third of the total square of the displacement over the surface of the sphere arises from radial motion, apart from any differences in the radial functions appearing in u_r and u_θ.] From Fig. 6 we observe that the agreement between theory and the experimental data for $1/Q_r$ is reasonable. On the other hand, the theoretical calculation of the frequency shift due to acoustic gas loading for S00 and S11 modes are between one and two orders of magnitude smaller than the experimentally observed frequency shifts, which are again not shown and will be discussed later.

The theoretical curves for Δf and $1/Q_r$ for the fundamental pure shear mode T02 are plotted in Fig. 4(a) and (b), respectively. Once again the theoretical values for Δf are negligible compared to those for the experimentally acquired data. However, this time there is a mass dependence exhibited in the theoretical curves as well as in the experimental data. The mass-dependent part of the experimental Δf and the theoretical Δf due to acoustic gas loading are both small compared to the total measured Δf, and both show a characteristic $\sqrt{M}$ dependence. Thus at least qualitatively, the data are consistent with the theoretical results once a mass-independent background due to the third-order elastic constant effect is subtracted from the data. (It can be assumed that the He data constitute the background data since the correction due to the acoustic gas loading would only decrease the experimental value at 100 bar by about 0.7%, or about 2.5 Hz.) Quantitatively, however, there is a discrepancy between the data and the theory as far as the size of the mass-dependent contribution to Δf is concerned, with the data showing a variation that is a few times larger than the theoretical variation.[24]

The attenuation data for helium and argon are plotted in Fig. 4(b). The theoretical curves pass through the data reasonably well, particularly when it is noted that the attenuation values are an order of magnitude smaller than the ones shown for the S00 and S11 modes. As mentioned before, this is to be expected since the coupling to the surrounding gas is through viscous damping and not through gas–pressure fluctuations caused by the radial displacement of the sample's surface. The actual Q's measured are in the range of 3×10^4 while the changes correspond to Q_r's which are an order of magnitude larger and thus represent changes in total Q of less than 10%. This fact accounts for the scatter of the data around the theoretical curves particularly for the helium data. These observed changes in Q almost correspond to the sensitivity in the measurements of Q in our apparatus.

Now let us discuss the perplexing experimentally ob-

served variations in the frequency shifts Δf for the spheroidal modes which have purposefully not been plotted. For the S00 mode, Δf is negative for Ar and He and positive for N_2. And, while Δf is negative for the three gases for the S11 mode, it does not depend monotonically on the mass of the pressurizing gas in either case. It is true, though, that the frequency shift due to the third-order elastic constants for these two modes should be negative. However, if there were to be a mass dependence, it would be expected that the order of the effect on the frequency change would be similar to that observed for $1/Q_r$, namely $\Delta f(N_2)$ should lie between Δf(He) and Δf(Ar), and the smallest effect should be observed for He. Since the present theory does give good agreement with the observed radiation loss, it should also give a reasonable account of the frequency shift produced by acoustic gas loading on this breathing mode. Thus we are left with the tentative deduction that some other effect is causing the differences in Δf observed experimentally for the different gases. It has been suggested (by Al Migliori) that this effect could be produced by gas diffusion into the oscillating sphere or into the springs holding the transducer in place. However, as was mentioned in Sec. I, there was no significant difference between the data taken when the pressure was being increased and when it was being decreased. So no hysteresis was observed. One would expect to notice hysteresis if significant gas diffusion was involved in this process. It was also mentioned in Sec. I that two different methods were used to produce contact between the transducers and the specimen, one used a spring and the other a weight. Again, no meaningful differences were found. In addition, the frequency shifts and $1/Q_r$'s observed for the T02 mode, and which were obtained during the same pressure runs, are consistent with the theoretical results, and with third-order elastic constant measurements reported by other researchers using alternate ultrasonic techniques. Therefore, it appears that gas diffusion is not the source of these perplexing results.

A calculation using a scattering approach is being carried out by D. Beck,[25] in order to determine if different theoretical results may be obtained concerning Δf while still retaining the proper values for $1/Q_r$. However, preliminary results indicate that essentially the same results as found in the present calculation are also obtained by Beck *et al.*[25] It may be possible that another mechanism, which is not related to third-order elastic constants or coupling of the specimen to the surrounding pressurizing gas, is producing the Δf effects observed for the S00 and S11 modes. However, until a source for these observed discrepancies is determined, it appears obvious that only the data obtained with the T02 mode may be used for determining third-order elastic constants. This is the assumption that was made by Isaak *et al.*[16] following our collaboration at the Physical Acoustics Summer School held in Asilomar, California in June 1997.

Since the resonance data for all three modes were obtained during the same pressure run for each individual gas, and the toroidal mode yields consistent results for both Δf and $1/Q_r$, but the spheroidal modes only yield consistent results for $1/Q_r$, it appears that the perplexing frequency shifts for the spheroidal modes must be caused by subtle experimental conditions. Therefore, new measurements are in progress in order to resolve the discrepancies observed for the experimentally measured frequency shifts of the spheroidal modes. It should be noted that there is one feature in the frequency shifts of the S00 mode and the S11 mode which is suggestive, and that is that the magnitude of the experimentally observed frequency shifts for the three gases are closer together by approximately a factor of 4 for the S11 mode than they are for the S00 mode. This is the same factor that is observed for the Q_r's for the two modes; and it has already been mentioned that this reduction is due to the fact that the radial fraction of the motion is less for the S11 mode than the S00 mode. Therefore, it appears that the perplexing frequency shifts may be associated with the radial motion of the sphere.

V. SUMMARY

Resonant Ultrasound Spectroscopy of a spherical sample of a fused quartz sphere in a pressurizing gas atmosphere was performed in order to try to understand the effect of acoustic gas loading on the resonant modes of a solid shape which is amenable to an exact theoretical solution. The acoustic gas-loading effect is a dynamic effect due to acoustic radiation created in the surrounding gas by the vibrating sample. It gives rise to a loss $1/Q_r$ and a shift in the resonant frequency Δf which have been related to the real part and the imaginary part of the impedance function Z by means of expressions Eqs. (29) and (28), respectively. Note that Eq. (61) provides a direct way to determine the acoustic gas-loading contribution to Δf in terms of the acoustic radiation loss $1/Q_r$ without having to evaluate the elastic displacements and stresses for the sphere. Thus if $1/Q_r$ can be deduced from experimental data, Δf due to acoustic gas loading can be immediately obtained from Eq. (61). The result is especially simple in the case of toroidal modes, where the right-hand side of Eq. (61) equals $-1/2$.

We found that the observed changes in $1/Q$ with gas pressure were reasonably well described by the acoustic gas-loading expression Eq. (29). This indicates that the change in $1/Q$ with pressure finds its origin in the acoustic gas-loading effect. We deduce that changes in background losses due to the presence of a gas and changes in intrinsic losses in the sample due to increasing pressure of the gas are negligible compared to measured values.

The primary reason for performing RUS experiments in a pressurizing gas is to try to obtain experimental values for third-order elastic constants, or equivalently, for pressure derivatives of second-order elastic constants. In general, the experimental Δf vs pressure curves contain contributions from third-order elastic constants, the change of sample dimensions with pressure, acoustic gas loading, and, possibly, some pressure-dependent background effects due to transducers or some other unknown source. It is straightforward to incorporate the change of sample dimensions into the analysis of the data (see, for example, Ref. 16). For the case of spheres at least, we are also able to include the effect of acoustic gas loading by means of Eq. (28). Consequently, third-order elastic constants can be deduced from the RUS data if there are no appreciable pressure-dependent back-

ground effects due to transducers or other unknown sources. Therefore, a critical issue is whether the experimental RUS data are consistent with the assumption that these pressure-dependent background effects are negligible. As mentioned earlier, the $1/Q$ results for all modes were consistent with this assumption. However, as summarized below, this is not the case for the Δf results for the spheroidal modes S00 and S11. This is in contrast to the Δf results for the T02 mode, which are consistent with the assumption that pressure-dependent background effects are negligible compared to the measured values of Δf.

The theoretical results for acoustic gas loading associated with the radial motion of the S00 and S11 modes properly describes the experimentally observed broadening of the Δf curves for these two modes as a function of pressure of the three gases used in the measurements. The broadening was less for the S11 mode, which has a lower fraction of the total energy in the radial motion component than does the purely radial S00 mode. The effect of gas pressure on the experimental Δf for these two modes was perplexing, since for the S00 mode it was as large as what would be expected for the third-order elastic constant effect and varied with the molecular mass of the gas in a nonmonotonic way. However, the effect was smaller for the S11 mode, and by the same proportion as it was for broadening the resonance curves. In contrast, the theoretical Δf due to acoustic gas loading is independent of the molecular mass of the gas and two orders of magnitude smaller than the observed spread in Δf for the different gases. Therefore, acoustic gas loading of the sphere cannot account for these anomalous experimentally observed frequency shifts. Experiments are in progress in order to ascertain the source of the excess frequency shift.

Since toroidal modes have zero radial displacement, the coupling to the surrounding gas is through the viscosity of the gas. This leads to acoustic gas-loading contributions to $1/Q$ and Δf that are proportional to the square root of the static pressure. For the T02 mode, we obtained reasonable agreement between the measured changes in $1/Q$ with pressure and the values obtained from our theoretical expression Eq. (29) for the losses due to acoustic radiation. Furthermore, for this mode, the frequency-shift data are qualitatively consistent with our theory, which predicts a very small mass-dependent contribution due to acoustic gas loading. Indeed, as shown by Isaak *et al.*,[16] the neglect of acoustic gas loading in the analysis of RUS data for the T02 mode leads to a value for the pressure derivative of the shear modulus that is near the values obtained by other measurement techniques. Therefore, it appears, for now, that the T02 mode should be the one used for evaluating third-order elastic constants.

ACKNOWLEDGMENTS

The authors would like to acknowledge interesting discussions with Don Beck, Albert Migliori, Jay Maynard, and Logan Hargrove. Research at UWM and UCLA was supported by the Office of Naval Research.

[1] N. Soga and O. L. J. Anderson, ''Elastic properties of tektites measured by resonant sphere technique,'' J. Geophys. Res. **72**, 1733–1739 (1967).
[2] I. Ohno, ''Free vibration of a rectangular parallelepiped crystal and its application to determination of elastic constants of orthorhombic crystals,'' J. Phys. Earth **24**, 355–379 (1976).
[3] T. Goto and O. L. Anderson, ''Apparatus for measuring elastic constants of single crystals by a resonance technique up to 1825 K,'' Rev. Sci. Instrum. **59**, 1405–1408 (1988).
[4] O. L. Anderson and D. G. Isaak, ''Elastic constants of mantle minerals at high temperature,'' in *Mineral Physics and Crystallography: A Handbook of Physical Constants*, edited by T. J. Ahrens (American Geophysical Union, Washington, DC, 1995), pp. 64–97.
[5] O. L. Anderson and K. Zou, ''Formulation for the thermodynamic functions for mantle minerals: MgO as an example,'' Phys. Chem. Miner. **16**, 642–648 (1989).
[6] O. L. Anderson, ''The relationship between the adiabatic bulk modulus and enthalphy for mantle-related minerals,'' Phys. Chem. Miner. **16**, 559–562 (1989).
[7] H. Demarest, ''Cube resonance method to determine the elastic constants of solids,'' J. Acoust. Soc. Am. **49**, 768–775 (1971).
[8] H. Oda, O. L. Anderson, D. G. Isaak, and I. Suzuki, ''Measurements of elastic properties of single crystal CaO up to 1200 K,'' Phys. Chem. Miner. **19**, 96–105 (1992).
[9] H. Oda, I. Suzuki, and I. Ohno, ''Partial derivatives of eigenfrequencies of a rectangular parallelepiped and a sphere of elastically anisotropic solid,'' J. Phys. Earth **41**, 271–289 (1993).
[10] J. Maynard, ''Resonant ultrasound spectroscopy,'' Phys. Today **49**, 26–29 (1996).
[11] R. G. Leisure and F. A. Willis, ''Resonant ultrasound spectroscopy,'' J. Phys.: Condens. Matter **9**, 6001–6029 (1997).
[12] A. Migliori and J. L. Sarrao, *Resonant Ultrasound Spectroscopy* (Wiley, New York, 1997).
[13] O. L. Anderson, ''The Beginnings of Resonant Ultrasound Spectroscopy and Its Application to Geophysics,'' Engineering Science Preprints-28, 28th Annual Meeting of the Society of Engineering Sciences, 10 pages (ESP28.910).
[14] I. Ohno, T. Nishitake, Y. Hinayana, and M. Kimura, ''The Resonance Method to Determine the Pressure and Temperature Variations of Elastic Constants,'' Engineering Science Preprints-28, 28th Annual Meeting of the Society of Engineering Science, 1991.
[15] H. Zhang, R. S. Sorbello, C. Hucho, J. Herro, J. R. Feller, D. E. Beck, M. Levy, D. Isaak, J. D. Carnes, and O. Anderson, ''Radiation impedance of resonant ultrasound spectroscopy modes in fused silica,'' J. Acoust. Soc. Am. **103**, 2385–2394 (1998).
[16] D. G. Isaak, J. D. Carnes, O. L. Anderson, and H. Oda, ''Elasticity of fused silica spheres under pressure using resonant ultrasound spectroscopy,'' J. Acoust. Soc. Am. **104**, 2200–2206 (1998).
[17] R. Meister, E. C. Robertson, R. W. Werre, and R. Raspet, ''Elastic moduli of rock glasses under pressure to 8 kilobars and geophysical implications,'' J. Geophys. Res. **85**, 6461–6470 (1980).
[18] D. Gerlich and G. C. Kennedy, ''Second pressure derivatives of the elastic moduli of fused quartz,'' J. Phys. Chem. Solids **39**, 1189–1191 (1978).
[19] W. M. Visscher, A. Migliori, T. M. Bell, and R. A. Reinert, ''On the normal modes of free vibration of inhomogeneous and anisotropic elastic objects,'' J. Acoust. Soc. Am. **90**, 2154–2162 (1991).
[20] H. B. Lamb, ''On the vibration of an elastic sphere,'' Proc. London Math. Soc. **13**, 189–212 (1882).
[21] E. R. Lapwood and T. Usami, *Free Oscillations of the Earth* (Cambridge University Press, Cambridge, England, 1981).
[22] See, for example, J. D. Jackson, *Classical Electrodynamics*, 2nd ed. (Wiley, New York, 1975).
[23] See, for example, L. Brekhovskikh and V. Goncharov, *Mechanics of Continua and Wave Dynamics* (Springer-Verlag, New York, 1985).
[24] In Ref. 16 a theoretical estimate of Δf due to acoustic gas loading appears to be in better agreement with experiment. However, the treatment in Ref. 16 is a qualitative one which assumes that the sphere is mass loaded due to a uniform layer of entrained gas in a thickness δ_v over the surface of the sphere and that the resonance frequency has a harmonic-oscillator dependence on total mass (sphere plus gas layer). One reason that this treatment leads to an over-estimate is that the T02 mode contains large regions where the displacement is relatively small, and so relatively little gas is entrained over those regions.
[25] D. Beck, R. S. Sorbello, J. Feller, and M. Levy (unpublished).

Using phase space diagrams to interpret multiple frequency drive sonoluminescence

Jeffrey A. Ketterling and Robert E. Apfel
Department of Mechanical Engineering, Yale University, New Haven, Connecticut 06520

(Received 9 April 1999; accepted for publication 30 August 1999)

The recent experimental results of J. Holzfuss, M. Rüggeberg, and R. Mettin [Phys. Rev. Lett. **81**, 1961 (1998)] in which a second harmonic drive system was used to generate sonoluminescence (SL) have been analyzed in the context of the dissociation hypothesis (DH) of D. Lohse and S. Hilgenfeldt [J. Chem. Phys. **107**, 6986 (1997)]. The second harmonic introduces two more variables that are under experimental control: a phase and an additional pressure term to the acoustic drive pressure. Diffusive equilibrium curves for a fixed gas concentration were calculated as was the Mach criterion. A phase space diagram was constructed to permit the prediction of regions of stable SL, unstable SL, stable non-SL, and unstable non-SL. These were compared to Holzfuss' experimental observations, and excellent quantitative agreement was seen. The results provide further evidence that the underlying assumptions of DH are sound. They also indicate the utility of DH for determining appropriate experimental conditions to achieve SL and for optimizing an experimental system. [S0001-4966(99)05112-7]

PACS numbers: 43.35.Ei [HEB]

INTRODUCTION

An air-filled bubble acoustically trapped in a sound field undergoes periodic radial oscillations. With the proper choice of experimental parameters, the bubble can emit a pulse of light each acoustic cycle resulting in single bubble sonoluminescence (SBSL).[1] Some of the interesting features of SBSL are its dependence on noble gas concentration,[2] light pulse lengths on the order of 100 ps,[3] and a spectrum that shows no distinct peaks.[4]

Over the laser few years, there has been an interest in increasing the energy output of SBSL. Several approaches have been suggested, each aiming to increase the expansion ratio (ER), a measure of the maximum bubble radius $R_{\max}$ divided by the ambient radius R_0. These approaches can be broken into methods that focus on (i) optimizing fixed experimental parameters such as drive frequency[5] and methods that focus on modifying the acoustic drive signal with (ii) harmonics[6] or with a (iii) pressure spike.[7,8] Both methods (i) and (ii) lend themselves to steady-state analysis, while method (iii) does not.

Rather than using a pressure spike, Holzfuss *et al.*[6] have recently attempted to increase the light output of SL by adding a second harmonic to the drive signal. This introduces two new variables since the phase ϕ and the drive pressure of the second harmonic are under experimental control. Figure 1 shows the key results taken from Figs. 1 and 4 of Ref. 6. Figure 1(a) indicates the z displacement of the bubble measured from the antinode as the phase of the second harmonic is varied with respect to the fundamental. This is in contrast to the single drive frequency case which displays minimal translation as the acoustic drive pressure P_a varies.[9] Also shown in Fig. 1(a) are points that displayed unstable behavior (•).

Figure 1(b) shows the results of the theoretically predicted z translation with the spatial mode profile of the experimental system included in the calculations. Comparison to Fig. 1(a) reveals close agreement. Finally, Fig. 1(c) shows the relative light intensity as the phase of the second harmonic was varied. What is interesting about Fig. 1(c) is that there were two stable ''islands'' of SL. Holzfuss *et al.*[6] also observed that the maximum intensity of light in Fig. 1(c) was twice that when only the fundamental drive frequency was used.

The goal in the remaining sections of this paper is to explain the above observations in terms of the dissociation hypothesis (DH) of D. Lohse and S. Hilgenfeldt.[10] DH permits the prediction of bubble behavior in the R_0 vs P_a phase space, based primarily on the dissolved gas content in the fluid. Stable non-SL is determined by the total amount of gas initially dissolved in the fluid, whereas stable SL is determined by the noble gas content. At low P_a the bubble dissolves or is unstable as it undergoes ''dancing'' behavior. As P_a is increased, the bubble begins to dissociate its diatomic gas content and enters a stable chemical equilibrium as the dissociation offsets growth by rectified diffusion.[11] With further increase in P_a, the diatomic gas completely dissociates, and only the noble gas remains. This view of SL has been shown to be consistent with experiment.[12–14]

The ability of DH to quantitatively explain the observations of Holzfuss *et al.*[6] would provide further proof of its utility as a predictive tool for steady-state SL experiments. First, the theoretical tools to assemble a phase space diagram are introduced, and a phase diagram for a single drive frequency is presented. Then the phase space diagrams for an ideal and for the experimental second harmonic drive system will be discussed. Finally, the ERs resulting for each case will be compared, and additional phase space predictions will be made.

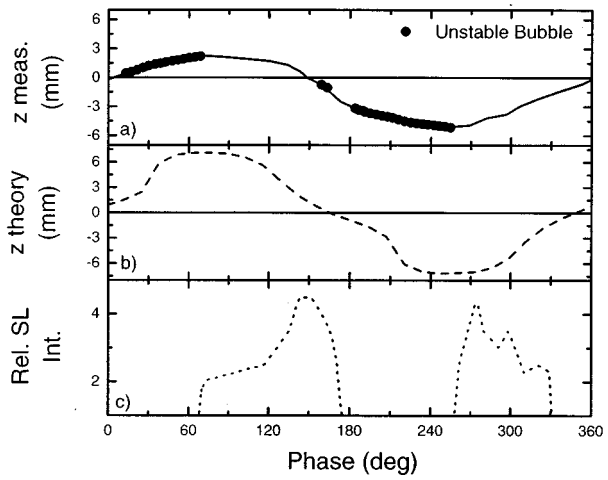

FIG. 1. Highlights of results from Figs. 1 and 4 of Ref. 6 showing the effect of the addition of a second harmonic on (a) experimental and (b) theoretical bubble translation, and (c) light intensity when phase was varied through 360°. Unstable behavior as experimentally observed is marked with a ●. As phase varied, the bubble underwent significant translation and two distinct regions of stable SL were observed.

I. THEORY

The theoretical tools to develop phase space diagrams based on DH are briefly introduced here. A more detailed description can be found in Refs. 10 and 15.

A. Rayleigh–Plesset equation

The radial oscillations of a bubble are described by the Rayleigh–Plesset equation[16]

$$R\ddot{R}+\frac{3}{2}\dot{R}^2=\frac{1}{\rho}(P_{\mathrm{gas}}(R,t)-P(t)-P_0)-4\nu\frac{\dot{R}}{R}-\frac{2\sigma}{R}+\frac{R}{\rho c_w}\frac{d}{dt}(P_{\mathrm{gas}}(R,t)-P(t)), \tag{1}$$

with internal gas pressure

$$P_{\mathrm{gas}}(R,t)=\left(P_0+\frac{2\sigma}{R_0}\right)\left(\frac{R_0^3-h^3}{R^3-h^3}\right)^{\gamma}, \tag{2}$$

where the acoustic drive pressure is $P(t)=-P_a\cos(wt)$. The ambient radius R_0 represents the static equilibrium size the bubble would have if the ambient pressure were 1 atm and no diffusive effects could occur. The expression for $P_{\mathrm{gas}}(R,t)$ includes a van der Waals hard core term $h=R_0/8.86$.[17]

The parameter values used in all the calculations to follow are ambient pressure $P_0=101\,325$ Pa, surface tension $\sigma=0.072$ N/m, sound speed in water $c_w=1481$ m/s^2, water density $\rho=1000$ kg/m^3, and water viscosity $\nu=10^{-6}$ m^2/s. The polytropic exponent is taken to be $\gamma=1$, arguments for which can be found in Ref. 10. The driving frequency used in the calculations is $\omega/2\pi=23.4$ kHz which results in a period of $T=43$ μs.

B. Diffusive equilibrium

In the presence of a sound field, an oscillating bubble can undergo growth or dissolution through the process of rectified diffusion.[11] Under the right conditions, it can also enter an equilibrium where its mass content remains steady over an acoustic cycle.[18] Diffusive equilibrium curves are found from[19]

$$C=\frac{C_\infty}{C_0}=\frac{1}{P_0}\frac{\int_0^T P_{\mathrm{gas}}(R,t)R^4(t)}{\int_0^T R^4(t)}, \tag{3}$$

where $P_{\mathrm{gas}}(R,t)$ was defined in Eq. (2), and $R(t)$ is the solution of Eq. (1). Gas saturation is normally referred to as the ratio $C=C_\infty/C_0$, where C_∞ is the concentration at some point far from the bubble and C_0 is the concentration at 1 atm. This equation gives the gas saturation necessary for a bubble to remain at diffusive equilibrium to within ≈10% for R_0.[20]

C. Mach criterion

The final item of interest is the location in phase space of the stable chemical equilibrium which arises as the rate of diatomic gas dissociation offsets the amount of mass entering the bubble each acoustic cycle. The actual calculation of the chemical equilibrium is very sensitive to how the temperature of the gas in the bubble is modeled during collapse.[10] However, the Mach criterion[15]

$$M=\frac{\dot{R}}{c_{\mathrm{gas}}}>1, \tag{4}$$

provides an excellent approximation that also shows good agreement with experimental data.[21] The Mach criterion indicates when the collapse is violent enough to launch a shock wave toward the center of the bubble. Since the collapse is more energetic, temperatures inside the bubble increase, permitting the diatomic gases to dissociate.

II. SINGLE DRIVE FREQUENCY

The case of just a single drive frequency will be dealt with first since it illustrates the main features of the phase space diagram. The key items of interest are diffusive equilibrium curves for the noble gas content used in the experiments and the Mach criterion.

Figure 2 shows a phase space diagram with the diffusive equilibrium curves $C=40\%$ (solid), $C=0.4\%$ (dashed), and $C=0.3\%$ (dotted). The $C=0.4\%$ and $C=0.3\%$ curves represent the argon gas content for the experimental range of air saturations: $C=40\%$ to 30%.[22] A positive slope represents a stable diffusive equilibrium while a negative slope represents an unstable equilibrium as indicated by the growth (g) and dissolution (d) trends next to each curve. The Mach criterion (dash-dotted) represents the path a bubble travels as it moves from stable non-SL to stable SL behavior. The true chemical equilibrium may lie somewhat to the right of the Mach criterion and could be slightly steeper.

For a gas saturation of 40% air, the P_a at which only the noble gas remains and SL begins is $P_a\approx1.26$ bar. This is the pressure at which the slope of the $C=0.4\%$ curve turns posi-

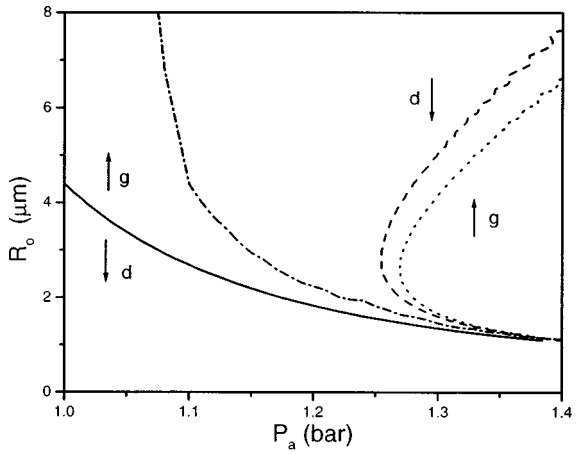

FIG. 2. Diffusive equilibrium curves computed for a single drive frequency of 23.4 kHz at $C=40\%$ (solid), $C=0.4\%$ (dashed), and $C=0.3\%$ (dotted). A positive slope indicates a stable equilibrium and a negative slope an unstable equilibrium as the growth (g) and dissolution (d) trends indicate. The Mach criterion (dash-dotted) provides an approximation of the stable chemical equilibrium.

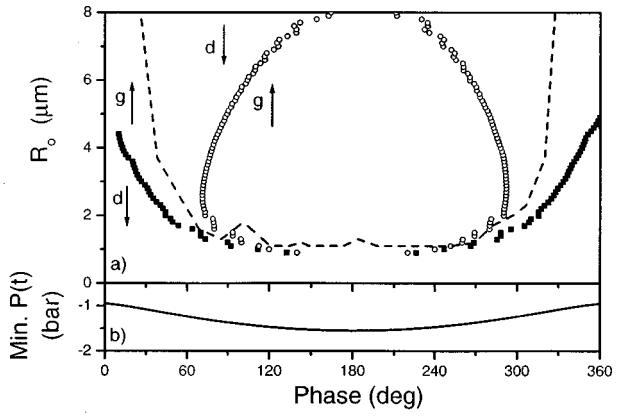

FIG. 3. Phase diagram (a) for an ideal second harmonic drive with an air saturation of 40%. The $C=40\%$ curve (■) represents an unstable equilibrium and the $C=0.4\%$ curve (○) a stable equilibrium as indicated by the growth (g) and dissolution (d) trends. The Mach criterion (dashed) approximates the stable chemical equilibrium. An increasing peak negative pressure for $P(t)$ (b) indicates a more violent collapse.

tive. Note that $P_a=1.25$ bar is not a stable point. A few features of stable SL behavior as P_a increases are worth noting. First, R_0 increases and the bubble gets brighter as P_a increases. Second, the ER *decreases* as P_a increases.[14,21] Third, there is a value of P_a above which instabilities cause the bubble to break up.[15] This extinction threshold pressure varies with gas concentration and drive frequency. These three points will be useful when discussing the phase space diagrams.

For simplicity, only the gas saturation of $C=40\%$ air will be used in the following analysis of the second harmonic drive system. The general analysis is not affected by this restriction, but specific parameter values will change slightly if a different total saturation is used.

III. IDEAL SECOND HARMONIC DRIVE

As a starting point for interpreting the experimental data we begin with the ''ideal'' second harmonic drive case having a drive signal at the pressure antinode of

$$P(t)=P_1\cos(\omega t)+P_2\cos(2\omega t+\phi). \tag{5}$$

The drive signal $P(t)$ is now described by the magnitude of each frequency component, P_1 and P_2 and the phase ϕ of the second harmonic. The values used by Holzfuss *et al.*[6] to generate Fig. 1 were $P_1=1.25$ bar and $P_2=0.3$ bar. These are also the values used for all the calculations presented here. Since the pressure amplitudes are now fixed, we can consider ϕ as an effective P_a when generating a phase diagram. This was clearly seen in Fig. 1 where the light intensity varied with ϕ, just as if P_a were being varied in a single drive frequency system.

Figure 3(a) shows the phase space diagram for the experimental case of a 40% air saturation. The diffusive equilibrium curves were computed with Eq. (3) using $P(t)$ as the drive pressure. The $C=40\%$ curve (■) represents an unstable equilibrium and the $C=0.4\%$ curve (○), a stable equilibrium as indicated by the growth (g) and dissolution (d) trends next to each curve. This phase space diagram differs somewhat from the earlier single drive frequency case, but it can be interpreted in the same way. We start by only examining the range of $\phi=0°$–$180°$ and describe the expected experimental behavior based on DH.

From $\phi=0°$–$30°$ the bubble behavior is determined by the $C=40\%$ curve. Because the curve is in the range of the typical seed size for levitation, some bubbles will tend to dissolve (d) while others will tend to grow (g) by rectified diffusion.[18,23] The bubbles that grow will display ''dancing'' behavior[1,13,24,25] as they repeatedly grow and pinch off when they intersect a shape stability threshold (not shown) at ≈ 7 μm or higher.[25]

From $\phi=40°$–$70°$ a seeded bubble begins above or grows to the Mach criterion (dashed). This indicates that the energy of collapse is now sufficient to dissociate the diatomic gases in the bubble, and the bubble can reach a stable non-SL equilibrium. If the Mach criterion were in fact the true chemical equilibrium, the bubble would travel along this path until only the noble gas content remained. However, since the true chemical equilibrium may actually lie to the right of the Mach criterion, the region of the stable non-SL may be smaller.

From $\phi=70°$–$100°$ the bubble only contains noble gas since the oxygen and nitrogen have been completely dissociated. Now the bubble is stable and luminescing, and its location in phase space is determined by the curve representing the argon concentration ($C=0.4\%$). As ϕ increases, the light intensity increases and the ER *decreases* until the bubble reaches the extinction threshold at ≈ 6 μm[25] (not shown), at which point it breaks up and no new bubble can be seeded. Beyond the extinction threshold, from $\phi=100°$–$180°$, no stable or unstable bubble can be acoustically trapped.

The instability at the extinction threshold occurs on a much faster time scale than the instability causing ''dancing'' behavior[15] and is still not completely understood. It may result from a build up of higher order shape modes,[21] from bubble translation caused by the instantaneous Bjerknes force,[9,26] or from a fast time scale instability such as the

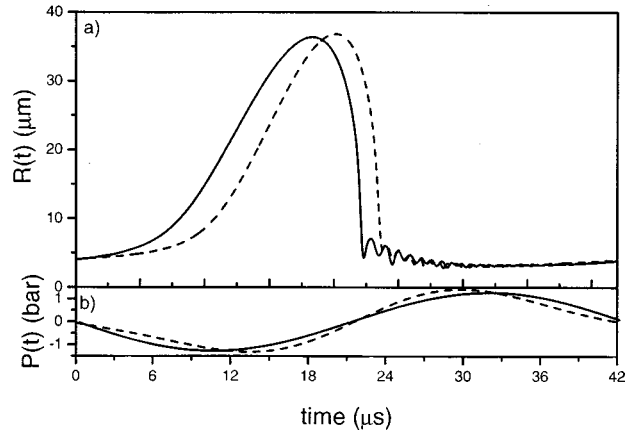

FIG. 4. Comparison of (a) $R(t)$ curves and (b) drive signals for a single drive frequency (solid) and an ideal second harmonic (dashed). Both cases represent a diffusively stable SL bubble with $R_0=4$ μm taken from the $C=0.4\%$ concentration curves in Figs. 2 and 3. For the single drive frequency, $P_a=1.27$ bar, and for the ideal second harmonic case, $P_1=1.25$ bar, $P_2=0.3$ bar, and $\phi=78°$. $R_{\max}$ for the ideal second harmonic case is slightly greater since it has more time to grow due to the small delay in its drive signal reaching the peak negative value.

Rayleigh–Taylor[27] or Richtmyer–Meshkov[28] instabilities. The boundary in phase space between unstable ''dancing'' behavior and extinction is not clearly defined. Loosely speaking, extinction is more likely to occur at higher drive pressures after following a path of stable SL and both the extinction threshold and shape instabilities occur at lower R_0 as P_a increases.[9,15,21,25,29,30]

The expected behavior described above for $\phi=0°$–$180°$ is nearly the same as for the single drive frequency case. In fact, from $\phi=180°$–$360°$ the phase diagram is just a mirror image of a single drive frequency case, and the behavior is therefore just the reverse of what was described above with the bubble showing stable SL from $\phi=260°$–$290°$ and stable or dancing non-SL behavior from $\phi=290°$–$360°$.

We can see why this symmetry arises by viewing the peak negative pressure (PNP) vs ϕ [Fig. 3(b)]. The PNP provides a means of relating the harmonic drive signal $P(t)$ to the single drive frequency amplitude P_a. For both cases, the negative pressure largely determines the $R_{\max}$ that the bubble reaches before undergoing inertial collapse.[31] Thus, an increase in the PNP leads to a larger $R_{\max}$ and a more violent collapse, just as with an increase in P_a. Based on these observations, we would expect to see an increasing PNP from $\phi=0°$–$180°$ since the violence of collapse is increasing with ϕ. This is indeed what is observed in Fig. 3(b). The PNP then decreases from $\phi=180°$–$360°$ leading to the symmetry of the phase diagram about $\phi=180°$.[32]

Now that we have a phase diagram for the ideal 40% air second harmonic drive system, we can compare the ideal second harmonic case to the single drive frequency case using the same initial conditions. The effect of the ideal second harmonic on the radial response $R(t)$ of a bubble can be seen in Fig. 4(a). The solid curve shows the $R(t)$ curve for a single drive frequency with $P_a=1.27$ bar and $R_0=4$ μm. These parameters represent a point on the $C=0.4\%$ curve from Fig. 2. This radial response can be compared to the same bubble driven by $P(t)$ [Eq. (5)] where $\phi=78°$ and $R_0=4$ μm (dashed). These parameter values correspond to the $C=0.4\%$ curve from the ideal second harmonic phase diagram (Fig. 3).

One interesting feature of Fig. 4(b) is that the drive signals look almost the same. Because P_2 is relatively small compared to P_1, the drive signal of the ideal second harmonic still maintains the general features of the fundamental frequency. However, $P(t)$ (dashed) reaches a PNP of -1.32 bar which is less than and delayed from the -1.27 bar PNP of $P_a(t)$ (solid). The more negative PNP for $P(t)$ allows the bubble to grow to a slightly larger $R_{\max}$. The time delay in the PNP leads to a delay in the growth and inertial collapse of the bubble.

Both these effects are visible in the $R(t)$ curves for each drive signal [Fig. 4(a)]. The bubble driven by $P_a(t)$ (solid) reaches $R_{\max}=36.39$ μm. The bubble driven by $P(t)$ (dashed) reaches $R_{\max}=36.86$ μm and has a delay in its growth and collapses. Because both cases have the same ambient radius ($R_0=4$ μm), the ER of the ideal second harmonic case is larger than the single drive frequency case by about 1.3%.

While this change in ER may seem small, it can in fact lead to substantially increased light output from the bubble. Moss *et al.*[33] have shown numerically that a 15% change in ER results in a nearly twofold increase in the number of photons emitted. Gaitan and Holt[14] have also experimentally found that with a single drive frequency,

$$\frac{\text{photons}}{\text{Vol}} \propto \left(\frac{R_{\max}}{R_0}\right)^{4.1}, \tag{6}$$

or the number of photons emitted per volume goes nearly as the fourth power of ER.

Based on Eq. (6) and assuming it can be extended to a system with multiple drive frequencies, a 1.3% increase in ER for the ideal second harmonic case would result in a bubble about 5% brighter than with just a single harmonic drive. Remember that the parameters for the two cases were chosen so that the gas concentration ($C=0.4\%$) and ambient radius ($R_0=4$ μm) were the same. The number of atoms available to emit light are therefore the same for each case. Thus, for the same initial conditions, the addition of the second harmonic truly leads to a brighter bubble as well as a higher energy concentration.

We should also mention that if P_2 were set to zero in the above analysis, the resulting bubble would dissolve or start ''dancing'' just as was observed by Holzfuss *et al.*[6] This behavior is seen in Fig. 2 where there is no stable equilibrium for $C=0.4\%$ at $P_a=1.25$ bar.

We have therefore established that a second harmonic drive can indeed lead to a brighter bubble for the same initial conditions. However, the phase space diagram discussed above and bubble behavior predicted from it clearly do not agree with the experimental results from Fig. 1. To obtain a phase diagram that corresponds to experiment, the spatial mode profile in the z direction must be considered.

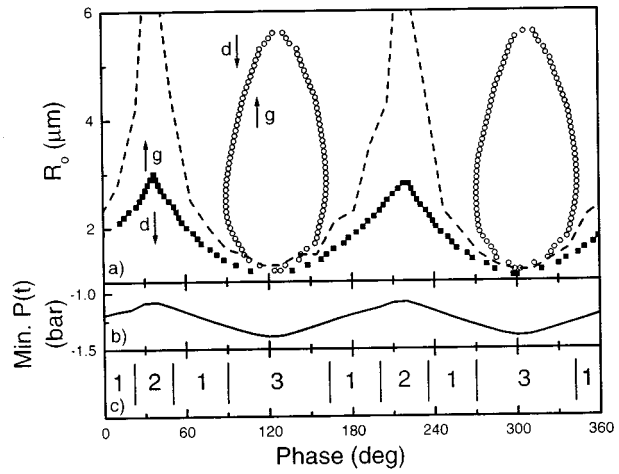

FIG. 5. (a) Phase space diagram for the experimental second harmonic drive for a 40% air saturation. The $C=0.4\%$ curve (○) and the Mach criterion (dashed) represent stable equilibria: The $C=40\%$ curve (■), unstable equilibrium. (b) An increasing peak negative pressure for $\hat{P}(t)$ indicates a more violent collapse. (c) ϕ is broken into regions of stable SL (3), unstable non-SL (2), and stable or unstable non-SL (1).

IV. EXPERIMENTAL SECOND HARMONIC DRIVE

As was seen in Fig. 1(a), the bubble undergoes a significant translation as ϕ varies. This translation arises from changes in the time-averaged Bjerknes force on the bubble, which counteracts the effect of buoyancy and pushes the bubble toward the antinode.[34] A similar translation occurs in single drive frequency systems, but is usually neglected, because its overall effect on bubble dynamics is minor.[26] It is normally assumed that the bubble rests at the antinode and that the z spatial profile of the standing wave can be ignored. However, this is not true of the experimental second harmonic drive system for which the translation in z must be considered when interpreting the experimental results. The translation in z means that the effective drive pressure varies as the bubble moves in the sound field.

We therefore use the spatial profile measured by Holzfuss *et al.*[6]

$$\hat{P}(t)=P_1\cos(\omega t)\cos\left(\frac{k}{2}z\right)+P_2\cos(2\omega t+\phi)\cos(2kz-\pi/2), \tag{7}$$

where the wave number $k=\omega/c_w$, and as before $P_1=1.25$ bar and $P_2=0.3$ bar. This description of the spatial profile is somewhat surprising for two reasons. First, the spatial term for P_1 is $k/2$ rather than the expected k. Second, if $z=0$, the P_2 term has no effect on the drive signal and the bubble responds as if only a single drive frequency were present. Thus, the Bjerknes force is the reason the bubble sees the second harmonic at all. The above points indicate the difficulty in achieving ideal one dimensional standing waves in an experimental system that is really a superposition of wave components in three dimensions.

Figure 5(a) shows the phase space diagram relevant to an experiment using a 40% air saturation when z translation is included in the calculations. The translation $z(\phi)$ was taken from Fig. 1(b) since this represents the theoretical translation. As in the ideal case, the $C=40\%$ curve (■) represents an unstable equilibrium, and the $C=0.4\%$ curve (○) represents a stable equilibrium. Trends for growth (g) and dissolution (d) are indicated next to each curve. The curves were computed with Eq. (3) with $\hat{P}(t)$ as the drive pressure. Also shown in Fig. 5(a) is the Mach criterion (dashed).

The first obvious feature of this phase diagram is that it looks like two of the ideal second harmonic phase diagrams (Fig. 3) placed back to back. This behavior results from the PNP swinging more negatively twice [Fig. 5(b)] while only once in the ideal case [Fig. 3(b)]. As the PNP becomes more negative, the bubble collapse becomes more violent, and the lower diffusive equilibrium curves being to stand out. As in the ideal case, we will focus on only one range of ϕ (37°–127°) due to the symmetry of the phase diagram. The analysis largely follows that for the ideal case and thus will not be dealt with in depth.

From $\phi=37°$–$45°$ the bubble still contains 40% air and the behavior is determined by the $C=40\%$ curve. Normally the bubble will lie above the curve when seeded, and will thus display dancing behavior. From $\phi=45°$–$90°$, the bubble collapse enters the regime where dissociation may occur. The bubble may therefore exhibit stable non-SL behavior as it reaches a chemical equilibrium, but as noted earlier, it may just as well continue dancing until $\phi=90°$. From $\phi=90°$–$127°$ the bubble now contains only noble gas, and it thus follows the $C=0.4\%$ curve. Near $\phi=127°$, the bubble approaches the extinction threshold and may display unstable behavior or break up. However, if we assume that the extinction threshold occurs at $R_0\approx 6$ μm,[25] then the bubble will remain stable even at $\phi=127°$. As the bubble travels along the $C=0.4\%$ curve and the PNP increases, its light emission will increase but the ER will *decrease*.

The behavior for the remaining range of ϕ is based on the above analysis. From $\phi=127°$–$220°$ the behavior is the mirror image of that from $\phi=37°$–$45°$. Then because of the symmetry of the PNP, the behavior from $\phi=37°$–$220°$ just repeats itself from $\phi=220°$–$397°$.

Using the above analysis, we can now predict the experimental behavior for a 40% air saturation [Fig. 5(a)]. In the range $\phi=90°$–$160°$ and $\phi=271°$–$343°$ there should be stable SL [region 3 of Fig. 5(c)], and the bubble should follow the $C=0.4\%$ curve. The intensity of the SL increases as the radius of the bubble increases, and since the bubble approaches the extinction threshold at its largest R_0 values, it could display some unstable behavior or extinction for a small range of ϕ in the middle of the SL regions.

In the range of ϕ where the bubble collapse is not violent enough to cause any dissociation, the bubble will display dancing motion (region 2). In the region where dissociation (region 1) is possible, the bubble may show stable non-SL behavior due to the chemical equilibrium, but it may also display dancing behavior. We therefore expect to see two regions where stable SL occurs. As ϕ increases through each region, the bubble reaches a maximum light output toward the center of the region and then decreases back down to zero. Outside of the SL ranges, the bubble most likely displays unstable dancing behavior.

Comparison of the predicted phase space behavior with

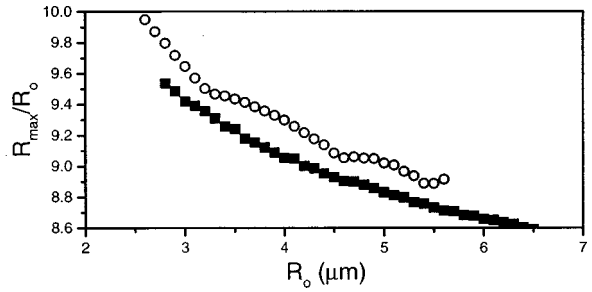

FIG. 6. Expansion ratios vs R_0 for a single drive frequency (■) and for the experimental second harmonic (○) for a 40% air saturation. The single drive frequency reprsents the stable portion of the $C=0.4\%$ curve in Fig. 2. The experimental second harmonic represents the $C=0.4\%$ curve from Fig. 5 in the range $\phi=270°-300°$.

the experimental data (Fig. 1) reveals excellent agreement. The experimental data show two regions of SL [Fig. 1(c)] from $\phi=67°-175°$ and $\phi=258°-331°$ which are nearly the same as the ranges predicted above. The SL regions also show a trend of increasing light intensity toward their center as predicted by DH. A small region of unstable SL [Fig. 1(a)] was observed near the center of the first SL region ($\phi\approx160°$), which is consistent with the bubble approaching the extinction threshold. In the region where no SL was observed, the bubble displayed dancing behavior except for $\phi>330°$, where it likely was able to reach a stable chemical equilibrium. Clearly, the overall behavior as ϕ varies is consistent with the earlier phase space predictions. However, a direct comparison of $R_0-\phi$ values is not possible, because R_0 values were not measured by Holzfuss *et al.*[6]

We can also compare the radial response of the experimental second harmonic case to the single drive frequency case, as was done for the ideal second harmonic drive case. This time we take $\phi=280°$ and $R_0=4$ μm from the stable $C=0.4\%$ curve in Fig. 5(a). The $R(t)$ responses and drive signals look essentially like those in Fig. 4 except that now $R_{max}=37.34$ μm, which is slightly greater than for the ideal second harmonic case. This represents an increase in ER of 2.6% over the single drive frequency case that had $P_a=1.27$ bar and $R_0=4$ μm. Based on Eq. (6), the bubble should be about 10% brighter for the same initial conditions.

The second harmonic can therefore lead to a brighter SL emission. However, the above comparison does not account for the 100% increase in light emission observed by Holzfuss *et al.*[6] when the second harmonic was added. The difference of 100% was not for the same values of R_0 in each case though. The maximum intensity for the single drive frequency case was found by adjusting P_a to just below the extinction threshold ($P_a\approx1.33$ bar), while the maximum intensity for the second harmonic case was taken from Fig. 5(c) at $\phi=150°$. Therefore, the bubbles do not have the same number of argon atoms inside them making a direct comparison more difficult. This can be partly resolved by looking at the ER of the bubble as it traverses its respective concentration curves.

V. EXPANSION RATIOS

Figure 6 shows the ER computed using the diffusively stable points along the $C=0.4\%$ curves for the single drive frequency case in Fig. 2 and the experimental second harmonic case in Fig. 5(a) in the range $\phi=270°-300°$. The data points are plotted against R_0 rather than ϕ, since the resulting relationship between ER and brightness is not ambiguous: for a fixed R_0, a larger ER leads to a brighter bubble. Since an increasing R_0 is the same as an increase in either P_a or the PNP of $P(t)$, a larger R_0 leads to a brighter bubble. However, as R_0 increases, the ER *decreases*.[14] The bubble gets brighter in spite of a less energetic collapse, because the emitting volume grows as does the number of argon atoms available to emit light, offsetting the fact that the photons emitted per unit volume decreases.

As can be seen in Fig. 6, for a fixed R_0 the harmonic drive case always has a larger ER by $\approx2.6\%$. Therefore, we expect the harmonic drive case to be about 10% brighter, as was estimated earlier. Since Holzfuss *et al.*[6] observed a maximum difference in SL intensity of 100% between the two cases, the bubbles were likely not at the same R_0. Because the values for R_0 and P_a were not measured, we can only estimate them and then determine how the brightness should differ between the two cases.

For example, if we assume the extinction threshold for the single drive frequency case occurs at $R_0=5$ μm and $P_a=1.3$ bar, then the resulting ER is 8.831 (Fig. 2). For the experimental second harmonic case, we take the brightest point at $\phi=306°$ and $R_0=5.6$ μm, which gives an ER of 8.916 [Fig. 5(a)]. This assumes that the extinction threshold occurs at a different R_0 for the two cases. Then, using Eq. (6) we find that the second harmonic case should appear about 45% brighter than with just the fundamental. Without knowing the values for R_0 and with the true air saturation ranging between 30% to 40%, the estimated maximum difference in intensity is quite reasonable. Clearly, knowing all of the experimental parameters would allow one to make better quantitative comparisons of light emissions.

Interestingly, Holzfuss *et al.*[6] reported that when further adjustments were made to P_1 and P_2 of $\hat{P}(t)$, the second harmonic drive case could be made 300% brighter than with just the fundamental. This would shift the position of the diffusive equilibrium used to determine the location of stable SL points in phase space. Thus, the radial response of the bubble would change and affect the ER. Since small changes in ER can lead to large changes in light emission,[35,36] a difference of 300% does not seem unreasonable and should be consistent with a phase space analysis using DH.

VI. PHASE SPACE PREDICTIONS

Having shown DH can be successfully applied to the second harmonic case with a 40% air saturation, we can also use DH to make predictions for other air saturations. Figure 7 shows a family of diffusive equilibrium curves computed with Eq. (3) using the function $z(\phi)$ from Fig. 1(b) to compute $\hat{P}(t)$. The curves range from a high concentration of $C=10\%$ (■) to a low concentration of $C=0.1\%$ (×). As the value of C decreases from 10%, the curves begin to wrap around, forming closed loops starting at $C\approx0.8\%$ (▲). Since the closed C curves are diffusively stable, these are the concentrations of noble gas needed in an experiment to achieve

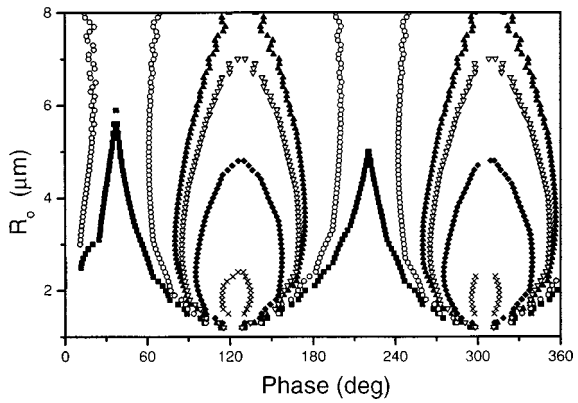

FIG. 7. Family of diffusive equilibrium curves for the experimental second harmonic drive. The curves represent $C=10\%$ (■), 3% (○), 0.8% (▲), 0.6% (▽), 0.3% (◆), and 0.1% (×). The curves that form closed loops represent noble gas concentrations at which stable SL can occur.

stable SL. Thus, for an air saturation of 30% the $C=0.3\%$ curve (◆) would determine the behavior for stable SL.

Based on Fig. 7 we can make the following predictions:

(i) When c is decreased, the ϕ ranges for the two islands of SL should decrease. This can be seen by comparing the $C=0.3\%$ and $C=0.1\%$ curves. Since the diameter of the closed C loops indicates the range of ϕ where SL is observed, the lower concentration clearly will span a smaller range.

(ii) Also, as C decreases, clear regions of stable non-SL should become visible to either side of the SL islands. Since the ϕ ranges of the SL islands decreases with decreasing C, this opens up a broader range of ϕ where chemical equilibrium can set in [regions 1 of Fig. 5(c)]. Therefore, as in the single drive frequency case,[13,25] a chemical equilibrium is more likely to occur. This effect should be clearly seen for a case with $C=0.1\%$.

(iii) When C is increased and the loops begin to ''open up,'' unstable behavior should become more visible in the center of each SL ϕ range. As the C curves steepen and cross the shape threshold at $R_0 \approx 5-6$ μm,[25] they will lie above the shape threshold over a larger range of ϕ. For the range of ϕ where the curve is above the threshold, the bubble grows to the threshold and pinches off, displaying a ''dancing'' unstable motion.[15] Extinction is also possible, but is not as likely since it was not observed by Holzfuss *et al.*[6] for a 40% air saturation. To reach the extinction threshold, one would need to further increase the PNP, which could not be done without adjusting P_1 and P_2 as has been observed.[22] Therefore, it seems more likely that unstable SL will be observed for the center ranges of ϕ as C increases, and these ranges will increase as C increases.

(iv) Finally, as C is decreased, the ER should increase but the SL intensity should *decrease*.[21] This is also as in the single drive frequency case where a more violent collapse does not necessarily result in a brighter bubble.[14] Since decreasing C also lowers R_0 for a fixed P_a, the emitting volume decreases.[21] Even though the ER increases for a decreasing value of C, the bubble appears fainter because there are fewer atoms available for emission.

VII. SUMMARY

We have shown that DH can be used to interpret the experimental results of Holzfuss *et al.*[6] While the data could not be directly compared to a theoretical phase space diagram because R_0 was not measured, all of the trends predicted by DH were observed in the data. In particular, the prediction that stable SL is determined by the noble gas content of the bubble agrees very well with the experimental results. Both cases revealed two ''islands'' of SL as ϕ was varied over 360°, and these ''islands'' occurred at nearly the same values of ϕ. The regions of ϕ where dancing was expected and a chemical equilibrium could occur also agreed very well with the phase space predictions based on DH.

For a bubble of the same size, R_0, and saturation C, it was found that the addition of a second harmonic to the drive signal can lead to a brighter bubble. This arises because the PNP of $\hat{P}(t)$ reaches a more negative value than the PNP of $P_a(t)$, permitting the bubble to grow to a larger $R_{\max}$. The ER of the second harmonic case is therefore larger, indicating a more violent and energetic collapse. Since both cases have the same number of emitting atoms, the second harmonic case is brighter because it has a higher energy concentration. This represents a true optimization over a single drive frequency case since both ER and brightness increase.

By adding additional harmonics, further optimization is possible.[6] Based on the analysis presented here, the phasing of the additional harmonics should be chosen so as to contribute to the negative pressure of the acoustic cycle, since this approach has the main effect on the ER via $R_{\max}$. Holt and Roy have proposed experiments along a similar line.[37] In the limit of an infinite number of harmonics, a negative pressure spike on top of the fundamental would be the ideal drive signal. Interestingly, this conclusion is the opposite of the positive pressure spike suggested by Moss *et al.*[7]

In real experimental systems, which are seldom ideal, unwanted harmonics could easily creep in to affect the acoustic drive signal. Depending on the phasing of the harmonics relative to the fundamental, they may either enhance or reduce the ER by a small amount, resulting in changes in light emission. This may explain why experimental groups working at the same drive frequency observe different maximum light intensities when using the same gas concentrations.[38]

In conclusion, the results presented here provide further evidence that the underlying assumptions of DH for steady-state SL conditions[10] are valid and point to the utility of using DH to determine the optimum experimental parameters. By first predicting where SL should occur, one can take some of the guess work out of performing SL experiments. As the focus on increasing the energy concentration of SL intensifies,[39] the ability to predict bubble behavior in advance of experiments[5] will become more and more important.

ACKNOWLEDGMENTS

We wish to thank J. Holzfuss for allowing us to use his experimental data and for helpful comments on this manu-

script. We also wish to acknowledge many valuable discussions with G. Holt, T. Matula, and S. Hilgenfeldt.

[1] D. F. Gaitan, L. A. Crum, C. C. Church, and R. A. Roy, ''Sonoluminescence and bubble dynamics for a single, stable, cavitation bubble,'' J. Acoust. Soc. Am. **91**, 3166–3183 (1992).
[2] R. Hiller, K. Weninger, S. J. Putterman, and B. P. Barber, ''Effect of noble-gas doping in single-bubble sonoluminescence,'' Science **266**, 248–250 (1994).
[3] B. Gompf, R. Günther, G. Nick, R. Pecha, and W. Eisenmenger, ''Resolving sonoluminescence pulse width with time-correlated single photon counting,'' Phys. Rev. Lett. **79**, 1405–1408 (1997).
[4] R. A. Hiller, S. J. Putterman, and K. R. Weninger, ''Time-resolved spectra of sonoluminescence,'' Phys. Rev. Lett. **80**, 1090–1093 (1998).
[5] S. Hilgenfeldt and D. Lohse, ''Predictions for upscaling sonoluminescence,'' Phys. Rev. Lett. **82**, 1036–1039 (1999).
[6] J. Holzfuss, M. Rüggeberg, and R. Mettin, ''Boosting sonoluminescence,'' Phys. Rev. Lett. **81**, 1961–1964 (1998).
[7] W. C. Moss, D. B. Clarke, J. W. White, and D. A. Young, ''Sonoluminescence and the prospects for table-top micro-thermonuclear fusion,'' Phys. Lett. A **211**, 69–74 (1996).
[8] K. Hargreaves, ''Influence of nonsinusoidal waveforms on single cavitation bubbles,'' Masters thesis, Univeristy of Washington (1998).
[9] S. M. Cordry, ''Bjerknes forces and temperature effects in single-bubble sonoluminescence,'' Ph.D. dissertation, University of Mississippi (1995).
[10] D. Lohse and S. Hilgenfeldt, ''Inert gas accumulation in sonoluminescing bubbles,'' J. Chem. Phys. **107**, 6986–6997 (1997).
[11] L. A. Crum, ''Acoustic cavitation series part five—Rectified diffusion,'' Ultrasonics **22**, 215–223 (1984).
[12] T. J. Matula and L. A. Crum, ''Evidence for gas exchange in single-bubble sonoluminescence,'' Phys. Rev. Lett. **80**, 865–868 (1998).
[13] J. A. Ketterling and R. E. Apfel, ''Experimental validation of the dissociation hypothesis for single bubble sonoluminescence,'' Phys. Rev. Lett. **81**, 4991–4994 (1998).
[14] D. F. Gaitan and R. G. Holt, ''Experimental observations of bubble response and light intensity near the threshold for single bubble sonoluminescence in an air–water system,'' Phys. Rev. E **59**, 5495–5502 (1999).
[15] S. Hilgenfeldt, D. Lohse, and M. P. Brenner, ''Phase diagrams for sonoluminescing bubbles,'' Phys. Fluids **8**, 2808–2826 (1996).
[16] T. G. Leighton, *The Acoustic Bubble* (Academic, London, 1994), pp. 302–305.
[17] R. Löfstedt, B. P. Barber, and S. J. Putterman, ''Toward a hydrodynamic theory of sonoluminescence,'' Phys. Fluids A **5**, 2911–2928 (1993).
[18] A. Eller and H. G. Flynn, ''Rectified diffusion during nonlinear pulsations of cavitation bubbles,'' J. Acoust. Soc. Am. **37**, 493–503 (1965).
[19] M. M. Fyrillas and A. J. Szeri, ''Dissolution or growth of soluble spherical oscillating bubbles,'' J. Fluid Mech. **277**, 381–407 (1994).
[20] P. H. Roberts and C. C. Wu, ''On rectified diffusion and sonoluminescence,'' Theor. Comput. Fluid Dyn. **10**, 357–372 (1998).
[21] J. A. Ketterling, ''An experimental validation of the dissociation hypothesis for sonoluminescence and an extension to the analysis of multiple frequency drives,'' Ph.D. dissertation, Yale University (1999).
[22] J. Holzfuss (private communication).
[23] M. M. Fyrillas and A. J. Szeri, ''Dissolution or growth of soluble spherical oscillating bubbles—The effect of surfactants,'' J. Fluid Mech. **289**, 295–314 (1995).
[24] B. P. Barber, C. C. Wu, R. Löfstedt, P. H. Roberts, and S. J. Putterman, ''Sensitivity of sonoluminescence to experimental parameters,'' Phys. Rev. Lett. **72**, 1380–1383 (1994).
[25] R. G. Holt and D. F. Gaitan, ''Observation of stability boundaries in the parameter space of single bubble sonoluminescence,'' Phys. Rev. Lett. **77**, 3791–3794 (1996).
[26] T. J. Matula, S. M. Cordry, R. A. Roy, and L. A. Crum, ''Bjerknes force and bubble levitation under single-bubble sonoluminescence conditions,'' J. Acoust. Soc. Am. **102**, 1522–1527 (1997).
[27] M. P. Brenner, D. Lohse, and T. F. Dupont, ''Bubble shape oscillations and the onset of sonoluminescence,'' Phys. Rev. Lett. **75**, 954–957 (1995).
[28] C. C. Wu (private communication).
[29] A. Prosperetti and Y. Hao, ''Modelling of spherical gas bubble oscillations and sonoluminescence,'' Philos. Trans. R. Soc. London, Ser. A **357**, 203–224 (1999).
[30] C. C. Wu and P. H. Roberts, ''Bubble shape instability and sonoluminescence,'' Phys. Lett. A **250**, 131–136 (1998).
[31] R. E. Apfel, ''Acoustic cavitation prediction,'' J. Acoust. Soc. Am. **69**, 1624–1633 (1981).
[32] Using a heuristical optimization algorithm with the condition of constant drive power. Holzfuss *et al.* (Ref. 6) found optimal drive conditions to be $\phi = 166.6°$, $P_1 = 1.026$ bar, and $P_2 = 0.798$ bar. These findings suggest that due to the nonlinearity of the bubble oscillations, the PNP is not the only factor influencing $R_{\max}$.
[33] W. C. Moss, D. A. Young, J. A. Harte, J. L. Levatin, B. F. Rozsnyai, G. B. Zimmerman, and I. H. Zimmerman, ''Computed optical emissions from a sonoluminescing bubble,'' Phys. Rev. E **59**, 2986–2992 (1999).
[34] L. A. Crum, ''Bjerknes forces on bubbles in a stationary sound field,'' J. Acoust. Soc. Am. **57**, 1363–1370 (1975).
[35] W. C. Moss, D. B. Clarke, and D. A. Young, ''Calculated pulse widths and spectra of a single sonoluminescing bubble,'' Science **276**, 1398–1401 (1997).
[36] L. Kondić, J. I. Gersten, and C. Yuan, ''Theoretical-studies of sonoluminescence radiation—Radiative-transfer and parametric dependence,'' Phys. Rev. E **52**, 4976–4990 (1995).
[37] R. G. Holt and R. A. Roy (unpublished material).
[38] S. J. Putterman (private communication).
[39] R. E. Apfel, ''Sonoluminescence: And there was light!'' Nature (London) **398**, 378 (1999).

Use of electrodynamic drivers in thermoacoustic refrigerators

Ray Scott Wakeland
Graduate Program in Acoustics, The Pennsylvania State University, University Park, Pennsylvania 16804

(Received 29 April 1999; accepted for publication 19 October 1999)

Some issues involved in matching electrodynamic drivers to thermoacoustic refrigerators are examined using an equivalent circuit model. Conclusions are that the driver should be chosen to have a large product $(Bl)^2/(R_eR_m)$; the suspension stiffness should be chosen to make the combined impedance of the mechanical and acoustical parts of the system entirely real at the operating frequency; and the piston area should be selected to maximize electroacoustic efficiency, or other desired parameter, by matching the acoustic load to the optimum mechanical load for the particular driver. Alternately, if the piston area is fixed, the operating frequency can be adjusted to make this same match. © *2000 Acoustical Society of America.* [S0001-4966(00)00602-0]

PACS numbers: 43.38.Dv, 43.35.Ud [SLE]

INTRODUCTION

The most common type of driver for use in thermoacoustic refrigeration applications is the ordinary electrodynamic loudspeaker. This paper examines some of the issues involved in matching an electrodynamic driver to a thermoacoustic refrigerator.

Most thermoacoustic refrigerators to date have had basic structures similar to those schematically depicted in Fig. 1. The driver is placed at the end of an acoustical resonator in which it creates a standing wave, as in Fig. 1(a). The back side of the driver is enclosed. The rear enclosure confines the working fluid (often a pressurized mixture of helium and argon) and provides equal mean pressures on the front and rear of the piston. This enclosed gas also provides a restoring force to the piston in the form of a gas spring.

Thermoacoustic refrigerators contain a heat-pumping element, called a ''stack,'' that is flanked by heat exchangers (not shown). For best efficiency, stacks are usually placed near pressure antinodes. In the example shown in Fig. 1(b), a volume is placed opposite the driver to act as an acoustic compliance, approximating an open end. If the driving frequency is chosen to make this a quarter-wavelength resonator, then the driver is at a location of high acoustic impedance, and the stack is placed near the driver (the dashed line is an approximate pressure amplitude profile). It is also possible to make resonators where the driver is at a position of low acoustic impedance, as in Fig. 1(c). Other arrangements are possible,[1] with the acoustic load seen by the face of the piston somewhere within this range from large to small.

This paper examines the questions of how to select an appropriate driver for a particular thermoacoustic application, and how the requirements differ depending on whether the driver is in a location of high or low impedance. The results are that the driver should be chosen to have a large product $(Bl)^2/(R_eR_m)$, defined below; the suspension stiffness should be chosen to make the combined impedance of the mechanical and acoustical parts of the system entirely real at the operating frequency; and the piston area should be selected to maximize electroacoustic efficiency (or other desired parameter) by matching the acoustic load to the optimum mechanical load for the particular driver. Alternately, if the piston area is fixed, the operating frequency can be adjusted to make this same match.

I. PHYSICAL MODEL AND EQUIVALENT CIRCUITS

The objective is to optimize the transfer of electrical power to acoustic power in the resonator. Two cases are considered. The first case is optimization of electroacoustic efficiency, the likely desired operating condition for a practical, working refrigerator. The second case, maximization of acoustic power in the resonator for maximum allowable electrical current in the voice coil, might be preferred for a small demonstration device.

The problem is analyzed using the simplified physical model shown in Fig. 2. The driver is modeled in the ordinary way, as a mass-spring-dashpot system driven by a coil of length l in a magnet gap with induction B. In this paper, B and l appear only as the force factor Bl, which is assumed to be a purely real number—''a typical situation prevailing with conventional moving-coil transducers.''[2] The piston has mass M_m and an area S that is not necessarily the same as the cross-sectional area of the resonator at that end. The mechanical compliance C_m, related to the mechanical stiffness k_m by $k_m=1/C_m$, includes the suspension stiffness and the effective spring constant of the gas in the enclosure. It is assumed that the enclosure is small enough that wave effects in the enclosure can be neglected at the (low) frequencies of interest. The resonator has a complex acoustic impedance ζ_a at the piston, the real part of which includes the dissipation due to the stack, heat exchangers, and resonator.

An equivalent circuit[3] of the simplified system is shown in Fig. 3(a). An $e^{j\omega t}$ time dependence is assumed throughout this paper. The electrical capacitance C_e has been included to allow for the possibility of adding a capacitor to improve the power factor of the device. In Fig. 3(b), all elements have been brought through the transformers into the mechanical mobility domain, with

$$X_e=\omega L_e-1/(\omega C_e), \tag{1a}$$

$$X_m=\omega M_m-k_m/\omega, \tag{1b}$$

$$R_a=\mathrm{Re}[S^2\zeta_a], \tag{1c}$$

$$X_a=\mathrm{Im}[S^2\zeta_a]. \tag{1d}$$

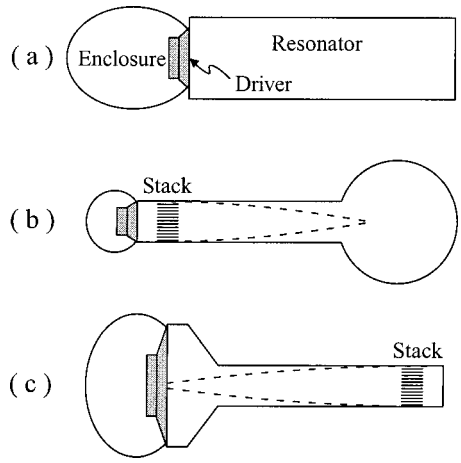

FIG. 1. (a) A typical thermoacoustic refrigerator comprises an acoustical resonator, a driver that creates a standing wave in the resonator, and a smaller ''enclosure'' behind the driver that holds in the working fluid. (b) A configuration that puts the driver at a pressure antinode. (c) An alternative configuration that puts the driver at a pressure node. The dashed lines represent the acoustic pressure swings.

The quantity $E/(Bl)$ has been assigned the symbol u_e because it has units of velocity. F_a is the force on the piston face due to the acoustical oscillations of the gas in the resonator, proportional to the pressure amplitude there; u_a is the velocity of the piston.

Converting all elements into the mechanical impedance domain results in Fig. 4.

The electroacoustic efficiency η is the ratio of the time-averaged acoustic power to the time-averaged total input power,

$$\eta = \frac{\mathrm{Re}[F_a u_a^*]}{\mathrm{Re}[F_e u_e^*]}. \tag{2}$$

The asterisk denotes complex conjugation, used here to facilitate taking the time-average of quantities represented in complex notation.

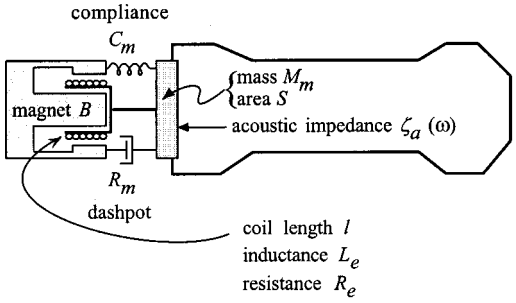

FIG. 2. The simple physical model used in this analysis.

Using $F_a = (R_a + jX_a)u_a$ and defining the total equivalent input impedance of the circuit as $Z_T \equiv F_e/u_e$, gives the form

$$\eta = \frac{\mathrm{Re}[(R_a + jX_a)u_a u_a^*]}{\mathrm{Re}[F_e(F_e^*/Z_T^*)]} = \frac{R_a}{\mathrm{Re}[1/Z_T]}\left|\frac{u_a}{F_e}\right|^2. \tag{3}$$

Defining an equivalent mechanical reactance X of the mechanical and acoustic impedances as

$$X \equiv X_m + X_a, \tag{4}$$

simplifies subsequent expressions. The total mechanical impedance can be obtained from Fig. 4 by adding in parallel the three legs of the circuit,

$$\frac{1}{Z_T} = \frac{R_e}{(Bl)^2} + \frac{jX_e}{(Bl)^2} + \frac{1}{(R_m + R_a) + jX}, \tag{5}$$

so

$$\mathrm{Re}\left[\frac{1}{Z_T}\right] = \frac{R_e}{(Bl)^2} + \frac{R_m + R_a}{(R_m + R_a)^2 + X^2}. \tag{6}$$

The ratio F_e/u_a is the impedance of the mechanical–acoustical leg only, so

$$\left|\frac{F_e}{u_a}\right|^2 = (R_m + R_a)^2 + X^2. \tag{7}$$

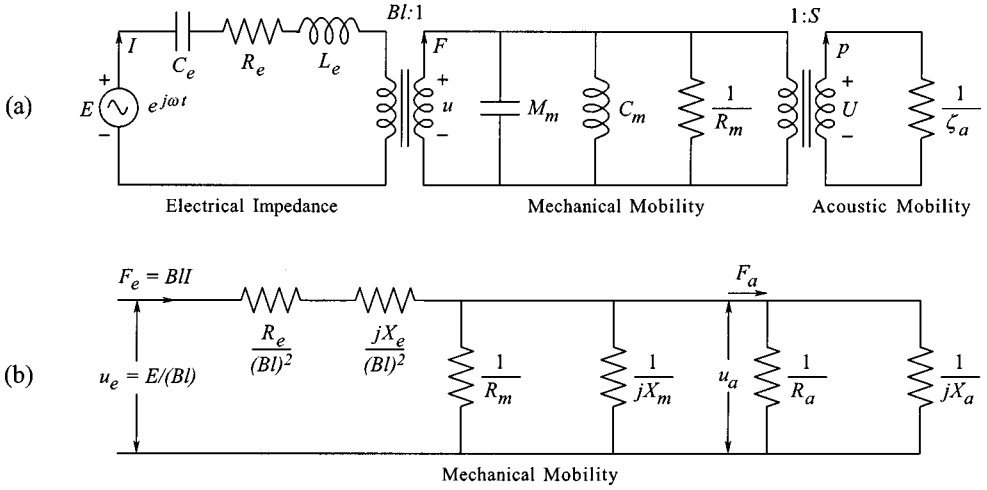

FIG. 3. Equivalent circuits for the physical model. Part (a) shows the electrical, mechanical, and acoustical parts of the system each in their respective domains, linked by transformer elements. Part (b) represents the same system, but with all parts converted to equivalent mechanical mobility elements.

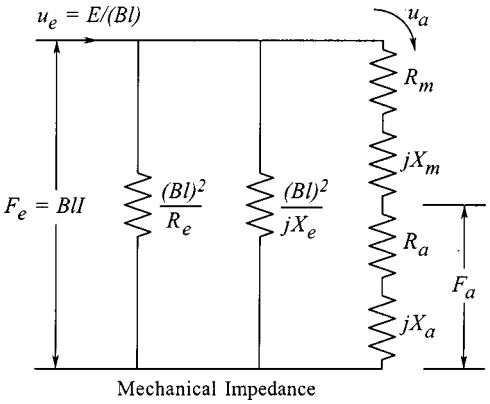

FIG. 4. Equivalent circuit in the mechanical impedance domain.

Substituting these expressions into Eq. (3), the electroacoustic efficiency is found to be given by[4]

$$\frac{1}{\eta}=\frac{R_eR_m}{(Bl)^2}\frac{R_m}{R_a}\left(1+\frac{R_a}{R_m}\right)^2+\left(1+\frac{R_m}{R_a}\right)+\frac{R_eR_m}{(Bl)^2}\frac{X^2}{R_mR_a}. \tag{8}$$

We would also like to find the conditions that will give the greatest possible acoustic power in the resonator without destroying the driver. One limit on the driver is the maximum current $I_{\max}$ that can be sustained before the voice coil burns up, so the case considered here is that of the time-averaged acoustic power at maximum current, $\Pi_a(I_{\max})$. Examination of Fig. 4 shows the acoustic power (i.e., the power in the resistive element R_a) to be

$$\Pi_a(I_{\max})=\frac{\mathrm{Re}[F_a u_a^*]}{2}=\frac{(BlI_{\max})^2}{2}\frac{R_a}{(R_m+R_a)^2+X^2}. \tag{9}$$

The factor of 1/2 assumes the use of peak (not root-mean-square) values for the amplitudes of oscillating variables such as forces, velocities, and currents.

II. THE REACTANCES X AND X_e

In Eqs. (8) and (9), both η and $\Pi_a(I_{\max})$ are maximized when $X=0$. That is, the combined equivalent impedance of the mechanical and acoustical parts of the device should be purely real. One way to satisfy this condition is to operate at a frequency of resonance or antiresonance of the acoustical resonator, where $X_a=0$, and to adjust the compliance of the driver so that the mechanical reactance X_m is also zero at this frequency. However, the $X=0$ condition can also be satisfied for any other frequency by adjusting the stiffness of the driver suspension (including the gas spring of the enclosure) so that[2] $X_m=-X_a$.

Both η and $\Pi_a(I_{\max})$ are independent of the electrical reactance X_e. If performance of the system is optimized by setting $X=0$, then the imaginary part of the total equivalent electrical input impedance of the system is simply the reactance of the electrical components, X_e. If the driver is inductive, as is likely for an electrodynamic device, then the total electrical impedance can be made real by the addition of a series capacitor, thereby eliminating the reactive component of the load seen by the driving amplifier without otherwise affecting the performance of the device.

In subsequent sections it is assumed that the stiffness of the driver suspension has been adjusted to make $X=0$.

III. OPTIMIZATION OF R_a AND PISTON AREA

In driving the acoustical resonator with $X=0$, the driver sees an equivalent mechanical resistance $R_a=S^2\,\mathrm{Re}[\zeta_a]$. By adjusting the piston area S, the value of R_a can be selected to optimize η or $\Pi_a(I_{\max})$. In this section, the derivatives with respect to R_a of Eqs. (8) and (9) have been set to zero to find the best values of R_a, and thus for S.

A. Adjusting R_a for maximum efficiency

The electroacoustic efficiency η is maximized when R_a is set to the value R_η such that

$$(R_a)_{\eta_{\max}}\equiv R_\eta=R_m\sqrt{\frac{(Bl)^2}{R_eR_m}+1}=R_m\sqrt{\beta+1}=\sigma R_m, \tag{10}$$

where $\beta\equiv(Bl)^2/(R_eR_m)$ and $\sigma=\sqrt{\beta+1}$. For this value of acoustic load, the efficiency takes on its maximum value of[5]

$$\eta_{\max}=\frac{\beta}{\beta+2\sqrt{\beta+1}+2}, \tag{11}$$

or, in terms of σ,

$$\eta_{\max}=\frac{\sigma-1}{\sigma+1}. \tag{12}$$

The number σ is a figure of merit for the driver, determining the maximum efficiency of the driver. For large σ, $\eta_{\max}\simeq 1-2/\sigma$.

From the point of view of efficiency, all drivers can be ranked in quality simply by calculating $\eta_{\max}$. The maximum efficiency depends only on the parameters Bl, R_e, and R_m. For this reason, it is useful to conceptually separate the piston and the suspension stiffness from the motive parts of the driver. The magnet and voice coil together form a linear electrical motor that is functionally separate from the piston. Although it is possible to connect any particular ''motor'' to any area of piston or suspension spring, it is actually only the *motor* that has a potential efficiency $\eta_{\max}$, independent of the rest of the device. To attain this maximum efficiency, the motor must work into the particular mechanical load R_η, which also depends only on the ''motor parameters'' Bl, R_e, and R_m.

Any acoustic load can be converted into the optimally efficient mechanical load for a particular driver motor by using the optimum piston area S_η given by

$$S_\eta=\sqrt{\frac{R_\eta}{\mathrm{Re}[\zeta_a]}}=\sqrt{\frac{\sigma R_m}{\mathrm{Re}[\zeta_a]}}. \tag{13}$$

While the driver may be said to be a ''high-impedance'' or ''low-impedance'' device depending on the acoustic load, it is important to remember that the thing which is ''high'' or ''low'' is the *acoustic* impedance at the piston face, which

TABLE I. Motor parameters for various drivers that have been used by thermoacoustics researchers. The first three are ''off-the-shelf'' loudspeakers. The STAR and SETAC drivers are custom designed and built moving-coil devices. The last three drivers are moving-magnet devices designed for single-frequency transduction at high efficiency and power.

Driver	Bl [N/A]	R_e [Ω]	R_m [kg/s]	σ	$\eta_{\max}$ [%]	Π_{electric} [W]
MW-142[a]	7.5	5.1	1.9	2.6	44	150
JBL 2206H[b]	18.1	5.3	9.5	2.7	47	300
Altec 290-16 K[c]	21.5	10.6	2.8	4.1	61	10
STAR[d]	15.3	8.2	1.8	4.1	61	20
SETAC[e]	18	1.7	2.2	9.4	81	200
B-300[f]	8.0	0.05	15	9.3	81	300
C-2[f]	41	0.24	48	12	85	2000
C-10[f]	85	0.52	80	13	86	10 000

[a]Morel Acoustics USA, Inc., 414 Harvard St, Brookline, MA 02446-2902. The numbers listed in the table are the measured values of a particular driver used at this lab.
[b]See Ref. 1.
[c]See Ref. 10.
[d]See Ref. 11.
[e]See Ref. 12.
[f]See Ref. 13.

depends on the piston area. The motor, by contrast, works most efficiently only at a single *mechanical* impedance, namely R_η, which is independent of S.

One of the most important consequences of this fact concerns the required piston excursion. The power provided to the acoustic load is $\Pi_a = |u_a|^2 R_a/2$, where u_a is the peak velocity of the piston. Since the value of R_a is fixed at R_η by the requirements of motor efficiency, the power requirement of the device dictates the piston velocity. Since a particular thermoacoustic device will also have a set operating frequency, the power of the device is directly linked to the piston stroke $d = 2u_a/\omega$. For a given frequency and power, an efficiently configured driver with a particular motor will have to have a certain fixed stroke, regardless of piston area and placement. If the driver is placed at a pressure node, the piston area will be large and the *volume velocity* will be large; the piston's linear velocity, however, is fixed by efficiency considerations. Assuming that optimum efficiency is a requirement, placing the same motor at the pressure antinode will necessitate the use of a smaller piston, but *cannot* reduce the required piston excursion. This contradicts the idea that piston excursion can be controlled by placing the driver at a pressure antinode, an idea that is found in some of the classic papers that are the primary references for the study of thermoacoustic engines. For example, Swift's article in the *Encyclopedia of Applied Physics*[6] states that ''...the loudspeaker-like driver was located at a pressure antinode of the standing wave, so that the acoustic power was delivered with high force and small displacement, easing engineering difficulties associated with the flexing portion of the driver.'' However, the electroacoustic efficiency was then maximized by making the piston area small, thereby increasing the displacement. The analysis presented here shows that the resulting displacement of maximum efficiency is the same regardless of the placement of the driver within the standing wave.

Table I lists motor parameters and maximum efficiencies and powers for some drivers that have been used by thermoacoustic researchers.

B. Adjusting R_a for maximum power

At maximum current, the acoustic power $\Pi_a(I_{\max})$ is maximized when $(R_a)_{\Pi_{\max}} \equiv R_\Pi = R_m$. This corresponds to a best piston area of $S_\Pi = \sqrt{R_m/\mathrm{Re}[\zeta_a]}$. Thus the best mechanical load for maximum (current limited) acoustic power is smaller than that for best efficiency by a factor of σ, and S_Π is smaller than S_η by a factor of $\sqrt{\sigma}$. For such a small piston, the driver may reach its stroke limit before it reaches its current limit. The important point is that piston sizes *smaller* than S_η can increase acoustic power output.

This provides another way to think about the earlier case of maximum efficiency. There are two loss mechanisms in the driver: electrical loss in the voice coil $\Pi_e = |I|^2 R_e/2$, and mechanical loss in the suspension $\Pi_m = |u_a|^2 R_m/2$. The piston area that minimizes the sum of these losses, $\Pi_m + \Pi_e$, gives maximum efficiency. For a fixed acoustic power, the mechanical loss can always be reduced by increasing piston area and thereby decreasing the necessary velocity; however, I is minimized for $S = S_\Pi < S_\eta$, so any increase of the piston area from S_η increases the electrical loss.

The main result for thermoacoustic applications is that trade-offs can be made between stroke, power, and efficiency. At fixed frequency and maximum current, reducing piston area from the most efficient value of S_η in order to increase acoustic power will not only degrade efficiency—it will necessarily increase the piston stroke as well, placing further demands on the suspension. On the other hand, using $S > S_\eta$ will result in decreased stroke, but also decreased efficiency and decreased maximum power delivery. The ways in which efficiency, acoustic power, and stroke depend on S (for fixed current and frequency) are shown in Fig. 5. The plot shows results of calculations for a particular high-efficiency driver designed for a thermoacoustic application, with $\sigma = 9.1$ and $\eta_{\max} = 80\%$ (the SETAC diver from Table I). The exact shapes of the curves depend on σ. The rapid increase in stroke as S is decreased from S_η means that limits on the stroke could make it impossible to reach S_Π, even if

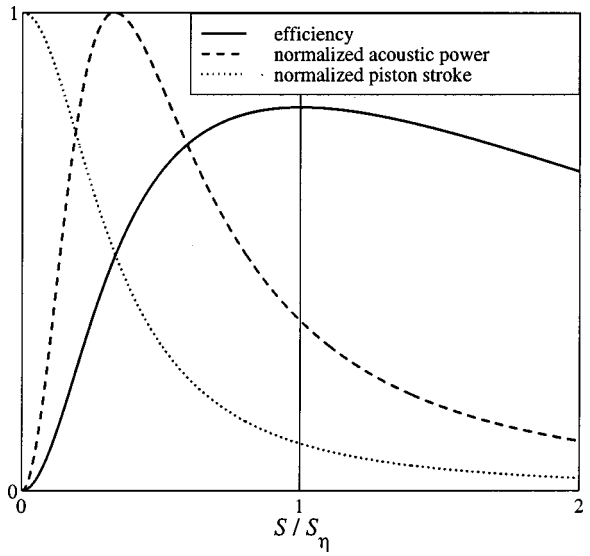

FIG. 5. Dependences of efficiency, acoustic power, and stroke as functions of piston area at a single frequency and current for the SETAC diver (see Table I), a high-efficiency driver designed for thermoacoustic refrigeration.

that were desired. In this case, adding a stroke-limit line to a plot such as Fig. 5 will give the absolute maximum power for the driver and the load required to attain it, and will show the penalty in efficiency from $\eta_{\max}$.

IV. OPTIMIZING R_a BY ADJUSTING OPERATING FREQUENCY

The foregoing discussion assumes that one can select the area of the piston. What if one wishes to use a driver ''off-the-shelf,'' in which case the piston area is already determined? Is it still possible to achieve optimum efficiency? Provided that the piston area is within a certain range, this can be done by adjusting the operating frequency of the device.

A. Selection of operating frequency for fixed piston area

In general, the piston area of optimum efficiency $S_\eta = \sqrt{R_\eta / \mathrm{Re}[\zeta_a]}$ is a function of frequency because the acoustic resistance $\mathrm{Re}[\zeta_a]$ is a function of frequency. As an example, consider a resonator consisting of a simple cylinder. The real and imaginary parts of the acoustic impedance[7] are shown in Figs. 6(a) and (b).

The dotted cursor lines show the lowest two frequencies for which ζ_a is purely real, ω_r (resonance) and ω_a (antiresonance). Near these frequencies the most efficient piston area S_η, shown in Fig. 6(c), takes on its smallest and largest values. If the piston area S is between these two values, then optimum efficiency can be achieved by operating at a frequency where $\mathrm{Re}[\zeta_a(\omega)] = S^2 R_\eta$. This design procedure assumes knowledge of the shape of the resistance curve for the resonator in question. This could be obtained with a measurement, or by modeling using a computer program such as DELTAE.[8]

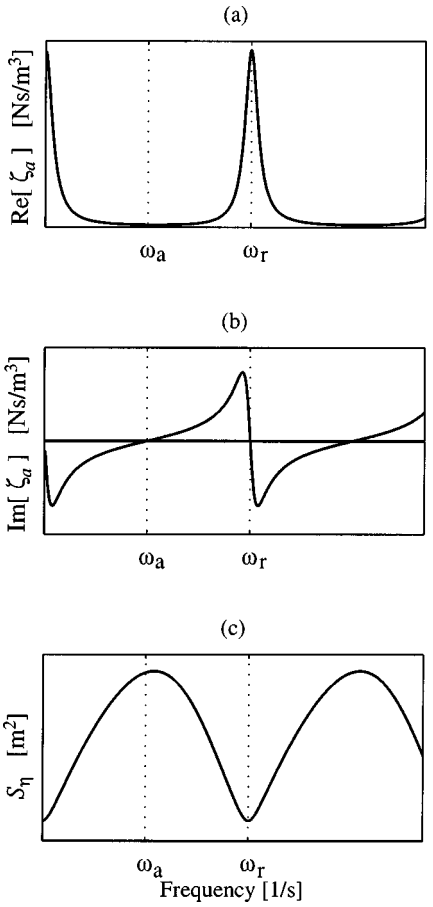

FIG. 6. The real. (a) and imaginary (b) parts of the acoustic impedance of a resonator. These particular curves are for a cylinder. Part (c) shows the optimum piston area S_η as a function of frequency.

B. Effect of operating frequency on required suspension stiffness

For a particular S, the acoustic resistance takes on the most efficient value at more than one frequency. Consider, for example, a driver with a piston that is slightly larger than $S_{\eta\,\min} = S_\eta(\omega_r)$; the designer must decide on an operating frequency either just above or just below ω_r. The two options have different consequences for the suspension.

Recall that efficient operation requires that $X = X_m + X_a = 0$. The mechanical reactance is $X_m = \omega M_m - k_m/\omega$, so the required driver suspension stiffness is

$$k_m = \omega^2 M_m + \omega X_a = \omega^2 M_m + \omega S^2 \,\mathrm{Im}[\zeta_a]. \tag{14}$$

The $\omega^2 M_m$ term means that k_m tends to increase with increasing frequency. Just above ω_r, however, $\mathrm{Im}[\zeta_a]$ is negative, so in some circumstances the required suspension stiffness may actually be *less* just above ω_r than just below it. Whether or not this occurs depends on the details of the resonator impedance curves. Maximum efficiency requires both $X = 0$, as expressed in Eq. (14), and $S^2 = R_\eta / \mathrm{Re}[\zeta_a]$. Combining these expressions gives

$$k_m = \omega^2 M_m + \omega R_n \frac{\mathrm{Im}[\zeta_a(\omega)]}{\mathrm{Re}[\zeta_a(\omega)]}. \tag{15}$$

Two example curves are plotted in Fig. 7. The lighter curves are for a very heavily damped resonator ($Q = 5$), for which

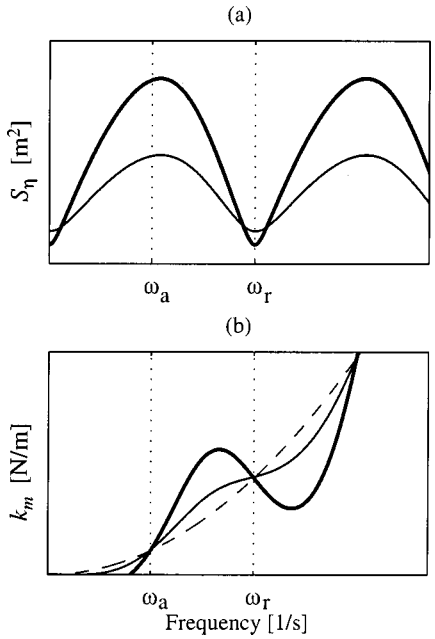

FIG. 7. Curves of optimum piston area (a) and the total spring constant needed to make the total impedance purely real (b). The lighter curves are for a highly damped resonator ($Q=5$), the heavier curves for a resonator with less damping ($Q=15$). The dashed curve in part (b) is the limiting value $k_m=M_m\omega^2$.

higher frequency always results in a need for higher k_m. The heavy curves are for a resonator typical of thermoacoustic refrigeration applications ($Q=15$). In this case, moving above ω_r results in enough resonator stiffness to decrease the demands on the mechanical spring k_m.

V. OTHER CONSIDERATIONS

This paper has examined only a few of the issues involved in using electrodynamic drivers in thermoacousitc refrigerators. There are others. For example, Ward has developed a method to minimize the pressure difference across the piston.[1] In a highly pressurized device with large pressure amplitudes, this pressure difference becomes a serious concern. Preliminary measurements made at this lab[9] provide some experimental support for the conclusions of this paper concerning attainability of maximum electroacoustic efficiency.

ACKNOWLEDGMENTS

Thanks to my advisor during this work, Steve Garrett. Thanks to George Mozurkewich for helpful conversations about efficiency, and Robert Keolian for many important corrections and improvements. Thanks to Matt Poese for measurements of the Morel Driver. This work was supported by the National Science Foundation and the Office of Naval Research.

[1] W. C. Ward, ''Cost-effective electrodynamic drivers with improved efficiency for thermoacoustic refrigerators,'' J. Acoust. Soc. Am. **100**, 2847(A) (1996).

[2] F. V. Hunt, *Electroacoustics: The Analysis of Transduction, and its Historical Background* (Acoustical Society of America, New York, 1982). (Original work published by Wiley, New York, 1954.) This is ''Case I'' on p. 140.

[3] L. L. Beranek, *Acoustics* (Acoustical Society of America, New York, 1986). (Original work published by McGraw-Hill, New York, 1954.) See, for example, Fig. 3.43.

[4] This is equivalent to expressions in Ref. 2 such as Eqs. (4.15) and (4.20) for the case where the force factor is purely real.

[5] Equivalent to Ref. 2, Eq. (4.30) for the case where the force factor is purely real.

[6] G. W. Swift, ''Thermoacoustic engines and refrigerators,'' in *Encyclopedia of Applied Physics* (Wiley-VCH, New York, 1997), Vol. 21, Section 5.3, p. 256.

[7] L. E. Kinsler, A. R. Frey, A. B. Coppens, and J. V. Sanders, *Fundamentals of Acoustics*, 3rd ed. (Wiley, New York, 1982), Sec. 9.5.

[8] W. C. Ward and G. L. Swift, ''Design environment for low amplitude thermoacoustic engines,'' J. Acoust. Soc. Am. **95**, 3671–3672 (1994); DELTAE is available at http://www.lanl.gov/thermoacoustics/ or contact Bill Ward at ww@lanl.gov

[9] R. W. M. Smith, R. M. Keolian, S. L. Garrett, and J. A. Corey, ''High-efficiency 2-kW thermoacoustic driver,'' J. Acoust. Soc. Am. **105**, 1072(A) (1999).

[10] M. Fitzpatrick, ''Electrodynamic driver for the Space Thermoacoustic Refrigerator (STAR),'' M.S. thesis, Physics Department, Naval Postgraduate School, 1988, DTIC Report No. ADA 192337, p. 80.

[11] D. A. Harris and R. E. Volkert, ''Design and calibration of an electrodynamic driver for the Space Thermoacoustic Refrigerator,'' M.S. thesis, Physics Department, Naval Postgraduate School, 1989, DTIC Report No. ADA 212022, pp. 30–42; S. L. Garrett, J. A. Adeff, and T. J. Hofler, ''Thermoacoustic refrigerator for space applications,'' AIAA J. Thermophys Heat Trans. **7**, 595–599 (1993).

[12] S. C. Ballister and D. J. McKelvey, ''Shipboard electronics thermoacoustic cooler,'' M.S. thesis, Physics Department, Naval Postgraduate School, 1995, DTIC Report No. ADA 300514, p. 17; S. L. Garrett, U.S. Patent No. 5,647,216, July 15, 1997.

[13] J. A. Corey and G. A. Yarr, ''HOTS to WATTS: The FPSE linear alternator system re-invented,'' in *Proceedings of the 27th Intersociety Energy Conversion Engineering Conference* (Society of Automotive Engineers, Warrendale, PA, 1992), pp. 5.289–5.294; U.S. Patent No. 5,389,844 (Feb. 14, 1995); CFIC, Inc./Resonant Power Group, 302 Tenth St., Troy, NY 12180.

Acoustical performance of an electrostrictive polymer film loudspeaker

Richard Heydt, Ron Pelrine, Jose Joseph, Joseph Eckerle, and Roy Kornbluh
SRI International, 333 Ravenswood Avenue, Menlo Park, California 94025

(Received 26 December 1998; accepted for publication 19 October 1999)

A new type of loudspeaker that generates sound by means of the electrostrictive response of a thin polymer film is described. Electrostrictive polymer film (EPF) loudspeakers are constructed with inexpensive, lightweight materials and have a very low profile. The films are typically silicone and are coated with compliant electrodes to allow large film deformations. Acoustical frequency response measurements from 5×5 cm (planar dimensions) prototype EPF loudspeakers are presented. Measurements of harmonic distortion are also shown, along with results demonstrating reduced harmonic distortion achieved with square-root wave shaping. Applications of EPF loudspeakers include active noise control and general-purpose flat-panel loudspeakers. © *2000 Acoustical Society of America.* [S0001-4966(00)00502-6]

PACS numbers: 43.38.Ja, 43.58.Vb [SLE]

INTRODUCTION

This paper discusses measurements of the sound produced by electrostrictive polymer film (EPF) loudspeakers. The goal of the work was to develop a lightweight loudspeaker that can be made essentially flat or can be contoured to a surface. The speaker may be useful for general audio applications in which a low profile is important. It may also have application to active noise control, where many systems require compact, lightweight sound sources. A previous paper[1] introduced the EPF loudspeaker and presented some modeling and preliminary test results. The present paper builds on the earlier work and discusses recent results.

In this paper, the term electrostriction is used to mean the stress and strain response of a material to an electric field. Polymer-film electrostriction has been investigated for use in ''artificial muscle'' actuators for robots, manipulators, unmanned vehicles, and other applications. These actuators produce thickness strains of up to 0.30 and actuation pressures of up to 1.9 MPa.[2] An acoustical actuator based on electrostriction of a polymer film was developed by Scheinbeim *et al.*[3] In Scheinbeim's actuator, sound is generated by a change in thickness of a film, or stack of films, caused by electrostriction. The EPF loudspeaker also operates by varying the thickness strain of the film. In contrast to Scheinbeim's device, however, the EPF loudspeaker generates sound by using out-of-plane film deformation resulting from the thickness strain. Because large out-of-plane film motions are possible, the EPF loudspeaker can produce significant sound power.

I. PRINCIPLE AND OPERATION OF THE EPF LOUDSPEAKER

Figure 1 illustrates the actuation of an EPF element. A polymer film is sandwiched between compliant electrodes and is squeezed by electrostatic forces when voltage is applied. The film thickness strain is equal (to a linear, first-order approximation) to the force per unit area of the film divided by the elastic modulus of the polymer,

$$s=\frac{\varepsilon_r\varepsilon_0E^2}{Y}=\frac{\varepsilon_r\varepsilon_0v^2}{h^2Y}, \tag{1}$$

where s is the strain in thickness, Y is the polymer-film elastic modulus, E is the electric field strength, ε_r is the relative dielectric constant of the polymer, ε_0 is the dielectric constant of free space, h is the film thickness, and v is the applied voltage. It is important to point out that the squeezing force in Eq. (1) assumes compliant electrodes.[4] These, along with a relatively high film dielectric constant, are important to achieving large strains. Figure 2 shows measured and predicted data for the thickness strain of a silicone film ($\varepsilon_r=2.8-3.0$) as a function of applied electric field strength.

Figure 3 is a schematic view of the EPF actuator, which shows a film with electrodes on top of a dense grid of holes. The closed plenum volume below the grid is at a slight negative pressure (alternatively, it could be slightly positive). The film thickness decreases when voltage is applied, and since the polymer is incompressible (Poisson ratio approximately 0.5), the film area increases. The plenum pressure causes the film ''bubble'' elements to deform uniformly downward, and the volume acceleration of the air resulting from film-element oscillations generates sound. In the future it may be possible to eliminate the differential static pressure across the film by mechanically biasing the film.

The EPF loudspeaker has a number of attractive features. With large film thickness strains, it is possible to obtain large volumetric displacements and correspondingly high radiated sound pressures from a very compact actuator. Plenum depth influences the acoustical output, but the plenum can be quite shallow (a few millimeters deep) and the speaker essentially flat. Furthermore, the design of Fig. 3 allows small- or large-area loudspeakers (the difference being the number of film elements) to be fabricated from the same set of processing steps. The layered structure of the EPF loudspeaker implies that it can eventually be built with batch processing methods.

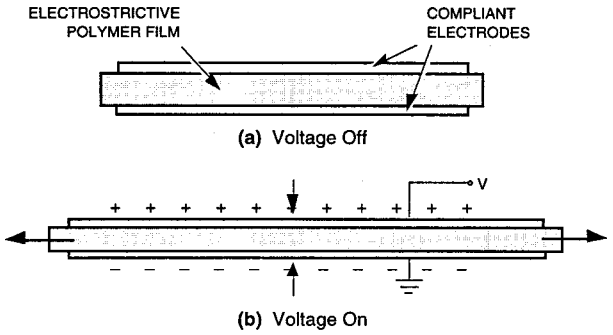

FIG. 1. Principle of electrostrictive-polymer film actuation.

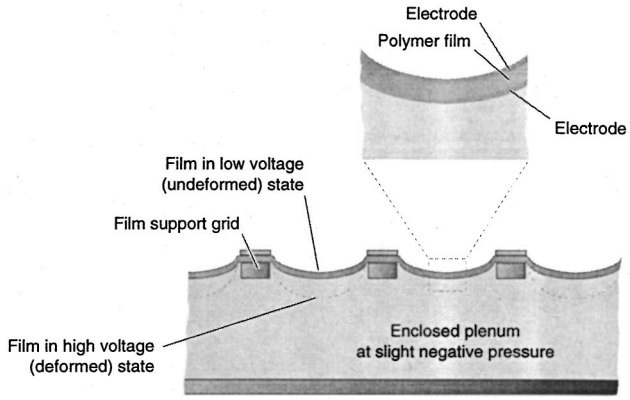

FIG. 3. Cross-sectional view of the electrostrictive-polymer-film loudspeaker, showing the design approach for obtaining out-of-plane displacement.

II. COMPARISON OF EPF WITH OTHER LOUDSPEAKER TECHNOLOGIES

A. Electrostatic loudspeakers

There are similarities and important differences between EPF loudspeakers and more familiar electrostatic loudspeakers. In an electrostatic loudspeaker, a thin, lightweight diaphragm is separated from a stationary, conducting electrode by a narrow air gap. ''Push–pull'' electrostatic loudspeakers (Fig. 4) have electrodes on both sides of the diaphragm. The diaphragm is a strong polymer (such as Mylar) with a thickness of 5 to 50 micrometers, and is held in tension on a rigid frame. The air gap spacing is on the order of a few millimeters. The diaphragm oscillates and radiates sound when a direct current (d.c.) bias voltage and alternating current (a.c.) drive voltage are applied between the diaphragm and stationary electrode. The applied d.c. bias is typically several thousand volts, and the a.c. voltage amplitude can be comparable.

Both electrostatic and EPF loudspeakers can produce high sound pressures by means of large diaphragm displacements, but the driving force on the film is greater in an EPF loudspeaker. One reason for this difference is that the relative dielectric constant equals one for the air gap of an electrostatic actuator, while it is always greater than one for a polymer film. A second reason is that the conversion of field energy to mechanical work occurs principally by narrowing the air gap in a rigid-electrode electrostatic actuator. In an EPF actuator with compliant electrodes, field energy is converted to work through narrowing or thinning of the film (thickness strain) and also by stretching the film (area increase). This results in a higher force per unit area than in a rigid-electrode electrostatic actuator of the same area.[4]

Electrostrictive polymer films can be driven at much higher electric field strengths than are possible with electrostatic loudspeakers. An air gap of a few millimeters in an electrostatic loudspeaker will break down at a field strength of about 3 V/μm. In comparison, the films of EPF loudspeakers are routinely driven at 20 V/μm and higher, and these field strengths result in large film displacements.

Another difference relates to applied voltage and gap width. When the diaphragm of an electrostatic actuator reaches a threshold displacement it becomes unstable and attaches itself to the stationary electrode. To get large diaphragm displacements without instability, the gap width and the applied voltage must be increased simultaneously. In other words, high sound pressures require large air gaps and large voltages. In contrast, there is no instability associated with film *displacement* in the EPF actuator. It is theoretically possible for an instability in film thickness strain to occur if the strain becomes very large. A model for the simplest case predicts instability at thickness strains larger than 0.33,[5] but this model ignores various effects that tend to increase the threshold, such as an increasing elastic modulus as film strain increases. Maximum thickness strains of 0.4 to 0.6 (depending on the specific film material) have been measured in the laboratory.

Finally, it is important to point out that since film thickness strain is related to applied electric field strength, it is

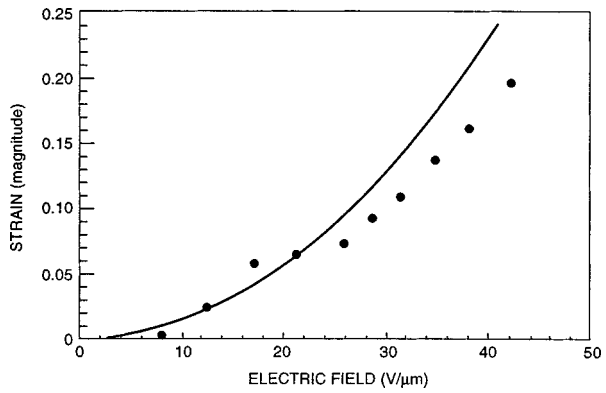

FIG. 2. Experimentally measured (points) and theoretically predicted (solid line) strain response of a silicone polymer.

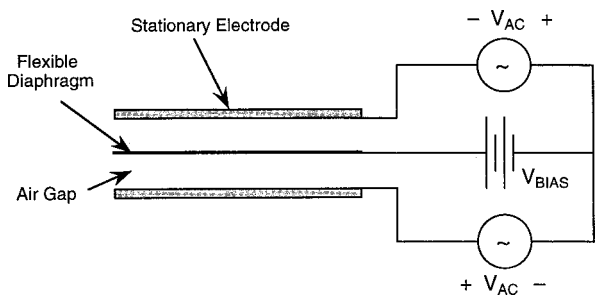

FIG. 4. Schematic drawing of a double-sided, or push–pull, electrostatic loudspeaker.

possible to produce the same thickness strain at lower voltage by reducing film thickness. This suggests the possibility of EPF loudspeakers operating at much lower voltages than are possible with electrostatic loudspeakers.

B. Electret transducers

An electret is a dielectric material with a permanent electrical polarization. Electrets used in electroacoustic applications may be permanently charged organic polymers, such as Teflon, or inorganic dielectrics, such as silicon dioxide. One of the first, and still most common, applications is the electret microphone, made practical in the 1960s by Sessler and West,[6] who used thin (25-μm) films of Teflon, metallized on one side. The diaphragms in more recent electret microphones are typically micromachined silicon.[7] Electrets have also been used as electroacoustic speakers, such as in earphones.[8] A significant advantage of electret microphones and speakers is that they require no external d.c. bias, although they often do not have the long-term stability of devices that operate with an external d.c. bias.

A basic similarity between EPF and electret transducers is that an electric field is applied across a dielectric film or diaphragm and the output is related to motion of the diaphragm. An obvious difference is that the EPF film is not permanently charged. A more important difference is that both electrodes of the EPF diaphragm are directly attached to the film, and the film is squeezed by the applied electric field. In contrast, for a typical electret transducer, one electrode is a metallized layer on one face of the diaphragm and the other is a stationary back plate. An electret loudspeaker is therefore more like an electrostatic loudspeaker, having both a stationary electrode and an air gap, than like an EPF actuator (which has neither). An electret loudspeaker has similar limitations on diaphragm motion as those of an electrostatic loudspeaker; the diaphragm will collapse into the back plate if threshold voltages and displacement amplitudes are exceeded.

III. EPF LOUDSPEAKER DESIGN

EPF loudspeakers are a new technology and a number of issues relating to design, fabrication, and performance are being investigated. This section describes the ''baseline'' EPF loudspeaker design and current methods of fabrication. In subsequent sections, recent experimental performance results for acoustical frequency response and harmonic distortion are presented.

Figure 5 is a schematic of the baseline speaker design. The films of most of the prototype EPF loudspeakers were made from Dow Corning HS3 silicone, a relatively soft polydimethyl siloxane (PDMS)-based silicone with an elastic modulus of 0.1 MPa. Other silicone elastomers of lower and higher modulus have been tested, but HS3, which has maximum elongations of over 300% and very good tear resistance, has given the best results to date. The films are spin-coated onto a wafer and released. Film thicknesses have ranged from 50 to 150 μm, with most being about 100 μm.

Compliant electrodes are a critical feature of EPF speakers. The electrodes must be sufficiently compliant to keep the film from being too stiff (which would lower strain), while remaining conductive enough at audible frequencies to distribute charge uniformly across the film. Electrodes consisting of graphite powder in a gelatin-glycerol-salt binder meet these requirements and are also convenient to fabricate. Graphite powder is first spread on the film. The binder is mixed as a solution of 50% isopropyl alcohol and 50% gelatin–water solution. Alcohol is added to enhance wetting of the graphite, along with glycerol (1 ml) to prevent drying, and salt (0.1 mg NaCl per 20 ml gelatin) to increase conductivity. The graphite layer is covered with approximately 0.039 ml of binder solution per square centimeter of electrode surface.

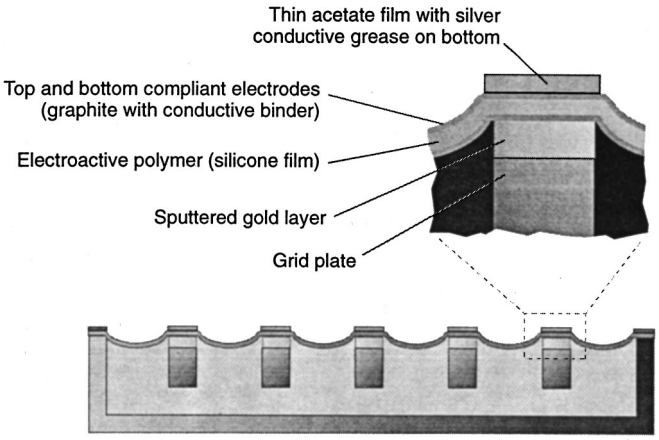

FIG. 5. Film and electrode layers in the baseline EPF loudspeaker design.

Loudspeaker acoustical performance will be degraded if the electrodes are not sufficiently conductive at the frequencies of interest. A sputtered gold layer on the grid below the film and conductive silver grease on top of the film (Fig. 5) act as charge-distribution layers. These layers lower the electrode resistance, which in turn lowers the exponential time constant (product of resistance and capacitance) governing the speed with which the film responds to applied voltage. The topmost layer is a flexible acetate film (25 to 100 μm in thickness) with holes matching the grid-plate pattern.

Figure 6 is a photograph of an EPF loudspeaker prototype. This speaker has an active area of 5×5 cm, with an array of 72 circular film elements, each 5.5 mm in diameter. The film thickness is 83 μm.

IV. LOUDSPEAKER PERFORMANCE

The acoustical output from an EPF loudspeaker is affected by several design parameters (Fig. 7), including the film-element (''bubble'') diameter, the total actuator area, the plenum depth, and the film prestrain. Operational parameters that affect output are the applied voltage across the film and the pressure in the plenum beneath the film.

As with electrostatic loudspeakers, EPF loudspeakers are driven with a d.c. bias voltage and an a.c. signal voltage. For driving a typical 100-μm film, d.c. bias voltages range from 1000 to 1500 V, and a.c. voltage zero-to-peak amplitudes are in the range from 100 to 600 V. Since film strain depends on electric field strength rather than voltage, thinner

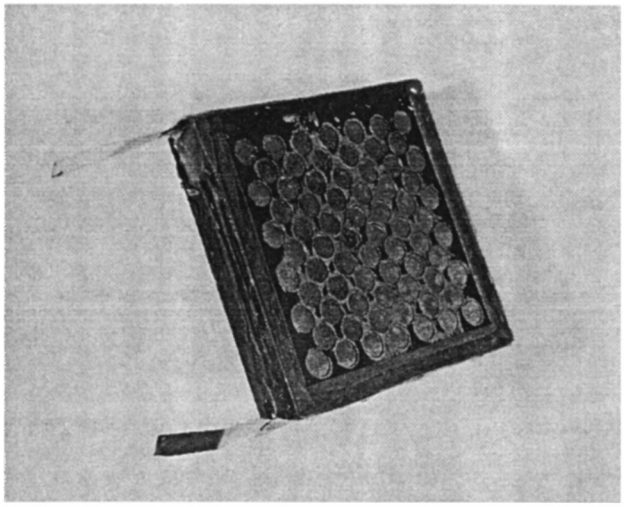

FIG. 6. Photograph of prototype EPF loudspeaker. The active surface area is 5×5 cm and the sound-radiating film elements are 5.5 mm in diameter. The depth of the plenum beneath the film is 5 mm. Film thickness is 83 μm.

films require lower voltages to generate the same acoustical output.

Figure 8 shows a measured spectrum of sound pressure level (SPL) produced by a loudspeaker similar to that of Fig. 6. The measurements were performed in a $3\times4\times9$ m anechoic chamber. A microphone was located 1 meter from the speaker along the centerline axis. The speaker was driven with a swept sine wave and the response was measured on a HP 35670 A dynamic signal analyzer. The Fig. 8 response is typical of the speakers tested. The SPL rises at a rate of approximately 18 dB per octave to a primary resonance, the frequency of which is determined by the film tension and the effective air load mass on the film bubble elements.[9] A null, or antiresonance, typically follows the primary resonance. The sharpness of the resonance and the depth of the antiresonance are affected by film and electrode materials and thickness, plenum pressure, and any added acoustical damping. The film-element oscillation at frequencies less than the resonance frequency is unimodal. The film oscillation at frequencies above resonance, which may feature higher-order vibrational modes, has not yet been measured. From the standpoint of loudspeaker design, it is noteworthy in Fig. 8 that the response was essentially flat up to at least 20 kHz. Off-axis SPL measurements have not been made to date.

Figure 9 shows the spectrum between 100 Hz and 5 kHz of the SPL produced on-axis at a distance of 1 m by a 5 $\times$5 cm loudspeaker. The response of the speaker was measured at ten applied voltages. The two response spectra in the

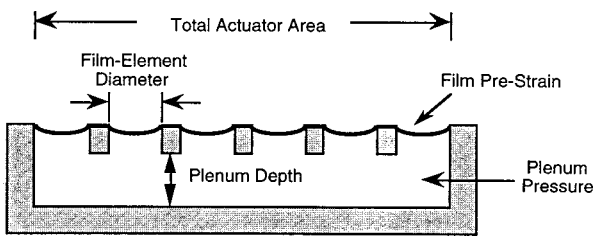

FIG. 7. Cross section of the EPF loudspeaker, showing the important design and operational parameters.

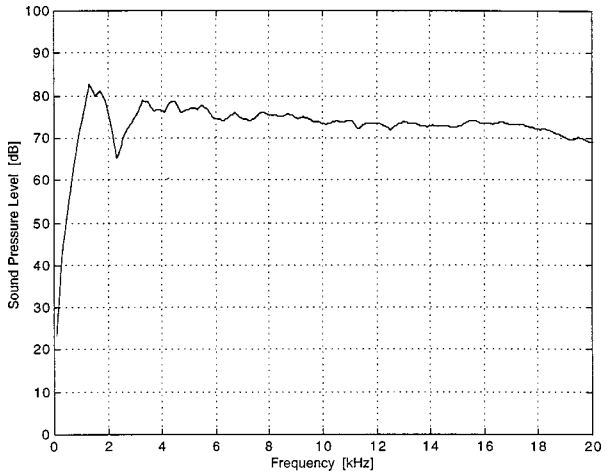

FIG. 8. Measured frequency response spectrum of an EPF loudspeaker. The sound pressure level is in decibels relative to 20 μPa and was measured at 1 meter along the principal axis.

figure correspond to the lowest (1000 V bias, 200 V a.c.) and highest voltages (1500 V bias, 600 V a.c.) used. The film thickness at zero voltage was 83 μm, which meant that a lower bound on the maximum field applied across the film was 25 V/μm. At the highest voltage, the SPL at 1 m was greater than 80 dB *re* 20 μPa at frequencies above resonance, and was 50 dB or more at frequencies above 390 Hz. Figure 9 represents the highest sound pressure level measured to date. However, it is estimated that the silicone film could have been driven at 2500 volts (total d.c. plus a.c.) without breakdown, with the speaker generating 3 to 5 dB greater SPL at each frequency.

These results show that moderately high sound pressure levels can be generated from EPF speakers of compact size. The plenum depth of the speaker in Fig. 9 was only 5 mm. Speakers with plenums of 5 and 20 mm have been tested. In general, the acoustic output was less with a smaller plenum depth, because the effective stiffness of the air enclosed within the plenum is greater. However, speaker plenum

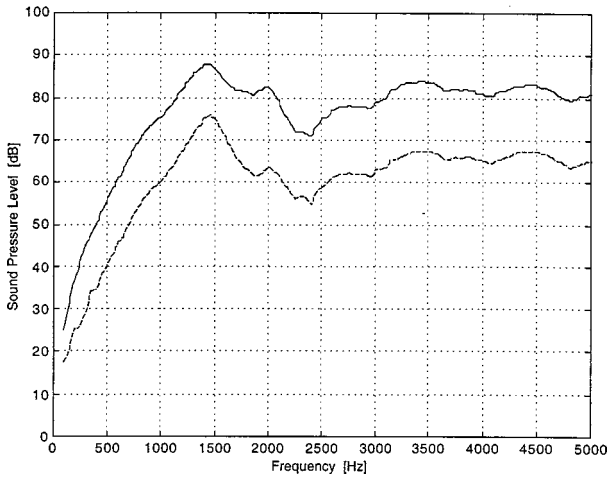

FIG. 9. Sound pressure levels *re* 20 μPa measured at 1 meter along the principal axis for a 5$\times$5 cm EPF loudspeaker: 1000 V bias, 200 V a.c. (lower curve), 1500 V bias, 600 V a.c. (upper curve). The silicone film was 83 μm in thickness and had 10% prestrain. Film elements were 5.5 mm in diameter, and plenum depth was 5 mm.

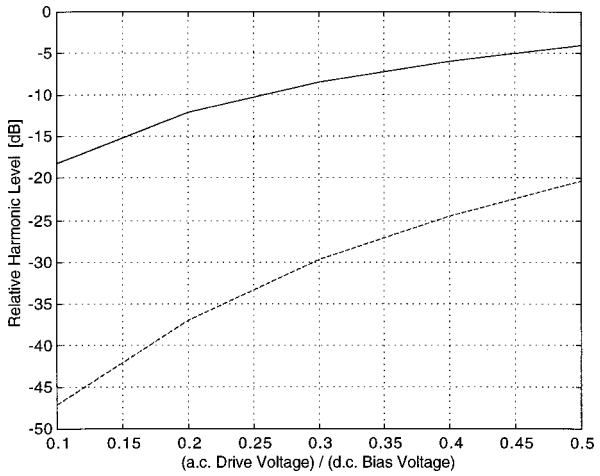

FIG. 10. Model prediction of second (solid line) and third (dashed line) harmonic levels as functions of the a.c.-to-d.c. voltage ratio. Harmonic level is expressed in decibels relative to the fundamental on-axis mean-square sound pressure at 1 m. The model assumed that the bias is 1500 V and that the film ''bubble'' elements have a height equal to one-fourth of the base diameter.

depths even less than 5 mm are feasible, if low-frequency performance is not critical.

The most important design parameter is the size of the radiating film elements. The diameter of the film elements for the Fig. 9 actuator was 5.5 mm. Larger film elements radiate more sound per unit area, so to increase the SPL from an EPF speaker of given overall size, one uses larger diameter film elements (assuming comparable area coverage is possible). Most of our work to date has involved 5.5-mm-diameter elements because good reliability and fabrication yield were achieved at this element size. However, loudspeakers with element diameters ranging from 1.5 to 25 mm have been fabricated. The primary resonance frequency drops as film-element diameter increases. Conversely, the resonance frequency increases with increasing film tension (the film of the loudspeaker of Fig. 9 was prestrained by 10%).

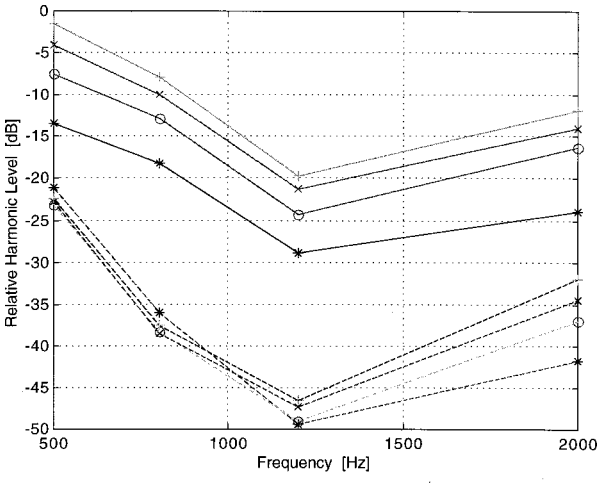

FIG. 11. Measured relative harmonic levels of an EPF loudspeaker with 5.5 mm film elements: second harmonic (solid lines), third harmonic (dashed lines). Harmonic levels are shown for four ratios of a.c.-drive-to-d.c.-bias voltage: 0.1 (*), 0.2 (○), 0.3 (×), 0.4 (+).

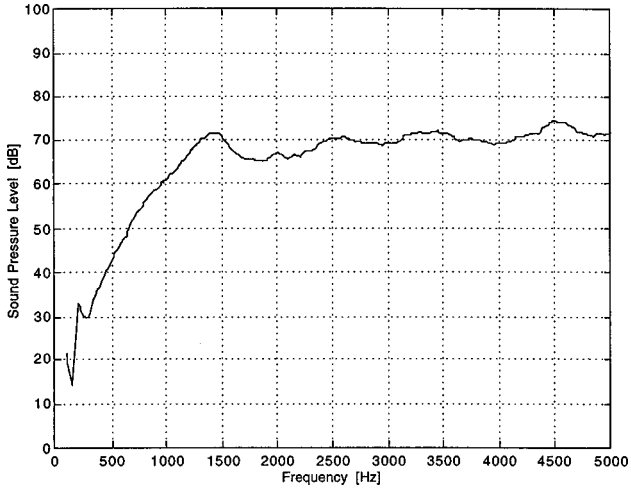

FIG. 12. Frequency response spectrum of the EPF loudspeaker corresponding to the relative harmonic distortion shown in Fig. 11. Applied voltage: 1400 V bias, 420 V a.c. Loudspeaker area is 2.5×2.5 cm. The SPL *re* 20 μPa was measured at 1 meter along the principal axis.

V. HARMONIC DISTORTION

The sound pressure radiated by a film bubble element is proportional to the volume acceleration of air caused by element expansion and contraction. Harmonics in the sound pressure are unavoidable even if each element of the loudspeaker deforms ''perfectly'' when voltage is applied. This is because the thickness strain of the film varies as the square of applied voltage (Fig. 2), which introduces second-order harmonics in the voltage–strain relationship, and because there is a nonlinear relationship between film thickness strain and film-element volume.

Figure 10 is an analytical prediction of harmonic distortion in the mean-square sound pressure produced by a sinusoidally excited electrostrictive-polymer film element. The model (described in Ref. 1) predicts the sound pressure radiated by a film element as a function of applied voltage and geometric parameters, including film thickness and film-element base diameter and height. The model assumes that the film maintains its basic shape (a spherical section) as it expands and contracts, and ignores dynamic effects such as resonance or modal behavior. Figure 10 shows that both second and third harmonics of the sound pressure signal increase as the a.c. drive voltage amplitude increases (they also increase with increasing d.c. bias). However, second harmonics dominate the distortion.

Figure 11 shows typical measured harmonic distortion levels for an EPF loudspeaker. The silicone film was 91-μm thick and the loudspeaker had 18 identical film elements 5.5 mm in diameter. Measurements were made at four frequen-

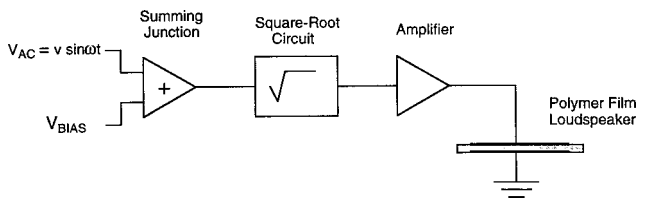

FIG. 13. Simplified schematic illustrating the approach for driving the loudspeaker with a square-root waveform.

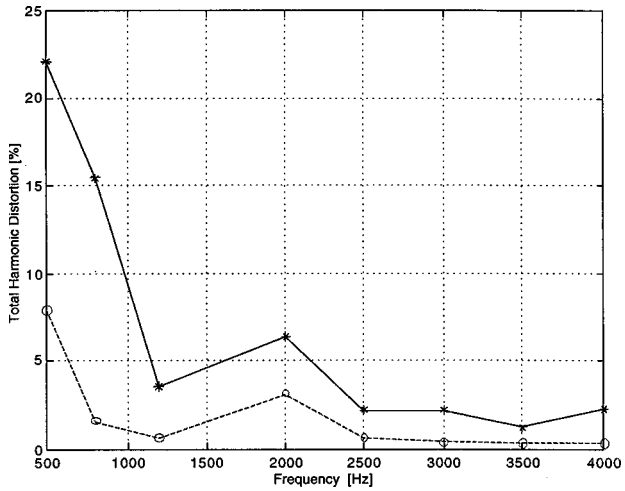

FIG. 14. Effect of square-root wave shaping on total harmonic distortion for a.c.-to-d.c.-bias ratio=0.1. Measurement with standard input (*), measurement with square-root wave shaping (○).

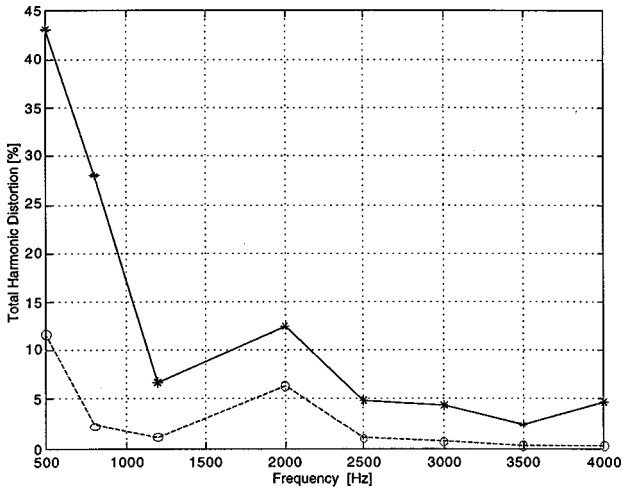

FIG. 15. Effect of square-root wave shaping on total harmonic distortion for a.c.-to-d.c.-bias ratio=0.2. Measurement with standard input (*), measurement with square-root wave shaping (○).

cies and four a.c. drive voltages, using a constant d.c. bias. The relative levels of the second harmonics were large and increased with a.c. voltage, as the analytical model predicts. However, the harmonic content varied strongly with frequency (the model predictions are frequency independent). The frequency dependence in the data can be understood from the shape of the frequency-response curve for this speaker, which is shown in Fig. 12. For fundamental frequencies well below the 1450-Hz resonance, relative harmonic levels were amplified because of the high sensitivity at the harmonic frequencies. In contrast, for fundamental frequencies near resonance and above, the sensitivity at harmonic frequencies was comparable to that at the fundamental.

We have demonstrated two methods by which harmonic distortion in EPF speakers can be reduced. One method is to drive the loudspeaker in a configuration analogous to the push–pull configuration of the electrostatic loudspeaker (Fig. 4). Push–pull operation of an EPF speaker requires drive electronics similar to that of Fig. 4 as well as some relatively simple modifications to the basic actuator geometry of Fig. 3. Push–pull test results are discussed in Ref. 10. A second method is to tailor the shape of the electrical waveform that drives the speaker. The wave shaping approach uses standard, single-actuator drive electronics along with the basic actuator geometry, but requires additional electronic circuitry to shape the waveform. In experiments to date, push–pull and wave shaping approaches have given comparable distortion reduction, although push–pull performance is somewhat better at low frequencies (500 Hz and less). Only the wave shaping test results are presented here.

The wave shaping tests emphasized the use of a square-root waveform; that is, in place of the standard d.c. bias plus a.c. drive input $[B+A\sin(\omega t)]$, the loudspeaker was driven with a signal $[B+A\sin(\omega t)]^{0.5}$. The motivation for this approach is that it compensates for the quadratic nonlinearity in the relation between applied voltage and film thickness strain. The drive-circuit configuration is illustrated schematically in Fig. 13.

Results from the square-root wave shaping tests are shown in Figs. 14 and 15. These figures plot measured total harmonic distortion (t.h.d.) at discrete frequencies between 500 and 4000 Hz, for two cases in which the a.c. amplitude (zero-to-peak) is equal to 10% of the d.c. bias and 20% of the d.c. bias, respectively. The t.h.d. is expressed as a percentage of the root-mean-square amplitude at the fundamental frequency. At 2500 Hz and above, square-root wave shaping reduced t.h.d. to 1% or less. The reductions in t.h.d. below resonance (1450 Hz) are also substantial, considering the initially high levels. Most of the t.h.d. decreases result from lower second harmonics; third harmonics remains about the same or decrease slightly. For these measurements, the t.h.d. with square-root wave shaping was greater than 10% only at 500 Hz for the case of 20% a.c. drive voltage.

VI. CONCLUSIONS

Sound generation has been demonstrated with loudspeakers in which the transduction is based on the electrostrictive response of a thin polymer film. More than 60 prototype EPF loudspeakers have been fabricated and tested. On-axis sound pressure levels of over 80 dB re 20 μPa at 1 meter have been measured in anechoic chamber tests. Two methods for reducing harmonic distortion have also been demonstrated. EPF loudspeakers are compact and lightweight, and are potentially useful in active noise control applications and as general-purpose flat-panel speakers.

[1] R. Heydt, R. Kornbluh, R. Pelrine, and V. Mason, ''Design and performance of an electrostrictive-polymer-film acoustic actuator,'' J. Sound Vib. **215**(2), 297–311 (1998).
[2] R. Kornbluh, R. Pelrine, and J. Joseph, ''Elastomeric dielectric artificial muscle for small robots,'' Proceedings of the Third IASTED International Conference on Robotics and Manufacturing, Cancun, Mexico, June 14–16 (1995).
[3] J. Scheinbeim and B. Newman, ''Electrostrictive Driving Device, Process for Sonic Wave Projection and Polymer Materials for use Therein,'' United States Patent 5,229,979, July 20, 1993.
[4] R. Pelrine, J. Kornbluh, J. Joseph, and S. Chiba, ''Electrostriction of polymer films for microactuators,'' Proceedings of 10th Annual International Workshop on Micro Electro Mechanical Systems (MEMS 97), Nagoya,

Japan, June 26–30, 1997, pp. 238–243.
[5] R. Pelrine, R. Kornbluh, and J. Joseph, ''Electrostriction of polymer dielectrics with compliant electrodes as a means of actuation,'' Sens. Actuators A **64**, 77–85 (1998).
[6] G. M. Sessler and J. E. West, ''Electret transducers: A review,'' J. Acoust. Soc. Am. **53**(6), 1589–1600 (1973).
[7] Q. Zou, Z. Tan, Z. Wang, J. Pang, X. Qian, Q. Zhang, R. Lin, S. Yi, H. Gong, L. Liu, and Z. Li, ''A novel integrated silicon capacitive microphone—floating electrode 'electret' microphone (FEEM),'' J. Microelectromechanical Systems **7**(2), 224–234 (1998).
[8] I. Busch-Vashniac, ''Response of an edge-supported circular membrane electret earphone. Parts I and II,'' J. Acoust. Soc. Am. **75**, 977–995 (1984).
[9] J. H. Streng, ''Sound radiation from circular stretched membranes in free space,'' J. Aud. Eng. Soc. **37**(3), 107–118 (1989).
[10] R. Heydt, R. Pelrine, J. Joseph, and J. Eckerle, ''Lightweight polymer film loudspeaker for active noise control,'' International Mechanical Engineering Conference and Exposition (IMECE), Anaheim, California, November 16–20, 1998.

Hybrid tool for quickly estimating the radiated acoustic power from a vibrating structure in a multiple-source environment

Olivier Beslin,[a] Olivier Foin, and Jean Nicolas
GAUS, Département de génie mécanique, Université de Sherbrooke, Sherbrooke, Quebec J1K 2R1, Canada

(Received 11 March 1999; accepted for publication 3 October 1999)

This paper presents a new hybrid method for predicting overestimating and underestimating indicators of the acoustic power radiated by a vibrating surface even in the presence of other surrounding acoustic sources. This method is applicable to plates or low curvature surfaces radiating in open acoustic fields. The method is hybrid in the sense that the vibration field is measured and the parietal pressure field is predicted considering two extreme academic cases ''baffled'' and ''unbaffled.'' Many simplifications are made and justified in order to save running time. The method is successfully validated in comparison with experimental results on both laboratory and real life structures. This method has led to a quick tool, allowing one to obtain a good approximation of the radiated power in a few minutes. It provides a natural extension of a classical analyzer for vibroacoustics engineering. © *2000 Acoustical Society of America.* [S0001-4966(00)04901-8]

PACS numbers: 43.50.Cb, 43.50.Yw [MRS]

INTRODUCTION

In a practical problem of noise reduction for a multiple-source noisy machine, the first step is to identify sources and to quantify the radiated acoustic power relative to each sources. However, in practice, it is often difficult to do it rigorously, as it is difficult to measure the acoustic power radiated by a particular part of a complex system without being contaminated by other close noisy parts. Very often, different natures of sources are superimposed (structure-borne noise, jet noise, fan noise, etc.), and they are so interactive that it is not possible to remove a source to quantify another one. For example, a PC fan radiates noise and simultaneously excites the steel tower case which radiates too, so that the fan cannot be stopped when quantifying the structure-borne sound radiated from the tower. Many other examples can be found in common machines (compressors, ventilation systems, etc.). Today, the classical way of estimating the radiated acoustic power remains intensimetry.[1,2] The undesirable contributions are masked using partial coverage with sound barriers materials. This remains often a rough solution because of unavoidable acoustic leaks through the partial coverage, the difficulty in properly defining scanning surfaces and sometimes the impossibility of using the intensity probe because of a lack of space (as an *in situ* engine car, for example).

Theoretically, two unknowns must be identified to estimate the acoustic power radiated from a vibrating structure: its vibration field and the parietal acoustic pressure loading the vibration field.

To identify the vibration field, two methods are available, simulation or direct measurement. For the simulating approach, the finite element method (FEM) is a good tool for predicting the first modes of the structure. However, this approach remains limited to low frequencies, because of the large amount of data that must be processed when a fine mesh is used. Moreover, for predicting a real vibration field, a great limitation of FEM is the impossibility of knowing the mechanical and acoustical excitations that must be introduced in the model to predict the good vibration response. Using FEM, measurements have to be done anyway to validate the model, so that in a practical case, the quicker way to identify the vibration field is to measure it.

To identify the pressure field, once again, simulation and direct measurement can be considered. In this case, the direct measurement method is not possible. More precisely, for estimating the radiated power, the resistive part of the pressure (the part which is in phase with the velocity vibration field) must be measured in the near acoustic field of the vibrating structure, in the area where the acoustic field is mainly reactive (out of phase with the velocity vibration field). In practice, because of the limited dynamics of transducers and measurement bench, it is impossible to extract the resistive part of the pressure field from the dominant reactive part. In such a case, advanced techniques like ''near-field acoustic holography'' have to be used to extract the parietal pressure.

In summary, one original way to overcome the previous limitations and difficulties is to use a hybrid method: measuring the vibration field and simulating the pressure field

In this way, several authors have attempted to develop new hybrid techniques which will be detailed in the following lines. A common feature of all these techniques is that they all start from the measurement of the vibration field. They are differentiated by the assumptions that they make when simulating the pressure field.

Lovat *et al.*[3] have proposed an ''equivalent monopoles'' technique. In this method, the pressure field is approximated as being generated by a superposition of a finite number of discrete monopolar sources in the infinite space. The diffraction induced by surrounding objects and vibrating structure shape is not taken into account. The vibrating surface is divided into elementary subsurfaces on which normal velocity is measured. Then, each subsurface is replaced by an equivalent monopole, with a strength proportional to the normal

[a]Electronic mail: Olivier.beslin@gme.usherb.ca

velocity and area of the subsurface. This technique is very easy to use and can be applied to odd shape structures, but it leads to an overestimation of the true power as it considers only monopolar terms. The division of the vibrating surface into discrete elementary elements require a fine mesh to reach accurate results in midrange frequencies.

Koopman, Fahnline, and Paddock[4,5] have proposed a more precise method that takes into account the acoustic field diffracted by the shape of the vibrating object and surrounding objects by ''measuring'' the Green's function of the problem. It can be used in the case of odd shape structures and not only for plane structures. This very interesting method is in two steps. First, the motionless structure is divided into elementary subsurfaces, and the radiation impedancies matrix of the structure is measured in the following way: A reference monopolar source is placed on an elementary subsurface and the acoustic pressure on all the subsurfaces is measured. This procedure is repeated for all the other positions of the reference monopolar source. In a second step, the structure is turned on and normal velocities on all the subsurfaces are measured. Then, the radiated acoustic power is calculated by multiplying the velocities vector by the radiation impedancies matrix. This method is interesting as it permits us to take into account the complete geometry of the structure, allowing a precise measurement of the radiated acoustic power. However, the measurement of the radiation impedancies takes a long time proportional to N^2 if N is the number of subsurfaces. Moreover, it requires a specially built transducers set.

An alternative to the Fahnline *et al.* approach is to simulate the matrix radiation resistances using a classical boundary element method (BEM) code[6,7] and to measure the real vibration field. This permits a simplified experimental procedure (no reference source needed). However, the vibrating surface and the surrounding geometries must be meshed and a diffraction calculation must be done with all the pre- and postprocessing that comes with a FEM modelization, so that it remains a heavy procedure for the one who wants a quick estimation of an *in situ* radiated power estimation.

The method the authors are proposing could be classified between Lovat and Koopman approaches. It has the simplicity of the Lovat approach for the measurement procedure but the predicted pressure field is closer to the reality than a discrete monopole distribution. The approach of Koopman is very fine; however, the authors' goal was to develop a simple tool, using classical transducers and a quick measurement procedure allowing an estimation in a few minutes in order to answer the daily needs of numerous vibroacoustics engineers in diagnostic procedures. This method is limited to plane or low curvature structures radiating in acoustic open fields. This method cannot work if the structure stands in a close cavity having low damped acoustic modes since no vibroacoustic coupling is taken into account. This is the price to pay for quickness. This open field assumption allows us, however, to answer numerous practical problems.

The methodology of the proposed method is summarized in Fig. 1. In a first step, normal accelerations or velocities are measured on a mesh, using accelerometers (or better, a scanning laser vibrometer). More precisely, a particular

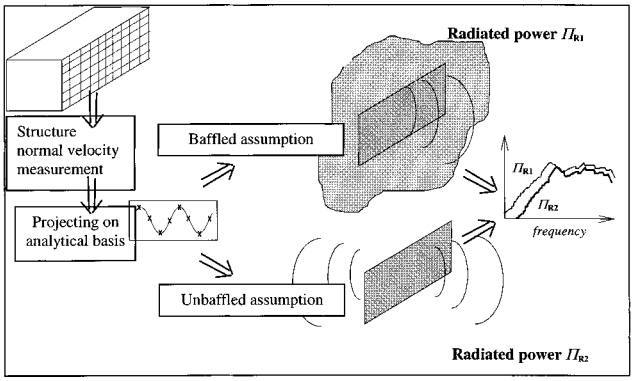

FIG. 1. Methodology.

point is chosen as a reference point and its acceleration autospectrum is measured. Transfer functions are measured between the reference point and a running point of the mesh. The measured data is then imported into a numerical code where the vibration field is expressed as an expansion over two-dimensional (2D) Fourier series. Then a minimum and a maximum indicator are calculated for estimating the acoustic power radiated from the vibration field. The first indicator is calculated considering the vibration field surrounded by an infinite baffle (Rayleigh integral) while the second indicator is calculated considering the vibration field alone in the infinite space (unbaffled case). These two extreme and academic situations allow a quick simulation since the influence of the surrounding objects is neglected. The baffled case results give an overestimation of the true radiated power while the unbaffled case gives an underestimation.

This paper presents several scientific and technical originalities. (i) The importation of the measured vibration field into a numerical model is done via a trigonometric functions basis set, which allows us to keep a physical meaning of all equations and consequently to physically justify the assumptions that are made for saving running time and memory. (ii) When calculating radiation impedancies, the trigonometric functions allow us to transform double surface integrals into single surface ones because of their well-known properties to simply transform sums of their arguments into product of sine functions. This cannot be made so easily using polynomial functions as in classical BEM codes. (iii) Technically, the method allows us to obtain an estimation of the radiated power from a vibrating surface surrounded by other sources without having to muffle or remove them. So, it really gives a good diagnostic tool for multi-source systems when intensimetry becomes tricky to handle in some extreme situations. (iv) No special measurement bench is needed, but simply a classical two-channel analyzer, accelerometers or a laser scanner and a personal computer with standard performances. (v) Hot spots of radiating power can be quickly identified. (vi) This method can be used in a ''try and fail'' procedure to test quickly the influence of a structural modification. (vii) The greater feature of this method (which was the goal the authors have initially set) is its blasting running time performances. This is a very important point since this is the reason why such a tool will be used or not in practice by engineers. Very often, in practical situations, measure-

ments have to be made on temporarily available costly machines because of industry constraints. In such situations, for the engineer it is very important to quickly obtain results and to be insured of its accuracy before leaving the machine.

The main results shown in this paper can be summarized as follows. (i) The proposed indicators actually allow a good estimation of the radiated power. (ii) The old classical Rayleigh integral remains a good approximation for describing radiation of structures even if they are not completely baffled. In all the cases we have tested, the baffled indicators were always closer to the reality than the unbaffled ones. (iii) Many simplifications can be made to save time without altering results. (iv) This new tool was revealed to be a natural complement of the analyzer since it provides a quasi-real-time estimation of the radiated acoustic power. For example, 455 measurement points can be processed from 64 to 6000 Hz with a frequency step of 4 Hz in less than 5 min on a Pentium II 333 MHz.

This paper is organized as follows. In Sec. I, the procedure for importing the vibration field into the semi-analytical formulation is described. In Secs. II and III we present the theoretical formulations for estimating the acoustic radiated power in the case of the baffled and unbaffled vibration fields, respectively. In Sec. IV we present all the approximations that have been made to save running time and memory size while keeping a good precision for estimating the acoustic power. Finally, in Sec. V, the efficiency of the method is demonstrated on three cases with increasing complexities, from the academic simply supported plate to a real life airplane fuselage part.

I. IMPORTING THE VIBRATION FIELD

The first step of this hybrid method is to import the measured vibration field into an analytical basis in order to have a vibration field expressed as if it was coming from a numerical or semi-analytical simulation program. In the proposed formulation, the vibration field is imported using a collocation method as following.

A. Presentation of the basis functions set

The displacement vibration field $w(M,t)$ is measured on a finite number of points belonging to a rectangular area of dimensions $a \times b$, of the vibrating structure, in order to set a vector $\{w_{pq}^{\text{mes}}\}$ of ''measured displacements.''

$$w_{pq}^{\text{mes}} \equiv w(M(x_p, y_q)) e^{j\omega t}, \quad (p,q) \in \Omega_w^{\text{mes}}, \tag{1}$$

where Ω_w^{mes} is defined as

$$\Omega_w^{\text{mes}} \equiv \{(p,q) \in N, \text{ such that } 1 \leqslant p \leqslant 2N_x \text{ and } 1 \leqslant q \leqslant 2N_y\}, \tag{2}$$

where N_x and N_y determine the size of a Cartesian mesh on the vibrating structure, and (x_p, y_q) Cartesian coordinates that will be defined in Eqs. (8) and (9).

Then, the measured vibration displacement field is imported into a basis of functions, in order to be expressed as follows:

$$w(M,t) = \sum_{(m,n) \in \Omega_w^{\psi}} w_{mn} \psi_{mn}\left(\frac{x}{a}, \frac{y}{b}\right) e^{j\omega t}, \tag{3}$$

where the $\{\psi_{mn}\}$ basis set is the classical two-dimensional Fourier basis

$$\psi_{mn}(\xi, \eta) \equiv e^{-j2\pi(m\xi + n\eta)} \tag{4}$$

and where $\{\Omega_w^{\psi}\}$ represents the set of integer couples defined by

$$\Omega_w^{\psi} \equiv \{(m,n) \in Z, \text{ such that } -N_x \leqslant m \leqslant N_x \text{ and } -N_y \leqslant n \leqslant N_y\}, \tag{5}$$

The expansion coefficients w_{mn} have to be identified.

The 2-D Fourier basis set (4) has been retained for several reasons: (i) It is a complete set (in the sense of global convergence in Fourier series) which allows a true representation of the vibration field. (ii) This set presents ''natural wavelength'' for describing flexion motion and finding assumptions based on physical criteria. (iii) When calculating radiation power, it greatly facilitates the calculation of radiation impedancies. As sums and products of trigonometric functions are easy to handle, it allows us to transform double-surface integrals into single-surface integrals.[8,9]

To identify the unknown expansion coefficients w_{mn}, a simple collocation method is used, which leads to solving the following linear system:

$$[P_{pqmn}]\{W_{mn}\} = \{W_{pq}^{\text{mes}}\}, \tag{6}$$

where P_{pqmn} matrix elements are defined by

$$P_{pqmn} \equiv \psi_{mn}\left(\frac{x_p}{a}, \frac{y_q}{b}\right). \tag{7}$$

B. Avoiding the nonuniqueness problem

It is well known, using collocation methods, that care must be taken in the choice of collocation points.[10] It must be ensured that collocation points do not coincide with the zeros of each ψ_{mn} function so that the expansion coefficient w_{mn} can always be defined. It is easy to verify that the following points mesh in $M(x_p, y_p)$ can satisfy this criteria:

$$x_p = \frac{a}{2}\left(\frac{3p+1}{3N_x+1}\right), \quad p = 0,1,...,2N_x, \tag{8}$$

$$x_q = \frac{b}{2}\left(\frac{3q+1}{3N_y+1}\right), \quad q = 0,1,2,...,2N_y. \tag{9}$$

The distance δx between two columns and δy between two rows is then

$$\delta x \equiv \frac{3}{2} a\left(\frac{1}{3N_x} + 1\right), \tag{10}$$

$$\delta y \equiv \frac{3}{2} b\left(\frac{1}{3N_y} + 1\right). \tag{11}$$

This mesh is summarized in Fig. 2.

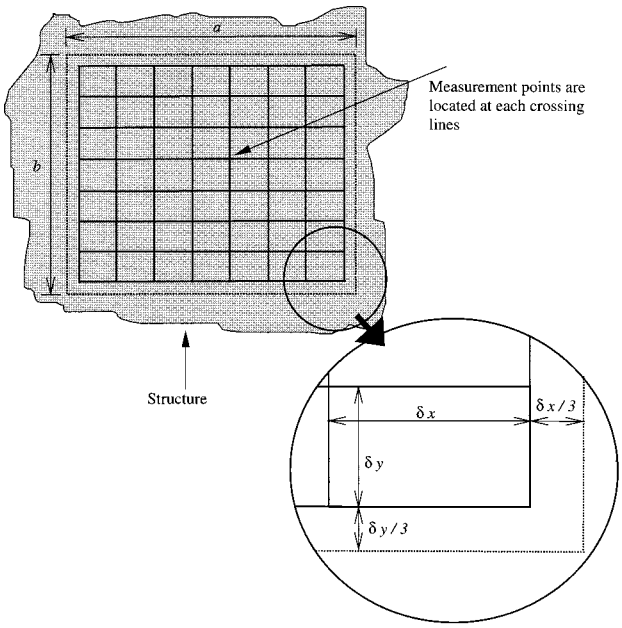

FIG. 2. Mesh measurement.

C. Spatial sampling criterion

If the mechanical parameters of the structure are unknown or if the structure is complex (containing stiffeners, rivets, multi-layered, variable thickness,...), it is difficult to calculate *a priori* a spatial sampling criterion since the dispersion law of such a structure is unknown. However, in the case of homogeneous platelike structure, some guidelines can be used as summarized in the following lines.

Let us call l_{mesh} the greatest distance between two successive rows (or two successive columns) of the measurement mesh. Following Shannon criterion, the minimum vibration wavelength that can be measured is $\lambda_{\min}=2l_{\text{mesh}}$. For a homogeneous platelike structure, the dispersion law of flexural waves in infinite plate $\lambda^2=\pi\sqrt{E/3\rho(1-\nu^2)}(h/f)$ can be used to approximate the correspondence between the wavelength λ and the frequency f, where E is the Young modulus, ρ is the density, ν is the Poisson ratio, and h is the thickness of the plate. Using this dispersion law, the following criterion can be announced: If measurements have to be made up to frequency $f_{\max}$, the mesh step l_{mesh} must be such as $l_{\text{mesh}}^2\leqslant(\pi/4)\sqrt{E/3\rho(1-\nu^2)}(h/f_{\max})$.

II. BAFFLED VIBRATION FIELD FORMULATION

The first radiated power indicator is calculated by prolonging the imported vibration field with an infinite baffle. It is well known in literature[11–14] that baffle assumption tends to overestimate the radiated power. This first indicator gives an overestimating indicator of the truly radiated power.

In the baffled case, the acoustic pressure field $p(M_0)$ generated by the vibration field is given by the well-known Rayleigh integral[11–14]

$$p(M_0)=-\rho_0\omega^2\int_S w(M)G_{k_0}(M,M_0)\,dS(M), \tag{12}$$

where ρ_0 is the air density, $G_{k_0}(M,M_0)$ is the semi-infinite space Green function,

$$G_{k_0}(M,M_0)=\frac{1}{2\pi}\frac{e^{-jk_0R}}{R} \tag{13}$$

with

$$R\equiv\sqrt{(x-x_0)^2+(y-y_0)^2+(z-z_0)^2}, \tag{14}$$

S is the surface of the vibrating field, $k_0=\omega/c_0$ is the wave vector, ω is the angular frequency, and c_0 is the sound celerity.

Let us call $\vec{n}$ the unit vector, normal to the surface S. Then the normal acoustic intensity $I_n(M_0)$ radiated by the vibration field is

$$I_n(M_0)\equiv\tfrac{1}{2}\,\mathrm{Re}\,(p(M_0)\,v_n^*(M_0)), \tag{15}$$

where M_0 is a point situated on the surface S, and $v_n(M_0)$ is the normal acoustic velocity. Because of normal velocity continuity condition between the fluid and the structure, the normal acoustic velocity can be related to the vibration displacement field as follows:

$$v_n^*(M_0)=-j\omega w^*(M_0). \tag{16}$$

The radiated acoustic power is defined by

$$\Pi_{\text{rad}}^{\text{baf}}=\int_S I_n(M_0)\,dS(M_0), \tag{17}$$

which can be rewritten using the pressure field expression (12):

$$\Pi_{\text{rad}}^{\text{baf}}=\frac{1}{2}\,j\rho_0\omega^3\int_S\int_S w(M)G_{k_0}(M,M_0)w^*(M_0)\times dS(M)\,dS(M_0), \tag{18}$$

which can be expressed introducing radiation impedances Z_{pqmn}^{baf},

$$\Pi_{\text{rad}}^{\text{baf}}=\frac{1}{2}\,\omega^2\sum_{(m,n)\in\Omega_w^{\psi}}\sum_{(p,q)\in\Omega_w^{\psi}} w_{mn}\,\mathrm{Re}\,(Z_{pqmn}^{\text{baf}})w_{pq}^*, \tag{19}$$

where Z_{pqmn}^{baf} is defined as

$$Z_{pqmn}^{\text{baf}}=j\rho_0\omega^3\int_S\int_S\psi_{mn}(M)G_{k_0}(M,M_0)\psi_{pq}^*(M_0)\times dS(M)\,dS(M_0). \tag{20}$$

This last expression can be summarized by the following matrix equation:

$$\Pi_{\text{rad}}^{\text{baf}}=\tfrac{1}{2}Z_0\omega^2\{w_{pq}^*\}^T\cdot[R_{pqmn}^{\text{baf}}]\cdot\{w_{mn}\}, \tag{21}$$

where R_{pqmn}^{baf} denotes the adimensional real part of $Z_{pqmn}^{\text{baf}}/Z_0$ with $Z_0=\rho_0c_0$ denoting the characteristic impedance of the air.

In summary, the calculation of the acoustic power radiated by the baffled vibration field is simply given by the matrix equation (21) and it requires the calculation of the frequency-dependent terms R_{pqmn}^{baf}.

III. UNBAFFLED VIBRATION FIELD FORMULATION

The second radiated power indicator is calculated considering the unbaffled vibration field. In this case, the pressure field generated by the vibration field is given by

$$p(M_0)=\int_S \overline{p}(M)\frac{\partial G_{k_0}(M,M_0)}{\partial n_M}\,dS(M), \tag{22}$$

where $\partial G_{k_0}/\partial n_M$ denotes the normal derivative of the infinite space Green's function on the surface S and where $\overline{p}(M)$ is the pressure drop across the surface S.

The continuity of normal velocities between the fluid and the structure can be expressed as

$$\rho_0\omega^2 w(M_0)=\frac{\partial p(M_0)}{\partial n_{M_0}}. \tag{23}$$

Inserting the pressure expression (22) into (23) leads to the following relation between the known vibration field displacement $w(M_0)$ and the unknown pressure drop $\overline{p}(M)$:

$$w(M_0)=\frac{1}{\rho_0\omega^2}\int_S \overline{p}(M)\frac{\partial^2 G_{k_0}(M,M_0)}{\partial n_{M_0}\partial n_M}\,dS(M). \tag{24}$$

This last expression is very difficult to handle to identify the pressure drop since it contains a double derivative of the singular Green's function. To circumvent this singularity, a variational form of Eq. (24) can be found in the literature.[15,16] It is shown that the solution $\overline{p}(M)$ satisfying Eq. (24) and vanishing at the boundary of the domain S (which is the case here) must also be the solution that minimizes the following functional F:

$$F(\overline{p}(M))\equiv\frac{1}{2}\frac{1}{\rho_0\omega^2}J(\overline{p}(M),\overline{p}(M)) + \int_S w(M)\overline{p}(M)\,dS(M), \tag{25}$$

where J denotes the quadratic functional defined as

$$J(\overline{p}(M),\overline{p}(M_0))\equiv-\int_S\int_S\left[k^2\overline{p}(M)\overline{p}(M_0)+\frac{\partial\overline{p}(M)}{\partial x}\times\frac{\partial\overline{p}(M_0)}{\partial x_0}+\frac{\partial\overline{p}(M)}{\partial y}\frac{\partial\overline{p}(M_0)}{\partial y_0}\right]\times G_{k_0}(M,M_0)\,dS(M)\,dS(M_0). \tag{26}$$

In order to identify the unknown pressure drop $\overline{p}(M)$, it is searched as an expansion on a functions basis $\{\phi_{ij}\}$, insuring the nullity of $\overline{p}(M)$ at the boundary of the domain S,

$$\overline{p}(M)=\sum_{(i,j)\in\Omega_{\overline{p}}}\overline{p}_{ij}\phi_{ij}(M),\quad (i,j)\in\Omega_{\overline{p}}, \tag{27}$$

where ϕ_{ij} functions are given by

$$\phi_{ij}(M)\equiv\sin\left(\frac{i\pi x}{a}\right)\sin\left(\frac{j\pi x}{b}\right) \tag{28}$$

and where $\Omega_{\overline{p}}$ is defined by

$$\Omega_{\overline{p}}\equiv\{(i,j)\in N/1\leqslant i\leqslant M_x \text{ and } 1\leqslant j\leqslant M_y\} \tag{29}$$

(M_x and M_y are adjusted for convergence).

The stationarity of functional F versus coefficients $\overline{p}_{ij}$ is classically expressed

$$\frac{\partial F}{\partial\overline{p}_{ij}}=0,\quad \forall(i,j)\in\Omega_{\overline{p}}, \tag{30}$$

which leads to the following linear system:

$$[A_{klij}]\cdot\{\overline{p}_{ij}\}=[S_{klmn}]\cdot\{w_{mn}\},\quad (k,l)\in\Omega_{\overline{p}},\ (i,j)\in\Omega_{\overline{p}},\ (m,n)\in\Omega_w^{\psi}, \tag{31}$$

where S_{klmn} is a transfer matrix from base $\{\psi_{mn}\}$ to base $\{\phi_{kl}\}$,

$$S_{klmn}\equiv\int_S\phi_{kl}(M)\psi_{mn}(M)\,dS(M),\quad (k,l)\in\Omega_{\overline{p}},\quad (m,n)\in\Omega_w^{\psi}, \tag{32}$$

and A_{klij} is a frequency-dependent matrix defined by

$$A_{klij}=M_{klij}-\frac{K_{klij}}{\omega^2}, \tag{33}$$

where K_{klij} and M_{klij} are defined as the following double-surface integrals:

$$M_{klij}\equiv\frac{1}{\rho_0 c_0^2}\int_S\int_S\phi_{kl}(M)G_{k_0}(M,M_0)\phi_{ij}(M_0)\times dS(M)\,dS(M_0), \tag{34}$$

$$K_{klij}\equiv\frac{1}{\rho_0}\int_S\int_S\left[\frac{\partial\phi_{kl}(M)}{\partial x}\frac{\partial\phi_{ij}(M_0)}{\partial x_0}+\frac{\partial\phi_{kl}(M)}{\partial y}\times\frac{\partial\phi_{ij}(M_0)}{\partial y_0}\right]G_{k_0}(M,M_0)\,dS(M)\,dS(M_0). \tag{35}$$

The normal acoustic intensity generated by the unbaffled vibration field is

$$I_n(M_0)=\tfrac{1}{4}\,\mathrm{Re}\,(\overline{p}^*(M_n)\,v_n(M_0)) \tag{36}$$

Similarly to the baffled case, the total acoustic power generated in a half-space by the unbaffled field is given by the flux of the acoustic intensity over the entire surface S, which leads to the following matrix equation:

$$\Pi_{\mathrm{rad}}^{\mathrm{unbaf}}=-\frac{\omega}{4}\,(\{\overline{p}_{ij}^*\}^T\cdot[S_{ijmn}]\cdot\{W_{mn}\}),\quad (i,j)\in\Omega_{\overline{p}},\ (m,n)\in\Omega_W^{\psi}. \tag{37}$$

In summary, the acoustic power radiated by the unbaffled vibration field is calculated as follows:

(i) First, the matrix equation (31) is solved in order to identify the pressure drop unknown $\overline{p}(M)$ via the expansion coefficients $\overline{p}_{ij}$.

(ii) Second, the radiated acoustic power is calculated with the matrix expression (37).

IV. SAVING CPU TIME AND MEMORY

The most time-consuming steps of the method can be summarized as follows.

(i) The linear system (6) must be solved to import the vibration field into the analytical basis (4).
(ii) The real part of the frequency-dependent terms Z^{baf}_{pqmn} [Eq. (20)] must be calculated for estimating the first (baffled) radiated power indicator.
(iii) The frequency-dependent terms K_{klij} and M_{klij} [Eqs. (34) and (35)] must be calculated for estimating the second (unbaffled) radiated power indicator.
(iv) The linear system (31) must be solved to calculate the second radiated power indicator.

This section presents the assumption that can be made to accelerate computing time and minimize memory size.

A. Linear systems resolutions

The matrix $[P_{pqmn}]$ in the linear system (6) that must be solved to import the measured data in the analytical basis is not frequency dependent; only the second-hand vector $\{w^{\text{mes}}_{pq}\}$ depends on frequency. Therefore, for saving time, a LU decomposition[17] (product of lower triangular by upper triangular matrices) of matrix $[P_{pqmn}]$ can be made instead of a classic ''Gauss pivot'' method.

If N is the rank of the matrix to be solved, the ''Gauss pivot'' method is an N^3 process that is called for each frequency point. With the LU method, the matrix is decomposed one time for all in an upper and a lower triangle matrix. Then, for each frequency point, two triangular systems have to be solved, which is only an N^2 process.

The other linear system (31) to be solved is frequency dependent, but matrix $[A_{klij}]$ is symmetric. In this case, a simple symmetric pivoting method is used.

B. Baffled vibration field

The first radiated power indicator requires the calculation of the frequency-dependent matrix, defined by the following double-surface integral terms:

$$R^{\text{baf}}_{mnpq}=\frac{jk_0}{2\pi}\int_S\int_S \psi_{mn}(M)\,\frac{\sin(k_0R)}{R}\,\psi^*_{pq}(M_0)\times dS(M)\,dS(M_0). \tag{38}$$

As shown in this section, several simplifications can be made to accelerate the running time of the program while keeping a good calculation precision.

1. The ''dominant diagonal terms'' assumption

A first way to save cpu time is to neglect the off-diagonal terms of the matrix R^{baf}_{mnpq}. Figure 3 represents 3-D plots of the relative magnitudes of R^{baf}_{mnpq} terms versus (m,n) and (p,q) sequences, for four different frequencies: (a) 100 Hz, (b) 500 Hz, (c) 1000 Hz, and (d) 5000 Hz. For this example the dimensions of the surface S were $a=1.36$ m and $b=0.54$ m. It can be observed in these four figures that the diagonal terms are always dominant, in comparison with off-diagonal terms. It must be noted also that at high frequency (5000 Hz here), the diagonal terms are tending toward the same value ''1.'' This fact will be used later in this section.

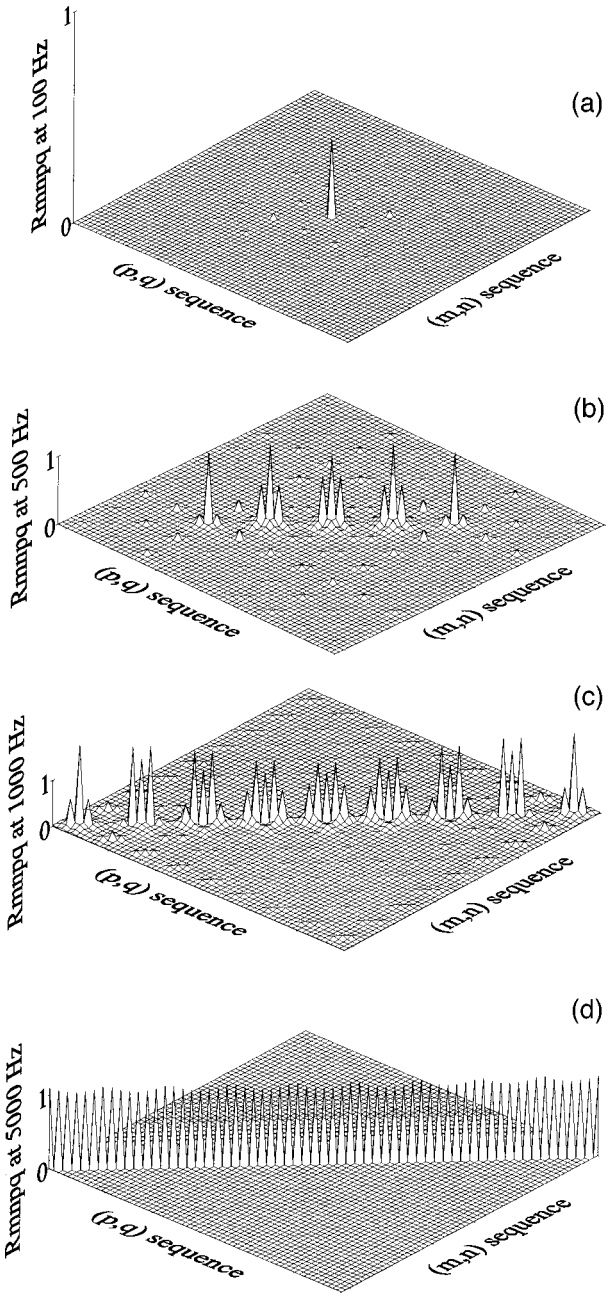

FIG. 3. Negligibility of extra diagonal terms in the matrices of the adimensional radiation resistances R_{mnpq} at (a) 100 Hz, (b) 500 Hz, (c) 1000 Hz, and (d) at 5000 Hz.

2. Frequency interpolation of radiation resistances

Radiation resistances R^{baf}_{mnpq} depend on frequency via the wave vector k_0 as it can be seen in definition (38).

Figure 4 represents examples of the frequency dependency of R^{baf}_{4411} and R^{baf}_{3333} terms (for $a=1.36$ m and $b=0.54$ m). It can be seen in Fig. 4 that the frequency dependency is smooth so that R^{baf}_{mnpq} terms can be interpolated instead of being calculated at each frequency point. For example, Fig. 4 shows the effect of interpolating using a 50-Hz frequency step. It can be observed that interpolated and exact data are quite comparable.

3. The overcritical wave vector assumption

As shown previously in Fig. 4, radiation resistances tend toward unity at high frequency so that it is not necessary to

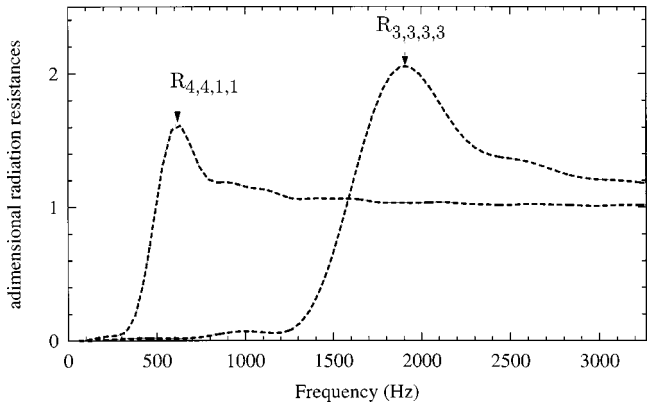

FIG. 4. Frequency interpolation of radiation resistances. Thin solid line: noninterpolated data, thick dashed lines: interpolated data (50-Hz steps).

compute them at each frequency step. However, they are not reaching the unity plateau at the same frequency point, it depends on *m*, *n*, *p*, *q*, indices. Instead of plotting radiation impedancies versus frequency, they can be plotted versus the adimensional parameter k_0/k_{mn} were k_{mn} is the ''wave vector'' relative to the basis function ψ_{mn} and defined as

$$k_{mn}=\sqrt{\left(\frac{2\pi m}{a}\right)^2+\left(\frac{2\pi n}{b}\right)^2}. \tag{39}$$

Figure 5 represents such a plot of radiation resistances versus the parameter k_0/k_{mn} for numerous different values of *m*, *n*, *p*, *q*. This time, all resistances present the same behavior versus the adimensional parameter k_0/k_{mn}. It can be seen in Fig. 5 that when k_0/k_{mn} is greater than 3, resistances can be approximated by unity with an error less than 10%, which is quite sufficient. This criteria has been retained in this presented method.

4. The unity radiation factor assumption

Classically, in the literature of radiating structures, the acoustic radiation of a vibrating structure is quantified by a radiation factor σ, defined as follows:

$$\sigma=\frac{\Pi^{\mathrm{rad}}}{SZ_0\langle\nu^2(M,t)\rangle_{S,T}}, \tag{40}$$

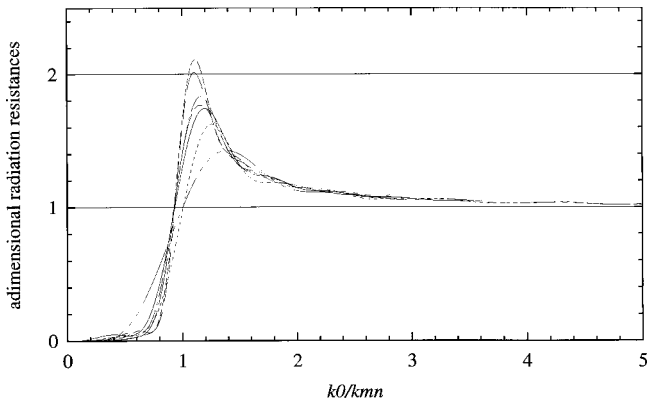

FIG. 5. Adimensional radiation resistances versus the adimensional frequency parameter k_0/k_{mn} with $k_0=\omega_0/c_0$.

where Π^{rad} is the acoustic power radiated by the structure, S is the area of the structure, Z_0 is the characteristic impedance of the fluid medium, and $\langle\nu^2(M,t)\rangle_{S,T}$ is the mean quadratic velocity over time and space of the vibrating structure.

It is well known in the literature[11,14] that at high frequency, beyond a critical frequency, the radiation factor tends toward unity. In this frequency area, the structure reaches a full effective radiating state. The program developed on this presented method calculates this radiation factor at each frequency point. When it is detected that the radiation factor is close to unity for several successive frequency points, the calculation of radiated acoustic power is greatly simplified by using expression (40), setting σ to unity, which leads to the simple expression

$$\Pi^{\mathrm{rad}}=SZ_0\langle\nu^2(M,t)\rangle_{S,T}. \tag{41}$$

Note that in expression (41), it is not necessary to import the measured velocity into the analytical basis so that no linear system has to solved; the quadratic velocity is directly obtained from the measured data as follows (using the notations of Sec. I A):

$$\langle\nu^2(M,t)\rangle_{S,T}=\frac{1}{(2N_x+1)(2N_y+1)}\sum_{(p\cdot q)\epsilon\Omega_W^{\mathrm{mes}}}|W_{pq}^{\mathrm{mes}}|^2. \tag{42}$$

C. Unbaffled vibration field

The second indicator of radiated acoustic power requires the calculation of the frequency-dependent terms A_{klij} as defined in Eqs. (33)–(35).

1. Frequency interpolation of matrix A

The frequency dependency of matrix M_{klij} is similar to R_{mnpq}^{baf} dependency so that it is treated in the same way. However, for the term K_{klij}/ω^2, the interpolation can be made before or after dividing by ω^2. It has been found that the best way to interpolate the K_{klij}/ω^2 term is to treat separately the real and imaginary part. Figure 6 represents an example of real part interpolation for the particular term K_{1212}. The effect of interpolating before dividing by ω^2 is shown in Fig. 6(a) while the effect of interpolating after dividing by ω^2 is reported in Fig. 6(b). It can be seen in Fig. 6 that the best way of interpolating the real part of K_{klij}/ω^2 is to first interpolate the term K_{klij} and then to divide by ω^2. This leads to a very smooth curve presenting a good slope continuity which matches well the noninterpolated curve. At the opposite, it is shown in Fig. 7 that for the imaginary part, dividing after interpolation leads to bad results. In this case, it is preferable to interpolate the global terms K_{klij}/ω^2. This gives a poorer quality of interpolation than for the real part, but it remains quite acceptable.

2. Stopping calculations at high frequency

It is well known in literature that the acoustic radiation power differences between a baffled and unbaffled structure are vanishing at high frequencies. The effect of ''acoustic short cut'' which is important at low frequencies, where the acoustic wavelengths are greater than the structure flexion wavelengths and/or surface dimensions, is decreasing versus frequency when the acoustic wavelength becomes shorter.

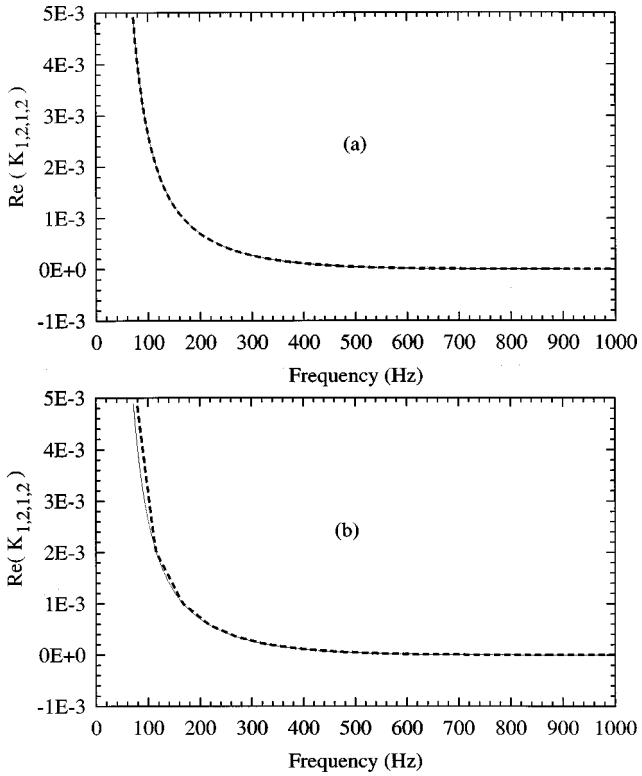

FIG. 6. Interpolation of the real part of elements of matrix K/ω^2. Solid line: noninterpolated data. Dashed lines: interpolated data (50-Hz frequency step). (a) Interpolating before dividing by ω^2. (b) Interpolating after dividing by ω^2.

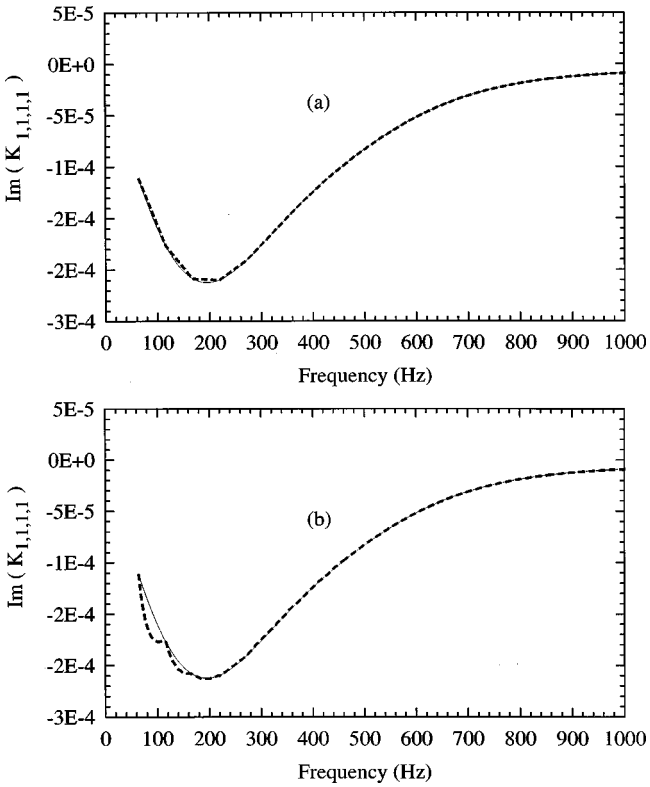

FIG. 7. Interpolation of the imaginary part of elements of matrix K/ω^2. Solid line: noninterpolated data. Dashed lines: interpolated data (50-Hz frequency step). (a) Interpolating after dividing by ω^2. (b) Interpolating before dividing by ω^2.

Then it is needless calculating the second power radiation indicator at high frequency when it gives the same results as the first indicator.

This argument is illustrated in Fig. 8 where the two power indicators are plotted for the case of a stiffened rectangular plate (complete characteristics of the stiffened plate are given in Sec. V A 2). It can be seen in Fig. 8 that both indicators are merging beyond around 1200 Hz. Stopping automatically, the calculation of the second indicator can be implemented very simply by comparing systematically both indicators. When the two results are closer than a user-defined criteria, for several successive frequency points, the calculation of the second indicator is skipped, allowing a great running time savings.

V. VALIDATION

This section presents the experimental validation of the proposed method. First, the method is tested on academic ''laboratory structures,'' having a low modal density and low damping properties. Finally, the efficiency of the method is demonstrated on a real life structure having a high modal density, heterogeneities, and higher damping.

A. Laboratory structures

1. A simply supported plate

The first tested structure was a rectangular aluminum homogeneous plate having dimensions $0.48\times0.42\,\mathrm{m}^2$, 6 mm thick. The experimental boundary conditions were very close to be simply supported. The plate was excited with a shaker. The excitation signal was a white noise (from 0 to 5600 Hz). The plate normal accelerations were measured on a regular mesh of 63 points (9 columns by 9 rows). Using the spatial sampling criterion defined in Sec. I C, this mesh can allow accurate results up to around 4000 Hz. However, it must be noted that the critical frequency of a 6-mm aluminum plate is around 2000 Hz. As explained in the end of Sec. IV B, over the critical frequency, the vibration field is no more imported in the trigonometric basis, the radiated acoustic power is directly calculated as being proportional to the mean quadratic velocity, and this mean quadratic velocity is directly calculated by averaging the quadratic velocities measured at the mesh points. This means that what is important is to import

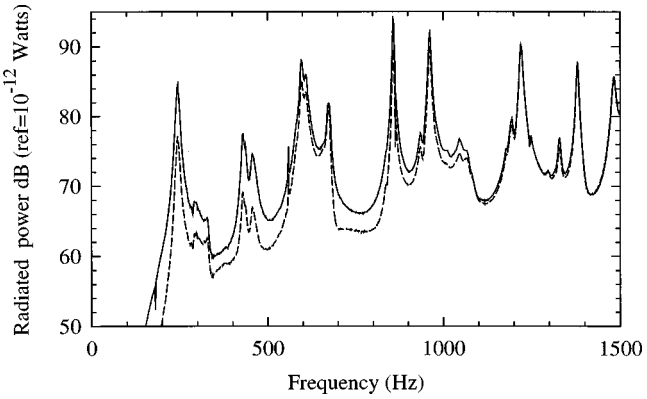

FIG. 8. Radiated acoustic power of a baffled (solid line) and unbaffled (dashed line) stiffened plate.

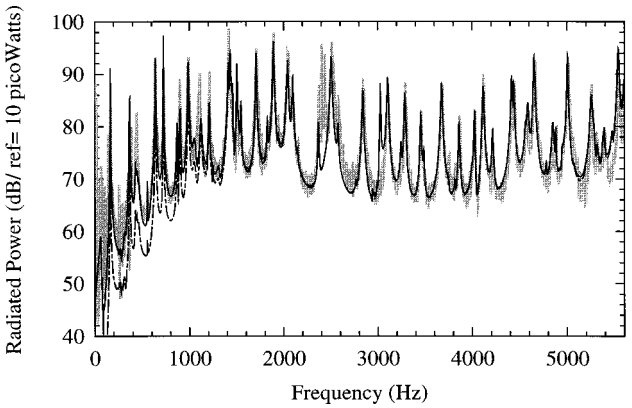

FIG. 9. Radiated acoustic power of a simply supported plate. Grey thick line: experimental; black solid line: baffled vibration field; black dashed line: unbaffled vibration field.

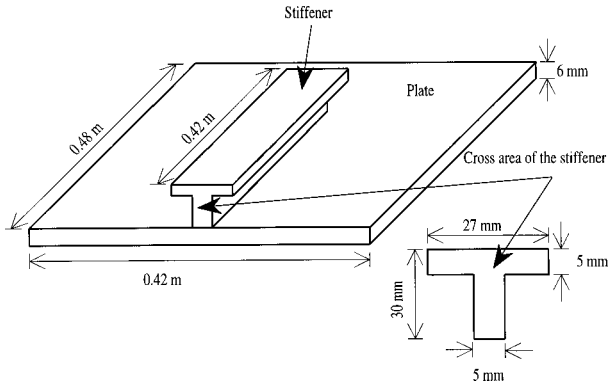

FIG. 10. Geometry of the stiffened plate.

accurately the vibration field up to 2000 Hz. Over this frequency, the vibration field is no more imported. This explains why radiated acoustic power results are good up to 5600 Hz. The plate was not baffled but a thick maintaining aluminum frame was surrounding the plate boundaries, acting as a strip baffle having a width of 5 to 6 cm. The whole system was standing vertically on a motionless table, the table acting as a partial reflecting surface. In summary, the plate was neither baffled nor unbaffled. It was only surrounded by some diffracting objects as it is the case in practical situations. The radiated acoustic power was directly measured with an intensity probe by scanning the surfaces of a virtual parallelepiped fronting the plate. The comparison between the direct measurement and the estimations of the radiated acoustic power is shown in Fig. 9. It can be seen that the method allows a good estimation of the radiated power. It can be seen that the baffled indicator is closer to the reality than the unbaffled one. This confirms the assumption repeatedly made in literature that the Rayleigh integral is often a good approximation when calculating the radiation of a vibrating structure, even if this structure is not extended with an infinite baffle. It must be noted that the intensity measurement shown here as a ''reference'' is not the exact radiated power since intensity measurement presents its own limitations (finite difference approximation for the acoustic velocity, influence of the reactive pressure field in the near field of the structure, etc.). This is particularly true in low frequencies where high levels have no physical meanings.

2. A stiffened plate

One can object that the case of a simply supported plate is not sufficient to validate the method, since the natural modes of such a plate are sine functions and that the method uses also sine (and cosine) functions as interpolation functions, which is a particularly ''advantageous'' case for a validation. In order to show that the method still works for more complex cases, the same type of measurement has been done with the same plate with an added strong T-shaped stiffener as shown in Fig. 10. In such a case, the mode shapes of the structure are no longer sine functions. The comparison between direct intensity measurement and estimating indicators is reported in Fig. 11. It can be seen that even in this case, the method works very well. Once again, the baffled indicator fits well the direct measurements, even in very low frequency.

B. A real life structure: An airplane fuselage

The method has been tested on part of an airplane fuselage as shown in Fig. 12. The typical dimensions of the panel were $1\times2.3\,\mathrm{m}^2$. The panel was curved with a curvature radius of 1.34 m. The thickness of the panel was variable from 0.8 to 2 mm. This aluminum panel was riveted on an array of 5 by 8 curved stiffeners (portions of rings). This structure is representative of a real life structure, with heterogeneities, ribs, rivets, complex damping mechanisms, etc.

The structure was excited with a shaker (white noise) and normal accelerations have been measured on a rectangular area of the panel (rectangle of $1.36\times0.54\,\mathrm{m}^2$). The acceleration measurements have been done with accelerometers, on 455 points (35 columns by 13 rows). The radiated acoustic power was estimated using a classic intensity probe.

Figure 13 shows the comparisons between the measured acoustic power and the minimal and maximal indicators computed from the acceleration measurement using the proposed method. The total running time to obtain this curves was less than 5 min on a 333-MHz PentiumII with 64 Meg RAM, which was quite a ''middle of the road'' PC at the time this article was written. Even for such a complex struc-

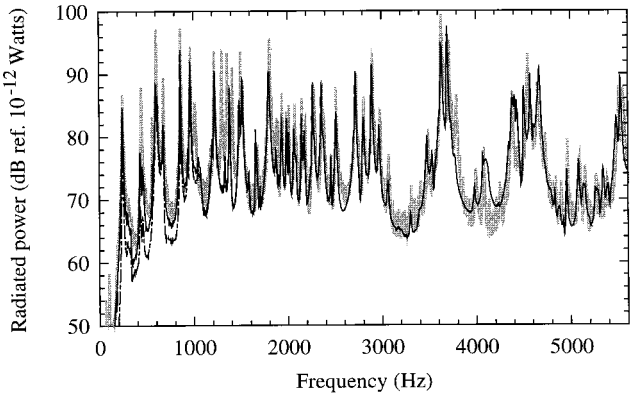

FIG. 11. Radiated acoustic power of a stiffened plate. Grey thick line: experimental; black solid line: baffled vibration field; black dashed line: unbaffled vibration field.

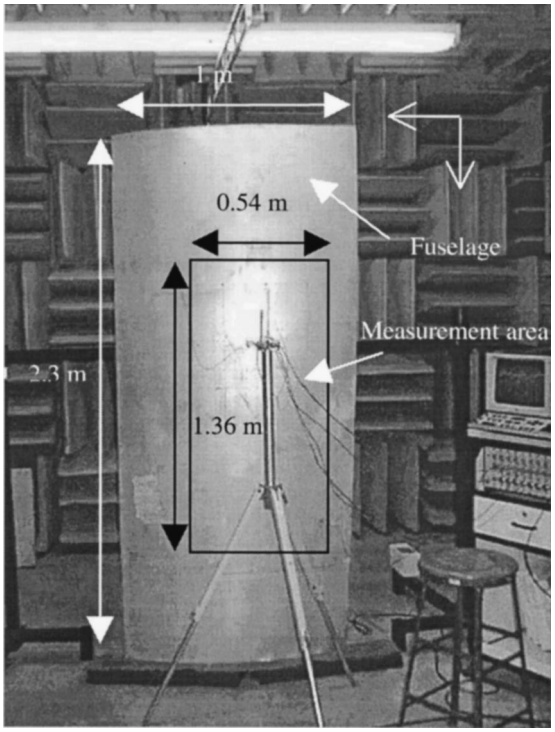

FIG. 12. Measurement on a portion of an airplane fuselage.

ture, it can be seen that the method works quite well on the large frequency spectrum, and the true radiated power is well contained in the estimators.

VI. CONCLUSION

A new hybrid method has been presented in this paper, which allows us to estimate the radiated acoustic power from a portion of a vibrating surface, using only measured normal velocities as input data. This paper can be summarize in three points:

A strategy has been set to develop a quick tool, using a standard measurement bench and a personal computer, which could help vibroacoustics engineers in quantifying the power of each source in a multiple-source environment, where classical techniques are not satisfactory. This method has led to an effective tool that can be considered as a natural complement of a classical analyzer for measuring almost in real time (about 5 min of computation) a good estimation of radiated acoustic power from vibrating surfaces.

Specific calculations have been used to accelerate running time. (i) A real situation has been approximated by two ''bounding'' simple cases: *baffled* and *unbaffled* vibration field. (ii) The vibration field has been expanded on a *2D Fourier basis* to easily transform quadruple integrals into double ones and to formulate calculus simplifications on a ''physical meaning'' basis. (iii) At each step of the program, simplifications have been successively made (i.e., *dominant diagonal terms* assumption, *frequency interpolation* of radiation resistances, *overcritical wave vector* assumption, *unity radiation factor* assumption).

Engineering applications of this tool are numerous. (i) Measurement of radiated power from subcomponents, structures, and subparts of structures valid in a heavily acoustically contaminated environment. (ii) Identification of high radiating zones to help designing quieter solutions. (iii) Prototyping tool for experimental ''try and fail'' procedures. Actually, it gives a quick answer to each new modifications with the great advantage of working on the real structure.

The effectiveness of the method has been demonstrated on simple and complex structures. Of course, the presented method is limited to rectangular domains and low curvature surfaces, but this is the price to pay to obtain a quick estimation. Nevertheless, it will answer numerous problems. Moreover, in practice, mesh measurements are often defined as rectangular areas to simplify the measurement procedure and the display of results.

The quickness of the method, coupled to a scanning laser vibrometer, opens the way to intelligent measurement methods where the measurement mesh could be defined by an interactive program which could adapt the measurement mesh to the vibration field characteristics in an interactive process.

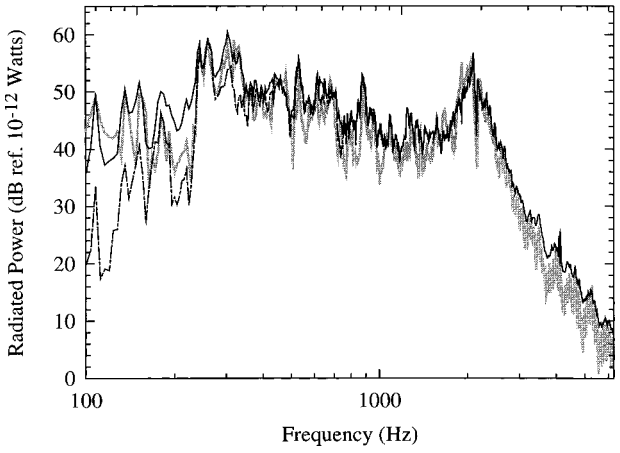

FIG. 13. Radiated acoustic power of an airplane fuselage part. Grey thick line: experimental; black solid line: baffled vibration field; black dashed line: unbaffled vibration field.

ACKNOWLEDGMENTS

The authors thank the IRSST for their financial support.

[1] F. J. Fahy, *Sound Intensity*, 2nd ed. (Spon, London, 1995).
[2] J. Nicolas and G. Lemire, ''Precision of active sound intensity measurement in a progressive and a nonprogressive field,'' J. Acoust. Soc. Am. **78**, 414–422 (1985).
[3] G. Lovat, T. Loyau, and J. L. Barbry, ''Calculation of the acoustic radiation of structures by using acceleration measurements and a monopolar distribution,'' in Proceedings of the Fourth International Congress on Sound and Vibration, St. Petersburg, Russia, 24–27 June 1996, edited by Malcom J. Crocker and Nicolay I. Ivanov, Vol. 2, pp. 873–880.
[4] J. B. Fahnline and G. H. Koopmann, ''A lumped parameter model for the acoustic power output from a vibrating structure,'' J. Acoust. Soc. Am. **100**, 3539–3547 (1996).
[5] E. Paddock, ''The use of acoustic radiation resistance measurements to assess the noise characteristics of ic engine components,'' Master thesis, The Pennsylvania State University, 1994.
[6] SYSNOISE, LMS Numerical Technologies nv, Interleuvenlaan 70, 3001 Leuven, Belgium.
[7] IDEAS, SDRC, 2000 Estman Drive, Milford, OH 45150.
[8] H. Nélisse, O. Beslin, and J. Nicolas, ''Fluid-Structure Coupling for an Unbaffled Elastic Panel Immersed in a Diffuse Field,'' J. Sound Vib. **198**, 485–506 (1996).

[9] H. Nélisse, O. Beslin, and J. Nicolas, ''A generalised approach for the acoustic radiation from a baffled or unbaffled plate with arbitrary boundary conditions, immersed in a light or heavy fluid,'' J. Sound Vib. **211**, 207–225 (1998).
[10] J. N. Reddy, *Applied Functional Analysis and Variational Methods in Engineering* (Krieger, Malabar, FL, 1991).
[11] M. C. Junger and D. Feit, *Sound, Structures, and Their Interaction* (Acoustical Society of America, Woodbury, NY, 1972).
[12] A. D. Pierce, *Acoustics, An Introduction to its Physical Principles and Applications* (McGraw–Hill, New York, 1981).
[13] P. M. Morse and K. U. Ingard, *Theoretical Acoustics* (Princeton Univ. Press, Princeton, NJ, 1968).
[14] M. Bruneau, *Introduction aux théories de l'acoustique* (Université du Maine, Le Mans, France, 1983).
[15] M. A. Hamdi, ''Une formulation variationnelle par équations intégrales pour la résolution de l'équation de Helmholtz avec des conditions aux limites mixtes,'' C. R. Acad. Sci. Paris, Ser. II, t.232, p. 17–20, Sjanvier, 1981.
[16] N. Atalla, J. Nicolas, and C. Gauthier, ''Acoustic radiation of an unbaffled vibrating plate with general elastic boundary conditions,'' J. Acoust. Soc. Am. **99**, 1484–1494 (1996).
[17] W. H. Press, S. A. Teokolsky, W. T. Vetterling, and B. P. Flannery, Numerical recipies in FORTRAN 77 (Cambridge Univ. Press, Cambridge, 1992), 963 pp.

Rotating machinery dynamics simulation. I. Rigid systems with ball bearing nonlinearities and outer ring ovality under rotating unbalance excitation

Fawzi M. A. El-Saeidy
Damro-Salman, Desouk, Kafr-El-Sheikh, Egypt

(Received 27 October 1998; accepted for publication 7 October 1999)

The radial clearance in rolling bearing systems, required to compensate for dimensional changes associated with thermal expansion of the various parts during operation, may cause dimensional attrition and comprise bearing life, if unloaded operation occurs and balls skid [D. Childs and D. Moyer, ASME J. Eng. Gas Turb. Power **107**, 152–159 (1985)]. Also, it can cause jumps in the response to unbalance excitation. These undesirable effects may be eliminated by introducing two or more loops into one of the bearing races so that at least two points of the ring circumference provide a positive zero clearance [D. Childs, *Handbook of Rotordynamics*, edited by F. Ehrich (McGraw-Hill, NY, 1992)]. The deviation of the outer ring with two loops, known as ovality, is one of the bearing distributed defects. Although this class of imperfections has received much work, none of the available studies has simulated the effect of the outer ring ovality on the dynamic behavior of rotating machinery under rotating unbalance with consideration of ball bearing nonlinearities, shaft elasticity, and speed of rotation. To fill this gap, the equations of motion of a rotor–ball bearing system are formulated using finite-elements (FE) discretization and Lagrange's equations. The analyses are specialized to a rigid-rotor system, by retaining the rigid body modes only in the FE solution. Samples of the results are presented in both time domain and frequency domain for a system with and without outer ring ovality. It is found that with ideal bearings (no ovality), the vibration spectrum is qualitatively and quantitatively the same in both the horizontal and vertical directions. When the ring ovality is introduced, however, the spectrum in both orthogonal planes is no longer similar. And magnitude of the bearing load has increased in the form of repeated random impacts, between balls and rings, in the horizontal direction (direction of maximum clearance) compared to a continuous contact along the vertical direction (direction of positive zero clearance). This underlines the importance of the vibration measuring probe's direction, with respect to the outer ring axes, to capture impact-induced vibrations. Moreover, when the harmonic excitation is increased for a system with ideal bearings, the spectral peaks above forcing frequency have shifted to a higher-frequency region, indicating some sort of a hard spring mechanism inherent in the system. Another observation, is that for the same external excitation, vibration amplitude at forcing frequency in the bearing force spectrum is the same for systems with or without outer ring ovality. © *2000 Acoustical Society of America.* [S0001-4966(00)00802-X]

PACS numbers: 43.55.At [PJR]

INTRODUCTION

Rotating machinery incorporating radial rolling element bearings is widely used in industrial applications. These rotor systems are highly nonlinear, and among the sources of nonlinearities are the bearing radial clearance, deadband, and nonlinear stiffness. However, the radial clearance between the rolling elements and the races is required to compensate for dimensional changes associated with differential thermal expansion of the parts during operation. The radial clearance may cause dimensional attrition and compromise bearing life, if unloaded operation occurs and balls skid.[1] Moreover, the bearing clearance can cause jumps in the response to unbalance excitation. Such undesirable effects may be eliminated by introducing two or more lobes into one of the bearing races so that at least two points of the ring circumference provide a positive zero clearance. In these cases of close clearance contact, the race is designed so that it may elastically deform to avoid excessive compression forces on the moving balls.[2] For an outer ring with two lobes, the circumferential deviation, known as ovality, is a special case of the outer ring out-of-roundness, which in turn is one of the bearing distributed defects. These distribution defects include misaligned rings, eccentric races, off-size rolling elements, and out-of-round components. Another class of the bearing imperfections is local defects that include pits, spalls, and cracks in the rolling surfaces as well as contamination of the lubricant; see, for example, Refs. 3–5. The main sources of the outer ring vibrations in ball bearings are the cyclic variations in the bearing compliance to load (these vibrations are present even in a geometrically perfect bearing) and the excitations generated by the rolling elements rolling over geometrical imperfections.[6] The contribution of the distributed geometrical imperfections to the bearing vibrations has received both extensive analytical and experimental

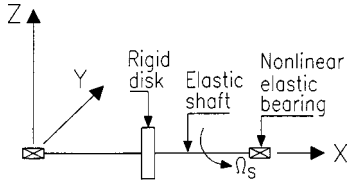

FIG. 1. Rotating shaft–ball bearings system.

studies.[7–11] The effect of the inner ring waviness and nonuniform diameters of the bearing rollers on vibrations of a rigid-rotor bearing system under a pure radial load due to the rotor weight was studied analytically and experimentally.[7] The bearing stiffness was modeled by a linear spring assuming weight to be supported on only two rollers at a time. And the relative displacements between the bearing inner and outer rings are assumed to be unaffected by both the elastic deformation of bearing and the rotor dynamics. The author ascribed poor agreement, especially for heavy loads, between the measured and calculated vibrations to approximations in the analytical model. The effect of the surface waviness and roughness of rings of preloaded roller bearings has been experimentally and analytically studied.[8] It was found that the outer ring imperfections can produce vibration spectra having tones at harmonics of the outer race ball passing frequency (outer race defect frequency). In Ref. 9, analytical expressions relating amplitudes of the imperfections on the bearing surfaces to the excitation forces of a thrust loaded ball bearing were presented. The Hertz equation for elastic contact was used to calculate ball forces where the relative approach between the races was approximated by a mean steady component (constant for all balls) due to applied load plus a smaller time-dependent component due to waviness. The second component is approximated by a spring constant equal to the slope of the load deflection curve at the mean deflection. Such approximations had left the author with a poor correlation between some of the measured and computed spectra. In Ref. 10, a theoretical linearized (with respect to displacement and form errors) model for the response of a shaft bearing system caused by waviness of both the outer and inner rings of axially loaded angular ball bearings has been presented. Examples for rigid-rotor bearing systems with system weight being neglected were presented. In Refs. 7–10, the bearing inner ring is rotating whereas the outer one is stationary.

In Ref. 11, the spectrum response due to distributed defects of axially loaded ball bearings with a rotating outer ring and a stationary inner one was analytically studied. The ball force is composed of a constant component plus a time varying, sinusoidal, one. The magnitude of both components is the same and assumed to be of the same value for all balls. Among defects considered is the outer ring ovality, and the model simulates only one malfunction at a time. A theoretical analysis of the vibration response of a rotating rigid shaft supported by two radial deep groove lubricated ball bearings under a rotating unbalance/inner ring surface waviness excitation was presented.[12] The bearings and their films are approximated by a set of nonlinear elastic springs and dampers and the analysis assumes continuous negative interference between the bearing balls and rings. In Refs. 7–12, the centrifugal action of the bearing rotating elements was neglected. Recently,[13] the axial and radial vibrations of a rigid shaft supported on a pair of geometrically perfect angular contact ball bearings as affected by the number of balls and the axial preload were theoretically studied. In Refs. 7–10 and 13, the external load (if it exists) is due to the shaft weight only. To the author's knowledge, the effect of the outer ring ovality and the shaft elasticity of systems incorporating radial ball bearings under a mass unbalance has not been studied before. This work simulates the outer ring ovality effect on vibrations of a rotor supported on nonlinear radial ball bearings and driven by a mass unbalance. Here we present a general formulation and a rigid shaft response.

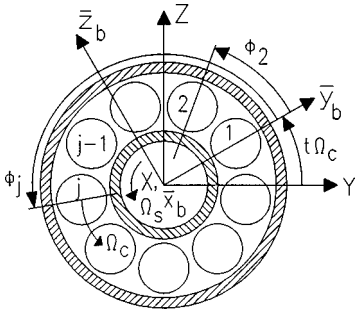

FIG. 2. Ball bearing elements and coordinate systems.

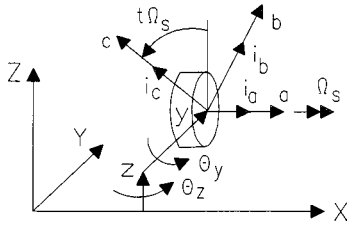

FIG. 3. Rotor deflected element.

I. ANALYTICAL MODEL

Figure 1 shows a rigid disk of a circular shape mounted through its center to an elastic shaft which in turn is mounted on two elastic radial ball bearings. These supporting bearings, however, are mounted into their rigid housings. The bearing details are shown in Fig. 2. In Fig. 1, the triad *XYZ* is a global coordinates system with its origin at the geometrical center of the shaft left bearing, where the *X* axis coincides with the shaft bearing's center line in the nonworking (zero speed) position of the system. The orientation of the de-

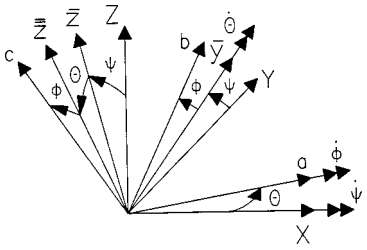

FIG. 4. Euler angles.

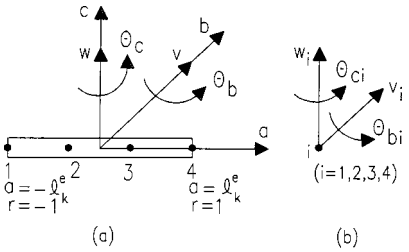

FIG. 5. Rotating shaft finite element.

flected rotor element in space (Fig. 3) is monitored using Euler angles (Fig. 4). The elastic rotating shaft is discretized using a C^0 four-node isoparametric beam finite element (Fig. 5) with four degrees of freedom (DOF) per node: two translational motions plus two total rotations. The C^0 beam finite elements were first used in rotor dynamics in Ref. 15, using a weak formulation, where the authors demonstrated the excellent performance of the C^0 elements compared to their counterparts of C^1, reported in the literature. The author[14] has presented a rotating shaft C^0 finite-element model using the finite-element displacement method taking into account translational motions, rotary inertia, shear deformations, gyroscopic moments, and mass unbalance forces. The advantages of our formulation compared to those of Ref. 15 are discussed in Ref. 14.

A. Shaft finite-element displacement field

In Fig. 4, *XYZ* is an inertial coordinate system and *abc* is a body-fixed coordinate system that rotates with the shaft differential element and represents its principal directions where i_a, i_b, i_c are unit vectors along axes *a*, *b*, *c* (Fig. 3). $\bar{x}\,\bar{y}\,\bar{z}$ is an auxiliary, moving frame system that initially coincides with *XYZ*. Euler angles are: (1) rotation ψ about the X axis results in Y coinciding with $\bar{y}$; (2) rotation θ about $\bar{y}$ results in the moving frame coinciding with $a\bar{y}\bar{z}$; and (3) spin ϕ about the *a* axis results in the moving frame coinciding with frame *abc*. The angular velocity vector is $\bar{\omega}=\bar{\omega}_a i_a+\bar{\omega}_b i_b+\bar{\omega}_c i_c$. Its components, expressed in the body coordinate system, are[14]

$$[\bar{\omega}_a\ \ \bar{\omega}_b\ \ \bar{\omega}_c]^T=[\dot{\psi}\cos\theta+\dot{\phi}\quad \dot{\psi}\sin\theta\sin\phi+\dot{\theta}\cos\phi\quad \dot{\psi}\sin\theta\cos\phi-\dot{\theta}\sin\phi]^T. \tag{1}$$

Figure 5(a) shows a typical four-node beam element of length $2l_k^e$ where *e* and *k* refer to an element and its number. A generic point located in a general position within the *k*th element has two translational motions v, w along *b*, *c* axes, respectively, plus two total rotations θ_b, θ_c around *b*, *c*. These local deformations are related to their global counterparts $d_k^e=[y\ z\ \theta_y\ \theta_z]^T$ by the transformation matrix $\bar{Q}_s$, such that

$$h_k^e=\bar{Q}_s d_k^e,\quad h_k^e=[v\ w\ \theta_b\ \theta_c]^T,$$

$$\bar{Q}_s=\begin{bmatrix} Q_s & 0_2\\ 0_2 & Q_s\end{bmatrix},\quad Q_s=\begin{bmatrix}\cos\Omega_s t & \sin\Omega_s t\\ -\sin\Omega_s t & \cos\Omega_s t\end{bmatrix}.$$

$\bar{0}_2$ is a 2×2 null matrix. The shaft *k*th finite element has 16-DOF [Fig. 5(b)] and its 16×1 global deformation vector, q_k^e, and the local counterpart, u_k^e, are $q_k^e=[y_j\ z_j\ \theta_{yj}\ \theta_{zj}]^T$, $u_k^e=[v_j\ \underline{w}_j\ \theta_{bj}\ \theta_{cj}]^T=\underline{A}_s\underline{q}_k^e$, $j=1,2,3,4$. In transformation matrix, $A_s=\mathrm{diag}[Q_s\ Q_s\ Q_s\ Q_s]$; each of its off-diagonal entries is a 4×4 null matrix. The global deformation vector, d_k^e, is related to the element nodal point variables vector, q_k^e, such that

$$d_k^e=Nq_k^e,\quad N=\begin{bmatrix} N_j & 0 & 0 & 0\\ 0 & N_j & 0 & 0\\ 0 & 0 & N_j & 0\\ 0 & 0 & 0 & N_j\end{bmatrix},\quad j=1,2,3,4. \tag{2}$$

N is 4×16 matrix of the element C^0 shape functions where N_1, N_2, N_3, $N_4=1/16[-(1-r)(1-3r)(1+3r), 9(1-r)\times(1-3r)(1+r), 9(1-r)(1+3r)(1+r), -(1-3r)(1+3r)\times(1+r)]$.

B. Shaft finite-element energy expressions

Utilize Eq. (1) and the assumption of small deflections and small angles of rotations $[\theta_y, \theta_z, \Omega_s=\theta\cos\psi, \theta\sin\psi, \dot{\phi}+\dot{\psi}$, $(\dot{\ })$ indicates differentiation with respect to time, $t]$ and follow the analyses of Ref. 14, the element kinetic energy $T_k^e=1/2(\dot{q}_k^e)^T M_k^e\dot{q}_k^e+1/2(\dot{q}_k^e)^T\bar{G}_k^e q_k^e+\rho_k^e\Omega_s^2 I_{pk}^e\det(J_k^e)$. I_{pk}^e is the element cross sectional area polar moment of inertia and $\underline{\rho}_k^e$ is the material mass density. M_k^e is the inertia matrix and G_k^e is the matrix due to gyroscopic effect, both defined in the *XYZ* frame. $\det(J_k^e)$ is a determinant of the Jacobian matrix, J_k^e.

$$(\bar{G}_k^e, M_k^e)=\int_{-1}^{1}(N)^T\left(\begin{bmatrix}\bar{0}_2 & \bar{0}_2\\ \bar{0}_2 & \rho_k^e\Omega_s I_{pk}^e\tilde{I}_2\end{bmatrix}N,\ \begin{bmatrix}\rho_k^e A_k^e I_2 & \bar{0}_2\\ \bar{0}_2 & \rho_k^e I_{dk}^e I_2\end{bmatrix}N\right)\det(J_k^e)\,dr.$$

$$\tilde{I}_2=\begin{bmatrix}0 & 1\\ -1 & 0\end{bmatrix},$$

I_2 is a 2×2 identity matrix, and A_k^e is the element cross sectional area. In Ref. 14, the element strain tensor $\epsilon_k^e=[\partial u/\partial a\ (\partial u/\partial b+\partial v/\partial a)\ (\partial u/\partial c+\partial w/\partial a)]^T$, where *a*, *b*, and *c* are the element spatial coordinates [Fig. 5(a)] and $u=u(a,b,c)=(c\,\theta_b-b\,\theta_c)$ is the axial displacement field of a point located in a general position in the cross section, from the centroidal axis, and stress vector $\sigma_k^e=\mathrm{diag}[E_k^e\ G_k^e\bar{K}_k^e\ G_k^e\bar{K}_k^e]^T$, where (E_k^e, G_k^e) are the moduli of elasticity and shear, respectively, and K_k^e is the cross sectional shear factor, along with the assumption of symmetrical cross section, were used to obtain the element potential energy

$$P_k^e=1/2(q_k^e)^T K_k^e q_k^e,\quad K_k^e=\int_{-1}^{1}(B_k^e)^T D_k^e B_k^e\det(J_k^e)\,dr,$$

$$D_k^e=\mathrm{diag}[\bar{K}_k^e G_k^e A_k^e\ \bar{K}_k^e G_k^e A_k^e\ E_k^e I_{dk}^e\ E_k^e I_{dk}^e],$$

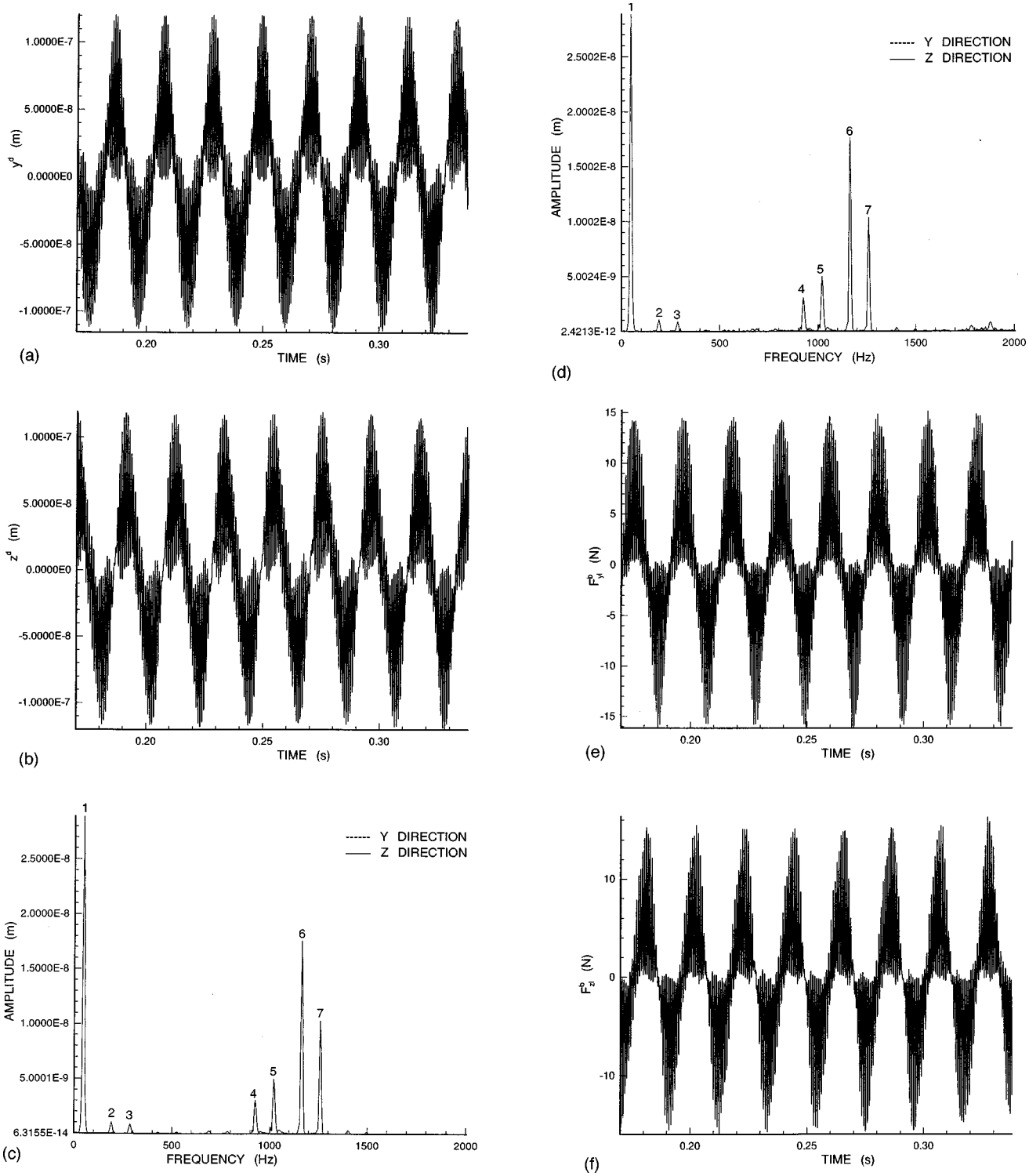

FIG. 6. (a) Time domain of y^d [light load (LL), ideal bearings (IBS)], (b) time domain of z^d (LL,IBS), (c) FFT of y^d and z^d (LL,IBS), (d) FFT of the left bearing motions (LL,IBS), (e) time domain of the left bearing force F^b_{yl} (LL,IBS), (f) time domain of the left bearing force F^b_{zl} (LL,IBS), (g) FFT of F^b_{yl} and F^b_{zl} (LL,IBS).

$$B^e_k=\begin{bmatrix} I_2\partial(J^e_k)^{-1}/\partial r & -\tilde{I}_2 \\ \overline{0_2} & I_2\partial(J^e_k)^{-1}/\partial r \end{bmatrix} N.$$

K^e_k, B^e_k, D^e_k are the element stiffness, global strain displacement, and material constants matrices. I^e_{dk} is the diametral moment of inertia. The matrix multiplication in the B^e_k's equation carries out differentiation of N with respect to r. Assume the kth finite-element mass unbalance to be uniformly distributed along the element length, then its generalized unbalance load vector is

$$F^e_{uk}=\int^1_{-1}(N)^T(\overline{Q_s})^T Q^e_{uk} Z^e_{uk} \det(J^e_k)\,dr,$$

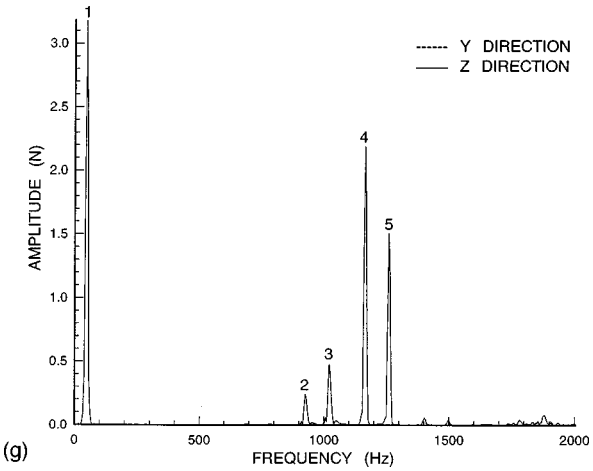

FIG. 6. (*Continued.*)

where $Z^e_{uk}=[\alpha^e_{bk}\ \alpha^e_{ck}\ 0\ 0]^T$, with α^e_{bk}, α^e_{ck} the mass center eccentricities along the *b*, *c* axes, and

$$Q^e_{uk}=\begin{bmatrix}\rho^e_k A^e_k \Omega_s^2 I_2 & \overline{0}_2\\ \overline{0}_2 & \overline{0}_2\end{bmatrix}$$

C. Discrete rigid disks

The *j*th disk kinetic energy, T^d_j, when expressed in the *XYZ* system, is $T^d_j=1/2(\dot{q}^d_j)^T M^d_j \dot{q}^d_j+1/2(\dot{q}^d_j)^T \overline{G}^d_j q^d_j+1/2 I^d_{pj}\Omega_s^2$, $q^d_j=[y^d\ z^d\ \theta^d_y\ \theta^d_z]^T$,

$$M^d_j=\begin{bmatrix} m^d_j I_2 & \overline{0}_2\\ \overline{0}_2 & I^d_{dj} I_2\end{bmatrix},$$

$$\overline{G}^d_j=\begin{bmatrix}\overline{0}_2 & \overline{0}_2\\ \overline{0}_2 & \Omega_s I^d_{pj}\tilde{I}_2\end{bmatrix}.$$

q^d_j, M^d_j, $\overline{G}^d_j$ are the disk global displacement vector and mass (inertia) and gyroscopic matrices, respectively. m^d_j is the mass, and I^d_{pj} and I^d_{dj} are as defined before but for the disk. Let α^d_{bj}, α^d_{cj} be the disk mass center eccentricities in the *b*, *c* directions, then its generalized unbalance force vector is

$$F^d_{uj}=(\overline{Q}_s)^T\begin{bmatrix} m^d_j\Omega_s^2 I_2 & \overline{0}_2\\ \overline{0}_2 & \overline{0}_2\end{bmatrix}[\alpha^d_{bj}\ \ \alpha^d_{cj}\ \ 0\ \ 0]^T.$$

D. Ball bearing with outer ring ovality

The advantages of the bearing model[14,16] compared to other existing analyses (see references listed in Ref. 14) are discussed in Ref. 14. This model is extended herein to account for outer ring ovality. Figure 2 depicts a ball bearing system without outer ring ovality and with uniform radial clearance where the global coordinate system *XYZ* has its origin at the bearing center with the *X* axis coinciding with the bearing axis. The frame $\overline{x_b y_b z_b}$ is a rotating coordinate system spinning with the bearing cage angular speed, Ω_c (rad/s), where the $\overline{x_b}$ axis coincides with the bearing axis. The bearing inner ring is lightly fitted on its shaft and is modeled as an integral part of it and thus rotates with the angular speed Ω_s. The bearing outer ring is fitted into its rigid and nonrotating housing. The bearing is treated as a 2-DOF system and is allowed to oscillate along, respectively, *Y*, *Z* axes, where coupling between bearing rotating elements and elastic rotating shaft is of the force-elastic oscillations type, i.e., the input to the bearing is shaft elastic motions and in return, the generated bearing loads are input to the shaft model.

Let the global vibrations of the *k*th rotating shaft element at its *l*th bearing point of action be y^b, z^b along the *Y*, *Z* directions that when transformed to the system $\overline{x_b y_b z_b}$ are given by

$$\overline{u}^b_{lk}=[\overline{v}^b\ \overline{w}^b]^T=Q_c q^b_{lk},$$

$$Q_c=\begin{bmatrix}\cos\Omega_c t & \sin\Omega_c t\\ -\sin\Omega_c t & \cos\Omega_c t\end{bmatrix}.\quad q^b_{lk}=[y^b\ z^b]^T.$$

The superscript *b* denotes bearing whereas the subscripts *l*,*k* stand for the bearing number and the element number. The relative displacement between the *l*th bearing outer and inner rings at the instantaneous position of the *j*th ball is $A_j=[\cos\phi_j\ \sin\phi_j]\overline{u}^b_{lk}$. A_j is measured in the spinning frame system where ϕ_j is the radial position of the *j*th ball measured relative to the rotating axis $\overline{y_b}$. The combined effect of the bearing clearance(s) and outer ring surface deviation is

$$\Delta^b_j=\Delta^b_o+\delta^b_o\cos 2(\Omega_c t+\phi_j). \tag{3}$$

Δ^b_j is the value of the bearing total clearance at the instantaneous position of the *j*th ball, Δ^b_o is the constant value of the bearing radial clearance, and δ^b_o is the amplitude of the outer ring out of roundness. In Eq. (3), δ^b_o should always be $\leqslant\Delta^b_o$, to avoid a negative interference between the rotating balls and the rings. Moreover, the formula is designed to produce an outer ring with elliptical deviation only. Other forms of deviation will be presented in paper(s) to follow. If $\delta^b_o=\Delta^b_o$, the time-dependent variation in the bearing clearance will simulate an outer ring ellipticity with a maximum clearance of a value of $2\Delta^b_o$ along the *Y* axis and a positive zero clearance along the *Z* axis. If $\overline{K}^b$ is the bearing stiffness constant, then in the bearing rotating frame the ball compression force, P_j, is

$$P_j=\begin{cases}\overline{K}^b(A_j-\Delta^b_j)^{3/2} & \text{for } A_j>\Delta^b_j \quad (M1)\\ -\overline{K}^b(|A_j+\Delta^b_j|)^{3/2} & \text{for } A_j<-\Delta^b_j \quad (M3)\\ 0 & \text{for } |A_j|<\Delta^b_j \quad (M2).\end{cases} \tag{4}$$

The horizontal and vertical components of the bearing force when expressed in the $\overline{x_b y_b z_b}$ frame are $[f^b_y\ f^b_z]^T_o=\sum_{j=1}^{Nb}P_j[\cos\phi_j\ \sin\phi_j]^T$, where *Nb* is the bearing number of balls. These forces when expressed in the *XYZ* frame are given by $[F^b_y\ F^b_z]^T_o=(Q_c)^T[f^b_y\ f^b_z]^T_o$. The inner ring global force vector is $F^b_{lk}=[F^b_y\ F^b_z]^T_i=[-F^b_y\ -F^b_z]^T_o$. The outer subscripts *i*, *o* denote bearing inner and outer races and the inner ones *y*, *z* stand for *Y*, *Z* directions. For the purpose of the element global load vector assembly, let inner ring global load vector, denoted by F^e_{lk}, be written in an expanded form as $F^e_{lk}=[(F^b_{lk})^T\ (M^b_{lk})^T]^T_i$. $M^b_{lk}=[M^b_y\ M^b_z]^T_i=[0\ 0]^T_i$ is the inner ring global loading moment vector. M^b_y, M^b_z are the moments around *Y*, *Z* axes.

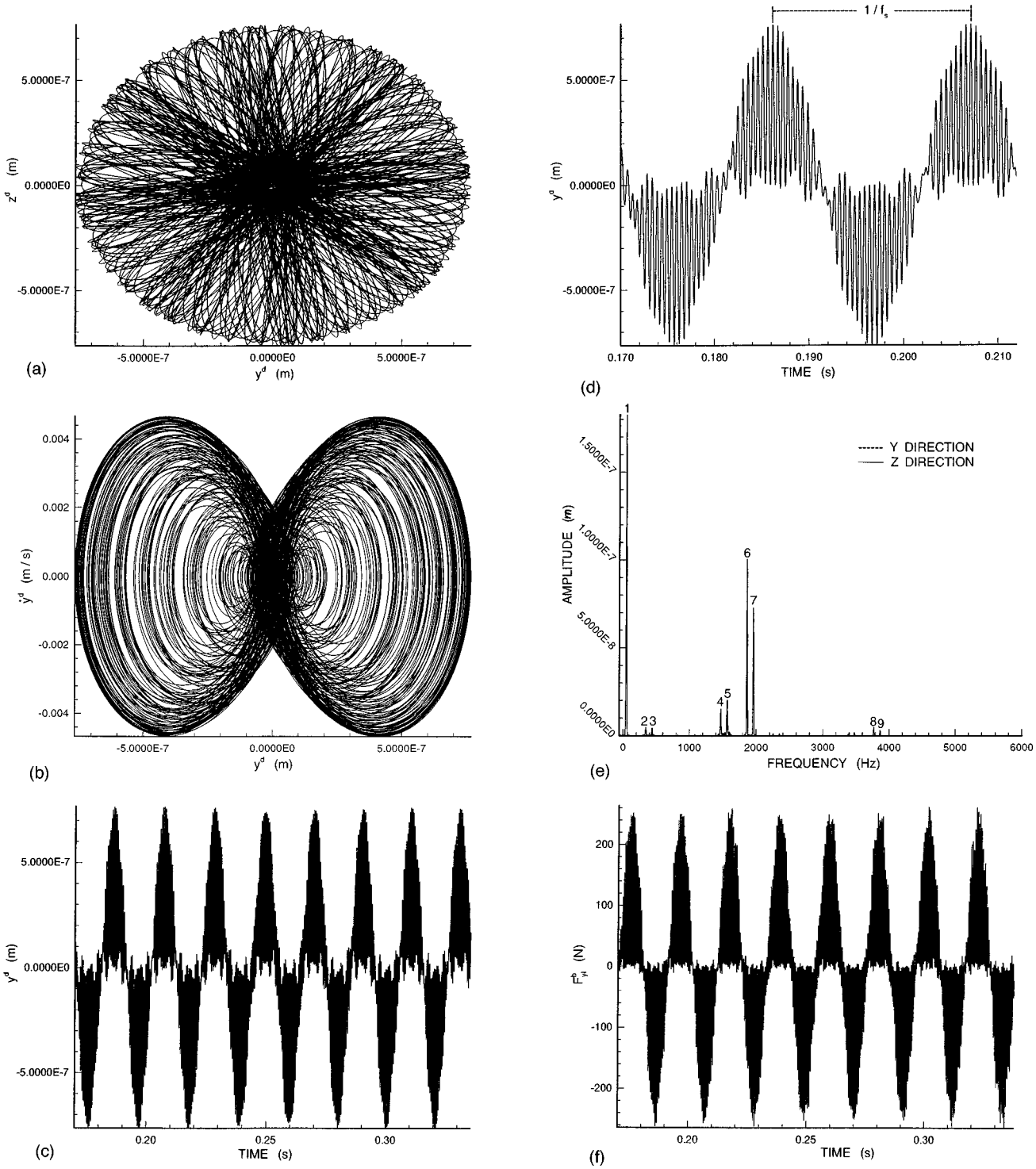

FIG. 7. (a) The disk whirl orbit [heavy load (HL), ideal bearings], (b) $\dot{y}^d$ vs y^d (HL,IBS), (c) time domain of y^d (HL,IBS), (d) the first portion of signal of (c), (e) FFT of y^d and z^d (HL,IBS), (f) time domain of the left bearing force F^b_{yl} (HL,IBS), (g) FFT OF F^b_{yl} and F^b_{zl} (HL,IBS).

E. Equations of motion and solution scheme

It is convenient to apply Lagrange's equations at the element level and then assemble into global matrices. Adjusting the dimension of F^e_{lk} to 16×1, the element external load vector is $Q^e_k = F^e_{uk} + \Sigma_{l=1}^{Neb} F^e_{lk}$, where *Neb* is the number of bearings supporting the *k*th shaft element. Using T^e_k, P^e_k (subsection Sec. I B), Q^e_k, and apply Lagrange's equations, the *k*th finite-element global equations of motion are $M^e_k \ddot{q}^e_k + G^e_k \dot{q}^e_k + K^e_k q^e_k = Q^e_k$. $G^e_k = 1/2[G^e_k - (G^e_k)^T]$ is the gyroscopic matrix. Similarly, for the *j*th rigid disk we get $M^d_j \ddot{q}^d_j + G^d_j \dot{q}^e_k = F^d_{uj}$. Let *Q*, *M*, *G*, *K* denote the system overall global load vector, mass, gyroscopic, and stiffness matrices. They are assembled from the individual elements using the one-dimensional (1D) array scheme for banded/sparse matrices.[17] If q denotes overall global displacement field, then equations of motion are $M\ddot{q} + Kq = Q - G\dot{q}$. Premultiplying by $(\Phi_N)^T$ and use transformations $[(q)^T(\dot{q})^T]^T = [(\Phi_N \eta)^T (\Phi_N \dot{\eta})^T]^T$ where η is the modal displacement

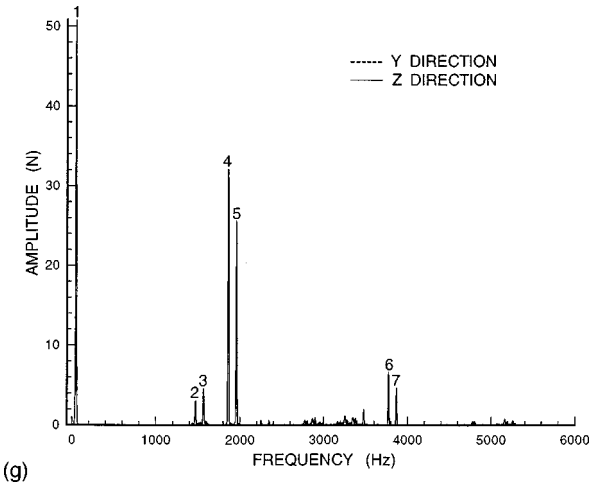

FIG. 7. (*Continued.*)

vector, we get $\ddot{\eta}+\underline{\omega}^2\eta=F$. $F=(\Phi_N)^TQ-(\Phi_N)^TG\Phi_N\dot{\eta}$ is the load vector expressed in the normal coordinates system. Φ_N is the normalized modal matrix obtained by solving the nonrotating shaft eigenvalue problem with free–free end conditions. $\underline{\omega}^2$ is the spectral matrix. The scheme used to solve for the rigid body motions is $\eta_p(t_j+\Delta t)=\eta_p(t_j)+\Delta t\,\dot{\eta}_p(t_j)+(\Delta t)^2F_p(t_j)$, $\dot{\eta}_p(t_j+\Delta t)=\dot{\eta}_p(t_j)+\Delta tF_p(t_j)$, $\ddot{\eta}_p(t_j+\Delta t)=F_p(t_j)$. $p=1,2,\ldots,Nr$ (=system total number of rigid body modes). The expressions η_p, $\dot{\eta}_p$ have been presented in Ref. 18 without derivation. In their derivation,[14] the force $F_p(t_j)$ is taken constant during time step, $t_{j+1}-t_j$ (i.e., Δt has to be small). A second constraint on Δt which is independent of the numerical integration scheme used comes from bearing nonlinearity. To change the contact mode from $M1$ to $M3$ or vice versa [Eq. (4)], the ball has to pass through $M2$ (no contact). To maintain this sequence of operation, Δt has to be small. That is, if Δt is large enough to cause a jump from $M1$ directly to $M3$ or vice versa without executing $M2$, this violates problem physics and causes bearing force and hence vibration amplitude to grow without limits, causing numerical instability. A small Δt introduces input energy/loss of input energy due to impact/loss of contact at the clearance boundary into the system smoothly, to avoid instability. Here, $\Delta t=2\times10^{-8}$ s provides accurate clearance simulation and results.

II. RIGID SHAFT RESULTS AND CONCLUSIONS

The system data are: Shaft: $\Omega_s=47.683\,72$ Hz, shaft length=0.5 m, shaft diameter=30 mm, $E^e=200$ GPa, Poisson's ratio=0.3, $\rho^e=7500$ kg/m^3, $K^e=0.883$; disk: $m^d=2$ kg, $I_p^d=0.03$ kg·m^2, $\alpha_b^d=\alpha_c^d=$variable; bearings: $Nb=9$, $D_b=9.525$ mm, bearing bore diameter=30 mm, outer bearing diameter=62 mm, bearing width=16 mm, inner race diameter=37.175 mm, outer race diameter=56.225 mm, inner raceway groove curvature radius=4.810 mm, outer raceway groove curvature radius=5.048 mm, $\Delta_{ol}^b=\Delta_o^b=$variable where Δ_o^b is the bearing radial clearance and subscripts l and r denote left and right bearings. $\delta_{ol}^b=\delta_{or}^b=$variable where δ_o^b is the amplitude of the ring ovality. The shaft is discretized with free–free end conditions and the eigenvalues problem of the system at rest is solved using the subspace iteration method with spectral shift to extract zero eigenvalues.[17] To simulate the rigid shaft motions, only the first four modes corresponding to zero eigenvalues are retained in the modal analysis. The solution is carried out for 16 shaft cycles and only the last 8 are reported.

A. System with ideal ball bearings

Figure 6(a) and (b) show time domains of the disk motions in the horizontal and vertical directions, respectively, for a light load ($\mu_b^d=\mu_c^d=50$ μm) and ideal bearings ($\Delta_{or}^b=\Delta_{ol}^b=\delta_{ol}^b=\delta_{or}^b=0$). Here the main period (not marked) of the reported eight shaft cycles is $1/f_s$ s ($f_s=\Omega_s$). Figure 6(c) shows spectra of y^d and z^d where $f_1=f_s$. The amplitudes are typically the same in each of the Y direction and the vertical direction. In other words, for a rotor–ideal bearings system under mass unbalance, the vibration signatures along the two principal directions should be identical. In Fig. 6(c), the other marked vibrations are $(f_2,f_3)=(190.35,286.10)=(4f_s,6f_s)$, $(f_4,f_5)=(925.06,1020.43)=(19f_s+f_c,21f_s+f_c)$, $(f_6,f_7)=(1163.48,1258.85)=(24f_s+f_c,26f_s+f_c)$ Hz. $f_c=18.979$ Hz is the cage frequency. The frequency spacing between the two vibrations of each pair is $2f_s$. The vibration pairs can also interpreted as whole numbers plus fractions of f_s, for example, $f_7=26.4f_s$. The left bearing orbit is similar to that of the disk (both not included), except for a minute difference which is attributed to the rocking (rotational) motions of the gyroscopically coupled system. The difference can be seen in fast Fourier transform (FFT) for the left bearing motions y_l^b, z_l^b along Y, Z axes shown in Fig. 6(d), compared to Fig. 6(c). The right bearing spectra (not shown) when compared to each of these two plots reflect a small dissimilarity in the energy content. Thus the rigid shaft vibrations can be modeled by retaining the rigid body modes only in the FE solution. The left bearing reaction forces are shown in Fig. 6(e) and (f) for horizontal and vertical loads, F_{yl}^b, F_{zl}^b, and their spectra are shown in Fig. 6(g), where the peaks, f_1-f_5, correspond, respectively, to f_1 and f_4-f_7 in each of Fig. 6(c) and (d).

Figure 7(a) illustrates disk orbit for a heavy load ($\mu_b^d=\mu_c^d=800$ μm) and ideal bearings. Because supporting bearings are identical and free from defects and external excitation is a mass unbalance, the trajectory envelope is almost a circle. The phase space $\dot{y}^d$ vs y^d is given in Fig. 7(b) and $\dot{z}^d$ vs z^d (not shown) is similar. For brevity, only the time domain plot of y^d is included in Fig. 7(c). The motion attractor is given in Fig. 7(d), on an expanded time scale, for the first portion of the record in Fig. 7(c) where the response has a main period of $1/f_s$ s. The marked one cycle comprises 39 equally spaced oscillations. That is, the frequency of each of these vibrations is $39f_s$ and this tone coincides with the peak $f_6=1859.665$ Hz$=39f_s$ in the spectrum depicted in Fig. 7(e) for y^d and z^d. Again, the energy content is the same for both oscillations and $f_1=f_s$. In Fig. 7(e), $(f_2,f_3)=(343.32,438.69)=(8f_s-2f_c,10f_s-2f_c)$ or $(7.2f_s,9.2f_s)$, $(f_4,f_5)=(1473.43,1568.79)=(30.9f_s,32.9f_s)$, $(f_6,f_7)=(1859.66,1955.02)=(39f_s,41f_s)$, $(f_8,f_9)=(3771.78,3867.15)=(79.1f_s,81.1f_s)$ Hz. F_{yl}^b in the time domain is

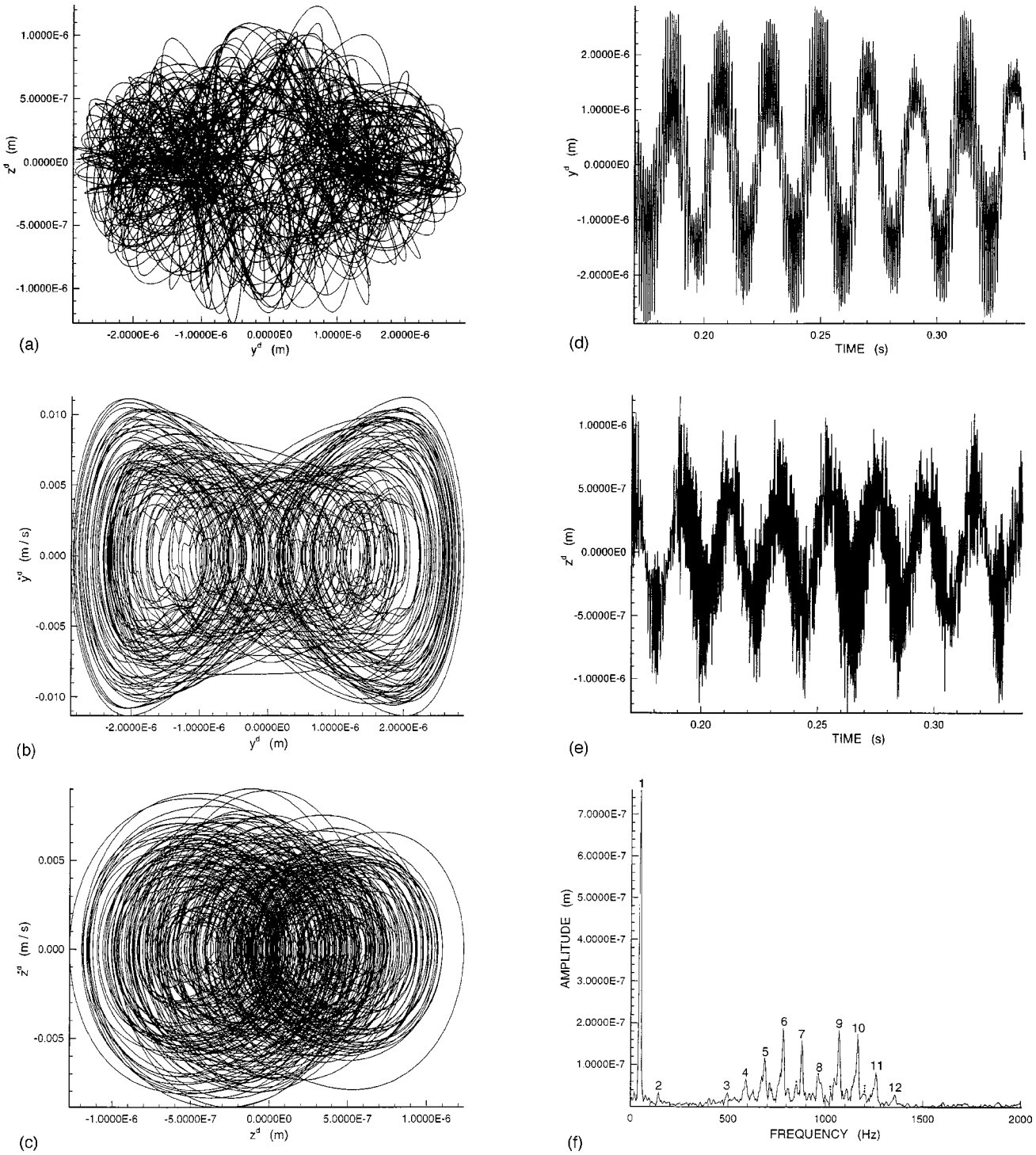

FIG. 8. (a) The disk whirl orbit [HL, defected bearings (DBS)], (b) $\dot{y}^d$ vs y^d (HL,DBS), (c) $\dot{z}^d$ vs z^d (HL,DBS), (d) time domain of y^d (HL,DBS), (e) time domain of z^d (HL,DBS), (f) FFT of y^d (HL,DBS), (g) FFT OF z^d (HL,DBS), (h) FFT of $\dot{y}^d$ (HL,DBS), (i) time domain of the left bearing force F^b_{yl} (HL,DBS), (j) time domain of the left bearing force F^b_{zl} (HL,DBS), (k) FFT of F^b_{yl} (HL,DBS), (l) FFT of F^b_{zl} (HL,DBS).

shown in Fig. 7(f). The F^b_{zl} plot is not shown; however, its FFT is given in Fig. 7(g), which shows the spectrum of F^b_{yl} as well as where f_1-f_7 coincide with f_1 and f_4-f_9 of Fig. 7(e), respectively. Increasing unbalance from 50 to 800 μm shifts vibrations above f_s to a higher region (the system becomes stiffer). Since the rotor system is linear axisymmetric and its bearing forces are nonlinear, the nonlinearity acts as a hardening spring.[2]

B. System with ball bearing outer ring ovality

For the system under the heavy load and $\Delta^b_{ol}=\Delta^b_{or}=\delta^b_{ol}=\delta^b_{or}=1$ μm, the disk orbit shown in Fig. 8(a) reflects the elliptical variation in clearance around bearing rings, the shaft-disk system has more freedom to oscillate along the Y direction whereas in the Z direction there is a continuous contact between the passing balls and the rings. This can be seen from the signals y^d, z^d in the time domain [Fig. 8(d)

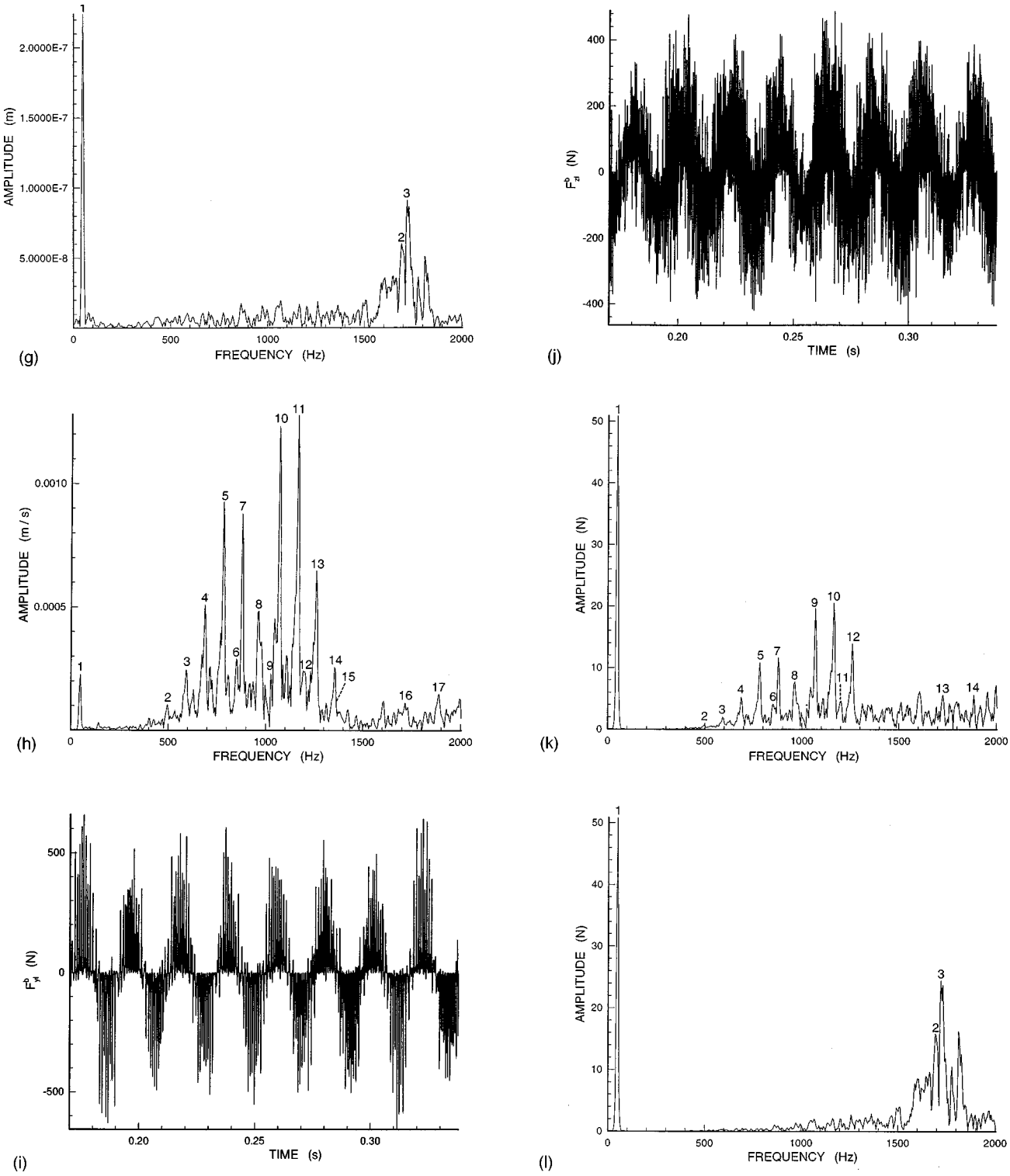

FIG. 8. (*Continued.*)

and (e)] and bearing forces [Fig. 8(i) and (j)]. As a result, the motions in the *XY* and *XZ* planes are no longer similar [see Fig. 8(b) and (c) for plots y^d vs $\dot{y}^d$, z^d vs $\dot{z}^d$]. Figure 8(f) and (g) show spectra for y^d and z^d where $f_1 = f_s$. The y^d spectrum is characterized by equispaced peaks: $f_3 - f_{12}$, with a spacing of $2f_s$. $f_5 = 4f_o$, the components marked (.,:,⋮) correspond to $(5f_o, 6f_o, 7f_o)$ and $f_{12} \approx 8f_o$ ($f_o = \mathrm{Nb}\, f_c = 170.811$ Hz is the outer ring ball passing frequency). Some of these vibrations are due to modulation of f_o harmonics, for example $f_7 = 877.38$ Hz is contributed by $5f_o + 1.23f_c$. The equispaced tones are not visible in Fig. 8(g), however, $(f_1, f_2, f_3) = (f_s, 9f_o, 9f_o + 2f_c)$. Figure 8(h) shows the spectrum of the disk velocity, $\dot{y}^d$, where $f_4 = 4f_o$. The bearings spectra for both displacement and velocity (not included) show that the equispaced spikes start to emerge at $4f_o$.

The left bearing forces in the time domain are depicted in Fig. 8(i) and (j). F^b_{yl} is characterized by a series of repeated random impacts between the bearing balls and its

rings whereas F_{zl}^{b} reflects a continuous contact. These patterns of variation are due to clearance variation as mentioned earlier. The maximum amplitude of F_{yl}^{b} exceeds that of F_{zl}^{b} by a factor of about 1.4. The dominant vibration, $f_1 = f_s$, has the same amplitude for both loads [see Fig. 8(k) and (l)]. In Fig. 8(k), the vibrations marked (4,6,.,11,13,14) are equal to $(4f_o, 5f_o, 6f_o, 7f_o, 10f_o, 11f_o)$ and the equispaced peaks are visible. From Figs. 7(g), 8(k), and (l), we see that amplitude of $f_1 = f_s$ is the same for the system with or without bearing ovality. As we can see, with the bearing ovality, the spectrum along the *Y* axis is different from that along the *Z* axis. That is, the orientation of the vibration measuring probe with respect to the outer ring axes is important, to capture the impact induced peaks. This finding is in agreement with the experimental observation for a ball bearing system with an outer ring with two localized defects.[5]

C. Conclusions

Analytical analyses are presented for the dynamic analysis of rotating machinery incorporating radial ball bearing nonlinearities and outer ring ovality subject to a mass unbalance. Rotating shaft finite elements, with shear deformation, rotary inertia, elastic bending, and gyroscopic effect, included along with Lagrange's equations, are employed to obtain equations of motion. The analyses are specialized to a rigid shaft system by retaining the rigid body modes only in the finite-element solution. Results in both time and frequency domains are discussed and the following concluding remarks pertain. (1) With ideal bearings, the response spectrum is qualitatively and quantitatively the same in both the horizontal and vertical directions. (2) With outer ring ovality, the spectra in both directions are dissimilar. In the maximum bearing clearance direction (*Y* axis), the spectrum is characterized by a bundle of equispaced vibrations above f_s, and harmonics of the outer ring ball passing frequency are prominent. The bearing dynamic force in the *Y* direction exhibits a pattern of repeated random impacts between the bearing balls and rings compared to continuous contact in the positive zero clearance direction (*Z* axis). Therefore, the vibration measuring probes' orientation with respect to outer ring axes is important, to capture impact induced vibrations. (3) With ideal bearings, increasing mass unbalance caused vibration peaks above f_s to shift to a higher-frequency region, and system nonlinearity acts as a hardening spring. (4) The adopted modeling approach, that is solving for a rigid shaft system using existing FE codes for rotor dynamics, may be of interest to the dynamicist.

[1] D. W. Childs and D. S. Moyer, ''Vibration characteristics of the HPOTP (high-pressure oxygen turbopump) of the SSME (space shuttle main engine),'' ASME J. Eng. Gas Turb. Power **107**, 152–159 (1985).
[2] D. Childs, *Handbook of Rotordynamics*, edited by F. Ehrich (McGraw-Hill, NY, 1992).
[3] O. Gustafsson and T. Tallian, ASLE Trans. **5**, 197–209 (1962).
[4] T. Igarashi and H. Hamada, Bull. JSME **25**, 994–1001 (1982).
[5] T. Igarashi and J. Kato, Bull. JSME **28**, 492–499 (1985).
[6] T. Tallian and O. Gustafsson, ASLE Trans. **8**, 195–207 (1965).
[7] C. Sunnersjö, J. Sound Vib. **98**(4), 455–474 (1985).
[8] Y. Su, M. Lin, and M. Lee, J. Sound Vib. **165**(3), 455–466 (1983).
[9] F. Wardle, Proc. Inst. Mech. Eng. **202**, 305–319 (1988).
[10] E. Yhland, ASME J. Tribol. **114**, 348–359 (1992).
[11] L. D. Meyer, F. F. Ahlgren, and B. Weichbrodt, ''An analytical model for ball bearing vibrations to predict vibration response to distributed defects,'' Trans. of ASME J. Mechanical Design **102**, 205–210 (1980).
[12] H. Rahnejat and R. Gohar, Proc. Inst. Mech. Eng. **199**, 181–193 (1985).
[13] N. Akturk, M. Uneeb, and R. Gohar, ASME J. Tribol. **119**, 747–753 (1997).
[14] F. M. A. El-Saeidy, ''Finite element modeling of rotor-shaft-rolling bearing systems with consideration of bearing nonlinearities,'' J. Vib. Control **4**, 541–602 (1998).
[15] T. C. Gmür and J. D. Rodrigues, ''Shaft finite elements for dynamics analysis,'' ASME J. Vibration and Acoustics **113**, 482–493 (1991).
[16] F. M. A. El-Saeidy, ''Finite element dynamic analysis of a rotating shaft with or without nonlinear boundary conditions subject to a moving load,'' Nonlinear Dynamics (to be published).
[17] F. M. A. El-Saeidy, DAMRO 1:A General Purpose Finite Element Program, 1993.
[18] M. L. Adams, J. Sound Vib. **71**(1), 129–144 (1980).

Reverberation time and maximum background-noise level for classrooms from a comparative study of speech intelligibility metrics

Sylvio R. Bistafa[a] and John S. Bradley
Institute for Research in Construction—Acoustics, National Research Council—Canada, 1500 Montreal Road, Ottawa, Ontario K1A 0R6, Canada

(Received 4 June 1999; revised 18 October 1999; accepted 27 October 1999)

Speech intelligibility metrics that take into account sound reflections in the room and the background noise have been compared, assuming diffuse sound field. Under this assumption, sound decays exponentially with a decay constant inversely proportional to reverberation time. Analytical formulas were obtained for each speech intelligibility metric providing a common basis for comparison. These formulas were applied to three sizes of rectangular classrooms. The sound source was the human voice without amplification, and background noise was taken into account by a noise-to-signal ratio. Correlations between the metrics and speech intelligibility are presented and applied to the classrooms under study. Relationships between some speech intelligibility metrics were also established. For each noise-to-signal ratio, the value of each speech intelligibility metric is maximized for a specific reverberation time. For quiet classrooms, the reverberation time that maximizes these speech intelligibility metrics is between 0.1 and 0.3 s. Speech intelligibility of 100% is possible with reverberation times up to 0.4–0.5 s and this is the recommended range. The study suggests ''ideal'' and ''acceptable'' maximum background-noise level for classrooms of 25 and 20 dB, respectively, below the voice level at 1 m in front of the talker.
[S0001-4966(00)03002-2]

PACS numbers: 43.55.Hy, 43.55.Fw, 43.71.Gv, 43.55.Br [JDQ]

INTRODUCTION

Reverberation and background noise control speech intelligibility in a room. Several objective speech intelligibility metrics that take into account both the room sound reflections and noise have been proposed.[1–5] Many of them can be measured in real rooms, and, for some, commercial measuring equipment is available. No thorough comparative study exists concerning the adequacy of the various speech intelligibility metrics that have been proposed. An approach for such a study could be experimental, evaluating the speech intelligibility metrics in rooms with different reverberation times and background-noise levels. Room acoustics simulations in a laboratory would avoid the difficulty of finding real rooms that cover the necessary range of the acoustical variables. However, both methods are costly and time consuming. When the sound field in the room is diffuse, analytical formulas for the speech intelligibility metrics can be developed. In this case, the room reverberant response results in an exponential decay, with the decay constant of the room inversely proportional to reverberation time. The influence of the background noise can be taken into account in the form of a noise-to-signal ratio, where the signal is the speech energy at the receiver position. Although the diffuse sound field condition is difficult to achieve in real rooms, when applied uniformly to all the speech intelligibility metrics, it provides conditions for these comparisons. Another possible approach for comparing speech metrics would be to use room acoustics computer simulations such as ray-tracing-type programs. This approach is also under development by the authors.

There have been a number of modern studies of speech intelligibility in classrooms such as that of Houtgast[6] who experimentally verified the effect of background noise on speech intelligibility in classrooms. Bradley[7] developed an acoustical energy-based useful-to-detrimental sound ratio, and correlated it with speech intelligibility test scores in real classrooms. He also derived optimum conditions, in terms of background noise and reverberation time, for rooms for speech.[8] Hodgson[9] surveyed almost 50 university classrooms with respect to speech intelligibility conditions, and recently measured and developed empirical prediction models of typical speech and background-noise levels in university classrooms.[10] However, no study has systematically verified the adequacy of different speech intelligibility metrics when applied to classrooms. It was felt that specific important issues particular to classroom acoustics, such as recommended reverberation time and classroom-noise criteria, could be obtained from a comparative study of available speech intelligibility metrics.

A survey of the available speech intelligibility metrics that take into account the room sound reflections and background noise reveals that they can be classified into three different categories. The first category includes speech intelligibility metrics that make use of the acoustical energy ratio concept. This concept classifies the available acoustical energy (direct+reflected+noise) into a useful part (direct+earlier arriving reflected) and a detrimental part (later arriving reflected+noise). The ratio of these has

[a]Visiting Scientist, Department of Mechanical Engineering, Polytechnic School, University of São Paulo, São Paulo, Brazil.

proven to be correlated to speech intelligibility by different authors.[1–3] The second category is used by just one type of metric known as the speech transmission index STI, and makes use of the concept of the modulation transfer function[4] $m(F)$. The third category is an experimental based procedure that gives an expected articulation score as a function of the reverberation time and the signal-to-noise ratio. The articulation score is that of a syllable articulation type of test in which the result is given as the articulation loss of consonants.[5] Although the form of these types of measures is quite different, a recent experimental study showed their values to be strongly correlated.[11]

All of the acoustic energy ratio-based speech intelligibility metrics make use of the concepts derived from the experimental results of Haas[12] in the beginning of the 1950s. These results, using speech sounds, show that reflections arriving at the listener with delays as long as 40 ms after the direct sound are not perceived as echoes. The listener perceives an increase in loudness, a pleasant modification of the quality of the sound, and an apparent spatial enlargement of the sound source. These conditions are considered useful for speech intelligibility because they give support to the source. Reflections, which arrive later, are subjectively judged as reverberation or even echoes in the most unfavorable cases. Reverberation and echoes, as well as noise, are detrimental to speech communication.

The inertia or the integrating properties of the hearing system, which lead to early reflections being subjectively summed with the direct sound to increase its apparent strength, were reported as early as 1935 by Aigner and Strutt.[13] They were the first to suggest an acoustic-energy-ratio-based formula to quantify the combined effects of room acoustics and background noise on speech intelligibility. They called their measure impression Q, which is given by

$$Q=(E_d+E_e)/(E_l+E_n), \tag{1}$$

where E_d is the direct sound energy, E_e is the useful part of the reflected sound energy, which comes to the ear not later than $\frac{1}{16}$ s after the direct sound, E_l is the remaining part of reflected sound energy coming later than $\frac{1}{16}$ s, and E_n is the noise energy. Aigner and Strutt went further by putting a lower threshold of $Q=1$ for a satisfactory ''sound impression.''

In fact, Q is what we call today a useful-to-detrimental sound ratio, and for $E_n=0$ we get what is called a useful-to-late sound ratio. Equation (1) essentially forms the basis of most speech intelligibility metrics that were later developed. The importance of the findings of Aigner and Strutt were perhaps too advanced to be appreciated at that time.

Lochner and Burger[1] further developed the useful-to-detrimental sound ratio concept in a long series of experiments. In their speech metric the useful part of the ratio included a weighted energy sum of early reflections. The weighting varied according to the amplitude and time of arrival of each early reflection. Latham[2] evaluated the Lochner and Burger procedure in a number of theaters, and only with minor modifications found it to be a quite successful predictor of speech intelligibility. Several authors suggested that a 50-ms early time limit was appropriate for speech. For example, Thiele[14] proposed an early-to-total sound ratio termed definition D (or ''Deutlichkeit''), and more recently Bradley[3,7] used the early-to-late sound ratio, called C_{50}, both to characterize the effects of a room on speech intelligibility. Bradley[3] also simplified Lochner and Burger's useful-to-detrimental sound ratio concept by using a simple unweighted sum of the useful (early) speech energy over the first 50 ms. U_{50}, the resulting useful-to-detrimental sound ratio, was found to be well correlated with articulation scores.

The speech transmission index STI is based on the concept of the modulation transfer function $m(F)$. In the beginning of the 1970s Houtgast and Steeneken[4] introduced this totally different concept for the use in the field of room acoustics. When the speech signal is transmitted through an enclosure, its amplitude modulation, rather than the carrier, contains the important information. The room reverberation and noise cause a decrease in the amplitude modulation. Here $m(F)$ quantifies the degree of preservation of the original speech amplitude modulations, as a function of modulation frequency, as it is transmitted throughout the room.

It can be shown[15,16] that the complex modulation transfer function equals, apart from a constant factor, the complex Fourier transform of the sound power density impulse response function. As originally proposed by Houtgast and Steeneken, the $m(F)$ only reflects the amplitude characteristic of modulation transfer and the phase characteristic is disregarded. Hence,

$$m(F)=\frac{\left|\int_0^\infty p(t)e^{-j2\pi Ft}\,dt\right|}{\int_0^\infty p(t)\,dt}, \tag{2}$$

where $p(t)$ is the room sound power density impulse response. Here $p(t)$ is nothing more than the time derivative of the sound decay curve.

Each $m(F)$ value is converted into an apparent signal-to-noise ratio, averaged, and normalized, resulting in a single figure of merit called the speech transmission index STI, ranging from zero to one, for each octave frequency band of interest. A procedure to obtain the STI as a single number, based on weighted STI values in seven octave frequency bands, from 125 Hz to 8 kHz, is given by Houtgast *et al.*[15] The STI also has a simplified version, called rapid speech transmission index RaSTI, and calculated only in the 500 Hz and 2 kHz octave frequency bands.[17] Both the STI and RaSTI were found to correlate well with speech intelligibility.[15,17]

Another measure of the intelligibility of speech in rooms known as the articulation loss of consonants $\mathrm{Al}_{\mathrm{cons}}$ was proposed by Peutz,[5] based on tests conducted under varying conditions of reverberation, distance to the source, and background noise. These tests resulted in the development of an empirical relationship, without background noise, where the articulation loss of consonants is expressed as a function of the distance to the source r, the room volume V, and the reverberation time T, in the form

$$\%\mathrm{Al}_{\mathrm{cons}}=\frac{200\cdot(rT)^2}{V}, \tag{3}$$

where $\%\mathrm{Al}_{\mathrm{cons}}$ is the articulation loss of consonants as a percentage. Equation (3) should be used with S.I. units, and is valid as long as the distance to the source is less than or equal to a certain *critical distance*, after which $\%\mathrm{Al}_{\mathrm{cons}}$ is constant and equal to $9T$. The critical distance r_c is given by $0.21\sqrt{V/T}$ in meters. The $\%\mathrm{Al}_{\mathrm{cons}}$ is normally evaluated with the reverberation time T given in the 2-kHz octave or one-third octave frequency band.

The logarithm of $\%\mathrm{Al}_{\mathrm{cons}}$ was found to be linearly related to the background noise, expressed as a signal-to-noise ratio, and having the reverberation time as a parameter. The expression for $\%\mathrm{Al}_{\mathrm{cons}}$ that incorporates both the room acoustics and the background noise will be presented later.

I. SPEECH INTELLIGIBILITY METRICS BASED ON THE ACOUSTICAL ENERGY RATIO

The impulse response completely defines the properties of a system such as a room. Thus, the steady-state response and the reverberant response can both be determined from the impulse response. For the analytical formulation of the various speech intelligibility metrics, it is first necessary to establish an expression to describe the room impulse response. Although the impulse response of a room can be found experimentally, it can also be obtained in analytical form, assuming the sound field in the room is diffuse.[18] Unfortunately, the assumption of a diffuse sound field is only an approximation to conditions in most rooms.

As shown elsewhere,[19] the stationary direct and reflected sound energy densities e_d and e_r are respectively given by

$$e_d = \frac{qP}{4\pi c r^2} \tag{4}$$

and

$$e_r = \frac{qP}{4\pi c r_h^2}, \tag{5}$$

where q and P are the directivity index and the sound power of the acoustic source, respectively, and c is the sound velocity. Here r is the distance from the acoustic source to the receiver, and r_h is the *reverberation distance*, defined as the distance for which the reflected sound energy density equals the direct sound energy density ($e_r = e_d$). The square of the reverberation distance is given by

$$r_h^2 = \frac{kVq}{4\pi c(1-\overline{\alpha})}. \tag{6}$$

In Eq. (6), V is the room volume, $\overline{\alpha}$ is the average sound absorption coefficient, and $k = 13.82/T$, where T is the reverberation time.

Assuming for simplicity that the direct and the reverberant fields are established at a distance r from the source at the same time $t=0$, it can be shown[18] that the sound power density describing the room impulse response for $t \geqslant 0$ is given by

$$p(t) = \frac{qP}{4\pi c}\left[\frac{1}{r^2}\,\delta(t) + \frac{k}{r_h^2}e^{-kt}\right], \tag{7}$$

where $\delta(t)$ is the Dirac delta function at $t=0$. The second term in Eq. (7) shows that for the diffuse field, the reflected sound power density decays exponentially with decay constant $-k$.

Once the impulse response is known, the sound energy density to arrive at the receiver position in the time interval $[0-t]$ can be found using the following integral operation:

$$e_{0-t} = \int_0^t p(t)\,dt. \tag{8}$$

The room stationary sound energy density $e = e_d + e_r$ is found by putting $t = \infty$.

We shall now develop the speech intelligibility metrics based on the useful-to-detrimental sound ratio concept under the fundamental assumption of diffuse sound field inside the enclosure. This ratio varies according to what is considered useful and detrimental sound energy for speech communication. There is no complete agreement on how to quantify these different energy portions of an impulse response. Several authors propose different forms for doing that, some of them simply recommend different values for the duration of the early time interval, while others suggest different prescriptions to quantify this ratio.

A. The impression *Q* in a reverberant enclosure with diffuse sound field

Once the enclosure impulse response function is known, Eq. (8) allows the determination of the sound energy density that exists between any specified time limits of integration, from zero to infinity. Hence an expression for the Aigner and Strutt[13] impression Q can now be obtained at a given receiver in any reverberant enclosure for which the assumption of diffuse sound field holds.

Equation (1) written in terms of sound energy densities is given by

$$Q = (e_d + e_e)/(e_l + e_n), \tag{9}$$

where e_d, e_e, and e_l are the sound energy densities of the direct, early, and late sounds, respectively, and e_n is the background noise energy density given by $\overline{p_n^2}/\rho c^2$. Here ρ is the air density, and $\overline{p_n^2}$ is the mean square value of a uniform and stationary noise pressure inside the room. For a threshold of separation of $\frac{1}{16}$ s for the early-reflected sound energy density, and with the help of Eqs. (7) and (8), Eq. (9) can be written as

$$Q = \frac{1 + (r_h/r)^2 - e^{-0.86/T}}{e^{-0.86/T} + 10^{(L_n - L_r)/10}}, \tag{10}$$

where $(L_n - L_r)$ can be taken as $10\,1g(\overline{p_n^2}/\overline{p_r^2})$, where $\overline{p_r^2}$ is the mean square value of the reflected sound pressure.

B. The definition D_{50}

Metrics using the ratio of energies concept began to be measured and correlated with speech intelligibility in the 1950s. One of the earliest attempts was due to Thiele,[14] who used the early-to-total sound energy ratio instead, and named it definition D. The early (useful) sound was considered to be the direct and the reflected sound energy that arrives at the

receiver position within 0.05 s after the direct sound. In this case, with the aid of Eqs. (7) and (8), an expression for D_{50} can be found in the form

$$D_{50}=\frac{1+(r_h/r)^2-e^{-0.69/T}}{1+(r_h/r)^2}. \tag{11}$$

Definition *D*, as it was originally proposed, does not take into account the detrimental effect of background noise. Its importance lies in the fact that it represents one of the earliest attempts to numerically quantify the influence of the acoustics of the room on speech intelligibility.

C. The useful-to-detrimental sound ratio U_{50}, and the useful-to-late sound ratio C_{50}

One of the most tested predictors of speech intelligibility in classrooms, which uses the useful-to-detrimental sound ratio concept, is in fact a variation of the impression *Q*. Bradley[7] found that a useful-to-detrimental sound ratio with an early time limit of 0.05 s, expressed in decibels and called U_{50}, is better suited for the evaluation of speech intelligibility in classrooms and other similar sized rooms:

$$U_{50}=10\lg\left[\frac{1+(r_h/r)^2-e^{-0.69/T}}{e^{-0.69/T}+10^{(L_n-L_r)/10}}\right]. \tag{12}$$

A useful-to-late sound-ratio-based speech intelligibility metric, called C_{50}, can also be obtained by putting the second term in the denominator of Eq. (12) equal to zero:

$$C_{50}=10\lg\left[\frac{1+(r_h/r)^2-e^{-0.69/T}}{e^{-0.69/T}}\right]. \tag{13}$$

D. Weighted useful-to-detrimental sound ratio

Lochner and Burger[1] found in experiments with single echoes that a fraction of the energy arriving within the time limit of 0.095 s is integrated with the direct sound. The fraction α depends on the strength of the reflection and delay time relative to the direct sound. This weighted useful-to-detrimental sound ratio was called signal-to-noise ratio R_{sn}, and can be calculated according to

$$R_{\mathrm{sn}}=10\lg\left[\frac{\int_0^{0.095}\alpha(t)p(t)\,dt}{\int_{0.095}^{\infty}p(t)\,dt+10^{(L_n-L_r)/10}}\right]. \tag{14}$$

Different curves for the fraction $\alpha(t)$ of the reflected sound energy, integrated with the direct sound energy by the hearing mechanism, were obtained for different levels and delay times relative to the direct sound. For the current calculations these were approximated by the linear relation for $\alpha(t)$:

$$\alpha(t)=1 \quad \text{for } 0\leqslant t<t_1,$$

$$\alpha(t)=\frac{t_2-t}{t_2-t_1} \quad \text{for } t_1\leqslant t\leqslant t_2, \tag{15}$$

and

$$\alpha(t)=0 \quad \text{for } t>t_2,$$

with $t_1=0.035$ s and $t_2=0.095$ s.

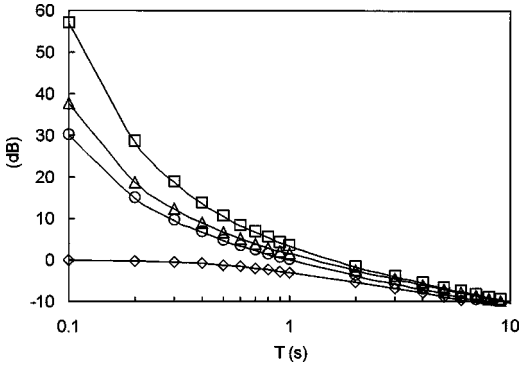

FIG. 1. Values of the useful-to-late sound ratios R'_{sn} (□), Q'_{dB} (△), C_{50} (○), and D_{50} in dB (◇), as a function of the reverberation time *T*.

When Eqs. (7) and (15) are substituted into Eq. (14), an expression for Lochner and Burger's signal-to-noise ratio R_{sn} can be found in the form

$$R_{\mathrm{sn}}=10\lg\left[\frac{1+(r_h/r)^2+1.21T(e^{-1.31/T}-e^{-0.48/T})}{e^{-1.31/T}+10^{(L_n-L_r)/10}}\right]. \tag{16}$$

E. The detrimental sound energy based on an ideal reverberant decay curve

A similar approach to that of Lochner and Burger was adopted by Niese,[20] who suggested the same form for $\alpha(t)$ as given by Eq. (15), but with different time limits, $t_1=0.017$ s and $t_2=0.033$ s, in order to calculate the useful sound energy. Niese considered as detrimental not all the reflected sound energy, but only that portion that arrives after $t_2=0.033$ s and which is in excess of an idealized impulse response. For enclosures with a diffuse sound field for which the impulse response is given by Eq. (7), Niese's idealized impulse response is never exceeded. The Niese approach to this problem is useful to identify strong detrimental reflections (echoes) in room impulse responses obtained experimentally.

F. Useful-to-detrimental sound ratios for $r\gg r_h$ in the absence of background noise

At receiver positions sufficiently far away from the sound source, for which $r\gg r_h$, and in the absence of background noise, the impression *Q* reduces to a useful-to-late sound ratio Q'. The corresponding expression, in decibels, is then given by

$$Q'_{\mathrm{dB}}=10\lg\left(\frac{1-e^{-0.86/T}}{e^{-0.86/T}}\right). \tag{17}$$

In the absence of background noise U_{50} will be equal to C_{50}, and R_{sn} will be given by Eq. (16), with the second term in the denominator equal to zero, which will be called R'_{sn}.

Figure 1 shows plots of the useful-to-late sound ratios R'_{sn}, Q'_{dB}, and C_{50} as a function of the reverberation time *T*, which were calculated with $r_h/r=0$ (because $r\gg r_h$). All three measures show an increase in the useful-to-late sound ratio as the reverberation time decreases, and tend asymptotically to infinity as the reverberation time approaches zero.

All three follow similar trends with only shifts in levels for the same reverberation time. Also shown in Fig. 1 is the curve for D_{50} in dB, which was calculated using Eq. (11), for $r_h/r=0$. It can be seen that D_{50} in dB follows a trend similar to the other three useful-to-late sound ratios, for reverberation times as low as 1 s or so, below which it tends asymptotically to zero instead. Therefore, as far as correlating the room acoustical effects with speech intelligibility is concerned, the useful-to-late sound ratios provide a larger change in dB than the useful-to-total sound ratio for the same change in reverberation time, when the reverberation time is less than about 1 s. This makes the useful-to-late sound ratios more convenient than the useful-to-total sound ratio for ''fine-tuning'' the reverberation time for best speech intelligibility. This is an important characteristic since it is generally accepted that the reverberation time for speech in small rooms such as classrooms should lie somewhere below 1 s.

G. The classroom noise-to-signal ratio

In the denominator of the expressions for all of the useful-to-detrimental sound ratios, the effects of the noise appear as a noise-to-signal ratio instead of the conventional signal-to-noise ratio. Since the noise-to-signal ratio $10^{(L_n-L_r)/10}$ is a form that naturally occurs in the derived formulas for the useful-to-detrimental sound ratios, it will be used throughout this paper rather than the conventional signal-to-noise ratio. Here L_n is the background-noise level, assumed to be stationary and uniform throughout the classroom, and L_r is the reflected sound pressure level. The latter is, in fact, the reflected speech level in the classroom that we will simply call the *classroom level* L_{clasrm}. The classroom level will then be given by

$$L_{\text{clasrm}}=L_{\text{sp1m}}+10\lg\left(\frac{1}{r_h^2}\right)\text{dB}, \tag{18}$$

where L_{sp1m} is the long-term anechoic speech level at 1 m straight ahead of the talker. For $c=344$ m/s, and considering that $k=13.82/T$, the substitution of Eq. (6) into Eq. (18) results in

$$L_{\text{clasrm}}=L_{\text{sp1m}}+10\lg\left[\frac{T}{0.0032\cdot V\cdot q}e^{-0.16(V/S)(1/T)}\right]\text{dB}. \tag{19}$$

According to Eyring's reverberation formula,[19] the exponential term in Eq. (19) is equal to $(1-\overline{\alpha})$. This quantity gives the fraction of the sound energy remaining in the room after the very first reflection at the room surface with area S. It is a function of the reverberation time T and the ratio V/S. Most regularly shaped rooms have volume-to-surface area ratios between 0.5 and 2.5 m. Rectangular shaped classrooms have a volume-to-surface area ratio around 1 m. In this case, in Eq. (19), $V/S=1$ m, and the classroom noise-to-signal ratio can be written as

$$10^{(L_n-L_r)/10}=10^{(L_n-L_{\text{clasrm}})/10}=\left[0.0032\frac{V\cdot q}{T}e^{0.16/T}\cdot 10^{(L_n-L_{\text{sp1m}})/10}\right]. \tag{20}$$

When Eq. (20) is substituted into the denominator of the useful-to-detrimental sound ratios, they can be readily calculated from the room volume, the reverberation time, the vocal output level at 1 m, the directivity, and the noise level. For a given room volume, this therefore allows the speech intelligibility metric to be determined as a function of the reverberation time and the expected noise-to-signal ratio. The latter is now more adequately defined as a function of parameters readily available at the design stage of a room, that is, the vocal (or other source) output at 1 m, the directivity straight ahead, and the expected background-noise level. The important consequence of this procedure is that a general comparison among the speech intelligibility metrics, which take into account both the room acoustics characteristics and the background noise, can now be made using the same common basis. That is, all the speech intelligibility metrics that have been proposed can be directly expressed as a function of the reverberation time, for rooms in which the assumption of a diffuse sound field is valid. In these rooms the reverberation decay is purely exponential, and, as experience shows, it is just an approximation to the actual acoustic field in real rooms. However, at the acoustical design stage one does not have any other analytical tool, and the calculation procedures presented here provide a useful means for estimating speech intelligibility from reverberation time and noise-to-signal ratios.

II. REVERBERATION TIME T^* THAT MAXIMIZES THE USEFUL-TO-DETRIMENTAL SOUND RATIO

Figure 1 shows that the useful-to-late sound ratios increase without bound as reverberation time tends to zero. This result, however, does not correspond to the whole picture of what happens in a real room. Background noise is always present. As the reverberation time decreases, the useful-to-late sound ratio increases while the reflected speech signal-to-noise ratio decreases for a given background noise. The former effect is beneficial while the latter is detrimental to speech intelligibility. The useful-to-detrimental sound ratio is therefore one type of speech intelligibility metric capable of taking both effects into account.

It is expected that there should be a reverberation time for which the useful-to-detrimental sound ratio is maximized, which should correspond to the condition for the best possible speech intelligibility for a given background noise. As shown in Fig. 2, that is indeed the case. Figure 2 is a plot of the useful-to-detrimental sound ratios R_{sn}, Q in dB, and U_{50}, for a 300-m^3 classroom, calculated using Eqs. (10), (12), and (16), respectively, in the reverberant field, that is, for $r_h/r=0$, and for three L_n-L_{sp1m} values, with $q=2$. It can now be seen that the incorporation of the noise-to-signal ratio, in the form given by Eq. (20), into the useful-to-late sound ratios R'_{sn}, Q'_{dB}, and C_{50}, puts a limit on the growth of the speech intelligibility metric as the reverberation time tends to zero. It also produces a reverberation time for which the useful-to-detrimental sound ratio is maximized. The reverberation time for which the speech intelligibility metric reaches its maximum value, for a given L_n-L_{sp1m} value, will be called T^*. It can be seen in Fig. 2 that T^* decreases as L_n-L_{sp1m} decreases, and that for reverberation times greater

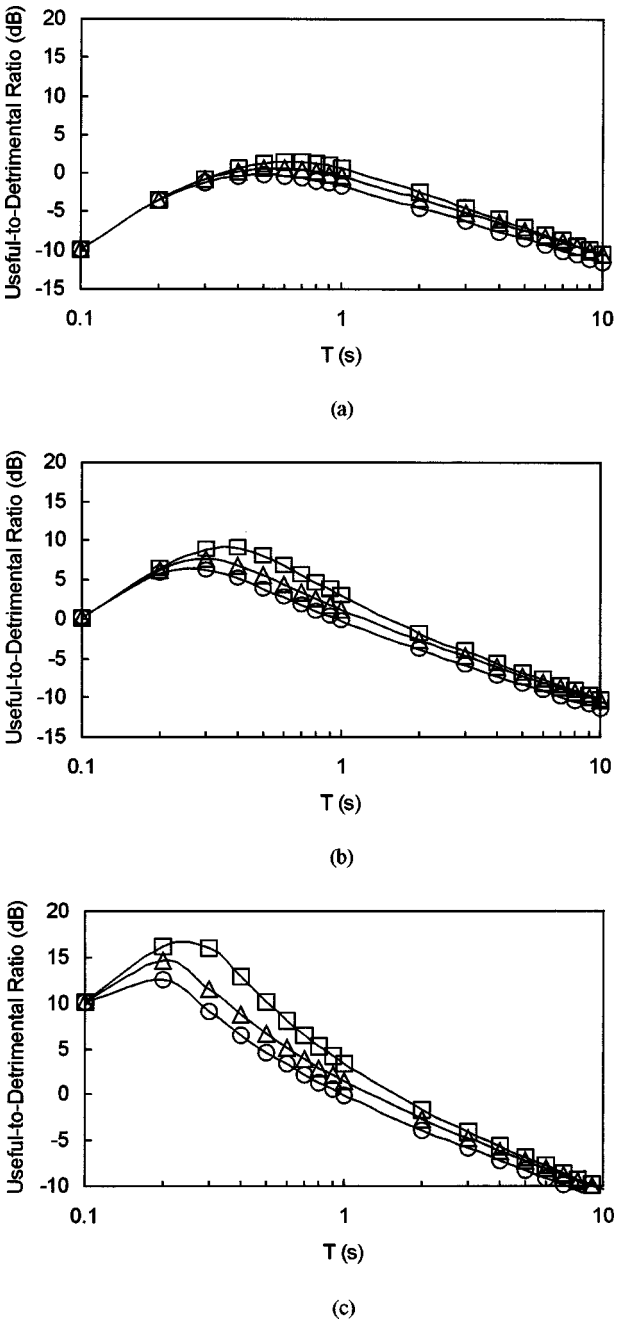

FIG. 2. Values of the useful-to-detrimental sound ratios R_{sn} (□), Q in dB (△), and U_{50} (○), as a function of the reverberation time T, for a 300-m^3 classroom and for $L_n - L_{sp1m}$ equal to (a) −10 dB, (b) −20 dB, and (c) −30 dB.

than about T^* the useful-to-detrimental sound ratios follow similar trends, with only small shifts in levels for the same reverberation time. Also, for reverberation times lower than about T^*, the values of the useful-to-detrimental sound ratios coincide for the same reverberation time.

T^* can be found by taking the useful-to-detrimental sound ratio derivative with respect to the reverberation time and setting it equal to zero. The solution of the resulting equation is T^*, which is the reverberation time for which the useful-to-detrimental sound ratio reaches a maximum value. A simpler procedure is to read them off curves such as those shown in Fig. 2. Table I shows T^* values for Q, R_{sn}, and U_{50}, which were calculated for three classrooms volumes and for five $L_n - L_{sp1m}$ values. These reverberation times are for a frequency band that represents the room acoustical conditions that are important for speech intelligibility, e.g., the 1-kHz band.

TABLE I. Reverberation time T^* that maximizes the speech intelligibility metric for three classroom volumes and for five $L_n - L_{splm}$ values. These reverberation times are for a frequency band that represents the room acoustical conditions that are important for speech intelligibility, e.g., the 1-kHz band.

$L_n - L_{splm}$ (dB)	Speech intelligibility metric	T^* (s) Classroom volume (m^3) 100	300	500
−10	Q	0.4	0.6	0.6
	R_{sn}	0.5	0.6	0.7
	U_{50}	0.4	0.5	0.6
	STI	0.5	0.7	0.8
	Al_{cons}	0.5	0.7	0.8
−15	Q	0.3	0.4	0.5
	R_{sn}	0.4	0.5	0.5
	U_{50}	0.3	0.4	0.4
	STI	0.3	0.4	0.5
	Al_{cons}	0.4	0.5	0.6
−20	Q	0.2	0.3	0.3
	R_{sn}	0.3	0.4	0.4
	U_{50}	0.2	0.3	0.3
	STI	0.2	0.3	0.4
	Al_{cons}	0.3	0.4	0.4
−25	Q	0.2	0.2	0.3
	R_{sn}	0.2	0.3	0.3
	U_{50}	0.2	0.2	0.2
	STI	0.2	0.2	0.3
	Al_{cons}	0.2	0.3	0.3
−30	Q	0.2	0.2	0.2
	R_{sn}	0.2	0.2	0.3
	U_{50}	0.1	0.2	0.2
	STI	0.1	0.2	0.2
	Al_{cons}	0.2	0.2	0.3

III. ARTICULATION FOR THE SPEECH INTELLIGIBILITY METRICS BASED ON THE ACOUSTICAL ENERGY RATIO

The speech intelligibility metrics based on the useful-to-detrimental sound ratio give an indication of how the time of arrival of speech energy in a reverberant enclosure will influence the perception of the speech. They are, in fact, physical measures based on different separations of useful and detrimental speech energy. In a previous section analytical expressions for each of these physical measures have been developed based on the assumption of diffuse sound field.

It is now necessary to relate these physical measures to the actual speech intelligibility experienced by listeners. The assessment of speech intelligibility is based on articulation tests. These basically consist of the production of speech test material at one point in a room and listeners who try to correctly identify the speech material at some other point. The percentage of correctly identified material is the articulation score. There are different types of speech test material

that result in different articulation scores. These can vary from complete sentences to single test words or even nonsense syllables, although they should all be representative of the range of sounds found in a particular language. Speech test material that includes some redundancy, such as complete sentences, can be easier to identify in adverse conditions and may lead to higher articulation scores than material such as nonsense syllables.

There have been few attempts to relate the results of different types of articulation tests in rooms. In addition each of the speech metrics described in this paper were usually developed and tested in terms of different articulation tests and thus it is very difficult to make precise comparisons. A further complication is that many of the earlier metrics were based on broadband acoustical measurements, while some newer metrics are based on octave-band measurements. For example, Lochner and Burger's signal-to-noise ratio R_{sn} was derived using unfiltered impulse responses, but newer metrics such as U_{50} and STI have been developed based on acoustical measurements filtered in octave bands.

A. The limiting distance

The distance beyond which the direct sound is of no significance anymore is known as the limiting distance r_l. The limiting distance can be defined as the distance for which the direct-to-reflected sound energy density is equal to -10 dB. In this case $r_l = \sqrt{10}\cdot r_h$. For a 300-m^3 classroom in which the reverberation time is 0.5 s, the limiting distance r_l is approximately 7.3 m. For the same conditions the reverberation distance r_h is approximately 2.3 m. For first-order estimates of speech intelligibility in the reverberant field, it seems possible to substitute for the rather general $r \gg r_h$ condition the more specific $r > r_l$ condition. This means that the results obtained in what follows are calculated for $r_h/r = 0$ (because $r \gg r_h$), but can be applied at distances from the sound source greater than r_l, for which the direct sound is of no significance anymore. This is a worst case scenario since at distances less than r_l there is an increasing contribution from the direct field as the receiver approaches the speaker. Therefore, we are on the safe side with respect to the evaluation of the overall speech intelligibility performance of the room.

B. Speech intelligibility for metrics that make use of the concept of *useful speech level*

The process of estimating speech intelligibility by two metrics to be discussed below requires the calculation of both the useful-to-detrimental sound ratio and the useful speech level at the receiver. These metrics consider that the reflected speech sound at the receiver is composed of two parts, a useful, earlier arriving reflected speech sound, and a detrimental, later arriving reflected speech sound. For an early arriving time limit for the reflected sound of $\frac{1}{16}$ s, as originally proposed by Aigner and Strutt,[13] the useful speech level $L_{p_{\mathrm{useful}}}$ is given by

$$L_{p_{\mathrm{useful}}} = L_{\mathrm{clasrm}} + 10\lg(1 - e^{-0.86/T}). \tag{21}$$

Speech intelligibility metrics that make use of the concept of useful speech level, and that incorporate both the room effects and the background noise, have been proposed by Lochner and Burger[1] and also by Mankovsky.[21] The latter reports on the use of the original Aigner and Strutt impression Q, as given by Eq. (1), with the name *factor of reverberation interference* or the *Sukharevsky–Strutt factor*. Mankovsky[21] shows that the impression Q, multiplied by the reverberation time T, and by a factor k_L which depends on the useful speech level, gives a good correlation with syllable articulation measurements carried out by various experiments. The Sukharevsky–Strutt factor Q'' is then given by

$$Q'' = k_L \cdot T \cdot Q, \tag{22}$$

where

$$k_L = 0.039 \cdot L_{p_{\mathrm{useful}}} \cdot e^{-L_{p_{\mathrm{useful}}}/70}. \tag{23}$$

Here k_L is the loudness reduction factor, originally proposed by Knudsen,[22] and results in the expected articulation due only to the influence of the speech level. Equation (23) is, in fact, a representation proposed by Mankovsky,[21] to a curve presented by Knudsen,[22] of articulation in percent versus speech levels at the receiver. In Eq. (23) Mankovsky[21] uses the useful speech level instead of the speech level as it originally appears in Knudsen's curve.[22]

Mankovsky[21] presents a curve of syllable articulation versus Q'', without detailing the type of syllable articulation test used. A fourth-order polynomial fit to his curve results in the following expression relating the speech intelligibility SI (%) to Q'', with R-square (coefficient of determination) equal to 0.997.

$$\mathrm{SI} = -23.6\cdot(Q'')^4 + 211.4\cdot(Q'')^3 - 694.5\cdot(Q'')^2 + 998.7\cdot(Q'') - 441.5 \quad (\%). \tag{24}$$

Although the curve relating SI (%) to Q'' presented by Mankovsky[21] is only given in the range $1.0 \leqslant Q'' \leqslant 2.1$ that corresponds to $50\% \leqslant \mathrm{SI} \leqslant 92\%$, Eq. (24) was found taking into account Q'' values also in the range $2.1 < Q'' \leqslant 3.0$, to extrapolate values of SI (%) to the range $92\% < \mathrm{SI} \leqslant 100\%$.

Figure 3 is a plot of speech intelligibility versus reverberation time, calculated using Eq. (24), having $L_n - L_{\mathrm{sp1m}}$ as a parameter, for a 300-m^3 classroom. The useful speech level was calculated with $L_{\mathrm{sp1m}} = 65$ dB and $q = 2$. To ensure good articulation Mankovsky[21] recommends that Q'' should not be less than 2. Also indicated in Fig. 3 is the ''minimum acceptable'' value for speech intelligibility of 90%, which corresponds to $Q'' = 2$. In Fig. 3, SI (%) values for $L_n - L_{\mathrm{sp1m}}$ equal to -10 dB are less than 50%, for any reverberation time, and were not plotted.

Lochner and Burger[1] also made use of the useful speech level concept in what they called *effective speech level* L_{efs}, which was here calculated according to

$$L_{\mathrm{efs}} = L_{\mathrm{clasrm}} + 10\lg[1 + 1.21\cdot T\cdot(e^{-1.31/T} - e^{-0.48/T})]. \tag{25}$$

Lochner and Burger[1] present curves of speech intelligibility versus the effective speech level L_{efs}, having their signal-to-noise ratio R_{sn} as a parameter. The articulation test

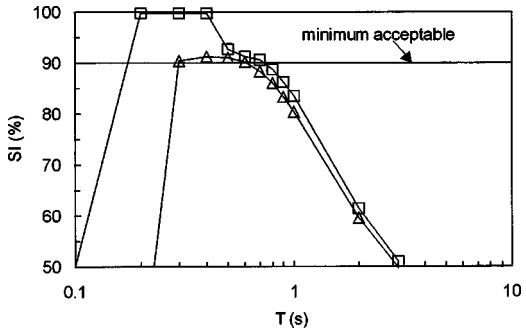

FIG. 3. Speech intelligibility given by a syllable articulation test, calculated using Eq. (24), with the Sukharevsky–Strutt factor Q'' given by Eq. (22), as a function of the reverberation time T, for a 300-m^3 classroom and for $L_n - L_{\mathrm{sp1m}}$ equal to -20 dB (△) and -30 dB (□). SI (%) values for $L_n - L_{\mathrm{sp1m}}$ equal to -10 dB are less than 50%, for any reverberation time T, and were not plotted. Indicated in this figure is the ''minimum acceptable'' value of 90% speech intelligibility recommended by Mankovsky (Ref. 21).

consisted of Afrikaans monosyllabic word lists, which, according to them, are similar to the Harvard PB-50 articulation test lists (50 phonetically balanced word lists).

Figure 4 is a plot of speech intelligibility versus reverberation time, extracted from the curves given by Lochner and Burger,[1] having $L_n - L_{\mathrm{sp1m}}$ as a parameter, for a 300-m^3 classroom. The effective speech level L_{efs} was calculated with $L_{\mathrm{sp1m}} = 65$ dB and $q = 2$.

C. Speech intelligibility for a modified version of Lochner and Burger's signal-to-noise ratio

Latham[2] used what he called a modified version of Lochner and Burger's signal-to-noise ratio R_{sn} to account for the effect of fluctuating background noise on speech intelligibility. In its modified version, the background noise was no longer considered as a stationary value, but considered instead in terms of its transient and spectral characteristics given by L_{10} and the preferred noise criteria curves (PNC curves), respectively. This modification has no effect on the present work since we are treating the background noise as being stationary. Latham's work is considered here because it provides a direct correlation between speech intelligibility and Lochner and Burger's signal-to-noise ratio R_{sn}, in its

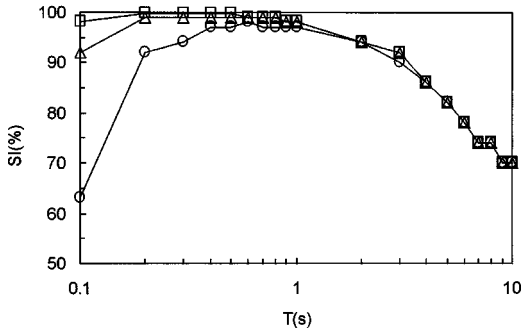

FIG. 4. Speech intelligibility given by a test using Afrikaan monosyllabic words, similar to the Harvard PB-50 Test, extracted from Lochner and Burger's curves (Ref. 1), with the effective speech level L_{efs} and the signal-to-noise ratio R_{sn} obtained using Eqs. (25) and (16), respectively, as a function of the reverberation time T, for a 300-m^3 classroom and for $L_n - L_{\mathrm{sp1m}}$ equal to -10 dB (○), -20 dB (△), and -30 dB (□).

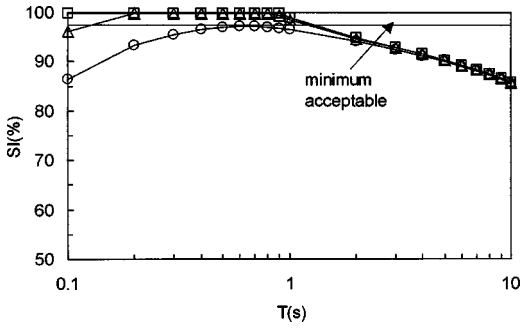

FIG. 5. Speech intelligibility given by the Fairbanks' Rhyme Test, calculated using Eq. (26), with $(\mathrm{S/N})'$ obtained from Eq. (16), as a function of the reverberation time T, for a 300-m^3 classroom and for $L_n - L_{\mathrm{sp1m}}$ equal to -10 dB (○), -20 dB (△), and -30 dB (□). Indicated in this figure is the ''minimum acceptable'' value of 97.5% speech intelligibility recommended by Latham (Ref. 2).

modified form, without taking into consideration the effective speech level L_{efs} as originally proposed by Lochner and Burger.[1] It is therefore a simpler procedure than that of Lochner and Burger's for estimating speech intelligibility.

Articulation tests were carried out by Latham in seven different auditoriums, in which the experimentally obtained impulse responses were filtered in the 1-kHz octave band to obtain the modified signal-to-noise ratio $(\mathrm{S/N})'$. The articulation test used was the Fairbanks' Rhyme Test. In this test, the task response consists of recognizing only the initial consonant of test words. Consonants contain most of the information but less of the energy in continuous speech. A third-order polynomial fit to the curve presented by Latham[2] results in the following expression relating the speech intelligibility SI (%) to $(\mathrm{S/N})'$, with R-square (coefficient of determination) equal to 0.993:

$$\mathrm{SI} = 0.0038 \cdot (\mathrm{S/N})'^3 + 0.0188 \cdot (\mathrm{S/N})'^2 + 0.7773 \cdot (\mathrm{S/N})' + 96.013 \quad (\%), \tag{26}$$

valid for $-23\,\mathrm{dB} \leqslant (\mathrm{S/N})' \leqslant 5$ dB in the 1-kHz octave band.

Figure 5 is a plot of speech intelligibility versus reverberation time, calculated using Eq. (26), with $(\mathrm{S/N})'$ obtained from Eq. (16), having $L_n - L_{\mathrm{sp1m}}$ as a parameter, for a 300-m^3 classroom. Also indicated in Fig. 5 is the ''minimum acceptable'' value of 97.5% speech intelligibility recommended by Latham.[2]

D. Speech intelligibility for U_{50}

Bradley[7] performed a series of articulation tests and acoustical measurements in ten occupied classrooms. The Fairbanks' Rhyme Test was applied to 12- to 13-year-old students in their regular classroom and class time. Room impulse responses were obtained with gunshots as the sound source. Using the useful-to-detrimental sound ratio calculated from the filtered impulse response in octave bands, he concluded that a threshold of sound separation of 0.05 s was better than 0.08 s for predicting speech intelligibility in classrooms. From the regression analyses carried out he proposed the following best-fit curve relating articulation scores to U_{50} values at 1 kHz:

$$\mathrm{SI} = -0.838 \cdot (U_{50})^2 + 1.027 \cdot (U_{50}) + 99.42 \quad (\%), \tag{27}$$

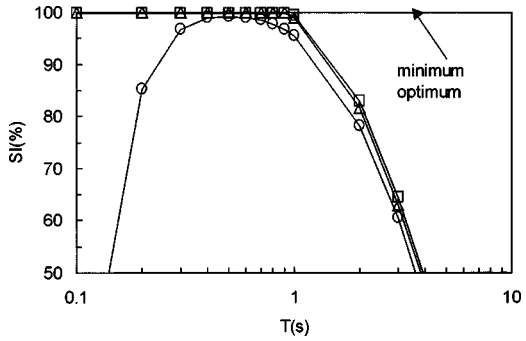

FIG. 6. Speech intelligibility given by the Fairbanks' Rhyme Test, calculated using Eq. (27), with U_{50} obtained from Eq. (12), as a function of the reverberation time T, for a 300-m^3 classroom and for $L_n - L_{\mathrm{sp1m}}$ equal to -10 dB (○), -20 dB (△), and -30 dB (□). Indicated in this figure is the ''minimum optimum'' value of 100% speech intelligibility recommended by Bradley (Ref. 8).

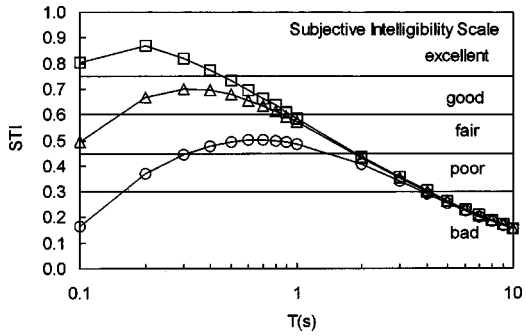

FIG. 7. Speech transmission index (STI) as a function of the reverberation time T, for a 300-m^3 classroom and for $L_n - L_{\mathrm{sp1m}}$ equal to -10 dB (○), -20 dB (△), and -30 dB (□). Indicated in this figure is the subjective intelligibility scale associated with different ranges of STI values (Ref. 17).

valid for $-10\,\mathrm{dB} \leqslant U_{50} \leqslant 0$ dB in the 1-kHz octave band.

Figure 6 is a plot of speech intelligibility versus reverberation time, calculated using Eq. (27), with U_{50} obtained from Eq. (12), having $L_n - L_{\mathrm{sp1m}}$ as a parameter, for a 300-m^3 classroom. Indicated in this figure is the ''minimum optimum'' value of 100% speech intelligibility recommended by Bradley.[8] This is a little higher than the limit of 97.5% recommended by Latham,[2] because Bradley considered that a more conservative limit was appropriate for such a simple test.

IV. THE SPEECH TRANSMISSION INDEX STI

If the room impulse response given by Eq. (7) is substituted into Eq. (2), an expression for the modulation transfer function $m(F)$, for $r_h/r = 0$, can be found in the form

$$m(F) = \left[1 + \left(\frac{2\pi}{13.82} F \cdot T\right)^2\right]^{-1/2} \cdot \left[1 + 10^{(L_n - L_{\mathrm{clasrm}})/10}\right]^{-1}. \tag{28}$$

For each room volume V, $m(F)$ is then calculated using Eq. (28), in each of the $14-F$ one-third octave-band speech modulation-frequency values F from 0.63 to 12.5 Hz, for each reverberation time T, having $L_n - L_{\mathrm{sp1m}}$ as a parameter. The corresponding STI value, for each reverberation time T, is then calculated using a procedure shown elsewhere.[15]

As revealed by Houtgast and Steeneken,[23] the speech transmission index STI has been demonstrated to have a broad range of validity. In addition to background noise and reverberation, it can take into account other types of speech disturbances including the effect of masking from a lower frequency band upon a higher one. It has also been found that the spectral shape of the interfering noise is not critical, and that it applies to various types of articulation test, although, of course, with not a unique (test-independent) relationship. It also appears to hold for languages other than Dutch.[17] The main body of articulation tests was performed with monosyllabic nonsense phonetically balanced words (PB words), for the Dutch language, of consonant–vowel–consonant type (C–V–C type). It has been recognized that for the major disturbances encountered in room acoustics, namely, reverberation and background noise, the STI calculation scheme as presented above will suffice. The STI calculations here include the same important simplification as the other speech metrics based on the acoustic energy ratio, that the reverberant field is assumed to be diffuse.

Since STI can vary considerably with frequency, one should determine the STI value in each octave frequency band from 125 Hz to 8 kHz, to obtain a weighted mean of these frequency-specific STIs.[15] In many cases only the 500-Hz and 2-kHz octave frequency bands are used as such when calculating the rapid STI (RaSTI). Therefore, implicit in the RaSTI calculation scheme[17] is the fact that in rooms for speech the analysis restricted to only the 500-Hz and the 2-kHz octave frequency bands will suffice. A further simplification introduced here has restricted the evaluation of STI in just one frequency band. This frequency band can be considered to be one that represents the room acoustical conditions that are important for speech intelligibility, e.g., the 1-kHz band. Otherwise, a more detailed room acoustic description would be necessary in terms of the reverberation time in other octave frequency bands, which is not within the scope of the present work.

Figure 7 is a plot of STI values versus reverberation time, having $L_n - L_{\mathrm{sp1m}}$ as a parameter, for a 300-m^3 classroom. Indicated in this figure is the subjective intelligibility scale associated with different ranges of STI values.[17]

Similar to Fig. 2, Fig. 7 also shows that for each $L_n - L_{\mathrm{sp1m}}$ value there is a reverberation time that maximizes STI, which we are calling T^*. Table I shows the reverberation times T^* that maximize STI for three classroom volumes and for five $L_n - L_{\mathrm{sp1m}}$ values. These reverberation times are for a frequency band that represents the room acoustical conditions that are important for speech intelligibility, e.g., the 1-kHz band.

V. THE ARTICULATION LOSS OF CONSONANTS $\mathrm{AI_{cons}}$

A common list of words used in syllable articulation tests is of the C–V–C (consonant–vowel–consonant) type. These are monosyllabic words, which are made up of phonemes. Phonemes are elementary speech sounds representative of all the vowels and consonants used in a particular language. When the subjects are asked to listen to these monosyllabic words in an articulation test, they in fact listen

to phonemes. As pointed out by Peutz,[24] individual phonemes are considered to be a neutral-form of message in that they are not recognizable by linguistic, logical, or any other than acoustic cues. This characteristic, at least in principle, makes the nonsense syllables a superior type of testing material and it is recognized as giving more accurate results, when compared to tests using words and sentences. On the other hand, the application of such a test requires that the subjects be thoroughly trained, meaning that the announcer must correctly pronounce the phonemes and the subjects must record in phonetic symbols what they have heard. The result is expressed as the percentage of syllables of which all three component sounds are perceived correctly.

Knudsen,[22] by quantifying the nature of errors in the syllable articulation test, found that the number of errors due to incorrectly perceived vowels was smaller than for consonants. The preponderance of the consonant errors was among the final consonants, probably as a result of the masking produced by the reverberation of the preceding vowel. This happens mainly because the energy and the duration of vowel sounds are greater than the consonant sounds. Nevertheless, most of the speech information is carried by the sound of consonants. The greater duration and energy of vowel sounds increases the masking of the consonant sounds by vowels as the reverberation time increases.

Peutz[5] also found that the articulation loss of vowels was much smaller than that for consonants. He then defined the articulation loss of consonants $\mathrm{Al}_{\mathrm{cons}}$, and the articulation loss of vowels Al_{v}, respectively, as the proportion of consonants and vowels wrongly perceived. Peutz obtained a better and more coherent set of relations regarding the influence of room acoustics on speech intelligibility in the form of articulation loss of consonants. He also found that no reliable numbers for the articulation loss of vowels could be obtained.

Articulation tests utilizing phonetically balanced, C–V–C type, nonsense words as well as meaningful ones, in the Dutch language, were anechoically taped, and later played back in rooms with different reverberation times, at various source-to-listener distances, and background-noise levels. Peutz[5] found that the articulation loss of consonants increases with increasing distance from the sound source up to the critical distance, after which it remains constant and equal to $9T$. The critical distance r_c in meters is given by $0.21\sqrt{V/T}$, with V in cubic meters and T in seconds. The critical distance r_c is approximately equal to the limiting distance r_l. For distances less than or equal to the critical distance, and without background noise, an empirical relation for $\%\mathrm{Al}_{\mathrm{cons}}$ was derived in the form of Eq. (3). Peutz[5] presented the results regarding the influence of background noise in graphical form, expressing $\%\mathrm{Al}_{\mathrm{cons}}$ as a function of the signal-to-noise ratio (S/N), and having the reverberation time T as a parameter.

The expression that follows was curve-fitted by us to the Peutz graphical results and gives $\%\mathrm{Al}_{\mathrm{cons}}$, taking into account, in analytical form, the room effects, represented by the reverberation time T in seconds, as well as the background noise represented by the noise-to-signal ratio (N/S) in dB:

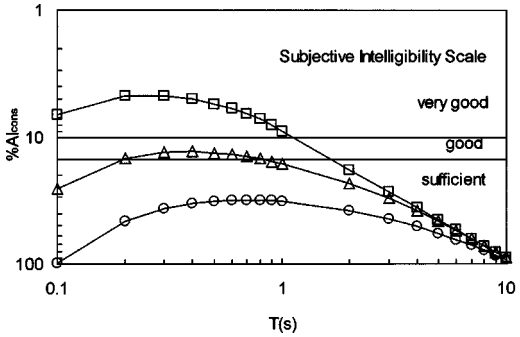

FIG. 8. Articulation loss of consonants $\%\mathrm{Al}_{\mathrm{cons}}$, as a function of the reverberation time T, for a 300-m^3 classroom and for $L_n - L_{\mathrm{sp1m}}$ equal to -10 dB (○), -20 dB (△), and -30 dB (□). Indicated in this figure is the subjective intelligibility scale associated with different ranges of $\%\mathrm{Al}_{\mathrm{cons}}$ values (Ref. 5).

$$\%\mathrm{Al}_{\mathrm{cons}} = K_C \cdot (1.071 \cdot T^{-0.0285})^{25+(\mathrm{N/S})}, \tag{29}$$

where $K_C = 9 \cdot T$ for $r > r_c$, and $K_C = 9 \cdot T \cdot (r/r_c)^2$ for $r \leqslant r_c$. Equation (29) is valid for $(\mathrm{N/S}) \geqslant -25$ dB. Normally $\%\mathrm{Al}_{\mathrm{cons}}$ is evaluated with the reverberation time T given in the 2-kHz octave or one-third octave frequency band.

Figure 8 is a plot of $\%\mathrm{Al}_{\mathrm{cons}}$ versus reverberation time, having $L_n - L_{\mathrm{sp1m}}$ as a parameter, for a 300-m^3 classroom. The $\%\mathrm{Al}_{\mathrm{cons}}$ was calculated using Eq. (29) for $r > r_c$, and, due to the fact that $r_c \approx r_l$, these results are therefore applicable to distances beyond the limiting distance r_l. Indicated in Fig. 8 is the subjective intelligibility scale associated with different ranges of $\%\mathrm{Al}_{\mathrm{cons}}$ values.[5]

Similar to Fig. 2, Fig. 8 also shows that for each $L_n - L_{\mathrm{sp1m}}$ value there is a reverberation time that maximizes $\%\mathrm{Al}_{\mathrm{cons}}$, which we are calling T^*. Table I shows the reverberation times T^* that maximize $\%\mathrm{Al}_{\mathrm{cons}}$ for three classroom volumes and for five $L_n - L_{\mathrm{sp1m}}$ values. These reverberation times are for a frequency band that represents the room acoustical conditions that are important for speech intelligibility, e.g., the 1-kHz band.

VI. RELATIONSHIPS AMONG THE SPEECH INTELLIGIBILITY METRICS

The results obtained so far show that the speech intelligibility metrics used in the present study, namely, useful-to-detrimental sound ratios, the STI, and $\mathrm{Al}_{\mathrm{cons}}$, are different in detail but indicate the same general trends. To study the relationship among these metrics, Bradley[11] calculated values of STI, U_{50}, and $\%\mathrm{Al}_{\mathrm{cons}}$ from experimentally obtained impulse responses, which covered a wide range of acoustical conditions, and for different speech-to-noise ratios. He then developed regression equations relating these metrics of speech intelligibility that permit conversions among them. The $\%\mathrm{Al}_{\mathrm{cons}}$ was for the 2-kHz octave-band results. The STI and U_{50} values used in these regression equations were obtained as single numbers, by weighting the octave-band values. They should be comparable to the results obtained in the present study, which are thought to represent broadband values of these speech metrics, but are derived assuming that the sound field in the room is ideally diffuse.

Contrary to what is generally assumed, it was verified[18] that no unique relationship, independent of the classroom

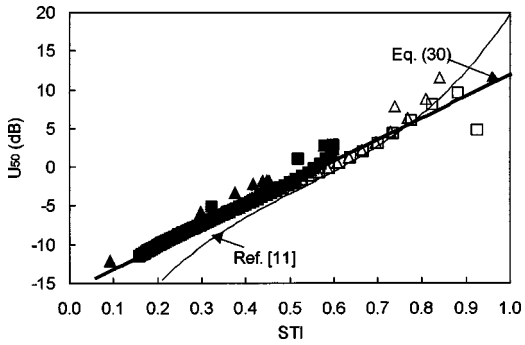

FIG. 9. Relationship between U_{50} and STI, with data points obtained from the results of the present study for two classroom volumes: 100 m^3 (■ □) and 500 m^3 (▲ △); for two $L_n - L_{sp1m}$ values: −10 dB (closed markers) and −30 dB (open markers); and for reverberation times in the range between 0.1 and 10 s.

volume and the noise-to-signal ratio, holds between $\%Al_{cons}$ and STI, and also between $\%Al_{cons}$ and U_{50}. This, however, is not the case with U_{50} and STI. A unique linear relationship seems to exist between them, independent of the classroom volume, and of the $L_n - L_{sp1m}$ value. This relationship can be seen in Fig. 9. The data points in this figure are from the results of the present study, obtained for two classroom volumes (100 and 500 m^3), two $L_n - L_{sp1m}$ values (−10 and −30 dB), and for reverberation times in the range between 0.1 and 10 s. Bradley's experimentally based relationship[11] is also shown in Fig. 9, which seems to be in good agreement with the results of the present study, for STI values greater than about 0.5. Also shown in Fig. 9, is a linear curve-fit to the data points, relating U_{50} to STI, which is given below as Eq. (30). This linear relation is more suited for the data points of the present study, which are valid for ideal exponential decays and classrooms with diffuse sound fields:

$$U_{50} = 28 \cdot \mathrm{STI} - 16. \tag{30}$$

No unique relationship was found between U_{50} and Q'', although the pair of speech intelligibility metrics U_{50} and R_{sn} are linearly related.[18] Figure 10 is a plot of U_{50} vs R_{sn}, with the data points obtained from the results of the present study, for two classroom volumes (100 and 500 m^3), two $L_n - L_{sp1m}$ values (−10 and −30 dB), and for reverberation

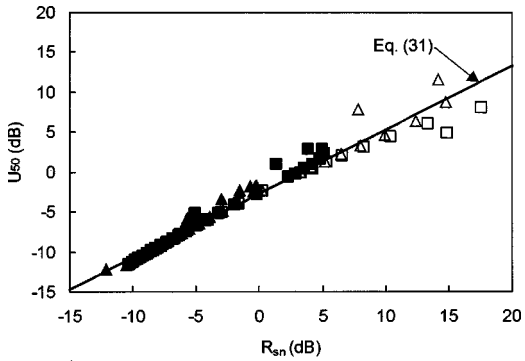

FIG. 10. Relationship between U_{50} and R_{sn}, with data points obtained from the results of the present study for two classroom volumes: 100 m^3 (■ □) and 500 m^3 (▲ △); for two $L_n - L_{sp1m}$ values: −10 dB (closed markers) and −30 dB (open markers); and for reverberation times in the range between 0.1 and 10 s.

times in the range between 0.1 and 10 s. As shown in Fig. 10, a unique linear relationship holds between U_{50} and R_{sn}, independent of the classroom volume and the $L_n - L_{sp1m}$ value. This relationship is given by

$$U_{50} = 0.8 \cdot R_{sn} - 2.7. \tag{31}$$

The above results show that the speech intelligibility metrics, U_{50}, R_{sn}, and STI, are very well correlated to each other, and that it is possible to establish a unique linear relationship for each pair, independent of the classroom volume and the value of $L_n - L_{sp1m}$. The proposed relationships given by Eqs. (30) and (31) are valid at least over the range of the acoustical variables used to obtain the data points of Figs. 9 and 10, respectively, which are based on ideal exponential decays and classrooms with diffuse sound fields.

According to Eqs. (30) and (31), for $U_{50} = 0$ dB, STI $= 0.6$, and $R_{sn} = 3.5$ dB. For $U_{50} = 0$ dB speech intelligibility is 100% based on the Fairbanks' Rhyme Test; and for $R_{sn} = 3.5$ dB, speech intelligibility is 98% based on a test similar to the Harvard PB-50 Test. STI $= 0.6$ corresponds to the limiting value between what is considered ''fair'' and ''good'' in the subjective speech intelligibility scale.[17] This comparison suggests that there may be differences in the prediction of speech intelligibility as given by different speech metrics.

VII. REVERBERATION TIMES FOR 100% SPEECH INTELLIGIBILITY, AND COST-EFFECTIVE REVERBERATION TIME

As can be seen in Figs. 3–6, there is for each speech intelligibility metric, and for some $L_n - L_{sp1m}$ curves, a range of reverberation times that correspond to 100% speech intelligibility. It is possible to obtain an equation, for each one of these metrics, that will give the aforementioned range of reverberation times. This can be done by knowing the value of the speech intelligibility metric for 100% speech intelligibility. Then, for a given classroom volume and $L_n - L_{sp1m}$ value, it is possible to solve the resulting equation for the desired range of reverberation time values. Also, we can define the cost-effective reverberation time as the T value for which 100% speech intelligibility is reached with the minimum amount of sound absorption. Then the cost-effective reverberation time is the highest value of T, which satisfies the above-mentioned equation identically. This procedure for obtaining these reverberation time values was pursued in an extended report.[18] A simpler procedure is to read the range of reverberation times for 100% speech intelligibility and the cost-effective reverberation time off the plots such as those shown in Figs. 3–6. This same simpler procedure could be also applied to different design goals, e.g., cost-effective reverberation time for 90% speech intelligibility.

Table II shows, for three classroom volumes and for five $L_n - L_{sp1m}$ values, the range of reverberation times that give 100% speech intelligibility, and the cost-effective reverberation time, for each acoustical energy ratio-based speech intelligibility metric, and also for STI and $\%Al_{cons}$. The values for STI and $\%Al_{cons}$ used to obtain the reverberation times for 100% speech intelligibility correspond to ''excellent'' [17] and ''very good'' [5] in the respective subjective intelligibility scales. The reverberation times listed in Table II are for a

TABLE II. Range of reverberation times to achieve 100% speech intelligibility and cost-effective reverberation time, as given by different speech intelligibility metrics, for three classroom volumes and for five $L_n - L_{\text{splm}}$ values. These reverberation times are for a frequency band that represents the room acoustical conditions that are important for speech intelligibility, e.g., the 1-kHz band.

$L_n - L_{\text{splm}}$ (dB)	Speech intelligibility metric	Range of reverberation times to achieve 100% speech intelligibility[a] (s)			Cost-effective reverberation time (s)		
		Classroom volume (m^3)					
		100	300	500	100	300	500
−10	Q''	⋯	⋯	⋯	⋯	⋯	⋯
	R_{sn}	⋯	⋯	⋯	⋯	⋯	⋯
	$(\text{S/N})'$	0.4–0.5	⋯	⋯	0.5	⋯	⋯
	U_{50}	0.2–0.9	⋯	⋯	0.9	⋯	⋯
	STI	⋯	⋯	⋯	⋯	⋯	⋯
	Al_{cons}	⋯	⋯	⋯	⋯	⋯	⋯
−15	Q''	⋯	⋯	⋯	⋯	⋯	⋯
	R_{sn}	⋯	⋯	⋯	⋯	⋯	⋯
	$(\text{S/N})'$	0.2–0.8	0.4–0.6	⋯	0.8	0.6	⋯
	U_{50}	0.1–1.0	0.2–0.9	0.2–0.8	1.0	0.9	0.8
	STI	⋯	⋯	⋯	⋯	⋯	⋯
	Al_{cons}	⋯	⋯	⋯	⋯	⋯	⋯
−20	Q''	0.3	⋯	⋯	0.3	⋯	⋯
	R_{sn}	0.2–0.5	⋯	⋯	0.5	⋯	⋯
	$(\text{S/N})'$	0.1–0.8	0.2–0.8	0.2–0.7	0.8	0.8	0.7
	U_{50}	1.1–1.0	0.1–1.0	0.1–0.9	1.0	1.0	0.9
	STI	0.2–0.4	⋯	⋯	0.4	⋯	⋯
	Al_{cons}	0.2–0.7	⋯	⋯	0.7	⋯	⋯
−25	Q''	0.2–0.4	0.2–0.3	⋯	0.4	0.3	⋯
	R_{sn}	0.1–0.5	0.2–0.5	0.2–0.4	0.5	0.5	0.4
	$(\text{S/N})'$	0.1–0.8	0.1–0.8	0.1–0.8	0.8	0.8	0.8
	U_{50}	0.1–1.0	0.1–1.0	0.1–1.0	1.0	1.0	1.0
	STI	0.1–0.4	0.2–0.4	0.3	0.4	0.4	0.3
	Al_{cons}	0.1–1.1	0.1–0.8	0.3–0.4	1.1	0.8	0.4
−30	Q''	0.1–0.4	0.1–0.4	0.2–0.4	0.4	0.4	0.4
	R_{sn}	0.1–0.5	0.1–0.5	0.1–0.5	0.5	0.5	0.5
	$(\text{S/N})'$	0.1–0.8	0.1–0.8	0.1–0.8	0.8	0.8	0.8
	U_{50}	0.1–1.0	0.1–1.0	0.1–1.0	1.0	1.0	1.0
	STI	0.1–0.4	0.1–0.4	0.2–0.4	0.4	0.4	0.4
	Al_{cons}	0.1–1.1	0.1–1.1	0.1–1.1	1.1	1.1	1.1

[a]The values for STI and Al_{cons} used to obtain the range of reverberation times correspond to ''excellent'' ($\geqslant$0.75) and ''very good'' ($\leqslant$10%) in the respective subjective intelligibility scales.

frequency band that represents the room acoustical conditions that are important for speech intelligibility, e.g., the 1-kHz band.

VIII. DISCUSSION

It can be seen in Table I that there is good agreement among the reverberation times T^* that maximize each one of the speech intelligibility metrics, especially for lower $L_n - L_{\text{sp1m}}$ values. Here T^* increases with the classroom volume and with the $L_n - L_{\text{sp1m}}$ value. This is due to the necessity of increasing the reflected sound in larger and/or noisier classrooms. In quieter classrooms, for $L_n - L_{\text{sp1m}}$ equal to −25 and −30 dB, T^* is almost independent of the classroom volume. Under this ideal condition, the reverberation time T^* that maximizes the speech intelligibility metrics is in the range between 0.1 and 0.3 s.

Table II shows that it is still possible to achieve 100% speech intelligibility for each specific speech intelligibility metric used in the present study, within a range of reverberation times as shown in this table. The aforementioned range of reverberation times varies according to each speech intelligibility metric considered. This is due to different articulation tests used to derive each metric, and, in the case of STI and $\%\text{Al}_{\text{cons}}$, is also due to a rather arbitrary way of establishing the cutoff values in the subjective speech intelligibility scale. Both factors also influence the different values for the cost-effective reverberation time as given by each speech intelligibility metric. Nevertheless, Table II shows that the cost-effective reverberation time can be at least double the reverberation time T^* that maximizes the speech intelligibility metrics. This means that for $L_n - L_{\text{sp1m}}$ values in the range between −30 and −25 dB, reverberation times of at least 0.4–0.5 s are still capable of guaranteeing 100% speech intelligibility. For some metrics the cost-effective reverberation time can be even higher while still giving 100% speech intelligibility. For conditions where 100% speech intelligibil-

ity is possible, a cost-effective reverberation time of 0.4 s is supported by 94% of the data in Table II, with $L_n - L_{sp1m}$ values in the range between -10 and -30 dB.

With respect to the effects of background noise on speech intelligibility, Table II shows 100% speech intelligibility in all classrooms, for $L_n - L_{sp1m}$ equal to -30 dB, according to all metrics considered in the present study. For $L_n - L_{sp1m}$ equal to -25 dB, Q'' indicates that 100% speech intelligibility is no longer possible in the 500-m^3 classroom, while STI indicates that ''excellent'' speech intelligibility is barely possible for a reverberation time of 0.3 s in this same classroom. All metrics indicate that for $L_n - L_{sp1m}$ equal to -20 dB, 100% speech intelligibility is only possible in the 100-m^3 classroom, while $(S/N)'$ and U_{50} indicate that 100% speech intelligibility can still be achieved in all classrooms. For $L_n - L_{sp1m}$ equal to -15 dB only $(S/N)'$ and U_{50} indicate that 100% speech intelligibility is still possible in all classrooms, with the exception of $(S/N)'$ in the 500-m^3 classroom. According to these same metrics, for $L_n - L_{sp1m}$ equal to -10 dB, 100% speech intelligibility is still possible in the 100-m^3 classroom. The reason why $(S/N)'$ and U_{50} are less restrictive with respect to the influence of background noise on speech intelligibility is due to the fact that they are based on the Fairbanks' Rhyme Test, which is considered to be a very simple type of articulation test. Therefore, different speech metrics may give different speech intelligibility results when the same room acoustical conditions are given.

A criterion should be adopted for the establishment of maximum background-noise levels in classrooms, based on the current comparative study of speech intelligibility metrics. Such a criterion could be that of a maximum $L_n - L_{sp1m}$ value that can still guarantee 100% speech intelligibility unanimously by *all* metrics considered in the present study. Taking into consideration the above discussion with respect to the effects of background noise on speech intelligibility, an $L_n - L_{sp1m}$ value of -20 dB satisfies this criterion for classrooms volumes less than or equal to 100 m^3, along with an $L_n - L_{sp1m}$ value of -25 dB for classrooms volumes less than or equal to 300 m^3, and an $L_n - L_{sp1m}$ value of -30 dB for classrooms volumes less than or equal to 500 m^3. It can be seen in Table II that an $L_n - L_{sp1m}$ value of -25 dB in the 500-m^3 classroom does not give 100% speech intelligibility only according to Q''. Therefore, -25 dB could be considered as a ''border line'' value for $L_n - L_{sp1m}$, in order to achieve 100% speech intelligibility in all three classrooms. Another way of putting it is to consider for standard classrooms in general an ''ideal'' and an ''acceptable'' value for $L_n - L_{sp1m}$ of -25 and -20 dB, respectively.

Therefore, based on the current analysis of speech intelligibility metrics, recommended desirable goals for acoustical conditions in classrooms are a reverberation time of 0.4–0.5 s or less, and a background-noise level 25 dB below the voice level measured at 1 m straight ahead of the talker.

IX. BASIC RECOMMENDATIONS FOR CLASSROOM ACOUSTICAL DESIGN

The results obtained in the present study allow us to make some basic recommendations for classroom acoustical design. More specifically, recommendations can now be made with respect to reverberation time and the classroom-noise criteria. These recommendations will be compared with other similar studies for classrooms. Of course, these recommendations are only based on the indications of the calculated intelligibility metrics assuming diffuse field conditions.

A. Recommended reverberation time

In a previous study,[7] in real classrooms, an optimum reverberation of 0.5 s was obtained. The present study shows that for very quiet classrooms, of standard sizes and shapes, the reverberation time T^* that maximizes the speech intelligibility metrics is in the range between 0.1 and 0.3 s. Nevertheless, in very quiet classrooms, 100% speech intelligibility can still be guaranteed, by *all* the speech intelligibility metrics used in this study, with a reverberation time of 0.4–0.5 s. Our findings agree with current recommendations given by the Acoustical Society of America[25] of 0.4–0.6 s, or less, for the reverberation time in occupied classrooms. For some metrics 100% speech intelligibility can still be obtained with higher reverberation times. Thus these new analyses do not lead to precise and unambiguous indications for recommended reverberation times. However, recent subjective studies[26] have suggested that optimum conditions for speech do not require such precision in assigning an optimum reverberation time.

Under the assumptions made, the reverberation time is the only physical parameter that characterizes the classroom acoustical conditions. Since reverberation time is a frequency-dependent quantity, the reverberation time recommended here should be equally applicable to all frequency bands that contribute to speech intelligibility. The present study suggests that in order to achieve 100% speech intelligibility in very quiet classrooms, the reverberation time should be 0.4–0.5 s. However, we are all aware of the practical difficulties in achieving these low reverberation time values at low frequencies, particularly in the 125- and 250-Hz octave frequency bands. Although it is convenient to have a low reverberation time at these frequency bands to reduce masking of the consonants sounds by vowels, most of the speech information is carried out by the sound of consonants, which comprises the higher frequency part of the speech spectrum. Therefore, it seems possible to relax somewhat the requirement to have the reverberation time at such low values in the 125- and the 250-Hz octave frequency bands. Another practical difficulty is to have a uniform reverberation time value in the octave frequency bands between 500 Hz and 4 kHz. In most rooms, reverberation time moderately decreases with increasing frequency above 500 Hz. Also, the reverberation time in the 1-kHz octave frequency band is approximately equal to the average value in the octave frequency bands between 500 Hz and 4 kHz. Therefore, the reverberation time recommended by the present study can be considered not only as that required for the 1-kHz octave frequency band, but also as the average value in the octave frequency bands between 500 Hz and 4 kHz.

B. Recommended room-noise criteria for classrooms

A maximum desirable goal for the background-noise level in classrooms is, of course, very much dependent on the voice level. In a previous related study,[8] maximum acceptable A-weighted background-noise levels of 35 and 42 dB were obtained for classrooms. These were calculated based on ''normal'' and ''raised'' A-weighted anechoic voice levels of 51 and 59 dB at 1 m, respectively. The more restrictive limits, derived assuming a ''normal'' voice level, can be described as ''ideal'' goals, while the limits derived from a ''raised'' voice level may better be referred to as ''acceptable'' goals.

Kingsbury[27] proposed maximum acceptable noise levels for classrooms based on an analysis of ventilation-type noises and using the *Articulation Index* procedure. Based on A-weighted anechoic voice levels of 61 to 63 dB at 1 m, he calculated that a NC-40 criterion would be acceptable in classrooms up to 200 m^3 and a NC-35 would be required for larger classrooms. These would approximately correspond to A-weighted levels of 48 and 43 dB, respectively.

Based on a survey of voice levels reported in the literature,[18] it was found that an anechoic voice level of 65 dB at 1 m in front of the talker is more representative of the average voice level produced by teachers in classrooms for children. This is equivalent to an A-weighted level of 63 dB, according to a relation between linear and A-weighted levels for voices provided by Pearsons *et al.*[28] The current study suggests an ''ideal'' and an ''acceptable'' value for $L_n - L_{\mathrm{sp1m}}$ of -25 and -20 dB, respectively (Sec. VIII); that is, a background-noise level 25 and 20 dB below the voice level at 1 m in front of the talker. This would correspond to an ''ideal'' A-weighted maximum background-noise level for classrooms of 38 dB. This is similar to other ''ideal'' goals for maximum background-noise levels, including the Acoustical Society of America[25] recommendation of an A-weighted level of 35 dB. The corresponding ''acceptable'' A-weighted maximum background-noise level for classrooms would be 43 dB. This is similar to other ''acceptable'' background-noise levels for classrooms and other similar rooms for speech.

The Acoustical Society of America[25] also recommends a classroom signal-to-noise ratio of 15 dB. For $L_n - L_{\mathrm{sp1m}}$ equal to -25 dB, it can be verified with the aid of Eq. (20), that this goal can be achieved with a reverberation time of at least 0.3 s in a 300-m^3 classroom. For $L_n - L_{\mathrm{sp1m}}$ equal to -20 dB, the reverberation time should be at least 0.7 s. This means that the ''ideal'' value for $L_n - L_{\mathrm{sp1m}}$ of -25 dB, together with the recommended reverberation time, provides conditions that achieve a classroom signal-to-noise ratio of more than 15 dB. The ''acceptable'' value for $L_n - L_{\mathrm{sp1m}}$ of -20 dB, together with the recommended reverberation time, would give, in a 300-m^3 classroom, a classroom signal-to-noise ratio of approximately 13 dB, which nevertheless can still be considered as an ''acceptable'' value for this parameter.

C. Extensions of the present work to other rooms for speech

The speech intelligibility metrics and the analytical formulations derived here can be applied to first-order estimates of speech intelligibility to be expected in other rooms for speech. Of course, the results will be less accurate if the sound diffusion condition is not met. There are, however, means of improving somewhat the accuracy of the predictions by modifications of these formulas. One of the simplifications introduced in the present study was to consider that the room volume-to-surface area ratio is equal to 1 m. For a more accurate prediction in rooms with shapes different from the regular rectangular shape found in most classrooms, for which the above-mentioned simplification holds, a more realistic estimate for V/S might be necessary. This, however, can be easily accommodated knowing the expected geometric configuration of the room under study. A probably more serious cause of inaccuracy using these analytical formulations in larger rooms is the decrease of the reflected sound energy density further away from the source. According to Barron,[29] Eq. (5) is found to predict the reflected sound energy density correctly at the source, but beyond, the reflected sound energy density is less. Barron proposes to take into account the decrease in the reflected sound energy density with distance by including an additional exponential term in Eq. (5), which depends on the distance from the source and the reverberation time. Following this proposal, Eq. (5) would read

$$e_{r_r} = \frac{qP}{4\pi c r_h^2} e^{-0.04 r/T}, \tag{32}$$

where e_{r_r} is the reflected sound energy density at a distance r from the source. The analytical formula for the speech intelligibility metric that results using Eq. (32) has the drawback that now the distance from the source r must also be specified in the reverberant field.

X. CONCLUSIONS

The following are the principal conclusions of this work:

(i) There is no difference in the overall behavior of the useful-to-late sound ratios R'_{sn}, Q'_{dB}, and C_{50}, only shift in levels for the same reverberation time.

(ii) When the useful-to-detrimental sound ratios R_{sn}, Q, and U_{50} are plotted versus reverberation time, they all follow similar trends, with only small shifts in levels for reverberation times greater than about T^*. For reverberation times lower than about T^*, the values of these useful-to-detrimental sound ratios coincide for the same reverberation time.

(iii) For very quiet classrooms of standard sizes and shapes, the reverberation time T^* that maximizes all the speech intelligibility metrics is in the range between 0.1 and 0.3 s.

(iv) For very quiet classrooms of standard sizes and shapes, 100% speech intelligibility is still possible with a reverberation time of at least 0.4–0.5 s, and this is the recommended range.

(v) Different ranges of reverberation time for 100% speech intelligibility given by different metrics, for a given $L_n - L_{\mathrm{sp1m}}$ value, are thought to be due to the different articulation testing methods used to derive each metric, and, in the case of STI and $\mathrm{Al}_{\mathrm{cons}}$, also due to a rather arbitrary way of establishing the cutoff values in the subjective speech intelligibility scale.

(vi) All the speech intelligibility metrics used in the present study are related to each other, however a unique relationship, independent of the classroom volume and the $L_n - L_{\mathrm{sp1m}}$ value, was only established between pairs of metrics involving STI, R_{sn}, and U_{50}.

(vii) When the same room acoustical conditions are given, different speech metrics may give different speech intelligibility results.

(viii) The ''ideal'' and the ''acceptable'' maximum background-noise levels for classrooms are respectively 25 dB and 20 dB below the voice level at 1 m in front of the talker.

(ix) The ''ideal'' maximum background-noise level, together with the recommended reverberation time, provides conditions that achieve a classroom signal-to-noise ratio of more than 15 dB.

ACKNOWLEDGMENTS

The first author is spending sabbatical leave, granted by the University of São Paulo, São Paulo, Brazil, with the Acoustic Group at the National Research Council—NRC Canada. The first author would like to acknowledge the personal financial support for the development of the classroom acoustic project currently underway, granted by Fundação de Amparo à Pesquisa do Estado de São Paulo—FAPESP.

[1] J. P. A. Lochner and J. F. Burger, ''The intelligibility of speech under reverberant conditions,'' Acustica **11**, 195–200 (1961).
[2] H. G. Latham, ''The signal-to-noise ratio for speech intelligibility—an auditorium acoustics design index,'' Appl. Acoust. **12**, 253–320 (1979).
[3] J. S. Bradley, ''Predictors of speech intelligibility in rooms,'' J. Acoust. Soc. Am. **80**, 837–845 (1986).
[4] T. Houtgast and H. J. M. Steeneken, ''The modulation transfer function in room acoustics as a predictor of speech intelligibility,'' Acustica **28**, 66–73 (1973).
[5] V. M. A. Peutz, ''Articulation loss of consonants as a criterion for speech transmission in a room,'' J. Audio Eng. Soc. **19**, 915–919 (1971).
[6] T. Houtgast, ''The effect of ambient noise on speech intelligibility in classrooms,'' Appl. Acoust. **14**, 15–25 (1981).
[7] J. S. Bradley, ''Speech intelligibility studies in classrooms,'' J. Acoust. Soc. Am. **80**, 846–854 (1986).
[8] J. S. Bradley, ''Uniform derivation of optimum conditions for speech in rooms,'' Report BRN 239 (National Research Council, Ottawa, Canada, 1985).
[9] M. Hodgson, ''UBC-Classroom acoustical survey,'' Can. Acoust. **24**(4), 3–10 (1994).
[10] M. Hodgson, R. Rempel, and S. Kennedy, ''Measurement and prediction of typical speech and background-noise levels in university classrooms during lectures,'' J. Acoust. Soc. Am. **105**, 226–233 (1999).
[11] J. S. Bradley, ''Relationships among measures of speech intelligibility in rooms,'' J. Aud. Eng. Soc. **46**, 396–405 (1998).
[12] H. Haas, ''The influence of a single echo on the audibility of speech,'' J. Audio Eng. Soc. **20**, 146–159 (1972).
[13] F. Aigner and M. J. O. Strutt, ''On a physiological effect of several sources of sound on the ear and its consequences in architectural acoustics,'' J. Acoust. Soc. Am. **6**, 155–159 (1935).
[14] R. Thiele, ''Richtungsverteilung und zeitfolge der schallruckwurfe in raumen,'' Acustica **3**, 291–302 (1953).
[15] T. Houtgast, H. J. M. Steeneken, and R. Plomp, ''Predicting speech intelligibility in rooms from the modulation transfer function I: General room acoustics,'' Acustica **46**, 60–72 (1980).
[16] M. R. Schroeder, ''Modulation transfer functions: Definition and measurement,'' Acustica **49**, 179–182 (1981).
[17] T. Houtgast and H. J. M. Steeneken, ''A multi-language evaluation of the RaSTI-method for estimating speech intelligibility in auditoria,'' Acustica **54**, 185–199 (1984).
[18] S. R. Bistafa and J. S. Bradley, ''A comparative study of speech intelligibility metrics and the derivation of optimum reverberation time and maximum background-noise level for classrooms,'' Report IR-778 (National Research Council Canada, Ottawa, Canada, 1999).
[19] H. Kuttruff, *Room Acoustics* (Elsevier Applied Science, London, 1991), pp. 114–123.
[20] H. Niese, ''Die messung der nutzschall-und echogradverteilung zur beurteilung der horsamkeit in raumen,'' Acustica **11**, 201–213 (1961).
[21] V. S. Mankovsky, *Acoustics of Studios and Auditoria* (Focal, London, 1971), pp. 75–79.
[22] V. O. Knudsen, *Architectural Acoustics* (Wiley, New York, 1932), pp. 373, 395–396.
[23] T. Houtgast and H. J. M. Steeneken, ''A review of the MTF concept in room acoustics and its use for estimating speech intelligibility in auditoria,'' J. Acoust. Soc. Am. **77**, 1069–1077 (1985).
[24] V. M. A. Peutz, ''Speech perception and information,'' in Proceedings of the 9th International Congress of Acoustics, Madrid, 1977, Vol. 1, p. 428.
[25] The Acoustical Society of America's response to a request for information on acoustics from the Office of Technical and Information Services—Architectural and Transportation Barriers Compliance Board, 27 July 1998, The Acoustical Society of America, 2 Huntington Quadrangle, Suite 1 NO 1, Melville, NY 11747.
[26] J. S. Bradley, R. D. Reich, and S. G. Norcross, ''On the combined effects of signal-to-noise ratio and room acoustics on speech intelligibility,'' J. Acoust. Soc. Am. **106**, 1820–1828 (1999).
[27] H. F. Kingsbury, ''Review and revision of room noise criteria,'' Noise Control Eng. J. **43**, 65–72 (1995).
[28] K. S. Pearsons, R. L. Bennett, and S. Fidell, ''Speech levels in various noise environments,'' Bolt, Beranek and Newman Inc. report to the U.S. Environmental Protection Agency, EPA Report 600-77-025, Canoga Park, CA (May 1977).
[29] M. Barron, *Auditorium Acoustics and Architectural Design* (E & FN SPON, London, 1993), pp. 418–419.

Broadband control of plate radiation using a piezoelectric, double-amplifier active-skin and structural acoustic sensing

Brody D. Johnson and Chris R. Fuller
Vibration and Acoustics Laboratories, Department of Mechanical Engineering, Virginia Polytechnic Institute and State University, Blacksburg, Virginia 24061

(Received 7 October 1998; accepted for publication 21 October 1999)

The potential of a piezoelectric, double-amplifier active-skin with structural acoustic sensing (SAS) is demonstrated for the reduction of broadband acoustic radiation from a clamped, aluminum plate. The active-skin is a continuous covering of the vibrating portions of the plate with active, independently controllable piezoelectric, double-amplifier elements and is designed to affect control by altering the continuous structural radiation impedance rather than structural vibration. In simulation, acoustic models are sought for the primary and secondary sources that incorporate finite element methods. Simulation indicates that a total radiated power attenuation in excess of 10 dB may be achieved between 250 and 750 Hz with microphone error sensing, while under SAS the radiated power is reduced by nearly 8 dB in the same frequency range. In experiment, the adaptive feed forward filtered-*x* LMS (least mean square) algorithm, implemented on a Texas Instruments C40 DSP, was used in conjunction with the 6I6O control system. With microphone error sensing, 11.8-dB attenuation was achieved in the overall radiated power between 175 and 600 Hz, while inclusion of SAS resulted in a 7.3-dB overall power reduction in this frequency band. © *2000 Acoustical Society of America.* [S0001-4966(00)00702-5]

PACS numbers: 43.55.Vn [PJR]

INTRODUCTION

Recent work in the areas of active noise control (ANC) and active structural acoustic control (ASAC) have shared a common trend: the pursuit of practical active control systems that may be applied in more generalized noise control environments. In such general environments, the necessary actuators and sensors must comply with predetermined space and weight requirements. Furthermore, the influence of the secondary system on the performance of the primary structure must also be considered in design. Example applications where such design issues are of prime concern arise in the automotive and aeronautical fields. In order to satisfy the constraints imposed in these and other applications, lightweight, compact, and robust control systems must be devised. This motive has led to the investigation of a wide variety of control approaches. One approach, discussed in this paper, consists of a complete covering of the radiating surface of a structure with a specially designed conformal skin. This skin may exhibit both passive and active characteristics and in many cases is comprised of a number of individual skin elements that make use of one or both of these tactics. In this approach one is concerned with sound radiated from the surface of the skin rather than the primary structure. Since the active-skin functions by modifying the radiation impedance, it is not necessary to directly modify the structural vibration and the approach is suitable for massive or stiff structures that have low mobility. The skin may also possess integrated sensing capabilities, such as structural acoustic sensing (SAS). SAS consists of the prediction of acoustic error from vibration information taken from a number of structurally mounted sensors. Maillard and Fuller have shown, both analytically and experimentally, that SAS is an effective technique for the estimation of an acoustic cost function in multichannel ASAC systems.[1,2]

An example of a passive–active skin, provided by Gentry, Guigou, and Fuller, is one that integrates a number of independent polyvinylidene fluoride (PVDF) actuators in a foam layer located on a vibrating piston.[3,4] This approach offers an increase in the low-frequency performance of the foam skin while still taking advantage of the passive properties of the foam at high frequency. For another skin approach, described in this paper, consider a primarily active-skin consisting of a number of independent skin cells, which are used to prevent radiation through the minimization of an acoustic cost function.[5] With this scheme, the skin cells must provide substantial control authority over the entire bandwidth of interest. Kugel and others have developed analytical models for the dynamic characterization of piezoelectric (PZT) acoustic transducers intended for use in an active-skin of this nature.[6]

Ross and Burdisso have also devised an interesting approach to the passive skin concept, by designing what is essentially a single degree of freedom (DOF) skin element.[7] When this passive device is applied to a vibrating surface, the mass component of the single DOF element is forced to vibrate at one level, while the base surrounding the mass element shares the original vibration level of the primary structure. Thus for frequencies above the resonance of this single DOF system, the mass and base elements vibrate out of phase. By determining the appropriate areas for the base and mass surfaces of the skin element, an acoustic dipole is created.

A number of examples of the skin concept in the control of sound were discussed in the previous paragraphs. In each of these examples the goal lies in the development of a com-

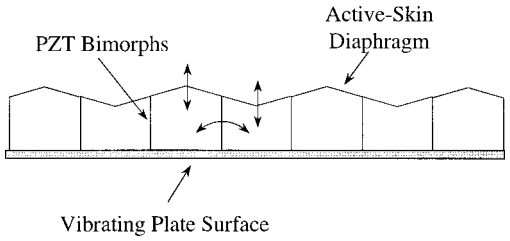

FIG. 1. The active-skin concept.

pact noise suppression system, albeit passive or active, that allows for application to a wider variety of noise control problems. It is such a system that will be evaluated here. The active-skin concept applied in this work is depicted in Fig. 1. By exciting the PZT bimorphs comprising the flexible leg elements of the active-skin, an amplified diaphragm response is obtained. The cell design employed here, shown in Fig. 2, provides two means of amplification of the acoustic response which are designed to provide a high level of diaphragm vibration with only a small space requirement. First, the use of bimorph PZT actuators, driven out of phase, provides an amplified flexural response of the legs of the cell. Since the cell legs are clamped at their base, the maximum leg displacement occurs at the joint between the legs and the cell diaphragm. By driving the two legs of a cell with opposite polarity, the diaphragm is forced to vibrate. Here the second stage of amplification is encountered as the response of the diaphragm tip is geometrically amplified with respect to the leg motion. The active-skin is then comprised of a number of these cells, each independently controllable. The independence of the individual cells provides the needed flexibility for attenuation of high-order modes, while also introducing the possibility of acoustic coupling between cells. This potential problem is handled by careful choices in error sensing and, in general, it is wise to use more error sensors than skin cells to prevent such interaction.

This work shall serve two main purposes. First, to develop a numerical model describing the active-skin system, as applied to plates, for investigation of the active-skin as a viable control approach in generalized structural radiation problems. Second, to verify the analytical findings by realizing the active-skin in experiment. The chosen primary structure is a clamped plate, which represents a building block common to many structures encountered in noise control applications, e.g., buildings, cars, machinery casings, etc.[8]

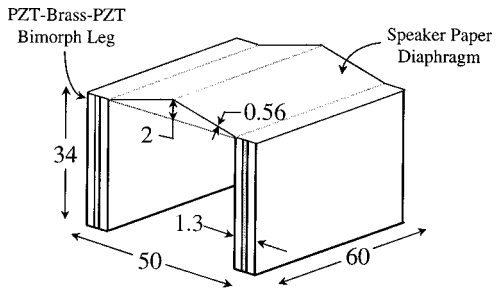

FIG. 2. The active-skin cell (dimensions in mm).

I. NUMERICAL ACTIVE-SKIN MODEL

In this section the numerical representation of the active-skin is introduced. The structural modeling techniques shall be discussed in the context of a single active-skin cell, as depicted in Fig. 2. This cell design makes use of bimorph PZT actuators on the legs of the cell and a light speaker paper material for the diaphragm. A description of the acoustic modeling approach follows, including the integration of SAS into the simulated error sensing. Once the necessary models are developed, a description of the control simulation is given. Finally, the setup of the virtual active-skin system is described, including the primary structure, skin cell, and error sensor locations.

A. Structural modeling

The IDEAS® finite element method (FEM) package was used for the creation of a 180-element, 210-node, representation of a single active-skin element.[9] A thin-shell element type was adopted for this model, providing six degrees of freedom (DOF) for each of the four nodes comprising an element. These DOF include translational motion along and rotational motion about the three coordinate axes. The element formulation also requires definition of the element thickness, mass density, modulus of elasticity, and Poisson's ratio for each element. For the purposes of this model, the materials are assumed to behave isotropically.

Having briefly introduced the FEM approach adopted in this analysis, a discussion of important mesh features will now be undertaken which pertain to the active-skin cell. First, as shown in Fig. 2, the bimorph PZT actuators are comprised of three layers of material, in which two 0.6-mm layers of PKI550 PZT sandwich a 0.1-mm layer of brass shim. The variation of material properties across this section is ignored for this model (along with the bonding layers), with PZT material properties assumed over the entire cross section. Similarity between the brass and PZT mechanical properties suggests that such an assumption should not significantly affect the modeling results. Second, three creased bends exist in the paper diaphragm of the active-skin cell. These bends, or hinges, are modeled by torsional springs, which act to impose resistance against the free rotation of the diaphragm about these creases. With this approach, the torsional stiffness may be tuned to match experimentally observed behavior. Clamped boundary conditions were assumed for nodes at the base of the PZT legs.

The simultaneous vector iteration approach is used to determine the mode shapes and resonant frequencies for the active-skin cell.[9,10] Each mode shape is expressed as a vector whose components represent the nodal displacements associated with a given mode. For such a multidegree of freedom system, the response to a harmonic input may be expressed as a summation over the orthogonal modes by

$$w(n,t)=\sum_{m=1}^{M} A_m \Phi_m(x,y)\sin(\omega t), \tag{1}$$

where w represents the displacement function, n refers to the nodal coordinate system, t is time, A_m is a complex modal amplitude, Φ_m is the mth mode shape, and ω is the excitation

frequency.[10] To determine the induced modal amplitudes for an arbitrary harmonic excitation, the assumed solution of Eq. (1) must be substituted into the transformed equation of motion, which reduces to

$$[\Phi]^T[M][\Phi]\{-\omega^2 A\}+[\Phi]^T[K][\Phi]\{A\}=[\Phi]^T\{F\}, \tag{2}$$

where Φ is the modal matrix, M is the mass matrix, K is the stiffness matrix, A represents the modal amplitude vector, and F is the nodal force vector. Further reduction of Eq. (2) yields the mth modal amplitude as

$$A_m=\frac{1}{m_d(\omega_m^2-\omega^2)}\{\Phi_m\}^T\{F\}, \tag{3}$$

where m_d is the normalization constant such that $\{\Phi_m\}^T[M]\{\Phi_m\}=m_d$, and ω_m is the natural frequency of the mth mode.

At this stage, it remains only to discuss the determination of a nodal force vector that appropriately represents the action of the piezoelectric actuators of the active-skin cell. The approach applied here was first proposed by Crawley and De Luis for the representation of one-dimensional piezoelectric actuators.[11] In 1991, Dimitriadis, Fuller, and Rogers developed an extension to two-dimensional scenarios, such as that encountered in this work.[12] The goal in the implementation of this model is to determine equivalent external edge moments to apply to the FEM models for characterization of the vibrational behavior of the active-skin cell. It should be noted that the approaches suggested in the references above do not directly apply here, due to the relative thickness of the piezoelectric material in the skin cell to the underlying structure. The models are used only to provide a more realistic loading of skin cell by application of the control voltage and, for purposes of simulation, are sufficient to meet this end.

B. Acoustic modeling

The objective of the acoustic modeling is to predict the far-field radiation from the active-skin. Since the skin may be effectively viewed as a baffled, planar radiator, it is the simple half-space radiation problem that requires attention. Under this limitation, the far-field radiated pressure depends only upon the normal surface velocity of the radiating structure. Each FEM element is treated as a component source of the complex radiating structure. When each of these component sources is small compared to the acoustic wavelength (maximum dimension $\ll\lambda$), the analysis will appropriately model the phase variation of the radiated pressure.[13] Thus under these assumptions, the pressure radiated to a point in the acoustic medium may be written in terms of Rayleigh's integral as

$$p(\vec{r})=\frac{j\omega\rho_0}{2\pi}\sum_S\left[\nu_n(\vec{r}_s)\frac{e^{-jk|r-r_s|}}{|\vec{r}-\vec{r}_s|}\right]dS, \tag{4}$$

where p is the observed acoustic pressure, ρ_0 is the density of the acoustic fluid, ν_n is the normal velocity, $\vec{r}$ is the position vector of the point at which the pressure is determined, and $\vec{r}_s$ is the position vector locating a surface element of the vibrating structure.[8]

From the FEM representation of a vibrating structure, the velocity of the structure at a number of defined nodal locations is known. Combining the nodal velocities with knowledge of the structure's geometry, the normal surface velocity may be computed for each element comprising the structure. This discretized normal surface velocity suggests that Rayleigh's integral must be approximated by a sum over the elements comprising the complex structure. This discretization takes the following form:

$$p(\vec{r})=\sum_{m=1}^{N}\frac{j\omega\rho_0}{2\pi}S_m\nu_m\frac{e^{-jkR_m}}{R_m}, \tag{5}$$

where the index m identifies an element of the vibrating structure, N is the total number of elements, S_m is the area of the mth element, ν_m is the normal velocity of the mth element, and R_m is the distance between the center of the mth element and the point in the acoustic medium at which the pressure is to be evaluated. As long as the maximum element dimension satisfies the above low-frequency assumption, a discretized evaluation of Eq. (4) will yield an accurate measure of the pressure radiated to desired points in the acoustic medium. Note that this method is most appropriately applied to planar, baffled radiators; however, when the size of a nonplanar source is small compared to the acoustic wavelength, it may also be represented in this manner.[13]

This modeling approach may also be modified for use in the study of structural acoustic sensing (SAS) with the active-skin. The basis of the SAS technique is that, for relatively simple geometries, the acoustic radiation may be predicted from a thorough knowledge of the surface velocity over a vibrating structure. In the previous paragraphs, a *complete* knowledge of this information was available, allowing for direct determination of the radiated pressure. The idea behind SAS is to accurately predict the radiated pressure from only a *partial* knowledge of the surface velocity field. As with the results in the previous paragraph, the radiated pressure will be expressed as a sum over a number of component radiators; however, here the component radiators will consist of a number of elements rather than one. In this work, the radiation from these areas is assumed to resemble a monopole, although an unlimited number of alternative pressure formulations may be assumed for the discretization.[1,2] For this model, the pressure estimate at a point in the acoustic medium may be written, in the frequency domain, as a summation of the accelerometer signals as

$$p(\vec{r})=\sum_{m=1}^{N}\frac{\rho_0}{2\pi}S_m a_m\frac{e^{-jkR_m}}{R_m}, \tag{6}$$

where the index m identifies an accelerometer of the SAS array, N is the total number of SAS sensors, S_m is the area of the radiating surface associated with the mth sensor, a_m is the normal acceleration at a point in the mth component area, and R_m is the distance between the mth sensor and the point in the acoustic medium at which the pressure is to be evaluated, which is defined by the position vector $\vec{r}$.

In order to implement SAS in real-time as a supplement to a time-domain feed forward algorithm, an array of digital filters modeling the various sensor paths is required.[1,2] The

appropriate digital filters necessary for modeling these transfer functions must be found using a numerical curve fit with a reasonable number of finite impulse response (FIR) filter weights. The difficulty in developing a practical SAS system lies in achieving an adequate representation of the acoustic radiation with a minimal number of structural sensors. These ideas will resurface below when SAS is applied in experiment with the active-skin.

C. Control simulation

In practice, the active-skin will be used as part of an adaptive control system making use of the filtered-x LMS feed forward algorithm.[14] In simulation it is impractical to mimic such an algorithm, prompting for an alternative means for time-domain evaluation of the control performance of the active-skin system. The method adopted in this work takes advantage of the quickness of a frequency-domain solution and the practicality of a time-domain approach. With this method, the optimal control compensator responses, $W(z)$, are determined in the frequency domain using linear quadratic optimal control (LQOC) theory.[15] This approach entails writing the quadratic cost function (a sum of the squared error) in terms of the disturbance and control inputs and subsequently determining the optimal control inputs which result in the minimization of this cost function. It is assumed in this analysis that the presence of the active-skin does not affect the acoustic radiation of the primary structure, limiting the analysis to the far-field control problem. Once the frequency responses have been isolated, the MATLAB® function INVFREQZ may be used to design digital filters for use in time-domain simulation.[16] This transformation uses a curve-fitting technique to provide the best possible *causal* representation (for a defined number of weights) of the desired complex frequency response. This transformation places a realistic limit on the performance of the control compensators, as found in experiment with a feed forward approach. Upon determination of the control compensators, an arbitrary time signal may be generated for the disturbance and fed through the primary and secondary control paths for evaluation of the control performance. Thus this hybrid approach to simulation entails the design of digital filters from frequency-domain transfer functions, along with the time-domain implementation of these filters with respect to a random disturbance, generated in MATLAB®.

D. Plate and active-skin coordinate systems

As mentioned earlier, in this work the active-skin is applied to a clamped, aluminum plate. The plate is rectangular, of dimensions $170\times150\times1.5$ mm, and is mounted in a baffle. A broadband disturbance is provided to the plate through a piezoelectric actuator ($38\times30\times0.1$ mm) located for effective excitation of the first six plate modes. The location of the disturbance actuator on the plate is shown in Fig. 3. The response of the plate is determined using a FEM approach analogous to that used with the active-skin cell. For brevity this model is not presented here, but let it be noted that the acoustic response of the plate is again determined from the structural response by means of Rayleigh's integral,

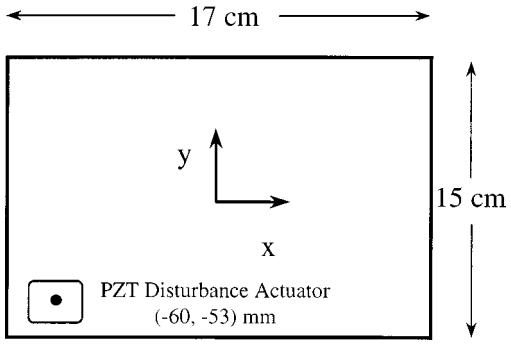

FIG. 3. The piezoelectric disturbance actuator.

which is evaluated in a discretized form. For the purposes of this work, the active-skin is mounted just above the surface of the plate, preventing vibrational coupling between the two structures. It is further assumed that the acoustic fields of these two structures may be determined separately and superposed for determination of the complete sound field. A typical configuration of the active-skin is represented by Fig. 4, with the origin of the coordinate system taken at the center of the plate.

In Sec. I C, the combined frequency-time-domain simulation approach was described. While a reference signal is not required for the frequency-domain determination of the optimal control compensator responses, a reference signal *is* necessary for the time-domain evaluation of these compensators under an arbitrary excitation. The ideal reference (the disturbance input) is assumed for this work. The error signals are sound pressure, measured or predicted (in the case of SAS) at a number of far-field locations. The sound pressure at a number of distinct observation points is also monitored for estimation of the global control performance. Both acoustic directivity and radiated sound power comparisons are made between the controlled and uncontrolled responses of the system.

II. NUMERICAL RESULTS

Three key results will be presented in this section. First, the tuned FEM model is presented and compared to experimentally measured resonant frequencies. Next, the complete active-skin model is used to demonstrate the effectiveness of this control approach in a 6I6O control system, which uses

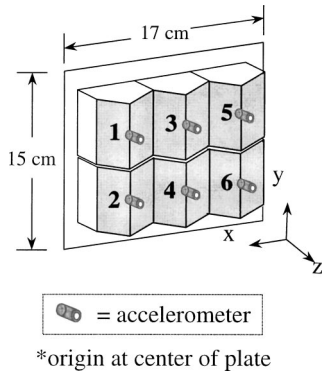

FIG. 4. 6I6O active-skin cell configuration.

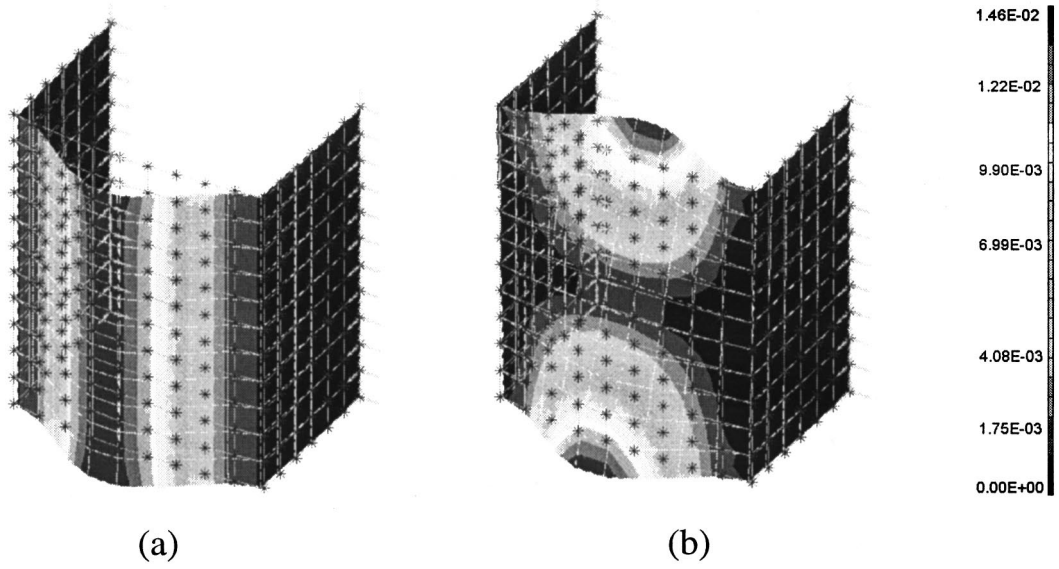

FIG. 5. Displacement magnitude: (a) first active-skin cell mode: 246 Hz (250 Hz) and (b) second active-skin cell mode: 374 Hz (390 Hz).

microphones as error sensors. Finally, an investigation of the effect of SAS on the active-skin is undertaken using the developed numerical model.

A. Structural modeling

The FEM approach to modeling the active-skin cell was outlined earlier in this paper. In order to tune the torsional springs used along the bends in the diaphragm of the active-skin cell, experiments were conducted in which the vibrational response of a single cell was observed for a broadband voltage excitation. In these experiments, a laser vibrometer was used to collect normal velocity data over the surface of the diaphragm. By computing the experimental frequency response function (FRF) relating the applied voltage to the cell vibration at various positions, the experimental modes and mode shapes of the active-skin cell were obtained. Only the first two modes made significant contributions to the observed response; therefore, it is the first two modes that will be presented here. Figure 5(a) displays the mode shape obtained from the FEM model for the first mode of the active-skin cell. Beneath this depiction, the FEM resonant frequency is given along with the experimentally observed value, the latter in parentheses. This mode dominates the frequency response except near the second resonance. Excitation of the first mode results in the desired diaphragm motion for efficient sound radiation. In Fig. 5(b), however, a less efficient radiating second mode is depicted. Here, the upper and lower halves of the diaphragm vibrate out of phase, resulting in reduced far-field radiation for low frequencies.

B. Microphone error sensing results

The first simulation performed with the active-skin is intended to show the potential of the secondary acoustic sources, the skin cells, for application to generalized structural radiation problems. Microphone error sensing is used to meet this end, before a more compact SAS sensing scheme is employed. Six cells are used for this embodiment of the active-skin, shown in Fig. 4. The accelerometers depicted in this figure are used only for simulation with SAS, below. the skin cells were distributed evenly over the surface of the plate and the microphones were positioned to sense all six radiating modes included in the analysis.

The time-domain portion of the simulation was performed with a sample rate of 1600 Hz, employing 96 coefficient FIR filters in the control path and 255 coefficient FIR filters serving as control compensators. This means that 255 FIR coefficients are used to model the optimal compensator frequency responses, as determined from LQOC theory. A target control bandwidth was chosen ranging from 250 to 750 Hz, encompassing six structural modes of the clamped aluminum plate. Figure 6 depicts the control performance in terms of the radiated sound power from the plate/skin system. An overall reduction in the acoustic power of 11.7 dB is observed between 250 and 750 Hz.

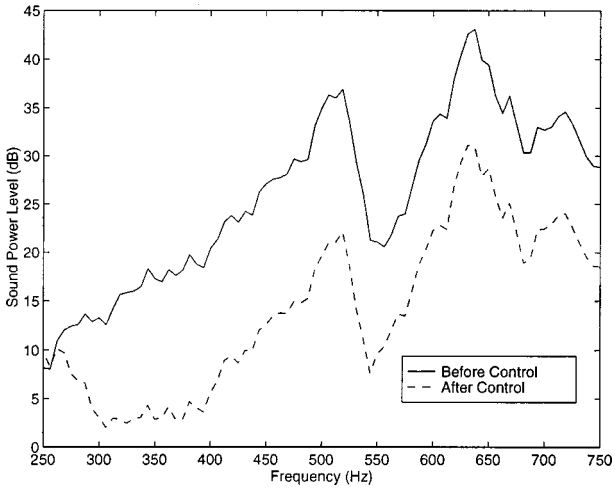

FIG. 6. Radiated acoustic power before and after control.

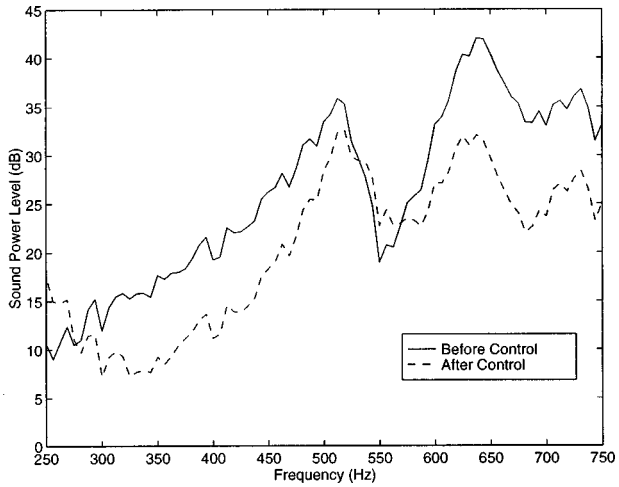

FIG. 7. Radiated acoustic power before and after control with structural acoustic sensing.

C. SAS error sensing results

Here, a SAS sensing scheme will be incorporated into the model of the previous section as a step toward a more practically realizable control system. The six active-skin cell locations from above were retained; however, an accelerometer is positioned at the center of the diaphragm of each skin cell, as depicted in Fig. 4. These sensors provide the structural information necessary for prediction of the acoustic error signals.

In order to isolate the effect of SAS on the control performance of this system, the simulation parameters from the previous control configuration are retained here. A comparison between the SAS-predicted and the analytically determined transfer functions relevant to the system was made prior to simulation. Only minor phase error (at high frequency) was evident from this comparison, suggesting that the SAS system provides an adequate model of both the control-to-error and disturbance-to-error paths. Implementation of this SAS active-skin system yields a 7.9-dB reduction in the overall sound power radiated from the plate/skin system. The radiated sound power frequency spectra for this simulation are shown in Fig. 7, respectively.

III. EXPERIMENTAL ACTIVE SKIN

Before presenting experimental results achieved with the active skin, it is necessary to first discuss the means for practical implementation of the active skin and the SAS error sensing technique. As mentioned above, the adaptive feed forward filtered-x LMS algorithm is applied through the use of a digital signal processor (DSP). Familiarity with algorithms of this nature shall be assumed and the unfamiliar reader is referred to the literature.[14,17,18] In the absence of far-field microphone error sensing, a second DSP is used to implement the SAS sensing scheme. Previous work with SAS has relied on the known radiation behavior of specialized geometries, while in this work a convenient experimental technique is used to determine relationships between the measured structural vibration and the desired far-field acoustic response. After a discussion of the application of SAS, the experimental setup will be introduced, which includes an improved skin cell design relative to that used in the numerical study.

A. Structural acoustic sensing in experiment

This section is devoted to the development of an experimental methodology for the prediction of the radiated acoustic pressure using a number of accelerometers, which are distributed over the radiating surfaces of the active skin. The accelerometer signals are used in conjunction with an array of specially designed digital filters to construct signals corresponding to the acoustic pressure at desired points in the far-field. For accurate prediction of the acoustic error, the influence of a given structural response on the acoustic pressure at a desired error location must be known. As discussed above, this relationship between the structural sensors and the error locations may be found using analytical methods. Alternatively, it is possible in some instances to measure the relationships directly. One way to do this is to excite each isolated area of the radiating surface independently, measuring the desired frequency response functions (FRF's) in the process. Fortunately, the individual skin cells of the active-skin provide a convenient means for the isolation of these influence functions. Thus the desired influence relationships are determined by exciting a single skin cell and directly measuring the transfer functions between an accelerometer mounted on the cell to each of the far-field microphones. This process yields the necessary information for relating the skin vibration to the measured acoustic response in the far-field, but fails to characterize the relationship between the plate vibration and the associated far-field acoustic disturbance. By placing a single additional accelerometer on the plate and issuing a disturbance to the plate via a shaker, a similar set of measurements may be made which characterizes the effect of the plate vibration on the net error. It is important to note that any ''cross-talk'' between the structural sensors would serve to dissolve the validity of this approach. This coupling is eliminated by mounting the skin cells on a perforate sheet (acoustically transparent) slightly above the surface of the plate. Once the influence functions have been determined, they must be incorporated into a real-time DSP code. Thus an array of digital filters modeling the various sensor paths is required.

B. Experimental setup

A rough schematic of this skin cell design is given in Fig. 8(a). In this sketch, the dashed lines depict an exaggerated motion of the skin cell frame, while solid black lines represent the motion of the diaphragm. This improved cell design includes piezoelectric material inside the frame, with an outer covering of steel for protection of the piezoelectric material. A stiff, lightweight carbon–graphite material is used for the diaphragm, preventing high-order diaphragm modes from dominating the response of the device. The actual devices used for this experimentation were designed and fabricated by the Material Research Laboratory at the Pennsylvania State University at State College, Pennsylvania.[6] One such device, which is approximately $55\times55\times20$ mm in size, is shown in Fig. 8(b). In this most recent design, the

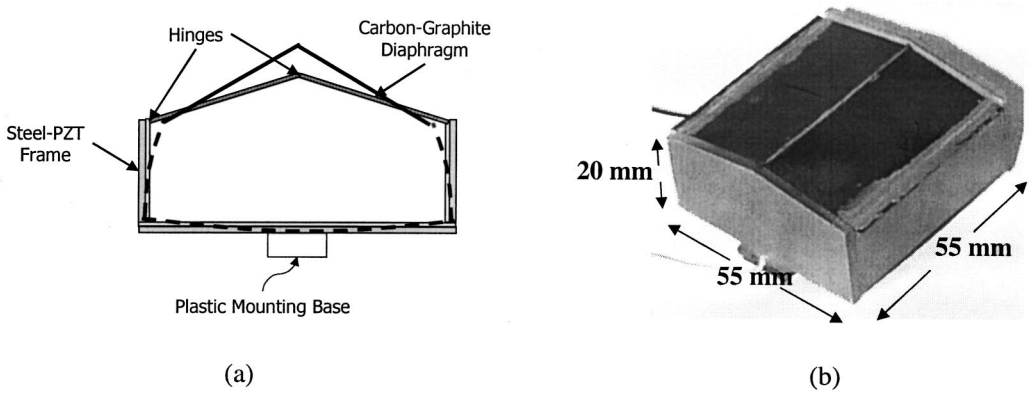

FIG. 8. The active-skin cell design: (a) schematic and (b) a single active-skin cell.

additional piezoelectric material employed on the bottom of the skin cell allows for even greater displacement of the cell diaphragm. Again, the active skin is implemented on a clamped, aluminum plate of dimensions $170\times150\times1.5$ mm. The plate is mounted in a baffle inside an anechoic chamber ($4.2\times2.5\times2.2$ m). A tubular hemisphere was used to support a number of microphones and a traverse boom was used to acquire in-plane acoustic directivity data over the 180°-space on the front side of the baffle. Sixteen microphones were mounted on the hemisphere, six for use as error sensors in microphone sensing configurations and an additional ten to provide a picture of the total radiated acoustic power. Note that each of these ten locations is distinct from the microphone error sensor locations. A schematic of the experimental setup is given in Fig. 9. Dashed lines are used with the microphones to indicate that either microphone or SAS sensing is adopted for a particular control configuration. As depicted in Fig. 9, a shaker mounted to the plate from the backside of the baffle disturbs the plate. The skin cells are mounted to a perforated aluminum support plate approximately 5 mm in front of the surface of the plate. An accelerometer is mounted to each radiating structure, one on each of the six skin cells and another on the backside of the plate. The signals from each accelerometer are passed along to the SAS filter DSP, see Fig. 9, where the SAS filtering is performed on a TI-C30 DSP. Thirty coefficients are employed in each of the 42 SAS paths at a 1300-Hz sample rate. A TI-C40 DSP is used to implement the filtered-*x* control algorithm at a sample rate of 2000 Hz, accepting error signals from the SAS filter DSP. With this sample rate, the control compensators and system identification filters may possess up to 175 and 96 FIR coefficients, respectively. The ideal reference (the disturbance input) is used in this work. The maximum filter length is applied in each control configuration. The limiting factor in the controllable bandwidth of this application of the active skin is the 1300-Hz sample rate of the SAS sensing. Hence, all control experiments are conducted for a band-limited random disturbance between 175 and 600 Hz to ensure accurate prediction of the far-field acoustic error.

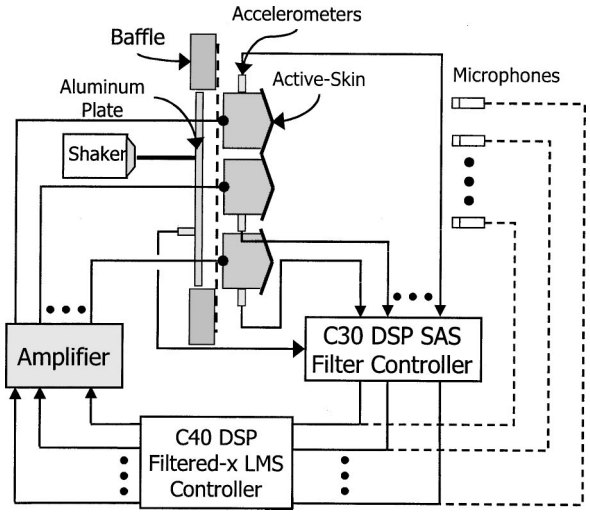

FIG. 9. The active-skin experimental setup.

IV. EXPERIMENTAL RESULTS

The primary objective of this work is to show the potential of the active-skin in the control of structural radiation; however, a secondary objective is to demonstrate the utility of such a skin in tandem with SAS. Thus the skin is employed first with far-field microphones serving as error sensors and second with the integration of SAS. The six-cell active-skin, mounted to a perforated aluminum sheet, is depicted in Fig. 10, showing the accelerometers mounted at the center of the diaphragm of each cell. Note that a seventh structural sensor is located on the backside of the aluminum plate. The following paragraphs summarize the results ob-

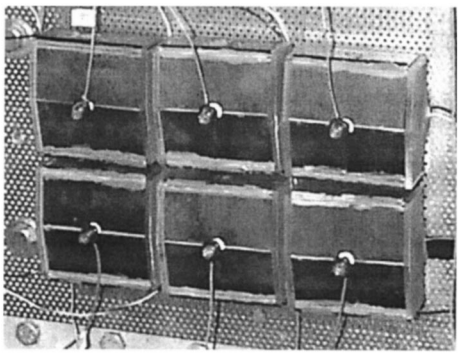

FIG. 10. The active-skin in a top-mounted structural acoustic sensing configuration.

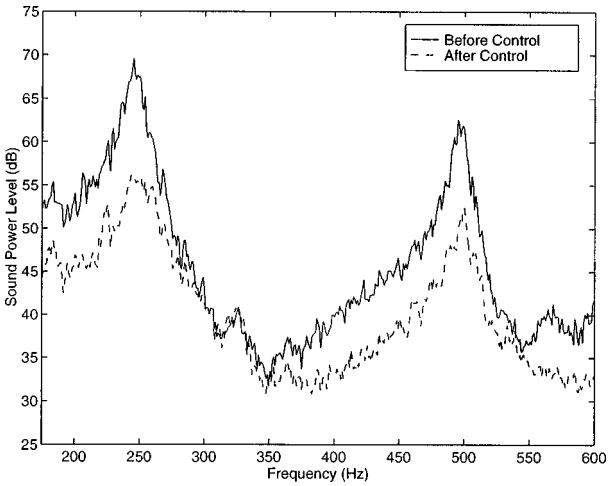

FIG. 11. Radiated sound power spectra, top-mounted accelerometer configuration with microphone sensing.

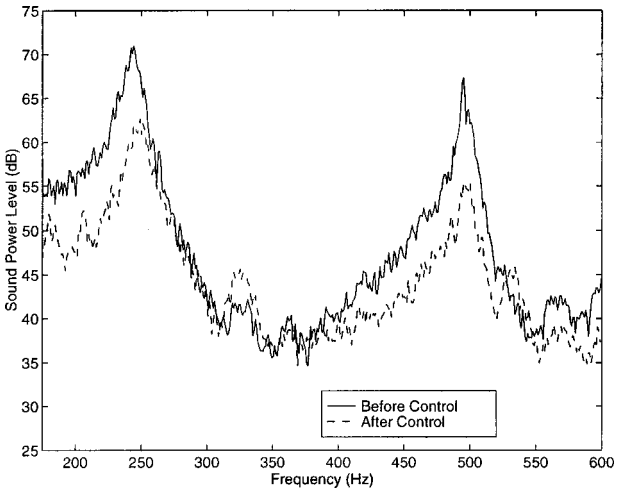

FIG. 12. Radiated sound power spectra, top-mounted accelerometer configuration with structural acoustic sensing.

tained for this mounting configuration under the aid of microphone and SAS sensing systems, respectively.

To set the pace for the SAS system, the microphone sensing setup is adopted first. For this 6I6O control system, the error microphones were distributed evenly over the tubular hemisphere described above. The shaker attached to the plate was driven with band-limited random noise between 175 and 600 Hz. While several plate modes are present in the frequency range investigated, the response of the plate is dominated by two modes due to the nature of the shaker loading. The filtered-*x* algorithm was employed with a sample rate of 2000 Hz and 175 coefficients were used in each of the six adaptive FIR control compensators. Following a three-minute period of system identification, the control compensators were allowed to adapt for two minutes. An estimate of the radiated sound power is given in Fig. 11 for the controllable bandwidth, which reveals significant attenuation around each resonant frequency of the aluminum plate. An impressive 9.5-dB reduction is achieved in the controlled power radiation from the plate-skin system in the 175- to 600-Hz bandwidth.

Having established a baseline performance for the active-skin, the primary objective of this work, as discussed above, is satisfied. The SAS system shall now be included to predict the acoustic error at each of the microphone locations used in the previous experiment. The 42 influence paths, relating the seven structural signals to each of the six error estimates, were obtained using the experimental procedure outlined in Sec. III A of this work. Once these paths have been identified, a straightforward application of the control algorithm is made. Again, a sample rate of 2000 Hz was used, in conjunction with 175 coefficient adaptive control compensators. A 1300-Hz sampling frequency was adopted with the SAS controller, using 30 coefficients in each of the SAS influence paths. A total radiated power reduction of 7.3 dB was attained over the 175 to 600 Hz bandwidth. The corresponding frequency spectra are given in Fig. 12.

V. CONCLUSIONS

In this work, both numerical and experimental methods were used to demonstrate the effectiveness of a piezoelectric double-amplifier active-skin in conjunction with SAS for the control of broadband radiation from a clamped, aluminum plate. A comparison between SAS and traditional sensing arrangements was made in both the numerical and experimental studies in order to validate the practically of an active-skin approach to systems where far-field microphone error sensing is impractical. FEM techniques were used to develop a structural model of a single active-skin element, which was, in turn, applied to the numerical determination of the acoustic radiation from this source. Integration of this structural-acoustic model into a combined frequency- and time-domain control approach led to the numerical evaluation of the 6I6O active-skin system. Numerical results indicate that the total radiated sound power may be reduced by as much as 11 dB using microphone sensing and by nearly 8 dB using SAS. In experiment, microphone error sensing led to an approximate attenuation of 10 dB in the total radiated sound power, while SAS error sensing yielded roughly a 7-dB attenuation. Significant attenuation in radiated sound power was achieved with each active-skin configuration. While the SAS configurations resulted in a lessened control performance with respect to the corresponding microphone sensing result, substantial reduction was still obtained. This degradation of control performance is suspected to depend on the maximum sample rate and filter lengths attainable with the SAS filter DSP. These results further suggest that the active-skin system is conducive to the inclusion of SAS, which makes the actuator-sensor system more compact and, hence, more practical than many previously developed ASAC or ANC systems.

The main conclusion drawn from this work is that the piezoelectric, double-amplifier active-skin system shows potential for application to broadband structural radiation problems, including those where far-field microphone sensing would represent an impractical error sensing scheme and when the radiating structure is relatively massive.

ACKNOWLEDGMENT

The authors gratefully acknowledge the funding of this research under Grant No. N00014-94-1-1140 by the Office of Naval Research, Dr. Kam Ng, Technical Monitor.

[1] J. Maillard and C. R. Fuller, ''Advanced time domain wave-number sensing for structural acoustic systems, Part I: Theory and design,'' J. Acoust. Soc. Am. **95**, 3252–3261 (1994).
[2] J. Maillard and C. R. Fuller, ''Advanced time domain wave-number sensing for structural acoustic systems, Part III: Experiments on active broadband radiation control of a simply-supported plate,'' J. Acoust. Soc. Am. **98**, 2613–2621 (1995).
[3] C. A. Gentry, C. Guigou, and C. R. Fuller, ''Smart foam for applications in passive/active noise radiation control,'' J. Acoust. Soc. Am. **101**, 1771–1778 (1997).
[4] C. A. Gentry, C. Guigou, and C. R. Fuller, ''Foam-PVDF smart skin for active control of sound,'' Proceedings of the 1996 Smart Structures and Materials Symposium, Industrial and Commercial Applications of Smart Structures Technologies, San Diego, California, Vol. 2721, pp. 26–37, February 1996.
[5] C. R. Fuller and B. D. Johnson, ''Control of structural radiation with an integrated piezoelectric double-amplifier skin,'' presented at the 1997 ONR Transducer Materials and Transducers Work Shop, State College, PA, April 1997.
[6] B. Xu, Q. M. Zhang, V. D. Kugel, W. Qingming, and L. E. Cross, ''Optimization of bimorph based double amplifier actuator under quasistatic situation,'' ISAF'96, Proceedings of the Tenth IEEE International Symposium on Applications of Ferroelectrics, 1996, Vol. 1034, p. 2; Vol. 1, pp. 217–220.
[7] B. W. Ross and R. A. Burdisso, ''Low frequency passive noise control of a piston structure with a weak radiating cell,'' J. Acoust. Soc. Am. **106**, 226–232 (1999).
[8] F. Fahy, *Sound and Structural Vibration* (Academic, London, 1985), Chap. 2, pp. 60–72.
[9] *I-DEAS Master Series User Guide Level 4: Model Solution and Optimization* (Structural Dynamics Research Corporation, Milford, Ohio, 1988), Chap. 6, pp. 6–7.
[10] L. Meirovitch, *Elements of Vibration Analysis*, 2nd ed. (McGraw-Hill, New York, 1975), Chap. 4, pp. 178–185.
[11] E. F. Crawley and Javier de Luis, ''Use of piezoelectric actuators as elements of intelligent structures,'' AIAA Paper 86-0878, pp. 1373–1385, October 1987.
[12] E. K. Dimitriadis, C. R. Fuller, and C. A. Rogers, ''Piezoelectric actuators for distributed vibration excitation of thin plates,'' Trans. ASME, J. Vib. Acoust. **113**, 100–107 (1991).
[13] L. E. Kinsler, A. R. Frey, A. B. Coppens, and J. V. Sanders, *Fundamentals of Acoustics*, 3rd ed. (Wiley, New York, 1982), Chap. 8, pp. 167–169.
[14] B. J. Widrow and S. D. Stearns, *Adaptive Signal Processing* (Prentice-Hall, Englewood Cliffs, NJ, 1985), Chap. 6, pp. 99–116.
[15] B. D. Johnson, ''Control of broadband structural radiation from structures using a piezoelectric double-amplifier active-skin,'' M.S. thesis, Department of Mechanical Engineering, Virginia Polytechnic Institute and State University, 1997.
[16] Mathworks, Inc., *MATLAB Signal Processing Manual* (Prentice-Hall, New York, 1995), Chap. 6, pp. 180–182.
[17] J. S. Vipperman, R. A. Burdisso, and C. R. Fuller, ''Active control of broadband structural vibration using the LMS adaptive algorithm,'' J. Sound Vib. **166**(2), 283–299 (1993).
[18] S. J. Elliot, P. A. Nelson, and I. M. Stothers, ''A multiple error LMS algorithm and its application to the active control of sound and vibration,'' IEEE Trans. Acoust., Speech, Signal Process. **35**, 1423–1434 (1987).

Performance of some sparseness criterion blind deconvolution methods in the presence of noise

Michael K. Broadhead and Lisa A. Pflug
Naval Research Laboratory, Ocean Acoustics Division, Code 7185, Stennis Space Center, Mississippi 39529

(Received 16 March 1998; accepted for publication 13 October 1999)

A comparison of the sparseness (simplicity) norm criterion blind deconvolution methods of Cabrelli and Wiggins is made in order to ascertain relative performance for underwater acoustic transient source signal estimation, especially in the presence of noise. Both methods perform well at high signal-to-noise ratios, producing source estimates that are significant improvements over the original received signal for classification purposes. At moderate and lower SNRs, the Cabrelli method tends to generate results that are superior to the Wiggins method. This is especially true for a damped sinusoid transient source, for which the Wiggins method fails completely at lower SNRs, while the Cabrelli method can still produce good source estimates. [S0001-4966(00)06601-7]

PACS numbers: 43.60.Gk, 43.30.Wi [JCB]

INTRODUCTION

An area of interest in several fields of underwater acoustics signal processing involves accounting for environmental distortion introduced into a propagating pulse (Broadhead *et al.*, 1993). One useful mathematical model representing this process is that of convolution, which in turn leads to the consideration of the deconvolution problem. When only the received signal is available, along with statistical information about the system transfer function or input, then the problem under consideration is called a ''blind'' deconvolution problem (Haykin, 1994). Such problems, with specific emphasis on underwater acoustics applications, are the subject of this paper.

In previous work we have discussed the blind deconvolution technique introduced by Wiggins (1978), and its application to underwater acoustics problems (Broadhead, 1995; Broadhead *et al.*, 1996). Wiggins' idea, based on intuition, was to use the varimax norm (or V-norm) as a measure of sparseness, which was a statistical property his signal model exploited. He termed this method ''minimum entropy'' (not to be confused with maximum entropy or minimum cross-entropy techniques), which, in hindsight, was not the most appropriate choice of terminology. However, the idea was fundamentally new—to develop a filter that would drive the received signal to a sparser representation in order to recover the underlying Green's function. This stimulated research on a wide range of related deconvolution methods (e.g., exponential transformation, parsimonious deconvolution, zero-memory, variable norm, etc.; see Walden, 1985).

This first period of research activity ended in the mid 1980's, and the higher order statistics community then took up the problem by considering the blind system identification problem with non-Gaussian input (refer to bibliography in Hatzinakos and Nikias, 1994). Modern terminology would cast Wiggins' method as a cumulant maximization technique (see, for example, Cadzow, 1996), although is seems that he has not as yet been universally recognized by that research community as the founder of such methods. By the time Walden's review paper was written, it was understood that Wiggins' method had less to do with entropy than with non-Gaussianity. The V-norm could be viewed, essentially, as kurtosis, which Wiggins' algorithm seeks to maximize. This is appropriate, since positive kurtosis is a measure of the degree of departure from a Gaussian distribution to one with a longer tail. This is consistent with sparseness (or simplicity) in the structure of the input random process to the blind deconvolution problem. This point of view allows one to view Wiggins' method as a higher order statistics method (Walden, 1985).

Another important paper on ''minimum entropy'' methods, that by Cabrelli (1984), appeared toward the end of the first period of research activity. As far as we can ascertain, his method is relatively unknown by the modern blind deconvolution community. Cabrelli developed a measure of simplicity (or sparseness) that he referred to as the D-norm. Otherwise, he proceeded much the same as Wiggins, and the resulting system of equations gave similar solutions for his test cases. Cabrelli noted that his algorithm should be more robust in the presence of noise. However, only two simulation examples are given in his paper to illustrate the successful application of his method in noise. The examples show successful estimation of two- and three-spike impulse response functions with levels of additive noise which are, for the underwater acoustics problem, considered to be very low.

In the present work, we study the relative performance of the Wiggins and Cabrelli methods with significantly varying levels of Gaussian noise in a realistic underwater acoustics propagation environment, and verify, at least to some degree, Cabrelli's conjecture. We also propose and test some variations of his algorithm.

I. PROBLEM MOTIVATION AND SIGNAL MODEL

When a sound pulse travels through the ocean, especially in shallow water, it reflects back and forth between the sea surface and the ocean bottom. Further interaction with geologic strata in the occan bottom may also occur, producing attenuation, scattering, and other distortions. Thus the pulse at the receiver, some distance from the source location,

can look quite different from the original pulse. Furthermore, the addition of noise will create even more distortion. An automatic pattern classifier may then fail to recognize a signal after these propagation distortions have been introduced.

In order to account for the effects of environmental distortion in signal processing schemes, a signal model is needed. In this paper, we do not explicitly include noise in the signal model, but rather seek algorithms that are stable in the presence of noise (considering also possible hybridization with noise reduction methods). We concentrate, then, on accounting for wave propagation effects (primarily multipath) in the signal model, by using the wave equation

$$\mathbf{D}_2\psi(\mathbf{r},t)=\overline{F}(\mathbf{r},t), \tag{1}$$

where

$$\mathbf{D}_2\equiv\rho\nabla\cdot\left(\frac{1}{\rho}\nabla\right)-\frac{1}{c^2(\mathbf{r})}\partial_{tt}. \tag{2}$$

Here, $c(\mathbf{r})$ is the sound speed, ρ is density, $\psi(\mathbf{r},t)$ is acoustic pressure, and $\overline{F}(\mathbf{r},t)$ is the sound source. Let us define the Green's function $\tilde{G}(\cdot)$, such that

$$\mathbf{D}_2\tilde{G}(\mathbf{r},t|\mathbf{r}',t')=\delta(\mathbf{r}-\mathbf{r}')\,\delta(t-t'), \tag{3}$$

and assume a separable source

$$\overline{F}(\mathbf{r},t)=F(\mathbf{r})S(t). \tag{4}$$

Now,

$$F(\mathbf{r}')S(t')\mathbf{D}_2\tilde{G}(\mathbf{r},t|\mathbf{r}',t')$$
$$=\mathbf{D}_2\tilde{G}(\mathbf{r},t|\mathbf{r}',t')F(\mathbf{r}')S(t'), \tag{5}$$

because $\mathbf{D}_2$ operates on unprimed coordinates. Hence,

$$\mathbf{D}_2\tilde{G}(\mathbf{r},t|\mathbf{r}',t')F(\mathbf{r}')S(t')$$
$$=F(\mathbf{r}')\,\delta(\mathbf{r}-\mathbf{r}')S(t')\,\delta(t-t'). \tag{6}$$

Furthermore,

$$\mathbf{D}_2\int_{-\infty}^{\infty}\int_V\tilde{G}(\mathbf{r},t|\mathbf{r}',t')F(\mathbf{r}')S(t')dV'\,dt'$$
$$=\int_V F(\mathbf{r}')\,\delta(\mathbf{r}-\mathbf{r}')dV'\int_{-\infty}^{\infty}S(t')\,\delta(t-t')dt'$$
$$=F(\mathbf{r})S(t)=\overline{F}(\mathbf{r},t). \tag{7}$$

This implies that

$$\psi(\mathbf{r},t)=\int_{-\infty}^{\infty}\int_V\tilde{G}(\mathbf{r},t|\mathbf{r}',t')F(\mathbf{r}')S(t')dV'\,dt'. \tag{8}$$

If we define

$$G(\mathbf{r},t,t')=\int_V\tilde{G}(\mathbf{r},t|\mathbf{r}',t')F(\mathbf{r}')dV', \tag{9}$$

then

$$\psi(\mathbf{r},t)=\int_{-\infty}^{\infty}G(\mathbf{r},t,t')S(t')dt'. \tag{10}$$

Note that, for a spatial point source, $G=\tilde{G}$. Since we assume that the environment changes on a time scale significantly greater than the acoustic propagation time scale, $G(\cdot)$ can be considered independent of the time origin. This property is called time invariance, and implies that

$$G(\mathbf{r},t,t')=G(\mathbf{r},t+t^*,t'+t^*), \tag{11}$$

where t^* is a (sufficiently small) time shift. This condition would be satisfied if $G(\cdot)$ only depended on $|t-t'|$, or

$$G(\mathbf{r},t,t')=G(\mathbf{r},|t-t'|). \tag{12}$$

No contribution from $G(\cdot)$ occurs until the first arrival time t_0 (due to causality). Let us assume that the pulse length (t_L) is less than (t_0), so that $t\geqslant t'$, for $t'\leqslant t_L$. Then,

$$G(\mathbf{r},t,t')=G(\mathbf{r},t-t'), \tag{13}$$

giving

$$\psi(\mathbf{r},t)=\int_{-\infty}^{\infty}G(\mathbf{r},t-t')S(t')dt', \tag{14}$$

which is the convolution equation.

Note that this development always holds for point sources, and also holds for extended sources when the separability condition is (at least approximately) appropriate. Henceforth, we will adopt the convolution equation as the basis for our signal model, where $S(t)$ is the source signature that is propagated, $G(\mathbf{r},t,t')$ encodes the multipath environmental distortion effects, and $\psi(\mathbf{r},t)$ is the received signal at range r and depth z. The source is placed at the origin at depth z', and $\mathbf{r}=(r,z)$ (we use cylindrical coordinates, and assume azimuthal symmetry). In a briefer form we could write

$$\psi(t)=S(t)*G(t), \tag{15}$$

where it is understood that $G(t)$ is associated with some fixed, specified source–receiver geometry.

II. THE DECONVOLUTION PROBLEM

To exploit the convolutional signal model to remove the environmental distortion introduced by $G(t)$ into measurements of a propagating $S(t)$, it is necessary to solve the following inverse problem: given $\psi(t)$ and $G(t)$, solve for $S(t)$. This is called the deconvolution problem, and has received much study. For some discussion of this problem and its literature in the area of ocean acoustics, see Broadhead *et al.* (1993).

In general, the classical single channel deconvolution problem is mathematically ill-posed. This implies that it may be difficult, even under the best conditions, to achieve stable and meaningful results. In the presence of uncertainties in $G(t)$, and with additive noise, the problem is exacerbated. Two potential remedies are the use of multichannel methods and regularization methods [see Broadhead *et al.* (1993) for further discussion]. In this paper, however, we set aside the deterministic approach and focus our attention on implementing a statistical interpretation of the signal model. This avoids the need for accurate knowledge of the source location, and complete environmental information, in order to calculate $G(t)$.

A. Reduced problem

We will, in general, assume knowledge of two things: (1) the received signal, and (2) some appropriate, exploitable statistical characterization of $G(t)$ [but, not $G(t)$ itself]. Under these ''blind'' conditions, and some appropriate parameterization associated with the signal model, we should be able to produce a class of candidate solutions. Our goal is to produce schemes such that (1) the candidate solution class contains one or more elements that are ''sufficiently close'' to $S(t)$, and (2) the class size is sufficiently small.

This reduced goal may not be adequate in general problems; but for classification the solution class can be presented to the classifier to see if there is any recognition. Then, in a sense, the classifier and its training signature set become part of the information exploited in the statistical approach. Of course, additional information or assumptions about the signal model invoked will help reduce ambiguity in the solution class. Also, when multiple received signals over significantly different transmission paths are available, significant ambiguity reduction can probably be accomplished. The results of that study will be published elsewhere.

B. Statistical signal model

Wiggins (1978) gives the key idea that we employ here in a slightly generalized form. We consider $G(t)$ to be a realization of a non-Gaussian random process, input to a linear system whose impulse response is $S(t)$. From previous calculations (Broadhead *et al.*, 1996), we know that non-Gaussianity is appropriate because of the high, positive kurtosis of $G(t)$. This is due to its sparseness (or simple structure, or lower entropy) relative to a Gaussian random signal.

How, then, do we accomplish the estimation of $S(t)$? The following approach is a generalization, and in some sense, an extension of Wiggins' approach. We wish to design a filter $f(t)$ that increases the sparseness measure of the received signal. The goal is to ''drive'' the received signal toward $G(t)$. The rationale is that the convolution process is a smearing process that moves the signal to less sparseness (i.e., it makes it more Gaussian). The main assumption is that increasing the non-Gaussianity will drive it towards $G(t)$.

After deconvolution is used to estimate the filter, an estimate of $S(t)$ is readily provided by the inverse filter $f^{-1}(t)$. Let $sp\{\cdot\}$ represent some sparseness measure. We seek $f(t)$ such that

$$sp\{f*\psi\} > sp\{\psi\}. \tag{16}$$

To do this, we can use a gradient operator (Cadzow, 1996). If

$$f*\psi \approx G, \tag{17}$$

then we have

$$\begin{aligned} &f^{-1}*f*\psi \approx f^{-1}*G, \\ &\psi \approx f^{-1}*G. \end{aligned} \tag{18}$$

Comparing to the initial assumption

$$\psi = S*G, \tag{19}$$

we conclude that

$$S \approx f^{-1}. \tag{20}$$

III. DECONVOLUTION METHODS

A. Wiggins' method

Wiggins (1978) used a measure of ''simplicity'' (or ''sparseness'') borrowed from factor analysis, i.e., the V-norm:

$$V(\mathbf{y}) = \sum_j y_j^4 \Big/ \left(\sum_j y_j^2 \right)^2. \tag{21}$$

Here we give Cabrelli's (1984) statement of Wiggins' algorithm (also see Walden, 1985). Consider N observed signals $\mathbf{x}_1 \ldots \mathbf{x}_N$. for each i $(i=1,...,N)$, and let $\mathbf{x}_i$ be represented by

$$x_i = s*g_i, \tag{22}$$

where $\mathbf{s}$ is the source signal, and $\mathbf{g}_i$ represents the propagation distortion. Suppose that each signal $\mathbf{x}_i$ is convolved with the same filter $\mathbf{f}$ in order to obtain an output

$$y_i = f*x_i = (f*s)*g_i. \tag{23}$$

To determine the filter, the varimax criterion is then applied to the outputs $\mathbf{y}_i$ in order to maximize $V(\mathbf{y})$ over all filters $\mathbf{f}=(f_1,\ldots,f_l)$ of fixed length l. Differentiating $V(\mathbf{y})$ with respect to the filter coefficients f_l, and equating to zero, a nonlinear system of equations is obtained which can be rewritten in matrix form as

$$\mathbf{R}(\mathbf{f}) \cdot \mathbf{f} = \mathbf{h}(\mathbf{f}), \tag{24}$$

where $\mathbf{R}=\mathbf{R}(\mathbf{f})$ is a Toeplitz matrix, and $\mathbf{h}=\mathbf{h}(\mathbf{f})$ is a column vector whose coefficients depend upon $\mathbf{f}$. Choosing an initial filter $\mathbf{f}^0=(0,...,0,1,0,...,0)$, an iterative algorithm can be generated by taking

$$\mathbf{f}^{n+1} = \{\mathbf{R}(\mathbf{f}^n)\}^{-1}\mathbf{h}(\mathbf{f}^n), \tag{25}$$

which leads to a satisfactory solution.

B. The *D*-norm and Cabrelli's method

Cabrelli used certain geometrical considerations to suggest another criterion for simplicity, which he called the D-norm, defined by

$$D(\mathbf{y}) = \max_{1 \le j \le m} |y_j| / \|\mathbf{y}\|, \tag{26}$$

where $\|\mathbf{y}\| = (\Sigma_j y_j^2)^{1/2}$ is the Euclidean norm. The D-norm leads to a nonitcrative algorithm for the multichannel blind deconvolution problem. The $N \times m$ matrix $\mathbf{Y}=(y_{ij})$ is defined by

$$y_{ij} = \sum_l f_l x_{i,j-l+1}, \tag{27}$$

where f is a filter to be determined, and the x_i are input channels of data. Let us rewrite the matrix $\mathbf{Y}$ as a Nm-dimensional vector, $\mathbf{Y} \equiv (y_{11},\ldots,y_{1m},y_{21},\ldots,y_{2m},\ldots, y_{N1},\ldots,y_{Nm})$. The D-norm applied to this vector yields

$$D(\mathbf{Y}) = \max_{i,j}(|y_{ij}|/\|\mathbf{Y}\|), \tag{28}$$

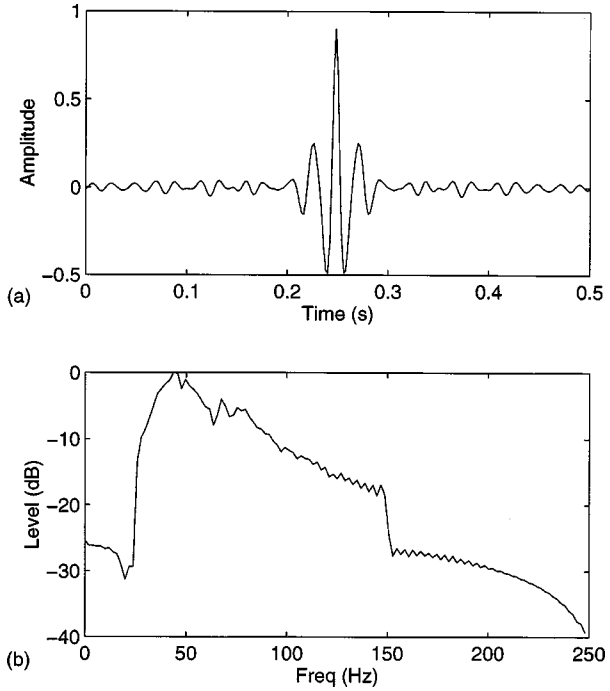

FIG. 1. The short pulse (a) time signal, and (b) energy spectrum.

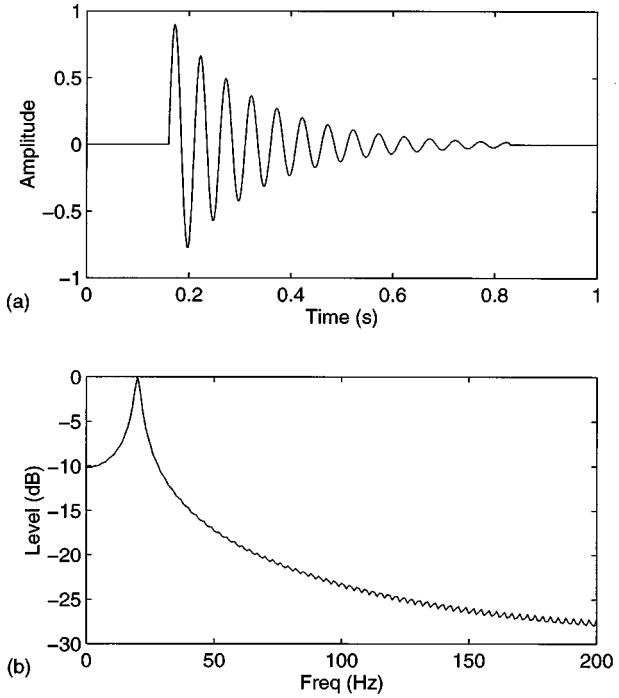

FIG. 2. The exponentially damped sinusoid (a) time signal, and (b) energy spectrum.

where $\|\mathbf{Y}\| = (\Sigma_{i,j} y_{ij}^2)^{1/2}$. The formation of the vector $\mathbf{Y}$ is based on the multichannel kurtosis norm introduced by Ooe and Ulrych (1979). With respect to Cabrelli's method, $\mathbf{Y}$ defines the sparseness measure over the set of all the filter outputs instead of summing the sparseness measure over the individual filter outputs. Use of this idea makes extension of the *D*-norm to multichannel [Eq. (28)] straightforward. The next step is to compute

$$\max_{i,j} \{\sup_{f \in \Re'} (|y_{ij}|/\|\mathbf{Y}\|)\}, \tag{29}$$

which can be found by considering $\partial \|\mathbf{Y}\| / \partial f_l$. The algorithm obtained requires the computation of

$$\mathbf{R} = \sum_i \mathbf{R}^i, \tag{30}$$

where $\mathbf{R}^i$ is the matrix of autocorrelations of the *i*th sample input, and $x_{i,j}$ is the transpose of $[x_{i,j}, x_{i,j-1}, \ldots, x_{i,j-(l-1)}]$, with $x_k = 0$ if $k \notin \{1,\ldots,m\}$. A set of filters is then generated by calculating

$$f^{ij} = \mathbf{R}^{-1} x^{ij}. \tag{31}$$

The filters are applied to the input to generate $\mathbf{Y}^{(ij)}$, and the algorithm terminates by computing $\max_{i,j}(|y_{ij}^{(ij)}|/\|\mathbf{Y}^{(ij)}\|)$. The filter is then the *i*th filter associated with the *D*-norm.

IV. DECONVOLUTION RESULTS

Two test transient signals are used to compare the performance of the Wiggins and Cabrelli deconvolution methods. The first transient is a short duration *pulse* shown with its amplitude spectrum in Fig. 1. The second is a longer duration exponentially *damped sinusoid*, shown with its amplitude spectrum in Fig. 2.

Multipath propagation-distorted versions of the signals are generated by convolution of the two source transients with three model Green's functions. The Green's functions were created using a time-domain parabolic equation model and realistic geoacoustic parameters for an experimental site in the Atlantic Ocean at the southern end of the Blake Plateau (Field and Leclere, 1993). The receiver depth is 250 m in a 915-m water column, and the Green's functions are calculated at 600 m, 4300 m, and 7900 m upslope from the receiver. Thus the Green's functions, shown at the three source-to-receiver ranges in Fig. 3, are realistic representations of those that occur in the ocean. Note that the closeness of the multipath interactions in the Green's functions occur over much shorter time durations than either of the test signals, indicating that the multipath arrivals in the propagated signals will not be visually separable.

The two blind deconvolution methods evaluated in this paper require sparse Green's functions, or high kurtosis, to work successfully. Each of the three Green's functions has a significantly large value of kurtosis, at 124.63, 37.98, and 27.33 for the 600-m, 4300-m, and 7900-m ranges, respectively.

To evaluate the performance of the deconvolution algorithms, the source estimate generated by the algorithm is compared to the known source signal using the peak absolute value of the correlation coefficient, given by

$$\gamma = \max \left| \frac{u \otimes v}{\sigma_u \sigma_v} \right| \tag{32}$$

for two functions u and v. Higher values of γ indicate more similarity between u and v, and $\gamma = 1$ indicates that the two signals are equal (within a scale factor). Although the classifiers used in practice will generally be much more sophis-

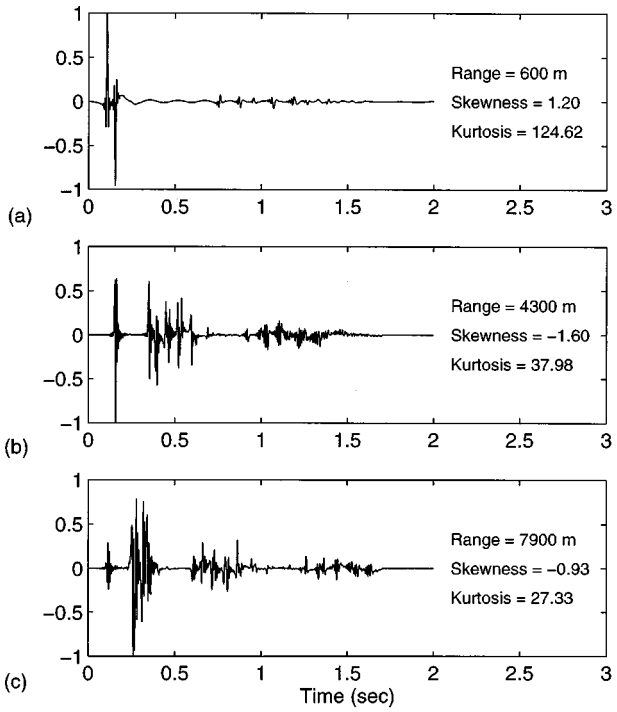

FIG. 3. Modeled Green's functions at 250 m depth and ranges of (a) 600 m, (b) 4300 m, and (c) 7900 m.

ticated and involve many signal features, the correlation coefficient is a convenient numerical measure of performance that lends itself to straightforward comparison between the deconvolution methods.

In this paper, determining whether a method is ''successful'' depends on three factors. If a classifier is designed to sort through each source estimate produced by a set of filter lengths, searching for a match to a known signal type, then a method is successful if it produces only one source estimate with a high correlation coefficient. However, if several source estimates with high correlation coefficients are produced, a classifier can identify a signal with more confidence. Thus the number of good source estimates for a given set of filter lengths is a second measure of a method's success. Finally, a method is conditionally successful if it produces source estimates that are superior to the unprocessed or original source estimate, which is the original received signal, corrupted by propagation. The term ''conditional'' encompasses the uncertainty of how much improvement will ultimately be enough to significantly improve classification capability.

A. Simulations without noise

The Wiggins and Cabrelli methods are initially compared using the two test signals with no additive noise. The Wiggins method requires that a convergence criterion be chosen for determining the stopping point for the iterations. It was found that a useful stopping criterion was when the current and previous source estimates have a correlation coefficient between them of 0.9999. The Wiggins and Cabrelli methods both occasionally require a small degree of prewhitening during the autocorrelation inversion. A value of 0.01% is found to be sufficient for stabilization in the cases where prewhitening is required, and is thus used for all test cases to preserve consistency, and reflect a realistic application scenario where instabilities cannot be predicted efficiently. Filter length in each method ranges from 1 to 50 points.

We also assume that it is reasonable to expect that an estimate of the signal passband would be available for use in the deconvolution routines. As such, the source estimates produced by the two deconvolution methods are subjected to a bandpass filter before processing as well as again preceding classification, i.e., before the correlation coefficient of the source estimate is calculated. For the pulse, the passband filter is defined over 25–150 Hz, and for the damped sinusoid, over 0–100 Hz. The primary effect of this step will be to improve SNR when we add noise.

The results from the two methods are shown in Figs. 4 and 5 for the pulse and damped sinusoid signals, respectively. These figures show the correlation coefficients for the source estimates versus filter length for the three test ranges of 600 m, 4300 m, and 7900 m. For completeness, the correlation coefficient for the original received signal, i.e., the source estimate that is available with no processing, is depicted by the dashed horizontal lines for the three ranges. Note that use of the original received signal for classification includes the initial application of the bandpass filter. The maximum correlation coefficients over filter length for the two methods are also provided in the legend boxes.

For both test signals, the Wiggins and Cabrelli methods produce several to many source estimates that are superior to the original received signal (the solid curves exceed the dashed lines). This indicates that, although filter length is an important parameter, the methods often produce good results for several filter lengths. Except for the pulse signal at the 4300-m range, the Wiggins method produces as many or more source estimates with correlation coefficients of 0.90 or higher for the tested filter lengths than the Cabrelli method, as indicated by the results in Table I. Also, as indicated by the maximum correlation coefficients in Figs. 4 and 5, the best source estimate over filter length is generated by the Wiggins method, rather than the Cabrelli method, in all but one case.

B. Simulations with noise

To assess the performance of the Wiggins and Cabrelli methods in noise, simulated independent Gaussian noise is generated and added to each received signal before application of the deconvolution algorithms. The SNR is defined as the ratio of signal and noise standard deviations, and converted to decibels (dB) for display. Again, in these simula-

TABLE I. Number of filter lengths (out of 50) for which the Wiggins and Cabrelli methods produce source estimates with correlation coefficients of at least 0.9.

		600 m	4300 m	7900 m
Pulse	Wiggins	10	31	0
	Cabrelli	0	35	0
Damped Sinusoid	Wiggins	23	3	26
	Cabrelli	0	0	18

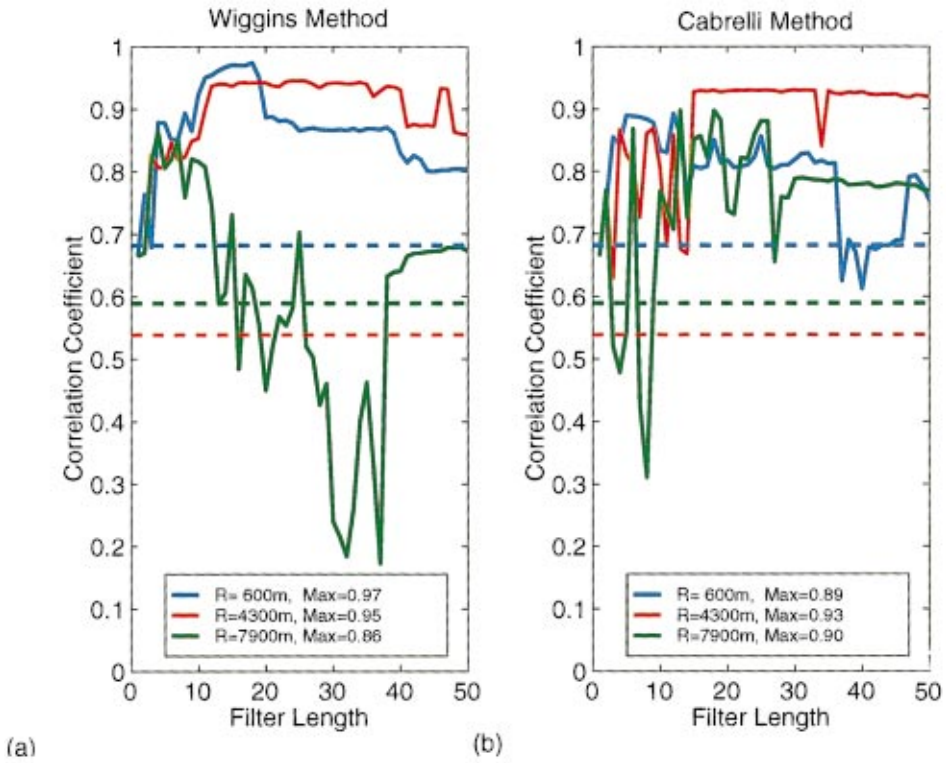

FIG. 4. Correlation coefficients between the known pulse source and the source estimates produced by the (a) Wiggins and (b) Cabrelli methods versus filter length. The correlation coefficients between the true source and the original received signal are denoted by dashed lines.

tions, the bandpass filter is applied twice: first, it is applied to the received signal before input to the deconvolution algorithm; and second, it is applied to the source estimate generated by the algorithm.

Results depicting the maximum correlation coefficients produced by the two methods for a series of SNRs from −10 dB to 30 dB are shown in Figs. 6 and 7 for the pulse and damped sinusoid signals, respectively. The correlation coefficients for the original received signal (no processing) are also included (solid curves).

At all three ranges, both the Wiggins and Cabrelli methods produce source estimates that are superior to the original received for the pulse signal (Fig. 6). At the 600-m range, the Wiggins method produces slightly better results than the Cabrelli method at SNRs above 22 dB, but the Cabrelli method produces better results at all the lower SNRs. In the 4300-m

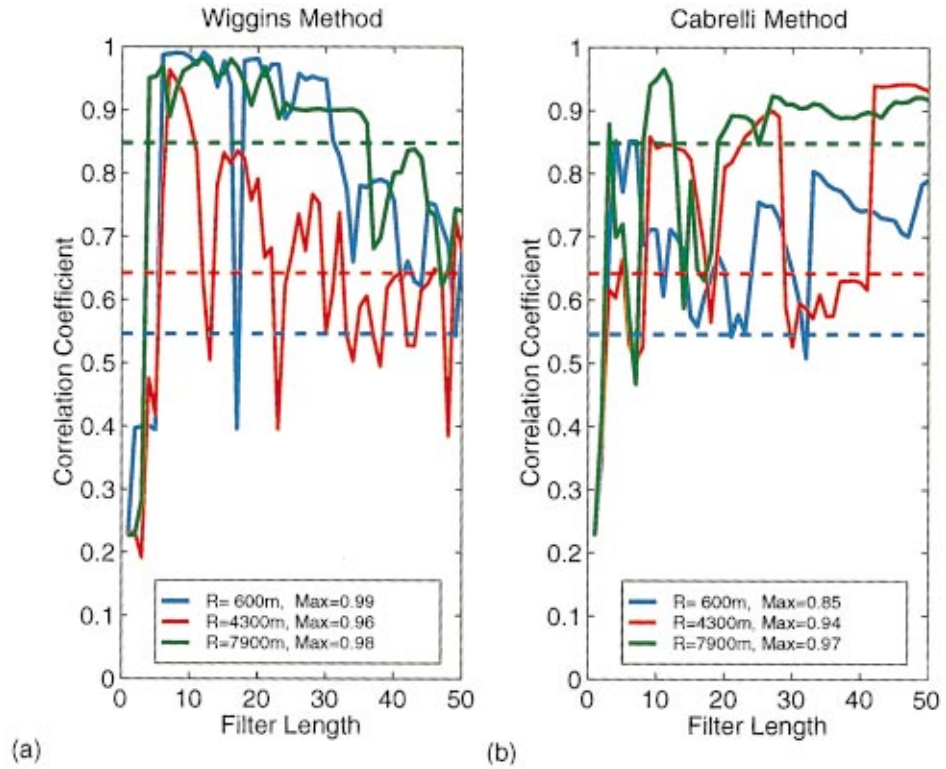

FIG. 5. Correlation coefficients between the known damped sinusoid source and the source estimates produced by the (a) Wiggins and (b) Cabrelli methods versus filter length. The correlation coefficients between the true source and the original received signal are denoted by dashed lines.

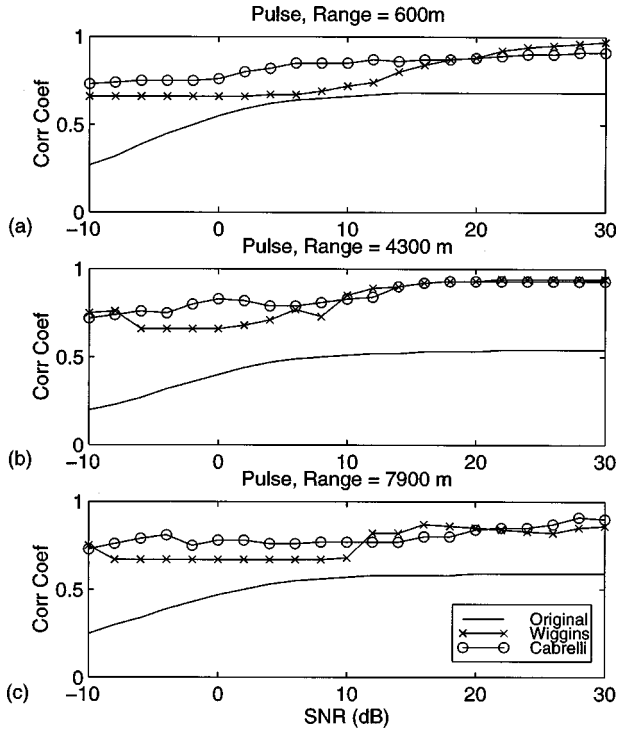

FIG. 6. Correlation coefficients between the known pulse signal and source estimates produced by the Wiggins (×) and Cabrelli (○) methods in Gaussian noise for ranges of (a) 600 m, (b) 4300 m, and (c) 7900 m. The solid lines indicate correlation coefficients for the original received signal.

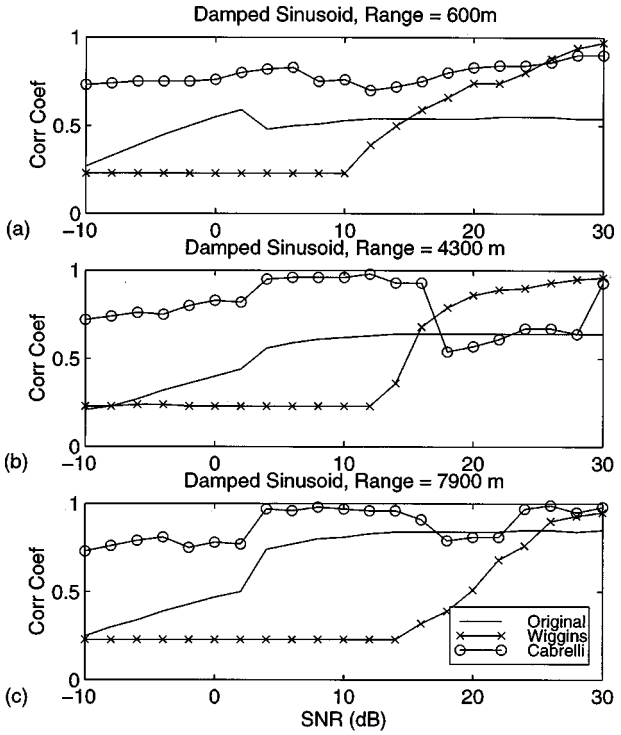

FIG. 7. Correlation coefficients between the known damped sinusoid signal and source estimates produced by the Wiggins (×) and Cabrelli (○) methods in Gaussian noise for ranges of (a) 600 m, (b) 4300 m, and (c) 7900 m. The solid lines indicate correlation coefficients for the original received signal.

range case, the Wiggins and Cabrelli methods produce comparable results at SNRs above 14 dB, but the Cabrelli method is superior at lower SNRs. In the 7900-m case, the Wiggins method performs better at SNRs between 14 dB and 20 dB, but the Cabrelli method performs better at all other SNRs. Below about 8 dB, at all three ranges, the best Wiggins methods source estimate occurs at a filter length of 1 (correlation coefficient=0.67). While this result seems better than the unprocessed signal, it is only because the particular source signal is a pulse-type signal, similar in form to the approximate delta function source estimate generated by the filter length of 1. Thus this moderately high correlation coefficient of 0.67 is strictly signal dependent, and cannot generally be expected to occur. In fact, it does not occur for the second test signal used in this paper.

Figure 7 depicts the deconvolution results for the damped sinusoid signal. In this case, the Wiggins method completely fails at SNRs below 10–14 dB while the Cabrelli method can still produce some good source estimates below 10 dB. That is, the Cabrelli source estimates are superior to the original received signal, and in some cases (SNRs of 4–16 dB for the 4300-m and 7900-m ranges) the source estimate correlation coefficients are quite high. For the 600-m case, the Wiggins method exceeds the Cabrelli method at only the highest SNRs. The inferior performance of the Cabrelli method from SNRs of 18–28 dB in the 4300-m case and 18–22 dB in the 7900-m case can be made superior to the Wiggins method by removing or reducing the prewhitening used in the autocorrelation matrix inversion. In the 4300-m case, for example, the correlation coefficients for the Cabrelli source estimates between 18 and 22 dB when prewhitening is removed are 0.95 or 0.96. While the Wiggins results shown here do not appear to be adversely affected by the level of prewhitening used, they may be for other test cases. A more sophisticated implementation of both of these algorithms would include a test for ill-conditioned matrices and a determination of the appropriate level of prewhitening.

Detailed results for the Wiggins and Cabrelli methods at SNR=10 dB are shown in Figs. 8 and 9 for the two test signals. For the pulse signal (Fig. 8), neither method produces source estimates with correlation coefficients above 0.90 for any of the three ranges tested. However, comparison of the two sets of curves indicates that the Cabrelli method produces a better selection of source estimates than the Wiggins method for the 4300-m and 7900-m ranges, many having higher correlation coefficients than the original received signal. The higher correlation coefficients are mostly between 0.70 and 0.85, however, and it is unknown whether this degree of improvement in the source signal estimate will translate into improved classification performance. For the damped sinusoid signal (Fig. 9), the Cabrelli method is obviously superior to the Wiggins method, generating four and seven source estimates with correlation coefficients above 0.90 for the 4900-m and 7900-m cases, as well as many source estimates that are improvements over the original received signal for all three ranges. This example illustrates that the Cabrelli method is, at least in some cases, more robust to additive noise than the Wiggins method.

V. CABRELLI METHOD WITH ALTERNATIVE NORMS

The Cabrelli method uses maximization of the *D*-norm to extract a source signature from received data. Alternative

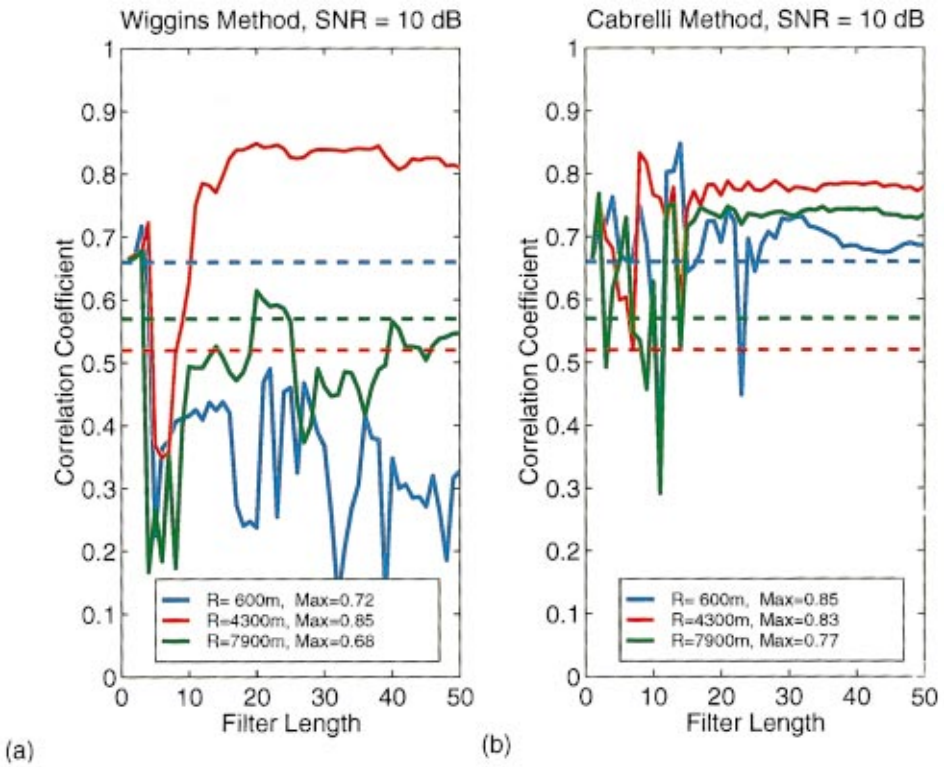

FIG. 8. Correlation coefficients between the known pulse source and the source estimates produced by the (a) Wiggins and (b) Cabrelli methods versus filter length for SNR=10 dB. The correlation coefficients between the true source and the original received signal are denoted by dashed lines.

norms can also be used in the Cabrelli method. As an example, we implement the Cabrelli algorithm with the *D*-norm at the final stage in the algorithm replaced by the *r*th order normalized cumulant

$$C_r = \sum_k y_k^r \Big/ \|y\|^r, \tag{33}$$

for cumulant orders $r=3$, 4, 5, and 6. For the damped sinusoid signal at range=7900 m, the fourth and sixth order cumulant norms give results comparable to the *D*-norm, as shown in Fig. 10 (no prewhitening is used in this example). In contrast, the third and fifth order cumulant norms do not produce good source estimates at most SNRs. This example is representative of the *r*th order results for the damped si-

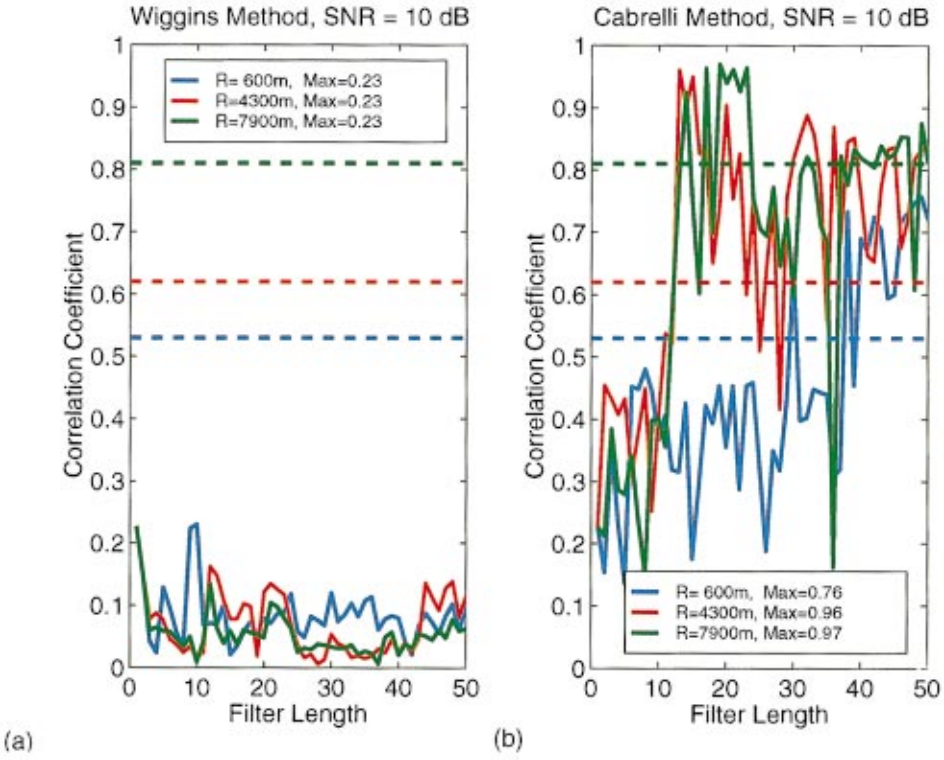

FIG. 9. Correlation coefficients between the known damped sinusoid source and the source estimates produced by the (a) Wiggins and (b) Cabrelli methods versus filter length for SNR=10 dB. The correlation coefficients between the true source and the original received signal are denoted by dashed lines.

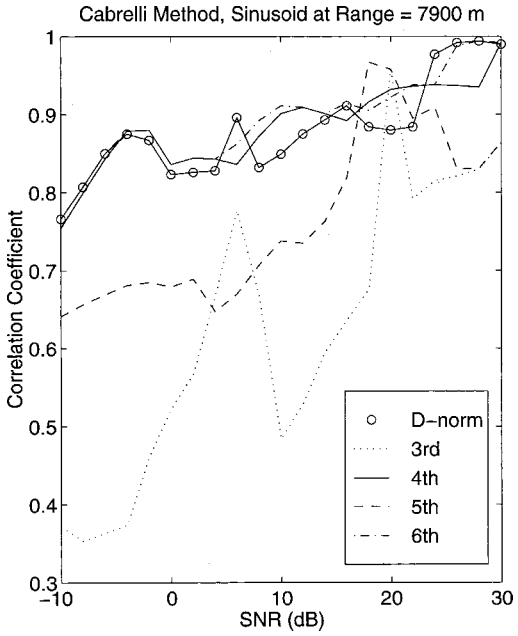

FIG. 10. Correlation coefficients for the Cabrelli method using the *D*-norm and *r*th order cumulant norms for the damped sinusoid signal at range=7900 m. No prewhitening is used in this example.

nusoid at the 600-m and 4300-m ranges. Since the Green's function in this example is close to symmetrically distributed (i.e., a skewness of -0.93), the poor performance with the odd order cumulants is not surprising. Odd order cumulants may work well, however, for other applications. Examples of successful odd order alternate norms in the Wiggins method can be found in Nandi (1997), and a comparison of alternate norms in the Wiggins and Cabrelli methods can be found in Pflug and Broadhead (1998).

VI. CONCLUSIONS

In this paper, we presented a general scheme for applying blind deconvolution as a preprocessor to improve classifier performance for passive acoustic transients. We also presented two particular algorithms from the literature and showed that they can perform well in an ocean acoustics setting (albeit, they were both developed for oil-exploration related problems in reflection seismology). Furthermore, we have given a relative performance comparison in the presence of significant levels of additive noise. The evaluation included using the correlation coefficient between the source estimate and true source to quantify similarity, and compared the level and frequency of occurrence of correlation coefficients produced for a predefined set of filter lengths. The two methods gave good results for both the pulse and damped sinusoid test signals when noise was absent or the SNR was high. At moderate and lower SNRs, the Cabrelli method tended to generate results that were superior to the Wiggins method. For the damped sinusoid signal, the Wiggins method failed completely below SNR=10 dB, producing source estimates that were more distorted than the original received signal. In contrast, the Cabrelli method at this and lower SNRs still produced some good source estimates. We also implemented a variation of the Cabrelli algorithm to accommodate third through sixth order cumulants and presented simulation results from the modified method that showed comparable results for the *D*-norm, fourth, and sixth order cumulant norms.

ACKNOWLEDGMENTS

This work was funded by the Office of Naval Research and the Naval Research Laboratory, NRL Contribution No. JA/7173–97-0058.

Broadhead, M. K. (**1995**). ''Broadband source signature extraction from underwater acoustics data with sparse environmental information,'' J. Acoust. Soc. Am. **97**, 1322–1325.

Broadhead, M. K., Field, R. L., and Leclere, J. H. (**1993**). ''Sensitivity of the deconvolution of acoustic transients to Green's function mismatch,'' J. Acoust. Soc. Am. **94**, 994–1002.

Broadhead, M. K., Pflug, L. A., and Field, R. L. (**1996**). ''Minimum entropy filtering for improving nonstationary sonar signal classification,'' Proc. of the 8th IEEE Signal Proc. Workshop on Statistical Signal and Array Proc., Corfu, Greece, June 24–26, pp. 222–225.

Cabrelli, C. A. (**1984**). ''Minimum entropy deconvolution and simplicity: A noniterative algorithm,'' Geophysics **50**, 394–413.

Cadzow, J. A. (**1996**). ''Blind deconvolution via cumulant extrema,'' IEEE Signal Process. Mag. **13**, 24–42.

Field, R. L., and Leclere, J. H. (**1993**). ''Measurements of bottom-limited ocean impulse responses and comparisons with the time domain parabolic equation,'' J. Acoust. Soc. Am. **93**, 2599–2616.

Hatzinakos, D., and Nikias, C. L. (**1994**). ''Blind equalization based on higher-order statistics,'' in *Blind Deconvolution*, edited by S. Haykin (Prentice-Hall, New Jersey).

Haykin, S. (**1994**). ''The blind deconvolution problem,'' in *Blind Deconvolution*, edited by S. Haykin (Prentice-Hall, New Jersey).

Nandi, A. K., Mampel, D., and Roscher, B. (**1997**). ''Blind Deconvolution of Ultrasonic Signals in Nondestructive Testing Applications,'' IEEE Trans. Signal Process. **45**, 1382–1390.

Ooe, M., and Ulrych, T. J. (**1979**). ''Minimum entropy deconvolution with an exponential transformation,'' Geophys. Prospect. **27**, 458–473.

Pflug, L. A., and Broadhead, M. K. (**1998**). ''Alternative Norms for the Cabrelli and Wiggins Blind Deconvolution Algorithms,'' Naval Research Laboratory, NRL/MR/7173–97-8069.

Walden, A. T. (**1985**). ''Non-Gaussian reflectivity, entropy, and deconvolution,'' Geophysics **50**, 2862–2888.

Wiggins, R. A. (**1978**). ''Minimum entropy deconvolution,'' Geoexploration **16**, 21–35.

A macro-mechanical model of the guinea pig cochlea with realistic parameters

David Brass
Institute of Laryngology and Otology, University College, London WC1X 8EE, England

(Received 5 April 1999; revised 14 September 1999; accepted 30 September 1999)

The post-mortem transfer function of the cochlea of the guinea pig was compared to the transfer function generated by a model with parameters derived from physical measurements of the guinea pig cochlea. Both the formulation and parameters of the model were carefully chosen to be realistic using evidence from published measurements. The fit between the transfer function of the model and recent mechanical measurements of the passive guinea pig cochlear response was good, with a root mean square ratio of 6.3 dB in amplitude and 0.33π rad in phase. The model was used to explore the effect of cochlear partition mode factor and duct geometry upon the mechanical response of the cochlea. Possible inadequacies of the model which could explain the remaining differences between the output of the model and measurements are discussed. © *2000 Acoustical Society of America.* [S0001-4966(00)04701-9]

PACS numbers: 43.64.Bt, 43.64.Kc [RDF]

INTRODUCTION

The mechanics of the cochlea are often divided into micro-mechanical and macro-mechanical parts, where ''micro-mechanics'' refers to the internal mechanics of the organ of Corti and ''macro-mechanics'' refers to the remainder of the mechanics of the cochlea. The micro-mechanics are thought to become important to the response of the cochlea at low levels of acoustic stimulation in the physiologically intact cochlea (see the review of de Boer, 1991). Hence, the mechanical response of the cochlea at high levels or in the recently post-mortem cochlea can be modeled by the passive macro-mechanics alone. Such a model will be developed in this paper.

This is not the first attempt to match the transfer function of a macro-mechanical model to mechanical measurements made in real cochleae in the passive state. Some examples of previous attempts are listed below:

(1) Viergever (1980) attempted to match the transfer functions generated by a two-dimensional, one degree of freedom model to the passive mechanical measurements of Johnstone and Yates (1974) and Wilson and Johnstone (1975) using realistic parameters. He largely failed to find a simultaneous match of both the amplitude and phase of the transfer function.
(2) Viergever and Diependaal (1986) corrected some of the deficiencies of Viergever's (1980) approach and achieved a good match to the mechanical data of Johnstone and Yates (1974) using a single degree of freedom, two-dimensional model solved using the Wentzel–Kramers–Brillioun (WKB) approximation. However, their model was a ''box model'' with scalae 1.4 mm high by 0.7 mm wide. Even at the place of observation this is not a very realistic size, either in cross-sectional area or ''aspect ratio''—the ratio of height to width (Fernandez, 1952; Stevens and Davies, 1938). When these dimensions are corrected the transfer function of the model cannot be made to match the mechanical data.
(3) Although not attempting to specifically match passive mechanical data, the model of Mammano and Nobili (1993) uses a realistic macro-mechanical model with parameters derived from measurements made from the guinea pig. However, the ''passive'' output of this model (shown in Fig. 5 below) fails to match mechanical measurements made in the guinea pig. In particular, the phase of the transfer function generated by this model fails to accumulate as quickly with increasing frequency as that measured in real cochleae. I think that this is due to the values of some of the parameters used, in particular the effective mass and effective width of the cochlear partition.

In this paper I shall use a model which is basically similar to that used by Mammano and Nobili (1993), except that the parameter values used are more carefully chosen and realistic. With the exception of some inherent problems, which will be discussed later, this model matches passive mechanical data quite well. (See the results of Fig. 5 below.)

The model developed in this study can be thought of as being ''realistic'' since its predicted transfer function closely matches mechanical measurements made in real cochleae while its mechanical parameters are carefully chosen to match published measurements. This is in contrast to the models of Viergever (1980) and Mammano and Nobili (1993) which fail to generate transfer functions which match mechanical measurements, and also the model of Viergever and Diependaal (1986) which, although matching the mechanical measurements, does not use realistic parameters.

Although the generation of a realistic macro-mechanical cochlea model can be seen as an end in itself, this study is intended to provide a starting point for more complete mechanical models of the cochlea which incorporate both realistic macro-mechanical and micro-mechanical features. Such

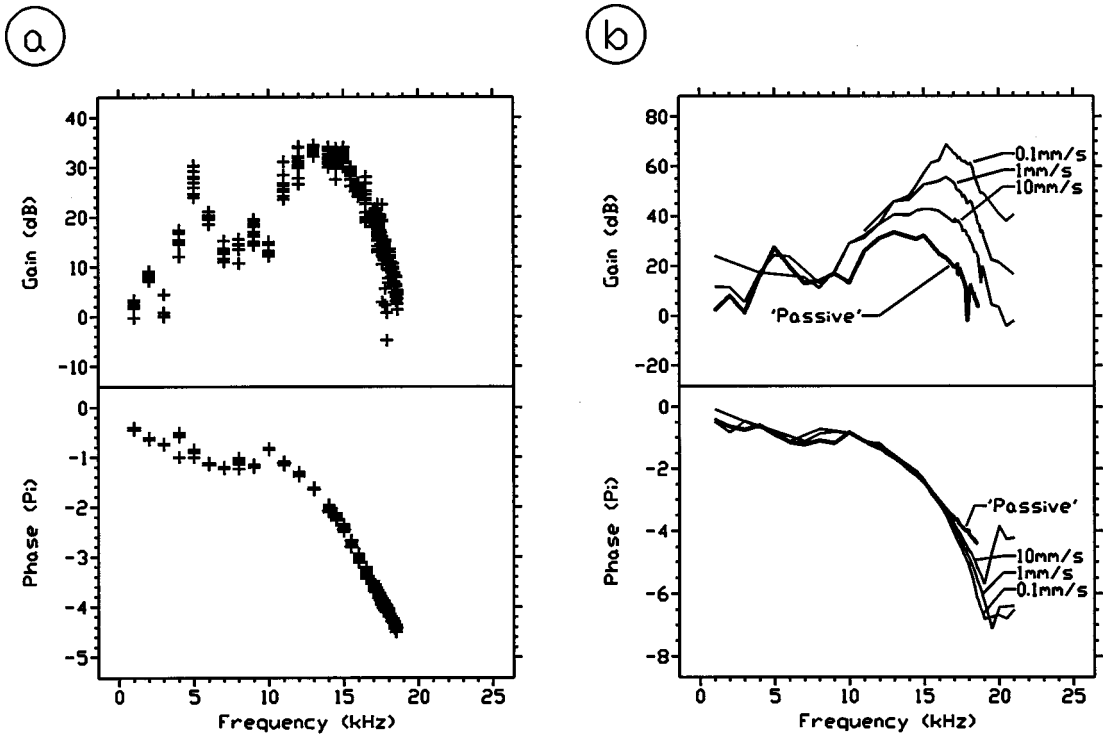

FIG. 1. The mechanical measurements (from Nuttall and Dolan, 1996b) with which the output of the model is to be compared. (a) Shows the gain and phase of the complex cochlear gain or transfer function (cochlear partition velocity/stapes velocity) from post-mortem measurements made in animal 2381. The cochlear partition velocity measurements were made close to the position of the first row of outer hair cells. All measurements, with stimulus velocity amplitudes from 0.2 to 400 mm/s, are shown, each marked as a separate cross. The phase is presented in units of pi radians (i.e., 2 units=1 cycle). (b) Comparison of the cochlear gain, for the same position in animal 2381, in the sensitive and post-mortem state. The gain measured in the sensitive state is shown for stapes velocity amplitudes of 0.1, 1, and 10 mm/s. The mean of the gain measured in the post-mortem state is shown, marked ''passive.''

a model can be thought of as a macro-mechanical model with additional features to simulate the micro-mechanics (see de Boer, 1991). For such a complete mechanical model of the cochlea to be realistic it must necessarily incorporate realistic macro-mechanics.

I. METHOD

A. The measurements to which the model response will be compared

A comprehensive set of measurements of the mechanical response of the guinea pig cochlea, both in a live, sensitive condition and recently post-mortem, were made by Nuttall and Dolan (1996a, b). From these results we can derive the complex transfer function from the stapes footplate to the point of measurement on the basilar membrane.

Unfortunately, measurements in the living, sensitive animal were not made at a high enough level (maximum acoustic stimulus 80–90 dB SPL) that the responses become completely passive. Evidence for this is provided by the fact that at these levels the transfer function remains nonlinear. However, there is a complete set of measurements made in a recently post-mortem animal (2381#2po.txt). We shall use these measurements to compare with the results of our model.

Figure 1(a) shows the gain and phase of the transfer function for this animal. As the post-mortem response is essentially linear at these levels, we can put together all of the responses, with stapes footplate velocity magnitudes of 0.2 to 400 mm/s. From these results we can derive both a mean transfer function and a measure of the noise and experimental variation of the measurements. The average 95% confidence interval of the mean of the transfer function is ± 2.3 dB in gain and ± 0.12 rad in phase.

Figure 1(b) shows the post-mortem transfer function together with transfer functions recorded from the same place in the same animal in its sensitive (active, nonlinear) state. The stapes velocity amplitudes of 0.1, 1, and 10 mm/s correspond to sound pressure amplitudes of around 30, 50, and 70 dB SPL at the best frequency. This figure shows that the ''passive'' response from the post-mortem state is similar to what we would expect in the sensitive state if the stapes velocity amplitude were increased further. This continuity between the trend of the high level responses and the post-mortem response is evidence that the post-mortem responses are the result of a simple ''switching off'' of the cochlear amplifier rather than other changes occurring in the mechanics of the cochlea.

Figure 2(a) shows a comparison between the passive cochlear mechanical transfer function measured in the guinea pig by Nuttall and Dolan (1996b) and some earlier measurements. To aid comparison between measurements made at different locations along the cochlear partition we assume a ''scaling symmetry'' as detailed by Zweig (1991). Figure 2(b) shows the measurements plotted against ''scaled frequency'' defined as

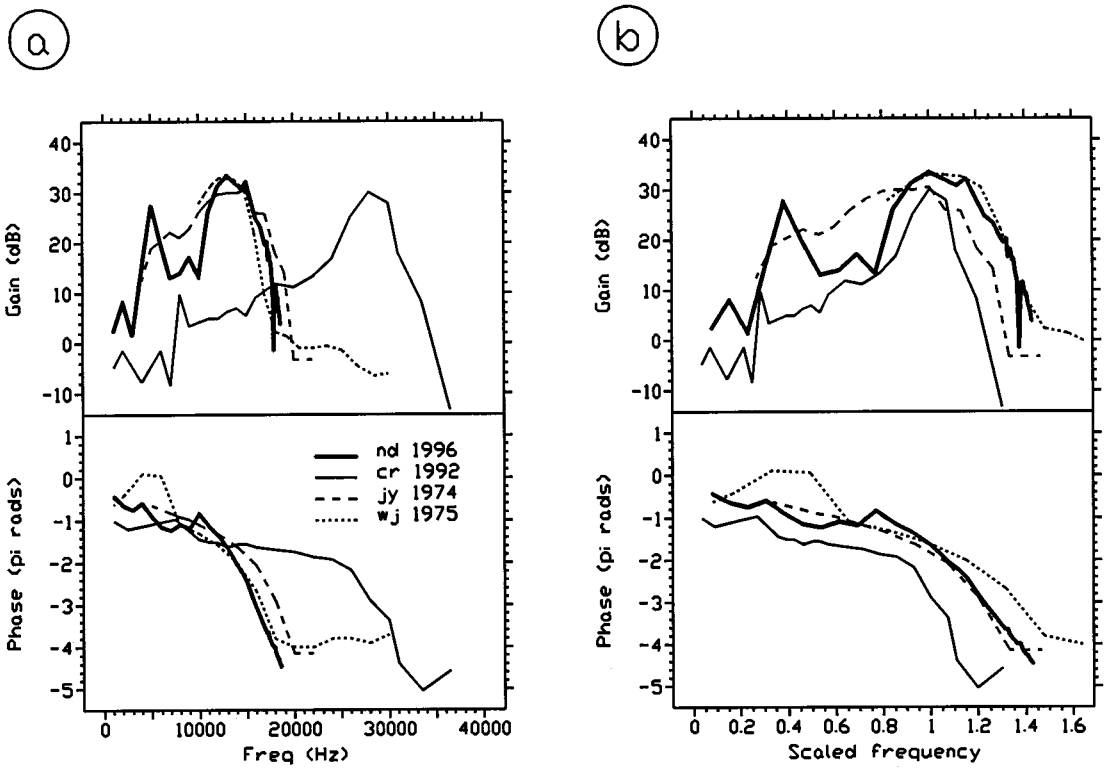

FIG. 2. (a) Comparison of the amplitude and phase from four sets of mechanical measurements of cochlear transfer function made from guinea pigs in a ''passive'' state. Key: **nd 1996**, from Nuttall and Dolan (1996b), mean of measurements from animal 2381 in a post-mortem state; **cr 1992**, from Cooper and Rhode (1992), measurements from animal GP60 with 100 dB SPL in the ear canal; **jy 1974**, from Johnstone and Yates (1974), measurements shown in their Fig. 3; **wj 1975**, from Wilson and Johnstone (1975), measurements from animal 160 made at location 6 with 100 dB SPL in the ear canal. (b) The same measurements as in (a) with frequency scaled according to Eq. (1).

$$\text{Scaled frequency} = \frac{f}{F_{\text{ch}}}, \tag{1}$$

where f is the frequency of measurement and F_{ch} is the characteristic frequency of the place of measurement (or frequency at which maximum amplitude of the transfer function occurs).

The validity of Nuttall and Dolan's (1996b) measurements is suggested by the qualitative similarity of all the measurements. However, there are substantial differences—with ratios of up to 20 dB in gain and 2π rad in phase. I suggest the following reasons for these differences (none of which invalidate Nuttall and Dolan's measurements):

(1) Differences in measurement techniques. Nuttall and Dolan (1996a) and Cooper and Rhode (1992) both used laser interferometry techniques, Johnstone and Yates (1974) used a Mossbauer technique, and Wilson and Johnstone (1975) used a capacitive probe technique that required the draining of the scala tympani. Each of these measurement techniques will disturb the cochlea macromechanics to a greater or lesser extent and thus give rise to differences between the sets of measurements.
(2) Differences between the measurement sites in each of the measurements. The site of recording of cochlear partition vibration can vary in both the longitudinal and radial directions. The transfer function of Cooper and Rhode (1992) was obviously measured at a site much more basal than the other measurements. A break down of scaling symmetry would cause this transfer function to be different from the others. Differences in transfer functions will also be caused by radial differences in measurement site. For instance, a transfer function measured at the edge of the basilar membrane will have a lower gain than one measured towards the center of the basilar membrane.
(3) Intraspecies differences between the cochleae of different guinea pigs.

B. The model

The geometry of the model of the cochlea used in this paper is shown in Fig. 3. The model consists of two straight semicircular sectioned fluid-filled tubes, of varying cross-sectional area, joined at a wall. Part of this wall, the cochlear partition, can move in response to the difference in pressure across it. The cochlear partition consists of a set of thin flexible parallel beams arranged perpendicular to the longitudinal direction, along which the x dimension varies. At the apical end of the cochlea ($x=L$) is an opening (representing the helicotrema) at which the pressure difference across the cochlear partition becomes zero.

The input to the model is the acceleration of the oval window ($j\omega V_s$) which is positioned at $x<0$. This movement, together with the corresponding motion of the round window, sets up a pressure difference across the cochlear partition. The cochlear partition responds by moving at velocity $V_{\text{cp}}[x]$, which is the output of the model. Each of the

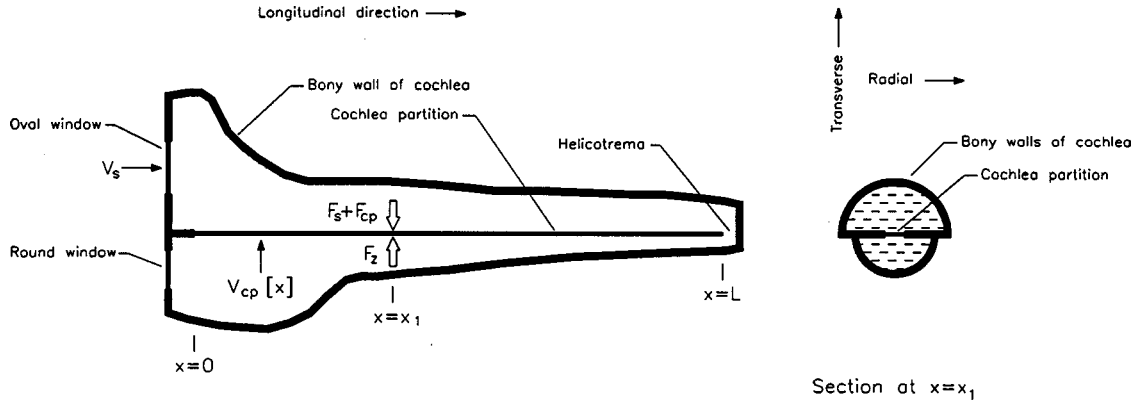

FIG. 3. Longitudinal and transverse sections of the geometry of the model used in this paper. Note that, for reasons of clarity, the scale in the longitudinal direction is smaller than that in the other directions.

thin beams making up the cochlear partition is restrained by an impedance $Z_{cp}[x]$. A force per unit length $F_z[x]$ along the cochlear partition is generated by $V_{cp}[x]$ acting across this impedance. This force is resisted by force per unit length $F_s[x]+F_{cp}[x]$. $F_s[x]$ is the force per unit length due to the motion of the oval window transmitted through the fluid to x. $F_{cp}[x]$ is the force per unit length due to the motion of the cochlear partition transmitted through the fluid to x.

Mechanically this model is believed to behave somewhat like the cochlea. However, for reasons of tractability and ease of computation of the solution method many simplifications and assumptions have been made. These simplifications and assumptions include: (1) only the cochlear partition and the round and oval windows are free to move, all other fluid boundaries are perfectly rigid; (2) the fluid filling the cochlea is inviscous and incompressible; (3) the motion of the fluid is irrotational and thus can be characterized in terms of potential flow; (4) all motions in the cochlea are linearly proportional to the forces generating them; (5) the cochlear partition can be characterized as a set of thin laterally uncoupled parallel beams; (6) the fluid-filled chambers of the cochlea are semicircularly sectioned and straight; (7) the parallel beams move as pistons (i.e., no variation of radial mode shape along cochlea) and only in a transverse direction; (8) the radial mode shape of the motion of the real cochlear partition can be simulated by reducing the effective width of the partition; (9) that the oval and round windows are positioned so that the force propagator is greatest at $x=0$; (10) that the round and oval windows are positioned far enough away from the cochlear partition that the ''local'' part of the force propagator is negligible;[1] (11) the Green's functions for the fluid flow are described well by the approximate formulas given in Mammano and Nobili (1993);[2] (12) in the case of the recently post-mortem (passive) cochlea the impedance restraining the cochlear partition ($Z_{cp}[x]$) can be characterized as a passive, linear, one degree of freedom, damped oscillator with characteristic that varies smoothly along the length of the duct; and (13) the stapes is driven from a velocity (infinitely high impedance) source.

A solution to the model is found using a modification of the solution method developed by Mammano and Nobili (1993) and Nobili and Mammano (1996). An outline of the solution method is given in Appendix A.

C. The parameters of the model used to calculate the Green's functions

The stapes force propagator and Green's functions were calculated according to the methods of Mammano and Nobili (1993). In order to calculate the functions three sets of geometric measurements are required:

Effective area of the round window. Fernandez (1952) measured the cross-sectional area of the oval window in the guinea pig to be about 1.41×10^{-6} m^2 (mean of six ears). However, since the edges of the oval window are constrained not to move, we cannot assume that it moves as a piston. We can define an ''equivalent area'' of the oval window:

$$A_{st}=A_{ow}\times\text{mode factor of oval window}, \tag{2}$$

where A_{st} is the equivalent area of the oval window; A_{ow} is the actual area of the oval window; and the mode factor is the ratio of the volume displaced by the oval window when the stapes is moved a given distance and the volume that would be displaced if the whole window were to move this distance as a piston.

The area of the stapes footplate in the guinea pig is about 0.88×10^{-6} m^2 (Littler, 1965, mean of eight ears). We shall assume that all of this area is fixed to the center of the oval window and vibrates like a piston. If the remaining part of the oval window vibrates with a linear mode shape, the mode factor is about 0.9. This gives an equivalent area of the oval window of about 1.26×10^{-6} m^2.

Cross-sectional area of the cochlea ducts. Fernandez (1952) gives the cross-sectional area of the scala vestibuli plus the scala media and of the scala tympani in the guinea pig (measured from two orthogonal mid-modiolar sections, average of three ears for each section). We shall use these values in this paper.

Effective width of the moving part of the cochlear partition. Both Guild (1927) and Fernandez (1952) give measurements of the width of the basilar membrane of the guinea pig. These measurements differ by less than 25%. What is more difficult to ascertain is exactly how much of the width of the cochlear partition moves and what the mode shape of that motion is.

Fernandez (1952) judges that all structures up to the osseous spiral lamina or the edge of the limbus are thin

enough to participate considerably in the motion of the cochlear partition. This assumption adds up to 25% to the effective width of the moving part of the cochlear partition, at the apical end of the cochlea. In this paper we shall use this larger width for the moving part of the cochlear partition (marked ''Y'') in Fig. 3 of Fernandez, 1952).

We can define a mode factor for the moving part of the cochlear partition in much the same way as for the oval window. The value of this mode factor depends upon the unknown transverse mode shape of the vibration of the cochlear partition. For instance, the mode factor could be 0.5 (if it behaved like a uniform beam clamped at both ends) or about 0.637 (if it behaved like a uniform beam hinged at both ends).

Many investigators have assumed that the cochlea partition behaves as a uniform clamped beam [e.g., in the original model of Mammano and Nobili (1993)]. However, two pieces of evidence lead me to conclude that the cochlear partition behaves as though it were hinged at its edges: (1) the sheet of transverse fibers which probably account for most of the stiffness of the cochlea becomes considerably thinner at its edges (Iurato, 1962) and (2) the inner hair cell stereocilia are mounted close to the modiolar edge of the cochlear partition which must be hinged if they are to bend appreciably in response to motion of the cochlear partition (Davis, 1958).

However, the cochlear partition probably does not have the mode shape of a uniform hinged beam. Variations in stiffness across its length and the loading of structures such as the organ of Corti will cause a complicated mode shape with an unknown mode factor (but probably less than 0.637). In this paper I shall set the default cochlear partition mode factor to be 0.637, but will also examine the effect of reducing it to 0.5.

D. The parameters of the cochlear partition

We shall model the impedance of the cochlear partition (in its passive state) as a single degree of freedom mass–spring–damper system. The impedance of the cochlear partition is

$$Z_{cp}[x,\omega]=H[x]+j(\omega M[x]-K[x]/\omega)$$
$$=M[x]\omega_0[x]\left\{\delta[x]+j\left(\frac{\omega}{\omega_0}\right)-\left(\frac{\omega_0[x]}{\omega}\right)\right\}, \tag{3}$$

where $H[x]$, $M[x]$, and $K[x]$ are the effective damping, mass, and stiffness per unit length respectively; $j=(-1)^{-1/2}$; $\omega=2\pi f$ is the angular excitation frequency; $\omega_0[x]=(K[x]/M[x])^{1/2}$ is the ''*in vacuo* resonance'' of the cochlear partition; and $\delta[x]=H[x](M[x]K[x])^{-1/2}$ is the damping coefficient.

Taking each of the parameters of Eq. (3) in turn, we have the following.

Mass per unit length of cochlear partition. Fernandez (1952) states that the cross-sectional area of the structures attached to the basilar membrane (CSA$[x]$) has a minimum of 12×10^{-9} m^2, increases to a maximum of 17×10^{-9} m^2 (17.5×10^{-3} m from the base), and falls to 15×10^{-9} m^2 near the apex. Since most of this mass is situated close to the center of the moving part of the cochlear partition and its density is close to that of water (ρ) we approximate the mass per unit length of the moving part of the cochlear partition as $M[x]=\rho\mathrm{CSA}[x]$. Figure 4(b) shows the mass per unit length of the moving part of the cochlear partition used in this paper. It is based upon an interpolation of the cross-sectional areas given in Fernandez (1952).

In vacuo *resonance of cochlear partition*. The ''*in vacuo* resonant frequency'' of the cochlea is the resonant frequency of a particular short section of the cochlear partition were it to be mechanically excited with the effect of the fluid coupling removed.

In a nonuniform transmission line model of the cochlea [such as the energy flow model of Lighthill (1991)], the place of the ''cutoff'' of a particular input frequency occurs at the place which has an *in vacuo* resonance equal to that input frequency. The ''cutoff place'' is the position along the cochlear partition at which energy of a particular frequency ceases to flow as propagating waves and flows in an evanescent mode. In the lightly damped case the cutoff place is marked in the response by a rapid change of phase gradient from its maximum to close to zero. Slightly basal to the cutoff place the group velocity of the propagating waves reaches its minimum (Lighthill, 1991). Spatially, the maximum of the amplitude of the response (the characteristic place) also occurs slightly basal to the cutoff place, and hence the place of the *in vacuo* resonance for the input frequency. This effect is clearly visible both in measurements of the mechanical response of the cochlea [see, for instance, Robles *et al.* (1986) and Nuttall and Dolan (1996a, b)] and in the results of various mechanical models [see, for instance, Steele and Taber (1979) and Kanis and de Boer (1993)].

The model used in this paper is not a transmission line model. Nevertheless, the same relationship between the *in vacuo* resonance and the cutoff point of the response holds true, except for very low frequencies at the very apical end of the cochlea.[3] For frequencies with *in vacuo* resonances at the apical end of the cochlea, reflection from the helicotrema invalidates the unidirectional energy flow argument above and the cutoff point occurs somewhat basally to the *in vacuo* resonance. Such effects do not concern us here since we are modeling measurements close to the basal end of the cochlea.

We can find an approximation to the *in vacuo* resonance by finding the characteristic frequency map for low-level inputs along the cochlea. Several such sets of measurements, made in guinea pig, are presented in Greenwood (1990). This data can be fitted reasonably well to the equation

$$F^{ch}[x]=45\,000\times2^{-410x}, \tag{4}$$

where $F^{ch}[x]$ is the characteristic frequency for a place x meters from the basal end of the cochlear partition.

The above equation gives a characteristic frequency half a turn basal of the helicotrema ($F^{ch}[0.01775]$) of 290 Hz. This corresponds with the direct mechanical measurements of Cooper and Rhode (1995).

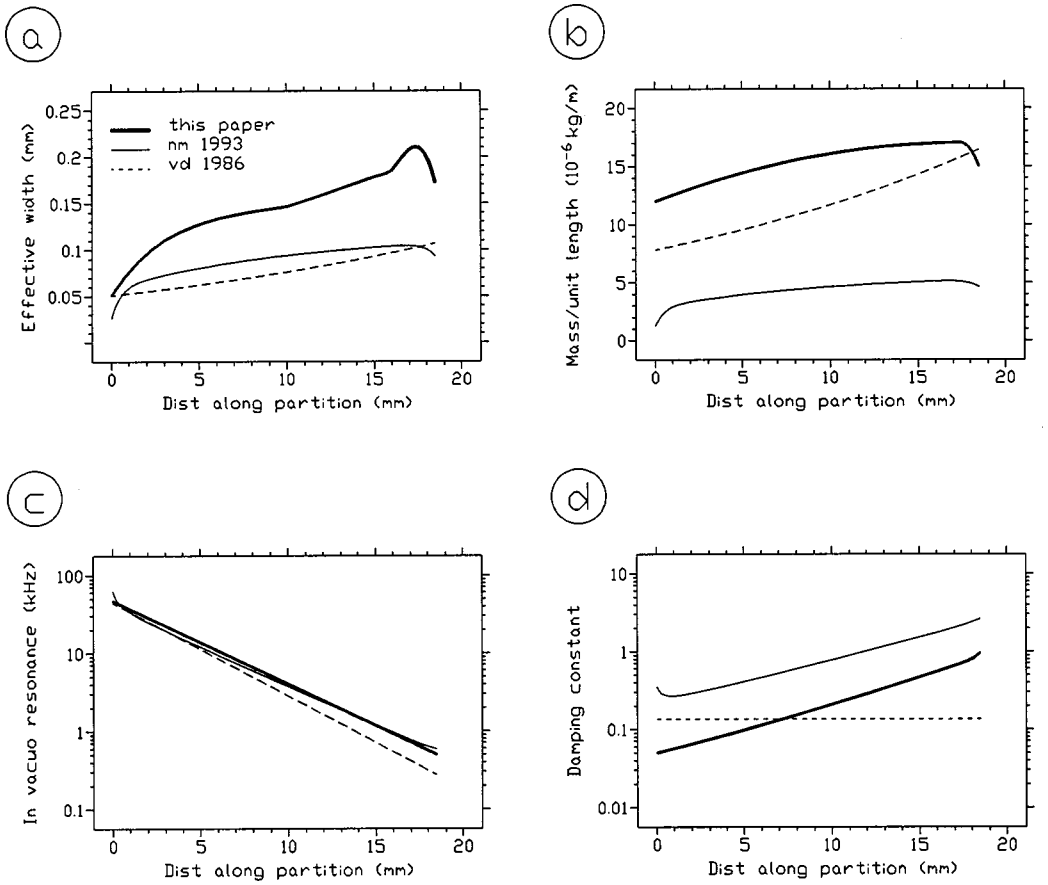

FIG. 4. Some of the parameters of the model used in this and other papers. Key: **this paper**, parameters used in this paper, **nm 1993**, parameters used by Mammano and Nobili (1993); **vd 1986**, parameters used by Viergever and Diependaal (1986) to fit to the passive guinea pig data of Johnstone and Yates (1974). (a) The effective width of the moving part of the cochlear partition used in each model. (b) The mass per unit length of the cochlear partition used in each model. (c) The *in vacuo* resonance of the cochlear partition used in each model. (d) The damping constant of the cochlear partition used in each model.

However, $F^{\mathrm{ch}}[x]$ is not equal to $(1/2\pi)\omega_0[x]$ since the characteristic place is slightly basal to the *in vacuo* resonance and hence $(1/2\pi)\omega_0[x]$ must be slightly higher than $F^{\mathrm{ch}}[x]$. An estimate of the difference at the basal end of the guinea pig cochlea can be found by comparing sensitive low-level amplitude and phase responses for animal 2381#2 from Nuttall and Dolan (1996b). At $F^{\mathrm{ch}}[x]=18$ kHz in this animal, $F^{\mathrm{ch}}[x]$ is about 20% lower than $(1/2\pi)\omega_0[x]$. At the apical end of the cochlea the difference is more difficult to estimate due to the irregularity of the response and lack of a definite point at which the gradient of the phase changes, probably due to reflections from the apex [see, for instance, the results of Cooper and Rhode (1995)]. However, the results of Cooper and Rhode (1995) suggest that the *in vacuo* resonance is about 600 Hz (or about one octave above $F^{\mathrm{ch}}[x]$) at $x=17.5$ mm. Logarithmically interpolating between these two points gives us the *in vacuo* resonance function that I will use in this paper:

$$\omega_0[x]=2\pi\times 47\,250\times 2^{-355x}. \tag{5}$$

Damping coefficient of cochlear partition. Mammano and Nobili (1993) derive an estimate of the damping per unit length ($H[x]$) from fluid mechanical considerations and estimated dimensions of the subtectorial space. Their dimensions for the subtectorial space correspond well with published pictures of sections of the organ of Corti. We shall use these values of $H[x]$ to find the damping constant of the cochlear partition in this paper.

Longitudinal coupling. Mammano and Nobili (1993) showed that realistic values of longitudinal coupling (shearing resistances of around 10^{-10} kg.m/s along the cochlear partition) made a significant contribution to the response of their active model of the cochlea.

Increasing the longitudinal coupling to these values in our passive model only makes a significant change to its transfer function at a small region just before the place of *in vacuo* resonance. This region is localized to a 0.1-mm-long section of the cochlea and the rest of the transfer function is changed insignificantly by the introduction of longitudinal coupling.

We attribute the negligible effect of longitudinal coupling to the fact that the damping forces are much larger than the shearing resistance in our passive model. In an active model, such as that of Mammano and Nobili (1993), the activity balances out the damping forces to the point where the shearing resistance becomes significant.

Place of measurement of motion of the cochlear partition. Nuttall and Dolan (1996a) do not state the longitudinal position on the cochlear partition from which responses were recorded. However, examination of the responses of animal 2381#2 from Nuttall and Dolan (1996b) (to which the response of the model will be compared) show that the phase

gradient change occurs at 18 900 Hz. If we take this to be the *in vacuo* resonance of the place of measurement, then according to our model's *in vacuo* frequency map the measurements were made at $x=3.72$ mm. This will be the place along the cochlear partition from which the model's output is taken in order to calculate the transfer function.

The discretization mesh of the model. The ''discretization mesh'' defines where the points $\{x_1, x_2, \ldots, x_N\}$ are placed along the longitudinal axis of the cochlear partition. As the time to find a solution increases as the cube of the number of mesh points, it is advantageous to use as few mesh points as is consistent with an accurate solution. In general, a regularly spaced discretization mesh is not optimal. The maximum phase gradient of high-frequency responses is much steeper than the maximum phase gradient of low-frequency responses. Therefore the discretization mesh is arranged to decrease its density (using an exponential function) by a factor of 20 from base to apex. Furthermore, the phase gradient of the response for a particular frequency increases markedly at around the place of the *in vacuo* resonance for that frequency. Therefore, the mesh density is increased, in a smooth manner (using a hyperbolic secant function), by a factor of up to 8 for about 1 mm either side of the place of the *in vacuo* resonance for the frequency being investigated.

All of the model results reported in this paper were generated using a nonuniform 400-point discretization mesh. Increasing the number of points to 600 made an insignificant difference to the solution (a ratio of only 0.4 dB in amplitude and 0.02π rad in phase). Reducing the number of points to 200 only changed the amplitude by a maximum of 1 dB and the phase by a maximum of 0.1π rad. This indicates that a 400-point nonuniform mesh is sufficient for an accurate solution.

With a 400-point discretization mesh a single run of the model (at one frequency) takes about 90 s on a 200-MHz Pentium based computer.

II. RESULTS

Figure 5 shows the amplitude and phase of the transfer function obtained by running the model with the parameters discussed above. These results were obtained by running the model at a selection of frequencies between 1 and 18.6 kHz (with the discretization mesh optimized for each frequency). The complex velocity transfer function between the stapes and the place of measurement on the cochlear partition was then plotted (in the log amplitude/phase domain) against frequency.

Also shown are the mean and 95% confidence intervals of the mechanical measurements made on the post-mortem guinea pig (2381#2po) by Nuttall and Dolan (1996b). The root mean square of the ratios between the mean of the Nuttall and Dolan (1996b) data and the output of the model is 6.3 dB in amplitude and 0.33π rad in phase. The maximum difference was 13 dB in amplitude and 0.5π rad in phase.

The fit between the model and the mechanical data is good at low frequencies (1–2 kHz) and follows the general trend of the data towards the peak of the amplitude (2–13 kHz). However, the transfer function of the model fails to follow the rapid amplitude transitions, particularly at 5 and 10 kHz where it is up to 12 dB different. I believe that these rapid amplitude transitions are due to reflection phenomena (such as standing waves) and cannot be simulated in a model with smoothly varying parameters, such as the one described in this paper. Beyond the peak the model transfer function matches the mechanical data quite well with both the phase and amplitude falling rapidly to the correct level. However, there are differences: both the amplitude and phase fall too late and too quickly, and the ''plateau'' in the phase response occurs too early.

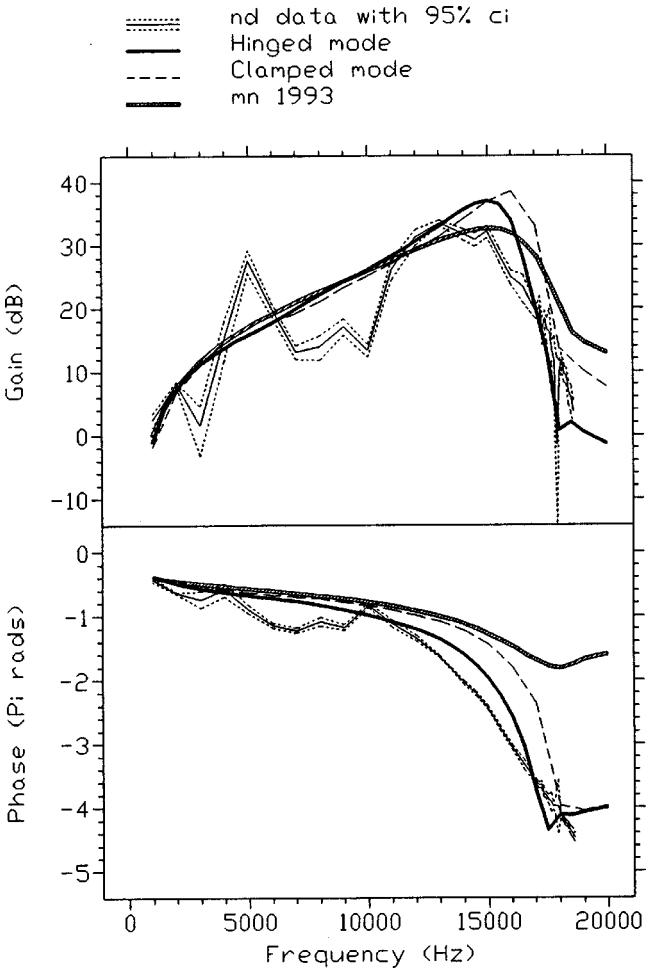

FIG. 5. Amplitude and phase of the cochlear transfer function both predicted by various models and from mechanical measurements made in the guinea pig. Key: **nd data with 95% ci**, mechanical measurement data from Nuttall and Dolan (1996b) animal 2381#2po, the solid line is the mean and the dotted lines enclose the 95% confidence interval at each frequency; **Hinged mode**, results from the model run with all parameters set as described in Sec. I C; **Clamped mode**, results from the model run with the cochlear partition mode factor set to 0.5; **mn 1993**, results from the passive model of Mammano and Nobili (1993).

A. The effect of reducing the cochlear partition mode factor

Figure 5 also shows the transfer function obtained when the mode factor of the cochlear partition was reduced from 0.637 (that of a uniform beam hinged at both ends) to 0.5 (that of a beam clamped at both ends). The differences between the two transfer functions are significant at frequencies

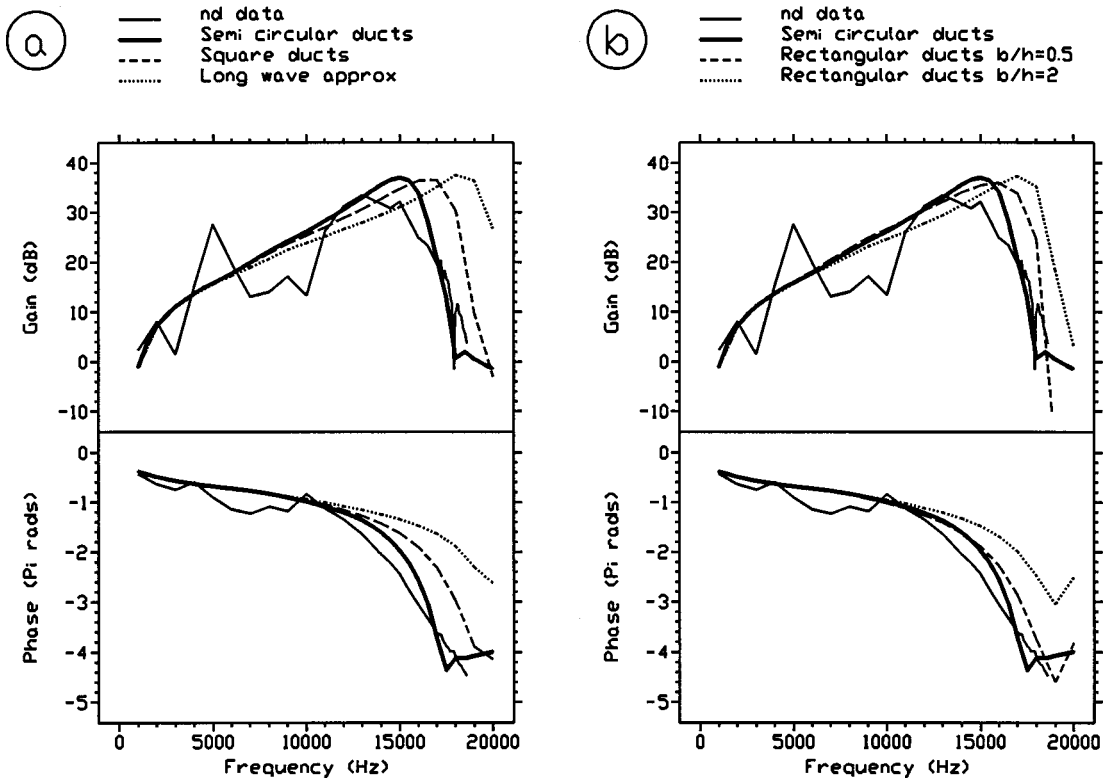

FIG. 6. Amplitude and phase of the cochlear transfer function from both the model and mechanical measurements made in the guinea pig. Key: **nd data**, mean of the mechanical measurement data from Nuttall and Dolan (1996b) animal 2381#2po; **Semi circular ducts**, results from the model run with all parameters set as described in Sec. I C; **Rectangular ducts b/h=2, Square ducts and Rectangular ducts b/h=0.5**, results from the model run with the Green's function describing a two-dimensional rectangular duct with aspect ratios (width of duct/height of duct) set to 0.5, 1, and 2, respectively; **Long wave approx**, results from the model in which pressure was not allowed to vary across the cross section of the duct.

between the peak amplitude and the *in vacuo* resonance (with ratio of up to 15 dB in amplitude and 1.5π rad in phase).

In view of this result, I conclude that any quantitative model of the cochlea must pay significant attention to the mode factor of the vibration of the cochlear partition if it is to generate accurate results. The model in this paper uses the mode factor of a simple hinged beam, on the basis of rather nebulous arguments. Obviously, some further investigation of this matter is required.

B. The effect of changing the geometry of the scalae

Figure 6 shows the effect of changing the geometry of the cross-sectional shape of the scalae, while their cross-sectional area remains the same.

Figure 6(a) compares a model with square sectioned ducts and a model in which pressure is constant across the cross section of the duct (the so-called ''long wave'' approximation) to our model with semi-circular sectioned ducts. The Green's function for the model with square sectioned ducts was derived using a 2D approximation outlined in Appendix B. There is a significant difference between the transfer functions generated by the models with different geometries, particularly after the peak amplitude frequency (a ratio of up to 35 dB and 2π rad between the long wave and semi-circular ducted models and up to 20 dB and 1.2π rad between the square and semi-circular ducted models). This demonstrates that neither the square ducted nor the long wave models are adequate representations of a semi-circular ducted cochlea.

The formulation of the approximation to the Green's function for the model with square ducts allows us to investigate the effect of altering the aspect ratio (width/height) of a rectangular duct. Figure 6(b) shows transfer functions generated by models with rectangular ducts with aspect ratios of 0.5, 1, and 2. There is a significant change in the transfer function (with ratios of up to 25 dB in amplitude and 1.5π rad in phase) caused by altering the aspect ratio.

I conclude that the cross-sectional shape of the scalae has a considerable effect upon the cochlear transfer function, and therefore that any quantitative model must reflect realistic scalae geometry. Although a semi-circular duct is probably the most realistic of the geometries considered in this paper, it probably still does not adequately reflect the true geometry of the guinea pig cochlea (see Stevens and Davis, 1938).

III. DISCUSSION

It can be seen from Fig. 5 that, although the transfer function predicted by the model in this paper follows the general trend and reproduces many of the features of the measured mechanical data, there are still quite large discrepancies between the measured and predicted transfer func-

tions. There are a very large number of possible reasons for these discrepancies. However, I suggest the reasons listed below as the most likely explanations:

(i) In the model used in this paper the scalae are assumed to have a semi-circular cross section. In the real guinea pig cochlea the scalae cross sections are not this shape (Stevens and Davis, 1938). Furthermore, in the real cochlea the shape of the scalae is further complicated by the coiling of the cochlea. The study in this paper has shown that the scalae cross-sectional shape has a significant effect upon the transfer function generated by the model. Modeling the complex shape of the real scalae probably requires a numerical method for finding the Green's functions.

(ii) In the model presented here the cochlear partition impedance is represented as the point impedance of a one degree of freedom oscillator. This is probably too simple a model. For instance, because the real cochlea must provide good coupling to the inner hell cell stereocilia, the micro-mechanics (hair cell stereocilia–tectorial membrane complex) must play a significant role in the partition impedance, even in the passive cochlea. To model these effects would require a multiple degree of freedom impedance model.

(iii) The round and oval windows are assumed to be somewhat basal to the end of the cochlear partition in the model presented in this paper. This allows us to assume that the cochlear partition is driven by a simple pressure difference across its basal end and to ignore any evanescent coupling effects between the window motion and the cochlear partition. In the real guinea pig cochlea the round and oval windows drive into the vestibule over the basal end of the cochlear partition. The proximity and position of the windows may well have a significant effect upon the mechanical response of the cochlea.

(iv) In the model presented here the parameter values are assumed to vary smoothly along the length of the cochlear partition. I have adopted these ''smooth'' parameters since the available measurements only provide a few points of reference, the rest of the data being derived by interpolation. The mechanical measurements show rapid fluctuations across frequency, which I believe can only be modeled by reflections caused by irregularities in some of the parameters. Irregularities in the parameters could be found by optimizing the model parameters, all along the length of the cochlea, so that the model output fits the mechanical data. Such a scheme (e.g., conjugate gradient minimization) would require large amounts of computing time since the model would have to be run many times and a single run of the model at many frequencies takes several tens of minutes (on a 200-MHz Pentium processor based computer).

(v) The model presented here is driven from a velocity (infinitely high impedance) source. This is obviously unrealistic since the real cochlea is driven via a finite impedance dependent upon the middle and outer ears and the driving arrangement used to deliver the sound stimulus. The driving impedance will affect the cochlea transfer function, in particular standing waves may occur at some frequencies. The rapid fluctuations in the real transfer function may be due to these factors. To investigate this would require the model to be driven from an impedance derived from a realistic model of the middle and outer ears and the driving arrangement. Such a model would require that the acoustic parameters of the driving arrangement as well as those of the middle and outer ears to be measured. These measurements were not published by Nuttall and Dolan (1996a), so such a model is not possible at present. It would be useful to those attempting to model the data if future publications of mechanical measurements included details such as the Thevenin parameters of the sound source.

(vi) Most of the parameter values used in this paper were obtained from rather old sources [for instance, many parameters were derived from Fernandez (1952)]. Since these sources were compiled, many advances have been made, both in measurement and reporting techniques, which could result in more accurate values for many of the parameters. It would be beneficial to make new measurements of many of the macro-mechanical structures of the cochlea of the guinea pig, and to report both means and individual differences between animals.

(vii) In the model presented here the mode factor of the cochlear partition was assumed to be that of a hinged uniform beam. In view of the complex structure of the cochlear partition this assumption is probably incorrect. It has been shown that even quite small variations of the cochlear partition mode factor can have significant effects upon the transfer function generated by the model. A realistic value for the cochlear partition mode factor can probably be found by a combination of mechanical measurements and theoretical studies.

(viii) The cochlea duct dimensions are changing rapidly at around our place of measurement. This could cause our approximation for the Green's function of the duct to become significantly inaccurate, giving rise to inaccuracies in our predicted transfer function. This matter could be resolved by finding a better approximation for the Green's functions, for instance, by using numerical methods.

(ix) The procedure for making mechanical measurements of the motion of the cochlear partition is very invasive. They involve gaining physical access to the inside of the cochlea, and in many cases the placing of a small mass upon the moving part of the cochlear partition. Disturbance of the mechanical process by such procedures probably accounts for the discrepancies between the measurements shown in Fig. 2. Modern measurements are carried out using the minimum of disturbance, to the point where the ''active process'' at low levels is still present. It is an implicit assumption of this study that modern measurements,

such as those performed by Nuttall and Dolan (1996a), accurately reflect the mechanics of the undisturbed cochlea. However, in view of the history of improving measurements being obtained by procedures that cause less perturbation of the cochlear mechanics, we must question the validity of all cochlear mechanical measurements.

(x) The guinea pigs used to obtain the mechanical measurements of cochlear response were different animals from those used to obtain the parameters of the model used in this paper. None of the sources of the model parameters include details of the variation of those parameters among individual animals. The possibility exists that this variation is quite wide. If this is the case, then we should properly only compare mechanical response measurements with a model using parameters from that animal.

(xi) In our model the ''output'' of the cochlear vibration is taken at a point of the greatest amplitude of vibration across the cochlear partition 3.72 mm from the base. In fact, the measurement was taken from a point on the cochlear partition below the outer hair cells. Given our ignorance of the mode of vibration of the cochlear partition, we cannot tell if this is the point of maximum amplitude of vibration, or, if it is not, then what proportion of the maximum vibration is present at this point. The point of measurement in the x direction (3.72 mm from the base) was chosen to match the frequency of the start of the ''phase plateau'' of the transfer function to the *in vacuo* resonance of the cochlear partition. In fact, even in our model, these frequencies do not quite match. The start of the phase plateau for an input of 18 900 Hz is some 0.25 mm basal to the *in vacuo* resonance for that frequency. This difference appears to be a function of damping with smaller damping reducing the difference. Other factors, such as longitudinal coupling, also affect this difference. In view of the foregoing, we may be comparing the transfer functions taken from a different point in the model and in the real cochlea from which the mechanical measurements were made.

IV. SUMMARY

(1) The post-mortem transfer function of the cochlea of the guinea pig was compared to the transfer function generated by a model [based upon that of Mammano and Nobili (1993)] with parameters derived from physical measurements of the guinea pig cochlea.

(2) The transfer function generated by the model is quantitatively quite similar to that measured in the real guinea pig cochlea. The model transfer function follows the general trend and has many of the features of the real data (see Fig. 5).

(3) Experiments with the model show the importance of cochlear partition mode factor and duct geometry upon the passive response of the cochlea (see Figs. 5 and 6).

(4) There are features of the real data which the model fails to simulate. In particular, there are rapid fluctuations across frequency in the real transfer function. These cause differences of up to 12 dB between the amplitudes of the transfer functions of the real guinea pig and the model (see Fig. 5).

APPENDIX A: OUTLINE OF THE GREEN'S FUNCTION SOLUTION METHOD USED IN THIS PAPER

The solution method can be derived from the assumption that the forces transmitted through the fluid in the cochlea are exactly balanced by the force generated by the impedance of the moving cochlear partition. At distance x along the cochlea this balance of forces, acting upon the cochlear partition, can be written

$$F_s[x]+F_{cp}[x]=F_z[x], \tag{A1}$$

where $F_s[x]$ is the force per unit length, acting at x, due to the motion of the stapes coupled via the cochlear fluid; $F_{cp}[x]$ is the force per unit length due to the combined motion of the whole of the cochlear partition coupled via the cochlear fluid; and $F_z[x]$ is the force per unit length due to the mechanical impedance of the moving cochlear partition. Figure 3 shows these forces diagrammatically. Note that all forces and velocities are expressed as amplitudes since the model is linear and we are working in the frequency domain.

Taking these forces one by one,

$$F_x[x]=-j\omega G_s[x]V_s, \tag{A2}$$

where V_s is the velocity of the stapes and $G_s[x]$ is the stapes force propagator, giving the force per unit length at x due to unit velocity of the stapes. The value of the stapes force propagator can be determined from fluid mechanical considerations. Details are given in Mammano and Nobili (1993) and Nobili and Mammano (1996):[1]

$$F_{cp}[x]=-j\omega\int_{x'=0}^{x'=L}\mathrm{G}[x,x']V_{cp}[x']\,dx', \tag{A3}$$

where $V_{cp}[x']$ is the velocity of the cochlear partition at x'; L is the length of the cochlear partition; and $\mathrm{G}[x,x']$ is the Green's function, giving force per unit length at x due to unit velocity at x':

$$F_z[x]=V_{cp}[x]Z_{cp}[x], \tag{A4}$$

where $Z_{cp}[x]$ is the impedance per unit length of the cochlear partition to transverse motion.

An approximate value of the Green's function in the cochlea can be determined from fluid mechanical considerations. For example, see the analysis of Mammano and Nobili (1993) and Nobili and Mammano (1996).[2] Such an analysis results in a Green's function that is the sum of a ''long range part'' (without a singularity at $x=x'$) and a ''singular part'' (with a singularity at $x=x'$). Equation (A3) can then be written

$$F_{cp}[x] = -\left[j\omega \int_{x'=0}^{x'=L} G_{lw}[x,x']V_{cp}[x']\, dx' \right] - \left[j\omega \int_{x'=0}^{x'=L} G_{sing}[x,x']V_{cp}[x']\, dx' \right], \quad \text{(A5)}$$

where G_{lw} and G_{sing} are the ''long range'' and ''singular'' parts of the Green's function, respectively.

We can discretize the model by defining a set of $N+1$ points along the cochlear partition $\{x_1, x_2, x_3, \ldots, x_N, x_{N+1}\}$ where $x_1 = 0 < x_2 < x_3 \ldots < x_N < x_{N+1} = L$. The model is thus discretized into N sections each of length $\Delta_n = x_{n+1} - x_n$. Using this discretization, Eq. (A5) can then be approximated by

$$\begin{aligned} F_{cp}[x_r] \approx & -j\omega \sum_{c=1}^{N} \frac{1}{2}\Delta_c (V_{cp}[x_c]G_{lw}[x_r, x_c] \\ & + V_{cp}[x_{c+1}]G_{lw}[x_r, x_{c+1}]) \\ & - j\omega \sum_{c=1}^{N} \left(\frac{1}{2}(V_{cp}[x_c] \right. \\ & \left. + V_{cp}[x_{c+1}]) \int_{x'=x_c}^{x'=x_{c+1}} G_{sing}[x_r, x']\, dx' \right). \end{aligned} \quad \text{(A6)}$$

Here $V_{cp}[x_{N+1}] = 0$, since force per unit length across the partition is zero at the helicotrema (at $x = L$). Finally, a set of simultaneous equations [with a similar form to Eq. (A1)] for the whole system can be written in matrix form:

$$(j\omega \mathbf{G^M} + \mathbf{Z^M})\mathbf{V^V} = -j\omega V_s \mathbf{S^V}, \quad \text{(A7)}$$

where $\mathbf{G^M}$ is a full square matrix of size $N \times N$, with elements

$$\mathbf{G^M} = \begin{cases} \int_{x'=x_1}^{x'=x_2} \frac{1}{2} G_{sing}[x_r, x']\, dx' + \frac{1}{2}\Delta_1 G_{lw}[x_r, x_1], & c = 1, \\ \int_{x'=x_c}^{x'=x_{c+1}} G_{sing}[x_r, x']\, dx' + \frac{1}{2}(\Delta_{c-1} + \Delta_c) G_{lw}[x_r, x_c], & c \neq 1, \end{cases} \quad r, c \in \{1, 2, \ldots, N-1, N\}, \quad \text{(A8)}$$

$$\mathbf{Z^M} = \text{diag}\,[\{Z_{cp}[x_1], Z_{cp}[x_2], \ldots, Z_{cp}[x_{N-1}], Z_{cp}[x_N]\}], \quad \text{(A9)}$$

$$\mathbf{V^V} = [\{V_{cp}[x_1], V_{cp}[x_2], \ldots, V_{cp}[x_{N-1}], V_{cp}[x_N]\}]^T, \quad \text{(A10)}$$

$$\mathbf{S^V} = [\{G_s[x_1], G_s[x_2], \ldots, G_s[x_{N-1}], G_s[x_N]\}]^T. \quad \text{(A11)}$$

We shall define the complex ''gain of the cochlea,'' or gain at x_n as $V_{cp}[x_n]/V_s$. In other words, $V_{cp}[x_n]$ when V_s is set to unity. If $G[x', x]$, $G_s[x]$, and $Z_{cp}[x]$ are known, then Eq. (A7) can be solved with $V_s = 1$, for any frequency of input, to find the gain of the cochlea at all points.

APPENDIX B: A TWO-DIMENSIONAL APPROXIMATION FOR THE GREEN'S FUNCTION OF A RECTANGULAR DUCT OF VARYING CROSS-SECTIONAL AREA

The Green's function for a rectangular duct of varying cross section can be approximated using a similar technique to that of Mammano and Nobili (1993). The Green's function can be expressed as the sum of a long range part, determined by the cross-sectional area all along the duct, and a singular part, determined by the geometry of the duct local to the singularity.

The force per unit length generated by the motion of the cochlear partition propagated by the cochlear fluid can be written

$$F_{cp}[x] = -j\omega \int_{x'=0}^{x'=L} ({}^{u}G[x,x'] + {}^{l}G[x,x'])V_{cp}[x']\, dx', \quad \text{(B1)}$$

where ${}^{u}G[x,x']$ is the Green's function representing the force transmitted by the fluid in the upper fluid space (scala vestibuli and scala media) and ${}^{1}G[x,x']$ is the Green's function for the lower fluid space (scala tympani).

Here ${}^{u}G[x,x']$ can be approximated by

$$\begin{aligned} {}^{u}G[x,x'] &\approx {}^{u}G_{lw}[x,x'] + {}^{u}G_{sing}[x,x'] \\ &\approx {}^{u}G_{lw}[x,x'] + {}^{u}G_{2d}[x,x'] - {}^{u}G_{lwc}[x,x'], \end{aligned} \quad \text{(B2)}$$

where

$${}^{u}G_{lw}[x,x'] = \rho\beta[x]\beta[x'] \int_{\epsilon=\text{Max}[x,x']}^{\epsilon=L} \frac{1}{{}^{u}h[\epsilon]\,{}^{u}b[\epsilon]}\, d\epsilon, \quad \text{(B3)}$$

which is the ''long range'' part of the upper fluid space Green's function (Mammano and Nobili, 1993):

$${}^{u}G_{2d}[x,x'] = \frac{\rho\beta[x]}{\pi\,{}^{u}b[x]} \int_{x'=0}^{x'=L} -\beta[x'] \left(Ln\left[2 \left| \cosh\left[\frac{\pi x}{{}^{u}h[x]} \right] - \cosh\left[\frac{\pi x'}{{}^{u}h[x]} \right] \right| \right] - \frac{\pi L}{{}^{u}h[x]} \right) dx', \quad \text{(B4)}$$

which is the Green's function for a two-dimensional ''box'' model (constant cross section rectangular duct) with height and width equal to the height and width of the fluid space at x (Diependaal, 1989):

$${}^{u}G_{lwc}[x,x'] = \rho\beta[x]\beta[x'] \frac{1 - \text{Max}\,[x,x']}{{}^{u}b[x]\,{}^{u}h[x]}, \quad \text{(B5)}$$

which is the long range part of the Green's function for a ''box model'' with height and width equal to the height and width of the fluid space at x (Diependaal, 1989); and $\beta[x]$ is the width of the moving part of the cochlear partition at x; ${}^{u}b[x]$ and ${}^{u}h[x]$ are the height and width of the rectangularly sectioned upper fluid space at x; ρ is the density of the fluid, and Max $[x1,x2]$ is a function returning the larger of $x1$ or $x2$.

A similar expression to approximation (B2) exists for ${}^{1}\mathrm{G}[x,x']$.

${}^{u}\mathrm{G}_{\mathrm{sing}}[x,x'] \approx {}^{u}\mathrm{G}_{2\mathrm{d}}[x,x'] - {}^{u}\mathrm{G}_{\mathrm{lwc}}[x,x']$ holds because the right-hand side of this expression is equal to the singular part of the Green's function of a two-dimensional box model with cross section equal to that of the varying cross section rectangular duct at x. The singular part of the Green's function decays rapidly as x moves away from the source at x'. It is therefore assumed that the characteristics of the singular part of the Green's function are mostly determined by the local dimensions of the duct.

Expression (B1) can be discretized using a similar procedure to that adopted by Diependaal (1989). Using the same coordinate system as was used in Appendix A, this yields

$$\mathbf{F}^{\mathbf{V}}_{\mathbf{cp}} = -j\omega \mathbf{G}^{\mathbf{M}}_{\mathbf{rect}} \cdot \mathbf{V}^{\mathbf{V}} = -j\omega ({}^{\mathbf{u}}\mathbf{G}^{\mathbf{M}}_{\mathbf{lw}} + {}^{\mathbf{u}}\mathbf{G}^{\mathbf{M}}_{\mathbf{2d}} - {}^{\mathbf{u}}\mathbf{G}^{\mathbf{M}}_{\mathbf{lwc}} + {}^{\mathbf{1}}\mathbf{G}^{\mathbf{M}}_{\mathbf{lw}} + {}^{\mathbf{1}}\mathbf{G}^{\mathbf{M}}_{\mathbf{2d}} - {}^{\mathbf{1}}\mathbf{G}^{\mathbf{M}}_{\mathbf{lwc}}) \cdot \mathbf{V}^{\mathbf{V}}, \tag{B6}$$

where

$$\mathbf{F}^{\mathbf{V}}_{\mathbf{cp}} = [\{F_{cp}[x_1], F_{cp}[x_2], \ldots, F_{cp}[x_{N-1}], F_{cp}[x_N]\}]^T, \tag{B7}$$

${}^{\mathbf{u}}\mathbf{G}^{\mathbf{m}}_{\mathbf{lw}}$, ${}^{\mathbf{u}}\mathbf{G}^{\mathbf{m}}_{\mathbf{2d}}$, ${}^{\mathbf{u}}\mathbf{G}^{\mathbf{m}}_{\mathbf{lwc}}$, ${}^{\mathbf{1}}\mathbf{G}^{\mathbf{m}}_{\mathbf{lw}}$, ${}^{\mathbf{1}}\mathbf{G}^{\mathbf{m}}_{\mathbf{2d}}$, and ${}^{\mathbf{1}}\mathbf{G}^{\mathbf{m}}_{\mathbf{lwc}}$ are full square Green's function matrices of size $N \times N$, with elements

$${}^{\mathbf{u}}\mathbf{G}^{\mathbf{M}}_{\mathbf{lw}}[r,c] = \begin{cases} \frac{1}{2}\Delta_c \rho \beta[x_r]\beta[x_c]S[r], & c=1, \\ \frac{1}{2}(\Delta_c + \Delta_{c-1})\rho\beta[x_r]\beta[x_c]S[r], & c>1 \quad \text{and} \quad c \leqslant r, \\ \frac{1}{2}(\Delta_c + \Delta_{c-1})\rho\beta[x_r]\beta[x_c]S[c], & c>1 \quad \text{and} \quad c>r, \end{cases} \tag{B8}$$

$$S[i] = \frac{1}{2}\sum_{k=i}^{N} \Delta_k \left(\frac{1}{{}^{u}b[x_k]{}^{u}h[x_k]} + \frac{1}{{}^{u}b[x_{k+1}]{}^{u}h[x_{k+1}]} \right),$$

$${}^{\mathbf{u}}\mathbf{G}^{\mathbf{M}}_{\mathbf{2d}}[r,c] = \begin{cases} -\frac{1}{2}\rho\beta[x_r]\beta[x_c]\dfrac{g^{+}_{2d}[x_r,\Delta_r]}{{}^{u}b[x_r]}, & r=1 \quad \text{and} \quad c=1, \\ -\frac{1}{2}\rho\beta[x_r]\beta[x_c]\dfrac{g^{-}_{2d}[x_r,\Delta_{r-1}]}{{}^{u}b[x_r]}, & r=2 \quad \text{and} \quad c=1, \\ -\frac{1}{2}\rho\beta[x_r]\beta[x_c]\dfrac{\Delta_c g^{0}_{2d}[x_r,x_c]}{{}^{u}b[x_r]}, & r>2 \quad \text{and} \quad c=1, \\ -\frac{1}{2}\rho\beta[x_r]\beta[x_c]\dfrac{(\Delta_c+\Delta_{c-1}) g^{0}_{2d}[x_r,x_c]}{{}^{u}b[x_r]}, & |r-c|>2 \quad \text{and} \quad c>1, \\ -\frac{1}{2}\rho\beta[x_r]\beta[x_c]\dfrac{\Delta_c g^{0}_{2d}[x_r,x_c] + g^{-}_{2d}[x_c,\Delta_{c-1}]}{{}^{u}b[x_r]}, & r>2 \quad \text{and} \quad c=r-1, \\ -\frac{1}{2}\rho\beta[x_r]\beta[x_c]\dfrac{g^{+}_{2d}[x_c,\Delta_c] + g^{-}_{2d}[x_c,\Delta_{c-1}]}{{}^{u}b[x_r]}, & r>1 \quad \text{and} \quad c=r, \\ -\frac{1}{2}\rho\beta[x_r]\beta[x_c]\dfrac{\Delta_c g^{0}_{2d}[x_r,x_c] + g^{+}_{2d}[x_c,\Delta_c]}{{}^{u}b[x_r]}, & c=r+1, \end{cases}$$

$$g^{0}_{2d}[x_r,x_c]=\frac{1}{\pi}\mathrm{Ln}\left[2\left|\cosh\left[\frac{\pi x_r}{h}\right]+\cosh\left[\frac{\pi x_c}{h}\right]\right|\right]-\frac{L}{h},$$

$$g^{+}_{2d}[x,\Delta]=\frac{1}{\pi}\left(\Delta\,\mathrm{Ln}\left[\sinh\left[\frac{\pi\Delta}{2h}\right]\right]-\frac{\Delta^2\pi\,\coth[\pi\Delta/2h]}{4h}-\frac{\Delta}{2}+2x\,\mathrm{Ln}\left[\frac{\sinh[\pi(2x+\Delta)/2h]}{\sinh[\pi x/h]}\right]+\Delta\mathrm{Ln}\left[\mathrm{Sinh}\left[\frac{\pi(2x+\Delta)}{2h}\right]\right]\right.$$
$$\left.-\frac{\Delta\pi(2x+\Delta)}{4h}\coth\left[\frac{\pi(2x+\Delta)}{2h}\right]-\frac{x\Delta\pi\,\coth[\pi x/h]}{2h}+\Delta\,\mathrm{Ln}[4]-\frac{\Delta\pi L}{h}\right),\tag{B9}$$

$$g^{-}_{2d}[x,\Delta]=\frac{1}{\pi}\left(\Delta\mathrm{Ln}\left[\sinh\left[\frac{\pi\Delta}{2h}\right]\right]-\frac{\Delta^2\pi\,\coth[\pi\Delta/2h]}{4h}-\frac{\Delta}{2}+2x\,\mathrm{Ln}\left[\frac{\sinh[\pi x/h]}{\sinh[\pi(2x-\Delta)/2h]}\right]+\Delta\,\mathrm{Ln}\left[\mathrm{Sinh}\left[\frac{\pi(2x-\Delta)}{2h}\right]\right]\right.$$
$$\left.-\frac{\Delta\pi(2x-\Delta)}{4h}\coth\left[\frac{\pi(2x-\Delta)}{2h}\right]-\frac{x\Delta\pi\,\coth[\pi x/h]}{2h}+\Delta\,\mathrm{Ln}[4]-\frac{\Delta\pi L}{h}\right),$$

$$h={}^{u}h[x_r],$$

$$\mathbf{{}^{u}G^{m}_{lwc}}[r,c]=\begin{cases}\frac{1}{2}\Delta_c\rho\beta[x_r]\beta[x_c]\dfrac{L-x_r}{{}^{u}h[x_r]\,{}^{u}b[x_r]}, & c=1,\\ \frac{1}{2}(\Delta_c+\Delta_{c-1})\rho\beta[x_r]\beta[x_c]\dfrac{L-x_r}{{}^{u}h[x_r]\,{}^{u}b[x_r]}, & c>1 \quad \text{and} \quad c\leqslant r,\\ \frac{1}{2}(\Delta_c+\Delta_{c-1})\rho\beta[x_r]\beta[x_c]\dfrac{L-x_c}{{}^{u}h[x_r]\,{}^{u}b[x_r]}, & c>1 \quad \text{and} \quad c>r,\end{cases}\tag{B10}$$

and the lower fluid space Green's function matrices ($\mathbf{{}^{1}G^{m}_{lw}}$, $\mathbf{{}^{1}G^{m}_{2d}}$, and $\mathbf{{}^{1}G^{m}_{lwc}}$) being defined in the same way as their upper fluid space counterparts, but with ${}^{1}h[x]$ and ${}^{1}b[x]$ substituted for ${}^{u}h[x]$ and ${}^{u}b[x]$.

Finally, we can find the solution for the whole system as before in Appendix A. To do this we solve the system of simultaneous equations:

$$(j\omega\mathbf{G^{M}_{rect}}+\mathbf{Z^{M}})\mathbf{V^{V}}=-j\omega V_s\mathbf{S^{V}}.\tag{B11}$$

[1]The stapes force propagator derived by Mammano and Nobili (1993) assumes that the geometry of the cochlea is such that the iso-potential surfaces of the potential fluid flow correspond to the cross sections of the cochlea ducts. In particular, the oval and round windows are assumed to be sufficiently far from the cochlear partition that the ''short range part'' of the stapes force propagator is negligible. Without detailed study of the geometry of the vestibule of the cochlea the validity of this assumption cannot be assessed.

[2]The Green's functions used by Mammano and Nobili (1993) are derived by assuming that the Green's function is the sum of two parts, the ''long'' and ''short'' range parts. The long range part corresponds to the solution derived using the ''long wavelength assumption'' of Wentzel–Kramers–Brillouin (WKB) models (de Boer, 1991). The short range part corresponds to the difference between the solution for the full three-dimensional geometry of the cochlea and that derived using the long wavelength assumption. This short range part is derived by assuming that the part of the cochlea close to the source is a cylinder of constant cross section. The cross-sectional area of this cylinder is equal to the sum of the cross-sectional areas of the upper and lower ducts around the source. The validity of this assumption is not known, particularly in the vestibule where the cross section of the ducts changes very rapidly. In addition, the cross-sectional areas of the upper and lower ducts vary by a ratio of up to 3.75:1 (Fernandez, 1952).

[3]Mammano and Nobili (1993) argue that since the total hydrodynamic loading of the cochlear partition greatly exceeds that of the total mass of the cochlear partition, we cannot directly relate the *in vacuo* resonance to the cutoff point. I would argue that since the local hydrodynamic loading falls to zero at the *in vacuo* resonance [see Steele and Taber (1979) for a lucid explanation of this phenomena in the 2D box model], the total hydrodynamic loading is irrelevant. Irrespective of these arguments, the place of the *in vacuo* resonance and the cutoff point are within a fraction of a millimeter of one another in the basal 85% of the cochlea, both in the model presented in this paper and in Nobili and Mammano's own model.

de Boer, E. (**1991**). ''Auditory physics. Physical principles in hearing theory. III,'' Phys. Rep. **203**, 125–231.

Cooper, N. P., and Rhode, W. S. (**1992**). ''Basilar membrane mechanics in the hook region of cat and guinea-pig cochleae: Sharp tuning and nonlinearity in the absence of baseline position shifts,'' Hearing Res. **63**, 163–190.

Cooper, N. P., and Rhode, W. S. (**1995**). ''Nonlinear mechanics at the apex of the guinea-pig cochlea,'' Hearing Res. **82**, 225–243.

Davis, H. (**1958**). ''Transmission and transduction in the cochlea,'' Laryngoscope **68**, 359–382.

Diependaal, R. J., and Viergeuer, M. A. (**1989**). ''Nonlinear and active two-dimensional cochlea models: Time-domain solution,'' J. Acoust. Soc. Am. **85**, 803–812.

Fernandez, C. (**1952**). ''Dimensions of the cochlea (guinea pig),'' J. Acoust. Soc. Am. **24**, 519–523.

Greenwood, D. D. (**1990**). ''A cochlear frequency-position function for several species—29 years later,'' J. Acoust. Soc. Am. **87**, 2592–2605.

Guild, S. R. (**1927**). ''The width of the basilar membrane,'' Science **65**, 67.

Iurato, S. (**1962**). ''Functional implications of the nature and submicroscopic structure of the tectorial and basilar membranes,'' J. Acoust. Soc. Am. **34**, 1386–1395.

Johnstone, B. M., and Yates, G. K. (**1974**). ''Basilar membrane tuning curves in the guinea pig,'' J. Acoust. Soc. Am. **55**, 584–587.

Kanis, L. J., and de Boer, E. (**1993**). ''Self-suppression in a locally active nonlinear model of the cochlea: A quasilinear approach,'' J. Acoust. Soc. Am. **94**, 3199–3206.

Lighthill, J. (**1991**). ''Biomechanics of hearing sensitivity,'' Trans. ASME, J. Vib. Acoust. **113**, 1–13.

Littler, T. S. (**1965**). *The Physics of the Ear* (MacMillan, New York), Appendix I.
Mammano, F., and Nobili, R. (**1993**). ''Biophysics of the cochlea: Linear approximation'' J. Acoust. Soc. Am. **93**, 3320–3332.
Nobili, R., and Mammano, F. (**1996**). ''Biophysics of the cochlea: Stationary nonlinear phenomenology,'' J. Acoust. Soc. Am. **99**, 2244–2255.
Nuttall, A. L., and Dolan, D. F. (**1996a**). ''Steady-state sinusoidal velocity responses of the basilar membrane in guinea pig,'' J. Acoust. Soc. Am. **99**, 1556–1565.
Nuttall, A. L., and Dolan, D. F. (**1996b**). JASMA-99-1556-disk, internet site: ftp://pinet.aip.org/epaps/journ_acoust_soc/E-JASMA-99-1556-disk.
Robles, L., Ruggero, M. A., and Rich, N. C. (**1986**). ''Basilar membrane mechanics at the base of the chinchilla cochlea,'' J. Acoust. Soc. Am. **80**, 1364–1374.
Steele, C. R., and Taber, L. A. (**1979**). ''Comparison of WKB calculation and experimental results for a two-dimensional cochlea,'' J. Acoust. Soc. Am. **65**, 1001–1006.
Stevens, S. S., and Davis H. (**1938**). *Hearing—Its Psychology and Physiology* (Wiley, New York), p. 270.
Viergever, M. (**1980**). ''Mechanics of the inner ear—a mathematical approach,'' Ph.D. thesis (Delft U. P.).
Viergever, M. A., and Diependaal, R. J. (**1986**). ''Quantitative validation of cochlea models using the Liouville Green approximation,'' Hearing Res. **21**, 1–15.
Wilson, J. P., and Johnstone, J. R. (**1975**). ''Basilar membrane and middle-ear vibration in guinea-pig measured using a capacitive probe,'' J. Acoust. Soc. Am. **57**, 705–723.
Zweig, G. (**1991**). ''Finding the impedance of the organ of Corti,'' J. Acoust. Soc. Am. **89**, 1229–1254.

Stochastic properties of cat auditory nerve responses to electric and acoustic stimuli and application to intensity discrimination

Eric Javel and Neal F. Viemeister
Departments of Otolaryngology and Psychology, University of Minnesota, Minneapolis, Minnesota 55455

(Received 26 October 1998; revised 24 August 1999; accepted 17 September 1999)

Statistical properties of electrically stimulated (ES) and acoustically stimulated (AS) auditory nerve fiber responses were assessed in undeafened and short-term deafened cats, and a detection theory approach was used to determine fibers' abilities to signal intensity changes. ES responses differed from AS responses in several ways. Rate-level functions were an order of magnitude steeper, and discharge rate normally saturated at the stimulus pulse rate. Dynamic ranges were typically 1–4 dB for 200 pps signals, as compared with 15–30 dB for AS signals at CF, and they increased with pulse rate without improving threshold or changing absolute rate-level function slopes. For both ES and AS responses, variability of spike counts elicited by repeated trials increased with level in accord with Poisson-process predictions until the discharge rate exceeded 20–40 spikes/s. AS variability continued increasing monotonically at higher discharge rates, but more slowly. In contrast, maximum ES variability was usually attained at 100 spikes/s, and at higher discharge rates variability reached a plateau that was either maintained or decreased slightly until discharge rate approached the stimulus pulse rate. Variability then decreased to zero as each pulse elicited a spike. Increasing pulse rate did not substantially affect variability for rates up to 800 pps; rather, higher pulse rates simply extended the plateau region. Spike count variability was unusually high for some ES fibers. This was traced to response nonstationarities that stemmed from two sources, namely level-dependent fluctuations in excitability that occurred at 1–3 s intervals and, for responses to high-rate, high-intensity signals, fatigue that arose when fibers discharged at their maximum possible rates. Intensity discrimination performance was assessed using spike count as the decision variable in a simulated 2IFC task. Neurometric functions (percent correct versus intensity difference) were obtained at several levels of the standard (I), and the intensity difference (ΔI) necessary for 70% correct responses was estimated. AS Weber fractions ($10 \log \Delta I/I$) averaged $+0.2$ dB ($\Delta I_{\mathrm{dB}} = 3.1$ dB) for 50 ms tones at CF. ES Weber fractions averaged -12.8 dB ($\Delta I_{\mathrm{dB}} = 0.23$ dB) for 50 ms, 200 pps signals, and performance was approximately constant between 100 and 1000 pps. Intensity discrimination by single cells in ES conditions paralleled human psychophysical performance for similar signals. High ES sensitivity to intensity changes arose primarily from steeper rate-level functions and secondarily from reduced spike count variability. [S0001-4966(99)07912-6]

PACS numbers: 43.64.Me, 43.64.Pg, 43.66.Ba [RDF]

INTRODUCTION

A major problem in hearing mediated by cochlear implants is the limited dynamic range over which useful information can be presented. The typical dynamic range in implanted humans is 4–10 dB for brief (100–200 μs phase) biphasic pulses presented to bipolar electrodes (Donaldson *et al.*, 1997), and it seldom exceeds 20 dB (Shannon, 1993). This is in sharp contrast with the dynamic range of more than 100 dB for normal acoustic hearing. Various compression schemes are used in implant processors in an attempt to map the useful acoustic range to the limited electric range. A potential problem with compression is that it may render important amplitude changes inaudible. The seriousness of this problem would be mitigated if sensitivity to intensity changes were significantly greater in electric hearing than in acoustic hearing. Psychophysical data indicate that intensity difference limens (DLs) in implanted humans vary considerably among subjects but are not appreciably smaller than those observed in normal acoustic hearing (Nelson *et al.*, 1996).

Intensity coding mechanisms for electric stimulation (ES) can be inferred from auditory nerve fiber (ANF) responses, but the data are too limited to permit much insight. It is known that ES rate-level functions are much steeper than those for acoustic stimulation (AS), dynamic range is correspondingly smaller, and dynamic range depends on stimulus pulse rate (Moxon, 1971; Hartmann *et al.*, 1984; Javel, 1990; Dynes and Delgutte, 1992). Steeper rate-level functions alone suggest that intensity discrimination should be much better for ES than for AS, since a smaller intensity increment would be needed to achieve a criterion change in discharge rate. However, it is generally thought that the psychophysical ability to discriminate intensity also depends on variability in responses to nominally identical stimuli. Such variability or ''internal noise'' is a characteristic of sensory

processing and is incorporated in all recent models of acoustic intensity discrimination.

Response variability in ES has only begun to be considered (Bruce *et al.*, 1999), and the role it plays in perceptual processing is not well understood. The impact of stochastic response properties in intensity discrimination by ANFs can be investigated directly using a simulated psychophysical task (Relkin and Pelli, 1987). Although such analyses have provided insights into basic aspects of intensity coding in AS conditions (Delgutte, 1987; Viemeister, 1983, 1988; Winslow and Sachs, 1988; Winter and Palmer, 1991), no comparable analyses exist for ES.

Several investigators have incorporated random noise sources into single-cell models for ES as a way of introducing probabilistic response behavior (Verveen, 1962; White *et al.*, 1987; Bruce *et al.*, 1999). Although this approach produces the needed effects, the stochastic properties of the noise and the effects of absolute and relative refractoriness, both of which affect the form of the variance function, are still uncertain. Bruce *et al.* (1997) took stochastic behavior into account in developing a neural population model for ES, and they applied it to intensity discrimination. However, their model was based on limited physiological data from undeafened and acutely deafened ears. It is not clear that the same results would have been obtained if model neurons were based on responses from chronically deafened cochleas, in which fibers often exhibit degraded stimulus coding capabilities (Shepherd and Javel, 1997).

Chronic deafness leads to variable, time-dependent loss of spiral ganglion cell peripheral processes, cell death, and reduction of average central-process axon caliber in surviving cells (Leake and Hradek, 1988; Spoendlin and Schrott, 1989). Biophysical models of neuronal excitability to electric stimuli predict an inverse relationship between response variability and the diameter of the node of Ranvier at the active spike initiation site, and they predict a direct relationship between node diameter and rate-level function slope (Verveen, 1962). Loss of peripheral processes necessarily causes spike initiation sites to shift to central processes, and, on average, central processes have larger diameters than peripheral processes (Liberman, 1980; Liberman and Oliver, 1984). This implies steeper, rate-level functions and reduced response variability, which translates into smaller intensity difference limens. On the other hand, deafness-induced reductions in average central-process caliber implies shallower rate-level functions and higher variability, and cell loss implies that fewer spikes are available for perceptual decision-making. These effects would increase intensity difference limens. Thus chronic deafness can have opposite effects on ES intensity discrimination.

The first part of this paper examines variability in ANF responses, with a particular emphasis on the statistical properties of driven activity. It will be shown that spike count variability behaves differently in ES than in AS, with ES variability typically being much smaller. It will also be shown that increasing pulse rate generally does not increase variability, at least for pulse rates up to 800 pps, and that some ES fibers exhibit time-dependent fluctuations in excitability, the effect of which is to increase variability.

The second part examines the role spike count variability plays in intensity coding. A detection theory approach is used to examine ANF's abilities to signal intensity changes, and single-cell performance is related to psychophysical performance in humans. It will be shown that fibers' abilities to discriminate intensity are substantially better in ES than in AS, and that steeper slopes of rate-level functions and decreased variability of spike counts both contribute to the effect. It will also be shown that single-cell performance matches perceptual findings in implanted humans relatively well, but it falls somewhat short of accounting for performance in normal acoustic hearing.

I. METHODS

Single ANF responses to electric and acoustic stimuli were recorded in cats. All AS animals and six ES animals possessed normal hearing prior to the experiment. Three other ES animals were deafened 6–12 weeks prior to single-unit experiments by co-administering kanamycin and ethacrynic acid in a single session (Xu *et al.*, 1993). This method effectively eliminates outer and inner hair cells, as evidenced by a lack of acoustic responsiveness and no random spontaneous activity in the great majority of fiber responses. It also produced 20%–40% peripheral process loss in the basal cochlear turn by 12 weeks post-deafening. One other ES animal was profoundly deafened as a kitten by serial kanamycin administration and experimented upon 3.7 years later.

Animals were anesthetized with pentobarbital (40 mg/kg, IM) and tracheostomized, and the animal's head was mounted in a stereotaxic frame. The skull overlying the lateral posterior fossa was exposed and opened, and a portion of the cerebellum was aspirated to reveal the cochlear nucleus and brainstem. Small cotton pledgets were wedged between the brainstem and skull wall to expose the eighth nerve at its point of exit from the internal auditory meatus. A Davies chamber was affixed to the skull, filled with warmed mineral oil, and sealed by a clear plastic cover plate on which a miniature hydraulic microdrive (FHC, Inc.) was mounted. The microdrive carried a 3M KCl-filled recording micropipette with an ac impedance of 20–30 MΩ at 1 kHz. The tip of the micropipette was visually positioned over the eighth nerve using an operating microscope, and the electrode was advanced into the nerve with a remote-controlled stepping motor.

ES animals were acutely implanted with a custom-built electrode array that was a smaller-diameter version of a Nucleus (Cochlear Corp.) implant. It possessed 0.3 mm platinum bands on 0.75 mm centers. Band diameters decreased from 0.6 mm at the basal end to 0.4 mm at the tip. To install the array, the bulla was opened from a posterolateral direction, the round window membrane was excised, and the array was gently inserted into scala tympani to a depth of approximately 6 mm. This located the apical-most band nominally at the 15 kHz cochlear place (Liberman, 1982).

Custom software was used to specify stimulus sequences consisting of digitally synthesized 50–100 μs phase biphasic pulse trains (ES animals) or CF tones (AS animals). The digital-to-analog conversion rate was 100–200 kHz. For AS

signals, conversion rates were chosen to put all aliased spectral components above 60 kHz. Unit activity was detected with probe stimuli consisting of 100 pps pulse trains presented at 1–2 mA in ES animals and 100 ms wide-band noise bursts presented at 70–80 dB SPL in AS animals. ES responses were obtained to pulse trains presented at user-specified rates, typically 200 pps, through an isolated voltage-to-current converter (Bak). ES signals were delivered in 50–400 ms trains to a bipolar electrode pair consisting of the most apical band and the second-or third-most apical band. AS signals were sinusoids of 50 ms duration presented through a calibrated Beyer DT-48 earphone in a closed system. The duty cycle was 25%–50% for ES signals and 33% for AS signals. Single-fiber responses were collected as input–output functions for 20–200 repetitions of signals presented in increasing order of intensity. Step sizes were 0.2–0.5 dB for ES signals and 5 dB for AS signals.

Action potentials recorded by the micropipette were amplified (WPI Instruments) and displayed on an oscilloscope. Stimulus artifact caused by ES signals was eliminated by microprocessor-controlled sample-and-hold blanking that began at pulse onset and was maintained for a user-specified time, normally slightly longer than the duration of the pulse. The rising phases of spikes were voltage discriminated using the oscilloscope's trigger circuit. Trigger pulses coincident with the onset of each oscilloscope sweep were led to custom timing hardware. Custom software was used to time incoming spikes to 10 μs accuracy and to analyze and display neural responses in real time.

Detailed information about methods, numbers of fibers recorded from each ES animal, and post-deafening cochlear morphology is provided in Shepherd and Javel (1997). ES responses described here are representative of data obtained from 200 fibers in undeafened ears and 158 fibers in deafened ears. AS responses shown here are based on data obtained from 43 fibers in one animal and are representative of similar data from several other animals. Protocols were reviewed and approved by the Creighton University Animal Care and Use Committee.

II. RESULTS

A. ANF responses

Representative raw and normalized rate-level functions for ES and AS conditions are shown in Fig. 1. ES and AS responses came from different animals, but data in each set came from the same ear. The ES data were obtained from a cat profoundly deafened for eight weeks prior to the single-cell experiment. They have been selected to show the range of thresholds and dynamic range that are typically encountered. Responses were elicited by 100 μs phase, 200 pps biphasic pulse trains presented for 50 ms. The curves in the lower left panel of Fig. 1 show the same data as in the upper left panel, except that threshold has been normalized to 0 dB and discharge rate is expressed as a percentage of the maximum expected rate of 200 spikes/s. We define threshold as the intensity eliciting a discharge rate of 10% of the maximum driven rate. For 200 pps signals this is 20 spikes/s.

AS responses are shown on the right side of Fig. 1 for comparison with the ES responses. These were selected on the basis of similar characteristic frequency (CF), except for the fibers with extremely high and low spontaneous rates, which were included for completeness. The responses exhibit typical variation in threshold and spontaneous and maximum discharge rates. Normalized responses (lower right panel) show that slopes are comparable across spontaneous rate (Sachs and Abbas, 1974), and some fibers exhibit sloping saturations (Sachs *et al.*, 1989).

Consistent with earlier reports (Moxon, 1971; Hartmann *et al.*, 1984; Javel *et al.*, 1987; Dynes and Delgutte, 1992), most ES fibers exhibited dynamic ranges of 1–4 dB. We define dynamic range as the intensity range over which discharge rate increases from 10% above the spontaneous rate to 90% of the maximum rate. While 1–4 dB dynamic ranges are typical for ES, they are much smaller than the 15–30 dB dynamic ranges normally observed in AS at CF.

Pulse-number distributions (PNDs) are one of several measures of stochastic behavior (Teich and Khanna, 1985). These are formed by plotting the proportion of times a fixed signal elicits a particular spike count. Representative PNDs for ES and AS conditions are shown by solid lines in Fig. 2. The dashed lines are the PNDs predicted by a Poisson process with the same mean rate as the corresponding neural data. The probability density function for a Poisson process is defined by $P=(\mu^N e^{-\mu})/N!$, where P is proportion of occurrences, μ is the mean count (discharge rate times duration), and N is the number of counts. Although it is known that variability of AS responses deviates from Poisson-process predictions because of absolute and relative refractoriness (Gray, 1967; Gaumond *et al.*, 1982; Johnson and Swami, 1983; Young and Barta, 1986), Poisson-process expectations form a convenient reference to which ES and AS response behavior may be compared. Figure 2 shows that distributions of AS and ES spike counts both deviate progressively more from Poisson-process predictions as discharge rate increases, and that ES variability is smaller than AS variability over most of the dynamic range.

Further information on spike count variability is provided in Fig. 3. These data came from the fibers whose rate-level functions were shown in Fig. 1, and the same symbols have been carried forward. The AS data (right panel) indicate that Poisson-process predictions (variance=mean and s.d. $=\sqrt{\text{mean}}$, denoted by the solid line) are maintained up to 1–2 counts per 50 ms trial or discharge rates of 20–40 spikes/s, and that variability falls increasingly short of Poisson-process predictions at higher discharge rates. Responses of fibers with different spontaneous rates all follow the same general trend. This implies that variability depends primarily on overall rate. Important aspects of the AS responses are that variability increases monotonically with level and that discharge rate saturation has no obvious effect on variability.

The ES data shown in the left panel of Fig. 3 also follow Poisson-process predictions up to 20–40 spikes/s and then depart at higher discharge rates. However, notable differences exist between ES and AS data. First, once ES variability departs from Poisson-process expectations, it tends to remain at a constant value or ''plateau'' until discharge rate

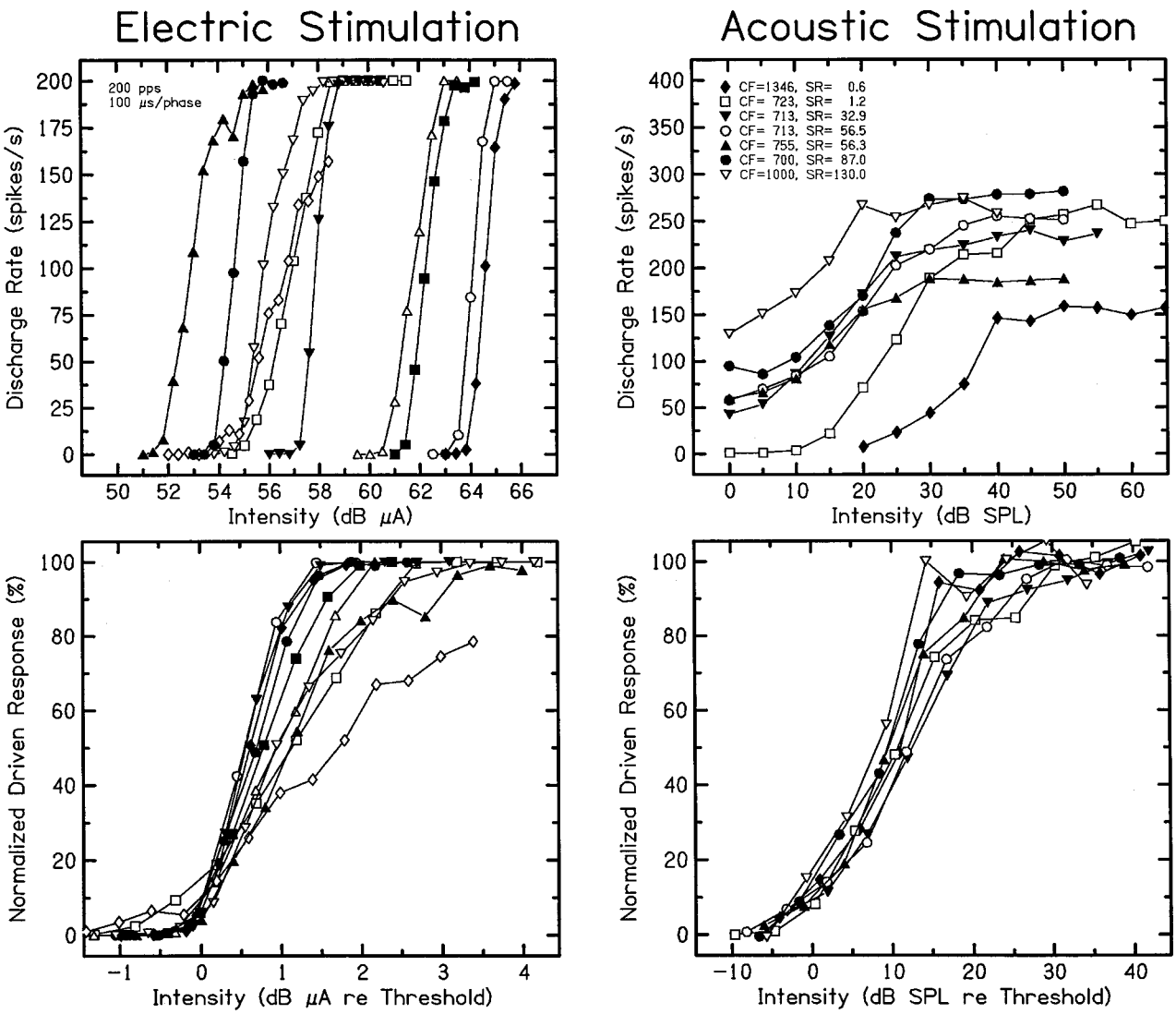

FIG. 1. Representative rate-level functions for ES at 200 pps (left) and AS at CF (right). Each set of functions came from the same ear. Raw rate-level functions are shown in the top row. The same functions, normalized for both discharge rate and intensity relative to threshold, are shown in the bottom row. SR denotes spontaneous rate.

approaches the stimulus pulse rate, in this case 200 pps or 10 counts per 50 ms trial. And second, variability rapidly decreases to zero when discharge rate approaches the stimulus pulse rate and responses become deterministic, i.e., every pulse elicits a spike.

The AS data in Fig. 3 resemble those reported by Young and Barta (1986), but average variability is slightly lower. The discrepancy stems from differences in the counting intervals. That is, Young and Barta considered only the steady-state portion of the response, and they purposely excluded spikes occurring during the (nonstationary) rapid and short-term adaptation periods at response onset (Westerman and Smith, 1984). Our data, on the other hand, include these spikes because the ''perceptual processor'' likely uses them. Analyses we performed on AS data, not shown here, indicated that the elevated discharge rates at response onset have relatively low variability. Although low variability at signal onset reduces overall variability, the effect is small for signals with all but the shortest durations. As evidence of this, one may note the similarity between Winter and Palmer's (1991) and Young and Barta's (1986) variability data, obtained using different counting intervals.

Figure 4 shows rate-level functions and variability data for signals presented at pulse rates ranging from 100 to 800 pps. Data for three fibers are shown. One fiber came from an undeafened ear, one came from an ear profoundly deafened for eight weeks prior to experimentation, and one came from an ear profoundly deafened for 3.7 years. Rate-level functions exhibit differences in slope across fibers. The fiber from the undeafened ear (top row) exhibits the type of response seen most often, i.e., a discharge rate that saturates at the pulse rate, no improvement in threshold with increasing pulse rate, and rate-level function slopes that remain constant in absolute terms (spikes/s/dB). The dependence of saturation rate on pulse rate produces a corresponding increase in dynamic range.

Discharge rates in the fiber from the eight-week-deafened ear (middle row) also saturated at the stimulus pulse rate, but thresholds increased with pulse rate. However, at least some of the threshold increase may be artifactual due

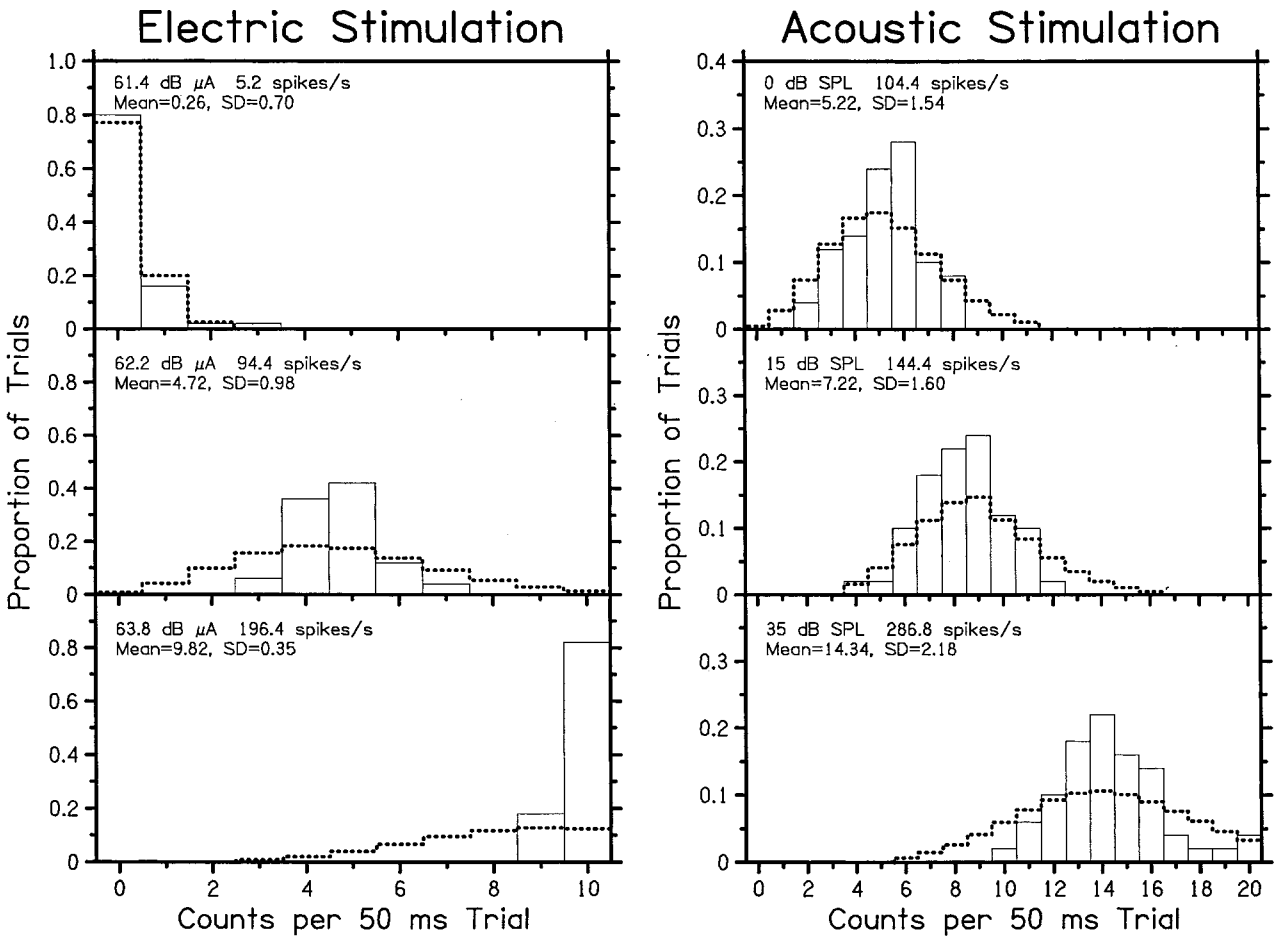

FIG. 2. PNDs obtained from ANFs at three intensities for ES at 200 pps (left) and AS at CF (right). Dashed lines denote the distribution of counts predicted by a Poisson process at the obtained mean rates.

to the fact that responses were collected in increasing order of intensity and pulse rate. That is, data at low intensities and high pulse rates were collected just after the fiber had finished responding at high discharge rates to the next-lower pulse rate, and the fiber may have been temporarily fatigued. Other fibers from this ear exhibited similar threshold increases with increasing pulse rate. Unlike either of the other two, the fiber from the long-term-deafened ear (bottom row) displayed large dynamic ranges and was unable to discharge at rates higher than 500–600 spikes/s.

The behavior of spike count variability for these fibers is shown in the right-hand column of Fig. 4. Variability initially increased with discharge rate in accord with Poisson-process predictions, and it deviated from predicted behavior when rates exceeded 20–40 spikes/s. This is similar to behavior shown previously in Fig. 3 for 200 pps signals. Variability decreased somewhat when the discharge rate exceeded 100 spikes/s, and it maintained a plateau value until the discharge rate approached the stimulus pulse rate. Variability increased at high pulse and discharge rates for the fibers from the undeafened and long-term-deafened ear, but not for the fiber from the short-term-deafened ear.

The point at which variability increases at high pulse rates and intensities appears to be related to the maximum sustained discharge rate a given fiber can generate. In Fig. 4, increases in spike count variability occurred at 700 spikes/s for the fiber from the undeafened ear and at 450 spikes/s for the fiber from the long-term-deafened ear. These were the highest sustained rates elicitable from those fibers. Absence of a variability increase for the fiber from the short-term-deafened ear likely stemmed from that fiber's ability to discharge at very high rates. Although it was not examined, we suspect that this particular fiber was capable of discharging in a sustained manner at rates >800 spikes/s.

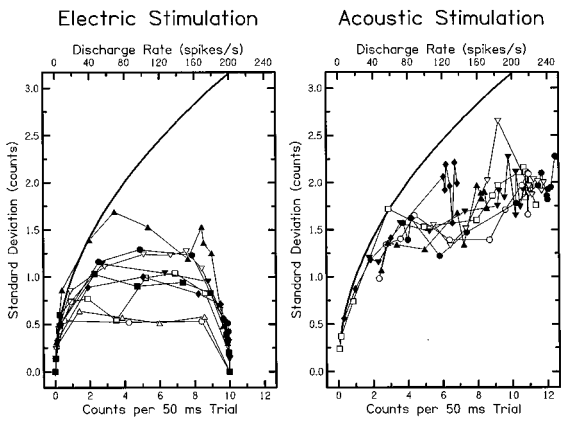

FIG. 3. Representative variability functions for ES at 200 pps (left) and AS at CF (right). Functions are from the same fibers whose rate-level functions are shown in Fig. 1, using the same symbols.

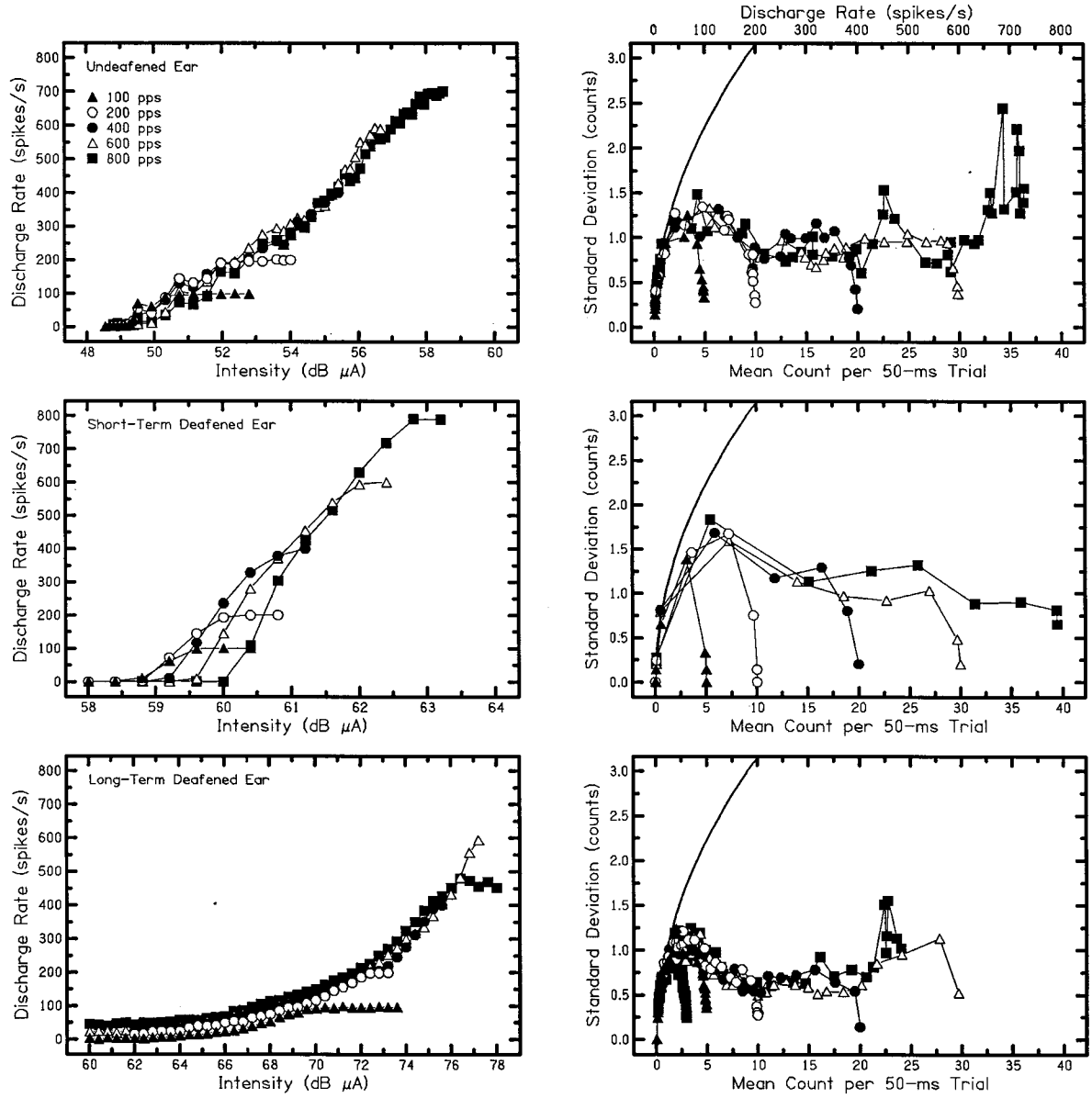

FIG. 4. Rate-level functions (left) and variability-count functions (right) for three ES fibers stimulated at pulse rates ranging from 100 to 800 pps.

Maximum discharge rates and variability of responses from other fibers in all three types of ear were distributed over a range similar to that shown in Fig. 4. That is, some fibers could discharge at high sustained rates, and consequently variability did not increase when stimuli at 800 pps elicited discharge rates of 800 spikes/s. However, other fibers could not discharge at high rates, and variability increased when discharge rate approached the maximum possible. Differences among fibers likely stem from variation in the duration of the absolute refractory period and the time constant for recovery from relative refractoriness. These differences exist in undeafened as well as short-term-deafened and long-term-deafened ears.

Distributions of maximum spike count variability observed for 50 ms, 200 pps signals are shown in the left-hand column of Fig. 5. They were obtained by forming a variability function for each fiber and noting the highest standard deviation. As previously indicated in Figs. 3–4, maximum ES variability normally occurs at 2–5 counts per 50 ms trial, or 40–100 spikes/s. Spike count variability in our sample formed two subtypes. One type, indicated in the upper left panel, displayed low variability. The other type, indicated in the lower left panel, exhibited variability that spanned a wide, generally high range. As discussed later, the two subtypes differed in the extent to which excitability varied from trial to trial. The dashed lines are a reference. They indicate the Poisson-process prediction that a mean count of 3 (corresponding to 60 spikes/s for a 50-ms trial) should possess a standard deviation of 1.73 counts. The data in Fig. 5 indicate that, like AS fibers, most ES fibers from deafened ears show less spike count variability than a Poisson process predicts, but a subset of fibers exhibits greater variability. Although our sample size is too small to draw firm conclusions, increased variability appears to be more prevalent in short-term-deafened animals, and a larger proportion of fibers exhibit high variability as duration of deafness increases. In our

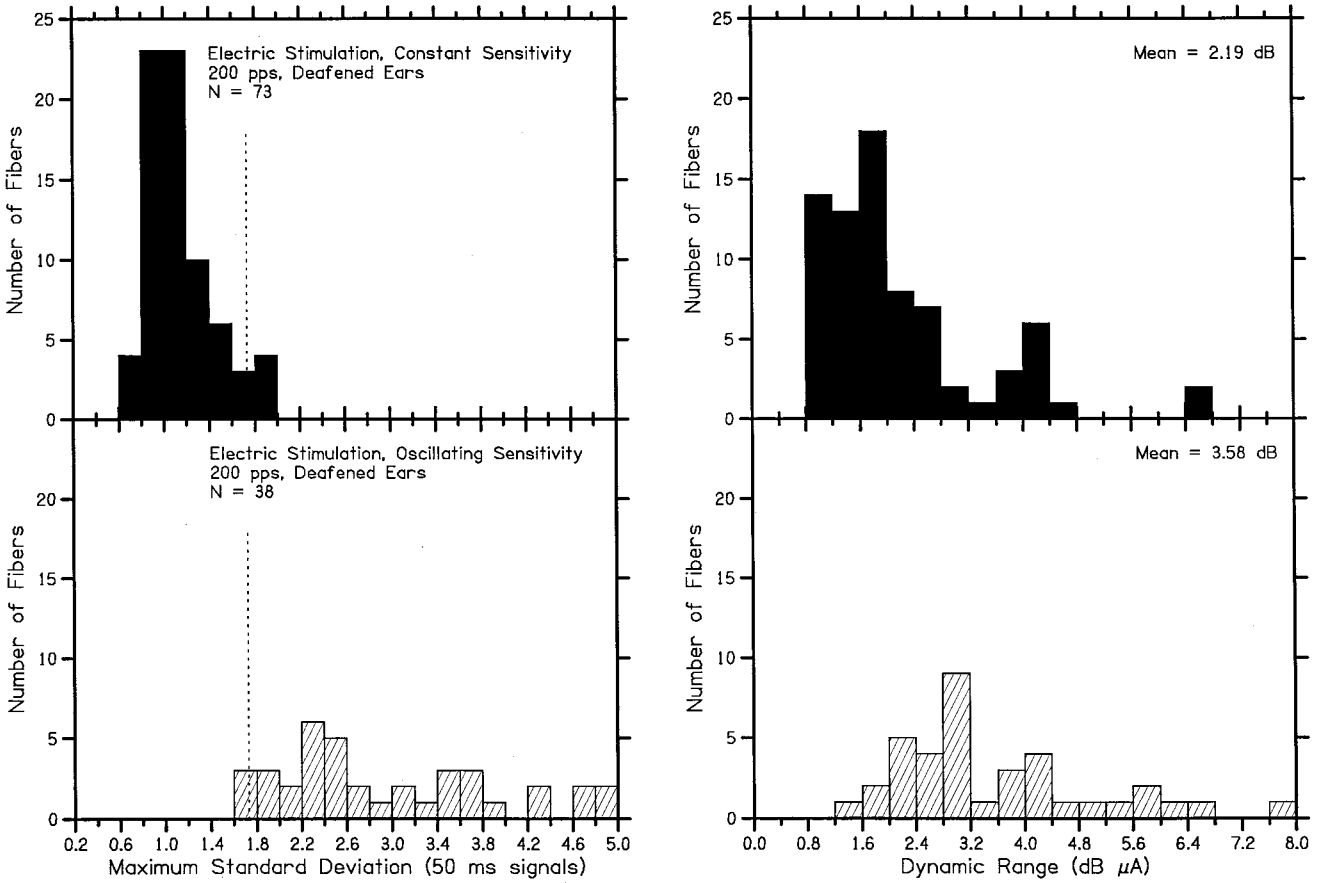

FIG. 5. Left: Distributions of maximum spike count variability for 50 ms, 200 pps stimuli from ES fibers in deafened ears whose excitability remained constant during data collection (top) and fibers whose excitability fluctuated over time (bottom). Right: Dynamic ranges of ES fibers with constant (top) and fluctuating (bottom) excitability.

sample, 34.3% of all fibers from short-term-deafened ears exhibited increased variability, but the proportion increased from 28% to 42% between 6 and 12 weeks post-deafening. In contrast, fibers exhibiting increased spike count variability were rarely encountered in either undeafened or long-term-deafened ears. Thus increased variability appears to be associated with active cochlear degeneration.

The right-hand panel of Fig. 5 shows distributions of dynamic range for the same fibers whose variability is depicted in the left-hand panel. These data indicate that ES fibers with high spike count variability also possess larger dynamic ranges than fibers with low variability (3.58 dB vs 2.19 dB). Differences between subtypes were statistically significant for both variability ($t=10.11$, $df=40.8$, $p<0.001$) and dynamic range ($t=4.86$, $df=60.0$, $p<0.001$).

Examples of rate-level and variability functions for ''high variability'' fibers are shown in Fig. 6. These data all came from the same eight-week-deafened ear. The rate-level functions had typical shapes but larger than normal dynamic ranges. However, in each case maximum spike count variability exceeded Poisson-process expectations for mean counts <7 per 50 ms, or <140 spikes/s. Further examination of these responses and others like them showed that in every case increased spike count variability was associated with periodic fluctuations in sensitivity. We call this phenomenon ''oscillating excitability.'' An analysis of responses to 200 pps pulse trains in a fiber from an eight-week-deafened cat is shown in Fig. 7. The fiber's rate-level function (upper left) displayed a rather broad dynamic range of 5.25 dB, and spike count variability (lower left) greatly exceeded Poisson-process predictions. Dot rasters (middle column) indicated that at near-threshold intensities the fiber only responded at 3 s intervals. As intensity increased the period of the response oscillations decreased to about 1 s, then progressively filled in, culminating in the fiber ultimately producing a spike for

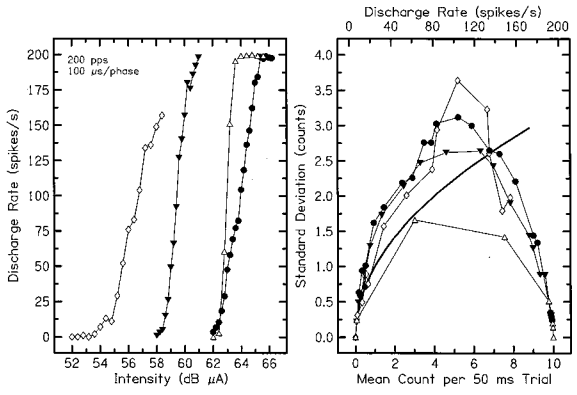

FIG. 6. Rate-level (left) and variability-count functions (right) for four fibers that exhibited oscillating excitability. All the fibers came from the same chronically deafened ear.

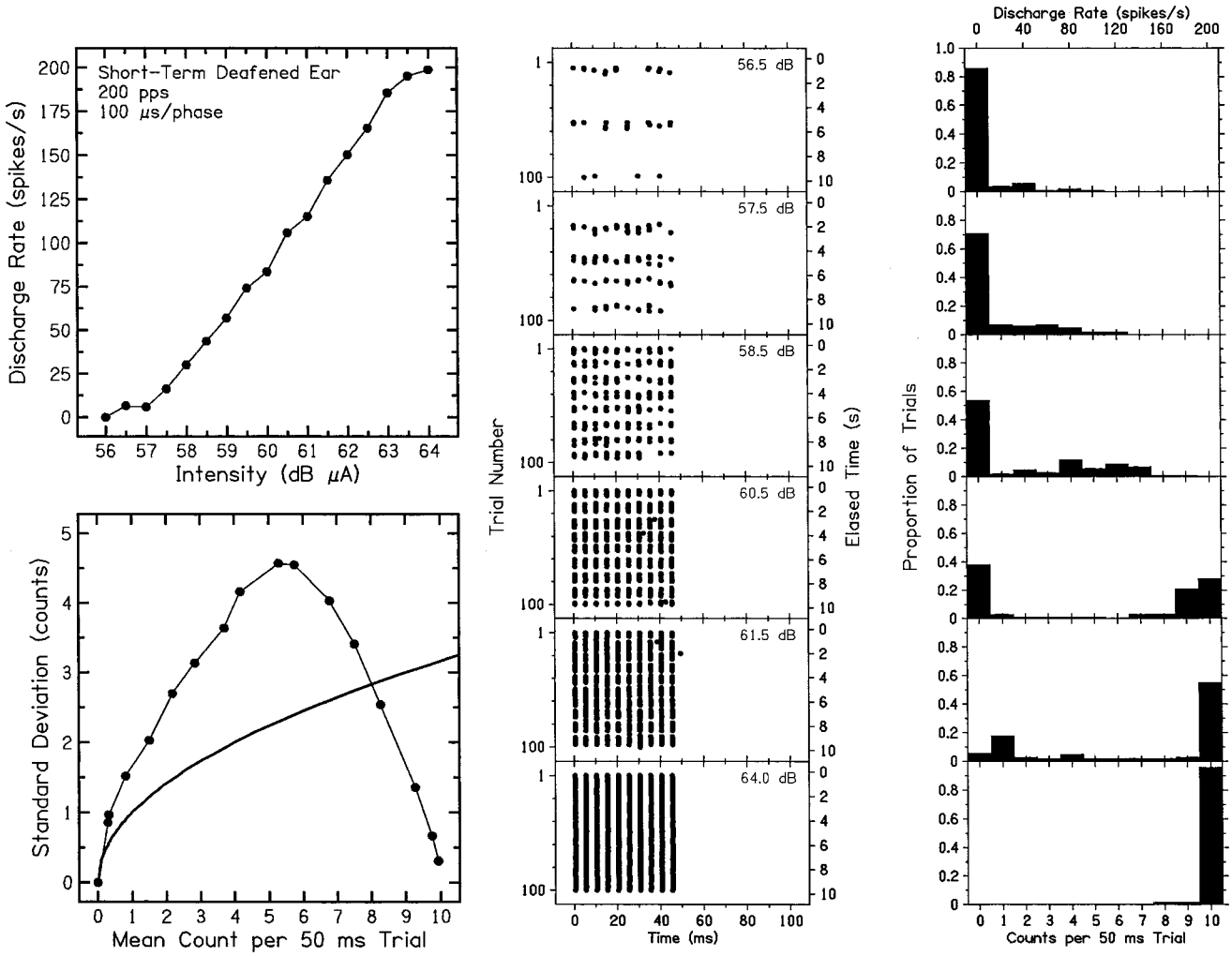

FIG. 7. Rate-level function (top left), variability-count function (bottom left), selected dot rasters (center), and PNDs (right) for a fiber that exhibited oscillating excitability. The fiber came from a chronically deafened ear.

every stimulus pulse. PNDs (right column) show two modes at intensities in which excitability fluctuated, corresponding to alternating periods of activity and inactivity. The large range of counts elicited by repeated trials explains the high spike count variability. Although the observation that fluctuations in excitability disappeared at high intensities is seemingly enough to rule out the possibility that the phenomenon is artifactual, we nonetheless performed several tests to prove that oscillating excitability did not arise from movement due to heart or respiration rate. It appears to be an intrinsic property of ANF responses that is especially prevalent in recently de-afferented ears, and fibers exhibiting the phenomenon were interspersed along the same electrode track with fibers whose trial-to-trial excitability remained constant. Thus ''oscillating excitability'' is one form of nonstationarity that causes increased variability in ES fiber responses. Its origin is unclear.

We also observed a second form of nonstationarity in ES fiber responses that occurred only at very high discharge rates. This consisted of a fatiguelike phenomenon in which discharge rate progressively decreased during a data collection run, leading to greater spread in PNDs and higher variability. Results of one analysis are provided in Fig. 8, which shows summaries of responses from an ES fiber in an undeafened ear that was stimulated by 800 pps trains at 58.3 dB μA for 50 trials of 100 ms duration. The left-hand panel shows running averages for mean count (solid line referred to left-hand axis) and spike count variability calculated over the 50-trial run (dashed line referred to right-hand axis). The discharge rate was initially high (760–770 spikes/s) and decayed with time to an overall rate of 680 spikes/s. Variability moved in the opposite direction, being initially low and increasing with time. Although the overall standard deviation of approximately 4 counts per 100 ms was considerably lower than Poisson-process predictions at 67–70 counts, namely 8.2–8.4 counts, it is nonetheless high for ES activity.

Analyzing these responses in five-trial blocks produced the data shown in the right-hand panel of Fig. 8. The discharge rate decreased by 100 spikes/s over the first 20–25 trials and then remained relatively constant. However, standard deviation in each five-trial block was only 1–2 counts per 100 ms. This is within the range of standard deviations observed at lower pulse rates (cf. Fig. 5). Thus increased spike count variability over the entire duration of the run stemmed from a progressive decrease in discharge rate over time, but moment-to-moment variability was considerably smaller.

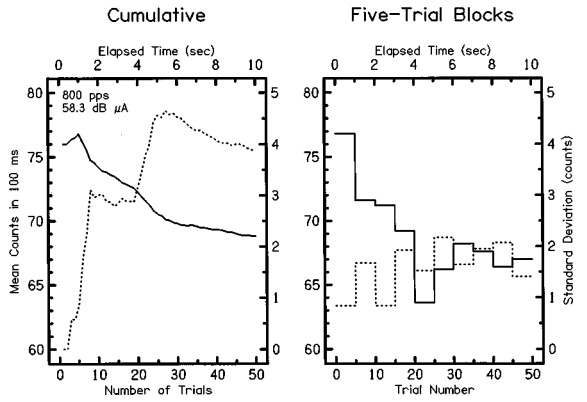

FIG. 8. Behavior of spike counts and their variance as a function of time. Left: Cumulative mean counts (solid line referred to left axis) and spike count variance (dashed line referred to right axis) over 50 presentations of a 100 ms ES signal at 800 pps signal and 58.3 dB μA. Right: The same data, plotted in five trial blocks. Discharge rate decreased from 770 spikes/s to 670 spikes/s during the course of the run. Variance did not change much from moment to moment, but fatigue increased overall variance substantially.

B. Intensity discrimination

The ability of ES and AS fibers to signal intensity differences was assessed in a simulated two-interval-forced-choice (2IFC) intensity discrimination task. Proportion correct discrimination $[P(C)]$ was estimated by computing the proportion of times the number of spikes elicited by a higher-intensity presentation $(I+\Delta I)$ exceeded the number elicited by the standard (I), for each pairing of stimulus presentations in the 20–200 set of trials. When the counts were equal, the number of correct responses was increased by 0.5, corresponding to a ''guess.'' Estimating performance this way avoids assumptions about the form of the probability distributions of counts and thus is advantageous over other measures, such as those based on d'. Although we did not make a detailed comparison, it appears that $P(C)$ based on d' (using means and standard deviations such as those shown in Figs. 3–4) is nearly identical to the direct estimation of $P(C)$ used here.

For a given value of I, a ''neurometric function'' (Movshon *et al.*, 1982; Relkin and Pelli, 1987) was constructed by estimating $P(C)$ for increasing values of ΔI. A sample of neurometric functions for ES and AS is shown in the upper and lower panels, respectively, of Fig. 9. ES stimuli were 200 pps pulse trains, and data are from fibers in two short-term-deafened ears. The fiber whose responses are indicated by unfilled inverted triangles exhibited oscillating excitability, and it was stimulated by 100 ms signals repeated at 200 ms intervals. The other fibers exhibited constant excitability and were stimulated by 50 ms signals repeated at 100 ms intervals. AS stimuli were 50 ms CF tones, repeated at intervals of 150 ms. The parameter is pedestal intensity I. In principle, these functions can be directly compared with psychometric functions for intensity discrimination by human observers. Unfortunately, neither the present data nor the human data are sufficiently detailed to make such a comparison informative.

The level difference at threshold $[\Delta I_{\mathrm{dB}}=10\log(1+\Delta I/I)]$ necessary for $P(C)=0.7$ was estimated from the

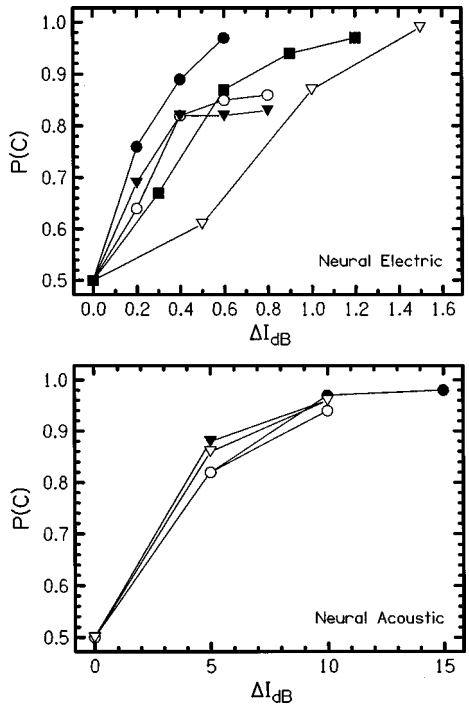

FIG. 9. Neurometric functions obtained in a simulated 2IFC intensity discrimination task in ES (top) and AS (bottom) conditions. ES stimuli were 50 ms presentations of 200 pps pulse trains, and AS stimuli were CF tones (AS). $P(C)$ is the proportion of times the number of counts elicited by a higher-intensity presentation $(I+\Delta I)$ exceeded the number elicited by the standard (I). If counts were equal, the response was taken to be correct with $P(C)=0.5$. Different symbols denote data from different fibers.

neurometric functions at each value of I. Thresholds were computed only when there were at least two points for which $P(C)$ was between 0.6 and 0.9 and were based on linear interpolation between the points closest to $P(C)=0.7$.

The upper panel of Fig. 10 shows Weber functions for several ES fibers from deafened ears. Discrimination thresholds have been converted to Weber fractions $(\Delta I/I)$ and are expressed in dB. This measure is preferable to ΔI_{dB} primarily because it is considerably less compressive. For reference, corresponding values of ΔI_{dB} are shown on the (nonlinear) right axis. At low intensities the Weber fraction for a given fiber increases with decreasing I, i.e., performance becomes worse as intensity decreases. This simply reflects absolute threshold. That is, when I is lower than the absolute threshold, there is no response to the standard and ΔI at threshold corresponds to the difference between the (constant) absolute threshold and signal intensity. At high intensities the discharge rate saturates and the Weber fraction becomes indeterminate because no intensity increase produces a reliable increase or decrease in spike count.[1] The rightmost points for each Weber function approximately reflect the saturation intensity. They essentially define the upper limit of the useful dynamic range for each fiber.

The Weber fraction is approximately constant when I is within the fiber's dynamic range. Some fibers exhibited greater sensitivity to intensity changes, for example, the fiber whose responses are indicated by inverted triangles. Ignoring this fiber, the smallest Weber fractions across fibers are generally seen at larger values of I. This trend suggests that

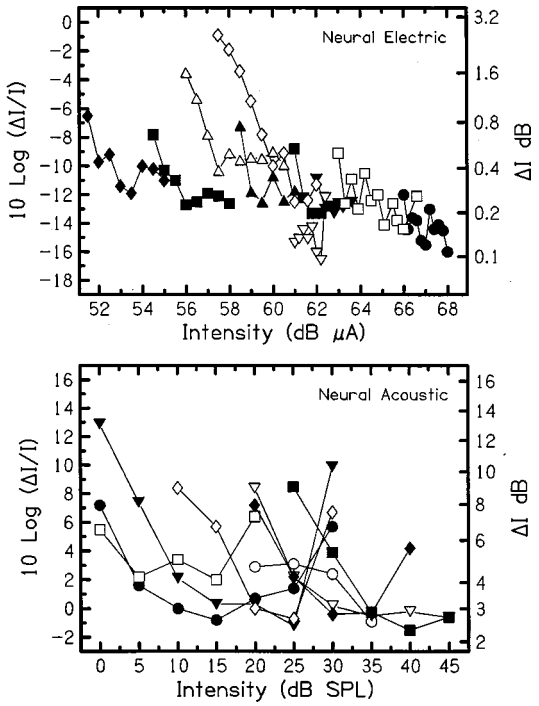

FIG. 10. Weber functions for intensity discrimination of 50 ms signals by several fibers in ES (top) and AS (bottom) conditions. Electric stimuli were 200 pps pulses, and AS stimuli were CF tones. Different symbols denote data from different fibers. Discrimination thresholds [$P(C)=0.7$] have been converted to Weber fractions ($\Delta I/I$) and are expressed in dB. Corresponding values of ΔI_{dB} are shown on the (nonlinear) right vertical axis for reference purposes.

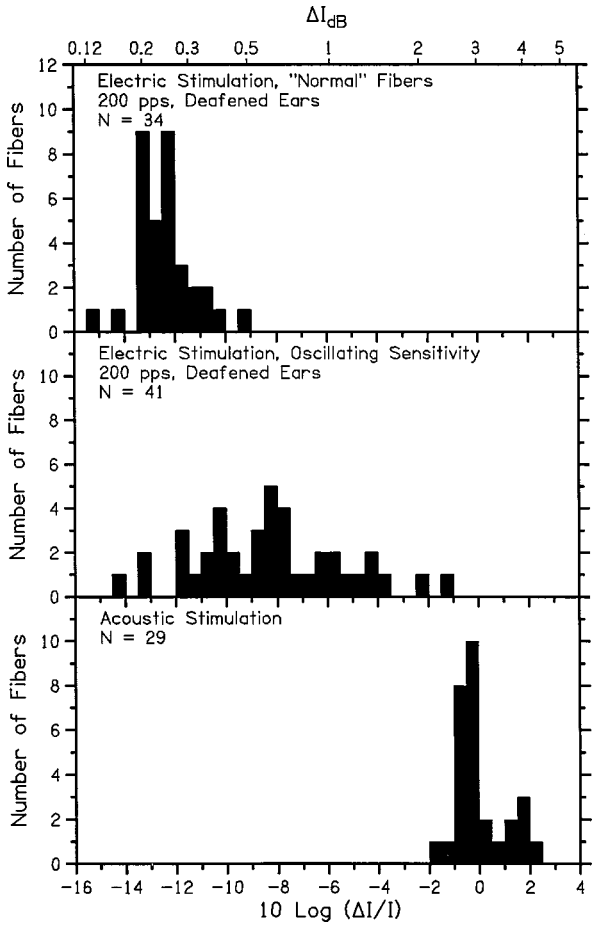

FIG. 11. Distributions of Weber fractions for intensity discrimination by ES fibers that did not exhibit oscillating excitability (top), ES fibers that did (middle), and AS fibers (bottom). ES signals were at 200 pps, and AS signals were at CF. Signal duration was 50 ms, and all AS fibers came from the same ear.

fibers with higher absolute thresholds may be slightly more sensitive to intensity changes. It is consistent with the notion that high-threshold neurons are stimulated on their central processes, which in turn have larger node diameters, steeper rate-level functions, and lower membrane noise. Sensitivity to intensity changes should also correlate with latency, which is generally shorter for central-process activation sites than for peripheral-process activation sites (Javel and Shepherd, 1999).

Weber functions for intensity discrimination in AS conditions are shown in the lower panel of Fig. 10. Stimuli were 50 ms CF tones repeated at 150 ms intervals, and all responses came from the same ear. The data are similar to those previously reported by Delgutte (1987) and Viemeister (1988), and the AS functions are presented here because (1) data were obtained under conditions closely comparable to those for ES and (2) the analysis was identical. Two major differences exist between the AS data and the ES data. As would be expected from the rate-level functions, the range over which performance improves is considerably larger for AS than for ES (note the difference in *X*-axis scales between the two panels in Fig. 10). More importantly, the asymptotic values for Weber fractions in ES are considerably smaller than the minimum values for AS.

Distributions of Weber fractions for ES and AS conditions, averaged over values obtained within each fiber's dynamic range, are shown in Fig. 11. Responses of ES fibers whose excitability remained constant across time are shown at the top; responses of ES fibers exhibiting oscillating excitability are shown in the middle; and responses of AS fibers are shown at the bottom. Mean performance was −12.8 dB for ES fibers displaying constant excitability, −8.1 dB for ES fibers displaying oscillating excitability, and +0.2 dB for AS fibers.

The effect of stimulus pulse rate on intensity discrimi-

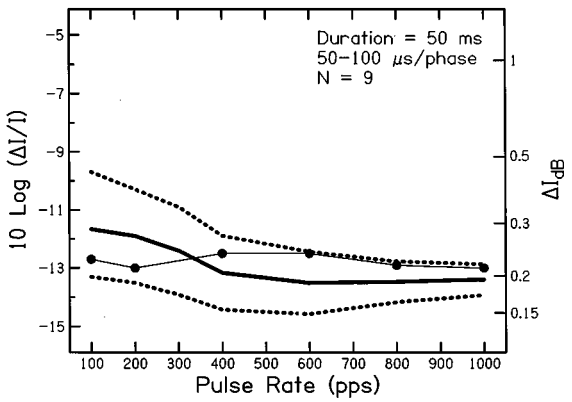

FIG. 12. Average intensity discrimination performance as a function of pulse rate for nine ES fibers from five animals, for 50 ms signals. Solid and dashed lines indicate mean ± 1 s.d. and filled symbols denote data from one of the fibers.

nation of 50 ms ES signals is shown in Fig. 12. Solid and dashed lines indicate mean ±1 s.d. for data from nine fibers in five animals, all of which were tested over the entire range of pulse rates. Filled symbols indicate data obtained from one of those fibers. Performance is not substantially different for pulse rates between 100 and 1000 pps. This might be expected on the basis of equivalent rate-level function slopes (when measured in absolute units of spikes/s/dB) and comparable spike count variability across pulse rate (Fig. 4).

III. DISCUSSION

A. ANF responses

Steeper rate-level functions and correspondingly reduced dynamic range in ES (Fig. 1) reflect the fact that direct electric stimulation is considerably more effective in eliciting spikes from spiral ganglion cells than synaptic neurotransmission. In addition, fibers can also respond at much higher sustained discharge rates in ES than in AS (Fig. 4). However, slopes of ES rate-level functions measured in absolute units of spikes/s/dB are generally no different at high pulse rates than at low pulse rates, and variability does not change. In terms of intensity discrimination, this implies that performance should not depend on pulse rate. This generalization holds for both single-fiber responses (Fig. 12) and psychophysical performance in implanted humans (Donaldson, personal communication).

Variability of both ES and AS spike counts conforms to Poisson-process predictions up to discharge rates of 20–40 spikes/s and then falls increasingly short of predicted behavior at higher discharge rates. Variability in AS conditions follows a monotonically increasing curve that resembles a power function. As noted earlier, several studies have shown that the discrepancy between observed behavior and Poisson-process predictions stems primarily from the effects of absolute and relative refractoriness. ES variability is smaller than AS variability in fibers whose excitability remains constant across time. Increasing pulse rate does not increase spike count variability in ES conditions, at least for pulse rates less than 800 pps in fibers capable of responding at high discharge rates (Fig. 4). Variability in ES responses is usually maximal at discharge rates of 100 spikes/s, and it often attains a plateau value that differs from fiber to fiber and is maintained throughout most of the remaining dynamic range. One of two behaviors occurs at high pulse and discharge rates, depending on the fiber's ability to respond in a sustained manner at discharge rates that exceed the stimulus pulse rate. For fibers that can do this, variability decreases to zero when responses become deterministic and each pulse elicits a spike. For fibers that cannot, variability increases when the discharge rate approaches the maximum possible rate. The maximum possible rate appears to depend on durations of absolute and relative refractory times, and these vary from fiber to fiber. ES variability becomes increasingly smaller than AS variability as discharge rates exceed 40 spikes/s, except in fibers exhibiting oscillating excitability.

Stochastic models of ES utilize rate-level functions whose shapes conform to integrated-Gaussian curves, and they predict a parabolic relationship between spike probability and variance in single-pulse and low-pulse-rate conditions (Bruce *et al.*, 1999). While some fibers exhibited parabolic variability functions for pulse rates of 200 pps (e.g., filled circles in Fig. 3), most did not. Also, parabolic variance curves were never observed in high-rate (>400 pps) stimulation, where refractory effects become significant. Bruce *et al.* (1999) showed that increasing absolute and relative refractory times flattens variability functions in predictable ways, and that choosing appropriate values can produce curves which conform to the observed data relatively well. An important point suggested by data presented here is that the duration of the absolute refractory period and the time constant of the relative refractory period both need to be increased substantially to account for ES variance curves. Furthermore, the existence of plateaus in many ES variability functions suggests that detailed shapes of rate-level functions differ for ES vs AS. That is, flattened variability functions argue that slopes of ES rate-level functions are constant over much of their extent. Our data also imply that integrated Gaussians, while convenient, do not describe shapes of ES rate-level functions precisely. That is, the facts that (1) ''true'' ES rate-level functions saturate at a very high discharge rates, (2) slopes do not vary appreciably across pulse rate, and (3) maximum possible discharge rates vary from fiber to fiber mean that low-pulse-rate stimuli only reveal part of the underlying function. Given this, a better description of ES rate-level functions would be provided by an integrated Gaussian that saturates at the maximum possible discharge rate, appropriately truncated at the stimulus pulse rate.

Related to the issue of internal noise, Rubinstein *et al.* (1997) presented preliminary neural modeling work that predicts a decrease in ES input–output slope when inter-spike intervals (ISIs) approach the absolute refractory time. The decreased slope stems from increased noise, which in turn arises because fewer ion channels are available for conducting spikes when ISIs are short. Thus as ISI decreases, neurons output spikes that have increasingly more variability, culminating in an inability to output any spikes when ISIs reach the absolute refractory time. The increase in variability we observed when neurons respond at their maximum possible rates (Fig. 4) is in general agreement with this concept. However, the observation that maximum possible discharge rates differ across fibers suggests corresponding differences in absolute and relative refractory times from cell to cell. Although our data suggest that these both increase in chronic profound deafness, a considerably larger sample size is needed to resolve this issue. The increased variability due to time-dependent fatigue (Fig. 8) apparently stems from a different source than refractoriness-related effects.

A recurrent theme in developing speech processing strategies for cochlear implants at the present time is that increasing pulse rates in each stimulation channel will change stochastic properties of ES responses such that they better approximate AS responses (Wilson *et al.*, 1994a). Changes in stochastic behavior can be approached from more than one point of view. On one hand, it can mean increased temporal spike dispersion, i.e., reduced phase-locking. However, since Hartmann and Klinke (1990) and Dynes and Delgutte (1992)

showed that ES responses to sinusoidal current are significantly phase-locked to at least 12 kHz, it appears that high-rate stimulation cannot substantially change this aspect of stochastic responsiveness. On the other hand, altered stochastic behavior can also mean increased spike count variability, as evidenced in PNDs with counts distributed over a larger range of values that better conform to Poisson-process predictions or AS behavior. Data in Fig. 4 show quite clearly that stimulation at rates up to 800 pps does not increase variability unless fibers discharge at their maximum possible rates, and even then the increase is relatively small. This suggests that increasing stimulation rates cannot alter the low-variability nature of intrinsic neural noise, and that a different approach is needed to increase variability. One way to achieve this is to add external noise to the signal (Wilson *et al.*, 1994b). While this certainly will succeed in increasing randomness, a problem is that all neurons activated by the signal will tend strongly to respond in a similar manner. However, although individual neurons may exhibit increased probabilistic response behavior when external noise is introduced, variability in the active neural population should not increase.

The phenomenon of ''oscillating excitability'' in ANF responses from chronically deafened ears (Figs. 6–7) has not been described previously. It resembles the ''rhythmic'' responses observed in auditory nerve activity in immature ears (e.g., Walsh and McGee, 1986). However, unlike responses of immature cells, oscillating excitability occurs at slower rates and its period varies with level. Although the proportion of fibers exhibiting oscillating excitability increased from 28% to 42% as duration of deafness increased from 6 to 12 weeks, our sample size is too small to draw firm conclusions about the prevalence of the phenomenon.

The origin of oscillating excitability is not clear. One possibility is that membrane potential slowly fluctuates over a wide range in de-afferented cells. Verveen's (1962) *in vitro* data, obtained intracellularly from frog sciatic nerve, show such fluctuations when voltage was clamped to high (-90 mV) potentials. This suggests the possibility that ion conductances responsible for resting potential change when de-afferentation silences a spiral ganglion cell. An interesting consequence of widely fluctuating membrane potentials is that cells may exhibit regular but low spontaneous discharge rates, even though the cell has no hair cell innervation. In our sample, several ANFs from deafened ears exhibited low (1–2 spikes/s) spontaneous activity that tended to occur at regular intervals.

It is also possible that oscillating excitability is a transient, ''start-up'' phenomenon which occurs only when electric signals force previously silent cells to respond, and it disappears when activity becomes frequent. Although oscillating excitability clearly occurs, more work is needed to establish its origin and impact on auditory perceptual processing in implanted humans.

B. Intensity discrimination

The difference in variability between ES and AS accounts for only about 4 dB of the large (approximately 13 dB) difference in intensity discrimination thresholds based on spike count.[2] The remainder reflects the steeper rate-level functions for ES. Rate-level functions for 200 pps signals in ES are 6–20 times steeper than those for CF tones in AS, as Fig. 1 illustrates. Consequently, a given intensity change produces a much larger change in count for ES, and the intensity change necessary to produce a criterion change in count is correspondingly smaller.

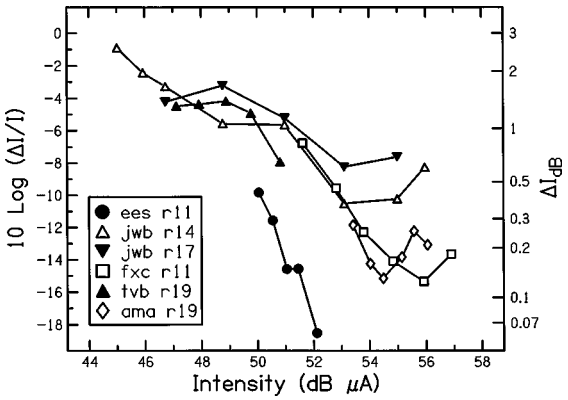

FIG. 13. Weber functions for intensity discrimination as a function of level by implanted humans, from Nelson *et al.* (1996). Different symbols denote data from different listeners. Corresponding values of ΔI_{dB} are shown on the (nonlinear) right axis for reference purposes.

Figure 13 shows human psychophysical data from Donaldson (personal communication) for ES intensity discrimination. Although the conditions are only partially comparable to those used in the present experiments,[3] it is interesting that the thresholds are similar to those shown for the ES neural data. Furthermore, by pooling selected fibers from Fig. 10 one can obtain a rough account of the psychophysical data, including the generally larger dynamic range. Such pooling would seem to require that responses of saturated fibers are ignored, similar to a situation that may exist in AS conditions (Viemeister, 1983, 1988; Delgutte, 1987; Winslow and Sachs, 1988).

The similarity between the ES neural data and the psychophysical data differs from the situation for AS. The Weber fraction for 50 ms, 1 kHz tones measured psychophysically is about -4 dB (Florentine, 1986)[4] versus -1 to $+2$ dB for data from individual cells (Fig. 10) and a mean performance of $+0.2$ dB across cells (Fig. 11). The smaller Weber fractions observed in psychophysical experiments can be reconciled with the neural data by assuming that spike counts are pooled over several fibers. More specifically, decisions based on optimally weighted counts from six to seven independent fibers would reduce the neural Weber fractions to those observed behaviorally. However, the major discrepancy between the neural and psychophysical AS data is not the difference in Weber fractions but the enormous difference in dynamic ranges. A multi-fiber, multi-population argument has been used to explain the psychophysical dynamic range for AS (Viemeister, 1988). Of course, the fiber populations involved in acoustic intensity coding would be different at different frequencies, and many fibers would be required to code intensity over the entire frequency and dynamic range of normal acoustic hearing.

The agreement between intensity discrimination perfor-

mance and dynamic range for ES fibers and implanted humans is surprising. Extending the argument above for AS, optimally weighting contributions from fewer than three ES fibers could reconcile the Weber fractions and the dynamic ranges. Although it is to be expected that deafness-induced cell loss would lead to fewer available fibers in implanted listeners, a functional population (per electrode) so small seems implausible. One possibility is that similar numbers of fibers are involved in ES and AS, but ES responses are not statistically independent. Rather, ES responses are positively correlated because of high synchronization to the pulsatile signals. In the limiting case, if responses across fibers were perfectly phase-locked and deterministic the Weber fraction for a combination of fibers would be the same as for one fiber.

Another possibility is that human performance is not determined by the stochastic behavior of ANF responses and that the major limitation is ''central noise,'' one source of which could be sub-optimal information weighting. In this case inputs from more than three fibers might be required to overcome the noise. This view suggests that the agreement between the human psychophysical data and physiological data from the auditory nerve is largely coincidental. Our opinion is that the agreement between neural and psychophysical performance in ES conditions is not coincidental. Rather, it is best explained by assuming statistical homogeneity in the population response to ES signals and in the dynamic ranges of active fibers.

Relative contributions of peripheral (stochastic) and central noise to perceptual performance could be examined by assessing intensity discrimination performance in ANF responses to stimulus conditions that affect randomness in peripheral activity. Two examples of these are long-pulsewidth signals (Dynes and Delgutte, 1992) and pulse rates >800 pps (Rubinstein *et al.*, 1997). With regard to the former, Ferguson *et al.* (1998) found that variability in behavioral thresholds to electrical stimuli increases with pulsewidth, in accord with ANF data and stochastic neural models. This suggests that peripheral neural processing plays a larger role than central processing, at least for tasks related to absolute threshold, and that central noise is both constant and of smaller magnitude than peripheral/stochastic noise. However, sufficient data to address the roles of peripheral versus central noise in other tasks, one of which is intensity discrimination, are not yet available.

ACKNOWLEDGMENTS

This work was supported in part by Grants Nos. P01 DC00110 and R01 DC00138 from NIDCD. The authors gratefully acknowledge the assistance of Robert K. Shepherd and Dan Clark in collecting the neural data, Gangesh K. Ganesan in conducting preliminary analyses (Ganesan, 1996), Gail S. Donaldson and David A. Nelson in providing the human psychophysical data, and two anonymous reviewers for their comments. Portions of this work were presented at the 21st Mid-Winter Meeting of the Association for Research in Otolaryngology (Viemeister *et al.*, 1998).

[1]Weber functions for ES must be U-shaped, similar to those shown for AS. They do not appear this way in the upper panel of Fig. 10 because for intensities eliciting discharge rates at and near the stimulus pulse rate, no value of ΔI produced the increase in discharge rate needed to estimate a difference limen. Hence, Weber fractions could not be estimated. This situation is particularly prevalent in ES because, unlike the situation in AS, discharge rate saturates abruptly at the pulse rate for low-rate (<600 pps) signals.

[2]To see this, consider performance in terms of d' rather than $P(C)$. For the present situation in which decisions are based on spike count,

$$d' = \frac{c(I+\Delta I) - c(I)}{\sigma_c},$$

where $c(I+\Delta I)$ and $c(I)$ are mean counts elicited by two signals differing in intensity and σ_c is the standard deviation of the counts at intensity I, assuming equal variance and a constant counting interval. Assuming linearity of the rate-level function in the coordinates of Fig. 1, this becomes

$$d' = \frac{S\Delta I_{\mathrm{dB}} T}{\sigma_c},$$

where S is the slope of the rate-level function in spikes/s/dB and T is the counting interval. From Fig. 2, σ_c is lower by approximately a factor of 2 for ES than for AS when I is within the dynamic range of the fiber. This reduction in variability increases d' by a factor of 2. For 50 ms signals, rate-level functions in ES are approximately 10 times steeper than those in AS when measured in absolute units of spikes/s/dB and estimated at the steepest portion of the function. Thus for a given change in level the overall d' should be a factor of 20 greater for ES. To express this in terms of discrimination thresholds, note that d' is proportional to ΔI_{dB} so, for the same d', ΔI_{dB} will be reduced by a factor of 2 by the reduction in σ_c and by 10 by the increase in S. From Fig. 5, ΔI_{dB} is approximately 3.2 dB for AS. The factor of 2 reduction decreases the Weber fraction by 3.9 dB (to −3.5 dB), and the factor of 10 reduction further decreases the Weber fraction by 10.5 dB (to −14.0 dB).

[3]The stimuli used by Nelson *et al.* (1996) were 200 μs phase, 125 pps biphasic pulse trains presented for 300 ms, and a 3IFC tracking procedure was employed to estimate the DL that yielded $P(C)=0.794$ ($d'=1.63$). The data shown in Fig. 13 were obtained with 100 μs phase, 200 pps biphasic pulse trains presented for 50 ms, and the DL was estimated for $P(C)=0.70$ in 2IFC ($d'=0.75$). Decreasing pulse duration from 200 to 100 μs phase would not affect the psychophysical DLs at equal sensation levels, nor would changing the pulse rate from 125 to 200 Hz (Donaldson, personal communication). Based on acoustic data (Florentine, 1986), decreasing duration from 300 ms to 50 ms would increase the Weber fraction by approximately 2 dB. The psychometric functions presented in Nelson *et al.* (1996) indicate that d' is a linear function of ΔI. Thus the Weber fraction would be reduced by $10\log(1.63/0.75)=3.4$ dB for $P(C)=0.7$ in 2IFC. The net result is that if the psychophysical data had been obtained under conditions comparable to those used for the neural data, the Weber fractions would be reduced by $3.4-2=1.4$ dB.

[4]Florentine (1986) used a 2IFC adaptive procedure that estimated the DL for $P(C)=0.71$. This performance level is nearly identical to the 0.70 value used to define DLs in our analysis. It is well known that acoustic Weber fractions decrease with the intensity of the standard, and it appears that this ''near miss'' to Weber's Law results from the nonlinear spread of excitation to frequency regions remote from that of the standard (for a review, see Plack and Carlyon, 1995). Florentine obtained a Weber fraction of −4 dB at 1 kHz and 40 dB SPL, the lowest level used in that study. We use the Weber fraction at this level because it is least likely to be affected by nonlinear spread of excitation and thus is comparable to the situation that likely exists throughout the lower part of the dynamic range in ES.

Bruce, I. C., Irlicht, L. S., White, M. W., O'Leary, S. J., Dynes, S., Javel, E., and Clark, G. M. (**1997**). ''A stochastic model of the electrically stimulated auditory nerve designed for the analysis of large-scale population response,'' Abst. Assn. Res. Otolaryngol. **20**, 57.

Bruce, I. C., Irlicht, L. S., White, M. W., O'Leary, S. J., Dynes, S., Javel, E., and Clark, G. M. (**1999**). ''A stochastic model of the electrically stimulated auditory nerve: Pulse-train response,'' Proc. IEEE Trans. Biomed. Eng. **46**, 630–637.

Delgutte, B. (**1987**). ''Peripheral auditory processing of speech information: Implications from a physiological study of intensity discrimination,'' in *The Psychophysics of Speech Perception*, edited by M. E. H. Schouten (Nijhoff, Dordrecht, The Netherlands), pp. 333–353.

Donaldson, G. S. (**1998**). Personal communication.
Donaldson, G. D., Viemeister, N. F., and Nelson, D. A. (**1997**). ''Psychometric functions and temporal integration in electric hearing,'' J. Acoust. Soc. Am. **101**, 3706–3721.
Dynes, S. B. C., and Delgutte, B. (**1992**). ''Phase-locking of auditory-nerve discharges to sinusoidal electric stimulation of the cochlea,'' Hearing Res. **58**, 79–90.
Ferguson, W. D., Smith, D. W., Finley, C. C., Pfingst, B. E., and Collins, L. M. (**1998**). ''Prediction of the variance in behavioral thresholds using a stochastic model of electrical stimulation,'' Abst. Assn. Res. Otolaryngol **21**, 290.
Florentine, M. (**1986**). ''Level discrimination of tones as a function of duration,'' J. Acoust. Soc. Am. **79**, 792–798.
Ganesan, G. K. (**1996**). ''Analyses and comparison of the responses of single ANFs to acoustic and electric stimulation,'' M.S. Thesis, University of Minnesota.
Gaumond, R. P., Molnar, C. E., and Kim, D. O. (**1982**). ''Stimulus and recovery dependence of cat cochlear nerve fiber spike discharge probability,'' J. Neurophysiol. **48**, 856–873.
Gray, P. R. (**1967**). ''Conditional probability analyses of the spike activity of single neurons,'' Biophys. J. **7**, 759–777.
Hartmann, R., and Klinke, R. (**1990**). ''Response characteristics of nerve fibers to patterned electrical stimulation,'' in *Models of the Electrically Stimulated Cochlea*, edited by J. M. Miller and F. A. Spelman (Springer-Verlag, New York), pp. 135–159.
Hartmann, R., Topp, G., and Klinke, R. (**1984**). ''Electrical stimulation of the cat cochlea: Discharge pattern of single auditory fibers,'' Adv. Audiol. **1**, 18–29.
Javel, E. (**1990**). ''Acoustic and electrical encoding of temporal information,'' in *Models of the Electrically Stimulated Cochlea*, edited by J. M. Miller and F. A. Spelman (Springer-Verlag, New York), pp. 247–292.
Javel, E., and Shepherd, R. K. (**1999**). ''Electrical stimulation of the auditory nerve. III. Response initiation sites and temporal fine structure,'' Hearing Res. (in press).
Javel, E., Tong, Y. C., Shepherd, R. K., and Clark, G. M. (**1987**). ''Responses of cat ANFs to biphasic electrical current pulses,'' Ann. Otol. Rhinol. Laryngol. **96** Suppl. 128, 26–30.
Johnson, D. H., and Swami, A. (**1983**). ''The transmission of signals by auditory-nerve fiber discharge patterns,'' J. Acoust. Soc. Am. **74**, 493–501.
Leake, P. A., and Hradek, G. T. (**1988**). ''Cochlear pathology of long term neomycin induced deafness in cats,'' Hearing Res. **33**, 11–34.
Liberman, M. C. (**1982**). ''The cochlear frequency map for the cat: Labeling ANFs of known characteristic frequency,'' J. Acoust. Soc. Am. **75**, 1441–1449.
Liberman, M. C. (**1980**). ''Morphological differences among radial afferent fibers in the cat cochlea: An electron-microscopic study of serial sections,'' Hearing Res. **3**, 45–63.
Liberman, M. C., and Oliver, M. E. (**1984**). ''Morphometry of intracellularly labeled neurons of the auditory nerve: Correlations with functional properties,'' J. Comp. Neurol. **223**, 163–176.
Movshon, J. A., Tolhurst, D. J., and Dean, A. F. (**1982**). ''How many neurons are involved in perceptual decisions?'' Invest. Ophthalmol. Visual Sci. **22**, 207.
Moxon, E. C. (**1971**). ''Neural and mechanical responses to electric stimulation of the cat's inner ear,'' Doctoral thesis, MIT.
Nelson, D. A., Schmitz, J. L., Donaldson, G. S., Viemeister, N. F., and Javel, E. (**1996**). ''Intensity discrimination as a function of stimulus level with electric stimulation,'' J. Acoust. Soc. Am. **100**, 2393–2414.
Plack, C. J., and Carlyon, R. P. (**1995**). ''Loudness perception and intensity coding,'' in *Hearing*, edited by B. C. J. Moore (Academic, New York), pp. 1223–160.
Relkin, E. M., and Pelli, D. G. (**1987**). ''Probe tone thresholds in the auditory nerve measured by two-interval forced-choice procedures,'' J. Acoust. Soc. Am. **82**, 1679–1691.
Rubinstein, J. T., Matsuoka, A. J., Abbas, P. J., and Miller, C. A. (**1997**). ''The neurophysiological effects of simulated auditory prosthesis stimulation,'' Second quarterly progress report (NIH Contract N01 DC-6-2111).
Sachs, M. B., and Abbas, P. J. (**1974**). ''Rate versus level functions for auditory-nerve fibers in cats: Tone-burst stimuli,'' J. Acoust. Soc. Am. **56**, 1835–1847.
Sachs, M. B., Winslow, R. L., and Sokolowski, B. H. A. (**1989**). ''A computational model for rate-level functions from cat auditory-nerve fibers,'' Hearing Res. **41**, 61–69.
Shannon, R. V. (**1993**). ''Psychophysics,'' in *Cochlear Implants: Audiological Foundations*, edited by R. S. Tyler (Singular, San Diego, CA), pp. 357–388.
Shepherd, R. K., and Javel, E. (**1997**). ''Electrical stimulation of the auditory nerve. I. Correlation of physiological responses with cochlear status,'' Hearing Res. **108**, 112–144.
Spoendlin, H., and Schrott, A. (**1989**). ''Analysis of the human auditory nerve,'' Hearing Res. **43**, 25–38.
Teich, M. C., and Khanna, S. M. (**1985**). ''Pulse number distribution for the neural spike train in the cat's auditory nerve,'' J. Acoust. Soc. Am. **77**, 1110–1128.
Verveen, A. A. (**1962**). ''Axon diameter and fluctuation in excitability,'' Acta Morphol. Neerlando-Scand. **5**, 79–85.
Viemeister, N. F. (**1983**). ''Auditory intensity discrimination at high frequencies in the presence of noise,'' Science **221**, 1206–1208.
Viemeister, N. F. (**1988**). ''Psychophysical aspects of auditory intensity coding,'' in *Auditory Function: Neurobiological Bases of Hearing*, edited by G. M. Edelman, W. E. Gall, and W. M. Cowan (Wiley, New York), pp. 213–242.
Viemeister, N. F., Javel, E., and Ganesan, G. K. (**1998**). ''Auditory nerve correlates of intensity discrimination for electrical stimuli,'' Abst. Assn. Res. Otolaryngol. **21**, 289.
Walsh, E. J., and McGee, J. (**1986**). ''The development of function in the auditory periphery,'' in *Neurobiology of Hearing: The Cochlea*, edited by R. A. Altschuler, R. P. Bobbin, and D. W. Hoffman (Raven, New York), pp. 247–282.
Westerman, L. A., and Smith, R. L. (**1984**). ''Rapid and short term adaptation in auditory-nerve responses,'' Hearing Res. **15**, 249–260.
White, M. W., Finley, C. C., and Wilson, B. S. (**1987**). ''Electrical stimulation of the auditory nerve: Stochastic response characteristics,'' in I.E.E.E. 9th Annual Conference of the Engineering in Medicine and Biology Society, pp. 1906–1907.
Wilson, B. S., Finley, C. C., Zerbi, M., and Lawson, D. T. (**1994a**). ''Speech processors for auditory prostheses,'' Seventh quarterly progress report (NIH Contract N01 DC-2-2401).
Wilson, B. S., Finley, C. C., Zerbi, M., and Lawson, D. T. (**1994b**). ''Speech processors for cochlear prostheses,'' Ninth quarterly progress report (NIH Contract N01 DC-2-2401).
Winslow, R. L., and Sachs, M. B. (**1988**). ''Single-tone intensity discrimination based on auditory-nerve rate responses in backgrounds of quiet, noise, and with stimulation of the crossed olivocochlear bundle,'' Hearing Res. **35**, 165–189.
Winter, I. M., and Palmer, A. R. (**1991**). ''Intensity coding in low-frequency auditory-nerve fibers of the guinea pig,'' J. Acoust. Soc. Am. **90**, 1958–1967.
Xu, S. A., Shepherd, R. K., Chen, Y., and Clark, G. M. (**1993**). ''Deaf animal models: Profound hearing loss in the cat following a single coadministration of kanamycin and ethacrynic acid,'' Hearing Res. **70**, 205–215.
Young, E. D., and Barta, P. E. (**1986**). ''Rate responses of ANFs to tones in noise near masked threshold,'' J. Acoust. Soc. Am. **79**, 426–442.

Temporal integration in the presence of off-frequency maskers

Sid P. Bacon, Michelle L. Hicks, and Krista L. Johnson
Psychoacoustics Laboratory, Department of Speech and Hearing Science, P.O. Box 871908, Arizona State University, Tempe, Arizona 85287-1908

(Received 20 July 1999; accepted for publication 25 October 1999)

Temporal integration was measured at a relatively low and a relatively high signal frequency under conditions of off-frequency masking. The masker was typically gated for 300 ms, and the signal was presented 70 ms after masker onset. In experiment 1, the signal frequency was 500 or 2000 Hz. Temporal integration was measured in quiet and in the presence of a masker whose frequency was lower or higher than the signal frequency. In all listening situations, there was less integration at 2000 Hz than at 500 Hz. This effect of frequency was particularly dramatic in the presence of a lower frequency masker, where there was almost no integration at 2000 Hz. Experiment 2 showed that this dramatic effect of frequency cannot be understood in terms of the underlying psychometric functions. Experiment 3 measured temporal integration at 750 and 2000 Hz for a large number of masker-signal frequency separations for both a tonal and a noise masker, and in conditions where the masker was gated or continuous. The results with the gated tonal masker largely confirmed the results of experiment 1. The results with the continuous tonal masker and the gated or continuous noise masker, however, were quite different. In those cases, the amount of temporal integration at both signal frequencies was more or less independent of the masker-signal separation; the masked temporal integration was nearly equal to the integration in quiet. Thus based on the conditions evaluated here, off-frequency masked temporal integration differs substantially from integration in quiet only for gated tonal maskers located considerably lower in frequency than the signal. It is unclear how to account for this finding, although it may be related to attentional factors. © *2000 Acoustical Society of America.* [S0001-4966(00)02102-0]

PACS numbers: 43.66.Ba, 43.66.Dc, 43.66.Mk, 43.66.Cb [RVS]

INTRODUCTION

Temporal integration generally refers to an improvement in threshold with increasing signal duration (e.g., Hughes, 1946; Green *et al.*, 1957; Plomp and Bouman, 1959; Zwislocki, 1960; Gerken *et al.*, 1990; Viemeister and Wakefield, 1991; Buus, 1999). It has been studied extensively and remains a topic of considerable interest, in large part because it is still unclear what mechanism underlies the improvement in threshold.

It has been shown that similar amounts of temporal integration occur in quiet and in broadband noise (Garner and Miller, 1947; Gengel, 1972; Chung and Smith, 1980), although the amount of integration may depend upon the noise level (Stephens, 1973; Oxenham *et al.*, 1997). In both quiet and broadband noise, the amount of integration is often smaller at higher frequencies (Hughes, 1946; Plomp and Bouman, 1959; Elliott, 1963; Sheely and Bilger, 1964; Watson and Gengel, 1969), although not always (Olsen and Carhart, 1966; Florentine *et al.*, 1988).

Considerably less is known about the influence of off-frequency masking on temporal integration. Such masking might not be expected to influence temporal integration in any fundamental way, and indeed Zwicker and Wright (1963) reported that a single, theoretically derived curve could equally as well account for temporal integration for a wide range of signal frequencies (500–3500 Hz) in quiet and in the presence of a critical-band-wide masker centered at 1000 Hz. Nevertheless, there are some inconsistencies in the literature regarding the influence of off-frequency masking on temporal integration, and in particular on whether there is an effect of signal frequency beyond that which might be observed in quiet.

In a series of studies, Fastl (1976, 1977, 1979) measured temporal integration for tonal signals with frequencies below, at, or above the (center) frequency of a tonal or critical-band-wide noise masker. He observed similar amounts of temporal integration for all conditions. Of particular relevance here, he (1976) found less integration at higher frequencies (6500–11 000 Hz) than at lower frequencies (300–600 Hz) in the presence of a critical-band masker, but noted that this effect of overall frequency was similar to that which he observed for tones masked by a broadband masker (he did not report integration in quiet). Indeed, the amount of integration at a given frequency region was similar for off-frequency and broadband maskers. Thus the results of Fastl suggest that off-frequency masking does not alter temporal integration.

Moore and Glasberg (1987) measured temporal integration at two signal frequencies (450 Hz and 1800 Hz) in quiet and in the presence of a tonal masker whose frequency was lower than that of the signal (signal-masker frequency ratio of 1.8). They observed similar amounts of temporal integration at the two signal frequencies in quiet, but less integration at the higher frequency in the presence of the off-frequency masker. The results of Moore and Glasberg thus suggest that off-frequency masking may alter temporal integration. In particular, their results suggest that there may be an effect of overall frequency on temporal integration in the

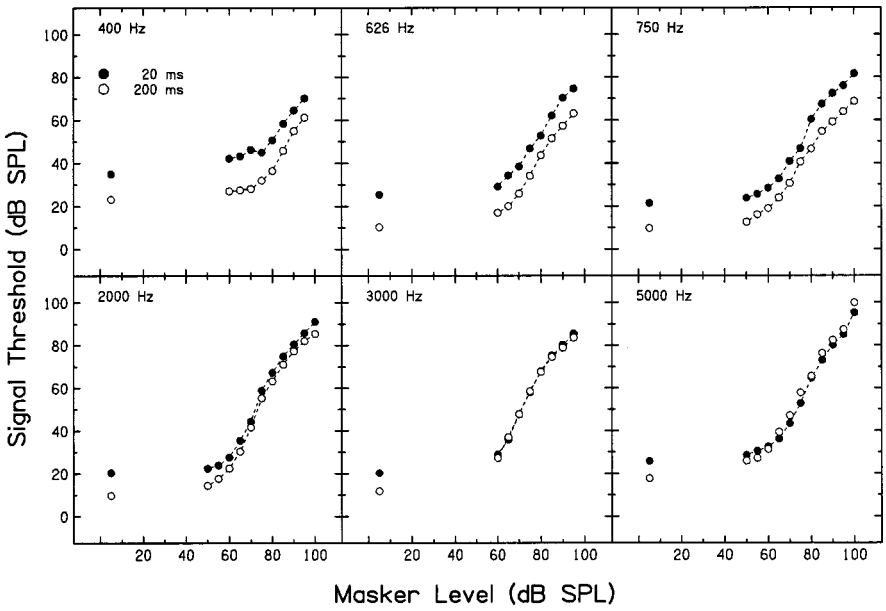

FIG. 1. Growth-of-masking functions from Bacon *et al.* (1999). The signal duration was 20 ms (filled circles) or 200 ms (unfilled circles). The signal frequency is indicated and varies across panels. The masker frequency was 3 ERBs below the signal frequency. Quiet thresholds are shown at the far left of each panel.

presence of off-frequency maskers in addition to any effect that might be observed in quiet and in broadband noise. It is unclear whether the difference across the studies of Fastl (1976) and Moore and Glasberg (1987) reflects individual differences or differences in the type of off-frequency masker (Fastl used a continuous band-pass noise, whereas Moore and Glasberg used a gated tone).

In the context of measuring growth-of-masking functions for two different signal durations, we have recently observed an effect of overall frequency on temporal integration in the presence of off-frequency, gated tonal maskers (Bacon *et al.*, 1999). The primary focus of that study was on the influence of overall frequency on the slope of the masking function, and thus temporal integration was not discussed nor were the data plotted in such a way as to reveal temporal integration. Some of the functions from that study are plotted in Fig. 1 to illustrate the effect of interest for the present study. The signal duration was 20 ms (filled circles) or 200 ms (unfilled circles). The signal frequency ranged from 400 to 5000 Hz, and is plotted across panels. In each case, the masker frequency was three equivalent rectangular bandwidths (ERBs; Glasberg and Moore, 1990) below the signal frequency, and the data are averaged across the subjects who were tested at that particular frequency (two different groups of subjects are represented, and each was tested at three of the frequencies). The amount of temporal integration observed in quiet (compare symbols at the far left in each panel) is more or less maintained throughout the masking function at the lower frequencies (top row), but not at the higher frequencies (bottom row). There is thus a clear effect of overall frequency on temporal integration under conditions of off-frequency masking, beyond the effect observed in quiet, consistent with the results of Moore and Glasberg (1987). Further, this effect is independent of masker level, at least once there is about 10 dB of masking.

The purpose of the present study was to explore this overall effect of frequency further. In experiment 1, we measured the threshold for several signal durations in quiet and in the presence of a gated tonal masker whose frequency was either above or below the signal frequency. In experiment 2, we measured psychometric functions to determine whether differences in masked temporal integration across signal frequency can be understood in terms of the slope of the underlying psychometric function. Finally, in experiment 3, we measured masked temporal integration for a wide range of masker-signal frequency separations in order to detail the effects of relative masker frequency. Moreover, we did this for both tonal and filtered-noise maskers that were either gated or continuous, in order to determine whether differences in the results of Moore and Glasberg (1987) and Bacon *et al.* (1999) on the one hand, and those of Fastl (1976) on the other, might be due to differences in masker type or masker gating.

I. EXPERIMENT 1. TEMPORAL INTEGRATION FUNCTIONS: GATED TONAL MASKER

The purpose of this experiment was to compare temporal integration functions (threshold versus signal duration) at a relatively low and a relatively high frequency in quiet and under two different masking conditions. In one, the masker was lower in frequency than the signal, and in the other it was higher in frequency than the signal. The two maskers were chosen to produce similar amounts of masking. These results will thus allow us to examine whether the effect of overall frequency on temporal integration observed by Moore and Glasberg (1987) and Bacon *et al.* (1999) is restricted to maskers lower in frequency than the signal.

A. Stimuli

The signal frequency was 500 or 2000 Hz. The signal was presented in quiet or in the presence of a tonal masker with a level of 80 dB SPL. The 500-Hz signal was paired with a masker whose frequency was 300 or 582 Hz, whereas the 2000-Hz signal was paired with one whose frequency was 1386 or 2250 Hz. These maskers are either 3 ERBs below or 1 ERB above their respective signal frequency. The signal was 20, 40, 80, or 160 ms in duration; when present,

the masker was 300 ms in duration. All durations include 5-ms $\cos^2$ rise/fall times. The delay between the onset of the masker and the onset of the signal was 70 ms, which resulted in the 160-ms signal being temporally centered within the masker. The sinusoidal signals and maskers were digitally generated and produced at a 20-kHz sampling rate. They were presented through separate channels of a digital-to-analog converter (TDT DA1); each channel was low-pass filtered at 8 kHz (Kemo VBF 25.01; 135 dB/oct). Within a block of trials, the level of the signal was varied adaptively via a programmable attenuator (Wilsonics PATT).

The cubic difference tone (CDT) is likely to provide a cue for signal detection in the conditions where the masker was located below the signal in frequency. Thus in those conditions, a noise was presented continuously to mask the CDT. The noise (GenRad 1381) was low-pass filtered (Kemo VBF 25.01; 135 dB/oct) at a cutoff frequency equal to the frequency of the CDT. The spectrum level of the noise was 20 dB SPL. The masker, signal, and low-pass noise were added together before being presented monaurally (right ear) through a TDH-49P headphone mounted in an MX/51 cushion.

At high signal levels, the signal might be detected in the nontest ear (Wegel and Lane, 1924; Bacon *et al.*, 1999). Thus in the masking conditions, a second noise (GenRad 1381) was presented continuously to the contralateral ear. It was filtered only by the TDH-49P headphone. The spectrum level of the noise was 10 dB SPL (see Bacon *et al.*, 1999).

B. Procedure

Testing was completed in a double-walled, sound-treated booth. An adaptive, two-interval, forced-choice (2IFC) paradigm was used. The signal was presented in one of the two intervals (chosen at random), and the subjects' task was to choose the interval that contained the signal. A three-down, one-up decision rule that tracked 79.4% correct (Levitt, 1971) was employed. Each run consisted of 50 trials. A 5-dB step size was used for the first two reversals, after which a 2-dB step size was used. The threshold estimate for a given run was obtained by averaging an even number of reversals, excluding the first two or three reversals. Runs were discarded on the rare occasions when the standard deviation of the threshold estimate was greater than 5 dB or when the number of reversals used for the threshold estimate was less than six. Three threshold estimates were averaged to produce a threshold for a given condition. If the standard deviation of this average was greater than 3 dB, an additional estimate was obtained and included in the average. This continued until the standard deviation was less than 3 dB, or a total of six estimates were obtained and averaged. Most (98%) of the thresholds had a standard deviation less than 3 dB.

C. Subjects

Four individuals participated. Of these, three were female and one was male. They ranged in age from 21 to 23 years, and had thresholds of 10 dB HL or lower (ANSI, 1989) for octave frequencies from 250 to 8000 Hz. Except for S1 (the third author), the subjects were paid for their participation.

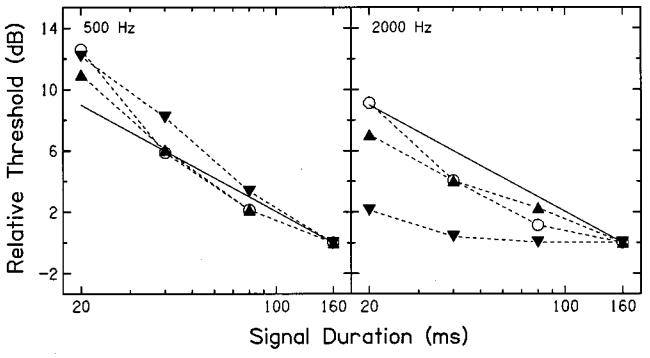

FIG. 2. Results from experiment 1, showing threshold as a function of signal duration. Results have been averaged across subjects. The threshold at each duration is referenced to the threshold for the 160-ms signal (actual thresholds are given in Table I). The signal frequency was 500 Hz (left panel) or 2000 Hz (right panel). For each frequency, listening was done in quiet (circles) or in the presence of an 80-dB-SPL masker that was either 1 ERB above (triangles) or 3 ERBs below (inverted triangles) the signal frequency. The solid line without symbols represents perfect power integration.

D. Results and discussion

The results were similar across the four subjects, and thus only their group average results are shown in Fig. 2. The thresholds have been referenced to the threshold for the 160-ms signal; the actual thresholds are given in Table I. First consider the results for the 500-Hz signal (left panel). Thresholds improve by about 11–13 dB as the duration of the signal increases from 20 to 160 ms, regardless of whether the listening is in quiet (circles) or in the presence of an 80-dB masker located lower (inverted triangles) or higher (triangles) in frequency than the signal. This amount of integration is slightly greater than the 9-dB improvement shown by the solid line without symbols that reflects perfect power integration (i.e., equal energy).

For the 2000-Hz signal (right panel), the amount of improvement with increasing signal duration depends upon the listening situation. There is about 9 dB of integration in quiet (circles), 7 dB in the presence of a masker higher in frequency than the signal (triangles), and only about 2 dB in the

TABLE I. Group mean thresholds (dB SPL) from experiment 1. The signal frequency was 500 or 2000 Hz. Thresholds were measured in quiet and in the presence of an 80-dB-SPL masker. The masker was either lower in frequency than the signal (300 or 1386 Hz) or higher in frequency than the signal (582 or 2250 Hz).

	Signal duration (ms)			
	20	40	80	160
500 Hz				
Quiet	28.4	21.7	17.9	15.8
Lower	53.8	49.8	44.9	41.6
Higher	60.4	55.4	51.5	49.4
2000 Hz				
Quiet	18.2	13.2	10.3	9.1
Lower	62.7	60.9	60.6	60.5
Higher	53.0	50.0	48.2	46.0

TABLE II. Slopes (dB/decade), intercepts, and r^2 values based on the fits to the temporal integration functions in Fig. 2. The signal frequency was 500 or 2000 Hz. Temporal integration was measured in quiet and in the presence of an 80-dB-SPL masker. The masker was either lower in frequency than the signal (300 or 1386 Hz) or higher in frequency than the signal (582 or 2250 Hz).

	500 Hz			2000 Hz		
	Slope	Intercept	r^2	Slope	Intercept	r^2
Quiet	−13.9	29.4	0.94	−10.1	21.2	0.93
Lower	−13.8	30.1	0.99	−2.3	4.7	0.75
Higher	−12.3	26.3	0.97	−7.6	16.6	0.99

presence of a masker lower in frequency than the signal (inverted triangles). This relative lack of integration in the latter condition is consistent with the results shown in Fig. 1, where there was little or no temporal integration for signal frequencies from 2000 to 5000 Hz when the masker frequency was 3 ERBs below the signal frequency, as in the present experiment.

Each function in Fig. 2 was fitted with a straight line chosen to minimize the squared deviations. The slopes (dB/decade), intercepts, and r^2 values based on those fits are shown in Table II. Except for one case (2000 Hz in the presence of the lower frequency masker), these slopes accounted for between 92% and 99% of the variance in the data. The following points are worth noting. First, the slope obtained in quiet is somewhat steeper at 500 Hz than at 2000 Hz, indicating slightly greater integration at the lower frequency, as has been observed by others (e.g., Plomp and Bouman, 1959; Sheely and Bilger, 1964; Watson and Gengel, 1969; Hicks and Bacon, 1999). Second, at 500 Hz, the slope is more or less independent of the masking situation. And finally, at 2000 Hz, the slope is dependent upon the masking situation. The value of the slope is greatest in quiet (−10.1), least in the presence of a lower frequency masker (−2.2), and intermediate in the presence of a higher frequency masker (−7.6). Thus the effect of overall frequency on temporal integration under conditions of off-frequency masking is most obvious for maskers lower in frequency than the signal; the effect for maskers higher in frequency appears to largely reflect the effect of frequency that exists in quiet. These results indicate that, at high signal frequencies, there is an effect of relative masker frequency on temporal integration. Importantly, this effect of relative frequency cannot be attributed to the differences in effective masker level (i.e., to differences in the amount of masking), given the results in Fig. 1 showing that there is little or no integration at high signal frequencies at essentially all masker levels (masker lower in frequency than the signal).

II. EXPERIMENT 2. PSYCHOMETRIC FUNCTIONS: GATED TONAL MASKER

One theory of temporal integration is multiple looks (Viemeister and Wakefield, 1991). This theory states that a subject takes multiple short looks at a relatively long signal and combines information from those looks to improve signal threshold. In particular, it is generally assumed that each look results in a given detectability (d'), and that the overall detectability for the signal increases with the square root of the number of looks, assuming that each look gives the same d' and that the information from the multiple looks is combined optimally. The amount of integration in dB will depend upon the slope of the psychometric function relating d' to signal level. If the function is shallow, a given change in d' (resulting from, say, combining information from multiple looks) will result in a large change in threshold. If the function is steep, however, that same change in d' will result in a much smaller change in threshold. This raises the possibility that the small amount of temporal integration for the high-frequency signal in the presence of the lower frequency masker might be the consequence of an especially steep psychometric function in that condition. The purpose of experiment 2 was to test this possibility.

A. Stimuli

Stimulus generation and timing was as in experiment 1. The signal frequency was 500 or 2000 Hz. Psychometric functions were measured for the 20-ms signal in quiet and in the presence of a masker 3 ERBs lower in frequency than the signal; the masker frequency was 300 Hz (500-Hz signal) or 1386 Hz (2000-Hz signal). The shortest signal that was used in experiment 1 was used here, as its duration is closest to the duration of a single look (Viemeister and Wakefield, 1991). As in experiment 1, when the masker was present, a continuous low-pass noise was presented to the test ear at a spectrum level of 20 dB to mask the CDT, and a continuous broadband noise was presented to the nontest ear at a spectrum level of 10 dB to limit ''cross hearing.''

B. Procedure

Performance was evaluated in a fixed-level, 2IFC procedure. The signal levels were chosen to bracket the threshold levels obtained in experiment 1. Each psychometric function consisted of two to seven (but typically four) levels, spaced 1-dB apart. The goal was to choose levels that would yield percent correct values between 60 and 90. Each block consisted of 55 trials. The first 5 trials were presented at a level 5 dB higher than the remaining 50 trials, in order to provide the subject with some practice at a relatively easy level; these practice trials were not included in the data analysis. Four blocks were run per level, and thus each point on the psychometric function was based on 200 trials.

C. Subjects

The same four subjects tested in experiment 1 participated.

D. Results and discussion

The percent correct values were converted to d' values. In Fig. 3, $\log d'$ is plotted as a function of level in dB. In order to display the psychometric functions for all four conditions for a given subject conveniently in a single panel, the functions are placed arbitrarily along the level axis. The filled symbols depict the results for the 500-Hz signal, whereas the unfilled symbols show results for the 2000-Hz signal. Circles represent the results in quiet, and inverted

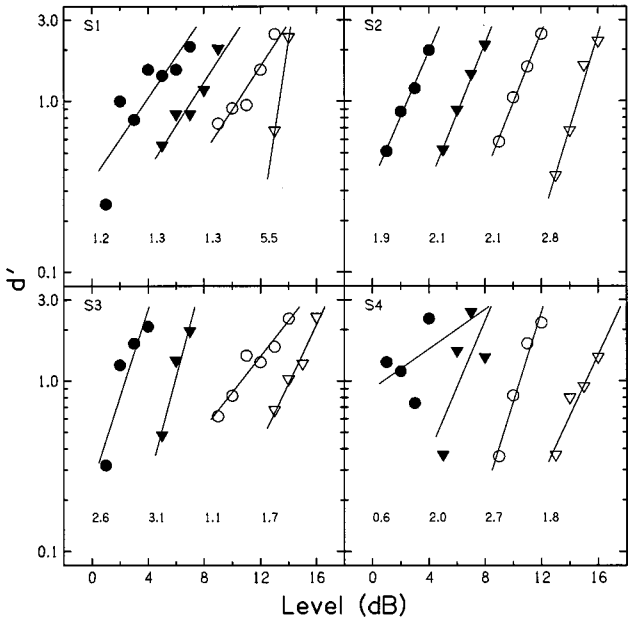

FIG. 3. Results from experiment 2, showing psychometric functions for the detection of a 20-ms signal. Results for the individual subjects are shown in separate panels. The functions are displaced arbitrarily along the level axis. The results for the 500-Hz signal are shown by filled symbols, whereas those for the 2000-Hz signal are shown by unfilled symbols. Listening was done in quiet (circles) or in the presence of a masker located 3 ERBs below the signal frequency (inverted triangles). The lines represent the best straight-line fits. The number below each function is the slope of the line, in terms of $\log d'$ vs log signal power.

triangles the results in the presence of a lower frequency masker. The number displaced below each function indicates the slope of the best-fitting straight line in terms of $\log d'$ versus log signal power. [Because the functions are plotted in terms of level in dB (i.e., 10 log signal power), the slopes of the lines in Fig. 3 are actually one-tenth the values displayed.]

Fifteen of the 16 psychometric functions included more than two points; of these, the fits were generally satisfactory: Most (11/15) r^2 values were greater than 0.91, although the range was from 0.13 to 0.99. When averaged across signal frequency and subjects, the slope in quiet was 1.7, which is somewhat greater than the value of 1.0 that is usually obtained in quiet or in broadband noise (e.g., Egan *et al.*, 1969; Buus *et al.*, 1986; Carlyon *et al.*, 1990). Variations from a slope of 1.0 have been observed previously (e.g., Carlyon *et al.*, 1990), and it is unclear whether the variations observed here reflect individual differences or differences in procedure.

The comparisons of particular interest are across conditions within a subject. In particular, the purpose of this experiment was to determine whether the lack of temporal integration at high frequencies in the presence of a lower frequency masker is due to an especially steep psychometric function in that condition. Only the results from S1 are consistent with this possibility: Her slope in that condition (5.5) is about four times greater than the slope obtained in the other three conditions. Subject S2 showed a similar trend, although her slope in the high-frequency masked condition (2.8) was only about 1.4 times greater than that in the other conditions. For the other two subjects (S3 and S4), the function was not steepest in the high-frequency masked condition. Hence, the results from the present experiment indicate that differences across signal frequency in terms of the amount of temporal integration under conditions of off-frequency masking (masker lower in frequency than the signal) generally cannot be understood in terms of differences in the underlying psychometric function. Psychometric functions from a fifth subject (S5), derived from adaptive tracks, were also consistent with this conclusion.

III. EXPERIMENT 3. EFFECTS OF MASKER-SIGNAL FREQUENCY RELATION, MASKER TYPE, AND MASKER GATING

Experiment 3 had three purposes. First, to extend the results from experiment 1 to more masker-signal frequency separations. We were particularly interested in confirming the effect of relative masker frequency at high signal frequencies, and mapping it in more detail. The other two purposes related to determining whether differences in the literature regarding the effects of overall frequency on temporal integration in the presence of off-frequency maskers might be due to differences in masker type or masker gating. In particular, using continuous noise maskers, Fastl (1976) did not observe an effect of overall frequency, whereas using gated tonal maskers, Moore and Glasberg (1987) and Bacon *et al.* (1999) did. Thus the second purpose of experiment 3 was to compare temporal integration in the presence of tonal and noise maskers, whereas the third purpose was to compare temporal integration in the presence of gated and continuous maskers. In the present experiment, we chose to use low-pass or relatively broad band-pass noise maskers instead of relatively narrow band-pass noise maskers, as used by Fastl. This was done to avoid the influence of inherent fluctuations of narrowband noise, which might depend upon signal duration, and hence might influence measures of temporal integration (i.e., the fluctuations might especially increase the detectability of long signals, due to more opportunities to ''listen in the dips'' of the fluctuating masker).

A. Stimuli

The sinusoidal signals and maskers were generated as described for experiment 1, with the exception that the continuous tonal masker was generated by a multi-function synthesizer (HP 8904A). The signal frequency was 750 or 2000 Hz. We chose 750 Hz as the lower frequency (rather than 500 Hz, as in experiments 1 and 2) to allow for a greater range of masker frequencies on the low-frequency side of the signal. As suggested by the data in Fig. 1, there should be little difference between 500 and 750 Hz in terms of masked temporal integration, at least for maskers located 3 ERBs below the signal frequency. The signal duration was 20 or 160 ms. When a masker was present, it was either gated for 300 ms (all timing includes the 5-ms $\cos^2$ rise/fall times) or presented continuously. The onset of the signal occurred 70 ms after the onset of the gated masker.

The frequency of the sinusoidal maskers ranged from -5 to 3 ERBs *re*: the signal frequency. The actual masker

frequencies were as follows. For the 750-Hz signal: 343, 408, 480, 560, 650, 750, 861, 985, and 1123 Hz. For the 2000-Hz signal: 1073, 1220, 1386, 1569, 1774, 2000, 2254, 2537, and 2851 Hz. When the masker and signal were equal in frequency, they were either 90° out of phase (gated masker) or their phase relation was uncontrolled and thus random from trial to trial (continuous masker). The sinusoidal masker was presented at a level of 80 dB SPL.

The noise maskers were either low pass or band pass, achieved by filtering broadband noise (GenRad 1381) by either a single low-pass filter or a low-pass and high-pass filter in series (Kemo VBF 25.01). The temporal characteristics were the same as those employed when using the tonal masker (i.e., the masker was either gated for 300 ms, including the 5-ms $\cos^2$ rise/fall times, or presented continuously, and the signal was presented 70 ms after the onset of the gated masker). The noise was gated via a digital gating function (TDT DA1) that was low-pass filtered (Kemo VBF 25.01) prior to multiplication.

Low-pass noise was used for maskers lower in frequency than the signal. The cutoff frequency ranged from −5 to 0 ERBs *re*: the signal frequency. Band-pass noise was used for maskers higher in frequency than the signal. The lower cutoff frequency ranged from 0 to 3 ERBs *re*: the signal frequency (thus the 0-ERB condition was tested twice, once with low-pass noise and once with band-pass noise). The upper cutoff frequency of the band-pass noise was fixed at twice the signal frequency. Thus in the two 0-ERB conditions, the bandwidth of the low-pass noise was equal to the bandwidth of the band-pass noise. The spectrum level of the noise masker was 60 dB SPL for the 750-Hz signal and 56 dB SPL for the 2000-Hz signal. This level was chosen so that, in the 0-ERB condition, the overall level of the noise at the output of the auditory filter centered at the signal frequency would be close to 80 dB SPL (i.e., the level of the tonal masker).

When the masker was a sinusoid, a continuous low-pass noise was presented at a spectrum level of 20 dB to mask the CDT. The cutoff frequency of the noise was equal to the CDT frequency. In all masking conditions, a noise was presented to the contralateral ear at a spectrum level of 10 dB to eliminate listening in the nontest ear.

B. Procedure

The procedure was the same as that used in experiment 1. Most (98%) of the thresholds had a standard deviation less than 3 dB.

C. Subjects

Two of the four subjects (S1 and S2) who participated in experiments 1 and 2 participated; the other two were unavailable. A third subject (S5) with normal hearing (the second author) participated. She had considerable listening experience in other psychoacoustic tasks, including simultaneous masking of both short- and long-duration signals. All three subjects were female and ranged in age from 21 to 29 years.

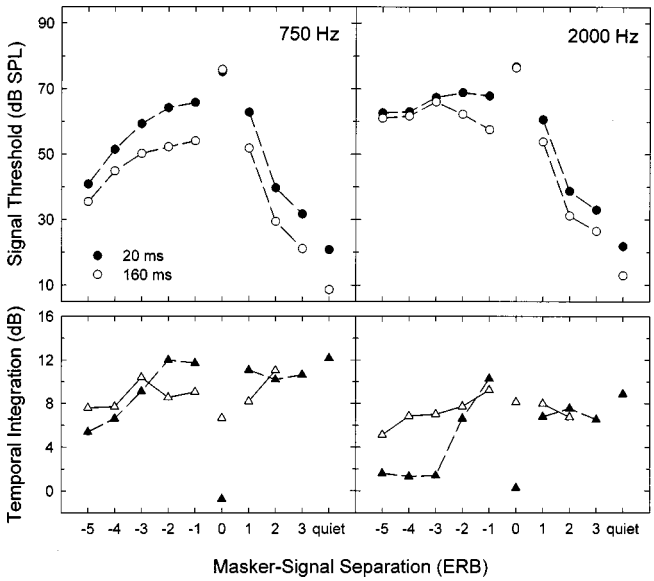

FIG. 4. Results from experiment 3 with a tonal masker. The signal frequency was 750 Hz (left panel) or 2000 Hz (right panel). The top row shows thresholds as a function of the masker-signal separation in ERBs. The masker was gated for 300 ms, and the signal duration was 20 ms (filled circles) or 160 ms (unfilled circles). The bottom row shows the difference between these thresholds (filled triangles). The unfilled triangles show the difference between thresholds for a 20-ms and 160-ms signal in the presence of a continuous tonal masker (thresholds not shown). Results obtained in quiet are at the far right of each panel.

D. Results and discussion

1. Gated tonal masker

The results for the tonal masker were similar across the three subjects, and thus only their group mean results are shown in Fig. 4. The circles in the top row show the thresholds for the two signal durations, whereas the filled triangles in the bottom row show the amount of temporal integration; both are plotted as a function of the masker-signal separation in ERBs. The unfilled triangles are discussed later (Sec. III D 3). The results in quiet are shown at the far right of each panel. First consider the results for the 750-Hz signal (left column). As expected, thresholds decrease as the masker moves further away from the signal, and this decrease is more abrupt for maskers higher in frequency than the signal. For all masker frequencies except 750 Hz (i.e., the 0-ERB condition), thresholds are lower for the 160-ms signal (unfilled circles), although the amount by which they are lower depends upon the masker-signal separation, at least for maskers lower in frequency than the signal. This is shown more clearly in the bottom panel (filled triangles). The amount of temporal integration in quiet is about 12 dB. This is maintained for masker-signal separations from −2 to 3 ERBs (except for the 0-ERB condition). For separations from −2 to −5 ERBs, the amount of temporal integration declines. This decline appears not to be due to the decreasing amount of masking, given that the masking produced at −5 ERBs is greater than that produced at 2 and 3 ERBs.

The pattern of thresholds for the 2000-Hz signal (right column) is similar to that for the 750-Hz signal, with the following three exceptions. First, the slope of the pattern on the low-frequency side is more gradual than at 750 Hz. Some

of this may be due to greater upward spread of masking at the higher signal frequency (Bacon *et al.*, 1999), although pilot results from S5 suggest that it is at least partly due to differences in the sensation level (SL) of the masker. At 2000 Hz, the SL of the masker does not change much as its frequency is lowered; at 750 Hz, however, the SL of the masker decreases considerably. When the SL of the masker was equated across the two signal frequencies (by lowering the level of the masker paired with the 2000-Hz signal), the slope of the pattern on the low-frequency side was more similar at the two signal frequencies. Second, for the 160-ms signal, thresholds do not decrease monotonically as the masker moves further away from the signal on the low-frequency side. Instead, the threshold is lowest when the masker is closest to the signal, and the thresholds at separations of −1 and −2 ERBs are lower than the threshold at −3 ERBs. This result is unlikely to be due to the detection of the CDT. For the two closest spacings, the spectrum level of the low-pass noise used to mask the CDT was increased from 20 to 40 dB SPL without affecting thresholds appreciably. A more plausible explanation for these results is that subjects were detecting beating between the masker and longer signal at the closest spacings, although the subjects did not report hearing any beating. Although the spacing between the masker and signal at a separation of −1 ERB is relatively large (226 Hz), Moore *et al.* (1998) have suggested that beating may play a role in masking for spacings greater than 200 Hz. Finally, the third difference in the results between the two signal frequencies is that, at 2000 Hz, the threshold for the 160-ms signal is not always noticeably lower than the threshold for the 20-ms signal. This is shown more clearly in the bottom panel (filled triangles). Except for the conditions (−1 and −2 ERBs) where thresholds for the 160-ms signal may have been influenced by beating, temporal integration is not observed for maskers lower in frequency than the signal. It does, however, exist for maskers higher in frequency than the signal. In those cases, there is about 7–8 dB of integration, compared to the 9 dB observed in quiet.

The results in Fig. 4 confirm the results of experiment 1 (where the masker-signal separation was −3 ERBs or 1 ERB). They also extend those results by showing that integration exists for a wide range of masker frequencies higher than the signal (for both signal frequencies); indeed, it appears that integration would exist for all such maskers, although we did not use maskers more than 3 ERBs above the signal frequency, as they would have produced little or no masking. The present results also extend previous results by showing that the amount of integration depends upon the spacing between a signal and a lower frequency masker. The amount of integration tends to decline as the masker moves further away from the signal on the low-frequency side, although there is clear evidence of temporal integration at 750 Hz even at the widest separation (−5 ERBs).

Although the results in Fig. 4 confirm differences across signal frequency in terms of masked temporal integration (Moore and Glasberg, 1987; Bacon *et al.*, 1999), they also reveal a pattern of temporal integration that is similar for the two signal frequencies: For both, temporal integration exists for maskers higher in frequency than the signal, but declines

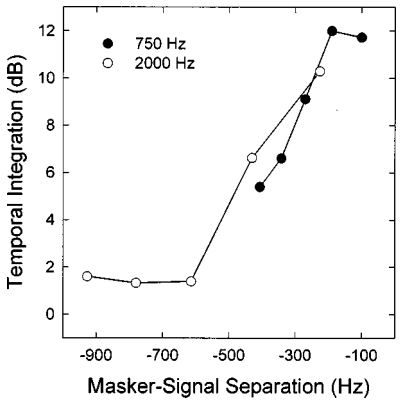

FIG. 5. The temporal integration results from Fig. 4 with a gated tonal masker located lower in frequency than the signal, re-plotted as a function of masker-signal separation in Hz.

(albeit more rapidly at 2000 Hz) as maskers move further away from the signal on the low-frequency side. As noted above, the integration at the higher frequency for separations of −1 and possibly −2 ERBs should be interpreted cautiously, as the thresholds for the long signal may have been influenced by beating. Although the pattern of thresholds at 750 Hz does not suggest that beating was a cue at this frequency, as it does at 2000 Hz, we cannot rule out the possibility that beating played a role at 750 Hz as well. In Fig. 5, we have re-plotted temporal integration for conditions where the masker was lower in frequency than the signal, but this time as a function of masker-signal separation in Hz. Inasmuch as the presence of integration at 2000 Hz is due to beating between the masker and long-duration signal, and the decline in integration as the masker moves further away from the signal results from a loss of the beating cue, then the overlap of the results at the two signal frequencies is consistent with the possibility that the results at *both* signal frequencies were influenced by beating between the masker and signal. This would explain why the decline in integration with masker-signal separation in ERBs was more immediate at the higher signal frequency.

The results in Fig. 5 suggest that, for maskers lower in frequency than the signal, temporal integration exists only (or primarily) when beating is a cue. This is obviously not the case for maskers higher in frequency than the signal, as temporal integration exists there for all masker-signal spacings, even those where beating would not be a cue (due to the large spacing in Hz and the considerably lower signal levels at masked threshold). In the General Discussion (Sec. V B), we address why temporal integration might differ for maskers higher versus lower in frequency than the signal.

The lack of integration observed in Fig. 4 in the on-frequency (0-ERB) condition at both signal frequencies is in contrast to the temporal integration measured by others (Fastl, 1979; Moore and Peters, 1997; Oxenham, 1998) for on-frequency tone-on-tone masking, although the effect they observed was only a few dB for a range of durations similar to those tested here. The lack of integration observed in Fig. 4 is also in contrast to the effect of duration on gated intensity discrimination (e.g., Carlyon and Moore, 1984; Florentine, 1986). Although it is unclear, this difference could re-

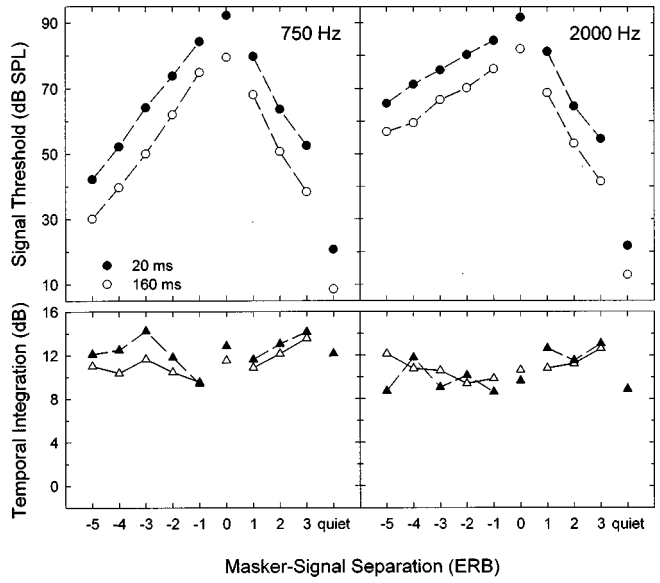

FIG. 6. As Fig. 4, but for a noise masker. See text for details regarding the spectral characteristics of the noise.

flect differences in stimulus gating: In studies of intensity discrimination, the pedestal and increment are gated together, whereas in the present study the masker and signal were gated asynchronously.

2. Gated noise masker

The results for the noise masker were similar across the three subjects, and thus only their group mean results are shown in Fig. 6. Recall that the 0-ERB condition was tested twice, once with low-pass noise and once with band-pass noise (located primarily above the signal frequency). Those thresholds were nearly identical, and thus were averaged for presentation. The pattern of threshold versus masker-signal separation (circles) is similar for both signal durations at the two signal frequencies, with the exception that the patterns are steeper on the low-frequency side at 750 Hz than at 2000 Hz. This difference across frequency was noted with the gated tonal masker as well. The fact that thresholds decline monotonically here but not in Fig. 4 for the 160-ms, 2000-Hz signal lends support to the conjecture that beating between the tonal masker and (long-duration) signal may have influenced some of the results in Fig. 4. Perhaps the most important finding revealed in Fig. 6 is that there is a considerable amount of temporal integration (filled triangles) for all masker frequencies at both signal frequencies. Further, the amount of masked temporal integration (averaged across masker frequency) is similar to the amount of integration in quiet: For 750 Hz, the two values are 12.5 and 12.2 dB, respectively; for 2000 Hz, the values are 10.5 and 8.9 dB, respectively. Although the amount of temporal integration is not independent of the relative masker frequency (e.g., it tends to increase with increasing masker-signal separation on the high-frequency side), the substantial integration at all separations contrasts with the results obtained with a gated tonal masker (bottom panels of Fig. 4); a possible cause of this difference is discussed below (Sec. V B). Furthermore, these results suggest that the effect of overall frequency on temporal integration under conditions of off-frequency masking (masker lower in frequency than the signal) observed by Moore and Glasberg (1987) and Bacon *et al.* (1999) was due to their use of a tonal masker. Such an effect is not observed with bandlimited noise maskers (Fastl, 1976; present study, Fig. 6).

3. Continuous tonal and noise maskers

For a given masker type (tonal or noise), the pattern of thresholds was similar whether the masker was gated or continuous, and thus those thresholds are not shown. In fact, for the noise masker, the thresholds were nearly the same, and hence the amount of integration was about the same. This can be seen in the bottom panels of Fig. 6, where the integration in the presence of the continuous masker (unfilled triangles) is shown along with the integration in the presence of the gated masker (filled triangles). The results are nearly overlapping for both signal frequencies, although at 750 Hz there tends to be a few dB more integration in the presence of the gated masker.

For the tonal masker, the thresholds were lower in the presence of the continuous masker. We discuss these and other gated-continuous threshold differences in detail in a separate paper, where the focus is on these differences and not on temporal integration (Hicks and Bacon, in preparation). For some conditions, thresholds for the longer signal decreased considerably more than did thresholds for the shorter signal when the masker was changed from gated to continuous. Consequently, the amount of temporal integration in those conditions increased. This can be seen in the bottom panels of Fig. 4, by comparing the unfilled triangles (continuous masker) to the filled triangles (gated masker). Temporal integration was not measured in the 3-ERB condition with a continuous masker, because pilot results from S5 indicated that the continuous masker produced relatively little masking in that condition. First consider the results for the 750-Hz signal (bottom left panel). In the presence of the continuous masker, the amount of integration is more or less independent of the masker-signal frequency separation, although it is a few dB less than that observed in quiet. Thus there is no clear indication of a decrease in temporal integration with increasing masker-signal separation for maskers lower in frequency than the signal, as there was when the masker was gated. Note that there is integration in the 0-ERB condition only for the continuous masker. This result should be interpreted somewhat cautiously, because the phase relation between the signal and masker was not controlled when the masker was continuous. This was the case for both signal durations, however, and so the difference between the thresholds for the two durations (i.e., the amount of integration) may have been unaffected by the random phase relation.

For the 2000-Hz signal (bottom right panel), temporal integration in the presence of the continuous masker (unfilled triangles) is less dependent on masker-signal separation than it is in the presence of the gated masker (filled triangles). Importantly, temporal integration now exists for frequency separations (-3 to -5 ERBs) where there was none in the presence of the gated masker. Thus these results suggest that the effect of overall frequency on temporal integration under

conditions of off-frequency masking (masker lower in frequency than the signal) observed by Moore and Glasberg (1987) and Bacon *et al.* (1999) was due specifically to their use of a *gated* tonal masker.

IV. GENERAL DISCUSSION

A. Temporal integration: Effects of frequency

1. In quiet

As noted in the Introduction, the issue of whether temporal integration decreases with increasing signal frequency is not clearly resolved in the literature. Although the intent of the present study was not to evaluate effects of frequency in quiet, by combining across the data reported in Fig. 1 (from Bacon *et al.*, 1999), Fig. 2, and Fig. 4, it is possible to evaluate the effects of frequency on temporal integration over a wide range of frequencies, from 400 to 5000 Hz. For signal frequencies at and below 750 Hz, the average amount of integration was 12.7 dB (range of 11.7–15.2). For frequencies above 750 Hz, the average was 9.1 (range of 8.1–10.7). Thus although the effect of frequency was not large, these data support the conclusion drawn by many others that there is less temporal integration at high frequencies than at low.

2. Under conditions of off-frequency masking

Although there can be a small effect of frequency on temporal integration in quiet or in broadband noise, the present study was motivated by our serendipitous finding of an even more dramatic effect of frequency in the presence of a tonal masker located lower in frequency than the signal (Bacon *et al.*, 1999; see Fig. 1). After noting this dramatic effect of frequency, we reviewed the literature and discovered that there had been very little previous research on temporal integration under conditions of masking by narrowband, off-frequency maskers. Further, the results of that research were inconclusive regarding the effect of overall frequency.

The present study suggests that the differences in the literature are due to differences in the masker. In experiment 3, we showed that the dramatic frequency effect only exists with a gated tonal masker. There was only a small frequency effect for a continuous tonal masker, or for a noise masker that was either gated or continuous; it was about the same as that seen in quiet. Thus it appears that the frequency effect observed in quiet and in broadband noise is also seen in the presence of an off-frequency noise or tonal masker (with the caveat that the tonal masker must be continuous). Although our data do not provide a critical evaluation of any of the models of temporal integration, the results suggest that regardless of the way in which temporal integration is achieved—via long-term integration (Zwislocki, 1969), multiple looks (Viemeister and Wakefield, 1991), or a matched filter (Dau *et al.*, 1997)—it is apparently largely unaffected by most maskers.

B. What is ''special'' about gated tonal maskers?

Although the relative lack of temporal integration appears to be unique to gated tonal maskers located lower in frequency than the signal, and understanding that situation may not provide much insight into temporal integration *per se*, it is of interest to speculate why temporal integration is so affected by these gated tonal maskers.

Although gated tonal maskers often produce more masking than do continuous tonal maskers, the greater masking cannot account for the unusual result produced by the gated tonal masker, as is clearly shown in Fig. 1, where the lack of integration exists for almost all masker levels. Instead, it appears that the aspect of gating *per se* disrupts the temporal integration process. One possibility is that it does this by drawing attention away from the signal. This places the interference at a rather central site, although that may not be unreasonable, given that the integration process itself is likely to be central to the auditory periphery (e.g., Viemeister and Wakefield, 1991; Dau *et al.*, 1997; Buus, 1999). Although the 70-ms delay between masker onset and signal onset may seem sufficient to avoid any ''distraction'' caused by gating the masker, there is clear evidence in the literature that so-called attention filters are considerably broader when the background noise is gated than when it is continuous. For example, Dai and Buus (1991) showed that attention was distributed over a broader frequency range (detectability of signals at unexpected, remote frequencies was higher) in the presence of a noise that was gated as opposed to one that was continuous. In their gated condition, the delay between masker onset and signal onset was 300 ms, more than a factor of 4 longer than the delay used in the present experiments. Thus the 70-ms delay is clearly short enough to result in a relatively broad attention or listening filter in the gated condition.

Preliminary results with S5 are consistent with the possibility that gating the masker *per se* disrupts the integration process. In these pilot conditions, a continuous tonal masker was paired with a gated masker. The continuous masker was 3 ERBs below the 2000-Hz signal, and it was presented at a level of 80 dB SPL (as in the main experiments). The gated masker was either 4 or 5 ERBs below the signal, and presented at a level of 50, 60, or 70 dB SPL. Thus the gated masker was both farther from the signal and lower in level than the continuous masker. Consequently, the gated masker should have produced no additional masking at the signal frequency in terms of spread of excitation. Nevertheless, the gated masker elevated thresholds, *but only for the 160-ms signal*. The 20-ms signal may have been unaffected because attention filters tend to be broader anyway for short signals (Wright and Dai, 1994). The gated masker thus reduced temporal integration. At both -4 and -5 ERBs, the elevation in threshold caused by the gated masker was independent of its level, confirming that its effect was not due to spread of excitation. Although the process by which the gated masker disrupts temporal integration is unclear, these preliminary results are consistent with the possibility that it is centrally mediated, perhaps related to broad attention filters.

If gating *per se* disrupts the temporal integration process, then one must address why temporal integration is only affected by gated tonal maskers located lower in frequency than the signal, given that the gating of a band-limited noise masker tends to broaden both the low- and high-frequency

sides of attention filters (Dai and Buus, 1991). One possibility is related to the asymmetry of the excitation pattern. In particular, if we assume that attention is drawn toward a relatively steep ''edge'' along the masker's excitation pattern, then attention will be drawn toward the low-frequency (apical) edge. For maskers higher in frequency than the signal, that edge likely will be masked by the signal. Thus a clear edge will exist during the entire masker presentation only for maskers lower in frequency than the signal. The potential importance of edges was also noted by Wright and Dai (1994), who suggested that the spectral edges of a band-limited noise could attract subjects' attention. As we saw in Fig. 4, however, temporal integration can exist for a gated tonal masker located lower in frequency than the signal, but only when beating is likely to influence the threshold for the long-duration signal. This suggests that, in those cases, the beating cue can compensate for the disruptive aspect of gating.

If a clearly audible, steep edge of the masker's excitation pattern is responsible for the effects of gating observed with tonal maskers, it is possible that we did not observe an effect of gating with our noise masker because we used a low-pass noise, which of course has no low-frequency edge to its excitation pattern. This possibility could be evaluated by using a relatively narrow band of noise. As mentioned in Sec. III, however, there are problems with using such a noise. In particular, the inherent fluctuations of the noise could result in lower thresholds, particularly for the longer signal, for conditions where the masker is lower in frequency than the signal (e.g., Mott and Feth, 1986; van der Heijden and Kohlrausch, 1995). This would lead to greater amounts of integration, but not as a result of the temporal integration process *per se*. Interestingly, if gating a relatively narrow noise similarly disrupted temporal integration, then differences in the literature between Moore and Glasberg (1987) and Fastl (1976) would have to be attributed solely to differences in gating, and not to differences in masker type.

ACKNOWLEDGMENTS

This research was supported by NIDCD Grant No. DC01376. We thank Brian Moore and an anonymous reviewer for their helpful comments on a previous version of this manuscript.

ANSI (**1989**). ANSI S3.6-1989, ''Specifications for audiometers'' (American National Standards Institute, New York).

Bacon, S. P., Boden, L. N., Lee, J., and Repovsch, J. L. (**1999**). ''Growth of simultaneous masking for $f_m < f_s$: Effects of overall frequency and level,'' J. Acoust. Soc. Am. **106**, 341–350.

Buus, S. (**1999**). ''Temporal integration and multiple looks, revisited: Weights as a function of time,'' J. Acoust. Soc. Am. **105**, 2466–2475.

Buus, S., Schorer, E., Florentine, M., and Zwicker, E. (**1986**). ''Decision rules in detection of simple and complex tones,'' J. Acoust. Soc. Am. **80**, 1646–1657.

Carlyon, R. P., and Moore, B. C. J. (**1984**). ''Intensity discrimination: A severe departure from Weber's law,'' J. Acoust. Soc. Am. **76**, 1369–1376.

Carlyon, R. P., Buus, S., and Florentine, M. (**1990**). ''Temporal integration of trains of tone pulses by normal and cochlearly impaired listeners,'' J. Acoust. Soc. Am. **87**, 260–268.

Chung, D. Y., and Smith, F. (**1980**). ''Quiet and masked brief-tone audiometry in subjects with normal hearing and with noise-induced hearing loss,'' Scand. Audiol. **9**, 43–47.

Dai, H., and Buus, S. (**1991**). ''Effect of gating the masker on frequency-selective listening,'' J. Acoust. Soc. Am. **89**, 1816–1818.

Dau, T., Kollmeier, B., and Kohlrausch, A. (**1997**). ''Modeling auditory processing of amplitude modulation. II. Spectral and temporal integration,'' J. Acoust. Soc. Am. **102**, 2906–2919.

Egan, J. P., Lindner, W. A., and McFadden, D. (**1969**). ''Masking-level differences and the form of the psychometric function,'' Percept. Psychophys. **6**, 209–215.

Elliott, L. L. (**1963**). ''Tonal thresholds for short-duration stimuli as related to subject hearing level,'' J. Acoust. Soc. Am. **35**, 578–583.

Fastl, H. (**1976**). ''Influence of test tone duration on auditory masking patterns,'' Audiology **15**, 63–71.

Fastl, H. (**1977**). ''Temporal masking effects: II. Critical band noise masker,'' Acustica **36**, 317–331.

Fastl, H. (**1979**). ''Temporal masking effects. III. Pure tone masker,'' Acustica **43**, 282–294.

Florentine, M. (**1986**). ''Level discrimination of tones as a function of duration,'' J. Acoust. Soc. Am. **79**, 792–798.

Florentine, M., Fastl, H., and Buus, S. (**1998**). ''Temporal integration in normal hearing, cochlear impairment, and impairment simulated by masking,'' J. Acoust. Soc. Am. **84**, 195–203.

Garner, W. R., and Miller, G. A. (**1947**). ''The masked threshold of pure tones a function of duration,'' J. Exp. Psychol. **37**, 293–303.

Gengel, R. W. (**1972**). ''Auditory temporal integration at relatively high masked-threshold levels,'' J. Acoust. Soc. Am. **51**, 1849–1851.

Gerken, G. M., Bhat, V. K. H., and Hutchison-Clutter, M. H. (**1990**). ''Auditory temporal integration and the power-function model,'' J. Acoust. Soc. Am. **88**, 767–778.

Glasberg, B. R., and Moore, B. C. J. (**1990**). ''Derivation of auditory filter shapes from notched-noise data,'' Hearing Res. **47**, 103–138.

Green, D. M., Birdsall, T. B., and Tanner, W. P. (**1957**). ''Signal detection as a function of signal intensity and duration,'' J. Acoust. Soc. Am. **29**, 523–531.

van der Heijden, M., and Kohlrausch, A. (**1995**). ''The role of envelope fluctuations in spectral masking,'' J. Acoust. Soc. Am. **97**, 1800–1807.

Hicks, M. L., and Bacon, S. P. (**1999**). ''Effects of aspirin on psychophysical measures of frequency selectivity, two-tone suppression, and growth of masking,'' J. Acoust. Soc. Am. **106**, 1436–1451.

Hicks, M. L., and Bacon, S. P. (**in preparation**). ''Simultaneous masking by gated and continuous maskers: Effects of signal duration, masker-signal frequency relation, and masker type,'' J. Acoust. Soc. Am.

Hughes, J. W. (**1946**). ''The threshold of audition for short periods of stimulation,'' Proc. R. Soc. London., Ser. B **133**, 486–490.

Levitt, H. (**1971**). ''Transformed up-down methods in psychoacoustics,'' J. Acoust. Soc. Am. **49**, 467–477.

Moore, B. C. J., Alcántara, J. I., and Dau, T. (**1998**). ''Masking patterns for sinusoidal and narrow-band noise maskers,'' J. Acoust. Soc. Am. **104**, 1023–1038.

Moore, B. C. J., and Glasberg, B. R. (**1987**). ''Factors affecting thresholds for sinusoidal signals in narrow-band maskers with fluctuating envelopes,'' J. Acoust. Soc. Am. **82**, 69–79.

Moore, B. C. J., and Peters, R. W. (**1997**). ''Detection of increments and decrements in sinusoids as a function of frequency, increment, and decrement duration and pedestal duration,'' J. Acoust. Soc. Am. **102**, 2954–2965.

Mott, J. B., and Feth, L. L. (**1986**). ''Effects of the temporal properties of a masker upon simultaneous masking patterns,'' in *Auditory Frequency Selectivity*, edited by B. C. J. Moore and R. D. Patterson (Plenum, New York).

Olsen, W. A., and Carhart, R. (**1966**). ''Integration of acoustic power at threshold by normal hearers,'' J. Acoust. Soc. Am. **40**, 591–599.

Oxenham, A. J. (**1998**). ''Temporal integration at 6 kHz as a function of masker bandwidth,'' J. Acoust. Soc. Am. **103**, 1033–1042.

Oxenham, A. J., Moore, B. C. J., and Vickers, D. A. (**1997**). ''Short-term temporal integration: Evidence for the influence of peripheral compression,'' J. Acoust. Soc. Am. **101**, 3676–3687.

Plomp, R., and Bouman, M. A. (**1959**). ''Relation between hearing threshold and duration for tone pulses,'' J. Acoust. Soc. Am. **31**, 749–758.

Sheeley, E. C., and Bilger, R. C. (**1964**). ''Temporal integration as a function of frequency,'' J. Acoust. Soc. Am. **36**, 1850–1857.

Stephens, S. D. G. (**1973**). ''Auditory temporal integration as a function of intensity,'' J. Sound Vib. **30**, 109–126.

Viemeister, N. F., and Wakefield, G. H. (**1991**). ''Temporal integration and multiple looks,'' J. Acoust. Soc. Am. **90**, 858–865.

Watson, C. S., and Gengel, R. W. (**1969**). ''Signal duration and signal frequency in relation to auditory sensitivity,'' J. Acoust. Soc. Am. **46**, 989–997.
Wegel, R. L., and Lane, C. E. (**1924**). ''Auditory masking of one pure tone by another and its possible relation to the dynamics of the inner ear,'' Phys. Rev. **23**, 266–285.
Wright, B. A., and Dai, H. (**1994**). ''Detection of unexpected tones with short and long durations,'' J. Acoust. Soc. Am. **95**, 931–938.
Zwicker, E., and Wright, H. N. (**1963**). ''Temporal summation for tones in narrow-band noise,'' J. Acoust. Soc. Am. **35**, 691–699.
Zwislocki, J. (**1960**). ''Theory of auditory summation,'' J. Acoust. Soc. Am. **32**, 1046–1060.

Psychophysical correlates of contralateral efferent suppression. I. The role of the medial olivocochlear system in "central masking" in nonhuman primates[a)]

David W. Smith[b)]
Hearing Research Laboratories, Division of Otolaryngology-Head and Neck Surgery, Duke University Medical Center, Durham, North Carolina 27710

Dennis A. Turner
Division of Neurosurgery, Duke University Medical Center, Durham, North Carolina 27710

Miriam M. Henson
Division of Otolaryngology-Head and Neck Surgery, The University of North Carolina–Chapel Hill, Chapel Hill, North Carolina 27709

(Received 31 March 1999; revised 21 June 1999; accepted 21 July 1999)

An extensive physiological literature, including experimental and clinical studies in humans, demonstrates that activation of the medial olivocochlear (MOC) efferent system, by either contralateral sound or electrical stimulation, can produce significant alterations in cochlear function and suggests a role for the MOC system in influencing the auditory behavior of binaural hearing. The present data are from psychophysical studies in nonhuman primates which seek to determine if the noted physiological changes in response to contralateral acoustic stimulation have a perceptual counterpart. Four juvenile Japanese macaques were trained to respond to the presence of 1-s sinusoids, presented to the test ear, in an operant reinforcement paradigm. Thresholds were compared for frequencies ranging from 1.0 to 4.0 kHz in quiet, with thresholds measured when continuous, two octave-band noise, centered on the test tone frequency, was presented in the contralateral ear. Contralateral noise was presented at levels of 10–60 dB above detection threshold for the test-tone frequency. While some variability was evident across subjects, both in the frequency distribution and magnitude (as a function of contralateral noise level), all subjects exhibited an increase, or suppression of thresholds in the presence of contralateral noise. On average, thresholds increased systematically with contralateral noise level, to a peak of 7 dB. In one subject, the threshold increase seen with contralateral noise was significantly reduced when the MOC was surgically sectioned on the floor of the IVth ventricle. The characteristics of the measured shifts in behavioral thresholds, in the presence of contralateral noise reported here, are qualitatively and quantitatively similar to both efferent physiological suppression effects and psychophysical central masking threshold shifts which have been reported previously. These data suggest that at least some aspects of ''central masking'' are efferent-mediated peripheral processes, and that the term ''central masking'' may be incorrect. © *2000 Acoustical Society of America.*
[S0001-4966(00)06701-1]

PACS numbers: 43.66.Ba, 43.66.Dc, 43.66.Cb, 43.64.Ld [RVS]

INTRODUCTION

The first description of the active mechanical behavior of outer hair cells (OHCs) was made over 10 years ago (Brownell *et al.*, 1985). Since that time, as the OHC's innervation is primarily from medial-olivocochlear efferents (MOCs), there has been an increasing awareness of the importance of the cochlear efferent system in modulating the activity of the OHCs and, as a result, of the auditory system as a whole. Numerous modeling and physiological studies have reported significant alterations in peripheral auditory function when the MOC efferent system is stimulated with either noise, presented in the contralateral ear, or electrical stimuli at the midline of the IVth ventricle.

In acute physiological preparations, activation of the MOC has been shown to produce alterations in cochlear potentials (Fex, 1967; Konishi and Slepian, 1970), cochlear mechanical and distortion responses (Mountain, 1980; Siegel and Kim, 1982), inner hair cell receptor potentials (Brown and Nuttall, 1984), ensemble background activity of the auditory nerve (Lima da Costa *et al.*, 1997) and responses of single auditory afferent nerve fibers (Buño, 1978; Wiederhold and Kiang, 1970; Warren and Liberman, 1989a, b; Kawase *et al.*, 1993). The MOC effects on cochlear function, whether suppressive (i.e., Warren and Liberman, 1989a, b; Kawase *et al.*, 1993) or enhancing (Neider and Neider, 1970;

[a)]These data were presented in preliminary form at 11th International Symposium on Hearing, 1–6 August, Belton Woods, Grantham, United Kingdom (Smith, 1998) and at the 22nd Midwinter Research Meetings of the Association for Research in Otolaryngology, 13–18 February 1999 (Smith *et al.*, 1999).

[b)]Corresponding author: Dr. David W. Smith, Hearing Research Laboratories, Division of Otolaryngology-Head and Neck Surgery, Box 3550, Duke University Medical Center, Durham, NC 27710; electronic mail: earsdws@duke.edu

Dolan and Nuttall, 1988; Kawase and Liberman, 1993; Kawase *et al.*, 1993; Lima da Costa, 1997), are reduced or blocked when efferent tracts are interrupted or eliminated.

Demonstration of MOC-mediated changes in cochlear function are not limited to acute physiological preparations in nonhuman species. With the advent of otoacoustic emission (OAE) measurement techniques (Kemp, 1978; Kemp and Chum, 1980; Kemp and Souter, 1988) it has become possible to measure the mechanical response of the OHCs and basilar membrane. Otoacoustic emissions reflect a reverse traveling wave resulting from OHC activity, whether spontaneously generated, or in response to acoustic stimulation (Probst *et al.*, 1991). Mott *et al.* (1986) have shown that contralateral acoustic stimulation can produce orderly shifts in the frequency, and reductions in the amplitude, of spontaneous otoacoustic emissions in humans. Numerous experimental studies in humans have shown that contralateral noise reduces the amplitude of OAEs (Collet *et al.*, 1990; Veuillet *et al.*, 1991; Rossi *et al.*, 1993; Williams and Brown, 1995). Like the acute physiological studies in nonhuman animals, the effects of contralateral stimulation on OAEs disappear following sectioning of the vestibular nerve in clinical patients (Williams *et al.*, 1993; Scharf *et al.*, 1994).

The physiological data are suggestive of a role for the cochlear efferent system in influencing hearing. Given the extent, and agreement, of the physiological literature on contralateral MOC activity, it is somewhat surprising that few, if any, analogous psychophysical data have been reported as indicating a perceptual counterpart.

Scharf *et al.* (1994) reported data from one patient who underwent a vestibular neurectomy for intractable vertigo, which should have the effect of removing all efferent innervation from the operated ear. While they present OAE suppression data which support that belief (contralateral suppression of OAE amplitude was eliminated following surgery), they report no difference between the operated and unoperated ears in the effectiveness of contralateral noise to increase thresholds. To determine if MOC activity could shift psychophysical thresholds, Strickland and Viemeister (1995) measured increases in threshold for a 20-ms sinusoidal stimulus in the presence of pulsed contralateral noise using a paradigm analogous to that employed with compound action potentials by Liberman (1989). The increase in threshold was 4–5 dB at frequencies of 1.0 to 4.0 kHz, but was not demonstrable in all subjects, or for pure-tone maskers. The investigators also reported a decrease in the selectivity of psychophysical tuning curves in the presence of the contralateral noise.

While not directly conceived to address the role of the MOC system in binaural interactions, the psychophysical literature on ''central masking'' provides evidence that contralateral sound activation does produce systematic changes in absolute thresholds. Central masking, where detection threshold for a brief tone in the test ear is increased by the presence of low-level sound presented in the contralateral ear, was first reported by Wegel and Lane (1924). In central masking, the magnitude of the threshold shift is dependent on the relative onset of the contralateral masker and test tone, with the largest threshold shifts occurring when the onset of the two signals is coincident in time (Zwislocki *et al.*, 1967). This paradigm, however, would not allow sufficient neural conduction time for the contralateral stimulation to reach the test cochlea (Lima da Costa *et al.*, 1997). With longer onset delays, where the onset of the contralateral masker precedes the onset of the target signal by more than 60–100 ms, allowing for adequate binaural neural conduction times, or with continuous contralateral maskers, the magnitude of contralateral suppression ranges, with contralateral noise level, between 2 and 6 dB depending on the contralateral noise level (Ingham, 1959; Lidén *et al.*, 1959; Dirks and Norris, 1966; Blegvad, 1967; Zwislocki *et al.*, 1967, 1971; Snyder, 1973; Benton and Sheeley, 1987).

When consideration is given to whether or not some aspects of central masking are dependent on MOC efferent mechanisms (i.e., where masker test-tone onset delays are sufficient for inter-cochlear neural conduction times), it is important to point out that many, if not most of the MOC physiological and central masking studies reported in the literature have employed comparable, if not identical, continuous contralateral stimulus paradigms (e.g., Kawase and Liberman, 1993; Kawase *et al.*, 1993; Puria *et al.*, 1996; Lima da Costa *et al.*, 1997). That so many efferent studies have employed a stimulus paradigm like that used in studies of central masking, produced comparable shifts in ipsilateral cochlear function, and showed that these effects are eliminated when the MOC tracts are sectioned, suggests that at least some aspects of central masking might be efferent-mediated peripheral processes. Indeed, several investigators have previously suggested that central masking is an efferent process (Lidén *et al.*, 1959; Blegvad, 1967; Winslow and Sachs, 1987; Warren and Liberman, 1989a).

In summary, the current physiological literature indicates that contralateral acoustic stimulation produces orderly changes in cochlear physiological function, which are known to be mediated by the MOC efferent tracts. While the psychophysical literature is suggestive of a role for the MOC efferent tracts in central masking, to date there has been no conclusive demonstration of that relationship. The present data are from psychophysical studies of central masking in nonhuman primates. The goal of this research was to demonstrate if the MOC efferent system plays a role, comparable to that played in contralateral efferent suppression, in central masking.

I. METHODS

A. Subjects

Four juvenile male Japanese macaques (*Macaca fuscata*), obtained as culls from a federally funded regional primate center, served as subjects in this study. All weighed between 3 and 6 kg at the outset of the study, and were maintained on a calorie-restricted diet to facilitate the use of food as a reward in an operant reinforcement paradigm for training and testing.

The care and use of the animals in this research was approved by the Duke University Institutional Animal Care and Use Committee.

B. Behavioral apparatus

All behavioral test sessions were carried out in two individual-sized, single-walled sound-attenuating chambers (Acoustic Systems, Austin, TX) which were housed inside a large, double-walled sound-attenuating room (Industrial Acoustics Company, Brooklyn, NY). The subjects were seated in custom-designed restraint chairs, which were fixed to the test chamber during testing to restrict the movement of the animal relative to the experimental apparatus. Head movement was restricted by placing the animal's muzzle through a set of uprights, and a stop behind the head. A feeder trough was mounted to the chair within easy reach of the animal's mouth. The wall directly in front of the subject contained a response key and a cue light which served to communicate the experimental conditions to the animal at all times. Stimulus presentation and all experimental parameters were under computer control.

C. Stimuli, transducers and calibration

Stimulus waveforms were computed by a PC-based array processor and generated by a rack-mounted digital-to-analog converter (Tucker-Davis Technologies, Gainesville, FL). The output of the digital-to-analog convertor was passed successively through two programmable attenuators (Tucker-Davis Technologies), an anti-aliasing filter, a passive attenuator to reduce line noise, to Etymotic ER-1 (Etymotic Research, Elk Grove Village, IL) insert earphones. Noise stimuli were created by passing the output of a waveform generator (Tucker-Davis Technologies), though a programmable filter (Tucker-Davis Technologies). As with the pure-tone stimuli, noise levels were controlled by feeding the signal through two programmable attenuators to the earphones. The transducer boxes were fixed to the head stop so that when the earphone tip was inserted into the ear canal, the tube of the earphone was out of the reach of the animal. The earphone terminated in a 10-mm long pediatric foam eartip, which was inserted approximately 6 mm into the ear canal after compression. Once inserted, the eartip expanded to a tight fit which was sufficient to hold the earphone in place, without moving, during the test sessions.

A separate calibration was performed for each insert earphone, *in vivo*. In this procedure, a subject was sedated and fitted with an insert earphone in one, or both ears. A calibrated probe microphone (B&K, Type 4134, adapted according to Sokolich, 1981) was inserted through the foam ear tip, and positioned within the ear canal, approximately 2-mm beyond the tip of the earphone. A periodic, pseudorandom electrical noise was presented to the earphone with a clock rate of 200 kHz, and a period of 20.48 ms. To ensure adequate energy for accurate measurements at high frequencies, where both transducer and probe microphone show reductions in sensitivity, the magnitude of the noise was flattened to 2.5 kHz, and then raised at 20 dB/decade to 40.0 kHz. The microphone signal was amplified by a B&K 2610 measuring amplifier and sampled by a custom, PC-based 18-bit, analog-to-digital convertor. Both the microphone signal and digital-to-analog convertor output were averaged by the collection computer over 200 cycles of pseudorandom noise. The spectra of the averaged signals were computed by Fourier Transform, and corrected according to the frequency/phase response of the probe microphone to compute the actual acoustic spectrum in the ear canal. Finally, the system transfer function was computed as a ratio of the two spectra.

Acoustic crosstalk was estimated by measuring in one ear, the presence of the pseudorandom noise presented to opposite ear. Interaural attenuation was approximately 50 dB at 100 Hz, increased gradually from 60 dB at 200 Hz to >70 dB at 500–700 Hz, and rose to >80 dB at frequencies above 1.0 kHz. Given the high-frequency limitations of both the ER-1 earphones and the B&K 4134 condensor microphones, acoustic crosstalk could not be measured above 10.0 kHz (>80 dB).

Pure-tone thresholds were measured for 1-s sinusoidal stimuli at frequencies between 73 Hz and 31.5 kHz. In general, the spectrum varied ± 8 dB between 50 Hz and 16.0 kHz, then decreased rapidly to approximately 20.0 kHz. Pure-tone frequencies were restricted in these studies to frequencies of 1–4.0 kHz because the spectrum was relatively flat (± 2 dB) within one octave of each test-tone frequency.

Contralateral noise was band limited, two-octave wide, centered at the test tone frequency. Contralateral noise levels were set relative to threshold in the contralateral ear for the pure-tone stimulus presented in the test ear. The noise, when presented, came on when the animal initiated a trial sequence by making contact with the lever, then remained on continuously so long as the subject maintained contact. Because of the normal shape of the threshold contour across frequency, the maximum noise levels presented varied with frequency, and were limited to different absolute levels based on acoustic crosstalk measurements.

D. Behavioral procedure

The behavioral procedures used in this study are comparable to those used previously and have been described in more detail elsewhere (Smith and Olszyk, 1997). The animals were trained using positive reinforcement in an operant reinforcement paradigm. Following presentation of a flashing cue light, the subject was trained to initiate a trial by making contact with the response lever. When contact was made, the light would remain on without flashing for the duration of the trial sequence. If the subject maintained contact with the lever through out the required hold intervals (1–8 s, with an average delay of 5 s), the test stimulus was presented and the animal was required to release the key to indicate signal detection. A correct response (i.e., releasing the key in the presence of the test signal) was followed by delivery of a 190-mg banana-flavored pellet (P. J. Noyes, Lancaster, NH) through the feeder trough. Releases of the lever at any other time (i.e., a false alarm) resulted in a 3–5-s timeout, during which the cuelight was extinguished and the subject was required to wait before initiating a subsequent trial sequence.

Stimulus intensity at the outset of a trial sequence was set at approximately 35 dB above the typical threshold for that frequency. Thresholds were determined using a tracking procedure, where stimulus intensity was adjusted on a trial-to-trial basis by decreasing the intensity 5 dB for the subsequent trial following a correct response. Likewise, a miss

resulted in a 5-dB increase in stimulus intensity for the subsequent trial. The change from a hit to a miss, or vice versa, defined a transition. Six transitions were presented and threshold for a given frequency was defined as the stimulus intensity at which 50% signal detection was reported.

Twenty percent of all trials were ''catch trials,'' where all experimental parameters were identical to a test-tone trial, except the test signal was withheld. As a routine procedure, data from sessions where the subject responded to more than 20% of the catch trials were not used in summary data calculations. In the present studies, however, there were no such sessions and the average response to catch trial rate was approximately 1%.

Data were collected in daily testing sessions lasting 2.5–3.5 h. Thresholds presented here were the average of at least 15 thresholds at each frequency.

E. Surgical procedures for section of the MOC efferent system

In order to determine if the increases in threshold observed in the presence of contralateral noise were influenced by the medial olivocochlear system, we attempted to cut the MOC fibers as they crossed the floor of the IVth ventricle in one subject. To section the MOC, subject M04 was anesthetized with acepromazine (1.65 mg/kg, i.m.) and isoflurane (2%, inhalation), and a midline incision was performed in the posterior occipital region, and several small holes were drilled in the posterior fossa. The posterior fossa was then thinned to the level of the dura, from the foramen magnum to the transverse sinus on either side. After the sinuses were identified, the dura was opened under the microscope, from the foramen magnum to superiorly and laterally at the edges of the sinuses on either side. The cerebellum was exposed and a Maroon retractor was placed in the muscle. The cerebellum was opened over the vermis in the midline, and the obex was located, beginning from the foramen magnum. The floor of the IVth ventricle was exposed from the obex to beyond the facial colliculus on each side, under the microscope. The remaining cerebellum was retracted superiorly using the Maroon retractor, and landmarks on the floor of the IVth ventricle were identified according to the descriptions given by May and MacQuone (1995). A small Beaver-blade knife was then used to make vertical knife cuts, parallel to the midline, on the floor of the IVth ventricle, just lateral to the facial colliculus on each side. Bilateral cuts in this manner should produce complete loss of MOC efferents to both ears. The cerebellum was then allowed to return to the usual position, and the dura was closed with a fine suture. The muscle and skin were then closed over the posterior fossa defect.

F. Histological evaluation of the MOC section

Control (normal) cochleae were prepared for histological examination as described by Sato *et al.* (1997), with the modification that the bones were decalcified in a microwave oven according to the protocol of Madden and Henson (1997).

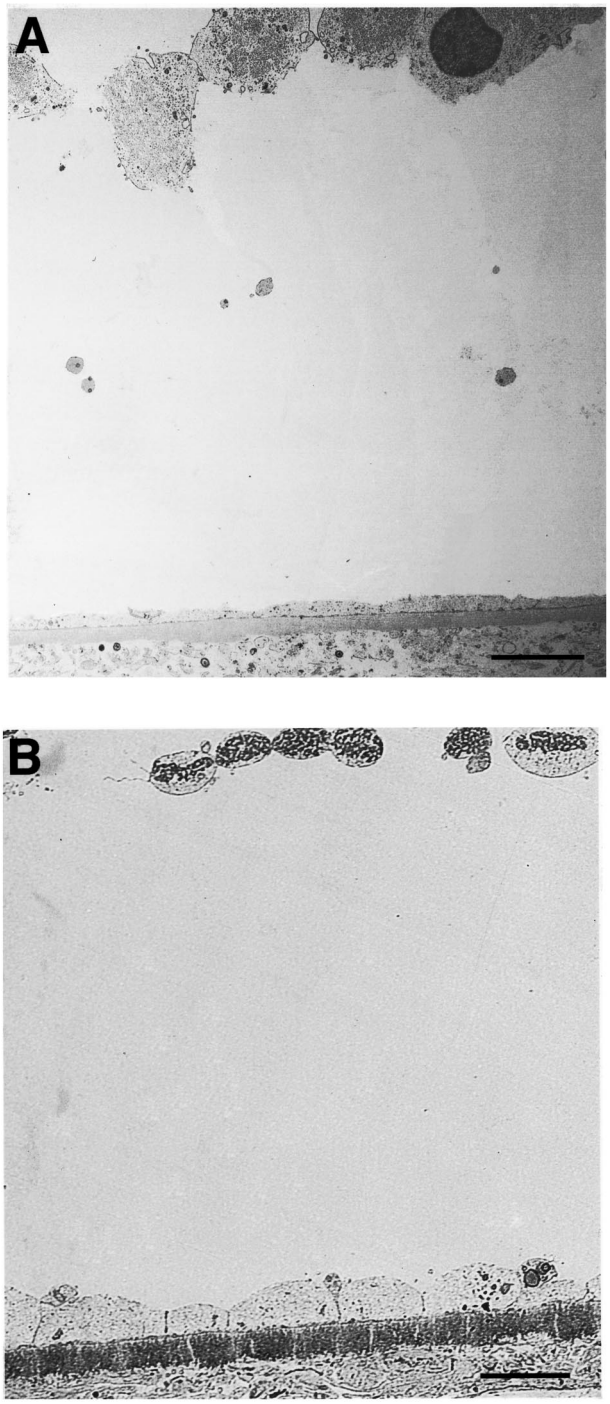

FIG. 1. (A) Cross-section of the tunnel of Corti in a normal, control cochlea, showing approximately one crossing bundle or group for each pillar cell. Typically, each group consists of one to several fibers. Bar=0.5 μm. (B) Cross sections of tunnel of Corti in the experimental cochleae, where very few crossing bundles could be found and there were long expanses where none could be seen. Bar=0.5 μm. Based on these findings, and the extensive TEM examination of the cochleae (see text for details), it was concluded that the lesion of the MOC in the cochlea was complete.

Forty-one outer hair cells from each of the right and left cochleae from subject M04 were examined in the transmission electron microscope for evidence of normal efferent endings. One ending was found in the right cochlea and two in the left. Although these were identified as ''probable'' efferent endings on the basis of position and size, no clear

synaptic specializations were observed. In addition, cross-sections of the tunnel of Corti were examined for the presence of tunnel crossing fibers (Fig. 1). In normal cochleae these were observed at regular intervals [Fig. 1(A)], approximately one crossing bundle or group for each pillar cell, with each group consisting of one to several fibers; in the experimental cochleae very few could be found and there were long expanses where none could be seen [Fig. 1(B)].

Based on these findings, it was concluded that the lesion of the MOC in the cochlea was complete.

II. RESULTS

A. Absolute thresholds

Contralateral noise levels in the present studies were set relative to detection threshold in the test ear (dB SL). The primary reason for this decision was that many auditory phenomena, including the active mechanical behavior of OHCs, are sensitive to the level above threshold at which they occur. Moreover, setting the contralateral noise in dB SL allows direct comparisons of changes at all frequencies, regardless of the absolute threshold level. Since our intention was to monitor changes in sensitivity by an interaction of the two ears, measuring normal thresholds in both ears was a necessary precursor to contralateral stimulation conditions.

At all test-tone frequencies used in the present studies, the absolute behavioral thresholds for these animals were comparable both across animals and with thresholds presented in the literature for other macaques species, and have been described in detail elsewhere (Smith and Olszyk, 1997). For each animal, thresholds measured in both right and left ears were within 6 dB at all test frequencies.

B. Changes in absolute threshold with continuous contralateral noise

Figure 2 presents threshold shifts at 1.0, 2.0 and 4.0 kHz, averaged across all four subjects, in the presence of contralateral noise at 10, 30 and 60 dB SL. On average, when measured in the presence of contralateral noise, presented at levels of 30 dB SL and above, thresholds were *increased*, or *suppressed*, relative to thresholds measured in quiet, in a manner that was intensity dependent. Across the test frequencies presented here, averaged thresholds were 1–2 dB higher in the presence of 30 dB SL noise, than when measured in quiet. When the contralateral noise was increased to 60 dB SL, thresholds were suppressed in a frequency-dependent manner, being, on average, 2.1 dB higher at 1.0 kHz, 4.1 dB higher at 2.0 kHz and 6.0 dB at 4.0 kHz, as compared with thresholds measured in quiet.

An examination of the group data from Fig. 2 suggests that thresholds are increased in an intensity and frequency-dependent manner. A statistical comparison of thresholds measured in noise with those measured in quiet demonstrated that thresholds at 2.0 and 4.0 kHz, measured in the presence of the 60 dB SL contralateral noise, were significantly higher than those measured in quiet (paired *t* test; $P<0.05$).

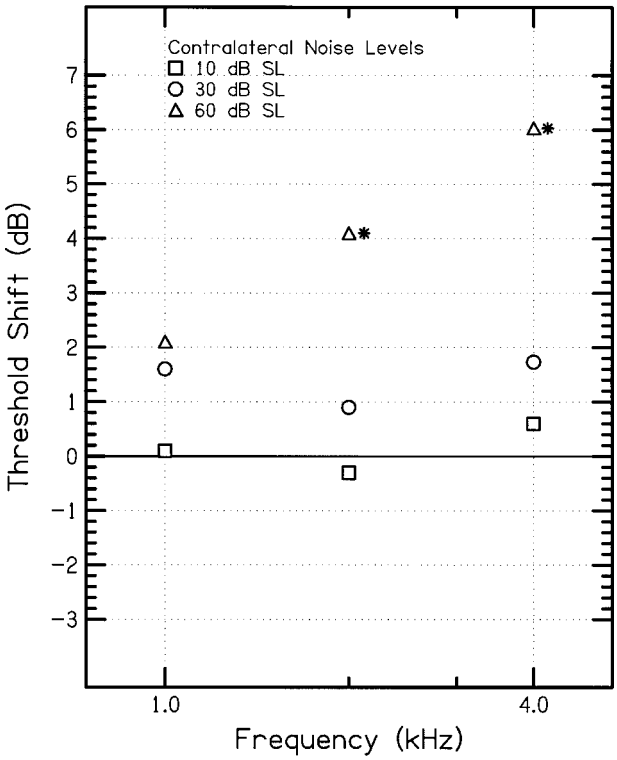

FIG. 2. Threshold shifts, averaged across subjects M03, M04, M05 and M06, measured in the presence of continuous contralateral noise (see text for details of the noise paradigm). Averaged thresholds are presented for the frequencies of 1.0, 2.0 and 4.0 kHz and contralateral noise levels of 10, 30 and 60 dB SL. The magnitude of the shifts was determined by subtracting the absolute threshold measured in quiet from the threshold measured with the same stimulus in the presence of continuous contralateral noise. Asterisks (*) denote threshold shifts where the averaged absolute thresholds in the presence of the contralateral noise are statistically greater than thresholds measured to the same stimuli in quiet (paired *t*; $P=0.05$).

C. Effects of MOC lesion on contralateral noise-induced threshold shifts

To determine if threshold increases measured in the presence of continuous contralateral noise were dependent on MOC activation, one subject underwent a surgical sectioning of the MOC on the floor of the IVth ventricle. The left panel of Fig. 3 shows the individual baseline, presurgery threshold shifts at 1.0, 2.0 and 4.0 kHz, as a function of contralateral noise level, for subject M04. There was a trend for thresholds to increase with contralateral noise level, reaching an average maximum of 5.0 dB at 1.0 kHz (60 dB SL noise level). A statistical comparison of thresholds measured in noise with those measured in quiet indicated that thresholds measured at 1.0, 2.0 and 4.0 kHz in the presence of 60 dB SL contralateral noise were significantly higher than those measured in quiet (paired *t* test; $P<0.05$).

Absolute thresholds for this animal were unaffected by the MOC lesion. Following surgery the significant increases in threshold seen with higher contralateral noise levels were substantially reduced, or eliminated (Fig. 3, right panel). At 1.0 and 2.0 kHz, a residual 2-dB increase in thresholds was apparent at both 1.0 and 2.0 kHz test frequencies, though this shift did not reach statistical significance.

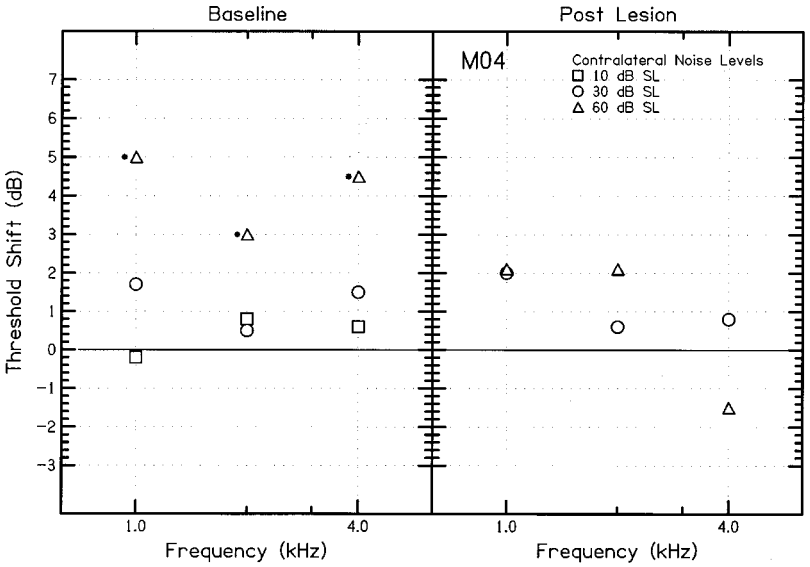

FIG. 3. The left panel shows average baseline, absolute threshold shifts measured in the presence of continuous contralateral noise (see text for details of the noise paradigm) for subject M04. Averaged thresholds are presented for the frequencies of 1.0, 2.0 and 4.0 kHz and contralateral noise levels of 10, 30 and 60 dB SL. The right panel shows average, absolute threshold shifts, following surgical lesiong of the MOC efferent system on the floor of the IVth ventricle. The magnitude of the shifts was determined by subtracting the absolute threshold measured in quiet from the threshold measured with the same stimulus in the presence of continuous contralateral noise. Asterisks (*) denote threshold shifts where the averaged absolute thresholds in the presence of the contralateral noise are statistically greater than thresholds measured to the same stimuli in quiet (paired t; $P=0.05$).

III. DISCUSSION

Behavioral thresholds were compared in quiet and in the presence of continuous, contralateral two octave-band noise. At contralateral noise levels of 30 dB SL and above, thresholds were increased, or suppressed, relative to those measured in quiet, in a manner that was both frequency and intensity dependent. Threshold shifts, however, only reached statistical significance for contralateral noise levels of 60 dB SL. Suppression reached a maximum, on average, of 6.0 dB at 4.0 kHz (60 dB SL noise level). These findings are in good agreement with earlier measurements of contralateral suppression in the same animals using continuous, contralateral broadband noise (Smith, 1998). This suppression was reduced or eliminated in one subject following elimination of the MOC via sectioning the crossed-olivocochlear bundle on the floor of the IVth ventricle.

Importantly, these psychophysical findings are in complete agreement, in terms of the frequency and intensity dependence and the magnitude of suppression, with both the extant physiological MOC contralateral suppression and central masking literatures.

A. Physiological mechanisms of contralateral noise-induced increases in threshold

In principle, contralateral noise could produce the noted threshold increases in the ipsilateral ear by at least three different peripheral physiological mechanisms: direct masking via acoustic crosstalk; acoustic/middle ear reflex; and medial olivocochlear suppression. It is also possible, of course, that purely central mechanisms might account for the data.

If the contralateral noise were sufficient in level to be detectable in the ipsilateral ear, transmitted as either an air borne or bone-conducted stimulus, thresholds would be increased by direct masking of the target stimulus. Several pieces of data, however, argue against acoustic crosstalk as having a role in the thresholds seen in with contralateral noise. First, we have estimated the interaural attenuation in our animals (see Methods section) and, at the frequencies where the threshold shifts are greatest, between 1.0 and 4.0 kHz, the interaural attenuation is, in general, >70–80 dB. Yet, data presented here and in our previous studies in these same animals (Smith, 1998), have shown that measurable threshold shifts are evident at contralateral noise levels as low as 30 dB SPL (e.g., 30 dB SL noise for a 0 dB SPL absolute threshold at 4.0 and 8.0 kHz).

Second, to determine what effects crosstalk might have on thresholds, we have measured shifts in threshold for the condition where a wide band noise is presented to the ipsilateral ear at levels of 30–70 dB SPL. In these four subjects, thresholds between 1.0 and 8.0 kHz were, on average, unaffected by noise at 30 dB SPL, and the average threshold was increased 7 dB when the noise level was increased to 40 dB SPL. This means that, to produce a threshold shift of, say, 5–7 dB (a shift comparable to that seen in the presence of contralateral noise), the noise level in the ipsilateral ear would need to be, for the noise bandwidth and transducers employed, approximately 30–40 dB SPL. Based on our acoustic crosstalk measurements preformed *in vivo*, at the affected frequencies, the contralateral noise levels necessary to produce 30–40 dB SPL of ipsilateral noise level would be greater than 100–110 dB SPL, far above those used in the present studies.

Finally, if the measured threshold shifts were solely a result of acoustic crosstalk, the MOC lesion should not have any measurable effect on the ability of the contralateral noise to influence ipsilateral thresholds. In subject M04, the ability of contralateral noise to influence thresholds was significantly reduced following the surgical sectioning of the MOC efferents.

Likewise, the general characteristics of the middle-ear reflex suggest it unlikely that contraction of the middle-ear muscles could account for the threshold elevations noted with contralateral noise. In most species, the acoustic reflex can be elicited by both ipsilateral and contralateral acoustic stimuli of >70 dB SPL (Pang and Peake, 1986), far exceeding the levels necessary to produce measurable alterations in threshold in the present studies, which were approximately 30–40 dB SPL. Furthermore, when activated, the acoustic reflex reduces acoustic transmission through the middle ear, primarily by increasing the stiffness of the ossicular chain by

contraction of the stapedius muscle. Thus, because only low-frequency transmission is stiffness dependent (i.e., <1.0 kHz), the increased impedance of the middle ear would not likely affect thresholds above 1.0 kHz (Pang and Peak, 1986), where the largest effects were observed in the present studies.

The medial olivocochlear neurons arise from regions in the brainstem surrounding the ipsilateral and contralateral medial superior olives, and reach out to synapse, characteristically, under the OHCs in the organ of Corti (cf. Warr *et al.*, 1986), where they play a primary role in influencing cochlear responses by modulating the mechanical behavior of the OHCs. Perhaps the most widely studied and best understood effect of MOC activity is that of suppressing contralateral OHC and cochlear activity (cf. Buňo, 1978; Siegel and Kim, 1982; Warren and Liberman, 1989a, b; Lima da Costa *et al.*, 1997). Many of these studies have reported increases in the various measures of neural/physiological threshold when the MOC is activated by contralateral noise (Mountain, 1980; Warren and Liberman, 1989a, b; Kawase *et al.*, 1993; Puria *et al.*, 1996; Lima da Costa *et al.*, 1997). They are thought to exert their influences over OHC mechanical behavior by altering the conductance of the hair cell membrane (Flock and Russell, 1976; Art *et al.*, 1984). In keeping with the current data, MOC physiological suppression is greatest at frequencies of 1.0 to 10.0 kHz (cf. Guinan and Gifford, 1988; Warren and Liberman, 1989b), with the magnitude of the suppression increasing in an intensity dependent manner. This frequency distribution corresponds to the areas of the basilar membrane which contain the highest density of MOC innervation (Guinan *et al.*, 1984; Liberman *et al.*, 1990; Sato *et al.*, 1997). In all of these studies, the effects of the MOC activation are eliminated when the MOC tracts are interrupted.

It is important to emphasize the high degree of correspondence between the magnitude of threshold shifts (i.e., suppression) produced by the presence of contralateral noise in the present study in nonhuman primates, and that reported in previous studies of ''central masking'' using comparable stimulus conditions in human observers: Numerous psychophysical studies have reported 2–6 dB increases in threshold under continuous contralateral noise (Ingham, 1959; Lidén *et al.*, 1959; Dirks and Norris, 1966; Blegvad, 1967; Snyder, 1973; Benton and Sheeley, 1987). Zwislocki *et al.* (1967, 1971) argued that central masking is best measured under stimulus conditions where the onset of the target signal is coincident with the onset of the contralateral masker: Under these conditions thresholds are elevated by as much as 12 dB, or more, depending on the masker level. With progressive increases in the delay between the onset of the masker and target signal, the magnitude of the threshold shift decreases to a steady state, intensity-dependent level of 2–6 dB by 60–120 ms. Indeed, Lima da Costa *et al.* (1997) have shown this steady-state suppression can be maintained for minutes, or hours. We argue here that this steady-state level is the same as that measured with continuous contralateral noise, both psychophysically (Ingham, 1959; Lidén *et al.*, 1959; Dirks and Norris, 1966; Blegvad, 1967; Snyder, 1973; Benton and Sheeley, 1987) and physiologically (Kawase *et al.*, 1993; Puria *et al.*, 1996; Lima da Costa *et al.*, 1997; Perry *et al.*, 1999), and is a peripherally based MOC response.

B. Rethinking ''central masking''

Numerous previous studies have measured changes in pure-tone thresholds with various contralateral stimuli in order to characterize the phenomenon of central masking (Ingham, 1959; Lidén *et al.*, 1959; Dirks and Norris, 1966; Blegvad, 1967; Zwislocki *et al.*, 1967, 1968; Zwislocki, 1971; Snyder, 1973; Benton and Sheeley, 1987). For lack of evidence of an appropriate peripheral mechanism, the effect was originally attributed to central processes (Ingham, 1957; Lidén *et al.*, 1959; Snyder, 1973), and this attribution may explain the lack of appreciation that these data may reflect the effects of the efferent system in auditory psychophysical phenomena. Importantly, the preponderance of the central masking literature was established before the first characterizations of the role of the MOC system in the physiology of peripheral auditory system function.

Two points are worth mentioning here: First, most previous psychophysical studies have used continuous contralateral maskers (Ingham, 1959; Lidén *et al.*, 1959; Dirks and Norris, 1966; Blegvad, 1967; Snyder, 1973; Benton and Sheeley, 1987), comparable to those used in the efferent physiological literature (cf. Kawase *et al.*, 1993; Puria *et al.*, 1996; Lima da Costa *et al.*, 1997; Perry *et al.*, 1999) and to those used in the present psychophysical studies. The similarities seen in the suppressive effects of these continuous contralateral stimuli on behavioral thresholds in humans and monkeys, and on compound action potentials, single afferent fiber responses, and otoacoustic emissions suggests a common mechanism. The repeated physiological demonstration that this suppression in greatly reduced, or eliminated, following interruption of the MOC tracts indicate these perceptual changes are likewise due at least in part to efferent activity.

Second, these efferent physiological demonstrations do not exclude the possibility that a purely ''central'' binaural interaction is also not at work. As described above, Zwislocki *et al.* (1967) has used pulsed maskers and test tones to show that the largest changes in thresholds occur when the onset of the masker is coincident with the onset of the test tone, and the masking effects decrease rapidly with delay between the onset of the two signals. This timing effect is far too fast to allow for input from one ear to neurally mediate a suppressive effect in the opposite ear. For example, the time constant for MOC activation, in the guinea pig, is greater than 10–50 ms (Wiederhold and Kiang, 1970; Brown and Nuttall, 1984; Lima da Costa *et al.*, 1997).

As a practical issue, the effects of contralateral noise on ipsilateral thresholds have long been known in the clinical literature where, when measuring thresholds in an impaired ear with more than a 40–60 dB threshold shift, it is suggested that one present masking noise in the contralateral, more sensitive ear to prevent detection of the intense test signal via transcranial conduction (Palva, 1954; Lidén *et al.*, 1959; Dirks and Malmquist, 1965; Martin *et al.*, 1962; Martin, 1972; Snyder, 1973; Studebaker, 1964, 1967). This lit-

erature suggests that a corrective factor of 5–10 dB should be subtracted from threshold shifts measured with the contralateral noise to compensate for increases in threshold due to ''central masking'' (Snyder, 1973). Lidén *et al.* (1959) and Blegvad (1967) suggested that this effect (central masking) is a peripheral phenomenon and is mediated by the efferent pathways. It is not clear, however, how the contralateral suppression process might be effected by the cochlear hearing loss and the associated OHC damage.

A reinterpretation of central masking results reported in the human psychophysical literatures in the context of the growing efferent literature, including the present study, suggests that the classical phenomenon of central masking may involve (at least) two different processes, each acting at a different level within the auditory system.

When equated for stimulus conditions, there can be little doubt that central masking under continuous contralateral noise, including long noise-target onset delays with pulsed maskers, is a psychophysical manifestation of medial olivocochlear efferent function. This phenomenon likely reflects the ''steady-state'' central masking response described originally by Zwislocki *et al.* (1967). As this process has been extensively characterized in numerous physiological studies as being determined by MOC activity, it may be better termed ''psychophysical contralateral efferent suppression,'' in keeping with the convention established in the physiological literature.

The present data and discussion do not, however, address the ''transient'' central masking response produced by pulsed contralateral maskers with noise-target onset delays of $<$100 ms (Dirks and Norris, 1966; Zwislocki *et al.*, 1967; Zwislocki, 1971). This function may very well reflect a purely central process, as the briefer noise-target delays are too short for adequate neural conduction times permitting contralateral efferent activity to directly affect ipsilateral cochlear activity. It is possible that the relatively large ''transient'' threshold shifts seen with masker-target signal onset delays of $<$20 ms might be attributed to other mechanisms, such as ''confusion,'' given the difficulty of the pulsed-masker paradigm (Trahiotis, *personal communication*). Warren and Liberman (1989b) have shown that the magnitude of contralateral efferent suppression decreases when contralateral stimuli are shorter than 100 ms which, as a result, produce masker-target onset delays of $<$100 ms. This finding indicates that the relatively larger transient central masking effects cannot be an efferent-mediated *peripheral* effect and should be termed, as it is currently referred to, as ''central masking.''

Finally, and importantly, this clarification of the role of the efferent system in ''central masking'' indicates that a substantial psychophysical literature on cochlear efferent function has existed for several decades in the form of central masking studies.

IV. SUMMARY

The changes in psychophysical thresholds produced by contralateral noise in the present study are both qualitatively and quantitatively similar to descriptions of contralateral physiological suppression in the extensive experimental and clinical physiological literatures, which are known to be produced by the MOC efferents. These comparisons, and the fact that many of the studies comprising both the psychophysical central masking and physiological MOC literatures employed comparable continuous contralateral noise stimulus paradigms, and yield comparable cochlear effects, suggest that the psychophysical threshold shift produced by contralateral noise, e.g., central masking, is likewise efferent mediated.

This notion is further supported by the fact that the contralateral noise effects measured in the present study, at least in one subject studied (M04), were reduced, or eliminated when the MOC was sectioned at the floor of the IVth ventricle. These data, therefore, indicate that central masking effects produced by long target stimulus/masker delays, or by continuous contralateral noise conditions, are mediated by peripheral, MOC efferent mechanisms.

ACKNOWLEDGMENTS

The authors are indebted to Dr. Jean-Marie Aran for insightful discussions concerning efferent function. We are also thankful for collaborations with Dr. Chris van den Honert concerning the calibration algorithm and the *in vivo* sound level measurements, and Dr. Bruce Weber for discussions concerning insert earphones. This paper benefitted from thoughtful comments by Dr. O.W. Henson, Jr., Dr. Emily Buss, Dr. John H. Grose, and Dr. Joseph W. Hall. This research was funded by the National Institutes of Health, National Institute for Deafness and Other Communication Disorders (DC 001692).

Art, J. J., Fettiplace, R., and Fuchs, P. A. (**1984**). ''Synaptic hyperpolarization and inhibition of turtle cochlear hair cells,'' J. Physiol. (London) **356**, 525–550.

Benton, S. L., and Sheeley, E. C. (**1987**). ''Effects of three contralateral maskers on pure-tone thresholds using manual audiometry,'' Audiology **26**, 227–234.

Blegvad, B. (**1967**). ''Contralateral masking and Békésy audiometry in normal listeners,'' Acta Oto-Laryngol. **64**, 157–165.

Brown, M. C., and Nuttall, A. L. (**1984**). ''Efferent control of cochlear inner hair cell responses in the guinea pig,'' J. Physiol. (London) **354**, 625–646.

Brownell, W. E., Bader, C. R., Bertrand, D., and Ribaupierre, Y. (**1985**). ''Evoked mechanical response of isolated cochlear outer hair cells,'' Science **227**, 194–196.

Buño, W. (**1978**). ''Auditory nerve fiber activity influenced by contralateral ear sound stimulation,'' Exp. Neurol. **59**, 62–74.

Collet, L., Kemp, D. T., Veuillet, E., Duclaux, R., Moulin, A., and Morgan, A. (**1990**). ''Effects of contralateral auditory on active cochlear micromechanical properties in human subjects,'' Hear. Res. **43**, 251–262.

Dirks, D. D., and Norris, J. C. (**1966**). ''Shifts in auditory thresholds produced by ipsilateral and contralateral maskers at low-intensity levels,'' J. Acoust. Soc. Am. **40**, 12–19.

Dirks, D., and Malmquist, C. (**1965**). ''Shifts in air conduction thresholds produced by pulsed and continuous contralateral maskers,'' J. Acoust. Soc. Am. **37**, 631.

Dolan, D. F., and Nuttall, A. L. (**1988**). ''Masked cochlear whole-nerve response intensity functions altered by electrical stimulation of the crossed olivocochlear bundle,'' J. Acoust. Soc. Am. **83**, 1081–1086.

Fex, J. (**1967**). ''Efferent inhibition in the cochlea related to hair cell DC activity: Study of postsynaptic activity of the crossed olivocochlear fibers in the cat,'' J. Acoust. Soc. Am. **41**, 666–675.

Flock, Å., and Russell, I. J. (**1976**). ''Inhibition of efferent nerve fibres, action on hair cells and afferent synaptic transmission in the lateral line canal of the burbot *Lota lota*,'' J. Physiol. (London) **257**, 45–62.
Guinan, Jr., J. J., and Gifford, M. L. (**1988**). ''Effects of electrical stimulation of efferent olivocochlear neurons on cat auditory-nerve fibers. III. Tuning curves and thresholds at CF,'' Hear. Res. **37**, 29–46.
Guinan, Jr., J. J., Warr, W. B., and Norris, B. E. (**1984**). ''Topographic organization of the olivocochlear projections from lateral and medial zones of the superior olivary complex,'' J. Comp. Neurol. **226**, 21–27.
Ingham, J. G. (**1959**). ''Variations in cross-masking with frequency,'' J. Exp. Psychol. **58**, 199–205.
Kawase, T., Delgutte, B., and Liberman, M. C. (**1993**). ''Antimasking effects of the olivocochlear reflex. II. Enhancement of auditory-nerve response to masked tones,'' J. Neurophysiol. **70**, 2533–2548.
Kawase, T., and Liberman, M. C. (**1993**). ''Antimasking effects of the olivocochlear reflex. I. Enhancement of compound action potentials to masked tones,'' J. Neurophysiol. **70**, 2519–2532.
Kemp, D. T. (**1978**). ''Stimulated acoustic emissions from the human auditory system,'' J. Acoust. Soc. Am. **64**, 1386–1391.
Kemp, D. T., and Chum, R. (**1980**). ''Properties of the generator of stimulated acoustic emissions,'' Hear. Res. **2**, 213–232.
Kemp, D. T., and Souter, M. (**1988**). ''A new rapid component in the cochlear response to brief electrical efferent stimulation,'' Hear. Res. **34**, 49–62.
Konishi, T., and Slepian, J. Z. (**1970**). ''Effects of the electrical stimulation of the crossed-olivocochlear bundle on cochlear potentials recorded with intracochlear electrodes in guinea pigs,'' J. Acoust. Soc. Am. **49**, 1762–1769.
Liberman, M. C. (**1989**). ''Rapid assessment of sound-evoked olivocochlear feedback: Suppression of compound action potentials by contralateral sound,'' Hear. Res. **38**, 47–56.
Liberman, M. C., Dodd, L. W., and Pierce, S. (**1990**). ''Afferent and efferent innervation of the cochlea: Quantitative analysis with light and electron microscopy,'' J. Comp. Neurol. **301**, 443–460.
Lidén, G., Nilsson, G., and Anderson, H. (**1959**). ''Masking in clinical audiometry,'' Acta Oto-Laryngol. **50**, 125–136.
Lima da Costa, D., Chibois, A., Erre, J.-P., Blanchet, C., Charlet de Sauvage, R., and Aran, J.-M. (**1997**). ''Fast, Slow and Steady-state effects of contralateral acoustic activation of the medial olivocochlear efferent system in awake guinea pigs: Action of gentamicin,'' J. Neurophysiol. **78**, 1826–1836.
Madden, V. J., and Henson, M. M. (**1997**). ''Rapid decalcification of temporal bones with preservation of ultrastructure,'' Hear. Res. **111**, 76–84.
Martin, F. N. (**1972**). *Clinical Audiometry and Masking* (Bobbs-Merrill, Indianapolis).
Martin, F. N., Bailey, Jr., H. A. T., and Pappas, J. J. (**1962**). ''The effect of central masking on thresholds for speech,'' J. Auditory Res. **5**, 293.
May, B. J., and McQuone, S. J. (**1995**). ''Effects of bilateral olivocochlear lesions on pure-tone intensity discrimination in cats,'' Aud. Neurosci. **1**, 385–400.
Mott, J. B., Norton, S. J., Neely, S. T., and Warr, W. B. (**1989**). ''Changes in spontaneous otoacoustic emissions produced by acoustic stimulation of the contralateral ear,'' Hear. Res. **38**, 229–242.
Mountain, D. C. (**1980**). ''Changes in endolymphatic potential and crossed olivocochlear bundle stimulation alter cochlear mechanics,'' Science **210**, 71–72.
Nieder, P., and Nieder, I. (**1970**). ''Crossed olivocochlear bundle: Electrical stimulation enhances masked neural responses to loud clicks,'' Brain Res. **21**, 135–137.
Palva, L. L. (**1954**). ''Masking in audiometry,'' Acta Oto-Laryngol. Suppl. **118**, 156.
Pang, X. D., and Peake, W. T. (**1986**). ''How do contractions of the stapedius muscle alter the acoustic properties of the middle ear?'' in *Peripheral Auditory Mechanisms*, edited by J. B. Allen, J. L. Hall, A. Hubbard, S. T. Neely, and A. Tubis (Springer-Verlag, New York), pp. 36–43.
Perry, B. P., McSwain, S. D., Conlon, B. J., and Smith, D. W. (**1999**). ''A comparison of efferent suppression of compound action potentials by simultaneous and non-simultaneous contralateral noise paradigms,'' Audiology **38**, 1–6.
Probst, R., Lonsbury-Martin, B. L., and Martin, G. K. (**1991**). ''A review of otoacoustic emissions,'' J. Acoust. Soc. Am. **89**, 2027–2067.
Puria, S., Guinan, J. J., and Liberman, M. C. (**1996**). ''Olivocochlear reflex assays: Effects of contralateral sound on compound action potentials versus ear-canal distortion products,'' J. Acoust. Soc. Am. **99**, 500–507.
Rossi, G., Actis, R, Solero, P., Rolando, M., and Pejrone, M. D. (**1993**). ''Cochlear interdependence and micromechanics in Man and their relations with the activity of the medial olivocochlear efferent system (MOES),'' J. Laryngol. Otol. **107**, 883–891.
Sato, M., Henson, M. M., and Smith, D. W. (**1997**). ''Normal synaptic morphology of outer hair cells in the organ of Corti of the Japanese Macaque,'' Hear. Res. **108**, 46–54.
Scharf, B., Magnan, J., Collet, L., Ulmer, E., and Chays, A. (**1994**). ''On the role of the olivocochlear bundle in hearing: A case study,'' Hear. Res. **75**, 11–26.
Sherrick, C. E., and Albernaz, P. L. M. (**1961**). ''Auditory threshold shifts produced by pulsed contralateral stimuli,'' J. Acoust. Soc. Am. **33**, 1381–1386.
Siegel, J. H., and Kim, D. O. (**1982**). ''Efferent neural control of cochlear mechanics? Olivocochlear bundle stimulation affects cochlear biomechanic non-linearity,'' Hear. Res. **6**, 171–182.
Smith, D. W. (**1998**). ''Effects of contralateral noise on absolute thresholds in non-human primates: Is ''central masking'' an efferent-mediated peripheral process?'' in *Psychophysical and Physiological Advances in Hearing*, edited by A. R. Palmer, A. Rees, A. Q. Summerfield, and R. Medis (Whurr Publishers, London), pp. 26–33.
Smith, D. W., and Olszyk, V. B. (**1997**). ''Auditory behavioral thresholds for Japanese macaques using insert earphones,'' Am. J. Primatol. **41**, 323–329.
Smith, D. W., Turner, D. A., and Hensen, M. M. (**1999**). ''The role of the medial olivocochlear efferent system in psychophysical 'central masking','' Abst. Assn. Res. Otolaryngol. **22**, 96, 24.
Snyder, J. M. (**1973**). ''Central masking in normal listeners,'' Acta Oto-Laryngol. **75**, 419–424.
Sokolich, W. G. (**1981**). Closed sound delivery system, U.S. Patent 4,251,686.
Strickland, E. A., and Viemeister, N. F. (**1995**). ''An attempt to find psychophysical evidence for efferent action in humans,'' Abst. Assn. Res. Otolaryngol. **18**, 690, 173.
Studebaker, G. A. (**1964**). ''Clinical masking of air- and bone-conduction stimuli,'' J. Speech Hear. Res. **29**, 32.
Studebaker, G. A. (**1967**). ''Clinical masking of the non-test ear,'' J. Speech Hearing Dis. **32**, 360.
Veuillet, E., Collet, L., and Duclaux, R. (**1991**). ''Effect of contralateral auditory stimulation on active cochlear micro-mechanical properties in human subjects: Dependence on stimulus variables,'' J. Neurophysiol. **65**, 724–735.
Warr, W. B., Guinan, J. J., and White, J. S. (**1986**). ''Organization of the efferent fibers: The lateral and medial olivocochlear systems,'' in *Neurobiology of Hearing: The Cochlea*, edited by R. A. Altschuler, D. W. Hoffman, and R. P. Bobbin (Raven, New York), pp. 333–348.
Warren III, E. H., and Liberman, M. C. (**1989a**). ''Effects of contralateral sound on auditory nerve responses. I. Contributions of cochlear efferents,'' Hear. Res. **37**, 89–104.
Warren III, E. H., and Liberman, M. C. (**1989b**). ''Effects of contralateral sound on auditory nerve responses. II. Dependence on stimulus variables,'' Hear. Res. **37**, 105–122.
Wegel, R. L., and Lane, C. E. (**1924**). ''The auditory masking of one pure tone by another and its probable relations to the dynamics of the inner ear,'' Phys. Rev. **23**, 266–285.
Wiederhold, M. L., and Kiang, N. Y. S. (**1970**). ''Effects of electrical stimulation of the crossed olivocochlear bundle on single auditory-nerve fibers in the cat,'' J. Acoust. Soc. Am. **48**, 950–965.
Williams, D. M., and Brown, A. M. (**1995**). ''Contralateral and ipsilateral suppression of the $2f1-f2$ distortion product in human subjects,'' J. Acoust. Soc. Am. **97**, 1130–1140.
Williams, E. A., Brookes, G. B., and Prasher, D. K. (**1993**). ''Effects of contralateral acoustic stimulation on otoacoustic emissions following vestibular neurectomy,'' Scand. Audiol. **22**, 197–203.
Winslow, R. L., and Sachs, M. B. (**1987**). ''Effect of electrical stimulation of the crossed olivocochlear bundle on auditory nerve response to tones in noise,'' J. Neurophysiol. **57**, 1002–1021.
Zwislocki, J. J. (**1971**). ''Central masking and neural activity in the cochlear nucleus,'' Audiology **10**, 48–59.
Zwislocki, J. J., Buining, E., and Glantz, J. (**1968**). ''Frequency distribution of central masking,'' J. Acoust. Soc. Am. **4**, 1267–1271.
Zwislocki, J. J., Damianopoulos, E. N., Buining, E., and Glantz, J. (**1967**). ''Central masking: Some steady-state and transient effects,'' Percept. Psychophys. **2**, 59–64.

The effects of frequency region and level on the temporal modulation transfer function[a)]

Elizabeth A. Strickland[b)]
Department of Audiology and Speech Sciences, Purdue University, West Lafayette, Indiana 47907

(Received 14 July 1999; revised 4 November 1999; accepted 8 November 1999)

Temporal modulation transfer functions (TMTFs) were measured using narrow-band AM and QFM noises with upper spectral edges from 0.6 to 4.8 kHz, and spectrum levels of 10 and 40 dB SPL. The cutoff frequency of the TMTF increases as the upper spectral edge is increased up to 4.8 kHz at low levels, and is constant at higher levels. Sensitivity increases with bandwidth if frequency region is constant. In a second experiment, these results were compared to predictions of a model incorporating peripheral and central limitations to modulation detection. To obtain an estimate of peripheral filtering, frequency selectivity was measured using the notched-noise method, with probe frequencies and levels chosen to parallel those in the first experiment. The TMTF data were then predicted using the model. Predicted cutoff frequencies as a function of the upper spectral edge of the test stimulus were lower than but parallel to those of the subjects at the lower stimulus level. The model predicted only a slight increase in cutoff frequency with level, and thus predicted an increase in cutoff frequency with frequency region at the higher level as well, in contrast to the measured data. These results suggest that there are peripheral and central limitations to temporal resolution, but the psychoacoustically derived auditory filter may be only an indirect measure of peripheral filtering, and/or a more complex model may be needed.
[S0001-4966(00)03902-3]

PACS numbers: 43.66.Ba, 43.66.Mk [SPB]

INTRODUCTION

One of the fundamental properties of the auditory system is the ability to follow time-varying changes in the amplitude of sounds. These dynamic changes carry much of the information in complex sounds of interest, such as speech and music. Because the auditory system must track, and perhaps compare, amplitude changes in different frequency regions, it is important to know whether temporal resolution varies with frequency region. The peripheral auditory system acts as a bank of overlapping filters whose bandwidths increase approximately proportionately with center frequency. Because the time constant of a linear filter is inversely related to the bandwidth, temporal resolution in the auditory system would be expected to increase with the frequency region of the signal, at least up to a point. There may be more central limits to temporal resolution which do not vary with frequency region. In a given frequency region, temporal resolution will be determined primarily by whichever of these factors is most limiting. For this reason, it might be expected that temporal resolution should vary with peripheral filtering in low-frequency regions, and should be constant in higher frequency regions, where central factors are the limitation.

Various methods have been used to estimate the temporal resolution of the auditory system. One method is to use a systems analysis approach, and measure the threshold modulation depth needed for detection of sinusoidal amplitude modulation of a carrier, yielding a temporal modulation transfer function (TMTF) (Viemeister, 1979). For test stimuli for which the bandwidth is at least twice the highest modulation frequency, the resulting function has the form of a low-pass filter (Dau *et al.*, 1997a). At low modulation frequencies, the system can easily follow the temporal fluctuations, and thus the limiting factor is the intensity resolution of the system. As the modulation frequency increases, the system cannot follow the amplitude changes as exactly, and the function begins to roll off. In carrier conditions where a low-pass TMTF can be observed, the cutoff frequency is generally considered to reflect the temporal resolution of the system.

Physiological measurements of the TMTF support the idea that there are two types of limits to temporal resolution. Greenwood and Joris (1996) have shown that TMTF cutoff frequencies measured in the auditory nerve in cats increase proportionally with cochlear place up to a place corresponding to approximately 3 kHz, and then begin to approach a constant limit. They suggest that this is consistent with temporal resolution being limited by mechanical filtering in lower frequency regions, and temporal filtering in higher frequency regions. The mechanical filtering is presumed to come from cochlear processing, while the temporal filtering could be stages after mechanical filtering but before neural discharge that limit the ability of the neural discharge to synchronize to the envelope of the signal. There could also be limitations more central than the VIIIth nerve.

Behavioral data in humans, however, have been less clear. Several studies have shown an increase in temporal resolution as frequency region was increased (Rodenburg, 1977; Patterson *et al.*, 1978; Viemeister, 1979; van Zanten,

[a)]Portions of this research were presented at the 131st meeting of the Acoustical Society of America, State College, Pennsylvania, June 1997 [J. Acoust. Soc. Am. Suppl. 1 **101**, S3150 (1997)].
[b)]Electronic mail: estrick@purdue.edu

1980; Bacon and Viemeister, 1985; Formby and Muir, 1988). In most of these studies, however, bandwidth increased with frequency region. Eddins (1993) and Dau *et al.* (1997b) found no effects of frequency region when bandwidth was kept constant, but bandlimiting was done after modulation, which decreases modulation depth at the highest modulation frequencies. Strickland and Viemeister (1997) and Eddins (1999) also found no effects of frequency region using AM and QFM noises, which are not filtered after modulation, for test stimuli with upper spectral edges at 1.2 kHz and above.

These data suggest that there may be an inconsistency between what is known about peripheral filtering and what is known about temporal resolution. If peripheral filtering does limit temporal resolution, it should be most apparent in lower frequency regions and at low signal levels, where the filter widths are narrowest. The aim of the first experiment was to measure temporal resolution as a function of frequency region and level, including lower frequency regions and levels.

I. EXPERIMENT 1

A. Methods

1. Stimuli

The test stimuli were AM and QFM noises, which are bandlimited stimuli which are not discriminable on the basis of long-term spectral cues. These stimuli avoid reduction in modulation depth which is caused by filtering after modulation (Strickland and Viemeister, 1997; Eddins, 1999). They have been described in detail in a previous paper (Strickland and Viemeister, 1997). Briefly, a narrow-band noise was created by adding together sinusoidal components, and each component in the noise was treated as a carrier. Sidebands were added at the carrier frequency plus and minus the modulation frequency. For AM noise, the sideband phases were shifted plus and minus π radians relative to the carrier phase,[1] as shown in Eq. (1)

$$\mathrm{AM}(t)=\sum_{c=l+\mathrm{mod}}^{h-\mathrm{mod}} A_c\Big[\cos(2\pi f_c t+\phi_c)+\frac{m}{2}(\cos(2\pi(f_c-f_{\mathrm{mod}})t+\pi+\phi_c)+\cos(2\pi(f_c+f_{\mathrm{mod}})t-\pi+\phi_c))\Big], \tag{1}$$

where A_c is Rayleigh distributed amplitude, ϕ_c is a random phase rectangularly distributed from 0 to 2π radians, and m is the modulation index (0 to 1). For the frequency terms, f_c is the frequency of each carrier component, f_l and f_h are the lower and upper spectral edges of the noise, f_{mod} is the modulation frequency, $f_{l+\mathrm{mod}}=f_l+f_{\mathrm{mod}}$, and $f_{h-\mathrm{mod}}=f_h-f_{\mathrm{mod}}$.

For QFM noise, the sideband phases were both shifted $\pi/2$ radians relative to the carrier phase, as shown in Eq. (2)

TABLE I. Conditions for experiment 1.

Bandwidth (Hz)	Upper spectral edge (Hz) 600	1200	2400	4800
400	S1–S5	S1–S4	S1–S4	S1–S4
800		S1–S5	S1–S4	S1–S4
1600			S1–S5	S1–S4
Broadband		S1, S2, S4, S5		

$$\mathrm{QFM}(t)=\sum_{c=l+\mathrm{mod}}^{h-\mathrm{mod}} A_c\Big[\cos(2\pi f_c t+\phi_c)+\frac{m}{2}\Big(\cos\Big(2\pi(f_c-f_{\mathrm{mod}})t-\frac{\Pi}{2}+\phi_c\Big)+\cos\Big(2\pi(f_c+f_{\mathrm{mod}})t-\frac{\Pi}{2}+\phi_c\Big)\Big)\Big]. \tag{2}$$

As shown by Strickland and Viemeister (1997, Fig. 3), the amplitude spectra of these stimuli have a central flat area, composed of carriers and sidebands, and a lower amplitude region flanking the central area, composed only of sidebands. The total bandwidth of the stimuli stays constant at f_h-f_l, and thus the width of the central area decreases and the width of the sidebands increases with f_{mod}.

Frequency region was varied by setting the upper spectral edge of the test stimuli, f_h, at 600, 1200, 2400, and 4800 Hz. Bandwidths used for each frequency region, and the subjects tested in each condition, are shown in Table I. The modulation frequency was set at 4 to 512 Hz in equal log steps, with the limitation that it could not exceed half the bandwidth of the test stimulus. Test stimuli were set at spectrum levels of 10 and 40 dB. As shown in Table I, four of the five subjects were also tested with a broadband noise carrier (10 to 10 000 Hz) at 30-dB spectrum level. Previous research has shown that with a broadband carrier, modulation detection thresholds are invariant with test stimulus level down to 20 dB SL (Viemeister, 1979; Bacon and Viemeister, 1985), and thus these results can be compared to narrow-band results at different levels.

In a previous study (Strickland and Viemeister, 1997), the data suggested that attending to frequency regions above the test stimulus might effectively increase the modulation depth for low modulation frequencies. To prevent this, and also to limit the frequency region available, a band of masking noise was presented above the test stimulus. The bandwidth was the same as that of the test stimulus, and the lower spectral edge was 50 Hz above the upper spectral edge of the test stimulus. In the same study, a combination tone at the modulation frequency was found to serve as a cue in discriminating between the AM and QFM noise. Therefore, a low-frequency masker was also presented, with the lower spectral edge at 100 Hz, and the upper spectral edge at 150, 300, and 600 Hz for test stimulus bandwidths of 400, 800, and 1600, Hz, respectively.

Test stimuli and masking noises were gated together, and were 500 ms in duration, including 10-ms raised-cosine ramps. The overall level of the test stimulus was set to be the same as that of a flat-spectrum noise of the same bandwidth

at the nominal spectrum level. The spectrum level of the masking noises was set 10 dB below the nominal spectrum level of the test stimuli.

The test stimuli were digitally generated and produced (TDT DA1) at a rate of 16 384 Hz. They were low-pass filtered at 6 kHz (Kemo VBF/23). The level was adjusted by programmable attenuators (TDT PA4). Stimuli were presented through one earphone of Sennheiser HD450 headphones to a listener seated in a double-walled sound-attenuating booth.

2. Procedure

Modulation frequency was fixed within a run, and modulation depth, in units of 20 log(m), was adjusted in an adaptive two-interval forced-choice procedure with a two-down, one-up stepping rule, to track 71% correct (Levitt, 1971). Seventy trials were presented in each block, and feedback was given after each trial. The initial step size was 3 dB, and was reduced to 1 dB after the first two reversals. The threshold estimate for each block was calculated from the average of the last even number of reversals at the smaller step size. Threshold values are based on the average of at least three blocks. If the modulation would have gone beyond 100% the track was terminated and not included in the threshold estimate.

In order to better define the skirt of the TMTF, in some conditions thresholds were also measured with modulation depth fixed and modulation frequency adjusted in logarithmic steps, a technique used previously by Formby (1985). The initial step size as ln(2)/2 (0.347), which was reduced to ln(2)/4 (0.173) after the first two reversals. The track was terminated if the bandwidth of the test stimulus would have been exceeded. Other details of the tracking were the same as those above.

3. Subjects

Subjects were two males and three females, with an average age of 23.8 years, and a range of 18 to 36 years. Each subject had thresholds for pure tones within laboratory norms for the ear tested, which was the left ear for all subjects. All subjects except S1, who is the author, were paid an hourly wage.

B. Results

1. Effect of frequency region on the TMTF with bandwidth fixed

TMTFs may be analyzed in terms of two parameters. These are sensitivity, defined as the absolute value of the low-frequency plateau, and the cutoff frequency, defined as the modulation frequency where thresholds have increased by 3 dB from the plateau. These may be estimated by fitting the transfer function of a one-pole Butterworth low-pass filter to the modulation detection thresholds using a least-squares algorithm, which will be done later in the paper.

In Fig. 1 average TMTFs are shown for constant bandwidths (across rows) and levels (across columns) as a function of frequency region. Symbols with downward arrows indicate that threshold could not be obtained due to termination of the track. Data points measured by adaptation on modulation frequency are plotted with the same symbols connected by separate lines, and are on the upper skirt of the functions. Looking first at the left column, where the spectrum level of the stimuli was 10 dB, it is clear that the cutoff frequency of the TMTF depends on frequency region. In the bottom panel, where the bandwidth is 400 Hz, the cutoff frequency is lower for $f_h = 600$ Hz than for higher frequency regions. In the middle panel, the cutoff frequency is lower for $f_h = 1200$ Hz than for higher frequency regions, when the bandwidth is 800 Hz. The cutoff frequency changes much less with frequency region in the top panel, where the 1600-Hz bandwidth means that only the two highest frequency regions could be tested. At this low level, the sensitivity is invariant with frequency region. When the spectrum level of the stimuli is 40 dB, in the right column, there is no effect of frequency region on the cutoff frequency of the TMTF at any bandwidth. There does tend to be a decrease in sensitivity of 3–5 dB for the lowest frequency region in each bandwidth. This could be due to upward spread of masking or modulation detection interference (MDI) from the low-frequency masker, which would be closer to the lower frequency stimulus than to any of the higher frequencies. All of the average effects are reflected in the individual subject data.

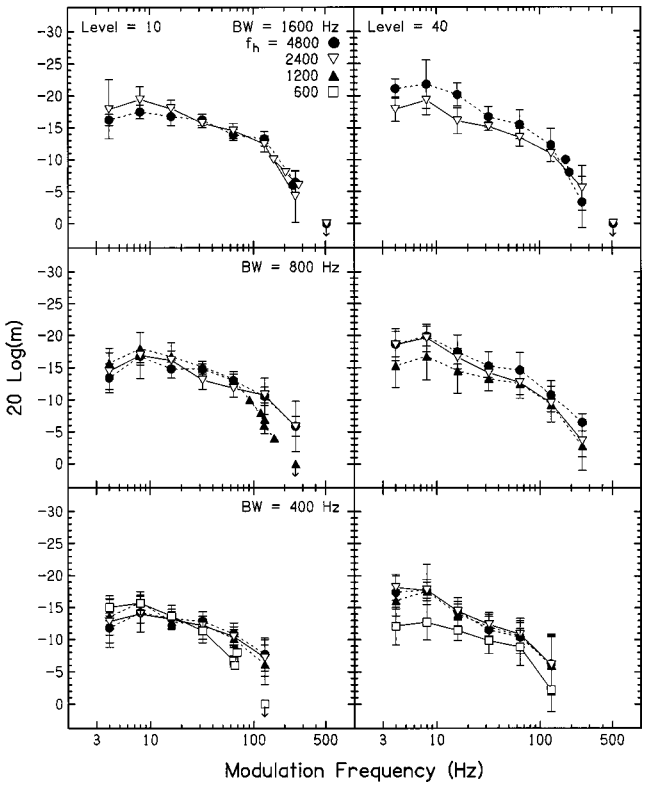

FIG. 1. Average TMTFs as a function of frequency region with bandwidth and level held constant. The test stimulus spectrum level is 10 dB in the left column and 40 dB in the right column. Bandwidths ranged from 400 Hz (bottom row) to 1600 Hz (top row).

2. Effects of audibility

To ensure that any effects of frequency region were not due to audibility limitations, threshold was measured for de-

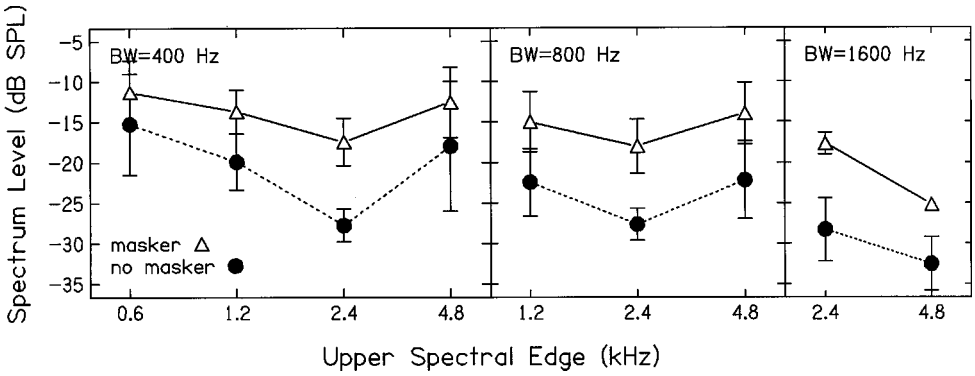

FIG. 2. Average thresholds for detection of a narrow-band noise in quiet (filled circles) or in the presence of notched noise at 0-dB spectrum level (open triangles).

tection of unmodulated flat-spectrum noise with the same upper spectral edges and bandwidths as the test stimuli. The average results for S1–S4 are shown in Fig. 2 (S5 was not tested). Thresholds were measured in quiet (filled circles) and with the masking noise set at 0-dB spectrum level (open triangles). This is the masker level when the test stimuli are at a spectrum level of 10 dB. For three of the four subjects, when the masking noise was present, threshold varied by less than 5 dB across the frequency range, indicating that there were no significant differences in audibility. Although there were differences in audibility across frequency regions for S3, they did not correlate with changes in TMTF cutoff frequency. As a further test of audibility effects, S1 was also tested at a spectrum level of 0 dB with $f_h = 4800$ Hz and a bandwidth of 400 Hz. Results for this subject are shown in Fig. 3, along with TMTFs at higher levels. Even at this low level, for this frequency region the cutoff frequency of the TMTF did not decrease with level. Therefore, the change in cutoff frequency with frequency region is not due to differences in stimulus audibility.

3. Effect of bandwidth and stimulus type on the TMTF

In Fig. 1, for a bandwidth of 400 Hz at a spectrum level of 10 dB, it would be possible to determine the cutoff frequency for the TMTF for $f_h = 600$ Hz, but the estimate would be less accurate for the higher frequency regions because the upper skirt of the TMTF is not well defined; that is, the function has barely begun to roll off. It is not until the bandwidth increases to 800 Hz for the lower level that it becomes evident that the cutoff frequency is lower for $f_h = 1200$ Hz than for higher frequency regions. The bandwidth of the test stimulus that can be used is limited by the upper spectral edge, but the highest modulation frequency that can be used is limited by the bandwidth. To accurately determine the TMTF cutoff frequency as a function of frequency region, comparisons must be made across different bandwidths as well.

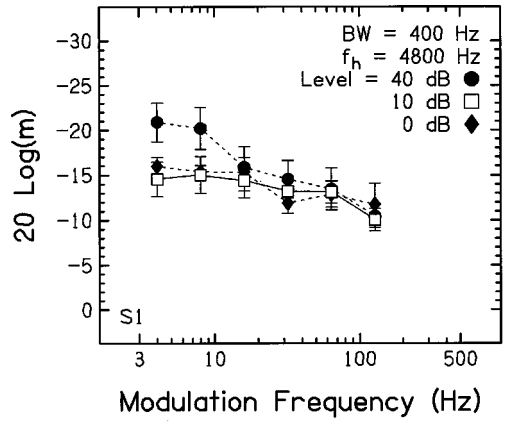

FIG. 3. TMTFs as a function of level for S1, with $f_h = 4800$ Hz and a bandwidth of 400 Hz. Note that the cutoff frequency does not decrease, even at the lowest level.

It has been shown previously that when the upper spectral edge of the test stimulus is fixed, the stimulus bandwidth does not affect the TMTF cutoff frequency when the spectrum level is 40 dB or greater (Strickland and Viemeister, 1997; Eddins, 1999). In the present study, this analysis was extended to lower frequency regions and to a lower level. TMTFs as a function of bandwidth are shown in Fig. 4 for a spectrum level of 10 dB, with frequency region the parameter across rows. Data are averages for either four or five subjects. At the highest modulation frequency, some subjects did not have measurable thresholds, and these points were averaged in as zeros. It is clear that there is no consistent change in cutoff frequency with bandwidth even at this lower level; that is, the functions are parallel. Sensitivity increases with bandwidth, by 2 to 3 dB per doubling, but does not vary with frequency region at this low level, as was shown in Fig. 1.

One reason TMTF cutoff frequency might be expected to depend on bandwidth is due to the way in which the test stimuli are generated. By choosing to hold total bandwidth constant, the bandwidth of the ''carrier band'' decreases as modulation frequency increases. For example, for a 400-Hz total bandwidth, the carrier bandwidth is 392 Hz when the modulation frequency is 4 Hz, and only 144 Hz when the modulation frequency is 128 Hz. Dau *et al.* (1997b) have shown that modulation detection thresholds decrease as *carrier* bandwidth increases. The decrease, in dB, is proportional to the log of the carrier bandwidth. To examine the effect that carrier bandwidth might have on the stimuli used in the present study, for which upper spectral edge was held constant, three subjects were also tested with stimuli for which the carrier bandwidth was held constant as a function of modulation frequency, with the upper edge of the carrier fixed at f_h. In Fig. 5, comparisons of modulation thresholds obtained with total bandwidth fixed (filled circles) and carrier bandwidth fixed (open triangles) are shown for a spectrum level of 40 dB SPL for S2 and S4. When the carrier

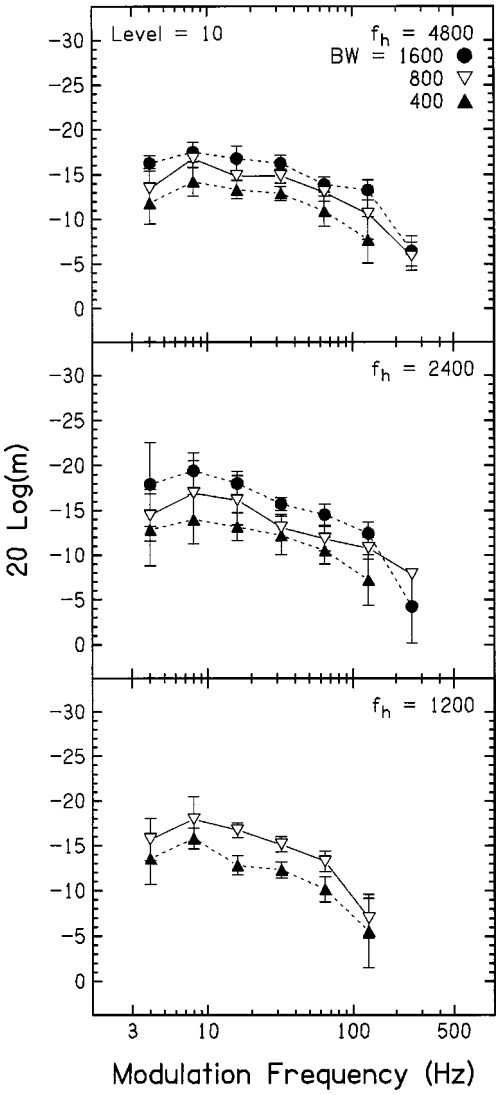

FIG. 4. Average TMTFs as a function of bandwidth for three frequency regions, replotted from Fig. 1.

bandwidth is fixed, thresholds are in general 1 to 2 dB lower at the two highest modulation frequencies than they are with the total bandwidth fixed, indicating that holding the total bandwidth constant does produce a bandwidth effect, but it is nearly negligible. These same effects were found for a stimulus level of 10 dB for S1 (not shown).

4. Effects of frequency region and level on the TMTF with varying bandwidth

The previous section showed that the test stimulus bandwidth does not affect the TMTF cutoff frequency; therefore, the effects of frequency region on the TMTF cutoff frequency may be compared across bandwidths. In Fig. 6, TMTFs are shown as a function of frequency region, with a bandwidth of 400 Hz when $f_h = 600$ Hz, a bandwidth of 800 Hz when $f_h = 1200$ Hz, and a bandwidth of 1600 Hz when $f_h = 2400$ Hz and 4800 Hz. The data are replotted from Fig. 1. The left panel shows TMTFs measured with test stimuli at a spectrum level of 10 dB. It is clear that cutoff frequency increases as f_h increases. In the right panel, the test stimuli were at 40-dB spectrum level. Also shown is the TMTF for a

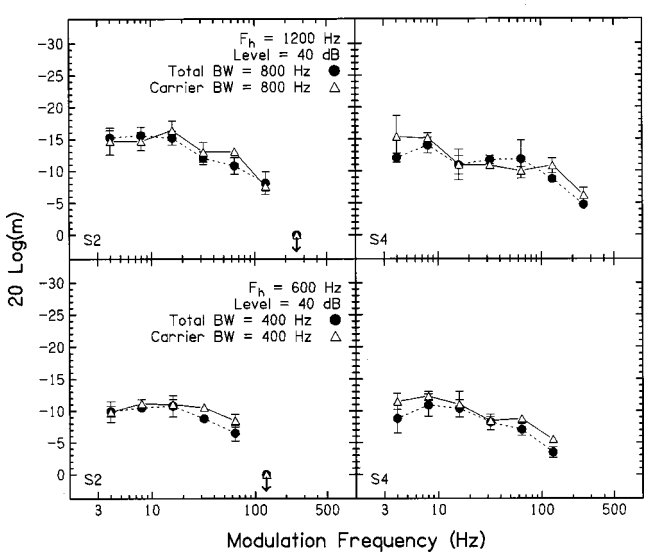

FIG. 5. TMTFs for S2 and S4 with total bandwidth held constant (filled circles) or carrier bandwidth held constant (open triangles) at a spectrum level of 40 dB.

broadband noise carrier that was at 30-dB spectrum level. For this high level, note that the cutoff frequency changes little if at all with frequency region. This is consistent with previous studies that have shown no effect of frequency region on cutoff frequency at this or higher test stimulus levels (Eddins, 1993, 1999; Dau *et al.*, 1997b; Strickland and Viemeister, 1997). Cutoff frequencies and sensitivities for these data are shown in Fig. 9.

II. EXPERIMENT 2: MODEL PREDICTIONS

A. Introduction

In experiment 1, it was demonstrated that the cutoff frequency of the TMTF increases with frequency region and level up to a point, and then plateaus. This is consistent with the idea advanced by Greenwood and Joris (1996) that there are peripheral and central limitations to temporal resolution, and whichever is more limiting will dominate in a given condition. The fact that TMTF cutoff frequency is lower in lower frequency regions and at lower levels, but constant in higher frequency regions and at higher levels, suggests that peripheral filtering could be a limitation in some conditions,

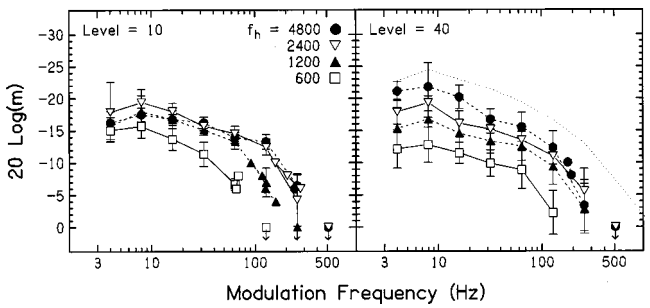

FIG. 6. Average TMTFs for the widest bandwidth in each frequency region, with a spectrum level of 10 and 40 dB.

because it is sharpest at lower frequencies and levels. The next step is to determine whether these results are predicted by models of temporal resolution.

Two types of models have been used to predict modulation detection by the auditory system. One has been called an ''envelope detector.'' This consists of one or more bandpass filters, a half-wave rectifier, and a low-pass filter (Rodenburg, 1977; Viemeister, 1977, 1979), and was developed specifically to model temporal resolution. The other is the modulation filterbank model developed by Dau *et al.* (1997a) to model such effects as adaptation and masking in addition to modulation detection. The first two stages are the same as those of the envelope detector. These are followed by an adaptation stage, a bank of modulation frequency filters, the addition of internal noise, and an optimal detector. This model captures aspects of modulation detection that are not well modeled by the envelope detector, such as effects of modulation masking.

For both models there are peripheral and central limitations to detection of modulation of noise carriers such as those used in experiment 1. The peripheral limitation is bandpass filtering. The central limitation is a low-pass filter in the envelope detector model, while in the modulation filterbank model, the limitation is the fact that the modulation filters broaden with modulation frequency. Therefore, more nonsignal modulation gets through at higher modulation frequencies, reducing detection of modulation. Thus, both models predict that peripheral filtering could limit temporal resolution at low carrier frequencies. For neither model is it clear, however, what should be used as an estimate of peripheral filtering in the first stage. When TMTFs for broadband carriers have been predicted using the envelope detector, a broad initial filter (2 or 4 kHz) has been necessary in order for the model to be sensitive enough (Viemeister, 1979; Forrest and Green, 1987). Both the envelope detector model and the modulation filterbank model have also been used to model TMTFs for narrow-band carriers using filters estimated from threshold for a pure tone in notched noise (Patterson *et al.*, 1987; Rosen *et al.*, 1995). At high test-stimulus levels, both models are able to successfully predict TMTFs for carriers in high-frequency regions, but predict a slightly sharper (Dau *et al.*, 1997b) or much sharper (Strickland and Viemeister, 1997) drop in threshold at high modulation frequencies in lower frequency regions than is shown by subjects. Neither model has been used with test stimuli at lower levels.

It is not clear why the predictions do not fit the data. One possibility that has been suggested is that listeners are able to combine temporal information across channels. This seems unlikely, because it would require that amplitude and phase information be preserved to a degree which may be beyond the capabilities of the auditory nerve (Viemeister, 1979; Strickland and Viemeister, 1997). Another possibility is that the problem could lie in the filter estimates. The measurement of frequency selectivity has been evolving since early studies of audition, and as techniques have changed, so have the filter estimates. Recent work by Rosen and his colleagues suggests that accurate filter estimates may be obtained by measuring threshold for a fixed-level probe as the level of a notched-noise masker is varied (Rosen and Baker, 1994). Using this method, filter widths broaden with frequency region and with level. Experiment 1 showed that TMTF cutoff frequencies also increase with frequency region and level until they plateau. Therefore, it is of interest to determine whether changes in filter shape can explain changes in the TMTF.

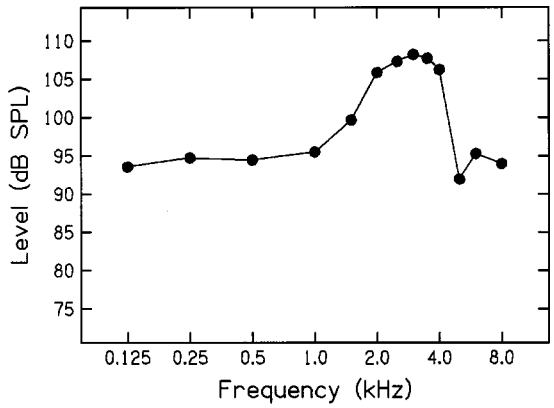

FIG. 7. Frequency response of the Sennheiser HD450 headphones.

The aim of experiment 2 was to measure frequency selectivity as a function of frequency region and level, derive filter functions, and then to use these filters in a model to predict modulation detection. The envelope detector model was used because this was a model the author had access to and had used before. For modeling the effects of frequency region and level on detection of modulation of noise carriers, the envelope detector model performs comparably to the modulation filterbank model in the conditions considered here.

B. Methods

1. Stimuli

The test stimuli in experiment 1 cover a range of frequencies. If the envelope detector is limited to one filter in the first stage, the modulation depth of the test stimulus will be maximized by the broadest filter. Therefore, the optimal filter to choose is one with the highest center frequency (CF) that passes the test stimulus but not the notched noise surrounding it. Probe frequencies of 500, 1000, and 2000 Hz were chosen, because these placed the filters in the upper end of the TMTF test stimulus regions. Rolloff of the headphone response precluded including a probe frequency of 4000 Hz. The response of the Sennheiser HD450s, as measured on KEMAR, has a 10–15-dB peak from just above 2 kHz to 4 kHz, as shown in Fig. 7. This was not compensated for in the stimulus levels. Probe levels were chosen to approximate the levels of the TMTF test stimuli after auditory filtering. It was assumed that the 3-dB bandwidth of the auditory filter was 10% of CF.

The probe was a 400-ms pure tone, temporally centered in the 500-ms notched-noise masker. Both masker and probe had 10-ms raised-cosine ramps. Probe level was fixed and masker level varied to estimate threshold at each notch width. The outer spectral edges of the noise were fixed at $0.2\times f_0$ and $1.8\times f_0$, where f_0 is the probe frequency. The

relative edge of the notch in the noise was designated by N, where $N=(|f-f_0|/f_0)$, and f is the inner spectral edge of the noise. The notch was placed either symmetrically about the probe, or asymmetrically, with the closer edge at N and the farther edge at $N+0.2$. For signal levels of 47 dB SPL and lower, N was set at 0 to 0.4 for the symmetric case, and 0 to 0.3 for the asymmetric case. For higher signal levels, N was set at 0 to 0.15, and where possible 0.2. Only narrower notch widths could be used at these levels because wider notch widths required higher masker levels to reach threshold, which would have exceeded the limits of the system and been uncomfortably loud for the subjects.

2. Procedure

The probe level was fixed within a run, and the masker level was adjusted in an adaptive two-interval forced-choice procedure with a two-up, one-down stepping rule, to track 71% correct (Levitt, 1971). Fifty trials were presented in each block, and feedback was given after each trial. The initial step size was 5 dB, and was reduced to 2 dB after the first two reversals. The threshold estimate for each block was calculated from the average of the last even number of reversals at the smaller step size. Threshold values are based on the average of at least three blocks. If the masker level would have exceeded the limits of the system, the block was terminated and not included in threshold determinations. Subjects were the same as those in experiment 1.

C. Results

1. Filter measurements

Thresholds were used to estimate filter shapes, using an adaptive least-squares fitting program. Data for probes at different levels were fit together for each subject and center frequency, by allowing the parameters to change with level (e.g., Rosen and Baker, 1994). The function used to fit the filters was a rounded exponential, as given in the following equation:

$$\text{roex}(p,w,t)=(1-w)(1+pg)\exp(-pg)$$
$$+w(1+tg)\exp(-tg),$$

where g is frequency normalized to the center frequency, p is the slope of the passband of the filter, t is the slope of the tail, and w determines which region is dominated by the passband and which by the tail (Patterson *et al.*, 1982). Parameters used in fitting the filters were lower and upper slopes (p_l and p_u), and a break point and tail on the low-frequency side (w_l and t_l) with a linear fit with level for each parameter. The filter fits include the weighting function of the headphones.

Filter 3-dB bandwidths are shown in Fig. 8. Also shown are 3-dB bandwidths for fourth-order gammatone filters (Holdsworth *et al.*, 1988) and estimates using the same fixed-probe method from Rosen *et al.* (1995). The average bandwidths for the low level are quite comparable to estimates by Rosen and the gammatone estimates. For the high level, the filter estimates in this study are consistently slightly larger than other estimates, particularly at 2 kHz. The extremely wide filter measured at the higher level at 2 kHz could well be due to the peak in the frequency response of the headphones as shown in Fig. 7. The weighting function may not be able to correct for the fact that the masker above the probe frequency dominated during the measurement. The filter bandwidths at 4 kHz were not measured; rather, the parameters from the 1-kHz filter were used.

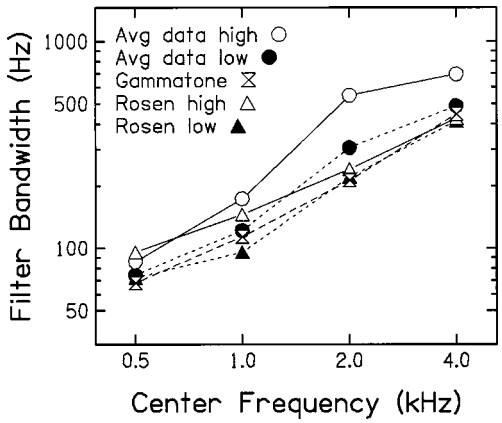

FIG. 8. Average filter 3-dB bandwidths calculated from filter functions fit for each subject. Filter functions were directly measured for center frequencies of 0.5, 1.0, and 2.0 kHz. 4.0-kHz data are extrapolated from the filter functions at 1.0 kHz. Filled circles are for probe levels corresponding to the 10-dB spectrum level stimuli in the previous experiment, open circles for the 40-dB spectrum level. Filled and open triangles are bandwidths calculated from measurements at the same levels by Rosen *et al.* (1995). Hourglass symbols show bandwidths for fourth-order gammatone filters.

2. Simulations

The envelope detector model was used to run simulations of a subset of the conditions from experiment 1. Bandwidths of 400, 800, 1600, and 1600 Hz were used with $f_h=600$, 1200, 2400, and 4800 Hz, respectively. Spectrum levels were 10 and 40 dB. In the simulations, the filters for each subject and condition were used in the first stage of the model. Because filters were only measured at one frequency within each frequency region, the filter parameters were extrapolated to nearby center frequencies as needed. The model was run under two different conditions. In the first, only one filter was used in the first stage. This filter was chosen to be the widest available within the stimulus region, and thus was placed near the upper edge of the stimulus frequency region. This will be called the single-channel model. In the second condition, as many independent filters as would fit in the stimulus region were used in the first stage, with the criterion for independence being that the filters were 3 dB down at the point where they overlapped. The number and center frequencies of the filters were determined individually for each subject and condition. This will be called the multichannel model. When the stimulus was broadband, only filters with CFs above 2 kHz were used, because with lower CFs the envelope spectrum and the stimulus spectrum overlap and the model does not perform well.

The decision statistic used in the model was the difference in the fourth moment of the envelope between the signal and nonsignal intervals (Hartmann and Pumplin, 1988). This particular statistic was chosen based on its performance in a previous study in predicting modulation thresholds for

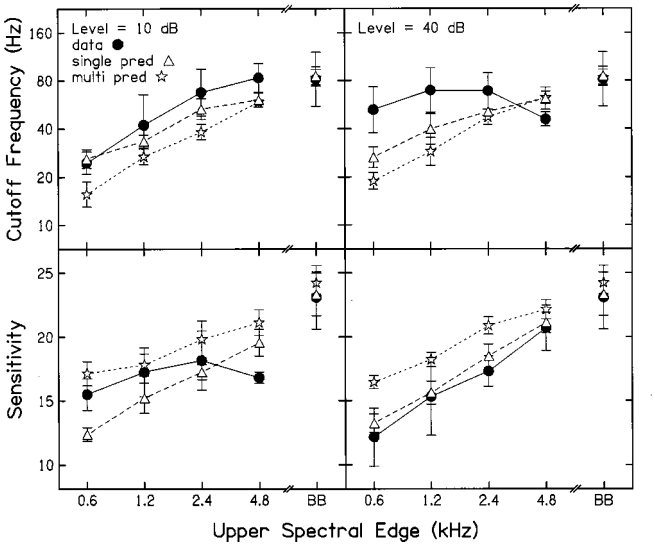

FIG. 9. Cutoff frequencies (top row) and sensitivity (bottom row) calculated by fitting the transfer function of a low-pass filter to each TMTF and taking the average.

TMTFs for broadband carriers that were as low as those measured for subjects, and in predicting some aspects of modulation masking[2] (Strickland and Viemeister, 1996). The cutoff frequency of the low-pass filter was set at 60 Hz, so that the model predicted the TMTFs for $f_h = 4800$ Hz well. This is close to the cutoff frequency that has been used in previous studies fitting results with broadband carriers (Viemeister, 1979; Forrest and Green, 1987). In the multichannel model, the differences in fourth moment were simply summed across channels.

An adaptive tracking procedure was used to get four threshold estimates in each condition, exactly as for the subjects in experiment 1. Thresholds were estimated by adapting on modulation depth, and also by adapting on modulation frequency with modulation depth held constant at -8 and -4 dB.

3. Predicted TMTFs as a function of frequency region

Cutoff frequencies and sensitivity were estimated by fitting the transfer function of a one-pole Butterworth low-pass filter to each TMTF using a least-squares criterion. This was done for TMTFs for each subject and condition for the data and the predictions of the two versions of the model. The cutoff frequencies (on a log scale) and sensitivity were then averaged for each condition. These are shown in Fig. 9. The cutoff frequencies are shown in the top panels. In order to quantify the results, analyses of variance were performed, with the data and the two model predictions analyzed as separate groups. There is clearly a three-way interaction between group, frequency region, and level [$F(6,36) = 16.418$, $p < 0.001$].[3] At a level of 10 dB, there is a significant effect of frequency region on cutoff frequency [$F(3,36) = 118.764$, $p < 0.001$]. A *post hoc* Tukey test showed that differences in cutoff frequency were significant up to $f_h = 2400$ Hz. There is a significant effect of group [$F(2,12) = 15.283$, $p = 0.001$], with a *post hoc* Tukey test showing a significant difference between the data and the predictions of the multichannel model. The models and the data show the same amount of change in cutoff frequency with frequency region, as there is not a significant interaction between group and frequency region [$F(6,36) = 2.051$, $p = 0.84$].

In contrast at the higher level, in the right panel, the effects of frequency region do depend on the group [$F(6,36) = 17.362$, $p < 0.001$]. For the subject data there is a small frequency effect [$F(3,12) = 4.755$, $p = 0.021$], with a Tukey test showing that the cutoff frequency for $f_h = 4.8$ kHz is significantly lower than that for $f_h = 1.2$ and 2.4 kHz. This frequency effect is driven by the results of one subject. For the other subjects, cutoff frequency was basically constant above $f_h = 1.2$ kHz. In contrast, both models predict an increase in cutoff frequency with frequency region.

The sensitivity values are shown in the bottom panels. Again, there is a three-way interaction between groups, levels, and frequency region [$F(6,36) = 7.854$, $p < 0.001$]. For the lower level, there is an interaction between group and frequency region [$F(6,36) = 9.596$, $p < 0.001$]. There is an effect of frequency for the subject data at the lower level [$F(3,12) = 3.814$, $p = 0.039$], but a Tukey test revealed that the only significant pairwise difference is between $f_h = 2.4$ kHz and $f_h = 0.6$ kHz. Both the single- and multichannel predictions show an increase in sensitivity with frequency region. At the higher level there is a significant effect of groups [$F(2,12) = 10.82$, $p = 0.002$], although a Tukey test revealed that no pairwise comparisons reached significance. There is also an effect of frequency region [$F(3,36) = 162.05$, $p < 0.001$].

The bandwidth of the test stimulus is increasing with frequency region up of $f_h = 2.4$ kHz. This means that the model predicts that sensitivity may depend on bandwidth and the number of peripheral channels that are used. For $f_h = 4.8$ kHz, two peripheral channels were combined, while for $f_h = 2.4$ kHz, four channels were combined. Sensitivity is greater when two larger channels are combined. Eddins (1999) has also shown that for a constant bandwidth, sensitivity may vary with frequency region. What is somewhat surprising is the fact that sensitivity for the subjects decreased as level increased, for $f_h = 0.6$ kHz and $f_h = 1.2$ kHz. Some subjects showed no decrease and others showed a substantial decrease, as is evident by the large error bars in the lower left-hand panel. As was noted in the results for Fig. 1, it is possible that there was either direct masking or MDI from the low-frequency masker in these conditions. Bacon and Viemeister (1985), who looked at TMTFs for low-pass test stimuli only showed an increase in sensitivity as level was increased.

Cutoff frequencies predicted by the single-channel model are higher than those for the multichannel model for lower frequency regions, and the multichannel model always predicts higher sensitivity than the single-channel model. This is due to the fact that all of the channels in the multichannel model can pass the lower modulation frequencies, and therefore that model predicts lower thresholds for the lower frequencies. At the higher modulation frequencies, fewer channels can pass the modulation, and therefore the thresholds predicted for the single- and the multichannel

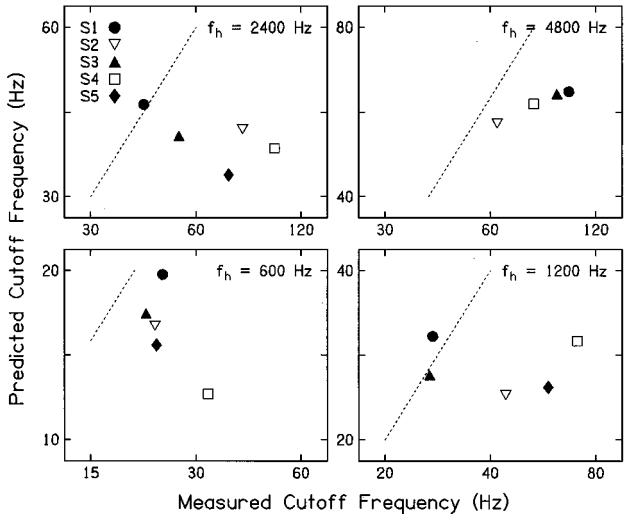

FIG. 10. Cutoff frequencies from TMTFs predicted by the multichannel model plotted against the cutoff frequencies from the measured data, for test stimuli at a spectrum level of 10 dB.

model are about the same. This leads to a higher cutoff frequency for the TMTF predicted by the single-channel model. In higher frequency regions, only a few filters fit into the test stimulus frequency range, so the model predictions converge. Although in general the predictions of the single-channel model are closer to the data than those of the multichannel model, the predicted sensitivity is too low at the lower level, and in general the predictions are far enough from the data to preclude favoring one model over the other. Dau *et al.* (1997b) were able to more successfully predict the effects of carrier bandwidth on thresholds using a multichannel version of the modulation filterbank model than a single-channel one.

4. Individual differences

At the lower level, the data show an increase in cutoff frequency with frequency region, which parallels that predicted by the models. This suggests that peripheral filtering could be a factor at this level. Therefore, it is of interest to examine whether measuring frequency selectivity individually for each subject led to a correlation between the measured and predicted cutoff frequencies of individual TMTFs. In Fig. 10 cutoff frequencies predicted by the multichannel model using each subject's estimated filter functions are plotted against cutoff frequencies estimated from each subject's TMTFs. If the predictions were exact, the data points would line up along the dashed line in each panel. As was already evident from Fig. 9, predicted cutoff frequencies are consistently lower than the measured ones, so the points fall below the line. If the predictions were at least correlated with the data, the order of the individual subject points for a given condition would be the same from left to right as from bottom to top. This holds true only when $f_h = 4800$ Hz, where the cutoff frequencies for the measured data are not significantly different from the broadband case, suggesting that peripheral filtering is not playing a major role. Thus, the individual frequency selectivity data do not improve the predictions of the model.

III. DISCUSSION

A. Measured TMTFs

The major finding in experiment 1 is the fact that TMTF cutoff frequency depends on frequency region at low levels but not at high levels. At a test stimulus spectrum level of 10 dB, the cutoff frequency increases with frequency region up to the broadband condition. Patterson *et al.* (1978) also presented data which show an increase in cutoff frequency with frequency region for a test stimulus spectrum level of 25 dB. At a spectrum level of 40 dB, the cutoff frequency of the TMTF remains nearly constant at the broadband cutoff frequency, regardless of frequency region. This is consistent with previous studies that have found no effect of frequency region on the TMTF cutoff frequency (Eddins, 1993, 1999; Dau *et al.*, 1997b; Strickland and Viemeister, 1997), which all used test stimulus spectrum levels at or above 40 dB. The data in the present study also show that regardless of level, when frequency region is held constant and stimuli are not filtered after modulation the effect of increasing bandwidth is to increase sensitivity but not cutoff frequency. This has been shown previously for test stimuli at high levels (Strickland and Viemeister, 1997; Eddins, 1999). However, even with bandwidth constant, Eddins (1999) has shown that sensitivity may also depend on frequency region, and as Fig. 9 shows may also decrease with level for some subjects. For similar conditions, TMTFs measured in this study are nearly identical to those measured by Eddins (1993, 1999) and by Dau *et al.* (1997b). This means that small differences in stimulus generation and the presence or absence of masking noises were not critical to the results.

The results of the present study are also consistent with results for gap detection found by Shailer and Moore (1983). Using bandlimited stimuli presented in notched-noise maskers, they found that gap detection threshold decreased with frequency region and level. Gap detection thresholds decreased in the same manner as the reciprocal of the bandwidth of estimated auditory filters up to a frequency of approximately 1 kHz.

The effects of frequency region and level found in the present study complement and extend the results found in a study done by Bacon and Viemeister (1985). In that study, TMTFs were measured for normal-hearing listeners as a function of level for two types of test stimuli. One was a broadband noise, and the other a noise which was low-pass filtered at 1.6 kHz and presented with a complementary masking noise high-pass filtered at 1.6 kHz. For the broadband noise, sensitivity decreased as the level of the test stimulus decreased below 20 dB SL, but the cutoff frequency did not. With the low-pass noise, sensitivity decreased slightly as level decreased, but the cutoff frequency also decreased.

Bacon and Viemeister speculated that the lower TMTF cutoff frequency seen for the low-pass noise as compared to the broadband noise was due to the smaller bandwidth, not the frequency region. However, coupled with the results of the present study, it is clear that in fact it is the frequency region and level of the test stimulus, and not the bandwidth, which are important in determining the TMTF cutoff fre-

quency. When stimuli are restricted to frequency regions at and above 2.4 kHz, regardless of bandwidth, the cutoff frequency of the TMTF does not change with level, as shown in Figs. 6 and 9. With a broadband test stimulus, for which higher frequency regions may be used, the cutoff frequency of the TMTF also does not change with level (Viemeister, 1979; Bacon and Viemeister, 1985).

The present results suggest that sensitivity increases with bandwidth if frequency region is held constant, as has been shown previously (Eddins, 1993, 1999; Strickland and Viemeister, 1997). However, as Eddins (1999) has shown, sensitivity may also depend on frequency region. Figure 9 shows that sensitivity may also decrease with level for some subjects, which may be due to masking or MDI from surrounding noises.

Taken together with the results of earlier studies, experiment 1 has several practical implications. Listeners will be more sensitive to modulation the wider the bandwidth of the modulated stimulus. Temporal resolution is limited by frequency region at low levels, but little if at all at higher levels. This suggests that for broadband signals, such as speech, at high levels the amplitude envelope may be equally well represented across frequency regions. For lower levels, the representation of the envelope will certainly vary across frequency regions. If listeners are restricted to the lower frequency regions due to damage to higher frequency regions, their temporal resolution will be poorer. This is constant with data of Bacon and Viemeister (1985) and data for the chinchilla from Henderson *et al.* (1984).

B. Predictions

Because previous studies have shown little or no effect of frequency region on TMTF cutoff frequency, it has been suggested that listeners may be able to combine temporal information across channels. This explanation seems even less likely given the dependence of cutoff frequency on frequency region at low levels. Why should listeners be able to combine information across channels at high levels but not at low? The results of experiment 1 suggest that there are in fact peripheral and central limits to temporal resolution. Experiment 2 was designed to determine whether a single- or multichannel envelope detector model could predict these results, if filters determined for each subject were used as the first stage in the model.

Looking at the model predictions in Fig. 9, clearly the models do not fit the data. Yet the pattern of the model predictions provide some clues to how modulation is processed. For cutoff frequencies at the lower level (top left panel), the data and the multichannel predictions are parallel across the frequency range, both increasing by approximately a factor of 3.6. This is in contrast to the 3-dB filter bandwidths, which increase by a factor of approximately 6.6 across this same range (see Fig. 8). So, the multichannel model, with a peripheral and central limitation, correctly predicts the slope of the cutoff frequencies, which the filter bandwidths alone would not.

The multichannel model predicts on average only a 10% increase in cutoff frequency as the test stimulus spectrum level increases from 10 to 40 dB. Because this is still below the limiting cutoff frequency for a broadband carrier, the model predicts the same frequency effects at a spectrum level of 40 dB as were seen at 10 dB. The subject data show an increase in cutoff frequency of 73% when $f_h = 600$ Hz. The cutoff frequency for the higher level is already nearly as high as the broadband cutoff frequency, and thus there is no frequency effect at the higher level. The cutoff frequencies from the subject data could be consistent with broader peripheral filters than were used in the model, and with a greater increase in filter width with level than the model filters showed. At first glance, the sensitivity results would seem to contradict this theory, however, as sensitivity would then be expected to increase more with level, instead of decreasing. Because masking noise surrounds the test stimuli, however, broader filters might pass masking noise as well as the signal, which would account for the decrease in sensitivity even though the cutoff frequency increases.

This suggests the possibility that frequency selectivity and the TMTF cutoff frequency at low levels both reflect the effects of peripheral filtering, but that the psychoacoustically derived auditory filter is not truly a measure of peripheral filtering. It seems quite likely that the outputs of peripheral filters may be processed by the central auditory system in different ways depending on the task. For example, peripheral filtering could be quite broad, but if listeners make comparisons across channels in detecting a tone in noise, the resulting frequency resolution could be quite precise. When doing a temporal resolution task, where broader filters are more advantageous, channels may be used differently. Another possibility is that different neural cues are used in the two tasks, resulting in different apparent ''filters.'' This could explain why even at the lower level, individual variability in frequency selectivity does not account for individual variability in TMTF cutoff frequency. This lack of correlation has also been found in other studies comparing temporal resolution and frequency resolution within the same subjects (Moore *et al.*, 1993; Holube *et al.*, 1998).

Coupled with this is the possibility that a more complex model could well be more successful at predicting the data. The modulation filterbank model (Dau *et al.*, 1997b, discussed in the introduction to experiment 2, filters the envelope spectrum into different frequency regions. Therefore, if a change in peripheral filter width with level were incorporated into the model, a small increase in peripheral filter width might cause a larger change in TMTF cutoff frequency than is predicted by the envelope detector model. Even with the addition of a modulation filterbank, however, if frequency selectivity is solely a measure of peripheral filtering, a high correlation would still be expected between the TMTF cutoff frequencies for the individual data and the individual predictions for each subject, which is not seen (Fig. 10).

ACKNOWLEDGMENTS

This research was partially supported by an NRSA Post Doctoral Fellowship. Sincere thanks to the many anonymous reviewers who provided helpful comments on various versions of this paper.

[1]AM can be created by any phase relationship between the sidebands such that one is in positive phase and the other is in negative phase by the same amount relative to the carrier phase. The phases used in this experiment were chosen so that the modulation would start and end in a valley.

[2]In that study, the ratio of the envelope maximum to the envelope minimum (max/min) was shown to perform the best in predicting effects of modulation masking such as effects of beats, phase effects between signal and masker modulation, and facilitation of detection of high-modulation frequencies with a low-modulation-frequency masker. For predicting TMTFs, however, the max/min is a less stable statistic, because it is based on only one peak and one valley in the envelope, and thus it predicts higher thresholds than the fourth moment. The max/min results could probably be improved by taking multiple maxima and minima, but that was not the focus of the present study.

[3]In the statistical analyses, data and predictions for S5 for $f_h = 4800$ Hz were estimated from the average of the other subjects.

Bacon, S. P., and Viemeister, N. F. (**1985**). ''Temporal modulation transfer functions in normal-hearing and hearing-impaired listeners,'' Audiology **24**, 117–134.

Dau, T., Kollmeier, B., and Kohlrausch, A. (**1997a**). ''Modeling auditory processing of amplitude modulation. I. Detection and masking with narrow-band carriers,'' J. Acoust. Soc. Am. **102**, 2892–2905.

Dau, T., Kollmeier, B., and Kohlrausch, A. (**1997b**). ''Modeling auditory processing of amplitude modulation. II. Spectral and temporal integration,'' J. Acoust. Soc. Am. **102**, 2906–2919.

Eddins, D. A. (**1999**). ''Amplitude-modulation detection at low- and high-audio frequencies,'' J. Acoust. Soc. Am. **105**, 829–837.

Eddins, D. A. (**1993**). ''Amplitude modulation detection of narrow-band noise: Effects of absolute bandwidth and frequency region,'' J. Acoust. Soc. Am. **93**, 470–479.

Formby, C. (**1985**). ''Differential sensitivity to tonal frequency and to the rate of amplitude modulation of broadband noise by normally hearing listeners,'' J. Acoust. Soc. Am. **78**, 70–77.

Formby, C., and Muir, K. (**1988**). ''Modulation and gap detection for broadband and filtered noise signals,'' J. Acoust. Soc. Am. **84**, 545–550.

Forrest, T., and Green, D. (**1987**). ''Detection of partially filled gaps in noise and the temporal modulation transfer function,'' J. Acoust. Soc. Am. **82**, 1933–1943.

Greenwood, D. D., and Joris, P. X. (**1996**). ''Mechanical and 'temporal' filtering as codeterminants of the response by cat primary fibers to amplitude-modulated signals,'' J. Acoust. Soc. Am. **99**, 1029–1039.

Hartmann, W. M., and Pumplin, J. (**1988**). ''Noise power fluctuations and the masking of sine signals,'' J. Acoust. Soc. Am. **83**, 2277–2289.

Henderson, D., Salvi, R., Pavek, G., and Hamernik, R. (**1984**). ''Amplitude modulation thresholds in chinchillas with high-frequency hearing loss,'' J. Acoust. Soc. Am. **75**, 1177–1183.

Holdsworth, J., Nimmo-Smith, I., Patterson, R., and Rice, P. (**1988**). ''Implementing a gammatone filter bank,'' Annex C of the SVOS Final Report (Part A: The Auditory Filter Bank).

Holube, I., Kinkel, M., and Kollmeier, B. (**1998**). ''Binaural and monaural auditory filter bandwidths and time constants in probe tone detection experiments,'' J. Acoust. Soc. Am. **104**, 2412–2425.

Levitt, H. (**1971**). ''Transformed up–down methods in psychoacoustics,'' J. Acoust. Soc. Am. **49**, 467–477.

Moore, B. C. J., Peters, R. W., and Glasberg, B. R. (**1993**). ''Detection of temporal gaps in sinusoids: Effects of frequency and level,'' J. Acoust. Soc. Am. **93**, 1563–1570.

Patterson, R. D., Johnson-Davies, D., and Milroy, R. (**1978**). ''Amplitude-modulated noise: The detection of modulation versus the detection of modulation rate,'' J. Acoust. Soc. Am. **63**, 1904–1911.

Patterson, R. D., Nimmo-Smith, I., Holdsworth, J., and Rice, P. (**1987**). ''An efficient auditory filterbank based on the gammatone function,'' Paper presented at a meeting of the IOC Speech Group on Auditory Modeling at RSRE, 14–15 December.

Patterson, R. D., Nimmo-Smith, I., Weber, D. L., and Milroy, R. (**1982**). ''The deterioration of hearing with age: Frequency selectivity, the critical ratio, the audiogram, and speech threshold,'' J. Acoust. Soc. Am. **72**, 1788–1803.

Rodenburg, M. (**1977**). ''Sensitivity of the auditory system to differences in intensity,'' Ph.D. dissertation, Erasmus University of Rotterdam, Netherlands.

Rosen, S., and Baker, R. J. (**1994**). ''Characterizing auditory filter nonlinearity,'' Hear. Res. **73**, 231–243.

Rosen, S., Baker, R. J., and Darling, A. M. (**1995**). ''Nonlinearities of human auditory filtering,'' in Abstracts of the Eighteenth Annual Midwinter Research Meeting of the Association for Research in Otolaryngology, 5–9 February 1995, St. Petersburg Beach, FL, Abstract Number 214, p. 54.

Shailer, M. J., and Moore, B. C. J. (**1983**). ''Gap detection as a function of frequency, bandwidth, and level,'' J. Acoust. Soc. Am. **74**, 467–473.

Strickland, E. A., and Viemeister, N. F. (**1996**). ''Cues for discrimination of envelopes,'' J. Acoust. Soc. Am. **99**, 3638–3646.

Strickland, E. A., and Viemeister, N. F. (**1997**). ''The effects of frequency region and bandwidth on the temporal modulation transfer function,'' J. Acoust. Soc. Am. **102**, 1799–1810.

van Zanten, G. A. (**1980**). ''Temporal modulation transfer functions for intensity modulated noise bands,'' in *Psychophysical, Physiological and Behavioural Studies in Hearing*, edited by G. van den Brink and F. A. Bilsen (Delft U.P., Delft, The Netherlands), pp. 206–209.

Viemeister, N. F. (**1977**). ''Temporal factors in audition: A systems analysis approach,'' in *Psychophysics and Physiology of Hearing*, edited by E. F. Evans and J. P. Wilson (Academic, London), pp. 419–427.

Viemeister, N. F. (**1979**). ''Temporal modulation transfer functions based upon modulation thresholds,'' J. Acoust. Soc. Am. **66**, 1364–1380.

On the relative influence of individual harmonics on pitch judgment[a)]

Huanping Dai
Boys Town National Research Hospital, Omaha, Nebraska 68131

(Received 16 November 1998; revised 29 April 1999; accepted 18 October 1999)

Spectral weighting functions were estimated in a pitch-comparison task to assess the relative influence of individual harmonics on listeners' pitch judgment. The stimuli were quasi-harmonic complex tones composed of the first 12 components, with fundamental frequencies ranging from 100 to 800 Hz. On each stimulus presentation the frequency of each harmonic was randomly jittered by a small amount. The perceptual weight for each harmonic was calculated as the correlation coefficient between the binary responses of the listener and the frequency jitters for that harmonic. Although in general the present results conform to previous ones showing the predominant role of several low-ranked harmonics, discrepancies exist in details. Contrary to some previous reports that the dominant harmonics were of fixed harmonic ranks regardless of their frequencies, the current results showed that the dominant harmonics were best described as close to a fixed absolute frequency of 600 Hz. © *2000 Acoustical Society of America.* [S0001-4966(00)00102-8]

PACS numbers: 43.66.Hg, 43.66.Ba, 43.66.Fe [RVS]

INTRODUCTION

The pitch of a harmonic complex tone is determined by information carried by not just the fundamental component but also the higher harmonics [see de Boer (1976), Green (1988), Moore (1993), and Hartmann (1996) for reviews]. These harmonics, however, do not make equal contributions to pitch perception. It is now widely agreed that harmonics that are resolved by the ear play the key role in determining the pitch (Wightman, 1973; Goldstein, 1973; Terhardt, 1974; Terhardt *et al.*, 1982a, b; Moore, 1992; Meddis and Hewitt, 1991a, b; Cohen, 1995). According to the principle of the dominance region, the pitch is derived primarily from just a few low-ranked harmonics (e.g., Ritsma, 1967, 1970).

The idea of a frequency dominance region in pitch perception has evolved through a series of studies (e.g., de Boer, 1956; Flanagan and Guttman, 1960; Plomp, 1967; Ritsma, 1967, 1970; Patterson and Wightman, 1976; Yost, 1982; Moore *et al.*, 1985; Houtsma and Smurzynski, 1990). A quantitative description of the dominance region has been given by the results of Moore *et al.* (1985). Under the assumption that pitch (P) is a weighted average of estimated fundamental frequencies based on individual harmonics,

$$P=\sum_{i=1}^{n} w_i(f_i/i), \tag{1}$$

where f_i is the estimated frequency of the ith harmonic and the weight, w_i, reflects the relative importance of each harmonic. They assessed the weights by measuring how much pitch is shifted by a change in the frequency of each harmonic. The results of their pitch-shift experiment showed that only the first four or five harmonics were effective; the contributions from the higher ones were insignificant.

In the present study, we set out to estimate the weighting functions based on the same rationale as that underlying the study by Moore *et al.* (1985), but using a different method. Unlike their approach in which the frequency of each component was shifted one at a time, the current procedure treated all the components equally by changing their frequencies randomly and simultaneously on each stimulus presentation. With a correlation technique, the weight associated with each harmonic was estimated as the correlation coefficient calculated between the frequency perturbations added to that harmonic and the listener's binary responses in a pitch comparison task. The reader is referred to Richards and Zhu (1994) for the theoretical basis of the correlation technique, and to Ahumada and Lovell (1971), Gilkey and Robinson (1986), Berg (1989), and Lutfi (1995) for the development and variations of this technique. We carried out the measurements over a relatively wide range of fundamental frequencies (from 100 to 800 Hz) in order to examine in greater detail whether the dominance region is best described in harmonic rank or absolute frequency (e.g., Ritsma, 1967, 1970; Plomp, 1967; Patterson and Wightman, 1976).

I. THE ASSUMPTIONS UNDERLYING THE MEASUREMENTS

The underlying assumption for our measurements comes from Goldstein (1973): the auditory system derives the pitch, P, of a complex tone based entirely on the frequencies of the individual components. Although its generality remains an open question, this assumption is probably reasonable for the stimuli used in the present study. For convenience of analysis, we normalize the frequencies by their harmonic ranks, and let η_i be the relative frequency f_i/i. The assumption then can be expressed as $P=P(\eta_1,\eta_2,\ldots,\eta_n)$. Note that η_i are random variables because of the frequency perturbations

[a)]Portions of this paper were presented at the 11th International Symposium of Hearing in Grantham, U.K., in 1997 and the joint 16th International Congress on Acoustics/135th meeting of the Acoustical Society of America in Seattle in 1998.

that the experimenter superimposed on individual harmonics. The change in pitch from a nominal value P_0 can be expressed in a Taylor series,

$$\Delta P = P - P_0 = \sum_{i=1}^{n} w_i \Delta \eta_i + \varepsilon + \xi, \tag{2}$$

in which $w_i = (\partial P / \partial \eta)_{\Delta \eta = 0}$ are the partial derivatives at the nominal pitch P_0, ε represents the higher-order terms of $\Delta \eta_i$, and ξ reflects contribution from internal noise. Within a small region surrounding P_0, in which ε can be ignored, the change in pitch is approximately a linear-weighted sum of the changes in the relative frequencies ($\Delta \eta_i$) plus an error term (ξ). Under the assumption that listeners use Eq. (2) as the decision statistic in judging the pitch of a complex tone, the weights, w_i, can be estimated using a correlation technique (Richards and Zhu, 1994).

In the present study, the weights are estimated in a two-interval, forced-choice, pitch-comparison task. The decision variable is assumed to be the pitch difference between the two observation intervals, denoted as $\Delta P_{(2,1)} = P_{(2)} - P_{(1)}$. Let $\Delta \eta_{i(2,1)}$ denote the difference between the perturbations added to the ith component in the second and first observation intervals. Then we have

$$\Delta P_{(2,1)} = \sum_{i=1}^{n} w_i \Delta \eta_{i(2,1)} + \xi_{(2,1)}. \tag{3}$$

Let R denote the binary response variable; the decision rule can be stated as $R=2$ (respond ''2'') if and only if $\Delta P_{(2,1)} > 0$, else $R=1$ (respond ''1''). The expected correlation coefficient between the response vector R and the perturbation vector $\Delta \eta_{i(2,1)}$ is proportional to the weight, w_i (Richards and Zhu, 1994). In the present study, we simply use the correlation coefficients to represent weights, i.e.,

$$w_i = \mathrm{CORR}[R, \Delta \eta_{(2,1)}]. \tag{4}$$

II. METHODS

Four normal-hearing college students participated. They received the signals in phase at the two ears through Sennheiser headphones (HD450), and were asked to indicate which observation interval had the higher pitch. They were instructed to respond to the holistic (virtual) pitch of the entire stimulus rather than the spectral pitches of individual components. No feedback was given.

The signals presented in both intervals can be described as

$$S_k = \sum_{j=1}^{12} a_j \sin[2\pi j (\eta_{j,k} t)] \quad (k = 1,2), \tag{5}$$

where the index k indicates the observation interval. They were quasi-harmonic complex tones consisting of the first 12 harmonics, each having a level of 60 dB SPL. The duration was fixed at 200 ms, including 10-ms, cosine-squared rise/fall times. The two complex tones on each trial were identical except for the random jitters η_i, added to individual components, which were drawn from a Gaussian distribution with a mean of f_0 and a standard deviation of $0.02 f_0$ (2% jitter at each harmonic). Eight fundamental frequencies (100 to 800 Hz) were tested. All signals were generated digitally (AP2, TDT), played at a sampling rate of 25 kHz (DA1, TDT), and low-pass filtered at 10 kHz (FLT5, TDT). After 1000 trials for each condition, the correlation coefficient (weights) for each harmonic was calculated.

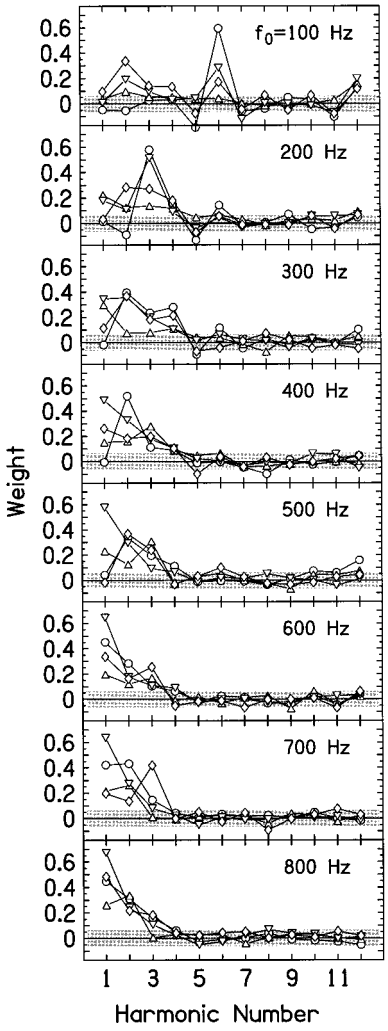

FIG. 1. Individual (circles, 01; downward triangles, 02; diamonds, 03; triangles, 04) weight (correlation coefficient) as a function of harmonic number obtained at eight fundamental frequencies. The shaded area indicates the 95% confidence interval, which is bounded by ± two standard errors around zero correlation.

III. RESULTS AND DISCUSSION

Figure 1 presents the individual weight as a function of harmonic number. The standard error was calculated as $\sigma_e = 1/\sqrt{N}$ for the null hypothesis of zero correlation (Lutfi, 1995). The 95% confidence interval in each panel is indicated by the shaded area, which is bounded by ±two standard errors. We define the dominance region as including harmonics with weights that are significantly greater than zero (i.e., above the shaded area). Although individual results vary considerably regarding the magnitudes of the weights, there is reasonably good agreement regarding the boundaries of the dominance regions. The mean results, which are presented in Fig. 2, capture the main features of the individual ones and will be the focus in our description.

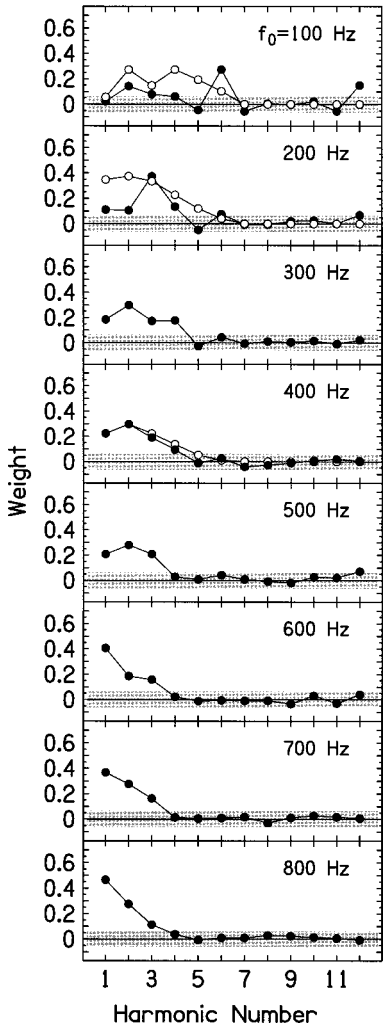

FIG. 2. Mean (filled circles) weight as a function of harmonic number obtained at eight fundamental frequencies. The shaded area indicates the 95% confidence interval. The weighting functions measured by Moore *et al.* (1985) at 100, 200, and 400 Hz are presented (open circles) for comparison.

With the exception of the results at $f_0 = 100$ Hz, which seem to show separate dominance regions at the second, sixth, and twelfth harmonics, the spectral weighting functions show a distinct dominance region. The upper boundary of the dominance region shifts from the fourth harmonic at lower fundamental frequencies ($200\,\text{Hz} \leqslant f_0 \leqslant 400\,\text{Hz}$) to the third harmonic at higher fundamental frequencies ($500\,\text{Hz} \leqslant f_0 \leqslant 800\,\text{Hz}$). The lower bound of the dominance region is not clearly defined; the dominance region often includes the fundamental component. For most cases the dominance region may be described as having a width of three to four harmonics. The peak of the weighting function (the most dominant component) tends to drift towards lower harmonic ranks with increasing fundamental frequency. In some cases, the fundamental component has the strongest influence on the pitch judgment. This pattern can be described by a simple rule in terms of absolute frequency: The harmonic close to 600 Hz appears to have the strongest influence on the pitch judgment. For harmonic complex tones with fundamental frequencies above 600 Hz, the fundamental components are closest to 600 Hz and are therefore dominant. These results, along with some others (e.g., Patterson and Wightman, 1976), disagree with the suggestion that the dominance region is roughly constant in harmonic rank (e.g., Ritsma, 1967, 1970).

To summarize in a simple way, the estimated dominance region has a fixed width in harmonic number (i.e., three to four) and a fixed location in absolute frequency (i.e., near 600 Hz). To apply this rule to arbitrary harmonic complex tone, the three or four components closest to 600 Hz will likely be the dominant harmonics.

For comparison, Fig. 2 also shows the weighting functions obtained by Moore *et al.* (1985) at 100, 200, and 400 Hz. Their estimated weights are rescaled so that the two weighting functions in each panel have the same maximum value. At $f_0 = 100$ and 200 Hz, the dominance regions described by their weighting functions are broader than ours. Two possible causes for this discrepancy are speculated. On the one hand, the weighting functions obtained in the present study may be narrower than the true functions. The reviewers of this paper, Dr. E. M. Burns and Dr. B. C. J. Moore, raised the possibility that the listeners of the present study might have sometimes responded not to the overall pitch of the complex sounds, but to the pitches of individual components. Such analytic listening mode would produce narrower weighting functions. On the other hand, the weighting functions estimated by Moore *et al.* may be broader than the true functions. Because in their procedure the individual harmonics were shifted one at a time, it was possible that the single shifted harmonic attracted undue attention, leading to wider estimated weighting functions.[1] While the cause of discrepancy remains to be determined at these fundamental frequencies, the two studies produced very similar results at $f_0 = 400$ Hz. Overall, they agree that dominant harmonics are likely to be among the first six components of the complex tone.

The possibility of analytic listening in the present study deserves some discussion. The sharply peaked weighting functions, the appearance of multiple dominance regions for the $f_0 = 100$ Hz condition, and the presence of negative weights (e.g., open circles at the fifth harmonic for fundamental frequencies of 100 and 200 Hz, Fig. 1) seem to fit this suspision. Although we did instruct our listeners to respond to the holistic pitch of the overall sound (i.e., the virtual pitch) and not to the individual spectral pitches, we did not have independent means for monitoring to what extent they were responding to the spectral pitches, whether consciously or not. The perceived pitch of a complex tone may be a compromise between the virtual pitch and spectral pitches (see, e.g., Hartmann, 1988). As the relative importance of each pitch type depends on many factors, sorting out their contribution to listeners' pitch judgment can be difficult. However, as far as our purpose of estimating the dominance region is concerned, separating the effect of virtual versus spectral pitches may not be a necessary requirement. According to Terhardt *et al.* (1982b), the virtual pitch is actually derived from the spectral pitches. As a result, harmonics that produce the dominant spectral pitches must also be the ones that produce the virtual pitch, although this does not necessarily imply that the spectral weighting functions for the two

pitch modes should have identical shapes. In many pitch-comparison or pitch-matching tasks, listeners may respond to whichever pitch mode that is prominent without actually realizing whether it is virtual or spectral. Accordingly, the weighting functions obtained in each condition simply reflect the dominance regions for the most prominent pitch mode, be it virtual or spectral.

A related concern, raised by Dr. Burns, is that jittering the frequencies in the current method may have enhanced the influence of spectral pitches relative to that of the virtual pitch. We do not have adequate information to address this concern. Nevertheless, there is no reason to suspect that the jitters should affect the shape of the weighting functions directly, because all components are treated simultaneous and equally (i.e., equal variance on a log-frequency scale) with the random jitters.

IV. GENERAL DISCUSSION

Although the phenomenon of a dominance region has been repeatedly observed in various studies, the reasons for its existence remain unclear. This may be due in part to the different manifestation of the dominance region when measured with different stimuli and different tasks. What we need to look for are the common mechanisms that govern the general phenomenon. Most pitch theories (e.g., Wightman, 1973, Goldstein, 1973, Terhardt, 1974, and more recently, Meddis and Hewitt, 1991a, and Cohen, 1995) account for the dominance phenomenon qualitatively. They assign great importance to harmonics that are resolved by the auditory system. For fundamental frequencies between 100 to 800 Hz, only the first seven or eight harmonics are reasonably well resolved. As a result, the lower-ranked harmonics will assume greater influence on pitch judgment than higher-ranked ones. Resolvability alone, however, is insufficient to explain the finding that the dominance region is often limited to only two or three harmonics. It does not explain why harmonics immediately above and below the dominant ones have little influence on pitch judgment, although they are often equally or even better resolved. Nor does it explain the presence of dominance region for dichotically presented harmonics. Thus, other mechanisms must play a role in shaping the dominance region. In this section we discuss possible mechanisms suggested by some existing pitch theories as well as the implications of the current results.

A. Wightman's pattern-transformation theory

In Wightman's (1973) theory, pitch is calculated based on the internal representation of the autocorrelation function of the stimulus waveform. Specifically, it is represented as the inverse of the estimated time delay ($\hat{\tau}$) of the first mode of the autocorrelation function, i.e., pitch$=1/\hat{\tau}$. The derivation of pitch by this model involves two stages. In the first stage, the neural excitation pattern of the complex tone is obtained. First, the power spectrum of the complex tone is weighted by the outer- and middle-ear transfer function. Here we used the approximated transfer function suggested by Glasberg and Moore (1990) based on equal-loudness contour at 100 Phon. Then, the excitation pattern is obtained by convolving the Roex filter function (e.g., Patterson and Moore, 1986) with the weighted stimulus power spectrum. We used the simple form of the Roex filter, $\mathrm{FLT}(f)=(1+pg)e^{-pg}$, in which $g=|f-f_c|/f_c$. The bandwidth parameter p was set to $p=4f_c/\mathrm{ERB}(f_c)$, in which $\mathrm{ERB}(f_c)=24.7(0.00437f_c+1)$ (Glasberg and Moore, 1990) is the equivalent-rectangular bandwidth of the filter. In the second stage, the internal representation of the autocorrelation function is obtained by taking the inverse Fourier transform of the neural excitation pattern. The pitch value is represented by the delay of the first mode, and the pitch strength is represented by the height of this mode. Because the current study does not concern pitch strength, we will not examine this aspect of the model.

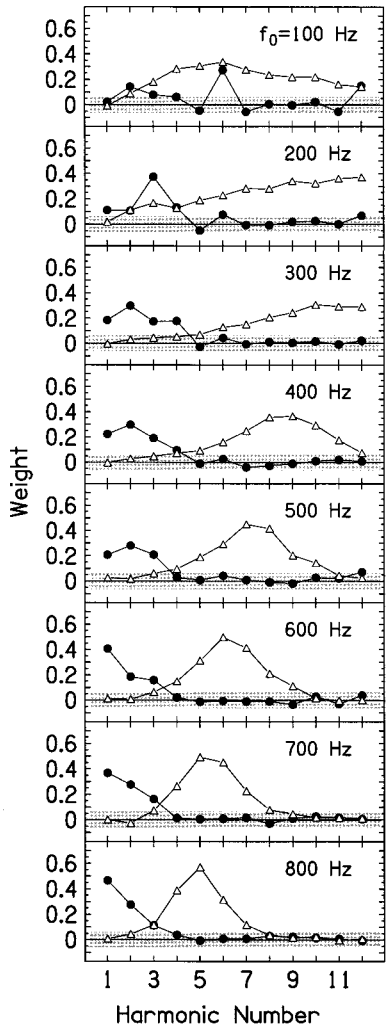

FIG. 3. Weighting function predicted by Wightman's (1973) pattern-transformation model (open triangles). The mean results shown in Fig. 2 are replotted for comparison.

Computer simulations were carried out in which the pitch extractor of Wightman's model performed the same pitch comparison task as the listeners of the current study. The simulation included 1000 trials at each of the eight fundamental frequencies. The weights were calculated as the correlation coefficients between the simulated binary responses and the perturbations (2%) added to the frequencies of individual harmonics. Figure 3 shows the results along with the mean weights taken from Fig. 2.

The weighting functions obtained from Wightman's

model largely reflect the shape of the outer- and middle-ear transfer function, showing a relatively broad dominance region with a peak around 3.6 kHz for fundamental frequencies above 200 Hz. Two other factors further influence the shape of the predicted weighting functions. On the one hand, the higher harmonics are expected to have greater influence on the pitch because their bigger jitters (in absolute frequency) will cause a bigger shift in the delay (τ) of the first mode in the autocorrelation function. On the other hand, the influences of the higher harmonics are offset by the smear of the peaks of their excitation patterns due to the reduced resolution. The combined effects of these two factors are revealed in simulations done without using any outer- and middle-ear transfer function. The predicted weight functions have a relatively broad peak near the sixth or seventh harmonic, and the shapes of the functions are largely independent of fundamental frequency.

Overall, given the particular set of outer- and middle-ear transfer functions and the auditory-filter function adopted here, the weighting functions derived from Wightman's model do not provide a good description of the measured weighting functions. Additional filtering or transfer functions must be included to improve the fit between the predicted and obtained weighting functions. It should be noted that this model as is has no free parameters.

B. Goldstein's optimal-processor theory

In the optimal-processor theory of Goldstein (1973), the pitch of a harmonic complex tone is the maximum-likelihood estimate of the fundamental frequency based on the estimated frequencies of individual harmonics. Obviously, the accuracy of the estimated pitch will depend on the accuracy of the estimated frequencies of the harmonics. Let f_i be the frequency of the ith harmonic. Then the maximum-likelihood estimate of the fundamental frequency is (as shown in the Appendix)

$$\hat{f}_0 = \sum_{i=1}^{n} w_i \left(\frac{f_i}{i} + \xi_i \right), \tag{6}$$

where ξ_i represents the internal noise that corrupts the estimate of f_i/i; it has zero mean and a variance of σ_i^2. The weight w_i is inversely proportional to σ_i^2:

$$w_i = \frac{K}{\sigma_i^2} \tag{7}$$

in which $K = 1/\Sigma_{i=1}^{n} 1/\sigma_i^2$ is a scaling constant, normalizing the sum of weights to unity. In words, Eq. (7) simply says that harmonics whose relative frequencies are estimated more accurately will assume greater importance.

The idea that the dominance region is determined by the error function $\sigma^2(f)$ [Eq. (7)] can be evaluated using existing approximations of the error functions. One approximation comes from frequency-difference limens (DLs) of simple tones measured in isolation, and we choose to use the results obtained by Wier *et al.* (1977). The second comes from frequency-difference limens of harmonics measured within complex tones, by Moore *et al.* (1984) for a fundamental frequency of 200 Hz. The third approximation is derived by Goldstein (1973), based on the musical intelligibility scores measured by Houtsma and Goldstein (1972).

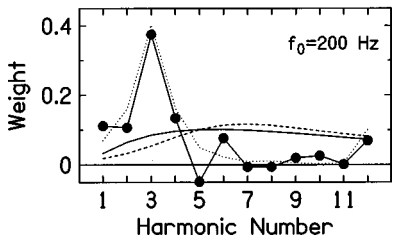

FIG. 4. Weighting functions based on Goldstein's model [Eq. (7)] using various approximations of the error function (solid line based on frequency DLs from Wier *et al.*, 1977; dashed line from Houtsma and Goldstein, 1972; dotted line based on frequency DLs from Moore *et al.*, 1984), and measured in the current study (circles) for $f_0 = 200$ Hz.

Figure 4 compares the weighting functions produced with various approximations of the error function with that measured in the current study at a fundamental frequency of 200 Hz (circles). The weighting functions derived from the frequency DLs obtained with simple tones (solid line) and from musical intelligibility scores obtained with two-tone complexes (dashed line) are much too flat to account for the experimental results obtained with 12-tone complexes (filled circles). This outcome echoed the previous finding by Goldstein (1973) that the error functions obtained with two-tone complexes did not provide a good description of Plomp's (1967) data obtained with 12-tone complexes. In contrast, the error function from the frequency DLs of harmonics measured within complex tones (dotted line) provides an excellent fit to the data. Consequently, the predicted weighting function would be narrower than that estimated by Moore *et al.* (1985) for the fundamental frequency of 200 Hz. The good fit between measured and predicted weighting functions reinforces the argument by Moore *et al.* (1984) that the error function is specific to the particular environment surrounding the harmonics.

One should keep in mind that DLs obtained in frequency discrimination tasks are not direct estimates of the error for estimating the frequencies of harmonics. Whether measured in isolation or within complex tones, discrimination can be influenced by unrelated cues. In Moore *et al.* (1984), cues may come from interactions among harmonics, particularly among higher ones. Despite these concerns, the procedure of Moore *et al.* is probably still the most reasonable among the existing ones for estimating the error functions for complex tones with many components.

The current results have two implications for Goldstein's model, depending on assumptions about whether the pitch processor adjusts the weights according to the external jitter of the frequencies. First, suppose the pitch processor is truly optimal in that it makes decisions based on distributions of both internal and external noises. Then the perceptual weights should be determined by the total error function, including both the internal and the external variability associated with the estimated frequencies of the harmonics. It is reasonable to assume that for the first six or seven harmonics the 2% external jitter dominates the internal variability, and thus the total error function is nearly flat for that part. Ac-

cording to Eq. (7), a flat error function should produce a flat weighting function, which is clearly inconsistent with the data.

Now suppose the pitch processor is only quasi-optimal in that it sets the weights for individual harmonics based entirely on the internal error function. In this case, the presence of the jitters should not affect the listeners' decision rules. This would be highly desirable for the application of the correlation technique. Then the estimated weighting functions can be used to reconstruct the internal error functions based on Goldstein's theory [Eq. (7)]. We will not attempt this task here except to state that the error functions derived this way are specific to the harmonic complex tones and thus dependent on the fundamental frequency.

C. Terhardt's virtual-pitch theory

In the virtual-pitch theory (Terhardt, 1974; Terhardt *et al.*, 1982a, b), the virtual pitch is derived from the spectral pitches of resolved harmonics. Each resolved harmonic has a set of subharmonics, and the predominant virtual pitch corresponds to the frequency where the maximum number of subharmonics from different harmonics coincide. The relative importance of different harmonics is described by a frequency weighting function derived empirically based on auditory data on complex tone stimuli (see Fig. 3 in Terhardt *et al.*, 1982b). This bell-shaped function has a maximum at 700 Hz, and its magnitude drops to half at frequencies around 100 and 5000 Hz. Terhardt *et al.* noted the striking similarity between their function and the frequency-region importance function deduced by Fletcher and Galt (1950) from speech intelligibility data. The weighting function used by Terhardt *et al.* also agrees with the present results in that the components around 600 to 700 Hz are assumed to be the most influential. However, their function is much too broad to produce the estimated perceptual weighting functions. Further filtering must be included to produce reasonable fits.

It has become clear from the above discussions of these models that they cannot produce the correct perceptual weighting function when a fixed frequency-weighting function is implemented. The predicted perceptual weighting functions are either too broad or tuned to the wrong frequencies, or both. The only satisfactory prediction is obtained using the error function based on frequency DLs measured within harmonic complex tone by Moore *et al.* (1984) for $f_0 = 200$ Hz. Although only Goldstein's model specifically employs error functions, the error functions can be easily incorporated in other models and can potentially improve their predictions.

ACKNOWLEDGMENTS

The author thanks David M. Green, Brian C. J. Moore, William Hartmann, and Doug Keefe for discussions, and Donna Neff and two formal reviewers, Edward M. Burns and Brian C. J. Moore, for many comments on earlier drafts of this paper. This research was supported by NIH/NIDCD Grant No. R29-DC01827.

APPENDIX: WEIGHTING FUNCTION PREDICTED BY GOLDSTEIN'S THEORY

The spectral weighting function as predicted by Goldstein's optimum-processor theory can be derived as follows. Let f_m be the frequency of the mth harmonic and y_m be the estimate of f_m/m. Assuming that y_m are Gaussian and independent variables with $E(y_m)=f_m/m$, and Var $(y_m)=\sigma_m^2$, the likelihood that y_m are generated with a fundamental frequency of f_0 is

$$L(f_0,y_1,y_2,\ldots)=K\prod_{m=1}^{n}\exp\left[-\frac{(y_m-f_0)^2}{2\sigma_m^2}\right], \tag{A1}$$

where K is a constant. The maximum-likelihood estimator of f_0 (the estimated pitch), $\hat{f}_0$, can be obtained by solving

$$\frac{\partial}{\partial f_0}L\equiv 0, \tag{A2}$$

which leads to

$$\hat{f}_0=\sum_{m=1}^{n} w_m y_m \tag{A3}$$

in which

$$w_m=\frac{1}{\sigma_m^2\Sigma_{j=1}^{n}1/\sigma_j^2}=\frac{Konst}{\sigma_m^2}. \tag{A4}$$

Equation (A4) is shown as Eq. (3) in the text.

Two points should be noted. First, the need to estimate the harmonic rank for each harmonic is avoided because in our cases the harmonic complex tones always have the complete first 12 harmonics. Second, in general, the variance σ_m^2 should be assumed to depend on f_m, thus also on f_0. Here, in differentiating L we treat σ_m^2 as a local constant, as did Goldstein (1973).

[1]B. C. J. Moore (personal communication) argued that since their weights within each harmonic complex tone sum to nearly unity, the effect of undue attention, if any, must have been small. Although reasonable in principle, this argument depends on how reliable the weight estimates are.

Ahumada, A., and Lovell, J. (**1971**). ''Stimulus features in signal detection,'' J. Acoust. Soc. Am. **49**, 1751–1756.

Berg, B. G. (**1989**). ''Analysis of weights in multiple observation tasks,'' J. Acoust. Soc. Am. **86**, 1743–1746.

de Boer, E. (**1956**). ''On the 'Residue' in Hearing,'' Ph.D. thesis, Amsterdam.

de Boer, E. (**1976**). ''On the 'residue' and auditory pitch perception,'' in *Handbook of Sensory Physiology*, edited by W. D. Keidel and W. D. Neff (Springer-Verlag, New York), Vol. V/3, pp. 479–583.

Cohen, M. A., Grossberg, S., and Wyse, L. L. (**1995**). ''A spectral network model of pitch perception,'' J. Acoust. Soc. Am. **98**, 862–879.

Flanagan, J. L., and Guttman, N. (**1960**). ''On the pitch of periodic pulses,'' J. Acoust. Soc. Am. **32**, 1308–1319.

Fletcher, H., and Galt, R. H. (**1950**). ''The perception of speech and its relation to telephony,'' J. Acoust. Soc. Am. **22**, 89–151.

Gilkey, R. H., and Robinson, D. (**1986**). ''Models of auditory masking: A molecular psychophysical approach,'' J. Acoust. Soc. Am. **79**, 1499–1510.

Glasberg, B. R., and Moore, B. C. J. (**1990**). ''Derivation of auditory filter shapes from notched-noise data,'' Hear. Res. **47**, 103–138.

Goldstein, J. L. (**1973**). ''An optimum processor theory for the central formation of the pitch of complex tones,'' J. Acoust. Soc. Am. **54**, 1496–1515.

Green, D. M. (**1988**). ''Audition: Psychophysics and Perception,'' in *Stevens' Handbook of Experimental Psychology, Vol. 1*, edited by R. C. Atkinson, R. J. Bernstein, G. Lindsay, and R. D. Luce (Wiley, New York), pp. 327–376.

Hartmann, W. M. (**1988**). ''Pitch perception and the segregation and integration of auditory entities,'' in *Auditory Functions*, edited by G. M. Edelman, W. E. Gall, and W. M. Cowan (Wiley, New York).

Hartmann, W. M. (**1996**). ''Pitch, periodicity, and auditory organization,'' J. Acoust. Soc. Am. **100**, 3491–3502.

Houtsma, A. J. M., and Goldstein, J. (**1972**). ''The central origin of the pitch of complex tones: Evidence from musical interval recognition,'' J. Acoust. Soc. Am. **51**, 520–529.

Houtsma, A. J. M., and Smurzynski, J. (**1990**). ''Pitch identification and discrimination for complex tones with many harmonics,'' J. Acoust. Soc. Am. **87**, 304–310.

Lutfi, R. A. (**1995**). ''Correlation coefficients and correlation ratios as estimates of observer weights in multiple-observation tasks,'' J. Acoust. Soc. Am. **92**, 1333–1334.

Meddis, R., and Hewitt, M. J. (**1991a**). ''Virtual pitch and phase sensitivity of a computer model of the auditory periphery. I. Pitch identification,'' J. Acoust. Soc. Am. **89**, 2866–2882.

Meddis, R., and Hewitt, M. J. (**1991b**). ''Virtual pitch and phase sensitivity of a computer model of the auditory periphery. II. Phase sensitivity,'' J. Acoust. Soc. Am. **89**, 2883–2894.

Moore, B. C. J. (**1992**). *Introduction to the Psychology of Hearing*, 2nd ed. (Academic, London).

Moore, B. C. J. (**1993**). ''Frequency analysis and pitch perception,'' in *Human Psychophysics*, edited by W. A. Yost, A. N. Popper, and R. R. Fay (Springer-Verlag, New York), pp. 56–115.

Moore, B. C. J., Glasberg, B. R., and Peters, R. W. (**1985**). ''Relative dominance of individual partials in determining the pitch of complex tones,'' J. Acoust. Soc. Am. **77**, 1853–1860.

Moore, B. C. J., Glasberg, B. R., and Shailer, M. J. (**1984**). ''Frequency and intensity difference limens for harmonics within complex tones,'' J. Acoust. Soc. Am. **75**, 550–562.

Patterson, R., and Moore, B. C. J. (**1986**). ''Auditory filters and excitation patterns as representations of frequency resolution,'' in *Frequency Selectivity in Hearing*, edited by B. C. J. Moore (Academic, London), pp. 123–177.

Patterson, R., and Wightman, F. (**1976**). ''Residue pitch as a function of component spacing,'' J. Acoust. Soc. Am. **59**, 1450–1459.

Plomp, R. (**1967**). ''Pitch of complex tones,'' J. Acoust. Soc. Am. **41**, 1526–1533.

Ritsma, R. J. (**1967**). ''Frequencies dominant in the perception of the pitch of complex sounds,'' J. Acoust. Soc. Am. **42**, 191–198.

Ritsma, R. J. (**1970**). ''Periodicity detection,'' in *Frequency Analysis and Periodicity Detection in Hearing*, edited by R. Plomp and G. F. Smoorenburg (Sijthoff, Leiden, The Netherlands), pp. 250–263.

Richards, V. M., and Zhu, S. (**1994**). ''Relative estimates of combination weights, decision criteria, and internal noise based on correlation coefficients,'' J. Acoust. Soc. Am. **95**, 423–434.

Terhardt, E. (**1974**). ''Pitch, consonance, and harmony,'' J. Acoust. Soc. Am. **55**, 1061–1068.

Terhardt, E., Stoll, G., and Seewann, M. (**1982a**). ''Pitch of complex signals according to virtual-pitch theory: Tests, examples, and predictions,'' J. Acoust. Soc. Am. **71**, 671–678.

Terhardt, E., Stoll, G., and Seewann, M. (**1982b**). ''Algorithm for extraction of pitch and pitch salience from complex tonal signals,'' J. Acoust. Soc. Am. **71**, 679–688.

Wier, C. C., Jesteadt, W., and Green, D. M. (**1977**). ''Frequency discrimination as a function of frequency and sensation level,'' J. Acoust. Soc. Am. **61**, 178–184.

Wightman, F. (**1973**). ''The pattern-transformation model of pitch,'' J. Acoust. Soc. Am. **54**, 407–416.

Yost, W. A. (**1982**). ''The dominance region and ripple noise pitch: A test of the peripheral weighting model,'' J. Acoust. Soc. Am. **72**, 416–425.

Extracting spectral envelopes: Formant frequency matching between sounds on different and modulated fundamental frequencies

Pascal Dissard and C. J. Darwin[a)]
Experimental Psychology, University of Sussex, Brighton BN1 9QG, United Kingdom

(Received 28 December 1998; revised 17 May 1999; accepted 18 October 1999)

The four experiments reported here measure listeners' accuracy and consistency in adjusting a formant frequency of one- or two-formant complex sounds to match the timbre of a target sound. By presenting the target and the adjustable sound on different fundamental frequencies, listeners are prevented from performing the task by comparing the absolute or relative levels of resolved spectral components. Experiment 1 uses two-formant vowellike sounds. When the two sounds have the same $F0$, the variability of matches (within-subject standard deviation) for either the first or the second formant is around 1%–3%, which is comparable to existing data on formant frequency discrimination thresholds. With a difference in $F0$, variability increases to around 8% for first-formant matches, but to only about 4% for second-formant matches. Experiment 2 uses sounds with a single formant at 1100 or 1200 Hz with both sounds on either low or high fundamental frequencies. The increase in variability produced by a difference in $F0$ is greater for high $F0$'s (where the harmonics close to the formant peak are resolved) than it is for low $F0$'s (where they are unresolved). Listeners also showed systematic errors in their mean matches to sounds with different high $F0$'s. The direction of the systematic errors was towards the most intense harmonic. Experiments 3 and 4 showed that introduction of a vibratolike frequency modulation (FM) on $F0$ reduces the variability of matches, but does not reduce the systematic error. The experiments demonstrate, for the specific frequencies and FM used, that there is a perceptual cost to interpolating a spectral envelope across resolved harmonics. [S0001-4966(00)00202-2]

PACS numbers: 43.66.Jh, 43.71.Es [RVS]

INTRODUCTION

This paper addresses the general question of what representations of sound mediate between a peripheral, spectral representation and the abstract categories of speech such as vowels. Specifically, it measures how accurately and consistently listeners can match a formant frequency in complex sounds under conditions which force them to use abstract representations of a sound's spectrum.

The idea behind the experiments is that if listeners have ready access to a particular representation such as a spectral envelope or a formant frequency, they should be able to make perceptual matches on the basis of that representation despite variation in other dimensions of the stimulus.

Although a number of experiments have been carried out on the ability of listeners to discriminate changes in formant frequency for single-formant sounds (see, for example, Lyzenga and Horst, 1995, 1997) or for multi-formant synthetic vowels (see for example, Kewley-Port and Watson, 1994; Kewley-Port, 1995; Kewley-Port *et al.*, 1996), these experiments can all be performed either by a simple identity match of (part of) the excitation pattern (Moore and Glasberg, 1983) or, where signal levels are roved, by profile analysis (Green, 1988)—comparing *relative* levels in the excitation pattern. Listeners need not extract either an interpolated spectral envelope or a formant frequency in order to perform the task.

By presenting sounds on different fundamental frequencies ($F0$), we can reduce the value to listeners of being able to compare absolute or relative levels at corresponding places in the excitation pattern. If they are to obtain a reliable, veridical match, they must then use a more abstract representation which is closer to the spectral envelope.

Whether the simple strategy of comparing corresponding places on the excitation pattern is useful depends on the relationship between the formant frequency and the fundamental frequency. When a formant is excited by high-numbered, unresolved harmonics, the spectral envelope is represented explicitly in the excitation pattern. Sounds on different fundamentals could then be matched by comparing absolute (or relative) levels of excitation patterns. However, when the formant frequency is a smaller multiple of $F0$, so that harmonics close to the formant peak are resolved, their local peaks prevent the spectral envelope being explicitly represented in the excitation pattern. If the spectral envelope is to be used by listeners, it must be derived from the excitation pattern. This process may have a perceptual cost: listeners may have relatively greater difficulty in making different-$F0$ matches for sounds presented on high $F0$'s than for sounds presented on low $F0$'s. The main object of this paper is to test whether there is such a perceptual cost.

How the spectral envelope might be extracted from an excitation pattern of resolved harmonics has not been dis-

[a)]Author to whom correspondence should be addressed. Electronic mail: cjd@biols.sussex.ac.uk

cussed in the literature, although the analogous problem of vernier acuity in spatial vision has received some attention. Observers can locate the spatial position of a spatially periodic pattern with a precision as high as 5–10-s arc, even though the pattern is coarsely sampled at an interval over ten times that amount (Morgan and Watt, 1982). They probably achieve this by interpolating luminance profiles on the basis of a few samples (Kontsevich and Tyler, 1998).

A number of papers have addressed the more complex problem of how the first formant frequency ($F1$) might be extracted. An early suggestion that listeners simply equate $F1$ with the frequency of the dominant harmonic (Mushnikov and Chistovich, 1972) has been discounted in favor of methods which either form a weighted sum of two (Carlson *et al.*, 1975; Assmann and Nearey, 1987) or more (Darwin and Gardner, 1985) harmonic frequencies close to the formant. Klatt (1986) has pointed out that such weighting models, together with alternative approaches such as spectral smoothing and linear predictive coding (LPC) analysis produce formant frequency estimates which are biased in the direction of the dominant harmonic. Such bias can produce formant estimation errors as large as 16%. In contrast, vowel identification experiments have found no explicit evidence for such shifts (Florén, 1979; Klatt, 1985). Experiment 2 of this paper provides evidence of such a bias.

The third issue addressed in this paper is whether adding frequency modulation (FM) to $F0$ changes the accuracy and veridicality of formant-frequency matches. In principle, a changing $F0$ can provide additional information about the value of the spectral envelope over a range of values around each harmonic, and, through amplitude modulation of the individual harmonics, information about the slope of the spectral envelope. However, previous work on the effects of vibratolike FM of $F0$ on the perception of formants or of vowels has given mixed results.

For example, on the one hand, McAdams and Rodet (1988) showed that differences in the slope of spectral envelopes could be discriminated and identified in the presence of a small amount of vibrato. They interpreted their data in terms of listeners using the spectral tracing produced by vibrato to discriminate and identify spectral envelopes with different formant frequencies (although whether the dynamic aspects of the stimulus were necessary was not established). On the other hand, Marin and McAdams (1991) could find no evidence for such spectral tracing increasing the prominence that vibrato gives a vowel against a background of other steady vowels. Similarly, rather little effect of vibrato on vowel identification thresholds was found by Demany and Semal (1990) for vowels ($F0 = 100$ Hz) masked either by noise or by a different-$F0$ pulse-train.

Beneficial effects of vibrato on vowel identification are, in principle, more likely to be found at high than at low $F0$'s since the sparser sampling of the spectral envelope can make vowel identification worse at high $F0$'s (Ryalls and Lieberman, 1982) although not invariably (Hillenbrand and Nearey, 1999). It is surprising then that Sundberg (1975, 1977) was unable to find such a beneficial effect. He examined the influence of ± 0.5 semitone ($\pm 3\%$) vibrato on the identification of 12 synthetic Swedish vowels with $F0$'s between 300 and 1000 Hz. Overall, the effects were small, and in the majority of cases where the vibrato affected the response, the vowel identification became somewhat harder when the stimulus was presented with than without vibrato. Carlson *et al.* (1975) also comment that a modulated $F0$ slightly decreased the reliability of vowel labelling judgements. In experiments 3 and 4 we ask whether FM improves listeners' ability to match single-formant sounds on different $F0$'s.

In summary, the experiments described in this paper measure listeners' ability to match a formant frequency in complex sounds under stimulus conditions which force them to use a representation of a sound's spectrum that is more abstract than a simple excitation pattern. Subjects adjust the frequency of a single formant of either a one- or a two-formant sound so that it matches a similar sound, which can be played on the same or a different $F0$. We use the within-subject standard deviation of matches as a measure of the difficulty of the task.

The first experiment, which establishes the viability of the technique, uses two-formant vowels, with subjects adjusting either the first or the second formant. The sounds that we have used last 500 ms. We use relatively long vowels in order to improve our chances of finding effects due to the dynamic changes in $F0$ that are introduced in experiments 3 and 4. Experiment 2 compares matching reliability for single-formant sounds when the target and the adjustable sounds have either the same $F0$ or different $F0$'s and when the target formant frequency is in a region of resolved harmonics (high $F0$) or of unresolved harmonics (low $F0$). Experiments 3 and 4 ask whether a sinusoidally modulated $F0$ increases the reliability of matching.

I. EXPERIMENT 1

A. Stimuli and procedure

On each trial subjects heard two 500-ms sounds: a target sound followed after 500 ms by an adjustable sound. They adjusted the frequency of one formant of a periodically excited two-formant complex to match the timbre of the similar target sound, by moving a roller-ball up or down. Instructions given to subjects were to match the timbre of the sounds, in other words to try to get the same quality of sound between target and adjustable sound. The adjustable sound could have either the same or a different fundamental frequency from the target ($F0$ values: 90, 120, 150 Hz). The pair of sounds could be repeated as often as necessary on each trial by pressing the roller-ball's button.

In experiment 1a, the second formant ($F2$) of both sounds was kept constant at 2100 Hz (bandwidth 200 Hz) and the target's first formant ($F1$) could be either 400, 550, or 700 Hz (bandwidth 100 Hz). In experiment 1b, $F1$ was fixed at 550 Hz and the target's $F2$ could be either 1500, 2100, or 2600 Hz. Within a block of trials the target could have either of the three formant values, but the $F0$ of the adjustable sound, and whether the target had the same $F0$ as the adjustable sound or a different $F0$ was fixed. When the $F0$'s were different, the $F0$ of the target sound also varied within a block of trials. Consequently, there were three different targets in blocks where the $F0$ was the same, and six

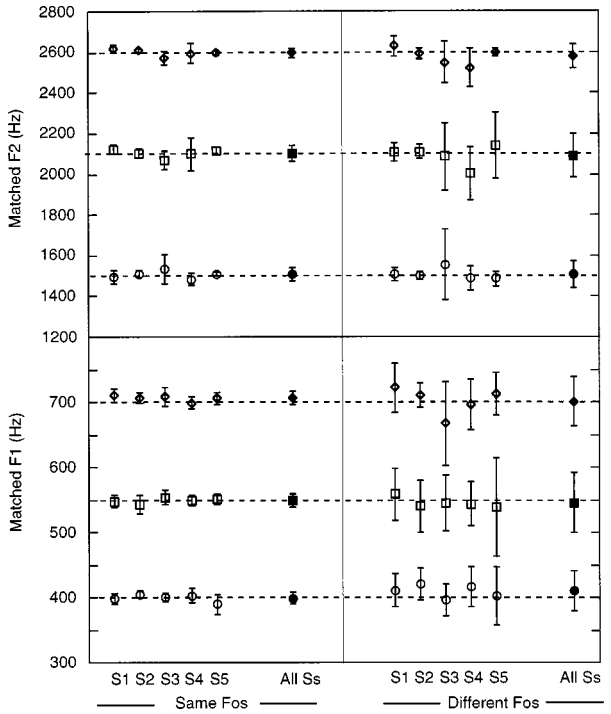

FIG. 1. Open symbols represent mean matches with standard deviations across five replications for individual subjects in experiment 1a ($F1$ matching), lower panel, and in experiment 1b ($F2$ matching), upper panel. Closed symbols represent average matches across subjects together with the average within-subject standard deviation.

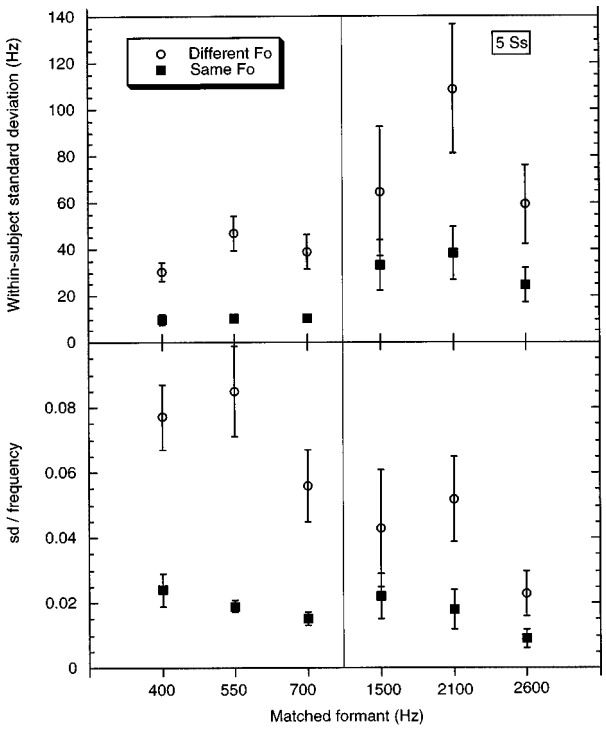

FIG. 2. The upper panel shows the mean within-subject standard deviations (and their across-subject standard errors) for formant matches in experiment 1. The lower panel plots the same data as a fraction of the center frequency of the matched formant.

different targets in blocks that had different $F0$'s. Each target sound was matched five times in a quasi-random order. The order of the 12 experimental blocks were randomized across subjects so that each block appeared equally in each serial position across subjects.

Sounds were synthesized in real time at 22.05 kHz using the parallel branch of SenSyn PPC™ (Sensimetrics, Cambridge, MA) incorporated into custom software. Formant amplitudes were set equal in the SenSyn tables and the overall output level was around 60 dB SPL. Voice source parameters were set to their default values, which are the same as described in Klatt (1980). Sounds were output through a Digidesign Protools board and presented through Sennheiser HD414 headphones in an IAC booth. An Apple Power Macintosh 7100 computer controlled the experiment.

At the beginning of each trial the formant frequency of the adjustable sound was chosen at random from the permitted range (150 to 850 Hz in experiment 1a, 1000 to 3100 Hz in experiment 1b). As subjects moved the roller-ball to adjust the formant frequency of the comparison sound a screen cursor also moved. The cursor was recentered after each sound pair so that subjects could not base their adjustment on the cursor's position. In experiment 1a, moving the cursor by half a screen led to a change of about 33 Hz (fine adjustment) or 100 Hz (coarse adjustment). In experiment 1b, the adjustment was either 33 Hz (fine) or 310 Hz (coarse). Subjects could toggle between the coarse and fine adjustments. If the formant frequency was adjusted outside the permitted range, it was reset to a random value within the range and a warning sound played.

Six subjects (including the two authors) participated in the experiment. Subjects were university students or staff and were paid for their services. All had pure-tone thresholds within the normal range at octave frequencies between 250 Hz and 4 kHz. Subjects were introduced to the task by undertaking between 10 and 40 trials with the experimenter providing feedback to ensure that they understood the task. One subject's data were removed because of grossly inconsistent matches for sounds that had the same $F0$.

B. Results

Average matches across five replications for individual subjects and their within-subject standard deviation are shown by the open symbols in Fig. 1. Within-subject standard deviations were calculated for each target/adjustable sound condition across the five replications. These standard deviations were then averaged across conditions to give the values plotted in Fig. 1. The filled symbols show the mean across all five subjects together with the average within-subject standard deviation.

Averaging across subjects, mean matches correspond closely to their target values, with no systematic differences whether or not the sounds differ in $F0$. However, as is apparent from the within-subject standard deviation error bars in Fig. 1, matches are more variable when the sounds have different $F0$'s than when they have the same $F0$ [$F(1,4) = 16.5$, $p < 0.02$]. These standard deviations are themselves plotted in Fig. 2 both as raw (Hz) values (upper panel) and as a proportion of the target formant value (lower panel). The increase in variability when the sounds have different $F0$'s rather than the same $F0$ is significant both for the raw

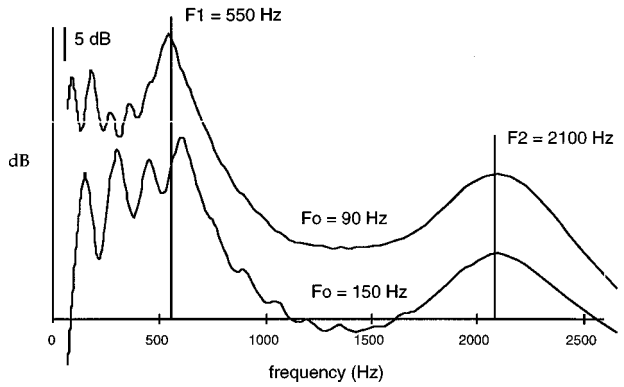

FIG. 3. Excitation patterns for two of the target sounds in experiment 1. Both sounds $F1$ at 550 Hz and $F2$ at 2100 Hz (marked by vertical lines). The upper curve has a fundamental frequency of 90 Hz, the bottom of 150 Hz. The curves are vertically displaced for clarity.

$[F(1,4)=16.5,\ p<0.02]$ and proportional scores $[F(1,4)=31.8,\ p<0.005]$.

Figure 2 also shows that a difference in $F0$ increases the proportional within-subject variability more for $F1$ matches than for $F2$ $[F(1,4)=20.4,\ p=0.01]$. The size of the $F0$ difference (i.e., 30 or 60 Hz) had no significant effect on match variability.

C. Discussion

The first experiment has shown that subjects can make formant matches across two-formant vowellike sounds on different fundamentals. However, the within-subject reliability of these matches is less than those made across sounds that have the same $F0$. Moreover, the difference in $F0$ impairs performance more for the $F1$ matches than for the $F2$ matches.

This pattern of results can be explained by considering the excitation pattern produced by the sounds we have used. When matches are being made between sounds that have the *same* $F0$, listeners do not need to extract the spectral envelope, but can simply match the absolute or relative levels of the excitation pattern at corresponding frequencies around the formant frequency. The resulting matches are accurate and show low within-subject variability. The variability of matches for sounds on the same $F0$ is comparable with discrimination threshold data from Lyzenga and Horst (1998). They found jnd's (equivalent to 63% correct and using a roving level) of 1%–3% for discrimination of changes to $F1$ in the presence of a static $F2$ (at around 2 kHz) on a fundamental of 100 Hz.

Placing sounds on *different* fundamentals complicates the listener's task in two ways. First, the sounds can no longer be adjusted to be identical: there is always a difference in pitch which can distract listeners from their timbral judgements. This complication applies to both the $F1$ matches and the $F2$ matches.

Second, for the $F1$ matches, where the harmonics close to the matched formant frequency are resolved by the cochlea, the excitation pattern shows marked variations with $F0$ around the formant frequency (corresponding to individual harmonic peaks). Figure 3 shows excitation patterns (Moore and Glasberg, 1983) for sounds with $F1$ at 550 Hz and $F2$ at 2100 Hz on $F0$ of either 90 or 150 Hz. Since the excitation pattern in the region of $F1$ is very different for sounds on different $F0$'s subjects cannot make veridical formant matches by simply matching relative levels of the excitation pattern.[1] However, a more abstract representation, such as the spectral envelope, would allow veridical matches to be made. On the other hand, for the $F2$ matches, where the harmonics close to the matched formant are *not* resolved, the excitation pattern varies little with $F0$ around the formant peak and so can be used as an explicit basis for the perceptual match.

This analysis provides a natural explanation for the changes that we have observed in within-subject variability. For both the $F1$ and $F2$ matches, variability increases when the matches are made between sounds with different $F0$'s primarily because of the distracting effect of a difference in $F0$. For the $F1$ matches, variability increases further because of the need for listeners to use a more abstract representation than explicit properties of the excitation pattern to match the formant frequency.

The above analysis is weakened by the fact that the comparison of resolved and unresolved harmonics is confounded with the different spectral regions of formants $F1$ and $F2$. It is also the case that part of the increase in variability produced by a difference in $F0$ could be due to vowel quality changes that cannot be compensated for by changing the single formant over which the subject has control. The next experiment uses simpler, single-formant stimuli which allow a more direct comparison of the effect of a difference in $F0$ for resolved and unresolved harmonics.

II. EXPERIMENT 2

Experiment 2 uses single-formant sounds and a slightly different experimental design to investigate whether the increased difficulty of making matches on different $F0$'s is greater when there are resolved harmonics in the region of the formant (for a formant on a high $F0$) than it is with unresolved harmonics in the region of the formant (with a low $F0$). A single formant at around 1100 Hz is used since at this frequency $F0$'s within a normal vocal range generate harmonics around the formant peak that are either clearly resolved ($F0$ around 250 Hz) or unresolved ($F0$ around 80 Hz). Figure 4 shows excitation patterns (Moore and Glasberg, 1983) for a single formant at 1100 Hz on two different fundamentals: 80 and 250 Hz. The harmonic ripple is not evident around the formant frequency for the low fundamental, but is clearly present for the high fundamental.

A. Stimuli and procedure

Listeners had to adjust the formant frequency of a periodically excited single-formant complex sound to match the timbre of a similar sound with a formant frequency of either 1100 or 1200 Hz (bandwidth 100 Hz). Three factors were varied orthogonally across 8 blocks of 20 trials: whether both sounds in a trial were from the low (80 or 90.4 Hz) or the high (221.2 or 250 Hz) $F0$ range, whether they had the same or a different $F0$ and whether the target sound had an $F0$ that was the higher or lower value in its range. On each trial

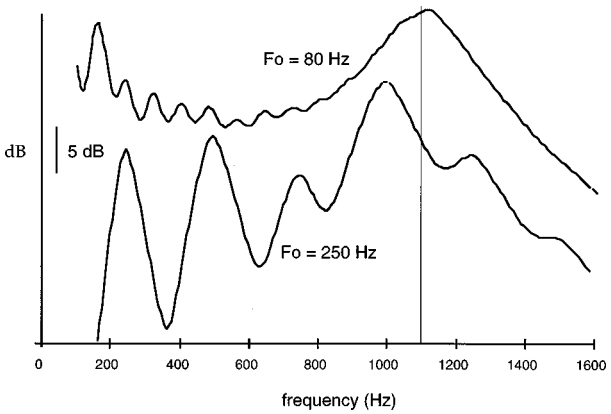

FIG. 4. Excitation patterns for two of the target sounds in experiment 2. Both sounds have a single formant at 1100 Hz (marked by the vertical line). The upper curve has a fundamental frequency of 80 Hz, the bottom of 250 Hz. The curves are vertically displaced for clarity.

the two sounds' fundamental frequencies ($F0$) were in the ratio 1:1.13. The specific values of $F0$ for each block of trials are shown in Fig. 5. Within blocks the target formant frequency was randomly either 1100 or 1200 Hz. Each target sound was matched ten times in a quasi-random order; the number of matches per condition was increased from that used in experiment 1 in order to increase the reliability of estimates of within-subject variability. Each block took about 30 min to complete and the order of experimental blocks was randomized across subjects.

Stimulus synthesis and presentation were similar to experiment 1a except that the permitted adjustment range was 800–1500 Hz. Eleven subjects (including the two authors), who were university students or staff, participated in the experiment. All had pure-tone thresholds within the normal range at octave frequencies between 250 Hz and 4 kHz. For each subject, matches that deviated from the mean by more than two standard deviations were classified as errors and were ignored. Such matches amounted to less than 3% of the total in this and subsequent experiments.

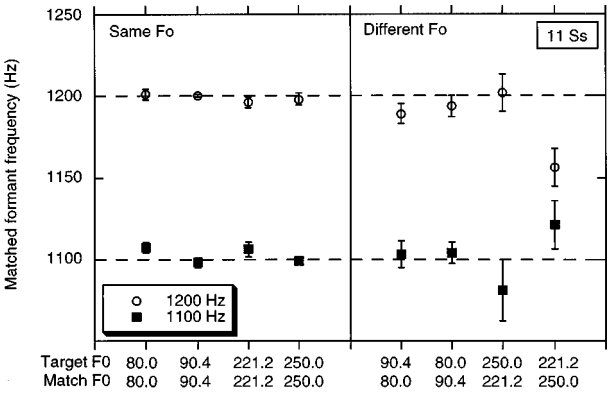

FIG. 5. Mean matched target formant frequencies in experiment 2 for target formant frequencies of 1100 and 1200 Hz. Error bars are standard errors of the mean over 11 subjects. The left panel shows matches made when the target and match had the same $F0$, the right-hand panel shows matches when they had different $F0$'s.

TABLE I. Dominant harmonic and estimated formant frequencies.

	Dominant harmonic		Burg-estimated formant	
Formant	$F0=221.2$	$F0=250$	$F0=221.2$	$F0=250$
1100	**1106**	*1000*	1092	1050
1200	*1106*	**1250**	1166	1210

B. Results and discussion

1. Mean matches

The mean matched formant frequencies for each condition across the 11 subjects are shown in Fig. 5 together with their standard error. Matches made on the same $F0$ are not systematically different from the target formant frequency and are very consistent across subjects.

The matches to sounds on different $F0$'s are also close to the target values when the $F0$'s are low (with unresolved harmonics near the formant peak), but there are significant discrepancies between the target and matched formant frequencies when the $F0$ is high, as seen in the four right-most data points in Fig. 5. The interaction is significant both as a four-way interaction involving all the data in the figure [$F(1,10)=9.9$, $p=0.01$] and as a simple interaction involving only the four right-most data points [$F(1,10)=9.1$, $p<0.02$]. This interaction between target formant frequency and the relative $F0$ of the target and the match, which is confined to those conditions where the target and the match are on different $F0$s and the individual harmonics are resolved, can be interpreted by examining how individual harmonics align with the formant frequency. For our target sounds, the harmonics close to the formant peak had an asymmetric level distribution, which varied depending on the particular $F0$'s and formant frequencies used. For some sounds the most intense harmonic was lower in frequency than the formant frequency, for others it was higher.

Table I shows the dominant (highest amplitude) harmonic for each of the four combinations of $F0$ and formant frequency in question. Harmonic frequencies in bold are above the formant frequency, those in *italics* are below the formant frequency. For example, for a 1200-Hz formant, the dominant harmonic from a 221.2-Hz $F0$ is at 1106, considerably below the true formant frequency. The interaction in the data could be due to listeners tending to hear the formant frequency as displaced in the direction of the dominant harmonic.

Klatt (1986) has pointed out that various methods of estimating formant frequencies such as spectral smoothing and LPC analysis are also prone to a similar displacement. That this is true for our stimuli is shown in Table I using LPC analysis as an example. This table gives formant frequency estimates of our stimuli using an implementation (Press, 1993) of the Burg method (identical results were obtained using an LPC covariance method). With these methods of estimating formant frequency an increase in $F0$ from 221.2 to 250 Hz decreases the estimated frequency for 1100 Hz by about 40 Hz but increases it by about the same amount for 1200 Hz. These shifts are similar to the perceptual data. Although this explanation is couched in terms of listeners

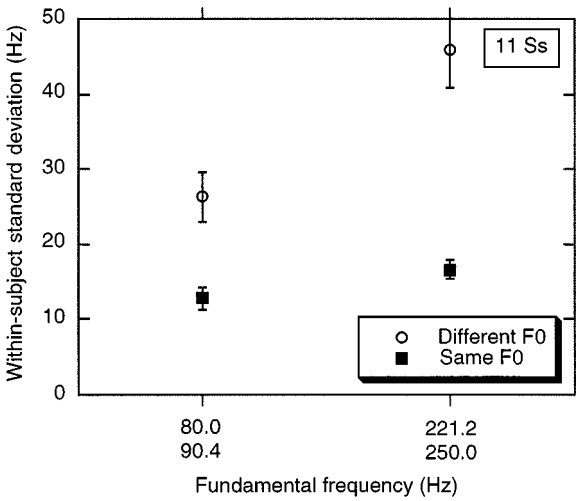

FIG. 6. Average within-subject standard deviations of matches in experiment 2 with their standard errors over 11 subjects.

making explicit formant frequency comparisons, it is important to reiterate that the demands of this experiment do not force listeners to use an explicit formant frequency, rather than the spectral envelope. A similar explanation could be couched in terms of the shape of the spectral envelope derived by spectral smoothing or by LPC analysis.

2. Match variability

Figure 6 shows the mean within-subject standard deviation of matches within each block of trials, together with the standard error of these means across the 11 subjects. Within-subject variability was not significantly different between the two matched formant values or between different values of $F0$ within an $F0$ range,[2] so Fig. 6 pools data across these dimensions. As in Experiment 1, while within-subject variability of matching was low for sounds on the same $F0$, it increased when the adjustable sound's $F0$ was different from the target's. This increase was significantly larger for sounds on high $F0$'s (with resolved harmonics) than for those on low $F0$'s (with unresolved harmonics) [$F(1,10)=7.1$, $p<0.025$].

These results have confirmed the main findings from experiment 1 using single-formant sounds. When the target and match sounds are on the same $F0$, formant frequency matches are on average veridical with low within-subject variability whether both sounds are presented on a low or a high $F0$. When the target and match sounds are on different $F0$'s, the variability of matching varies with the range of $F0$. On low $F0$'s variability increases significantly from the case where $F0$'s are the same. On high $F0$'s however, there is a significantly larger increase in within-subject variability. This interaction can be attributed to the need for listeners to interpolate a spectral envelope when the individual harmonics near the formant peak are resolved.

In addition, this experiment has shown that when individual harmonics near the formant peak are not resolved, the mean matches to sounds on different $F0$'s deviate significantly from veridicality. This result is explicable if listeners tend to perceive the formant peak as shifted towards the dominant harmonic—a shift which is also seen in formants estimated from our sounds by the Burg or LPC covariance methods.

3. Testing an excitation pattern match model of matching

We have interpreted the results of this experiment and experiment 1 on the assumption that listeners cannot perform the matching task for resolved harmonics on different $F0$'s on the basis of explicit properties of the excitation pattern. The following section tests this assumption.

It is possible that listeners might solve the formant matching task even when sounds are on different fundamentals by minimizing the discrepancy between the excitation pattern of the target vowel and that of the adjustable vowel as suggested for same-$F0$ formant discrimination by Sommers *et al.* (1996). We tested whether this strategy is feasible by measuring the rms error (in units of log power) between excitation patterns for various combinations of single-formant sounds. Excitation patterns were calculated using the formula proposed by Moore and Glasberg (1983), using 44 channels spaced at 3% frequency increments from 500 to 1836 Hz. The upper panel of Fig. 7 shows the rms dB error between a fixed formant at either 1100 or 1200 Hz and $F0$ of 250 Hz, and a variable formant with an $F0$ of 221.2 Hz whose frequency is given on the abscissa. The middle panel is similar except the $F0$'s of the fixed and variable formants are reversed. In the lower panel the $F0$'s of the two formants are the same at 250 Hz. The figure also shows the mean matched position for each condition from the experimental data, together with error bars that show the average within-subject standard deviation.

As one would expect, when there is no difference in fundamental (in the bottom panel), there is a clear minimum in the rms difference score, which corresponds with the matched value. However, when there *is* a difference in fundamental (top two panels), the minima are much shallower and the actual minima correspond neither to the true (synthesized) formant values nor to the experimental matched ones.

Let us assume that in the control condition (for which the $F0$'s are the same) listeners are adopting a strategy of finding the minimum error in the excitation pattern. Let us also assume that the variability of listeners' performance on the matching task is limited by the accuracy with which they estimate the average rms difference. If we take an accuracy of 1 dB as an arbitrary value, we can then covert this into a measure of the accuracy with which the minimum is defined. In the bottom panel, each curve remains within 1 dB of the minimum value over an average range of about 45 Hz. This value corresponds to about 1.4 times ± 1 standard deviation of the matching scores. If listeners are employing a similar strategy in matching the conditions with different $F0$'s, we would expect this ratio to remain constant. In fact, the corresponding figure for the upper panel is 200 Hz corresponding to 2.6 times ± 1 standard deviation of the appropriate matching scores, and for the middle panel 280 Hz, again corresponding to 2.6 times ± 1 standard deviation of the appropriate matching scores.

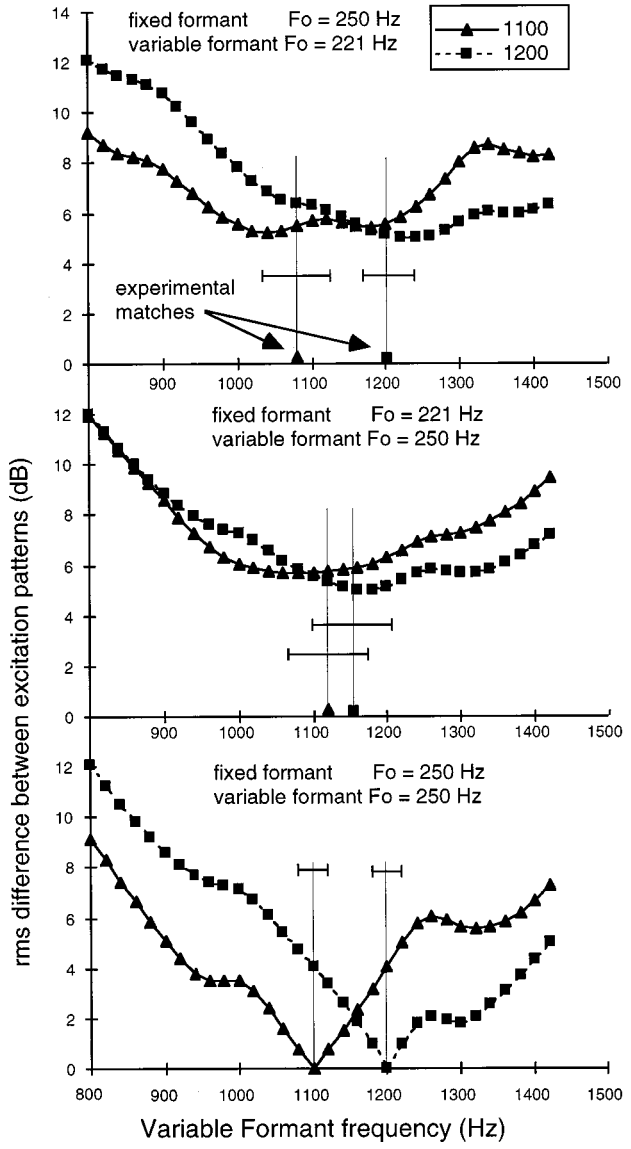

FIG. 7. The rms difference in dB between excitation patterns of single-formant sounds. In the upper panel, a fixed formant at either 1100 or 1200 Hz and $F0$ of 250 Hz is compared with a variable formant with an $F0$ of 221.2 Hz whose frequency is given on the abscissa. The middle panel is similar except the $F0$'s of the fixed and variable formants are reversed. In the lower panel the $F0$'s of the two formants are the same at 250 Hz. The vertical lines show the mean matched position (± 1 within-subject s.d.) for each condition from the experimental data.

Therefore, with different $F0$'s, subjects do better by a factor of about 2 than predicted by this excitation pattern model from their performance on the same $F0$. Since it is also likely that some aspect of their absolutely inferior performance with different $F0$'s arises because of the distracting effect of a difference in pitch, a direct comparison of excitation patterns does not provide an adequate model for explaining listeners' performance on this task.

III. EXPERIMENT 3

The aim of experiment 3 is to examine whether adding frequency modulation (FM) to $F0$ changes the accuracy and veridicality of formant-frequency matches.

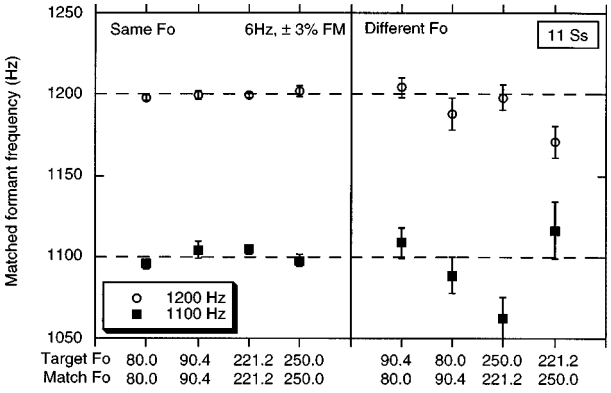

FIG. 8. Mean matched formant frequencies with standard errors over 11 subjects in experiment 3 for stimuli with frequency-modulated $F0$'s.

In our experimental paradigm we look for two possible effects of vibrato on formant matching. First, vibrato might generally make the task harder since it replaces a steady sound with one that is changing in an irrelevant dimension ($F0$). If this factor is at work, then matches ought to be more variable with FM than with a steady $F0$ in all conditions, but in particular, matches on the *same* $F0$ might show larger within-subject variation with vibrato than without. Second, if the spectral-envelope tracing produced by vibrato is useful to listeners, then different-$F0$ matches on high $F0$'s would be both more veridical and show less within-subject variability with vibrato than without.

A. Stimuli and procedure

The stimuli and procedure were similar to experiment 2 except that the steady $F0$'s of experiment 2 were replaced with $F0$'s that were frequency-modulated at 6 Hz and $\pm 3\%$ depth. The same 11 subjects participated in this experiment after they had taken experiment 2.

B. Results

1. Mean matches

The mean matched formant frequencies are show in Fig. 8. The overall pattern of the data is very similar to that from the previous experiment without FM. Matches on the same $F0$ are veridical and consistent across listeners. Matches on different $F0$'s are also close to the target values when the $F0$'s are low (with harmonics near the formant peak unresolved), but there are again significant discrepancies between the target and matched formant frequencies when the $F0$ is high. The pattern of this interaction is identical to that in the previous experiment and is again significant both as a four-way interaction involving all the data in Fig. 8 [$F(1,10) = 37.4$, $p = 0.001$] and as a simple interaction involving only the four right-most data points [$F(1,10) = 14.8$, $p < 0.005$].

2. Match variability

The average within-subject standard deviations of matches are shown in Fig. 9. Matches to sounds on the same $F0$ show similar variability in this experiment to those in the previous one where there was no FM. It is thus unlikely that FM is distracting listeners from the matching task. However,

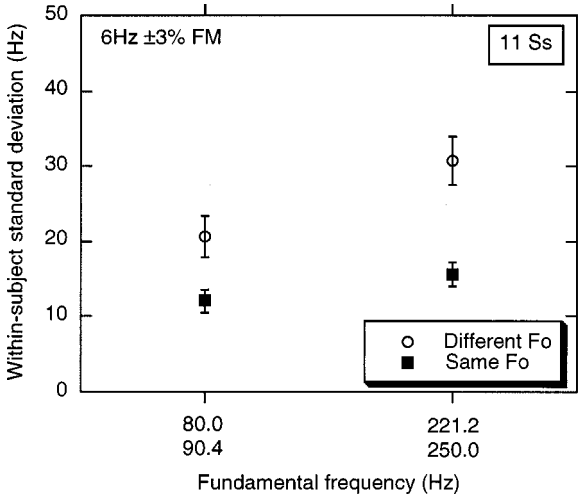

FIG. 9. Average within-subject standard deviations of matches in experiment 3 with standard errors over 11 subjects.

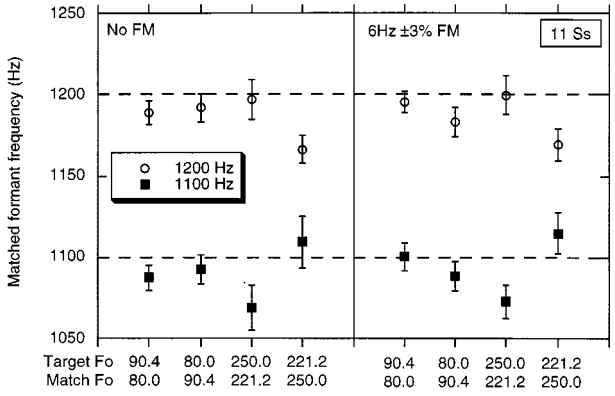

FIG. 10. Mean matched formant frequencies with standard errors over 11 subjects in experiment 4 for stimuli with or without frequency-modulated $F0$'s.

the variability of matches with different $F0$'s is lower in this experiment, giving a marginally significant interaction between the two experiments and same/different $F0$ [$F(1,10) = 4.7$, $p = 0.06$]. Although this reduction in variability of the more difficult conditions between the two experiments could be due to the introduction of FM, it could also be due to increasing practice of listeners on the task, since this experiment was conducted subsequent to experiment 2 and on the same listeners. The next experiment removes this ambiguity.

IV. EXPERIMENT 4

The previous experiment showed a marginally significant decrease of within-subject variability for matches to sounds on different, high $F0$'s when the $F0$ is modulated. To show that this increased consistency with FM is not due to subjects being more practised, experiment 4 presents the different-$F0$ conditions used in experiments 2 (no FM) and 3 (FM) in counter-balanced order.

A. Stimuli and procedure

The different-$F0$ conditions from experiments 2 and 3 were used, with the order of blocks with FM or no FM counterbalanced across subjects. The 11 subjects from experiments 2 and 3 participated after they had taken experiment 3.

B. Results and discussion

All the matches in this experiment were done on sounds that had different $F0$'s. The mean matched formant frequencies for all conditions and their standard errors across 11 subjects are shown in Fig. 10. The pattern of mean matches is very similar whether the sounds had frequency modulation or not and replicates the pattern seen in the different-$F0$ conditions of experiments 2 and 3. For matches made on a low $F0$, giving unresolved harmonics in the region of the formant, matches are generally veridical and are little affected by whether the target or the match has the higher $F0$. On the other hand, matches made on a high $F0$, are less veridical and again interact with the relative $F0$ of the target and mask. The three-way interaction between $F0$ range, target formant frequency, and specific $F0$ values is highly significant [$F(1,10) = 35.1$, $p < 0.001$], but does not interact with whether the $F0$ has FM or not [$F(1,10) = 0.01$].

In contrast to the absence of any effect of FM on the mean matched formant frequencies, FM reduces the within-subject variability of matches made on high $F0$'s (resolved harmonics), compared with those made on low $F0$'s (unresolved harmonics). This significant interaction [$F(1,10) = 5.8$, $p < 0.05$] is illustrated in Fig. 11 and shows that the corresponding difference between experiments 2 and 3 was not simply due to the fact that subjects took experiment 3 after experiment 2 and were therefore more practised at the task. The mere presence of FM does not appear to have a general distracting effect, since even in the low-$F0$ condition, FM matches are not significantly more variable than are the no-FM matches.

In summary, this experiment provides direct evidence that frequency-modulating $F0$ improves listeners' reliability at matching a formant frequency that is cued by resolved harmonics. However, although matches were less variable with FM, they were no more veridical: the tendency for matches with unresolved harmonics to be influenced by the

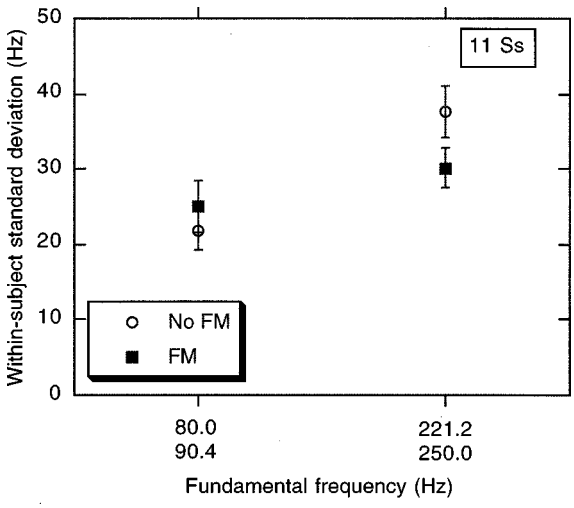

FIG. 11. Average within-subject standard deviations of matches in experiment 4 with standard errors over 11 subjects for stimuli matched on different $F0$'s, with or without FM.

frequency of the dominant harmonic is just as strong with FM as without it.

V. SUMMARY AND GENERAL DISCUSSION

The four experiments described here have explored how a difference in $F0$ affects listeners' ability to match sounds according to formant frequency. When the individual harmonics close to a formant peak are resolved by the cochlea, and so produce individual peaks in the excitation pattern, a difference in $F0$ prevents listeners from performing the matching task by simply comparing across corresponding frequencies the absolute or relative levels of the excitation patterns produced by the target and adjustable sounds—a strategy which accounts for much of the data on formant-frequency discrimination.

The main result is that a difference in $F0$ increases the variability of matches for sounds with resolved harmonics more than it increases the variability of those with unresolved harmonics. This increase in variability is probably due to the need to interpolate a spectral envelope in order to perform the task with resolved harmonics but not with unresolved. It is not necessary for listeners to explicitly extract the formant frequency in order to perform the task. We plan to report in a subsequent paper experiments which require listeners to match sounds which also differ in bandwidth. The bandwidth difference prevents listeners from performing the matching task on the basis of the (interpolated) spectral envelope, thereby forcing them to use a more abstract representation such as the envelope peak (formant frequency).

An unexpected finding was the way that small differences in $F0$ affected the mean values of the matched formant frequencies with resolved harmonics. It is probable from experiments on vowel identification that have manipulated the amplitude of individual resolved harmonics close to the $F1$ frequency (Carlson *et al.*, 1975; Darwin and Gardner, 1985) that the perceived formant frequency is influenced by the amplitude of the small number of resolved harmonics close to the formant peak—although it has been claimed that it is simply determined by the frequency of the harmonic closest to the formant frequency (Mushnikov and Chistovich, 1972). The effect that we found could be explained by listeners' formant frequency estimates (or spectral envelope interpolations) being unduly influenced by the dominant harmonic in the spectrum. A similar effect was also shown by automatic formant frequency estimation using the Burg method.

The experiments have also shown that giving the fundamental frequency vibratolike FM reduces the variability of matches. The matches carried out with FM, however, still demonstrate the same effect of the dominant harmonic as those without FM. This failure of FM to produce more veridical matches (as defined by the synthesis procedure) argues against listeners being sensitive to the spectral envelope tracing produced by FM, but further experiments using deeper modulation and more systematic variation of the alignment of harmonic frequencies and formant peaks are needed to test this speculation. Given the lack of any change in the veridicality of matches produced under FM, the reason for the reduced variability of FM matches may be more to do with the greater perceptual integrity of the timbral percept from the $F0$-modulated vowels than from the steady-state ones. FM has been shown to increase perceptual integration for harmonically related sounds (McAdams, 1989; Darwin *et al.*, 1994) even though differences in FM cannot be used to segregate different sound sources (Gardner and Darwin, 1986; Gardner *et al.*, 1989; Carlyon, 1991; Culling and Summerfield, 1995).

In summary, the formant-matching task introduced here has been shown to be sensitive to the increased perceptual difficulty of extracting a spectral envelope from resolved rather than unresolved harmonics. In addition, it has demonstrated a beneficial effect of FM in reducing the variability of subjects' formant-frequency matches. It therefore provides a tool for further investigation of the intermediate representations that listeners employ for complex sounds. The experiments have also demonstrated a specific effect of the alignment of harmonics with a formant peak on subjects' perception of the formant. Our data are compatible with shifts of the perceived formant frequency towards the strongest resolved harmonic—an effect also shown in automatic methods of formant extraction.

ACKNOWLEDGMENTS

P. Disscard was supported by Grant No. GR/L03422 from the UK EPSRC. Paul Russell wrote the software for formant matching based on SenSyn for the PowerPC. We are grateful to Rob Hukin for technical assistance, to Dr. George Mather for discussions on vernier acuity, to Peter Assmann and another anonymous reviewer for numerous helpful suggestions, and to Oded Ghitza for drawing our attention to Dennis Klatt's 1986 paper.

[1]This assertion is tested in the context of experiment 2.

[2]The largest within-subject standard deviations for matches on the same $F0$ in Fig. 6 occur for the two conditions where a harmonic frequency is closest to the formant frequency (1100/221.2 and 1200/250). In discrimination experiments, formant frequency thresholds are also larger when a harmonic frequency is close to a formant frequency (Kewley-Port and Watson, 1994; Lyzenga and Horst, 1995).

Assmann, P. F., and Nearey, T. M. (**1987**). ''Perception of front vowels: the role of harmonics in the first formant region,'' J. Acoust. Soc. Am. **81**, 520–534.

Carlson, R., Fant, G., and Granstrom, B. **(1975)**. ''Two-formant models, pitch and vowel perception,'' in *Auditory and Analysis and Perception of Speech*, edited by G. Fant and M. A. A. Tatham (Academic, London).

Carlyon, R. P. (**1991**). ''Discriminating between coherent and incoherent frequency modulation of complex tones,'' J. Acoust. Soc. Am. **89**, 329–340.

Culling, J. F., and Summerfield, Q. (**1995**). ''The role of frequency modulation in the perceptual segregation of concurrent vowels,'' J. Acoust. Soc. Am. **98**, 837–846.

Darwin, C. J., and Gardner, R. B. (**1985**). ''Which harmonics contribute to the estimation of the first formant?'' Speech Commun. **4**, 231–235.

Darwin, C. J., Ciocca, V., and Sandell, G. R. (**1994**). ''Effects of frequency and amplitude modulation on the pitch of a complex tone with a mistuned harmonic,'' J. Acoust. Soc. Am. **95**, 2631–2636.

Demany, L., and Semal, C. (**1990**). ''The effect of vibrato on the recognition of masked vowels,'' Percept. Psychophys. **48**, 436–444.

Florén, Å. **(1979)**. ''Why does [a] change to [ɔ] when $F0$ is increased?: Interplay between harmonic structure and formant frequency in the perception of vowel quality,'' PERILUS (Institute of Linguistics, University of Stockholm) **1**, 13–23.

Gardner, R. B., and Darwin, C. J. (**1986**). ''Grouping of vowel harmonics by frequency modulation: absence of effects on phonemic categorisation,'' Percept. Psychophys. **40**, 183–187.
Gardner, R. B., Gaskill, S. A., and Darwin, C. J. (**1989**). ''Perceptual grouping of formants with static and dynamic differences in fundamental frequency,'' J. Acoust. Soc. Am. **85**, 1329–1337.
Green, D. M. **(1988)**. *Profile Analysis* (Oxford U.P., New York).
Hillenbrand, J., and Nearey, T. M. (**1999**). ''Identification of resynthesised /hVd/ utterances: Effects of formant contour,'' J. Acoust. Soc. Am. **105**, 3509–3523.
Kewley-Port, D. (**1995**). ''Thresholds for formant-frequency discrimination of vowels in consonantal context,'' J. Acoust. Soc. Am. **97**, 3139–3146.
Kewley-Port, D., and Watson, C. S. (**1994**). ''Formant-frequency discrimination for isolated english vowels,'' J. Acoust. Soc. Am. **95**, 485–496.
Kewley-Port, D., Li, X. F., Zheng, Y. J., and Neel, A. T. (**1996**). ''Fundamental-frequency effects on thresholds for vowel formant discrimination,'' J. Acoust. Soc. Am. **100**, 2462–2470.
Klatt, D. H. (**1980**). ''Software for a cascade/parallel formant synthesizer,'' J. Acoust. Soc. Am. **67**, 971–995.
Klatt, D. H. (**1985**). ''The perceptual reality of a formant frequency,'' J. Acoust. Soc. Am. **78**, S81–S82.
Klatt, D. H. **(1986)**. ''Representation of the first formant in speech recognition and in models of the auditory periphery,'' in Proceedings of the Montreal symposium on speech recognition; McGill University, Montreal, pp. 5–7.
Kontsevich, L. L., and Tyler, C. W. (**1998**). ''How much of the visual object is used in estimating its position?'' Vision Res. **38**, 3025–3029.
Lyzenga, J., and Horst, J. W. (**1995**). ''Frequency discrimination of band-limited harmonic complexes related to vowel formants,'' J. Acoust. Soc. Am. **98**, 1943–1955.
Lyzenga, J., and Horst, J. W. (**1997**). ''Frequency discrimination of stylized synthetic vowels with a single formant,'' J. Acoust. Soc. Am. **102**, 1755–1767.
Lyzenga, J., and Horst, J. W. (**1998**). ''Frequency discrimination of stylized synthetic vowels with two formants,'' J. Acoust. Soc. Am. **104**, 2956–2966.
Marin, C. M. H., and McAdams, S. (**1991**). ''Segregation of concurrent sounds. II. Effects of spectral envelope tracing, frequency-modulation coherence, and frequency-modulation width,'' J. Acoust. Soc. Am. **89**, 341–351.
McAdams, S. (**1989**). ''Segregation of concurrent sounds. I: Effects of frequency modulation coherence,'' J. Acoust. Soc. Am. **86**, 2148–2159.
McAdams, S. and Rodet, X. **(1988)**. ''The role of FM-induced AM in dynamic spectral profile analysis,'' in *Basic Issues in Hearing*, edited by H. Duifhuis, J. W. Jorst, and H. P. Wit (Academic, London)
Moore, B. C. J., and Glasberg, B. R. (**1983**). ''Suggested formulae for calculating auditory-filter bandwidths and excitation patterns,'' J. Acoust. Soc. Am. **74**, 750–753.
Morgan, M. J., and Watt, R. J. (**1982**). ''Mechanisms of interpolation in human spatial vision,'' Nature (London) **299**, 553–555.
Mushnikov, V. N., and Chistovich, L. A. (**1972**). ''Method for the experimental investigation of the role of component loudness in the recognition of a vowel,'' Sov. Phys. Acoust. **17**, 339–344.
Press, W. H., Teukolsky, S. A., Vettering, W. T., and Flannery, B. R. **(1993)**. *Numerical recipes in C* (Cambridge C.U.P.).
Ryalls, J. H., and Lieberman, P. (**1982**). ''Fundamental frequency and vowel perception,'' J. Acoust. Soc. Am. **72**, 1631–1634.
Sommers, M. S., and Kewley-Port, D. (**1996**). ''Modeling formant frequency discrimination of female vowels,'' J. Acoust. Soc. Am. **99**, 3770–3781.
Sundberg, J. (**1975**). ''Vibrato and vowel identification,''Speech Transmission Laboratory, Quartery Progress and Status Report (KTH, Stockholm) STL-QPSR **2-3**, 49–60.
Sundberg, J. (**1977**). ''Vibrato and vowel identification,'' Arch. Acoust. **2**, 257–266.

Effectiveness of spatial cues, prosody, and talker characteristics in selective attention

C. J. Darwin[a] and R. W. Hukin
Experimental Psychology, University of Sussex, Brighton BN1 9QG, United Kingdom

(Received 26 May 1999; accepted for publication 22 October 1999)

The three experiments reported here compare the effectiveness of natural prosodic and vocal-tract size cues at overcoming spatial cues in selective attention. Listeners heard two simultaneous sentences and decided which of two simultaneous target words came from the attended sentence. Experiment 1 used sentences that had natural differences in pitch and in level caused by a change in the location of the main sentence stress. The sentences' pitch contours were moved apart or together in order to separate out effects due to pitch and those due to other prosodic factors such as intensity. Both pitch and the other prosodic factors had an influence on which target word was reported, but the effects were not strong enough to override the spatial difference produced by an interaural time difference of ± 91 μs. In experiment 2, a large ($\pm 15\%$) difference in apparent vocal-tract size between the speakers of the two sentences had an additional and strong effect, which, in conjunction with the original prosodic differences overrode an interaural time difference of ± 181 μs. Experiment 3 showed that vocal-tract size differences of $\pm 4\%$ or less had no detectable effect. Overall, the results show that prosodic and vocal-tract size cues can override spatial cues in determining which target word belongs in an attended sentence. © *2000 Acoustical Society of America.* [S0001-4966(00)01302-3]

PACS numbers: 43.66.Pn, 43.71.Es [RVS]

INTRODUCTION

This paper addresses the general problem of how listeners attend to a particular sound source over time. Cherry's original paper on the ''cocktail-party effect'' (Cherry, 1953) and subsequent work on auditory selective attention by Broadbent (1953) and others (Spieth *et al.*, 1954) emphasized the spatial nature of auditory attention. A number of recent papers have studied the consequences for audition of our ability to direct attention, either intentionally or automatically, to a particular spatial direction (Spence and Driver, 1994; Teder and Näätänen, 1994; Mondor and Zattore, 1995; Quinlan and Bailey, 1995). Auditory attention, though, cannot be purely concerned with selecting between spatially distinct sound sources, since attention is possible, though more difficult, between sources that are not spatially separated. Indeed, there is a variety of demonstrations of listeners' ability to attend selectively to particular frequency regions (Scharf *et al.*, 1987; Schlauch and Hafter, 1991; Hubner and Hafter, 1995). For a complex and highly constrained sound source such as speech, the simple strategy of attending to a particular frequency is of doubtful value. There is a variety of more complex, nonspatial perceptual properties of a speech signal that could be used to maintain attention across time such as its pitch contour and, more abstractly, individual characteristics of the talker (Broadbent, 1952) or of the transmission channel (Egan *et al.*, 1954). More recently, on the basis of EEG data, Woods and colleagues (1984) have argued that selective attention to speech (either silent or with shadowing) is directed not just to a particular spatial location but rather to the ensemble of a particular location and talker. This paper looks at the effectiveness of two properties that help to define a particular talker across time: prosodic continuity and vocal-tract size.

In an earlier paper (Darwin and Hukin, 1999), which was primarily concerned with the use of spatial cues such as interaural time difference (ITD) in auditory grouping and selective attention, we showed that listeners could use differences in ITD of a few tens of microseconds (μs) to decide which of two synchronized target words came from one of two simultaneous sentences. The sentences were spoken in a monotone by the same talker, and were resynthesized to be accurately on a constant fundamental frequency (F_0). Somewhat surprisingly, we found that listeners made very little use of F_0 continuity in doing this task. Differences in F_0 between the two sentences of up to four sentences had very little influence on listeners' preferences. When the two sentences had the same ITD, listeners showed little preference for the target word on the same F_0 as the attended sentence; when the target words were cross-spliced they continued to report the target word that shared spatial location with the attended sentence, tolerating an F_0 jump during the target word. Such ineffectiveness of F_0 continuity was surprising since previous work using rather different paradigms had shown that continuity of prosody or just of F_0 could be useful in assigning speech across time to the same or to different talkers (Darwin, 1975; Darwin and Bethell-Fox, 1977). Speech separation algorithms had similarly found continuity of F_0 to be useful (Parsons, 1976; Weintraub, 1987).

The first experiment in the present paper uses a similar task to that used in the earlier paper to investigate the effectiveness of natural (rather than monotonous) prosody, and uses resynthesized speech to compare the effectiveness of F_0 and level changes produced by varying sentence stress. The experiment titrates these changes against differences in lateral position cued by ITD.

[a]Electronic mail: c.j.darwin@biols.susx.ac.uk

I. EXPERIMENT 1

This experiment first examines how effective the prosodic cues present in naturally spoken sentences are at helping listeners to track a particular utterance in the presence of a second utterance from the same talker. The two sentences could also differ in ITD, and the experiment compares the effectiveness of these two types of cue.

The basic design of the experiment is similar to the first experiment reported in our previous paper: the listener hears the same two carrier sentences on each trial, is asked to attend to one of them, and to report which of two target words occurs in the attended sentence. The same two targets words are present on each trial, so the experiment is strongly weighted towards measuring how effective the different cues are at enabling listeners to track a particular sound source over time, rather then how well listeners can detect or recognize a word.

Unlike our previous experiments, in which the sentences had a monotonous F_0 contour, this experiment uses sentences that are spoken with natural intonation. The sentence stress is placed either towards the beginning of the sentence or towards the end, so that on each trial the two constituent sentences have globally different intonation contours. This change in intonation contour affects the way the pitch, amplitude, and durations of the individual words vary across the sentence. Listeners might be using any or all of these cues to help them to identify which word was spoken as part of the attended sentence. Our paradigm makes it unlikely that rhythmic differences are contributing to listeners' performance, since the two target words start at the same time and have similar durations.

In order to assess whether a difference in fundamental frequency (over and above any difference in intensity) is contributing to the ability of subjects to follow a particular sentence, we manipulate the overall level of the pitch contour. In one manipulation we change the overall pitch level for the whole of each sentence in order to bring the average F_0s in the two target words together, and in the other, we move them further apart. If listeners are using the F_0 contour to help them to track a particular sentence, we could expect them to do this better when the F_0 contours are moved apart, and worse when they are moved together. In order to maintain good speech quality while changing the pitch contour of the speech, we use the pitch-synchronous overlap–add (PSOLA) method of resynthesis. PSOLA is a waveform-based resynthesis method that allows independent manipulation of the pitch and duration of speech while maintaining good speech quality. The method was introduced by Moulines and Charpentier (1990) and its perceptual effect on simple speech-like sounds has recently been evaluated (Kortekaas and Kohlrausch, 1997, 1999).

In this experiment, we also vary the lateral position of the two sentences by giving the two sentences of a pair different ITDs—the dominant lateralization cue for complex sounds (Wightman and Kistler, 1992). In our previous experiment, using sentences spoken and resynthesized on a monotonous F_0 contour, listeners were able to use a small difference in ITD to track one sentence over time. Listeners continued to report the target word with the same ITD as the carrier sentence when the target words were cross-sliced so that there was a discontinuity (of up to four semitones) in the monotonous pitch contour. Experiment 1 thus pitted the effectiveness of prosodic cues against differences in ITD by cross-splicing target words between pairs of sentences, so that one target word had the appropriate prosody but the wrong ITD and *vice versa*.[1]

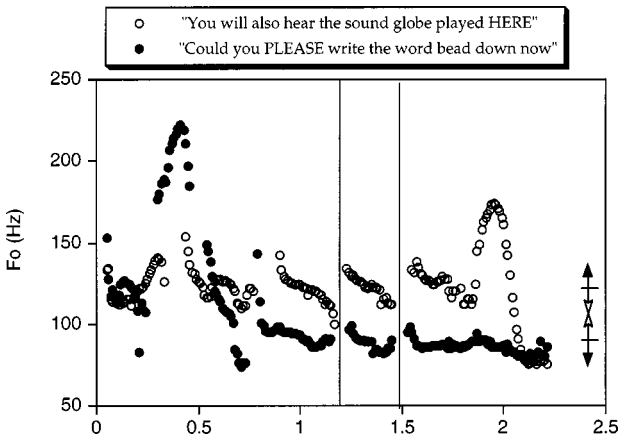

FIG. 1. F_0 values used for PSOLA resynthesis for one of the four original pairs of sentences used in experiment 1. The vertical lines at around 1.5 s delimit the target words ''bead'' and ''globe.'' The open-headed arrows show the change in F_0 to the whole sentence for the together condition, where the F_0 contours for the target words overlap; the filled arrows show the change in F_0 to the whole sentence for the apart condition.

A. Stimuli

Two sentences with each of two target words (''Could you please write the word bead/globe down now'' and ''You'll also hear the sound bead/globe played here'') were recorded by a male, native speaker of British English (C.J.D.). Each sentence was spoken in two versions, one with the main sentence stress early in the sentence (on ''please'' and ''also''), and once with the stress late in the sentence (on ''now'' and ''here''). These eight sentences were recorded on DAT tape and subsequently digitized at 22 050 Hz. Each sentence was between 2.20 and 2.41 s long. Sentences were paired so that a pair contained both carrier sentences, both target words, and both sentence stress positions (early, late). These constraints gave four different pairings. Within each pair, minor durational adjustments were made in order to (i) equate the durations of the two target words by adding/removing individual pitch periods from their centers, and (ii) align the onset of the two target words by adding a short period of silence to the beginning of one sentence in a pair. The target words started between 1.2 and 1.3 s from the start of their respective carrier sentences.

The F_0 contour of each sentence was obtained automatically using ESPS/WAVES+ software (Sensimetrics, Cambridge, MA) and checked for accuracy against the waveform. These original contours for two of the sentences are shown in Fig. 1. Three different resyntheses were then made for each sentence pair using a WAVES+ resynthesis tool (Möhler and Dogil, 1995) based on the PSOLA method (Moulines and Charpentier, 1990) which allowed the F_0 contours of the sentences to be increased or decreased in frequency. These three F_0 conditions were: *original*, in which the F_0 values

TABLE I. Allocation of prosodic and spatial cues across the different experimental conditions. (The vocal tract manipulation is only made in experiments 2 and 3.)

	F_0 Together	F_0 Original	F_0 Apart
Normal	+ITD $0F_0$ +Intensity	+ITD $+F_0$ +Intensity (+Vocal tract)	+ITD $++F_0$ +Intensity
Swapped	−ITD $0F_0$ +Intensity	−ITD $+F_0$ +Intensity (+Vocal tract)	−ITD $++F_0$ +Intensity

were unchanged; *together*, in which the two sentences' F_0 contours were both shifted in order to make the values of F_0 during the two target words similar (F_0 contours of the sentence whose target word had a higher F_0 were shifted down 12% and the F_0 contours of the other sentence were shifted up 15%—the symmetry was introduced to maintain quality of resynthesis); *apart*, in which the two sentences' F_0 contours were shifted the opposite way in order to make their values of F_0 during the two target words more different (the sentence that had the higher-F_0 target was raised by 15% Hz, the one with the lower- F_0 target was lowered by 12%).

Two different splicing conditions were generated from these resynthesized sentence pairs. A *normal* condition which retained the sentences as described in the previous paragraph, and a *swapped* condition in which the target words were swapped between the two sentences of a pair. Notice that this cross-splicing was done *after* the F_0 contours of the sentence pair had been altered but *before* sentences were given different ITDs (which was done by the computer program that presented the sounds to listeners). Thus, in the normal condition prosodic cues act in the same direction as the spatial cue to reinforce the choice of a particular target word, whereas in the swapped condition, the prosodic cues oppose the spatial cue. Table I summarizes the allocation of the two prosodic cues (intensity, F_0) and one spatial cue (ITD) in the different conditions of experiment 1.

B. Procedure

The 13 listeners were native speakers of British English aged between 21 and 52 who had pure-tone thresholds within the normal range at octave frequencies between 125 Hz and 8 kHz. They had all taken part in the experiment reported in the earlier paper, which had used a similar paradigm and broadly similar stimuli.

Listeners were tested individually. They were told that they would always hear the same two carrier sentences which might come from the same or different positions. Six listeners were asked to attend to one of the sentences and seven to the other sentence. They were asked to press the ''b'' or ''g'' key according to whether the attended sentence contained the target word ''bead'' or ''globe,'' respectively. On each trial the listener heard both carrier sentences and both target words.

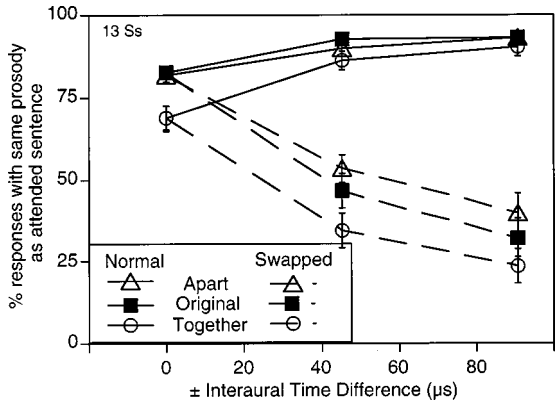

FIG. 2. Percentage of trials on which listeners reported the target word that had been originally spoken in the attended sentence (chance performance is 50%). Two sentences were presented at the same time; their interaural time differences could be different and the F_0 contours of both original sentences could be manipulated so as to move the F_0's of the two simultaneous target words either together or further apart from their original values. In the normal condition, one of the target words has both the same prosody and the same ITD difference as the attended sentence. In the swapped condition, the target that has the same prosody as the attended sentence has the opposite ITD.

Pairs of files, prepared as described above, were digitally mixed at presentation with ITDs of 0, ±45.3, ±90.7 μs (both sentences were therefore played to both ears). These ITDs correspond to 0, ±1, ±2 samples at 22 050 Hz (the terminology ''±1 sample'' indicates that one of the sentences led in one ear by one sample, and the other sentence led in the other ear by one sample). The ITDs were paired symmetrically, so that if one sentence and target word had an ITD of +2 samples, the other had an ITD of −2 samples. Which sentence of a pair had the positive and which the negative ITD was randomly varied from trial to trial (with the 0 ITD conditions doubled).

Each listener thus heard each of 144 trial types (4 sentence pairs×2 cross-splicing conditions×3 F_0-contour types×6 ITD conditions) 5 times to give a total of 720 trials. Stimuli were presented through a Digidesign Protools interface attached to a Power Mac 7100 which also controlled the experiment. The output of the Protools interface was connected to Tucker-Davis PA4 attenuators which were used to set the overall level for the experiment. Subjects listened over Sennheiser HD414 headphones in a double-walled IAC booth. The sentences, when mixed at each headphone, gave an average level of 68 dB SPL through a flat-plate coupler.

C. Results and discussion

Figure 2 shows the percentage of trials on which listeners reported the target word that had been originally spoken in the attended sentence (and so had the appropriate prosody for the attended sentence) as a function of ITD. Overall, the obvious difference between the normal conditions (solid lines) in which the prosodic cues and ITD work together, and the swapped conditions (dashed lines) where ITD opposes the prosodic cues, shows the effect of ITD in opposing the prosodic cues. However, we first examine the power of the

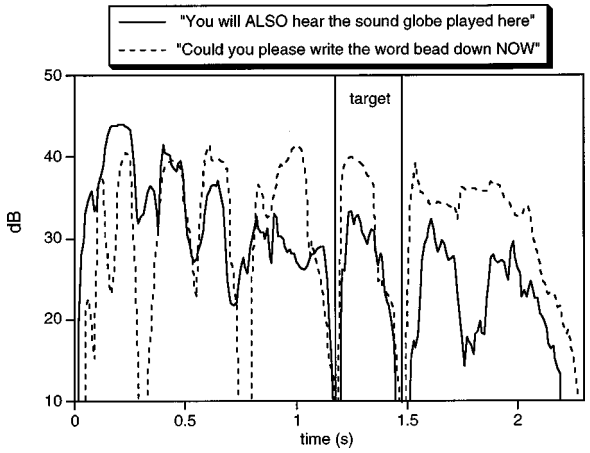

FIG. 3. Amplitude contours of the two sentences of a pair from experiment 1. In this example the target from the sentence with early sentence stress is about 10 dB less intense than the target from the sentence with late sentence stress.

prosodic cues alone by looking at the results from the conditions where the ITD was zero (and so the distinction between normal and swapped does not exist).

1. ITD=0

When both sentences are presented with an ITD of zero, listeners prefer the target with the same prosody as the attended sentence substantially above chance (83%) for the original condition (with the prosody unchanged). This level of performance is made possible by the prosodic differences between the two sentences. Specifically, the F_0 contour of the attended sentence makes some contribution to listeners' ability to track the attended sentence; changing the pitch contours of both sentences, so that the two target words have similar F_0's (together condition), reduces performance by 14% ($t_{12}=3.9, p<0.001$). This change (produced by a 27% change in the frequency of F_0) is comparable to the 11% improvement in performance produced by a four-semitone (26% change in frequency) monotonous difference in F_0 in our previous experiment (Experiment 1, Darwin and Hukin, 1999). It shows that, in the absence of other cues, listeners can use the continuity of a natural F_0 contour to track a sentence across time, but, like the continuity of a monotonous F_0 contour, it is not a particularly strong effect. Strengthening the prosodic cues by moving the F_0 contours apart does not further increase listeners' preference.

In the together condition, where there is a little difference between the F_0 contours of the target words, other prosodic cues maintain listeners' preferences well above chance at 69% ($t_{12}=4.8, p<0.002$). Listeners are probably using intensity differences between the target words to achieve this level of performance. Figure 3 shows the intensity contours of the two sentences of one pair. In the region of the target word, the sentence with the late stress is around 10 dB more intense than the sentence with the early stress.

2. Normal ITD≠0

When the original sentences are also separated by a difference in ITD, preference for the target word sharing the same prosody as the attended sentence increases from 83% at 0 μs to 93% at ± 91 μs. This change is significant ($t_{12}=5.1, p<0.002$). Changes to the F_0 contour do not significantly alter this already very high level of performance.

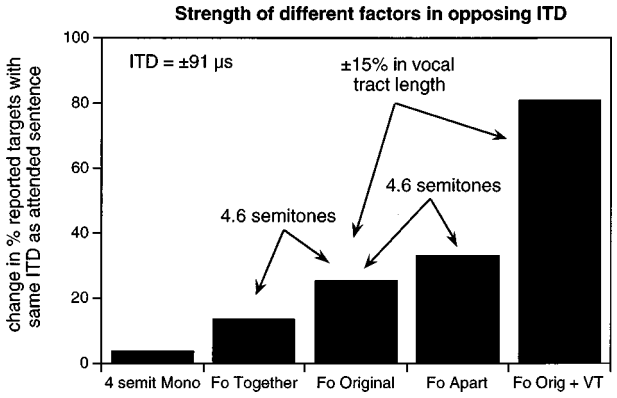

FIG. 4. The strength of different prosodic factors in opposing ITD is illustrated by plotting how the percent of reported targets that have the same ITD as the attended sentence changes when ITD is opposed (swapped condition), rather than reinforced (normal condition), by the prosodic cues listed on the abscissa. A large percent change indicates an effective prosodic cue. All the date in this figure are from the same 13 subjects. The left-hand bar comes from experiment 1 of Darwin and Hukin (1999). The next three bars are from experiment 1 of the present paper; the right-hand bar is from experiment 2.

3. Swapped ITD≠0

Opposing prosodic cues with a difference in ITD clearly reduces the number of trials on which listeners report the target word that has the same prosodic cues as the attended sentence $F_{1,12}=72.9, p<0.0001$. This reduction is greater for the larger difference in ITD, $F_{1,12}=49.6, p<0.0001$. An ITD of ± 45 μs is sufficient to counter the prosodic cues present in this experiment (performance is 50% for the swapped original condition) and with an ITD of ± 91 μs listeners consistently report the target that has the same ITD as the attended sentence rather than the target that has the correct prosody. These levels of performance are lower than in the normal original, zero ITD condition by 36% for ± 45 μs and 51% for ± 91 μs.

Strengthening the prosodic cues by moving the F_0 contours apart increases the chance of listeners reporting the target word with the same prosody as the attended sentence; conversely, weakening the prosodic cues by moving the F_0 contours together decreases it: the total increase in reports of the target with the same prosody between the together and apart conditions is about 18%. The main effect of the F_0 manipulation (together, original, apart) is significant in the swapped conditions when ITD is not zero ($F_{1,12}=44.7, p<0.0001$).

We can now compare the effectiveness in opposing ITD of the natural intonation contours from this experiment, with the monotone manipulations from our earlier experiment. Figure 4 shows how effective different prosodic factors are in opposing an ITD of ± 91 μs. The score shows how much listeners' preference for the target that had the same ITD as the attended sentence was reduced when the ITD cue was opposed rather than reinforced by the prosodic cue(s) shown

on the abscissa. A small difference shows that listeners tend to follow ITD; a large difference shows that they tend to follow the other cues. The left-hand bar illustrates data from our previous experiment, and shows the difference between a condition where a four-semitone difference in monotone F_0 is acting with or against an ITD of ± 91 μs. There is very little (3%) change, reflecting the weakness of the monotonous F_0 cue. The next three bars illustrate data from the together, original, and apart conditions of the present experiment. Although these prosodic manipulations are insufficient to override the ITD difference, they exercise a greater influence than the monotonous F_0. The together condition is significantly more influenced by prosody than the four-semitone monotone condition, $t_{11}=2.47$, $p<0.02$, and the others progressively more different. A 4.6 semitone difference of F_0 between the together and normal conditions produces a 12% change, and a further 4.6 semitone difference between the normal and apart conditions gives a further 8% change.

In summary, first this experiment has extended, to sentences with natural intonation, our previous result that a difference in ITD between two sentences substantially helps listeners decide which of two simultaneous target words belong to an attended sentence. A difference of ITD of ± 91 μs (equivalent to about $\pm 12°$ separation in azimuth) gives a change of about 50% when opposed to the natural prosodic cues.

Second, the experiment has shown that normal prosodic changes also help listeners: the prosodic cues naturally present here give a performance that is 33% above chance. Specifically removing the F_0 contribution to the prosodic cues (leaving substantial amplitude differences), reduces this figure by 14%, to 19% above chance.

Third, the experiment (in conjunction with experiment 1 of our previous paper) has shown that, for comparable semitone differences, a natural F_0 contour is slightly more effective at maintaining a listener's attention in the face of an opposing ITD difference than a monotonous contour.

II. EXPERIMENT 2

Both the first experiment in our previous paper and the present experiment 1 used two simultaneous sentences spoken by the same talker. It is substantially more natural to have two different talkers speaking at the same time. Globally shifting formant frequencies is an effective way of altering the individuality of a voice (without changing voice pitch or fundamental frequency) and corresponds to an alteration in vocal-tract length. Individuals with longer vocal tracts have lower formant frequencies; those with shorter vocal tracts have higher formant frequencies. Men and women differ on average by about 17% in vocal-tract length (Peterson and Barney, 1952), but an upward or downward shift of 8% in formant frequencies is sufficient to reduce the recognition of individual voices to chance (Kuwabara and Takagi, 1991). Although it is technically possible to resynthesize speech so that only formant frequencies (the resonant frequencies of the vocal tract) are changed, it was simpler (and allowed better speech quality) for us to change the whole spectral envelope, so that not only formant frequencies but also voice source characteristics were changed. When this is done, it is likely that formant frequency changes, rather than changes to the individual characteristics of the voice source, are responsible for most of the change in individuality (Zhu and Kasuya, 1998). It is important to stress, however, that the manipulation that we used leaves the fundamental frequency of the voice unchanged: the same harmonic frequencies are present as in the original voice, but the spectral envelope that defines the amplitudes of those harmonics is transposed up or down in frequency.

In this experiment, we produced two apparently different talkers from the original sentences used in experiment 1 by globally changing the spectral envelope (including formant frequencies) by $\pm 15\%$. For convenience, we will refer to the change as producing a voice from a longer or a shorter vocal tract.

A. Stimuli

The original sentences from experiment 1 were modified to produce two different talkers, with the same F_0 and durations as the originals but with a different spectral envelope and consequently a different apparent vocal-tract size. To produce the longer vocal-tract voice, the PSOLA algorithm that had been used in experiment 1 was used together with the program DSP DESIGNER (Zola Technologies) to: (i) raise F_0 and globally reduce the duration by 15%, (ii) resample the file at a 15% higher sampling frequency and then set the playback rate back to the original value (22 050 Hz). The end results of these manipulations was to produce sentences that had the same durations and F_0s as the originals, but which had the spectral envelope (including formant resonances and voice source properties) lowered by 15%. To produce the shorter vocal-tract voice the opposite manipulations were made. The resulting voices, although still plausibly natural, were very clearly different individuals, neither of whom sounded like the original talker.

The sentences were paired as in experiment 1 with the additional constraint that each pair contained one long vocal-tract sentence and one short vocal-tract sentence. As in experiment 2, target words could be swapped between the sentences of a pair before the sentences were allocated an ITD. In the swapped condition, the target word that had the same ITD as the attended sentence had a prosody and vocal-tract size that was appropriate for the unattended sentence.

B. Procedure

The procedure was similar to that from experiment 1 except that ITDs of 0, ± 45.3, ± 90.7, and ± 181.4 μs were used. The longest ITD value was introduced after the first four subjects had been run. Again, the ITD manipulation was made at the time of presentation. The same 13 listeners from experiment 1 took part.

C. Results and discussion

Figure 5 shows the percentage of trials on which listeners reported the target word that had originally belonged to the attended sentence (and so shared its prosody and vocal-tract size). The data from this experiment are plotted with

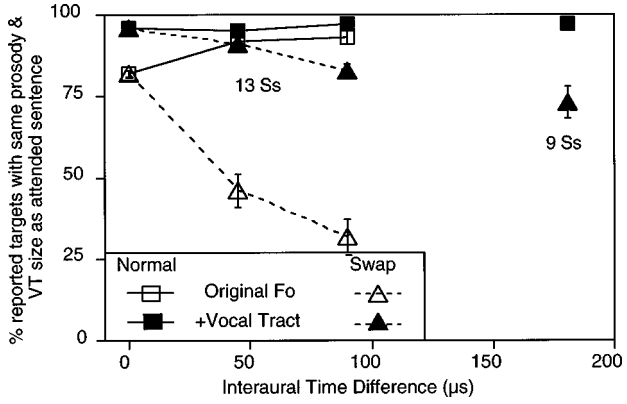

FIG. 5. Percentage of trials on which listeners reported the target word that had been originally spoken in the attended sentence (chance performance is 50%). The solid squares show the results from experiment 3 in which two sentences were presented at the same time, one with each of two different vocal-tract lengths. In the swapped conditions, the original target word has the opposite ITD, and the other target word has the same ITD as the attended sentence. Open triangles replot comparable data from experiment 1 without the difference in vocal-tract length. Only nine listeners contributed data at the longest ITD.

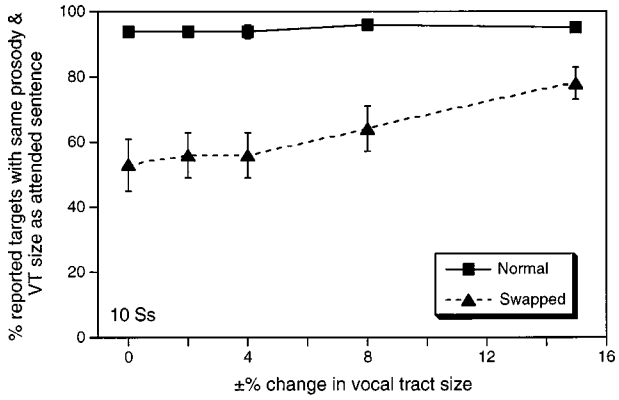

FIG. 6. Percentage of trials in experiment 3 on which listeners reported the target word that had been originally spoken in the attended sentence. In the normal conditions, one of the target words has the same prosody, vocal-tract size, and ±91 μs ITD difference as the attended sentence. In the swapped condition the target with the same prosody and vocal-tract size as the attended sentence has the opposite ITD.

solid symbols; data from the same listeners from experiment 1 (without the vocal-tract change) are plotted as open symbols.

Introducing a difference of ±15% in vocal-tract size clearly has a large effect; even without a difference in ITD, listeners' preferences are almost 100% when the two voices differ in vocal-tract size. In addition, when an increasing ITD acts against prosodic and vocal-tract size cues, listeners have a strong tendency to stay with the vocal tract rather than the spatial position. Although there is some significant progressive reduction as ITD increases in the swapped condition in the number of reported targets derived from the attended sentence, the reduction is small ($F_{2,16}=7.9$, $p<0.02$ for nine listeners across three ITDs, $F_{1,12}=10.3, p<0.01$ for 13 listeners on the two smaller ITDs). Similarly, introducing an opposing ITD of ±91 μs only reduces the number of these targets reported from 98% to 86%. This contrasts with a reduction in experiment 1, which lacked the vocal-tract cue, from 93% to 32%. With a larger opposing ITD of ±181 μs (corresponding to a spatial separation of about ±50°D) listeners still prefer the original target word (that has the same vocal-tract size and the same prosody as the attended sentence) on 73% of trials.

This experiment has shown that a substantial difference in vocal-tract size between two talkers produces a powerful cue for selective attention. As illustrated in Fig. 4, the effects that we have found with our vocal-tract manipulation have been substantially larger than those found for our prosodic manipulations. However, our vocal-tract manipulation is larger, compared with naturally occurring values, than is our prosodic manipulation as shown in the data of Peterson and Barney (1952). Their data shows an average[2] female/male formant ration of 1.17, but an average female/male ratio for F_0 of 1.7 (nine semitones). Consequently, our experiment 2 uses an F_0 range (9.2 semitones between together and apart) that is comparable to the average male/female difference, but a vocal tract difference (30% between the short and the long manipulations) that is at the top of the range of scaling values. Experiment 3 examines the effect of smaller vocal-tract manipulations.

III. EXPERIMENT 3

This experiment asked how changes to the difference in vocal-tract size between two talkers influence the listener's selection of which word belongs in the attended sentence. It is similar in design to the first two experiments but uses a range of vocal-tract size differences with a single prosodic condition which are opposed by a single ITD.

A. Method and procedure

The original prosody condition from experiment 2 at an ITD of ±91 μs was used together with four more conditions with changes of vocal-tract size of ±2, ±4, ±8, and ±15% produced by the same PSOLA and DSP DESIGNER algorithms as in experiment 2. As in the previous experiments, for the normal conditions a particular target word had the same ITD, prosody, and vocal-tract size as one of the sentences, whereas in the swapped condition, if a target word had the same ITD as one sentence, it had the same prosody and vocal-tract size as the other sentence.

Each subject heard each of 80 trial types (4 sentence pairs×5 vocal-tract sizes×2 ITD conditions×normal/swapped) 6 times to give a total of 240 trials. The ten listeners had all taken part in experiment 2.

B. Results and discussion

The overall results for the experiment are shown in Fig. 6 as the percent of target words that shared the same prosody and, where appropriate, vocal-tract length with the attended sentence.

When prosodic, vocal tract, and ITD differences all operate in the same direction, listeners perform the task almost perfectly with scores of over 90% in all conditions. When an ITD of ±91 μs opposes the prosodic and vocal-tract cues, listeners report fewer of the targets that have the same

prosody and vocal-tract size. With no difference in vocal-tract size, the prosodic cues in the experiment are sufficient to give about 54% of the reported target words, which is somewhat larger than the corresponding condition in the previous experiment. With the largest vocal-tract difference augmenting the prosodic cues, this figure increases to about 78%. However, most of the change occurs for the two larger vocal-tract sizes. There is no significant change in performance across the 0%, ±2%, and ±4% vocal-tract length differences. Differences from the 0% condition only begin to appear with the ±8% change in vocal tract with a 9% increase in reported targets that share the same vocal tract as the attended sentence $t_9 = 3.2$, $p < 0.01$. This size difference (16.6% between the short and the long) is comparable to that between male and female talkers, and so is ecologically comparable to an F_0 differences of around nine semitones which gave about a 20% increase in reported targets in experiment 2. This increase is somewhat larger than that produced by the ±8% vocal-tract change, indicating that the apparently dominant effects of a change in vocal tract in the previous experiment are due to the unnaturally large vocal-tract size changes used.

IV. GENERAL DISCUSSION

The experiments described in this paper have presented some new data on the relative roles of spatial cues, prosodic cues, and cues to an individual voice in auditory attention. The experiments have shown that natural prosodic variations are more effective than a monotonous pitch at overriding spatial cues in determining which of two possible target words belongs with a particular attended sentence. Part of their effectiveness is due to amplitude differences between target words in different prosodic contexts, and part is due purely to F_0 differences. The experiments have also shown that a difference in vocal-tract size that is comparable to or larger than the average male/female difference can also override spatial cues.

The task that we have used, though having the virtue of simplicity and requiring a minimum of preparatory signal processing, does not separate out the immediate allocation of attention from a more leisurely assessment of the whole stimulus. Listeners were under no time pressure to make their response and the target word occurred relatively late in the sentence. Since there were only two response alternatives, they could also have brought some variety to a repetitive task by listening to the ''nonattended'' sentence, though because of the symmetry of the stimulus pairings, such a strategy would not have influenced the overall results. However, our own impression in doing the task is that when there is a substantial change in vocal-tract size in the attended sentence, the word with the appropriate vocal-tract size in the unattended sentence ''pops out'' at you. We plan to pursue the questions raised in these experiments by trying to obtain some measure of the allocation of spatial attention in the temporal vicinity of this intrusion and also by testing whether it still occurs under a task such as close shadowing.

Although speech separation algorithms have exploited spatial differences and F_0 differences between competing messages, we know of no attempt to exploit vocal-tract length differences. Although vocal-tract length differences would be of limited value in initially separating simultaneous sounds, they could, along with spatial and prosodic cues, help in solving the problem of source continuity.

ACKNOWLEDGMENTS

This research was supported by Grant No. G9801285 from the UK MRC to the first author.

[1]This experiment was an extension and replication of a pilot experiment carried out by Catherine Brown as a student project.

[2]With a range across vowels from 1.02 to 1.27 reflecting the fact that males have a relatively larger pharynx (Fant, 1964).

Broadbent, D. E. (**1952**). ''Failures of attention in selective listening,'' J. Exp. Psychol. **44**, 428–433.

Broadbent, D. E. (**1953**). ''The role of auditory localization in attention and memory span,'' J. Exp. Psychol. **47**, 191–196.

Cherry, E. C. (**1953**). ''Some experiments on the recognition of speech, with one and with two ears,'' J. Acoust. Soc. Am. **25**, 975–979.

Darwin, C. J. (**1975**). ''On the dynamic use of prosody in speech perception,'' in *Structure and Process in Speech Perception*, edited by A. Cohen and S. G. Nooteboom (Springer, Berlin), pp. 178–194.

Darwin, C. J., and Bethell-Fox, C. E. (**1977**). ''Pitch continuity and speech source attribution,'' J. Exp. Psychol.: Hum. Percept. Perform. **3**, 665–672.

Darwin, C. J., and Hukin, R. W. (**1999**). ''Auditory objects of attention: the role of interaural time-differences,'' J. Exp. Psychol. Hum. Percept. Perform. **25**, 617–629.

Egan, J. P., Carterette, E. C., and Thwing, E. J. (**1954**). ''Some factors affecting multichannel listening,'' J. Acoust. Soc. Am. **26**, 774–782.

Fant, G. (**1964**). ''A note on vocal tract size factors and nonuniform *F*-pattern scalings,'' Speech Transmission Laboratory, Stockholm STL-QPSR **4**, pp. 22–30.

Hubner, R., and Hafter, E. R. (**1995**). ''Cueing mechanisms in auditory signal-detection,'' Percept. Psychophys. **57**, 197–202.

Kortekaas, R. W., and Kohlrausch, A. (**1999**). ''Psychoacoustical evaluation of PSOLA. II. Double-formant stimuli and the role of vocal perturbation,'' J. Acoust. Soc. Am. **105**, 522–535.

Kortekaas, R. W. L., and Kohlrausch, A. (**1997**). ''Psychoacoustical evaluation of the pitch-synchronous overlap-and-add speech-waveform manipulation technique using single-formant stimuli,'' J. Acoust. Soc. Am. **101**, 2202–2213.

Kuwabara, H., and Takagi, T. (**1991**). ''Acoustic parameters of voice individuality and voice-quality control by analysis-synthesis method,'' Speech Commun. **10**, 491–495.

Möhler, G., and Dogil, G. (**1995**). ''Test environment for the two level model of Germanic prominence,'' Eurospeech 1995; Madrid, pp. 1019–1022.

Mondor, T. A., and Zatorre, R. J. (**1995**). ''Shifting and focusing auditory spatial attention,'' J. Exp. Psychol: Hum. Percept. Perform. **21**, 387–409.

Moulines, E., and Charpentier, F. (**1990**). ''Pitch synchronous waveform processing techniques for text-to-speech synthesis using diphones,'' Speech Commun. **9**, 453–467.

Parsons, T. W. (**1976**). ''Separation of speech from interfering speech by means of harmonic selection,'' J. Acoust. Soc. Am. **60**, 656–60.

Peterson, G. H., and Barney, H. L. (**1952**). ''Control methods used in a study of the vowels,'' J. Acoust. Soc. Am. **24**, 175–184.

Quinlan, P. T., and Bailey, P. J. (**1995**). ''An examination of attentional control in the auditory modality—further evidence for auditory orienting,'' Percept. Psychophys. **57**, 614–628.

Scharf, B., Quigley, S., Aoki, C., Peachey, N., and Reeves, A. (**1987**). ''Focused auditory attention and frequency selectivity,'' Percept. Psychophys. **42**, 215–223.

Schlauch, R. S., and Hafter, E. R. (**1991**). ''Listening bandwidths and frequency uncertainty in pure-tone signal-detection,'' J. Acoust. Soc. Am. **90**, 1332–1339.

Spence, C. J., and Driver, J. (**1994**). ''Covert spatial ordering in audition: Exogenous and endogenous mechanisms,'' J. Exp. Psychol.: Hum. Percept. Perform. **20**, 555–574.

Spieth, W., Curtis, J. F., and Webster, J. C. (**1954**). ''Responding to one of

two simultaneous messages,'' J. Acoust. Soc. Am. **26**, 391–396.
Teder, W., and Näätänen, R. (**1994**). ''Event-related potentials demonstrate a narrow focus of auditory spatial attention,'' NeuroReport **5**, 709–711.
Weintraub, M. (**1987**). ''Sound separation and auditory perceptual organization,'' in *The Psychophysics of Speech Perception*, edited by M. E. H. Schouten (Martinus Nijhoff, Dordrecht), pp. 125–134.
Wightman, F. L., and Kistler, D. J. (**1992**). ''The dominant role of low-frequency interaural time differences in sound localization,'' J. Acoust. Soc. Am. **91**, 1648–1661.
Woods, D. L., Hillyard, S. A., and Hansen, J. C. (**1984**). ''Event-related brain potentials reveal similar attentional mechanisms during selective listening and shadowing,'' J. Exp. Psychol.: Hum. Percept. Perform. **10**, 761–777.
Zhu, W. Z., and Kasuya, H. (**1998**). ''Perceptual contributions of static and dynamic features of vocal tract characteristics to talker individuality,'' IEICE Trans. Fundam. Electron. Commun. Comput. Sci. **E81A**, 268–274.

Spectral characterization of jitter, shimmer, and additive noise in synthetically generated voice signals

Peter J. Murphy[a)]
Department of Electronic and Computer Engineering, University of Limerick, Limerick, Ireland

(Received 8 March 1999; revised 16 July 1999; accepted 29 July 1999)

Alteration of the harmonic structure in voice source spectra, taken over at least two periods of the waveform, may occur due to the presence of fundamental frequency ($f0$) perturbation, amplitude perturbation, additive noise, or changes within the glottal source signal itself. In order to make accurate inferences regarding glottal-flow dynamics or perceptual evaluations based on spectral measurements taken from the acoustic speech waveform, investigation of the spectral features of each aperiodic component is required. Based on a heuristic development involving a consideration of the partial sum of the Fourier series taken for two periods of a jittered, shimmered, and (additive, random) noise-contaminated signal, the corresponding spectral characteristics are hypothesized. Subsequent to this, the Fourier series coefficients are calculated for the two periods in order to test the hypotheses. Definite spectral differences are found for each aperiodic component; based on these findings differential quantitative spectral measurements are suggested. Further supportive evidence is obtained through use of Fourier transform and periodogram-averaged calculations. The analysis is carried out on synthetically generated glottal-pulse waveforms and on radiated speech waveforms. A discussion of the results is given in terms of voice aperiodicity in general and in terms of their implication for future studies involving human voice signals. [S0001-4966(99)01212-6]

PACS numbers: 43.70.Gr [AL]

INTRODUCTION

Many authors (e.g., Hillenbrand, 1987; Muta *et al.*, 1988; Fujimura, 1968) have observed that the presence of aperiodicities in the glottal-source signal gives rise to alteration in the harmonic structure of voiced speech. For example, Muta *et al.* (1988) report that ''glottal source perturbations distort the harmonic structure and thus affect both noise measures and harmonic strength measures'' (p. 1299). If the aim is to categorize or make direct inferences about specific glottal-source characteristics based on spectral analysis of a number of periods of the radiated speech waveform (e.g., abduction quotient [H_1-H_2, ratio (usually expressed in dB) between first and second harmonic energies], spectral tilt [H_1-A_1, ratio (usually expressed in dB) of first harmonic energy to first formant energy], etc. as per the recent studies by, e.g., Hanson, 1997; Holmberg *et al.*, 1995), then it is important to recognize the extent that jitter, shimmer, and additive noise affect the spectral composition.

Hillenbrand (1987) explains, in detail, the measurement problems associated with determining aperiodicities in speech signals. He concludes that there are strong measurement interactions among the three variables (jitter, shimmer, and additive noise) and that ''caution should be exercised in interpreting measures of perturbation and noise in terms of specific aspects of the laryngeal vibratory cycle'' (p. 458). For example, adding increasing amounts of jitter not only affects perturbation but also reduces the harmonics-to-noise ratio (HNR) of the signal. Alternatively, adding noise to the signal causes an increase in the measured jitter and shimmer as well as reducing the HNR. Furthermore, in the case of jitter, it is noted that for the radiated speech waveform, the consequence of this perturbation is the concomitant introduction of shimmer, irrespective of any measurement difficulties that may arise. This is a result of two characteristics of the vocal-tract filtering action, namely, the different resonant contributions from the vocal-tract transfer function due to the differing harmonic frequencies of the jittered signals and the overlay of energy from one cycle to the next due to the impulse response of the vocal tract. In acknowledgment of the difficulties of measuring jitter, shimmer, and additive noise in the time domain, a spectral analysis may provide an interesting alternative. Hillenbrand (1987) also gives a brief qualitative spectral evaluation of the three perturbation measures in the appendix of his paper.

A study of the spectral characteristics of aperiodicities may also be useful for interpreting some of the many interesting results reported in aperiodicity/perceptual correlation studies such as Hillenbrand (1988) or Martin *et al.* (1995). A recent study by Gauffin *et al.* (1996) has shown ''that different patterns of jitter and shimmer sequences with the same average period to period variability are rated differently'' (p. 260). They go on to conclude that ''this indicates that methods using period to period variability as a way to rate perceptual voice qualities might fail. Differences in the narrowband spectra of the stimuli may explain the differences in perceptual rating of the stimuli'' (p. 260).

Klingholtz and Martin (1985), noting that ''no quantitative data have been collected regarding the influence of shimmer and jitter on the voice spectrum'' (p. 169), at-

a)Electronic mail: peter.murphy@ul.ie

tempted to quantify the level of jitter in voice signals. The method involves the correlation of HNR with increasing levels of jitter for synthesized vowel-like data, consisting of exponentially damped sinewaves of frequency equal to the first formant. The authors conclude that ''the perturbed signals were synthesized by a simple model which describes jitter and shimmer phenomenologically. Therefore further investigation is necessary with a more refined model to simulate various types of laryngeal pathology'' (p. 174). The discrete-time model described in the next section, with its separately modeled glottal source, vocal-tract transfer function, and radiation load components, satisfies this refined model criterion. The spectral analysis approaches used in the present study include Fourier series, Fourier transform, and a periodogram-averaged analysis. The heuristic Fourier series approach facilitates a close examination of the theme of time/frequency equivalency.

I. METHOD

A. Synthesis data

A discrete-time system model of speech production is implemented in order to produce the synthesis data. The Rosenberg (1971) glottal-pulse model is used as the source excitation. It incorporates most of the important features of glottal waves estimated by inverse filtering and high-speed motion pictures and takes the form

$$g_r(n) = 0.5\left[1-\cos\left(\frac{\pi n}{N_1}\right)\right] \quad 0 \leqslant n \leqslant N_1$$
$$= \cos\left[\frac{\pi(n-N_1)}{2N_2}\right] \quad N_1 < n \leqslant N_1+N_2$$
$$= 0 \quad \text{otherwise}, \tag{1}$$

where n = sample number and N_1, N_2 = opening and closing phases of the glottal cycle.

To create a sequence of such waveshapes, an impulse-train generator produces a sequence of unit impulses which are spaced by the desired fundamental period. This sequence is then convolved with the glottal-pulse shape in order to produce the desired repetitive waveform. Since the goal is to study abnormalities of the voicing source, it is at the source that perturbation is introduced. Shimmer, which can be defined in general terms as the variation in amplitude of the glottal source from period to period, is introduced simply by adding a random variable gain factor to the impulse train prior to convolution with the glottal pulse. This variation in amplitude is implemented using MATLAB'S (The Math Works, Cambridge, MA) random-number generator ''randn(n)'' which produces a Gaussian distribution of random numbers with a mean of zero and a variance of 1. Therefore, in order to introduce a standard deviation of a given percent, denoted by ''per,'' a calculation similar to the following is implemented:

$$A' = A[100 + \text{per} \times \text{randn}(n)]/100, \tag{2}$$

where A = impulse train amplitude and n = sample number.

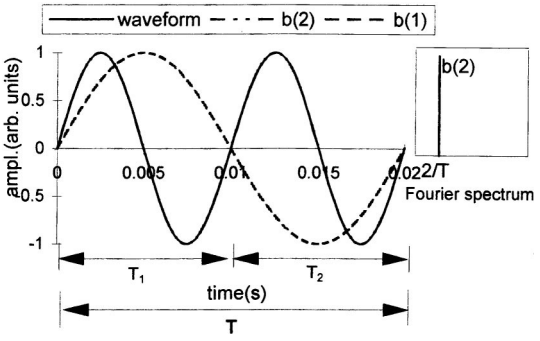

FIG. 1. Two periods of a sine wave with $T_1 = T_2 = T/2$. The sine terms for the first two Fourier coefficients (b_1 and b_2) are shown (b_2 is coincident with the waveform).

A per value of 4, for example, means that an originally constant amplitude impulse train, A, now has a Gaussian-distributed amplitude with a standard deviation equal to 4% of the original amplitude.

The introduction of random noise and random perturbation follows a similar strategy. Random additive noise is introduced by adding the multiplication of the average of the glottal-pulse wavelet by a random-noise generator of a user specified variance, denoted per to the glottal waveform (g_r). The noise is added according to the following equation:

$$g_r' = g_r + \text{mean}(g_r) \times [100 + \text{per randn}(n)]/100. \tag{3}$$

Two variations of jitter (the variation in the fundamental frequency from cycle to cycle) are synthesized: cyclic variation of the fundamental frequency, e.g., varying $f0$ from, say, 100 to 104 to 100 Hz and repeating in this fashion, and random variation, e.g., 102, 98, 101, 103 Hz, etc. Cyclic jitter is synthesized in order to investigate the proposal by Gauffin *et al.* (1996) that conventional jitter measurements indicating the same value may arise from vocal-fold motions which produce very different spectral characteristics. In both the cyclic and random-jitter synthesis, all periods are scaled versions of the unperturbed waveform periods. The glottal pulses are now used to excite the vocal tract, the transmission properties of which are based on the behavior of a set of concatenated lossless acoustic tubes (Rabiner and Schafer, 1978). Radiation at the lips is modeled by a first-order difference equation.

B. Spectral characterization

The possible spectral characterizations of each perturbation measure are first postulated based on a heuristic development that refers directly to the analytical expression for Fourier series expansion. This is a useful exercise because it provides a nonmathematical description of how the Fourier series gathers its spectral estimates and hence motivates an intuitive feeling for the time/frequency relationships under investigation. The spectra for the synthesis files are then produced (i.e., Fourier series evaluated) in order to test the hypotheses. In applying the Fourier series [Eq. (4)] two periods of a perfectly periodic sine wave with a total time record length T are considered, as shown in Fig. 1. (The glottal pulse is considered in later developments.)

$$s(t)=\frac{a_0}{2}+\sum_{k=1}^{\infty}\left[a_k\cos\left(\frac{2k\Pi t}{T}\right)+b_k\sin\left(\frac{2k\pi t}{T}\right)\right], \quad (4)$$

where

$$a_k=\frac{2}{T}\int_0^T s(t)\cos\left(\frac{2k\Pi t}{T}\right)dt, \quad (5)$$

and

$$b_k=\frac{2}{T}\int_0^T s(t)\sin\left(\frac{2k\Pi t}{T}\right)dt, \quad (6)$$

where t=time, T=time for one period, a_0=mean value of waveform, and $s(t)$=periodic time domain waveform.

$$h_k=(a_k^2+b_k^2)^{1/2}, \quad (7)$$

where h_k=amplitude of kth harmonic.

The basis behind the method is that if each waveform of period T_1 is exactly the same, then harmonics will only appear in the spectrum at integer multiples of $1/T_1=2/T$. If the waveforms differ in any respect, then energy appears in the spectrum at integer multiples of $1/T$. It should be noted, therefore, that, in this development, odd harmonics signify some form of perturbation and even harmonics represent the unperturbed waveform. In the present case (a sine wave), a single spectral peak at $f=1/T_1$ is obtained for the unperturbed signal, the harmonic energy at all other locations being equal to zero.

To see how the Fourier series arrives at this estimate, the sine terms of the series for each harmonic location k/T are considered (cosine terms are zero for odd functions). Fitting the first harmonic, $1/T$ Hz, to the waveform in Fig. 1 and taking the sum for the Fourier coefficient, $b_1=1/T$, it can be seen that [in consideration of Eq. (6) and Fig. 1] what is obtained in the positive half of the cycle is also obtained in the negative half of the cycle with all contributions to the sum adding to zero. A similar result is obtained for all higher terms in the series, except for $2/T$ when the contributions add constructively. This is a completely general analysis not specific to sine waves. In the case of a sine wave, it is possible to obtain the estimate analytically by substituting $\sin(2\times 2\pi t/T)$ into Eq. (6) (see the Appendix) to obtain

$$b_k=1, \quad \text{for } k=2, \quad (8)$$

$$b_k=0, \quad \text{for } k\neq 2. \quad (9)$$

Therefore, showing that the heuristic development is correct, i.e., energy is present at the ''$2\times 1/T$'' harmonic (b_2) and zero at all higher harmonics.

The glottal-pulse waveform is examined in Fig. 2. Fitting the $1/T_1=2/T$ Hz waveform, it is seen that the contributions to b_2 (at $2/T$) add constructively, giving amplitude of the ''fundamental,'' at the first even harmonic. All higher even harmonics $[k\times(2/T)]$ sum in similar fashion, giving spectral contributions dependent on the frequency characteristics of the waveshape; the glottal pulse having a low-pass nature as illustrated in the caption in Fig. 2. Now, considering the Fourier sine terms at $1/T$ Hz, the contributions are

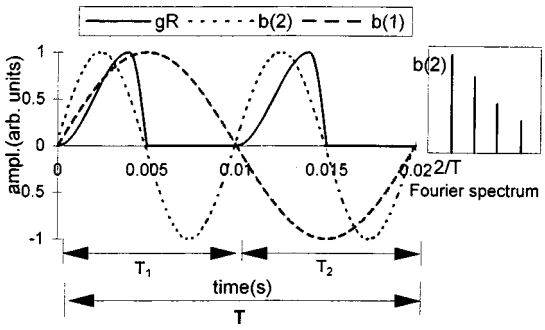

FIG. 2. Two periods of a glottal-flow waveform with $T_1=T_2=T/2$. The sine terms for the first two Fourier coefficients (b_1 and b_2) are shown.

symmetrical but opposite and sum to zero. All higher odd harmonic energy contributions sum to zero in similar fashion.

Shimmer is introduced as shown in Fig. 3. The contributions to b_2 are reduced due to the decreased amplitude of the second period of the waveform. All higher even harmonics are similarly reduced, and the reduction is in accordance with the spectral energy contributions for that frequency. The contributions to b_1 do not cancel due to the amplitude difference in the glottal waveform. A similar result occurs for all higher odd harmonics and again this is in accordance with the spectral energy contributions for that frequency. Because the waveform cannot be shifted to be even or odd, the cosine terms of the series should also be considered. For the glottal pulse shown in Fig. 3 (and Fig. 2), the same arguments that were used for the sine terms hold true for the cosine terms. Shimmer is introduced above with a reduction in the amplitude of the waveform (Fig. 3). This could just as easily have been an increase in amplitude giving rise to increased even harmonics, and in the case of random shimmer we would expect the overall effect (i.e., the average of several consecutive two-cycle analyses) to sum to zero, leaving the amplitude of the even harmonics unperturbed. A similar effect is predicted for the averaged odd harmonics which would represent the average amplitude difference between the shimmered waveforms.

In the case of jitter, the analysis is somewhat different. In this instance the Fourier series coefficients are separated by $1/T'$ Hz (Fig. 4). As the two periods are not equal, a contribution exists at $1/T'$ Hz. Notice also that there is a

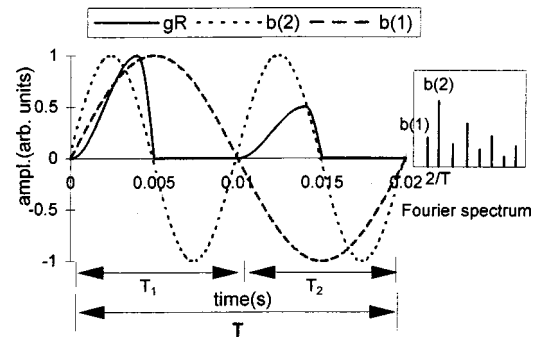

FIG. 3. Two periods of a glottal-flow waveform with $T_1=T_2=T/2$, with the amplitude of the waveform in the second period reduced to illustrate shimmer. The sine terms for the first two Fourier coefficients (b_1 and b_2) are shown.

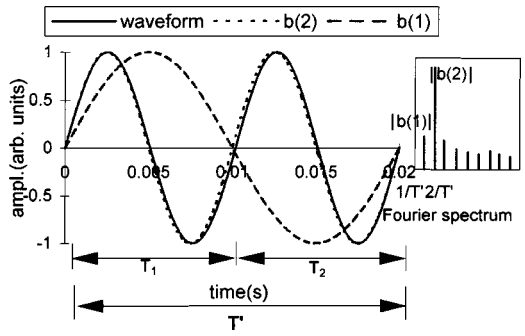

FIG. 4. Two periods of a sinewave with $T_1 \neq T_2 \neq T/2$, illustrating jitter. The sine terms for the first two Fourier coefficients (b_1 and b_2) are shown.

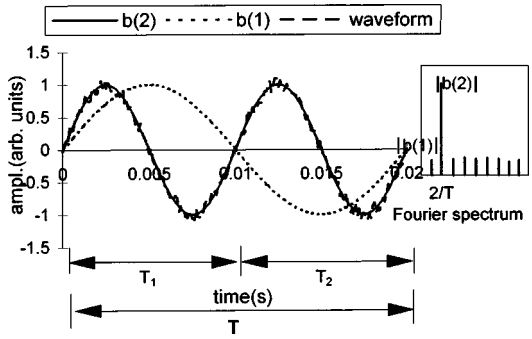

FIG. 5. Two periods of a sinewave with $T_1 = T_2 = T/2$, in the presence of additive noise. The sine terms for the first two Fourier coefficients (b_1 and b_2) are shown (b_2 is coincident with the waveform).

reduction in the amplitude contributions at $2 \times 1/T'$ Hz as the series coefficients no longer match the ''fundamental frequency,'' $1/T_1$. The situation is analogous to ''leakage'' that occurs when a noninteger number of periods are present in the analysis frame (Harris, 1978). Because the signal periods T_1 and T_2 are not submultiples of the series coefficients, higher harmonics appear in the spectrum and with respect to the sine wave, all of these are noise components.

A jittered glottal-flow waveform is now considered: a flow waveform of period T_1 is followed by a second waveform of period T_2. It is important to realize in this development that the signal consists of period length $T' = T_1 + T_2$ with harmonic frequencies at integer multiples of $1/T'$. However, a consideration of the coefficients that would result from a signal with fundamental frequency $1/T_1$ (0 to T_1) and an independent signal of fundamental frequency $1/T_2$ (T_1 to T') (each in a T' analysis frame) is instructive for an understanding of the amplitude variation in harmonic structure of the $1/T'$ signal. The $1/T_1$ signal in the T' window is denoted $1/T_1'$ (i.e., a flow waveform of period T_1 in a T' analysis window, i.e., zero from T_1 to T'). The $1/T_2$ signal in the T' frame is denoted $1/T_2'$ (zero from 0 to T_1). For the $1/T_1'$ and $1/T_2'$ signals the harmonics are spaced at integer multiples of $1/T'$. In calculating the spectral energy contributions for the unperturbed two cycle waveform it has been shown that the amplitude at even harmonic locations adds constructively and the amplitude at odd harmonic locations cancels. As the periods in question are not equal this is no longer the case. As the harmonic number (k) increases, the difference between the $k \times 1/T_1$ and $k \times 2/T_1'$ harmonic increases ($k \times 1/T_1$ lags further behind $k \times 2/T_1'$), hence reducing the contributions to the $2/T_1'$ coefficients. In similar fashion, the $k \times 1/T_2$ harmonics become further separated from the $k \times 2/T_2'$ harmonics ($k \times 1/T_2$ further advances $k \times 2/T_2'$), as the harmonic number increases. The overall effect provides reduced energy at even harmonics and reduced cancellation (or increased energy) at odd harmonics. This process continues until an upper frequency location, governed by Eq. (10), is reached. At this point, the energy contributions from the signal harmonics provide approximately equal contributions to both the odd and even harmonics (i.e., when an integer plus a half sub-periods of T' match T_1 and an integer minus a half sub-periods of T' match T_2). After passing this frequency location the odd analysis harmonic begins to receive a larger share of the energy contributions until a maximum boost at odd harmonics is obtained according to Eq. (11). The process then begins to reverse as the even harmonics begin to receive a greater share of the energy contributions and the odd harmonics receive less. A crossover point is again reached when an integer plus one and a half-subperiods of T' match T_1 and an integer minus one and a half sub-periods of T' match T_2. When T_1 and T_2 differ by two sub-periods of T' the even harmonics receive maximum reinforcement of energy [and the odd minimum, Eq. (11)]. The process then begins to repeat itself:

$$(m - n \times 0.5) \times 1/T_1 = (m + n \times 0.5) \times 1/T_2, \tag{10}$$

for m and n both integer,

$$n \times 1/T_1 = m \times 1/T_2 = (m + n) \times 1/T', \tag{11}$$

for n and m both integer; n-m even (0,2, . . .), harmonic enforcement; n-m odd (1,3, . . .), subharmonic reinforcement. Superimposed on this harmonic interplay between the ''individual signal harmonics'' and the analysis Fourier coefficients, the energy at higher harmonics decreases (due to the characteristics of the signal) as the harmonic number increases. Therefore, the contributions at harmonic and between-harmonic locations are dependent on the level of jitter and on the unperturbed waveform characteristics.

It is impossible to differentiate between cyclic and random jitter using a two-cycle analysis scheme. In the case of cyclic jitter, the above-mentioned ''odd analysis harmonic'' is equal to the subharmonic frequency. For random jitter, the above-mentioned trends are still valid, but the random variability introduced has a large bearing on the overall spectral characteristics. The Fourier series calculation could be extended to include more periods of the waveform (as a single analysis period), in order to investigate random jitter more accurately, but, as will be shown in Sec. II, it is more convenient to take a Fourier transform viewpoint.

Considering the addition of mean zero, random noise to the sinewave (Fig. 5), it can be seen that spectral energy is present at harmonic locations other than the frequency of the sinewave. As the variance of the noise increases, the variance of the spectral estimates increases also. The sine wave signal ($k = 2$, say) plus noise may be represented by the following equation:

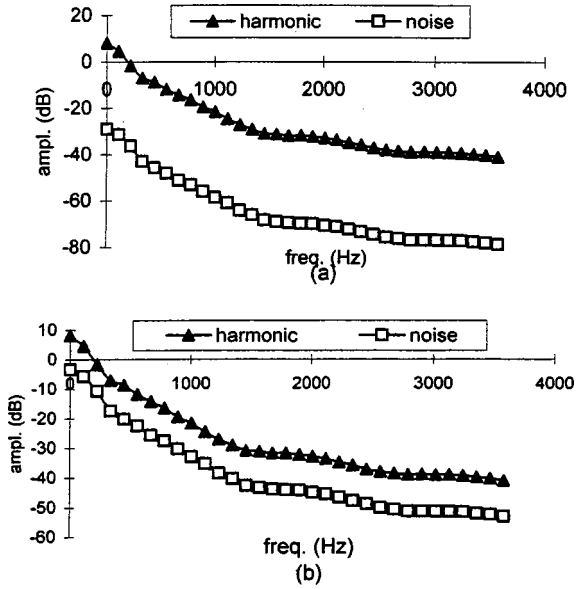

FIG. 6. Two-cycle Fourier series analysis for glottal-flow waveforms with 2% (a) and 32% (b) s.d. random shimmer (noise is estimated at between-harmonic locations).

$$s(t)=\sin\left(\frac{2\times 2\Pi t}{T}\right)+q(t), \tag{12}$$

where $q(t)$ is the noise component.

It has been shown in the Appendix that the Fourier series for the sine wave gives zero energy at all frequency locations except $2\times 1/T$. Therefore, for $k\neq 2$,

$$a_k=\frac{2}{T}\int_0^T q(t)\,\frac{\cos(2\Pi kt)}{T}\,dt, \tag{13}$$

and

$$b_k=\frac{2}{T}\int_0^T q(t)\,\frac{\sin(2\Pi kt)}{T}\,dt. \tag{14}$$

Since $q(t)$ is random, it can be inferred that it provides (on average) roughly equal energy contributions to all harmonics in the spectrum. A more formal analysis of the Fourier transform of a random noise signal can be found in, e.g., Blackman and Tukey (1959).

The above development, through a heuristic implementation of the Fourier series and a brief reference to the Fourier transform, leads to a descriptive, spectral characterization of shimmer, jitter, and additive noise, respectively. In summary, for shimmered signals the level of the even harmonics is unchanged and the level of odd harmonics increases with the increasing variance of the shimmer. The contributions to the odd harmonic at a given frequency are in direct relation to the contributions to the unperturbed signal for the nearest even harmonic. Jitter gives reduced harmonic levels and energy is introduced at between-harmonic locations. The contributions at a given harmonic or between-harmonic location are dependent on the frequency characteristics of the unperturbed signal, with enforcement of spectral energy occurring at intervals determined by the magnitude of the jitter component. Additive noise has no effect on the energy at averaged harmonic locations as long as the signal strength is greater than the strength of the noise signal at these harmonic locations. Energy is introduced between harmonics with a flat spectral characteristic. Therefore, both the jittered and shimmered signals are dependent on the characteristics of the signal being perturbed and the additive noise is independent of the signal characteristics. These conclusions are in agreement with the jitter and shimmer results reported by Klingholtz and Martin (1985) and with the additive noise and jitter observations reported by Hillenbrand (1987). In the study undertaken by Klingholtz and Martin (1985), the harmonic level estimated in shimmer is found to remain constant, whereas Hillenbrand found the harmonic levels to be significantly reduced in comparison to the spectra for jitter and additive noise signals. The present description supports the former observation (Hillenbrand's report may have been a result of the particular synthesis used, where there appear to be unusually high noise levels at the formant locations in the spectra illustrated). The present deduction is also supported by a formal mathematical study of shimmered signals recently developed by Michaelis (1999).

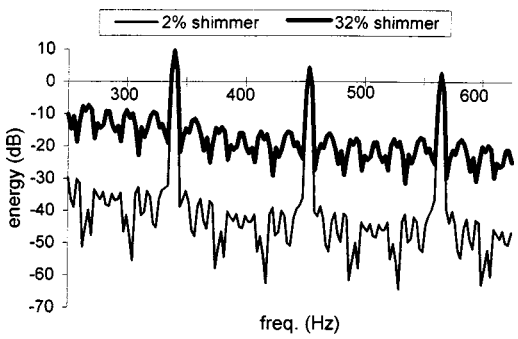

FIG. 7. Fourier transform estimates of the s.d. 2% and s.d. 32% shimmered signals illustrating the increased variance of the 32%-s.d. signals between-harmonic energy.

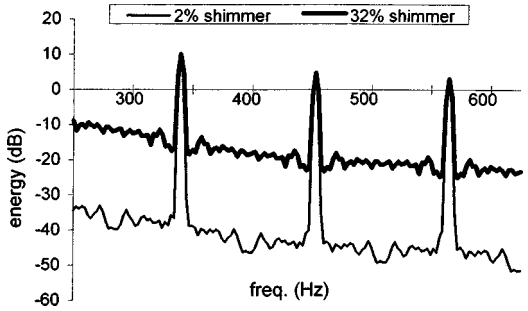

FIG. 8. Periodogram-averaged or power spectral density estimate for the test shimmer signals of (a) s.d. 2% and (b) 32% s.d. illustrating equal harmonic strengths for each signal and an increased noise level for the s.d. 32% shimmer signal.

II. ANALYSIS AND RESULTS

A. Source signals

To test the hypotheses based on the Fourier series development, spectra for the glottal pulses with six levels of additive noise, jitter (two types), and shimmer are examined. In addition to the two-cycle Fourier series analysis, a Fourier transform analysis and a periodogram-averaged analysis are

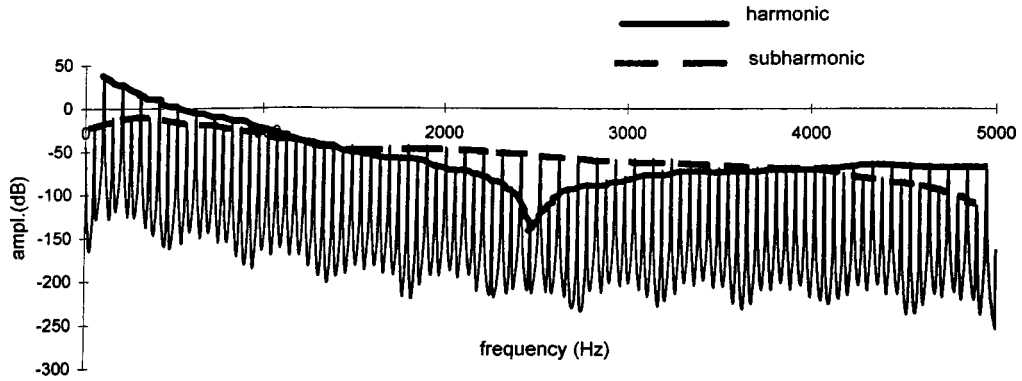

FIG. 9. Periodogram-averaged estimate of the 5% cyclic jitter signal showing a maximum in subharmonic signal strength at ~2530 Hz (22nd 115-Hz harmonic matches the 23rd 110-Hz harmonic) with a corresponding minimum in the even harmonic at this location. The even harmonic is maximally boosted at 5 kHz with a corresponding minimum in the odd harmonic. Harmonic reinforcement locations are governed by Eqs. (10) and (11).

also performed for the shimmered and jittered signals. Figure 6 illustrates the two-cycle Fourier series analysis for shimmer values of s.d. 2% and 32%. The Fourier series coefficients are computed every two cycles for an analysis interval of 1 s and the mean of the Fourier coefficients are plotted. It can be seen that increases in shimmer cause the noise floor to go up in a consistent manner for all frequencies (i.e., in accordance with the signal characteristic). The harmonic levels themselves remain unperturbed and the source spectrum envelope is maintained. The noise component reaches a higher level for the 32%-s.d. shimmered signal. In considering the Fourier transform estimate (4096 points at 10-kHz sampling, Hamming window) of the same signal (Fig. 7), a similar trend to the two-cycle analysis plot is observed. As the transform provides only a single estimate at each frequency location (as opposed to an averaged estimate), an increased variance of the between-harmonics becomes apparent. The variance of the estimates increases as the shimmer level increases. The periodogram plots (Fig. 8) are an average of six 4096-point spectra hopped 1024 points. The averaging reduces the variance of the spectral estimates. The temporal equivalent is the mean of the glottal wavelets (harmonics) and the mean difference of the glottal wavelets (between-harmonics).

Although a two-cycle Fourier analysis scheme is instructive for examining the underlying nature of the harmonic structure for jittered signals, a Fourier transform analysis using several periods (1024 sample points sampled at 10 kHz) of the waveform offers a less restrictive approach. For cyclic jitter (Fig. 9) the main characteristic is the introduction of a strong subharmonic regime. The amplitude in the harmonic spectrum is seen to follow an interesting trend governed by Eqs. (10) and (11).

Random jitter is now considered. For a perfectly periodic signal (within the analysis frame), the estimate at a given frequency location is the convolution of the Fourier transform of the window function with the Fourier transform of the signal at that frequency. Hence, there is a broadening of the spectral peak due to the window function. This is shown in Fig. 10 for the 110-Hz glottal waveform with a random jitter component of s.d. 4%. As the frequency increases, the spread of the signal about the higher harmonics increases, reducing the amplitude at $k\times 110$ Hz locations. Hillenbrand (1987) also observed that jitter leads to a more prominent smearing of the harmonic structure at higher frequencies. If the jitter component is large, the broadening of the harmonic peaks gives way to the contributions becoming individually resolved, giving rise to a more irregular-looking spectrum. However, some reappearance of harmonic structure is also evidenced. This is due to a combination of the broadening of the Gaussian distribution of spectral energy about higher harmonics and the reinforcement that takes place at higher frequency locations where the difference between a jittered harmonic matches a lower (or higher)

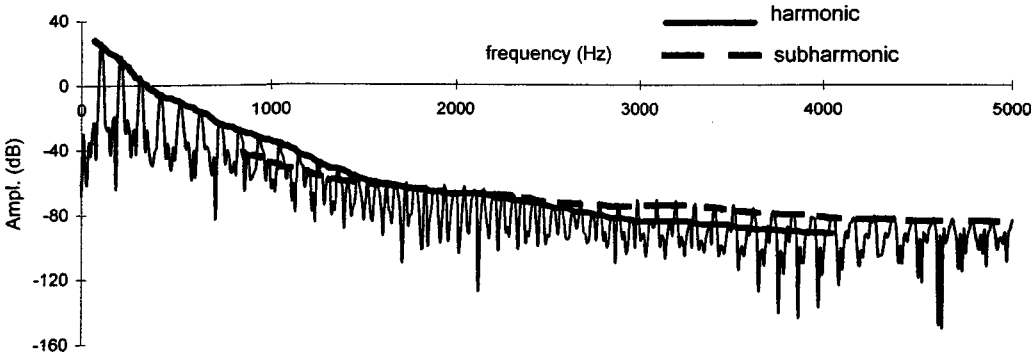

FIG. 10. Fourier transform (1024 points at 10-kHz sampling) of a 4% randomly jittered signal. Region 1 (0–1.2 kHz): initial spectral broadening of harmonics gives way to spectral decomposition centered around harmonic locations. Region 2 (1.2–3 kHz): A subharmonic regime is introduced as the Gaussian distributions centered at harmonic locations begin to have significant overlay with adjacent jittered harmonic distributions. Region 3 (3–5 kHz): The overlay increases to such an extent that a single peak is found at subharmonic locations with broadened spectral bandwidths.

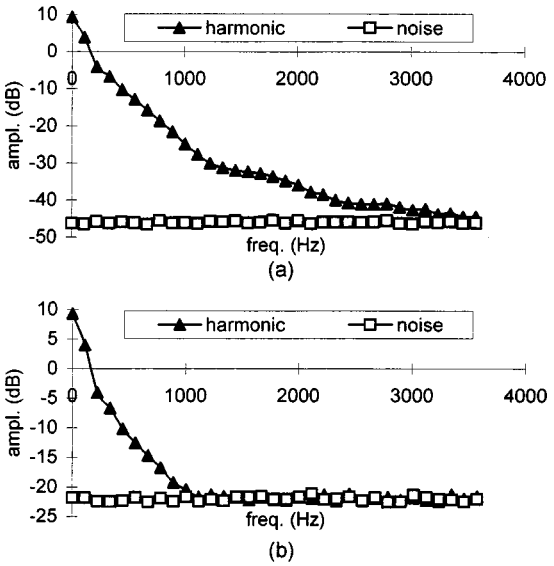

FIG. 11. Two-cycle Fourier series analysis for glottal-flow waveforms in the presence of random additive noise of (a) 2% s.d. and (b) 16% s.d. The noise spectrum, which is approximately flat, moves upward for the increased noise level (noise is estimated at between-harmonic locations).

110-Hz harmonic as mentioned in the discussion on cyclic jitter.

Figure 11 shows the effect of adding random Gaussian noise to the glottal source. The level of the harmonics in the averaged two cycle spectrum is unaffected except as the noise floor moves upwards, in a sense consuming the lower-level harmonics as it moves. The noise spectrum is white, i.e., constant for all frequencies, as expected. An examination of the signal-plus-noise spectrum indicates that traditional HNR estimators may overestimate the level of harmonics due to the presence of noise at higher frequency locations. This similarly has consequences for spectral tilt measurements.

B. Radiated speech waveform

Until now, the spectral consequences of aperiodicities were examined directly as introduced at the glottal source. Guided by this source analysis, it is now expedient to investigate the spectral alterations that occur due to vocal-tract filtering of aperiodic waveforms. In the case of shimmer and additive noise, the process is reasonably straightforward if a separable source/filter arrangement is assumed. The situation is shown in Fig. 12(a) and (b). Upon filtering, HNR remains the same for the shimmered signal but decreases for the additive noise signal (see Murphy, 1999 for a quantitative illustration). HNR(f) remains the same for all frequencies (f) for the shimmer signals and the noise floor moves up equally for all frequencies in the additive noise case.

The effects of the vocal-tract filtering on the jittered signals are more complex. As briefly alluded to in the Introduction, this stems from two consequences of the vocal-tract filtering, namely, the excitation of the vocal tract with differing harmonic frequencies on a period-by-period basis, and the difference in overlay in energy from one cycle to the next due to the convolution of the impulse response of the vocal tract with different length periods. The exact quantification of the effect of vocal-tract filtering on jittered signals in terms of spectral measurements such as the HNR is not easy to determine as the relationship of the fundamental frequency to the resonant frequencies (and the bandwidths of the resonant frequencies) must be taken into consideration. An investigation into the magnitude of these effects is required. Quantitative data detailing the effects of overlay energy into adjacent cycles are also of interest. Hillenbrand (1988) states that the HNR reduces for signals with the same absolute jitter values as the fundamental frequency increases. It is difficult to postulate whether overlay energy or the difference in the location of the source harmonics is the prominent component in determining this trend.

Two glottal-pulse waveforms (100 and 200 Hz) with equal jitter values of 3% are examined by way of example. The variance in overlay energy for these signals is greater for the higher frequency signal since the periods are spaced more closely together. A three-percent jitter value gives rise to a 3-Hz variation for the 100-Hz signal and a 6-Hz variation for the 200-Hz signal, this variation doubles with each doubling of frequency. However, this apparently higher source spectrum variability for the higher frequency signal is somewhat compensated for over a set frequency range due to the lower density (half) of harmonics. Although the 100-Hz signal has double the density of harmonics, if the glottal-flow waveforms are scaled versions of each other (each with -12 dB/oct), at a given frequency location, the 200-Hz signal will have higher amplitude values. This fact may be very important in determining which factors (overlay or harmonic shift) dominate in determining the $f0$ trend. The remaining variable is the location of the harmonics with respect to the formant peaks, which is $f0$-dependent, but not in a linearly increasing fashion. Therefore, it is difficult to conclude whether the overlay or harmonic shift is dominant in determining the ratio; further experimentation is required in order to test which term dominates.

For the jittered signals used in the present study, the effect of the filtering action on the harmonic structure is evident [Fig. 12(c) and (d)]. However, the overriding harmonic characteristics (excluding the vocal-tract transfer function) are still very similar to those of the source spectra. The radiated, cyclic jitter waveform has the same subharmonic pattern as that for the source waveform, reflecting both the regularity of the overlay energy into consecutive periods and the repeating nature of the differential harmonic excitation. The filtering of the random jitter signal introduces more prominent secondary variations as the overlay and differential harmonic excitation occur in a random fashion. Early harmonics are broadened and the predicted reappearance of harmonic structure in the region of the third formant (for the given combination s.d. jitter and average fundamental frequency) is less obvious.

III. DISCUSSION

A. Relationship between analysis variables (jitter, shimmer, and additive noise) and aperiodicities found in human voice signals

As overall descriptive categorizations of aperiodicity in voice signals, the labels of jitter, shimmer, and additive noise

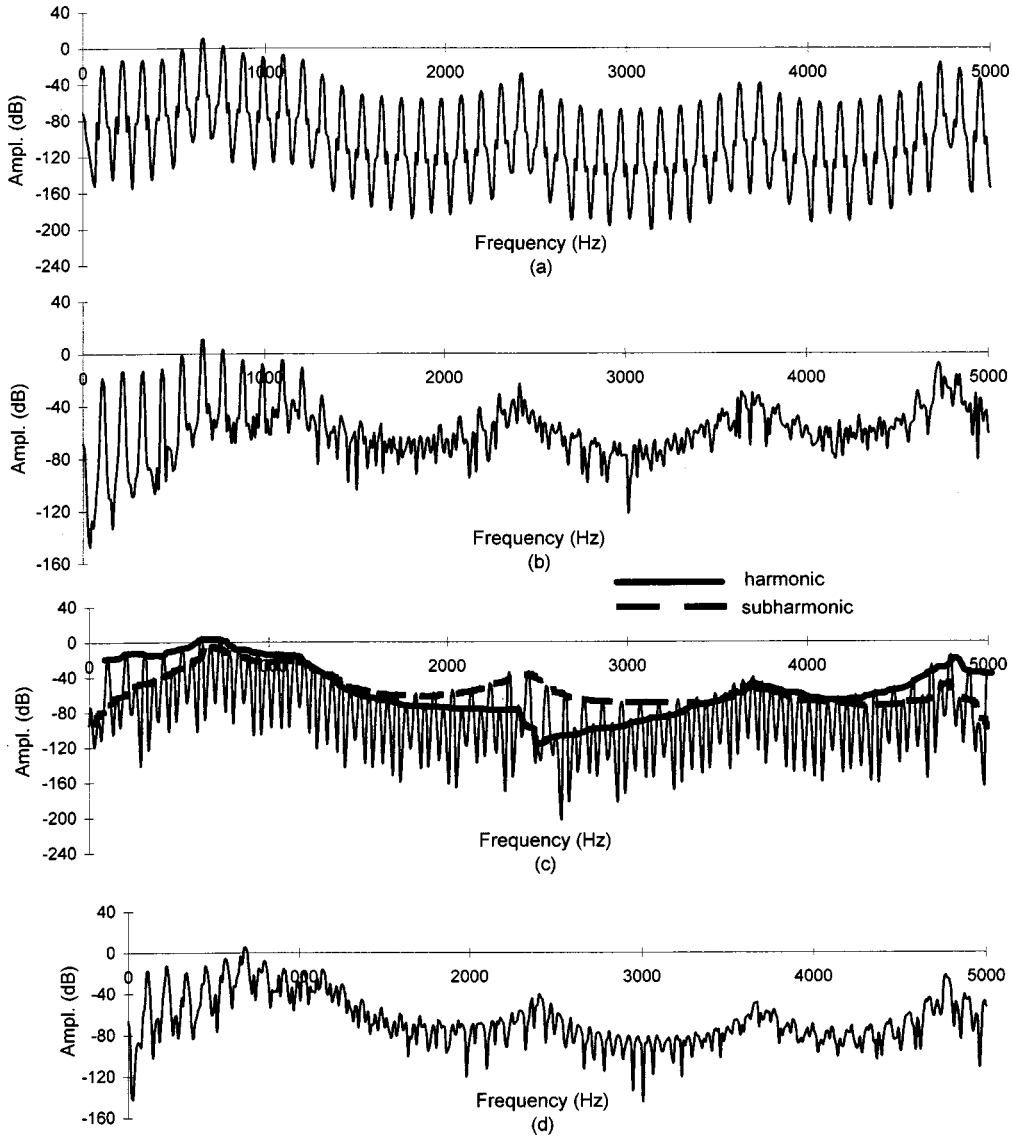

FIG. 12. Fourier transform estimates (1024 points at 10-kHz sampling) of the radiated speech waveforms for the four aperiodic components of (a) 4% s.d. shimmer, (b) 4% s.d. additive noise, (c) 5% cyclic jitter, and (d) 5% s.d. random jitter.

are perhaps useful classifications of unidimensional changes. In a similar manner, waveshape change could conceivably provide another useful variable. However, this is not to imply that these parameters are the most salient or independent aperiodic components found in voice signals. Attempting to describe the precise nature of aperiodicities in voice signals in physical, physiological, and perceptual terms is still the subject of wide-ranging investigations. In the meantime, gross descriptions have found some application, in terms of perceptual and physical correlations. In general auditory perceptual terms, additive noise is associated with breathiness, with moderate amounts of jitter and shimmer being associated with roughness. In general physical terms, noise is associated with turbulent flow at the glottis and perturbation (jitter and shimmer) is associated with vocal-fold instability.

Random jitter, cyclic jitter, random shimmer, and additive noise are the aperiodic components synthesized and investigated in the present study. Further discussion of jitter, shimmer, and additive noise in voice signals can be found in Murphy (1999). Description of the new aperiodic component synthesized in the present study (cyclic jitter) is given presently. The term ''cyclic'' refers to the fact that the aperiodic component repeats itself in a periodic or cyclic fashion every second (in this case, but could also be every third, fourth, etc.) period of the unperturbed waveform. Cyclic jitter is synthesized in the present investigation; however, other (or combinational) cyclic perturbations can also be synthesized, e.g., cyclic shimmer. Voice signals containing cyclic shimmer are perceived as having a rough voice quality when the amplitude variation is less than approximately 50 percent and as having a pitch an octave lower when this 50-percent threshold is exceeded (Titze, 1994). This voice quality is referred to as vocal creak and may be perceived as fry phonation when a subharmonic appears in the spectrum at a frequency location less than 70 Hz. Creaky voice may occur during normal phonation, particularly during voice onset/offset episodes. Cyclic jitter may also be present during voice onset/offset characteristics (and during sustained phonations) in addition to, or in place of, cyclic shimmer (see, e.g., Askenfelt and Hammarberg, 1986; Svec *et al.*, 1996).

TABLE I. Summary of spectral characteristics of shimmer, random jitter, cyclic jitter, and additive noise. Harmonic levels, noise levels, and HNRs in comparison to those of a periodic waveform.

Acoustic index/ perturbation type	Harmonic level (H)	Noise level (N)	Harmonics-to-noise ratio (HNR)
Periodic waveform	Finite	Zero	Infinite
Shimmer	Unchanged (on averaging)	Increase in direct proportion to signal characteristics at that frequency.	Reduced. Constant for all frequencies.
Random jitter	Reduced and variable. Dependent on the magnitude of the jitter.	Increases (signal dependent). Amplitude of noise is in general greater at lower frequencies. Harmonic bandwidth broadening and introduction of subharmonics.	Reduced. Dependent on magnitude of jitter and fundamental frequency.
Cyclic jitter	Reduced and variable. Dependent on the magnitude of the jitter.	Increased. A subharmonic regime is introduced.	Reduced. Dependent on magnitude of jitter and fundamental frequency.
Random additive noise	Unchanged (on averaging) when harmonic levels are greater than noise levels.	Increased. Independent of signal.	Reduced. Decreases with increasing frequency.

When jitter is the ''period doubling/tripling'' determinant (as opposed to shimmer), the resultant subharmonic pattern is more complicated and depends on the relationship between the original fundamental frequency and the magnitude of the jitter component, as shown in Sec. II.

IV. CONCLUSION

Definite differences in spectral composition are shown to exist between signals containing cyclic jitter, random jitter, shimmer, and additive noise. The nature of the alterations in harmonic structure due to the different aperiodic components is first postulated using a graphical analysis of the Fourier series calculation. This is an important development for two separate reasons. First, it allows for an examination of the aperiodicities in their most basic form (two cycles), based upon which greater complexity is introduced and examined, namely, more cycles of the waveform and the filtering action of the vocal tract. Second, the analysis facilitates a closer understanding of how the Fourier series gathers its spectral estimates. It therefore provides a useful, nonmathematical tool for predicting the spectral features of varying time-domain parameters. This approach to the investigation of time/frequency equivalency avoids the use of complicating parameters such as bandwidths and windowing, which make comparisons difficult, as noted by Qi and Hillman (1997).

The postulates regarding the harmonic alterations are tested using Fourier series, Fourier transform, and periodogram-averaged analyses. The methods prove complimentary. A summary of the results from these spectral analyses is given in Table I. As stated in the Introduction, one of the aims of the present study is to investigate whether perturbation measurements can be extracted from frequency domain data. The results illustrated in Table I and Fig. 12 suggest that this may be possible, at least for univariate data. Referring to Table I, it can be seen that a constant value of HNR(f) for all ''f'' indicates shimmer. Therefore, once constancy of this measurement is checked for at all frequency locations, it can then be used to provide a direct indication of the level of shimmer in the speech waveform.

Examination of the graphs for random jitter [Fig. 12(d)] and additive noise [Fig. 12(b)] reveal severe deterioration in harmonic structure for each aperiodicity. However, the noise level for the additive noise simulation rises above the level of the signal spectral characteristics, whereas the noise level in the jittered signal maintains the same level as the signal characteristic. Therefore, a measurement of the HNR from 1 to 4 kHz indicates an aperiodicity of either additive noise or jitter, but a subsequent measurement of the noise level will reveal which of the two is actually present. Alternatively, a spectral tilt measurement will differentiate the two spectra. It should also be noted that the additive noise spectra have important implications for presently used spectral tilt and HNR measurements; new methods are required in order to eliminate the noise contamination of higher harmonics in such measurements. In addition, the use of a set frequency range is problematic when quantifying spectral characteristics of signals with different fundamental frequencies (see

Murphy, 1999, for a discussion of these issues).

The subharmonic regime of the cyclic jitter spectra suggest a method for quantifying jitter levels for this type of perturbation. For the spectrum shown in Fig. 12, the minimum amplitude for the even harmonic appears at 2.53 kHz for the 110-Hz signal. Therefore, 23 periods of this waveform (period T_1) match 22 periods of a T_2 waveform at this point, giving a jitter value of 5%. Plotting consecutive narrow-band spectra for continuous speech could be developed in order to track the onset of octave-lowering pitch variations more accurately, as suggested previously by Fujimura (1988).

Tracking the amplitude variations of the harmonic and subharmonic regimes of jittered waveforms should help to predict the perceived pitch of such signals. In general, spectral characterizations of aperiodicities should help in the interpretation of results obtained in aperiodicity/perceptual correlation studies. The present results [Fig. 12(c), cyclic jitter spectrum, and Fig. 12(d), random jitter spectrum] show that an equal jitter index may arise from waveforms with very different spectral characteristics. Further studies using auditory-processed spectra will help to explain some of the effects of aperiodicity on the perception of voice quality.

Finally, the results presented have implications for the application of studies such as the recent work by Hanson (1997) (i.e., determining glottal characteristics from the radiated speech spectrum), to the study of pathological voice types. In consideration of the spectral changes brought about due to the affects of jitter, taking H_1-A_1 (level of first harmonic to first formant) and H_1-H_2 (level difference between the first and second harmonic) measurements from spectra obtained from several periods of the waveform is not recommended for jittered waveforms. For shimmered and noise-contaminated signals, the averaged H_1-H_2 and H_1-A_1 ratios remain unaffected so long as the unperturbed fundamental frequency is tracked in the case of shimmer, and the signal harmonics are greater than the noise variance for the noise-contaminated signal. When noise levels are high, extracting the Fourier coefficients (as opposed to harmonic energies) from pitch-synchronous spectra and averaging the coefficients to give the H_1-H_2 and H_1-A_1 ratios is suggested. Further analysis is required for quantitative qualification of these issues.

ACKNOWLEDGMENTS

Partial support for this work was provided by a Health Research Board Grant (No. 01-95) while the author was with the Department of Physics, Royal College of Surgeons in Ireland, and by a joint Dublin Institute of Technology/Trinity College, Dublin (DIT/TCD) seed-funding scheme. The author is grateful to Dr. Eugene Coyle and Dr. Bob Lawlor, School of Control Systems and Electrical Engineering, DIT, and Dr. Pauline Sloane, School of Clinical Speech and Language Studies, TCD, for participating in the DIT/TCD scheme and for fruitful discussions of the present work. The author also wishes to thank Dr. Dirk Michaelis for communicating his work on shimmered signals and Dr. Maurílio Nunes Vieira for many helpful editorial suggestions.

APPENDIX

$$b_k=\frac{2}{T}\int_0^T \sin\frac{2\times 2\Pi t}{T}\sin\left(\frac{2k\Pi t}{T}\right)dt. \tag{A1}$$

Setting $k=2$, the integrand becomes

$$b_2=\frac{2}{T}\int_0^T \sin^2\left(\frac{2\times\pi t}{T}\right)dt=\frac{2}{T}\int_0^T\frac{1}{2}\left(1-\cos\left(\frac{8\pi t}{T}\right)\right)dt, \tag{A2}$$

$$=\frac{2}{T}\left[\frac{t}{2}-\frac{T}{2\times 8\times\Pi}\sin\left(\frac{8\pi t}{T}\right)\right|_0^T\Bigg]=1, \tag{A3}$$

and for $k\neq 2$, Eq. (A1) becomes

$$b_k=\frac{2}{T}\int_0^T\frac{1}{2}\left[\cos\left(\frac{(2-k)\times 2\pi t}{T}\right)-\cos\left(\frac{(2+k)\times 2\pi t}{T}\right)\right]dt, \tag{A4}$$

where we have used the trigonometric identity

$$\sin A\sin B=\tfrac{1}{2}[\cos(A-B)-\cos(A+B)], \tag{A5}$$

$$\frac{2}{T}\left[\frac{1}{2}\left(\frac{T}{2\pi(2-k)}\right)\sin\left(\frac{(2-k)2\pi t}{T}\right)-\frac{1}{2}\left(\frac{T}{2\pi(2+k)}\right)\sin\left(\frac{(2+k)2\pi t}{T}\right)\right]\Bigg|_0^T=0. \tag{A6}$$

Askenfelt, A. G., and Hammarberg, B. (**1986**). ''Speech waveform perturbation analysis: A perceptual-acoustical comparison of seven measures,'' J. Speech Hear. Res. **29**, 50–64.

Blackman, R. B., and Tukey, J. W. (**1959**). *The Measurement of Power Spectra* (General, Toronto, Ontario).

Fujimura, O. (**1968**). ''An approximation to voice aperiodicity,'' IEEE Trans. Audio Electroacoust. **AU-16**, 68–72.

Fujimura, O. (**1988**). ''A note on voice fundamental frequency (pitch) in irregular voice,'' in *Vocal Fold Physiology: Voice Production, Mechanisms and Functions*, edited by O. Fujimura (Raven, NY).

Gauffin, J., Granqvist, S., Hammarberg, B., and Hertegård, S. (**1996**). ''Irregularities in the voice: A perceptual experiment using synthetic voices with subharmonics,'' in *Vocal Fold Physiology: Controlling Complexity and Chaos*, edited by P. J. Davis and N. H. Fletcher (Singular, San Diego).

Hanson, H. M. (**1997**). ''Glottal characteristics of female speakers; Acoustic correlates,'' J. Acoust. Soc. Am. **101**, 466–481

Harris, F. J. (**1978**). ''On the use of windows for harmonic analysis with the discrete Fourier transform,'' Proc. IEEE **66**, 51–142.

Hillenbrand, J. (**1987**). ''A methodological study of perturbation and additive noise in synthetically generated voice signals,'' J. Speech Hear. Res. **30**, 448–461.

Hillenbrand, J. (**1988**). ''Perception of aperiodicities in synthetically generated voices,'' J. Acoust. Soc. Am. **83**, 2361–2371.

Holmberg, E. B., Hillman, R. E., Perkell, J. S., Guiod, P. C., and Goldman, S. L. (**1995**). ''Comparisons among aerodynamic, electroglottographic, and acoustic spectral measures of female voice,'' J. Speech Hear. Res. **38**, 1212–1223.

Klingholtz, M., and Martin, F. (**1985**). ''Quantitative spectral evaluation of shimmer and jitter,'' J. Speech Hear. Res. **28**, 169–174.

Martin, D., Fitch, J., and Wolfe, V. (**1995**). ''Pathological voice type and the acoustic prediction of severity,'' J. Speech Hear. Res. **38**, 765–771.

Michaelis, D. (**1999**). Personal communication.

Murphy, P. J. (**1999**). ''Perturbation free measurement of the harmonics-to-

noise ratio in voice signals using pitch synchronous harmonic analysis,'' J. Acoust. Soc. Am. **105**, 2866–2881.

Muta, H., Baer, T., Wagatsuma, K., Muraoka, T., and Fukuda, H. (**1988**). ''A pitch synchronous analysis of hoarseness in running speech,'' J. Acoust. Soc. Am. **84**, 1292–1301.

Qi, Y., and Hillman, R. E. (**1997**). ''Temporal and spectral estimations of harmonics-to-noise ratio in human voice signals,'' J. Acoust. Soc. Am. **102**, 537–543.

Rabiner, L., and Schafer, R. (**1978**). *Digital Processing of Speech Signals* (Prentice–Hall, Englewood Cliffs, NJ).

Rosenberg, A. E. (**1971**). ''Effect of glottal pulse shape on the quality of natural vowels,'' J. Acoust. Soc. Am. **84**, 583–588.

Svec, J. G., Schutte, H. K., and Miller, D. G. (**1996**). ''A subharmonic vibratory pattern in normal vocal folds,'' J. Speech Hear. Res. **39**, 135–143.

Titze, I. R. (**1994**). *Principles of Voice Production* (Prentice–Hall, Englewood Cliffs, NJ).

Quantitative assessment of second language learners' fluency by means of automatic speech recognition technology

Catia Cucchiarini, Helmer Strik, and Lou Boves
A²RT, Department of Language and Speech, University of Nijmegen, P.O. Box 9103, 6500HD Nijmegen, The Netherlands

(Received 15 December 1998; revised 13 July 1999; accepted 29 September 1999)

To determine whether expert fluency ratings of read speech can be predicted on the basis of automatically calculated temporal measures of speech quality, an experiment was conducted with read speech of 20 native and 60 non-native speakers of Dutch. The speech material was scored for fluency by nine experts and was then analyzed by means of an automatic speech recognizer in terms of quantitative measures such as speech rate, articulation rate, number and length of pauses, number of dysfluencies, mean length of runs, and phonation/time ratio. The results show that expert ratings of fluency in read speech are reliable (Cronbach's α varies between 0.90 and 0.96) and that these ratings can be predicted on the basis of quantitative measures: for six automatic measures the magnitude of the correlations with the fluency scores varies between 0.81 and 0.93. Rate of speech appears to be the best predictor: correlations vary between 0.90 and 0.93. Two other important determinants of reading fluency are the rate at which speakers articulate the sounds and the number of pauses they make. Apparently, rate of speech is such a good predictor of perceived fluency because it incorporates these two aspects. © *2000 Acoustical Society of America.*
[S0001-4966(00)04401-5]

PACS numbers: 43.70.Kv, 43.71.Es, 43.71.Gv, 43.71.Hw [JMH]

INTRODUCTION

The term fluency is routinely used by teachers and researchers to describe both native and non-native language performance. The fact that fluency is a frequently applied notion might suggest that there is general agreement as to its precise meaning. However, a review of relevant literature reveals that the term fluency has been used to refer to a wide range of different skills and different speech characteristics (e.g., Leeson, 1975; Fillmore, 1979; Brumfit, 1984; Lennon, 1990; Schmidt, 1992; Chambers, 1997).

In spite of this great variation, though, there is general agreement on two matters. First, although it is obvious that fluency can be used to describe written performance (Lennon, 1990), most authors restrict the use of the term to the oral modality. Furthermore, although some authors have underlined the importance of fluency-related factors in receptive processes (Leeson, 1975; Segalowitz, 1991), there seems to be a tacit agreement among teachers and researchers that fluency mainly refers to productive language performance. However, even this more restricted definition of fluency as a descriptor of oral production is amenable to different interpretations.

In considering the various possibilities, we may draw a distinction between fluency with respect to native language performance and fluency in the context of foreign language teaching and testing. In the latter case, fluency is viewed as an important criterion by which non-native performance can be judged (Riggenbach, 1991), despite the vagueness of the exact meaning of the concept. This is clear from the fact that fluency is often included in tests and evaluation schemes. With respect to native speakers' oral performance, fluency may be used to characterize the performance of a speaker, but does not really constitute an evaluation criterion. The term dysfluent, on the other hand, is often used in connection with certain speech disorders such as stuttering, where dysfluent speech is characterized by ''an abnormally high frequency and/or duration of stoppages in the forward flow of speech'' (Peters and Guitar, 1991).

In considering native speakers' oral production Fillmore (1979) identifies four different abilities that might be subsumed under the term fluency: (a) ''the ability to talk at length with few pauses,'' (b) ''the ability to talk in coherent, reasoned, and ''semantically dense'' sentences,'' (c) ''the ability to have appropriate things to say in a wide range of contexts,'' and (d) ''the ability...to be creative and imaginative in...language use.''

In foreign language teaching and testing, various definitions of fluency are also found. For instance, in communicative language teaching the emphasis has been on fluency as opposed to accuracy. According to the definition provided by Brumfit (1984, p. 57) fluency is ''the maximally effective operation of the language system so far acquired by the student.'' In this definition of fluency, native-speaker-like performance does not constitute the target to be achieved (Brumfit, 1984, p. 56). Alternatively, nativelike performance is viewed as the final goal in the more common interpretation of fluency as a synonym for oral command of a language. In everyday language use, this definition may be extended to indicate overall language proficiency (Lennon, 1990; Chambers, 1997). Finally, in a more restricted sense, the term fluency has been used to refer to one aspect of oral proficiency, in particular the temporal aspect (Nation, 1989; Lennon, 1990; Riggenbach, 1991; Schmidt, 1992; Freed, 1995; Towel *et al.*, 1996). However, even when the term fluency is used in this more limited sense, there is still uncertainty as to what exactly contributes to perceived fluency. It is this—

admittedly rather vague—temporal interpretation of fluency that will be the focus of the present paper.

In trying to define the temporal aspect of fluency, it has often been assumed that the goal in language learning consists of producing ''speech at the tempo of native speakers, unimpeded by silent pauses and hesitations, filled pauses...self-corrections, repetitions false starts and the like'' (Lennon, 1990). However, quantitative studies of pause-related phenomena have revealed that native speech is not always smooth and continuous, but exhibits a lot of hesitations and repairs (Raupach, 1983; Lennon, 1990; Riggenbach, 1991). This would seem to imply that the presence of hesitation phenomena is not sufficient to distinguish between natives and non-natives and that the difference rather lies in the frequency and distribution of these phenomena, as suggested by Möhle (1984). As a matter of fact, studies that have compared a number of quantitative fluency measures in L1 and L2 speech of the same speaker have shown that there may be considerable differences between the two speech types (Möhle, 1984; Towell *et al.*, 1996).

In an attempt to gain more insight into the temporal aspects of fluency, Lennon (1990), Riggenbach (1991), and Freed (1995) carried out studies in which samples of spontaneous speech produced by non-native speakers of English were judged by experts on fluency and were then analyzed in terms of quantitative variables such as speech rate, phonation-time ratio, mean length of runs, and number and length of pauses. The results of these studies show that fluency ratings are affected by quantitative variables such as speech rate and number of pauses. In addition, these studies also reveal that studying the relationship between fluency ratings and temporal variables in spontaneous speech may be rather complex, because in this case the fluency ratings turn out to be affected by nontemporal properties of speech utterances, such as grammar, vocabulary, and accent (Lennon, 1990; Riggenbach, 1991; Freed, 1995).

The aim of the research reported in this paper is to determine whether expert fluency ratings of read speech can be predicted on the basis of temporal measures of speech quality. The decision to limit this investigation to read speech is related to the methodological complexities involved in studying fluency in spontaneous speech. If the present approach appears to be feasible, it will be applied to spontaneous speech too. Identifying quantitative correlates of perceived fluency is important with a view to developing objective testing instruments for fluency assessment. An important characteristic of the present investigation is that the quantitative variables are calculated automatically. In turn this suggests that if the objective measures used in this study appear to be able to predict perceived fluency, this approach may have potential for the development of automatic tests of fluency in read speech.

The goal of this study will be pursued by relating expert fluency ratings of speech read by native and non-native speakers of Dutch with a set of quantitative measures of speech quality that are supposed to be related to perceived fluency. In this way it can be determined to what extent expert judgments of fluency can be predicted on the basis of automatically obtained temporal measures of speech quality. In other words, the expert fluency ratings will constitute the reference for the evaluation of the automatic fluency measures. Of course, this will be possible only if the expert ratings exhibit acceptable levels of reliability. To this end, we will ask different groups of raters to evaluate the same material on fluency. Moreover, each rater will be asked to score part of the material twice so that it will possible to establish reliability.

In addition, these analyses will make it possible to determine the contribution of the various quantitative variables to perceived fluency. In turn this will shed some light on the determinants of fluency in read speech.

Furthermore, since the data gathered in this investigation concern both natives and non-natives, this will offer the possibility of determining whether native and non-native speakers differ on the fluency ratings and on the temporal variables. It is clear that distinguishing between these two groups is not the aim of a fluency test, which, instead, should distinguish between fluent and nonfluent speakers. However, for the development of a test of this kind, data on native performance are necessary to establish benchmarks. Moreover, given that fluency is often equated with nativelike performance (see above), it is interesting to determine whether the two groups of natives and non-natives significantly differ from each other on the variables under study.

I. METHOD

A. Speakers

The speakers involved in this experiment are 60 non-native speakers (NNS) and 20 native speakers of Dutch (NS). The 60 NNS all lived in The Netherlands and were attending or had attended courses in Dutch as a second language. They were selected to obtain a group that was sufficiently varied with respect to mother tongue, proficiency level, and gender.

Table I shows how the 60 non-native speakers were distributed according to these three variables. Some comment about this table is in order. First, the speakers in the ''beginner'' category had been attending the course for some months. This was thought to be necessary for the learners to be able to read the sentences. Second, it is clear from this table that the speakers were not evenly distributed over the categories. This has to do with the availability of the speakers. Even if it were possible to find the same number of speakers for each category, then they have to be prepared and have to find the time to carry out the task. So, eventually, there were more women and more speakers of the intermediate and advanced levels. Furthermore, the number of speakers differed for the various mother tongue groups. It is clear, though, that for the purpose of the present experiment, complete symmetry in the sample is not really required.

Four of the NS subjects, two men and two women, were speakers of the Standard variety of Dutch (SDS: Standard Dutch Speakers), while the other 16 NS, speaking an accented variety of Dutch, were selected to obtain a heterogeneous group with respect to region of origin and gender. The rationale behind including the four SDS is that the presence of clear ''anchor stimuli'' has been shown to be an important help in keeping the reference standard stable (Flege and

TABLE I. Distribution of the 60 non-native speakers according to the selection variables mother tongue, proficiency level, and gender.

	Beginner		Intermediate		Advanced		
	Female	Male	Female	Male	Female	Male	Total
Arabic	1		1	2	1	1	6
Turkish	1			1	1		3
Chinese/Japanese		1	1	1			3
Spanish/Italian/Portuguese	1		3	1	5	2	12
Russian/Polish/Serbo Cr.	1		3	1	5	2	12
English	2		1	1		2	6
German	1		3	2	2	1	9
French		1	2	1	1		5
Swedish/Danish/Norwegian	1		3				4
Total	8	2	17	10	15	8	60

Fletcher, 1994). However, we do not expect the SDS and the NS to be different with respect to fluency, so in the analyses they will be treated as one group of native speakers.

B. Speech material

Each speaker read two different sets of five phonetically rich sentences designated group 1 and group 2 (see Appendix). In preparing the sentences, the following criteria were adopted:

(i) the sentences should be meaningful and should not sound strange;
(ii) the sentences should not contain unusual words which NNS are unlikely to be familiar with, foreign words or names, or long compound words which are particularly difficult to pronounce;
(iii) the content of the sentences should be as neutral as possible. For instance, the sentences should not contain statements concerning characteristics of particular countries or nationalities;
(iv) each set of five sentences should contain all phonemes of Dutch at least once.

The average duration of each set is 30 s. With two sets this amounts to 1 min of speech per speaker. All speakers read the same sentences over the telephone. The sentences to be read were printed on paper together with the instructions. Consequently, the subjects had the possibility of rehearsing before reading the sentences over the telephone. They had not explicitly been encouraged to do so, but since they had received the material beforehand, they had the chance to rehearse. Moreover, they had the possibility of starting the recording session all over again if they felt something had gone wrong. However, this happened only in one case.

As the recording system was connected to an ISDN line, the input signals consist of 8-kHz 8-bit *A*-law coded samples. The subjects were allowed to call from their homes, from telephone booths, or from the first author's office. Two subjects resorted to the latter possibility, while all the others called from their homes. Since the recordings did not take place in sound-treated booths, the recording conditions were different from those in a studio.

All speech material was checked and orthographically transcribed before being used for the experiment. Although with read speech the content of the sentences should be known beforehand, one cannot be sure that the speaker will read exactly what is on paper. Furthermore, speakers may repeat part of the words or sentences, and make restarts and repairs.

In transcribing the material, special symbols were used for four categories of nonspeech acoustic events,

(a) filled pauses: uh, er, mm, etc.
(b) speaker noise: lip smack, throat clear, tongue click, etc.
(c) intermittent noise: noise that occurs incidentally during the call such as door slam and paper rustle.
(d) stationary noise: continuous background noise that has a rather stable amplitude spectrum such as road noise or channel noise.

Repetitions, restarts, and repairs were transcribed exactly as they were pronounced. The transcriptions were carried out at SPEX (SPEX), a university expertise center that specializes in database construction and validation.

C. Raters

Since in this experiment a specific aspect of speech production had to be evaluated, raters with a high level of expertise were required. Different categories of raters seemed to qualify as experts: phoneticians, because they are expert on pronunciation in general; teachers of Dutch as a second language (L2) for obvious reasons. However, it turned out that, in practice, pronunciation problems (including all fluency-related temporal phenomena) of people learning Dutch as L2 are usually not addressed by language teachers, but by specially trained speech therapists. Since it is possible that the ratings vary with the background of experts, a group of three phoneticians and a group of three speech therapists, expert on pronunciation problems of Dutch L2 learners, were selected for this investigation.

Furthermore, since previous studies had revealed that the reliability of expert fluency ratings was rather low (Lennon, 1990; Riggenbach, 1991; Freed, 1995), we decided to add a third group of experts to get more information on the degree of reliability that can be attained. It turned out that finding speech therapists for this task was easier than finding phoneticians, so the third group of experts consisted of three

TABLE II. Distribution of the speech material among the three raters in each group. The cells in italics contain the material used for determining inter-rater reliability, while the material in bold was used for intrarater reliability calculation.

		Material for comparison man–machine				Added material for reliability analyses					
					Total 1			Total 2	Duplications for intrarater reliability		Grand total sum 1 and 2
Rater 1	group 1	20 NNS1	6 NS1	*4 SDS*	30	*13 NNSA1*	*5 NSA1*	18	**5NNSD11**	**1NSD11**	48
	group 2	20 NNS1	6 NS1	*4 SDS*	30	*14 NNSA2*	*4 NSA2*	18	**4NNSD12**	**2NSD12**	48
Rater 2	group 1	20 NNS2	6 NS2	*4 SDS*	30	*13 NNSA1*	*5 NSA1*	18	**5NNSD21**	**1NSD21**	48
	group 2	20 NNS2	6 NS2	*4 SDS*	30	*14 NNSA2*	*4 NSA2*	18	**4NNSD22**	**2NSD22**	48
Rater 3	group 1	20 NNS3	6 NS3	*4 SDC*	30	*13 NNSA1*	*5 NSA1*	18	**5NNSD22**	**1NSD31**	48
	group 2	20 NNS3	6 NS3	*4 SDC*	30	*14 NNSA2*	*4 NSA2*	18	**4NNSD32**	**2NSD32**	48
		132(44×3) sets for inter-rater reliability analyses							**36(12×3) sets for inter-rater reliability**		

other speech therapists who are expert on pronunciation problems of Dutch L2 learners.

D. Expert fluency ratings

The speech material was transferred from disc on a DAT tape adopting different orders for the different raters, as will be described below. All raters listened to the speech material and evaluated it individually. This was done to enhance flexibility (each rater could thus carry out the task at the most suitable time) and to avoid raters influencing each other.

Each rater received two tapes which contained the group 1 and the group 2 sentences, respectively. The material was scored on a scale ranging from 1 to 10. The scores were not assigned to each individual sentence, but to each set of five phonetically rich sentences. No specific instructions were given as to how to assess fluency. However, before starting with the evaluation proper, each rater listened to five sets of sentences spoken by five different speakers, which were intended to familiarize the raters with the task they had to carry out and to help them anchor their ratings. As a matter of fact, the five speakers were chosen so as to give an indication of the range that the raters could possibly expect.

Since it was not possible to have all raters score all speakers (it would cost too much time and it would be too tiring for the raters), the 80 speakers were proportionally assigned to the three raters in each group. Each rater was assigned 20 NNS, 6 NS with regional accents (since there were only 16 of these speakers, 2 of them were scored by two raters instead of by only one) and all 4 speakers of the standard variety. For each speaker, two sets of sentences (group 1 and group 2) had to be evaluated, which makes 60 sets of five sentences for each listener. Furthermore, 36 sentence sets were added to allow calculation of intrarater reliability and inter-rater reliability.

In assigning speakers to raters, we took the selection variables into account to avoid overloading raters with speakers of one gender, L1, or level of proficiency. The way in which the speakers were divided over the various raters is illustrated in Table II. Each rater scored the same 20 NNS, the same 6 NS and all 4 SDS twice, once for the group 1 sentences and once for the group 2 sentences, so that 30 scores per rater per sentence group were obtained. The speakers were presented in different random orders in the two sentence groups, to minimize possible ordering effects on the scores. However, the four SDS were presented at regular intervals, so that the raters would be reminded of how the sentence was supposed to sound in the standard language, as was explained above (see also Flege and Fletcher, 1994). In Table II the distribution of the speakers is clarified by distinguishing three groups of 20 NNS (one for each rater) i.e., 20 NNS1, 20 NNS2, 20 NNS3, and three groups of 6 NS, 6 NS1, 6 NS2, and 6 NS3. Since the four SDS were scored by all three raters in a group, both for the group 1 and the group 2 sentences, the same label 4 SDS is used in Table II for all three raters. The scores assigned by the raters to this part of the material were subsequently compared with the automatic measures calculated for the same material. For this reason this material will be referred to as the man–machine comparison material.

The 36 sentence sets that were added for calculating inter-rater and intrarater reliability were selected so as to have a balanced set of NNS and NS and of group 1 and group 2 sentences. The sentence sets produced by the four SDS were also included in the inter-rater reliability analyses, because they had been scored by all three raters in a group. Consequently, we did not need to add extra SDS sentence sets. Eventually, we selected 27 NNS sets and 9 NS sets and 18 group 1 sets and 18 group 2 sets, as is clear from Table II, under added material. The 13 NNS and the 5 NS sets selected for group 1 and the 14 NNS and the 4 NS sets selected for group 2 were the same for all raters, so the labels 13 NNSA(dded) 1(group 1), 5 NSA1, 14 NNSA2, and 4 NSA2 are used in Table II for all raters.

The number of sentence sets that were eventually used for inter-rater reliability analyses amounts to 44 (36 extra plus the 4 SDS for group 1 and the 4 SDS for group 2, indicated in italic in Table II) per rater, i.e., 132 for all three raters, as appears from the italic cell in the bottom row of Table II.

For the intrarater reliability analyses, on the other hand, 12 sentence sets that were present both in the man–machine comparison material and in the inter-rater reliability material were chosen for each rater. The 12 sets to be scored twice by each rater were selected so as to have nine NNS and three NS and six group 1 sets and six group 2 sets, as appears from the bold cells in Table II, under duplicated materials. Given

that the five NNS and one NS in group 1 and the four NNS and the two NS in group 2 differed for the three raters, different lables are used, i.e., 5 NNSD (uplicated) 1(rater 1)1(group 1), 1 NSD11, 4 NNSD12, 2 NSD12, 5 NNSD21, 1 NSD21, 4 NNSD22, 2 NSD22, 5 NNSD31, 1 NSD31, 4 NNSD32, 2 NSD32.

To summarize, each rater had to evaluate 30+18 sets of sentences (the 6 sets for intrarater reliability were a subset of these 48 sets) of group 1 and 30+18 sets of sentences of group 2. These numbers are indicated in the Total 1 and Total 2 columns in Table II, as well as the grand total for each rater for each group, 48. Since this amount of material was too much for one rating session, it was divided over two sessions. Therefore, two tapes were prepared, one containing 48 sets of sentences of group 1 and the other containing 48 sets of sentences of group 2. The duration of each of the tapes was about 30 min. The first tape contained the five training sets mentioned above. After having rated tape 1, the raters had to pause for a while before starting with tape 2.

The scores assigned to the two sets of sentences by each speaker were subsequently averaged to obtain one score for each speaker. The scores assigned by the three raters were then combined to compute correlations with the machine scores. This way 80 human-assigned fluency scores were obtained, which were subsequently compared with the various quantitative measures.

E. Automatic assessment of fluency

1. The automatic speech recognizer

To calculate the quantitative measures, the continuous speech recognizer (CSR) described in Strik *et al.* (1997) was used. Feature extraction is done every 10 ms for frames with a width of 16 ms. The first step in feature analysis is a fast Fourier transform (FFT) to calculate the spectrum. The energy in 14 mel-scaled filter bands between 350 and 3400 Hz is then calculated. Next, a discrete cosine transformation is applied to the log filterband coefficients. The final processing stage is a running cepstral mean subtraction. Besides 14 cepstral coefficients (c0–c13), 14 delta coefficients are also used. This makes a total of 28 feature coefficients.

The continuous speech recognizer (CSR) uses acoustic models (39 Hidden Markov Models, HMMs), language models (unigram and bigram), and a lexicon. The lexicon contains orthographic and phonemic transcriptions of the words to be recognized. The continuous density HMMs consist of three parts of two identical states, one of which can be skipped. One HMM was trained for nonspeech sounds and one for silence. For each of the phonemes /l/ and /r/ two models were trained, a distinction was made between prevocalic (/l/ and /r/) and postvocalic position (/L/ and /R/). For each of the other 33 phonemes one HMM was trained.

The HMMs were trained by using part of the Polyphone corpus (den Os *et al.*, 1995). This corpus is recorded over the telephone and consists of read and (semi-) spontaneous speech of 5000 subjects with varying regional accents. For each speaker 50 items are available. Five of these 50 items are the so-called phonetically rich sentences, which contain all phonemes of Dutch at least once. Each speaker read a different set of sentences. In this experiment the phonetically rich sentences of 4019 speakers were used for training the CSR.

The trained CSR was subsequently used to analyze the utterances read by the 80 speakers. For each utterance a Viterbi alignment between the speech signal and the orthographic transcription was obtained. This Viterbi alignment is also a segmentation at the phone level and contains information about the boundaries of phones. Consequently, the segmentation contains information about the position of speech and nonspeech parts (pauses, dysfluencies, etc.). The accuracy of forced alignment was checked only for a small sample of the material. In general the segmentation appeared to be correct, although the boundaries were not always placed where a human listener would probably have placed them. This aspect, however, is not really crucial for the present article, because here we do not use the information about the position of the phone boundaries in the speech parts, but we are concerned with the automatic calculation of the phonemes present in an utterance. This calculation was determined on the basis of the transcriptions, i.e., it is the number of units actually produced and not the number of units the speakers were supposed to realize on the basis of the text they had to read. The resulting segmentation was used to calculate a number of quantitative measures that are described in detail below.

2. Quantitative measures of fluency

Previous studies of temporal phenomena in native and non-native speech have identified a number of quantitative variables that appear to be related to perceived fluency. In this context the term ''temporal'' does not refer exclusively to timing-related variables such as speaking rate, utterance duration, and pausing, but it also covers hesitation phenomena such as filled pauses, repetitions, and restarts (Grosjean, 1980).

Early studies of temporal phenomena were aimed at gaining more insight into psycholinguistic processes in one language (Goldman-Eisler, 1968). Subsequently, the analysis of temporal phenomena was applied in cross-linguistic investigations (Grosjean and Deschamps, 1975; Grosjean, 1980) and in studies of second language acquisition (Dechert and Raupach, 1980a, 1980b; Möhle, 1984). Recently, temporal variables have been employed in studies on perceived fluency and fluency development such as Nation (1989), Lennon (1990), Riggenbach (1991), Freed (1995), Towell *et al.* (1996).

On the basis of the literature on temporal variables in L2 acquisition and perceived fluency, the following measures were selected for investigation:

(a) *ros* = rate of speech = # phonemes/total duration of speech including sentence-internal pauses
(b) *ptr* = phonation/time ratio = 100% × total duration of speech without pauses/total duration of speech including sentence-internal pauses
(c) *art* = articulation rate = # phonemes/total duration of speech without pauses

TABLE III. Intrarater and inter-rater reliability coefficients (Cronbach's α) for the three rater groups.

	Intrarater reliability			Inter-rater reliability	
	Rater 1	Rater 2	Rater 3	NNS & NS	NNS
Phoneticians	0.97	0.94	0.95	0.96	0.96
Speech therapists 1	0.94	0.97	0.96	0.93	0.88
Speech therapists 2	0.90	0.76	0.91	0.90	0.83

(d) *#p* = # of silent pauses = # of sentence-internal pauses of no less than 0.2 s
(e) *tdp* = total duration of pauses = total duration of all sentence-internal pauses of no less than 0.2 s
(f) *mlp* = mean length of pauses = mean length of all sentence-internal pauses of no less than 0.2 s
(g) *mlr* = mean length of runs = average number of phonemes occurring between unfilled pauses of no less than 0.2 s
(h) *#fp* = # filled pauses = # of uh, er, mm, etc.
(i) *#dy* = # dysfluencies = # of repetitions, restarts, repairs

The first seven variables *(ros, ptr, art, tdp, #p, mlp, mlr)* correspond to the Primary Variables in Grosjean's (1980) taxonomy, i.e., ''variables that are always present in language output.'' The only differences are that we use phonemes as units instead of syllables and that we distinguish between number, total length, and mean length of silent pauses (see also Towell *et al.*, 1996). The latter two variables ($\#fp$ and $\#dy$) pertain to Grosjean's (1980) Secondary Variables, i.e., variables that are not necessarily present in speech. In addition, these variables seem to be infrequent in read speech (Grosjean, 1980), which would suggest that they are not good indicators of fluency in read speech. However, since it is not known how often they occur in read speech of non-natives, they are included in the present investigation.

In previous investigations, these variables were calculated manually (Möhle, 1984; Nation, 1989; Lennon, 1990; Riggenbach, 1991; Freed, 1995; Towell *et al.*, 1996), while in the present study the measures were calculated automatically by means of an automatic speech recognizer, as was explained in the previous section.

The various fluency scores for the individual sentences were subsequently averaged over the five sentences in each set and then over the two sets of each speaker. This way a set of 80 (60 NNS+20 NS) scores was obtained for each measure, which were then compared with the human-assigned fluency scores.

II. RESULTS

In presenting the results of the present experiment, we will first pay attention to the expert fluency ratings. In particular, we will consider the issues of intrarater and inter-rater reliability. Subsequently, the relationship between the expert fluency ratings and the quantitative measures will be addressed. Finally, the differences between native and non-native speakers, both on the fluency ratings and on the quantitative measures, will be examined.

A. Reliability of expert fluency ratings

The fluency ratings assigned by the three groups of experts were first analyzed to determine intrarater and inter-rater reliability. Intrarater reliability was calculated on the basis of 12×2 scores for each rater, while the computation of inter-rater reliability was based on 44×3 scores for each group of raters (44 sentence sets that were scored by all three raters in each group). The results of these analyses are shown in Table III.

As appears from Table III, intrarater reliability is very high for all raters, with the exception of rater 2 in the second group of speech therapists, who reaches only 0.76. Inter-rater reliability appears to be very high for all three groups. Since native speakers consistently receive higher scores than the non-native speakers, their presence has the effect of increasing the correlation between the scores assigned by the three raters. For this reason, reliability was computed for two different conditions: (1) NS & NNS (both groups of speakers), (2) NNS (only foreign speakers). As is clear from Table III, even in the least favorable condition (NNS), the reliability coefficients are still rather high.

Besides considering inter-rater reliability, we also checked the degree of inter-rater agreement. Closer inspection of the data revealed that the means and standard deviations varied between the raters in a group, but also between the raters in different groups who rated the same speech material (see Table IV).

A low degree of agreement within a group of raters has obvious consequences for the correlation coefficient computed between the combined scores of the raters and another set of data (i.e., the ratings by another group or the machine scores). This is so, because straightforward combination of the scores would amount to pooling measurements made with different yardsticks. When such a heterogeneous set of measurements is submitted to a correlation analysis with homogeneous measures, the ''jumps'' at the splicing joints lower the correlation. The same is true when several groups are compared: differences in correlation may be observed, which are a direct consequence of differences in the degree of agreement between the ratings.

Therefore, we decided to normalize for the differences in the values by using standard scores instead of raw scores. For this normalization we used the means and standard deviations of each rater in the overlap material, because in this case all raters scored the same samples. For individual raters, these values hardly differed from the means and standard deviations for the total material, as is clear from Table IV.

The effect of normalizing the data is evident from Table V, which shows the correlation coefficients between the

TABLE IV. Means and standard deviations for the three raters in each group for the overlap material (the sentence sets used for determining inter-rater reliability) and for all the material scored by each rater.

		Rater 1		Rater 2		Rater 3	
		$\bar{x}$	sd	$\bar{x}$	sd	$\bar{x}$	sd
Phoneticians	overlap material	5.41	2.91	6.09	2.39	6.18	3.06
	all material	5.36	2.69	5.95	2.13	5.99	2.86
Speech therapists 1	overlap material	7.16	2.50	6.84	3.26	7.80	2.47
	all material	7.06	2.37	7.08	3.00	7.61	2.42
Speech therapists 2	overlap material	7.36	2.90	5.75	1.89	6.98	2.72
	all material	7.42	2.98	5.57	1.73	6.91	2.61

groups of raters before and after normalization. Since it is known that measurement errors affect the magnitude of the correlation coefficient, the correction for attenuation was applied (Ferguson, 1987), to allow direct comparisons between the various coefficients.

These correlations are so high that we can conclude that all nine raters involved in this experiment adopt similar definitions of fluency. Given the advantages of normalization, standard scores will be used also in the rest of the analyses in this study.

B. Quantitative measures as indicators of perceived fluency

Before turning to the correlations among the fluency ratings and the temporal measures, we will first present the means and standard deviations of the nine temporal measures and the correlations among them.

The data in Table VI confirm that filled pauses and dysfluencies are indeed very infrequent in this type of speech. For this reason they will not be involved in the rest of the analyses presented in this paper. The mean value for articulation rate appears to be below the average of 15 phonemes per second indicated by Levelt (1989, p. 22) as average in normal speech. This is not surprising if we consider that these data refer to natives and non-natives and that articulation rate should be lower in non-natives (Towell *et al.*, 1996). Furthermore, since these data pertain to read speech, articulation rate should be lower than the average 15 phonemes per second also for native speakers. This point will be addressed in more detail in Sec. II C.

The correlations among the remaining seven quantitative variables are shown in Table VII. It is clear that all seven variables are relatively highly correlated with each other, but there are differences. For example, *ros*, *ptr*, *#p*, *tdp*, and *mlr* are highly correlated with each other (>0.86). *art*, on the other hand, is highly correlated only with *ros*, while its correlations with the other variables are moderate (between 0.61 and 0.75). A clear exception is *mlp*, which shows moderate correlations with all other variables.

To establish which of the quantitative variables analyzed can be successfully used as a predictor of fluency in read speech, the correlations among the quantitative variables and the fluency ratings assigned by the experts were calculated. For the same reason as explained in Sec. III A, these correlations were calculated both for the whole group of speakers (natives and non-natives) and for the non-natives only. The results of these analyses, corrected for attenuation, are shown in Table VIII.

From Table VIII it appears that all quantitative variables are strongly correlated with the fluency ratings, with the exception of *mlp*. For all three groups of raters, the highest correlation is found for *ros*. Moreover, it appears that the correlations for the non-natives are of the same order of magnitude as those for the whole group of speakers.

To determine whether a combination of variables allows us to make better predictions, we submitted these data to a multiple regression analysis in which the temporal variables are used as the predictors and the fluency ratings as the criterion. From Table V it appears that the fluency scores assigned by the three groups of raters are highly correlated with each other. For this reason we decided to use the mean scores in the regression analysis. The results of this analysis show that the variable that explains the greatest amount of variance is *ros*: *R* is 0.93. The second variable that is added in the stepwise procedure is *#p*. However, the increase in explained variance is marginal: Multiple *R* rises to 0.94.

C. Differences between natives and non-natives

In this section we analyze both the fluency ratings and the seven quantitative measures to determine whether the two groups of natives and non-natives significantly differ on these variables. To this end, the two sets of data were submitted to a *t*-test for comparison of means. The results of these analyses are shown in Table IX. From this table it appears that the native speakers involved in this study were systematically found to be significantly more fluent than the non-natives. It is clear that not only the mean scores differ considerably between the two speaker groups, but also the standard deviations, thus indicating that the group of NS is more homogeneous in this respect than the group of NNS. In addition, Table IX reveals that also for the native speakers in

TABLE V. Correlations among the groups of raters before and after normalization.

	Raw scores	Standard scores
Phoneticians-speech therapists 1	0.92	0.94
Phoneticians-speech therapists 2	0.82	0.90
Speech therapists 1-speech therapists 2	0.83	0.90

TABLE VI. Means and standard deviations for the nine quantitative variables.

	Rate of speech	Phonation/ time ratio	Articulation rate	Number of pauses	Tot. duration of pauses	Mean length of pauses	Mean length of runs	Number of filled pauses	Number of dysfluencies
$\bar{x}$	10.44	85.29	12.12	5.76	2.43	0.33	24.71	0.11	0.49
sd	2.24	8.81	1.59	5.39	2.66	0.15	9.83	0.31	0.70

this experiment, articulation rate is indeed lower than the 15 phonemes per second indicated by Levelt (1989, p. 22) as average in normal speech.

Furthermore, Table IX shows that the native and the non-native speakers of Dutch in this study significantly differ from each other on all quantitative variables investigated. In other words, native speakers do appear to speak faster and to pause less than non-native speakers.

III. DISCUSSION

In this paper we have presented the results of a study on perceived fluency in which a dual approach was adopted: fluency ratings assigned by experts to read speech produced by natives and non-natives were compared with a number of quantitative measures that were automatically calculated for the same speech fragments. Reading material was purposely chosen in this study because it offers the possibility of reducing the impact of some linguistic factors known to affect fluency ratings (Riggenbach, 1991; Freed, 1995), while concentrating on the temporal variables as much as possible. A possible disadvantage of this choice is that it is not known whether the various degrees of fluency, or lack thereof, should be attributed to speech problems or to reading problems. However, if we consider that reading is often used in examinations in second or foreign language acquisition as a way of assessing fluency, then we may conclude that using read speech is less far-fetched than one might think at first.

The results of this study show that it is possible to obtain reliable ratings of fluency: reliability was high for all three groups of experts (Cronbach's α varied between 0.90 and 0.96). On the one hand, this may be surprising if we consider that the raters involved in this experiment were given no specific instructions for assessing fluency and that in previous studies low degrees of reliability were obtained (Riggenbach, 1991; Freed, 1995). On the other hand, we had deliberately chosen read speech material so that the raters would be less distracted by other factors than those under study, as explained above. In read speech, grammar and vocabulary can be kept constant. However, accent can still vary and can possibly affect the fluency ratings. In spite of this the raters achieved high reliability.

The major goal of this investigation was to determine whether automatically obtained quantitative measures of fluency can be used to predict expert fluency ratings. The results presented above show that automatic scoring of fluency in read speech is possible. As a matter of fact, six automatic measures showed correlations with the fluency scores which varied in magnitude between 0.81 and 0.93. *ros* appears to be the best predictor of perceived fluency (correlations vary between 0.90 and 0.93). According to the results of the regression analysis, the inclusion of other variables in the regression equation does not add much to the amount of explained variance, which is not surprising given that all variables are strongly correlated with each other (see Table VII) and that the correlations among *ros* and the fluency ratings are already so high. Moreover, it should be noted that the magnitude of the correlations among the fluency ratings and the temporal measures very much resembles those between the fluency ratings of the experts, which varied between .90 and 0.94 and which constitute a sort of upper bound for the man–machine correlations.

With respect to the contribution of the different variables to perceived fluency, Table VIII reveals that the fluency ratings are strongly affected by *ros*, *art*, *ptr*, *#p*, *tdp*, and *mlr*, while *mlp* has a smaller effect. This suggests that for perceived fluency the frequency of pauses is more relevant than their length. In other words, the difference between fluent and nonfluent speakers lies in the number of the pauses they make, rather than in their length, and the longer *tdp* of nonfluent speakers is caused by a greater number of pauses rather than by longer pauses. These findings are in line with those of previous investigations (see Chambers, 1997) and are corroborated by the analyses of the differences between natives and non-natives: Table IX shows that the

TABLE VII. Correlations among seven quantitative variables.

	Phonation/time ratio	Articulation rate	Number of pauses	Tot. duration of pauses	Mean length of pauses	Mean length of runs
Rate of speech	0.91	0.96	−0.87	−0.86	−0.71	0.88
Phonation/time ratio		0.75	−0.97	−0.96	−0.73	0.94
Articulation rate			−0.72	−0.71	−0.61	0.74
Number of pauses				0.97	0.63	−0.91
Tot. duration of pauses					0.67	−0.86
Mean length of pauses						−0.76

TABLE VIII. Correlations among the fluency ratings by the three rater groups and the quantitative measures, for the whole group ($n=80$) and for the non-natives only ($n=60$).

	Phoneticians		Speech therapists 1		Speech therapists 2	
	NNS & NS	NNS	NNS & NS	NNS	NNS & NS	NNS
Rate of speech	0.93	0.88	0.91	0.93	0.90	0.91
Phonation/time ratio	0.86	0.80	0.89	0.86	0.89	0.89
Articulation rate	0.88	0.82	0.85	0.86	0.81	0.79
Number of pauses	−0.84	−0.82	−0.89	−0.89	−0.89	−0.90
Tot. duration of pauses	−0.81	−0.79	−0.86	−0.86	−0.86	−0.87
Mean length of pauses	−0.66	−0.50	−0.62	−0.52	−0.65	−0.55
Mean length of runs	0.85	0.81	0.86	0.84	0.88	0.89

differences between natives and non-natives with respect to *mlp* are significant; however, these differences are relatively smaller than those concerning *#p* and *tdp*.

So, these results suggest that two important factors for perceived fluency in read speech are the rate at which speakers articulate the sounds and the number of pauses they make. *ros* appears to be such a good predictor of perceived fluency because it is a complex variable that incorporates the two aspects of articulation rate (number of segments) and pause time (*tdp*) (Chambers, 1997). *tdp* is of course dependent on the number of pauses, but the same *tdp* may be caused by a few long pauses or by many short pauses. In *ros*, this difference cannot be seen. In other words, although *ros* appears to be a very good predictor of reading fluency, it is possible that for certain purposes, for instance diagnostic ones, one may want to know how a specific score was obtained. In this case, adding the variable *#p* may be informative.

A possible limitation of these results is that they only indicate a strong relationship between objective measures of temporal speech characteristics on the one hand and expert fluency ratings on the other, but they do not provide information as to how varying articulation rate and/or pause time would affect the fluency ratings. In other words, we are not in a position to make strong claims about the causal relationships obtaining between the objective measures and the fluency ratings. One way of investigating this would be by compressing and expanding the speech under study, although this is not as simple as it might seem. Another possibility would be to use speech where a different relationship between articulation rate and pause time obtains, such as spontaneous speech. Since we are now working to extend the automatic approach to spontaneous speech, in the near future we will probably be able to address the issue of the causal relationship on the basis of spontaneous speech measurements. In any case, it is clear that this is a rather complex issue that deserves a series of studies on its own (see also, Butcher, 1981).

The results of this study indicate that automatically calculated temporal measures of speech could be used to develop objective tests of fluency, at least in read speech. In this sense this study is an answer to Lennon's call for more research along the lines of his own study, ''but with larger sample groups'' (Lennon, 1990), for ''comparisons between learner and native-speaker performance'' (Lennon, 1990), for ''machine analysis of spoken text which...might be particularly useful when expert judges are not available to make an assessment'' (Lennon, 1990) and ''to develop standardized techniques for fluency assessment that would be independent of variation between individual raters'' (Lennon, 1990). With respect to testing, however, it should be pointed out that in this study we were primarily exploring the possibilities of this approach and were not actually constructing a fluency test. This might explain why, for example, our focus was on reliability and less on agreement. In some cases agreement turned out not to be very high and we decided to use standard scores to combine the scores of the three raters in each group. The degree of agreement does play a crucial role in constructing a fluency test, because it contributes to establishing the cutoff point. However, since we are still in the development stage, agreement was less important in the present experiment, while reliability was our main concern.

TABLE IX. Results of *t*-tests for the fluency ratings of the three rater groups and for seven quantitative variables.

			t-test				
	$\bar{x}$ NS	sd NS	$\bar{x}NNS$	sd NNS	*t*-value	df	*p*
Phoneticians	0.88	0.39	−0.32	0.70	9.55	59.98	0.000
Speech therapists 1	0.91	0.13	−0.27	0.79	11.07	67.55	0.000
Speech therapists 2	0.86	0.33	−0.30	0.83	8.90	75.77	0.000
Rate of speech	12.74	1.35	9.68	1.94	6.54	78	0.000
Phonation/time ratio	93.17	2.79	82.66	8.57	8.27	78	0.000
Articulation rate	13.65	1.19	11.61	1.37	5.97	78	0.000
Number of pauses	1.42	1.23	7.20	5.47	−7.62	73	0.000
Tot. duration of pauses	0.45	0.42	3.10	2.76	−7.18	66.68	0.000
Mean length of pauses	0.20	0.13	0.38	0.13	−5.24	78	0.000
Mean length of runs	34.26	5.85	21.52	8.77	7.36	49.2	0.000

The potential of this approach for automatic fluency assessment is all the more important if we consider that these results pertain to telephone speech. Consequently, the resulting acoustic registrations differ in many ways from those made in a studio or a (usually quiet) office environment. Here we will mention only the most relevant ones.

First of all, in telephone speech only the bandwidth of 300–3400 Hz is used. Second, not just one high-quality microphone was used, but many different telephone microphones. Finally, and probably most important, relatively high-level acoustic background signals are frequently present, which is usually not the case with laboratory speech. We do consider these conditions as ''normal and realistic'' in the sense that later on, when this technology will be used in applications over the telephone, conditions will most probably be similar. However, it should be underlined that these conditions make automatic speech recognition more difficult.

The data collected in this study were also analyzed to determine whether the two groups of native and non-native speakers significantly differ on perceived fluency and on seven quantitative measures of fluency. The results reveal significant differences between the two groups on all variables. As mentioned above, these results indicate that natives and non-natives are more different from each other with respect to pause frequency than to pause length. Furthermore, these findings are interesting in the light of the discussion on the effectiveness of temporal variables in distinguishing between native and non-native speakers. Although it is true that not all native speakers are completely fluent (Riggenbach, 1991), these results show that, on average, they are more fluent, produce fewer pauses, and articulate faster than non-native speakers.

IV. CONCLUSIONS

On the basis of the results of the present investigation we can draw the following conclusions. First, expert listeners are able to evaluate fluency with a high degree of reliability. Second, expert fluency ratings of read speech are mainly influenced by two factors: speed of articulation and frequency of pauses. Third, expert fluency ratings can be accurately predicted on the basis of automatically calculated measures such as rate of speech, articulation rate, phonation–time ratio, number and total duration of pauses, and mean length of runs. Of all these measures, rate of speech appears to be the best one. Fourth, native speakers are more fluent than non-natives and the temporal measures are significantly different for the two groups.

To conclude, these findings indicate that temporal measures of fluency may be employed to develop objective testing instruments of fluency in read speech. In turn, the fact that these measures can be automatically calculated by means of automatic speech recognition techniques suggests that this approach may contribute to developing automatic tests of fluency, at least for read speech. If we then consider that these results were obtained with telephone speech, then it seems that this approach is likely to have important consequences for the future of fluency assessment.

ACKNOWLEDGMENTS

This research was supported by SENTER (an agency of the Dutch Ministry of Economic Affairs), the Dutch National Institute for Educational Measurement (CITO), Swets Test Services of Swets and Zeitlinger, and KPN. The research of Dr. H. Strik has been made possible by a fellowship of the Royal Netherlands Academy of Arts and Sciences. The authors would like to thank Tim Bunnell and an anonymous reviewer for their valuable comments and suggestions.

APPENDIX

Group 1 sentences

(1) Vitrage is heel ouderwets en past niet bij een modern interieur.
(2) De Nederlandse gulden is al lang even hard als de Duitse mark.
(3) Een bekertje warme chocolademelk moet je wel lusten.
(4) Door jouw gezeur zijn we nu al meer dan een uur te laat voor die afspraak.
(5) Met een flinke garage erbij moet je genoeg opbergruimte hebben.

Group 2 sentences

(1) Een foutje van de stuurman heeft het schip doen kapseizen.
(2) Gelokt door een stukje kaas liep het muisje keurig in de val.
(3) Het ziet er naar uit dat het deze week bij ons opnieuw gaat regenen.
(4) Na die grote lekkage was het dure behang aan vervanging toe.
(5) Geduldig hou ik de deur voor je open.

Brumfit, C. (**1984**). *Communicative Methodology in Language Teaching: The Roles of Fluency and Accuracy* (Cambridge University Press, Cambridge).

Butcher, A. (**1981**). ''Phonetic correlates of perceived tempo in reading and spontaneous speech,'' *Work in Progress*, Phon. Lab. Univ. Reading, pp. 105–117.

Chambers, F. (**1997**). ''What do we mean by fluency?,'' System **4**, 535–544.

Dechert, H. W., and Raupach, M. (**1980a**). *Temporal Variables in Speech: Studies in Honour of Frieda Goldman-Eisler* (Mouton, The Hague).

Dechert, H. W., and Raupach, M. (**1980b**). *Towards a Cross-Linguistic Assessment of Speech Production* (Lang, Frankfurt).

den Os, E. A., Boogaart, T. I., Boves, L., and Klabbers, E. (**1995**). ''The Dutch Polyphone Corpus,'' *Proceedings Eurospeech95*, pp. 825–828.

Ferguson, G. A. (**1987**). *Statistical Analysis in Psychology and Education* (McGraw-Hill, Singapore).

Fillmore, C. J. (**1979**). ''On fluency,'' in *Individual Differences in Language Ability and Language Behavior*, edited by C. Fillmore, D. Kempler, and W. S.-Y. Wang (Academic, New York), pp. 85–101.

Flege, J. E., and Fletcher, K. L. (**1992**). ''Talker and listener effects on degree of perceived foreign accent,'' J. Acoust. Soc. Am. **91**(1), 370–389.

Freed, B. F. (**1995**). ''What makes us think that students who study abroad become fluent?,'' in *Second Language Acquisition in a Study-Abroad Context*, edited by B. F. Freed (Benjamins, Amsterdam), pp. 123–148.

Goldman-Eisler, F. (**1968**). *Psycholinguistics: Experiments in Spontaneous Speech* (Academic, New York).

Grosjean, F. (**1980**). ''Temporal variables within and between languages,'' in *Towards a Cross-Linguistic Assessment of Speech Production*, edited by H. W. Dechert and M. Raupach (Lang, Frankfurt), pp. 39–53.

Grosjean, F., and Deschamps, A. (**1975**). ''Analyse contrastive des variables temporelles de l'Anglais et du Francais: Vitesse de parole et variables composantes, phénomènes d'hésitation,'' Phonetica **31**, 144–184.
Leeson, R. (**1975**). *Fluency and Language Teaching* (Longman, London).
Lennon, P. (**1990**). ''Investigating fluency in EFL: A quantitative approach,'' Language Learning **3**, 387–417.
Levelt, W. J. M. (**1989**). *Speaking. From Intention to Articulation* (MIT Press, Cambridge, MA).
Möhle, D. (**1984**). ''A comparison of the second language speech production of different native speakers,'' in *Second Language Productions*, edited by H. W. Dechert, D. Möhle, and M. Raupach (Narr, Tübingen), pp. 26–49.
Nation, P. (**1989**). ''Improving speaking fluency,'' System **3**, 377–384.
Peters, T. J., and Guitar, B. (**1991**). *Stuttering. An Integrated Approach to its Nature and Treatment* (William and Wilkins, Baltimore).
Raupach, M. (**1980**). ''Temporal variables in first and second language speech production,'' in *Temporal Variables in Speech: Studies in Honour of Frieda Goldman-Eisler*, edited by H. W. Dechert and M. Raupach (Mouton, The Hague), pp. 263–270.
Raupach, M. (**1983**). ''Analysis and evaluation of communicative strategies,'' in *Strategies in Interlanguage Communication*, edited by C. Faerch and G. Kasper (Longman, London), pp. 263–270.
Riggenbach, H. (**1991**). ''Toward an understanding of fluency: A microanalysis of non-native speaker conversations,'' Discourse Process. **14**, 423–441.
Schmidt, R. (**1992**). ''Psychological mechanisms underlying second language fluency,'' Stud. Second Language Acquisition **14**, 357–385.
Segalowitz, N. (**1991**). ''Does advanced skill in a second language reduce automaticity in the first language?,'' Language Learning **41**, 59–83.
SPEX http://lands.let.kun.nl/spex.
Strik, H., Russel, A., Van den Heuvel, H., Cucchiarini, C., and Boves, L. (**1997**). ''A spoken dialog system for the Dutch Public Transport Information Service,'' International J. Speech Technol. **2**, 121–131.
Towell, R. (**1987**). ''Approaches to the analysis of the oral language development of the advanced learner,'' in *The Advanced Language Learner*, edited by J. A. Coleman and R. Towell (CILT, London), pp. 157–181.
Towell, R., Hawkins, R., and Bazergui, N. (**1996**). ''The development of fluency in advanced learners of French,'' Appl. Linguistics **1**, 84–119.

The recognition of isolated words and words in sentences: Individual variability in the use of sentence context

Ken W. Grant[a] and Philip F. Seitz[b]
Walter Reed Army Medical Center, Army Audiology and Speech Center, Washington, DC 20307-5001

(Received 8 March 1999; revised 27 October 1999; accepted 1 November 1999)

Estimates of the ability to make use of sentence context in 34 postlingually hearing-impaired (HI) individuals were obtained using formulas developed by Boothroyd and Nittrouer [Boothroyd and Nittrouer, J. Acoust. Soc. Am. **84**, 101–114 (1988)] which relate scores for isolated words to words in meaningful sentences. Sentence materials were constructed by concatenating digitized productions of isolated words to ensure physical equivalence among the test items in the two conditions. Isolated words and words in sentences were tested at three levels of intelligibility (targeting 29%, 50%, and 79% correct). Thus, for each subject, three estimates of context ability, or *k* factors, were obtained. In addition, auditory, visual, and auditory–visual sentence recognition was evaluated using natural productions of sentence materials. Two main questions were addressed: (1) Is context ability constant for speech materials produced with different degrees of clarity? and (2) What are the relations between individual estimates of *k* and sentence recognition as a function of presentation modality? Results showed that estimates of *k* were not constant across different levels of intelligibility: *k* was greater for the more degraded condition relative to conditions of higher word intelligibility. Estimates of *k* also were influenced strongly by the test order of isolated words and words in sentences. That is, prior exposure to words in sentences improved later recognition of the same words when presented in isolation (and vice versa), even though the 1500 key words comprising the test materials were presented under degraded (filtered) conditions without feedback. The impact of this order effect was to reduce individual estimates of *k* for subjects exposed to sentence materials first and to increase estimates of *k* for subjects exposed to isolated words first. Finally, significant relationships were found between individual *k* scores and sentence recognition scores in all three presentation modalities, suggesting that *k* is a useful measure of individual differences in the ability to use sentence context. © *2000 Acoustical Society of America.* [S0001-4966(00)03802-9]

PACS numbers: 43.71.An, 43.71.Gv, 43.71.Ky [JMH]

INTRODUCTION

Most speech communication occurs in circumstances that permit both auditory and visual processing of the speech signal. With few exceptions, listeners are able to integrate the visual cues derived from speechreading (i.e., lipreading) with audition to improve their speech recognition (Sumby and Pollack, 1954; ANSI, 1969).

The recognition performance when optical and acoustic phonetic information are available is determined by at least three factors: (1) the ability to extract cues from the auditory and visual signals, (2) the ability to integrate these cues, and (3) the ability to use one's language knowledge to constrain the number of possible response alternatives (Grant and Walden, 1996; Grant *et al.*, 1998; Grant and Seitz, 1998). This last factor includes knowledge of what constitutes a well-formed word within the language, knowledge of word frequency and word familiarity, and the use of morpho-syntactic, semantic, and situational cues (collectively denoted as ''context''). The ability to make use of sentence context also involves working memory capacity, information processing speed, vocabulary size, and inference-making skills (Rönnberg *et al.*, 1998). In the study described here, we focused on an individual's ability to use context in sentence identification, and how individual differences in the ability to make use of sentence context may relate to auditory, visual, and auditory–visual recognition of sentence materials. Although it is important ultimately to delineate how each of these different context factors differs across individuals, the present study is much more limited in scope. We felt that it was important first to determine whether estimated differences in subjects' ability to make use of context could account for a significant proportion of variance in typical speech-recognition measures obtained under auditory, visual, and auditory–visual conditions. If an individual's ability to make use of context failed to explain significant amounts of the variability in speech recognition typically observed across hearing-impaired listeners, then the desire to further explore the various context factors might seem less well motivated.

The extent to which contextual cues may assist in speech recognition depends upon the nature of the speech sample, as well as potential individual differences in the ability to use contextual information. For example, identifying *nonsense* consonant–vowel–consonant (CVC) syllables requires that sufficient stimulus cues for each consonant and vowel segment be received accurately. However, with *meaningful*

[a]Electronic mail: grant@tidalwave.net
[b]Current affiliation: United States Department of State, Foreign Service.

CVC words, lexical constraints make it possible to identify words correctly without having to resolve all of the individual segments (e.g., /buk/ is not a real word, whereas /bʊk/ is, thus restricting the choice of back-rounded vowel). Similarly, words presented in isolation under auditory or auditory–visual conditions are usually harder to identify than words presented in sentences (Miller *et al.*, 1951; Boothroyd and Nittrouer, 1988). In order to understand the relationship between segment, word, and sentence-recognition performance, these contextual variables must be quantified.

One of the most familiar tests of the effects of linguistic context on speech intelligibility is the Speech Intelligibility in Noise (SPIN) test, designed to distinguish between the reception of acoustic cues and the ability to make use of linguistic information stored in long-term memory (Kalikow *et al.*, 1977). The SPIN test sought to control the amount of linguistic information by testing speech intelligibility under conditions of controlled word predictability. Sentence contexts with high (PH) and low (PL) word predictability were generated, and the difference in intelligibility between the word score in PH sentences and PL sentences (i.e., PH-PL) was used as a measure of the individual's use of context. Earlier studies using the SPIN test by Hutchinson (1989) and Schum and Matthews (1992) described results where a number of elderly listeners had PH-PL scores that were lower than expected based on normative data. The finding that some subjects demonstrate less facilitation from contextual information than others must be considered when interpreting any observed speech communication difficulties.

SPIN word scores are based on the intelligibility of the final word from each PH and PL sentence. Therefore, one has to perceive enough of the initial portion of the sentence in order to make use of semantic and syntactic information. In the SPIN test, the words comprising the low- or high-context portion of each sentence typically are subjected to the same speech-to-babble distortion as are the target words at the end of each sentence. If two listeners obtain different PH-PL scores at the same signal-to-noise (S/N) level, it does not necessarily mean that the listener with the greater difference score is able to make better use of context than the other. It is possible that the two listeners are affected differently by the speech babble interference, and the listener with the smaller PH-PL difference was not able to resolve the initial context portion of the sentence as well as the other listener. Stated differently, SPIN performance may be affected by factors related to audibility and other auditory processing differences, and not solely to the use of contextual information (Humes *et al.*, 1994).

A second problem in measuring a listener's ability to use contextual information with SPIN sentences is accounting for the interaction between PL scores and PH-PL difference scores. Because of the interdependence between PL and PH-PL scores, very low or very high PL scores necessarily limit PH-PL difference scores. Bilger *et al.* (1984) noted that raw scores reflect two different skills: the ability to listen in noise and the ability to use context, and suggested that it might be useful to transform raw scores into their normal deviates prior to any subtraction.

To circumvent some of the problems with the SPIN test, a more general approach to quantifying the effects of lexical, semantic, and morpho-syntactic context was suggested by Boothroyd and Nittrouer (1988). Using probability theory, phonemic and semantic redundancies inherent in a speech corpus can be represented quantitatively by simple power-law equations. In Eq. (1), the probability of recognizing a word is assumed to be equal to the joint probability of recognizing its component parts, or segments. If each of these parts is statistically independent and equally recognizable, then

$$P_w = P_p^n, \tag{1}$$

where P_w is the probability of recognizing the whole word, P_p is the probability of recognizing each independent segment, and n is the number of parts, or segments, in the word. However, in the case of real words, the segments are not independent due to coarticulation and structural properties of the lexicon, and the recognition of the whole word does not require that all segments be received. Therefore, for real words

$$P_w = P_p^j, \tag{2}$$

where $1 \leqslant j \leqslant n$. Application of this equation to several sets of data showed that for monosyllabic CVC words, j was approximately 2.5 (Boothroyd and Nittrouer, 1988; Rabinowitz *et al.*, 1992). Hence, for these simple three-segment stimuli, subjects responded as if the words consisted of about 2.5 independent parts (each part containing the equivalent of 1.2 phonemes) rather than three independent parts.

Equation (3), developed by Boothroyd and Nittrouer (1988), relates word recognition in isolation to word recognition in sentences,

$$P_s = 1 - (1 - P_w)^k, \tag{3}$$

where P_s is the recognition probability for words in sentences, P_w is the recognition probability for words in isolation, and k is a free parameter reflecting the degree of predictability or context of the sentence materials. The exponent k represents the effective proportional increase in the number of channels of independent information due to contextual constraints. To obtain an estimate of k, one acquires speech-recognition scores for words presented in isolation (or in nonsense sentences) and for words presented in sentences. Thus, a criticism applied to SPIN measures, namely that the recognition of the final word is affected by the audibility of previous words, and not necessarily due to contextual information, is circumvented because all of the words in the sentence are treated equally in contributing to the overall amount of contextual information. Further, because k is a ratio of two logarithms, rather than a simple difference score (as in the SPIN test), the dependence of contextual information on isolated word intelligibility is theoretically avoided.[1]

Figure 1 shows the predicted relationship between word recognition in isolation and word recognition in meaningful sentences for different k factors. The figure predicts that word recognition in meaningful sentences is predicted to be better than isolated word recognition for all values of $k > 1$

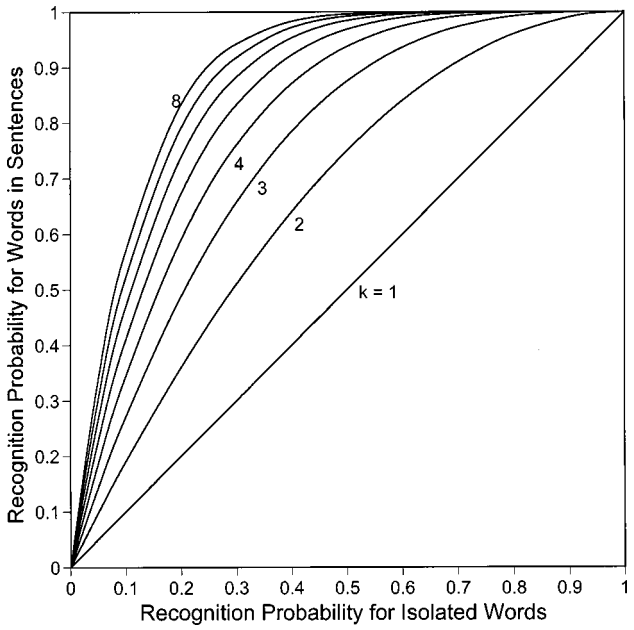

FIG. 1. Predicted isolated word recognition and word recognition in meaningful sentences for different *k* factors (after Boothroyd and Nittouer, 1988).

(with the exception of isolated word-recognition scores of zero and 100% correct) and that the difference in percent correct between words in sentences and isolated words grows more rapidly as *k* increases. Thus, for highly contextual materials, small improvements in isolated word recognition translate to large improvements in the recognition of words in sentences.

In the literature, *k* has been interpreted primarily as a property of the stimulus materials. Word and sentence-recognition scores collected from many subjects for a given corpus of speech materials are plotted and iteratively fit so as to determine a single *k* value that minimizes the variability across subjects. A lingering question, however, is whether *k* can be used to differentiate between *individual subjects* regarding their ability to use context in everyday communication. One practical concern in addressing this question is revealed by the convergence of the family of curves at either very low or very high isolated word-recognition accuracy. The theoretical curves displayed in Fig. 1 suggest that in order to demonstrate differences in *k* among individual subjects or different speech materials, it is important to control for the overall intelligibility of words presented in isolation. Isolated word-recognition scores near 30% yield the greatest range of intelligibility scores for words in meaningful sentences. On the other hand, word-recognition scores below 20% or above 80% correct show a greatly compressed range of word-in-sentence scores. It is important to point out that because *k* is a ratio of logarithms, only isolated word-recognition scores of zero or 100% correct are theoretically problematic. For example, even with isolated word-recognition scores as high as 95% correct, a large range of *k* values is possible, although very difficult to show statistically (e.g., for this case, the word-in-sentence recognition score would have to be 99.99% correct or higher to obtain *k* values greater that 3.0). Therefore, it is prudent to control for the range of isolated word-recognition scores making it feasible to demonstrate a range of *k* for individual subjects.

A second concern with treating *k* as a property of an individual rather than a property of the stimulus is that the traditional method for obtaining *k* values assumes that *k* is constant across various levels of isolated word intelligibility for a fixed speech corpus. In our application of *k* as an attribute of individuals and not materials, it follows that the amount of contextual knowledge applied to the recognition of words in sentences under unfavorable listening situations would be identical to that obtained under highly favorable listening situations. That is, an individual with a specified *k* would be predicted to perform according to the appropriate iso-*k* contour line as shown in Fig. 1. However, there is no *a priori* reason to adopt this assumption, and, in fact, it is reasonable to think that listeners may be able to modulate the degree to which contextual information is applied depending on the quality of the incoming speech signal. Thus, the recognition of speech stimuli with easily accessible information (such as clear speech presented to normally hearing listeners) might be less dependent on internal linguistic constraints than speech stimuli with less accessible information (such as conversational speech presented to hearing-impaired listeners). We will return to this point later.

Two recent studies have made use of the model of Boothroyd and Nittrouer and are germane to the present investigation. Rabinowitz *et al.* (1992) studied consonant recognition, vowel recognition, NU6 words, low-context sentences (IEEE, 1969) and high-context sentences (Boothroyd *et al.*, 1985) in 20 postlingually deafened cochlear implant users. Significant correlations across subjects were found between segment (consonants and vowels) and word intelligibility, and between word and sentence intelligibility ($r>0.85$). For low-context sentence materials such as IEEE/Harvard sentences, the average *k* value was found to be approximately 1.14 (recall that a *k* of 1.0 implies no contextual information). For sentence sets with a higher degree of predictability [City University of New York (CUNY) sentences], *k* was approximately 4.5 (Rabinowitz *et al.*, 1992). Thus, *k* is dependent on the different morpho-syntactic and semantic characteristics of the test materials, and any variability in *k* values due to individual differences would likely be located around the stimulus-dependent *k* value.

Recently, Olsen *et al.* (1997) investigated the relationship between phoneme, isolated word, and sentence recognition in noise for listeners with normal and impaired hearing. Sentence lists were constructed from lists of CVC words (2–8 words per sentence) so that the key words comprising the sentence measures were the same words tested in isolation (at least orthographically).[2] The sentences were syntactically correct but were of low context, making them similar to SPIN-PL sentences. During testing, subjects were first presented with a list of words, immediately followed by the corresponding sentences made from those same words. Thus, although subjects were not informed that the same words would be presented in sentences, it is highly likely that prior exposure to the isolated word materials inflated the scores for the corresponding sentence materials. Because the calculation of *k* involves forming the ratio of the logarithms of the error terms for sentences and isolated words, procedural ef-

fects that increase sentence recognition relative to word recognition necessarily will increase the estimate of *k*. Presumably, a reverse ordering of the test conditions would cause a reduction in the estimate of *k*. The design of the present study will allow us to examine this issue in more detail.

The Olsen *et al.* study also demonstrated large individual differences across both normal-hearing and hearing-impaired subjects. For example, normal-hearing subjects who recognized isolated words with about 40% accuracy showed markedly different abilities when recognizing words in sentences (scores between 20%–85%). Olsen *et al.* (1997) offered no specific explanation regarding these apparent individual differences, but the data show that large individual differences exist even for subjects who acquired language under normal conditions.

In summary, context factors in language processing (e.g., the use of syntactic and semantic information to facilitate speech understanding) are often cited as important determinants of both unimodal and bisensory speech recognition (e.g., Massaro, 1987; Boothroyd and Nittrouer, 1988; Erber, 1996; Montgomery and Demorest, 1988; DeFilippo, 1990; Nittrouer and Boothroyd, 1990). In past studies on auditory–visual speech recognition in hearing-impaired subjects, large individual differences have been readily observed. Whether some of these differences in performance across individuals are due to differences in the ability to make use of context is not known. In this study, the ability of hearing-impaired individuals to use sentence context was investigated. However, no attempt is made to control for the various factors that comprise contextual information or the resources required on the part of individual to use context (such as memory, vocabulary, and speed of processing). Instead, we simply quantify possible individual differences in context use among hearing-impaired subjects by obtaining estimates of individual *k* values (essentially the difference in speech-recognition performance for isolated words and for words in sentences). This was achieved by measuring isolated word and words-in-sentence recognition at several different levels of isolated word intelligibility. Finally, individual estimates of *k* were used to predict auditory, visual, and auditory–visual recognition for sentences presented in a background of continuous speech–shaped noise. These latter conditions were included for two main purposes. First, they provide baseline measures on sentence-recognition performance to test the hypothesis that the ability to make use of context is a primary factor in determining individual differences in speech recognition. Second, if *k* is predictive of speech-recognition performance across modality, it would lend support to the idea that *k* is a measure of a subject's ability to deploy higher-level knowledge sources, independent of the modality in which the speech is presented. Overall, the results obtained from this study should be useful in evaluating whether an individual's ability to use context is an important factor in determining speech-recognition performance.

I. METHODS

This study included three parts: (1) establishing three different conditions of intelligibility (targeting 29%, 50%, and 79% correct) separately for each hearing-impaired listener using isolated words, (2) obtaining estimates of *k* for individual HI subjects at each of the three intelligibility levels, and (3) measuring auditory, visual, and auditory–visual sentence recognition. For auditory and auditory–visual sentence recognition, a continuous background of speech-shaped noise was presented.

A. Subjects

The subjects were 34 hearing-impaired (HI) adults (32 male, 2 female) between the ages of 33 and 85 years ($\bar{\chi}=67.7$; s.d.$=11.3$). Subjects had a wide variety of hearing losses and configurations ranging from normal hearing to moderate hearing loss in the low frequencies (average pure tone thresholds at 0.5, 1, and 2 kHz between 3 and 52 dB HL in the better ear) and mild-to-severe hearing loss in the high frequencies (average pure-tone thresholds at 3, 4, 6, and 8 kHz between 18 and 88 dB HL in the better ear re: ANSI, 1989). One subject had normal hearing through 6 kHz in the left ear and a moderate-to-severe loss in the right. Although the exact causes of the hearing losses were not known, most of the subjects had a history of noise exposure due to military service. All hearing losses were of sensorineural origin (as confirmed by air- and bone-conduction testing and middle-ear admittance testing) and occurred postlingually. There was no history of chronic middle-ear disease or retrocochlear signs and all subjects were fitted with hearing aids at least 1 year prior to participation in the study. All subjects were native speakers of American English with normal or corrected-to-normal vision (static visual acuity equal to or better than 20/30 as measured with a Snellen chart from a distance of 20 ft). All testing was conducted binaurally using headphones. Unfiltered speech levels (see below) were set at approximately 40 dB SL relative to the subject's better ear, or at the subject's most comfortable listening (MCL) level, whichever was lower. Subjects provided informed consent and were paid for their participation.

B. Stimuli

Speech materials consisted of isolated words and words in sentences taken from the IEEE/Harvard (1969) sentence set. This set consists of 720 phonetically balanced low-context sentences each containing five key words. The sentences are organized into 72 lists with 10 sentences per list. Estimates of *k* for individual subjects required a comparison between word recognition in isolation and word recognition in meaningful sentences. Approximately 2000 isolated key words from the IEEE set (40 lists), as well as all of the necessary non key words to construct sentences were recorded separately by a male talker, low-pass filtered (8.5 kHz), and digitized at 20 kHz with 16-bit amplitude quantization. Sentences were constructed by concatenating key words and non key words together so that in the main comparison between isolated words and words in context, physically identical key words were used. This process ensured that any differences observed in key-word recognition scores between the two sets of materials could only be due to morpho-syntactic and semantic context and not due to coar-

ticulation, prosodic information, or any other physical signal alteration that occurs between words spoken in isolation or in sentence context.

In creating concatenated sentence materials, care was taken to make the resultant sentences sound as natural as possible.[3] Thus, when recording the non key words, phrases rather than isolated words were recorded whenever possible. For example, for the sentence ''The birch canoe slid on the smooth planks,'' the non key word ''The'' and the non key phrase ''on the'' were recorded along with the remaining five key words (''birch,'' ''canoe,'' ''slid,'' ''smooth,'' and ''planks''). The concatenated sentence thus consisted of the pieces the, birch, canoe, slid, on the, smooth, and planks. The intensity of all non key words and nonkey word phrases was scaled to be 0.7 times the original level. This amplitude scaling was chosen to make concatenated sentences appear as natural as possible. Concatenated sentences were approximately 1.2 times longer than their fluently produced counterparts. Whereas the test sentences sounded somewhat unnatural because of the absence of appropriate intonation and stress, they were nevertheless quite intelligible and easily understood by our HI subjects.

To test sentence recognition in noise, naturally produced IEEE sentences spoken by a female talker were used. All 720 IEEE sentences were originally videotaped at the Massachusetts Institute of Technology, and the auditory and visual images were transferred to an optical disk recorder (Panasonic TQ-3031F). The audio portion of each sentence was digitized (16-bit A/D, 20-kHz sampling rate), normalized in level so that all sentences had the same overall rms, and stored on computer for later playback. The computer independently controlled the visual and audio playback for each sentence, allowing for precise alignment of the audio and visual signals (± 2 ms). The noise used to mask the sentence materials was a 20-s sample of white noise that was shaped according to the long-term average magnitude spectrum of the IEEE sentences. The duration of the noise sample used on each trial was equal to the sentence duration plus 100 ms. This was accomplished by positioning a pointer randomly in the noise file and extracting the appropriate duration of shaped noise.

C. Procedures

1. Establishing equivalent intelligibility conditions across listeners for isolated words

The intelligibility of auditorily presented isolated words was controlled by bandpass filtering. Three bandpass filters with different bandwidths, each centered at 1.0 kHz, were determined independently for each subject using an adaptive tracking procedure that controlled the bandwidth of the filter (TDT PF1). Three different tracking algorithms, each run separately, were used: 1-down 2-up (targeting 29% correct—filter 1), 1-down 1-up (targeting 50% correct—filter 2), and 3-down 1-up (targeting 79% correct—filter 3). Subjects were presented randomized lists of isolated key words (up to 200 unique IEEE key words for each filter bandwidth estimate) and were required to repeat back verbally what they heard. Scoring was performed online by the experimenter. The filter bandwidth initially was increased or decreased symmetrically in semitone steps according to the specific decision rule for the three different adaptive tracks (getting narrower after correct responses and broader after incorrect responses). After four track reversals, the step size was decreased to a quarter tone and continued at the smaller step size until an additional eight reversals were recorded. The final bandwidth was computed from the geometric mean of the last eight reversals. Each subject was tested for a minimum of nine tracks (three tracks per filter). A fourth track was run if any of the three filter bandwidth estimates differed by more than five quarter tones and the final average was then based on all four estimates. The order of tracks was randomized separately across subjects.

2. Estimating individual k factors

To estimate k, the recognition of words in isolation and words in sentences was tested under each of the three filter conditions described above (hereafter labeled filter 1, filter 2, and filter 3). Five hundred key words were tested per filter condition. Because some of the IEEE key words are repeated within and across lists of sentences, the total number of unique key words presented was 1048 (instead of 1500). Half of the subjects ($n=17$) received isolated words prior to being tested with the concatenated sentence materials, whereas the other half received sentences first. Within each group (words first or sentences first), the test materials were randomized separately for each subject, although the same words were used for all subjects in a given filter condition. Thus, each subject obtained three isolated word scores (based on the average of 500 words each) and three sentences scores (based on the same 500 words used for isolated words). The three estimates of k for each subject (one per filter condition) were computed using Eq. (3).

3. Measuring auditory, visual, and auditory–visual speech recognition in noise

Speech recognition in continuous speech-shaped noise was evaluated following the estimation of individual k factors. Fifteen lists of IEEE sentences (50 key words per list) not previously presented were used to evaluate each of the three receiving modalities (five lists per modality). The signal-to-noise ratio for auditory and auditory–visual conditions was fixed at 0 dB S/N for all subjects. Whereas isolated words and concatenated sentences used to estimate k were spoken by a male speaker, the IEEE sentences used for speech recognition in noise were spoken by a female speaker. For visual and auditory–visual conditions, the subjects were seated approximately 5 ft away from a 19-in. television monitor (SONY PVM 2030). Listening was conducted binaurally under headphones (Beyer model DT 770) at approximately 85 dB SPL. The subjects gave their responses verbally and the number of correct key words was scored online by the experimenter. The final score for each condition (auditory, visual, and auditory–visual) was the average of five lists (50 key words per list).

TABLE I. Average bandwidth for three filter conditions targeting 29% (filter 1), 50% (filter 2), and 79% (filter 3) correct isolated word recognition, respectively, for 34 hearing-impaired subjects. Filters were logarithmically centered at 1 kHz.

	Bandwidth (Hz)		
Subject	Filter 1	Filter 2	Filter 3
1	76	209	730
2	76	176	730
3	142	451	1370
4	586	1666	3915
5	443	1292	4461
6	1439	2051	2686
7	461	1413	2051
8	118	1402	2652
9	161	466	3624
10	76	339	900
11	85	281	1056
12	122	330	2701
13	108	549	1687
14	146	414	1225
15	231	1277	3782
16	218	980	2925
17	133	504	1800
18	62	269	1077
19	192	1038	4758
20	593	1056	2814
21	76	561	1042
22	168	723	1095
23	58	198	693
24	80	296	1529
25	395	832	1905
26	118	612	2220
27	146	514	1518
28	163	560	1957
29	93	273	872
30	73	367	1081
31	261	634	1289
32	313	820	1608
33	85	687	1873
34	870	1353	3084
Mean	246.1	723.3	2020.9
Standard error	48.3	81.2	191.8

II. RESULTS

A. Filter bandwidths

Filter conditions corresponding to roughly 29%, 50%, and 79% intelligibility, established for each subject during the tracking task with isolated words, resulted in average bandwidths of 246, 723, and 2021 Hz, respectively (see Table I). However, because there was a wide range of hearing loss across subjects, there was also a great amount of variability in the final filter bandwidths. To determine whether various characteristics of the subject's hearing loss were good predictors of filter bandwidth, a canonical correlation was used with bandwidth as the dependent measure and hearing loss at single frequencies (1 and 2 kHz) and average frequencies (0.5, 1, and 2 kHz; 2 and 4 kHz; 2, 3, and 4 kHz; 2, 3, 4, 6, and 8 kHz; and 3, 4, 6, and 8 kHz) as the independent measures. As might be expected, the bandwidth for the narrowest filter condition was most highly correlated with hearing loss measured at 1 kHz ($r=0.69$, $p<0.0001$) since the filters were centered at 1 kHz. For the two broader filter conditions, the hearing loss at higher and lower frequencies became important in determining the final bandwidth. For example, for filter condition 2 (targeting 50% word intelligibility), the average pure-tone three-frequency loss at 0.5, 1, and 2 kHz ($r=0.64$, $p<0.0001$) was the best predictor of bandwidth, whereas for filter condition 3 (targeting 79% word intelligibility), the hearing loss at 2 kHz ($r=0.79$, $p<0.0001$), and the average three-frequency loss at 2, 3, and 4 kHz ($r=0.72$, $p<0.0001$) were the most important frequencies for determining filter bandwidth. Thus, for broader filters with higher intelligibility, the high-frequency hearing loss, and especially the loss at 2 kHz, became increasingly more important in determining the final filter bandwidth.

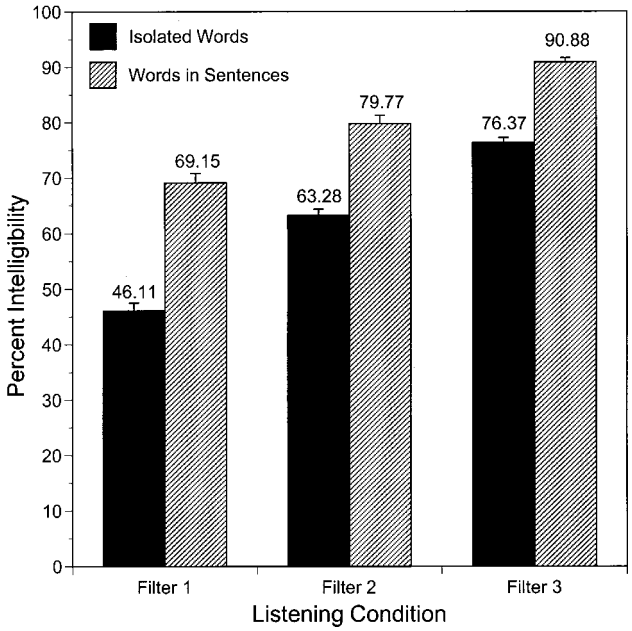

FIG. 2. Isolated word and words in sentence scores obtained for the three filter conditions. Error bars show +1 standard error.

B. Estimates of *k*

Isolated word and word-in-sentence scores obtained for the three filter conditions are shown in Fig. 2. The mean isolated word scores, based on 500 words each (10 blocks of 50 words), were 46%, 63%, and 76% correct, respectively. The corresponding words-in-sentence scores were 69%, 80%, and 91% correct, respectively. Thus, even though the sentence materials were constructed by concatenating words together (and therefore lacked normal prosody and coarticulation among syllables), the meaningful sequence of the words and well-formed grammatical structure of the sentences significantly enhanced word intelligibility.

Prior exposure to either isolated words or words in sentences facilitated the recognition of speech materials presented later. Figure 3 shows the effect of presentation order on the intelligibility of isolated words and words in sentences. Recall that half the subjects (group 1; $n=17$) were exposed to words in isolation prior to receiving concatenated sentence materials, whereas the remaining subjects (group 2; $n=17$) were exposed to concatenated sentences prior to iso-

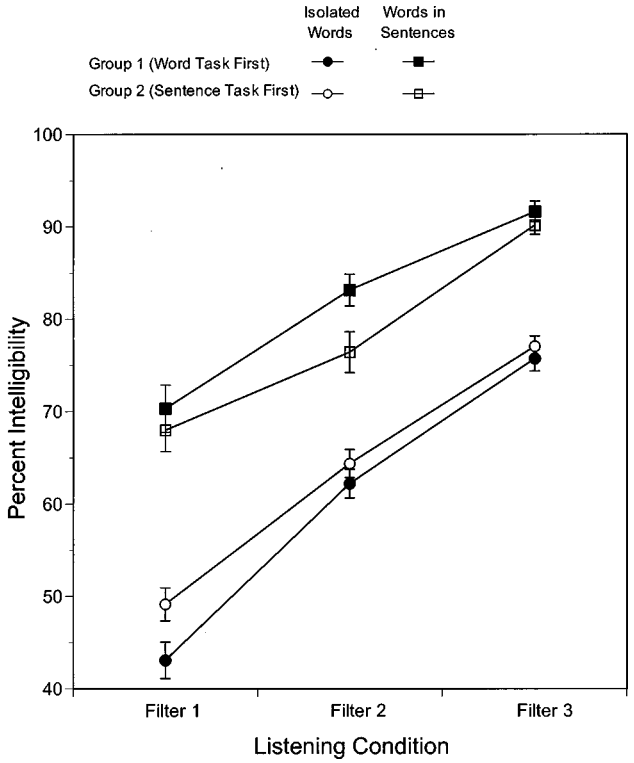

FIG. 3. Same as Fig. 2 but broken out for the two groups of subjects. Group 1 (filled symbols) received isolated words prior to sentences, group 2 (open symbols) received sentences prior to being exposed to isolated words. Square symbols show percent correct scores for words-in-sentences, circle symbols show percent correct scores for isolated words. Error bars show ±1 standard error.

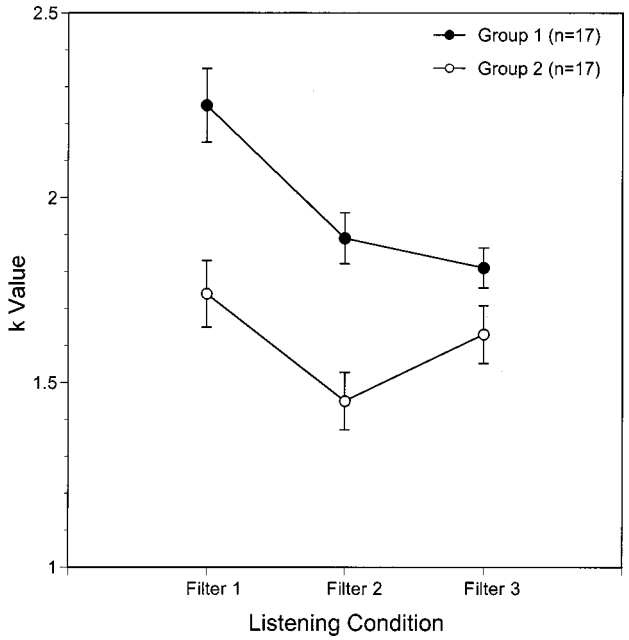

FIG. 4. Group mean k values for the three filter conditions. Filled circles =group 1 (words first); filled triangle=group 2 (sentences first). Error bars show ±1 standard error.

lated words. The facilitating effects of prior exposure can be measured by comparing the difference in intelligibility scores for words received first (group 1) versus words received second (group 2) and for sentences received first (group 2) versus sentences received second (group 1). Averaged across filter conditions, the facilitation effect on isolated word recognition due to prior exposure to concatenated sentences was 3.7%, and the facilitation effect on word-in-sentence recognition due to prior exposure to isolated words was 3.2%.

Although these differences in intelligibility due to test order may seem small at first, they have a significant effect on the estimates of individual k factors. Because k is related directly to the difference in intelligibility between isolated word and word-in-sentence scores, experimental variables, like test order, that affect intelligibility will also affect estimates of k. By testing concatenated sentences after exposure to isolated words (group 1), the word-in-sentence scores were enhanced relative to what they would have been had there been no prior exposure, and the estimated k values were relatively large. This is illustrated in Fig. 3 by the greater separation between isolated word and word-in-sentence scores for group 1 subjects. Conversely, by testing isolated words after exposure to concatenated sentences (group 2), the word scores were enhanced relative to what they would have been had there been no prior exposure (thereby making the difference between isolated words and concatenated sentences smaller), and the estimated k values were relatively small. Figure 4 shows the estimated group mean k values for each filter condition. A repeated measures analysis of variance was carried out on the k values with one between-subjects factor (test order) and one within-subjects factor (filter condition) at three levels. The results showed significant main effects of test order [$F(1,32)=15.74$, $p<0.001$] and filter condition [$F(2,64)=20.60$, $p<0.001$]. The analysis also showed a significant interaction between test order and filter [$F(2,64)=5.04$, $p<0.01$]. This interaction may be seen in Fig. 4 as the more similar performance for the two groups with filter 3 than with the other two filter conditions.

Post hoc analyses (paired t-tests with Bonferonni adjustment) of the data revealed that the estimated k values obtained for filter 2 were significantly smaller than for filter 1 for both groups of subjects. However, whereas the k values for filter 3 were essentially the same as those measured for filter 2 for group 1, the k values for filter 3 were significantly larger than those measured for filter 2 for group 2. At present, we have no explanation for this result, especially considering that the words tested across groups for any given filter condition were identical.

With the exception of filter condition 3, group 2, the average k values obtained for the two groups of subjects decreased with increasing signal clarity, at least over the range of intelligibility tested. That is, as more stimulus information becomes available due to a broadening of the listening band, there appears to be less contextual information employed by the subjects. Note that this result is counter to the theoretical predictions of Boothroyd and Nittrouer (1988). Under their formulation, k is expected to be constant regardless of the level of isolated word intelligibility, as long as the speech materials remain fixed. However, given that contextual constraints are used to reduce ambiguity of missing or distorted information due to signal degradation, it may

be that as the intelligibility of the signal increases, the relative importance of contextual processing diminishes. This is not to imply that there is no benefit of context for signals with relatively high intelligibility. According to Eq. (3), k values above 1.0 indicate some information due to context. As Fig. 4 shows, all mean k values were well above 1.0, even for group 2, whose k values are probably smaller than those typically reported given the prior exposure to sentence materials. Averaged across filter conditions, the mean k value for group 1 was 1.98, whereas the mean value for group 2 was 1.61. According to Boothroyd and Nittrouer (1988), this means that the morpho-syntactic information contained in IEEE sentences represents an effective increase of 60%–100% in the number of channels of statistically independent information available from the stimulus alone.

An important question regarding the potential use of k as an indication of individual skill in using contextual information is whether estimates of k are stable across different listening conditions. To address this question, Pearson correlation coefficients for all pairs of k across filter conditions were computed. A significant correlation across filter conditions indicates that a subject's ranking with regard to contextual ability is consistent relative to other subjects. The correlation between adjacent filter conditions (i.e., filter 1 versus filter 2, and filter 2 versus filter 3) was highly significant ($r_{12}=0.78$, $p_{12}<0.0001$ and $r_{23}=0.69$, $p_{23}<0.0001$, respectively), accounting for roughly 50%–60% of the variance across subjects. The correlation for filter 1 versus filter 3 was more modest ($r_{13}=0.46$, $p<0.01$), but nevertheless significant. The significance of these correlations is critical for the hypothesis that k, a presumed measure of subject ability to make use of contextual information, tends to travel with the subject from one task to the next. That is, a subject with a high k value on one task is likely to have a high k value on some other task.

C. Relation between *k* and auditory, visual, and auditory–visual sentence recognition

Sentence recognition in noise measured at 0 dB S/N for auditory and auditory–visual conditions, as well as sentence recognition for speechreading alone, is shown in Fig. 5. Auditory sentence recognition, shown along the abscissa, ranged from 9% to 87% ($\bar{\times}=49\%$). Visual sentence recognition (filled circles) ranged from 0% to 24% ($\bar{\times}=4\%$), whereas auditory–visual sentence recognition (filled triangles) ranged from 56% to 99% ($\bar{\times}=84\%$). The solid line represents the unity function auditory=visual and auditory=auditory–visual. The fact that all data for the auditory–visual condition lie well above the unity line indicates that all subjects derived benefit from combining auditory and visual cues.

Our original hypothesis concerning the role of context ability in sentence recognition was that subjects with greater k values would, in general, have higher recognition scores for words in sentences than subjects with lower k values. However, sentence scores are influenced by a number of factors other than context, such as a subject's ability to extract auditory and visual segmental and prosodic cues and the ability to integrate these cues (for auditory–visual recognition). Therefore, to determine whether individual k factors influence a subject's sentence recognition score, these other potentially confounding factors have to be addressed. In the present study, no direct data were obtained regarding segmental or prosodic cue extraction ability in either auditory, visual, or auditory–visual modalities. However, at least for auditory speech recognition, this ability is known to be determined primarily by audibility of specific speech cues, which in turn may be estimated by the subjects hearing loss, especially for high frequencies. This estimate of auditory cue extraction ability can be further augmented by data obtained in the filter-tracking phase of the current study, in that one can assume that listeners who can identify isolated words through narrow filters have better suprathreshold abilities to extract auditory cues than listeners who require broader filter bandwidths to achieve the same level of word-recognition performance (Noordhoek *et al.*, 1998, 1999).

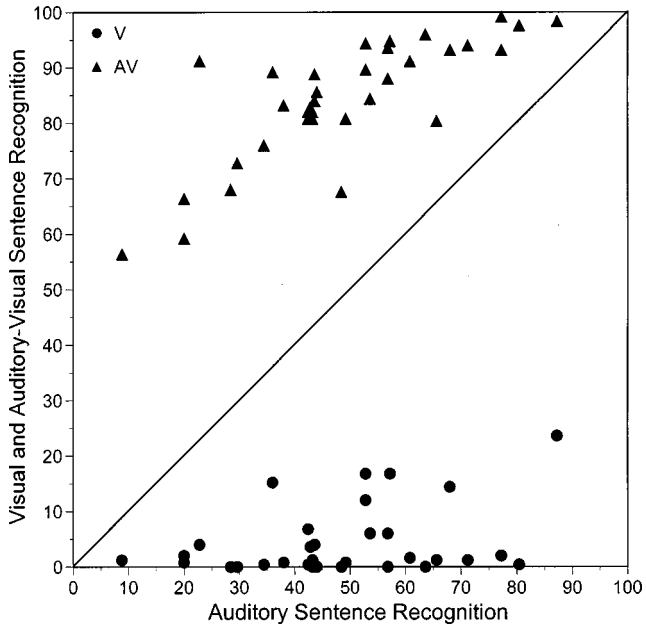

FIG. 5. Sentence recognition in noise measured at 0 dB S/N for auditory, visual, and auditory–visual conditions. Filled circles=*V* condition; filled triangles=auditory–visual condition. The location of any symbol with respect to the abscissa shows the score for the auditory condition.

To determine whether an individual's k value is useful in explaining some of the individual differences typically observed in sentence-recognition tasks, three separate stepwise multiple linear regression analyses were carried out with sentence recognition for each of the three modalities (auditory, visual, and auditory–visual) as dependent variables and with k, age, high-frequency hearing loss (3–8 kHz), and filter bandwidth determined in the tracking tasks as independent variables. Not surprisingly, auditory factors presumably related to acoustic cue extraction (i.e., high-frequency puretone thresholds and filter bandwidth) were significantly correlated with both auditory and auditory–visual sentence recognition. For the visual-only condition, age was the most important factor whereas hearing loss and filter bandwidth did not contribute significantly to the amount of variance explained. Importantly, however, the mean k values for each

TABLE II. Predicting sentence recognition (P_s) in noise. Equations indicate final subset model from a multilinear forward stepwise linear regression ($\alpha = 0.15$). Predictor variables were age, average high-frequency hearing loss from 3–8 kHz (HL), mean *k* value, filter 1 bandwidth (*F*1), filter 2 bandwidth (*F*2), and filter 3 bandwidth (*F*3). The amount of variance explained by each factor is also shown (in percent).

	Predictors	Variance	*F* value	*p* value
I. Auditory sentence recognition in noise				
$P_s = C + 21.106k - 0.558\text{HL} - 0.012F2$				
($r^2 = 0.498$, $p < 0.001$)	HL	33.3	11.5562	0.0019
	k	13.3	7.9260	0.0085
$C = 51.248$	*F*2	3.2	4.2737	0.0474
II. Visual sentence recognition				
$P_S = C + 5.252k - 0.262\text{age}$				
($r^2 = 0.316$, $p < 0.003$)	Age	23.6	10.4735	0.0029
	k	8.0	3.6111	0.0667
$C = 12.724$				
III. Auditory–visual sentence recognition in noise				
$P_S = C + 14.704k - 0.370\text{HL} - 0.009F1$				
($r^2 = 0.564$, $p < 0.0001$)	HL	33.8	17.8620	0.0002
	k	19.4	13.3227	0.0010
$C = 81.158$	*F*1	3.2	3.1186	0.876

subject (averaged over the three filter conditions) remained a significant factor in the final subset model for all three modalities.[4] Approximately 50% of the variance in the auditory-alone condition and approximately 56% of the variance in the auditory–visual condition could be accounted for with each individual subject's average *k*, better ear high-frequency hearing loss (average pure-tone thresholds from 3–8 kHz), and filter 2 bandwidth and filter 1 bandwidth, respectively (see Table II). In both of these conditions, hearing loss was the far more important factor accounting for between 33%–34% of the variance. The proportion of total variance accounted for by *k* was 19.4% for the auditory–visual condition and 13.3% for the auditory condition. In the visual-only condition, age and average *k* accounted for roughly 32% of the variance. Here too, *k* accounted for relatively little variance (8%) with age accounting for 23.6% of the total variance explained.

III. DISCUSSION AND CONCLUSIONS

There can be little doubt that sentence context facilitates word recognition and examples are readily found in the literature. For instance, in the ANSI standard for calculating the articulation index (ANSI, 1969), Fig. 15 (p. 23) shows that the recognition of words when presented in isolation versus meaningful sentences at a fixed signal-to-noise ratio can vary by over 50 percentage points, depending on the speech materials. Even when the words are physically identical, as in the present experiment, recognition rates for words in sentences were between 14%–30% better than for words presented in isolation. As Boothroyd and Nittrouer (1988) noted, this facilitation occurs for at least two basic reasons: (1) within a word, lexical redundancy serves to reduce the ambiguity of a given phoneme based on a knowledge of its position within the word and the phonemes surrounding it, and (2) within a sentence, the identity of a target word can be guessed with better than chance accuracy because of semantic and morpho-syntactic constraints imposed by the words preceding and following it. Lexical redundancy is primarily responsible for facilitating word recognition relative to nonsense words or isolated syllables (Boothroyd and Nittrouer's *j* factor), whereas semantic and morpho-syntactic redundancy is primarily responsible for facilitating the recognition of words in sentence relative to words in isolation (Boothroyd and Nittrouer's *k* factor).

Past work on the facilitating effects of intra- and inter-word redundancy has focused primarily on differences across materials. Far fewer studies have focused on the possibility that individuals differ with respect to the amount of facilitation derived from these different sources of linguistic redundancy (*viz.*, Lyxell and Rönnberg, 1987a, 1987b, 1989; Rönnberg *et al.*, 1998 for exceptions). In the present study, isolated-word and word-in-sentence recognition scores based on 500 items each were used to derive *k* estimates. Further, three such estimates were made for each subject at different levels of isolated word intelligibility. The large number of trials per subject, although clinically unfeasible, was nevertheless deemed necessary to stabilize individual performance.

Given our overall objective of obtaining estimates of subject ability to make use of sentence context and applying this information to predict sentence-recognition scores, the first point to be established was that individuals do indeed vary in the amount of facilitation derived from sentence context, and that the positioning among individual subjects (good to poor users of context) was relatively stable for different conditions of distortion. Results showed a range of individual *k* values averaged across intelligibility (i.e., filter condition) between 1.2 and 2.5. This represents a large range in the amount of information derived from sentence context when viewed in terms of additional channels of information (Boothroyd and Nittrouer, 1988). Thus, individuals clearly differ with regard to the amount of contextual facilitation they can achieve.

An important question regarding the estimates of subjects' ability to make use of sentence context pertains to the stability of the measurements. If *k* reflects a specific factor or

primary ability of subjects to use context to facilitate word recognition, then the rank ordering of individuals with respect to *k* should not vary with changes in task difficulty. The significant correlation of *k* values across filter conditions implies that the ordering of subjects with regard to their ability to make use of context cues was fairly stable. The correlation between filter conditions 1 and 2 ($r=0.78$) has the greatest reliability because the isolated word scores fell within the region most sensitive for demonstrating differences in *k* values (see Fig. 1). Correlations involving filter condition 3 are more suspect because several of the *k* estimates for this filter condition were compromised by ceiling effects (due to perfect performance for the recognition of words in sentences). Nevertheless, the remaining two correlations (filter 1 versus filter 3 and filter 2 versus filter 3) were also significant, though somewhat more modest. Thus, using *k* as a measure of an individual subject's ability to use context to facilitate word recognition appears to be stable across several conditions of distortion.

Like most measures of human perceptual performance, *k* is subject to the effects of different test methodologies. Thus, whereas the relative position of an individual with respect to other subjects was fairly stable (good context users were good regardless of test condition), the absolute amount of contextual facilitation depended on how the measurements were made. Even with no feedback, a large stimulus set size, and an open response format, subjects showed a strong learning effect depending on whether they received isolated words first or sentences first. In the recent study by Olsen *et al.* (1997), where sentence tests were administered immediately following isolated word tests, we would have to conclude that their *k* estimates may be somewhat high. One implication of the learning effects associated with test order is that the estimates of isolated words correct and words in sentences should be carried out with lists that do not contain the same words but that have been pretested to be of equal expected mean performance levels.

In addition to being subject to the effects of test order, *k* estimates also depend on the isolated word-recognition score, unlike the theoretical functions described by Boothroyd and Nittrouer (1988). Specifically, *k* decreased as isolated word recognition improved. A decrease in *k* was observed for 32 of 34 subjects when comparing the results for filter 1 versus filter 2. Thus, it appears that listeners compensate for reduced stimulus information by increasing their reliance on contextual information. Similar conclusions have been reached for read and spoken word recognition, especially under conditions of stimulus distortion (Stanovich and West, 1979; Cohen and Faulkner, 1983; Wingfield *et al.*, 1985; Madden, 1988; Ben-Dror *et al.*, 1991). For example, Stanovich and West (1979) measured good and poor third-grade readers' ability to rapidly spot real words, pseudowords, and nonwords. Overall, search times were significantly longer for poor readers than for good readers. Moreover, the effect of orthographic structure, measured by the difference in search time between spotting real words versus pseudo-or nonwords, tended to be greater for the poorer readers. In another study, Stanovich and Pachella (1977) demonstrated that reaction times were more affected by stimulus probability (e.g., context) when the clarity of the stimulus was decreased. These results, as with the present results for aurally presented words, suggest that the various factors contributing to word recognition (visual or auditory peripheral analyses, use of lexical redundancy, semantic constraints, morpho-syntactic constraints, etc.) may be employed flexibly so that a reduction in one process can be compensated for by greater reliance on other processes. In other words, as the stimulus becomes degraded (reduced bottom-up information) there is a tendency for subjects to rely more heavily on top-down information. The fact that the vast majority (32 of 34) of subjects had higher *k* values for filter 1 than for filter 2 suggests that the tendency to rely less on contextual information as signal clarity improves is common to individual hearing-impaired listeners in spite of large differences in the amount of hearing loss and age.

In a review article, Elliott (1995) equated the ability to use contextual information in speech to that of verbal auditory closure. Elliot further suggested that if this ability represented a primary factor of human perceptual behavior, it should provide useful information regarding an individual's speech comprehension skill. In terms of the present experiment, this means that *k*, to the extent that it is modality independent, should help explain some of the differences in auditory, visual, and auditory–visual speech recognition. This was demonstrated by multiple stepwise regression in which an attempt was made to predict auditory, visual, or auditory–visual sentence-recognition scores using a number of different subject variables such as age, hearing loss, filter bandwidth, and *k*. The final subset model for each modality included *k*, indicating that the ability to use semantic and morpho-syntactic constraints in sentences is a significant subject factor in predicting speech recognition regardless of the test modality. By including the average *k* value with the other factors listed in Table I, the amount of variance accounted for was increased by approximately 13%, 8%, and 19% for auditory, visual, and auditory–visual conditions, respectively. Whereas the amount of variance that can further be explained by adding context to other subject variables may be relatively small, it is nevertheless a significant factor in explaining some of the intersubject variability in sentence recognition.

This last point deserves additional comment. In speech recognition and in reading, the ability to use one's knowledge of the language to compensate for missing or incomplete signal information has been regarded as an important factor in explaining individual differences in performance. Whereas individual *k* values were significant factors in determining speech-recognition performance, the amount of variance explained was moderate to small. This may have been due to the conditions under which the speech-recognition scores were obtained. Recall that the speech materials were presented at approximately 85 dB SPL and 0 dB S/N for all subjects with no adjustments for the varying amounts of hearing loss across the study group. Thus, it is likely that individual differences in signal audibility existed across subjects for the auditory and auditory–visual conditions. Because differences in audibility have been shown repeatedly to be a dominant factor in predicting speech-

recognition performance, the importance of intersubject differences in the ability to use contextual information might have been reduced. Had the sentence-recognition tests been conducted at different levels depending on the subjects hearing status, so that the speech was equally audible for all subjects, the amount of variance explained by *k* might have been larger.

Another important factor to consider when interpreting the results of the regression analyses is that *k* values were obtained under rather constrained conditions (auditory only, concatenated ''unnatural'' sentences). It is possible that in addition to being dependent on the specific speech corpus and perceiver attributes, *k* may also be dependent on modality. Therefore, predicting visual and auditory–visual performance from auditory derived *k* factors may have led to an underestimate of the association. However, at present we know of no data to suggest that the knowledge base used when employing contextual information in speech recognition is in any way different across modalities. In fact, the premise of the present experiment that led us to construct concatenated sentence materials was that once certain stimulus variables, like coarticulation and prosody, were controlled so that the stimulus information for words in isolation and words in sentences were identical, any differences observed in the recognition rates would have to be ascribed to use of higher-order processes that are essentially signal independent (and modality independent).

The amount of additional variance accounted for in the speechreading condition by individual *k* factors was only 8%. Given that all subjects had normal or corrected-normal vision, why might this be so? One possibility is that the speechreading scores were extremely low overall and rather skewed. Thus, the limited range of speechreading scores may have compromised the regression analysis and produced an artificially low correlation between *k* values and speechreading scores. Another possibility is that speechreaders have particular difficulty extracting prosodic cues, such as word boundaries, creating greater ambiguity when confronted with sentences rather than isolated word productions (Erber and McMahon, 1978). Thus, the problem for the speechreader is primarily related to the extraction of relevant signal cues and not one of deployment of higher-level knowledge sources regarding semantic and syntactic information. Under this interpretation, it is not surprising that measures pertaining to a subject's ability to make use of context would have little to do with overall speechreading scores.

It is also well established that individual differences in speechreading ability are known to be quite substantial across a variety of test materials (Demorest and Bernstein, 1992; Watson *et al.*, 1996) despite ''normal'' visual acuity. In these studies, normal or corrected-normal visual acuity was assumed based on subject reports. In the present study, subjects passed a visual screening (Snellen chart) with 20/30 or better visual acuity. However, this measure was taken at a distance of 20 ft, whereas all visual speech testing was done at approximately 5 ft. It is possible that the subjects may have exhibited different degrees of visual acuity at this closer distance.

In addition to possible visual acuity deficits, a predominant factor in visual speech recognition seems to be age. In the present study, age accounted for approximately 24% of the variance in *V* scores. Aging is known to have detrimental effects on visual function, especially with regard to motion detection and contrast sensitivity (Wood and Bullimore, 1995). It is possible that there are substantial individual differences related to these visual measures within the study group. Thus, heterogeneity in basic visual function impacts speechreading performance and limits the extent to which we can observe the effects of differences in individual *k* factors. In future studies, it may be necessary to screen more carefully for visual anomalies in elderly subjects before presuming normal visual acuity.

IV. SUMMARY

Word recognition in sentences is determined by a number of factors including the ability to recognize phonemes (auditorily and /or visually), the ability to integrate cues across modality (under auditory–visual conditions), the ability to use intraword redundancy (lexical redundancy), and the ability to use semantic and morpho-syntactic constraints in sentence contexts (Boothroyd and Nittrouer's *k* factor). The present study focused on the role of sentence context in facilitating word recognition and whether understanding an individual subject's ability to use context would help explain some of the variability commonly observed in speech communication. The results indicated that the use of sentence context to facilitate word recognition varies substantially across hearing-impaired subjects. Furthermore, subjects with high *k* factors performed slightly better than subjects with lower *k* factors on sentence recognition in all three receiving modalities (auditory, visual, and auditory–visual). The *k* factor for an individual depends to a large degree on the speech materials used in the test, as shown in earlier studies. But it also depends on the order in which isolated words or words in sentences are presented, as well as on the clarity of the signal information available to each subject, at least for isolated word recognition scores between 29%–75% correct.

ACKNOWLEDGMENTS

Portions of this research were presented at the 134th Meeting of the Acoustical Society of America, San Diego, CA, 3 December 1997 [Grant, K. W., and Seitz, P. F. (1997). ''The recognition of isolated words and words in sentences: Individual variability in the use of sentence context,'' J. Acoust. Soc. Am. **102**, 3132.] This research was supported by Grant Numbers DC00792 and DC01643 from the National Institute of Deafness and Other Communication Disorders to Walter Reed Army Medical Center, and by the Clinical Investigation Service, Walter Reed Army Medical Center, under Work Unit # 2548. All subjects participating in this research provided written informed consent prior to beginning the study. We would like to thank James Hillenbrand, Arthur Boothroyd, and two anonymous reviewers for their helpful comments and suggestions. The opinions or assertions contained herein are the private views of the authors and are not to be construed as official or as reflecting the

views of the Department of the Army or the Department of Defense.

[1]Solving for k in Eq. (3) gives $k=\log(1-P_s)/\log(1-P_w)$, where the quantity $(1-P_s)$ is the error rate for words presented in sentences and $(1-P_w)$ is the error rate for words presented in isolation.

[2]Words spoken in isolation and in sentences differ with respect to many variables. In sentences, words tend to be shorter in duration, are influenced by coarticulation and prosody, and undergo numerous phonological transformations (e.g., vowel neutralization and phonetic substitutions, as in the transformation from ''Did you eat?'' [/dɪd yu it/] to ''Jueet?'' [/dʒit/]). This study minimized these differences across materials by concatenating isolated words to form sentences, thus eliminating these complex transformations and ensuring that differences in the intelligibility of isolated words and sentences were due mainly to semantic and morpho-syntactic context.

[3]Another option for keeping words in isolation and words in sentences physically identical was to excise words from naturally spoken sentences (Wingfield *et al.*, 1994). However, subjective impressions of the two methods (concatenated words versus excised words) led us to believe that the former method would be better tolerated and appear more natural to hearing-impaired subjects.

[4]Of special interest is the fact that hearing loss (pure-tone averages at 0.5, 1, and 2 kHz, 2–8 kHz, 3–8 kHz, or individual tonal thresholds at 1 and 2 kHz) and average k were uncorrelated ($-0.017<r<0.059$). This lends further support that k reflects an ability of individual subjects to make use of higher-level language constraints independent of stimulus quality.

American National Standards Institute (ANSI) **(1969)**. ''American National Standard Methods for the Calculation of the Articulation Index,'' ANSI S3.5-1969, American National Standards Institute, New York.

American National Standards Institute (ANSI) **(1989)**. ''Specifications for Audiometers,'' ANSI S3.6-1989, American National Standards Institute, New York.

Ben-Dror, I., Pollatsek, A., and Scarpati, S. (**1991**). ''Word identification in isolation and in context by college dyslexic students,'' Brain Lang. **40**, 471–490.

Bilger, R. C., Nuetzel, J. M., Rabinowitz, W. M., and Rzeckowski, C. (**1984**). ''Standardization of a test of speech perception in noise,'' J. Speech Hear. Res. **27**, 32–48.

Boothroyd, A., Hnath-Chislm, T., and Hanin, L. **(1985)**. ''A sentence test of speech perception: Reliability, set-equivalence, and short-term learning,'' City University of New York, Report Number RCl10.

Boothroyd, A., and Nittrouer, S. (**1988**). ''Mathematical treatment of context effects in phoneme and word recognition,'' J. Acoust. Soc. Am. **84**, 101–114.

Cohen, G., and Faulkner, D. (**1983**). ''Word recognition: age differences in contextual facilitation effects,'' Br. J. Psychol. **74**, 239–251.

DeFilippo, C. L. (**1990**). ''Speechreading training: Believe it or not!,'' ASHA **32**, 46–48.

Demorest, M. E., and Bernstein, L. E. (**1992**). ''Sources of variability in speechreading sentences: A generalizability analysis,'' J. Speech Hear. Res. **35**, 876–891.

Elliott, L. L. (**1995**). ''Verbal auditory closure and the speech perception in noise (SPIN) Test,'' J. Speech Hear. Res. **38**, 1363–1376.

Erber, N. P. (**1996**). *Communication Therapy for Adults with Sensory Loss*, 2nd ed. (Clavis, Clifton Hill, Victoria, Australia).

Erber, N. P., and McMahon, D. A. (**1978**). ''Effects of sentence context on the recognition of words through lipreading by deaf children,'' J. Speech Hear. Res. **19**, 112–119.

Grant, K. W., and Seitz, P. F. (**1998**). ''Measures of auditory–visual integration in nonsense syllables and sentences,'' J. Acoust. Soc. Am. **104**, 2438–2450.

Grant, K. W., and Walden, B. E. (**1996**). ''Evaluating the articulation index for auditory–visual consonant recognition,'' J. Acoust. Soc. Am. **100**, 2415–2424.

Grant, K. W., Walden, B. E., and Seitz, P. F. (**1998**). ''Auditory–visual speech recognition by hearing-impaired subjects: Consonant recognition, sentence recognition, and auditory–visual integration,'' J. Acoust. Soc. Am. **103**, 2677–2690.

Humes, L. E., Watson, B. U., Christensen, L. A., Cokely, C. G., Halling, D. C., and Lee, L. (**1994**). ''Factors associated with individual differences in clinical measures of speech recognition among the elderly,'' J. Speech Hear. Res. **37**, 465–474.

Hutchinson, K. M. (**1989**). ''Influence of sentence context on speech perception in young and older adults,'' J. Gerontol. **44**, 36–44.

Institute of Electrical and Electronic Engineers **(1969)**. *IEEE Recommended Practice for Speech Quality Measures* (IEEE, New York).

Kalikow, D. H., Stevens, K. N., and Elliott, L. L. (**1977**). ''Development of a test of speech intelligibility on noise using sentence materials with controlled word predictability,'' J. Acoust. Soc. Am. **61**, 1337–1351.

Lyxell, B., and Rönnberg, J. (**1987a**). ''Guessing and speechreading,'' Br. J. Audiol. **21**, 13–20.

Lyxell, B., and Rönnberg, J. **(1987b)**. ''Necessary cognitive determinants for speechreading skills,'' in *Adjustment to Acquired Hearing Loss: Analysis, Change, and Learning*, edited by J. G. Kyle (Anthony Row, Chippenham, Witshire), pp. 48–54.

Lyxell, B., and Rönnberg, J. (**1989**). ''Information processing skills and lipreading,'' Br. J. Audiol. **23**, 339–347.

Madden, D. J. (**1988**). ''Adult age differences in the effect of sentence context and stimulus degradation during visual word recognition,'' Psychol. Aging **3**, 167–172.

Massaro, D. M. **(1987)**. *Speech Perception by Ear and Eye: a Paradigm for Psychological Inquiry* (Erlbaum, Hillsdale, NJ).

Miller, G. A., Heise, G. A., and Lichten, W. (**1951**). ''The intelligibility of speech as a function of the context of the test material,'' J. Exp. Psychol. **41**, 329–335.

Montgomery, A. A., and Demorest, M. **(1988)**. ''Issues and developments in the evaluation of speechreading,'' in *New Reflections on Speechreading*, edited by C. DeFilippo and D. Sims (A. G. Bell Association for the Deaf, Washington, DC), pp. 193–214.

Nittrouer, S., and Boothroyd, A. (**1990**). ''Context effects in phoneme and word recognition by young children and older adults,'' J. Acoust. Soc. Am. **87**, 2705–2715.

Noordhoek, I. M., Houtgast, T., and Festen, J. M. (**1999**). ''Measuring the threshold for speech reception by adaptive variation of the signal bandwidth. I. Normal-hearing listeners,'' J. Acoust. Soc. Am. **105**, 2895–2902.

Noordhoek, I. M., Houtgast, T., and Festen, J. M. (**1998**). ''Minimum bandwidth required for speech reception by normal-hearing and hearing-impaired listeners,'' J. Acoust. Soc. Am. **103**, 3051.

Olsen, W. O., Van Tasell, D. J., and Speaks, C. E. (**1997**). The Carhart Memorial Lecture, American Auditory Society, Salt Lake City, Utah 1996. ''Phoneme and word recognition for words in isolation and in sentences,'' Ear Hear. **18**, 175–88.

Rabinowitz, W. M., Eddington, D. K., Delhorne, L. A., and Cuneo, P. A. (**1992**). ''Relations among different measure of speech reception in subjects using a cochlear implant,'' J. Acoust. Soc. Am. **92**, 1869–1881.

Rönnberg, J., Samuelsson, S., and Lyxell, B. **(1998)**. ''Conceptual constraints in sentence-based lipreading in the hearing-impaired,'' in *Hearing by Eye II: The Psychology of Speechreading and Audiovisual Speech*, edited by R. Campbell, B. Dodd, and D. Burnham (Erlbaum, Mahwah, NJ), pp. 143–153.

Schum, D. J., and Matthews, L. J. (**1992**). ''SPIN test performance of elderly hearing-impaired,'' J. Am. Acad. Audiol. **3**, 303–307.

Stanovich, K. E., and Pachella, R. G. (**1977**). ''Encoding, stimulus-response compatibility, and stages of processing,'' J. Exp. Psychol. Hum. Percept. Perform. **3**, 411–421.

Stanovich, K. E., and West, R. F. (**1979**). ''The effect of orthographic structure on the word search performance of good and poor readers,'' J. Exp. Child Psychol. **28**, 258–267.

Sumby, W. H., and Pollack, I. (**1954**). ''Visual contribution to speech intelligibility in noise,'' J. Acoust. Soc. Am. **26**, 212–215.

Watson, C. S., Weiguang, Q., Chamberlain, M. M., and Xiaofeng, L. (**1996**). ''Auditory and visual speech perception: Confirmation of a modality-independent source of individual differences in speech recognition,'' J. Acoust. Soc. Am. **100**, 1153–1162.

Wingfield, A., Poon, L. W., Lombardi, L., and Lowe, D. (**1985**). ''Speed of processing in normal aging: Effects of speech rate, linguistic structure, and processing time,'' J. Gerontol. **40**, 579–585.

Wingfield, A., Alexander, A. H., and Cavigelli, S. (**1994**). ''Does memory constrain utilization of top-down information in spoken word recognition? Evidence from normal aging,'' Lang. Speech **37**, 221–235.

Wood, J. M., and Bullimore, M. A. (**1995**). ''Changes in the lower displacement limit for motion with age,'' Ophthalmic Physiol. Opt. **15**, 31–36.

Suprasegmental and segmental timing models in Mandarin Chinese and American English

Jan P. H. van Santen[a] and Chilin Shih
Lucent Technologies Bell Laboratories, 700 Mountain Avenue, Room 2D-431, Murray Hill, New Jersey 07974-0636

(Received 12 March 1998; revised 15 July 1999; accepted 15 October 1999)

This paper formalizes and tests two key assumptions of the concept of suprasegmental timing: *segmental independence* and *suprasegmental mediation*. Segmental independence holds that the duration of a suprasegmental unit such as a syllable or foot is only minimally dependent on its segments. Suprasegmental mediation states that the duration of a segment is determined by the duration of its suprasegmental unit and its identity, but not directly by the specific prosodic context responsible for suprasegmental unit duration. Both assumptions are made by various versions of the *isochrony hypothesis* [I. Lehiste, J. Phonetics **5**, 253–263 (1977)], and by the *syllable timing hypothesis* [W. Campbell, Speech Commun. **9**, 57–62 (1990)]. The validity of these assumptions was studied using the syllable as suprasegmental unit in American English and Mandarin Chinese. To avoid unnatural timing patterns that might be induced when reading carrier phrase material, meaningful, nonrepetitive sentences were used with a wide range of lengths. Segmental independence was tested by measuring how the average duration of a syllable in a fixed prosodic context depends on its segmental composition. A strong association was found; in many cases the increase in average syllabic duration when one segment was substituted for another (e.g., *bin* versus *pin*) was the same as the difference in average duration between the two segments (i.e., [b] versus [p]). Thus, the [i] and [n] were not compressed to make room for the longer [p], which is inconsistent with segmental independence. Syllabic mediation was tested by measuring which locations in a syllable are most strongly affected by various contextual factors, including phrasal position, within-word position, tone, and lexical stress. Systematic differences were found between these factors in terms of the intrasyllabic locus of maximal effect. These and earlier results obtained by van Son and van Santen [R. J. J. H van Son and J. P. H. van Santen, ''Modeling the interaction between factors affecting consonant duration,'' Proceedings Eurospeech-97, 1997, pp. 319–322] showing a three-way interaction between consonantal identity (coronals vs labials), within-word position of the syllable, and stress of surrounding vowels, imply that segmental duration cannot be predicted by compressing or elongating segments to fit into a predetermined syllabic time interval. In conclusion, while there is little doubt that suprasegmental units play important predictive and explanatory roles as phonological units, the concept of suprasegmental timing is less promising. [S0001-4966(00)01202-9]

PACS numbers: 43.72.Ar, 43.72.Ja, 43.70.Fq, 43.70.Pf, 43.71.Hw [JLH]

INTRODUCTION

In most research on timing in speech, results are reported in the form of the effects of various contextual factors on segmental duration (Crystal and House, 1988a, 1988b, 1988c; Klatt, 1976; Umeda, 1975, 1977; van Santen, 1992). These contextual factors typically involve features of phonological units: prominence of *words*, locations of *words* in *phrases*, and stress of *syllables*. While there is little disagreement about the validity of these factors, the emphasis on segmental duration as the focus of timing research has been called into question for various reasons.

First (Olive *et al.*, 1993), the definitions of certain segmental boundaries are either unclear, as in glide to vowel transitions, or somewhat arbitrary, as in vowel to nasal transitions, where the acoustic correlates of the oral closure are used rather than the opening of the velic port.

Second, phenomena in speech that appear complicated when studied at the surface level can often be understood at the articulatory level (Browman and Goldstein, 1990; Coleman, 1992; Stevens and Bickley, 1991), in particular in terms of asynchronies between articulatory gestures. In fact, the deletion or insertion of segments in certain contexts certainly poses a problem for segmental duration modeling, yet can be explained easily in such articulatory terms.

Third, since contextual factors rarely cause uniform changes in a segment, timing should be studied at the subsegmental level. For example, certain contextual factors (e.g., phrase boundaries) have a nonuniform effect on the time course of a segment (Edwards and Beckman, 1988; de Jong, 1991), where later parts of the segment are increasingly more expanded when we compare phrase-final with phrase-medial positions. Likewise, it is known that the durations of steady-state and glide parts of certain diphthongs are affected differently by the same contextual factors (Gay,

[a]Current address: Oregon Graduate Institute, 20000 NW Walker Road, Beaverton, Oregon 97006; electronic mail: vansanten@ece.ogi.edu

1968; Hertz, 1990; van Santen *et al.*, 1992; van Santen, 1996).

While these first three reasons are based on indisputable facts, the fourth—suprasegmental timing—is of a more theoretical nature. Here, it is claimed that one should focus on durations of phonological units larger than the phoneme (suprasegmental units) such as syllables (Campbell, 1990; Campbell and Isard, 1991; Campbell, 1992), feet (Lehiste, 1977), or interperceptual center groups, or intervals spanner between the onsets of successive words (IPCGs) (Barbosa and Bailly, 1995). The basis for this claim is the hypothesis that speakers tend to impose [(Campbell and Isard, 1991), p. 37] ''higher-level rhythmic regularity'' on speech, meaning that they control the durations of suprasegmental units with more precision than segmental duration. If one focuses on segmental duration, one cannot capture these suprasegmental regularities adequately. To illustrate, if it were the case that speakers keep the durations of feet constant (*isochrony*), then a system of segmental duration rules would have to incorporate total foot duration in their prediction of segmental duration, because otherwise it is difficult and certainly unprincipled to model segmental durations in such a way that the durations in a foot would be precisely constant. The obvious way to model segmental duration in the face of constant foot duration is to adjust segmental durations to fit into the constant foot interval.

In this paper, we are concerned with which factors do and do not affect the durations of suprasegmental units and their constituent segments. Isochrony can be viewed as a particularly extreme hypothesis, which states that no factors affect the durations of suprasegmental units. Less extreme hypotheses include Lehiste's version of the isochrony hypothesis according to which duration of a foot is affected by its internal structure (Lehiste, 1977), and the syllable timing hypothesis, according to which the duration of a syllable is affected by a host of prosodic factors (Campbell and Isard, 1991).

A factual basis for these suprasegmental hypotheses may come from what can be called *constituency effects* in timing (van Santen, 1997). For example, vowel duration can be shortened by 10% for every doubling of sentence length (van Santen, 1992); syllables are shorter in longer words (Klatt, 1976; Port, 1981; van Santen, 1992); vowels can be shorter when they are preceded by certain tautosyllabic consonant clusters than by single consonants (e.g., the /t/ is longer in ''top'' than in ''stop.'') These and similar phenomena can be interpreted as a general trend for the duration of a unit (e.g., word) to decrease as the number of units in the larger unit (e.g., sentence) increases.

The common hypothesis underlying the work by Campbell, Bailly, and Lehiste is that some of these constituency effects can be best understood by speakers attempting to keep constant the actual durations of the suprasegmental units. Thus syllables are shortened in longer words because speakers tend to keep overall word duration (or foot duration, with which word duration is statistically correlated) constant. To put this idea in perspective, we mention some alternative hypotheses that might explain constituency effects.

First, it might be that these constituency effects have little to do with the numbers of units contained in larger units but are the result of boundary phenomena. Most syntactic boundaries cause some degree of lengthening in preboundary syllables (Klatt, 1975), and, by logical necessity, there are fewer units affected by boundary lengthening effects in a larger unit. Second, the /t/ being shorter in stop than in top can better be characterized as involving an (unaspirated) allophone of /t/ due to being preceded by /s/; it is unlikely that the duration of /t/ will be influenced much, if at all, when we change top into the syllable ''torn,'' whose rhyme is likely to be longer by an amount roughly equal to the duration of /s/.

In summary, some of these claimed constituency effects may not exist, while as a group they may be quite heterogeneous and involve factors unrelated to the concept of constituency. Hence, there may not be much need for the ability of suprasegmental timing hypotheses to provide a unified explanation of these effects.

Although the empirical case for suprasegmental timing in the form of these constituency effects is not strong, recent developments in text-to-speech systems have produced new interest in suprasegmental timing. A key reason for this is the following. Prediction of timing in earlier text-to-speech systems involved rules that were based on separate empirical studies in each of which the effects of a small number of factors was measured. Typical rules were of the type ''lexical stress increases vowel duration by 35%.'' In the system, rules such as these were applied successively, starting with an intrinsic phoneme duration (Allen *et al.*, 1987). The obvious drawback is that one cannot infer from separate studies how factors interact whose joint effects were not measured in a single experiment. In addition, experiments often involved different speakers, textual materials, and segmentation conventions, and hence have incompatibilities that endanger the meaningfulness of the resulting rule system. What was obviously needed were large, single-speaker speech corpora in which all factors vary. But when, after increases in computer power and storage, such speech corpora became available, new problems were encountered. Because prediction of segmental durations depends on many interacting factors, and the sizes of carefully labeled and segmented speech corpora are necessarily still limited, *sparsity problems* arose (van Santen, 1994, 1997): the number of context–phoneme combinations that can occur in the language is astronomic, and cannot be covered by any reasonably sized corpora.

Under the syllable timing hypothesis, described in more detail below, sparsity becomes a significantly lesser issue. According to this hypothesis, durations of syllables are largely independent of the particular phonemes they contain, while durations of segments depend on their larger prosodic context only through the precomputed overall syllable duration; one does not have to model how a particular phoneme (e.g., /t/) behaves in a particular prosodic context (e.g., stressed phrase-final syllable). This drastically reduces the sparsity of the data, because the feature space has become much smaller by the elimination of the interaction between prosodic factors that do not directly affect segments and phonemic factors that hardly affect syllable durations.

A key role in the introduction of suprasegmental timing

in speech synthesis has been played by the *syllable timing model* (Campbell and Isard, 1991; Campbell, 1992). The important contribution of this model is that it is the first explicit formalization of the suprasegmental timing idea. Our aim here, however, is not to narrowly focus on the details of this model, but to formalize and then test its broader underlying assumptions. In addition, the logic that we develop should be applicable to any larger unit, including the foot.

I. OVERVIEW OF THE PAPER

We have performed our analyses for two languages, Mandarin Chinese and American English, and anticipate performing similar analyses for other languages, once appropriate data become available. The two languages differ in some key issues pertaining to the current study: English is a stress language (and reportedly a stress-timed language where the duration of stress groups is relatively constant), while Mandarin is a tone language (and reportedly a syllable-timed language where syllable duration is relatively constant). English has a complicated syllable structure, with consonant clusters both in the onset and coda position of a syllable, while Mandarin has simple syllable structure with heavy restrictions on coda consonants, disallowing intrasyllabic consonant clusters. No doubt, given the difference between these two languages, we expect to see language-specific aspects in the fine details of the results. But, what is more interesting is to see to what degree these two very different languages converge on the evidence supporting segmental timing.

It is extremely important to point out that in both languages we used meaningful sentences that varied significantly in length and syntactic structure. As a consequence, we avoided any of the artifacts that can be associated with recordings involving repeated sentences, or sentences consisting of a repeated carrier phrase having a ''slot'' that contains a target word that varies from one utterance to the next. It is not unlikely that certain positive findings (e.g., Port *et al.*, 1987) on suprasegmental unit duration constancy are caused in part by such speaking conditions, because they appear to encourage repetitive behavior from the speakers.

The outline of the paper is as follows. In the next section, Sec. I, we discuss the syllable timing model as proposed by Campbell and Isard (1991) and show that this model makes two broad assumptions: *segmental independence* and *syllabic mediation*. In Sec. III, we first develop the mathematical justification of our empirical tests of segmental independence, and then report results. Section IV has the same structure, and focuses on syllabic mediation.

II. SYLLABLE TIMING

A. The syllable timing model

We describe here the model as proposed in Campbell and Isard (1991), and then generalize it in Sec. II B. Barbosa and Bailly (1995) used the same model, but applied to IPCGs instead of to syllables. The model can be split up into two parts. First, a hypothesis about which factors affect the duration of a syllable; there is no explicit mathematical model here—these factors are used as input for a neural net. Second, a mathematical model specifying the durations of a segments given a precomputed syllabic duration.

1. Factors affecting and not affecting syllabic duration

According to Campbell (1990) and to Campbell and Isard (1991), the duration of a syllable depends on the following factors:

(1) Number of phonemes in the syllable.
(2) The nature of the syllabic peak (tense versus lax vowel versus diphthong versus sonorant consonant).
(3) Position of the syllable in the foot.
(4) Position of the syllable in the phrase and clause.
(5) Stress assigned to the syllable, and nature of pitch movement.
(6) Function/content role of the parent word.

We will call factors 3–6 the *prosodic factors*, and their joint combinations *prosodic contexts*. The key assumption here is the minimal dependence of syllabic duration on constituent segments (factors 1 and 2). Basically, these factors capture some measure of *phonological syllable length*, without specific reference to the identities and intrasyllabic locations of its segments.

This assumption predicts that in identical contexts (as characterized in terms of factors 3–6) the syllables ''lit'' and ''sit'' should have the same duration, because the number of phonemes is the same and the syllabic peaks are identical.

Note that if one includes a more detailed description of the segmental makeup of a syllable, the hypothesis becomes indistinguishable from segmental timing. Specifically, if we replace factors 1 and 2 by a full characterization of the identities and locations of all constituent segments, then the above factors contain all information required to compute segmental duration in the usual way [e.g., via Klatt's model (Allen *et al.*, 1987)], and we can then trivially compute syllable duration by adding up the predicted durations of the constituent segments.

We will refer to the assumption that syllabic duration depends on segments only through phonological syllable length as the segmental independence assumption.

2. Segmental duration

In applications of the model, syllabic durations are predicted using a neural net. The training data consist of a list of feature vectors and associated durations for each syllable in the corpus.

Now, suppose that for a given syllable $s = \langle p_1, p_2, \ldots, p_n \rangle$ (where the p_i's represent phonemes) in context c, the neural net predicts that the syllabic duration is given by some quantity of Δ ms. Thus

$$\mathrm{DUR}(s,c) = \mathrm{DUR}(\langle p_1, p_2, \ldots, p_n \rangle, c) = \Delta. \tag{1}$$

Let the mean and standard deviation of the log-transformed durations in the speech corpus of the segment p_i be denoted by μ_i and σ_i. Then, we can solve for k_s in the following equation:

$$\Delta = \sum_{i=1}^{n} e^{\mu_i + k_s \sigma_i}. \quad (2)$$

Once we have determined the solution for k_s, $k_s(\Delta)$, the duration of the ith segment is given by

$$\mathrm{DUR}(p_i, s, c) = e^{\mu_i + k_s(\Delta)\sigma_i}. \quad (3)$$

Here, $k_s(\Delta)$ is the (unique) solution to Eq. (2). Note that its value depends only on what the syllable is (s) and on the duration of the syllable (Δ), but not directly on the context (c) responsible for giving syllable s duration Δ. This follows because in Eq. (2) no reference is made to context c. Hence, when there are two contexts c and c' such that

$$\mathrm{DUR}(s, c) = \mathrm{DUR}(s, c'), \quad (4)$$

it follows that the resulting estimates for k_s must be the same, so that the durations of the individual segments must also be the same. Thus, when we find two occurrences of the same syllable (e.g., ''lit'' in phrase-medial stressed context vs phrase-final unstressed context; with some luck, they could have identical durations), then the durations of the /l/, /i/, and /t/ should be the same in both contexts.

The parameter σ_i is of some theoretical interest, because it allows for the possibility that phonetic segments vary in terms of *elasticity* (Campbell and Isard, 1991): Segments differ in terms of the amount of systematic variation of their durations. Whether this degree of freedom is needed to understand differences among phonemes belonging to the same class (e.g., vowels) is not certain, however. Elsewhere, we found that in American English all vowels are stretched and compressed by identical percentages by all factors considered in a large-scale study of duration (van Santen, 1992), yet the intrinsic durations of these vowels varied considerably.

There is a broader principle here, which is that segmental duration is completely determined by (1) a precomputed syllabic duration (Δ), and (2) its identity (p_i). We call this the *syllabic mediation assumption*.

Note that the particular version of this assumption in the model, via the parameters μ_i, k_s, and σ_i, is not critical. In fact, it would not matter at all if there were no relation between μ_i and the mean of the log-transformed durations of p_i. Also, note that it would not matter if we would annotate μ_i and σ_i by intrasyllabic-positional markers (e.g., $\mu_{1,\mathrm{onset}}$, $\sigma_{2,\mathrm{nucleus}}$, and $\mu_{1,\mathrm{coda}}$). What matters is the fact that segmental duration does not directly depend on context c, but only indirectly—via Δ.

While there are additional assumptions implicit in Eq. (2)—such as the assumption that it does not matter where in a syllable a segment occurs (e.g., no difference in the duration of /t/ in ''pit'' versus ''tip'')—these will not be addressed in this paper.

3. Amendments to the model

While the above formulation brings out the raw essence of the model, important modifications have been added by Campbell. We discuss here these amendments, and to what extent they change this essence.

The first amendment is that for phrase-final syllables, Eq. (2) is replaced by

$$\Delta = \sum_{i=1}^{n} e^{\mu_i + 0.75^{(n-i)} k_s \sigma_i}. \quad (5)$$

This is a significant relaxation of the syllabic mediation assumption. Now it does not predict that the durations of /l/, /i/, and /t/ should be the same in phrase-medial stressed context vs phrase-final unstressed context. This change was prompted, of course, by the well-known fact that phrase boundaries have a strongly asymmetric stretching effect on syllables, affecting the nucleus and coda much more than the onset.

The second amendment seems at first glance a technical detail—it was proposed (C92, p. 218) to change the estimated value of $k_s(\Delta)$, reducing its absolute value by a small quantity (0.075). Could it be that this modification makes it conceivable that syllables consisting of intrinsically short phonemes (such as /l/ are somewhat shorter than factors 3–6 dictate, and vice versa for syllables consisting of intrinsically long phonemes (such as /s/)? The result of that would be that there now would be a difference in duration between syllables lit and sit.

We strongly suspect that this is not the case, however. Suppose that, for some context c, the common predicted value of $\Delta(\text{''}pay\text{''}|c)$ and $\Delta(\text{''}say\text{''}|c)$ is 400 ms, the mean durations of /eɪ/, /s/, and /p/ are 135, 120, and 90 ms, respectively, and their standard deviations 45, 40, and 30 ms. Then, after taking the logarithms of these means and standard deviations, we find that $\hat{k}_{\mathrm{pay}} = 0.157$ and $\hat{k}_{\mathrm{say}} = 0.120$. When we subtract from this the correction quantity of 0.075, 0.157 changes into 0.082 and 0.120 changes into 0.045. Substituting these values for k_{pay} and k_{say} in the equations, we obtain $\Delta'(pay|c) = 303$ ms and $\Delta'(say|c) = 302$. We found the same results—less than 5-ms differences in either direction—over a wide range of values of the correction quantity (ranging from 0.004 687 5 to 1.2), and of Δ (125, 250, and 400 ms.) These counterexamples show that it is *not* the case that modification of the estimates of k allows the model to account for our finding reported below that the durations of $\Delta(pay|c)$ and $\Delta(say|c)$ differ, and certainly not for our finding that this difference is roughly equal to the difference between the average durations of /p/ and /s/ (30 ms).

B. The concept of syllable timing generalized

We elaborate on the syllable timing hypothesis using the diagrams in Fig. 1. These diagrams depict *functional relationships* (in the broad mathematical sense of the word ''function'') between factors (in rectangular boxes) and durations (enclosed by ellipsoids), with an arrow from A to B indicating that B *depends on* A.

This dependency relation is quite general, and includes subset relations [as between contextual factors and phrasal location in panel (b); the latter being a special case of the former], arithmetic relations [as between segmental duration and syllable duration in panel (c), the latter being the sum of the former], and factorial mappings [as between contextual

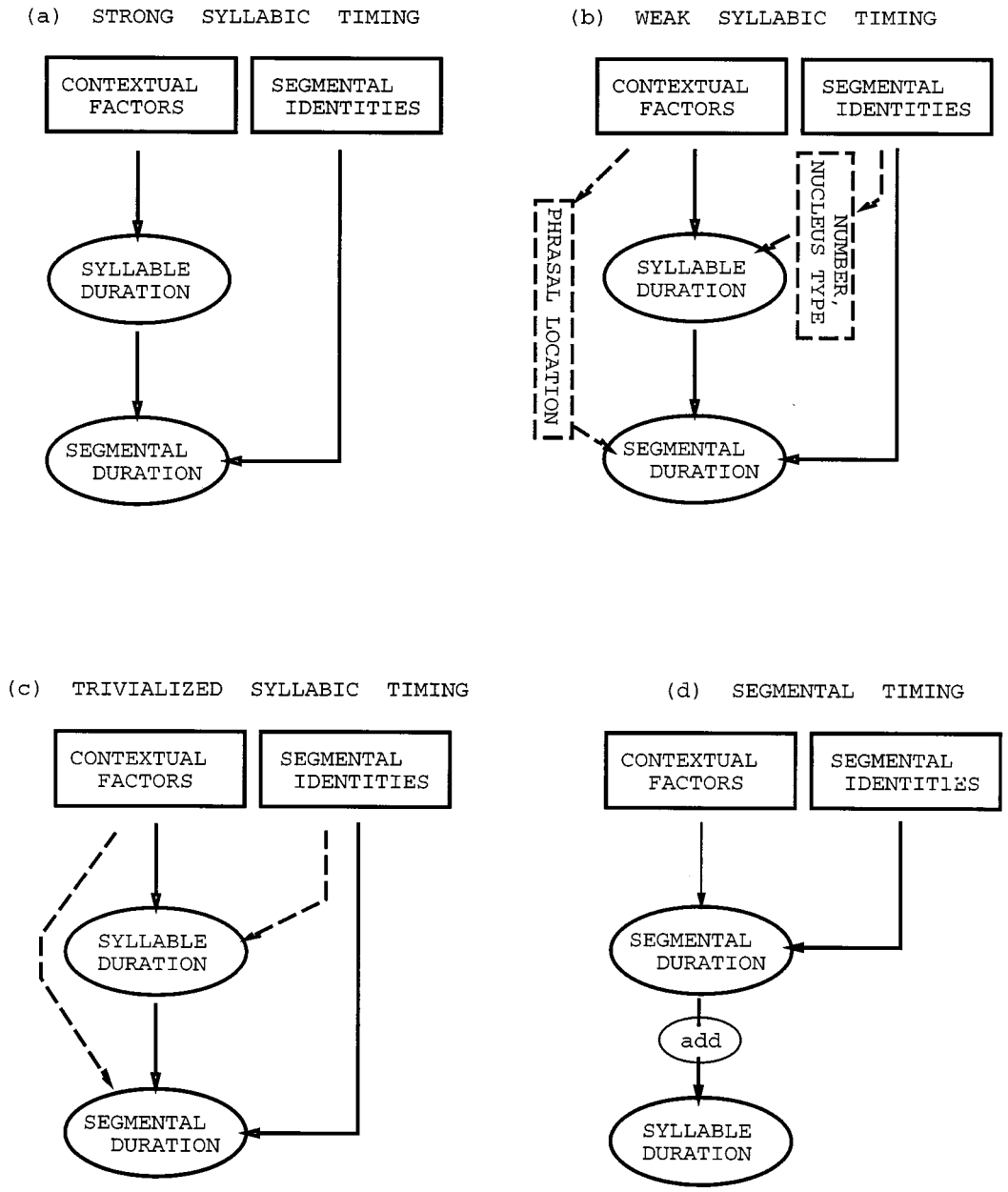

FIG. 1. Functional relations between a syllable and its segments.

factors and syllable duration in panel (a), the latter being computed from the former via duration rules, duration models, or neural nets].

Panel (a) shows the first version of the hypothesis (which we label the *strong syllabic liming hypothesis*, and is much stronger than either Campbell's or Barbosa and Bailly's proposals). It states that the duration of a syllable is completely independent of the segments it contains (which we call strong *segmental independence*), and that the duration of a segment in a syllable depends only on the duration of the syllable and the identity of the segments (which we call strong *syllabic mediation*). In other words, there is a set of *contextual factors* that has only indirect effects on segmental duration, via the syllable. This set consists of all factors affecting duration of the syllable and the segment, but excludes any factors derived from (or depending on) the segmental composition of the syllable. The effects of the contextual factors on segmental duration are completely mediated by the syllable, while the segmental factors have no effect on syllable duration.

However, as Campbell, and Barbosa and Bailly, were well aware, the strong syllable timing hypothesis is obviously wrong. First, syllables consisting of more segments have longer durations (e.g., the syllable ''string'' in the word ''stringing'' is longer than the syllable ''ring'' in the word ''ringing''). Hence, the duration of a syllable is not completely independent of its segments—at the very least, it depends on their number.

Second, two occurrences of the same syllable can have the same overall duration, yet the durations of the segments differ, contradicting the syllabic mediation assumption. For example, consider the syllable ''pin'' in phrase-final unstressed context versus in phrase-medial stressed context, and suppose that the two syllables have the same overall

durations—which is conceivable, because both stress and phrase-finality have lengthening effects. But when that happens, the [n] is likely to be longer in phrase-final unstressed pin than in phrase-medial stressed pin. Thus, segmental duration depends not only on syllable duration and segmental identity, but also on whether the syllable is phrase-final and stressed, and on the location of the segment within the syllable.

The second hypothesis [the weak syllable timing hypothesis; panel (b)] takes some of these facts into account, while preserving the overall structure of the strong syllable timing hypothesis (Campbell and Isard, 1991; Campbell, 1992). It is assumed that syllable duration is at least partly determined by segments (by their number and the type of nucleus), and that segmental duration is influenced directly by at least one contextual factor—phrasal location. In panel 1(b), this is accomplished by two ''bypasses.'' These additions lead to significant deviations from the strong syllabic timing hypothesis, but because of the limited amount of information flowing through the bypasses, strong constraints on speech timing remain.

The third diagram [panel (c)] assumes that the flow of information through these bypasses is not limited at all. Now, if all factors directly affect segmental duration, then, because the duration of a syllable can be computed by adding the durations of its segments, the third diagram can be simplified into the fourth diagram [panel (d)], which we labeled *segmental timing*. In this diagram the contextual factors are used to predict segmental duration directly, while syllable duration is the sum of all the segments contained therein.

In summary, the essence of the syllable timing hypothesis consists of the following two key assumptions:

(1) *Segmental independence*. The duration of syllable in a fixed context is only minimally dependent on its segmental composition.
(2) *Syllabic mediation*. The duration of any segment in a syllable can be predicted from the predicted duration of the syllable, the identity of the segment, and only minimal information about contextual factors.

The question addressed in this paper is not whether the strong syllable timing hypothesis is correct, because we know it is not. What is at stake is to what degree the segmental independence and syllabic mediation assumptions are incorrect—*how much* information flows through the bypasses.

III. SEGMENTAL INDEPENDENCE: EFFECTS OF INTRINSIC SEGMENTAL DURATION ON SYLLABLE DURATION

This section investigates the segmental independence assumption by *measuring relations between segmental and syllable durations for a fixed syllable structure in a fixed context*. By analyzing the relation between these two types of duration we will be able to draw strong conclusions about segmental independence, using the following argument.

Suppose that we analyze syllables that all occur in the same context, have the same syllable structure (including not only the number of segments but also their order, thereby distinguishing not only between a consonant followed by a vowel-(CV) and CVC but also between CVCC and CCVC), and have the same nucleus type. Then, the weak syllable timing hypothesis predicts that syllable duration should be constant except for random variability. This is the case because the only factor distinguishing between these syllables are the *details* of their segmental makeup such as whether a syllable starts with a [t] or a [b]; according to the weak syllable timing hypothesis, these details do not matter. If we then show that within this very restricted context, syllable duration nevertheless varies systematically with the intrinsic durations of constituent segments, this would be a powerful violation of this prediction. A similar logic was used by Beckman (1982), who showed that, in Japanese, segments are not shortened when other segments in the same mora have long intrinsic durations.

We are aware that analyzing correlations between durations is hazardous if we were to analyze durations of *individual occurrences*, because segmentation errors could induce positive correlations (Ohala and Lyberg, 1976). For example, when the left boundary of the ''*p*'' in pin is put too early in some specific occurrence of pin, and too late in another occurrence, then this will induce a positive correlation between the durations of ''*p*'' and pin. However, we analyzed correlations between *average* durations (interpreted as estimates of intrinsic durations), where each average was computed from many instances. Such correlations cannot easily be accounted for by segmentation errors, in particular when each average is based on many observed durations, or when the two sets of averages are based on different subsets of the data base. Moreover, by showing that the durations have an expected pattern where, say, syllables starting with voiceless stops are longer than those starting with voiced stops, the contribution of segmentation errors to the correlation becomes even less likely.

To discuss the relation between syllabic and segmental duration more clearly, we introduce some notation, and in the process discuss the relation between segmental independence and the concept of (intrasyllabic) *compensatory timing*.

Consider syllables of the type CV—a consonant followed by a vowel, and let cv be an instance. $\mathrm{DUR}(cv)$ is the intrinsic duration of cv in some fixed context, $\mathrm{DUR}(c|cv)$ the duration of c in cv, and $\mathrm{DUR}(v|cv)$ the duration of v in cv. By definition,

$$\mathrm{DUR}(cv)=\mathrm{DUR}(c|cv)+\mathrm{DUR}(v|cv). \tag{6}$$

Also, $\mathrm{DUR}(c\cdot)$ is the mean duration of all CV syllables starting with c, and $\mathrm{DUR}(\cdot v)$ the mean duration of all CV syllables ending on v. Likewise, $\mathrm{DUR}(c|c\cdot)$ is the duration of c averaged over all vowels v, and $\mathrm{DUR}(v|\cdot v)$ the duration of v averaged over all consonants c.

Next, if we let the vowels range from 1,...,V and consonants from 1,...,C

$$\mathrm{DUR}(c\cdot)=(1/V)\sum_{v=1}^{v=V}\mathrm{DUR}(cv), \tag{7}$$

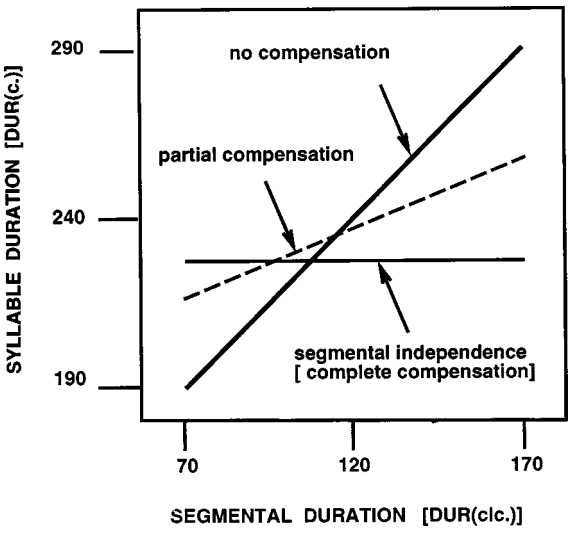

FIG. 2. Relation between syllable and segmental duration with complete, partial, or no compensation. Note that the two axes are drawn on the same scale.

and

$$\mathrm{DUR}(\cdot v)=(1/C)\sum_{c=1}^{c=C}\mathrm{DUR}(cv). \tag{8}$$

All quantities defined thus far are descriptive statistics that can be computed directly from data. We now introduce simple linear effects models for these quantities, describing compensatory effects of these segments on each others' durations

$$\mathrm{DUR}(c|cv)=D_{\mathrm{inherent}}(c)-E_{\mathrm{compensatory}}(v), \tag{9}$$

and

$$\mathrm{DUR}(v|cv)=D_{\mathrm{inherent}}(v)-E_{\mathrm{compensatory}}(c). \tag{10}$$

These equations state that the duration of a consonant or vowel may depend on the identities of the remaining segments in the syllable. When there is no compensatory effect, then $E_{\mathrm{compensatory}}=0$.

It is easy to show that Eqs. (6)–(10) imply a functional relationship between average syllable duration for syllables containing a particular consonant (or vowel) and the average duration of that consonant (or vowel)

$$\mathrm{DUR}(c\cdot)=\mathrm{DUR}(c|c\cdot)-E_{\mathrm{compensatory}}(c)+(1/V)\sum_{v=1}^{v=V}D_{\mathrm{inherent}}(v), \tag{11}$$

and

$$\mathrm{DUR}(\cdot v)=\mathrm{DUR}(v|\cdot v)-E_{\mathrm{compensatory}}(v)+(1/C)\sum_{c=1}^{c=C}D_{\mathrm{inherent}}(c). \tag{12}$$

This implies, first, that if there is no compensatory timing [i.e., $E_{\mathrm{compensatory}}(c)=0$], then a graph displaying syllable duration $[\mathrm{DUR}(c\cdot)]$ as a function of segmental duration $[\mathrm{DUR}(c|c\cdot)]$ is a line with a slope of 1 (see Fig. 2) and an intercept of

$$(1/V)\sum_{v=1}^{v=V}D_{\mathrm{inherent}}(v);$$

and likewise for vowel duration.

Second, if we make the additional assumption that the amount of compensatory shortening inflicted by consonant c on a vowel is larger for intrinsically longer consonants, than Eq. (11) also implies that the slope of the line (or curve, because the relation between intrinsic duration and compensatory effect is not necessarily linear) becomes shallower as the overall degree of compensatory shortening becomes more severe. If we, for the purposes of illustration, do assume a linear relationship with slope $(1-\alpha)$ and intercept $-\beta$

$$E_{\mathrm{compensatory}}(c)=(1-\alpha)D_{\mathrm{inherent}}(c)-\beta, \tag{13}$$

then

$$\mathrm{DUR}(c\cdot)=\alpha\,\mathrm{DUR}(c|c\cdot)+(1/V)\sum_{v=1}^{v=V}D_{\mathrm{interent}}(v)+\beta, \tag{14}$$

then, when α is 1 (no compensation), the curve is a line with slope 1, and when α is 0 (complete compensation), the curve is a horizontal line.

The point here is that segmental independence implies *complete*—not partial—compensatory timing for syllables having the same structure and occurring in the same prosodic context. To show that segmental independence does not hold, it is sufficient to demonstrate a systematic relationship between segmental and syllabic duration (i.e., $\alpha>0.0$), but we do not need to show complete lack of compensation (i.e., $\alpha=1$). However, our results below show that in most cases studied α is in fact quite close to 1.0. This constitutes particularly strong evidence against segmental independence.

A. Segmental independence in American English

1. Method

For American English, the same database was used as described in van Santen (1992). The database consists of 2017 isolated sentences read by an American English male speaker. Vowel onset was determined by the first zero crossing at which the formant structure characteristic for the vowel was visible; the consonantal aspiration, if present, was not included in the vowel duration. Vowel offset was determined similarly. Two cases require special attention. First, vowel-to-vowel boundaries were measured by determining the location of an amplitude minimum (corresponding to either a definite or a weak glottal stop) in the formant transition region. In the absence of a clearly defined minimum, the midpoint of the transition region was used. When no well-defined formant transition region could be found, the point temporally midway between the two vowel centers was used. Here, vowel centers were determined on the basis of energy peaks and proximity to target vowel formant values. Second, transitions from vowels to or from approximants could typically be detected by a visible discontinuity; if not, the midpoint of the transition region was used; and when no transition region was detectable, fixed formant values were used, for example, the boundary of /w/ and the following vowel is

TABLE I. Consonant class labels used for American English.

Class	Symbol
Voiced stops	*B*
Voiceless stops	*P*
Voiced fricatives	*Z*
Voiceless fricatives	*S*
/h/	*H*
Voiced affricate	*J*
Voiceless affricate	*C*
Nasal	*N*
Liquids, glides	*L*

placed at the point where the F_2 value of /w/ passes 900 Hz; the boundary between /r/ and a following vowel is placed at the point where the F_3 value of /r/ passes 1750 Hz.

2. Results

We analyzed the two most frequently occurring syllable types—consonant–vowel (CV) and consonant–vowel–consonant (CVC). Table I shows the symbols used for denoting consonant classes as defined in terms of voicing and manner. We first analyzed stressed word-initial CV syllables in phrase-medial words having two or three syllables.

Syllable duration was highly predictable from the intrinsic durations of the onset and the nucleus, as measured by product-moment correlation coefficients of 0.912 ($t_7=5.88$, $p<0.001$) and 0.959 ($t_{15}=12.20$, $p<0.001$). The slopes were 0.889 and 0.959, statistically indistinguishable from 1.0. Hence, for these syllables, virtually no compensatory timing takes place.

Next, we analyzed stressed word-final CVC syllables in accented phrase-medial words. Correlations between syllable duration and the segmental durations were 0.677 ($t_5=2.06$, $p<0.05$) for the onset consonant, 0.777 ($t_{11}=4.09$, $p<0.001$) for the vowel, and 0.650 ($t_4=1.71$, $p<0.1$) for the coda consonant. Slopes were 1.122, 0.929, and 1.009.

For the effects of consonants in onsets in both syllable types, both voicing and manner of the segment play a role: voiceless fricatives>voiceless stops>voiced stops >voiced fricatives. Vowels showed a clear separation between four classes: diphthongs, long vowels ([æ] and [ɑ]), medium-length vowels ([i], [ɔ˞], [u]), and vowels ([ɛ], [ɪ] [ʌ], [ʊ]). Please see Figs. 3 and 4.

B. Segmental independence in Mandarin Chinese

1. Method

The Mandarin data were a subset of a database designed for the study of duration (van Santen, 1993; Shih and Ao, 1994, 1996). The original database consists of 424 sentences chosen by a greedy algorithm, which maximizes the coverage of a set of predefined factors, including phone combinations and phones in prosodic contexts. The sentences were recorded by a male Mandarin speaker from Beijing. The recorded speech was segmented with the same standards described above for the English database. This database contains 19 150 syllables or 49 671 phones.

Three syllable types of Mandarin Chinese were analyzed: CV, CVC, and CGV (here, ''C'' indicates nonglide consonants, and ''G'' glide consonants). For the CVC case, effects of the final consonant could not be measured because the coda in the language is highly constrained: only nasal /ŋ/ and /n/, and retroflex /ɹ/ are allowed, and these three codas have very similar durations (77, 75, and 63 ms, respectively, in our database), making it meaningless to analyze correlations between segmental and syllabic duration for codas.

Besides syllable type, within-word position was also varied (word-initial final): Contextual factors kept constant were tone (deaccented neutral tones were excluded), prominence (syllables with discourse prominence were excluded), number of syllables in word (at least two), and position in phrase (neither phrase-initial nor phrase-final).

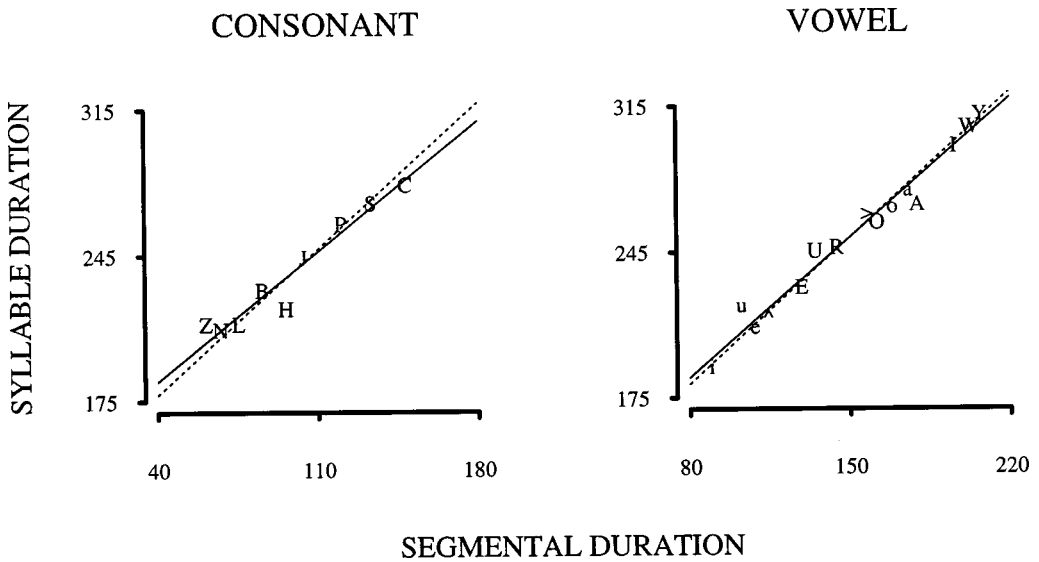

FIG. 3. Effects of consonant (left panel) and vowel (right panel) identity on CV syllable duration (linear, given in ms), for American English. The consonant symbols in the left and right panels represent consonant classes, see Table I. The vowel symbols in the center panel correspond to IPA symbols as follows: Y=/ɔɪ/, W=/aʊ/, I=/aɪ/, A=/eɪ/, a=/æ/, o=/ɑ/, O=/oʊ/, >=/ɔ/, R=/ɔ˞/, U=/u/, E=/i/, ʌ=/ʌ/, e=/ɛ/, u=/ʊ/, *i*=/ɪ/.

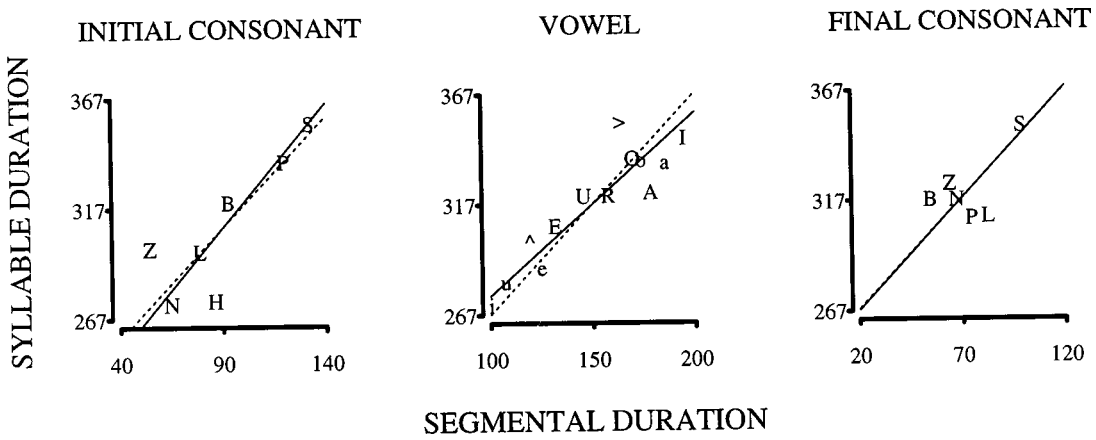

FIG. 4. Effects of consonant (left and right panels) and vowel (center panel) identity on CVC syllable duration.

2. Results

Table II shows overall statistics for the relation between segmental and syllable duration for six syllable types. As in American English, syllable duration correlates strongly with segmental duration.

Figure 5 shows mean durations pooled across all three syllable types and two within-word locations, that have been additively *corrected* for the effects of syllable type and location. By this, the following is meant. We predicted durations using multiple regression, with as predictive factors syllable type and location, using a standard dummy-coding scheme. The residuals can then be considered as durations that have been corrected for the effects of these factors. Table III shows the correlations within each of the syllable types.

It is critical that the relation between syllable duration and onset consonant duration cannot be reduced to a simple categorization such as voiced vs voiceless consonants. Thus, syllable duration depends in a detailed way on the identity of the onset consonant, including both voicing and manner. It is not impossible that, given enough data, we also might have been able to show effects of place of articulation (which are much smaller).

The results for vowels are less clear, which may be due, at least in part, to the intrinsic duration range to be smaller for vowels (50 ms) than for consonants (100 ms). This might be the result of the well-known *restriction of range* phenomenon, where the correlation between two random variables decreases as we reduce the range of one variable. Nevertheless, there is also a statistically significant association.

TABLE II. Consonant class labels used for Mandarin Chinese, sorted in decreasing order of segmental duration.

Class	Symbol	Segmental duration	Syllable duration
Voiceless fricatives s, ʂ, ʃ	*S*	113	248
Aspirated affricates	*C*	101	224
Voiceless fricatives f, h	*h*	93	232
Voiceless aspirated stops	*P*	80	210
Glides	*Y*	63	200
Nasals in onsets	*n*	59	212
Other voiced consonants	*v*	51	203
Unaspirated affricates	*Z*	38	183
Unaspirated stops	*B*	10	165

C. Summary of segmental independence results

In both languages, we found large and systematic variations in syllable duration, despite the fact that the syllables were matched in terms of internal structure and occurred in equivalent contexts. According to the weak syllable timing hypothesis, this variation should have been small and random. The systematicity was shown by powerful correlations between intrinsic segmental and syllabic duration, involving detailed classification of the segments. These results contradict the assumption of segmental independence. We conclude that the duration of a syllable of a given type in a given context depends on the details of its segmental makeup, specifically, on those phonetic features that are the primary determinants of *segmental* duration—voicing and manner. In terms of the diagrams in Fig. 1, these results suggest that syllable duration is influenced by segmental identities directly [as in panel (c)], and not as in the weak syllable timing hypothesis merely through the number of segments or a coarse characterization of the nucleus.

In several cases, the slopes of the line relating segmental duration to syllable duration were statistically not significantly different from 1.0, indicating minimal amounts of compensatory timing.

To clarify how to interpret these results, we emphasize that they do not establish the phonological reality of segments. Rather, they establish that the durational behavior of syllables cannot be understood without taking into account the detailed properties of their constituents. The results are neutral as to whether one should describe these constituents as a sequence of phonetic segments or as a set of quasi-independent asynchronous streams of features.

IV. SYLLABIC MEDIATION: EFFECTS OF SUPRASEGMENTAL FACTORS ON SEGMENTAL DURATION

We test here the following implication of syllabic mediation: when the exact same syllable (e.g., two instances of [ba:]) occurring in two contexts has the same duration, then the segmental durations should also be the same.

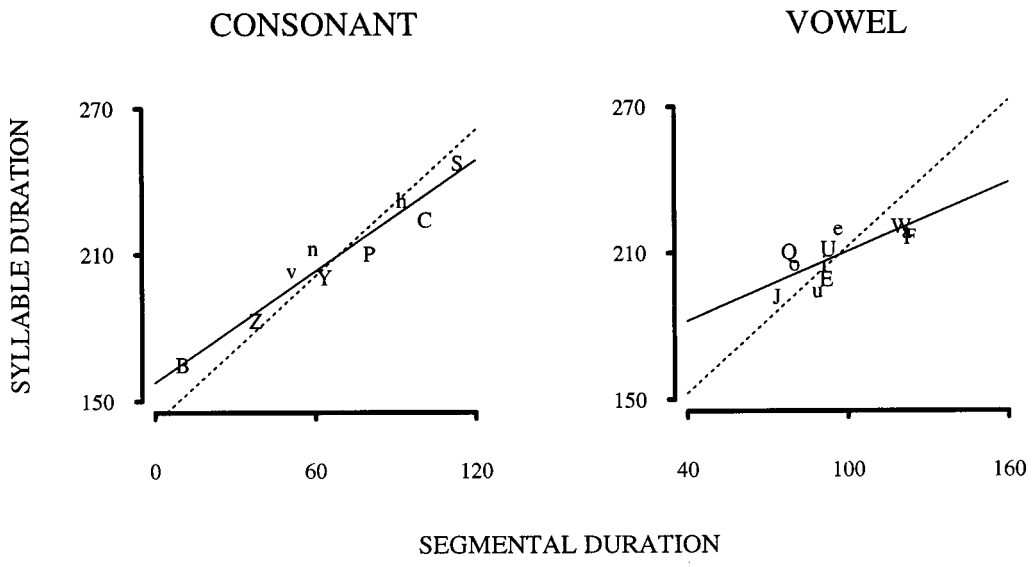

FIG. 5. Effects of consonant (left panel) and vowel (right panel) identity on syllable duration, combined over three syllable types (CV, CVC, and CGV) and over word position (word-initial, word-final), for Mandarin Chinese. The data in the left panel are the same as given in Table II. The consonant symbols in the left panel represent consonant classes as shown in Table II. The vowel symbols in the right panel correspond to IPA symbols as follows: F=/æ/, a =/ɑ/, W=/aʊ/, e=/ɛ/, U=/ü/, E=/ʌ/, i=/i/, u=/u/, o=/o/, O=/oʊ/, J=/ɨ/.

As pointed out in Sec. II, the weak syllable timing hypothesis makes an exception for the effect of phrase boundaries. That is, segmental duration depends not only on syllable duration and segmental identity, but also on whether the syllable is phrase-final and on the position of the segment within the syllable. In other words, phrasal location has a special *syllabic influence profile*, whereby segments in different intrasyllabic locations are affected by different amounts by changes in phrasal location.

In this section, we show that many contextual factors, not only phrasal location, have a nonuniform, unique syllabic influence profile, where some factors affect mostly syllable onset duration, and others the duration of the nucleus, or the coda. This implies that segmental duration depends on the constellation of contextual factors to a much greater degree than can be comfortably handled by the weak syllable timing hypothesis.

A brief not here on the logical connection between influence profiles and syllabic mediation. In practice, it is difficult to obtain contextual constellations that produce nearly identical syllable durations (e.g., because the effects of stress would have to be exactly the same as the effects of phrase finality). Syllable influence profiles allow us to estimate segmental durations that would be obtained had we been able to find such constellations, using the following argument. We define the syllabic influence profile of a two-leveled factor as follows. For each within-syllable position, we compute the ratio of the segmental durations in the ''long'' versus ''short'' level of the factor (e.g., stressed versus unstressed, or phrase-final versus phrase-medial); the graph of these ratios across within-syllable position is the syllabic influence profile. We say that two profiles *have different shapes* when it is impossible to transform one into the other by multiplying it with some constant. It follows that if we find some constant that produces the same profile averages (i.e., average over within-syllable locations), then for at least one within-syllable location the values of the two profiles will still be different. Thus, when we find that two contextual constellations produce profiles with different shapes, then by extrapolation (e.g., had we been able to find boundaries that are a little bit stronger, or stress levels that are a little bit weaker) it follows that contextual constellations that would have produced the same overall syllable durations would not produce the same segmental durations. Of course, we are making a tacit assumption here, which is that contextual effects are multiplicative in nature. There is increasingly more evidence, however, that to a first order of approximation this is true for most contextual effects on duration (van Santen, 1992; Shih and Ao, 1994, 1996; Möbius and van Santen, 1996).

TABLE III. Correlations (slopes) for relation between syllable-initial consonant or vowel and syllable duration, for Mandarin Chinese. Except for the value of 0.21, all correlations are significant at $p<0.05$.

Syllable type	Within-word position	Consonant	Vowel
CV	initial	0.89 (0.70)	0.76 (0.81)
	final	0.91 (0.63)	0.21 (0.43)
CVC	initial	0.96 (0.84)	0.60 (0.70)
	final	0.96 (0.75)	0.89 (0.91)
CGV	initial	0.95 (0.94)	0.94 (0.55)
	final	0.90 (0.96)	0.99 (0.78)

The factors that will be analyzed are word initiality, tone (Mandarin Chinese), word emphasis (Mandarin Chinese), lexical stress (American English), and phrasal position.

A. Syllabic mediation in American English

We analyzed the effects of three factors for CV and CVC syllables:

(1) *Phrase boundaries*, comparing word-final syllables in phrase-medial and utterance-final position.

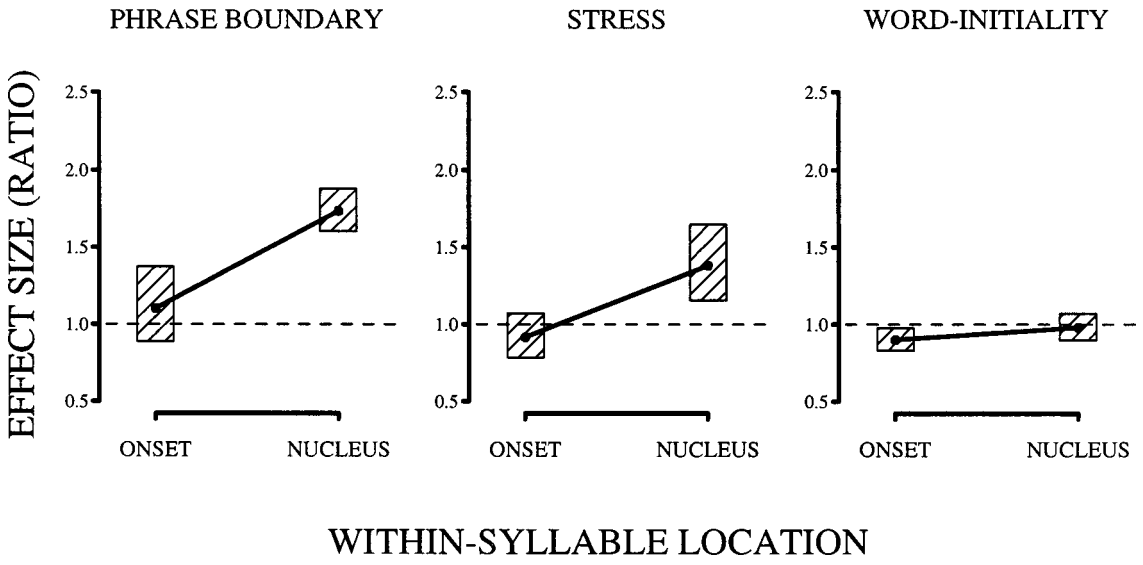

FIG. 6. Syllable influence profiles for contextual factors on durations of onsets and nuclei in CV syllables in American English. Error bars indicate 95% confidence intervals.

(2) *Within-word position*, comparing non-word-final syllables in word-initial and non-word-initial position.
(3) *Lexical stress*, comparing unstressed with primary stressed.

Analyses of variance were performed on the logarithm of duration (thereby analyzing ratios, or *change percentages*, as in the figures, instead of differences). We were primarily interested in showing nonuniformity of lengthening ratios across within-syllable positions (which corresponds to a two-way interaction between within-syllable location and contextual factor), and showing that these nonuniform influence patterns differed across contextual factors [which corresponds to a three-way interaction between within-syllable location, type of contextual factor (phrase boundary versus stress versus word initiality), and within-contextual-factor-level (longer versus shorter, e.g., phrase-final vs phrase-medial for the phrase boundary factor]. In each of these analyses, we also included some of the remaining factors in the analysis (listed as ''additional factors'') that the database did not allow us to keep constant; these factors were assumed not to interact with the factors of interest. Segmental identity was treated as a nested (within the within-syllable location factor) fixed-effects factor. Table IV shows which factors were involved in these analyses.

Key findings were the following (also see Figs. 6 and 7 and Table IV): First, word initiality had no main effect [CV case: $F(1,1530)=0.2196$, $p>0.5$; CVC case: $F(1,880)=0.58$, $p>0.5$] and did not interact with position in the syllable [CV case: $F(1,1530)=3.78$, $p>0.5$; CVC case: $F(1,880)=2.62$, $p>0.05$].

Second, phrase boundary had main effects [CVC case, phrase boundary: $F(1,5497)=1873.38$, $p<0.001$; CV case,

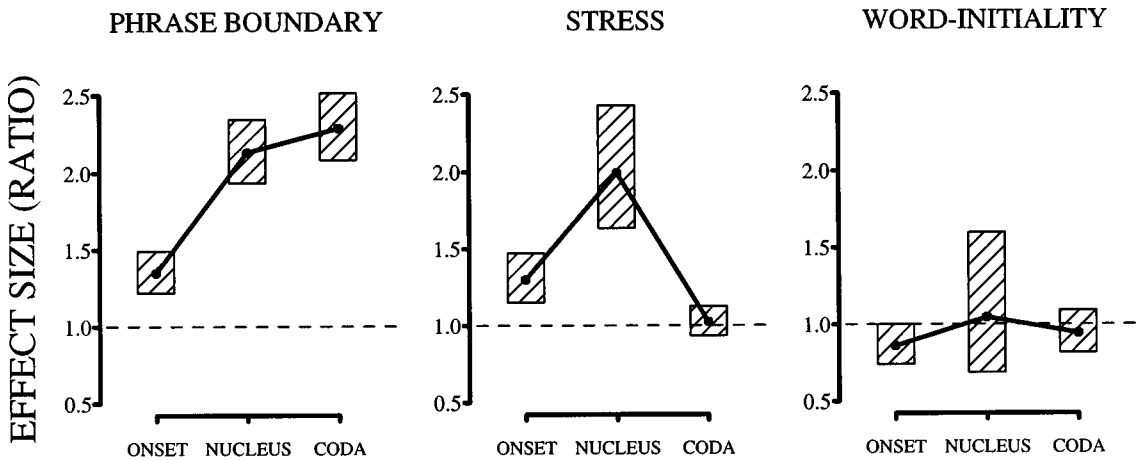

FIG. 7. Syllable influence profiles for contextual factors on durations of onsets, nuclei, and codas in CVC in American English.

TABLE IV. Restrictions and additional factors for each of the three contrasts shown in Figs. 6 and 7 for American English (CV syllables; CVC syllables between parentheses).

Contrast	Restrictions	Additional
Phrase-final vs not phrase-final	Exclude affricates	Segmental identity
	Exclude schwa	
	At least 4 words	
	Word-final	
	Primary stress	
	Accented	
Word-initial vs not word-initial	Exclude affricates	Segmental identity
	Exclude schwa	
	At least 4 words	
	Not phrase-initial	
	Not phrase-final	
	Not word-final	
	Primary stress	
	Accented	
Stress 1 vs stress 0	Exclude affricates	Segmental identity
	Exclude schwa	
	Not phrase-initial	
	At least 4 words	
	Not phrase-final	
	Not phrase-final	
	Word-final (Only word final)	
	Accented	

phrase boundary: $F(1,750)=255.73$, $p<0.001$] and interacted with within-syllable location [CVC case, phrase boundary: $F(1,5497)=87.77$, $p<0.001$; CV case, phrase boundary: $F(1,750)=170.56$, $p<0.001$].

Third, stress had main effects [CVC case, stress: $F(1,1216)=228.88$, $p<0.001$; CV case, stress: $F(1,710)=55.64$, $p<0.001$] but interacted with position in the syllable only in CVCs [CVC case, stress: $F(1,1216)=58.71$, $p<0.001$; CV case, stress: $F(1,710)=0.12$, $p>0.5$].

Fourth, the critical three-way interaction between within-syllable location, type of contextual factor, and within-contextual-factor was significant for CVCs and for CVs and for CVs [CVC case: $F(4,7639)=93.55$, $p<0.001$; CV case: $F(2,3007)=44.25$, $p<0.001$].

We reach the conclusion that different contextual factors have different, nonuniform influence profiles, with the differences particularly pronounced for CVCs due to the lack of effect of stress on codas.

B. Syllabic mediation in Mandarin Chinese

We analyzed the effects of four factors for CV and CVC syllables:

(1) *Phrase boundaries*, comparing word-final, utterance-medial syllables in phrase-medial and phrase-final position.
(2) *Within-word position*, comparing syllables in word-initial and non-word-initial position.
(3) *Tone*, comparing the deaccented tone 0 with full tones 1–4.
(4) *Stress*, comparing stress 0 with stress levels 1 and 2.

TABLE V. Restrictions and additional factors for each of the four contrasts shown in Figs. 8 and 9 (Mandarin Chinese).

Contrast	Restrictions	Additional
Phrase-final vs not phrase-final	Tones 1–4	Segmental identity
	Stress 0	Word-initial vs not word-initial
	Word-final	
	Not phrase-initial	
	Not utterance-final	
Word-initial vs not word-initial	Tones 1–4	Segmental identity
	Stress 0	
	Polysyllabic word	
	Not phrase-initial	
	Not phrase-final	
Tone 1–4 vs tone 0	Not phrase-initial	Segmental identity
	Not phrase-final	Within-word position
	Stress 0	
Stress 1,2 vs stress 0	Not phrase-initial	Segmental identity
	Not phrase-final	Within-word position
	Tones 1–4	

Table V lists additional restrictions as well as additional factors.

Figures 8 and 9 show that phrase boundaries primarily affect the nucleus and coda, while word initiality primarily affects the onset. The effects of tone and stress are more evenly spread over onset, nucleus, and coda. Results are quite similar for CV and CVC syllables.

Analyses of variance on the logarithm of duration supported these impressions. For CV syllables, we found significant effects (at $p<0.001$ or better). All analyses uniformly yielded *F*-ratios with 1 and degrees of freedom (df), where df exceeded 3000, and had values in excess of 9.0; we do not separately report these analyses for the interaction between within-syllable location and phrase boundary, tone, stress, and word initiality, indicating that ratios for the two locations indeed differed for each of these factors.

Moreover, the critical three-way interaction between within-syllable location, type of contextual factor (phrase boundary versus tone versus stress versus word initiality), and within-contextual-factor (longer versus shorter, e.g., phrase-final versus phrase-medial for the phrase boundary factor) was also significant.

C. Summary of syllabic mediation results

Syllabic mediation implies that contextual constellations that produce the same syllable duration should also cause the durations of the constituent segments to be the same. This was tested by analyzing the syllabic influence profiles of various two-level (''long'' versus ''short'') contextual factors, defined as the ratios of the long to the short durations as a function of within-syllable position. We found that the effects on segmental duration depend on a complicated interaction between within-syllable position and which contextual

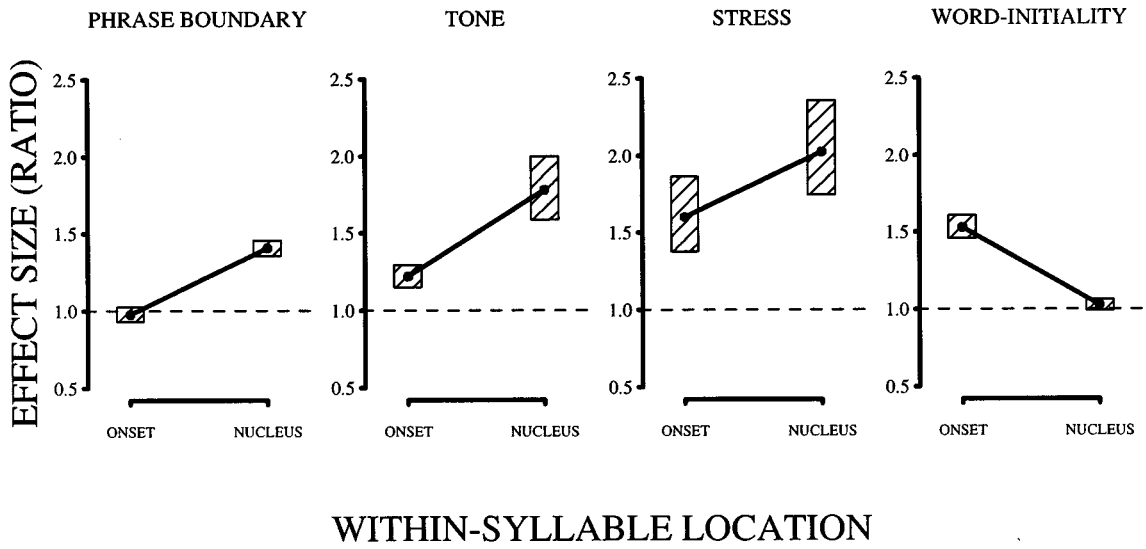

FIG. 8. Syllable influence profiles for various contextual factors on durations of onsets, nuclei, and codas in CV syllables in Mandarin Chinese.

factor was involved. It seems that these factors, far from operating on the syllable as a unit, have strikingly uneven effects across the syllable.

Recent results by van Son and van Santen (1997) cast further doubt on syllabic mediation. The effects of stress of surrounding vowels on intervocalic consonants in word-initial, word-medial, and word-final syllables were studied. For labials, it was found that the effects of stress (measured as ratios or as differences) were roughly the same in the three syllabic positions. However, for coronals these effects differed strongly. Specifically, stress of surrounding vowels had a much larger effect in word-medial positions than in either word-final or word-initial positions. (Of course, the word-medial prestressed position provides the typical context in which *flapping* occurs.) These, and related results show that effects of prosodic factors such as syllabic stress and position of the syllable in a word have to be understood in conjunction with specific features of the segments involved, not only in conjunction with the intrasyllabic position of the segments. These results cannot be understood by prosodic factors determining overall syllable duration, and segmental durations being adjusted to fit in this syllable interval.

V. CONCLUSIONS

In this paper, we argued that various forms of the syllable timing concept all share two assumptions, which we called *syllabic mediation* and *segmental independence*. The former refers to the assumption that the duration of a segment depends only on the duration of the syllable, its identity, and its position in the syllable; and the latter to the assumption that the duration of the syllable is independent of the identities of the segments it contains.

The data showed that the duration of a syllable is highly dependent on the intrinsic duration of the segments it contains. Specifically, durations of syllables having exactly the same structure (e.g., CVC) and occurring in nominally identical prosodic contexts vary systematically with the intrinsic

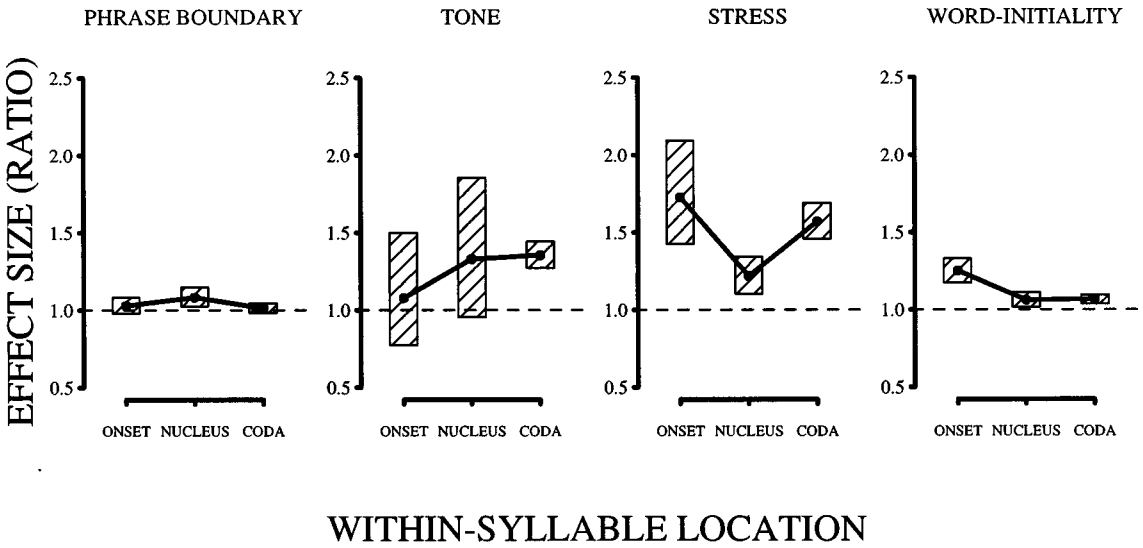

FIG. 9. Syllable influence profiles for various contextual factors on durations of onsets, nuclei, and codas in CVC syllables in Mandarin Chinese.

durations of their segments. In other words, one cannot predict and understand syllable duration unless one takes the identities of the constituent segments into account. But, when the syllable timing model does this, the key attractive property—decomposition of the feature space into prosodic factors that do not directly affect segments and phonemic factors that hardly affect syllable durations—is lost. As we remarked in the Introduction, this property could have been a major tool in dealing with data sparsity.

The data also showed that contextual factors differ in terms of which parts of the syllable they affect: Some factors primarily affect onsets, others onsets and nuclei, and still others nuclei and codas. In other words, syllable duration by itself does not dictate segmental duration.

We reach the following conclusion. There is little controversy that suprasegmental units (words, syllables, IPCGs) play a role as phonological entities in explaining and predicting speech timing. In addition, it may very well be that certain effects involving these entities are of a compensatory nature. For example, we know that vowels in long words are shorter than vowels in short words; also, it appeared that some degree of compensation takes place at the intrasyllabic level in Mandarin Chinese. Nevertheless, in the two languages studied these compensatory effects are quite weak, and come nowhere near to obscuring the effects of intrinsic segmental duration on overall syllable duration.

We want to conclude by sketching a hypothesis of why speech would not be produced in terms of suprasegmental temporal units. We propose that higher-level speech production processes are concerned with speech timing only in a loose sense, and issue fairly imprecise requests for local (i.e., on the scale of up to a few syllables) accelerations and decelerations down the line of command to lower-level speech production processes. That is: they are commands of the type: ''pronounce this important word very slowly,'' but not: ''pronounce this syllable in 192 ms,'' nor ''make sure that these syllables are produced with the same total duration.'' Moreover, except perhaps for certain types of poetry or reiterant speech, these local speaking rate requests are determined to a significant degree by the semantics of discourse. Of course, the *pattern* of which words in a phrase require special emphasis—and hence local deceleration—does not follow some simple (e.g., alternating) sequence, but is the result of syntactic and semantic constraints. Hence, it would be unlikely that the pattern of local speaking rate commands issued by these higher-level speech production processes would exhibit any type of constancy or repetitiveness. Semantics, redundancy, and the desire to communicate efficiently may even be responsible for certain ''compensatory'' phenomena that typically have been interpreted as reflecting the speaker's desire for isochrony, such as the fact that vowels are shorter in longer words: It simply may be that syllables in long words are lexically more redundant than syllables in short words, and hence do not require particularly careful pronunciation. Elsewhere (van Santen, 1992) we showed not only that vowels in longer words are shorter than vowels in shorter words, but also, using a partial correlation technique, that this is not due to any effects of stress group length—which obviously increases with word length.

The actual durations of the resulting articulatory actions are a function both of these top-down requests and of various physiological and mechanical constraints. Since articulatory actions in speech are largely *nonrepetitive* (i.e., in nonreiterant speech the articulatory path hardly ever passes through the same subpath twice in articulatory space), there is no reason to suspect that articulatory actions involve *pendulum-like muscle behavior* such as in rhythmic music, sawing, or nodding one's head. Hence, the physiological and mechanical constraints are unlikely to execute rhythmic local speaking rate commands in a rhythmic fashion.

If this proposal is correct, then we should not expect *rhythmicity* in speech in the sense of any constancies of suprasegmental unit durations.

Allen, J., Hunnicut, S., and Klatt, D. H. **(1987)**. *From Text to Speech: The MITalk System* (Cambridge University Press, Cambridge).

Barbosa, P., and Bailly, G. (**1995**). ''Characterization of rhythmic patterns for text-to-speech synthesis,'' Speech Commun. (in press).

Beckman, M. (**1982**). ''Segment duration and the 'mora' in Japanese,'' Phonetica **39**, 113–135.

Browman, C. P., and Goldstein, L. (**1990**). ''Tiers in articulatory phonology, with some implications for casual speech,'' *Papers in Laboratory Phonology I: Between the Grammar and Physics of Speech*, edited by J. Kingston and M. E. Beckman (Cambridge University Press, Cambridge), pp. 341–376.

Campbell, W. N., and Isard, S. D. (**1991**). ''Segment durations in a syllabic frame,'' J. Phonetics **19**, 37–47.

Campbell, W. N. (**1990**). ''Analog i/o nets for syllable timing,'' Speech Commun. **9**, 57–61.

Campbell, W. N. **(1992)**. ''Syllable-based segmental duration,'' in *Talking Machines: Theories, Models, and Designs*, edited by G. Bailly and C. Benoit (Elsevier, Amsterdam), pp. 211–224.

Coleman, J. S. **(1992)**. ''Synthesis-by-rule without segments of rewrite-rules,'' in *Talking Machines: Theories, Models, and Designs*, edited by G. Bailly and C. Benoit (Elsevier, Amsterdam), pp. 43–60.

Crystal, T. H., and House, A. S. (**1988a**). ''The duration of American-English stop consonants: An overview,'' J. Phonetics **16**, 285–294.

Crystal, T. H., and House, A. S. (**1988b**). ''Segmental durations in connected-speech signals: Current results,'' J. Acoust. Soc. Am. **83**, 1553–1573.

Crystal, T. H., and House, A. S. (**1988c**). ''Segmental durations in connected-speech signals: Syllabic stress,'' J. Acoust. Soc. Am. **83**, 1574–1585.

de Jong, K. (**1991**). ''An articulatory study of consonant-induced vowel duration changes in English,'' Phonetica **48**, 1–17.

Edwards, J., and Beckman, M. E. (**1988**). ''Articulatory timing and the prosodic interpretation of syllable duration,'' Phonetica **45**, 156–174.

Gay, Th. (**1968**). ''Effect of speaking rate on diphthong formant movements,'' J. Acoust. Soc. Am. **44**, 1570–1573.

Hertz, S. R. **(1990)**. ''The Delta programming language: An integrated approach to nonlinear phonology, phonetics, and speech synthesis,'' in *Papers in Laboratory Phonology I: Between the Grammar and Physics of Speech*, edited by J. Kingston and M. E. Beckman (Cambridge University Press, Cambridge), pp. 215–257.

Klatt, D. H. (**1975**). ''Vowel lengthening is syntactically determined in connected discourse,'' J. Phonetics **3**, 129–140.

Klatt, D. H. (**1976**). ''Linguistic uses of segmental duration in English: Acoustic and perceptual evidence,'' J. Acoust. Soc. Am. **59**, 1209–1221.

Lehiste, I. (**1977**). ''Isochrony reconsidered,'' J. Phonetics **5**, 253–263.

Möbius, B. M., and van Santen, J. P. H. **(1996)**. ''Modeling segmental duration in German text-to-speech synthesis,'' in Proceedings ICSLP, Philadelphia, pp. 2395–2399.

Ohala, J. J., and Lyberg, B. (**1976**). ''Comments on 'temporal interactions within a phrase and sentence context' [J. Acoust. Soc. Am. **56**, 1258–1265 (1974)],'' J. Acoust. Soc. Am. **59**, 990–992.

Olive, J. P., Greenwood, A., and Coleman, J. S. **(1993)**. *Acoustics of American English Speech: A Dynamic Approach* (Springer, New York).

Port, R. F., Dalby, J., and O'Dell, M. (**1987**). ''Evidence for mora timing in Japanese,'' J. Acoust. Soc. Am. **81**, 1574–1585.

Port, R. F. (**1981**). Linguistic timing factors in combination. J. Acoust. Soc. Am. **69**, 262–273.
Shih, C., and Ao, B. **(1994)**. ''Duration study for AT&T Mandarin text-to-speech system,'' in *Workshop on Speech Synthesis* (ESCA, New Paltz, NY), pp. 29–32.
Shih, C., and Ao, B. **(1996)**. ''Duration study for the Bell Laboratories Mandarin text-to-speech system,'' in *Progress in Speech Synthesis*, edited by J. P. H. van Santen, R. W. Sproat, J. P. Olive, and J. Hirschberg (Springer, New York).
Stevens, K. N., and Bickley, C. A. (**1991**). ''Constraints among parameters simplify control of Klatt formant synthesizer,'' J. Phonetics **19**, 161–174.
Umeda, N. (**1975**). ''Vowel duration in American English,'' J. Acoust. Soc. Am. **58**, 434–445.
Umeda, N. (**1977**). ''Consonant duration in American English,'' J. Acoust. Soc. Am. **61**, 846–858.
van Santen, J. P. H., Coleman, J. C., and Randolph, M. A. (**1992**). ''Effects of postvocalic voicing on the time course of vowels and diphthongs,'' J. Acoust. Soc. Am. **92**(4, Pt. 2), 2444(A).
van Santen, J. P. H. (**1992**). ''Contextual effects on vowel durations,'' Speech Commun. **11**, 513–546.
van Santen, J. P. H. (**1993**). ''Perceptual experiments for diagnostic testing of text-to-speech systems,'' Comput. Speech Lang. **7**, 49–100.
van Santen, J. P. H. (**1994**). ''Assignment of segmental duration in text-to-speech synthesis,'' Comput. Speech Lang. **8**, 95–128.
van Santen, J. P. H. **(1996)**. ''Segmental duration and speech timing,'' in *Computing Prosody*, edited by Y. Sagisaka, W. N. Campbell, and N. Higuchi (Springer, New York).
van Santen, J. P. H. **(1997)**. ''Prosodic modeling in text-to-speech synthesis,'' in Proceedings of Eurospeech-97, Rhodes, Greece.
van Son, R. J. J. H., and van Santen, J. P. H. **(1997)**. ''Modeling the interaction between factors affecting consonant duration,'' in Proceedings Eurospeech-97, Rhodes, Greece.

Anisotropy of ultrasonic propagation and scattering properties in fresh rat skeletal muscle *in vitro*

Karen A. Topp and William D. O'Brien, Jr.
Bioacoustics Research Laboratory, Department of Electrical and Computer Engineering, University of Illinois at Urbana-Champaign, 405 North Mathews Avenue, Urbana, Illinois 61801

(Received 13 February 1999; revised 1 May 1999; accepted 6 October 1999)

The anisotropy of frequency-dependent backscatter coefficient, attenuation, and speed of sound is assessed in fresh rat skeletal muscle within 5 h *post-mortem*. Excised rat semimembranosus and soleus muscles are measured in 37 °C Tyrode solution, with the muscle fibers at 90° and 45° orientations to the incident sound beam. Reflected and through transmission signals from either a 6- or 10-MHz focused transducer give frequency dependent information in the 4–14 MHz range. The attenuation coefficient in each muscle is consistently a factor of 2.0 ± 0.4 lower for propagation perpendicular to the fibers than at 45°, whereas speed of sound shows a much milder anisotropy, and is slightly faster for the 90° orientation. The largest anisotropy is seen in the backscatter coefficient, most notably in the semimembranosus where the magnitude at 90° is over an order of magnitude greater than at 45°, with the frequency dependence in both cases giving a power law between 1.5 and 2.0. © *2000 Acoustical Society of America.* [S0001-4966(00)05401-1]

PACS numbers: 43.80.Cs, 43.80.Ev [FD]

INTRODUCTION

The variation of acoustic properties with direction of the incident sound field relative to the orientation of the medium being studied is known as acoustic *anisotropy*. Anisotropy in ultrasonic parameters characterizing biological tissue has been reported for a number of tissues with oriented structures, primarily myocardium,[1–8] in which Miller *et al.* have shown that attenuation is over a factor of 2 greater along the muscle fibers than perpendicular to them,[3] that speed of sound also has a maximum along the muscle fibers,[4] and that backscatter exhibits a maximum for incident sound perpendicular to the fibers and a minimum for for parallel incidence.[1,8] Tendon[5–7,9] and kidney[10] have also been studied for their anisotropic properties. The use of skeletal muscle to investigate ultrasound parameter anisotropy has primarily looked at bovine muscle; mostly attenuation[9,11–13] with an additional study each of speed[9] and integrated backscatter coefficient.[11] Investigations using dog,[14] rabbit,[14,15] and frog[15] muscles have measured speed of sound alone.

The great majority of the work cited above has been performed on samples which were fixed, frozen, or *post-rigor*, and the few studies using fresh tissue have measured only a single parameter at a time.[2,13,15] The aim of this study is to characterize the anisotropy of the frequency-dependent backscatter coefficient $\sigma_b(f)$, attenuation $\alpha(f)$, and speed of sound c, all measured at effectively the same time, in freshly excised rat skeletal muscle. Samples are measured in 37 °C Tyrode solution[16] to prolong the viability of the tissue and to create conditions as similar as possible to *in vivo*, which should be more clinically relevant than previous non-fresh anisotropy studies. Results are presented for ten rat soleus muscles, and ten rat semimembranosus muscles, both muscle types characterized by having straight and parallel muscle fibers.

I. METHODS

A. Muscle specimen preparation

The two muscle types studied here are both parallel-fiber skeletal muscles found in the leg of the rat; the soleus in the lower leg (the calf) and the semimembranosus in the upper lateral thigh. Adult rats (Sprague Dawley, Harlan, Indianapolis) were used for this study on fresh muscle, rather than using larger animals, since surplus rats from other investigations were readily available. Each muscle was excised from the rat within 15 min of when it was euthanized by CO_2. The experimental protocol was approved by the campus' Laboratory Animal Care Advisory Committee and satisfied all campus and NIH rules for the humane use of laboratory animals.

The excised semi-membranosus muscles were roughly rectangular in shape with typical relaxed dimensions of 2.0–2.5 cm long, 1.2–1.5 cm wide, and 0.5–0.7 cm thick; the sample is interrogated through its ''thickness'' which is remarkably flat and parallel over the region investigated, as determined from the acoustically detected front and back surfaces (see below). The soleus muscle samples were typically 2.0 ± 0.4 cm long between the tendons at each end. The fibers run neatly between tendons, lying straight and nearly parallel as the muscle is slightly thicker in the middle and tapers gradually to the ends. The muscle is interrogated through the thickest section, typically 0.3–0.4 cm thick (and 0.4–0.6 cm wide).

The microstructure of the two muscle types is shown in the stained microscope images of Fig. 1, in which the muscle fibers are seen in cross-section. The predominant feature in both images is the closely packed arrangement of muscle fibers, each surrounded by its sheath of connective tissue.

Within 5 min of excision, the muscles were fastened to a measurement holder such that the fibers were at a ~10%–20% stretch from relaxation. Soleus muscles were tied with suture through the tendons at each end, and the larger semi-

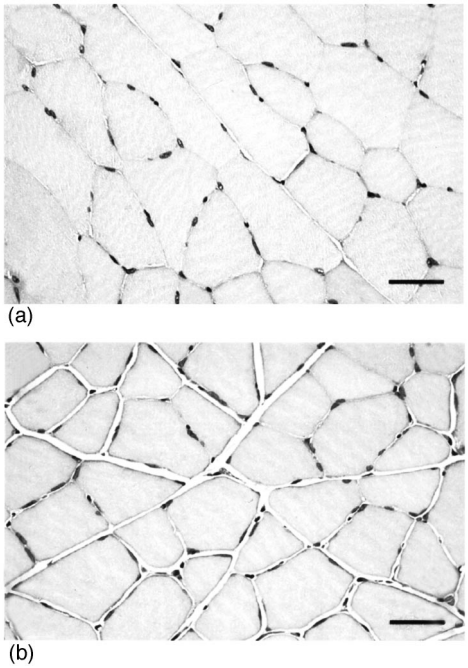

FIG. 1. Photomicrographs of the two rat muscle types, with the semimembranosus in the top panel (a) and the soleus below (b). The length scale in each image is determined by the bar which represents 50 μm. Muscle specimens were fixed in 10% neutral-buffered formalin, sectioned perpendicular to the fiber direction to 3 μm, and stained with hematoxylin and eosin for evaluation.

membranosus samples were held in place by a small stainless steel clip at each end. The sample was immediately immersed in a 37 °C Tyrode solution[16] (which was prepared with distilled degased water to limit gas formation) where it remained for all measurements. Tyrode solution is a nutritive medium containing the salts and glucose necessary to preserve cellular function in the tissue and thus maintain the viability of the sample for several hours. By removing a second (soleus) muscle from an animal, and holding it in similar conditions during the course of the experiment, we ascertained that the measured sample does not go into rigor for at least 4–5 h after death, by which time the acoustic measurements are completed.

B. Acquisition of data

The muscle sample, transducer, and needle hydrophone were all immersed in a temperature controlled ($37\pm0.5\,^{\circ}$C) Tyrode bath in an arrangement that allowed both transmission through, and reflection from, the same spatial locations in the muscle (see Fig. 2). The sample was held at the focus of either a 6-MHz or 10-MHz (Panametrics V309, V311) spherically focused transducer (both 1.27 cm diameter, 5 cm radius of curvature) which was excited by a Panametrics 5900 pulser/receiver. The reflected signal, and the through transmission signal from the 0.6-mm diameter needle hydrophone (Medicoteknisk Institut 1094) just behind the sample, were both received and amplified by the pulser/receiver and displayed on a LeCroy 9354 TM digitizing oscilloscope, set at 250 Ms/s. A dedicated PC recorded and stored the rf-signals from the oscilloscope for processing off-line.

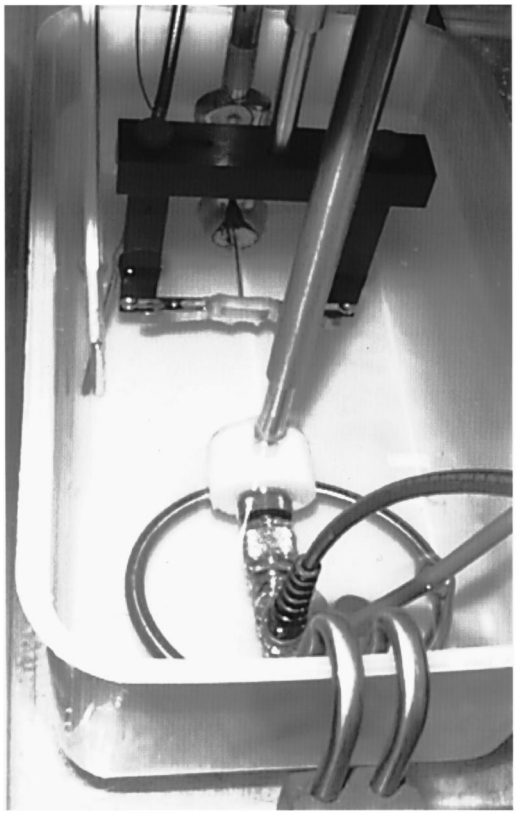

FIG. 2. Photograph showing the experimental apparatus. To determine the scale, note the semimembranosus muscle shown here is fastened in a holder whose black top bar measures 11 cm long. The needle hydrophone is directly behind the muscle, and the transducer is in the foreground. A heating coil and mechanical stirrer are seen below the transducer, and the heater's thermostat and a thermometer are seen to the left of the sample. All components are immersed in 37 °C Tyrode solution.

The muscle holder is moved within the sound field by a micropositioning system, which allows translational and rotational movement with a positional accuracy of 2 μm and 0.02 degrees, respectively. Two orientations with respect to the muscle fibers were measured: 90° (perpendicular) and 45°. (The effect of oblique incidence of the sound beam on the muscle surface in Tyrode was calculated for the 45° case to give a pressure transmission coefficient of greater than 0.998, in comparison to the normal incidence value of 0.999.) At each orientation, a 5×5 grid of spatial samples each separated by 700 μm (greater than both transducers' -6-dB spot size) was measured, with the muscle moved axially as necessary to ensure that the focal point of the transducer was at its center. Two rf-waveforms were captured for each spatial point: (a) a backscattered temporally averaged waveform (of 500 echoes) encompassing the entire muscle depth and both surfaces (to be gated off-line), which is used to find $\sigma_b(f)$ as well as the thickness of the sample at that spot; and (b) a transmission signal through the muscle. Between each spatial point measurement, the muscle is positioned out of the beam path to record (c) a reference transmission signal through the Tyrode solution alone. The two transmission rf-signals, (b) and (c), each averaged 100 times, are used to find $\alpha(f)$ and c. At the end of the experiment, a reference reflection signal for the σ_b measurement is collected from a flat Plexiglas plate positioned where the axial

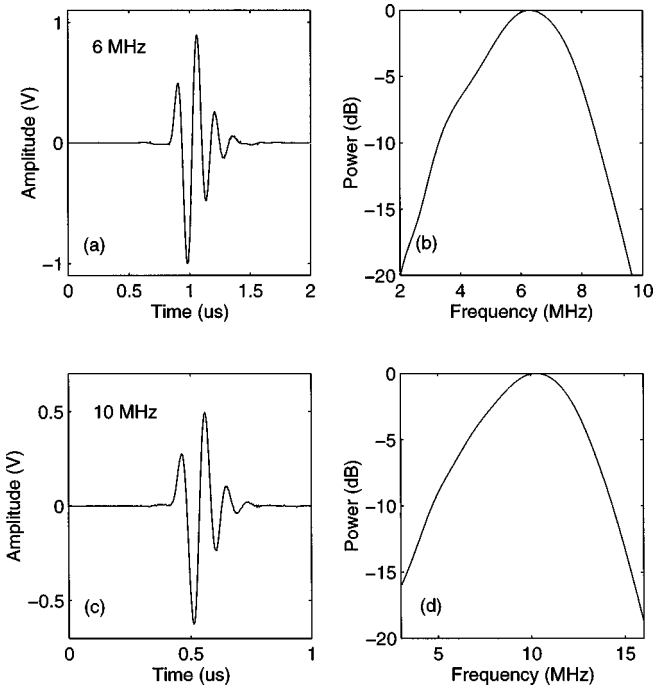

FIG. 3. Waveforms and power spectra of the two transducers used in this study; (a) and (b) from the 6-MHz transducer; (c) and (d) from the 10-MHz transducer. The waveforms are temporal averages of 100 echoes and were sampled at 250 MS/s.

center of the muscle had been. Figure 3 shows the waveforms and corresponding spectra of the echo of each of the transducers from the Plexiglas plane reflector.

The freshness of the muscle samples was fundamental to the protocol of this study. Since the acquisition of data for each muscle took approximately 3 h (due to the spatial sampling and extensive signal averaging after nearly 1 h of positioning and setup time), each muscle was interrogated with only one of the two transducers to ensure that all measurements were completed within 4–5 h before the onset of rigor.

To ensure that the differences we may see at the two orientations were not a function of the aging of the muscle, six of the ten rat muscles of each type were measured at 90° orientation first before being turned to 45°, and four in reverse order. No difference was seen between these two populations in any of the measured acoustic parameters.

The effect of refraction of the sound beam through the muscle samples held at 45° has been carefully considered: A calculation of the beam through the thickest specimens of 7 mm (and most samples were thinner), using speeds of sound 1590 m/s and 1537 m/s for the muscle and Tyrode solution, respectively, gives a 0.36-mm lateral shift of the beam relative to the incident beam axis. This is about half the size of the hydrophone diameter, and about one-quarter of the −3-dB transducer beamwidth at the hydrophone. Since the hydrophone is mounted on micrometer positioners, a ''reoptimization'' of its position was attempted after turning the sample from 90° to 45°, but no increase in the through transmission signal magnitude was seen, and it was decided that less error was introduced into the measurement by simply leaving the relative positions of the transducer and hydrophone fixed. To check the refraction effect on a known isotropic, homogeneous substance, the attenuation at 45° and 90° through a 0.5-cm wide disk of Dow Corning silicone fluid (with Reynolds plastic wrap windows) was measured in water with the same equipment and without repositioning the hydrophone. The larger discrepancy in speeds of sound between water and silicone fluid (1486 m/s and 1390 m/s, respectively, at room temperature) made the calculated lateral beam shift 0.43 mm when the 0.5-cm disk was held at 45° to the incident beam axis. The measured attenuation of the silicone oil for the two orientations was less than 5% different over the whole frequency range of the 5-MHz transducer; thus we concluded that for the muscle samples, with more similar speeds of sound to the surrounding fluid bath, the refraction effect would cause only a few percent decrease at most in the received signal power at 45°, and could be ignored.

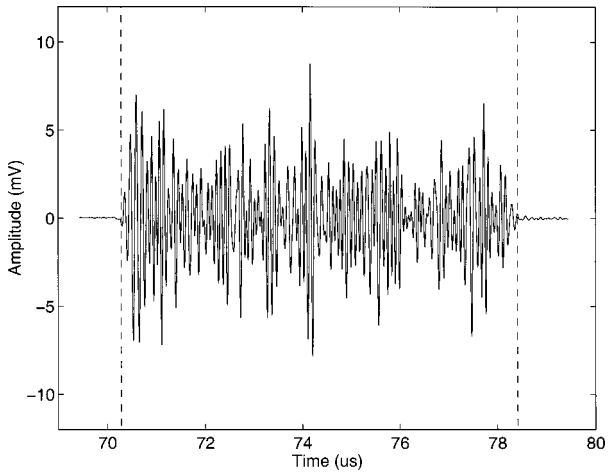

FIG. 4. The backscattered signal from a rat semi-membranosus muscle at 90° orientation to the sound beam. Dashed vertical lines are determined from an algorithm to find muscle surfaces $t_{1,2}$.

C. Analysis of data

Attenuation measurements require knowledge of the sample thickness, but since it is difficult to physically measure fresh tissue thickness, we use a technique employing the pulse times-of-flight (TOF) to the hydrophone with and without the specimen in the beam path (T_m and T_w, respectively), and the TOF back to the transducer from both muscle surfaces (t_1 front, t_2 back). See Fig. 4 for an example of the backscattered signal with the $t_{1,2}$ surfaces determined by an algorithm which looks for the first and last points which are greater than three times the baseline amplitude. (This baseline is defined as the average of the absolute value of the first 100 points—0.4 μs—of the captured waveform, which are arranged to be before the front surface of the sample.) Note the time difference between front and back surfaces is corrected in the analysis for the transmitted pulse duration, Δ (0.42 μs and 0.23 μs for the 6- and 10-MHz transducers, respectively). We calculate the speed of sound in the muscle, c_m, by:[17]

$$c_m = c_w\left[1+\frac{2(T_w-T_m)}{t_2-t_1-\Delta}\right], \tag{1}$$

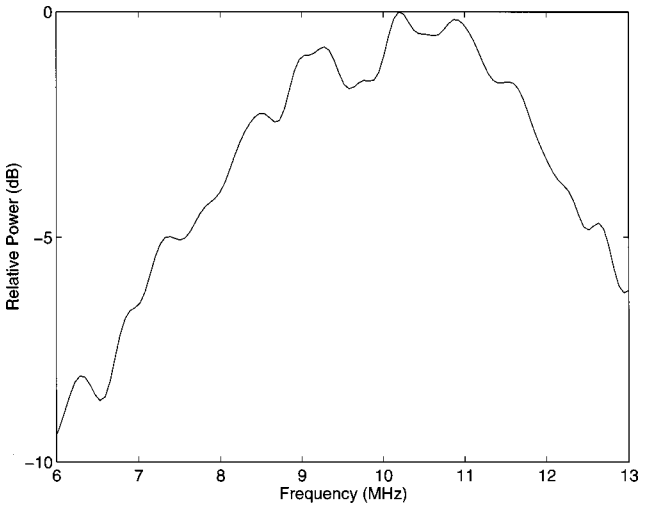

FIG. 5. Example of the echo spectrum from a semimembranosus muscle sample, measured with the 10-MHz transducer.

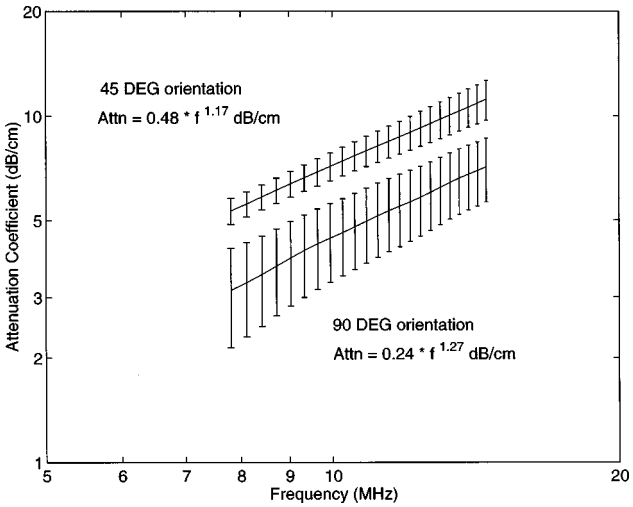

FIG. 6. Example of attenuation coefficient in a single muscle (semimembranosus #1) at 45° and 90°. Data are shown over the −5-dB bandwidth of the received hydrophone signal for the 10-MHz transducer, although the fit (not shown) is performed over −3 dB. Expressions for the best fit to each orientation are given in the figure, where f is in MHz. Error bars are the standard deviation of the 25 spatial samples in each case.

where c_w is the measured speed of sound in the Tyrode solution (1538 m/s at 37 °C). Then $c_m(t_2-t_1-\Delta)/2$ is the thickness of the muscle at that point. With thicknesses known, attenuation is then calculated by the insertion loss technique, in which the power spectrum of the signal transmitted through the sample is simply compared to the power spectrum received without the sample in the sound path.

Absolute backscatter coefficient is determined according to the method of Insana and Hall[18,19]

$$\sigma_b(f)=\frac{0.36R_1^2\gamma^2}{A_0\Delta z}e^{+4(\alpha_m-\alpha_0)(R_s+\Delta z/2)}\frac{\langle|S(f)|^2\rangle}{|R(f)|^2}, \qquad (2)$$

where R_1 is the average distance between the transducer and the near surface of the sampled volume, A_0 is the area of the transducer aperture, Δz is the axial length of the sampled volume, R_s is the distance from the muscle front face to the near surface of the sampled volume, α_m and α_0 are the frequency-dependent attenuation coefficients of the sample (measured for each case) and Tyrode solution (assumed similar to water), respectively, and $\langle|S(f)|^2\rangle$ is the spatially averaged power spectral estimate from the laterally sampled, diffraction corrected, Hanning gated[20] backscattered waveforms. [See Fig. 5 for an example of $\langle|S(f)|^2\rangle$ from a semimembranosus muscle.] $|R(f)|^2$ is the reference power spectral estimate obtained from the reflection against the Plexiglas plane reflector—with amplitude reflection coefficient $\gamma=0.35$—evaluated at axial distance $R_1+\Delta z/2$. Note that a factor of 4 error in our previous backscatter analysis[21] has been found and corrected.

The gated window depth for backscatter analysis of the semimembranosus muscles was 5 μs (4 mm), starting 1 μs below the front surface (to avoid surface reflections), and for the thinner soleus muscles was necessarily smaller, 3 μs (2.4 mm) at 0.5 μs below the front surface, to ensure the same sampling volume on all samples of the same muscle type. To check the effect of window gate length, the semimembranosus data were also analyzed with a 3-μs window, starting also at 1 μs below the front surface. This analysis showed no significant difference to that with the 5-μs gate, as determined by the best fits to both analyses of the same data having the same amplitude and power law exponent within a few percent.

II. RESULTS

The attenuation coefficient in each muscle shows a distinct difference between measurement with the muscle fibers at 90° and 45° to the incident sound beam. An example of $\alpha(f)$ for a single muscle (semimembranosus #1) is shown in Fig. 6 where the lines are the spatial averages over a given muscle orientation and the error bars the standard deviation of the 25 spatial samples. In 17 of the 20 muscle samples measured, the error bars of the two orientations were well separated like this; in the other three, there was some over-

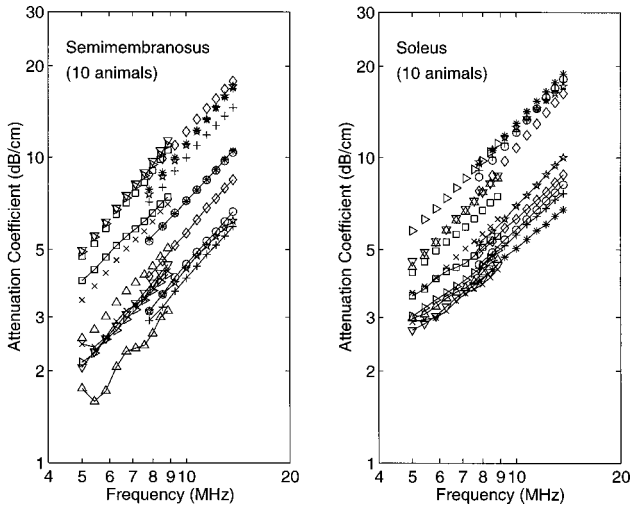

FIG. 7. Attenuation coefficient at 45° and 90° for the ten rat semimembranosus and ten rat soleus muscles. Different symbols represent individual muscles, where the higher valued data of each pair are the 45° orientation. For ease of distinction, the 90° orientation data have been connected with lines.

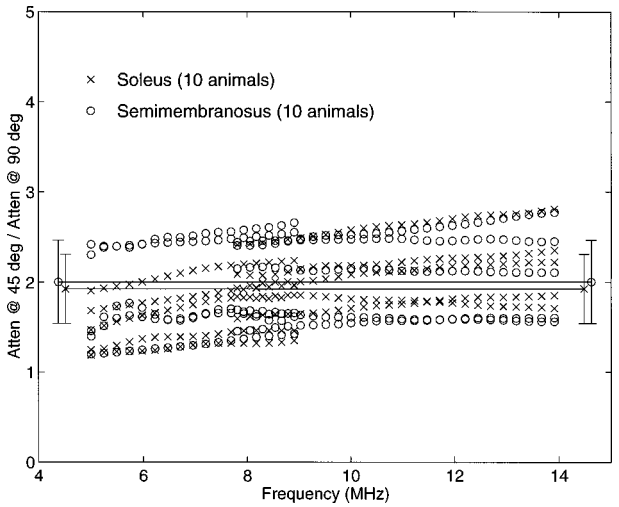

FIG. 8. Ratio of $\alpha(f)$ at 45° vs 90° for all 20 muscle samples. Solid lines represent the frequency-independent average of the $\alpha(f)_{45°}/\alpha(f)_{90°}$ ratio over the measured frequency range, and the error bars the standard deviation, for each muscle type ($N=10$).

lap. The average $\alpha(f)$ values for all 20 samples are shown in Fig. 7, where different symbols in each graph represent individual animals. Again, due to the time sensitivity of our measurements, a single muscle could not be measured with sufficient thoroughness at both orientations by both transducers, and so measurements on each sample are limited to the useful bandwidth of one transducer. For the purpose of distinction, the 90° orientation data are represented with both symbols and solid lines. The 45° data are always higher than 90°. Although the two orientations among all samples are not entirely separate, the ratio within each muscle stays fairly consistent (see Fig. 8). For both muscle types, the value of $\alpha(f)_{45°}/\alpha(f)_{90°}$ is very near to 2 (± 0.4) over the measured frequency range.

The averaged speed of sound values are given in Table I and plotted in Fig. 9. The difference between the two orientations in fresh muscle is only on the order of 0.5%, and the error bars here, due to the method of measuring thickness at each sampled location, have values close to the difference between orientations. Paired t-test analysis of the two orientations for each muscle type give probabilities of 0.006 and 0.0008 for the semimembranosus and soleus, respectively, that the speeds of sound for each orientation are from the same population. The observation that c at 90° is larger than at 45° contrasts with previous work[9,14,15] showing faster propagation parallel to muscle fibers. We note here that none of the previous work has been performed on rat muscle, nor

TABLE I. Average speeds of sound±standard deviation (m/s) in freshly excised rat semimembranosus and soleus muscles at 37 °C as a function of muscle fiber orientation to the sound field. $N=10$ for each muscle type. Measurements were taken with either a 6- or 10-MHz center frequency transducer. Standard deviation of the spatially averaged speed within one muscle is typically ~4 m/s, but can be up to ~7 m/s.

Semimembranosus	speed (m/s)	Soleus	speed (m/s)
90°	1589±5	90°	1582±3
45°	1581±5	45°	1576±4

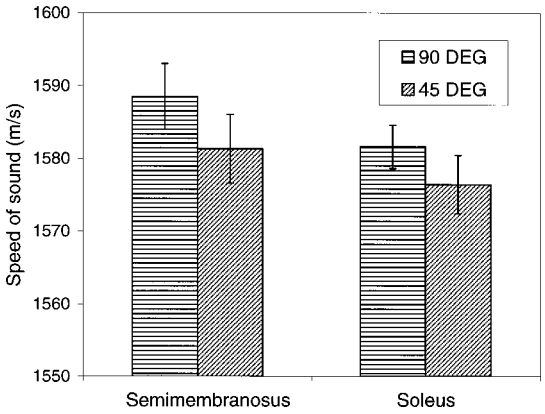

FIG. 9. Speeds of sound averages for the ten semimembranosus and ten soleus muscles measured at 45° and 90°.

apparently on samples that are measured this soon *post-mortem*. For a comparison between our fresh muscle measurements and *post-rigor* rat muscle, two of the same muscle samples for each type were measured one day later (*post-rigor*) after overnight storage in saline in the refrigerator. The speed of sound in each case decreased by close to 1%, indicating some softening, but the propagation speed for the four samples remained faster for the 90° orientation (but the difference was less: 0.2%–0.3% for the *post-rigor* samples).

The backscatter coefficient as a function of frequency is plotted in Fig. 10 for the ten semimembranosus muscles, and in Fig. 11 for the ten soleus. The symbols in each graph represent a different animal, and again the 90° orientation data are joined with solid lines to distinguish them from the values at 45°. In the semimembranosus, the power-law fit (straight line) to the 90° population is clearly a factor of ~30 or more higher than the fit to all the 45° backscatter data, and within each animal, the difference in orientations is at least an order of magnitude. The soleus backscatter data show a similar degree of anisotropy, with fits to the ensemble at each

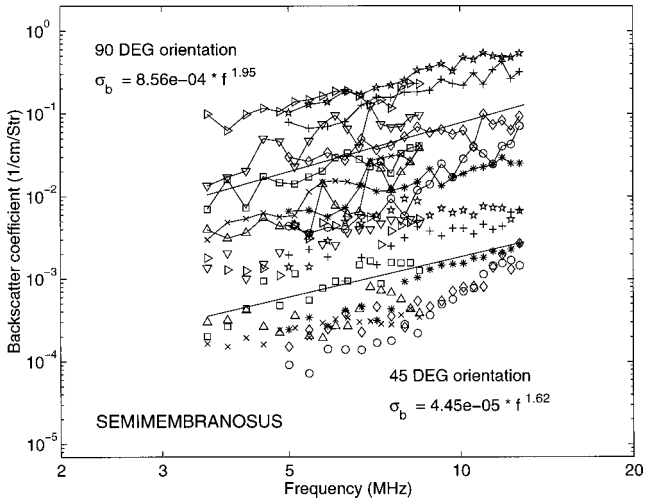

FIG. 10. Backscatter coefficient at 45° and 90° for the ten semimembranosus muscles. Symbols represent individual muscles, and the 90° data have been connected with solid lines to distinguish them from those measured at 45°. Straight lines are power-law fits to all samples at the given orientation. Expressions for each fit are given in the figure (in units of $cm^{-1}\,Str^{-1}$, with f in MHz).

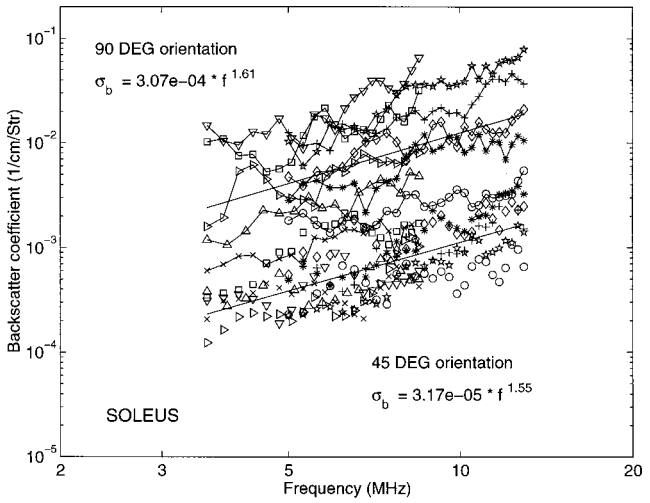

FIG. 11. Backscatter coefficient at 45° and 90° for the ten soleus muscles. Symbols represent individual muscles, and the 90° data have been connected with solid lines to distinguish them from those measured at 45°. Straight lines are power-law fits to all samples at the given orientation. Expressions for each fit are given in the figure (in units of $\mathrm{cm}^{-1}\,\mathrm{Str}^{-1}$, with f in MHz).

orientation a factor 10 apart. Note that $\sigma_b(f)$ values taken by the same method on a homogeneous, isotropic tissue phantom show no difference at all in magnitude or frequency dependence, within experimental uncertainty. The frequency dependence for both muscles and both orientations ranges between $f^{1.5}$ and f^2, with the 90° orientation typically having a slightly higher frequency dependence. A regression analysis of the log–log fits to each muscle and orientation gives $r^2 \approx 0.8$ in each of the four cases ($N=10$).

III. DISCUSSION AND CONCLUSIONS

Distinct differences are observed in the ultrasonic parameters of rat skeletal muscle held with muscle fibers at 90° and 45° to the sound beam. Attenuation values within each muscle show a distinctive increase as the muscle fibers are turned from 90° to 45°, and the ratio of $\alpha_{45°}/\alpha_{90°}$ is consistent at ~2 across the frequency range measured here. This amount of anisotropy is in good agreement with earlier measurements on frozen and *post-rigor* bovine skeletal muscle[9,11–13] and fresh canine myocardium[3] which showed ratios of 1.9 to 3.4 for attenuation parallel versus perpendicular to the muscle fibers ($\alpha_{0°}/\alpha_{90°}$); if one assumes a roughly sinusoidal variation of attenuation with angle of insonification (as seen in the oriented-fiber tissue phantom and canine myocardium samples of Miller *et al.*[3]), this would correspond to $\alpha_{45°}/\alpha_{90°}$ ratios of 1.5 to 2.2.

Speeds of sound in both muscles are seen here to be slightly faster for the 90° orientation, contrary to previous work on fixed and frozen muscle samples,[4,9] and fresh dog,[14] rabbit,[14,15] and frog[15] skeletal muscle. In all cases the difference between speeds measured parallel and perpendicular to the sound beam is on the order of 1% or less, and thus the accuracy of the method for determining sample thickness (which is easier for frozen and fixed tissue) becomes crucial. Although the possibility of systematic error in our determinations of fresh sample thickness exists, a statistical analysis of our propagation speeds at 45° and 90° orientations indicates that our means are distinct. [Note also, an indication of our similar ability to measure speed at both orientations is given by the standard deviation (s.d.) values for the 25 spatial samples of a given muscle and orientation. In comparing s.d.s between orientation groups, the average s.d.s were 3.9 m/s and 4.5 m/s for the 90° and 45° measurements, respectively, with the range in both cases 2–7 m/s.] As a check of our speed of sound technique, a sample of bovine semitendinosis (beef eye of round, grocer preparation) was cut, with sides parallel to muscle fibers, to the approximate size of a rat semimembranosus (0.5 cm thick). Using the same equipment and analysis techniques, including the threshold detection of front and back surfaces to determine sample thickness, the speed of sound was measured with the muscle fibers at 45° and 90° orientations. For this bovine muscle, the speed of sound was measured to be larger at 45° (1553.4 $\pm$3.5 m/s at 21 °C) than at 90° (1547$\pm$3.5 m/s at 21 °C) in agreement with earlier studies on speed of sound in muscle.[4,9,14,15]

The 0.4%–0.5% greater speed in the 90° measurements of rat skeletal muscle seen here may be particular to the rat, in which speed of sound measurements have not previously been measured. The role of freshness was checked with our four *post-rigor* muscle samples, measured in the same manner; although the speeds of sound decreased for the day-old muscles by ~1%, the propagation perpendicular to the muscle fibers remained faster than that at 45°. (The anisotropy did appear to decrease somewhat from ~0.5% to ~0.2% but since only 4 samples were measured compared to the 20 fresh, a quantitative comparison is not valid.) It was not the purpose of this work to examine the *post-mortem* time dependent effects on sound speed, and more measurements will be required to determine under which conditions mammalian skeletal muscle may have faster or slower propagation speeds at a given orientation; but in any case, the anisotropy of speed of sound in fresh tissue is not large.

Backscatter coefficient is the most anisotropic of the measured ultrasound parameters. The average $\sigma_b(f)$ values of the two measured orientations are separated by over an order of magnitude for both the semimembranosus and soleus muscles. The frequency dependence of the backscatter, averaging between $f^{1.5}$ and f^2, is not significantly different between muscles, and although the 90° orientation typically has a slightly higher frequency dependence in a given muscle, the ensemble average for the soleus muscle smears out this difference. (Note that although there is significant variability of the backscatter coefficient values from sample to sample, and the fact that each sample was not measured over the entire frequency range does compromise the frequency dependence, we believe the ensemble of ten samples of each muscle type represents a reasonable statistical sample for showing the magnitude differences and rough frequency dependence of each orientation.)

The frequency dependence of scattering can provide information as to the size of scatterer; Lizzi *et al.*[22] have found a relationship between the frequency dependence of the backscatter (expressed in dB/MHz) and the effective diameter of the scatterers in ocular tissue. Although they assume approximately spherical scatterers, we find it interesting to consider their model in examining our muscle samples of

presumably elongated scatterers. In using their spectral slope relationship, we find from our data an ''effective scatterer diameter'' of approximately 60 μm. Interestingly, a morphometric study of soleus muscle fiber in male and female rats[23] determined a 63–64 μm diameter of the predominantly (90%) type I (slow-twitch) muscle fibers. Our microscope images of both the soleus and semimembranosus muscle (Fig. 1) also indicate muscle fiber diameters on the order of 60 μm. This suggests that the effective scatterers in rat skeletal muscle might be the myofibers, instead of the smaller sarcomeres or myofibrils, or the larger myofiber bundles.

In summary, anisotropy in rat skeletal muscle has been quantified here by characterizing attenuation, speed of sound, and backscatter coefficient as a function of the muscle fiber orientation to the sound field. The anisotropy of speed is seen to be quite small, but attenuation differs by a factor of 2 with 90° and 45° orientation, and backscatter by over an order of magnitude. The mechanisms which produce the anisotropy in these parameters must be related to orientation of the elastic tissue structure, and it seems likely that scatterers of the size of the muscle fibers are involved. More work must be done, however, to uncover the physical causes of the observed ultrasound interaction with biological tissue.

ACKNOWLEDGMENTS

We thank Professor James Zachary, Kandice Spraker, Jim Blue, Professor Phil Best, and Jennifer Mitchell for advice and assistance with the animals, and Professor Timothy Hall for helpful discussions of backscatter data analysis. Special thanks to Professor Zachary for facilitating the microscope images. This work was supported in part by CA09067 from the National Institutes of Health.

[1] J. G. Mottley and J. G. Miller, ''Anisotropy of the ultrasonic backscatter of myocardial tissue: I. Theory and measurement *in vitro*,'' J. Acoust. Soc. Am. **83**, 755–761 (1988).
[2] E. I. Madaras, J. Perez, B. E. Sobel, J. G. Mottley, and J. G. Miller, ''Anisotropy of the ultrasonic backscatter of myocardial tissue: II. Measurements *in vivo*,'' J. Acoust. Soc. Am. **83**, 762–769 (1988).
[3] J. G. Mottley and J. G. Miller, ''Anisotropy of the ultrasonic attenuation in soft tissues: Measurements *in vitro*,'' J. Acoust. Soc. Am. **88**, 1203–1210 (1990).
[4] E. D. Verdonk, S. A. Wickline, and J. G. Miller, ''Anisotropy of ultrasonic velocity and elastic properties in normal human myocardium,'' J. Acoust. Soc. Am. **92**, 3039–3050 (1992).
[5] B. K. Hoffmeister, E. D. Verdonk, S. A. Wickline, and J. G. Miller, ''Effect of collagen on the anisotropy of quasi-longitudinal mode ultrasonic velocity in fibrous soft tissues: A comparison of fixed tendon and fixed myocardium,'' J. Acoust. Soc. Am. **96**, 1957–1964 (1994).
[6] B. K. Hoffmeister, S. M. Handley, E. D. Verdonk, S. A. Wickline, and J. G. Miller, ''Estimation of the elastic stiffness coefficient c_{13} of fixed tendon and fixed myocardium,'' J. Acoust. Soc. Am. **97**, 3171–3176 (1995).
[7] B. K. Hoffmeister, S. E. Gehr, and J. G. Miller, ''Anisotropy of the transverse mode ultrasonic properties of fixed tendon and fixed myocardium,'' J. Acoust. Soc. Am. **99**, 3826–3836 (1996).
[8] C. S. Hall, E. D. Verdonk, S. A. Wickline, J. E. Perez, and J. G. Miller, ''Anisotropy of the apparent frequency dependence of backscatter in formalin fixed human myocardium,'' J. Acoust. Soc. Am. **101**, 563–568 (1997).
[9] W. D. O'Brien, Jr. and J. E. Olerud, ''Ultrasonic Assessment of Tissue Anisotropy,'' 1995 IEEE Ultrasonics Symposium Proceedings, pp. 1145–1148 (1995).
[10] M. F. Insana, T. J. Hall, and J. L. Fishback, ''Identifying acoustic scattering sources in normal renal parenchyma from the anisotropy in acoustic properties,'' Ultrasound Med. Biol. **17**, 613–626 (1991).
[11] V. Roberjot, P. Laugier, and G. Berger, ''Anisotropy in bovine skeletal muscle in vitro: Frequency dependent attenuation and backscatter coefficient over a wide range of frequencies,'' 1994 IEEE Ultrasonics Symposium Proceedings, pp. 1467–1470 (1994).
[12] D. Shore, M. O. Woods, and C. A. Miles, ''Attenuation of ultrasound in *post rigor* bovine skeletal muscle,'' Ultrasonics **24**, 81–87 (1986).
[13] D. K. Nassiri, D. Nicholas, and C. R. Hill, ''Attenuation of ultrasound in skeletal muscle,'' Ultrasonics **17**, 230–232 (1979).
[14] D. E. Goldman and J. R. Richards, ''Measurement of high-frequency sound velocity in mammalian soft tissues,'' J. Acoust. Soc. Am. **26**, 981–983 (1954).
[15] C. R. Mol and P. A. Breddels, ''Ultrasound velocity in muscle,'' J. Acoust. Soc. Am. **71**, 455–461 (1982).
[16] We use a recipe for Tyrode solution from the laboratory of Professor P. Best, Dept. of Physiology, University of Illinois (in mM units): 137 NaCl, 5.4 KCl, 1$MgCl_2$, 0.33 NaH_2PO_4, 10 HEPES (buffer), 2$CaCl_2$; adjust *p*H to 7.4 with NaOH; add dextrose to 290 osmolarity. Original reference: M. V. Tyrode, ''The mode of action of some purgative salts,'' Arch. Internat. Pharm. Thérap **20**, 205–223 (1910).
[17] C.-Y. Wang and K. K. Shung, ''Variation in ultrasonic backscattering from skeletal muscle during passive stretching,'' IEEE Trans. Ultrason. Ferroelectr. Freq. Control **45**, 504–510 (1998).
[18] M. F. Insana and T. J. Hall, ''Parametric ultrasound imaging from backscatter coefficient measurements: image formation and interpretation,'' Ultrason. Imaging **12**, 245–267 (1990).
[19] M. F. Insana, R. F. Wagner, D. G. Brown, and T. J. Hall, ''Describing small-scale structure in random meda using pulse-echo ultrasound,'' J. Acoust. Soc. Am. **87**, 179–192 (1990).
[20] See for example, A. V. Oppenheim and R. W. Schafer, *Digital Signal Processing* (Prentice-Hall, Englewood Cliffs, NJ, 1975).
[21] E. L. Madsen, F. Dong, G. R. Frank, B. S. Garra, K. A. Wear, T. Wilson, J. A. Zagzebski, H. L. Miller, K. Shung, S. H. Wang, E. J. Feleppa, T. Liu, W. D. O'Brien, Jr., K. A. Topp, N. T. Sanghvi, A. V. Zaitsev, T. J. Hall, J. B. Fowlkes, O. D. Kripfgans, and J. G. Miller, ''Interlaboratory comparison of ultrasonic backscatter, attenuation, and speed measurements,'' J. Ultrasound Med. **18**, 615–631 (1999).
[22] F. L. Lizzi, M. Astor, T. Liu, C. Deng, D. J. Coleman, and R. H. Silverman, ''Ultrasonic spectrum analysis for tissue assays and therapy evaluation,'' Int. J. Imaging Syst. Technol. **8**, 3–10 (1997). For an earlier work, see also F. L. Lizzi, M. Ostromogilsky, E. J. Feleppa, M. C. Rorke, and M. M. Yaremko, ''Relationship of Ultrasonic Spectral Parameters to Features of Tissue Microstructure,'' IEEE Trans. Ultrason. Ferroelectr. Freq. Control **34**, 319–329 (1987).
[23] I. Ustunel and R. Demir, ''A Histochemical, morphometric and ultrastructural study of gastrocnemius and soleus muscle fiber type composition in male and female rats,'' Acta Anat. (Basel) **158**, 279–286 (1997).

Spectral cues and perception of the vertical position of targets by the big brown bat, *Eptesicus fuscus*

J. M. Wotton[a] and J. A. Simmons
Department of Neuroscience, Box 1953, Brown University, Providence, Rhode Island 02912

(Received 12 April 1999; revised 11 October 1999; accepted 11 October 1999)

Big brown bats (*Eptesicus fuscus*) were trained to discriminate between vertical angles subtended by paired beads suspended from fishing line. Bats were rewarded for choosing the smaller of the two angles presented. The difference between the angles was changed systematically using a transformed up–down procedure and the bats' ability to detect the difference was measured at different vertical locations. When the beads were centered at +20° (above the horizon), at 0° (the horizon), and at −20° (below the horizon), vertical angle acuity (VAA) was maintained between 2.9° and 4.1°. At more extreme vertical positions both bats showed loss of acuity; when the beads were centered around −40°, VAA was 6.7° or 8.3° and at +40, VAA was worse than 21° (the largest difference tested). When the tragi of both ears were bent down and glued to the side of the face, bats showed severe loss of acuity for beads centered at −20° (VAA 18.3° and 20.1°), but maintained their angle acuity for beads centered at +20° (VAA 3.8° and 4.9°). The results are consistent with the spectral cues created by the filtering of the external ear. © *2000 Acoustical Society of America.* [S0001-4966(00)05901-4]

PACS numbers: 43.80.Lb, 43.80.Ka, 43.66.Qp [WA]

INTRODUCTION

The shape and structure of the external ear provides information vital for vertical localization because the head and ears act as spatially dependent filters for sound (Blauert, 1969; Butler and Belendiuk, 1977; Hebrank and Wright, 1974). This filtering creates spectral cues that human subjects appear to use in localizing the elevation of a sound source (e.g., Asano *et al.*, 1990; Wightman and Kistler, 1989; Middlebrooks, 1992). Spatially dependent spectral peak and notch cues are produced by the external ears of humans (Shaw, 1974,1982; Searle *et al.*, 1975; Wightman and Kistler, 1989), cats (Musicant *et al.*, 1990; Rice *et al.*, 1992), ferrets (Carlile, 1990), the pallid bat (Fuzessery, 1996), and the big brown bat, *Eptesicus fuscus* (Wotton *et al.*, 1995). The frequency notches created by cat, ferret, and human ears occur for sound sources both above and below the horizon. However, by comparison, the changes in the primary notch frequency information for *Eptesicus* are not symmetrical around the horizon and it appears that distinctly different cues may be used to determine location above and below the horizon. The primary notch cue is prominent for locations near and below the horizon, while systematic changes in the magnitude of a peak and secondary notches could provide information for locations above the horizon (Wotton *et al.*, 1995).

If the cues are different above and below the horizon, then the acuity of the bat may differ too. One aim of this study is to see if the vertical location of the targets influences the bats' vertical angle acuity (VAA). Minimum audible angle measurements have been made for the passive sound localization ability of *Eptesicus* and reveal acuity of 14° (Koay *et al.*, 1998). However, for echolocating bats the available data for behavioral acuity are in terms of discriminating angle differences. Paired objects are strung in front of the bat and it chooses the pair that subtends the smallest angle. This task presumably utilizes the localization process; bats must locate the position of each object in order to compare the angles or to compare the absolute location of each object with the others. Near the horizon, the acuity of angle discrimination by *Eptesicus* is about 3° to 3.5° for vertical angles (Lawrence and Simmons, 1982a) and 1.5° for horizontal angles (Masters *et al.*, 1985; Simmons *et al.*, 1983).

The echolocation sound emitted by *Eptesicus* is a frequency-modulated (FM) sweep, ranging from about 100 kHz down to 25 kHz, with two or three harmonics (Simmons *et al.*, 1979; Simmons, 1987). Combining the directional properties of the sonar emission and the ear creates an area of greatest echolocation directional information of about ±30° in azimuth (for *Eptesicus*, Simmons *et al.*, 1995; and other bat species, e.g., Grinnell and Schnitzler, 1977; Schnitzler and Grinnell, 1977; Fuzessary *et al.*, 1992) and in elevation (Simmons *et al.*, 1995; Wotton *et al.*, 1997). It seems likely that bats would display the best acuity for objects within the region that contains the clearest differences in location information. Comparison of the spectra produced by the combined echolocation signal shows the spectral information available to the bat to distinguish different locations (Wotton *et al.*, 1997). For positions above the horizon and within the 0° to +30° range, the spectra have different gradients and peak/notch transitions, but at higher elevations (such as 50° and 60°) the spectra are almost indistinguishable. Systematic notch frequency differences occur in spectra for positions within the range 0° to −30°. At much lower elevations the notch frequency remains constant but other less systematic spectral differences exist. If bats are using spectral location information to perform VAA discrimina-

[a]Present address: Department of Biology, Gustavus Adolphus College, 800 College St., St. Peter, MN 56082.

tions, then we predict that the VAA of bats would be best within the range ±30° in elevation. At extremely high elevations, bats would perform poorly and at extremely low elevations the unsystematic nature of the spectral information could result in a loss of acuity. We aim to test the VAA of the bats with targets positioned within ±30° in elevation and at more extreme angles above and below this range.

Simmons and Grinnell (1988) suggested that reverberations of sound between the pinna and tragus create the primary acoustic cues for vertical localization. Manipulating the tragus of *Eptesicus* affects the neural sensitivity for elevations below the horizon but not those above the horizon (Grinnell and Grinnell, 1965). Removal of the tragus severely alters the notch cue but appears to have less effect on the peak cue in the external ear transfer functions (Wotton *et al.*, 1995). Notch frequency is known to influence elevation-dependent behavior of *Eptesicus* near and below the horizon (Wotton *et al.*, 1996). Lawrence and Simmons (1982a) showed that deflecting the position of the tragus interfered with the ability of *Eptesicus* to discriminate vertical angles. The bats' VAA was estimated to be altered from about 3° (intact ear) to 12° to 14° (tragus deflected). These bats were discriminating near or below the eye–nostril horizon, presumably utilizing the information provided by the notch cue. It is not known if the same poor discrimination performance would occur if the bats were examining targets positioned above the horizon. If *Eptesicus* uses another cue for encoding direction above the horizon, then we would predict that manipulating the tragus should not interfere with the bats' VAA in this region.

This study aims to use a similar paradigm to that of Lawrence and Simmons (1982a) in order to test the bat's vertical angle acuity (VAA) for objects at different vertical locations and to examine the consequences of bending the tragi for discriminations above and below the horizon.

I. METHODS

A. Bats

Two big brown bats, *Eptesicus fuscus* (see Kurta and Baker, 1990) were used in this experiment. The bats (Wom and Acro) were obtained from houses in Rhode Island and southeastern Massachusetts. Both were maintained at body weights between 13 and 15.5 grams. Their diet consisted of the larvae of *Tenebrio* (mealworms) and they were given vitamin supplements in freely available water. The bats were hand-fed daily during the training or experimental sessions (5 or 6 days a week) and on rest days they were given food in a dish. They were kept on a reversed light/dark schedule (lights out between 7 am and 7 pm) at a room temperature of about 26 °C.

B. Apparatus

Behavioral experiments were conducted in a dimly lit, anechoic room (3.5-m-wide×4.5-m-long×2.3-m-high). The bat was placed on a small Y-shaped platform (7-cm-wide at base×14-cm-long) which was 1.2 m above the floor. Small wooden beads (diameter about 1.5 cm) were suspended on fishing line (10 lb. test) strung 50 cm in front of the platform

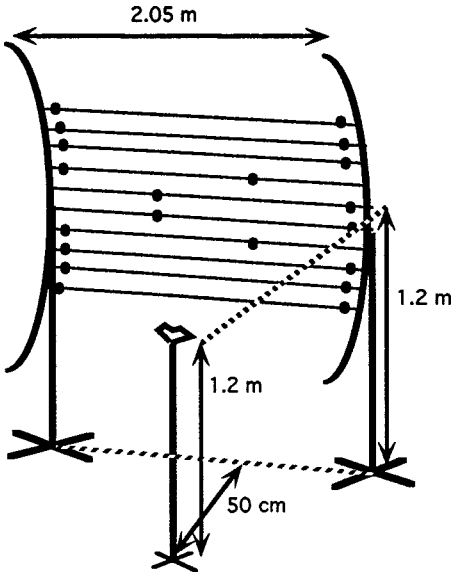

FIG. 1. Diagrammatic view of the experimental apparatus. Rows of fishing line were suspended horizontally between two large, vertically aligned, semicircular rods. The rods were 2.05 m apart. Two wooden beads were threaded on each line. The bat was placed on the Y-shaped platform facing the bead array (distance 50 cm from array). The fishing lines were separated vertically by known distances to provide specific vertical angles relative to the behavior platform (not all lines are shown in the figure). This is a slightly off-centered view of the equipment.

(see Fig. 1). The fishing line was strung taut between two large semicircular curved aluminum rods (length of rod end-to-end 1.94 m) aligned vertically and supported by wooden bases (height 1.53 m, cross base 1.23 m). The center of the semicircle of each rod was positioned at 1.20 m to be level with the platform. The two rods were 2.05 m apart with the platform in the middle. Attached to each of the curved rods were 20 clamps, with two protruding screws at the top and bottom of each clamp. The fishing line was tied to one screw on the left rod and to one screw at the same height on the right rod. Forty lines were strung between the two rods and on each line two beads were suspended. As the rods were semicircular, every line was at a distance of approximately 50 cm from the bat. The entire apparatus resembled a large, curved, horizontal abacus.

The vertical angular separation of the lines was set by the position of the clamps and each line was labeled with the vertical angle relative to the horizontal plane of the platform. The fishing line at the level of the platform was labeled 0°. The fishing lines tied to the top and bottom of the same clamp were separated by an angle of 2° and the lines tied to adjacent clamp screws (e.g., bottom of one clamp and top of the next) were separated by an angle of 1°.

C. Experimental procedure

1. Initial training

Bats were individually trained using a two-alternative forced-choice (2AFC) procedure (similar to the procedure outlined in Simmons, 1973, 1979). At the beginning of a trial the bat was placed at the base of a Y-shaped platform where it could make one of two responses, walking down either the right or left arm of the platform; only one response was

rewarded. After the bat completed its response, it was removed from the platform and the trial was ended. If the bat flew away before the end of a trial, that trial was canceled and a new one begun when the bat was returned to the platform.

To train the bats to choose between different vertical angular separations, two Styrofoam balls close together (separated vertically by 2–3 cm) were mounted on one rod and two balls separated vertically by 15–20 cm on the other. Bats were rewarded with a mealworm for correctly choosing to walk down the arm of the platform with the ball separation of 2–3 cm. When the bats performed this task to a level of 75% correct they were transferred to the ''abacus'' apparatus. Both bats had two practice sessions to allow them to become accustomed to this new equipment before experimental data were collected.

2. Bead-pair discrimination

Two beads were aligned vertically on the left side of the platform and two beads were aligned vertically on the right side of the platform; the horizontal angle was approximately 10° to 15° from the midline of the platform for each side. Beads at different elevations were chosen for the left or right bead pair to alter the vertical angular separation. Bats were rewarded for choosing the side with the smaller angular separation between the bead pair. All beads not in use for a trial were pushed far away to the sides of the apparatus near the clamps (see Fig. 1).

The side with the rewarded stimulus was chosen on a pseudorandom schedule with no more than three consecutive correct responses to the same side. To avoid giving obvious cues indicating that the rewarded side was being changed, the experimenter always walked to the abacus between trials and shuffled the beads.

Lawrence and Simmons (1982a) used the method of limits, with the larger angle being decreased each day until the two rod pairs subtended the same angle. However in our experiment, the difference between the vertical separation of the bead pairs was varied in steps according to a transformed up–down procedure described by Levitt (1971). After three consecutive correct responses the angular difference between the stimuli was reduced by 2° for the next trial; after any incorrect response the difference was increased by 2° for the next trial. After three reversals (change from a run in one direction to a run in the other direction), the change in stimulus step size was reduced to 1°. As recommended by Wetherill and Levitt (1965), testing continued until at least six or eight reversals were obtained in order to estimate the required difference level. This particular choice of response grouping caused the observations to converge on the difference level which produces a 79%-correct threshold (Levitt, 1971).

3. Experimental manipulation

Lawrence and Simmons (1982a) used pairs of brass rods with an angular separation centered on 0° in elevation. To verify the results of the Lawrence and Simmons experiment, the bead pairs in this experiment were initially centered on 0°. For example, to test an 8° difference, beads in one pair could be at elevations of +7° and −7° (angular separation 14°) and at elevations of +3° and −3° in the other pair (angular separation 6°). The vertical positions of the individual beads in a pair were changed to test different angle separations, but each pair was still centered as closely as possible on 0°.

To determine if VAA is altered when the discrimination is performed at different elevations, bats were also tested with bead pairs centered on four other elevations (+20°, −20°, +40°, or −40°). To produce the necessary angles around ±40°, the clamps and fishing line were shifted up or down the aluminum rods prior to the start of the experiment. Each of the five elevation conditions was conducted on a separate day and eight run reversals were obtained for each bat on that day. Thus, the transformed up–down procedure enabled a measurement of VAA in a single experimental session. The initial angle difference tested at the beginning of each experiment was 8°.

Within an experimental block the rewarded angle was varied as little as possible. The beads were not equally spaced (beads on the same clamp were separated by 2° and on adjacent clamps by 1°); consequently, it was sometimes necessary to adjust both bead pairs in order to produce the appropriate angle differences. VAA was determined by the bat's ability to discriminate the difference between the larger and smaller angles, not the absolute angle of bead pairs. For example, a bat displaying a VAA of 6° could be discriminating between one bead pair of 4° and the other of 10° or between a bead pair of 6° and the other of 12°. The rewarded angle was 5° during the conditions ±40° and varied for the other locations as follows; at 0° elevation either 6° or 3°; +20° elevation either 3° or 4°; at −20° elevation either 5° or 6°.

The effect of tragus manipulation on the VAA of bats for beads centered above (+20°) and below (−20°) the horizon was also tested. The tragi of both ears were bent down and glued to the fur on the sides of the face using superglue (as done by Lawrence and Simmons, 1982a). At the conclusion of the experimental session the glue was removed with acetone and the tragi resumed their normal position. The +20° condition and −20° condition were both tested in the same experimental session. Wom did the +20° condition first, then the −20° condition, Acro did the two tasks in the reverse order. Wom did the experiment first and as a consequence the experimenter's choices of the initial angle differences for Acro were influenced by Wom's performance. Six run reversals were obtained for each bent-tragus condition.

D. Head-aim system

The acoustic aim of the bat's head was monitored throughout part of this experiment. Head aim was determined by the relative amplitude of each of the bat's sonar emissions measured at four microphones arranged in a diamond-shaped array located 1.5 m from the Y-shaped platform (described in Wotton *et al.*, 1996). Measurements of head angle were made from videotape of bats and used to calibrate the acoustic head-aim system to spatial coordinates. The mean position (in elevation and azimuth) of acoustic aim

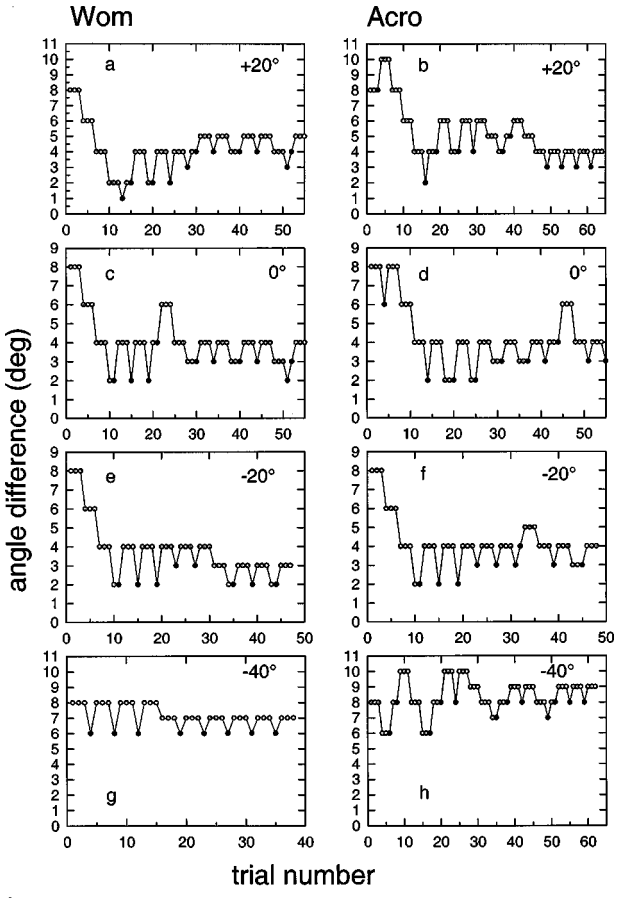

FIG. 2. The angle difference tested in each trial is plotted as a function of the trial number. Each panel shows the results for Wom and Acro (respectively) for a different experiment with the beads centered at a different vertical position: (a) and (b) +20°; (c) and (d) 0°; (e) and (f) −20°; (g) and (h) −40°. For all plots, open circles indicate a trial in which the bat responded correctly and was rewarded. Filled circles indicate an incorrect choice. The angle difference tested decreased only after three consecutive correct responses and any incorrect response resulted in an increase in the next tested angle difference.

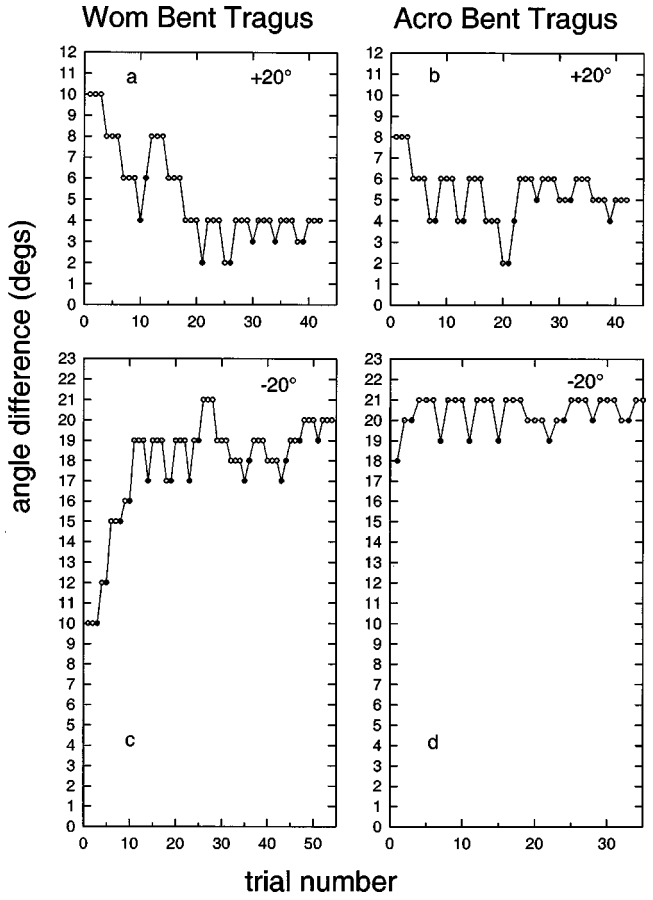

FIG. 3. In the bent-tragus conditions the angle difference tested in each trial is plotted as a function of the trial number. Panels (a) and (b) show the results of the experiment with the beads centered around +20° for Wom and Acro, respectively, and panels (c) and (d) with the beads centered around −20° for Wom and Acro, respectively (open circles correct choice; filled circles incorrect choice).

was recorded for each experimental trial in a session and converted to head angle using the calibration regression equation (Wotton *et al.*, 1996).

II. RESULTS

A. VAA (Vertical angle acuity)

Figures 2 and 3 display the results of individual VAA performance for each experimental session as a function of trial number (open symbols, correct response; closed symbols, incorrect response). The stimulus difference level required for the bat to perform at 79%-criterion level for each condition was calculated by averaging the midpoint value of every second run (i.e., the up runs). These thresholds of VAA are shown in Fig. 4 as a function of elevation.

1. Performance at +20°, 0°, −20° in elevation

Figure 4 shows that the VAAs of both bats were very similar at these three elevations. Respectively, Wom and Acro performed for VAAs of 3.4° and 3.9° with beads at 0°; at +20° elevation for VAAs of 3.7° and 4.1°; and at −20° elevation for VAAs of 2.9° and 3.4°. VAAs of 3.6° for Wom

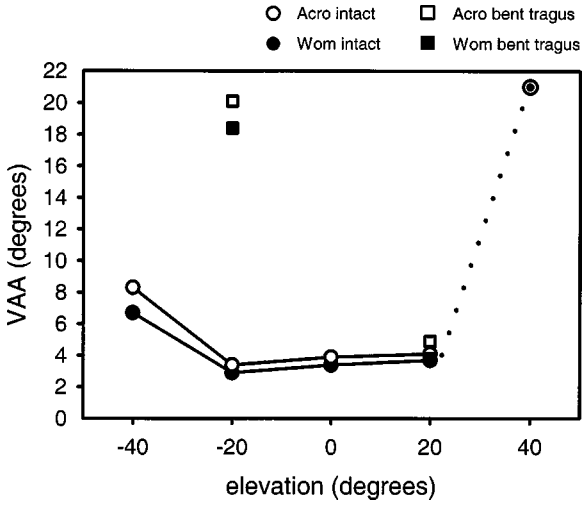

FIG. 4. The VAA required to produce 79%-correct performance was calculated by averaging the second runs (up-runs) for each experimental session. VAA is plotted as a function of experimental elevation (open symbols: Acro, closed symbols: Wom; circles: intact ear, squares: bent tragus). The dotted line to the symbol (circle with dot) indicates that this VAA was not measured and the acuity is at least greater than the point shown.

and 4.0° for Acro were calculated (using six reversals) from the second practice session (at 0° elevation) and provide an indicator of performance reliability.

2. Performance at +40° and −40° in elevation

Both bats were tested with the bead pairs centered on +40° but an estimate of VAA could not be obtained. Neither bat was able to perform the task at the largest angular difference possible (21°) at this elevation. The VAA for both bats was therefore greater than 21°; this is indicated by the dotted line in Fig. 4.

The VAA at −40° elevation was poor when compared to those conducted within the ±20° range (Fig. 4). The results of VAA performance were 6.7° for Wom and 8.3° for Acro.

A repeated measures analysis of variance (ANOVA) revealed significant differences between the four measurements (at +20°,0°,−20°,−40°) of VAA ($F_{(3,3)}=49$; $p=0.005$). Two hypotheses were tested using ANOVA contrasts (SYSTAT software). Moving the location from 0° to ±20° did not significantly change VAA ($F=25$; $p=0.13$). A comparison of VAA at the −40° elevation with those at the locations within the ±20° region approached but did not attain significance ($F=48$; $p=0.09$). If the alpha value for the test of significance is relaxed to a less conservative value (e.g., 0.10) then the difference between the VAA at this elevation and the others becomes statistically significant. Figure 4 clearly suggests that VAA at elevation −40° is different, but with only two subjects these statistical comparisons do not have much power.

3. Tragus manipulation

The vertical angle difference acuity was retested at +20° and −20° for both bats with their tragi bent. With the bead pairs centered on +20° in elevation, Wom and Acro displayed VAA of 3.8° and 4.9°, respectively. With the bead pairs centered on −20°, the VAA at criterion level was 18.4° and 20.1°, for Wom and Acro, respectively (see Figs. 3 and 4). Figure 4 shows that the performance with bent tragus is poorer than that of the intact ear at −20°.

Comparison of VAA between the conditions with the tragus intact and with the tragus bent when the bead pairs were centered on +20° revealed no significant difference in acuity (paired *t*-test, $t=-1.3$, $p=0.42$). However, when the beads were centered at −20°, the VAA was significantly larger with bent tragi compared to the performance with intact ears (paired *t*-test, $t=-26.8$, $p=0.02$).

B. Head aim

Figure 5 shows the mean and standard error of head angle in elevation for the experimental sessions for which these data are available. During the +20°, 0°, and −20° conditions, bats maintained fairly stable head angle with means ranging between about +7° and 0°. There were small differences in mean head aim between these conditions but these were not systematic and do not suggest that bats were aiming at the targets. For both bats, the mean head aim in the −40° condition was lower than the other locations by 5° to 10°.

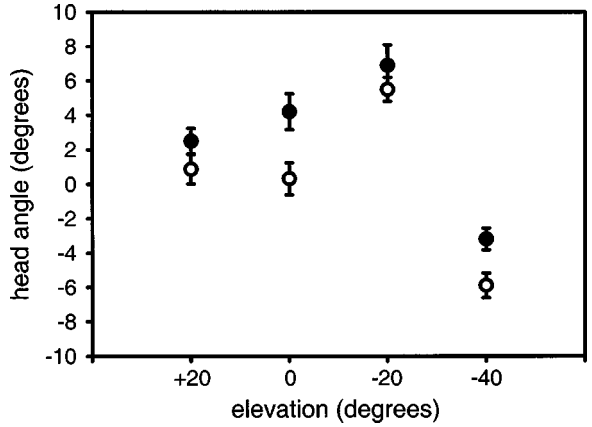

FIG. 5. The mean and standard error of the head angle for the two bats plotted as a function of experimental elevation (open symbols: Acro; closed symbols: Wom).

III. DISCUSSION

Discriminating between paired objects subtending different angles is not a direct measure of angle *difference* acuity. We cannot be certain that the bats were computing the subtended angles and using this metric as the basis of comparison. It is possible that bats were determining the relative location of the upper bead in each pair and/or the lower bead in each pair. Thus, the bats could simply have determined the bead pair that contains the lowest/highest bead and chosen the alternative bead pair. Regardless of the strategy employed, knowledge of the location of the beads is used and therefore spectral localization information predicts the performance of the bats in this task.

Although there were several minor methodological differences between this experiment and that conducted by Lawrence and Simmons (1982a), the results of the VAA for all the bats were very similar. Lawrence and Simmons found that for a 75% threshold the bats' acuity was about 3° to 3.5° when the targets were centered on 0°. Our experiment with the beads centered on 0° produced VAAs of between 3.4 and 3.9 at 79% threshold. If the large initial up-run value for Acro is removed, then both bats perform at 3.4° acuity [see Fig. 2(b)]. The results from the practice session indicate that the measurements of the bats' performance were quite reliable.

The combined echolocation spectral information shows that there is a region of best directional information between ±30° in elevation (Simmons *et al.*, 1995; Wotton *et al.*, 1997), and as a consequence we predicted that the VAA of bats should be best in this range. The performance of the bats was fairly consistent within this range of elevations and the measurements of VAA were smallest. Moving the beads from a center around 0° to a center around −20° or +20° did not significantly alter the bats' VAA. The change in acuity was within about 0.5°. Bats may be using different acoustic information above the horizon (e.g., peak cues) and below the horizon (e.g., notch cues) to make these judgments, but it

is not clear that this results in any meaningful difference in acuity for localizing above and below the horizon at these elevations.

The primary notch cue in the ear transfer function is contained in the frequency band corresponding to the first harmonic of the bat's echolocation sound. The peak cue and secondary notches are contained within the higher harmonics. Atmospheric attenuation severely reduces the efficacy of the higher frequencies of the second harmonic at distances of several meters (Lawrence and Simmons, 1982b). If the bat depends on the higher frequencies for localizing above the horizon, then we might expect differences of angle acuity to become apparent if this experiment were conducted at these long distances.

The *center* of the bead pairs had quite a large range in location (from $+20°$ to $-40°$) but the bats maintained their mean vertical head angle within a fairly narrow range ($+7°$ to $-6°$). A previous behavioral experiment investigated simulated targets at elevations between $\pm 20°$ and also revealed that bats have very limited head movement in the vertical dimension (mean head angles between $+5°$ to $-8°$: Wotton *et al.*, 1996). Both studies used the same Y-shaped platform in a 2AFC paradigm and this may influence the ability of the bat to move freely. This restricted head movement is advantageous for these localization experiments. If bats do not point at the targets, then they do not shift the spectral ''focus.'' Within the $\pm 20°$ range, the differences between head angles of the bats at various locations were not systematic; therefore, the bats did not appear to compensate for target location with head movements.

The combined echolocation information reveals that at extremely high elevations the spectra of different locations appear almost indistinguishable (Wotton *et al.*, 1997). When bats were tested with beads centered about $+40°$ it was not possible to get a measurement of acuity. The beads were separated to the greatest difference possible (21°) to no avail. Both bats performed the task at chance (50% correct). This bead configuration meant that the beads in the smallest angle were at 40° and 42° and the beads in the largest angle were at 31° and 54°. Although head-aim data are not available for the $+40°$ condition, it is apparent that bats were unable to compensate for loss of acuity by head adjustment.

At the extremely low elevations, the spectra are quite distinguishable but the changes are not systematic. When the bats were tested with the beads centered on $-40°$, they were able to perform the task demonstrating VAAs of 6.7° and 8.3°. For both bats, acuity at $-40°$ was approximately double that found within the $\pm 20°$ region.

The average head aim of both bats was about 5° to 10° lower in the $-40°$ condition than in the other three conditions. Whether this is simply statistical fluctuation or a deliberate effort by the bat to adjust to the lower targets is not clear. The respective head angle values for Wom and Acro were $-3°$ and $-6°$, which are within the range found for simulated targets (located between $\pm 20°$) (Wotton *et al.*, 1996). The lower head aim might have assisted the bat in this condition, but perhaps not enough to prevent some loss of acuity. Presumably, the bats need to aim about 20° below the horizon to shift the hypothesized region of best focus to encompass all the beads used in the pairs (range between $-34°$ and $-50°$). However, the bats may have moved the echolocation focus to a level that frequently included the upper bead in the bead pairs and sporadically included the lower bead.

The performance of the bats in the $-40°$ condition reveals that they may have been using different strategies to solve the task. Wom's behavioral function [Fig. 2(g)] shows that at angle differences of 7° or 8° the task was performed perfectly but at 6° Wom *always* chose the wrong side. It is possible that the lowest bead was essentially moving in and out of focus for Wom. Usually the lowest bead would indicate the incorrect alternative. When she perceived the lowest bead she was able to determine that there were two bead pairs and chose correctly. When the lowest bead disappeared, she may have been comparing one bead pair to a single bead at a higher elevation. The lowest bead would now belong to the bead pair subtending the smallest angle that was actually the correct choice. The strategy of locating the lowest bead would lead the bat to preferentially make the incorrect choice. Acro did not display the same shift in the expected correct responses at each stimulus level. For a 2AFC experiment, chance performance would be about 50% correct with some variation due to chance. Wom makes 0/8 correct choices compared to Acro 4/6 at the 6° difference stimulus level. These differences in the expected percentage of correct response could be due to chance, or perhaps the two bats used different strategies to solve the task. For all conditions, Wom performed with better acuity than Acro.

Whether the beads are centered around 0° or $\pm 20°$, there appears to be little difference in acuity. However, when more extreme vertical angles are examined it is clear that acuity above and below the horizon is quite different. At these greater elevations the disparity between localizing above and below the horizon is pronounced. The ears of flying bats are oriented slightly down and therefore do not point at objects well above the bat. The sonar emission of *Eptesicus* has a main lobe and a ventral lobe (Hartley and Suthers, 1989); consequently the area ensonified by the emission is not symmetrical around the horizon. If an object (such as an insect) is in the extreme lower portion of space, the bat should be able to resolve angle differences between the target and surrounding objects (such as leaves of trees) and be able to localize the target. It seems less likely that the bat will find the insect in the extreme upper portion of space.

Human vertical localization performance is best near the horizon with systematically increasing errors at higher and lower elevations (Makous and Middlebrooks, 1990). Similarly, deterioration of horizontal acuity at extreme azimuths has also been observed in humans (Makous and Middlebrooks, 1990) and cats (Heffner and Heffner, 1988).

A. Tragus influence

Bending the tragus in a live animal alters the acoustic information available and influences the behavior of bats (Grinnell and Grinnell, 1965; Lawrence and Simmons, 1982a). Acoustic measurements of the transfer functions of live *Eptesicus* are unavailable and cadaver ears provide the only estimate of the spectral changes due to this experimen-

tal manipulation. In cadaver ears, tragus removal dramatically disrupts spectra below the horizon and in particular alters the notch information. At all elevations the absolute amplitude of the main peak is also altered with tragus removal, but the changes in peak amplitude with elevation remain systematic (Wotton *et al.*, 1995). The same effects are true for the transfer functions of a cadaver ear that has had the tragus bent rather than removed (unpublished data, 1991, Wotton). We predicted that the performance of the bats should be impaired for this task below the horizon but less affected above the horizon.

When the beads were centered on $+20°$ there was no significant difference between the bats' performance with intact ears and with the tragi glued down. Differences in performance between the two conditions were within one degree. However, when the beads were centered on $-20°$, large, significant differences in performance occurred between the intact ear condition and the tragus-manipulated condition. Bending the tragus and gluing it to the side of the face for each ear greatly disrupted the bats' ability to resolve vertical angles below the horizon.

The bats' performance was impaired in the tragi-bent condition, but they were still able to do the task at some level. Although the notch cue may no longer be as useful, the bats presumably had access to additional elevation cues. Examination of the spectra for these positions below the horizon after tragus removal shows that there are still coarse differences in peak levels, gradients, and secondary notch frequencies (Wotton *et al.*, 1995). The cues introduced by reverberations between pinna and tragus are clearly important for localizing below the horizon but are not the sole representation of elevation.

Lawrence and Simmons (1982a) estimated the ability of the bat to resolve angle differences (around the horizon) with the tragus bent down to be about 12° to 14° acuity. This experiment measured the acuity (for beads centered at $-20°$) to be about 18° to 20°. This minor difference in the results between the two experiments could be due to the different elevations (0° or $-20°$) or the technique for measurement. Both experiments used only a single experimental session of bent tragi to prevent annoying the bats where they would no longer do the task and also to avoid any possible adaptation effects. Lawrence and Simmons used the method of limits for their intact ear experiment, but this was not possible for the bent-tragi condition. Instead, they used one stimulus level (correct choice angle of 6.5°, incorrect choice angle of 11°) with bent tragi and compared the performance to that of the same stimulus with intact ears. The threshold with tragus deflected was extrapolated from the psychometric function. In our experiment we used an up–down procedure for both bent-tragi and intact ears to obtain a measurement in a single session.

Lawrence and Simmons (1982a) enucleated the eyes of one of their bats to demonstrate that the bats were not using visual cues. The visual abilities of the two bats used in this experiment were not (to the best of our knowledge) impaired. Although the bats were performing the task under low-light conditions, the possibility that bats could have been using some visual information cannot be completely excluded. However, it does seem unlikely that if the bats were relying on visual information that they would be able to easily perform the task at both $\pm 20°$ with intact ears, but display impaired performance only at $-20°$ with tragus bent down.

IV. CONCLUSION

The bats' angular difference acuity for objects contained within a range of about $\pm 20°$ in elevation is very similar, regardless of the vertical location of the objects. Beyond this range, the bats' vertical acuity is poorer, and especially degraded for targets above the horizon. Reverberations of sound between the tragus and pinna create cues which bats use to localize below the horizon. Distortion of the tragus alters the ability of the bat to discriminate vertical angles below the horizon but has little effect on discrimination above the horizon.

ACKNOWLEDGMENTS

We would like to thank the anonymous reviewers for their valuable suggestions that have greatly improved this manuscript. The research was supported by ONR Grant No. N000014-89-J-3055, by NIH Grant No. DC00521, by NIMH Research Scientist Development Award No. MH00521, and by NIMH Training Grant No. MH19118. We are grateful to C.Ken DeLucia for carpentry assistance.

Asano, F., Suzuki, Y., and Sone, T. (**1990**). ''Role of spectral cues in median plane localization,'' J. Acoust. Soc. Am. **88**, 159–168.

Blauert, J. (**1969**). ''Sound localization in the median plane,'' Acustica **22**, 205–213.

Butler, R. A., and Belendiuk, K. (**1977**). ''Spectral cues utilized in the localization of sound in the median sagittal plane,'' J. Acoust. Soc. Am. **61**, 1264–1269.

Carlile, S. (**1990**). ''The auditory periphery of the ferret. II. The spectral transformations of the external ear and their implications for sound localization,'' J. Acoust. Soc. Am. **88**, 2180–2204.

Fuzessery, Z. M. (**1996**). ''Monaual and binaural spectral cues created by the external ears of the pallid bat,'' Hear. Res. **95**, 1–17.

Fuzessery, Z. M., Hartley, D. J., and Wenstrup, J. J. (**1992**). ''Spatial processing within the mustache bat echolocation system: possible mechanisms for optimization,'' J. Comp. Physiol. A **170**, 57–71.

Grinnell, A. D., and Grinnell, V. S. (**1965**). ''Neural correlates of vertical localization by echo-locating bats,'' J. Physiol. (London) **181**, 830–851.

Grinnell, A. D., and Schnitzler, H. U. (**1977**). ''Directional sensitivity of echolocation in the horseshoe bat, *Rhinolophus ferrumequinum*. II: Behavioral directionality of hearing,'' J. Comp. Physiol. A **116**, 63–76.

Hartley, D. J., and Suthers, R. A. (**1989**). ''The sound emission pattern of the echolocating bat, *Eptesicus fuscus*,'' J. Acoust. Soc. Am. **85**, 1348–1351.

Hebrank, J., and Wright, D. (**1974**). ''Spectral cues used in the localization of sound sources on the median plane,'' J. Acoust. Soc. Am. **56**, 1829–1834.

Heffner, R. S., and Heffner, H. E. (**1988**). ''Sound localization acuity in the cat: Effect of azimuth, signal duration, and test procedure,'' Hear. Res. **36**, 221–232.

Koay, G., Kearns, D., Heffner, H. E., and Heffner, R. S. (**1998**). ''Passive sound localization ability of the big brown bat (*Eptesicus fuscus*),'' Hear. Res. **119**, 37–48.

Kurta, A., and Baker, R. H. (**1990**). ''*Eptesicus fuscus*,'' Mamm. Species **356**, 1–10.

Lawrence, B. D., and Simmons, J. A. (**1982a**). ''Echolocation in bats: The external ear and perception of the vertical position of targets,'' Science **218**, 481–483.

Lawrence, B. D., and Simmons, J. A. (**1982b**). ''Measurements of atmospheric attenuation at ultrasonic frequencies and the significance for echolocation by bats,'' J. Acoust. Soc. Am. **71**, 585–590.
Levitt, H. (**1971**). ''Transformed up–down methods in psychoacoustics,'' J. Acoust. Soc. Am. **49**, 467–477.
Makous, J. C., and Middlebrooks, J. C. (**1990**). ''Two-dimensional sound localization by human listeners,'' J. Acoust. Soc. Am. **87**, 2188–2200.
Masters, W. M., Moffat, A. J. M., and Simmons, J. A. (**1985**). ''Sonar tracking of horizontally moving targets by the big brown bat, *Eptesicus fuscus*,'' Science **228**, 1331–1333.
Middlebrooks, J. C. (**1992**). ''Narrow-band sound localization related to external ear acoustics,'' J. Acoust. Soc. Am. **92**, 2607–2624.
Musicant, A. D., Chan, J. C. K., and Hind, J. E. (**1990**). ''Direction-dependent spectral properties of cat external ear: New data and cross-species comparisons,'' J. Acoust. Soc. Am. **87**, 757–781.
Rice, J. J., May, B. J., Spirou, G. A., and Young, E. D. (**1992**). ''Pinna-based spectral cues for sound localization in cat,'' Hear. Res. **58**, 132–152.
Schnitzler, H.-U., and Grinnell, A. D. (**1977**). ''Directional sensitivity of echolocation in the horseshoe bat, *Rhinolophus ferrumequinum*. I. Directionality of sound emission.'' J. Comp. Physiol. A **116**, 51–61.
Searle, C. L., Braida, L. D., Cuddy, D. R., and Davis, M. F. (**1975**). ''Binaural pinna disparity: Another auditory localization cue,'' J. Acoust. Soc. Am. **57**, 448–455.
Shaw, E. A. G. (**1974**). ''Transformation of sound pressure level from the free field to the eardrum in the horizontal plane,'' J. Acoust. Soc. Am. **56**, 1848–1861.
Shaw, E. A. G. (**1982**). ''External ear response and sound localization,'' in *Localization of Sound: Theory and Applications*, edited by R. Gatehouse (Amphora, Groton, CT), pp. 30–41.
Simmons, J. A. (**1973**). ''The resolution of target range by echolocating bats,'' J. Acoust. Soc. Am. **54**, 157–172.
Simmons, J. A. (**1979**). ''Perception of echo phase information in bat sonar,'' Science **204**, 1336–1338.
Simmons, J. A. (**1987**). ''Acoustic images of target range in the sonar of bats,'' Nav. Res. Rev. **39**, 11–26.
Simmons, J. A., Fenton, M. B., and O'Farrell, M. J. (**1979**). ''Echolocation and pursuit of prey by bats,'' Science **203**, 16–21.
Simmons, J. A., Ferragamo, M., Saillant, P. Haresign, T., Wotton, J. M., Dear, S. P., and Lee, D. N. (**1995**). ''Auditory dimensions of acoustic images in echolocation,'' in *Hearing by Bats*, edited by A. N Popper and R. R. Fay (Springer, New York), pp. 146–190.
Simmons, J. A., and Grinnell, A. D. (**1988**). ''The performance of echolocation: Acoustic images perceived by echolocating bats,'' in *Animal Sonar Systems*, edited by P. Nachtigall (Plenum, New York).
Simmons, J. A., Kick, S. A., Lawrence, B. D., Hale, C., Bard, C., and Escudie, B. (**1983**). ''Acuity of horizontal angle discrimination by the echolocating bat, *Eptesicus fuscus*,'' J. Comp. Physiol. A **153**, 321–330.
Wetherill, G. B., and Levitt, H. (**1965**). ''Sequential estimation points on a psychometric function.'' Br. J. Math. Stat. Psychol. **18**, 1–10.
Wightman, F. L., and Kistler, D. J. (**1989**). ''Headphone simulation of free-field listening. II: Psychophysical validation,'' J. Acoust. Soc. Am. **85**, 868–878.
Wotton, J. M., Haresign, T., and Simmons, J. A. (**1995**). ''Spatially dependent acoustical cues generated by the external ear of the big brown bat, *Eptesicus fuscus*,'' J. Acoust. Soc. Am. **98**, 1423–1445.
Wotton, J. M., Haresign, T., Ferragamo, M. J., and Simmons, J. A. (**1996**). ''The influence of sound source elevation and external ear notch cues on the discrimination of spectral notches by the big brown bat, *Eptesicus fuscus*,'' J. Acoust. Soc. Am. **100**, 1764–1776.
Wotton, J. M., Jenison, R. L., and Hartley, D. J. (**1997**). ''The combination of echolocation emission and ear reception enhances directional spectral cues of the big brown bat, *Eptesicus fuscus*,'' J. Acoust. Soc. Am. **101**, 1723–1733.

LETTERS TO THE EDITOR

This Letters section is for publishing (a) brief acoustical research or applied acoustical reports, (b) comments on articles or letters previously published in this Journal, and (c) a reply by the article author to criticism by the Letter author in (b). Extensive reports should be submitted as articles, not in a letter series. Letters are peer-reviewed on the same basis as articles, but usually require less review time before acceptance. Letters cannot exceed four printed pages (approximately 3000–4000 words) including figures, tables, references, and a required abstract of about 100 words.

C-scan imaging in molten zinc by focused ultrasonic waves

Ikuo Ihara and Cheng-Kuei Jen
Industrial Materials Institute, National Research Council of Canada, Boucherville, Québec J4B 6Y4, Canada

Demartonne Ramos França
Department of Electrical Engineering, McGill University, Montréal, Québec H3A 2A7, Canada

(Received 1 March 1999; accepted for publication 22 October 1999)

Ultrasonic images of a small steel object immersed in molten zinc at 600 °C are obtained with high spatial resolution using a focused ultrasonic pulse-echo technique. The focused ultrasonic waves are generated by a spherical acoustic lens which has been machined at the probing end of a clad buffer rod. The backscattered echoes from the object surface have a signal-to-noise ratio of 35 dB at 10 MHz in molten zinc. The ability to provide high spatial resolution measurements in molten metal is demonstrated by comparing the results obtained in molten zinc with those obtained in water. © *2000 Acoustical Society of America.* [S0001-4966(00)01102-4]

PACS numbers: 43.20.Mv, 43.35.Yb, 43.35.Zc, 43.58.Ls [DEC]

INTRODUCTION

Ultrasonic pulse-echo techniques are effective means for the characterization of acoustic properties of materials and for imaging voids or flaws inside materials. Due to their convenience, low cost and robustness, these techniques are widely used in material research and in various industries.[1] However, the application of these techniques in a molten metal bath at high temperatures seems to be difficult because of several reasons, including the limit of piezoelectricity to temperatures below the Curie temperature, the difficulty of having reliable and long lasting ultrasonic coupling at elevated temperatures and the requirement of high thermal shock and corrosion resistance sensors. Nevertheless, to perform ultrasonic imaging in such conditions would be valuable and, in particular, allow the detection of flaws, like cracks at the bottom of vessels containing liquid metals, or the inspection of objects immersed in liquid metal baths such as the bottom electrode of an aluminum electrolytic cell. The technique would be also of interest for detecting foreign particles present in the bath, these particles being known to have potentially adverse effects on the thin metallic sheet products derived from molten metal baths.

The objective of this investigation is to perform ultrasonic imaging in molten zinc, with the requirements of both high signal-to-noise ratio (SNR) and high spatial resolution at 600 °C, a temperature higher than the melting point of zinc (419 °C). Our technique follows a standard approach of mounting the ultrasonic transducer (UT) on the cooled end of a buffer rod.[2] We then achieve high spatial resolution by realizing an acoustic lens at the probing end, which is at the opposite side of the cooled UT end of a clad buffer rod. This clad buffer rod, consisting of a core and a cladding, provides superior wave guidance with high SNR at elevated temperature.[3,4] The acoustic lens, which is a spherical cavity machined at the probing end, is for generating and receiving focused ultrasonic waves. Scanned images with high resolution in molten zinc will be produced using the common C-scan imaging technique. For the demonstration of high resolution imaging capability, the scanned images obtained in molten zinc will be compared to those obtained in water.

I. WAVEGUIDE AND LENS

The clad buffer rod used for this work consisted of a mild steel core with a tapered shape (10.6 and 7.0 mm in diameter at the ends, 130.0 mm long) and a thermal sprayed stainless steel cladding (1.0 mm thick).[5] The thermal sprayed stainless steel cladding provides sufficient thermal shock resistance in this work. The longitudinal velocities in the core and cladding at room temperature are about 5930 and 2300 m/s, respectively. The porous structure of the cladding layer produced by thermal spray leads to not only its high ultrasonic loss but also low ultrasonic impedance. In previous works[3–5] it was experimentally verified that the mismatch of the ultrasonic impedance between the core and the cladding provides superior wave guidance performance over nonclad rods. The stainless steel cladding also protects the mild steel core against the interaction with molten zinc. In addition, the use of the tapered shape is also effective for reducing unwanted spurious echoes due to dispersion, multipaths, mode conversion and beam spread.[6] To provide high spatial reso-

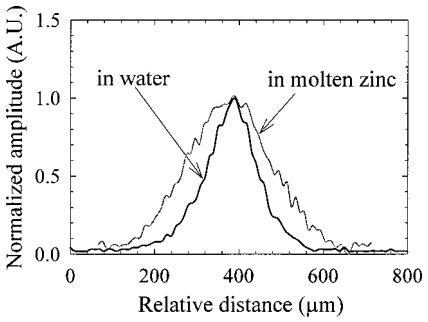

FIG. 1. Lateral variation of the reflected echo in the focal plane of the acoustic lens in water and in molten zinc. The data for water and molten zinc have been normalized to the same peak amplitude.

lution, a spherical concave surface of 7 mm diameter was machined at the probing end of the clad tapered buffer rod. It is used as an acoustic lens for generating and receiving focused ultrasonic waves. The lens has a radius of 4.75 mm and an aperture diameter of 7.0 mm. The lateral resolution *dr* and the focusing depth *dz* of the acoustic lens can be roughly estimated from the following formulas:[7] $dr = Kr\lambda F/D$ and $dz = 4Kz\lambda(F/D)$,[2] where λ is the wavelength, F the focal length, D the aperture diameter, and Kr and Kz are constants close to unity, respectively. From these formulas, setting $Kr = Kz = 1$, dr and dz at 10 MHz are found to be about 388 and 2150 μm in molten zinc, and 136 and 498 μm in water, respectively. With respect to the longitudinal velocities at 600 °C, values of 5500 m/s for the steel buffer rod and 2800 m/s for molten zinc were used for the estimation. We have previously verified the good focusing ability of a similar acoustic lens machined at an end of another clad buffer rod of the same kind by performing imaging experiments in water.[8]

In order to investigate the focusing ability of the acoustic lens, the lateral resolution was evaluated by using a thin stainless wire (0.38 mm in diameter) as a target immersed in molten zinc or in water. A 10 MHz broadband UT with a 6.35 mm diameter was used. This 0.38 mm diameter rod was laterally scanned across the focal point in the lens focal plane. The variation of the amplitude of the backscattered echo from the wire is shown in Fig. 1 for both in water and molten zinc. As expected, the lateral resolution in molten zinc is slightly worse than that in water. Nevertheless, this result demonstrates that the ultrasonic waves can be focused onto a small spot of about one wavelength to provide high lateral resolution even in molten zinc. Since molten zinc is corrosive, it can affect the focusing behavior of the acoustic lens by distorting the spherical concave shape if the lens is immersed in molten zinc for a long period of time. It is noted that, in this work, no significant deterioration of the lens was observed for an immersion time of about two hours. Based on this result, an attempt was then made to perform ultrasonic imaging in the molten zinc bath.

II. EXPERIMENTAL RESULTS

For imaging demonstration, a small steel object with the three letters NRC engraved on its surface was immersed both in water and in molten zinc with the grooves upward facing

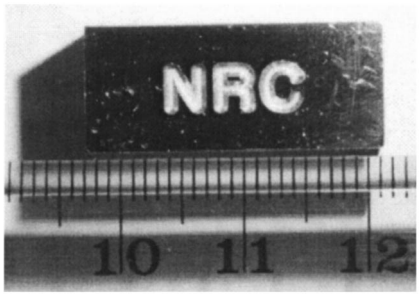

FIG. 2. Picture of the test steel specimen showing the three letters, NRC, engraved on the surface.

the lens (see Fig. 2). The width and depth of the grooves are 1.2 and 0.4 mm, respectively. The rod was lowered into the bath so the surface of the steel object was brought into focus of the acoustic lens, with the ultrasonic waves incident normally. The scanning was performed with a displacement step size of 200 μm. A 10 MHz broadband UT with a 6.35 mm diameter was again used and operated in the pulse-echo mode. The variations of the peak amplitude or time delay of the reflected echo coming from the focal zone, which are mainly caused by the irregularity of the object surface, are used for imaging. Figure 3 shows typical reflected echoes from water/steel and molten zinc/steel interfaces. We can observe that the reflected echo from the molten zinc/steel interface has also a good SNR, which is almost the same as the one from the water/steel interface. The measured SNR of these echoes is about 35 dB, which is quite sufficient for performing ultrasonic imaging. The definition of SNR is the ratio of the amplitude of the desired signal over that of the noise of the receiver electronics. It is noted in Fig. 3 that the amplitude of the reflected echo from the molten zinc/steel interface is larger than the one from the rod end. This can be explained by the small mismatch of ultrasonic impedances between the rod and molten zinc and good wetting between them, which cause a large amount of ultrasonic energy to be transmitted from the clad steel buffer rod into molten zinc.

From these reflected echoes, ultrasonic images in water and in molten zinc at 600 °C are obtained and shown in Figs. 4 and 5, respectively. Each of these images took about 30 min for the completion of scanning. We used directly the raw data without any signal processing, although image quality could be improved by signal processing techniques. Higher

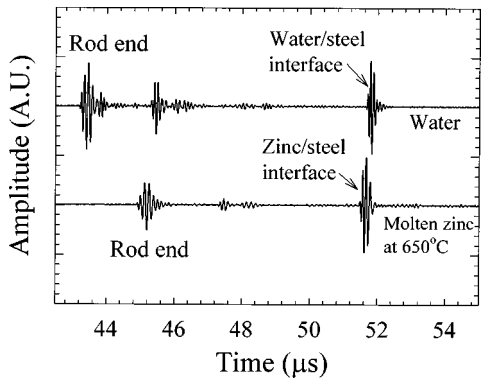

FIG. 3. Reflected echoes at 10 MHz from water/steel and molten zinc/steel interfaces.

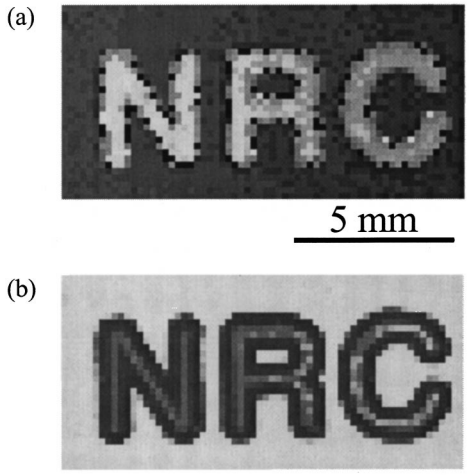

FIG. 4. Ultrasonic images of ''NRC'' in water: obtained (a) by plotting the time delay of the echo, (b) by plotting the echo amplitude.

intensity in the time delay or amplitude images corresponds to a longer time delay and to a higher amplitude, respectively. In the amplitude plot of Figs. 4 and 5 we can observe a dark zone delimiting the letters NRC. This is caused by a weaker echo at the locations where the surface is inclined and curved by engraving. It is noted that, since the wave velocity in molten zinc at 600 °C is about two times the one in water, the variation of time delay in water is about two times larger than that in molten zinc. It is also noted that the images obtained in water as shown in Fig. 4 have a slightly better spatial resolution than those obtained in molten zinc as shown in Fig. 5. This is in agreement with the results shown in Fig. 1. Both images from the molten zinc bath shown in Fig. 5 have sufficient quality to identify the letters NRC. Also, we can observe many dirty spots in both images in molten zinc shown in Fig. 5. It is considered that such spots are caused by the irregularity of chemical compound layers, such as oxide films formed on the steel sample surface due to chemical reactions at high temperature, or by the deterioration of the acoustic signal because of the ultrasonic scattering induced by impurities floating in molten zinc, and not by the inhomogeneity of acoustic impedance of the sample material itself. Although there is a steep temperature gradient in the buffer rod due to a large temperature difference between the immersed and air cooled parts, no marked influence on both images in Fig. 5 has been observed provided that the temperature gradient is kept nearly constant.

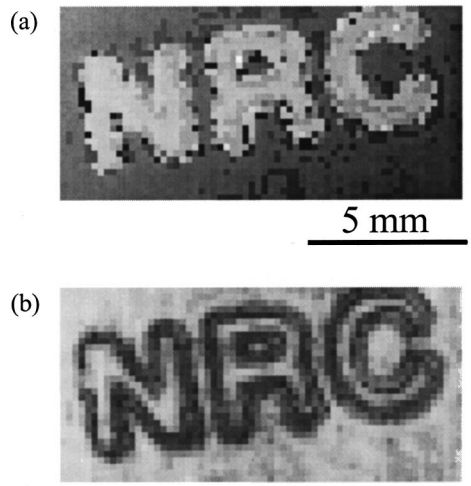

FIG. 5. Ultrasonic images of ''NRC'' in molten zinc: obtained (a) by plotting the time delay of the echo, (b) by plotting the echo amplitude.

III. CONCLUSION

In conclusion, this work establishes that the pulse-echo technique using the developed focusing clad buffer rod can be applied for imaging in molten zinc at 600 °C. The present method appears to provide a useful means to perform ultrasonic imaging in liquid metal at high temperature. The developed clad buffer rods provide higher SNR than those that have been reported with nonclad buffer rods operating in a similar frequency range, i.e., around 10 MHz. These results (detection of a thin wire and images) also show that the presented technique has the potential to detect small particles such as inclusions or impurities dispersed in molten metals and this will be the object of future work. In addition, this focused ultrasonic wave technique could be used to perform not only imaging but also quantitative and microscopic materials characterizations in molten metals, such as the phase velocity and attenuation determinations, which are similar to those performed by means of an acoustic microscope at room temperature.[8,9]

ACKNOWLEDGMENTS

The authors would like to thank H. Hébert and B. Marple of Industrial Materials Institute of National Research Council of Canada for their help on the ultrasonic data acquisition and molten zinc experiments, respectively. Financial support of the Natural Sciences and Engineering Research Council of Canada (NSERC) is gratefully appreciated. I. Ihara and D. R. França acknowledge the fellowships awarded to them by NSERC and by CNPq, Brazil, respectively.

[1] R. A. Lemons and C. F. Quate, ''Acoustic Microscopy,'' in *Physical Acoustics XIV*, edited by W. P. Mason and R. N. Thurston (Academic, London, 1979), pp. 1–92.
[2] L. C. Lynnworth, *Ultrasonic Measurements for Process Control: Theory, Techniques, Applications* (Academic, London, 1989), pp. 142–145.
[3] C.-K. Jen and J. G. Legoux, ''High performance clad metallic buffer rods,'' Proceedings of 1996 IEEE Ultrasonics Symposium, San Antonio, 1996, pp. 771–776.
[4] C.-K. Jen, K. T. Nguyen, J.-G. Legoux, I. Ihara, H. Hébert, and D. Ramos França, ''Novel clad ultrasonic buffer rods for the monitoring of industrial materials processing,'' Proceedings of 1st Pan American Conference on NDT, Toronto, 1998, pp. 99–106.
[5] C.-K. Jen and J. G. Legoux, U.S. Patent 5,828,274 (1998).
[6] C.-K. Jen, L. Piché, and J. F. Bussiere, ''Long isotropic buffer rods,'' J. Acoust. Soc. Am. **88**, 23–25 (1990).
[7] G. S. Kino, *Acoustic Waves: Devices, Imaging, and Analog Signal Processing* (Prentice-Hall, Englewood Cliffs, NJ, 1987), pp. 182–194.
[8] I. Ihara, C.-K. Jen, and D. R. França, ''Materials evaluation using long clad buffer rods,'' Proceedings of 1998 IEEE Ultrasonics Symposium, Sendai, 1998, pp. 803–807.
[9] J. Kushibiki and N. Chubachi, ''Material characterization by line-focus-beam acoustic microscope,'' IEEE Trans. Sonics Ultrason. **32**, 189–212 (1985).

Coupling of velocity dispersion curves of leaky Lamb waves on a fluid-loaded plate

Kohji Toda and Kenji Motegi
Department of Electronic Engineering, National Defense Academy, Hashirimizu, Yokosuka 239-8686, Japan

(Received 27 March 1998; accepted for publication 22 October 1999)

The coupling of velocity dispersion curves of leaky Lamb waves is studied based on analytical calculations to clarify the problem of repulsion and crossing of the curves. Two curves, corresponding to the 4th and 5th modes, are closely observed while artificially varying the properties of virtual materials, in the combination of piezoelectric ceramic and glass. The imaginary part of the Lamb-wave velocity is essential for distinguishing the coupling phenomena. The behaviors of the velocity values as functions of two variables, material property and the product of frequency and thickness of the plate, are analogous to the Riemann sphere defined by a mathematical function of $\omega = z^{(1/2)}$ (both z and ω are complex) inside the domain containing the point $z = 0$ on the complex plane. © *2000 Acoustical Society of America.*
[S0001-4966(00)01002-X]

PACS numbers: 43.20.Bi, 43.40.Rj, 43.40.Dx [DEC]

INTRODUCTION

The interactions mode crossing and mode repulsion appear in velocity dispersion curves of both leaky and nonleaky waves on various substrates, including a piezoelectric ceramic plate, and were discussed in some articles.[1–9]

In Ref. 6, an artificial plate was introduced from the elastic properties of aluminum in the analysis of wave propagation, and the exchange of propagation characteristics of Lamb waves in passing through a repulsion region was presented. The other interaction, mode crossing, was observed in Ref. 9 by computing the wave equation in an aluminum plate with free surfaces, presenting the discontinuity of the velocity dispersion curve at the crossing point. These references discussed either the mode repulsion or the mode crossing and did not consider the relation between the two phenomena.

If a plate of wave-propagation medium is immersed in water, some part of acoustic energy of the Lamb waves is radiated into water, resulting in the attenuation of the leaky Lamb waves in the plate and the radiation of longitudinal waves into water. The radiation efficiency (C) of the longitudinal wave in water depends on the imaginary value of the complex Lamb wave velocity. At the crossing point, where the phase velocities of the neighboring modes are the same, the imaginary parts of the complex velocity do not usually coincide. This implies that at the crossing point of the dispersion curves, a plate can sustain two different leaky Lamb wave modes, which propagate in the plate with a same phase velocity but with different radiation efficiencies. By dealing with a plate immersed in water instead of a plate with free surfaces, the separation of the two neighboring dispersion curves, especially at crossing points, might become clear.

The behavior of Lamb-wave velocity dispersion curves depends on the plate materials. To investigate the two types of interaction closely, virtual materials exposed to water are introduced using the elastic and piezoelectric constants of existing glass and piezoelectric ceramic, and the properties of the virtual materials are gradually shifted. The incorporation of piezoelectric ceramic would be valid for designing an ultrasound transducer. The 4th and 5th modes of the leaky Lamb waves are closely observed in terms of crossing and repulsion phenomena. The complex velocity values, which are usually seen as a function of fd, are regarded here as a function defined on the two-dimensional fd-q plane, where fd is the product of frequency f and plate thickness d, and q is a parameter determining the elastic and piezoelectric properties of the plate. An analogy of a Riemann sphere deriving from a mathematical function defined on the complex plane is helpful for understanding the behaviors of the velocity values of the two modes on the fd-q plane.

I. MODEL OF A VIRTUAL MATERIAL

Figure 1 shows the phase velocity dispersion curves of leaky Lamb waves propagating in a thin glass plate exposed to water on one surface as a function of fd. The glass is No. 7059 by Corning Co. and the material constants of the glass re elastic stiffness tensor (c_G), permittivity tensor (ε_G), and density (ρ_G). The glass is a borosilicate glass, having the amorphous structure. Numbers 0 to 5 in the figure correspond to the names of six lowest-order modes. It should be noted that the two curves for the 2nd and 3rd modes approach each other but fail to cross at around $fd = 3$ MHz·mm (mode repulsion), while curves for the 4th and 5th modes cross at around $fd = 5.2$ MHz·mm (mode crossing). Figure 2 shows calculated velocity dispersion curves of Lamb waves for a piezoelectric ceramic (TDK: 101A) as a substrate material. The ceramic is a $Pb(Zn \cdot Ti)O_3$ family, having the perovskite structure. The material constants used in the calculation are elastic stiffness tensor (c_p), piezoelectric constant tensor (e_p), permittivity tensor (ε_p), and density (τ_p), which are listed in Table I. It is noted that the curves for the 4th and 5th modes do not cross and that the two curves do not even approach each other. The relation between the 4th- and 5th-mode curves in the two materials is totally different as can be seen in Figs. 1 and 2.

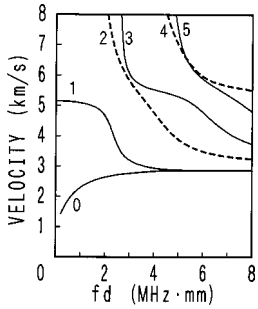

FIG. 1. Calculated phase velocity dispersion curves of the lowest six modes of leaky Lamb waves in glass plate loaded with water on one surface as a function of the product of frequency f and plate thickness d.

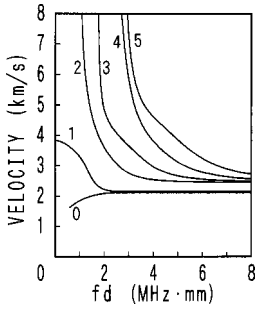

FIG. 2. Calculated phase velocity dispersion curves of the lowest six modes of leaky Lamb waves in a piezoelectric ceramic plate (TDK: 101A) loaded with water on one surface as a function of fd.

We will focus on the two velocity curves for the 4th and 5th modes while the elastic and piezoelectric properties of the plate change gradually from those of the glass to those of the ceramic. Virtual piezoelectric materials are introduced using the elastic constants of the two existing materials, glass and piezoelectric ceramic. The elastic stiffness tensor c_v, piezoelectric constant tensor e_v, permittivity tensor ε_v, and density ρ_v of the virtual materials are defined as follows:

$$c_v = c_p \cdot q + c_G \cdot (1-q), \tag{1}$$

$$e_v = e_p \cdot q, \tag{2}$$

$$\varepsilon_v = \varepsilon_p \cdot q + \varepsilon_G \cdot (1-q), \tag{3}$$

$$\rho_v = \rho_p \cdot q + \rho_G \cdot (1-q), \tag{4}$$

where q is a real parameter between 0 and 1. When q is equal to 1 or 0, the virtual plate is a piezoelectric ceramic or a glass, respectively. The multiplication and addition in Eqs. (1) to (3) are conducted for each tensor element. This virtual material is piezoelectric and the poling axis is always in the thickness direction of the plate.

Numerical calculation of the velocities was conducted by developing the Farnell's method.[10] The equation of motion in the plate and in water, the relating equation between the piezoelectricity and the strain in the ceramic, and Gauss' law from Maxwell's equations are formulated. Then, the mechanical and electrical boundary conditions on the plate surfaces are considered. Finally, proper combinations of frequency and Lamb-wave velocity are obtained by demanding that the determinant of the boundary condition matrix should be zero.

The Lamb-wave velocities are complex numbers. The real part is the phase velocity of the leaky wave propagating along the plate while the imaginary part is associated with the radiation efficiency of the longitudinal wave into water.[11] When the phase velocities of two different modes approach so closely, it is sometimes difficult to determine whether the two curves repel or cross. In these cases the imaginary parts of the complex velocities can be referred to successfully to distinguish the two curves, which will be described in the next section.

II. CALCULATION

Numerical analysis was carried out for the q values from 0 to 1 in an increment of 0.1. The velocity curves for the 4th and 5th modes cross for q equal to 0 and 0.1, while the two modes repel or do not even approach each other for q equal to or beyond 0.2. Figure 3 shows the phase velocity curves for the 4th and 5th modes for $q=0.1$ and $q=0.2$. The imaginary value of the complex velocity, on the other hand, takes quite a different behavior compared with the above relation. Instead of presenting the calculated results of imaginary parts of the velocities, radiation efficiency (C) is introduced here to understand the physical meaning of the role of the imaginary parts more clearly. C is the ratio of energy that is transferred in the form of mode conversion from the Lamb wave to the longitudinal wave in water while the Lamb wave propagates by one wavelength, and is defined as follows:[11]

$$C = 1 - \exp\left(4\pi \frac{v_I}{v_R}\right), \tag{5}$$

where v_g and v_I are the real and imaginary part of the complex velocity, respectively. Figure 4 shows the calculated C values as a function of fd, for two q values of 0.1 and 0.2. In the case of $q=0.1$, where the phase velocities of the two modes do cross at the fd values of 4.9 MHz·mm, C values for the same fd values are far apart, which implies that there are two different types of leaky Lamb waves in the plate, with the same frequency and same phase velocity but with two different radiation efficiencies. The velocity curves of the two modes repel each other for $q=0.2$, at around the fd values of 4.5 MHz·mm, while the two C curves corresponding to the two modes cross at around the same fd values. It means that the velocity dispersion curves for the two propagation modes exchange their propagation characteristics in terms of radiation efficiency (highly radiative, or less radiative) when the velocity curves pass through the repulsion region of the phase velocity.

To observe more detailed behavior of the velocity dispersion curves of the two modes around the repulsion and crossing points, two-dimensional space (fd-q plane) is introduced. fd value can change from 0 to infinity, while q value is between 0 and 1. A rectangular domain ABCD is focused on the plane as shown in Fig. 5. The coordinates of the points A, B, C, and D are (4.4, 0.1), (5.0, 0.1), (5.0, 0.2), and (4.4, 0.2), respectively. The velocities of the 4th and 5th modes are calculated as a function of the position of point T on the fd-q plane which has the coordinates of (fd,q) when T moves continuously along the closed path in the order of points A, B, C, D, and A. At the starting point A, the 4th-

TABLE I. Nonzero material constants of the piezoelectric ceramic (101A, TDK Co.) in the engineering notation. (The x_1 and x_3 axes are chosen parallel to the wave propagation direction and the poling axis of the ceramic, respectively.)

Elastic stiffness $\times 10^{10}$ N/m^2						Piezoelectric constant C/m^2			Permittivity		Density kg/m^3
c_{P11}	c_{P12}	c_{P13}	c_{P33}	c_{P44}	c_{P66}	e_{P31}	e_{P33}	e_{P15}	$\varepsilon_{P11}/\varepsilon_0$	$\varepsilon_{P33}/\varepsilon_0$	ρ_P
c_{P22}	c_{P21}	c_{P23}		c_{P55}		e_{P32}		e_{P24}	$\varepsilon_{P22}/\varepsilon_0$		
		c_{P31}									
		c_{P32}									
14.9	8.45	8.72	13.0	2.53	3.24	−2.63	14.3	11.6	719	540	7700

mode phase velocity is 7094 m/s. As *T* moves from point A to point B, the velocity smoothly declines to become 6144 m/s at point B. The velocity declines further as *T* moves from point B to point C to become 5641 m/s at point C. Then the velocity gradually gets larger as *T* moves from point C to point D to become 6502 m/s at point D. It grows larger again when *T* moves from point D to point A, the terminal point, to become 8666 m/s. This velocity 8666 m/s is the 5th-mode velocity at point A.

A similar series of calculations was conducted by starting at point A as earlier but with the 5th mode velocity of 8666 m/s this time. In the moving route of *T*, the similar tendency on the phase velocity variation as those in the 4th mode is recognized. Finally, at point A after one round, the phase velocity coincided with the 4th mode velocity at the point A.

III. DISCUSSION

Numerical calculation of the leaky Lamb waves velocities along a closed loop on the fd-q plane indicates that the phase velocity obtained at the terminal point after one round is not the same as the initial value at the starting point. Physical meaning of sweeping q value is regarded as a gradual transition of the material properties of the plate; on the other hand, sweeping *fd* value corresponds to transitional change of the thickness *d* of the plate along the direction of the wave propagation while keeping a constant frequency.

Figure 6 shows a schematic diagram for explaining the phenomenon mentioned above. Three-dimensional space is introduced whose arbitrary point *S* represents a combination of three values of *fd*, *q*, and phase velocity. On the two planes of $q=0.1$ and $q=0.2$ in Fig. 6, the velocity dispersion curves for the 4th (solid curve) and the 5th (dashed curve) modes are drawn. The two curves for the 4th and 5th modes cross on the plane of $q=0.1$ but fail to cross on the plane of $q=0.2$. The symbols a, b, c, d, e, f, g, and h in this figure represent the points (4.4, 0.1, 8666), (5.0, 0.1, 6072), (5.0, 0.2, 5439), (4.4, 0.2, 6311), (4.4, 0.1, 7094), (5.0, 0.1, 6144), (5.0, 0.2, 5641), and (4.4, 0.2, 6502), respectively. Two points a and e in Fig. 6 are projected to point A in Fig. 5. Similarly, points b and f are to point B, points c and g to point C, and the points d and h to point D. Four dotted curves connecting b with c, d with e, f with g, and h with a in Fig. 6 correspond to transitional shift of the *q* value retaining the same *fd* value. When the point *T* in Fig. 5 moves along the closed loop of ABCDA just once, the point *S* moves along the curve efgha in Fig. 6, which is not along a closed loop.

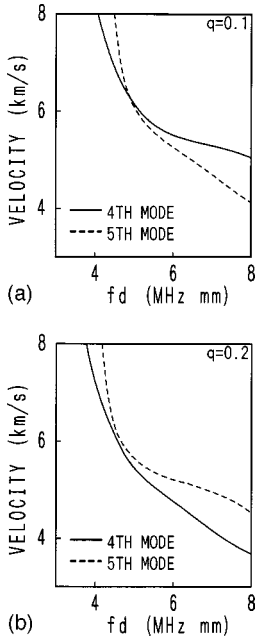

FIG. 3. Calculated phase velocity curves of the 4th and 5th modes for two *q* values. (a) $q=0.1$, (b) $q=0.2$.

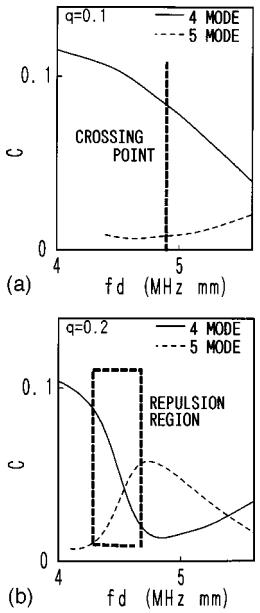

FIG. 4. Calculated *C* values of the 4th and 5th modes as a function of *fd* for two *q* values. (a) $q=0.1$, (b) $q=0.2$.

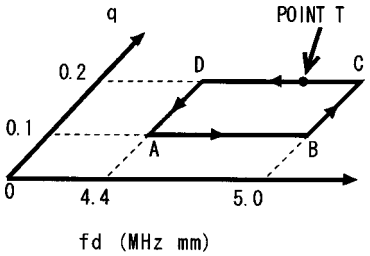

FIG. 5. Schematic diagram of geometrical relation of a rectangular domain ABCD on two-dimensional space (*fd*-*q* plane).

When the point T moves along the same loop once again, the point S moves along the curve abcde. This indicates that the phase velocity values of the 4th and 5th modes are in the form of two different branches of a two-valued function defined on the fd-q plane.

Other closed loops on the fd-q plane were used as paths along which the point T moves. It turned out that the same phenomenon of two-valuedness occurs if a loop contains the neighborhood of somewhere around the point $(fd,q)=(4.7,0.15)$, but it does not occur if a loop does not contain the neighborhood. This suggests that there is a singular point within the neighborhood. The phase velocities of the 4th and 5th modes can not be separated and are regarded as two different branches of a two-valued function in the domain containing the singular point or in the domain surrounding the singular point. But they can be isolated into the 4th-mode and the 5th-mode values and are regarded as two single-valued functions in the domain that is not containing nor surrounding the singular point.

Let us call the above phenomenon, two-valuedness of the velocities and the existence of a singular point, mode coupling from now on. The mode coupling is analogous to the behavior of mathematical function on the complex plane $\omega=z^{(1/2)}$ (both z and ω are complex) in the domain including the point $z=0$. It is expected that there is a special value of $q_0(0.1<q_0<0.2)$ and that the plane of $q=q_0$ contains the predicted singular point. We consider that the behaviors of the curves for the 4th and 5th modes in the case of $q=q_0$ are different from the phenomena of mode repulsion or mode crossing that are often observed on the velocity dispersion curves of existing materials. Because in the case of a plate with a right value of q_0, the complex velocity of the two modes completely coincides at the singular point, which is not the case in mode repulsion, where only the imaginary part coincides, nor in mode crossing, where only the real part coincides. The mode repulsion happened because the q value was a little beyond q_0, and the mode crossing occurred because q value was a little under q_0. So we suspect that both mode repulsion and mode crossing are two phenomenon that seem to occur when the mode coupling is observed at a fixed q-value.

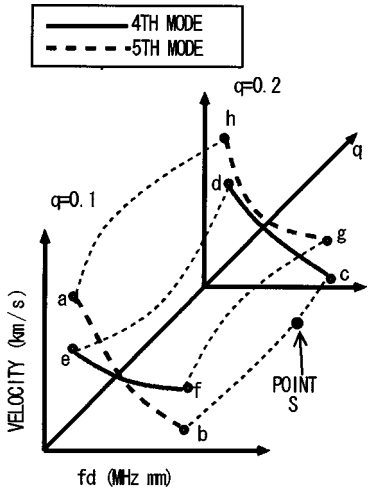

FIG. 6. Phase velocity variation on the *fd*-*q* plane, where an arbitrary point *S* represents a combination of three values of *fd*, *q*, and phase velocity.

IV. CONCLUSION

The mode repulsion and crossing of the velocity dispersion curves of Lamb waves in a virtual material were studied based on numerical analysis of wave propagation. Two-valuedness of the phase velocities and the existence of a singular point were found in the specific region of the *fd*-plane, in the combination of two particular materials, glass and ceramic. Consideration on the imaginary parts of velocity dispersion curves of leaky Lamb waves was useful for understanding the phenomenon of mode repulsion and mode crossing. The 4th- and 5th-mode phase velocity values as a function defined on the fd-q plane constituted two different branches of a two-valued function in the vicinity of a singular point. Further analytical studies on this matter are now developing on other leaky waves as well as on nonleaky waves along with experimental studies.

[1] A. Sawaguchi and K. Toda, Jpn. J. Appl. Phys. **30**, 191 (1991).
[2] K. Toda and Y. Akutsu, Jpn. J. Appl. Phys. **33**, 5385 (1994).
[3] K. Toda and K. Motegi, Jpn. J. Appl. Phys. **34**, 2886 (1995).
[4] O. Poncelet and M. Deschamps, J. Acoust. Soc. Am. **102**, 292 (1997).
[5] H. Moritake, M. Inoue, and K. Toda, Jpn. J. Appl. Phys. **36**, 6088 (1997).
[6] H. Uberall, B. Hosten, M. Descamps, and A. Gerard, J. Acoust. Soc. Am. **96**, 908 (1994).
[7] J. Dickey, G. Maidanick, and H. Uberall, J. Acoust. Soc. Am. **98**, 2365 (1995).
[8] X. L. Bao, H. Franklin, P. K. Raju, and H. Uberall, J. Acoust. Soc. Am. **102**, 1246 (1997).
[9] Q. Zhu and W. G. Mayer, J. Acoust. Soc. Am. **93**, 1893 (1993).
[10] G. W. Farnell, *Elastic Surface Waves, Surface Wave Filters*, edited by H. Matthews (Wiley, New York, 1977), Chap. 1, p. 26.
[11] K. Toda and K. Ibuki, Ferroelectrics **73**, 419 (1987).

Contribution to the hydroacoustic ocean monitoring of the UN Test Ban Treaty; signal classification by an autonomous buoy system

Dieter Brecht and Lothar Ginzkey
Federal Armed Forces Underwater Acoustics and Marine Geophysics Research Institute (FWG), Klausdorfer Weg 2-24, 24148 Kiel, Germany

(Received 24 May 1999; revised 4 November 1999; accepted 12 November 1999)

A concept for the detection of nuclear underwater explosions in the ocean with an autonomous, battery supplied hydroacoustic monitoring station is described. According to 26 Article IV of the Comprehensive Test Ban Treaty (CTBT), a low-cost station can be used as a quick temporary substitute in order to provide for cases of breakdown of a permanent facility. The on-board detector uses robust criteria to reduce false alarms caused by the background of natural events. For suspicious events, the typical characteristics are transmitted by a surface buoy satellite link to the data center. The classification technique has been tested with real data. With simple rules, an effective false alarm suppression can be achieved without losing sensitivity against suspicious in-water explosions. © *2000 Acoustical Society of America.* [S0001-4966(00)04202-8]

PACS numbers: 43.30.Lz, 43.30.Xm [DLB]

INTRODUCTION

The CTBT includes a global surveillance network covering the continents, the oceans, and the atmosphere. Hydroacoustic monitoring stations like the autonomous buoy system presented here record the typical signatures of illegal nuclear underwater explosions which, due to the excellent acoustic conductivity of the ocean, provide simple and unique classification clues.

The characteristic sound-speed profile of the deep ocean establishes a global waveguide at about 1500-m depth, allowing hydroacoustic events in the ocean to be detected over tremendous distances and even far below the yield of 1 Kt TNT equivalent as required by the treaty. The acoustic energy of earthquakes or explosions is trapped within the SOFAR channel and, without touching the sea surface or bottom, spreads out with little attenuation over the whole ocean. As long as the path between source and sensor is not blocked by underwater mountains or the continental shelf, a single hydrophone station can be sufficient to cover a complete ocean.

The CTBT prohibits nuclear tests in general (atmosphere, in-water, underground). The surveillance of the treaty is ensured by a global network of 170 seismic, 11 hydroacoustic, 60 infrasound, and 80 radionuclide monitoring stations. The few hydroacoustic stations play a key role for localization and classification of offshore nuclear tests.

(a) In the southern hemisphere, where the seismic network is sparse, the localization accuracy is improved considerably, well beyond the required value of 1000 km^2. Detections at three stations, requiring three to four stations per ocean, are sufficient for an independent high-accuracy localization.
(b) The SOFAR channel represents a low-pass filter waveguide of about 100-Hz rolloff. Unlike seismic signals, this comparably large bandwidth provides simple and reliable classification clues to distinguish the typical hydroacoustic signature of in-water explosions from the background of earthquakes and other natural events.

Five of the 11 hydroacoustic stations use island-based seismometer receivers and are used for localization only. Since only the six genuine hydrophone stations of the network provide the required bandwidth to obtain the essential and obvious classification clues, a backup station seems essential.

In this letter, we present the detection concept of an autonomous buoy station. Unlike the permanent stations, it is battery powered and does not depend on laborious cable connections to the shore. It can be deployed temporarily on short notice in case of malfunction of fixed stations. The signal processing is adapted to the requirements of autonomous operation. The constraints in power consumption and data transfer rate require an efficient on-board capability of false alarm reduction, preclassification, and data reduction.

I. TYPICAL ACOUSTIC EVENTS IN THE OCEAN

Many sources contribute to the background of nonstationary acoustic noise. Typical sources are seismic and volcanic activity, biologic sounds of fish/mammals (Ref. 1, standing in for many) and man-made noise including military, scientific, and exploration activities.

Underwater explosions can be distinguished because of their typical signature. Figure 1 shows the (uncalibrated) spectrogram of a nearby (7 km) in-water explosion which clearly depicts the typical characteristics. The signal is very short and impulsive in the time domain. The bandwidth is high, containing frequencies far beyond 100 Hz. Furthermore, the signal shows a clear bubble pulse structure. In-water explosions often cause an oscillating gas bubble which, after the initial expansion phase, collapses and expands again. The delay T of the first bubble pulse is a func-

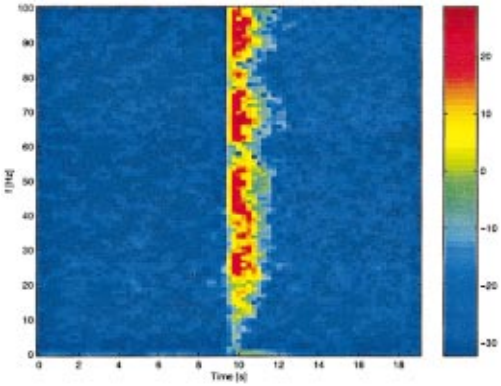

FIG. 1. Chemical explosion with bubble pulse structure.

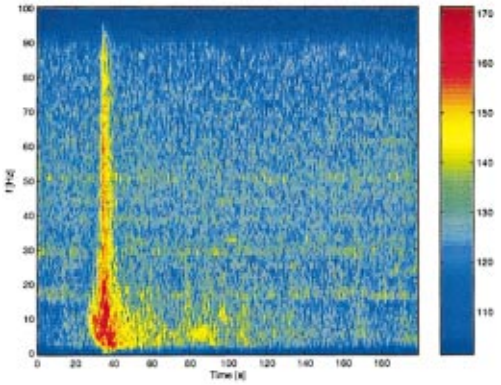

FIG. 3. Nuclear explosion, Mururoa, 27 October 1995.

tion of source depth z [m] and yield w [kg], given by[2]

$$T = \frac{Kw^{1/3}}{(z+10.06)^{5/6}}.$$

The experimental values $z=90\,\mathrm{m}$, $w=0.82\,\mathrm{kg}$, and $K=2.11$ for TNT give $T=42.5\,\mathrm{ms}$. In the spectrogram, the delay can be seen as a periodic structure with $\Delta f = 1/T = 23.5\,\mathrm{Hz}$. The autocorrelation for the time series of this event yields the exact value $T=42.5\,\mathrm{ms}$. Consequently, this is a strong indicator for an in-water explosion.

Figure 2 shows a signal which was recorded at the SOSUS station Point Sur. The origin was a seismic refraction experiment near Japan,[3] at a distance of 8000 km. Despite the long propagation path, the signal maintains a large bandwidth because all frequencies up to 100 Hz are guided by the SOFAR channel almost without attenuation. Despite its extraordinary duration, probably caused by the propagation conditions, the signal still shows the typical bubble pulse structure which is consistent with the reported values of depth and charge.

Nuclear and chemical explosions cannot be discriminated by their waveforms. The only classification clue is their significant difference in charge yield, which can be estimated if the signal is detected by at least three stations and the origin can be determined.

Hydroacoustic signals of nuclear in-water explosions have not been available to the authors. Figure 3 shows the spectrogram of an island nuclear explosion. It is one of the six French tests (27.10.95) conducted at Mururoa between September 95 and January 96. Despite the long, principally waterborne propagation path of 6800 km, the signal remains short and shows a large bandwidth. There is no bubble pulse structure because the test was conducted in the atoll. Like most of the waveforms used in this study, the raw data have been received via Internet access from the Prototype International Data Center (PIDC).

The coupling efficiency of the seismic energy into the SOFAR channel is, especially for higher frequencies, highly dependent upon the experimental setup, the local geology, and the bathymetry at the source location. Consequently, the signatures of the recorded nuclear explosions show a larger variety as compared to underwater explosions.

Figure 4 shows a typical seismic event from an earthquake near Japan, received at a distance of about 8080 km. Unlike a typical explosion, the seismic signal is longer, rises and falls slowly, and all frequencies above 30 Hz are lacking completely. Due to the long propagation path in rock with strong attenuation, seismic waves typically do not contain higher frequencies (above $\approx$20 Hz) which could couple into the SOFAR channel. These events with sources generally deep below the ground can therefore easily be distinguished from those in or near to the water column and be rejected as false alarms.

One of the most critical sources of false alarms are volcanic eruptions. Figure 5 shows events from Hawaii, July 22, 1996, recorded at Point Sur at a distance of 3700 km. The pulse length is short and the bandwidth considerably higher than for earthquake signals.

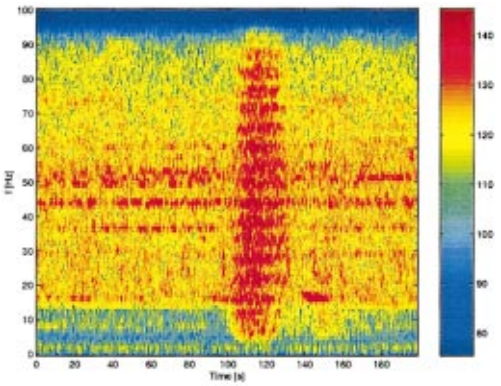

FIG. 2. Chemical explosion with bubble pulse structure.

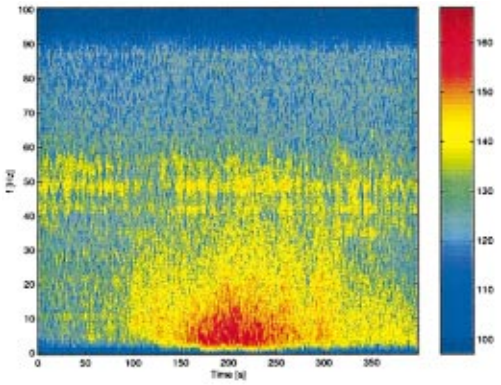

FIG. 4. Undersea earthquake near Japan.

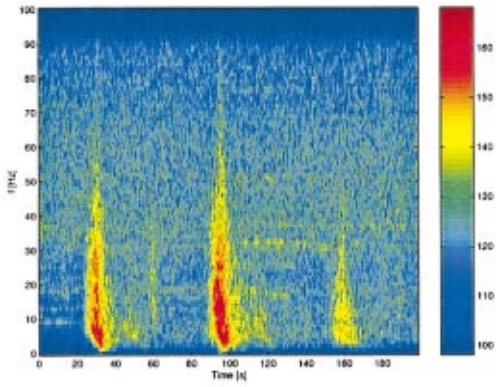

FIG. 5. Volcanic events from Hawaii, 22 July 1996.

These types of events show a great variety. While in most cases the spectrum allows discrimination from in-water explosions, there are still examples where even an analyst can hardly distinguish the signatures from those of not-in-water explosions. The buoy station would classify these events as suspicious and transmit them for expert analysis, allowing the fusion and joint evaluation of detections from other stations.

Further false alarms can occur due to unknown man-made sources or mammals in the vicinity of the station (Fig. 6). These signals are mostly short and often concentrated in a certain frequency band. They can mostly be screened due to their duration.

II. DESCRIPTION OF THE BUOY STATION

The hydrophone is suspended at SOFAR axis depth between a deep sea mooring (Fig. 7) and the submerged main float, which decouples the hydrophone from the motion of the surface buoy and contains most of the electronics and batteries. The spar buoy surface unit carries only the satellite communication interface and exposes just a small area to the wind and sea wave forces.

A novelty is the newly developed cable connection to the buoy. Two special swivels transmit the data by inductive couplers. Thus the buoy can turn freely to avoid cable kinks, which have been the weak point of deep sea sensor moorings with satellite links.

The system can be launched and installed easily with a single rope and operates autonomously for up to 2 years,

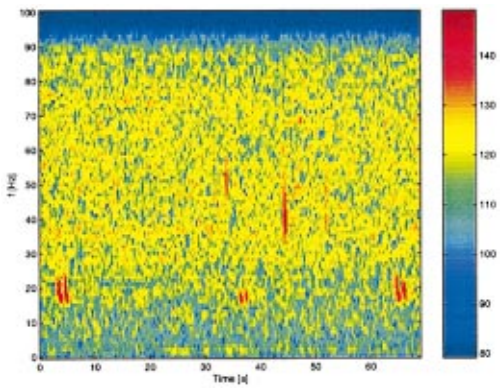

FIG. 6. Mammal calls.

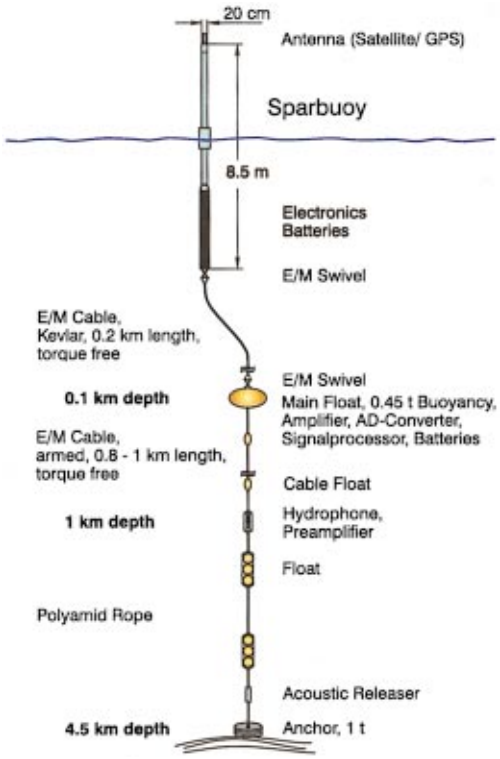

FIG. 7. Scheme of the autonomous monitoring station.

which is sufficient even for long-term tasks. Due to the limited energy reserves, the electronics has to be especially energy efficient and data transfer is limited to occasional satellite connections ($\leqslant$4/day) with low total data rate (we assume 50 events of 3×128 bytes/day). The buoy needs its own signal processing capability, performing detection, and feature extraction. Only for events classified as suspicious, the significant features will be transmitted to the data center for detailed post-analysis.

III. DETECTION AND FEATURE EXTRACTION

Most of the time, the electronic unit is in a low-energy mode. The hydrophone output is sampled at 256 Hz and stored into a RAM ring buffer of 64 min capacity. Only once an hour, the signal processing unit is activated to scan and analyze the buffer data. The quick detection algorithm is based on the short-time averaged (1 s) power signal, which has to exceed the long-time average (60 s) by at least 10 to 25 dB. A first classification and false alarm reduction is performed according to the peak power and pulse duration, rejecting short spikes (fish, etc., $T<1$ s) and long earthquake signals ($T>40$ s). Both excess level and duration are adjustable via satellite.

Although the number of detections will rarely exceed five per hour at this stage, the remaining detections can be limited to a maximum number, selecting the most interesting ones according to peak power. This limits the analysis effort in case of extraordinary false alarm situations due to exploration activity, for example.

The feature extraction is based on the spectrogram analysis, using a fast Fourier transform (FFT) with a 256-samples (1s) Hanning window, 3/4 overlap. For each

frequency-bin (width 1 Hz×1/4 s), the signal represents the mean power (μPa^2/Hz), with a weighted time-averaging according to the squared window function. The spectrogram is summed up into six nonoverlapping frequency bands by averaging the corresponding frequency bins. For each of the smoothed bands ($f=1-2$, 3–5, 6–10, 11–20, 21–40, 41–100 Hz), we derive characteristic features for further analysis:

(i) peak level and noise level
(ii) time of peak, onset, end
(iii) mean time, time spread, higher moments
(iv) total energy
(v) pulse shape: times of $-10,-15,...,-30$ dB down-points from peak.

The following features are derived from the spectrum:

(i) center frequency (max of energy)
(ii) cutoff frequency: crossing of signal/noise spectra
(iii) slope and shape above center-f
(iv) bubble pulse delay (cepstrum/autocorrelation)
(v) noise spectrum ($\Delta f=2$ Hz, on request).

Reasonable data reduction was achieved by observing the sufficient accuracy for the parameters. Most frequencies and times, for example, are in units of bins with width 1 Hz and 1/4 s, relative to a reference time and can be coded in 1 byte. This allows a sufficient time window of 64 s per report.

Based on robust features like the cutoff frequency, the events can now be further classified as ''explosionlike'' or ''false alarm.'' Only for those events classified as explosionlike, the features will be stored in a permanent buffer and occasionally transferred by satellite connection. The data of rejected events are lost and can not, like in most stationary stations, be later requested and reanalyzed on demand. In order to make sure that no interesting event is lost, conservative classification rules are applied. Based on the features, a more detailed analysis according to source type and travel path will be done in the International Data Center (IDC). This post-classification can be done off line, using sophisticated neural net[4] or fuzzy logic approaches.

IV. CLASSIFICATION RULES

The decision to transmit or not relies on simple and robust clues: the peak power and detection threshold (A), the signal duration (B), and the cutoff frequency (C). The classification results were tested with a real data set, including various representations of different event types, as shown in Sec. I.

As in the testing phase of the buoy, we begin by applying only rules A, B. This screens almost all spiky events and many of the long earthquake signals. The other events pass this step. The smaller in-water explosions can also be screened by increasing the detection threshold, as nuclear versions would be significantly louder. The threshold is remotely adjustable, allowing the false alarm rate to be controlled according to the testing goals.

The high-frequency content (rule C), available after feature extraction, rejects all events without significant frequencies above 40 Hz. This screens out all earthquakes while keeping all in-water explosions.

From the Mururoa nuclear test signals, those four with a typical signature (Fig. 3) are easily detected. Another three signals were available which, due to poor coupling or misidentification, show a seismic/volcanic signature and are not selected, as expected. The ''volcanoes'' can not be screened completely and generate unavoidable false alarms. This is tolerable because these events are quite rare. Thus the cutoff-frequency limit can even be slightly reduced without allowing false alarms from the far more common seismic signals.

The option is in preparation to transmit original signals for extraordinary events, where expert examination, including listening to the real signal, is considered indispensable. These would then be selected by applying much stronger criteria, based on further features like bubble pulse evidence.

V. CONCLUSIONS

An autonomous buoy station has been developed to detect and record hydroacoustic events, such as nuclear explosions in the ocean. The global surveillance network of the CTBT uses the typical hydroacoustic signatures of underwater explosions as a key classification clue.

The station is designed as a temporary replacement in case of breakdown of one of the only six fixed hydrophone stations of the IMS. It operates autonomously and independent of local infrastructure, making it deployable quickly and at reasonable costs by a ship of opportunity. The limitations in energy consumption and data link require an on-board capacity of classification, false alarm suppression, and data reduction.

Large chemical or nuclear explosions in the ocean can be identified by means of their specific signature. The classification algorithms designed for this task use simple and robust features like peak power, duration, and high-frequency content. Characteristic features of the signature are extracted and transmitted for post analysis.

The classification rules were tested using data from existing fixed stations. The classifier reliably detected all interesting in-water explosions, even though the available test signals from chemical explosions had yields far below the nuclear threshold. In an operational version, most of them could be screened as man-made noise by increasing the detection threshold. Even most island-based nuclear explosions are easily detected, like those from the French 1995 test series. Background events of different seismic, biologic, or man-made sources are effectively suppressed, giving a reasonable false alarm and data rate.

[1] M. A. McDonald and C. G. Fox, ''Passive acoustic methods applied to fin whale population density estimation'' J. Acoust. Soc. Am. **105**, 2643–2651 (1999).
[2] R. Urick, *Principles of Underwater Sound*, 3rd ed. (McGraw-Hill, New York, 1993).
[3] D. A. Brumbaugh and R. Le Bras, ''Hydroacoustic signals from a ground-truth data set of marine explosions,'' Technical Report SAIC-98/3008, Science Applications International Corporation, McLean, VA, 1998.
[4] P. Dysart and H. Laney, ''Hydroacoustic phase identification,'' Technical Report SAIC-97/Science Applications International Corporation, McLean, VA, 1997.

On a numerical truncation approximation algorithm for transfer matrix method

Krishnan Balasubramaniam[a)]
Department of Aerospace Engineering and Mechanics, Mississippi State University, Mississippi State, Mississippi 39762

(Received 31 March 1999; accepted for publication 10 November 1999)

A numerical truncation technique is described for reducing the numerical instability problems associated with the utilization of the transfer matrix method, especially in cases where the frequency of ultrasound, the number of layers, or the thickness of the layers become very large. This rather simplistic modification to the numerical coding extends the transfer matrix method to a wide range of applications, without any complex and computationally intensive reformulation. © *2000 Acoustical Society of America.* [S0001-4966(00)04102-3]

PACS numbers: 43.35.Cg [HEB]

INTRODUCTION

Modeling of acoustic wave propagation in layered elastic media is important because of the extensive range of problems which can be addressed. A popular and widely reported method for modeling wave propagation in layered structures is the transfer matrix method, which has been credited to Thomson[1] and has been well documented.[2–14]

It is a well-known fact that one of the characteristics of the technique is the occurrence of numerical instabilities, even for layered isotropic structures. The numerical instabilities have been observed especially when the overall thickness of the structure or the frequency of the harmonic ultrasonic wave becomes very high or when the intermediate elastic supports are very stiff.[9,10] The numerical difficulties also increase at higher oblique incidence angles (near grazing angles). They are reported to be dependent on the ''*fdr*,'' parameter which is a product of the frequency (f), thickness (d), and number of ply groups (r).[12] Here, ply groups is defined as the superlayer repetitions (a superlayer being a combination of ply groups that can repeat or have mirror images). Thus, for thick laminates (high *fdr* values) having a large number of ply groups, the transfer matrix method does not provide a reliable model. This results in a limitation of the model application to very thin layered structures composed of simple stacking sequences. Moreover, inverse problems like stacking sequence identification and elastic constant inversion become increasingly more difficult to solve.

The cause of these computational problems is traced to the loss of precision that occurs when performing normal arithmetic calculations using computers of limited precision. In the transfer matrix method, the global transfer matrix is related to the local transfer matrices by

$$A=\prod_{k=1}^{k=n} A_k,$$

where A_k is the local transfer matrix of the kth layer of an n-layered laminate. In this method, the relatively insignificant inaccuracies in computation are amplified by the large number of matrix premultiplications when computing the global transfer matrix A from the local transfer matrices A_k, as in the case of a large number of ply groups. Furthermore, the matrices A_k contain terms like $e^{i\alpha\xi d_k}$, where α is the ratio of the wave number component in the thickness direction to that along the surface in the incident plane, i.e., a partial wave solution; ξ is the wave number in the wave number component along the surface in the incident plane; and d_k is the thickness of the kth layer. Here, small precision errors are amplified by the exponential term, especially for high thicknesses.

There are several publications which have addressed the stability issue and suggested improvements to reduce the instability. For instance, Dunkin[8] had developed a delta operator technique which has since been improved by Kundu and Mal,[10] Levesque and Piche,[11] and Castaings and Hosten.[12] This method uses up to 20th-order delta matrices and is computationally intensive. The method involves computing subdeterminants of local transfer matrices and is aimed at preventing the accumulation of precision errors during computation of the global transfer matrix. Most work[6] has been concentrated on isotropic materials utilizing the delta-2 operator. However, Castaings and Hosten[12] have adapted the technique to anisotropic media (composite laminates) where the delta-3 operator has been introduced. Delta operators do indeed provide a much-improved transfer matrix formulation, but nevertheless, they result in significantly increasing computational time as a result of a large number of extra subdeterminant computations. The computational time on a Sun SPARC Server was determined to increase by 30–40 times for a typical thick composite laminate case study. Speed of computation is even more critical during the use of inverse techniques for determining the material properties, where the procedure has to be frequently repeated during a typical inverse search process.[13] Furthermore, as reported by Castaings and Hosten,[12] closed-form analytical expressions for the local transfer matrix elements and subdeterminants need to be found using a mathematical software that performs symbolic operations. This leads to the development of a considerably new formulation of the technique which can sometimes result in very complex coding for numerical

a)Electronic mail: balas@ae.msstate.edu

TABLE I. Material properties of the graphite–epoxy composite used in the analysis (Ref. 7).

Viscoelastic graphite/epoxy ($\rho = 1500\ \mathrm{kg/m^3}$)									
Elastic constant C_{ij} (GPa)	C_{11}	C_{22}	C_{33}	C_{12}	C_{13}	C_{23}	C_{44}	C_{55}	C_{66}
	132.00	12.30	12.10	6.90	5.90	5.50	3.32	6.21	6.15
Viscoelastic constant η_{ij} (GPa-μs)	η_{11}	η_{22}	η_{33}	η_{12}	η_{13}	η_{23}	η_{44}	η_{55}	η_{66}
	0.400	0.037	0.043	0.001	0.016	0.021	0.009	0.015	0.020

analysis for both the forward and the inverse solutions. For thick structures with periodic repetition of layers, Floquet wave techniques may be applicable.[13]

I. NUMERICAL TRUNCATION ALGORITHM

An approximation algorithm by numerically truncating the higher end values was attempted, with considerable success without compromising computational speed. Loss of accuracy and validity of the results is always a concern during any truncation process. The truncation algorithm discussed here provided results which compare very well with the results obtained using the delta operator technique[12] and was found to be stable for a wide range of case studies.[14,15] The technique is simple, almost trivial, and no significant change in the traditional analytical expressions for the transfer matrix method is required. In this remedy, the error amplification caused by the exponential terms was limited by setting a maximum threshold value on the real part of the exponent $(i\alpha\xi d_k)$. To account for the ply-group dependence, the maximum threshold was set to $25/r$. Hence, the following condition was imposed:

$$\text{IF REAL } (i\alpha\xi d_k) > 25/r \text{ THEN REAL } (i\alpha\xi d_k) = 25/r.$$

Here, ξ is equal to $(2\pi f)/c$, where f is the frequency and c is the phase velocity of the partial mode. Hence, the *fdr* parameter, which influences the onset of instabilities, is inherent in the numerical truncation algorithm. The selection of 25 as the threshold was based on several numerical convergence studies conducted on graphite–epoxy composite laminates. A numerical approach to solving the instability problems with the transfer matrix method has also been suggested elsewhere.[16]

In this letter, only fluid-loaded laminates constructed from fiber-reinforced composite materials (graphite–epoxy) were considered. The reflection and transmission factor characteristics for a longitudinal wave obliquely incident on the laminate will be employed in order to demonstrate the capability of a numerical truncation technique. Numerical experiments were carried out on the viscoelastic graphite/epoxy material used by Deschamps and Hosten.[7] The viscoelastic material properties are listed in Table I. The three commonly encountered stacking sequences, *viz.*, unidirectional, cross-ply, and quasi-isotropic, were investigated. Reflection factor versus incidence angle θ plots in the $\phi = 0°$ incidence plane were studied because numerical problems arise at oblique incidence. All multioriented laminates were assumed to be composed of equal-thickness ply groups, i.e., $d_k = d(\text{total laminate thickness})/r$. All routines were coded in FORTRAN 77 and executed on SUN workstations using double precision and double complex data types.

The behavior of reflection factor, with and without numerical truncation, for a unidirectional laminate was examined in a case study where numerical instabilities have been reported earlier.[7] The frequency and laminate thickness parameters were those used in Deschamps and Hosten,[7] i.e., frequency $(f) = 2.242$ MHz and thickness $(d) = 3.434$ mm. The plots of the reflection factor versus incidence angle without and with numerical truncation are shown in Fig. 1(a) and

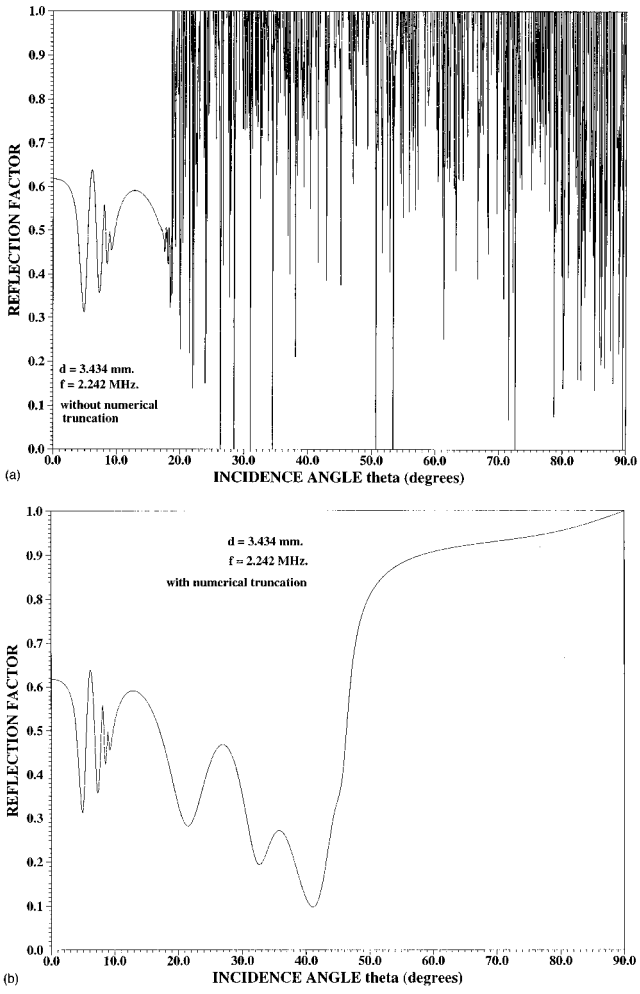

FIG. 1. (a) Computed reflection factor response without any numerical truncation for a viscoelastic unidirectional graphite–epoxy composite laminate with thickness $(d) = 3.434$ mm, at frequency $(f) = 2.241$ MHz at a plane of incidence along the fibers. (b) Computed reflection factor response with numerical truncation correction for a viscoelastic unidirectional graphite–epoxy composite laminate with thickness $(d) = 3.434$ mm, at frequency $(f) = 2.241$ MHz at a plane of incidence along the fibers.

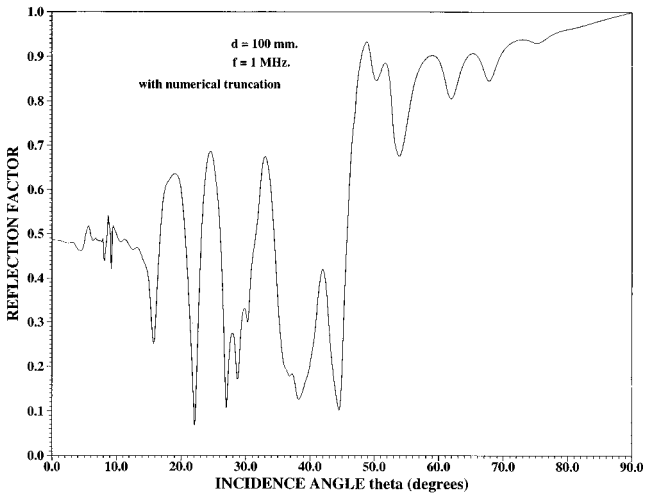

FIG. 2. Computed reflection factor response with numerical truncation for a very thick viscoelastic cross-ply $[0/90]_{4S}$ graphite–epoxy composite laminate with thickness $(d)=100$ mm, at frequency $(f)=1.00$ MHz at a plane of incidence along the fibers.

(b), respectively. As can be observed, without numerical truncation [Fig. 1(a)], the transfer matrix formulation is computationally stable till around an incidence angle $\theta=18°$, after which instabilities creep in. On the other hand, incorporating numerical truncation [Fig. 1(b)] stabilizes the computation, with the reflection factor being computed right up to $\theta=90°$. Furthermore, computation with truncation agrees extremely well with the result published by Deschamps and Hosten[7] for the same case—especially the experimental one at high angles of incidence and for several other case studies.[15] In fact, their numerical computation, in spite of using an improved transfer matrix algorithm, does not match well with experiments at incidence angles greater than 50°.

Next, the stability of the formulation with truncation was examined for a very thick composite laminate. The case study involved 100-mm-thick laminated plates at an incident frequency $f=1$ MHz $(fd=100\,\text{MHz mm})$. Figures 2–4 show the reflection factor plots for $[0°/90°]_{4S}$, $[0°/90°/+45°/-45°]_{4S}$, $[0°/90°]_{8S}$ laminates. It can be noted from Figs. 2–4 that the reflection factor computation is stable, while the results obtained without employing the numerical truncation were highly unstable. However, from Fig. 4, for $[0°/90°]_{8S}$ where the number of ply-group repetitions $r=16$ is doubled, as compared to $[0°/90°]_{4S}$ where $r=8$, some instabilities seem to appear around $\theta=30°$. Nevertheless, when the laminate thickness was reduced to $d=50$ mm $(fd=50\,\text{MHz mm})$, no instabilities were observed. This demonstrates that the numerical truncation may not be stable for all values of *fdr*. Yet, based on the laminate layups and high *fd* values used in the case studies here, representing extreme cases for many practical composite structures, the numerical truncation significantly reduces the computational instabilities.

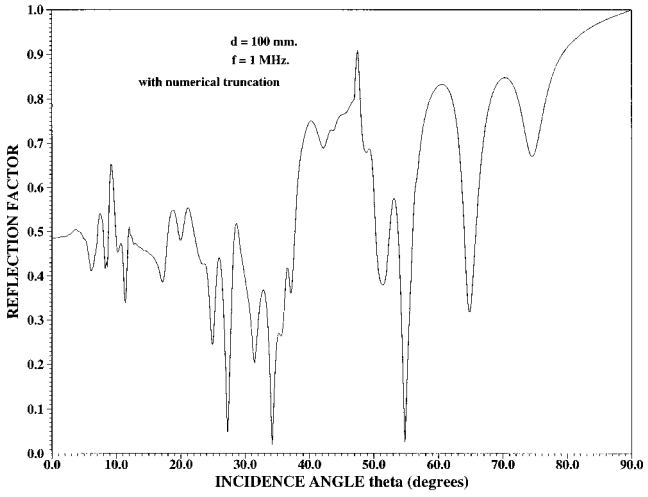

FIG. 3. Computed reflection factor response with numerical truncation for a very thick viscoelastic $[0/90/+45/-45]_{4S}$ graphite–epoxy composite laminate with thickness $(d)=100$ mm, at frequency $(f)=1.00$ MHz at a plane of incidence along the fibers.

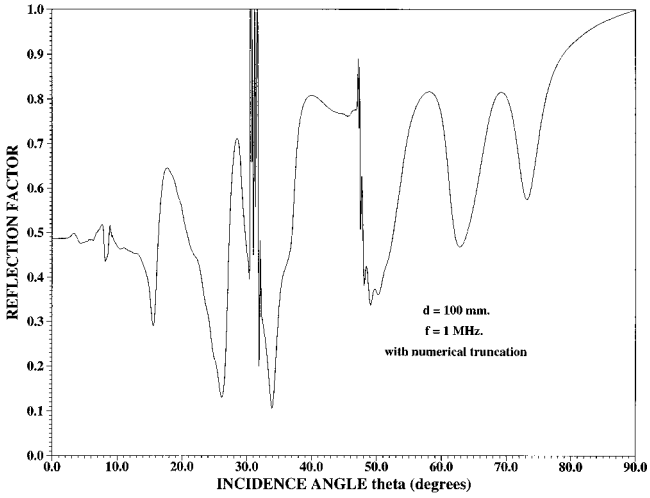

FIG. 4. Computed reflection factor response with numerical truncation for a very thick viscoelastic $[0/90]_{8S}$ graphite–epoxy composite laminate with thickness $(d)=100$ mm, at frequency $(f)=1.00$ MHz at a plane of incidence along the fibers. This shows some numerical instabilities near 30-deg angle of incidence.

II. CONCLUSION

The numerical truncation method, discussed in this letter, involves limiting the exponential terms involved to a certain threshold in order to prevent instabilities due to precision inaccuracies and computational limitation in handling large numbers. Alternative methods such as the delta operator technique have been shown to solve this problem, but these technique require extensive reformulation and significantly add to the computational time. In contrast, the numerical truncation algorithm is simpler and does not compromise computational speed. Numerical truncation was examined for unidirectional, cross-ply, and quasi-isotropic viscoelastic laminates. It was observed that despite some limitations on the thickness, *vis-a-vis* ply-group repetitions, the method can be applied successfully to a wider range of laminate stacking sequences, ultrasonic frequencies, and thicknesses where the traditional transfer matrix method demonstrates instabilities.

[1] W. T. Thomson, ''Transmission of elastic waves through a stratified solid medium,'' J. Appl. Phys. **21**, 89–93 (1950).
[2] L. M. Brekhovskikh, *Waves in Layered Media* (Academic, New York, 1960).
[3] A. H. Nayfeh, *Wave Propagation in Layered Anisotropic Media with Applications to Composites* (North-Holland, Amsterdam, 1995).
[4] A. H. Nayfeh and D. E. Chimenti, ''Elastic wave propagation in fluid-loaded multi-axial anisotropic media,'' J. Acoust. Soc. Am. **89**, 542–549 (1991).
[5] A. K. Mal and Y. Bar-Cohen, ''Ultrasonic characterization of composite laminates,'' in Wave Propagation in Structural Composites, edited by A. K. Mal and T. C. T. Ting, AMD-90 (American Society of Mechanical Engineers Press, New York, 1988), pp. 1–17.
[6] B. Hosten and M. Castaings, ''Transfer matrix of multilayered absorbing and anisotropic media. Measurements and simulations of ultrasonic wave propagation through composite materials,'' J. Acoust. Soc. Am. **94**, 1488–1495 (1993).
[7] M. Deschamps and B. Hosten, ''The effects of viscoelasticity on the reflection and transmission of ultrasonic waves by an orthotropic plate,'' J. Acoust. Soc. Am. **91**, 2007–2015 (1992).
[8] J. W. Dunkin, ''Computation of modal solutions in layered elastic media at high frequencies,'' Bull. Seismol. Soc. Am. **55**, 335–358 (1965).
[9] B. Hosten, ''Bulk heterogeneous plane waves propagation through viscoelastic plates and stratified media with large values of frequency domain,'' Ultrasonics **29**, 445–449 (1991).
[10] T. Kundu and A. K. Mal, ''Elastic waves in a multi-layered solid due to a dislocation source,'' Wave Motion **7**, 459–471 (1985).
[11] D. Lévesque and L. Piché, ''A robust transfer matrix formulation for the ultrasonic response of multilayered absorbing media,'' J. Acoust. Soc. Am. **92**, 452–467 (1992).
[12] M. Castaings and B. Hosten, ''Delta operator technique to improve the Thomson–Haskell-method stability for propagation in multilayered anisotropic absorbing plates,'' J. Acoust. Soc. Am. **95**, 1931–1941 (1994).
[13] C. Potel and J. F. de Belleval, ''Acoustic propagation in anisotropic periodic multilayered media: A method to solve numerical instabilities,'' J. Appl. Phys. **74**(4), 2208–2215 (1993).
[14] N. S. Rao, M.S. thesis, Mississippi State University, MS (1997).
[15] Y. Ji, Ph.D. dissertation, Mississippi State University, MS (1996).
[16] B. Hosten, ''Bulk heterogenous plane waves propagation through viscoelastic plates and stratified media with large values of frequency domain,'' Ultrasonics **29**, 445–449 (1991).

Performance limits of the broadband generalized sidelobe cancelling structure in an isotropic noise field

Sven E. Nordholm and Yee Hong Leung
Australian Telecommunications Research Institute, Curtin University of Technology, Bentley WA 6102, Australia

(Received 2 August 1995; revised 15 September 1999; accepted 29 October 1999)

In acoustic applications, the signal source of interest is generally broadband and the background noise field is predominantly isotropic. In this letter, the performance of the broadband generalized sidelobe canceller, optimized with respect to an isotropic noise field, is analyzed and compared against the performance of the conventional summing beamformer. The comparison is based on an ideal continuous-time infinite-length generalized sidelobe canceller with the aim of determining the performance limits of this beamforming structure. © *2000 Acoustical Society of America.* [S0001-4966(00)02402-4]

PACS numbers: 43.60.Gk [JCB]

INTRODUCTION

It is well known that an adaptive beamformer can outperform its corresponding conventional summing beamformer, but at a higher implementation cost.[1,2] Therefore, it is important to have an understanding of the precise nature of the adaptive beamformer's superior performance. In this paper, the generalized sidelobe canceller (GSC) form of the adaptive beamformer, also known as the Griffiths–Jim beamformer,[2–4] is studied. The study makes references to acoustic applications such as hands-free mobile phones and sonar where the signals of interest are broadband and the background noise field is predominantly isotropic.[5–8] This paper aims to determine, analytically, the amount of additional noise suppression the broadband GSC is able to achieve relative to the conventional summing beamformer in an isotropic noise environment.

Although this paper considers only the GSC, the results presented here are, in fact, quite general. For example, it can be shown that the GSC is equivalent to other beamforming structures such as the linearly constrained minimum variance (LCMV) beamformer.[2,9] The motivation for studying the GSC stems from the fact that the optimum GSC is defined by an optimization problem that is unconstrained. Fourier techniques can thus be applied to simplify the solution to this problem.

At this juncture, it should be pointed out that the aim of this paper is simply to explore the performance limits of adaptive beamformers. In this connection, the optimum GSC derived in this paper will be idealized in the sense that it will be a continuous-time, infinite length, and (possibly) noncausal processor.

The paper is organized as follows. In Sec. I, the optimum GSC is derived. The performance of this GSC, relative to the conventional summing beamformer, is analyzed in Sec. II. In Sec. III, a series of numerical studies is presented to illustrate the GSC's superior performance.

I. THE OPTIMUM GENERALIZED SIDELOBE CANCELLER

The general structure of a broadband GSC is shown in Fig. 1. It consists of an array of L sensors, located at $\mathbf{r}_l$, $l=1,...,L$. The function of the presteering delays T_l, $l=1,...,L$, is to time align the target signal $s(t)$ arriving from direction θ. The output of the lth delay element can thus be written as

$$z_l(t)=s(t)+n_l(t-T_l)+i_l(t-T_l), \tag{1}$$

where $n_l(t)$ denotes the spatially uncorrelated noise sensed by the lth the sensor, and $i_l(t)$ denotes the spatially correlated, or isotropic, noise sensed by this sensor.

The spatial and frequency responses of the main beam, or reference, signal $r(t)$ are shaped by the gains g_l, $l=1,...,L$, and the filter $h_0(t)$, respectively. The spatial and frequency responses of the auxiliary beams are determined by the filters $h_n(t)$, $n=1,...,N$. The function of the $L\times N$ blocking matrix $\mathbf{B}$, $L>N$, is to prevent $s(t)$ from reaching the combined output $y(t)$ of the auxiliary beams.

The optimum GSC is found as follows. Define first the following signal vectors:

$$\mathbf{z}(t)=[z_1(t) \quad \cdots \quad z_L(t)]^T, \tag{2}$$

$$\mathbf{g}=[g_1 \quad \cdots \quad g_L]^T, \tag{3}$$

$$\mathbf{n}(t)=[n_1(t-T_1) \quad \cdots \quad n_L(t-T_L)]^T, \tag{4}$$

$$\mathbf{i}(t)=[i_1(t-T_1) \quad \cdots \quad i_L(t-T_L)]^T, \tag{5}$$

$$\mathbf{x}(t)=[x_1(t) \quad \cdots \quad x_N(t)]^T, \tag{6}$$

and

$$\mathbf{h}(t)=[h_1(t) \quad \cdots \quad h_N(t)]^T, \tag{7}$$

where the superscript T signifies transpose.

Next, it is assumed that $s(t)$, $n_l(t)$, and $i_l(t)$ are stationary and mutually uncorrelated. Let $S_s(f)$ denote the spectral density of $s(t)$, and $\mathbf{R_n}(\tau)$ and $\mathbf{R_i}(\tau)$ denote the covariance matrices of $\mathbf{n}(t)$ and $\mathbf{i}(t)$, respectively, i.e.,

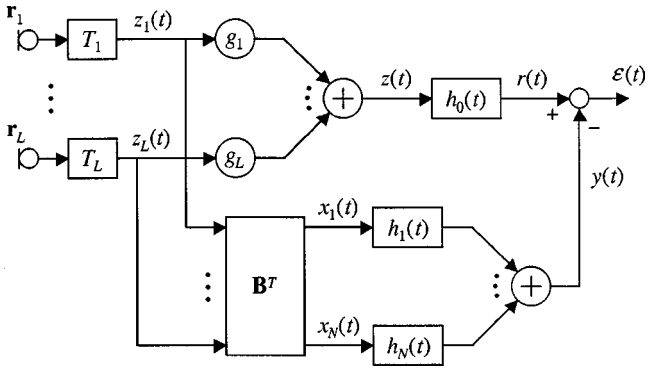

FIG. 1. Structure of a generalized sidelobe canceller.

$$\mathbf{R}_{\mathbf{n}}(\tau)=E[\mathbf{n}(t)\mathbf{n}^T(t+\tau)] \tag{8}$$

and

$$\mathbf{R}_{\mathbf{i}}(\tau)=E[\mathbf{i}(t)\mathbf{i}^T(t+\tau)]. \tag{9}$$

The optimum generalized sidelobe canceller is given by the solution to the following optimization problem

$$\min_{\mathbf{h}(t)} E[\varepsilon^2(t)]. \tag{10}$$

According to Wiener filter theory, the above problem can be solved by invoking the orthogonality condition[10]

$$E[\mathbf{x}(t)\varepsilon(t+\tau)]=\mathbf{0}, \quad \forall\tau. \tag{11}$$

In the frequency domain, Eq. (11) is equivalent to

$$\mathbf{s}_{\mathbf{x}r}(f)=\mathbf{s}_{\mathbf{x}y}(f), \tag{12}$$

where

$$\mathbf{s}_{\mathbf{x}r}(f)=[S_{x_1r}(f) \quad \cdots \quad S_{x_Nr}(f)]^T \tag{13}$$

and

$$\mathbf{s}_{\mathbf{x}y}(f)=[S_{x_1y}(f) \quad \cdots \quad S_{x_Ny}(f)]^T. \tag{14}$$

The cross-spectral term $\mathbf{s}_{\mathbf{x}r}(f)$ can be found as follows. First, note that $s(t)$ is blocked by $\mathbf{B}$. Thus

$$\mathbf{x}(t)=\mathbf{B}^T[\mathbf{n}(t)+\mathbf{i}(t)]. \tag{15}$$

Accordingly,

$$\mathbf{r}_{\mathbf{x}\mathbf{z}}(\tau)=E[\mathbf{x}(t)\mathbf{z}(t+\tau)]=\mathbf{B}^T[\mathbf{R}_{\mathbf{n}}(\tau)+\mathbf{R}_{\mathbf{i}}(\tau)]\mathbf{g}, \tag{16}$$

whereupon

$$\mathbf{s}_{\mathbf{x}r}(f)=H_0(f)\cdot\mathbf{s}_{\mathbf{x}\mathbf{z}}(f)=H_0(f)\cdot\mathbf{B}^T[\mathbf{S}_{\mathbf{n}}(f)+\mathbf{S}_i(f)]\mathbf{g}, \tag{17}$$

where $H_0(f)$, $\mathbf{S}_{\mathbf{n}}(f)$, and $\mathbf{S}_{\mathbf{i}}(f)$ are the Fourier transforms of $h_0(t)$, $\mathbf{R}_{\mathbf{n}}(\tau)$, and $\mathbf{R}_{\mathbf{i}}(\tau)$, respectively.

Similarly, the cross-spectral terms $\mathbf{s}_{\mathbf{x}y}(f)$ can be found. First, observe that

$$[\mathbf{r}_{\mathbf{x}y}(\tau)]_n=E\left[x_n(t)\cdot\sum_{i=1}^{N} h_i(t+\tau)*x_i(t+\tau)\right]. \tag{18}$$

Therefore,

$$[\mathbf{s}_{\mathbf{x}y}(f)]_n=\sum_{i=1}^{N} H_i(f)S_{x_nx_i}(f) \tag{19}$$

and hence

$$\mathbf{s}_{\mathbf{x}y}(f)=\mathbf{S}_{\mathbf{x}}(f)\cdot\tilde{\mathbf{h}}(f)=\mathbf{B}^T[\mathbf{S}_{\mathbf{n}}(f)+\mathbf{S}_{\mathbf{i}}(f)]\mathbf{B}\cdot\tilde{\mathbf{h}}(f), \tag{20}$$

where

$$\tilde{\mathbf{h}}(f)=[H_1(f) \quad \cdots \quad H_N(f)]^T. \tag{21}$$

Finally, substituting Eqs. (17) and (20) into Eq. (12) yields the optimum filters

$$\tilde{\mathbf{h}}(f)=H_0(f)\cdot\{\mathbf{B}^T[\mathbf{S}_{\mathbf{n}}(f)+\mathbf{S}_{\mathbf{i}}(f)]\mathbf{B}\}^{-1}\cdot\mathbf{B}^T[\mathbf{S}_{\mathbf{n}}(f)+\mathbf{S}_{\mathbf{i}}(f)]\mathbf{g}. \tag{22}$$

The spectral density of the output signal from the optimum GSC is given by

$$\begin{aligned}S_{\varepsilon}(f)&=S_r(f)-S_y(f)\\&=|H_0(f)|^2\{S_s(f)+\mathbf{g}^T[\mathbf{S}_{\mathbf{n}}(f)+\mathbf{S}_{\mathbf{i}}(f)]\mathbf{g}\}\\&\quad-|H_0(f)|^2\mathbf{g}^T[\mathbf{S}_{\mathbf{n}}(f)+\mathbf{S}_{\mathbf{i}}(f)]\mathbf{B}\cdot\{\mathbf{B}^T[\mathbf{S}_{\mathbf{n}}(f)\\&\quad+\mathbf{S}_{\mathbf{i}}(f)]\mathbf{B}\}^{-1}\cdot\mathbf{B}^T[\mathbf{S}_{\mathbf{n}}(f)+\mathbf{S}_{\mathbf{i}}(f)]\mathbf{g}.\end{aligned} \tag{23}$$

Note $\mathbf{S}_{\mathbf{n}}(f)$ and $\mathbf{S}_{\mathbf{i}}(f)$ are, by definition, Hermitian. This fact was made use of in deriving Eq. (23).

II. PERFORMANCE ANALYSIS

A. Signal model

Suppose that element self-noise is uncorrelated from sensor to sensor. Suppose further that the spectral density of $n_l(t)$ is independent of l and is given by $S_n(f)$. It then follows that

$$\mathbf{S}_{\mathbf{n}}(f)=S_n(f)\cdot\mathbf{I}. \tag{24}$$

Suppose next that isotropic noise has spectral density $S_i(f)$ and that its cross-spectral density matrix can be decomposed as follows:

$$\mathbf{S}_{\mathbf{i}}(f)=S_i(f)\cdot\mathbf{E}^H\mathbf{Q}(f)\mathbf{E}, \tag{25}$$

where the superscript H signifies conjugate transpose, $\mathbf{Q}(f)$ is a normalized matrix that describes the spatial correlation of isotropic noise, as seen by the sensors, and

$$\mathbf{E}=\mathrm{diag}(e^{-j2\pi/T_1},\ldots,e^{-j2\pi/T_L}). \tag{26}$$

Models of $\mathbf{Q}(f)$ for various isotropic noise fields can be found Refs. 6 and 7. In the case of a spherical isotropic noise field, $\mathbf{Q}(f)$ is given by

$$[\mathbf{Q}(f)]_{ij}=\mathrm{sinc}\left(\frac{2\pi f}{c}\|\mathbf{r}_i-\mathbf{r}_j\|\right), \tag{27}$$

where c is the speed of signal propagation in the acoustic medium.

The blocking matrix $\mathbf{B}$ can take a number of forms.[3] The following $L\times(L-1)$ matrix can be implemented easily in hardware:

$$\mathbf{B}^T=\begin{bmatrix}1 & -1 & 0 & \cdots & 0\\0 & 1 & -1 & \cdots & 0\\\vdots & & & & \vdots\\0 & \cdots & 0 & 1 & -1\end{bmatrix}. \tag{28}$$

In the sequel, it is assumed that

$$\mathbf{g}=\frac{1}{L}\mathbf{1}, \tag{29}$$

i.e., the main beam is not shaded. Note Eqs. (28) and (29) yield the following useful identity

$$\mathbf{B}^T\mathbf{g}=\mathbf{0}. \tag{30}$$

B. Performance index

The aim of this paper is to quantify the gain in noise suppression the GSC has over a summing beamformer with the same number of elements. This gain can be characterized by comparing the spectral density of the residual noise in the main beam, i.e., the summing beamformer, against the same in the output of the GSC. That is,

$$\rho(f)=\frac{S_r(f)-|H_0(f)|^2S_s(f)}{S_\varepsilon(f)-|H_0(f)|^2S_s(f)}. \tag{31}$$

Substituting Eqs. (23)–(25) and (30) into Eq. (31) and defining the scalar $\eta(f)$ and the Hermitian matrix $\mathbf{Q}'(f)$ as follows,

$$\eta(f)=\frac{S_n(f)}{S_i(f)} \tag{32}$$

and

$$\mathbf{Q}'(f)=\mathbf{E}^H\mathbf{Q}(f)\mathbf{E}, \tag{33}$$

it follows that

$$\rho(f)=\frac{1}{1-\alpha(f)}, \tag{34}$$

$$\alpha(f)=\frac{\mathbf{g}^T\mathbf{Q}'\mathbf{B}\{\mathbf{B}^T[\eta\mathbf{I}+\mathbf{Q}']\mathbf{B}\}^{-1}\mathbf{B}^T\mathbf{Q}'\mathbf{g}}{\mathbf{g}^T(\eta\mathbf{I}+\mathbf{Q}']\mathbf{g}}, \tag{35}$$

where, for convenience, the frequency argument in $\eta(f)$ and $\mathbf{Q}'(f)$ has been dropped.

C. High-frequency performance

Suppose frequency is high such that the wavelength is shorter than twice the smallest interelement spacing. The sinc functions in $\mathbf{Q}(f)$ are then small and $\mathbf{Q}'(f)$ can be approximated by

$$\mathbf{Q}'(f)\cong\mathbf{I}+\mathbf{\Delta}(f), \tag{36}$$

where the matrix $\mathbf{\Delta}(f)$ is small in the sense that the magnitudes of all its elements are much smaller than one. Substituting Eq. (36) into Eq. (35) gives

$$\alpha(f)\cong\frac{\mathbf{g}^T\mathbf{\Delta}\mathbf{B}\{\mathbf{B}^T\mathbf{B}\}^{-1}\mathbf{B}^T\mathbf{\Delta}\mathbf{g}}{(1+\eta)^2/L}. \tag{37}$$

Now, noting that $\mathbf{B}\{\mathbf{B}^T\mathbf{B}\}^{-1}\mathbf{B}^T$ is a projection matrix, it can be readily verified using Rayleigh's principle that $\alpha(f)$ is bounded above by $\lambda_{\max}(\mathbf{\Delta}^2)/(1+\eta)^2$. Therefore, at very high frequencies, $\rho(f)\to 1$ since $\mathbf{\Delta}(f)\to\mathbf{0}$, and the GSC loses its superior noise suppression characteristics.

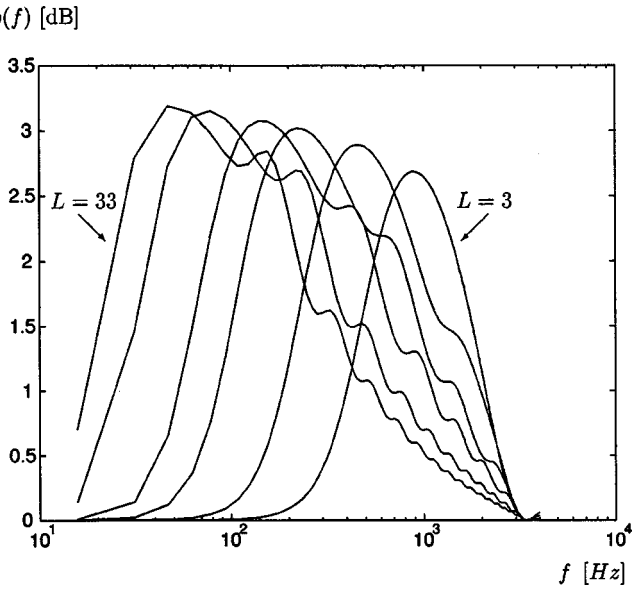

FIG. 2. Gain function of a uniform linear array with −30 dB element noise, 0-db isotropic noise, and $L=3$, 5, 9, 13, 23, and 33.

D. Low-frequency performance

At low frequencies, the sinc functions in $\mathbf{Q}'(f)$ approach unity and so $\mathbf{Q}'(f)$ can be approximated by

$$\mathbf{Q}'(f)\cong\mathbf{1}\mathbf{1}^T+\mathbf{\Xi}(f), \tag{38}$$

where the matrix $\mathbf{\Xi}(f)$ is small in the sense that the magnitudes of all its elements are much smaller than one. Suppose $\eta(f)>\lambda_{\max}(\mathbf{\Xi})$. Then, substituting Eq. (38) into Eq. (35), noting that $\mathbf{1}\mathbf{1}^T=L^2\mathbf{g}\mathbf{g}^T$, and invoking Eq. (30) yields

$$\alpha(f)\cong\frac{\mathbf{g}^T\mathbf{\Xi}\mathbf{B}\{\mathbf{B}^T\mathbf{B}\}^{-1}\mathbf{B}^T\mathbf{\Xi}\mathbf{g}}{\eta(\eta/L+1)}. \tag{39}$$

At very low frequencies, $\rho(f)\to 1$ since $\mathbf{\Xi}(f)\to\mathbf{0}$. Therefore, the performance of the GSC degrades again to that of the summing beamformer.

III. NUMERICAL EXAMPLE AND DISCUSSION

In the following numerical study, the array was selected to be a uniform linear array with an interelement spacing of 0.05 m. The array was presteered towards broadside so that $T_l=0$, $l=1,...,L$, and $\mathbf{Q}'(f)=\mathbf{Q}(f)$. The element self-noise and the isotropic noise were assumed to be flat from 0 to 3800 Hz with a noise level, relative to $s(t)$, of −30 and 0 dB, respectively. The velocity of sound is 340 m/s. Figure 2 plots $\rho(f)$ against f for various numbers of array elements.

As can be seen, the frequency at which $\rho(f)$ peaks decreases with increasing number of elements. This follows since, with a larger array aperture, the optimum GSC is able to suppress lower-frequency (longer wavelength) noise more effectively.

In contrast, the maximum of $\rho(f)$ is only weakly dependent on the number of elements. This follows since the additional terms that are appended to the $L\times L$ matrix $\mathbf{Q}(f)$ as L is increased are small.

Finally, it is observed that the total noise gain of the conventional summing beamformer, relative to the total

noise gain of the GSC, increases with increasing L. The relative total noise gain is given by the integral of $\rho(f)$ over frequency. This result is expected since, with more elements, the GSC should be able to find, by virtue of its optimality, a more effective way to suppress noise.

[1] J. E. Hudson, *Adaptive Array Principles* (Peregrinus, London, UK, 1981).
[2] B. D. Van Veen and K. M. Buckley, ''Beamforming: A Versatile Approach to Spatial Filtering,'' IEEE Acoust., Speech, Sig. Process. Mag. **5**, 4–24 (1988).
[3] L. J. Griffiths, and C. W. Jim, ''An Alternative Approach to Linearly Constrained Adaptive Beamforming,'' IEEE Trans. Antennas Propag. **30**, 27–34 (1982).
[4] S. Nordholm, I. Claesson, and P. Eriksson, ''The Broadband Wiener Solution for Griffiths-Jim Beamformers,'' IEEE Trans. Signal Process. **40**, 474–478 (1992).
[5] N. Dal Degan and C. Prati, ''Acoustic Noise Analysis and Speech Enhancement Techniques for Mobile Radio Applications,'' Signal Process. **15**, 43–56 (1988).
[6] B. F. Cron, B. C. Hassell, and F. J. Keltonic, ''Comparison of theoretical and experimental values of spatial correlation,'' J. Acoust. Soc. Am. **37**, 523–529 (1965).
[7] H. Cox, ''Spatial Correlation in arbitrary noise fields with application to ambient sea noise,'' J. Acoust. Soc. Am. **54**, 1289–1301 (1973).
[8] P. M. Schultheiss, ''Some Lessons from Array Processing Theory,'' in *Aspects of Signal Processing-Part 1*, edited by G. Tacconi (Reidel, Dordrecht, 1977), pp. 309–331.
[9] M. H. Er and A. Cantoni, ''Transformation of Linearly Constrained Broadband Processors to Unconstrained Partitioned Form,'' IEE Proc. Part H (Microwaves, Antennas and Propagation) **133**, 209–212 (1986).
[10] A. Papoulis, *Probability, Random Variables, and Stochastic Processes*, 3rd ed. (McGraw-Hill, New York, 1991).

Echo suppression in the horizontal and median sagittal planes

Brad Rakerd
Department of Audiology and Speech Sciences, Michigan State University, East Lansing, Michigan 48824

William M. Hartmann
Department of Physics, Michigan State University, East Lansing, Michigan 48824

Joy Hsu[a)]
Polytechnic School, Pasadena, California 91106

(Received 25 January 1999; revised 13 September 1999; accepted 30 October 1999)

Experiments were performed to measure two kinds of suppression threshold for running speech: echo threshold, defined here as the minimum level at which it was possible to detect that an echo was present, and masked threshold, defined as the minimum level at which it was possible to detect that a lagging sound was present at all. Both thresholds were measured using a geometry in which sound sources and reflections were distributed over the horizontal plane (left, front, and right locations) and a geometry in which they were distributed over the median sagittal plane (front, overhead, and rear locations). The predominant sound localization cues are different for these two geometries, and the experiments measured the consequences of this difference for suppression. Echo thresholds were found to have a comparable dependence on the delay of the lagging sound for the horizontal and median sagittal planes. Masked thresholds, which were systematically 8–15 dB lower than echo thresholds, also showed a comparable dependence on delay for the two planes. Overall, these results support the idea that echo suppression is functionally similar whether locations are cued by interaural differences in time and intensity, or by spectral features introduced by the head-related transfer function. [S0001-4966(00)02202-5]

PACS numbers: 43.66.Ba, 43.66.Qp [DWG]

INTRODUCTION

In a room, a sound comes to a listener many times over. It arrives first direct from its source, and thereafter from all around as the sound reflects and re-reflects from room surfaces. The reflected copies are a potential distraction for the listener, but they rarely distract to any great extent because a remarkable neural process suppresses their perception as echoes (Blauert, 1983). The present paper is motivated by a recent finding regarding the neurophysiology of echo suppression (Litovsky and Yin, 1994; Yin and Litovsky, 1994; Litovsky *et al.*, 1997). Recordings made in the inferior colliculus of cat point to an equivalence of suppression for sound sources and reflections spatially separated from one another in the horizontal plane (HP) and sources and reflections separated in the median sagittal plane (MSP). This comparison is interesting because the predominant directional cues are different for the two planes. In the HP, interaural difference cues are paramount (Mills, 1958; Durlach and Colburn, 1978). In the MSP, the most important cues are spectral shape cues introduced by the ears, head, and upper torso, which act as acoustical filters with different frequency responses for different angles of sound incidence (Shaw and Teranishi, 1968; Hebrank and Wright, 1974; Searle *et al.*, 1976; Middlebrooks and Green, 1991). Evidence of equivalence for the HP and the MSP argues for a suppression mechanism that is realized in the nervous system at a level where the locations of sources and reflections are represented abstractly, indifferent to the particulars of their spatial cuing.

The present study made a psychophysical comparison of echo suppression in the HP and the MSP, in complement to the neurophysiological comparison. It focused on human listeners' echo suppression for speech, which lasts for tens of milliseconds (Haas, 1951; Lochner and Burger, 1958), a time constant of the same order as that of the suppression that has been measured neurophysiologically. There were two experiments.

I. EXPERIMENT 1—ECHO THRESHOLD

Experiment 1 measured listeners' *echo threshold* for connected speech, defined here as the level at which a delayed copy of the speech was just barely audible as an image distinct from the direct sound. Measurements were made in the HP and the MSP, at delay times of 20, 40, 60, and 80 ms. The speech samples were newspaper articles, read aloud in an anechoic room by a female talker and by a male talker. Forty-five minutes of their speech were recorded onto digital audio tape and played back as needed for the experiment.

Five subjects participated in the study, S1, S2, and S3 were young adult listeners (two females, one male; ages 17 to 20 years) with normal hearing thresholds and no prior experience in psychophysical listening studies. S4 and S5 were older listeners (both males, ages 45 and 59), with some high-frequency hearing loss. S4 and S5 were experienced listeners. Subjects S1, S4, and S5 were authors.

The subjects were tested individually, in a 3.0 m (wide) $\times$4.3 m (long)$\times$2.4 m (high) anechoic room (IAC #107840). During testing, a subject sat still, facing straight ahead. A metal guidebar rested atop the subject's head and helped the subject maintain a fixed head position. For the HP condition, three loudspeakers were placed at the height of the subject's

[a)]Present address: Stanford University, Stanford, CA 94305.

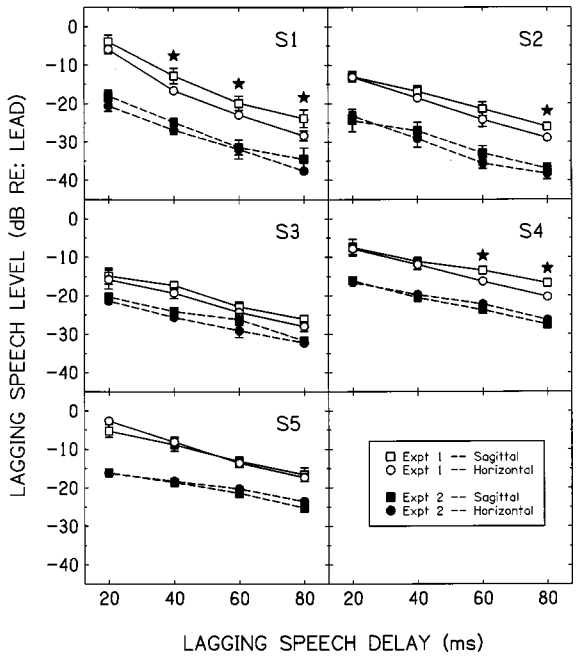

FIG. 1. Open symbols connected by solid lines show echo thresholds for running speech measured in experiment 1. Filled symbols connected by dashed lines show masked thresholds measured in experiment 2. Results are given separately for each subject (different figure panels). Thresholds (in dB *re*: the level of the lead) are plotted as a function of the delay time between leading and lagging copies of the speech. Plots with circles are for sources in the horizontal plane; plots with squares are for sources in the median sagittal plane. Error bars show ±1 standard deviation over test runs. Stars highlight instances in which error bars for the two planes do not overlap.

ears, and 120 cm away. One speaker was directly in front of the subject; the others were 90 deg off to the left and right. For the MSP condition, loudspeakers were placed directly in front, directly above, and directly behind the subject's head.

Test runs were done separately for the HP and the MSP. On each test trial, we directed a leading copy of the speech to one loudspeaker in the plane under test, and a lagging copy to the same speaker or to a different speaker in that plane. The subject was given control over the level of the lagging copy. At the highest level, which was 10 dB above that of the lead, the lagging copy was audible as an echo, distinct from the direct sound. The subject was instructed to reduce the level down to the point where the echo was as faint as possible while still remaining audible. Across trials, the leading and lagging loudspeakers were randomly varied, as was the delay time of the lag. One complete test run included all possible combinations of these variables (3 lead locations × 3 lag locations × 4 delay times = 36 trials). Subjects typically took about 20 min to complete a run. They did a total of four runs in the HP condition and four in the MSP condition. The order of these runs was random and different for each subject.

The results of experiment 1 are given by the open-symbol plots in Fig. 1. Echo thresholds (measured in dB *re*: the level of the leading sound) are plotted separately for each subject (different figure panels) and for the HP (open circles) and the MSP (open squares). Each plot gives a subject's mean threshold as a function of the lagging speech delay time. Error bars (in some cases smaller than the plotting symbols) indicate ± one standard deviation over the four runs that a subject did in each plane. All five subjects performed similarly in the HP and the MSP. For both planes, there was substantial suppression at the 20-ms delay time and progressively decreasing suppression with increasing delay times. There was a marked linear trend to the results. Best-fit lines (which accounted for over 90% of the variance in both planes) had nearly equal mean slopes for the HP (−0.25 dB/ms) and the MSP (−0.23 dB/ms).

For two subjects (S3 and S5), echo threshold levels for the HP and the MSP were close together at every value of the delay, never differing by more than the standard deviation over runs shown by the error bars. For the other three subjects (S1, S2, and S4), HP and MSP thresholds did diverge by amounts greater than the standard deviation at one or more values of the delay. Stars in Fig. 1 highlight the instances where this was the case (six in all). In every starred case, the HP echo threshold was lower than the corresponding MSP threshold. This effect was even present in the results for the one location that was common to both planes (center in the HP, front in the MSP).[1] Given that fact, and the fact that test runs were done separately for the HP and the MSP, we conclude that the plane difference reflects a context-sensitive shift in the subjects' criteria for decision making about echo thresholds. Just why this shift consistently favored slightly lower thresholds for the HP is unclear.

II. EXPERIMENT 2—MASKED THRESHOLD

Even after the level of a lagging sound is reduced to the point where an echo is no longer perceptible, audible loudness and coloration effects remain. Experiment 2 determined how much additional attenuation would be required to eliminate all audible effects of the lagging sound. The design of this *masked threshold* experiment was the same as for experiment 1, but the instructions to the subjects were different. Subjects were instructed to reduce the level of the lagging speech until they could barely detect that it was present at all. To aid in finding this point, subjects were given a push-button to press to remove the lagging sound altogether. On each test trial, they switched the lagging sound in and out and adjusted its level for as long as needed to find the masked threshold point. The subjects of this experiment were the same as for experiment 1. They completed all testing for that experiment before undertaking this one.

The results of experiment 2 are given by the filled-symbol plots in Fig. 1. Masked thresholds for all five subjects were 8 to 15 dB below the corresponding echo thresholds, with similar functions for the HP and the MSP. Best fit lines for the masked threshold data had identical mean slopes of −0.20 dB/ms for the HP and the MSP. Masked thresholds for the HP and the MSP were never further apart than the error bars for any subject at any delay time.

III. DATA ANALYSIS

A. Correlations

Figure 1 provides visible evidence that the subjects performed similarly in both experiments and in both planes. A correlation analysis was done to get a measure of the

TABLE I. Correlations among echo thresholds measured in experiment 1 and masked thresholds measured in experiment 2 for the horizontal plane (HP) and the median sagittal plane (MSP).

	Echo threshold		Masked threshold	
	HP	MSP	HP	MSP
Echo Threshold				
HP	···			
MSP	0.98	···		
Masked Threshold				
HP	0.93	0.89	···	
MSP	0.95	0.93	0.98	···

strengths of those relationships. Correlations were computed over the 20 values for each experiment/plane representing thresholds for each of the five subjects measured at each of the four delay times. Table I shows the correlation matrix. All of the correlations were high (0.89 or above), indicating a parallel dependence on lagging speech delay time throughout. Two correlations speak directly to the HP–MSP comparison that is at the heart of the present study. The correlation between HP and MSP echo thresholds measured in experiment 1 was 0.98. The correlation between HP and MSP masked thresholds measured in experiment 2 was 0.98 as well.

B. Individual source locations

Over the course of an experimental run, stimuli were presented from nine different combinations of leading and lagging loudspeakers. Statistical comparisons showed that there were significant differences among the nine for echo threshold results in the HP [$F(8,32)=2.27$; $p<0.05$] and for both echo and masked threshold results in the MSP [echo: $F(8,32)=7.30$; $p<0.001$; masked: $F(8,32)=8.59$; $p<0.001$]. There was no significant difference among the loudspeaker combinations for the masked threshold results in the HP ($p>0.05$). All of the loudspeaker-combination effects were statistically independent of the delay-time factor that was of chief interest in this study (no significant interaction with delay in any analysis; $p>0.05$).

Figure 2(A) plots the echo threshold results for the HP as a function of the different lead-lag loudspeaker combinations. The plot shows that thresholds for loudspeaker combinations that were in the same location (e.g., lead left, lag left) were comparable to thresholds for combinations that were in different locations (e.g., lead left, lag right). We found this result throughout. There was no statistical difference between same-location and different-location combinations in any analysis ($p>0.05$). Yang and Grantham (1997) also found no consistent effect of loudspeaker separation (including no separation) on echo thresholds measured in the HP with click stimuli.

Figure 2(A) shows that echo thresholds were uniformly lower when the lead speaker was at the center than when it was at the left or right. (Thresholds for the center-left, center-center, and center-right combinations were the three lowest in the set). Seraphim (1961) also noted a disparity in echo suppression for speech between center and side locations in

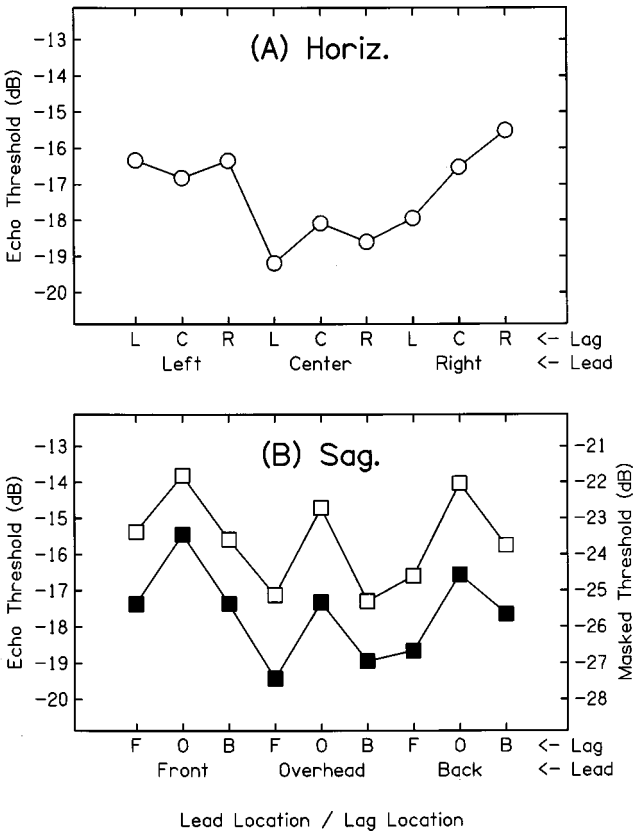

FIG. 2. Threshold results (in dB *re*: the level of the lead) averaged over all five subjects and four lagging delay times, and plotted a function of the different loudspeaker combinations used to present leading and lagging copies of the speech. (A): Echo thresholds (open circles) for loudspeakers arrayed in the horizontal plane (left, center, right locations). (Masked threshold, not plotted, showed no significant differences in this plane; see text.) (B): Echo (open squares) and masked (filled squares) thresholds for loudspeakers in the median sagittal plane (front, overhead, back locations).

the horizontal plane. In that instance, a lagging speech sound at the center was found to be suppressed more easily than a sound off to the side. Here the center location proved less effective than the side locations as an echo suppressor.

Figure 2(B) gives lead-lag plots of echo and masked thresholds for the MSP. Both plots show a generalized weakness for the overhead location, relative to front and back. When leading, overhead weakly suppressed reflections coming from the other two locations (over-front and over-back had the lowest thresholds in the set of nine). When lagging, overhead was itself readily suppressed by leads from front and back (front-over and back-over had the highest thresholds). A substantial majority of the variation in both the echo and masked thresholds could be attributed to this result, which amounted to an effective 2-dB reduction in the strength of the overhead source in the MSP. Results for the front location and the back location were comparable overall for both echo thresholds and masked thresholds.

IV. SUMMARY AND CONCLUSIONS

When listening to speech in a room, a listener is rarely aware of acoustical reflections or reverberation. This is because the listener's brain suppresses the perception of speech echoes for tens of milliseconds after the arrival of a direct

sound (Haas, 1951; Lochner and Burger, 1958). In two experiments, we measured thresholds associated with this effect for sound sources and reflections distributed in the horizontal plane and in the median sagittal plane.

Experiment 1 measured a listener's echo threshold—the level at which an echo was barely audible—as a function of the delay time between leading and lagging copies of running speech. Results were overall similar for the horizontal and median sagittal planes, particularly with respect to their delay-time dependence. One difference between the planes was that measured echo thresholds were slightly lower for the horizontal plane than for the median sagittal plane in several instances. We tentatively attributed that result to response bias. Experiment 2 measured a listener's masked threshold—the level at which any effect of lagging speech was barely audible—again, as a function of delay time. The results were comparable for the HP and the MSP in every important respect. Finally, a correlation analysis showed a high level of similarity between the HP and MSP results for both the echo ($r=0.98$) and masked ($r=0.98$) threshold experiments.

The present psychophysical findings of equivalence in echo suppression for the HP and the MSP can be interpreted two ways. It is possible that the suppression occurs at a neural processing site that is indifferent to source location. Alternatively, the findings may be seen as consistent with recent neurophysiological evidence (Litovsky and Yin, 1994; Yin and Litovsky, 1994; Litovsky *et al.*, 1997) for an echo suppression mechanism mediated by higher auditory centers where binaural and spectral cues to location are combined.

ACKNOWLEDGMENTS

This work was supported by National Institutes of Health (NIDCD) Grant No. DC00181. The National Science Foundation provided support for Joy Hsu, through the Michigan State University High School Honors Science Program (Grant No. ESI-94-52753). We thank David Perrott for many useful comments on a previous version of this article.

[1]One-ninth of all the trials for the two planes were identical, with leading and lagging speech sounds coming from directly ahead of the listener in both cases (center location in the HP, front location in the MSP). An analysis of these trials showed the same disparity between the two planes that was shown for the larger set of stimuli (consistently lower echo thresholds for the HP).

Blauert, J. (**1983**). *Spatial Hearing: The Psychophysics of Human Sound Localization* (MIT Press, Cambridge, MA).

Durlach, N. I., and Colburn, H.S. (**1978**). ''Binaural phenomena,'' in *Handbook of Perception*, Vol. 4, edited by E. C. Carterette and M. P. Friedman (Academic, New York), pp. 365–466.

Haas, H. (**1951**), ''Über den Einfluss eines Einfachechos auf die Hörsamkeit von Sprache [On the influence of a single echo on the intelligibility of speech],'' Acustica **1**, 49–58.

Hebrank, J., and Wright, D. (**1974**). ''Spectral cues used in the localization of sound sources on the median plane,'' J. Acoust. Soc. Am. **56**, 1829–1834.

Litovsky, R. Y., and Yin, T. C. T. (**1994**). ''Physiological correlates of the precedence effect: free-field recordings in the inferior colliculus of the cat,'' Assoc. Res. Otolaryngol. **85**, 337 (Abstract).

Litovsky, R. Y., Rakerd, B., Yin, T. C. T., and Hartman, W. M. (**1997**). ''Psychophysical and physiological evidence for a precedence effect in the median sagittal plane,'' J. Neurophysiol. **77**, 2223–2226.

Lochner, J. P. A., and Burger, J. F. (**1958**). ''The subjective masking of short time delayed echoes, their primary sounds, and their contributions to the intelligibility of speech,'' Acustica **8**, 1–10.

Middlebrooks, J. C., and Green, D. M. (**1991**). ''Sound localization by human listeners,'' Annu. Rev. Psychol. **42**, 135–159.

Mills, A. W. (**1958**). ''On the minimum audible angle,'' J. Acoust. Soc. Am. **30**, 237–346.

Searle, C. L., Braida, L. D., Cuddy, D. R., Davis, M. F., and Colburn, H. S. (**1976**). ''Model for auditory localization,'' J. Acoust. Soc. Am. **60**, 1164–1175.

Seraphim, H. P. (**1961**). ''Über die Wahrnehmbarkeit mehrerer Rückwürfe von Sprachshall [On the perception of multiple reflections of speech sounds],'' Acustica **11**, 80–91.

Shaw, E. A. G., and Teranishi, R. (**1968**). ''Sound pressure generated in an external ear replica and real human ears by a nearby point source,'' J. Acoust. Soc. Am. **78**, 524–533.

Yang, X., and Grantham, W. (**1977**). ''Echo suppression and discrimination aspects of the precedence effect,'' Percept. Psychophys. **59**, 1108–1117.

Yin, T. C. T., and Litovsky, R. (**1994**). ''Physiological studies of the precedence effect in the inferior colliculus of the cat,'' in *Advances in Hearing Research: Proceedings of the 10th International Symposium on Hearing*, edited by G. A. Manley, G. M. Klump, C. Koppl, and H. Oeckinghaus (World Scientific, Singapore).

A speech corpus for multitalker communications research

Robert S. Bolia, W. Todd Nelson, and Mark A. Ericson
Air Force Research Laboratory, Wright-Patterson Air Force Base, Ohio 45433

Brian D. Simpson
Department of Psychology, Wright State University, Dayton, Ohio 45435

(Received 1 October 1999; revised 18 October 1999; accepted 19 October 1999)

A database of speech samples from eight different talkers has been collected for use in multitalker communications research. Descriptions of the nature of the corpus, the data collection methodology, and the means for obtaining copies of the database are presented. © *2000 Acoustical Society of America.* [S0001-4966(00)00902-4]

PACS numbers: 43.66.Pn, 43.72.Kb [JMH]

INTRODUCTION

Several recent experiments at the Air Force Research Laboratory have investigated the utility of spatial audio displays for augmenting speech intelligibility in multitalker communications environments (Bolia *et al.*, 1999; Nelson *et al.*, 1998a; Nelson *et al.*, 1998b; Simpson *et al.*, 1999). Some of the goals of this research included: (1) an empirical determination of the maximal number of channels for which the benefits of spatialization may be realized in a spatial audio display designed to aid in the segregation of simultaneous, context-independent speech sources; (2) an evaluation of the efficacy of four different spatialization schemes for this task; and (3) the manner in which these factors interact with the sex of the target talker. In order to accomplish these goals, a large number of speech samples from talkers of both sexes were required. The purpose of this article is to describe the methods employed in collecting these speech samples, as well as the form of the resulting corpus, with the intent that other researchers in the field might benefit from their availability.

I. COORDINATE RESPONSE MEASURE (CRM)

The task selected for the sequence of investigations cited above was a version of the Coordinate Response Measure (CRM), a nonstandardized communication performance task adapted from similar tasks by Moore (1981) as a measure of speech intelligibility more relevant to military environments than standardized tests such as the Modified Rhyme Test. The phrases in the CRM consist of a call sign and a color–number combination, all embedded within a carrier phrase. Hence a typical sentence would be ''Ready baron, go the blue five now,'' where baron is the call sign, and blue five is the color–number combination. In the performance of the task, each listener is assigned a call sign, and responds by indicating the color–number combination spoken by the talker who uttered his or her call sign. If the listener does not hear his or her call sign spoken, he or she does not respond (or, equivalently, reports the absence of his or her target call sign). Possible dependent measures thus include the percentage of correct call sign detections and the percentage of correctly identified color–number combinations, as well as their associated reaction times.

The nature of the phrases in the CRM suggests its utility for measuring speech intelligibility in multichannel communications environments. McKinley *et al.* (1994) and Ericson and McKinley (1997) have employed it for such a purpose, and other researchers have devised and used similar tests (Koehnke *et al.*, 1998). Given a collection of multiple talkers speaking simultaneously, each speaking a different call sign and a different color–number combination, it is possible to interpret the percentage of correct call sign detections as a measure of the effectiveness of masking by competing speech signals, since, in order to make a correct detection, a listener must be able to distinguish his or her call sign from a collection of simultaneously spoken call signs. One can then interpret the percentage of correctly identified color–number combinations as a measure of a listener's ability to selectively attend to a single channel while ignoring irrelevant channels, since a listener must attend to a particular talker/location (i.e., the talker/location from which his or her call sign was spoken) in order to correctly identify the color–number combination emanating from that talker/location. In addition, it may also be desirable to perform a signal detection analysis using the detection portion of the task, from which can be gained measures of sensitivity (d') and response bias (β and/or c). The relatively context-free nature of the phrases ensures that changes in speech intelligibility are due to specific experimental manipulations rather than to contextual clues found in natural discourse.

Previous studies employing the CRM, such as those conducted by Ericson and his colleagues (Ericson and McKinley, 1997; McKinley and Ericson, 1997; McKinley *et al.*, 1994), have used live talkers as speech stimuli. Due to the large number of talkers required, as well as the need for precise control of stimulus onset, it was determined that digital recordings of talkers would be preferable to live talkers for the series of investigations cited above (Bolia *et al.*, 1999; Nelson *et al.*, 1998a, 1998b; Simpson *et al.*, 1999). It was for this reason that the speech corpus described herein was collected.

Factorial combinations of eight call signs (''arrow,'' ''baron,'' ''charlie,'' ''eagle,'' ''hopper,'' ''laker,'' ''ringo,'' ''tiger''), four colors (''blue,'' ''green,'' ''red,'' ''white''), and the numbers between one and eight yielded a total of 256 phrases, all of which were recorded by each of

the eight talkers, for a total of 2048 phrases. Four males and four females, between the ages of 18 and 26, participated as talkers. None of the talkers had any reported or readily detectable speech pathology.

II. METHODS OF COLLECTION

The recording of the phrases was conducted in a sound-attenuated room of dimensions 3.93×3.40×3.50 m, normally used for conducting audiometric examinations. The walls and ceiling of the room were lined with sound-absorbing foam to reduce reflections; the floor was covered with commercial carpet. During the recordings, the talker was seated in an immobile office-type chair in one corner of the room. A Bruel & Kjaer Type 4165 1/2-inch microphone connected to a Bruel & Kjaer 2639 preamplifier was placed in a microphone stand approximately 3 cm in front of the talker. The output of the microphone was amplified using a Bruel & Kjaer Type 5935 dual microphone supply, and the resulting waveform digitized at the sample rate of 40 kHz by means of a Tucker-Davis Technologies (TDT) DD1 combined analog-to-digital/digital-to-analog converter. The recorded phrase was then converted back to an analog signal using the same TDT DD1, amplified via a Crown D-75 amplifier, and presented to the experimenter over Sennheiser HD-560 headphones.

The process of recording the phrases was controlled by a computer program. The talker was presented with a visual display containing the phrase he/she was to speak. Recording began when the talker pressed a key on the computer keyboard, and continued for a period of 3 sec. If the recorded phrase appeared to be ''correct,'' the experimenter accepted it and proceeded to the next phrase; if it were incomplete or spoken at an inappropriate pace, the experimenter rejected it and recorded it anew. Speaking rate was regulated by having the talker listen to a ''standard'' phrase—previously recorded by one of the experimenters—immediately prior to each recording, and pace himself/herself according to the pace of the standard. The latter practice ensured that, across talkers, similar phrases were of similar duration.

Once the corpus had been recorded in its entirety, all incipient silence was removed from each waveform for the purpose of synchronized playback. This and all subsequently described manipulations were accomplished with Cool Edit, a commercially available software product for the analysis and processing of acoustic waveforms. Following the synchronization of phrase onsets, each of the speech signals was bandpass filtered, with a passband extending from 80 Hz to 8 kHz. All of the phrases in the set were then scaled to have the same root-mean squared average power. Additionally, a second set of files was created from the original recordings in which the initial word ''ready'' was removed, so that the phrases could be synchronized at the onset of the call sign instead of the carrier phrase. All other manipulations to these phrases were identical to those in the first set.

III. AVAILABILITY OF CORPUS

The speech corpus described herein is available free of charge to researchers who send a blank recordable compact disk with a self-addressed postage-paid return envelope to the first author at the following address: Robert S. Bolia Air Force Research Laboratory (AFRL/HECP) 2255 H. St. Wright-Patterson Air Force Base, OH 45433-7022.

ACKNOWLEDGMENTS

The authors would like to acknowledge Michael L. Ward, of Veridian, and Dennis L. Allen, of Sytronics, Inc., for their contributions to the collection and modification of the speech samples; Raymond Slyh, of the Air Force Research Laboratory, for his helpful insights; Sue Vadnais and Anitha Reddy, both of whom participated in the collection of the speech samples as part of a summer internship program sponsored by Alliance for Education; and James Hillenbrand and two anonymous reviewers, for their helpful comments on an earlier draft of this article. A portion of this research was supported by the Air Force Office of Scientific Research.

Bolia, R. S., Ericson, M. A., Nelson, W. T., McKinley, R. L., and Simpson, B. D. (**1999**). ''A cocktail party effect in the mediam plane?,'' J. Acoust. Soc. Am. **105**, 1390–1391.

Ericson, M. A., and McKinley, R. L. (**1997**). ''The intelligibility of multiple talkers separated spatiallly in noise,'' in *Binaural and Spatial Hearing in Real and Virtual Environments*, edited by R. H. Gilkey and T. R. Anderson (Lawrence Erlbaum Associates, Mahwah, NJ), pp. 701–724.

Koehnke, J., Besing, J., Abouchaera, K. S., and Tran, T. V. (**1998**). ''Speech recognition for known and unknown target message locations,'' *Abstracts of the Twenty-First Midwinter Meeting of the Association for Research in Otolaryngology* (ARO, Mt. Royal, NJ), p. 105.

McKinley, R. L., and Ericson, M. A. (**1997**). ''Flight demonstration of a 3-D auditory display,'' in *Binaural and Spatial Hearing in Real and Virtual Environments*, edited by R. H. Gilkey and T. R. Anderson (Lawrence Erlbaum Associates, Mahwah, NJ), pp. 683–699.

McKinley, R. L., Ericson, M. A., and D'Angelo, W. R. (**1994**), ''3-dimensional auditory displays: Development, applications, and performance,'' Aviat., Space Environ. Med. **65**, 31–38.

Moore, T. J. (**1981**). ''Voice communication jamming research,'' *AGARD Conference Proceedings 311: Aural Communication in Aviation* (AGARD, Neuilly-Sur-Seine, France), pp. 2:1–2:6.

Nelson, W. T., Bolia, R. S., Ericson, M. A., and McKinley, R. L. (**1998a**). ''Monitoring the simultaneous presentation of multiple spatialized speech signals in the free field,'' Proceedings of the 16th International Congress on Acoustics and the 135th Meeting of the Acoustical Society of America, 2341-2342.

Nelson, W. T., Bolia, R. S., Ericson, M. A., and McKinley, R. L. (**1998b**). ''Monitoring the simultaneous presentation of spatialized speech signals in a virtual environment,'' Proceedings of the 1998 IMAGE Conference, pp. 159–166.

Simpson, B. D., Bolia, R. S., Ericson, M. A., and McKinley, R. L. (**1999**) ''The effect of sentence onset asynchrony on call sign detection and message intelligibility in a simulated 'cocktail party','' J. Acoust. Soc. Am. **105**, 1024.

Directional hearing is only weakly dependent on the rise time of acoustic stimuli

Rüdiger Krahe[a)]
Institute of Biology, Department of Behavioral Physiology, Humboldt University, Invalidenstr. 43, D-10115 Berlin, Germany

Ole Næsbye Larsen
Centre for Sound Communication, Institute of Biology, Odense University, Campusvej 55, DK-5230 Odense M, Denmark

Bernhard Ronacher
Institute of Biology, Department of Behavioral Physiology, Humboldt University, Invalidenstr. 43, D-10115 Berlin, Germany

(Received 14 May 1999; revised 30 September 1999; accepted 25 October 1999)

First-spike latency differences between left and right auditory-nerve fibers have been proposed as one of the physiological cues for sound localization. Since first-spike latency depends not only on stimulus intensity, but also on the steepness of the amplitude rise of a sound stimulus, differences in first-spike latency are not a simple function of interaural level differences but also a function of stimulus rise time. We therefore investigated whether rise time influences human directional hearing in a localization paradigm. Subjects tended to localize a 3-kHz tone pulse with a long (18-ms) rise time further to the side than one with a short (2-ms) rise time delivered from the same source. The small size of this effect and its large inter-individual variability, however, suggest that it is of minor importance for human directional hearing. © *2000 Acoustical Society of America.*
[S0001-4966(00)01902-0]

PACS numbers: 43.66.Qp, 43.66.Pn, 43.66.Mk, 43.66.Ba [DWG]

INTRODUCTION

Sound direction may be inferred from monaural spectral cues and from a comparison of the inputs to the two ears. The physical cues available for this comparison are interaural differences in level (interaural level differences: ILDs) and in time (interaural time delays: ITDs). The difference in the timing of neuronal activity between left and right auditory pathway induced by the physical ITD may be enlarged by the ILD, due to the dependence of first-spike latency on stimulus intensity (Kitzes *et al.*, 1978; Heil and Irvine, 1997). These ILD-dependent differences in latency have been proposed to be the basis for ILD processing in the central nervous system (Yin *et al.*, 1985). Differences in the timing of first spikes may also be important for the precedence effect (or law of the first wavefront; Wallach *et al.*, 1949), i.e., the observation that in reverberant environments the first incoming wavefront of a sound stimulus is the most salient cue for directional hearing. However, there is strong physiological evidence that first-spike temporal differences do not only depend on ILD (and, of course, on ITD) but also on the rise time of the respective stimulus. The first-spike latency of auditory-nerve (AN) fibers is determined by the steepness of the envelope rise which in turn depends on rise time and peak level (in case of a linear rise function; Heil and Irvine, 1996, 1997). For shallow slopes (long rise time and/or low intensity) latency-intensity functions steeply decrease to approach the minimum latency of the respective cell asymptotically (Fig. 1). The shape of this curve has an important implication: For a given ILD and stimulus intensity, a long-rise-time stimulus will lead to a large latency difference (ΔT in Fig. 1) between the AN fibers of the two ears while latency differences will be small for short-rise-time stimuli. Therefore, if our central nervous system heavily relies on first-spike latency differences for assessing the angle of sound incidence, directional hearing may be influenced by the rise time of the respective stimulus. Due to larger latency differences, a long-rise-time stimulus could convey a more lateralized percept of the sound than a short-rise-time stimulus delivered from the same source.

To test this hypothesis we conducted a localization experiment under free-sound-field conditions. Subjects had to decide whether the second stimulus of a pair of sequentially presented stimuli was delivered from a more frontal or a more lateral position than the first stimulus. We predicted that subjects localize long-rise-time stimuli further to the side than short-rise-time stimuli, due to the larger latency differences induced by the long rise time.

I. METHODS

The free-field experiment was performed in the anechoic room at Odense University and was approved by the local ethics committee according to Danish guidelines. The three authors and nine inexperienced subjects from the Institute of Biology at Odense University volunteered for the experiments (six females, age range 24–41 years; six males, age range 24–49 years). All subjects were checked for normal hearing with a standard audiometer (Bosch type KS 5).

[a)]Present address: Department of Biology, University of California, Riverside, Riverside, CA 92521.

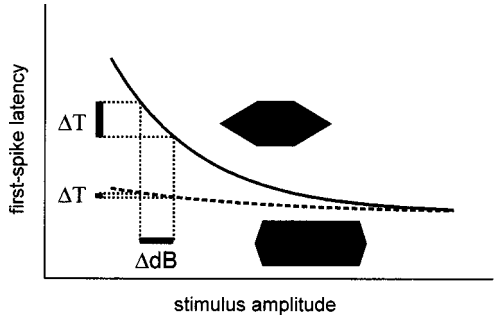

FIG. 1. Sketch depicting the relationship between first-spike latency of an auditory-nerve fiber and stimulus amplitude, for two different rise times (dashed line: short rise time; solid line: long rise time). The black hexagons represent the respective stimulus envelopes as a function of time. From the curve for a single fiber one may deduce the latency difference (ΔT) for a given ILD (ΔdB) between the responses of two fibers of similar characteristics, one in each auditory nerve.

The stimuli were 20-ms tone pulses with carrier frequencies of 0.75 kHz, 3 kHz, or 5 kHz, respectively. The tone pulses were linearly amplitude modulated with a rise time of 18 ms directly followed by a decay of 2 ms (long-rise-time stimuli) or with a rise time of 2 ms directly followed by a decay of 18 ms [short-rise-time stimuli; see insets in Fig. 2(a)]. Each trial consisted of two stimuli of the same carrier frequency separated by a pause of 1 s. The first stimulus of each trial—the reference stimulus—was always delivered from a loudspeaker situated at 30° to the left of the subject, the second from one of seven speakers, chosen in a pseudo-random order. Speaker positions were 10°, 22°, 26°, 30°, 34°, 38°, and 50° to the left of the subject. This speaker arrangement was chosen after preliminary tests had shown that the task was too easy when the reference speaker was positioned at 0°. All possible stimulus combinations were employed: (1) both stimuli with long rise time, (2) both with short rise time, (3) first long, second short, (4) first short, second long [see Fig. 2(a)]. The subjects had to decide whether the percept of the second sound source was located frontal or lateral relative to the first one. Thus the experiment was a *relative* localization task, not an absolute one. One session consisted of 56 trials (four stimulus combinations, seven speakers, two presentations, and one carrier frequency). Most subjects attended two sessions per day. Data for a given carrier frequency are based on eight to ten sessions per subject. Five subjects participated in the 0.75-kHz condition, 12 subjects in the 3-kHz, and 6 subjects in the 5-kHz conditions.

During an experiment a subject was seated in a chair in the anechoic room, the ceiling, walls, and floor of which were covered with 55-cm-long mineral wool wedges (room dimensions: 2.3×2.7×3.5 m between wedge tips; room anechoic above approx. 200 Hz; floor made without wire mesh). The subject's head rested comfortably on a chin holder. The seven speakers were located in a horizontal semicircle 2.58 m from the middle of the subject's head with their diaphragm centers at the height of the subject's ears. Subjects were instructed to fixate on a cross on the wall and keep their head as immobile as possible during a session. After each trial, listeners reported their decision (''frontal'' or ''lateral'') via an intercom to the control room. No information on the correctness of the decision was given.

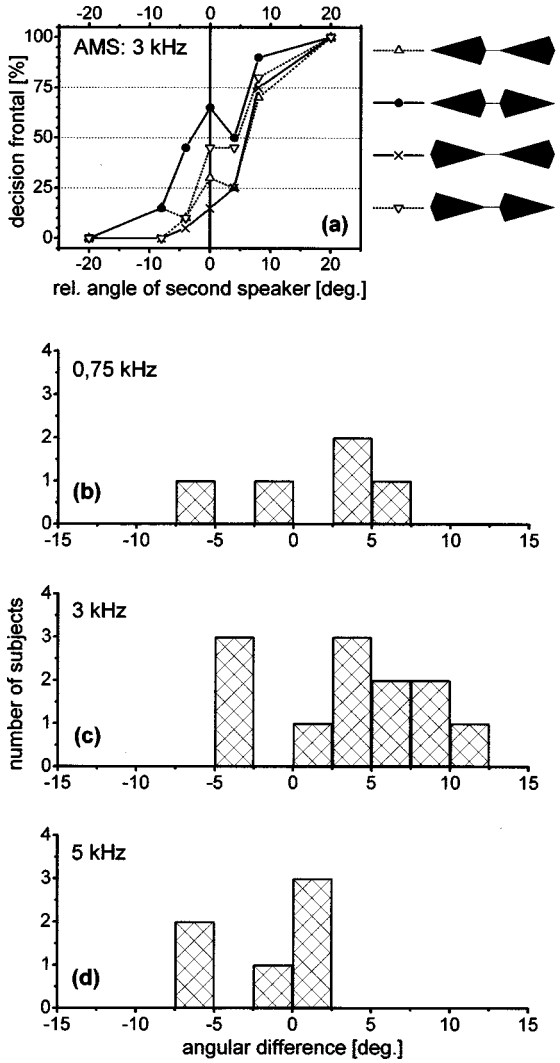

FIG. 2. (a) Psychometric functions describing the probability for a typical subject (AMS) to perceive the second tone pulse delivered from a more frontal position than the reference tone pulse. Abscissa: Actual angle of sound incidence of second tone pulse relative to the position of the reference speaker. Positive angles denote speaker positions frontal to the reference speaker. Carrier frequency: 3 kHz. The dashed lines with open triangles indicate the response to the control stimuli (upward triangles for long–long and downward triangles for short–short). (b), (c), (d) Histograms of the differences between the 50% values of the psychometric functions for the short–long combination and the long–short combination. Positive values indicate that the curve for long–short was shifted laterally relative to the curve for short–long, corresponding to the prediction. The carrier frequency was 0.75 kHz in (b), 3 kHz in (c), and 5 kHz in (d).

The stimulus waveforms had been calculated and stored digitally in a personal computer. Following D/A conversion by a two-channel 12-bit DT2821 board (DATA TRANSLATION) at a 40-kHz sampling rate, the signals were fed through a manual attenuator (HATFIELD INSTRUMENTS, type 2125), a custom-built reconstruction filter (6-kHz low pass), and a stereo power amplifier (DENON type POA-2400). A custom-built digital switch routed the signal to the chosen speaker. The speakers (JBL, type Control 1G, two-way speakers) were selected such that the sound intensity varied as little as possible at the position occupied by the subject's head (variation from speaker to speaker was 1.9–

3.6 dB as measured with a half inch microphone, Brüel & Kjaer type 4133, connected to a measuring amplifier, B&K type 2636). Stimulus intensity during the experimental sessions was set to 45 dB SPL (peak), measured without a subject being present.

For each subject we calculated the percentage of decisions ''frontal'' as a function of the angle between the reference sound source 1 and sound source 2, with each percentage value based on 16 to 20 decisions. The percentage data were arcsine transformed and linear regressions were calculated. In order to exclude the saturation ranges, only the values between 10% and 90% and the first value equal to or below 10% and equal to or above 90%, respectively, were included. To measure the influence of the envelope cues on localization we first determined the intersection of the regression line with the horizontal for 50% decisions ''frontal'' for both long–short and short–long stimulus combinations and then calculated the angular difference between these two intersections [cf. Fig. 2(b)–(d)].

II. RESULTS

The subjects reported whether they perceived the second stimulus from a more frontal or a more lateral position than the first stimulus. The probability of the decision ''frontal'' is shown in Fig. 2(a) for subject AMS as a function of the angle between the source of the second tone pulse and the reference speaker (at 30° to the left) for the four different stimulus combinations. The prediction was that the psychometric curves would be shifted to more lateral positions when a long-rise-time stimulus was referenced to a short-rise-time stimulus and vice versa. The shift was calculated from the intersections of the linear regressions with the 50% horizontal [Fig. 2(a)]. These angular differences are shown for all subjects in the histograms in Fig. 2(b), (c), and (d). Values close to 0° indicate that the regressions for the long–short and short–long condition were virtually identical for the respective subjects. At 0.75 kHz and at 5 kHz there was no obvious deviation from a distribution around 0° [Fig. 2(b) and (d); $p=0.9$ for 0.75 kHz; $n=5$; $p=0.6$ for 5 kHz; $n=6$; Wilcoxon's matched pairs signed rank test (Sachs, 1992)]. At 3 kHz we observed a statistically significant shift of the distribution to positive values ($p=0.05$, $n=12$). Thus at least for 3 kHz, the prediction that long-rise-time stimuli are localized further to the side than stimuli with a short rise time was upheld. The median of the angular difference was 3.7°. This rather moderate median value and the occurrence of negative values in a quarter of the subjects tested, however, indicate that the effect of rise time on directional hearing in the free sound field is not very robust [Fig. 2(c)].

In most cases (17/23) the psychometric curves for the control trials (long–long and short–short) fell between the curves for the test stimuli (long–short and short–long), indicating that a lateral shift of the test curves was not simply due to a long or a short rise being presented as the reference stimulus. As one would expect for a relative localization task, we found no systematic shift of the curves for long–long relative to those for short–short ($p>0.1$; $n=12$ for 3 kHz). Neither did the 50% intersections for long–long or short–short deviate from 0° ($p>0.1$).

In order to test whether stimulus combination affected the steepness of the psychometric curves [Fig. 2(a)], we compared the slopes of the respective regression lines. The slope was calculated from the angular difference between the 25-% and 75-% intersection points of the regression lines. This angular-difference threshold thus is a measure analogous to the minimum audible angle described by Mills (1958). The slopes for the long–long, short–short, long–short, and short–long conditions did not differ significantly according to a Kruskal–Wallis test ($H=2.086$, 1.128, and 2.21 for 0.75 kHz, 3 kHz, and 5 kHz, respectively; $df=3$ in each case).

Carrier frequency, however, significantly affected the steepness of the psychometric curves. The angular-difference thresholds for 0.75 kHz were only half as large as the thresholds for both 3 kHz and 5 kHz ($p<0.001$ and $p<0.01$, respectively; Kruskal–Wallis test), whereas angular-difference thresholds did not differ significantly between 3 kHz and 5 kHz. This conforms well with the finding that at frequencies below 1.5 kHz ITDs in the stimulus fine structure are the most salient directional cue, overriding possibly conflicting envelope delays (Henning, 1983; see also Zurek, 1993).

III. DISCUSSION

Our study was aimed at testing the hypothesis that long rise times of sound pulses entail stronger directional cues than very short ones presumably due to larger first-spike latency differences between left and right AN fibers (Fig. 1). We found a statistically significant influence of rise time only at 3 kHz. The effect pointed in the predicted direction [Fig. 2(c)]. However, the small absolute size of the effect and the large inter-individual variance indicate that rise time is not a robust determinant of directional information, at least under our experimental conditions.

This outcome is somewhat surprising since interaural disparities at stimulus onset are important indicators of the direction to a sound source, especially in reverberant environments (Wallach *et al.*, 1949; Zurek, 1987), and it seems plausible that first-spike latency differences are involved in this analysis. According to physiological data, these latency differences depend on stimulus rise time (Heil and Irvine, 1997). At least at 0.75 kHz, the negative result of our experiment [Fig. 2(b)] may be due to ringing of the auditory filters. It is reasonable to assume that ringing reduces the actual differences between the long- and short-rise-time stimulus envelopes at the level of the cochlea. However, since ringing effects increase with decreasing center frequency and the concurrent decreasing bandwidth of auditory filters (de Boer and Kruidenier, 1990; Evans, 1989) this explanation cannot account for the effects of rise time at 3 kHz. We cannot exclude that a much larger sample size or well-trained listeners might have rendered statistically significant results (note that the decisions of the three authors did not differ from those of the nine inexperienced subjects). Our interest, however, was in the existence of a behaviorally relevant effect of rise time upon sound localization. This can be excluded as

the effects found are still in the range of the minimum audible angle as determined by Mills (1958; see also Hartmann, 1983).

Since the physiological evidence for the dependence of first-spike latency differences on rise time is strong (cat: Heil and Irvine, 1997; for comparable work on insects: Adam, 1977; Krahe and Ronacher, 1993), it is conceivable that directional hearing relies more heavily on other neuronal cues. An ultimate reason for this may be that a strong dependence of directional hearing on latency differences would entail the risk of localization errors since the latency difference not only depends on stimulus direction (ILD) but also on the shape of stimulus onset and on intensity. In this context it is interesting to note that owls, which rely heavily on acoustic cues for locating prey, do not use onset transients for sound localization but rather focus on ongoing ITDs (Moiseff and Konishi, 1981). In a behavioral paradigm, Martin and Webster (1987) also found evidence that cats do not use transient temporal disparities to a significant amount. However, since humans undoubtedly can use temporal onset disparities (Wallach *et al.*, 1949; Zurek, 1987), we tentatively suggest that our nervous system rates other onset cues higher than just the first-spike temporal difference arising between left and right auditory pathway.

ACKNOWLEDGMENTS

This work would have been impossible without the collaboration of members of the Odense laboratory who volunteered as experimental subjects. We gratefully acknowledge the very helpful comments of Drs. Peter Heil, Walter Metzner, the anonymous referees, and the editor at various stages of the manuscript. The Centre for Sound Communication is financed by the Danish National Research Foundation. This research was supported by the Deutsche Forschungsgemeinschaft (grant to B.R.).

Adam, L. J. (**1977**). ''The oscillatory summed action potential of an insect's auditory nerve (*Locusta migratoria, Acrididae*). I. Its original form and time constancy,'' Biol. Cybern. **26**, 241–247.

de Boer, E., and Kruidenier, C. (**1990**). ''On ringing limits of the auditory periphery,'' Biol. Cybern. **63**, 433–442.

Evans, E. F. (**1989**). ''Cochlear filtering: A view seen through the temporal discharge patterns of single cochlear nerve fibres,'' in *Cochlear Mechanisms*, edited by J. P. Wilson and D. T. Kemp (Plenum, New York), pp. 241–248.

Hartmann, W. M. (**1983**). ''Localization of sounds in rooms,'' J. Acoust. Soc. Am. **74**, 1380–1391.

Heil, P., and Irvine, D. R. F. (**1996**). ''On determinants of first-spike latency in auditory cortex,'' NeuroReport **7**, 3073–3076.

Heil, P., and Irvine, D. R. F. (**1997**). ''First-spike timing of auditory-nerve fibers and comparison with auditory cortex,'' J. Neurophysiol. **78**, 2438–2454.

Henning, G. B. (**1983**). ''Lateralization of low-frequency transients,'' Hearing Res. **9**, 153–172.

Kitzes, L. M., Gibson, M. M., Rose, J. E., and Hind, J. E. (**1978**). ''Initial discharge latency and threshold considerations for some neurons in cochlear nuclear complex of the cat,'' J. Neurophysiol. **41**, 1165–1182.

Krahe, R., and Ronacher, B. (**1993**). ''Long rise times of sound pulses in grasshopper songs improve the directionality cues received by the CNS from the auditory receptors,'' J. Comp. Physiol. A **173**, 425–434.

Martin, R. L., and Webster, W. R. (**1987**). ''The auditory spatial acuity of the domestic cat in the interaural horizontal and median vertical planes,'' Hearing Res. **30**, 239–252.

Mills, A. W. (**1958**). ''On the minimum audible angle,'' J. Acoust. Soc. Am. **30**, 237–246.

Moiseff, A., and Konishi, M. (**1981**). ''Neuronal and behavioral sensitivity to binaural time differences in the owl,'' J. Neurosci. **1**, 40–48.

Sachs, L. (**1992**). *Angewandte Statistik* (Springer, Berlin).

Wallach, H., Newman, E. B., and Rosenzweig, M. R. (**1949**). ''The precedence effect in sound localization,'' Am. J. Psychol. **62**, 315–336.

Yin, T. C. T., Hirsch, J. A., and Chan, J. C. K. (**1985**). ''Responses of neurons in the cat's superior colliculus to acoustic stimuli. II. A model of interaural intensity sensitivity,'' J. Neurophysiol. **53**, 746–758.

Zurek, P. M. (**1987**). ''The precedence effect,'' in *Directional Hearing*, edited by W. A. Yost and G. Gourevitch (Springer, New York), pp. 85–105.

Zurek, P. M. (**1993**). ''A note on onset effects in binaural hearing,'' J. Acoust. Soc. Am. **93**, 1200–1201.

Variability in the characterization of the headphone transfer-function

Abhijit Kulkarni[a] and H. Steven Colburn[b]
Hearing Research Center and Department of Biomedical Engineering, Boston University, Boston, Massachusetts 02215

(Received 22 January 1997; revised 1 February 1999; accepted 24 September 1999)

In simulations of virtual acoustic space, stimuli are filtered with HRTFs and presented over headphones. An equalization filter is specified to compensate for the spurious coloration introduced by the headphone delivery system on the stimulus at the listener's eardrum. The purpose of this letter is to report the variability in the response of supra-aural headphones arising from the positioning of the headphone cushion during normal usage. The headphone responses were obtained on the KEMAR acoustical mannequin. It is shown that the variability in the measurements due to headphone cushion placements makes it difficult to specify a compensation filter for canceling the headphone characteristics. This makes the stimulus waveform at a listener's eardrum unpredictable and could have an important consequence on the perceptual adequacy of virtual displays. © *2000 Acoustical Society of America.* [S0001-4966(00)04301-0]

PACS numbers: 43.66.Yw, 43.66.Sr, 43.66.Qp [JWH]

INTRODUCTION

The process of virtual sound synthesis requires the filtering of the sound stream to each ear with two transfer functions. The first, called the head-related transfer function (HRTF), is the directional transform from source to ear. The second function is the nondirectional inverse headphone transfer function, which is required to compensate for the headphone transducer characteristic. The purpose of this paper is to document the large variability in the characterization of the headphone transfer function and hence also in its inverse. Headphone transfer function data collected from a popular headphone (Sennheiser HD520) are presented for repeated placements on a KEMAR mannequin. This variability, however, appears to be common to the general class of circumaural/supra-aural headphones. These observations are consistent with Shaw (1966).

I. BACKGROUND

Consider a sound source S having a pressure spectrum $S(j\omega)$ and the resulting signal $X(j\omega)$ at some point P in the ear canal. Note that for the purposes of this study we only need to consider the acoustical signal at one ear. The analysis applies for either ear. The signal $X(j\omega)$ can be mathematically related to the source spectrum $S(j\omega)$ by the relation

$$X(j\omega)=S(j\omega)H(j\omega), \tag{1}$$

where $H(j\omega)$ is the HRTF from the source S to the point P in a listener's earcanal. Due to the acoustical issues involved, the point P at which the HRTFs are measured is chosen to be either in close proximity to the eardrum (Wightman and Kistler, 1989) or at the entrance to the earcanal (Searle *et al.*, 1975). For the virtual synthesis of the sound source S, a listener is stimulated over headphones such that the pressure signal at the point P in the earcanal equals $X(j\omega)$. If the transfer function from the headphone input to the point P is denoted by $H_H(j\omega)$, such an equivalence can be established if the electrical signal input to the headphone $S_E(j\omega)$ is specified by

$$S_E(j\omega)=\frac{X(j\omega)}{H_H(j\omega)}=S(j\omega)\frac{H(j\omega)}{H_H(j\omega)}. \tag{2}$$

Hence, the virtual synthesis filter is the ratio of the HRTF $H(j\omega)$ and the headphone transfer function $H_H(j\omega)$. Note that $H_H(j\omega)$ is nondirectional; it embodies the headphone transducer characteristic in addition to the acoustical transfer function between the headphone transducer and point P in the ear canal. It is easy to see that when $S_E(j\omega)$ is delivered over the headphones, the resulting signal at the point P equals that due to the natural sound source S:

$$S_E(j\omega)H_H(j\omega)=S(j\omega)H(j\omega)=X(j\omega). \tag{3}$$

The measurement of HRTFs, which has been researched extensively (e.g., Wightman and Kistler, 1989), involves the placement of miniature microphones in the ear canals of listeners. The headphone transfer function $H_H(j\omega)$ is normally obtained for the same placement of the microphones. Due to different shapes and sizes of the pinna, HRTFs for different listeners have idiosyncratic spectral features so that individually measured HRTFs are believed to be required for veridical synthesis of virtual space (Wenzel *et al.*, 1993). Similarly, the headphone transfer function also differs for different listeners. Because of different shapes and sizes of the ear canal and pinna, the acoustical coupling between the headphone transducer and the ear canal differs for each listener and hence is typically specified individually. In a comprehensive study of headphone transfer functions, Moller *et al.* (1995a, b) concluded that there was significant intersubject variability among individuals and suggested that individualized equalization of the headphone response is preferable. Moller and colleagues also reported intrasubject

[a]Electronic mail: abhijit@enga.bu.edu
[b]Electronic mail: colburn@bu.edu

variability at the high frequencies, which are consistent with the data reported by Wightman and Kistler (1989). The goal of this study was to characterize the headphone transfer function, and its variability over placements using a commonly available supra-aural headphone. We then assessed the equalization that can be achieved to compensate for its response.

II. METHODS

The headphone used in this study was the Sennheiser HD-520. The headphone transfer function was measured on the KEMAR mannequin with ''large'' pinnae[1] and $\frac{1}{2}$-in. Etymotic ER-11 microphones fitted in DB-100 Zwislocki couplers. The KEMAR microphone has a flat response (to within ± 0.5 dB) between 200 kHz and 14 kHz. The headphone was placed over the mannequin's ears and the transfer function from headphone to eardrum was obtained using Golay code techniques (Golay, 1961; Foster, 1986). The probe stimulus was constructed on a TMS320C25 Spectrum board housed in a IBM-386 computer. It was delivered to the headphone driver via a D/A converter after suitable amplification from a Crown D-75 amplifier. The output from the KEMAR microphones was measured from an A/D converter and processed on the Spectrum signal processing board to obtain a 1024-tap finite-impulse-response filter at a sampling rate of 50 kHz.

A total of 20 transfer function measurements were obtained from the mannequin. On each measurement the headphone was removed and repositioned on the mannequin in order to estimate the variability resulting from repeated placements of the headphone. The headphones were positioned in a normal way on each trial such that the pinna was completely enclosed by the earphone cushion. Special care was taken to ensure that the cushions were not placed awkwardly, but rather, as might be expected, to be positioned by a human subject during a listening session.

Inverse headphone transfer functions were constructed for each of the 20 measurements. The inverse functions were constructed in MATLAB using inverse Fourier transform techniques and implemented as linear-phase finite impulse response (FIR) filters. If a headphone impulse response is denoted by $h_H[n]$ and the corresponding transfer function denoted by $H_H(j\omega)$, the inverse filter $h_H^{-1}[n]$ can be obtained by performing the basic operation

$$h_H^{-1}[n] = \mathrm{F}^{-1}\{1/H_H(j\omega)\}, \tag{4}$$

where F^{-1} denotes the inverse Fourier transform operator. A windowing function was introduced in the operand of the inverse Fourier operator of Eq. (4) to prevent regions of low spectral energy in $H_H(j\omega)$ from contributing to a numerically unstable result. Specifically, a window having a value of one between 200 and 16 000 Hz and tapered edges (raised cosine) outside this interval was used. The effect of using an inverse filter to cancel the headphone transfer function obtained for a different placement of the headphone cushions was simulated. We arbitrarily combined different inverse functions with different headphone transfer functions to evaluate the implications of such a mismatch for the spectrum of the signal received at the drum.

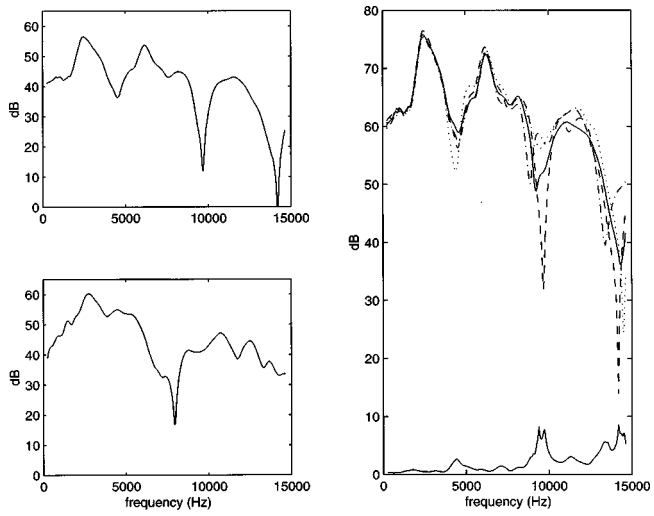

FIG. 1. Top-left panel: Representative headphone response magnitude spectrum from the Sennheiser HD-520 headphones. Lower-left panel: A representative HRTF magnitude spectrum shown for comparison. Right panel: The mean headphone transfer-function computed from 20 measurements is shown as a solid line in the upper set of curves. Also shown are three representative measurements (dashed, dotted, and dot-dashed lines) of the headphone transfer-function obtained for three different placements of the headphone-cushions. The curves are shown on a relative dB scale. The standard deviation of the 20 measurements is shown in the lower curve of the right panel on the same scale as the measurements.

III. RESULTS

The magnitude-spectrum of a headphone response $H_H(j\omega)$ for a particular placement of the cushions is shown in the top-left panel of Fig. 1. Note that there are significant spectral features in the headphone frequency response (as measured at the eardrum). In fact, the spectral features in the headphone transfer function are comparable to those observed in HRTFs. A representative HRTF magnitude spectrum $|H(j\omega)|$ is shown in the lower-left panel of Fig. 1 for comparison. As expected, the $\frac{1}{4}$-wavelength ear canal resonance around 2.7 kHz is common to both the HRTF and the headphone transfer function. The magnitude of peaks and notches in the headphone transfer function magnitude spectrum and the representative HRTF magnitude spectrum are comparable.

The mean headphone transfer function obtained by averaging the 20 measurements is shown by the solid line in the top set of curves in the right panel of Fig. 1. The ordinate scale is a relative scale in decibels. Also shown, displaced vertically for clarity, are three representative headphone transfer functions obtained for three different placements of the headphone cushions. The three measurements were chosen arbitrarily and do not represent the extreme variations in the data. Despite this, the different spectral features in the three measurements is striking. The standard deviation, in dB, for the 20 headphone transfer functions is shown by the solid curve at the bottom of the panel (on the same scale). The standard deviation curve indicates significant variability in the characterization of the headphone transfer function. In

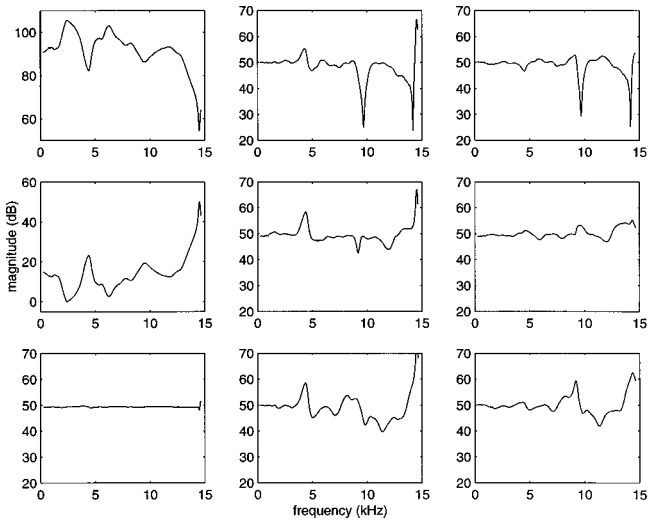

FIG. 2. Representative headphone response magnitude spectrum (top-left panel) and the corresponding inverse-filter magnitude spectrum (middle-left panel) for a given placement of the headphones. The equalized headphone response is shown in the bottom-left panel. Equalized headphone transfer functions for three different headphone-cushion placements using the inverse filter shown in the middle-left panel are shown in the middle column. The equalization for the same placements using the inverse filter computed from the mean headphone transfer-function shown in Fig. 1 is shown in the right column.

fact, due to the large variability in the data, it is difficult to consider the mean transfer function to be representative of the data in general. To confirm that the source of variability was in fact due to the headphone placement, we also obtained five transfer-function measurements for a fixed headphone placement. The resulting standard deviation was within 0.1 dB throughout the frequency range. Therefore, the variability seen in Fig. 1 must result from changes in headphone placements. It can be noted from Fig. 1 that presenting virtual stimuli through uncompensated headphones will result in unwanted spectral characteristics at the eardrum which will be different for each placement of the headphone. In order to preserve the fidelity of the directional spectrum at the eardrum the headpone characteristic needs to be compensated.

In the top-left panel of Fig. 2 we show a representative headphone response magnitude spectrum for a given placement of the headphones. The magnitude spectrum of the inverse filter corresponding to this placement is shown in the middle-left panel of the figure. In the bottom-left panel of Fig. 2, we show the effective, compensated headphone frequency response when the headphone impulse response and inverse filter are arranged in cascade. As shown, the inverse filter is able to achieve the desired compensation (i.e., a flat response). In contrast, in the three panels of the middle column of Fig. 2, ''compensated'' headphone transfer functions are shown when the same inverse filter is combined with the headphone transfer functions obtained for three different placements of the headphone cushions. It may be noted that the inverse filtering operation is not only ineffective in not compensating for the headphone characteristics, but also sometimes more deleterious than not having an inverse filter at all. Finally, in the three panels of the right column of Fig. 2 are shown the equalization of the headphone transfer functions used in the middle panels using an inverse filter constructed from the mean headphone transfer function (shown in Fig. 1). As expected, because the mean headphone transfer function is not representative of the data set in general, a mean inverse filter is unable to equalize the filter functions completely. However, on comparing the results in the middle column and the right column of Fig. 2, it can be seen on average that the mean inverse filter performs better than an inverse filter computed for a unique headphone placement. In both cases, however, the spurious spectral detail in the signal is significant. In fact, the magnitudes of these unwanted spectral features are as prominent as features in the HRTF. Because the spectral detail in the HRTF is associated with directional cues, such unwanted features could clearly have a deleterious perceptual consequence.

IV. DISCUSSION

The use of virtual acoustical stimuli is becoming increasingly popular in psychophysical experiments. It is often considered that the spectral signal delivered at the listener's eardrum should be identical to that arising from a natural source. Hence, considerable effort is often expended to measure HRTFs that are listener specific. However, as seen from the data presented above, headphone systems may introduce a significant coloration on the acoustical stimuli. In fact, the spectral features in headphone transfer functions are very similar to the directional features reported in HRTFs. There is a need to compensate for these spurious features in order to prevent them from having a deleterious perceptual effect during the synthesis of virtual acoustical space. The purpose of this paper is to bring to light the large variability in the measured headphone transfer function for a single headphone-head combination. In particular, choosing to compute inverse filters to equalize for the headphone response by measuring the headphone transfer function for each individual listener does not resolve this ambiguity, but may amplify it. In general, this variability is a cause of concern for virtual space synthesis and its consequences need to be carefully evaluated.

The variability in the headphone transfer characteristics arises primarily from the variable coupling of the headphone cushion to the ear for different placement. The acoustics of the coupling is sensitive to the specific placement of the cushion around the ear. An exact acoustical model that explains the phenomenon is not within the scope of this paper. A simple model which may be used to qualitatively explain the phenomenon is shown in Fig. 3. The top panel of Fig. 3 shows a generalized series of blocks describing the acoustical elements of interest. The headphone signal P_H couples to the earcanal via the two-port[2] labeled SOURCE-COUPLING. The signal at the entrance of the earcanal, P_E, couples to the eardrum via the second two-port, which is labeled EAR-CANAL. The transformation between the entrance of the ear canal and the eardrum is fixed and it is the variability associated with the source-coupling that is responsible for the variable features in the measured spectrum.

At low frequencies the pressure within the earphone cavity can be considered the same everywhere (spatial variation is ignored) and the source-coupling two-port can be re-

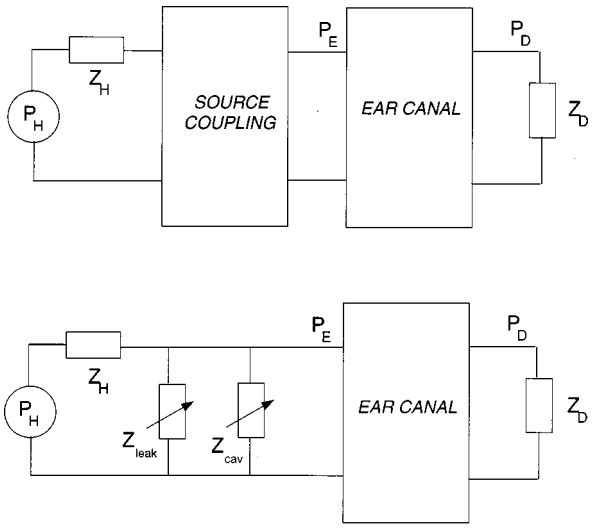

FIG. 3. Circuit model of headphone acoustics. P_H, P_E, and P_D represent the pressures at the headphone equivalent source, at the entrance to the ear canal, and at the eardrum respectively. Z_H and Z_D are the acoustic impedances of the headphone and looking into the eardrum; respectively. Top panel: A general circuit comprised of two-ports is shown in the top panel. The variability in the measurements arises due to the variability in coupling between the headphone and the ear canal. Lower panel: The source of the variability at the low frequencies is illustrated in the lower panel. The fit-dependent parameters Z_{leak} and Z_{cav} are the lumped acoustic impedances of the leakage of volume velocity to the atmosphere and of the cavity itself.

duced to the circuit shown in the lower panel of Fig. 3. Here the paths for volume velocity between the headphone transducer and the ear canal entrance have been separated into a leakage path out of the earcup (Z_{leak}) and a path into the cavity comprising the earphone cup and the pinna (Z_{cav}). The pressure at the entrance of the ear canal is then described by

$$P_E = P_H \frac{Z_{\text{leak}} Z_{\text{cav}}}{Z_{\text{leak}} Z_{\text{cav}} + Z_H (Z_{\text{leak}} + Z_{\text{cav}})}. \tag{5}$$

where all quantities are functions of frequency.

Because of the variability in Z_{leak} and Z_{cav}, the pressure waveform (P_E) at the ear canal entrance and therefore at the eardrum (P_D) is variable and depends upon the specific placement of the headphone. This result is consistent with Shaw (1966) who had reported large intrasubject variability in the frequency response of circum-aural and supra-aural headphones, and suggested that they were not suitable for exacting applications. This result is also consistent with the results of Domnitz (1976) who reported similar findings in measurements on human subjects wearing circumaural headphones for frequencies below 1 kHz. We note that the behavior of the two-port describing the coupling is complicated at high frequencies and we do not provide a specific analysis of the two-port at those frequencies.

Note that the variability reported here arises from normal usage of the headphones. It should be expected to arise during different runs of an experiment during which the headphone is repositioned. It is therefore impossible to specify a unique inverse filter that can equalize for the headphone response. Consequently, in spite of the care taken to measure HRTFs and headphone characteristic from individual listeners, the pressure waveform at the listener's eardrum is unpredictable, at least with circumaural headphones or supra-aural headphones. The often-reported lack of veridical perception of virtual stimuli could also be the outcome of this result.

A specific recommendation to eliminate this variability is beyond the scope of this manuscript. Our results suggest that a mean inverse filter computed from averaging the response for several headphone placements performs better on average compared to an inverse filter computed for a given headphone placement. Averaging across measurements made from multiple listeners may also be useful. Even a mean filter, however, is inadequate to compensate for the extreme variations in headphone responses. A possible approach may take the form of a stimulus monitoring system as proposed and used by Domnitz (1976). Note, however, that Domnitz used stimuli only up to 1 kHz. The difficulty in monitoring the frequency response increases with frequency and a system to monitor frequencies above a few kHz would be difficult to implement. In any case, this clearly makes the stimulus delivery system more complicated than those used in many current virtual displays.

ACKNOWLEDGMENTS

This work was supported by National Institutes of Health, NIDCD Grant No. RO1DC00100.

[1]The large pinna model corresponds to part number DB-065 and DB-066 available from Knowles Electronic, Inc.

[2]A two-port network is a generalization of a system having a pair of input terminals and a pair of output terminals. The behavior of a two-port is characterized by its impedances (input and output) and its transfer function.

Domnitz, R. H. (**1976**). ''Headphone monitoring system for binaural experiments below 1 kHz,'' J. Acoust. Soc. Am. **58**, 510–511.

Foster, S. H. (**1986**). ''Impulse response measurement using Golay codes,'' Proc. of ICASSP, Tokyo, Japan, pp. 929–932.

Golay, M. J. (**1961**). ''Complementary series,'' IRE Trans. Inf. Theory **7**, 82–87.

Kulkarni, A. (**1993**). ''Auditory Imaging a Virtual Acoustical Environment,'' Masters Thesis, Boston University.

Moller, H., Hammershoi, D., Jensen, C. B., and Sorensen, M. F. (**1995a**). ''Transfer characteristics of headphones measured on human ears,'' J. Aud. Eng. Soc. **43**, 203–217.

Moller, H., Jensen, C. B., Hammershoi, D., and Sorensen, M. F. (**1995b**). ''Design criteria for headphones,'' J. Aud. Eng. Soc. **43**, 218–232.

Searle, C. L., Braida, L. D., Cuddy, D. R., and Davis, M. F. (**1975**). ''Binaural pinna disparity: another auditory localization cue,'' J. Acoust. Soc. Am. **57**, 448–455.

Shaw, E. A. G. (**1966**). ''Earcanal pressure by circumaural and supraaural earphones,'' J. Acoust. Soc. Am. **39**, 471–479.

Wenzel, E. M., Arruda, M., Kistler, D. J., and Wightman, F. L. (**1993**). ''Localization using nonindividualized head-related transfer-functions,'' J. Acoust. Soc. Am. **94**, 111–123.

Wightman, F. L., and Kistler, D. J. (**1989**). ''Headphone stimulation of free-field listening I: stimulus synthesis,'' J. Acoust. Soc. Am. **85**, 858–867.